A MULTI-WAVELENGTH STUDY OF LUMINOUS INFRARED GALAXIES ACROSS COSMIC TIME

A DISSERTATION SUBMITTED TO THE GRADUATE DIVISION OF THE UNIVERSITY OF HAWAIʻI AT MĀNOA IN PARTIAL FULFILLMENT OF THE REQUIREMENTS FOR THE DEGREE OF

DOCTOR OF PHILOSOPHY

IN

ASTRONOMY

DECEMBER 2017

By
JASON KAI CHU

Dissertation Committee:

David B. Sanders, Chairperson
Lisa J. Kewley
Rolf-Peter Kudritzki
Joshua E. Barnes
Kimberly Binsted

We certify that we have read this dissertation and that, in our opinion, it is satisfactory in scope and quality as a dissertation for the degree of Doctor of Philosophy in Astronomy.

DISSERTATION COMMITTEE

_____

Chairperson

_____

_____

_____

_____

To my wife Laurie, for the unconditional love you have and continue to give me

Acknowledgements

I give much gratitude to my wife Laurie for her love and steadfast support, and to my family who taught me the value of education. I am also extremely grateful to my adviser David Sanders for supporting and guiding me through my dissertation, and for giving me travel opportunities. I also thank my dissertation committee and Bahram Mobasher who supported me scientifically and/or financially while I conducted this research. I would like to thank the staff at the NASA *Herschel* Science Center for their assistance in processing the *Herschel* data, and to David Sanders and Kirsten Larson for proposing and designing the *Herschel* observations. In addition I thank the University of Hawai'i Time Allocation Committee for the critical observing time needed to complete a part of this dissertation. I would also like to extend my gratitude towards Marc Kassis, Lucas Rizzi, Jim Lyke, Scott Dahm, Heather Hershey, and all of the staff members at the W. M. Keck Observatory for making all of my observations possible, and the MOSFIRE instrument team for designing and delivering one of the most sensitive near infrared instruments ever. I also thank Tian-Tian Yuan who generously helped me reduce and analyze my MOSFIRE spectra, and the COSMOS collaboration for obtaining all of the rich datasets on which part of this work depended on. I wish to thank Trevor Jim and Kevin Jim for the arduous task of converting and correcting the UH Thesis macros so that they would work properly with modern forms of Latex, and to Jason Surace, Joe Jensen, Chris Dudley, Jeff Goldader, and the many others who created the initial versions of the macros. Finally I wish to give recognition to Susan Lemn, who tirelessly processed my never-ending deluge of travel completions for observing runs on Maunakea.

Abstract

Luminous infrared galaxies (LIRGs) are galaxies in which their infrared emission dominates their bolometric luminosities, and are considered some of the most extreme objects in the universe with their elevated star formation rates and/or presence of a powerful active galactic nucleus (AGN). In the local universe many of these objects are found to be in systems of gravitationally interacting or merging galaxies. In this work I present a statistically complete far-infrared and submillimeter census of local LIRGs in the Great Observatories All-Sky LIRG Survey (GOALS) sample using the *Herschel Space Observatory*. The resulting image atlas shows each of the 201 GOALS systems at six different wavelengths between 70–500 μm, and is optimized to reveal both high and low surface brightness structures. In addition flux densities of companion galaxies in merging systems are measured where possible, as well as the total flux for each system. Using these results in conjunction with data from other infrared space missions, I construct the first complete view of the near-infrared to submillimeter spectral energy distributions (SEDs) of LIRGs. I compare the properties of the SEDs with respect to their total infrared luminosity, submillimeter luminosity and spectral index, infrared color, and to previous SED models from the literature. Furthermore I investigate the radio-infrared correlation on a subset of the GOALS sample using infrared maps at 24, 70, and 100 μm, and radio maps at 20 cm for the nucleus and entire galaxy. I find a deficit in the nuclear 24 μm flux due to silicate absorption for the majority of objects above $10^{11.6} L_{\odot}$, which suggests the presence of powerful AGN not seen at lower infrared luminosities. Finally, to understand the role of LIRGs in the early universe when the star formation rate was much higher, I study the properties of their

rest-frame optical emission lines in the context of other star-forming and AGN galaxies at redshift $z \sim 2.3$. I find the vast majority of high redshift LIRGs displaying both star-forming and AGN-like properties, which suggests that they are powered by both intense star formation as well as powerful AGN similar to their low redshift cousins.

Table of Contents

List of Tables

List of Figures

Chapter 1

Introduction

One of the foremost goals in astronomy is to understand how galaxies formed and evolved over cosmic time. The cold dark matter model is largely successful in describing the growth of large scale structures in the universe as a result of minute fluctuations in the cosmic microwave background (i.e., Mo et al. 1996; Springel et al. 2006). From these initial fluctuations, galaxies gradually grew in mass and size through a bottom-up hierarchical formation process driven predominantly by gravity (i.e., White & Rees 1978; Barnes & Hernquist 1992). Throughout cosmic time it is believed galaxies built up their mass by successively merging and interacting with other galaxies. Thus our goal is to have a complete understanding of all the physical processes driving the evolution of distant galaxy populations in the early universe into the galaxies we see in the local universe.

1.1 Luminous Infrared Galaxies

It was discovered that many interacting galaxies in the local universe have bolometric luminosities dominated by their infrared (IR) emission ($L_{\rm IR} \equiv L(8-1000\ \mu{\rm m})$, for an overview see Sanders & Mirabel 1996). These luminous and ultra-luminous infrared galaxies [LIRGs: $11 \leq \log(L_{\rm IR}/L_{\odot}) < 12$, ULIRGs: $12 \leq \log(L_{\rm IR}/L_{\odot}) < 13$, or (U)LIRGs collectively] were first discovered in the 1970s in small numbers (i.e., Kleinmann & Low 1970b,a; Rieke & Low 1972) as peculiar objects with a steeply rising mid-infrared (MIR)

slope. However with the launch of the *Infrared Astronomical Satellite* (*IRAS*, Neugebauer et al. 1984) in 1983, thousands of (U)LIRGs were unexpectedly discovered in the first all-sky survey at mid- and far-infrared (FIR; $60 \lesssim \lambda \lesssim 200$ μm) wavelengths.

Many studies at infrared and other wavelengths support the conclusion that (U)LIRGs are powered by dust-enshrouded major mergers of gas-rich galaxies (i.e., Toomre & Toomre 1972). The interaction and subsequent merging of two gas-rich disk galaxies into a single galaxy indelibly alters the fundamental properties of the progenitors. Furthermore, studies of (U)LIRGs revealed evidence of above average to extreme star formation rates (SFRs) as well as the presence of active galactic nuclei (AGN) in many of them (Sanders & Mirabel 1996). Gravitational torques and angular momentum loss from the merger event can drive gas inwards into the merging galaxies (i.e., Barnes & Hernquist 1996) causing a rapid increase in the star formation rate from cloud-cloud collisions, and a surge in mass accretion rate onto the supermassive black holes (SMBHs) in the nuclei. The intense infrared luminosity originates from the interstellar dust (produced by asymptotic giant branch stars) absorbing optical and ultraviolet (UV) radiation from the ongoing star formation and AGN activity, and re-radiating the energy in the infrared. The typical equilibrium temperature of these "cold" dust particles is approximately 30 K, which produces an idealized blackbody spectral energy distribution (SED) peaking around 100 μm.

Until recently, many studies of luminous infrared galaxies both near and far were hampered by a lack of adequate coverage in the FIR and submillimeter ($200 \lesssim \lambda \lesssim 850$ μm) wavelength regimes, insufficient spatial resolution at FIR and submillimeter wavelengths, and/or insufficient sensitivity. As a result many studies relied heavily on extrapolations, models, and/or assumptions that may bias their conclusions. This can happen in nearby (U)LIRGs where we lack a complete and high resolution characterization of the FIR emission from (U)LIRGs, a limitation primarily stemming from the Earth's atmosphere being entirely opaque to all FIR and some submillimeter radiation. At high redshifts where they are fainter and harder to detect, it is still unclear as to whether starbursts, AGN activity, or both are responsible in generating the observed FIR luminosities. In this dissertation, I focus

on removing the need for these assumptions by using the latest advances in astronomical instrumentation to directly probe nearby and distant (U)LIRGs.

1.2 Local Luminous Infrared Galaxies

In the first part of my dissertation I focus on the (U)LIRGs closest to Earth ($z \lesssim 0.1$, or $d \lesssim 460$ Mpc), which are the most amenable for a detailed study due to their proximity and relative brightness. The Revised Bright Galaxy Sample (RBGS, Sanders et al. 2003) consists of 629 mid- and far-infrared selected objects from the *IRAS* all-sky catalog. Within this catalog I select the 201 objects with $\log(L_{\rm IR}/L_{\odot}) \geq 11$ comprising the Great Observatories All-Sky LIRG Survey (GOALS, Armus et al. 2009) sample, a statistically complete, flux-limited sample of the most nearby infrared galaxies. This lower limit in luminosity was chosen to reflect the point above which the infrared galaxy luminosity function (LF) begins to show a significant deviation in shape from that of optically selected galaxies (see Figure 1.1). The GOALS sample has been the subject of an intensive, multi-wavelength observing campaign spanning the entire electromagnetic spectrum from radio to X-ray energies, and is the ideal laboratory to study this class of galaxies in detail.

Much work has already been done in studying the properties of these nearby objects. For example it was found that there is a strong correlation between the optical morphological classification of local (U)LIRGs and their infrared luminosity (Larson et al. 2016), and that the merger rate increased as a function of $L_{\rm IR}$ (Veilleux et al. 2002), as shown in Figure 1.2. In addition Veilleux et al. (1995) showed that the fraction of (U)LIRGs hosting AGN increases with $L_{\rm IR}$, while Yuan et al. (2010) showed using optical spectroscopy that the most luminous (U)LIRGs harbor the most powerful AGN in their sample. Finally Soifer et al. (1987) showed that the space density of (U)LIRGs is comparable to that of Seyfert galaxies in the local universe, while Sanders et al. (1988) was the first to suggest that (U)LIRGs evolve from their dust-enshrouded phase into an optically selected quasi-stellar object (QSO).

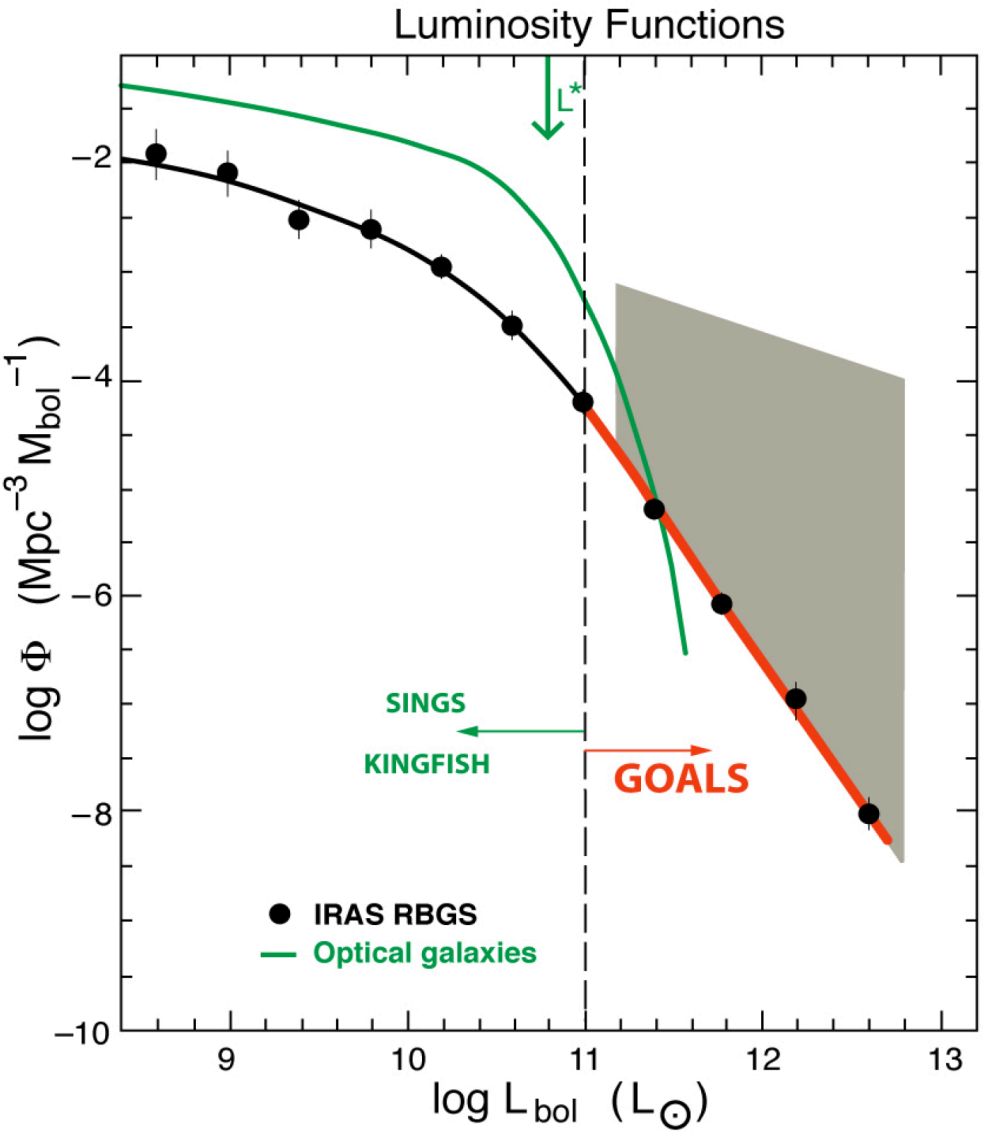

Figure 1.1 The luminosity function (LF, Φ) for IR selected galaxies. The black curve and filled circles represent the local LF as determined from all galaxies in the *IRAS* RBGS sample (Sanders et al. 2003). The green curve represents the LF for optically selected normal galaxies in the local universe (Schechter 1976). The high-luminosity (i.e. GOALS) tail of the LF (red curve) evolves strongly with redshift represented by the grey shaded area, increasing by $\sim 10^3$ between $z = 0$ (bottom) and $z = 2.5$ (top) (i.e., Blain et al. 2002; Le Floc'h et al. 2005; Casey et al. 2012).

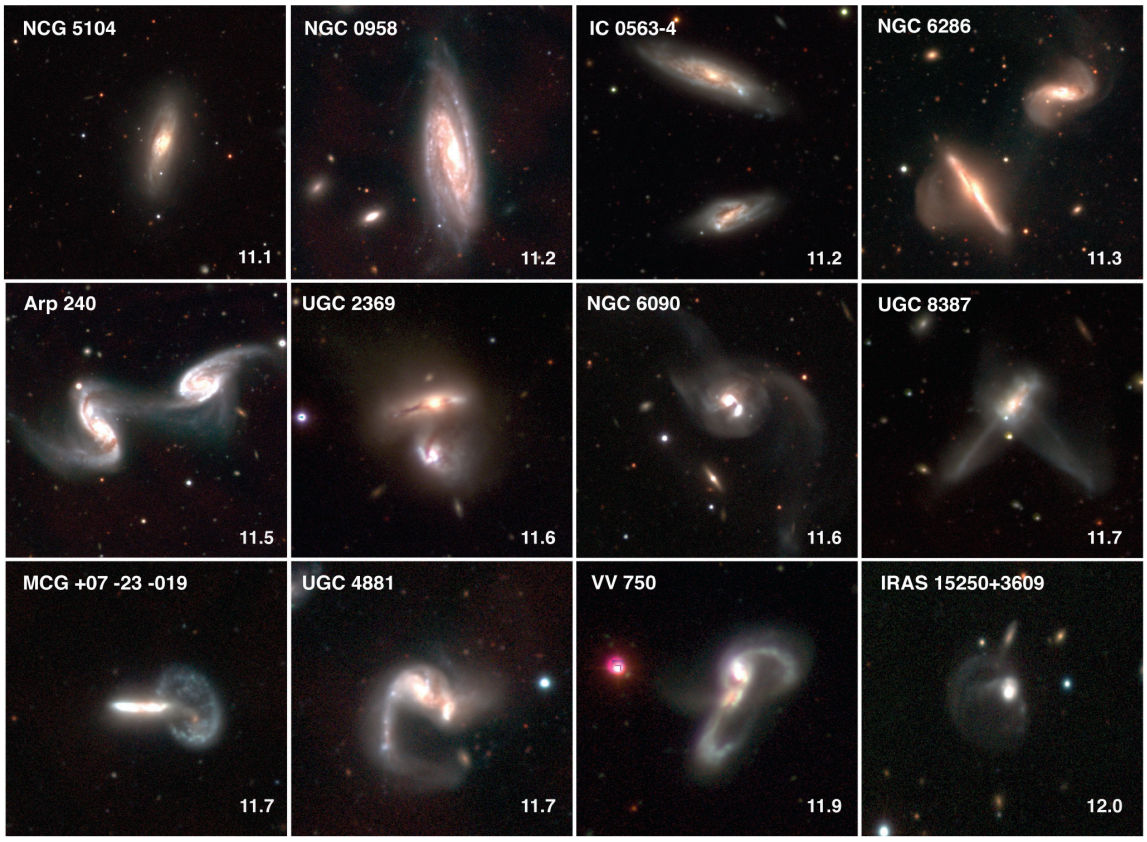

Figure 1.2 Optical BVI images of GOALS galaxies as a function of increasing $L_{\rm IR}$ for a representative subset of the sample. The $\log(L_{\rm IR}/L_{\odot})$ luminosity is given in the lower right corner of each panel. These images illustrate the progression of isolated objects and widely separated pairs at lower luminosities to highly disturbed objects at the highest luminosities (Veilleux et al. 2002).

However many of these studies were limited to wavelengths less than approximately 100 μm, which is only half of the infrared SED bump in (U)LIRGs. The original *IRAS* mission provided the first four crucial photometric data points at 12, 25, 60, and 100 μm. Observations with the *Spitzer Space Telescope* (Werner et al. 2004) launched in 2003 gave us our first high resolution look of the GOALS sample in the near- and mid-infrared (3–8 μm, 24 μm). In addition the Wide-Field Infrared Survey Explorer (*WISE*, Wright et al. 2010) launched in 2009 also covers the MIR (12 and 22 μm). Although submillimeter imaging of some (U)LIRGs were available (Dunne et al. 2000), the lack of sensitive FIR and submillimeter imaging for the entire sample makes it difficult to constrain the properties of the cold dust component. This resulted in a large amount of uncertainty in the FIR and submillimeter properties of (U)LIRGs where they emit the bulk of their energy. However with the launch of the high resolution FIR *Herschel Space Observatory* in 2009, we can now directly measure the long wavelength tail ($\lambda > 100$ μm) of the FIR SED bump.

1.3 High Redshift Luminous Infrared Galaxies

Although *IRAS* detected many (U)LIRGs in the local universe ($z \lesssim 0.4$), they become many times more numerous at higher redshifts (i.e., Blain et al. 2002; Le Floc'h et al. 2005; Casey et al. 2012). Figure 1.1 shows how the LF increases by a factor of $\sim 10^2$–10^3 as one moves from $z = 0$ to $z = 2.5$. Similarly, in Figure 1.3 Casey et al. (2012) showed that (U)LIRGs increasingly dominate the integrated star formation rate density (SFRD, or SFR per comoving volume) as one probes higher redshifts. Many studies have also shown that the integrated star formation rate in the universe peaks at around $z \sim 2$ (i.e., Madau & Dickinson 2014; Bourne et al. 2017), an epoch sometimes referred to as "cosmic noon." On the other hand the X-ray luminosity density, which is a reliable tracer of all but the most obscured AGN activity has a similar peak at $z \sim 2$, indicating a peak in AGN activity and SMBH growth rate density (i.e., $\dot{\rho}$) at that redshift (Aird et al. 2015). In Figure 1.4 I show their estimate of the total SMBH accretion rate density compared to the star formation rate

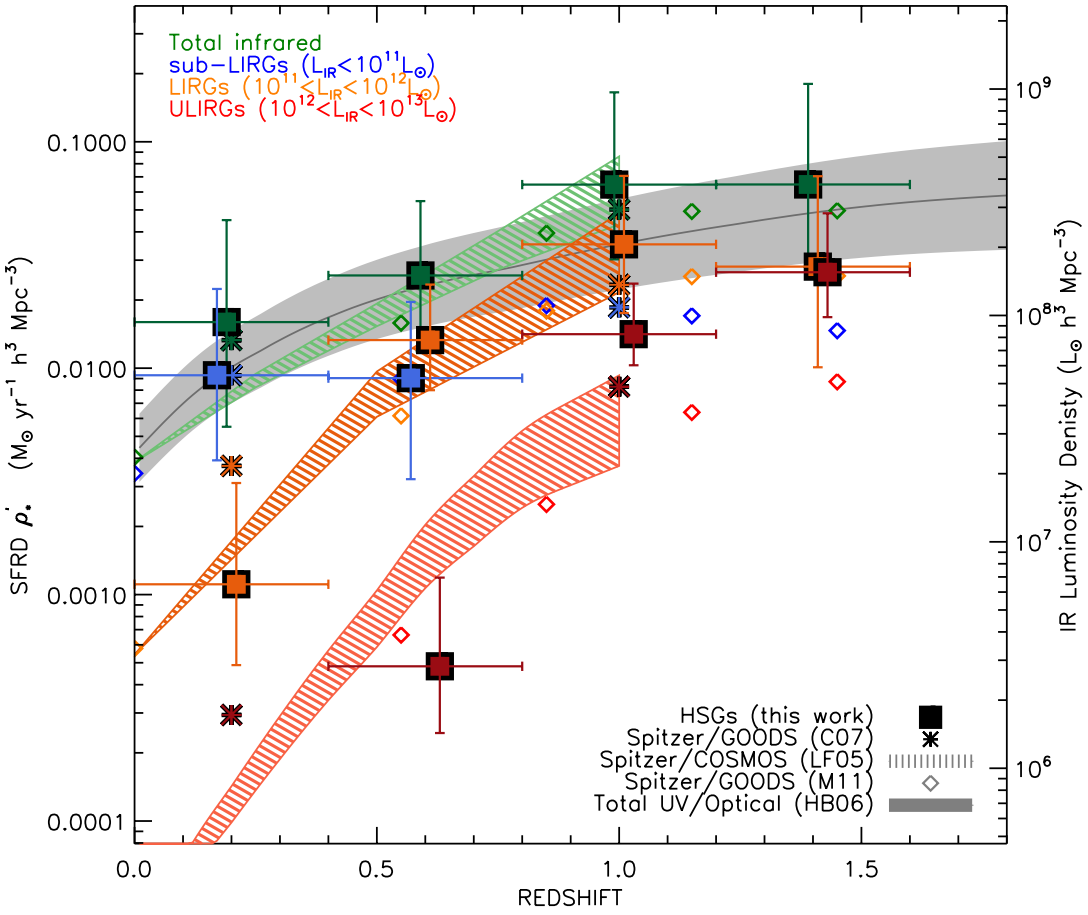

Figure 1.3 The star formation rate density (SFRD) as a function of redshift for all luminous IR galaxies (green), LIRGs (orange), ULIRGs (red), and non-infrared luminous star forming galaxies (blue), from Casey et al. (2012). Squares denote *Herschel*-selected galaxies while diamonds represent *Spitzer*-selected galaxies. By $z \sim 1$ IR galaxies become the dominant site of star formation in the universe.

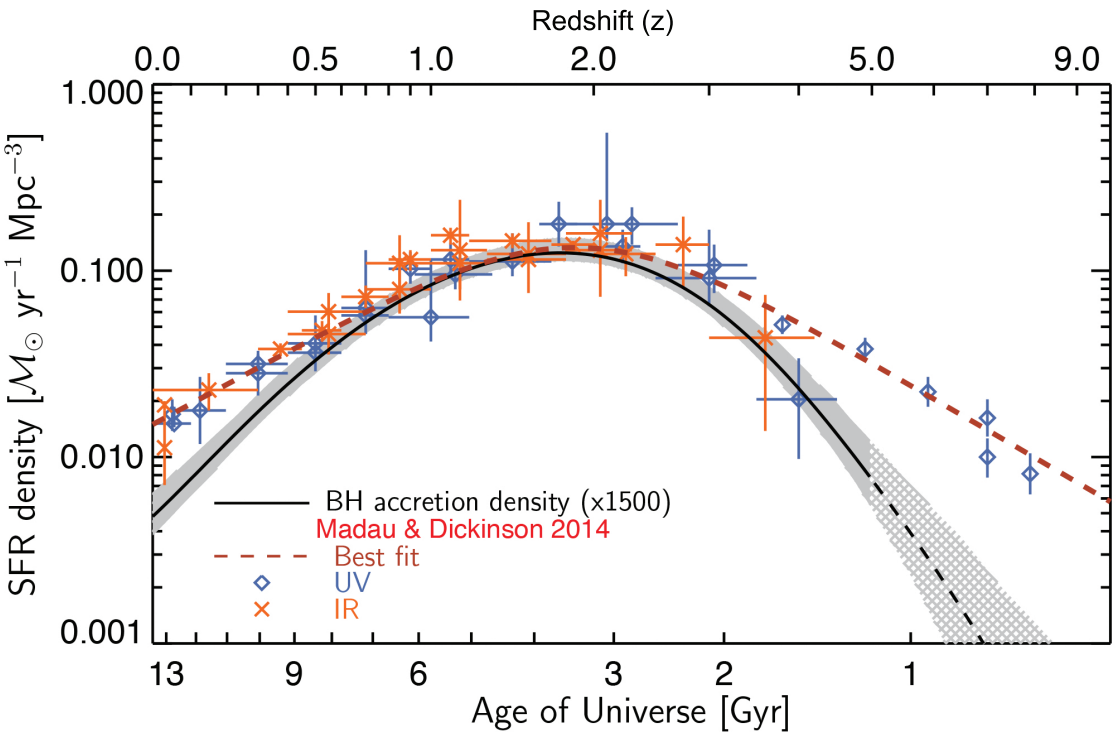

Figure 1.4 The black hole accretion rate density (multiplied arbitrarily by $\times 1500$ for visualization) as a function of redshift along with the SFRD relation of Madau & Dickinson (2014), from Aird et al. (2015). Both relations appear to peak just below $z = 2$ when the universe was about 3 Gyr old.

density peaking at a redshift just below $z = 2$. Given the fact that luminous IR galaxies are where the majority of stars formed at high redshifts, and the peak in star formation and AGN activity at $z \sim 2$, it is necessary to have a better understanding of (U)LIRGs at these redshifts. In addition it is important to understand how they evolved from the high redshift universe into the galaxies we see today.

However what powers (U)LIRGs at $z \gtrsim 2$ whether it is star formation, AGN activity, or both, is still a subject of debate. Detailed FIR imaging of distant (U)LIRGs is extremely challenging, given the redshift effect and difficulty in detecting their faint FIR signatures at $z \sim 2$ and beyond. Although *Herschel* has been successful in detecting the brightest $z \sim 2$ (U)LIRGs, the typical angular extent of these objects ($\sim 2''$) is significantly smaller than the telescope's resolution ($\sim 6''$), limiting any photometric or structural analysis to

the integrated flux of the galaxy. This makes a high resolution spatial study of these objects on a galactic scale impossible. Instead it is easier and more efficient to study the population of high redshift (U)LIRGs using NIR multi-object spectroscopy which is accessible using ground based facilities. Spectra of these high redshift (U)LIRGs can reveal a wealth of information about the physical conditions of the gas in the interstellar medium (ISM), as it is a direct reflection of star formation, AGN accretion, and/or other energetic processes occurring within a galaxy. Therefore I devote a part of my dissertation work to obtain spectra on a statistically significant sample of (U)LIRGs and characterizing their ISM properties in the context of other emission line galaxies.

1.4 Dissertation Overview

This dissertation aims to quantitatively study the multi-wavelength properties of (U)LIRGs in both the local and high redshift universe. Specifically I address the following questions:

1. What are the far-IR and submillimeter properties of (U)LIRGs in the local universe, and how do they change with infrared luminosity?

2. In what ways are local (U)LIRGs similar or different from lower luminosity infrared galaxies?

3. How does the true IR and submillimeter spectral energy distribution of (U)LIRGs compare to model predictions?

4. What is the spatial distribution of infrared flux in local (U)LIRGs, and how does that correlate with the radio flux and distribution?

5. In the local universe it is generally accepted that (U)LIRGs are powered by a combination of star formation and AGN, but what powers (U)LIRGs at "cosmic noon?"

In Chapter 2 I present the a detailed description of the full *Herschel*-GOALS image atlas and photometric measurements. These are the most sensitive and high resolution FIR and

submillimeter maps of a statistically complete sample of luminous infrared galaxies. This chapter has been submitted and published in the *Astrophysical Journal Supplement Series*.

In Chapter 3 I combine the new FIR and submillimeter fluxes measured from Chapter 2, with other infrared data to construct median-averaged spectral energy distributions as a function of infrared luminosity. These data constitute the first complete picture of the infrared spectral energy distributions of luminous infrared galaxies. This chapter will be submitted for publication in the *Astrophysical Journal Letters*.

In Chapter 4 I study the radial distribution of the MIR flux in local luminous infrared galaxies, and compare them to the radial distribution of the radio flux. In addition I compute the infrared to radio flux ratio for our sample for the nuclear and disk components of each galaxy. This work was done before the FIR *Herschel* data were available. Because of this I include an addendum at the end of the chapter incorporating additional insights gained using the *Herschel* data once they became available. This chapter will be submitted for publication in the *Astrophysical Journal*.

In Chapter 5 I characterize the rest-frame optical emission line properties of $z \sim 2.3$ (U)LIRGs, star forming galaxies, and AGN using NIR spectra obtained using the W. M. Keck Observatory. Specifically I measure the fluxes of emission lines to determine what is the most likely source(s) powering (U)LIRGs during epoch of cosmic noon. This chapter will be submitted for publication in the *Astrophysical Journal*.

Finally in Chapter 6 I provide concluding remarks and summarize the main results of this dissertation. Furthermore I provide an outline for future work that may be done to expand on the results presented in this dissertation.

References

Aird, J., Coil, A. L., Georgakakis, A., Nandra, K., Barro, G., & Pérez-González, P. G. 2015, MNRAS, 451, 1892

Armus, L., Mazzarella, J. M., Evans, A. S., Surace, J. A., Sanders, D. B., Iwasawa, K., Frayer, D. T., Howell, J. H., Chan, B., Petric, A., Vavilkin, T., Kim, D. C., Haan, S., Inami, H., Murphy, E. J., Appleton, P. N., Barnes, J. E., Bothun, G., Bridge, C. R., Charmandaris, V., Jensen, J. B., Kewley, L. J., Lord, S., Madore, B. F., Marshall, J. A., Melbourne, J. E., Rich, J., Satyapal, S., Schulz, B., Spoon, H. W. W., Sturm, E., U, V., Veilleux, S., & Xu, K. 2009, PASP, 121, 559

Barnes, J. E. & Hernquist, L. 1992, Nature, 360, 715

—. 1996, ApJ, 471, 115

Blain, A. W., Smail, I., Ivison, R. J., Kneib, J.-P., & Frayer, D. T. 2002, Phys. Rep., 369, 111

Bourne, N., Dunlop, J. S., Merlin, E., Parsa, S., Schreiber, C., Castellano, M., Conselice, C. J., Coppin, K. E. K., Farrah, D., Fontana, A., Geach, J. E., Halpern, M., Knudsen, K. K., Michałowski, M. J., Mortlock, A., Santini, P., Scott, D., Shu, X. W., Simpson, C., Simpson, J. M., Smith, D. J. B., & van der Werf, P. P. 2017, MNRAS, 467, 1360

Casey, C. M., Berta, S., Béthermin, M., Bock, J., Bridge, C., Budynkiewicz, J., Burgarella, D., Chapin, E., Chapman, S. C., Clements, D. L., Conley, A., Conselice, C. J., Cooray,

A., Farrah, D., Hatziminaoglou, E., Ivison, R. J., le Floc'h, E., Lutz, D., Magdis, G., Magnelli, B., Oliver, S. J., Page, M. J., Pozzi, F., Rigopoulou, D., Riguccini, L., Roseboom, I. G., Sanders, D. B., Scott, D., Seymour, N., Valtchanov, I., Vieira, J. D., Viero, M., & Wardlow, J. 2012, ApJ, 761, 140

Dunne, L., Eales, S., Edmunds, M., Ivison, R., Alexander, P., & Clements, D. L. 2000, MNRAS, 315, 115

Kleinmann, D. E. & Low, F. J. 1970a, ApJ, 161, L203

—. 1970b, ApJ, 159, L165

Larson, K. L., Sanders, D. B., Barnes, J. E., Ishida, C. M., Evans, A. S., U, V., Mazzarella, J. M., Kim, D.-C., Privon, G. C., Mirabel, I. F., & Flewelling, H. A. 2016, ApJ, 825, 128

Le Floc'h, E., Papovich, C., Dole, H., Bell, E. F., Lagache, G., Rieke, G. H., Egami, E., Pérez-González, P. G., Alonso-Herrero, A., Rieke, M. J., Blaylock, M., Engelbracht, C. W., Gordon, K. D., Hines, D. C., Misselt, K. A., Morrison, J. E., & Mould, J. 2005, ApJ, 632, 169

Madau, P. & Dickinson, M. 2014, ARA&A, 52, 415

Mo, H. J., Jing, Y. P., & White, S. D. M. 1996, MNRAS, 282, 1096

Neugebauer, G., Habing, H. J., van Duinen, R., Aumann, H. H., Baud, B., Beichman, C. A., Beintema, D. A., Boggess, N., Clegg, P. E., de Jong, T., Emerson, J. P., Gautier, T. N., Gillett, F. C., Harris, S., Hauser, M. G., Houck, J. R., Jennings, R. E., Low, F. J., Marsden, P. L., Miley, G., Olnon, F. M., Pottasch, S. R., Raimond, E., Rowan-Robinson, M., Soifer, B. T., Walker, R. G., Wesselius, P. R., & Young, E. 1984, ApJ, 278, L1

Rieke, G. H. & Low, F. J. 1972, ApJ, 176, L95

Sanders, D. B., Mazzarella, J. M., Kim, D., Surace, J. A., & Soifer, B. T. 2003, AJ, 126, 1607

Sanders, D. B. & Mirabel, I. F. 1996, ARA&A, 34, 749

Sanders, D. B., Soifer, B. T., Elias, J. H., Neugebauer, G., & Matthews, K. 1988, ApJ, 328, L35

Schechter, P. 1976, ApJ, 203, 297

Soifer, B. T., Sanders, D. B., Madore, B. F., Neugebauer, G., Danielson, G. E., Elias, J. H., Lonsdale, C. J., & Rice, W. L. 1987, ApJ, 320, 238

Springel, V., Frenk, C. S., & White, S. D. M. 2006, Nature, 440, 1137

Toomre, A. & Toomre, J. 1972, ApJ, 178, 623

Veilleux, S., Kim, D.-C., & Sanders, D. B. 2002, ApJS, 143, 315

Veilleux, S., Kim, D.-C., Sanders, D. B., Mazzarella, J. M., & Soifer, B. T. 1995, ApJS, 98, 171

Werner, M. W., Roellig, T. L., Low, F. J., Rieke, G. H., Rieke, M., Hoffmann, W. F., Young, E., Houck, J. R., Brandl, B., Fazio, G. G., Hora, J. L., Gehrz, R. D., Helou, G., Soifer, B. T., Stauffer, J., Keene, J., Eisenhardt, P., Gallagher, D., Gautier, T. N., Irace, W., Lawrence, C. R., Simmons, L., Van Cleve, J. E., Jura, M., Wright, E. L., & Cruikshank, D. P. 2004, ApJS, 154, 1

White, S. D. M. & Rees, M. J. 1978, MNRAS, 183, 341

Wright, E. L., Eisenhardt, P. R. M., Mainzer, A. K., Ressler, M. E., Cutri, R. M., Jarrett, T., Kirkpatrick, J. D., Padgett, D., McMillan, R. S., Skrutskie, M., Stanford, S. A., Cohen, M., Walker, R. G., Mather, J. C., Leisawitz, D., Gautier, III, T. N., McLean, I., Benford, D., Lonsdale, C. J., Blain, A., Mendez, B., Irace, W. R., Duval, V., Liu, F., Royer, D., Heinrichsen, I., Howard, J., Shannon, M., Kendall, M., Walsh, A. L., Larsen, M., Cardon, J. G., Schick, S., Schwalm, M., Abid, M., Fabinsky, B., Naes, L., & Tsai, C.-W. 2010, AJ, 140, 1868

Yuan, T., Kewley, L. J., & Sanders, D. B. 2010, ApJ, 709, 884

Chapter 2

The Great Observatories All-Sky LIRG Survey: *Herschel* Image Atlas and Aperture Photometry

Note: *This chapter was originally published in the Astrophysical Journal Supplement Series, Volume 229, Issue 2 as Chu et al. (2017).*

Abstract

Far-infrared (FIR) images and photometry are presented for 201 Luminous and Ultraluminous Infrared Galaxies [LIRGs: $\log(L_{\rm IR}/L_{\odot}) = 11.00 - 11.99$, ULIRGs: $\log(L_{\rm IR}/L_{\odot}) = 12.00 - 12.99$], in the Great Observatories All-Sky LIRG Survey (GOALS) based on observations with the *Herschel Space Observatory* Photodetector Array Camera and Spectrometer (PACS) and the Spectral and Photometric Imaging Receiver (SPIRE) instruments. The image atlas displays each GOALS target in the three PACS bands (70, 100, and 160 μm) and the three SPIRE bands (250, 350, and 500 μm), optimized to reveal structures at both high and low surface brightness levels, with images scaled to simplify comparison of structures in the same physical areas of $\sim$100 $\times$ 100 kpc^2. Flux densities of companion galaxies in merging systems are provided where possible, depending on their angular separation and the spatial resolution in each passband, along with integrated system fluxes (sum of components). This dataset constitutes the imaging and photometric component of the GOALS *Herschel* OT1 observing program, and is complementary to atlases presented for the *Hubble Space Telescope* (Evans et al. in prep.), *Spitzer Space*

Telescope (Mazzarella et al. in prep.), and *Chandra X-ray Observatory* (Iwasawa et al. 2011). Collectively these data will enable a wide range of detailed studies of AGN and starburst activity within the most luminous infrared galaxies in the local Universe.

2.1 Introduction

The Great Observatories All-Sky LIRG Survey (GOALS, Armus et al. 2009), combines both imaging and spectroscopic data for the complete sample of 201 luminous and ultra-luminous infrared galaxies [LIRGs: $11 \leq \log(L_{\rm IR}/L_{\odot}) < 12$, ULIRGs: $12 \leq \log(L_{\rm IR}/L_{\odot}) < 13$, or (U)LIRGs collectively] selected from the IRAS Revised Bright Galaxy Sample (RBGS, Sanders et al. 2003). The full RBGS contains 629 objects, representing a complete sample of extragalactic sources with IRAS 60 μm flux density, $S_{60} > 5.24$ Jy, covering the entire sky above a Galactic latitude of $|b| > 5^{\circ}$. The median redshift of objects in the GOALS sample is $\langle z \rangle = 0.021$, with a maximum redshift of $z_{\rm max} = 0.0876$. As the nearest and brightest 60 μm extragalactic objects, they represent a sample that is the most amenable for study at all wavelengths.

The primary objective of the GOALS multi-wavelength survey is to fully characterize the diversity of properties observed in a large, statistically significant sample of the nearest (U)LIRGs. This allows us to probe the full range of phenomena such as normal star formation, starbursts, and active galactic nuclei (AGN) that power the observed far-infrared emission, as well as to better characterize the range of galaxy types (i.e., normal disks, major and minor interactions/mergers, etc.) that are associated with the (U)LIRG phase. A secondary objective is to provide a data set that is ideally suited for comparison with (U)LIRGs observed at high redshifts.

GOALS currently includes imaging and spectroscopy from the *Spitzer*, *Hubble*, *GALEX*, *Chandra*, *XMM-Newton*, and now *Herschel* space-borne observatories, along with complementary ground-based observations from ALMA, Keck, and other telescopes. The GOALS project is described in more detail at http://goals.ipac.caltech.edu/.

Due to limitations in angular resolution, wavelength coverage, and sensitivity of pre-*Herschel* (*IRAS*, *ISO*, *Spitzer*, *AKARI*) far-infrared (FIR) data, the spatial distribution of FIR emission within the GOALS sources, and the total amount of gas and dust in these systems, are poorly determined. The *Herschel* data will allow us for the first time to directly probe the critical FIR and submillimeter wavelength regime of these infrared luminous systems, enabling us to accurately determine the bolometric luminosities, infrared surface brightnesses, star formation rates, and dust masses and temperatures on spatial scales of 2 – 5 kpc within the GOALS sample.

This paper presents imaging and photometry for all 201 (U)LIRGs and (U)LIRG systems in the IRAS RBGS that were observed during our GOALS *Herschel* OT1 program. A more complete description of the GOALS sample is given in §2.2. The data acquisition is described in §2.3 and data reduction procedures are discussed in §2.4. The image atlas is presented in §2.5, and photometric measurements are given in §2.6. Section 2.7 contains a discussion of basic results, including comparisons with prior measurements, and a summary is given in §2.8. A reference cosmology of $\Omega_\Lambda = 0.72, \Omega_\mathrm{m} = 0.28$ and $H_0 = 70$ km sec.$^{-1}$ Mpc^{-1} is adopted, however we also take into account local non-cosmological effects by using the three-attractor model of Mould et al. (2000).

2.2 The GOALS Sample

The IRAS RBGS contains a total of 179 LIRGs and 22 ULIRGs; these 201 objects comprise the GOALS sample (Armus et al. 2009), a statistically complete flux-limited sample of infrared-luminous galaxies in the local universe. In addition to the *Herschel* observations reported here, the GOALS objects have been the subject of an intense multi-wavelength observing campaign, including VLA 20 cm (Condon et al. 1990, 1996), millimeter wave spectral line observations of CO(1→0) emission (Sanders et al. 1991), sub-millimeter imaging at 450 μm and 850 μm (Dunne et al. 2000), near-infrared images from 2MASS (Skrutskie et al. 2006), optical and K-band imaging (Ishida 2004), as well as space-based

imaging from the *Spitzer Space Telescope* (IRAC and MIPS, Mazzarella et al. in prep), *Hubble Space Telescope* (ACS, Evans et al. in prep.), *GALEX* (NUV and FUV, Howell et al. 2010), and the *Chandra X-ray Observatory* (ACIS, Iwasawa et al. 2011). Extensive spectroscopy data also exist on the GOALS sample, such as in the optical (Kim et al. 1995) and with *Spitzer* IRS in the mid-infrared (Stierwalt et al. 2013). *Herschel* PACS spectroscopy was obtained in Cycles 1 and 2 targeting the [C II] 157.7 μm, [O I] 63.2 μm, and [O III] 88 μm emission lines and the OH 79 μm absorption feature for the entire sample, as well as the [N II]122 μm line in 122 GOALS galaxies (Díaz-Santos et al. 2013, 2014, 2017). In addition, *Herschel* SPIRE FTS spectroscopy were obtained to probe the CO spectral line energy distribution from $J = 4 \rightarrow 3$ up to $J = 13 \rightarrow 12$ for 93 of the GOALS objects (Lu et al. 2014, 2015, 2017), as well as the [N II]205 μm emission line for 122 objects Zhao et al. (2013, 2016).

Out of the original list of 203 GOALS systems, two were omitted from our *Herschel* sample, making for a final tally of 201 objects. IRAS F13097–1531 (NGC 5010) was part of the original RBGS sample of Sanders et al. (2003), however due to a revision in the redshift of the object it was much closer than thought. This caused the resulting far-IR luminosity to drop significantly below the LIRG threshold of $10^{11} L_{\odot}$. The other object we excluded from our sample is IRAS 05223+1908, which we believe is a young stellar object (YSO), due to the fact that its spectral energy distribution (SED) peaks in the submillimeter part of the spectrum.

Table 2.1 presents the basic GOALS information. Column 1 is the index number of galaxies in the GOALS sample, and correspond to the same galaxies in Tables 2.2, 2.3, 2.4, and 2.5. Column 2 is the IRAS name of the galaxy, ordered by ascending RA. Galaxies with the "F" prefix originate from the *IRAS* Faint Source Catalog, and galaxies with no "F" prefix are from the Point Source Catalog. Column 3 is a list of common optical counterpart names. Columns 4 and 5 are the *Spitzer* 8 μm centers of the system in J2000 from Mazzarella et al. (in prep.). For galaxy systems with two or more components, the coordinate is taken to be the geometric midpoint between the component galaxies. Column 6 gives the angular

diameter distance to the galaxy in Mpc, from Mazzarella et al. (in prep.). Column 7 is the map size used in the atlas, denoting the physical length of a side in each atlas image in kpc. Column 8 is the systemic heliocentric redshift of the galaxy system, and Column 9 is the measured heliocentric radial velocity in km $\sec^{-1}$, that corresponds to the redshift. Both of these columns take into account cosmological as well as non-cosmological effects (see Mould et al. 2000). Finally Column 10 is the indicative 8–1000 μm infrared luminosity in $\log(L_{\rm IR}/L_{\odot})$ of the entire system from Armus et al. (2009). Similar to Columns 8 and 9, the $L_{\rm IR}$ values in Table 2.1 take into account the effect of the local attractors to D_A, than one would normally obtain from pure cosmological effect.

2.3 *Herschel Space Observatory* Observations

The *Herschel Space Observatory* (Pilbratt et al. 2010) imaging observations of the GOALS sample took place between the dates of March 2011 through June 2012, through our Cycle 1 open time observing program OT1_dsanders_1 (PI: D. Sanders, Program ID #1279). A total of 169 galaxy systems were observed by the Photoconductor Array Camera and Spectrometer (PACS, Poglitsch et al. 2010) instrument in imaging mode under our proposal, with data from the remaining 32 galaxy systems from other guaranteed time (GT) or open time key programs (KPOT) obtained from the Herschel Science Archive (HSA). In addition we observed 160 targets with the Spectral and Photometric Imaging Receiver (SPIRE, Griffin et al. 2010), with the remaining 41 targets from other GT and KPOT programs extracted from the HSA. In total, 84.9 hours of observations were completed under our specific GOALS program, with 61.6 hours for PACS and 23.3 hours for SPIRE.

Broad-band imaging were obtained in the three PACS bands at 70 μm, 100 μm, and 160 μm, and the three SPIRE bands at 250 μm, 350 μm, and 500 μm. The normalized filter transmission curves are shown in Figure 2.1. Each SPIRE band has two curves associated with the filter, corresponding to the point source responsitivity (solid) and extended source

Table 2.1 Basic GOALS Data

#	IRAS Name	Optical Name	Right Ascension	Declination	D_A	Map Size	Redshift	Velocity	$L_{\rm IR}$
—	—	—	HH:MM:SS	DD:MM:SS	Mpc	kpc	—	km s^{-1}	$\log\left(\frac{L}{L_\odot}\right)$
1	F00073+2538	NGC 23	00 : 09 : 53.36	+25 : 55 : 27.7	63.3	100	0.01523	4566	11.12
2	F00085-1223	NGC 34, Mrk 938	00 : 11 : 06.56	−12 : 06 : 28.2	81.5	100	0.01962	5881	11.49
3	F00163-1039	Arp 256	00 : 18 : 50.37	−10 : 22 : 05.3	111.4	150	0.02722	8159	11.48
4	F00344-3349	ESO 350-IG 038, Haro 11	00 : 36 : 52.49	−33 : 33 : 17.2	85.4	100	0.0206	6175	11.28
5	F00402-2349	NGC 232	00 : 42 : 49.32	−23 : 33 : 04.3	91.3	150	0.02217	6647	11.44
6	F00506+7248	MCG+12-02-001	00 : 54 : 03.88	+73 : 05 : 05.9	67.7	100	0.0157	4706	11.50
7	F00548+4331	NGC 317B	00 : 57 : 39.72	+43 : 47 : 47.7	74.1	100	0.01811	5429	11.19
8	F01053-1746	IC 1623, Arp 236	01 : 07 : 47.54	−17 : 30 : 25.6	82.2	100	0.02007	6016	11.71
9	F01076-1707	MCG-03-04-014	01 : 10 : 08.93	−16 : 51 : 09.9	134.8	100	0.03349	10040	11.65
10	F01159-4443	ESO 244-G012	01 : 18 : 08.27	−44 : 27 : 51.9	87.7	100	0.02104	6307	11.38
11	F01173+1405	CGCG 436-030	01 : 20 : 02.63	+14 : 21 : 42.3	82.2	100	0.03123	9362	11.69
12	F01325-3623	ESO 353-G020	01 : 34 : 51.26	−36 : 08 : 14.4	82.2	100	0.016	4797	11.06
13	F01341-3735	ESO 297-G011/012	01 : 36 : 23.76	−37 : 19 : 51.9	72	100	0.01732	5191	11.16
14	F01364-1042		01 : 38 : 52.79	−10 : 27 : 12.1	191.1	150	0.04825	14464	11.85
15	F01417+1651	III Zw 035	01 : 44 : 30.56	+17 : 06 : 09.0	112.6	100	0.02794	8375	11.64
16	F01484+2220	NGC 695	01 : 51 : 14.34	+22 : 34 : 56.0	130.4	100	0.03247	9735	11.68
17	F01519+3640	UGC 01385	01 : 54 : 57.78	+36 : 55 : 07.9	76.9	100	0.01875	5621	11.05
18	F02071-1023	NGC 838	02 : 09 : 31.84	−10 : 09 : 30.7	53.3	130	0.01285	3851	11.05
19	F02070+3857	NGC 828	02 : 10 : 09.53	+39 : 11 : 24.7	73.6	100	0.01793	5374	11.36
20	F02114+0456	IC 214	02 : 14 : 00.77	+05 : 10 : 13.8	122.4	175	0.03022	9061	11.43
21	F02152+1418	NGC 877	02 : 17 : 56.46	+14 : 31 : 58.2	52.9	75	0.01305	3913	11.10
22	F02203+3158	MCG+05-06-036	02 : 23 : 20.47	+32 : 11 : 33.6	135.7	100	0.03371	10106	11.64
23	F02208+4744	UGC 01845	02 : 24 : 07.97	+47 : 58 : 11.9	65	100	0.01561	4679	11.12
24	F02281-0309	NGC 958	02 : 30 : 42.84	−02 : 56 : 20.5	77.6	100	0.01914	5738	11.20
25	F02345+2053	NGC 992	02 : 37 : 25.46	+21 : 06 : 02.8	56.4	50	0.01381	4141	11.07
26	F02401-0013	NGC 1068	02 : 42 : 40.72	−00 : 00 : 47.9	15.8	50	0.00379	1137	11.40
27	F02435+1253	UGC 02238	02 : 46 : 17.46	+13 : 05 : 44.6	88.5	100	0.02188	6560	11.33
28	F02437+2122		02 : 46 : 39.13	+21 : 35 : 10.4	94.4	50	0.02331	6987	11.16
28	F02437+2123[a]		02 : 46 : 45.05	+21 : 33 : 23.5	94.4	50	0.02331	6987	11.16

continued on the next page

Table 2.1. (continued) Basic GOALS Data

#	IRAS Name	Optical Name	Right Ascension	Declination	D_A	Map Size	Redshift	Velocity	$L_{\rm IR}$
—	—	—	HH:MM:SS	DD:MM:SS	Mpc	kpc	—	km s^{-1}	$\log\left(\frac{L}{L_\odot}\right)$
29	F02512+1446	UGC 02369	02 : 54 : 01.79	+14 : 58 : 26.0	127.7	100	0.03188	9558	11.67
30	F03117+4151	UGC 02608	03 : 15 : 01.47	+42 : 02 : 08.6	95.5	100	0.02334	6998	11.41
30	F03117+4151[a]	UGC 02612	03 : 15 : 14.58	+41 : 58 : 50.0	95.5	100	0.02334	6998	11.41
31	F03164+4119	NGC 1275	03 : 19 : 48.18	+41 : 30 : 42.0	72.4	100	0.01756	5264	11.26
32	F03217+4022		03 : 25 : 05.37	+40 : 33 : 32.2	95.5	100	0.02337	7007	11.33
33	F03316-3618	NGC 1365	03 : 33 : 36.40	−36 : 08 : 25.9	17.7	65	0.00546	1636	11.00
34	F03359+1523		03 : 38 : 47.07	+15 : 32 : 54.1	141.8	100	0.0354	10613	11.55
35	F03514+1546	CGCG 465-012	03 : 54 : 15.95	+15 : 55 : 43.4	90.1	75	0.02222	6662	11.20
35	F03514+1546[a]	CGCG 465-011	03 : 54 : 07.67	+15 : 59 : 24.3	90.1	75	0.02222	6662	11.20
36	03582+6012		04 : 02 : 32.47	+60 : 20 : 40.0	123.5	100	0.03001	8997	11.43
37	F04097+0525	UGC 02982	04 : 12 : 22.68	+05 : 32 : 49.1	72.3	100	0.0177	5305	11.20
38	F04118-3207	ESO 420-G013	04 : 13 : 49.70	−32 : 00 : 25.3	49.8	50	0.01191	3570	11.07
39	F04191-1855	ESO 550-IG 025	04 : 21 : 20.04	−18 : 48 : 48.4	130	100	0.03209	9621	11.51
40	F04210-4042	NGC 1572	04 : 22 : 42.81	−40 : 36 : 03.1	85.1	100	0.02038	6111	11.30
41	04271+3849		04 : 30 : 33.09	+38 : 55 : 47.8	77.8	100	0.01881	5640	11.11
42	F04315-0840	NGC 1614	04 : 33 : 59.95	−08 : 34 : 46.6	65.7	100	0.01594	4778	11.65
43	F04326+1904	UGC 03094	04 : 35 : 33.81	+19 : 10 : 18.0	100.9	100	0.02471	7408	11.41
44	F04454-4838	ESO 203-IG001	04 : 46 : 49.55	−48 : 33 : 30.6	212	100	0.05291	15862	11.86
45	F04502-3304	MCG-05-12-006	04 : 52 : 04.96	−32 : 59 : 26.0	78.3	100	0.01875	5622	11.17
46	F05053-0805	NGC 1797	05 : 07 : 44.84	−08 : 01 : 08.7	61.6	100	0.01481	4441	11.04
46	F05053-0805[a]	NGC 1799	05 : 07 : 44.59	−07 : 58 : 09.0	61.6	80	0.01481	4441	11.04
47	F05054+1718	CGCG 468-002	05 : 08 : 20.46	+17 : 21 : 57.8	75.1	100	0.01819	5454	11.22
48	05083+2441		05 : 11 : 27.46	+24 : 45 : 41.1	94.8	100	0.02307	6915	11.26
49	F05081+7936	VII Zw 031	05 : 16 : 46.39	+79 : 40 : 12.9	216.2	200	0.05367	16090	11.99
50	05129+5128		05 : 16 : 55.96	+51 : 31 : 56.9	113.7	100	0.02743	8224	11.42
51	F05189-2524		05 : 21 : 01.45	−25 : 21 : 46.2	172	100	0.04256	12760	12.16
52	F05187-1017		05 : 21 : 06.53	−10 : 14 : 46.2	115.4	100	0.02827	8474	11.30
53	05368+4940	MCG+08-11-002	05 : 40 : 43.70	+49 : 41 : 41.6	80.6	100	0.01916	5743	11.46
54	F05365+6921	NGC 1961	05 : 42 : 04.55	+69 : 22 : 42.8	57.5	100	0.01312	3934	11.06

continued on the next page

Table 2.1. (continued) Basic GOALS Data

#	IRAS Name	Optical Name	Right Ascension	Declination	D_A	Map Size	Redshift	Velocity	$L_{\rm IR}$
—	—	—	HH:MM:SS	DD:MM:SS	Mpc	kpc	—	km s^{-1}	$\log\left(\frac{L}{L_\odot}\right)$
55	F05414+5840	UGC 03351	05 : 45 : 48.03	+58 : 42 : 03.6	63.9	100	0.01486	4455	11.28
56	05442+1732		05 : 47 : 08.49	+17 : 33 : 29.1	77.4	100	0.01862	5582	11.30
57	F06076-2139		06 : 09 : 45.84	−21 : 40 : 28.3	153.3	100	0.03745	11226	11.65
58	F06052+8027	UGC 03410	06 : 14 : 13.75	+80 : 27 : 47.1	56.9	100	0.01308	3921	11.10
59	F06107+7822	NGC 2146	06 : 18 : 37.82	+78 : 21 : 24.0	17.4	50	0.00298	893	11.12
60	F06259-4708	ESO 255-IG007	06 : 27 : 22.39	−47 : 10 : 49.4	160.3	100	0.03879	11629	11.90
61	F06295-1735	ESO 557-G002	06 : 31 : 46.45	−17 : 38 : 00.7	89.5	100	0.0213	6385	11.25
62	F06538+4628	UGC 03608	06 : 57 : 34.41	+46 : 24 : 10.6	90.4	100	0.02135	6401	11.34
63	F06592-6313		06 : 59 : 40.26	−63 : 17 : 52.4	99.4	100	0.02296	6882	11.24
64	F07027-6011	AM 0702-601	07 : 03 : 26.33	−60 : 16 : 02.7	132.6	150	0.03132	9390	11.64
65	07063+2043	NGC 2342	07 : 09 : 15.04	+20 : 37 : 10.7	75	110	0.0176	5276	11.31
66	F07160-6215	NGC 2369	07 : 16 : 37.73	−62 : 20 : 36.4	46.6	70	0.01081	3240	11.16
67	07251-0248		07 : 27 : 37.62	−02 : 54 : 54.8	338.2	200	0.08756	26249	12.39
68	F07256+3355	NGC 2388	07 : 28 : 46.38	+33 : 50 : 22.9	59.7	220	0.01379	4134	11.28
69	F07329+1149	MCG+02-20-003	07 : 35 : 43.44	+11 : 42 : 34.8	72	100	0.01625	4873	11.13
69	F07329+1149[a]	NGC 2416	07 : 35 : 41.53	+11 : 36 : 42.1	72	100	0.01625	4873	11.13
70	08355-4944		08 : 37 : 01.87	−49 : 54 : 30.0	112.1	100	0.0259	7764	11.62
71	F08339+6517		08 : 38 : 23.18	+65 : 07 : 15.2	83.1	100	0.01911	5730	11.11
72	F08354+2555	NGC 2623	08 : 38 : 24.11	+25 : 45 : 16.5	81.1	100	0.01851	5549	11.60
73	08424-3130	ESO 432-IG006	08 : 44 : 28.07	−31 : 41 : 40.5	72.1	100	0.01616	4846	11.08
74	F08520-6850	ESO 060-IG016	08 : 52 : 31.28	−69 : 01 : 57.0	191.8	100	0.04632	13885	11.82
75	F08572+3915		09 : 00 : 25.35	+39 : 03 : 54.0	235.7	200	0.05835	17493	12.16
76	09022-3615		09 : 04 : 12.69	−36 : 27 : 01.5	241.4	200	0.05964	17880	12.31
77	F09111-1007		09 : 13 : 37.69	−10 : 19 : 24.6	221.4	200	0.05414	16231	12.06
78	F09126+4432	UGC 04881	09 : 15 : 55.10	+44 : 19 : 54.0	164.7	150	0.03953	11851	11.74
79	F09320+6134	UGC 05101	09 : 35 : 51.59	+61 : 21 : 11.9	163.8	100	0.03937	11802	12.01
80	F09333+4841	MCG+08-18-013	09 : 36 : 34.02	+48 : 28 : 18.8	109.8	150	0.02594	7777	11.34
81	F09437+0317	Arp 303, IC 0563/4	09 : 46 : 20.70	+03 : 03 : 30.4	89.3	150	0.02	5996	11.23
82	F10015-0614	NGC 3110	10 : 03 : 59.57	−06 : 29 : 08.5	75.2	95	0.01686	5054	11.37

continued on the next page

Table 2.1. (continued) Basic GOALS Data

#	IRAS Name	Optical Name	Right Ascension	Declination	D_A	Map Size	Redshift	Velocity	$L_{\rm IR}$
—	—	—	HH:MM:SS	DD:MM:SS	Mpc	kpc	—	km s^{-1}	$\log\left(\frac{L}{L_\odot}\right)$
83	F10038-3338	ESO 374-IG 032	10 : 06 : 04.65	−33 : 53 : 06.1	145.9	130	0.0341	10223	11.78
84	F10173+0828		10 : 20 : 00.24	+08 : 13 : 32.8	203.5	200	0.04909	14716	11.86
85	F10196+2149	NGC 3221	10 : 22 : 19.98	+21 : 34 : 10.6	63.9	80	0.01371	4110	11.09
86	F10257-4339	NGC 3256	10 : 27 : 51.30	−43 : 54 : 14.0	38.2	50	0.00935	2804	11.64
87	F10409-4556	ESO 264-G036	10 : 43 : 07.51	−46 : 12 : 44.1	95.9	100	0.02101	6299	11.32
88	F10567-4310	ESO 264-G057	10 : 59 : 01.70	−43 : 26 : 25.2	80.5	100	0.0172	5156	11.14
89	F10565+2448		10 : 59 : 18.15	+24 : 32 : 34.2	147.6	100	0.0431	12921	12.08
90	F11011+4107	MCG+07-23-019	11 : 03 : 53.98	+40 : 51 : 00.4	147.6	100	0.03452	10350	11.62
91	F11186-0242	CGCG 011-076	11 : 21 : 10.26	−02 : 59 : 20.8	110.5	100	0.0249	7464	11.43
92	F11231+1456	IC 2810	11 : 25 : 47.31	+14 : 40 : 21.2	146	200	0.034	10192	11.64
93	F11255-4120	ESO 319-G022	11 : 27 : 54.18	−41 : 36 : 51.7	77.4	100	0.01635	4902	11.12
94	F11257+5850	NGC 3690, Arp 299	11 : 28 : 32.35	+58 : 33 : 43.3	49.7	100	0.01032	3093	11.93
95	F11506-3851	ESO 320-G030	11 : 53 : 11.73	−39 : 07 : 49.0	40.3	50	0.01078	3232	11.17
96	F12043-3140	ESO 440-IG058	12 : 06 : 51.78	−31 : 56 : 52.8	107	100	0.0232	6956	11.43
97	F12112+0305		12 : 13 : 46.02	+02 : 48 : 42.2	295.1	200	0.07332	21980	12.36
98	F12116+5448	NGC 4194	12 : 14 : 09.71	+54 : 31 : 35.5	42.3	50	0.00834	2501	11.10
99	F12115-4656	ESO 267-G030	12 : 14 : 12.81	−47 : 13 : 42.5	93	100	0.01849	5543	11.25
99	F12115-4656[a]	ESO 267-G029	12 : 13 : 52.28	−47 : 16 : 25.4	93	100	0.01849	5543	11.25
100	12116-5615		12 : 14 : 22.08	−56 : 32 : 32.7	121.3	100	0.0271	8125	11.65
101	F12224-0624		12 : 25 : 03.90	−06 : 40 : 52.1	118.7	100	0.02636	7902	11.36
102	F12243-0036	NGC 4418	12 : 26 : 59.74	−00 : 53 : 32.1	36.3	60	0.00727	2179	11.19
103	F12540+5708	UGC 08058, Mrk 231	12 : 56 : 14.25	+56 : 52 : 24.8	176.8	150	0.04217	12642	12.57
104	F12590+2934	NGC 4922	13 : 01 : 24.89	+29 : 18 : 39.6	105.9	100	0.02359	7071	11.38
105	F12592+0436	CGCG 043-099	13 : 01 : 50.28	+04 : 20 : 00.8	162.6	150	0.03748	11237	11.68
106	F12596-1529	MCG-02-33-098	13 : 02 : 20.02	−15 : 46 : 01.8	76.3	100	0.01592	4773	11.17
107	F13001-2339	ESO 507-G070	13 : 02 : 52.42	−23 : 55 : 17.8	101.5	100	0.0217	6506	11.56
108	13052-5711		13 : 08 : 18.73	−57 : 27 : 30.3	101.6	100	0.02123	6364	11.40
109	F13126+2453	IC 0860	13 : 15 : 03.49	+24 : 37 : 07.6	55.6	100	0.01116	3347	11.14
110	13120-5453		13 : 15 : 06.37	−55 : 09 : 22.5	135.5	120	0.03076	9222	12.32

continued on the next page

Table 2.1. (continued) Basic GOALS Data

#	IRAS Name	Optical Name	Right Ascension	Declination	D_A	Map Size	Redshift	Velocity	$L_{\rm IR}$
—	—	—	HH:MM:SS	DD:MM:SS	Mpc	kpc	—	km s^{-1}	$\log\left(\frac{L}{L_\odot}\right)$
111	F13136+6223	VV 250a	13 : 15 : 32.82	+62 : 07 : 37.4	133.1	150	0.03107	9313	11.81
112	F13182+3424	UGC 08387	13 : 20 : 35.37	+34 : 08 : 22.2	105	100	0.0233	6985	11.73
113	F13188+0036	NGC 5104	13 : 21 : 23.09	+00 : 20 : 33.2	87.5	100	0.01861	5578	11.27
114	F13197-1627	MCG-03-34-064	13 : 22 : 21.73	−16 : 43 : 06.2	79.5	100	0.01654	4959	11.28
115	F13229-2934	NGC 5135	13 : 25 : 44.02	−29 : 50 : 00.4	59.3	100	0.01369	4105	11.30
116	13242-5713	ESO 173-G015	13 : 27 : 23.79	−57 : 29 : 21.8	33.3	50	0.00973	2918	11.38
117	F13301-2356	IC 4280	13 : 32 : 53.40	−24 : 12 : 25.5	79.8	100	0.01631	4889	11.15
118	F13362+4831	NGC 5256	13 : 38 : 17.52	+48 : 16 : 37.2	122.1	100	0.02782	8341	11.56
119	F13373+0105	Arp 240, NGC 5257/8	13 : 39 : 55.34	+00 : 50 : 09.5	103.8	150	0.02261	6778	11.62
120	F13428+5608	UGC 08696, Mrk 273	13 : 44 : 42.12	+55 : 53 : 13.1	160.6	100	0.03778	11326	12.21
121	F13470+3530	UGC 08739	13 : 49 : 13.94	+35 : 15 : 26.2	78.7	90	0.01679	5032	11.15
122	F13478-4848	ESO 221-IG010	13 : 50 : 56.92	−49 : 03 : 18.8	61.6	100	0.01034	3099	11.22
123	F13497+0220	NGC 5331	13 : 52 : 16.32	+02 : 06 : 18.0	145.2	100	0.03304	9906	11.66
124	F13564+3741	Arp 84, NGC 5394/5	13 : 58 : 35.80	+37 : 26 : 20.5	57.3	100	0.01161	3482	11.08
125	F14179+4927	CGCG 247-020	14 : 19 : 43.27	+49 : 14 : 11.9	114.1	100	0.02574	7716	11.39
126	F14280+3126	NGC 5653	14 : 30 : 10.44	+31 : 12 : 55.8	58.8	70	0.01188	3562	11.13
127	F14348-1447		14 : 37 : 38.29	−15 : 00 : 24.2	330.3	300	0.08273	24802	12.39
128	F14378-3651		14 : 40 : 59.04	−37 : 04 : 32.0	276.4	200	0.06764	20277	12.23
129	F14423-2039	NGC 5734	14 : 45 : 10.02	−20 : 53 : 30.9	65.2	110	0.01375	4121	11.15
130	F14547+2449	VV 340a, Arp 302	14 : 57 : 00.51	+24 : 36 : 45.2	146.5	155	0.03367	10094	11.74
131	F14544-4255	IC 4518A/B	14 : 57 : 43.27	−43 : 07 : 56.3	77.5	100	0.01589	4763	11.23
132	F15107+0724	CGCG 049-057	15 : 13 : 13.07	+07 : 13 : 32.1	63.7	80	0.013	3897	11.35
133	F15163+4255	VV 705	15 : 18 : 06.24	+42 : 44 : 41.5	169.2	200	0.03984	11944	11.92
134	15206-6256	ESO 099-G004	15 : 24 : 57.98	−63 : 07 : 29.4	129.3	100	0.02928	8779	11.74
135	F15250+3608		15 : 26 : 59.42	+35 : 58 : 37.8	228.1	150	0.05516	16535	12.08
136	F15276+1309	NGC 5936	15 : 30 : 00.85	+12 : 59 : 22.1	65.3	100	0.01336	4004	11.14
137	F15327+2340	Arp 220, UGC 09913	15 : 34 : 57.23	+23 : 30 : 11.3	84.8	140	0.01813	5434	12.28
138	F15437+0234	NGC 5990	15 : 46 : 16.41	+02 : 24 : 55.6	62.8	80	0.01281	3839	11.13
139	F16030+2040	NGC 6052	16 : 05 : 12.87	+20 : 32 : 33.0	75.2	90	0.01581	4739	11.09

continued on the next page

Table 2.1. (continued) Basic GOALS Data

#	IRAS Name	Optical Name	Right Ascension	Declination	D_A	Map Size	Redshift	Velocity	$L_{\rm IR}$
—	—	—	HH:MM:SS	DD:MM:SS	Mpc	kpc	—	km s^{-1}	$\log\left(\frac{L}{L_\odot}\right)$
140	F16104+5235	NGC 6090	16 : 11 : 40.84	+52 : 27 : 27.2	129.2	100	0.02984	8947	11.58
141	F16164-0746		16 : 19 : 11.75	−07 : 54 : 03.0	121.3	100	0.02715	8140	11.62
142	F16284+0411	CGCG 052-037	16 : 30 : 54.89	+04 : 04 : 41.3	112.8	100	0.02449	7342	11.45
143	16304-6030	NGC 6156	16 : 34 : 52.55	−60 : 37 : 08.0	47	75	0.01088	3263	11.14
144	F16330-6820	ESO 069-IG006	16 : 38 : 12.64	−68 : 26 : 42.3	193.6	200	0.04644	13922	11.98
145	F16399-0937		16 : 42 : 40.11	−09 : 43 : 13.7	121.4	100	0.02701	8098	11.63
146	F16443-2915	ESO 453-G005	16 : 47 : 30.21	−29 : 20 : 14.2	96.4	140	0.02088	6260	11.37
147	F16504+0228	NGC 6240	16 : 52 : 58.90	+02 : 24 : 03.3	110.5	100	0.02448	7339	11.93
148	F16516-0948		16 : 54 : 23.72	−09 : 53 : 20.9	102.3	100	0.02253	6755	11.31
149	F16577+5900	NGC 6286, Arp 293	16 : 58 : 27.81	+58 : 56 : 47.5	83.9	100	0.01835	5501	11.37
150	F17132+5313		17 : 14 : 20.45	+53 : 10 : 31.6	210.1	200	0.05094	15270	11.96
151	F17138-1017		17 : 16 : 35.68	−10 : 20 : 40.5	81.2	100	0.01734	5197	11.49
152	F17207-0014		17 : 23 : 21.97	−00 : 17 : 00.7	182.1	175	0.04281	12834	12.46
153	F17222-5953	ESO 138-G027	17 : 26 : 43.35	−59 : 55 : 55.2	94.3	100	0.02078	6230	11.41
154	F17530+3447	UGC 11041	17 : 54 : 51.82	+34 : 46 : 34.2	75	100	0.01628	4881	11.11
155	F17548+2401	CGCG 141-034	17 : 56 : 56.65	+24 : 01 : 02.0	89.8	100	0.01983	5944	11.20
156	17578-0400		18 : 00 : 28.61	−04 : 01 : 16.3	67	100	0.01404	4210	11.48
157	18090+0130		18 : 11 : 35.91	+01 : 31 : 41.3	126.6	125	0.02889	8662	11.65
158	F18131+6820	NGC 6621, Arp 81	18 : 12 : 57.46	+68 : 21 : 38.7	92.4	100	0.02065	6191	11.29
159	F18093-5744	IC 4687	18 : 13 : 39.56	−57 : 44 : 00.9	76.7	100	0.01735	5200	11.62
160	F18145+2205	CGCG 142-034	18 : 16 : 37.26	+22 : 06 : 42.6	83.2	100	0.01868	5599	11.18
161	F18293-3413		18 : 32 : 41.10	−34 : 11 : 27.0	83	100	0.01818	5449	11.88
162	F18329+5950	NGC 6670A/B	18 : 33 : 36.00	+59 : 53 : 20.3	122.4	100	0.0286	8574	11.65
163	F18341-5732	IC 4734	18 : 38 : 25.75	−57 : 29 : 25.4	71.2	100	0.01561	4680	11.35
164	F18425+6036	NGC 6701	18 : 43 : 12.52	+60 : 39 : 11.6	60.8	100	0.01323	3965	11.12
165	F19120+7320	VV 414, NGC 6786	19 : 10 : 59.19	+73 : 25 : 04.2	107.5	100	0.02511	7528	11.49
166	F19115-2124	ESO 593-IG008	19 : 14 : 31.15	−21 : 19 : 06.3	201.8	150	0.04873	14608	11.93
167	F19297-0406		19 : 32 : 22.30	−04 : 00 : 01.1	335.1	200	0.08573	25701	12.45
168	19542+1110		19 : 56 : 35.78	+11 : 19 : 04.9	260.1	200	0.06496	19473	12.12

continued on the next page

Table 2.1. (continued) Basic GOALS Data

#	IRAS Name	Optical Name	Right Ascension	Declination	D_A	Map Size	Redshift	Velocity	$L_{\rm IR}$
—	—	—	HH:MM:SS	DD:MM:SS	Mpc	kpc	—	km s^{-1}	$\log\left(\frac{L}{L_\odot}\right)$
169	F19542-3804	ESO 339-G011	19 : 57 : 37.60	−37 : 56 : 08.4	85.3	100	0.0192	5756	11.20
170	F20221-2458	NGC 6907	20 : 25 : 06.58	−24 : 48 : 32.9	49.1	60	0.01064	3190	11.11
171	20264+2533	MCG+04-48-002	20 : 28 : 31.98	+25 : 43 : 42.3	63.6	75	0.0139	4167	11.11
172	F20304-0211	NGC 6926	20 : 33 : 06.13	−02 : 01 : 38.9	85.7	100	0.01961	5880	11.32
173	20351+2521		20 : 37 : 17.73	+25 : 31 : 37.5	141.3	100	0.0337	10102	11.61
174	F20550+1655	CGCG 448-020, II Zw 096	20 : 57 : 24.01	+17 : 07 : 41.6	150	100	0.0361	10822	11.94
175	F20551-4250	ESO 286-IG019	20 : 58 : 26.78	−42 : 39 : 00.5	177.4	100	0.043	12890	12.06
176	F21008-4347	ESO 286-G035	21 : 04 : 11.11	−43 : 35 : 36.1	76.4	100	0.01736	5205	11.20
177	21101+5810		21 : 11 : 29.28	+58 : 23 : 07.9	161.2	100	0.03904	11705	11.81
178	F21330-3846	ESO 343-IG013	21 : 36 : 10.73	−38 : 32 : 37.8	82.6	100	0.01906	5714	11.14
179	F21453-3511	NGC 7130	21 : 48 : 19.54	−34 : 57 : 04.7	70.4	100	0.01615	4842	11.42
180	F22118-2742	ESO 467-G027	22 : 14 : 39.97	−27 : 27 : 50.3	74.7	100	0.0174	5217	11.08
181	F22132-3705	IC 5179	22 : 16 : 09.13	−36 : 50 : 37.2	50.2	50	0.01141	3422	11.24
182	F22287-1917	ESO 602-G025	22 : 31 : 25.48	−19 : 02 : 04.0	104.7	100	0.02504	7507	11.34
183	F22389+3359	UGC 12150	22 : 41 : 12.21	+34 : 14 : 56.8	89.6	100	0.02139	6413	11.35
184	F22467-4906	ESO 239-IG002	22 : 49 : 39.84	−48 : 50 : 58.3	175.6	100	0.04303	12901	11.84
185	F22491-1808		22 : 51 : 49.35	−17 : 52 : 24.9	302.2	200	0.07776	23312	12.20
186	F23007+0836	NGC 7469, Arp 298	23 : 03 : 16.84	+08 : 53 : 00.9	68	100	0.01632	4892	11.65
187	F23024+1916	CGCG 453-062	23 : 04 : 56.55	+19 : 33 : 07.1	103.7	100	0.0251	7524	11.38
188	F23128-5919	ESO 148-IG002	23 : 15 : 46.75	−59 : 03 : 15.8	182.4	100	0.0446	13371	12.06
189	F23135+2517	IC 5298	23 : 16 : 00.67	+25 : 33 : 24.3	112.7	100	0.02742	8221	11.60
190	F23133-4251	NGC 7552	23 : 16 : 10.81	−42 : 35 : 05.5	23.2	50	0.00536	1608	11.11
191	F23157+0618	NGC 7591	23 : 18 : 14.89	+06 : 34 : 17.8	69.1	90	0.01653	4956	11.12
192	F23157-0441	NGC 7592	23 : 18 : 22.19	−04 : 24 : 57.4	101	100	0.02444	7328	11.40
193	F23180-6929	ESO 077-IG014	23 : 21 : 04.59	−69 : 12 : 54.1	171.5	100	0.04156	12460	11.76
194	F23254+0830	NGC 7674, HCG 96	23 : 27 : 57.73	+08 : 46 : 51.0	119.4	100	0.02892	8671	11.56
195	23262+0314	NGC 7679	23 : 28 : 46.62	+03 : 30 : 41.4	71.3	100	0.01714	5138	11.11
195	23262+0314[a]	NGC 7682	23 : 29 : 03.91	+03 : 31 : 59.9	71.3	100	0.01714	5138	11.11
196	F23365+3604		23 : 39 : 01.32	+36 : 21 : 08.2	253.3	200	0.06448	19331	12.20

continued on the next page

Table 2.1. (continued) Basic GOALS Data

#	IRAS Name	Optical Name	Right Ascension	Declination	D_A	Map Size	Redshift	Velocity	$L_{\rm IR}$
—	—	—	HH:MM:SS	DD:MM:SS	Mpc	kpc	—	km s^{-1}	$\log\left(\frac{L}{L_\odot}\right)$
197	F23394-0353	MCG-01-60-022	23 : 42 : 00.91	−03 : 36 : 54.4	92.4	100	0.02324	6966	11.27
197	F23394-0353[a]	MCG-01-60-021, Mrk 933	23 : 41 : 46.04	−03 : 39 : 42.3	92.4	100	0.02324	6966	11.27
198	23436+5257		23 : 46 : 05.44	+53 : 14 : 01.7	139.3	100	0.03413	10233	11.57
199	F23444+2911	Arp 86, NGC 7752/3	23 : 47 : 01.73	+29 : 28 : 16.2	71.1	100	0.01708	5120	11.07
200	F23488+1949	NGC 7771	23 : 51 : 13.55	+20 : 07 : 41.2	58.5	200	0.01427	4277	11.40
201	F23488+2018	Mrk 331	23 : 51 : 22.73	+20 : 34 : 55.4	73.8	100	0.01848	5541	11.50

Basic properties of each object in the GOALS sample. See §2.2 for a description of each column.

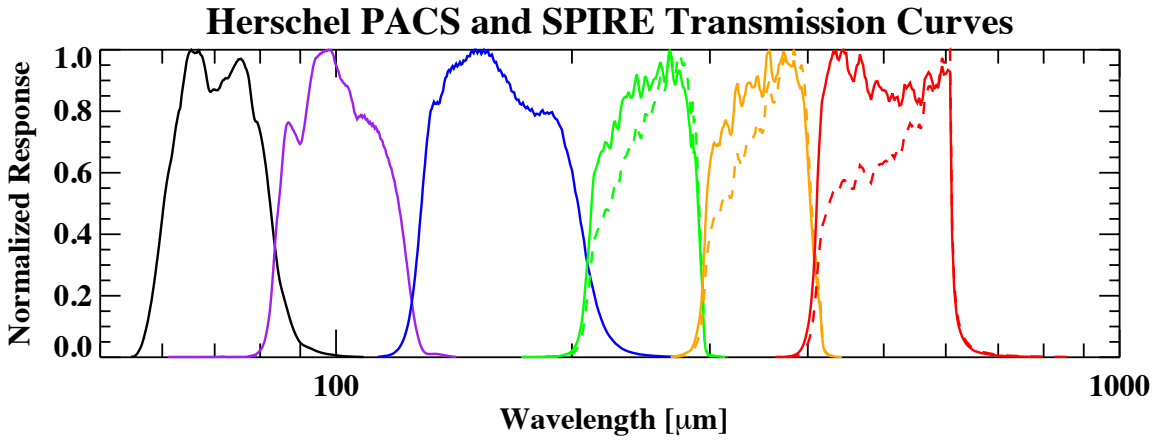

Figure 2.1 The normalized filter transmission curves for our *Herschel* data. From left to right are the PACS 70 μm, 100 μm, 160 μm channels, followed by the SPIRE 250 μm, 350 μm, and 500 μm channels. For the SPIRE bands, the point source response is shown with a solid curve, while the extended source response is shown with a dashed curve. Note the large difference in response for the SPIRE 500 μm transmission curve.

responsitivity (dashed), which is important since some of the objects in our sample are extended even at SPIRE wavelengths (i.e., the LIRG IRAS F03316–3618/NGC 1365).

Within the GOALS sample there are eight systems consisting of widely separated pairs where two separate PACS observations were needed, but only one SPIRE observation was made since its field of view was larger. These galaxies are denoted in both Tables 2.1 and 2.2, giving a total of $201 + 8 = 209$ observation datasets. We note for the galaxy system IRAS F07256+3355 which has three components, only two are visible in the PACS imagery, due to the smaller field of view of PACS. The third component (NGC 2385) is far to the west and still within SPIRE's larger field of view. Using the SPIRE fluxes as a rough proxy for infrared luminosity strength, NGC 2385 contributes very little to the overall infrared luminosity of the system. IRAS F23488+1949 also has a third component (NGC 7769) to the NNW in the SPIRE images, but is outside of the PACS scan area. However from the SPIRE fluxes NGC 7769 appears to have a moderate contribution to the system's infrared luminosity. In sum we achieved a very high degree of coverage and completeness for each GOALS object with *Herschel*.

2.3.1 Photoconductor Array Camera and Spectrometer (PACS) Observations

The Photoconductor Array Camera and Spectrometer (PACS, Poglitsch et al. 2010) is one of three far-infrared instruments onboard the *Herschel Space Observatory* and covers a wavelength range between 60 – 210 μm. In the photometer mode it can image two simultaneous wavelength bands centered at 160 μm, and at either 70 μm or 100 μm. These three broad bands are referred to as the blue channel (60 – 85 μm), green channel (85 – 130 μm) and red channel (130 – 210 μm). For any given observation, the blue camera observes at either 70 μm or 100 μm, while the red camera only observes at 160 μm. A dichroic beam-splitter with a designed transition wavelength of 130 μm directs the incoming light into the blue and red cameras, and a filter in front of the blue camera selects either the blue or green band.

The detectors for both the blue and red cameras comprise a filled bolometer array of square pixels that instantaneously samples the entire beam from the telescope's optics. The layout of the blue camera's focal plane consists of 4 $\times$ 2 subarrays, with 16 $\times$ 16 pixels in each subarray. Similarly the red camera consists of 2 $\times$ 1 subarrays with 16 $\times$ 16 pixels each. On the sky each bolometer pixel subtends an angle of $3\farcs2 \times 3\farcs2$ and $6\farcs4 \times 6\farcs4$ for the blue and red cameras respectively. There exists gaps between each of the subarrays in both cameras, which must be filled in by on-sky mapping techniques (i.e., scan mapping). Both the blue and red cameras were designed to image the same $3\farcm5 \times 1\farcm75$ field of view on the sky at any given instant.

In the photometer mode there are two astronomical observing templates (AOT) available, in addition to a PACS/SPIRE parallel observing mode. For our *Herschel* GOALS program we used the scan map technique for all of our astronomical observing requests (AOR), which is ideal for mapping large areas of the sky and/or targets where extended flux may be present. Our scan map observations involve slewing the telescope at constant speed along parallel lines separated by $15''$ from each other, perpendicular to the scan direction. Two example PACS observation footprints are shown in Figure 2.2 panels (a) and (c),

overlaid on images from the Digital Sky Survey (DSS). The area of maximum coverage is the inner region centered on the red box, where the requested observation is centered. For the GOALS observations we chose to observe 7 scan legs in each scan and cross-scan using the $20''$/sec scan speed, with scan leg lengths ranging between $3 - 6'$ depending on the size of the target. At this scan speed the beam profiles for each wavelength have mean FWHM values of $5\farcs6$, $6\farcs8$, and $11\farcs3$ for the 70 μm, 100 μm, and 160 μm channels respectively.

Before each PACS photometer observation is a 30 sec. chopped calibration measurement between two internal calibration sources (the calibration block), followed by 5 sec. of idle for telescope stability before the science observation is executed. As the telescope is scanned across the sky during science observations, all of the bolometer pixels are read out at a frequency of 40 Hz, even during periods where the telescope was turning around for the next scan leg. However due to satellite data-rate limitations, all PACS data are averaged over four frames effectively downsampling the data to 10 Hz. The result is a data timeline of the flux seen by each detector pixel as a function of time (and by extension position on the sky) as the telescope is scanned over the target field.

In order to accurately reconstruct the image, two scan map AORs at orthogonal angles are required. This is because as the telescope scans a field, the offsets of each bolometer subarray, and even each pixel, may be different from its neighbor resulting in stripes or gradients in the final reconstructed map. However if the same field is scanned in two orthogonal directions, many of these map artifacts can be successfully removed, by virtue of multiple different bolometers sampling each patch of the sky. Furthermore in order to maximally sample a given sky pixel by as many bolometer pixels as possible, we chose our scan angle to be 45° and 135° with respect to the detector array. The orthogonal scans similarly help remove drifts in the bolometer timelines, which are time-dependent variations in the detector or subarray offsets, caused by for example cosmic ray hits and other instrument effects. For our survey the typical PACS scan duration is about 200 sec., however larger maps with deeper coverage can be as long as $\sim$1900 sec. Since two scans are needed for each target in the blue and green filter, there are two pairs of scan and

cross-scan in the red channel, giving us better sensitivity. Unfortunately due to unforeseen consequences, several galaxy components in IRAS F02071–1023 and IRAS F07256+3355 had sufficient coverage by only one of the scans, which resulted in more noise along the scan direction around the target.

Since by definition all of the objects in the GOALS sample have an *IRAS* 60 μm flux of at least 5.24 Jy, the galaxies or galaxy systems are bright enough such that only one repetition was needed for each PACS scan and cross scan. With one pair of scan and cross-scan observations, we achieved a 1-σ point source sensitivity of approximately 4 mJy in the central area, and approximately 8 mJy averaged over the entire map for both blue and green observations. By combining all four red channel scans and cross-scans we achieved a 1-σ point source sensitivity of about 6 mJy in the central area, and about 12 mJy averaged over the entire map. On the other hand the extended flux sensitivities for one repetition (one scan and cross-scan pair) are 5.3 MJy sr^{-1}, 5.2 MJy sr^{-1}, and 1.7 MJy sr^{-1} for the 70 μm, 100 μm, and 160 μm channels respectively.

2.3.2 Spectral and Photometric Imaging Receiver (SPIRE) Observations

The Spectral and Photometric Imaging Receiver (SPIRE, Griffin et al. 2010) is a submillimeter camera on *Herschel* that operates between the 194-671 μm wavelength range. In the imaging mode, it can simultaneously observe in three different broad bandpasses ($\lambda/\Delta\lambda \sim 3$), centered at 250 μm, 350 μm, and 500 μm. Similar to PACS, SPIRE images a field by scan mapping, where the instrument field of view ($4' \times 8'$) is scanned across the sky to maximize the spatial coverage. The three detector arrays use hexagonal feedhorn-coupled bolometers, with 139, 88, and 43 bolometers for the PSW (250 μm), PMW (350 μm), and PLW (500 μm) channels respectively. The beam profiles for each wavelength have mean FWHM values of $18\farcs1$, $25\farcs2$, and $36\farcs6$ for the 250 μm, 350 μm, and 500 μm photometer arrays, and mean ellipticities of 7%, 12%, and 9% (the beam shape changes slightly as a function of off-axis angle).

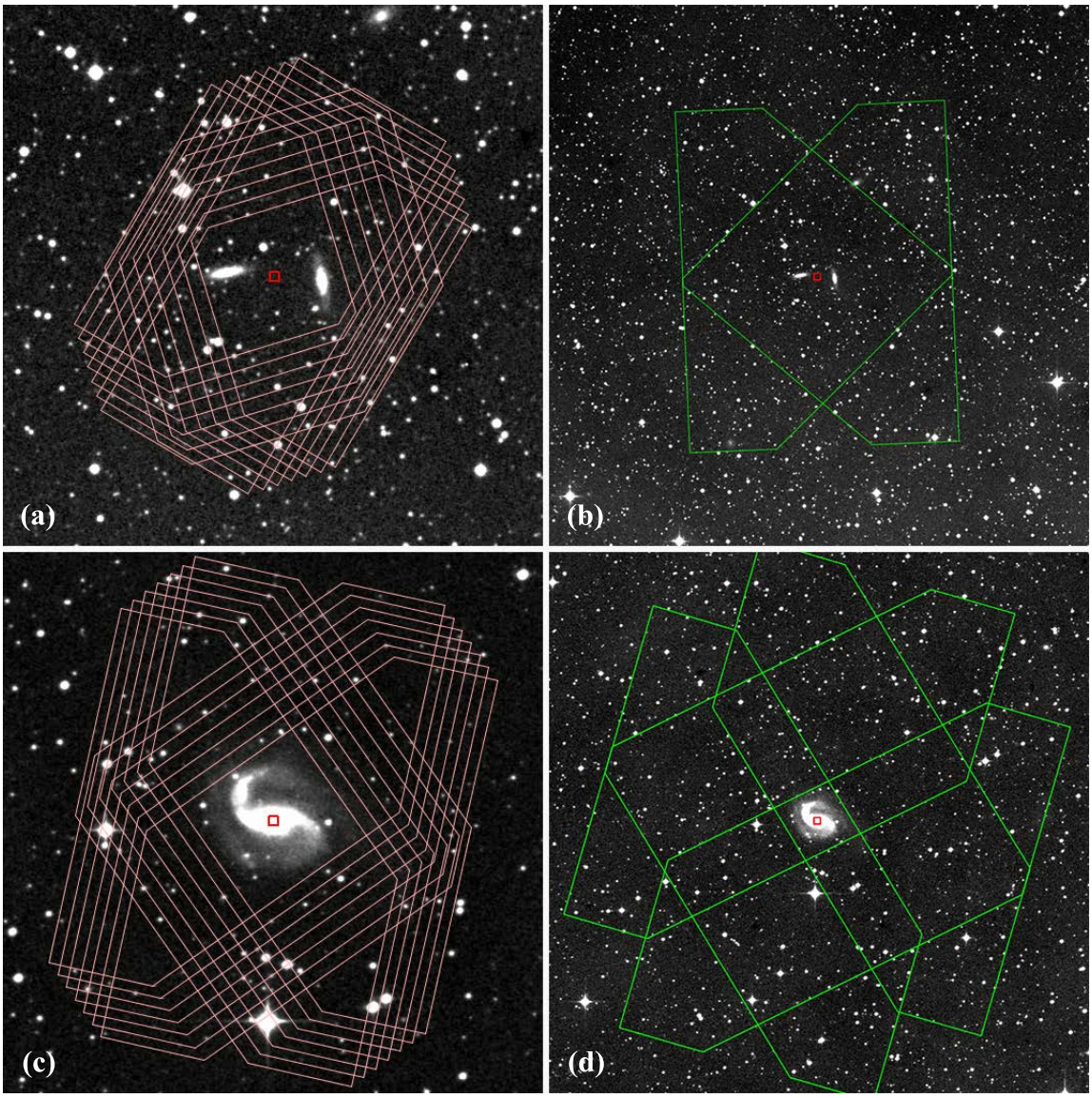

Figure 2.2 The PACS and SPIRE observation footprints for two galaxies, IRAS F18145+2205 (CGCG 142-034) in the top row, and IRAS F20221-2458 (NGC 6907) on the bottom. These figures were generated using HSPOT, the Herschel observation planning tool, while the background images used are from DSS. The red box in each panel indicates the central coordinate for each observation. The PACS observations are shown in panels (a) and (c), which show a $9' \times 9'$ field of view around the target coordinate. Each scan leg in one direction is repeated several times (nominally 7 times) for maximal coverage of the source galaxy (or galaxies). The SPIRE observations are shown in panels (b) and (d), and have a $25' \times 25'$ field of view, which is much larger than the PACS field of view. Panel (b) shows a small map scan, while the bottom panel shows a large map scan.

There are three main observing modes available: point source photometry, field/jiggle mapping, and scan mapping. For our observing program (dsanders_OT1_1) we chose the scan-map mode at a scan rate of 30″/sec., since it gave the best data quality and also larger field of view for the final map than the other two mapping modes. Nominal scan angles of 42.4° and 127.2° with respect to the detector arrays were used to maximize sky coverage by as many detectors as possible, and to minimize the effect of individual bolometer drift during data processing. Like PACS, two scans are needed for data redundancy as well as cross-linking, however the scan and cross-scan with SPIRE are observed within a single AOR. Within our program, the vast majority of our targets were observed in the small map mode (∼150 targets), while the rest were taken in the large map mode (∼20 targets). The typical scan durations are ∼170 sec. for small maps (∼5′× 5′ guaranteed map coverage area), and up to ∼2200 sec. for large maps. In Figure 2.2 panels (b) and (d) we show two example observations using SPIRE. The top panel shows a small map mode observation, while the bottom panel shows a large map mode observation. In both cases the SPIRE detector is scanned over the target coordinate (shown by the red box) from the top left to the bottom right, and then from the top right to the bottom left.

Due to the extremely sensitive design of the *Herschel* optics and SPIRE instrument, only one repetition was observed for every target in our observing program. The SPIRE instrument has a confusion limit of 5.8, 6.3, and 6.8 mJy beam^{-1} for the 250 μm, 350 μm, and 500 μm channels, which is defined as the standard deviation of the flux density in the limit of zero instrument noise (Nguyen et al. 2010). On the other hand the instrument noise is about 9, 7.5, and 10.8 mJy beam^{-1} at 250 μm, 350 μm, and 500 μm for one repetition (scan and cross-scan) at the nominal scan speed of 30″/sec. Since many of our targets have extended features, SPIRE's 1-σ sensitivities to extended flux are at the 1.4 MJy sr^{-1}, 0.8 MJy sr^{-1}, and 0.5 MJy sr^{-1} levels for 250 μm, 350 μm, and 500 μm for one repetition. These flux levels are already dominated by confusion noise, and is more than enough to detect any cold dust components in our sample.

2.3.3 Observing Log

Table 2.2 below lists the observing log for our data sample. Column 1 is the galaxy reference number, and column 2 is the IRAS name of the galaxy, ordered by ascending RA. Column 3 is the common optical counterpart names to the galaxy systems. Columns 4 – 7 are the observation IDs for PACS imaging. Blue corresponds to a wavelength of 70 μm, while green corresponds to 100 μm. Each blue and green observation pair simultaneously observes the red 160 μm channel. Two orthogonal observations are made at each wavelength to reduce imaging artifacts. We note that four galaxies in our sample do not have 100 μm observations available since they were from other programs that did not observe them: IRAS F02401-0013 (NGC 1068), IRAS F09320+6134 (UGC 05101), IRAS F15327+2340 (Arp 220), and IRAS F21453-3511 (NGC 7130). Column 8 is the PACS observation duration for each scan and cross-scan, unless otherwise noted. We note these are *not* exposure times, but instead the amount of time for each scan and cross-scan. Columns 9 – 10 are the observation dates (in YYYY-MM-DD) for each pair of PACS scan and cross-scan, unless otherwise noted, while column 11 is the Program ID of the PACS program from which the data were obtained. We list the PID corresponding to each number in Table 2.2's caption. The bulk of the data ($\sim$80%) are from OT1_sanders_1, with most of the remaining data from KPGT_esturm_1 and KPOT_pvanderw_1. Column 12 is the SPIRE observation ID which includes all three 250 μm, 350 μm, and 500 μm observations. The scans and cross-scans for each target is combined into one observation. Column 13 is the SPIRE observation duration, which is similar to the PACS duration. Column 14 is the SPIRE observation date, and column 15 is the PID of the SPIRE program from which the data were obtained, similar to the PACS PID column.

2.4 Data Processing and Reduction

The data processing for our *Herschel* data was performed using the Herschel Interactive Processing Environment (HIPE, Ott 2010) version 14 software tool, which provides the

Table 2.2 *Herschel* GOALS Observation Log

			PACS								SPIRE			
#	IRAS Name	Optical Name	Blue 1 Obs. ID	Blue 2 Obs. ID	Green 1 Obs. ID	Green 2 Obs. ID	Duration (sec.)	Blue Obs. Date	Green Obs. Date	PACS PID[a]	Obs. ID	Duration (sec.)	Obs. Date	SPIRE PID[a]
1	F00073+2538	NGC 23	1342225471	1342225472	1342225469	1342225470	198	2011-07-24	2011-07-24	1	1342234681	169	2011-12-18	1
2	F00085-1223	NGC 34, Mrk 938	1342212463	1342212464	1342212465	1342212466	276	2011-01-10	2011-01-10	3	1342199384	445	2010-06-29	3
3	F00163-1039	Arp 256	1342212700	1342212701	1342212702	1342212703	485	2011-01-15	2011-01-15	2	1342234694	169	2011-12-18	1
4	F00344-3349	ESO 350-IG 038	1342210636	1342210637	1342197713	1342197714	65[c]	2010-12-01	2010-06-04	10	1342199386	307	2010-06-29	10
5	F00402-2349	NGC 232	1342238073	1342238074	1342237438	1342237439	240	2012-01-21	2012-01-13	1	1342234699	1217	2011-12-18	1
6	F00506+7248	MCG+12-02-001	1342237174	1342237175	1342237172	1342237173	198	2012-01-11	2012-01-11	1	1342199365	169	2010-06-29	4
7	F00548+4331	NGC 317B	1342213944	1342213945	1342213946	1342213947	347	2011-02-08	2011-02-08	2	1342238255	169	2012-01-27	1
8	F01053-1746	IC 1623, Arp 236	1342212754	1342212755	1342212846	1342212847	65	2011-01-16	2011-01-18	2	1342199388	169	2010-06-29	2
9	F01076-1707	MCG-03-04-014	1342225341	1342225342	1342225343	1342225344	198	2011-07-23	2011-07-23	1	1342234709	169	2011-12-18	1
10	F01159-4443	ESO 244-G012	1342225365	1342225366	1342225363	1342225364	198	2011-07-23	2011-07-23	1	1342234726	169	2011-12-18	1
11	F01173+1405	CGCG 436-030	1342238031	1342238090	1342238088	1342238089	198	2012-01-20	2012-01-21	1	1342237499	169	2012-01-14	1
12	F01325-3623	ESO 353-G020	1342225351	1342225352	1342225353	1342225354	198	2011-07-23	2011-07-23	1	1342234721	169	2011-12-18	1
13	F01341-3735	ESO 297-G011/012	1342213629	1342213630	1342213631	1342213632	485	2011-02-01	2011-02-01	2	1342234720	169	2011-12-18	1
14	F01364-1042		1342238034	1342238035	1342238036	1342238037	198	2012-01-20	2012-01-20	1	1342236227	169	2012-01-02	1
15	F01417+1651	III Zw 035	1342238021	1342238022	1342238023	1342238024	198	2012-01-20	2012-01-20	1	1342237555	307	2012-01-15	1
16	F01484+2220	NGC 695	1342238017	1342238018	1342237464	1342237465	198	2012-01-20	2012-01-13	1	1342238266	169	2012-01-27	1
17	F01519+3640	UGC 01385	1342237168	1342237169	1342237166	1342237167	198	2012-01-11	2012-01-11	1	1342238260	169	2012-01-27	1
18	F02071-1023	NGC 838	1342238855	1342238856	1342238853	1342238854	303	2012-02-09	2012-02-09	1	1342237533	1324	2012-01-14	1
19	F02070+3857	NGC 828	1342237468	1342237469	1342224932	1342224933	198	2012-01-13	2011-07-28	1	1342239822	169	2012-03-01	1
20	F02114+0456	IC 214	1342238796	1342238798	1342238799	1342238797	240	2012-02-08	2012-02-08	1	1342238274	169	2012-01-27	1
21	F02152+1418	NGC 877	1342238869	1342238870	1342238867	1342238868	240	2012-02-09	2012-02-09	1	1342238267	1217	2012-01-27	1
22	F02203+3158	MCG+05-06-036	1342223872	1342223873	1342223874	1342223875	347	2011-07-10	2011-07-10	2	1342238262	169	2012-01-27	1
23	F02208+4744	UGC 01845	1342237995	1342237996	1342237997	1342237998	198	2012-01-19	2012-01-19	1	1342239799	169	2012-02-29	1
24	F02281-0309	NGC 958	1342238801	1342238802	1342223580	1342223581	198	2012-02-08	2011-07-03	1	1342238277	169	2012-01-27	1
25	F02345+2053	NGC 992	1342238873	1342238874	1342238871	1342238872	198	2012-02-09	2012-02-09	1	1342239830	169	2012-03-01	1
26	F02401-0013	NGC 1068	1342189194	1342189195	...	...	909	2010-01-12	2010-01-12	8	1342189425	1076	2010-01-17	8
27	F02435+1253	UGC 02238	1342238792	1342238793	1342238794	1342238795	198	2012-02-08	2012-02-08	1	1342238270	169	2012-01-27	1
28	F02437+2122		1342238875	1342238876	1342238879	1342238880	198	2012-02-09	2012-02-09	1	1342239829	307	2012-03-01	1
28	F02437+2123[b]		1342238877	1342238878	1342238881	1342238882	198	2012-02-09	2012-02-09	1	...	...	...	...
29	F02512+1446	UGC 02369	1342223858	1342223859	1342223860	1342223861	347	2011-07-10	2011-07-10	2	1342239831	169	2012-03-01	1
30	F03117+4151	UGC 02608	1342241466	1342241467	1342241464	1342241465	198	2012-03-15	2012-03-15	1	1342239819	169	2012-03-01	1
30	F03117+4151[b]	UGC 02612	1342241649	1342241651	1342241650	1342241652	198	2012-03-17	2012-03-17	1	...	...	...	...
31	F03164+4119	NGC 1275	1342216022	1342216023	1342204217	1342204218	153	2011-03-14	2011-09-09	2	1342203614	307	2010-08-24	2
32	F03217+4022		1342248716	1342248717	1342248714	1342248715	198	2012-07-26	2012-07-26	1	1342239950	169	2012-03-01	1
33	F03316-3618	NGC 1365	1342222495	1342222496	1342222497	1342222498	1217	2011-06-11	2011-06-11	3	1342201436	999	2010-07-14	3
34	F03359+1523		1342248700	1342248701	1342248698	1342248699	198	2012-07-26	2012-07-26	1	1342239948	307	2012-03-01	1
35	F03514+1546	CGCG 465-012	1342241695	1342241696	1342241693	1342241694	198	2012-03-18	2012-03-18	1	1342239946	169	2012-03-01	1
35	F03514+1546[b]	CGCG 465-011	1342248702	1342248703	1342248704	1342248705	198	2012-07-26	2012-07-26	1	...	...	...	...
36	03582+6012		1342242575	1342242576	1342242573	1342242574	198	2012-03-28	2012-03-28	1	1342239801	169	2012-02-29	1
37	F04097+0525	UGC 02982	1342249943	1342249944	1342250109	1342250110	198	2012-08-20	2012-08-23	1	1342239938	169	2012-03-01	1
38	F04118-3207	ESO 420-G013	1342237452	1342237453	1342237450	1342237451	198	2012-01-13	2012-01-13	1	1342227719	169	2011-09-01	1
39	F04191-1855	ESO 550-IG 025	1342241947	1342241948	1342241945	1342241946	198	2012-03-20	2012-03-20	1	1342239857	169	2012-03-01	1
40	F04210-4042	NGC 1572	1342237422	1342237423	1342241686	1342241687	198	2012-01-12	2012-03-18	1	1342227720	169	2011-09-01	1
41	04271+3849		1342243496	1342243497	1342243494	1342243495	198	2012-03-24	2012-03-24	1	1342229106	169	2011-09-21	1

continued on the next page

Table 2.2. (continued) *Herschel* GOALS Observation Log

			PACS								SPIRE			
#	IRAS Name	Optical Name	Blue 1 Obs. ID	Blue 2 Obs. ID	Green 1 Obs. ID	Green 2 Obs. ID	Duration (sec.)	Blue Obs. Date	Green Obs. Date	PACS PID[a]	Obs. ID	Duration (sec.)	Obs. Date	SPIRE PID[a]
42	F04315-0840	NGC 1614	1342243096	1342243097	1342243410	1342243411	198	2012-03-21	2012-03-24	1	1342203628	169	2010-08-24	4
43	F04326+1904	UGC 03094	1342241971	1342241972	1342241973	1342241974	198	2012-03-20	2012-03-20	1	1342239944	169	2012-03-01	1
44	F04454-4838	ESO 203-IG001	1342240271	1342240272	1342240273	1342240274	198	2012-03-04	2012-03-04	1	1342227722	307	2011-09-01	1
45	F04502-3304	MCG-05-12-006	1342238887	1342238888	1342238889	1342238890	198	2012-02-09	2012-02-09	1	1342229237	169	2011-09-22	1
46	F05053-0805	NGC 1797	1342242528	1342242529	1342242526	1342242527	198	2012-03-28	2012-03-28	1	1342227717	169	2011-09-01	1
46	F05053-0805[b]	NGC 1799	1342242523	1342242524	1342242522	1342242525	198	2012-03-28	2012-03-28	1	...	...	...	...
47	F05054+1718	CGCG 468-002	1342242680	1342242681	1342242678	1342242679	198	2012-03-29	2012-03-29	1	1342227711	169	2011-09-01	1
48	05083+2441		1342241327	1342241328	1342217496	1342217497	198	2012-03-13	2011-03-30	1	1342229651	169	2011-09-23	1
49	F05081+7936	VII Zw 031	1342242561	1342242562	1342242559	1342242560	198	2012-03-28	2012-03-28	1	1342229130	169	2011-09-21	1
50	05129+5128		1342242748	1342242749	1342242746	1342242747	198	2012-03-30	2012-03-30	1	1342229110	307	2011-09-21	1
51	F05189-2524		1342242080	1342242081	1342242082	1342242083	198	2012-03-20	2012-03-20	1	1342203632	169	2010-08-24	4
52	F05187-1017		1342242516	1342242517	1342242518	1342242519	198	2012-03-28	2012-03-28	1	1342239929	169	2012-03-01	1
53	05368+4940	MCG+08-11-002	1342242752	1342242753	1342242750	1342242751	198	2012-03-30	2012-03-30	1	1342229112	169	2011-09-21	1
54	F05365+6921	NGC 1961	1342242565	1342242566	1342242563	1342242564	240	2012-03-28	2012-03-28	1	1342227742	1217	2011-09-02	1
55	F05414+5840	UGC 03351	1342242738	1342242739	1342242740	1342242741	198	2012-03-30	2012-03-30	1	1342229115	169	2011-09-21	1
56	05442+1732		1342242668	1342242669	1342242666	1342242667	198	2012-03-29	2012-03-29	1	1342229653	169	2011-09-23	1
57	F06076-2139		1342242546	1342242547	1342242544	1342242545	198	2012-03-28	2012-03-28	1	1342227695	307	2011-09-01	1
58	F06052+8027	UGC 03410	1342242734	1342242735	1342242732	1342242733	198	2012-03-30	2012-03-30	1	1342229131	583	2011-09-21	1
59	F06107+7822	NGC 2146	1342194051	1342194053	1342194052	1342194054	1934	2010-04-07	2010-04-07	5	1342191186	2167	2010-02-25	5
60	F06259-4708	ESO 255-IG007	1342236648	1342236649	1342236646	1342236647	198	2012-01-06	2012-01-06	1	1342226643	307	2011-08-16	1
61	F06295-1735	ESO 557-G002	1342242713	1342242714	1342242711	1342242712	198	2012-03-29	2012-03-29	1	1342227706	169	2011-09-01	1
62	F06538+4628	UGC 03608	1342242777	1342242778	1342242779	1342242780	198	2012-03-30	2012-03-30	1	1342229649	169	2011-09-23	1
63	F06592-6313		1342233607	1342233608	1342233605	1342233606	198	2011-12-05	2011-12-05	1	1342229669	169	2011-09-23	1
64	F07027-6011	AM 0702-601	1342233595	1342233596	1342233597	1342233598	198	2011-12-05	2011-12-05	1	1342229671	169	2011-09-23	1
65	07063+2043	NGC 2342	1342231560	1342231561	1342231562	1342231563	198	2011-10-29	2011-10-29	1	1342230778	169	2011-10-10	1
66	F07160-6215	NGC 2369	1342233603	1342233604	1342233601	1342233602	198	2011-12-05	2011-12-05	1	1342229670	169	2011-09-23	1
67	07251-0248		1342242707	1342242708	1342242709	1342242710	198	2012-03-29	2012-03-29	1	1342230794	307	2011-10-11	1
68	F07256+3355	NGC 2388	1342244897	1342244898	1342242774	1342244896	303	2012-04-24	2012-03-30[d]	1	1342229477	1324	2011-09-22	1
69	F07329+1149	MCG+02-20-003	1342242701	1342242702	1342242699	1342242700	198	2012-03-29	2012-03-29	1	1342229463	583	2011-09-22	1
69	F07329+1149[b]	NGC 2416	1342242698	1342242697	1342220575	1342242696	198	2012-03-29	2011-05-04[e]	1	...	...	...	...
70	08355-4944		1342226690	1342226691	1342227293	1342227294	198	2011-08-17	2011-08-24	1	1342226978	307	2011-08-20	1
71	F08339+6517		1342252800	1342252801	1342252802	1342252803	198	2012-10-08	2012-10-08	1	1342229120	307	2011-09-21	1
72	F08354+2555	NGC 2623	1342232226	1342232227	1342232228	1342232229	198	2011-11-11	2011-11-11	1	1342206174	169	2010-10-10	4
73	08424-3130	ESO 432-IG006	1342233390	1342233391	1342233392	1342233393	198	2011-12-01	2011-12-01	1	1342230798	169	2011-10-11	1
74	F08520-6850	ESO 060-IG016	1342236932	1342236933	1342236934	1342236935	198	2012-01-07	2012-01-07	1	1342226637	307	2011-08-16	1
75	F08572+3915		1342244254	1342244255	1342232234	1342232235	198	2012-04-13	2011-11-11	1	1342230749	445	2011-10-10	6
76	09022-3615		1342233591	1342233592	1342233593	1342233594	198	2011-12-05	2011-12-05	1	1342230799	445	2011-10-11	6
77	F09111-1007		1342233398	1342233399	1342233396	1342233397	198	2011-12-02	2011-12-02	1	1342245553	307	2012-05-11	1
78	F09126+4432	UGC 04881	1342232391	1342232392	1342232393	1342232394	198	2011-11-17	2011-11-17	1	1342245571	169	2012-05-11	1
79	F09320+6134	UGC 05101	1342220800	1342220801	...	...	111	2011-04-29	2011-04-29	7	1342204962	169	2010-09-21	7
80	F09333+4841	MCG+08-18-013	1342209451	1342209452	1342209453	1342209454	403	2011-11-17	2011-11-17	2	1342230740	307	2011-10-10	1
81	F09437+0317	Arp 303, IC 0563/4	1342221138	1342221139	1342221140	1342221141	485	2011-05-16	2011-05-16	2	1342245559	169	2012-05-11	1
82	F10015-0614	NGC 3110	1342247307[f]	1342247308[f]	1342247305[f]	1342247306[f]	198	2012-06-23	2012-06-23	1	1342234843	169	2011-12-18	1
83	F10038-3338	ESO 374-IG 032	1342237954	1342237955	1342233370	1342233371	198	2012-01-06	2011-12-01	1	1342234831	307	2011-12-17	1

continued on the next page

Table 2.2. (continued) *Herschel* GOALS Observation Log

			PACS								SPIRE			
#	IRAS Name	Optical Name	Blue 1 Obs. ID	Blue 2 Obs. ID	Green 1 Obs. ID	Green 2 Obs. ID	Duration (sec.)	Blue Obs. Date	Green Obs. Date	PACS PID[a]	Obs. ID	Duration (sec.)	Obs. Date	SPIRE PID[a]
84	F10173+0828		1342246207	1342246208	1342246209	1342246210	198	2012-05-27	2012-05-27	1	1342247235	307	2012-06-22	1
85	F10196+2149	NGC 3221	1342231649	1342231650	1342231651	1342231652	198	2011-10-30	2011-10-30	1	1342246610	169	2012-06-03	1
86	F10257-4339	NGC 3256	1342201183	1342201184	1342211985	1342211986	262	2010-07-24	2010-12-16	2	1342200126	307	2010-12-16	2
87	F10409-4556	ESO 264-G036	1342237950	1342237951	1342237952	1342237953	198	2012-01-06	2012-01-06	1	1342236204	169	2012-01-02	1
88	F10567-4310	ESO 264-G057	1342237948	1342237949	1342237946	1342237947	198	2012-01-06	2012-01-06	1	1342236203	169	2012-01-02	1
89	F10565+2448		1342233408	1342233409	1342233410	1342233411	198	2011-12-02	2011-12-02	1	1342234869	445	2011-12-18	6
90	F11011+4107	MCG+07-23-019	1342233414	1342233415	1342233412	1342233413	198	2011-12-02	2011-12-02	1	1342247231	169	2012-06-22	1
91	F11186-0242	CGCG 011-076	1342223691	1342223692	1342223693	1342223694	198	2011-07-04	2011-07-04	1	1342234862	169	2011-12-18	1
92	F11231+1456	IC 2810	1342223678	1342223679	1342223458	1342223459	198	2011-07-04	2011-06-22	1	1342222886	169	2011-06-20	1
93	F11255-4120	ESO 319-G022	1342237944	1342237945	1342237942	1342237943	198	2012-01-06	2012-01-06	1	1342234822	169	2011-12-17	1
94	F11257+5850	NGC 3690, Arp 299	1342210600	1342210601	1342211104	1342211105	485	2010-11-30	2010-12-13	2	1342199344	459	2010-06-29	2
95	F11506-3851	ESO 320-G030	1342237940	1342237941	1342237938	1342237939	198	2012-01-06	2012-01-06	1	1342200129	169	2010-07-09	4
96	F12043-3140	ESO 440-IG058	1342237936	1342237937	1342225087	1342225088	198	2012-01-06	2011-08-01	1	1342236196	169	2012-01-02	1
97	F12112+0305		1342223929	1342223930	1342223612	1342223613	198	2011-07-11	2011-07-03	1	1342234880	169	2011-12-18	1
98	F12116+5448	NGC 4194	1342233545	1342233546	1342235145	1342235146	198	2011-12-04	2011-12-25	1	1342230869	169	2011-10-11	1
99	F12115-4656	ESO 267-G030	1342234409	1342234410	1342234411	1342234412	198	2011-12-16	2011-12-16	1	1342234819	583	2011-12-17	1
99	F12115-4656[b]	ESO 267-G029	1342234413	1342234414	1342234415	1342234416	198	2011-12-16	2011-12-16	1	...	...	...	...
100	12116-5615		1342227110	1342227111	1342227112	1342227113	198	2011-08-23	2011-08-23	1	1342226974	169	2011-08-20	1
101	F12224-0624		1342224336	1342224337	1342224338	1342224339	198	2011-07-17	2011-07-17	1	1342234857	307	2011-12-18	1
102	F12243-0036	NGC 4418	1342224340	1342224341	1342224163	1342224164	240	2011-07-17	2011-07-14	1	1342234883	1217	2011-12-18	1
103	F12540+5708	UGC 08058, Mrk 231	1342199861	1342199862	1342206704	1342206705	65	2010-07-05	2010-10-18	2	1342201218	169	2010-07-26	2
104	F12590+2934	NGC 4922	1342233366	1342233367	1342233012	1342233013	198	2011-12-01	2011-11-25	1	1342234903	307	2011-12-18	1
105	F12592+0436	CGCG 043-099	1342224902	1342224903	1342224904	1342224905	198	2011-07-28	2011-07-28	1	1342234886	307	2011-12-18	1
106	F12596-1529	MCG-02-33-098	1342234383	1342234384	1342234381	1342234382	198	2011-12-15	2011-12-15	1	1342234810	169	2011-12-17	1
107	F13001-2339	ESO 507-G070	1342236638	1342236639	1342236640	1342236641	198	2012-01-06	2012-01-06	1	1342234813	169	2011-12-17	1
108	13052-5711		1342227119	1342227120	1342227117	1342227118	198	2011-08-23	2011-08-23	1	1342226971	169	2011-08-20	1
109	F13126+2453	IC 0860	1342233537	1342233538	1342234367	1342234368	198	2011-12-03	2011-12-15	1	1342234902	169	2011-12-18	1
110	13120-5453		1342227288	1342227289	1342227286	1342227287	198	2011-08-24	2011-08-24	1	1342226970	445	2011-08-20	6
111	F13136+6223	VV 250a	1342209024	1342209025	1342209026	1342209027	347	2010-11-04	2010-11-04	2	1342229508	307	2011-09-22	1
112	F13182+3424	UGC 08387	1342235368	1342235369	1342233010	1342233011	198	2011-12-25	2011-11-25	1	1342198191	169	2010-06-12	4
113	F13188+0036	NGC 5104	1342234375	1342234376	1342234373	1342234374	198	2011-12-15	2011-12-15	1	1342236168	169	2012-01-01	1
114	F13197-1627	MCG-03-34-064	1342236913	1342236914	1342236915	1342236912	198	2012-01-07	2012-01-07	1	1342236178	169	2012-01-01	1
115	F13229-2934	NGC 5135	1342237916	1342237917	1342237918	1342237919	198	2012-01-06	2012-01-06	1	1342202248	169	2010-08-07	4
116	13242-5713	ESO 173-G015	1342237930	1342237931	1342237928	1342237929	198	2012-01-06	2012-01-06	1	1342203562	169	2010-08-23	4
117	F13301-2356	IC 4280	1342237910	1342237911	1342237912	1342237913	198	2012-01-06	2012-01-06	1	1342236191	169	2012-01-02	1
118	F13362+4831	NGC 5256	1342233497	1342233498	1342234363	1342234364	198	2011-12-03	2011-12-15	1	1342232709	169	2011-11-09	1
119	F13373+0105	Arp 240, NGC 5257/8	1342213606	1342213607	1342213608	1342213609	485	2011-02-01	2011-02-01	2	1342234798	169	2011-12-17	1
120	F13428+5608	UGC 08696, Mrk 273	1342208444	1342208445	1342210432	1342210433	153	2010-11-09	2010-11-18	2	1342201217	307	2010-07-26	2
121	F13470+3530	UGC 08739	1342234226	1342234227	1342234224	1342234225	198	2011-12-05	2011-12-05	1	1342236144	169	2012-01-01	1
122	F13478-4848	ESO 221-IG010	1342227128	1342227129	1342227130	1342227131	198	2011-08-23	2011-08-23	1	1342238293	169	2012-01-28	1
123	F13497+0220	NGC 5331	1342213598	1342213599	1342213600	1342213601	347	2011-02-01	2011-02-01	2	1342236165	169	2012-01-01	1
124	F13564+3741	Arp 84, NGC 5394/5	1342211285	1342211286	1342211287	1342211288	550	2010-12-17	2010-12-17	2	1342236140	1253	2012-01-01	1
125	F14179+4927	CGCG 247-020	1342235352	1342235353	1342234361	1342234362	198	2011-12-25	2011-12-15	1	1342232717	169	2011-11-09	1
126	F14280+3126	NGC 5653	1342234240	1342234241	1342233523	1342233524	198	2011-12-05	2011-12-03	1	1342236146	169	2012-01-01	1

continued on the next page

Table 2.2. (continued) *Herschel* GOALS Observation Log

			PACS								SPIRE			
#	IRAS Name	Optical Name	Blue 1 Obs. ID	Blue 2 Obs. ID	Green 1 Obs. ID	Green 2 Obs. ID	Duration (sec.)	Blue Obs. Date	Green Obs. Date	PACS PID[a]	Obs. ID	Duration (sec.)	Obs. Date	SPIRE PID[a]
127	F14348-1447		1342236610	1342236611	1342236612	1342236613	198	2012-01-06	2012-01-06	1	1342238301	445	2012-01-28	6
128	F14378-3651		1342238053	1342238054	1342225403	1342225404	198	2012-01-20	2011-07-24	1	1342238295	445	2012-01-28	6
129	F14423-2039	NGC 5734	1342237184	1342237185	1342237186	1342237187	240	2012-01-12	2012-01-12	1	1342227731	1217	2011-09-01	1
130	F14547+2449	VV 340a, Arp 302	1342235382	1342235383	1342235384	1342235385	198	2011-12-25	2011-12-25	1	1342234779	169	2011-12-17	1
131	F14544-4255	IC 4518A/B	1342225308	1342225309	1342225306	1342225307	198	2011-07-23	2011-07-23	1	1342240003	169	2012-03-02	1
132	F15107+0724	CGCG 049-057	1342236624	1342236625	1342236626	1342236627	198	2012-01-06	2012-01-06	1	1342203077	169	2010-08-15	4
133	F15163+4255	VV 705	1342234242	1342234243	1342234244	1342234245	198	2011-12-05	2011-12-05	1	1342229532	169	2011-09-22	1
134	15206-6256	ESO 099-G004	1342238067	1342238068	1342238065	1342238066	198	2012-01-20	2012-01-20	1	1342229209	169	2011-09-22	1
135	F15250+3608		1342235398	1342235399	1342235400	1342235401	198	2011-12-25	2011-12-25	1	1342234775	445	2011-12-17	6
136	F15276+1309	NGC 5936	1342236904	1342236905	1342236902	1342236903	198	2012-01-07	2012-01-07	1	1342238324	169	2012-01-28	1
137	F15327+2340	Arp 220, UGC 09913	1342189033	1342189034	...	...	293	2010-01-06	2010-01-06	8	1342188687	619	2009-12-29	8
138	F15437+0234	NGC 5990	1342225290	1342225291	1342225292	1342225293	198	2011-07-22	2011-07-22	1	1342238312	169	2012-01-28	1
139	F16030+2040	NGC 6052	1342225429	1342225430	1342225427	1342225428	198	2011-07-24	2011-07-24	1	1342229560	169	2011-09-23	1
140	F16104+5235	NGC 6090	1342233360	1342233361	1342233358	1342233359	198	2011-12-01	2011-12-01	1	1342229529	307	2011-09-22	1
141	F16164-0746		1342241414	1342241415	1342262221	1342262222	198	2012-03-14	2013-01-28	1	1342229568	169	2011-09-23	1
142	F16284+0411	CGCG 052-037	1342241365	1342241366	1342241367	1342241368	198	2012-03-14	2012-03-14	1	1342229572	169	2011-09-23	1
143	16304-6030	NGC 6156	1342241537	1342241538	1342241539	1342241540	198	2012-03-16	2012-03-16	1	1342229213	169	2011-09-22	1
144	F16330-6820	ESO 069-IG006	1342241669	1342241670	1342241667	1342241668	198	2012-03-17	2012-03-17	1	1342230810	169	2011-10-11	1
145	F16399-0937		1342238822	1342238823	1342238824	1342238825	198	2012-02-09	2012-02-09	1	1342229188	169	2011-09-22	1
146	F16443-2915	ESO 453-G005	1342241448	1342241449	1342241450	1342241451	198	2012-03-15	2012-03-15	1	1342229199	169	2011-09-22	1
147	F16504+0228	NGC 6240	1342213938	1342213939	1342213936	1342213937	71	2011-02-08	2011-02-08	2	1342203586	332	2010-08-23	2
148	F16516-0948		1342238828	1342238829	1342238826	1342238827	198	2012-02-09	2012-02-09	1	1342229189	169	2011-09-22	1
149	F16577+5900	NGC 6286, Arp 293	1342209331	1342209332	1342209333	1342209334	485	2010-11-10	2010-11-10	2	1342229148	169	2011-09-21	1
150	F17132+5313		1342234345	1342234346	1342234343	1342234344	198	2011-12-15	2011-12-15	1	1342229150	307	2011-09-21	1
151	F17138-1017		1342241454	1342241455	1342241456	1342241457	198	2012-03-15	2012-03-15	1	1342229190	169	2011-09-22	1
152	F17207-0014		1342241373	1342241374	1342241375	1342241376	198	2012-03-14	2012-03-14	1	1342203587	169	2010-08-23	4
153	F17222-5953	ESO 138-G027	1342241671	1342241672	1342241673	1342241674	198	2012-03-17	2012-03-17	1	1342229216	169	2011-09-22	1
154	F17530+3447	UGC 11041	1342231901	1342231902	1342231903	1342231904	198	2011-11-05	2011-11-05	1	1342229169	169	2011-09-22	1
155	F17548+2401	CGCG 141-034	1342231911	1342231912	1342231909	1342231910	198	2011-11-05	2011-11-05	1	1342229175	169	2011-09-22	1
156	17578-0400		1342241377	1342241378	1342241379	1342241380	198	2012-03-14	2012-03-14	1	1342229187	169	2011-09-22	1
157	18090+0130		1342241357	1342241358	1342231115	1342231116	198	2012-03-13	2011-10-18	1	1342229185	169	2011-09-22	1
158	F18131+6820	NGC 6621, Arp 81	1342212029	1342212030	1342212031	1342212032	403	2010-12-16	2010-12-16	2	1342220865	169	2011-05-13	1
159	F18093-5744	IC 4687	1342207063	1342207064	1342207065	1342207066	485	2010-09-21	2010-10-25	2	1342204955	169	2010-10-25	4
160	F18145+2205	CGCG 142-034	1342231915	1342231916	1342231913	1342231914	198	2011-11-05	2011-11-05	1	1342229176	169	2011-09-22	1
161	F18293-3413		1342240663	1342240664	1342240661	1342240662	198	2012-03-06	2012-03-06	1	1342204954	169	2010-09-21	4
162	F18329+5950	NGC 6670A/B	1342232433	1342232434	1342235330	1342235331	198	2011-11-17	2011-12-25	1	1342229139	169	2011-09-21	1
163	F18341-5732	IC 4734	1342241541	1342241542	1342241543	1342241544	198	2012-03-16	2012-03-16	1	1342229222	169	2011-09-22	1
164	F18425+6036	NGC 6701	1342232435	1342232436	1342235328	1342235329	198	2011-11-17	2011-12-25	1	1342229137	169	2011-09-21	1
165	F19120+7320	VV 414, NGC 6786	1342220812	1342220813	1342220814	1342220815	403	2011-04-29	2011-04-29	2	1342220623	169	2011-05-08	1
166	F19115-2124	ESO 593-IG008	1342216478	1342216479	1342216476	1342216477	198	2011-03-21	2011-03-21	1	1342215995	169	2011-03-13	1
167	F19297-0406		1342241615	1342241616	1342241617	1342241618	198	2012-03-16	2012-03-16	1	1342230837	445	2011-10-11	6
168	19542+1110		1342244232	1342244233	1342244234	1342244235	198	2012-04-12	2012-04-13	1	1342230847	169	2011-10-11	1
169	F19542-3804	ESO 339-G011	1342216466	1342216467	1342216464	1342216465	198	2011-03-20	2011-03-20	1	1342230821	169	2011-10-11	1
170	F20221-2458	NGC 6907	1342232508	1342232509	1342217433	1342217434	240	2011-11-19	2011-03-30	1	1342230828	1217	2011-10-11	1

continued on the next page

Table 2.2. (continued) *Herschel* GOALS Observation Log

			PACS								SPIRE			
#	IRAS Name	Optical Name	Blue 1 Obs. ID	Blue 2 Obs. ID	Green 1 Obs. ID	Green 2 Obs. ID	Duration (sec.)	Blue Obs. Date	Green Obs. Date	PACS PID[a]	Obs. ID	Duration (sec.)	Obs. Date	SPIRE PID[a]
171	20264+2533	MCG+04-48-002	1342244230	1342244231	1342244228	1342244229	198	2012-04-12	2012-04-12	1	1342233320	169	2011-11-30	1
172	F20304-0211	NGC 6926	1342243832	1342243833	1342232514	1342232515	198	2012-04-06	2011-11-19	1	1342218992	169	2011-04-10	1
173	20351+2521		1342218714	1342218715	1342218716	1342218717	198	2011-04-17	2011-04-17	1	1342233323	169	2011-11-30	1
174	F20550+1655	II Zw 096	1342243838	1342243839	1342243840	1342243841	198	2012-04-06	2012-04-06	1	1342233327	169	2011-11-30	1
175	F20551-4250	ESO 286-IG019	1342217438	1342217439	1342232496	1342232497	198	2011-03-30	2011-11-19	1	1342230815	445	2011-10-11	6
176	F21008-4347	ESO 286-G035	1342217440	1342217441	1342232498	1342232499	198	2011-03-30	2011-11-19	1	1342230813	169	2011-10-11	1
177	21101+5810		1342235326	1342235327	1342235324	1342235325	198	2011-12-25	2011-12-25	1	1342220627	169	2011-05-08	1
178	F21330-3846	ESO 343-IG013	1342243782	1342243783	1342232500	1342232501	198	2012-04-06	2011-11-19	1	1342244162	169	2012-04-12	1
179	F21453-3511	NGC 7130	1342218550	1342218551	...	...	115	2011-04-11	2011-04-11	7	1342210527	169	2010-11-23	7
180	F22118-2742	ESO 467-G027	1342234426	1342234427	1342234428	1342234429	198	2011-12-16	2011-12-16	1	1342245428	169	2012-05-06	1
181	F22132-3705	IC 5179	1342234099	1342234100	1342234101	1342234102	198	2011-12-14	2011-12-15	1	1342244158	169	2012-04-11	1
182	F22287-1917	ESO 602-G025	1342244875	1342244876	1342244877	1342244878	198	2012-04-23	2012-04-23	1	1342234670	169	2011-12-18	1
183	F22389+3359	UGC 12150	1342222924	1342222925	1342235322	1342235323	198	2011-06-22	2011-12-25	1	1342220870	169	2011-05-13	1
184	F22467-4906	ESO 239-IG002	1342233627	1342233628	1342232476	1342232477	198	2011-12-05	2011-11-18	1	1342234738	307	2011-12-19	1
185	F22491-1808		1342235609	1342235610	1342235611	1342235612	198	2011-12-26	2011-12-26	1	1342234671	445	2011-12-18	6
186	F23007+0836	NGC 7469, Arp 298	1342211775	1342211776	1342211777	1342211778	485	2010-12-27	2010-12-27	2	1342196915	169	2010-05-24	4
187	F23024+1916	CGCG 453-062	1342237366	1342237367	1342237364	1342237365	198	2012-01-12	2012-01-12	1	1342234765	169	2011-12-19	1
188	F23128-5919	ESO 148-IG002	1342211955	1342211956	1342209486	1342209487	71	2010-12-15	2010-11-18	2	1342209299	169	2010-11-09	2
189	F23135+2517	IC 5298	1342234090	1342234091	1342234092	1342234093	198	2011-12-14	2011-12-14	1	1342234766	169	2011-12-19	1
190	F23133-4251	NGC 7552	1342211631	1342211632	1342211633	1342211634	121	2010-12-27	2010-12-27	2	1342210528	639	2010-11-23	2
191	F23157+0618	NGC 7591	1342236592	1342236593	1342236590	1342236591	198	2012-01-06	2012-01-06	1	1342234758	169	2011-12-19	1
192	F23157-0441	NGC 7592	1342221802	1342221803	1342221804	1342221805	198	2011-05-28	2011-05-28	1	1342234750	169	2011-12-19	1
193	F23180-6929	ESO 077-IG014	1342232486	1342232487	1342234424	1342234425	198	2011-11-18	2011-12-16	1	1342230804	169	2011-10-11	1
194	F23254+0830	NGC 7674, HCG 96	1342237355	1342237356	1342237353	1342237354	198	2012-01-12	2012-01-12	1	1342234929	445	2011-12-18	9
195	23262+0314	NGC 7679	1342237347	1342237348	1342221786	1342221787	198	2012-01-12	2011-05-28	1	1342234755	583	2011-12-19	1
195	23262+0314[b]	NGC 7682	1342237351	1342237352	1342237349	1342237350	198	2012-01-12	2012-01-12	1	...	...	...	...
196	F23365+3604		1342237856	1342237857	1342225459	1342225460	198	2012-01-05	2011-07-24	1	1342234919	445	2011-12-18	6
197	F23394-0353	MCG-01-60-022	1342221749	1342221750	1342237337	1342237338	240	2011-05-27	2012-01-12	1	1342234751	583	2011-12-19	1
197	F23394-0353[b]	Mrk 933	1342221801	1342221799	1342221800	1342221798	240	2011-05-28	2011-05-28	1	...	...	...	...
198	23436+5257		1342237876	1342237877	1342237874	1342237875	198	2012-01-05	2012-01-05	1	1342236249	169	2012-01-03	1
199	F23444+2911	Arp 86, NGC 7752/3	1342225463	1342225464	1342225465	1342225466	303	2011-07-24	2011-07-24	1	1342234921	1324	2011-12-18	1
200	F23488+1949	NGC 7771	1342222930	1342223182	1342223183	1342223181	198	2011-06-22	2011-06-23	1	1342199379	169	2010-06-29	4
201	F23488+2018	Mrk 331	1342225242	1342225243	1342225240	1342225241	240	2011-07-22	2011-07-22	1	1342234682	583	2011-12-18	1

The observing log for our *Herschel* data, see §2.4.3 for a description of each column. [a]PI list: 1 = OT1_sanders_1; 2 = KPGT_esturm_1; 3 = GT1_msanchez_2; 4 = KPOT_pvanderw_1; 5 = KPOT_rkennicu_1; 6 = OT1_dfarrah_1; 7 = GT1_lspinogl_2; 8 = cwilso01_1 (including KPGT); 9 = OT1_mcluver_2; 10 = KPGT_smadde01_1. [b]These are very widely separated galaxy pairs that required two *Herschel* PACS observations. [c]Green 1 and Green 2 have durations of 65 sec., Blue 1 has a duration of 141 sec. and Blue 2 has a duration of 153 sec. [d]Green 2 was observed on 2012-04-24. [e]Green 2 was observed on 2012-03-29. [f]Rescheduled to replace previous PACS observations: 1342245766 1342245767 1342245764 1342245765.

means to download, reduce, and analyze our data. All of our data reduction routines are derived from the standard pipeline scripts found within HIPE, where the programming language of choice is Jython (a Java implementation of the popular Python language). In addition to handling the data processing, HIPE also downloads and maintains all of the instrument calibration files needed for the data processing.

2.4.1 PACS Data Reduction

Choosing a PACS Map Maker

Due to the bolometer and scanning nature of the PACS instrument, it was important to determine the best map-making software to translate the time ordered data (TOD) into an image. The PACS bolometers (indeed all bolometers) produce noise that increases as one approaches lower temporal frequencies, commonly referred to as $1/f$ noise, that must be removed by the map-maker. If this noise is left uncorrected in the time ordered data, the result would be severe striping or even gradients across the image. In addition the map making software must also remove the bolometers' common mode drift (which is a changing offset as function of time) from the TOD, termed *pre-processing*, as well as cosmic ray hits and individual bolometer drift. The PACS team released a Map-making Tool Analysis and Benchmarking report[1] in November 2013 with an update in March 2014 that characterized in detail the six different map making packages available to reduce PACS data. We summarize the information presented in this report below to decide upon the best map making software to use, since it was important that all of the *Herschel* data on our sample were processed uniformly.

The PACS team tested the performance of six different publicly available map-making packages: MADMap (Microwave Anisotropy Dataset mapper, Cantalupo et al. 2010), SANEPIC (Signal And Noise Estimation Procedure Including Correlation, Patanchon et al.

[1] `http://herschel.esac.esa.int/twiki/pub/Public/PacsCalibrationWeb/pacs_mapmaking_report_ex_sum_v3.pdf`

2008), Scanamorphos (Roussel 2013), JScanam (Jython Scanamorphos[2]), Tamasis (Tools for Advanced Map-making, Analysis and SImulations of Submillimeter surveys, Barbey et al. 2011), and Unimap (Piazzo et al. 2015) (see §2 and §4 of the Map-making Tool and Analysis Benchmarking report for a description of each code). We did not consider the PACS high pass filter (HPF) reduction software, since HPF maps are background-subtracted and will miss a significant amount of extended emission outside approximately one beam area. To evaluate each of the packages, a combination of simulated and real data from PACS were used. Except in a few cases, most of our fluxes are within the Benchmarking report's "bright flux regime" of 0.3 – 50 Jy, while the "faint flux regime" is defined to be 0.001 – 0.1 Jy (see Figure 2.5). Below we summarize the five tests performed on each map maker from the benchmarking report:

1) A power spectrum analysis which tests the map maker's ability to remove noise while preserving extended fluxes over large angular sizes on the map. This tests each code's performance in removing the $1/f$ noise from the PACS data, and consequently how well gradients and stripes are removed from the maps.

2) A difference matrix is computed for each map maker's output, which evaluates differences in fluxes for individual sky pixels over the entire image. $(S - S_{\rm true})$ is computed for each pixel and plotted against $S_{\rm true}$, and the resulting scatter, offset, and slope is evaluated.

3) Each map maker's performance in point source photometry is compared to fluxes measured from the HPF maps for both bright (0.3 – 50 Jy) and faint (0.001 – 0.1 Jy) cases. Since the HPF maps produced by HIPE are designed specifically for the case of point sources, they provide the most accurate reference point source fluxes.

4) Extended source photometry tests each map maker's ability to recover extended flux over large areas of the map. To assess this, each code's output is compared to IRAS data on M31 from the Improved Reprocessing of the IRAS Survey (IRIS, Miville-Deschênes & Lagache 2005).

[2]This is the HIPE/PACS implementation of the Scanamorphos algorithm however they both differ in many assumptions, hence why they were tested separately.

5) The noise characteristics each map maker introduces into the final map are evaluated. This includes statistical tests on the pixel-to-pixel variance as well as the shape of the overall distribution of fluxes in each map pixel. The noise patterns are also evaluated with regard to how isotropic the noise appears in the maps.

Considering the results of these extensive tests, it was difficult to select the best map maker for our PACS data. We rejected the High Pass Filter method outright since many of our galaxies are easily resolved at the PACS wavelengths, and would therefore have a significant amount of extended flux missed by the HPF pipeline. We decided against using SANEPIC since it significantly overestimated the true flux for both bright and faint point source photometry. We also ruled out using Tamasis since it has a tendency to introduce more pronounced noise along the scan directions. This left us with four remaining choices: JScanam, MADMap, Scanamorphos, and Unimap. We finally decided on using JScanam to reduce all of our PACS data, as it gave the best balance between photometric accuracy and map quality. Specifically, it reproduced a power spectrum closest to the original, it had the flattest $(S - S_{\rm true})$ vs. $S_{\rm true}$ plot, and it yielded the most accurate photometry for both point and extended sources in both channels.

For a small fraction of our maps where JScanam could not remove all of the image artifacts (usually gradients due to non-optimal baseline subtraction), we used Unimap to process the data, since it performed just as well as JScanam. Unlike JScanam, Unimap approaches map making differently, using the Generalized Least Square (GLS) approach, which is also known as the Maximum Likelihood method if the noise has a Gaussian distribution. For a very few cases where even Unimap did not produce optimal results, we resorted to using MADMap. This map maker requires that the noise properties of the detectors are determined *a-priori*, from which a noise filter can be generated to filter out the $1/f$ noise. Finally, despite that not all of the PACS maps were generated using the same map maker, we note that the resulting photometry from all three map makers are remarkably consistent as shown in the Benchmarking report (and addendum) from the

PACS team, hence giving one the freedom to use the map maker that produces the best image quality.

PACS Map Making With JScanam

All of our *Herschel*-GOALS PACS data were reduced in HIPE 14 using the latest available PACS calibration version 72_0 released in December 2015. In order to alleviate the processing time for all 211 objects, we started our data processing from the Level 1 products downloaded from the HSA. These Level 1 data products have the advantage of an improved reconstruction of the actual *Herschel* spacecraft pointing, which reduces distortions on the PSF due to jitter effects. Compared to previous maps from our data processing, the new maps have slight shifts of up to $\sim 1\farcs5$, and slightly smaller PSFs in unresolved GOALS objects.

Since each PACS scan and cross-scan are separate observations, JScanam requires two observations each for the blue and green data. On the other hand the red channel data are observed simultaneously regardless if the blue or green filter is used, so we have four observations in the red channel. Processing for both the blue and red cameras are identical, with the red data requiring a further step of combining the two pairs of scan and cross-scan data. Below we describe the key steps in the data reduction process.

After loading each scan and cross-scan observation context from HSA into HIPE, the first step was to execute the task `photAssignRaDec` to assign the RA and declination coordinates to each pixel in each frame which allows JScanam to run faster. The next step was to remove the unnecessary frames taken during each turnaround in the scan or cross-scan using the `scanamorphosRemoveTurnarounds` task. We opted to use the default speed limit which is $\pm 50\%$ of our nominal scan speed ($20''$/sec.), so any frames taken at scan speeds below $10''$/sec. or above $30''$/sec. were removed. After turnaround removal the `scanamorphosMaskLongTermGlitches` task in JScanam goes through the detector timelines and masks any long term glitches.

At this point we have a detector timeline of flux detected by the bolometers as a function of time with the turnarounds and long term glitches removed. Using the `scanamorphosScanlegBaselineFitPerPixel` task, our next step is to subtract a linearly fit baseline from each bolometer pixel of every scan leg, with the intention of creating a "naive" map for source masking purposes. This is done iteratively where the most important parameter is the `nSigma` variable, which controls the threshold limit for source removal. For our data any points above `nSigma`=2 times the standard deviation of the unmasked data are considered real sources, until the iteration converges.

The next step is to join the scan and cross-scan data together for a higher signal-to-noise map to create the source mask. In the `scanamorphosCreateSourceMask` task we set a `nSgima`=4, so that any emission above 4 standard deviations is masked out. At this point it is not necessary to mask out all of the faint extended emission, only the brightest regions. After the source mask is determined, they are applied to the individual scan and cross-scan timelines and the real processing begins.

With the `galactic` option set to "true" in `scana- morphosBaselineSubtraction`, we only want to remove an offset in the time ordered data over all the scan legs, and subtract it from all the frames. This is done by calculating a median offset over only the unmasked part of the data which importantly does not include any bright emission, and subtracting it from each pixel's timeline. This is so that extended flux is treated correctly when subtracting the baseline (due to the telescope's own infrared emission) from the signal timelines, even in cases where the emission is not concentrated in a small region. We emphasize this does not imply the subtraction of the Galactic foreground emission from our maps.

Once the baseline is removed we need to identify and mask the signal drifts produced by the calibration block observation. In previous versions of our reduction, these drifts have produced very noticeable gradients in our final maps. To do this the task `scanamorphosBaselinePreprocessing` assumes that the scan and cross-scan are orthogonal to each other, which would result in gradients in different directions. The drift removal is also based on the assumption that the drift power increases with the length

of the considered time ($1/f$ noise). For this reason the first iteration removes the drift component over the longest time scale which corresponds to the entire scan (or cross-scan). After that drifts are removed over four scan legs, and finally over one scan leg, with the remaining drift in each successive iteration becoming weaker. In order to actually calculate the drift in each iteration, a single scan (or scan legs) is back projected over itself in the orthogonal direction, which transforms the generally increasing or decreasing signal drift into oscillatory drifts that cancel out on large time scales. The orthogonal back projected timeline is then subtracted from the scan timeline, and the difference which represents the drift is fitted by a line.

At this point the scan and cross-scan data have been cleaned enough to be combined. Since signal drifts were only eliminated over timescales down to one scan leg, the next step is to remove them from over time scales shorter than one scan leg. These drifts are due to for example cosmic ray hits on the PACS instruments, which produce different effects on the time ordered data depending on which part is hit. If an individual bolometer or bolometer wall is hit, it only affects those bolometer(s). However if a cosmic ray hits the readout electronics, it introduces a strong positive or negative signal for all of the bolometers read by the electronics, which can be anything from a single bolometer to an entire detector group. These jumps typically last a few tens of seconds before settling to the previous level again, and would result in stripes across the final map if not properly removed.

To remove these individual drifts, we use the task `scanamorphosIndividualDrifts` to first measure the scan speed and calculate the size of a map pixel that can hold six subsequent samples of a detector pixel crossing it. We use a threshold of `nSigma`=5 which is large enough to include the strongest drifts but still masking out the real source. Then the average flux value and standard deviation from the detector pixels crossing that map pixel is calculated, along with the number of detector pixels falling into that map pixel. Using the threshold noise value (from the calibration files), we eliminate any individual detector fluxes for that map pixel that has a standard deviation greater than the noise threshold.

The missing values are then linearly interpolated, and the individual drift is subtracted from the detector timeline.

After all of the individual drifts are corrected, the time ordered data are saved and we project the timelines from both the scans and cross-scans into our final map using the `photProject` task. We use a pixel scale of $1\farcs6$ pixel^{-1} for the 70 μm and 100 μm maps, and a pixel scale of $3\farcs2$ pixel^{-1} for the 160 μm maps. By default the `photProject` task assumes in projection an active pixel size of 640 μm, however if we 'drizzle' the projection we can assume smaller PACS pixels. This allows us to reduce the noise correlation between neighboring map pixels and also sharpens the PSF. We used a `pixfrac` of 0.1, which controls the ratio between the input detector pixel size and the map pixel size. At this point the 70 μm and 100 μm maps are finished. For the 160 μm data, both pairs of scan and cross-scan are identically processed separately, and then combined in the end using `photProject` again.

2.4.2 SPIRE Data Reduction

Choosing a SPIRE Map Maker

Similar to the PACS instrument, the SPIRE detectors exhibit certain effects that are characteristic to bolometers. Namely, they introduce an increasing amount of noise as the length of the considered time increases ($1/f$ noise), as well as constant and changing offsets (drifts) which could result in stripes or gradients in the final image. Therefore any map maker for SPIRE must be able to remove these instrumental effects, while preserving flux (point source and extended) and creating distortion-free maps. The SPIRE team released a Map Making Test Report[3] in January 2014 that benchmarked in depth seven different map making codes, several of which were also present in the PACS Map Making report. The map makers that participated in the benchmarking were the Naive Mapper, Destriper in two flavors (P0 and P1), Scanamorphos, SANEPIC, and Unimap. The two flavors of the Destriper differ in the polynomial order used to subtract the baseline, where

[3] `http://arxiv.org/pdf/1401.2109v1.pdf`

P0 corresponds to a polynomial order of 0 (i.e., the mean) and P1 corresponds to an order of 1. Two additional super-resolution map makers were also tested, however we did not consider them for processing our SPIRE data. For a summary of each map maker we refer the reader to the SPIRE Map Making Test Report.

For the Map Making Test Report, the authors tested these five map makers based on a variety of benchmarks that are very similar to the PACS Map-Making Tool Analysis and Benchmarking report. A combination of real and simulated SPIRE data were used, covering the full variety of science cases such as faint vs. bright sources, extended vs. point sources, and complex vs. empty fields. The simulated SPIRE data have the advantage of comparing each of the map makers' outputs to the "truth" image, allowing for an unbiased comparison between all of the map making codes. These simulated observations were synthesized from two different layers: a truth layer based on a real or artificial source, and a noise layer from real SPIRE observations so that both instrumental and confusion noise is accurately represented. Below we summarize the four metrics and performance results for the five possible map makers:

1) Using simulated data, the deviation of each map maker's output is compared to the original synthetic data. To quantify the deviation from truth, a scatter plot of $(S - S_{\rm true})$ is plotted against $S_{\rm true}$, and the resulting slopes, relative deviations, and absolute deviations are compared.

2) The 2D power spectrum of each map makers' output is compared to the "truth" image. The goal here is to quantify how well $1/f$ noise is removed from the maps while leaving real fluxes (point and extended) intact, as well as how high spatial frequency (small spatial scale) fluxes are treated.

3) Using the simulated data, point source photometry from each of the map makers were compared to the "truth" images. This tests how well point source fluxes are recovered by each map maker in both the bright ($S \approx 300$ mJy) and faint ($S \approx 30$ mJy) regimes.

4) Finally, extended source photometry was tested between all the map makers using the synthetic data. A simulated exponential disk with an e-folding radius of $90''$was used, and fluxes were measured using aperture photometry.

Using the results from these tests, we concluded that the best map maker to use was the Destriper P0 mapper. It performed remarkably well among the other map makers, especially in cases where complex extended emission is present. Although the Map Making report warned about its inability to properly remove the "cooler burp" effect, the most recent version of Destriper P0 in HIPE 14 was updated to include proper treatment of this instrument effect. On the other hand Destriper P1 compared unfavorably, especially in introducing artificial gradients in many cases. The Naive Mapper was also ruled out due to it frequently over-subtracting the background where extended emission is present. The map maker SANEPIC showed significant deviations from the "truth" map, because the code makes some incorrect assumptions about the data. Finally, although Scanamorphos can handle faint pixels very well, it showed significant deviations in the bright pixel case ($S > 0.2$ Jy). This is important since many galaxies in our sample are nearby and thus quite bright.

In HIPE 14, we used a more advanced version of the Destriper code called the "SPIRE 2-Pass Pipeline" that was released by the SPIRE instrument team. The basic pipeline processing steps and settings follow exactly that of the Destriper P0 (or P1 if the user so chooses) map maker, with the added benefit of producing exceptionally clean maps to be used in the final *Herschel* Science Archive. Specifically, the 2-Pass Pipeline mitigates residual faint tails and glitches in the timeline, which if not removed can produce ringing effects. The primary aim of this pipeline is to produce maps with better detections of outliers in the TOD such as glitches, glitch tails, and signal jumps, and remove any Fourier ringing that would result from failed outlier detections. As an overview, the first pass runs a stripped down version of the pipeline using only the bare minimum tasks that excludes any Fourier analysis. This includes running the Second Level Deglitching task to produce

a mask over the glitches, which is then applied back to the Level 0.5 products[4]. Then a second pass of the pipeline is executed identical to the original Destriper map maker.

SPIRE Map Making With 2-Pass Pipeline and Destriper P0

Our final SPIRE maps were reduced in HIPE 14 using the latest calibration version `SPIRECAL_14_2` released in December 2015. Below we summarize the key data reduction steps, however a more detailed description on the photometer pipeline can be found within Dowell et al. (2010).

Our data processing begins with the Level 0 data products downloaded from HSA, which are the raw data formatted from satellite telemetry containing the readout in ADU from each SPIRE bolometer. After an observation is loaded into HIPE, the first step is to execute the Common Engineering Conversion and format it into Level 0.5 products. These products are the uncalibrated and uncorrected timelines measured in Volts, and contain all of the necessary information to build science-grade maps.

The first step in processing our data from Level 0.5 to Level 1 is to join all the scan legs and turnarounds together. The turnaround occurs when the spacecraft turns around after a scan leg to begin another scan. We opted to use the turnaround data to include as much data within our maps as possible. Next the pipeline produces the pointing information for the observation, based on the positions of the SPIRE Beam Steering Mechanism as well as the offset between SPIRE and the spacecraft itself (referred to as the Herschel Pointing Product). This results in the SPIRE Pointing Product which is used later on in the pipeline. After calculating the pointing information, the pipeline corrects for any electrical crosstalk between the thermistor-bolometer channels. The thermistors measure the temperature of the array bath as a function of time so that later we may accurately subtract the instrument thermal contribution, or temperature drift from the data timelines.

The next step is the signal jump detector, which detects and removes jumps in the thermistor timelines that would otherwise cause an incorrect temperature drift correction.

[4]The Level 0.5 products are the output after running the raw satellite telemetry through the engineering pipeline.

To do this, the module subtracts baselines and smoothed medians from the thermistor timelines to identify any jumps. After deglitching the thermistor timelines, we must deglitch any cosmic ray hits on the bolometers themselves. This is an important step since any glitches that are not removed would manifest itself as image artifacts on the final maps. The pipeline does this in two steps, where the first step is to remove glitches that occur simultaneously in groups of connected bolometer detectors. This can occur when a cosmic ray hits the substrate of an entire photometer array, and can leave an imprint of the array on the final map. The second step is to run the wavelet deglitcher on the timeline data, which uses a complex algorithm to remove glitches in Fourier space.

After deglitching the detector timelines, a low pass filter response correction is applied to the TOD. This is to take into account the delay in the electronics with respect to the telescope position along a scan, in order to ensure a match between the astrometric timeline from the telescope, and the detector timeline from the instrument. At this point we can apply the flux conversion to the detector timelines, changing the units from Volts to Jy beam^{-1}. The next step involves corrections to the timelines due to temperature drifts, which are caused by variations of the detector array bath temperatures. First, with the `coolerBurpCorrection` flag set to `true`, the pipeline flags data that were affected by the "cooler burp" effect. Observations taken during this effect, usually in the first $\sim$8 hours of SPIRE observations, can create unusual temperature drifts. The temperature drift correction step then removes low frequency noise by subtracting a correction timeline for each detector using data and calibration information. The "cooler burp" is also removed at this stage by applying additional multiplicative factors to the correction timeline.

Next we apply a bolometer time response correction which corrects any remaining low-level slow response from the bolometers. This is done by multiplying the timelines in Fourier space by an appropriate transfer function obtained from a calibration file containing the detector time constants. After this step we attach the RA and declination to the data timelines by using the SPIRE Pointing Product generated earlier. Since many of our objects are extended in nature, we must apply an additional extended emission gain correction for

individual SPIRE bolometers. This is because the pipeline so far assumes uniform beams across the array, whereas in reality there exists small variations among different bolometers due to their positions on the array.

We then use the Destriper to remove striping from the final maps. Since the dominant fluxes seen by SPIRE are from the telescope itself, the science signal is very small in comparison. Therefore to isolate the science signal we must subtract out thermal contributions from the telescope. However even after doing this, there are still large differences in residual offsets between different bolometers due to variations in the thermal and electronic aspects of the system, resulting in striping. This is where the Destriper P0 comes in, which effectively takes as input SPIRE Level 1 context, and outputs destriped Level 1 timelines. To do this we first subtract a median baseline as an initial guess, then we use a polynomial order of 0 to iteratively update the offsets in the TOD for each detector until an optimal solution is found. This algorithm effectively normalizes the map background to zero, however we do include the true background using data from the *Planck* High Frequency Instrument (HFI) for the PMW and PLW arrays (see §2.6.2). After destriping we run the optional second level deglitching in order to remove any residual glitches that may still remain.

At this point the data have been processed to Level 1, and in the case of the first pass, only tasks that don't involve any manipulation in Fourier space were omitted. The resulting second level deglitching mask from the first pass of this pipeline is applied to the Level 0.5 data, and the entire process is repeated in a second pass, this time including operations in Fourier space.

The final step in our SPIRE data reduction is to project the drift-corrected, deglitched, and destriped timelines into our Level 2 science grade map. To do this we use a Naive Mapper, which simply projects the full power seen by a bolometer onto the nearest map pixel. The final map pixel scales used were $6''$, $10''$, and $14''$ for the PSW, PMW, and PLW arrays respectively. For each instant of time on each bolometer's timeline, the measured flux is added to the total signal map and a value of 1 is added to the coverage map. Once

this is done for all bolometer timelines, the total signal map is divided by the coverage map to obtain the flux density map.

Although the 2-pass pipeline does an excellent job of removing all SPIRE image artifacts, approximately twenty of the maps still exhibited stripes and residual glitches in the final map. These maps were reprocessed by first using the SPIRE bolometer finder tool to identify the misbehaving bolometer, and then masking the affected portions in that bolometer's Level 1 timeline. The data were then rerun through the Naive Mapper to produce a clean and deglitched Level 2 science grade map.

2.5 The *Herschel*-GOALS Image Atlas

In the following pages in Figure 2.3 we present the entire *Herschel* atlas of the GOALS sample, ordered by ascending RA. The archived[5] *Herschel* GOALS maps are in standard `*.fits` format with image units of Jy pixel^{-1}. Each page consists of six panels for the 70 μm, 100 μm, 160 μm, 250 μm, 350 μm, and 500 μm channel maps.

The IRAS name of each galaxy or galaxy system is shown at the top, along with their common names from optical catalogs. Each of the six panels are matched and have the exact same map center as well as field of view. The center coordinates of the *Herschel* atlas images are listed in Table 2.1. For galaxy systems with multiple components, the center coordinate is chosen to be roughly equidistant from all components. The field of view for each panel is shown on the bottom left of the 70 μm panel, and represents the physical length of one side of each panel. A scale bar also indicates the physical length of 10 kpc at the distance of the galaxy (derived from the angular diameter distance in Table 2.1), along with the equivalent angular distance. The circle on the bottom right of each panel represents the beam size at that wavelength. Finally the right ascension and declination coordinates are indicated in J2000 sexagesimal as well as decimal format. The sexagesimal RA coordinates have the hour portion truncated for all but the center tick mark, to keep the tick name sizes manageable.

[5] `http://irsa.ipac.caltech.edu/data/GOALS/overview.html`

Since many objects appear as point sources at some or all of the *Herschel* wavelengths, the morphologies of these galaxies will be dominated by the PSF at that wavelength. In the case of PACS, the PSF is characterized by a narrow circular core elongated in the spacecraft z-direction, at 70 μm and 100 μm. In addition there is a tri-lobe pattern at the several percent level at all three wavelengths, however it is strongest at 70 μm. Finally, there are knotty structured diffraction rings at the sub-percent level, again most apparent at 70 μm and 100 μm. In the case of SPIRE, the PSF appears mostly circular, however for the brightest objects, airy rings are also visible.

In order to show as much detail in these maps, we used an inverse hyperbolic sine (asinh) stretch function to maximize the dynamic range of visible structures. Also to keep all the PACS images uniform, the background for each image was adjusted such that the background is very close to zero. The format in our *Herschel* atlas matches that of companion image atlases from *Hubble Space Telescope*-ACS (Evans et al. in prep.) and *Spitzer*-IRAC/MIPS (Mazzarella et al. in prep.), allowing one to study the morphological properties of these galaxies from 0.4 μm to 500 μm.

2.6 *Herschel*-GOALS Aperture Photometry

In this section we discuss the manner in which the broadband photometry were determined for our sample. Both PACS and SPIRE photometry were obtained using the `annularSkyAperturePhotometry` routine found in HIPE. At first we attempted to measure fluxes by using an automated routine to determine the appropriate circular aperture sizes for each galaxy, based on data from the MIPS instrument on *Spitzer*. Unfortunately this approach does not work well for our sample, due to the extended nature of some GOALS systems and galaxies.

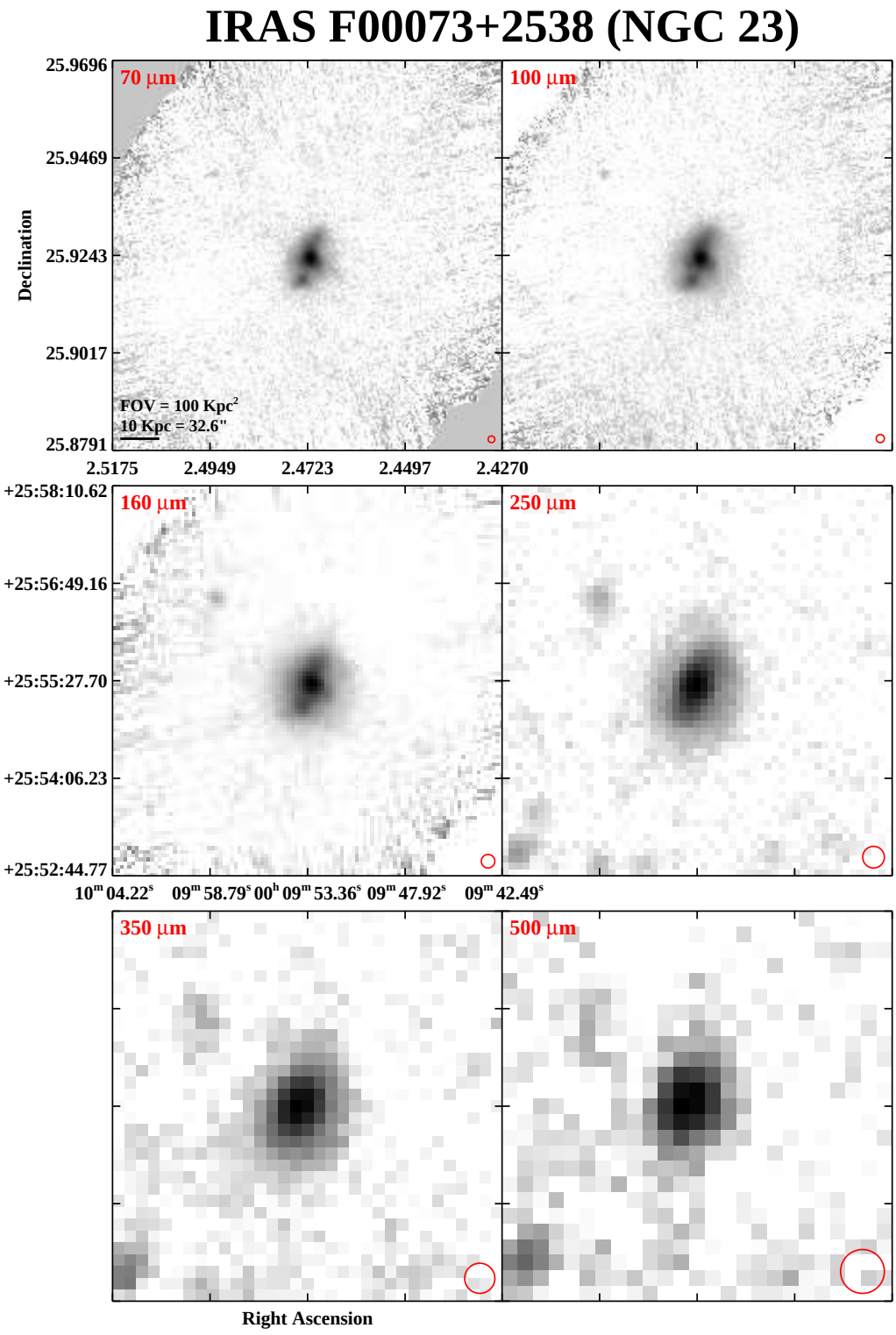

Figure 2.3 The *Herschel* GOALS atlas, displaying imagery of local LIRGs and ULIRGs in the three PACS bands and three SPIRE band. See §2.5 for the information presented in each atlas.

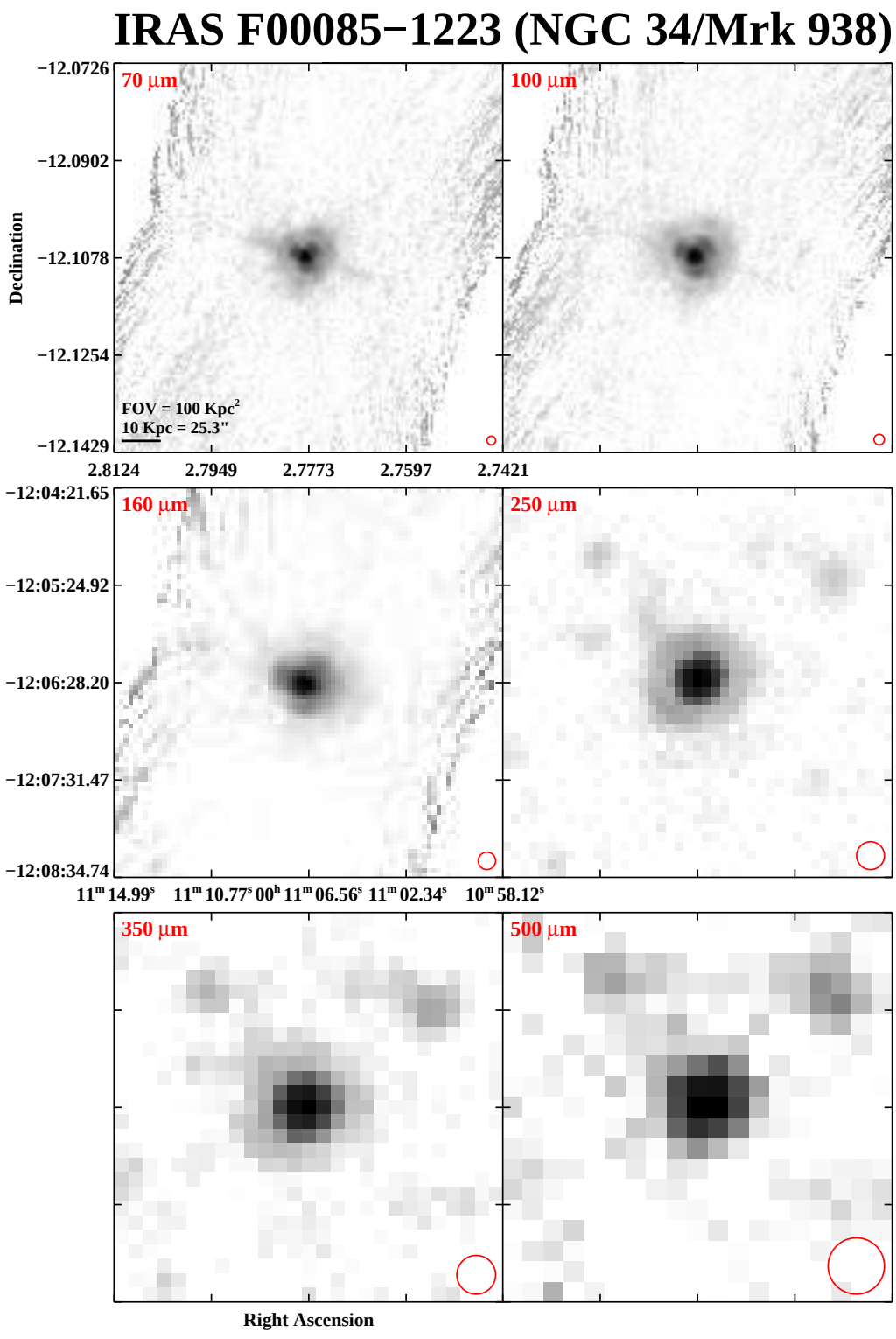

Figure 2.3 continued (page 2 of 209).

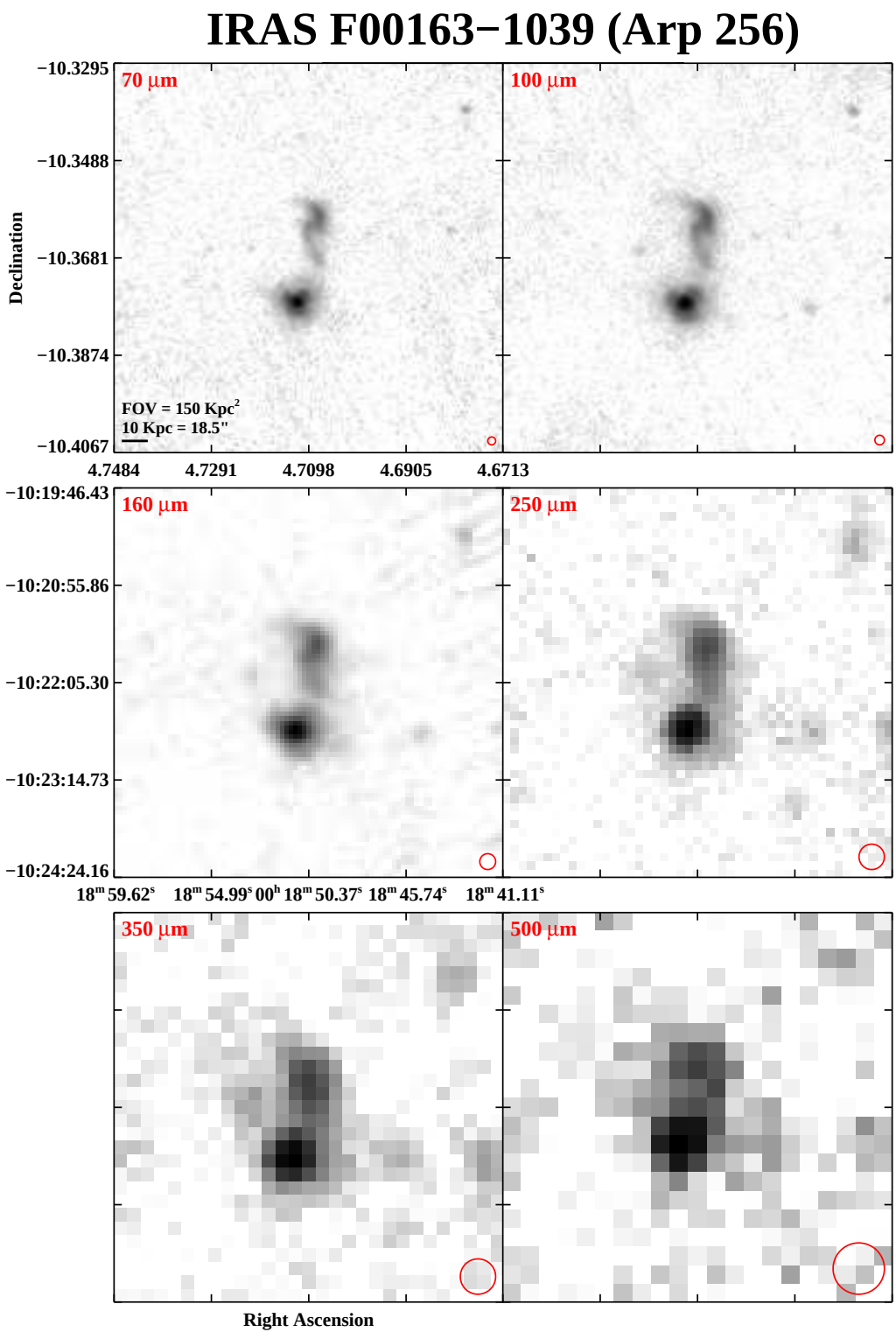

Figure 2.3 continued (page 3 of 209).

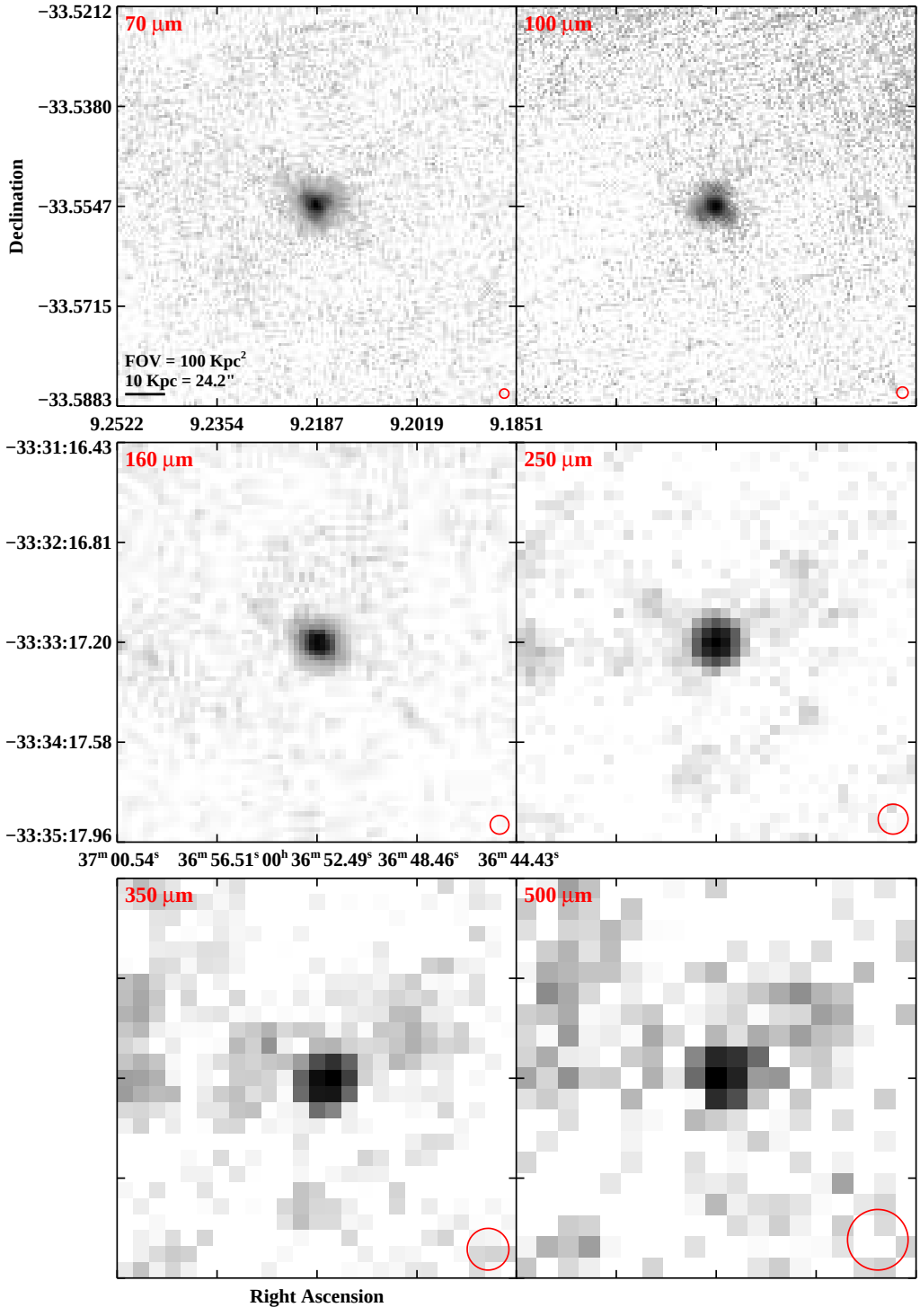

Figure 2.3 continued (page 4 of 209).

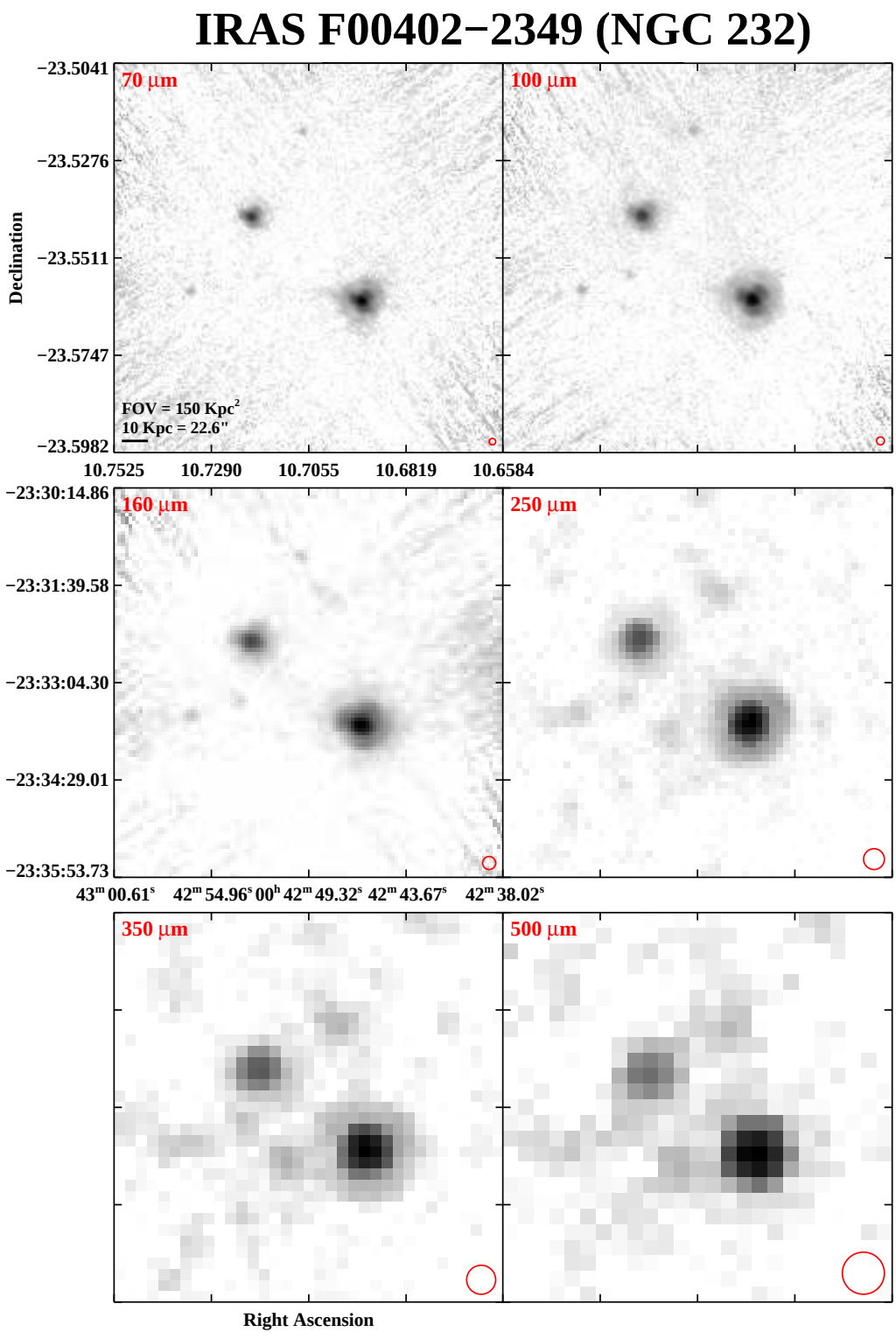

Figure 2.3 continued (page 5 of 209).

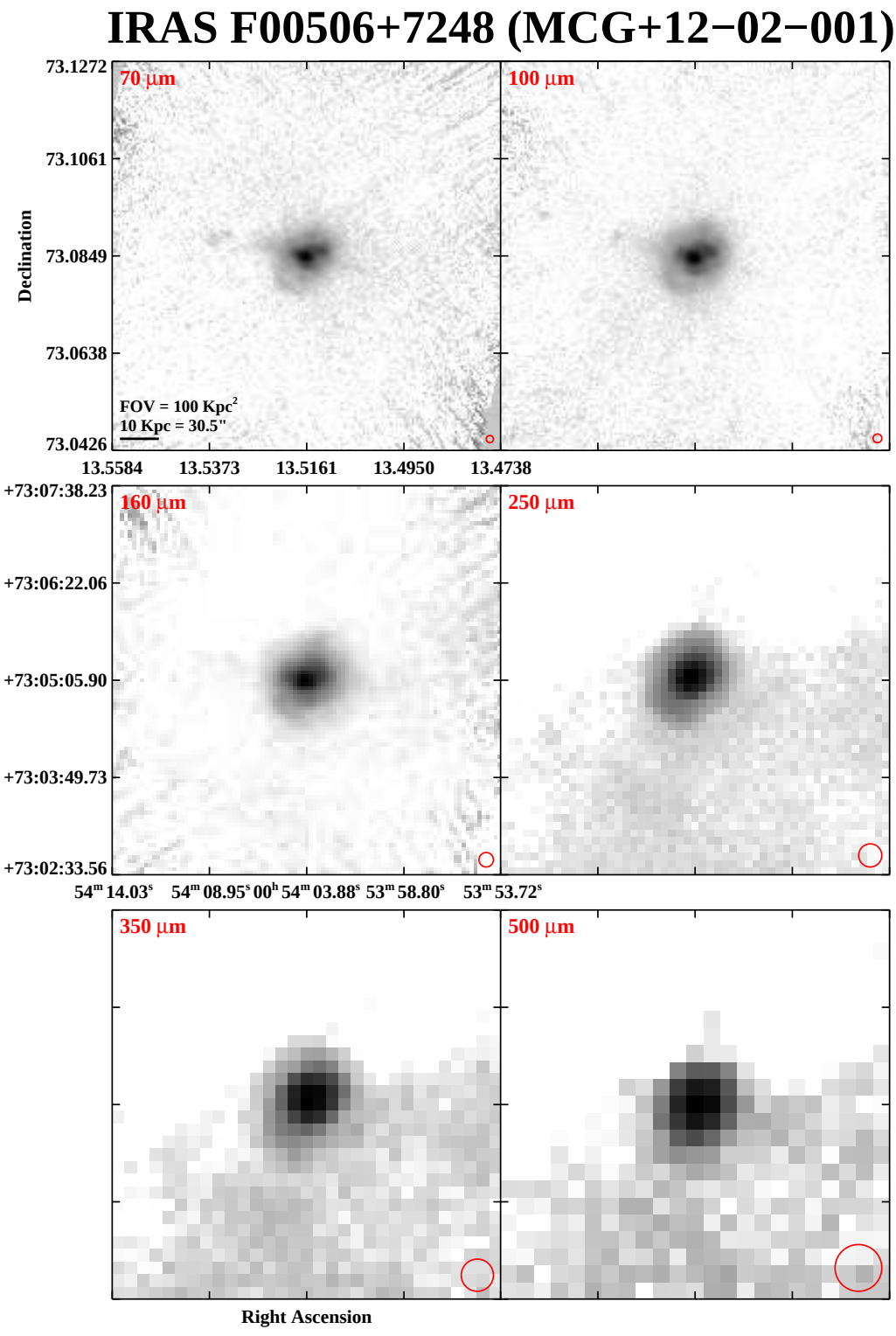

Figure 2.3 continued (page 6 of 209).

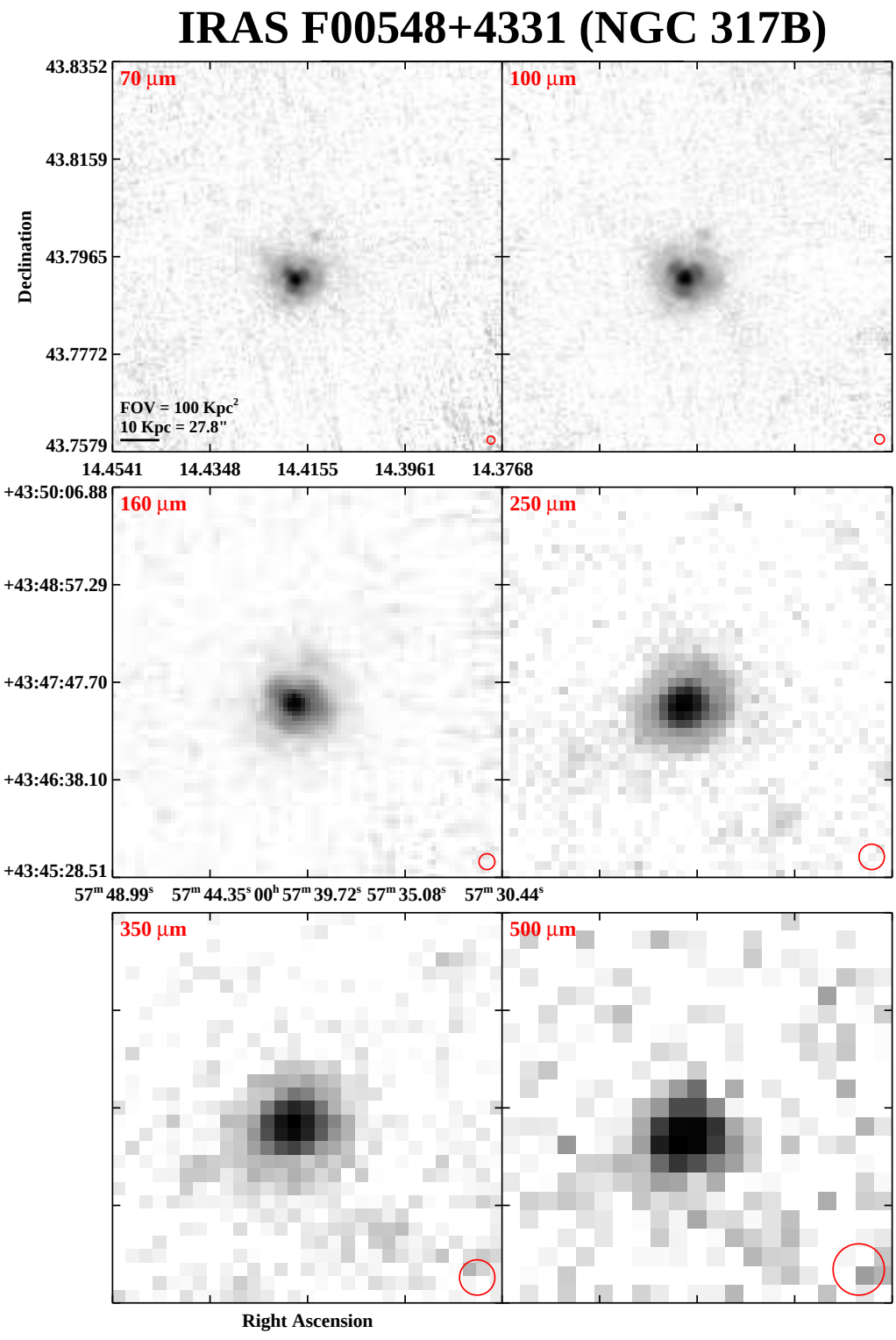

Figure 2.3 continued (page 7 of 209).

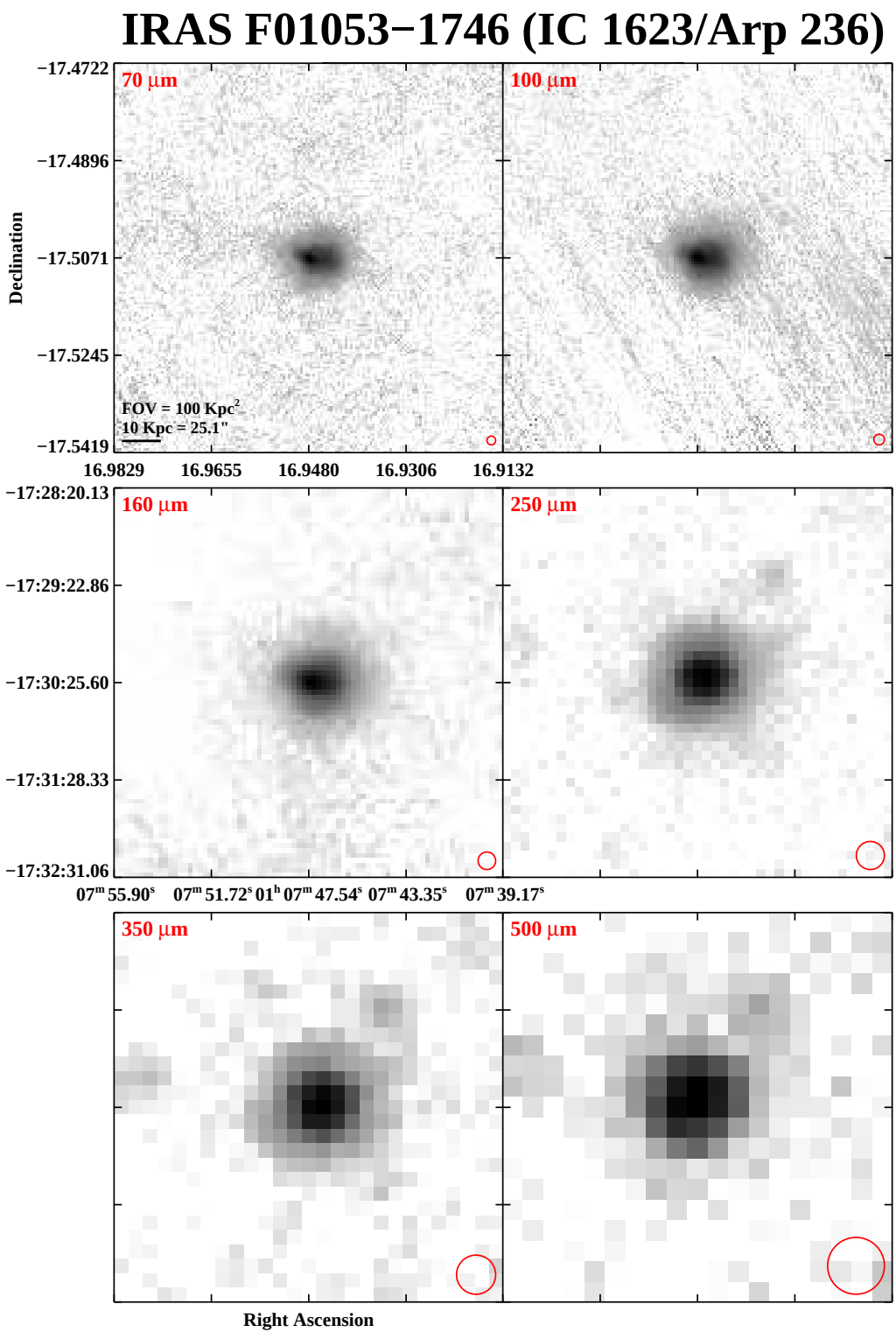

Figure 2.3 continued (page 8 of 209).

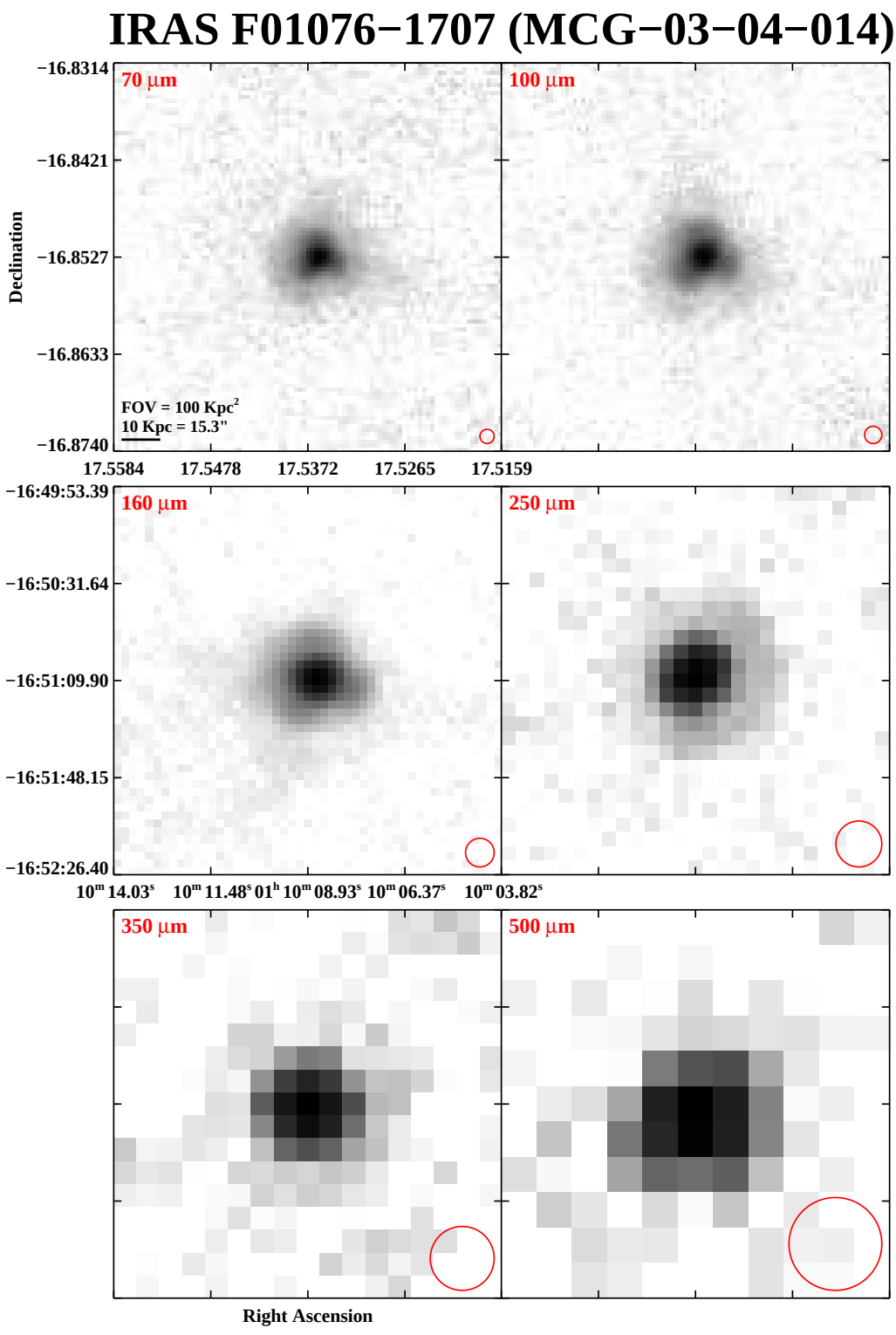

Figure 2.3 continued (page 9 of 209).

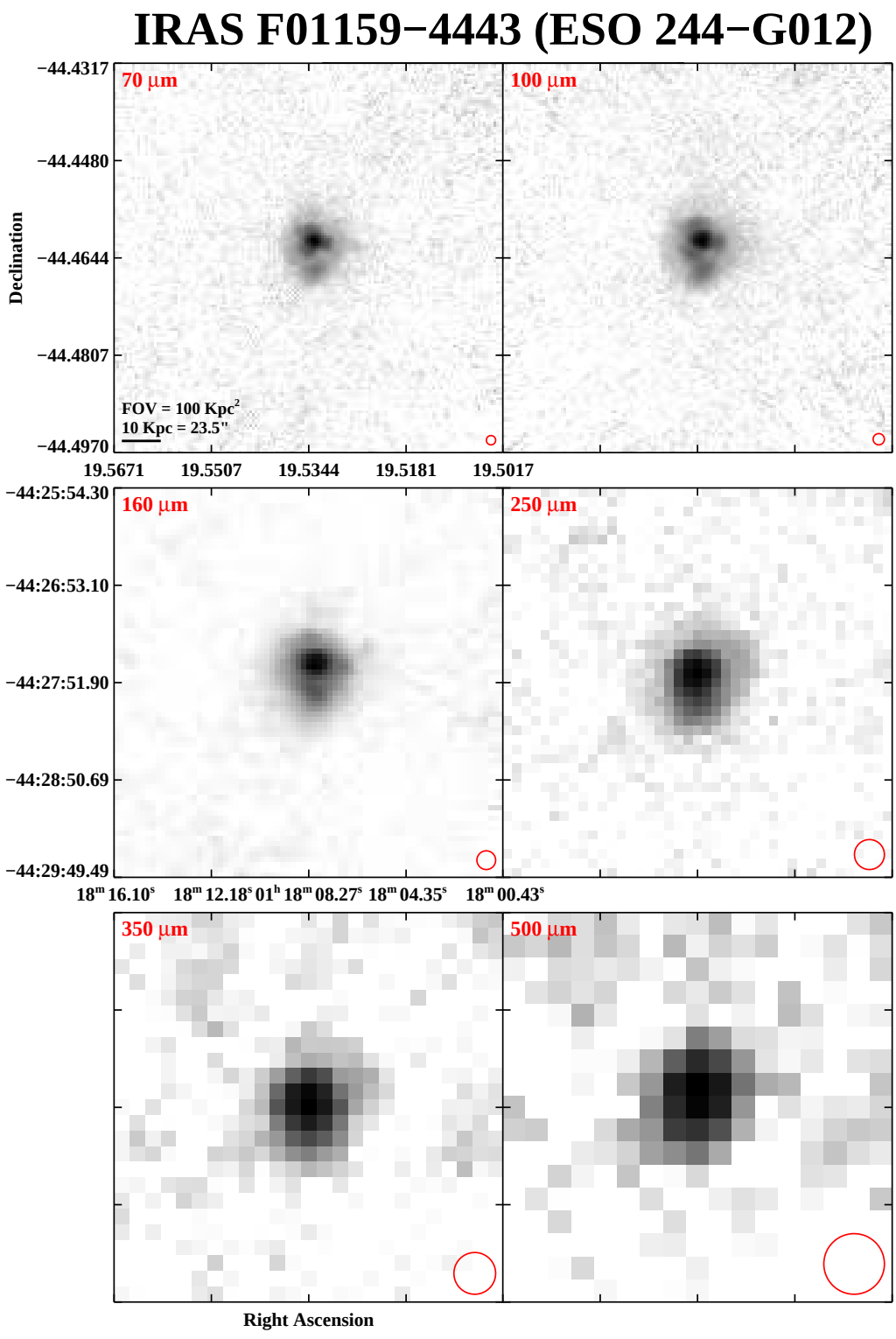

Figure 2.3 continued (page 10 of 209).

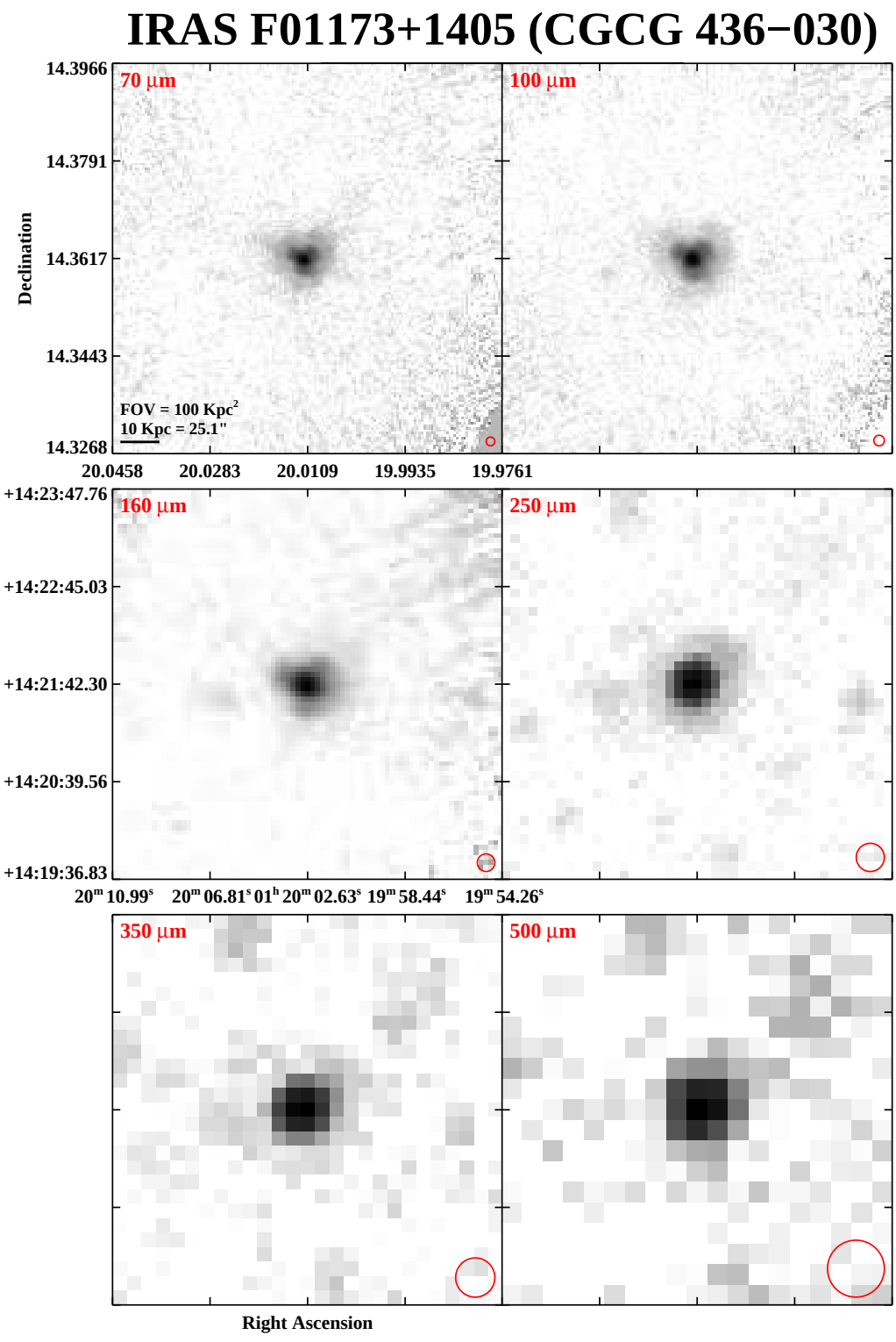

Figure 2.3 continued (page 11 of 209).

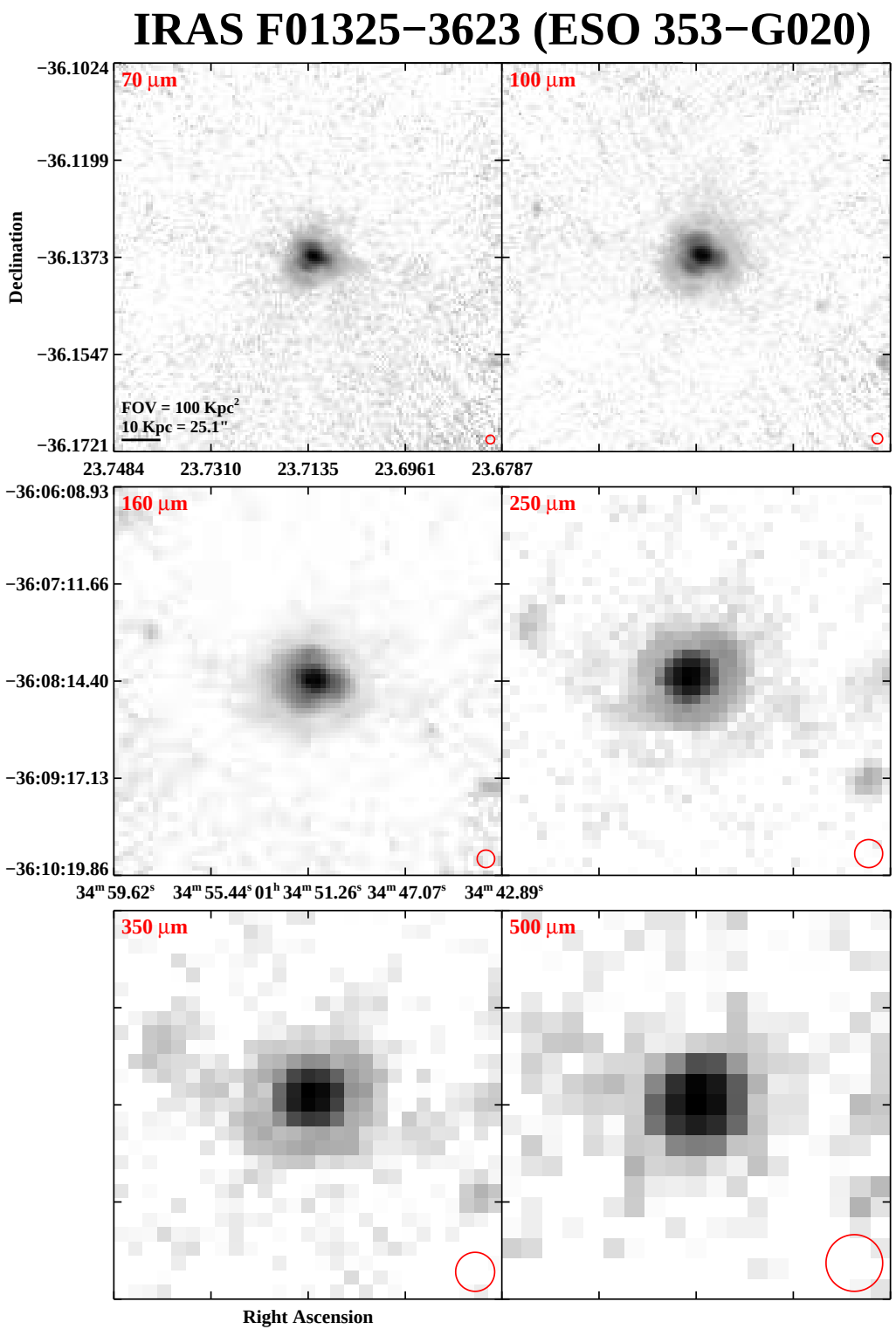

Figure 2.3 continued (page 12 of 209).

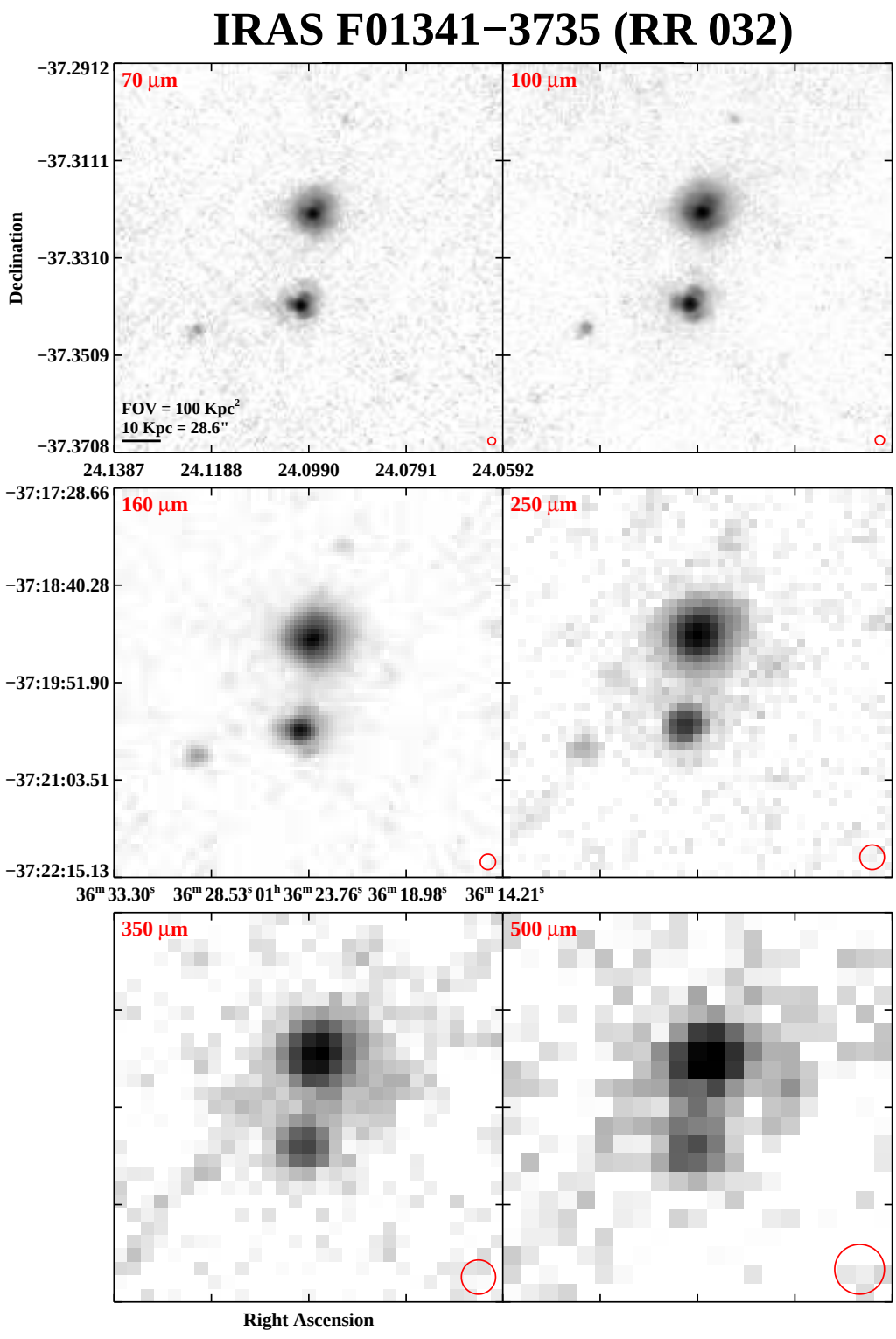

Figure 2.3 continued (page 13 of 209).

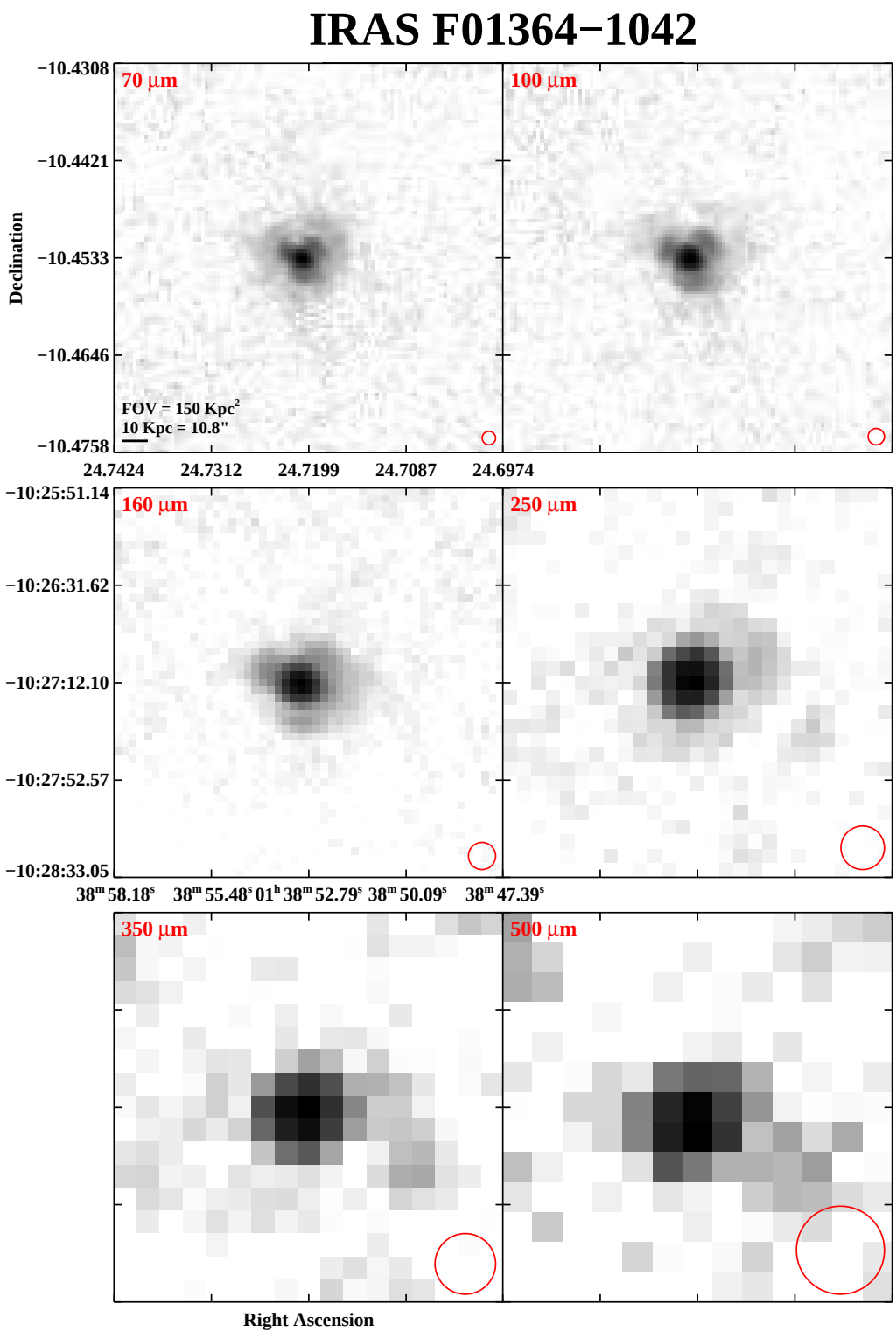

Figure 2.3 continued (page 14 of 209).

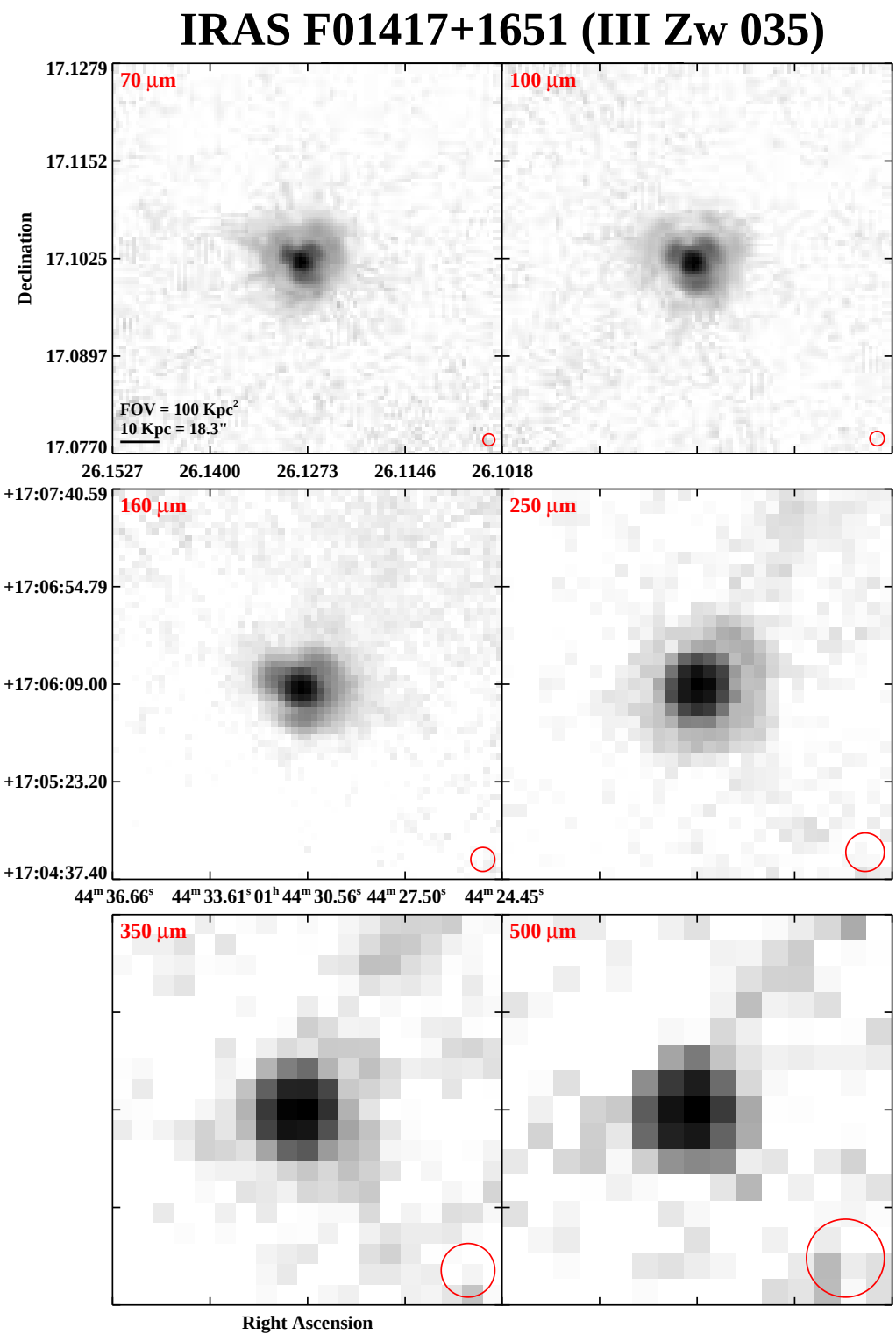

Figure 2.3 continued (page 15 of 209).

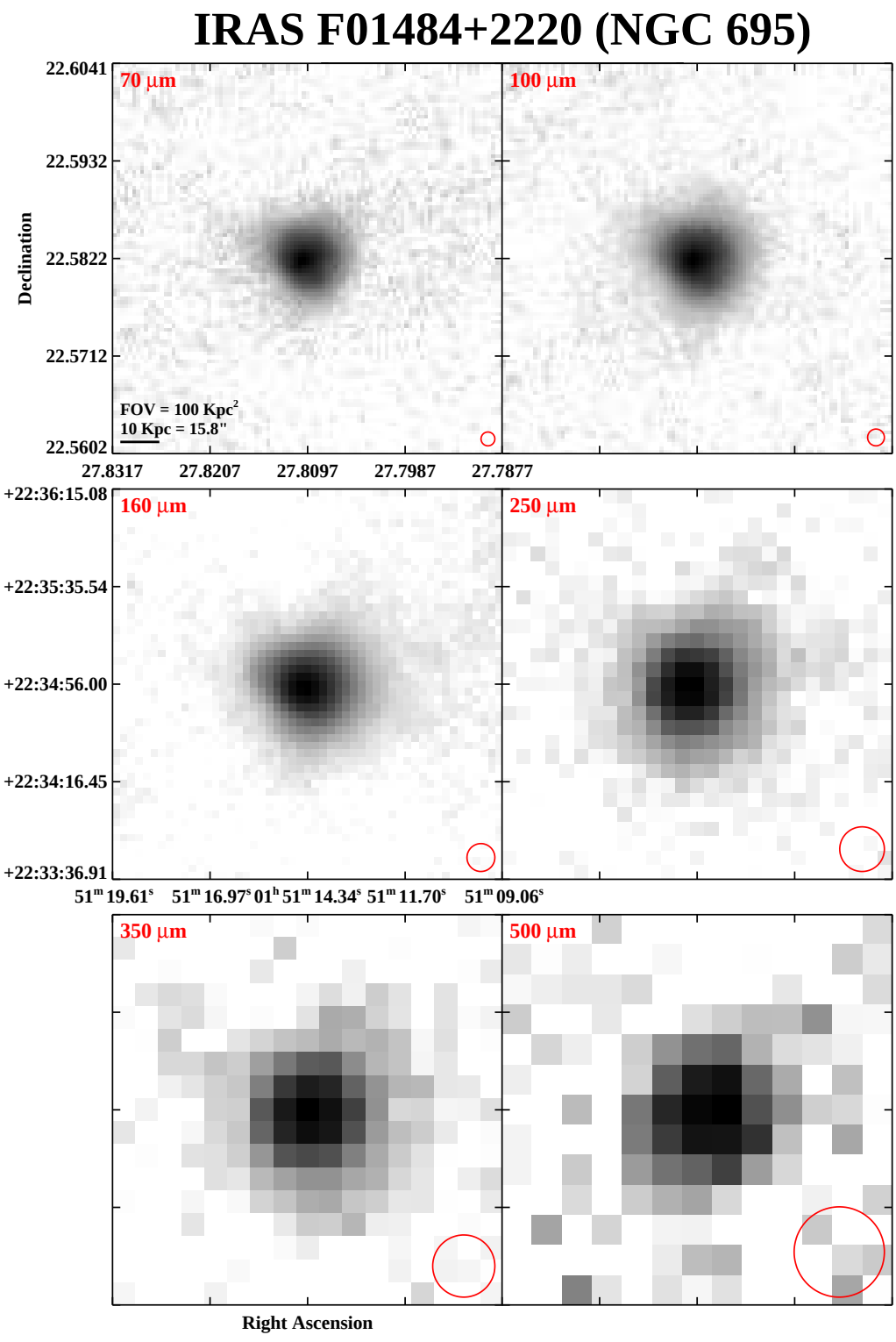

Figure 2.3 continued (page 16 of 209).

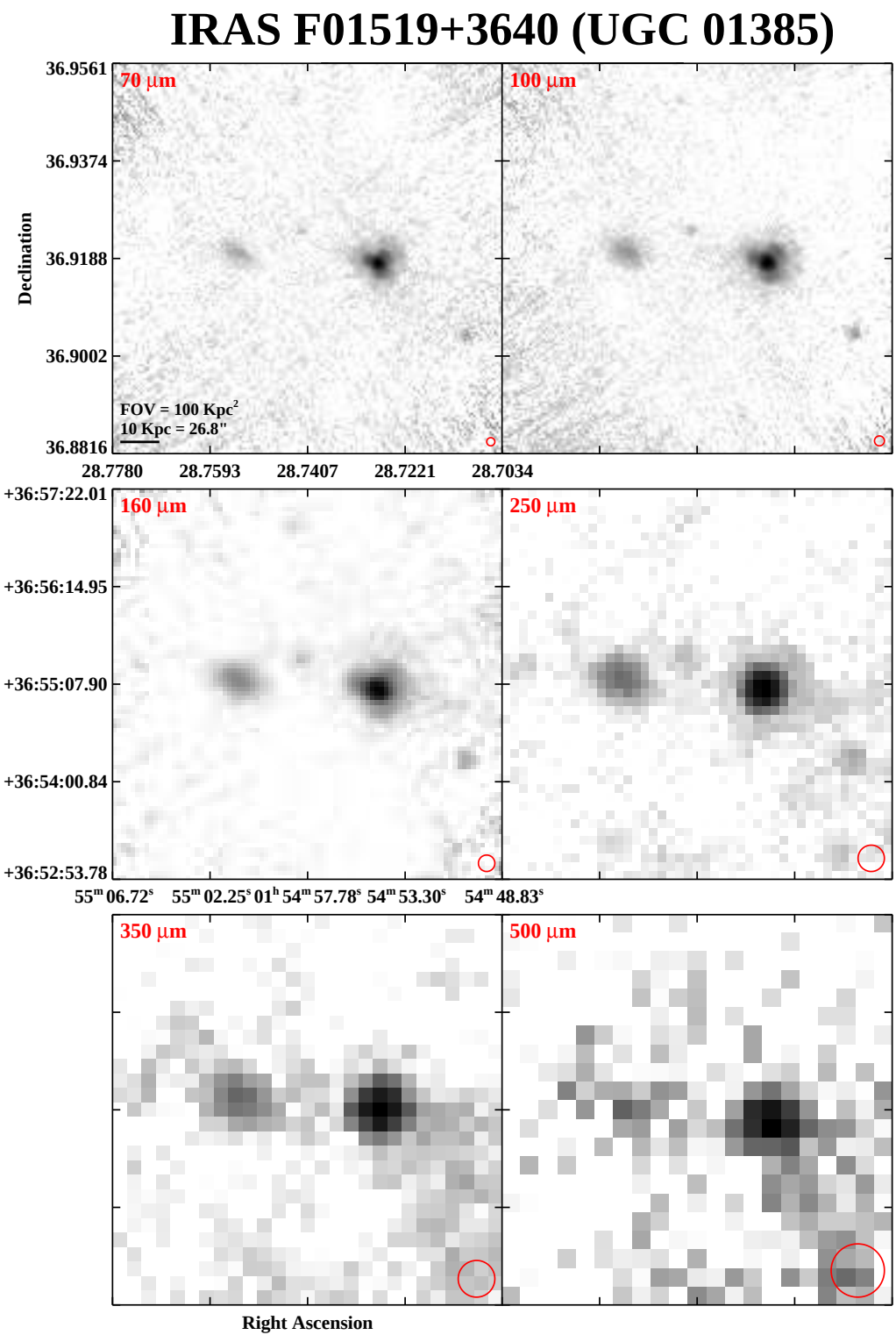

Figure 2.3 continued (page 17 of 209).

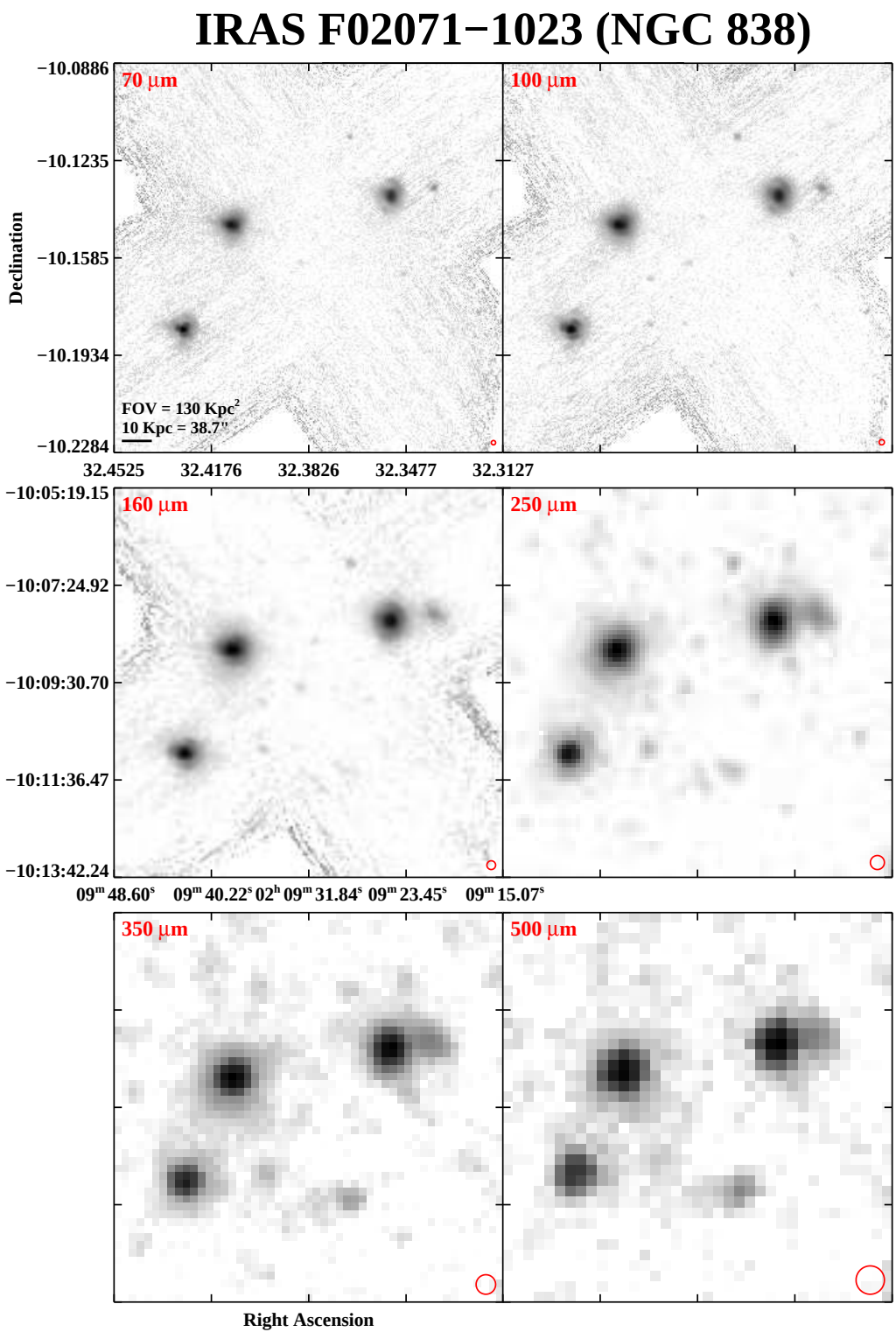

Figure 2.3 continued (page 18 of 209).

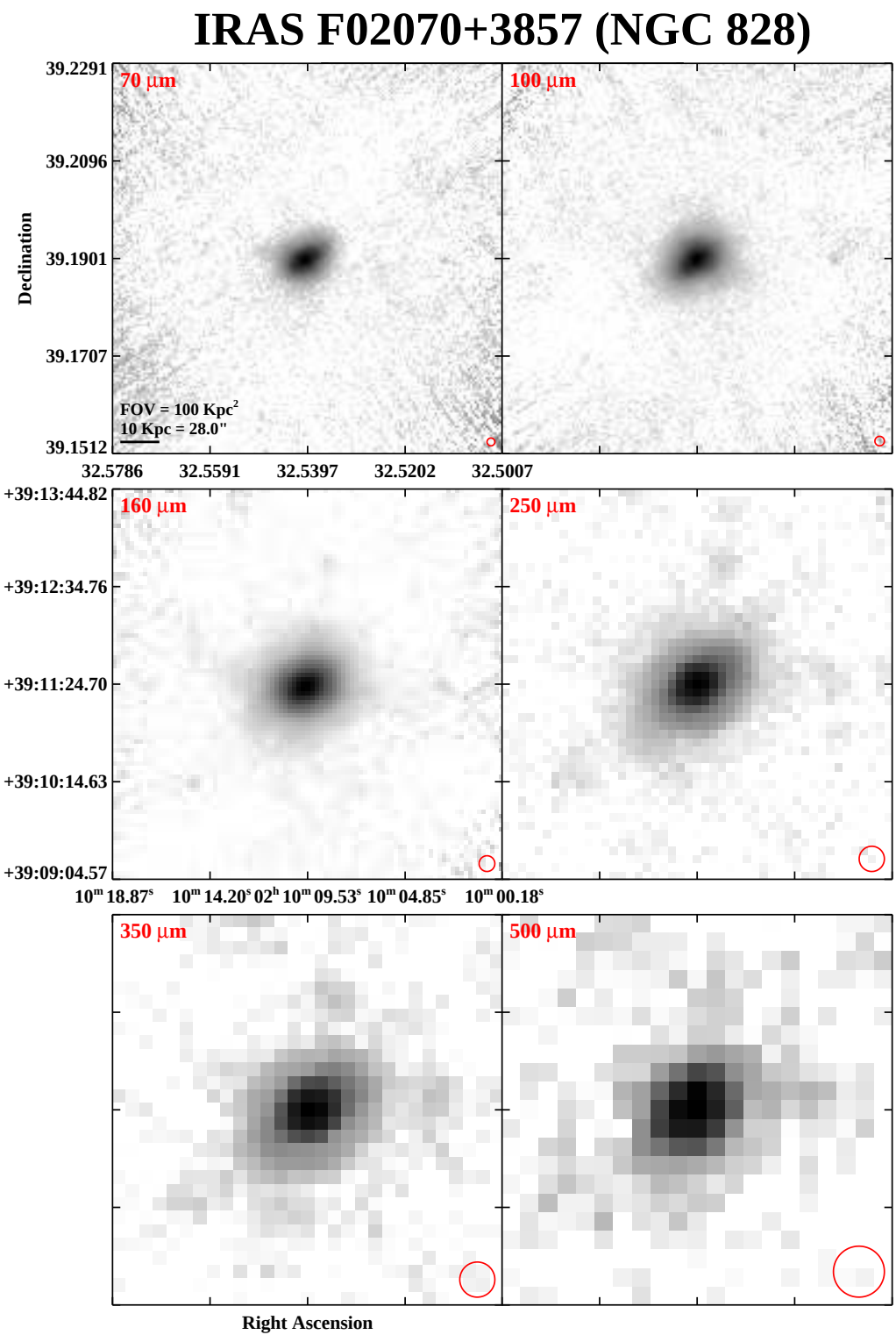

Figure 2.3 continued (page 19 of 209).

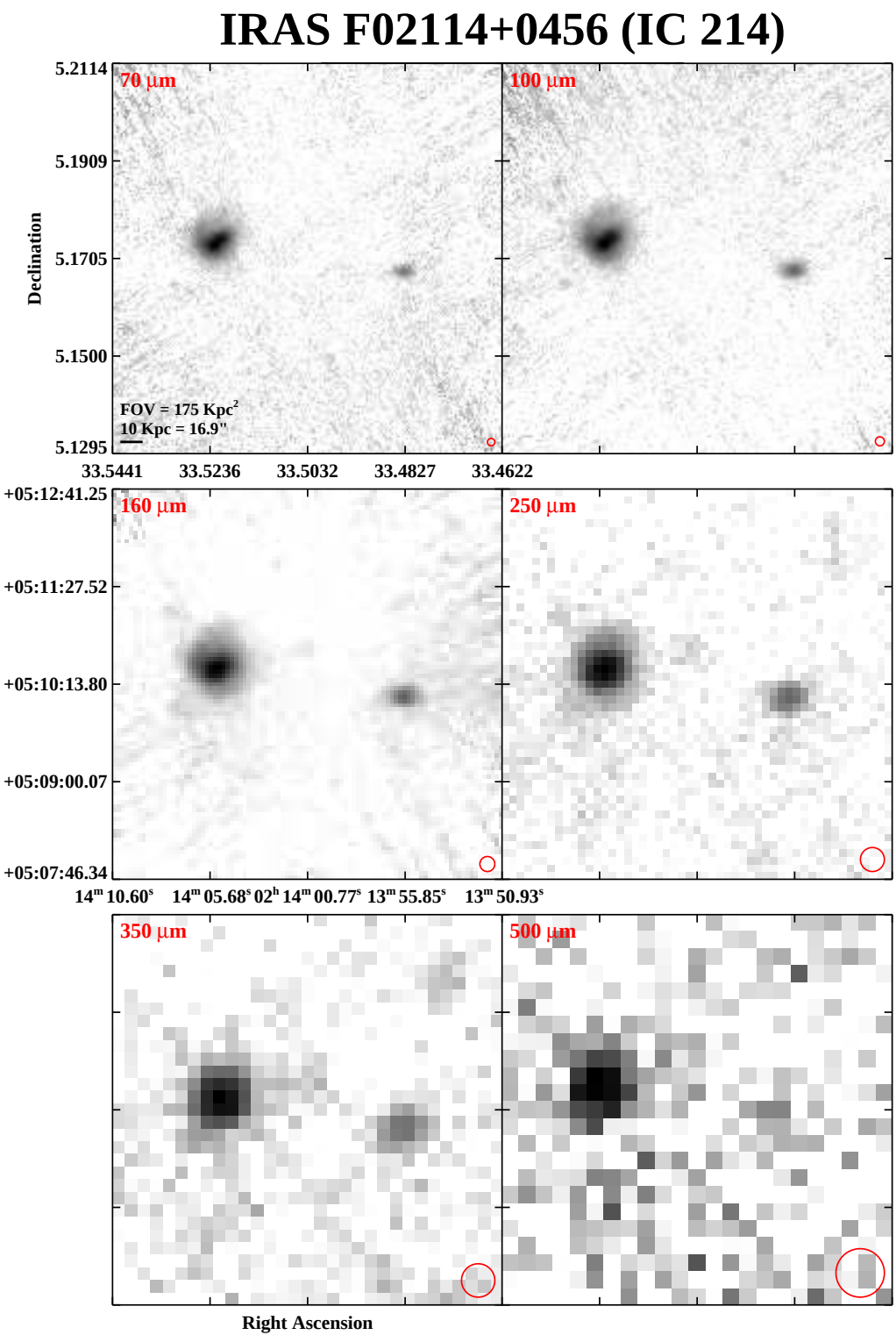

Figure 2.3 continued (page 20 of 209).

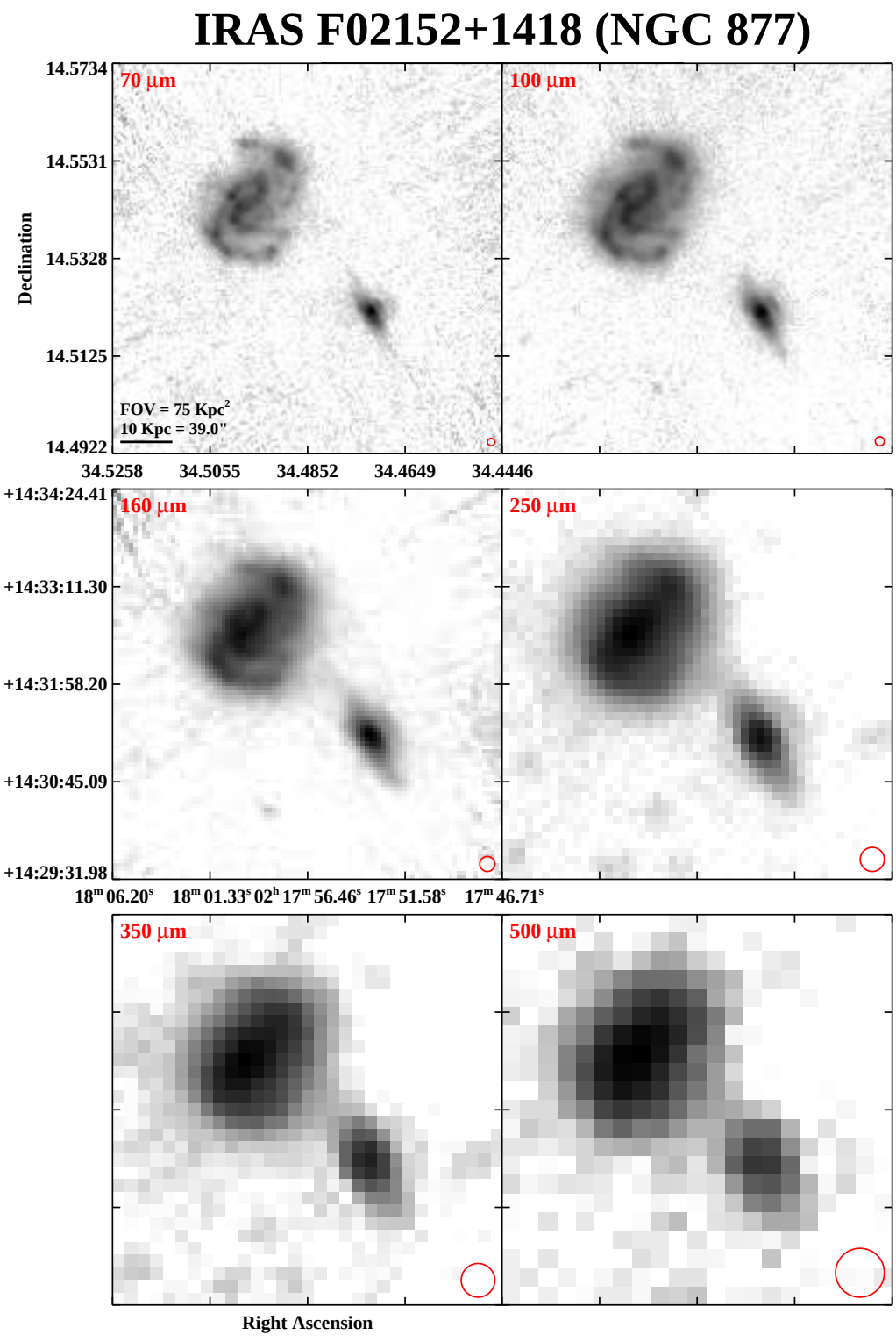

Figure 2.3 continued (page 21 of 209).

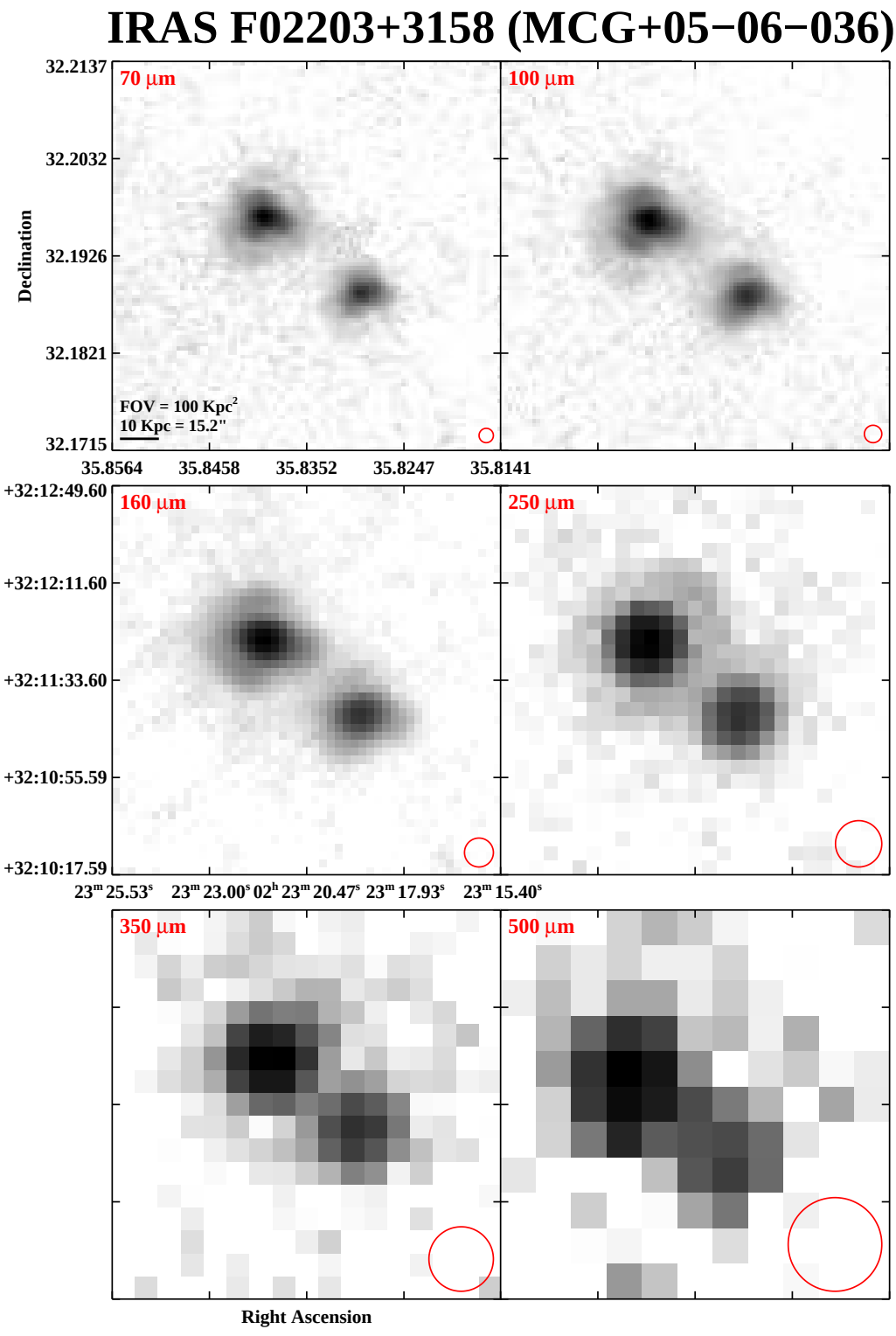

Figure 2.3 continued (page 22 of 209).

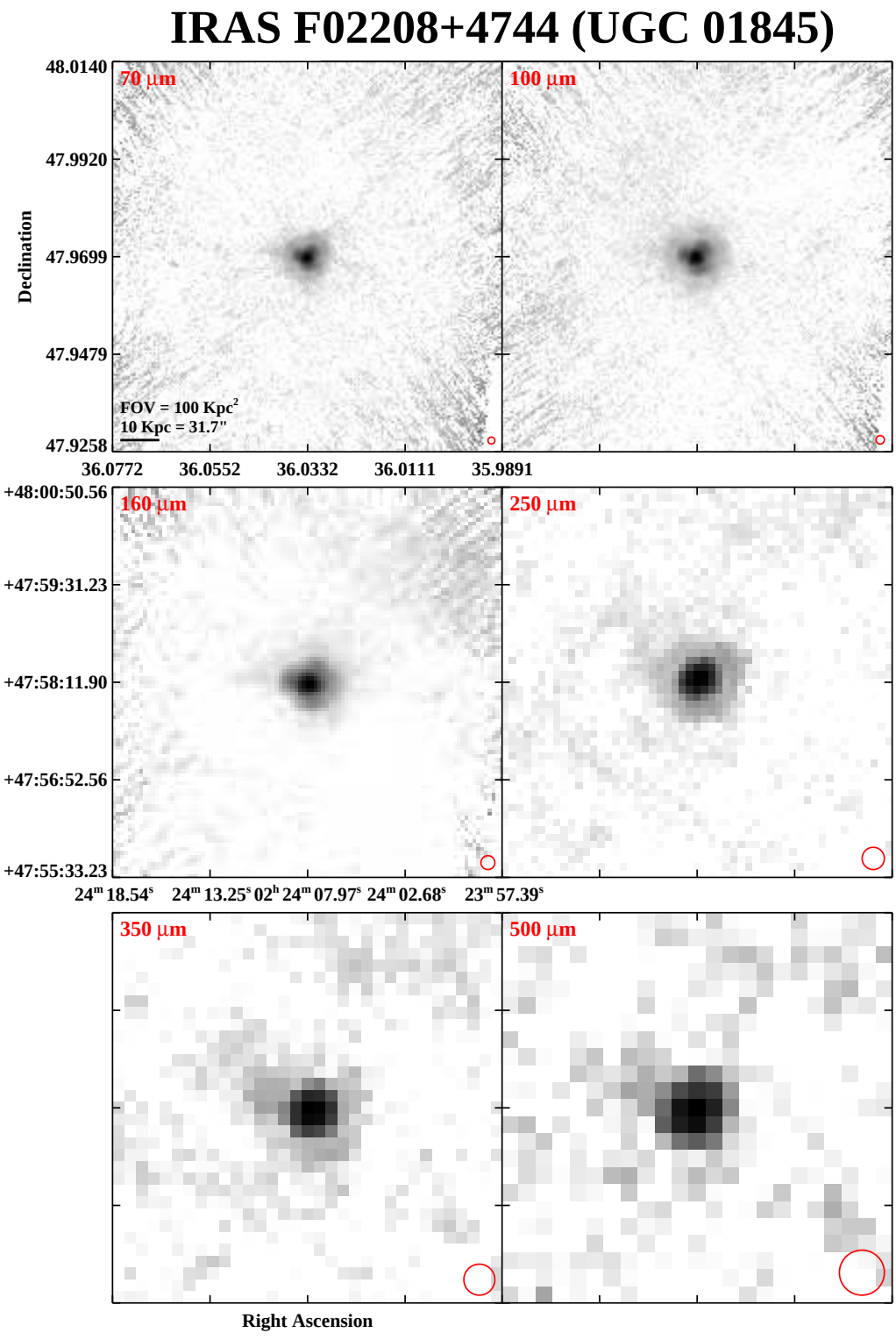

Figure 2.3 continued (page 23 of 209).

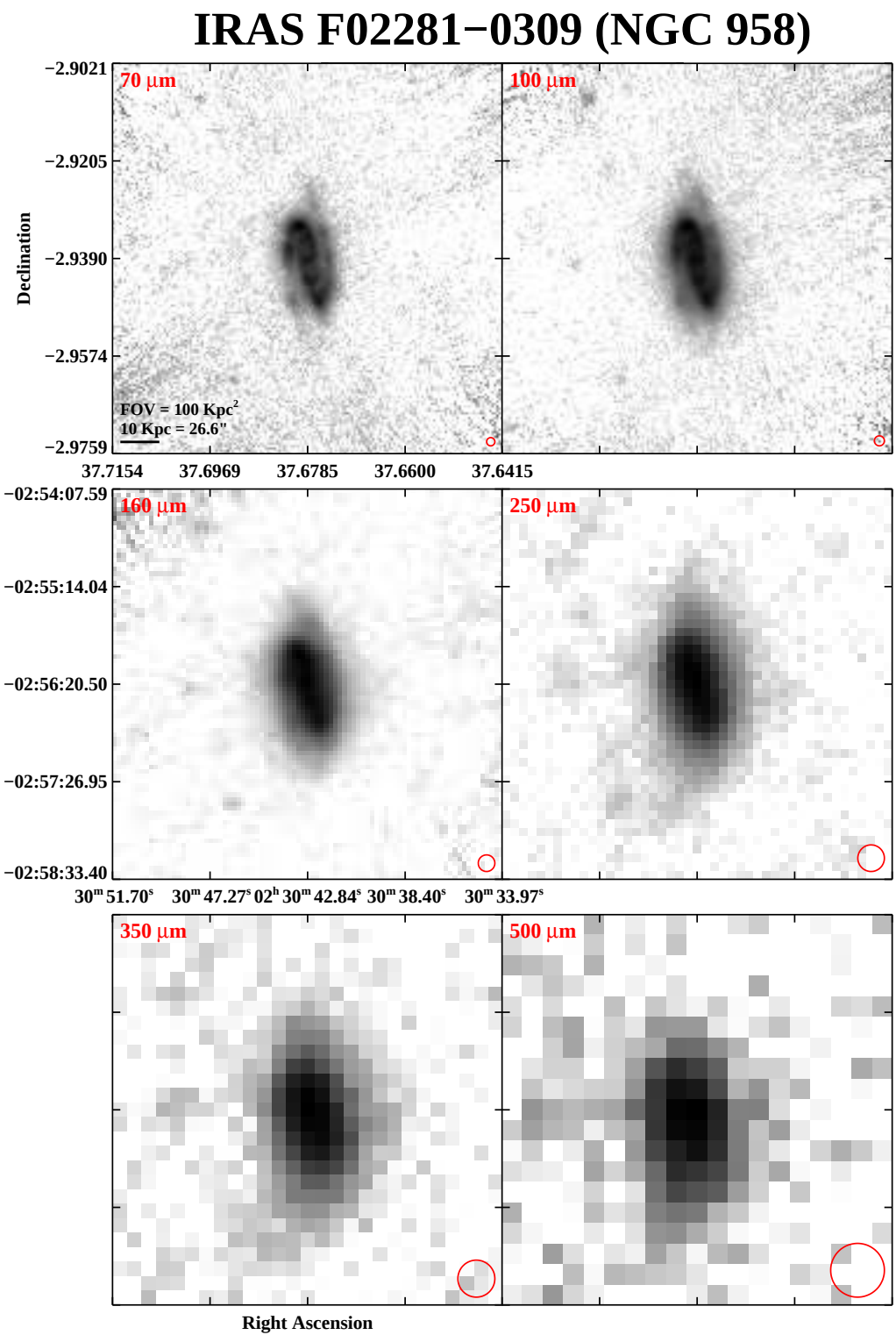

Figure 2.3 continued (page 24 of 209).

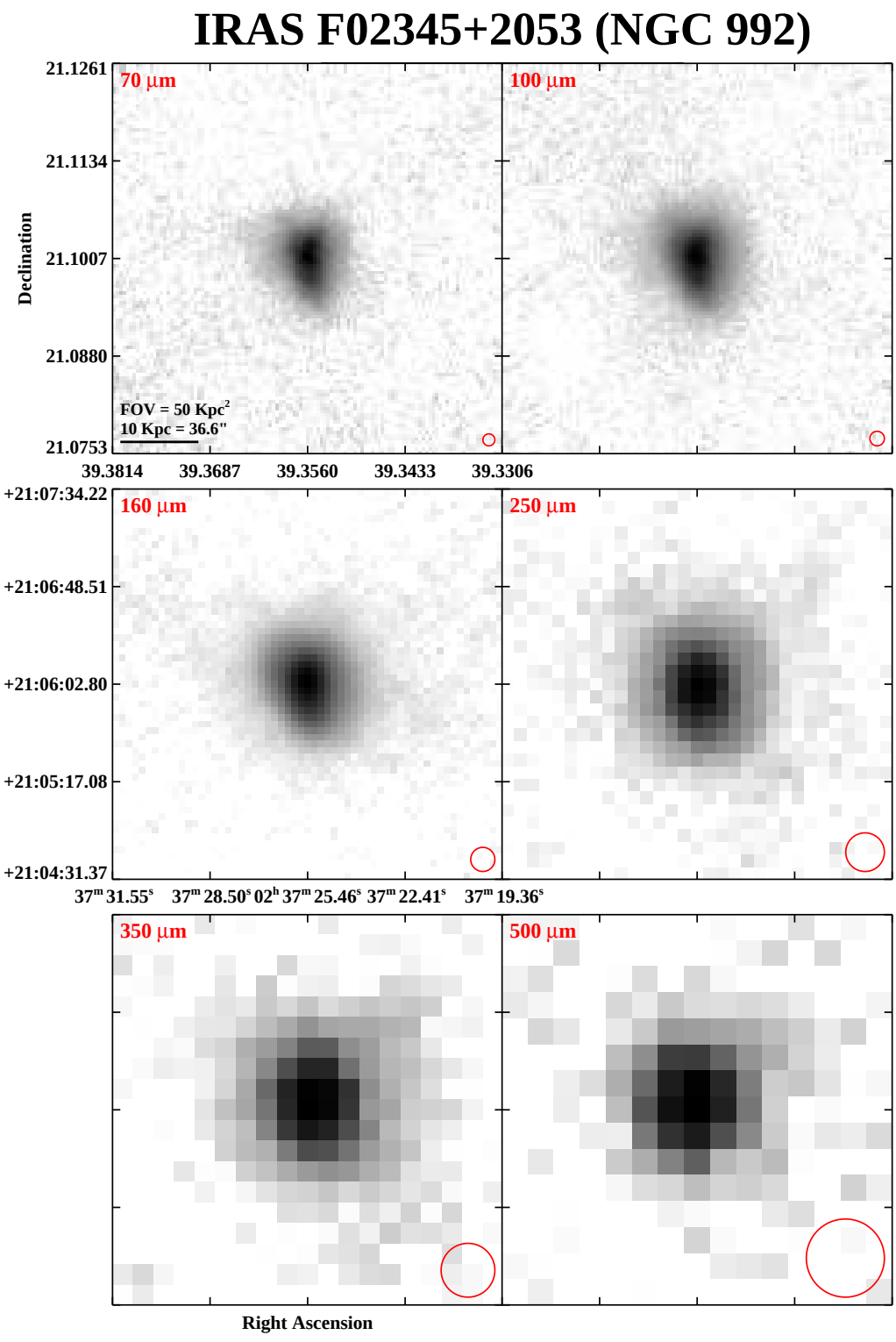

Figure 2.3 continued (page 25 of 209).

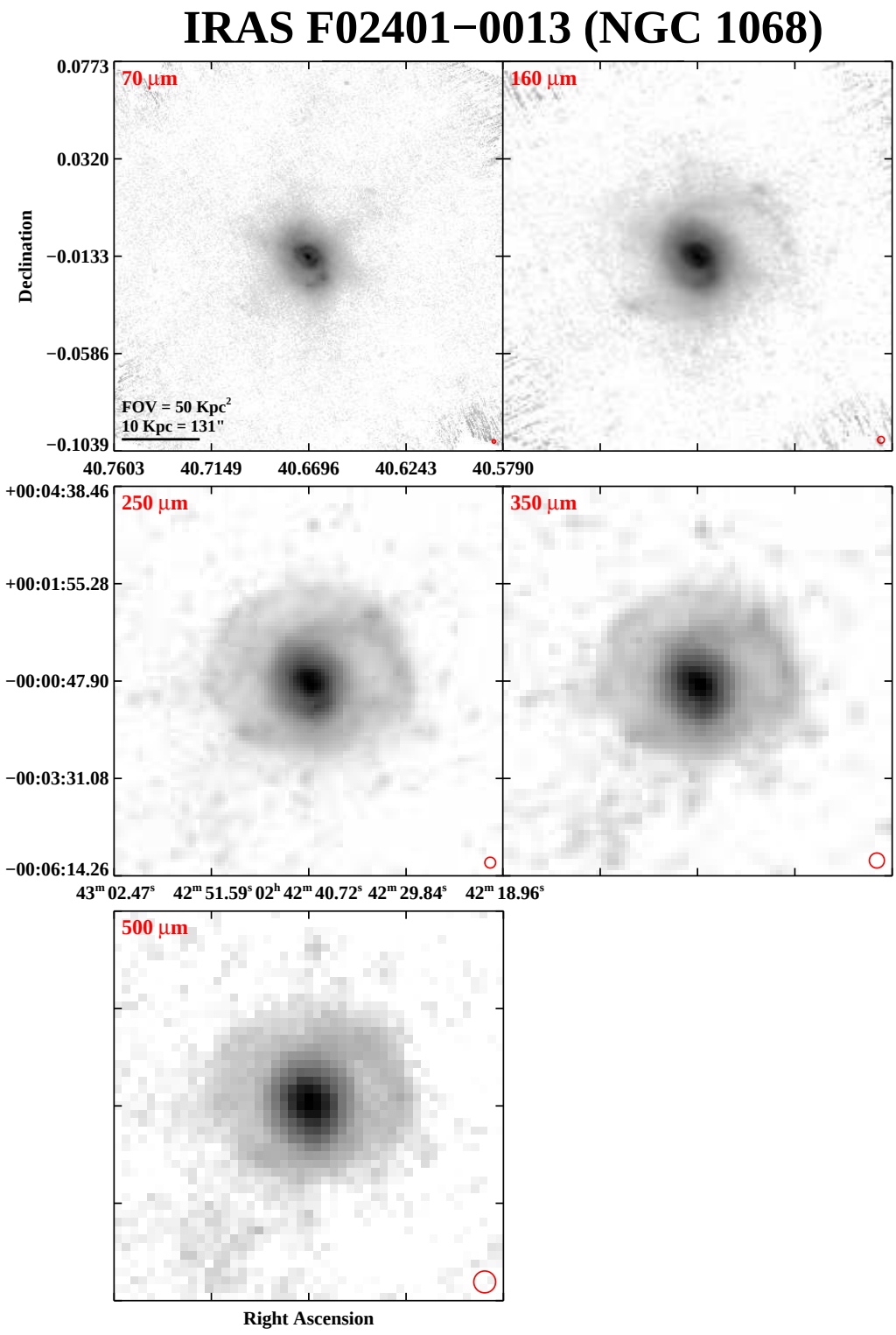

Figure 2.3 continued (page 26 of 209).

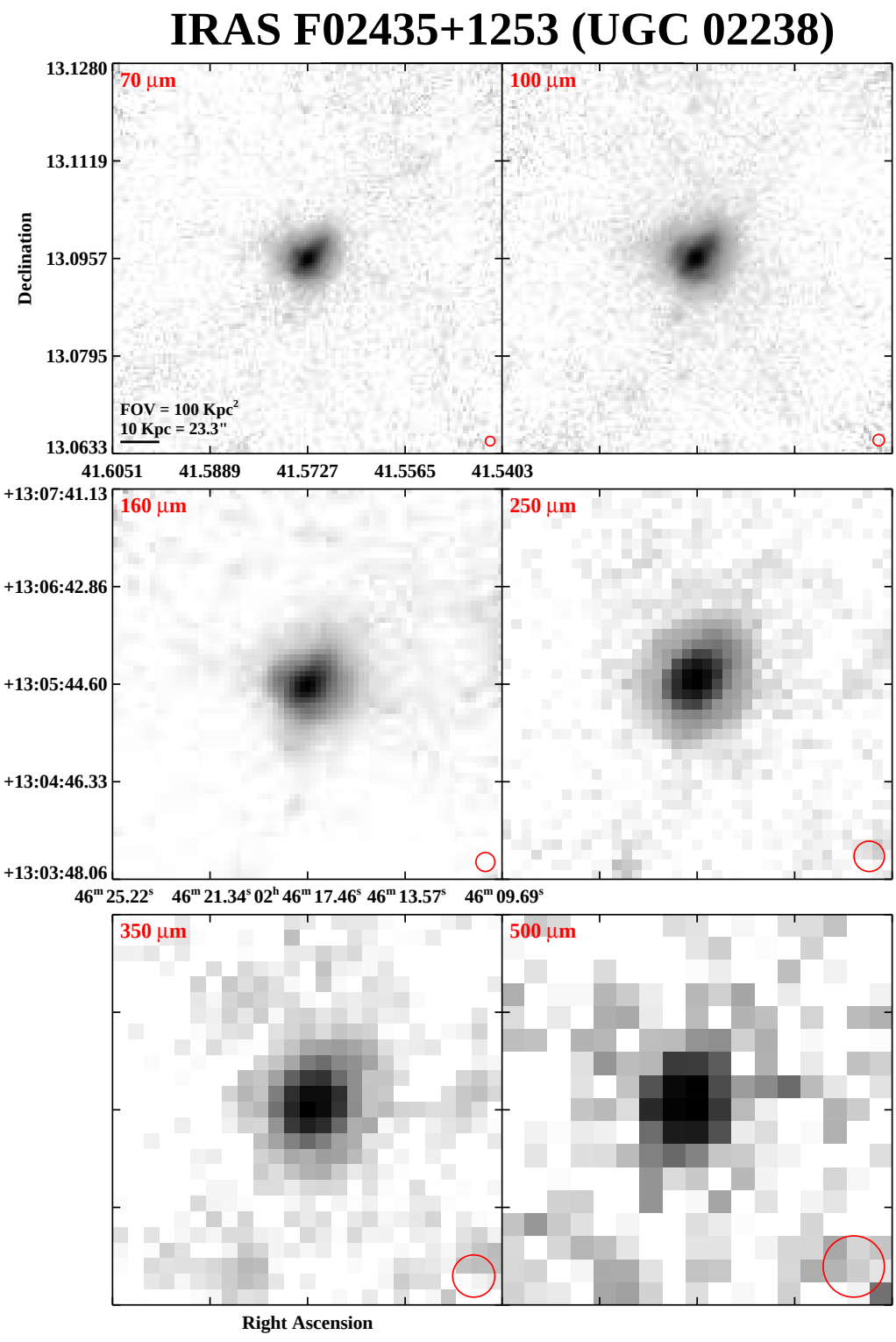

Figure 2.3 continued (page 27 of 209).

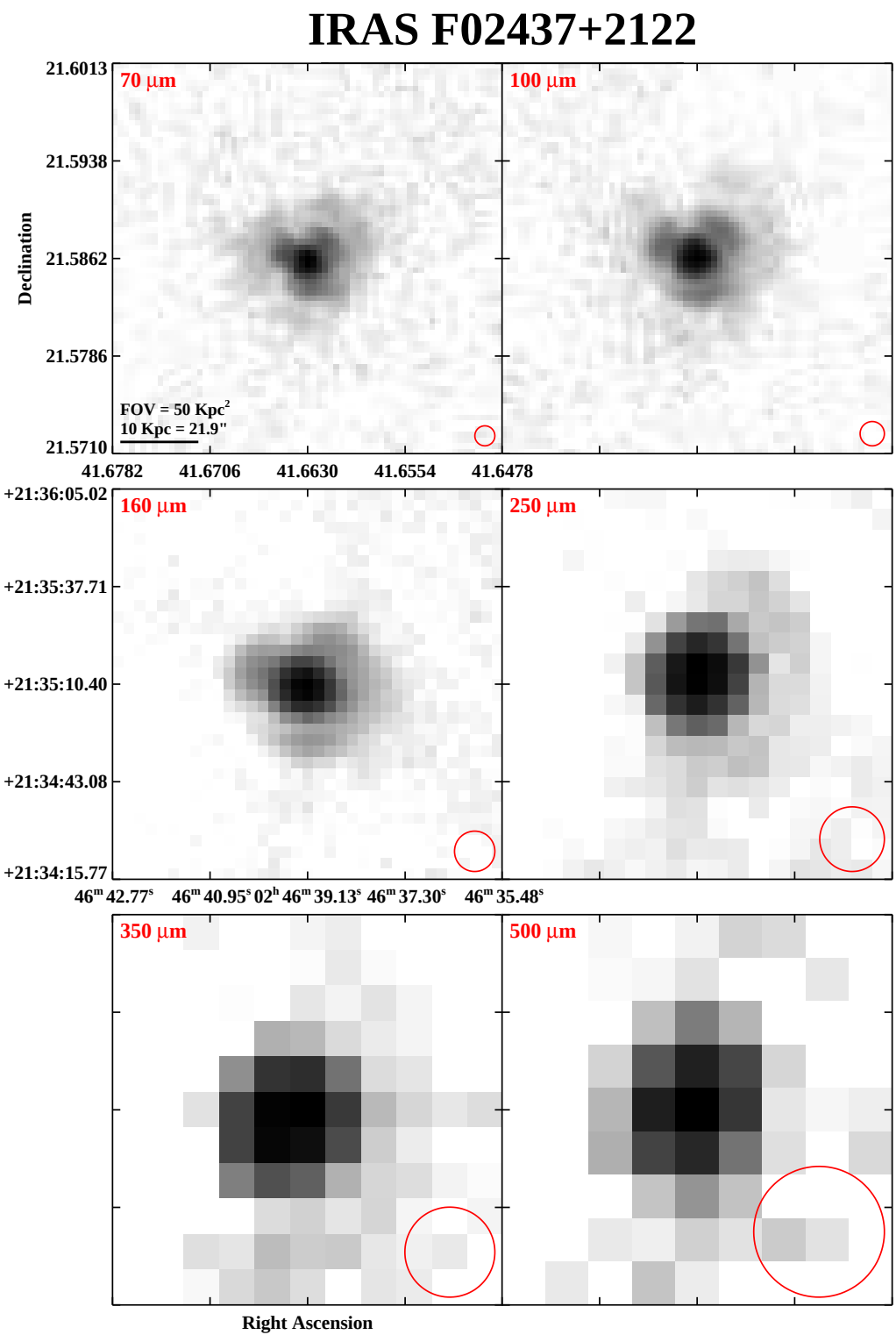

Figure 2.3 continued (page 28 of 209).

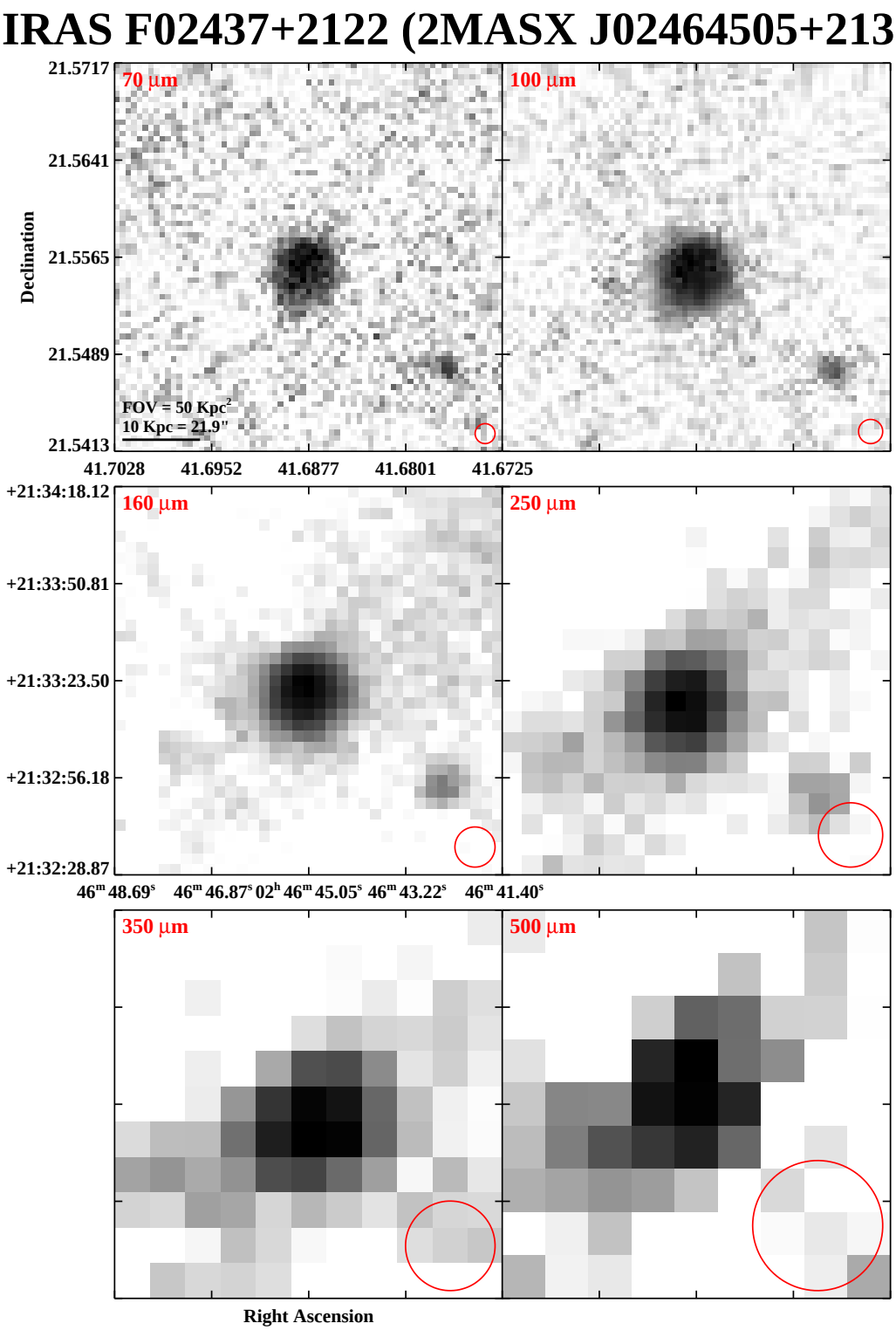

Figure 2.3 continued (page 29 of 209).

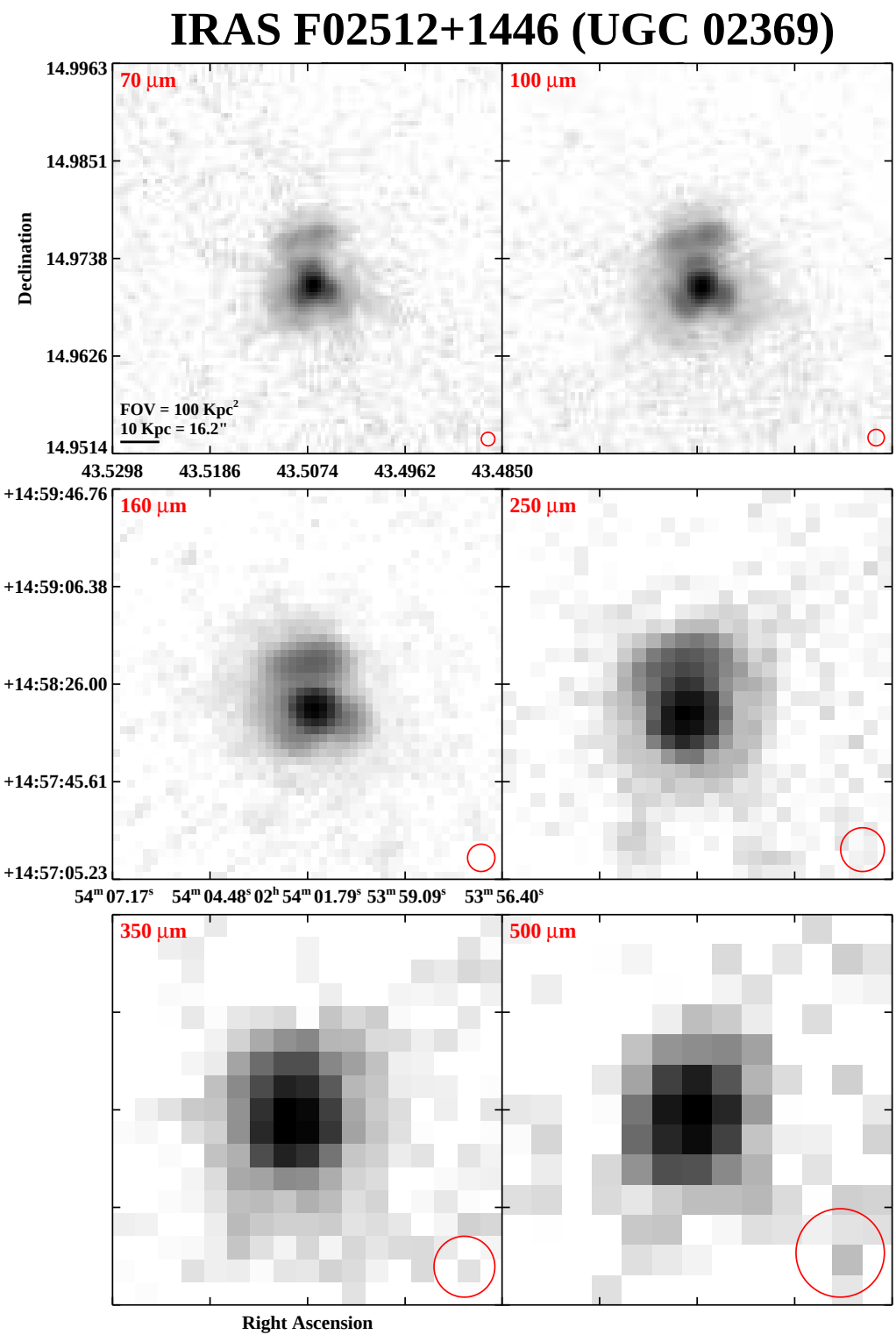

Figure 2.3 continued (page 30 of 209).

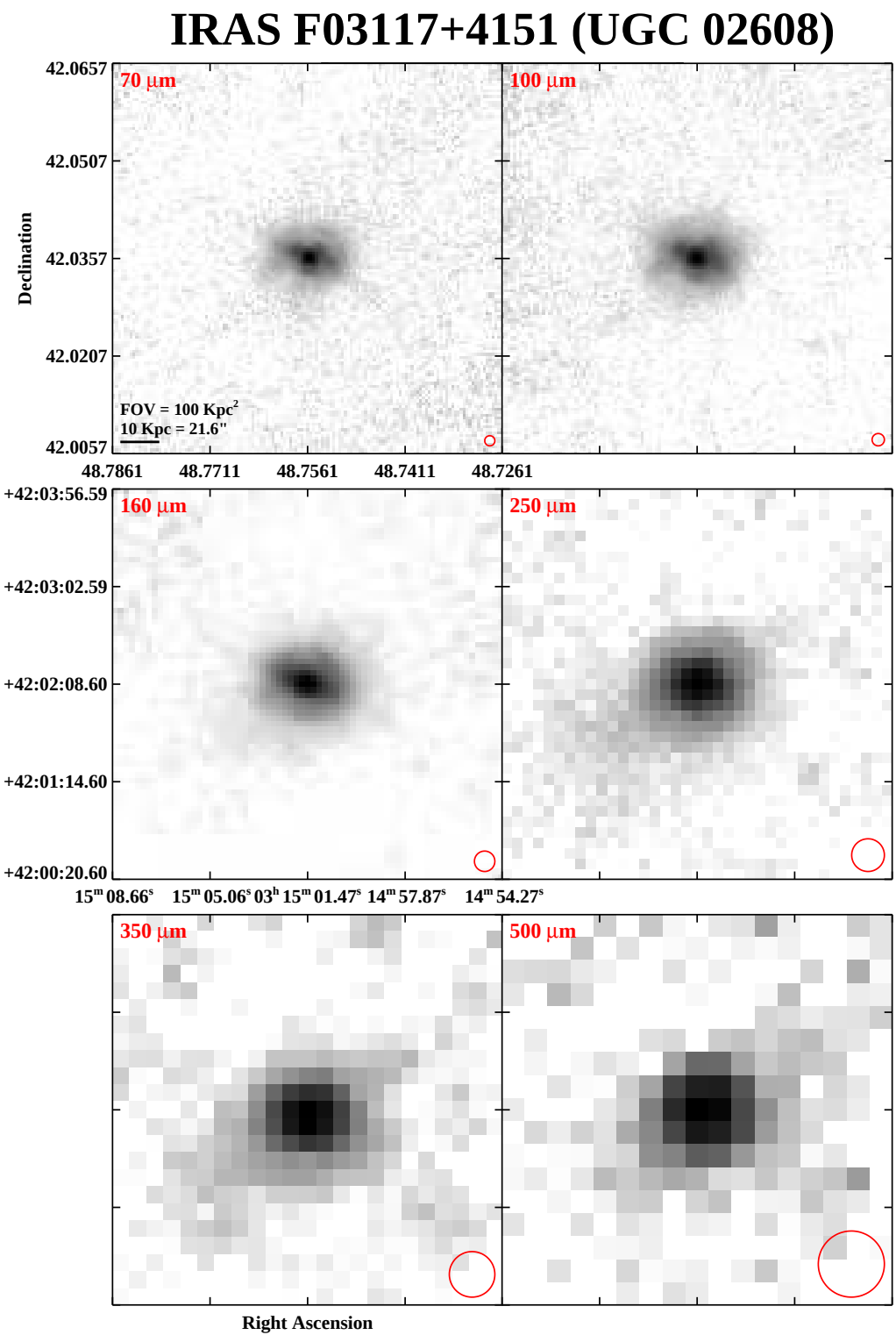

Figure 2.3 continued (page 31 of 209).

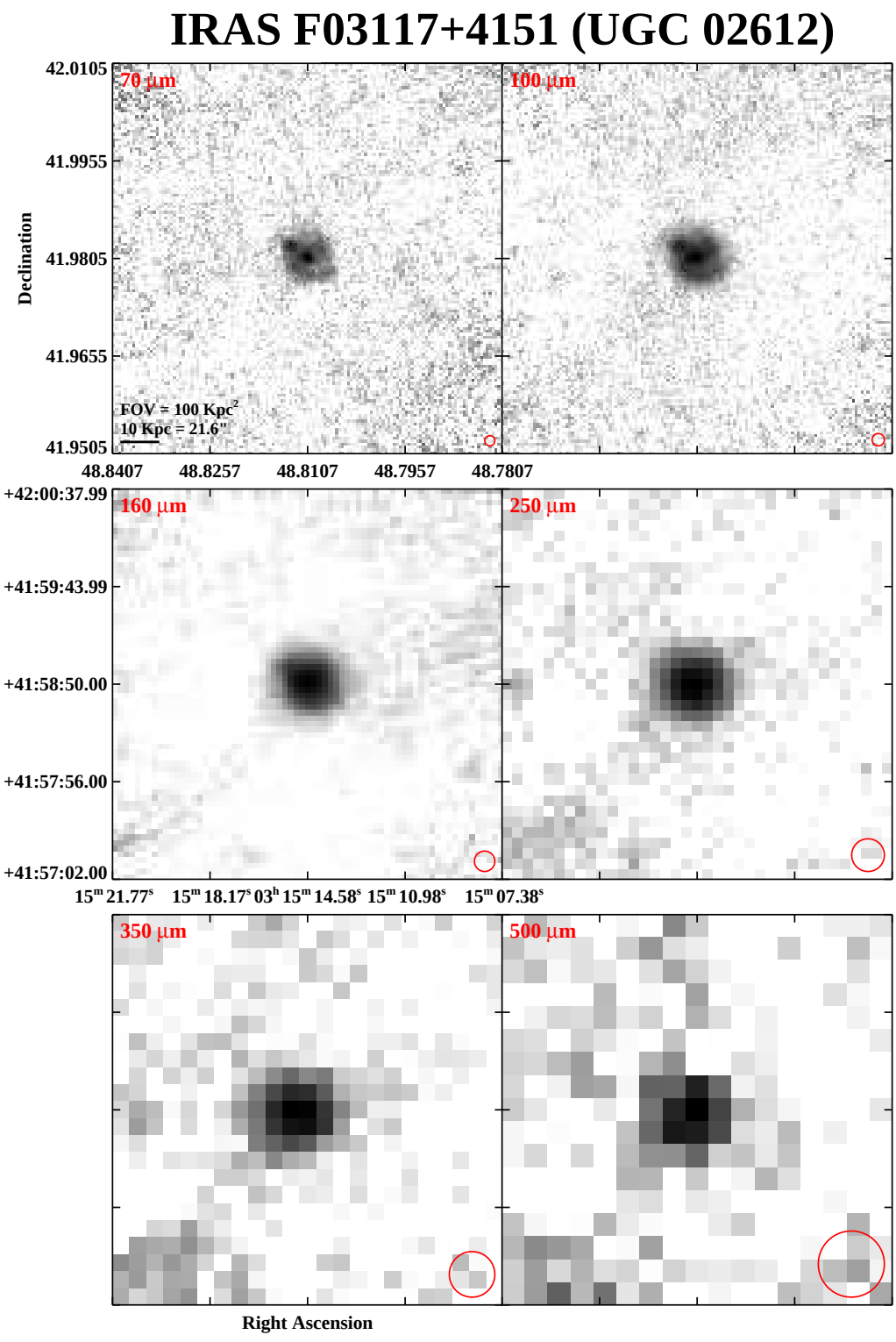

Figure 2.3 continued (page 32 of 209).

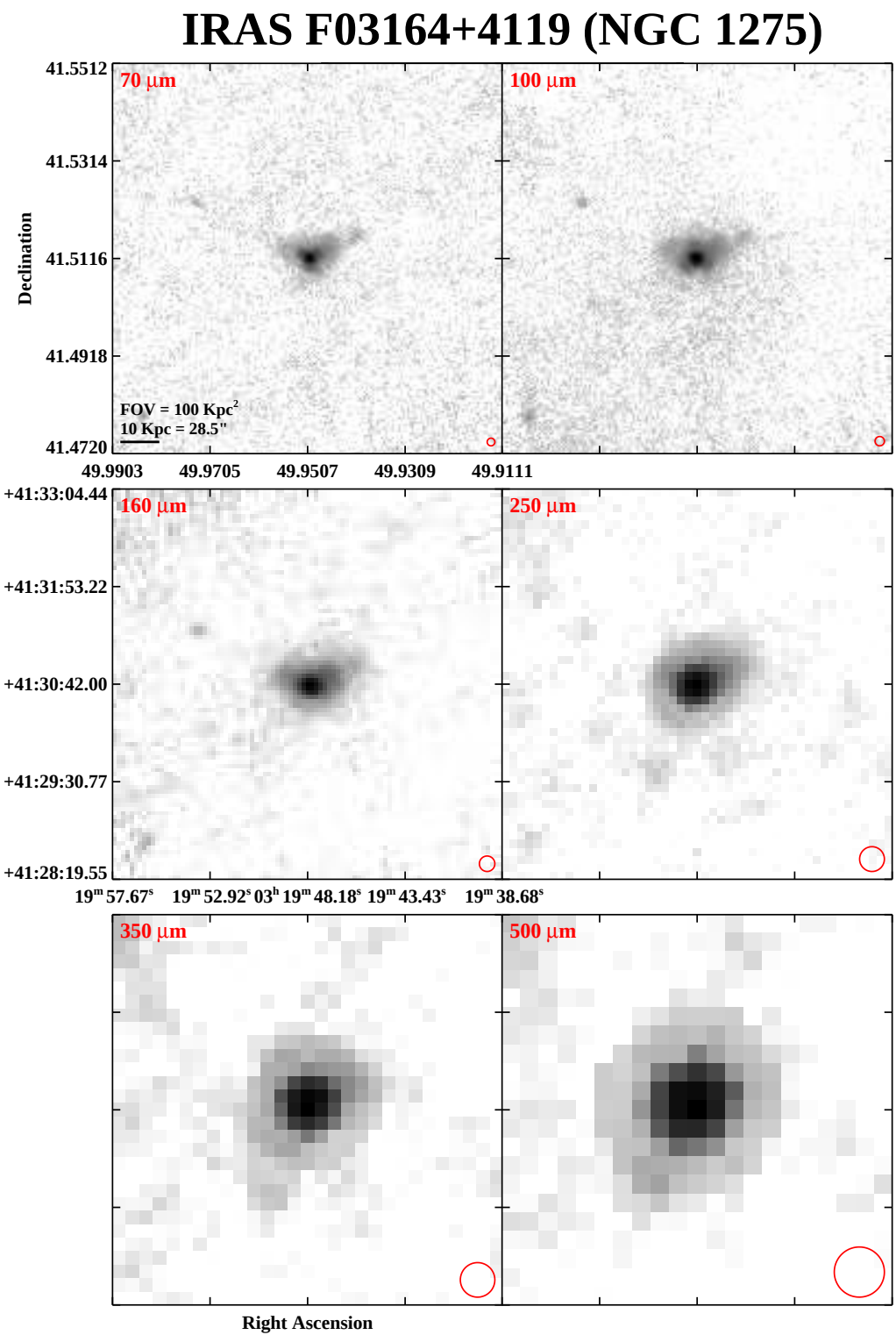

Figure 2.3 continued (page 33 of 209).

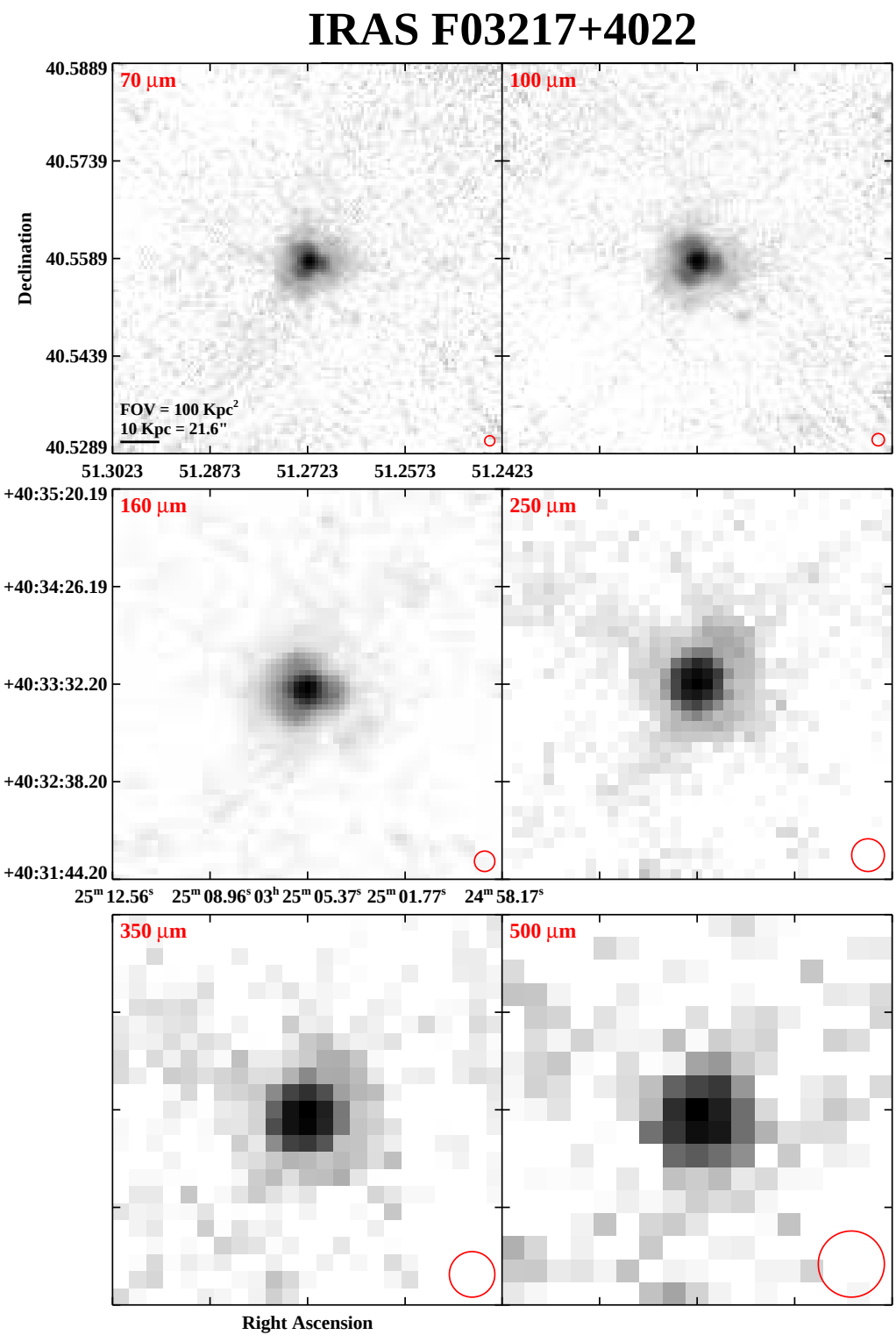

Figure 2.3 continued (page 34 of 209).

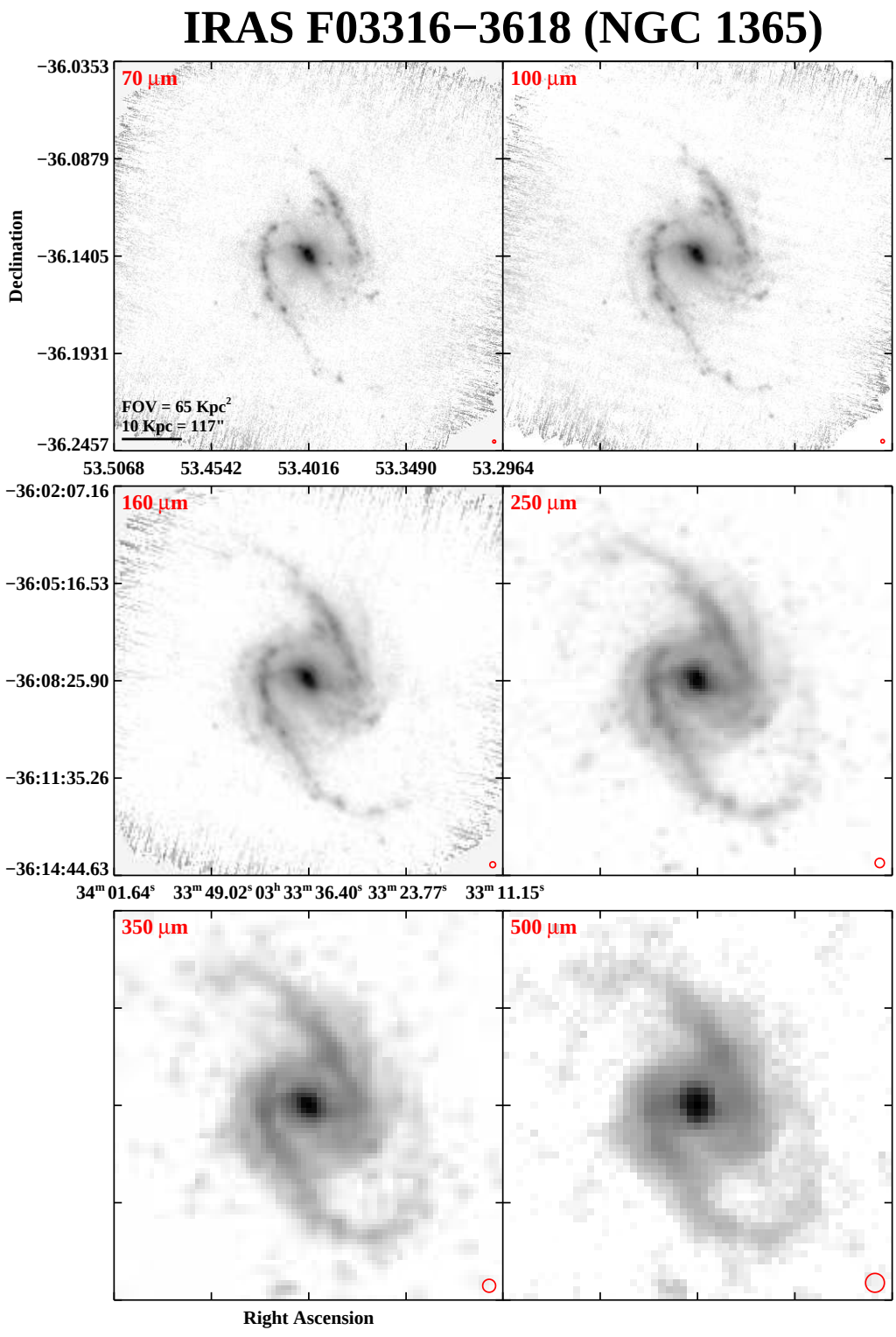

Figure 2.3 continued (page 35 of 209).

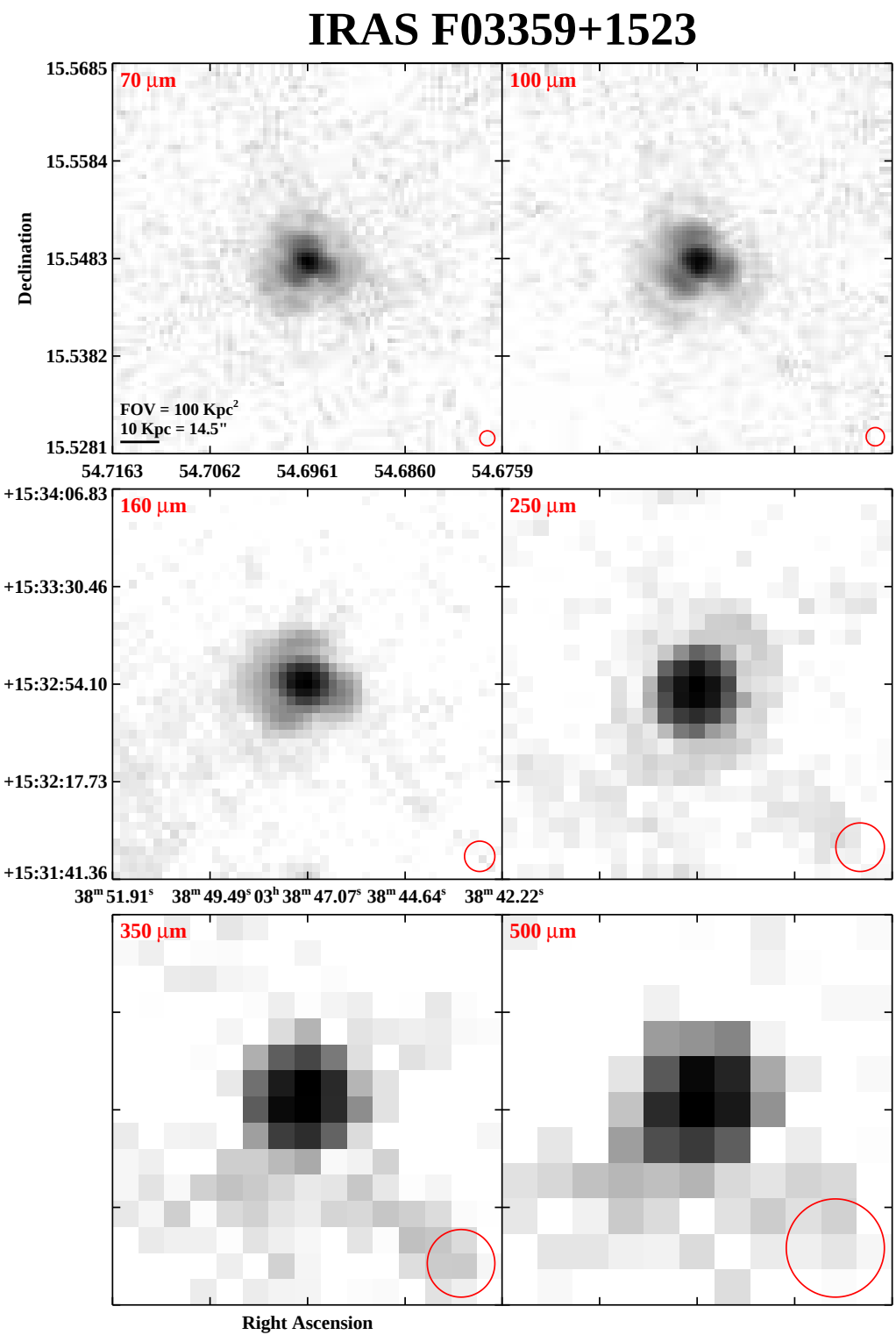

Figure 2.3 continued (page 36 of 209).

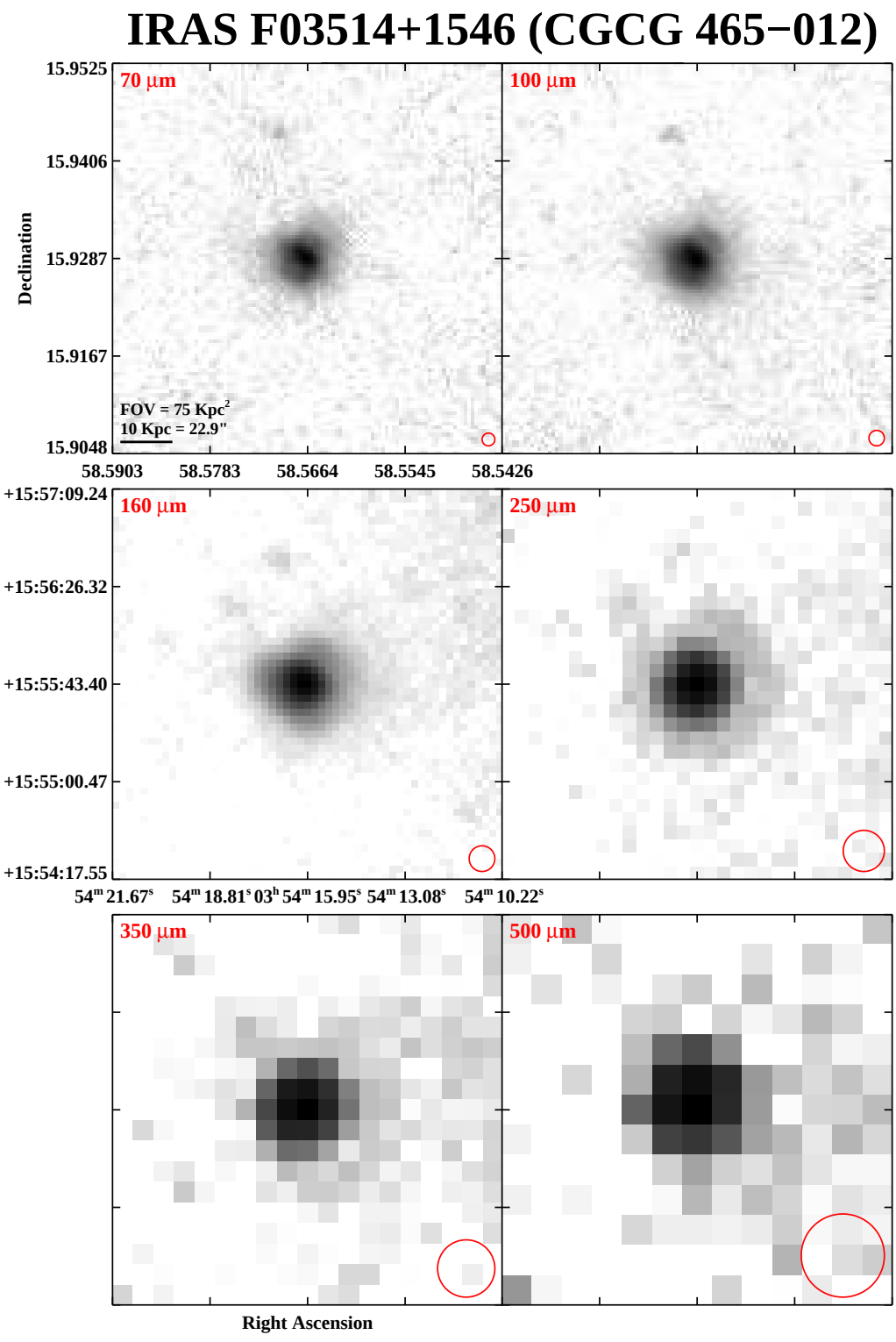

Figure 2.3 continued (page 37 of 209).

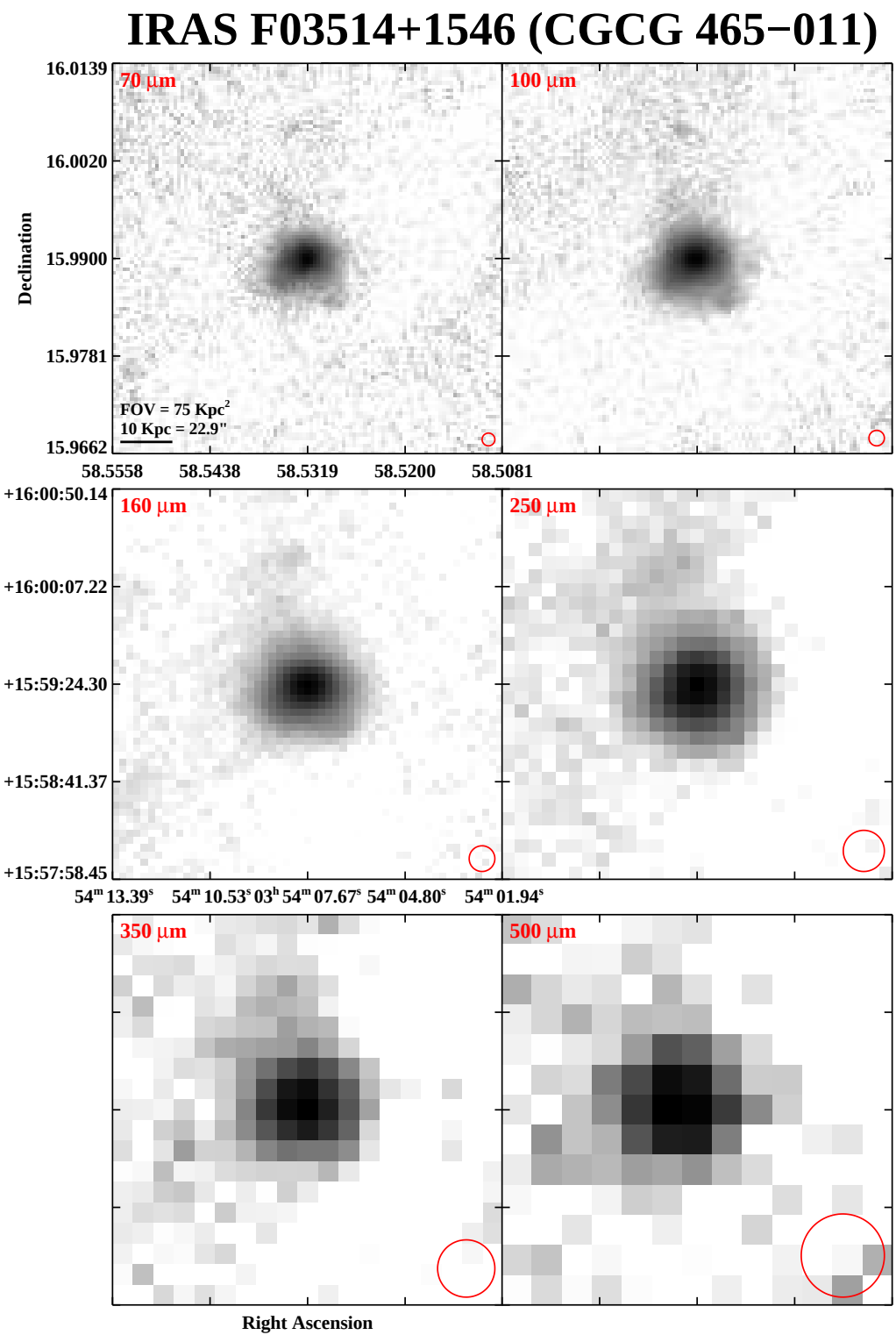

Figure 2.3 continued (page 38 of 209).

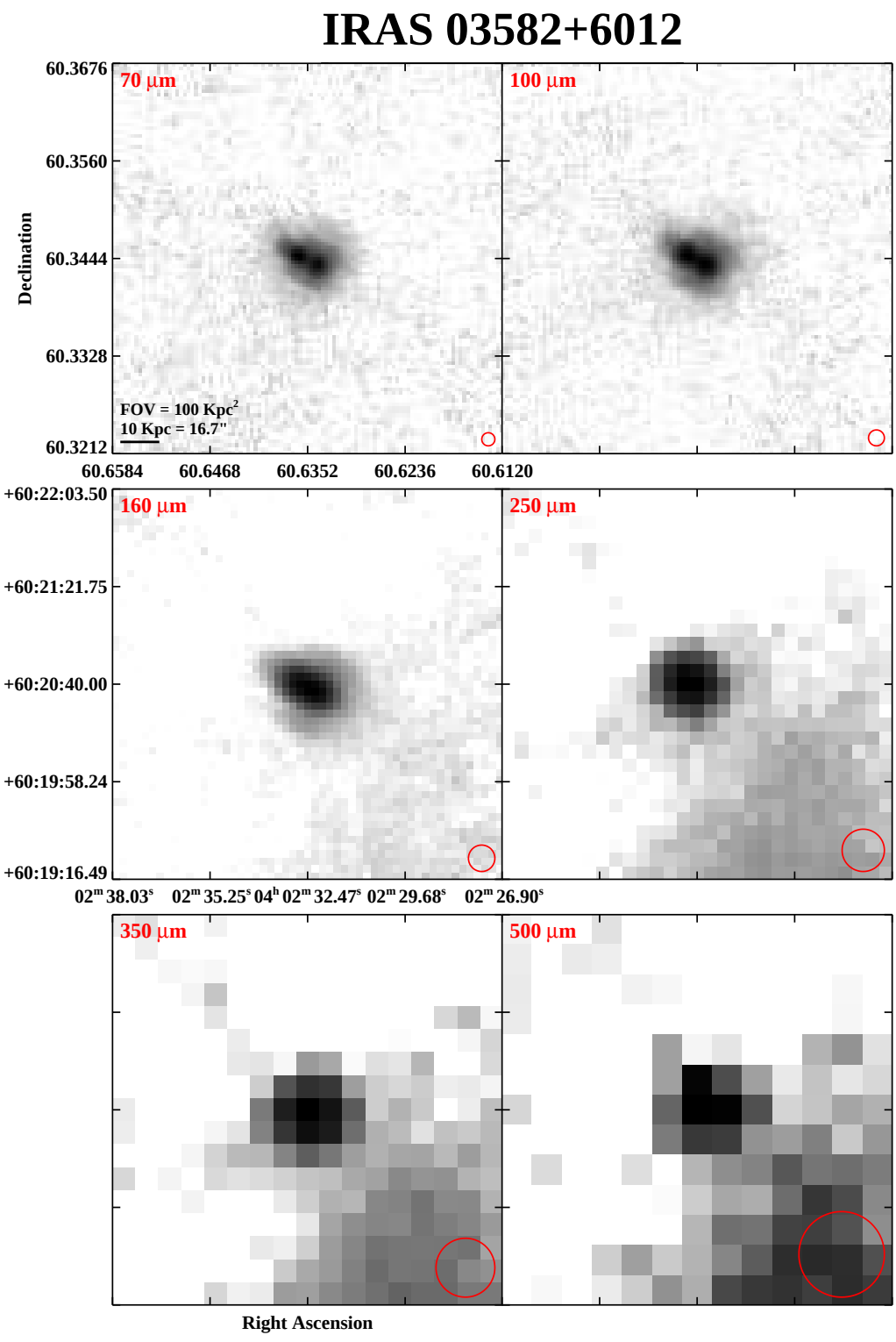

Figure 2.3 continued (page 39 of 209).

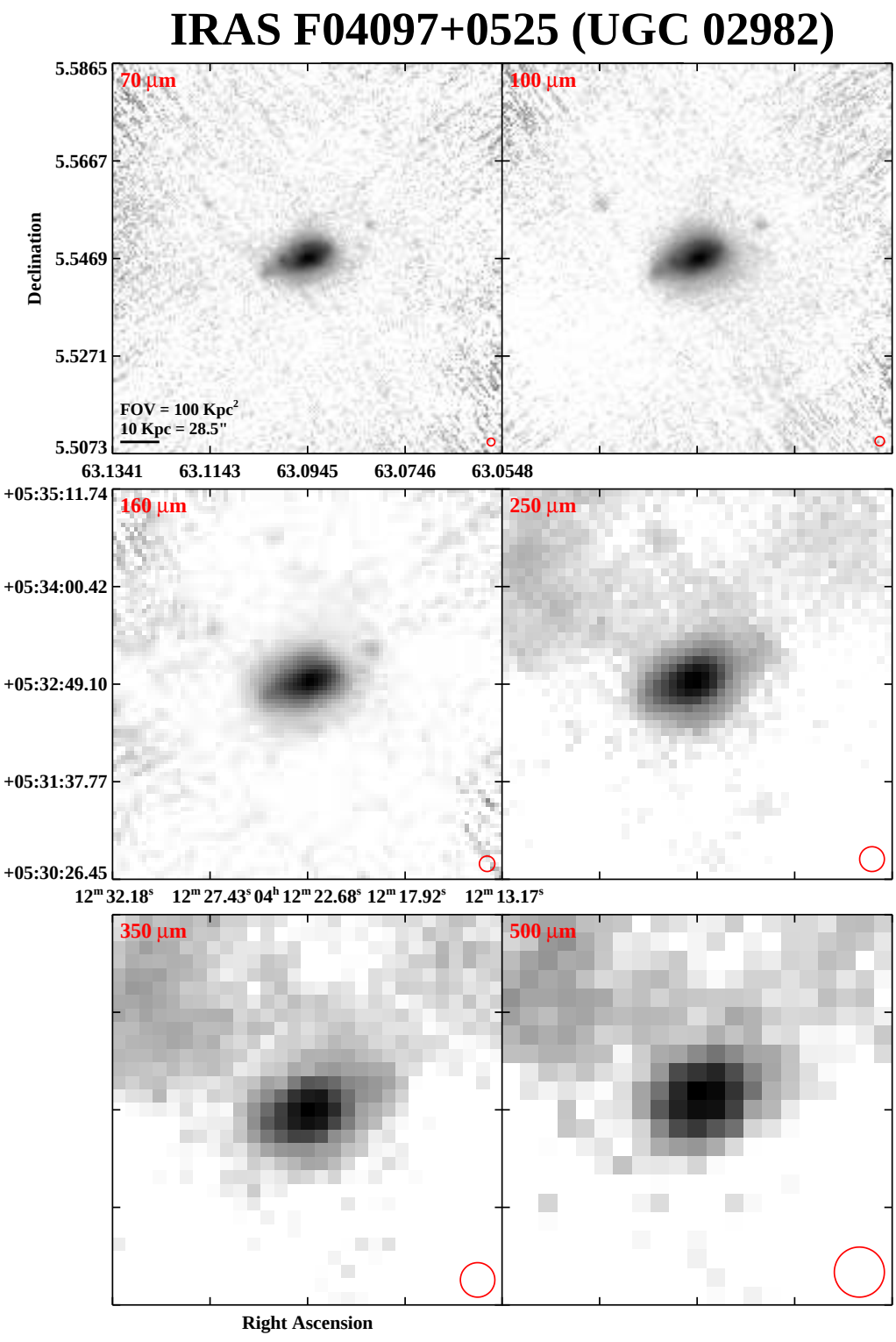

Figure 2.3 continued (page 40 of 209).

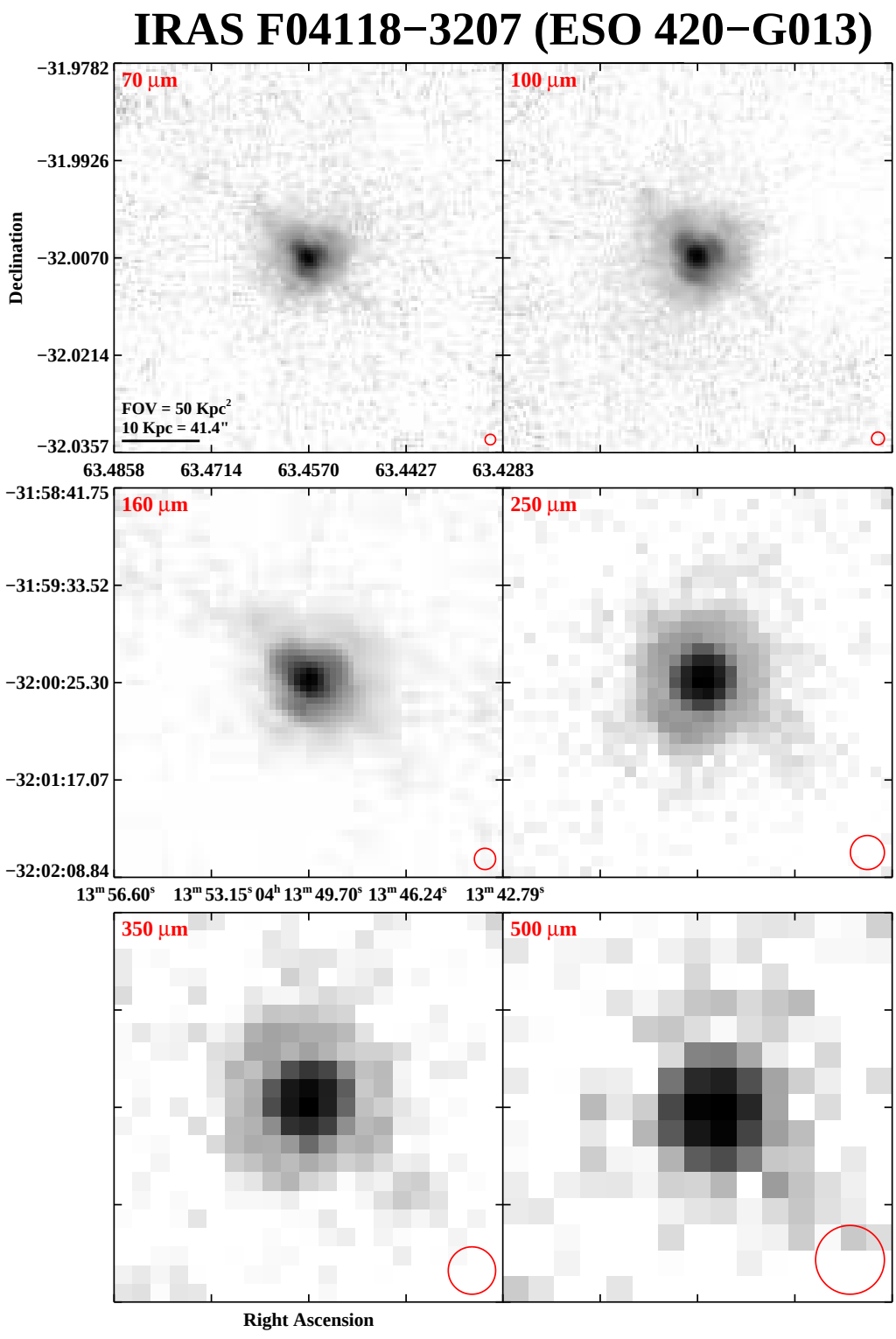

Figure 2.3 continued (page 41 of 209).

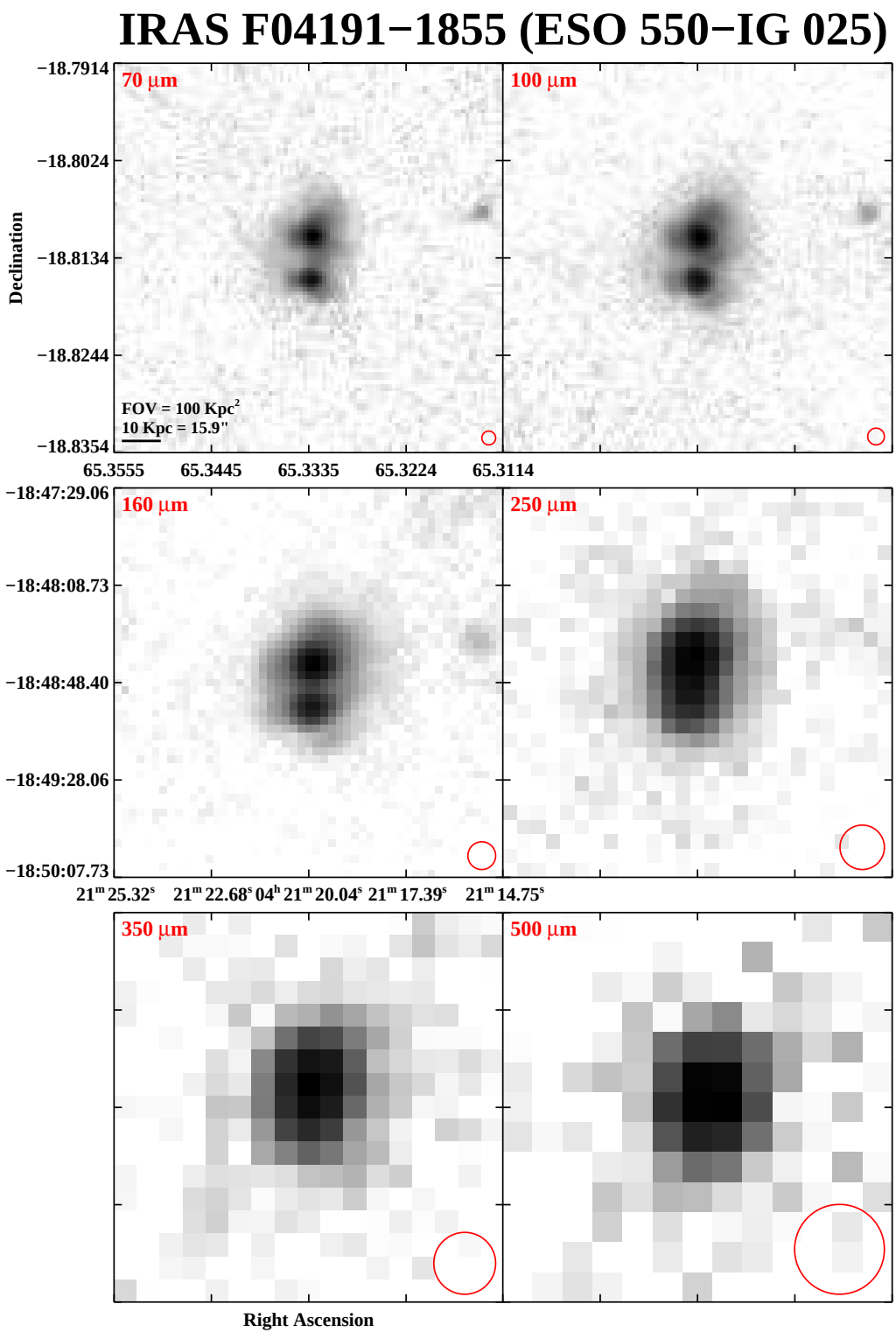

Figure 2.3 continued (page 42 of 209).

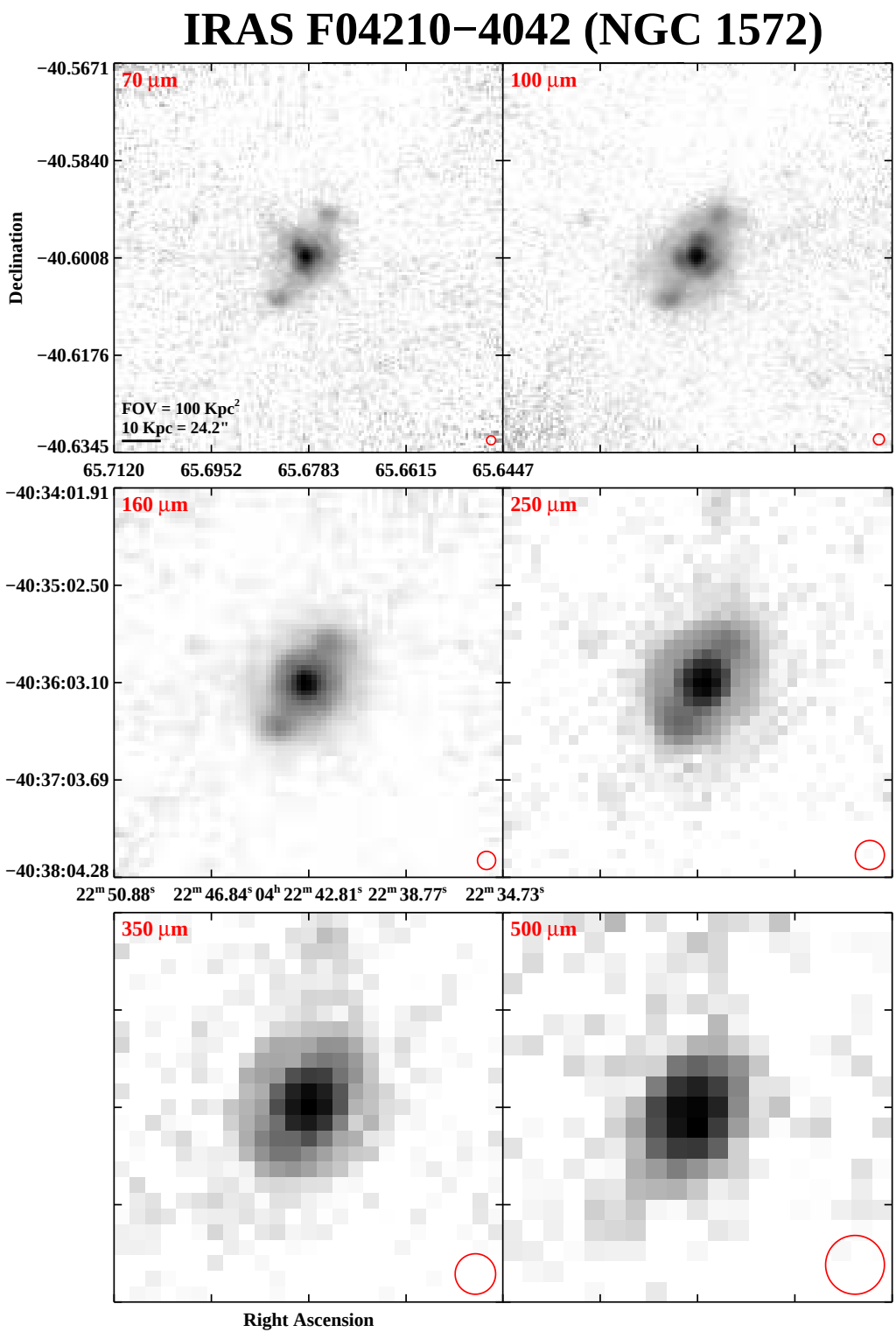

Figure 2.3 continued (page 43 of 209).

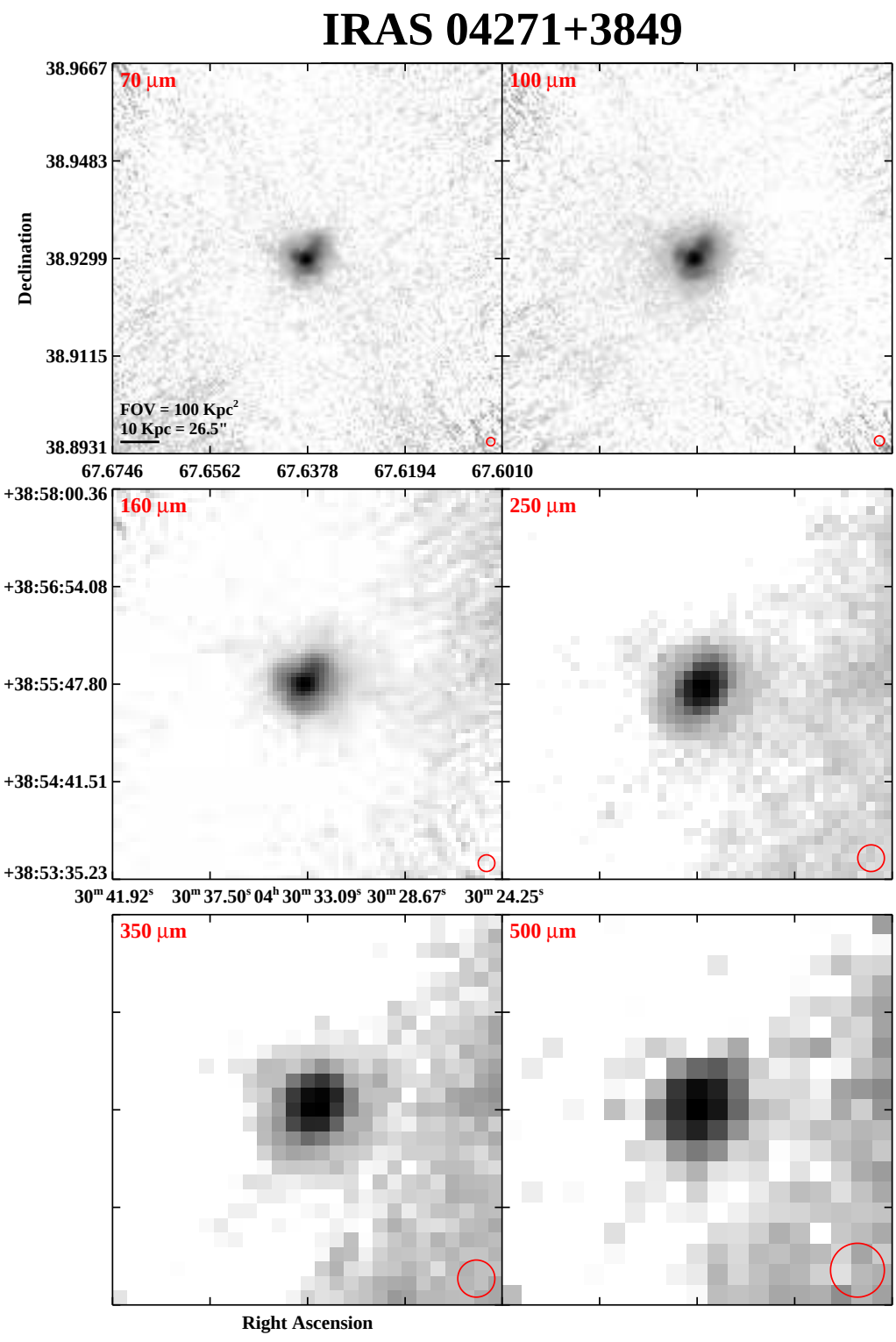

Figure 2.3 continued (page 44 of 209).

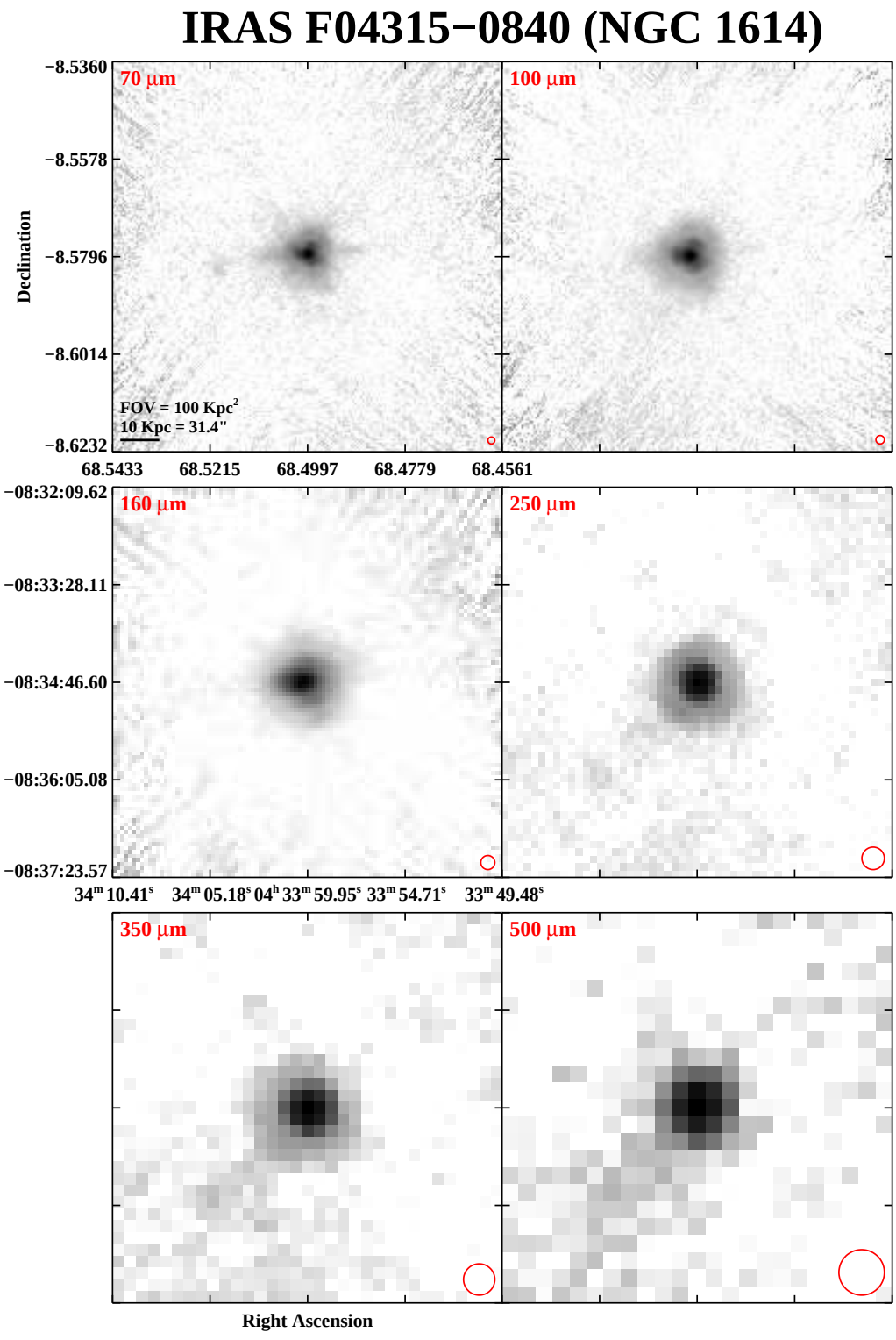

Figure 2.3 continued (page 45 of 209).

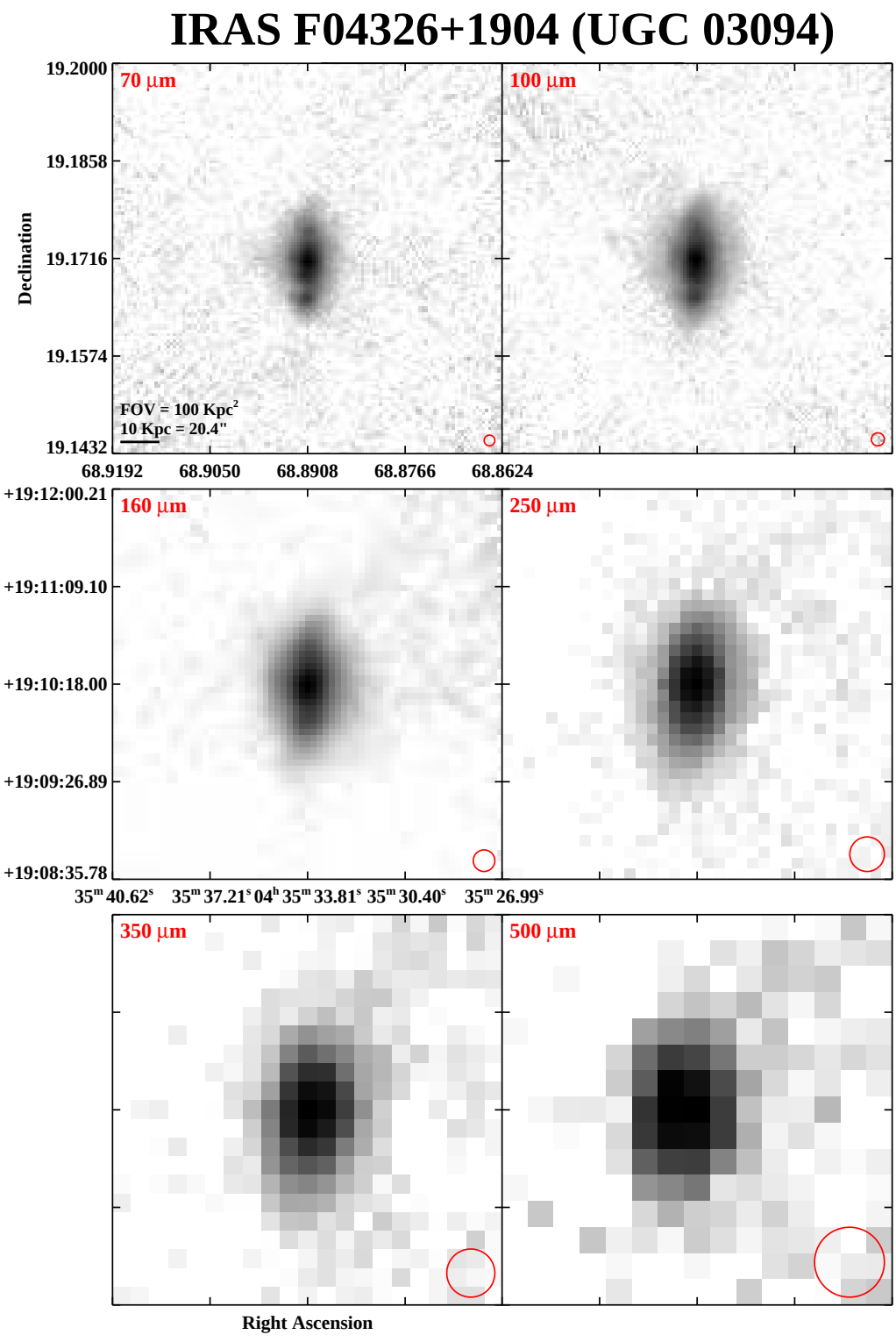

Figure 2.3 continued (page 46 of 209).

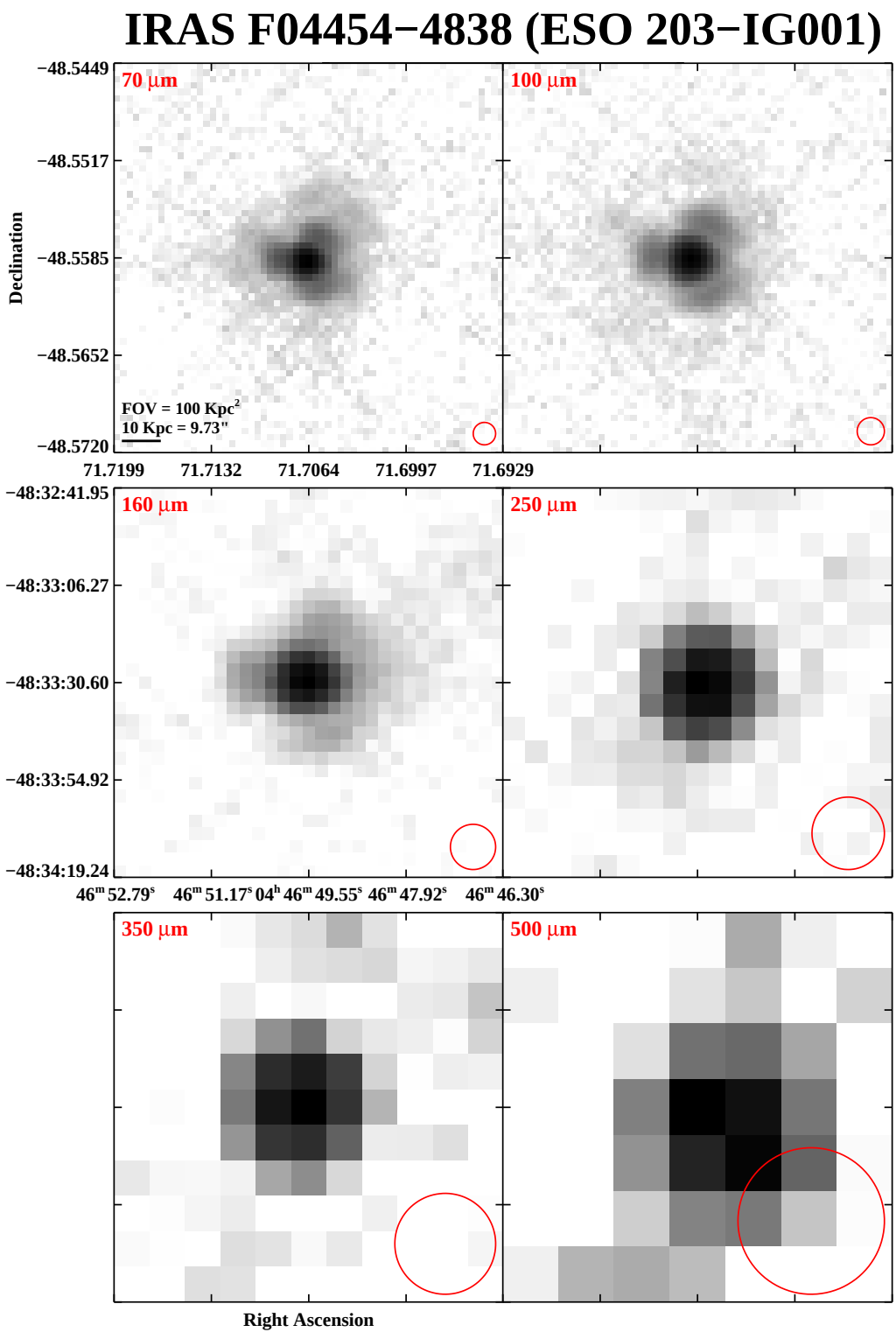

Figure 2.3 continued (page 47 of 209).

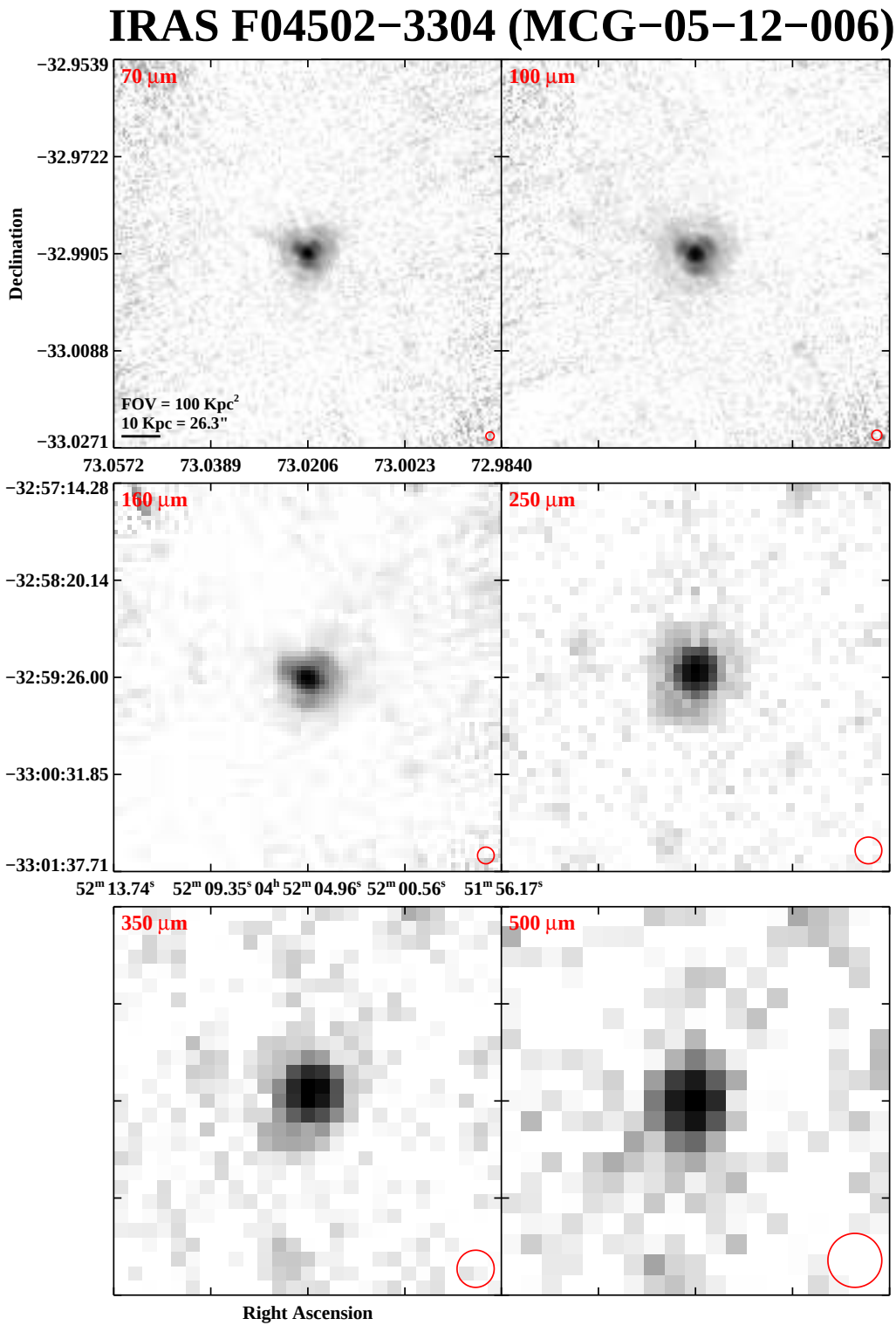

Figure 2.3 continued (page 48 of 209).

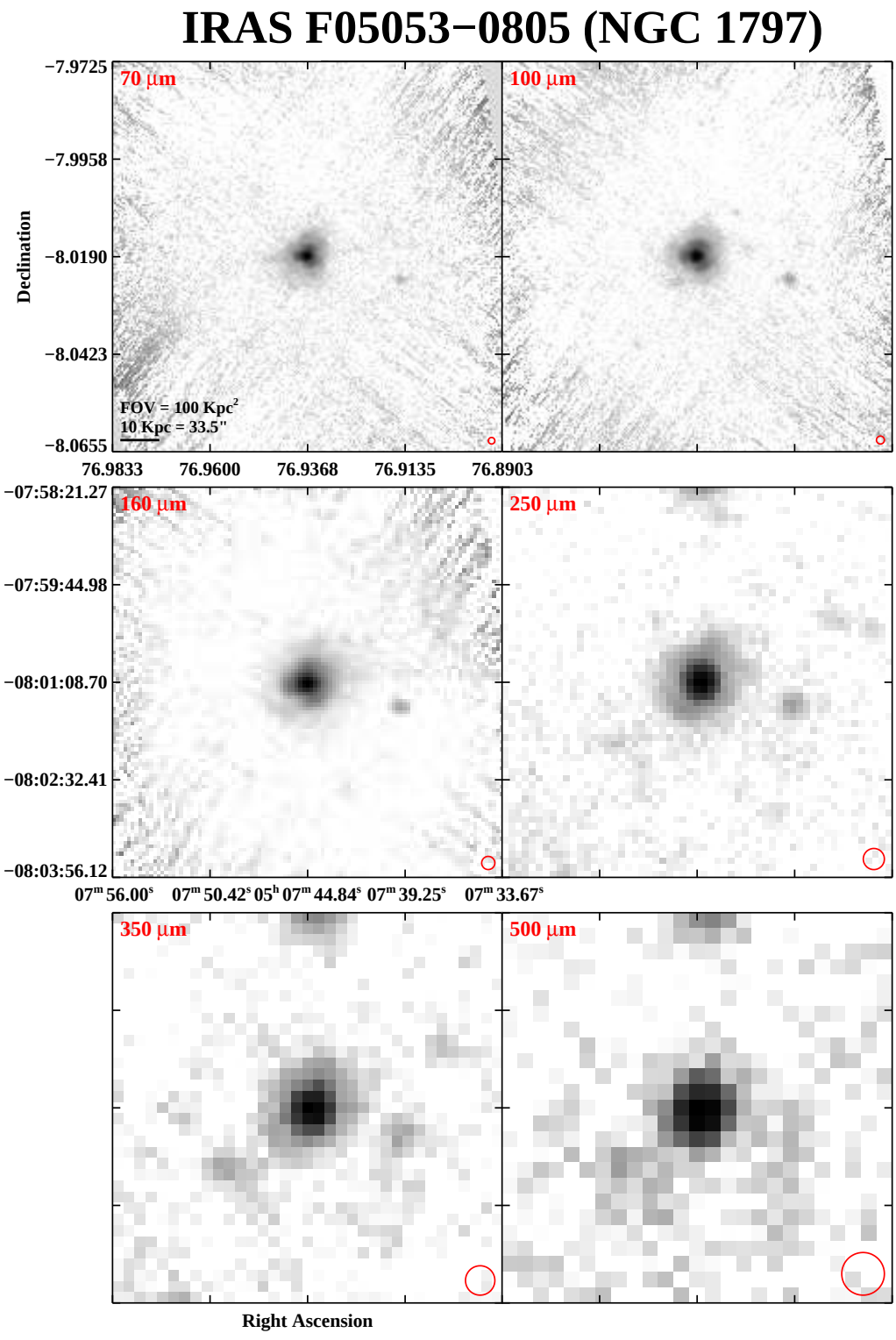

Figure 2.3 continued (page 49 of 209).

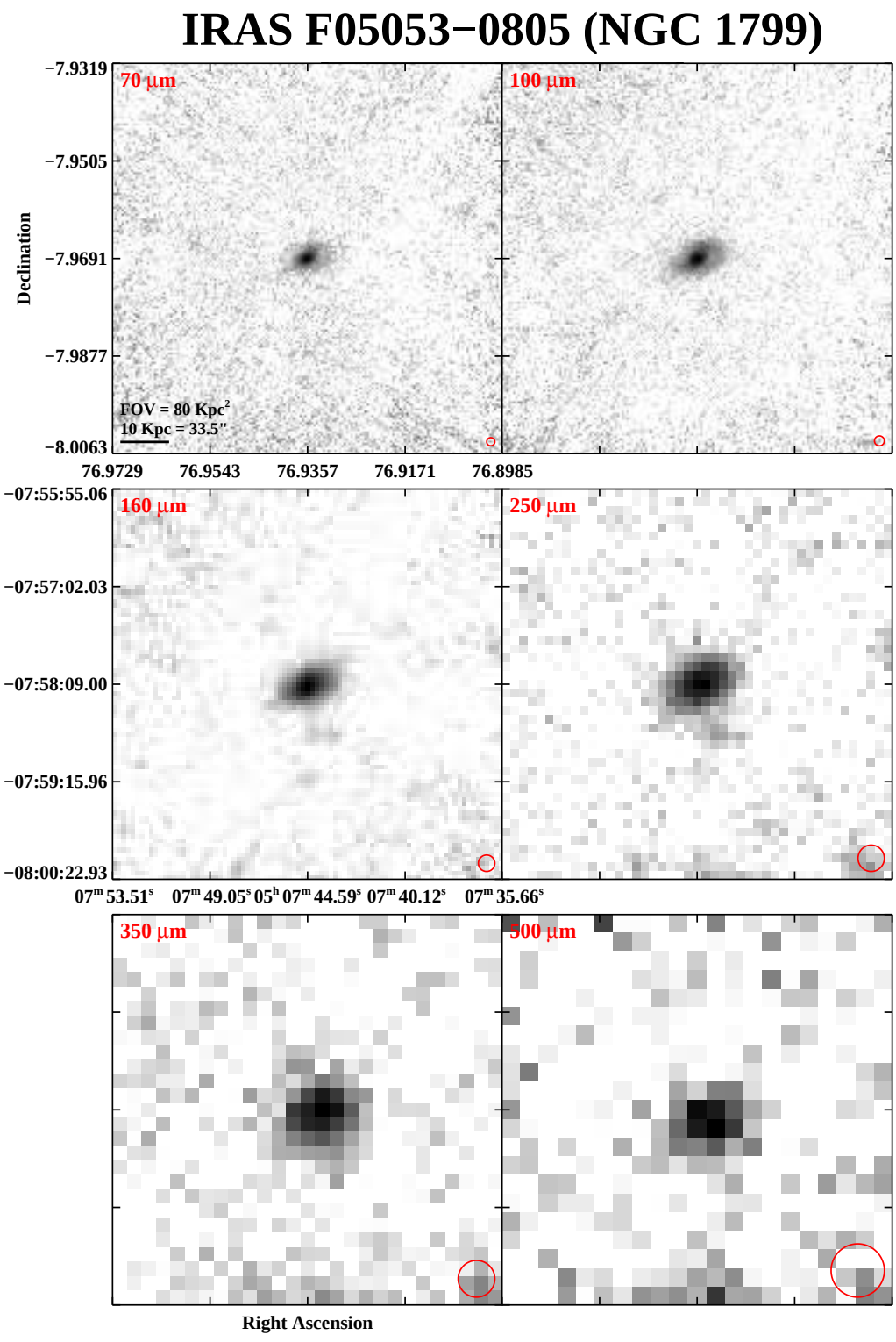

Figure 2.3 continued (page 50 of 209).

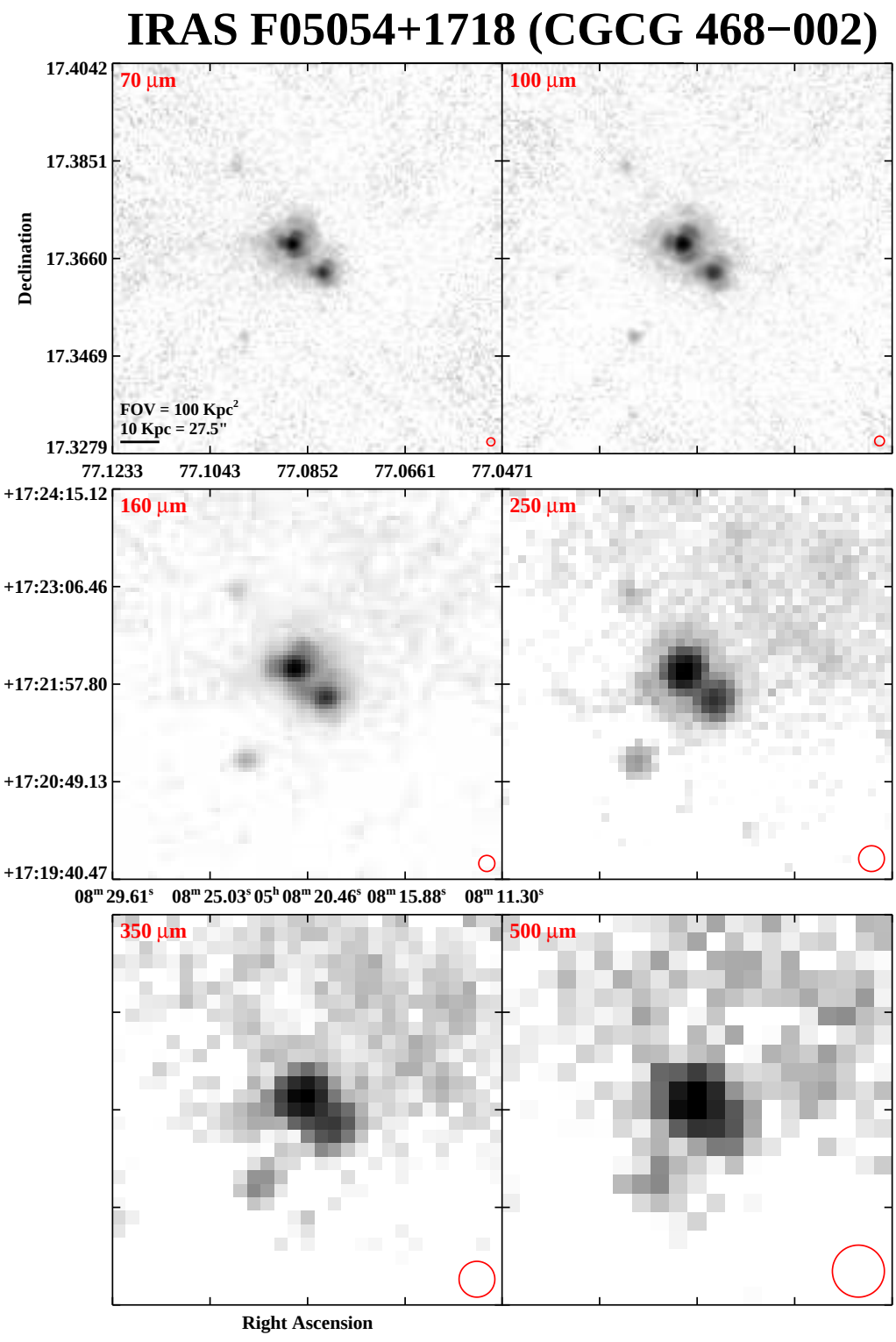

Figure 2.3 continued (page 51 of 209).

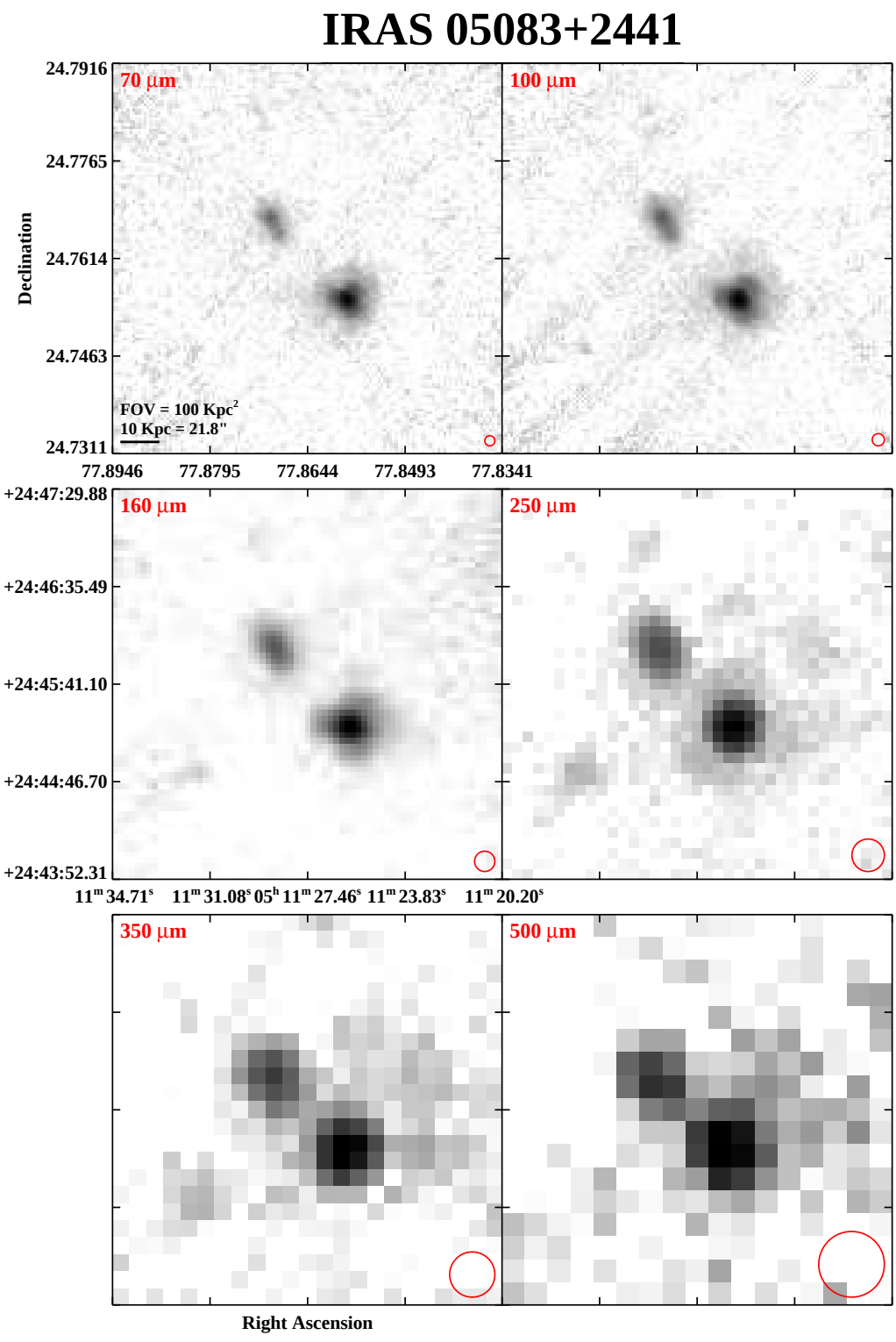

Figure 2.3 continued (page 52 of 209).

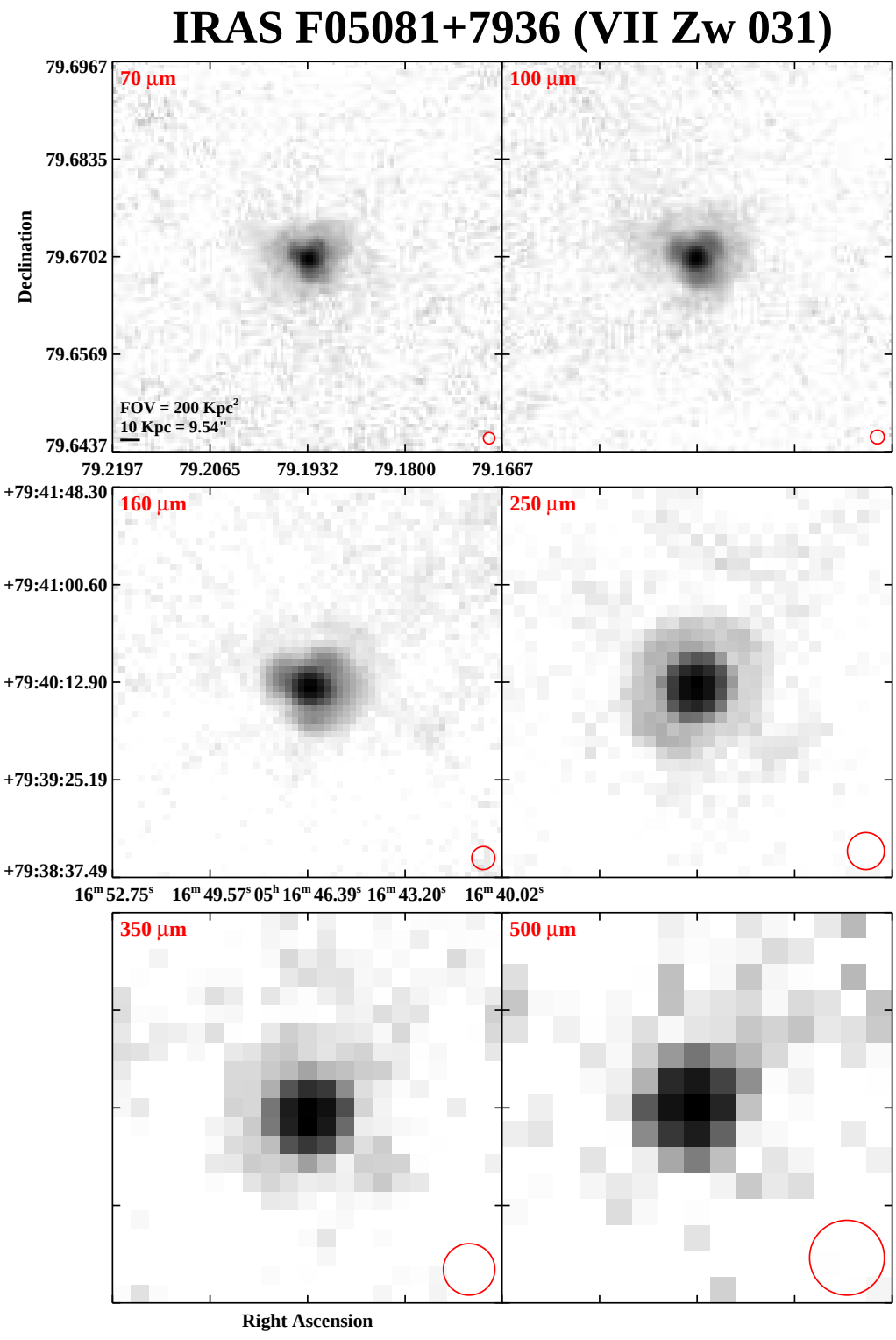

Figure 2.3 continued (page 53 of 209).

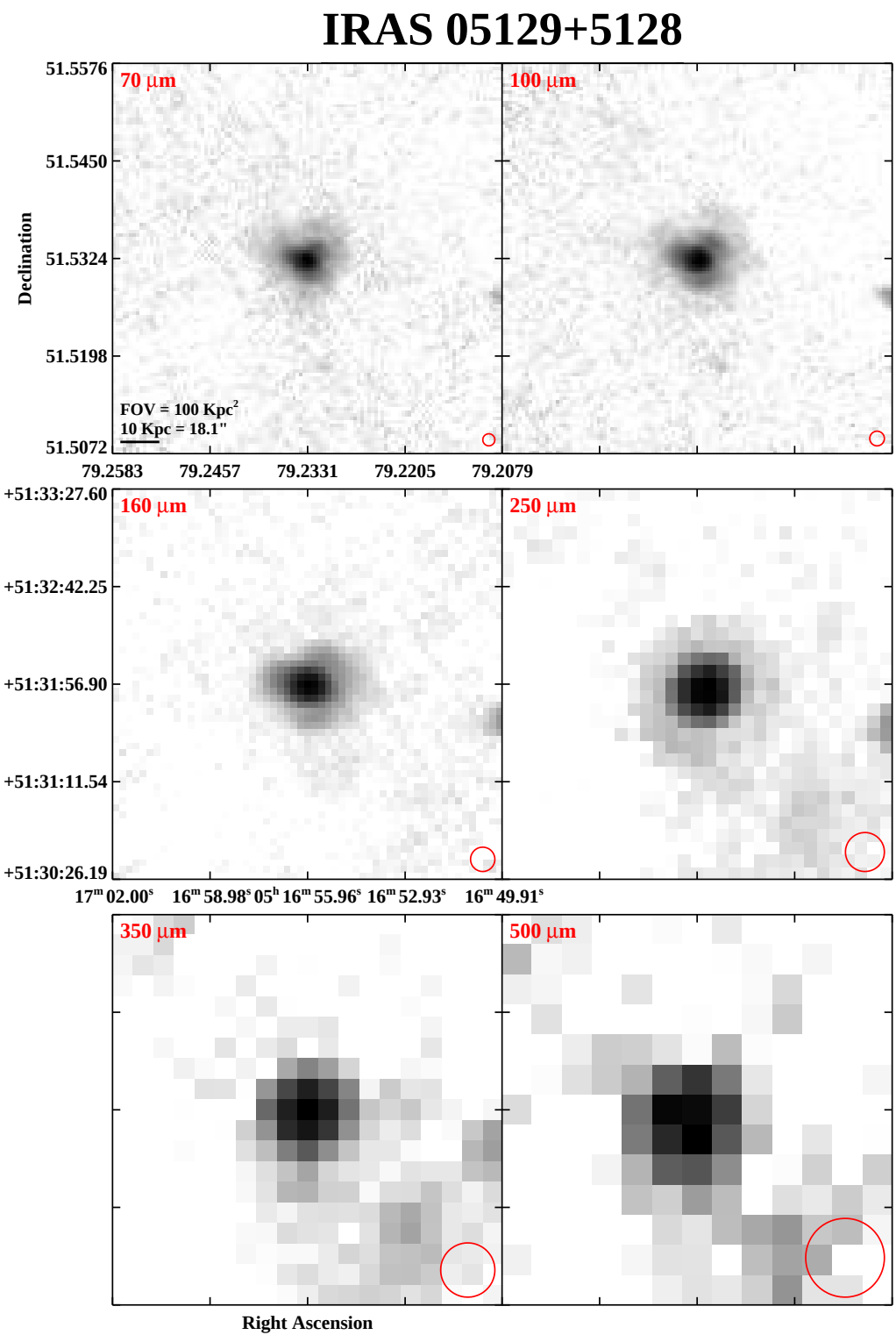

Figure 2.3 continued (page 54 of 209).

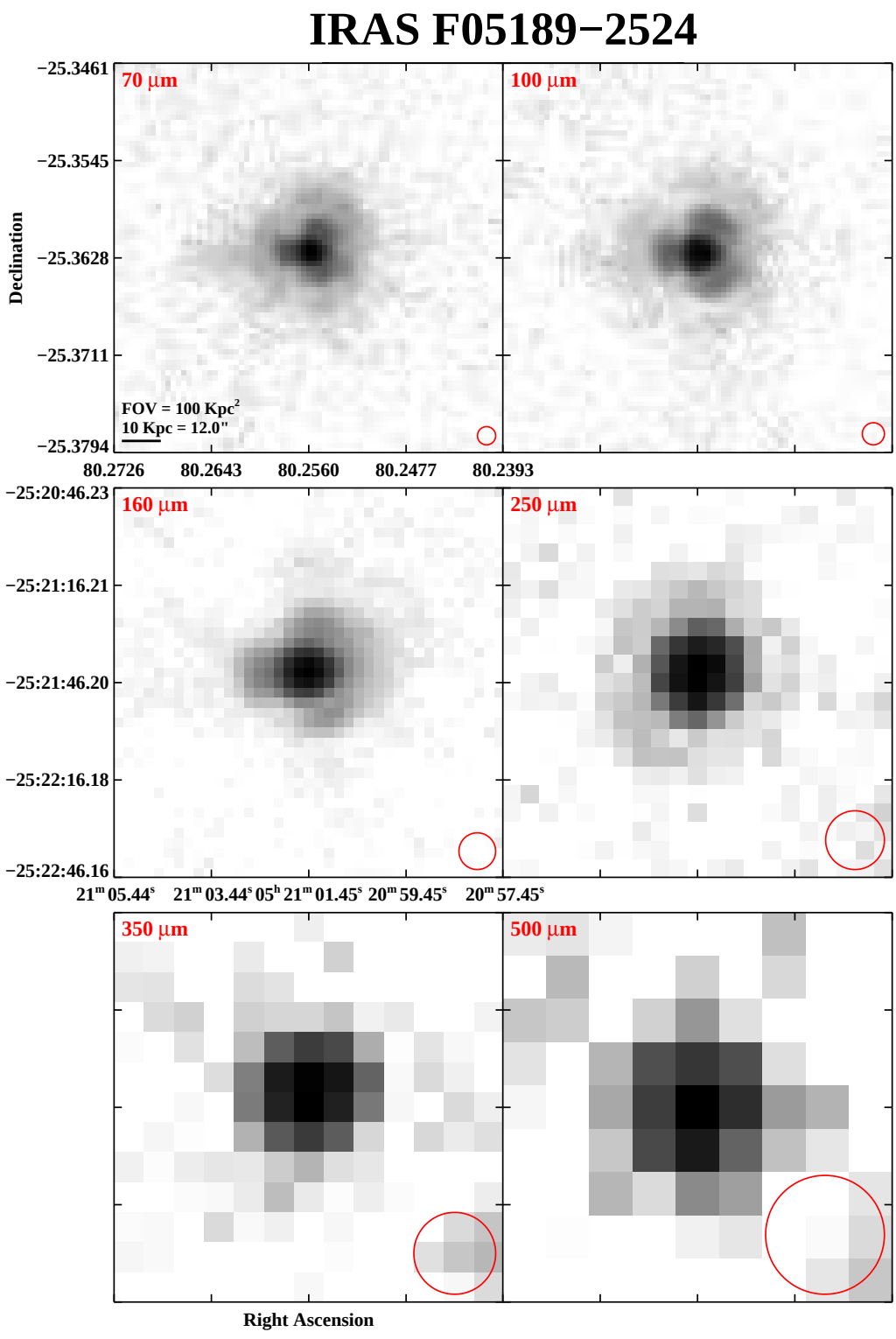

Figure 2.3 continued (page 55 of 209).

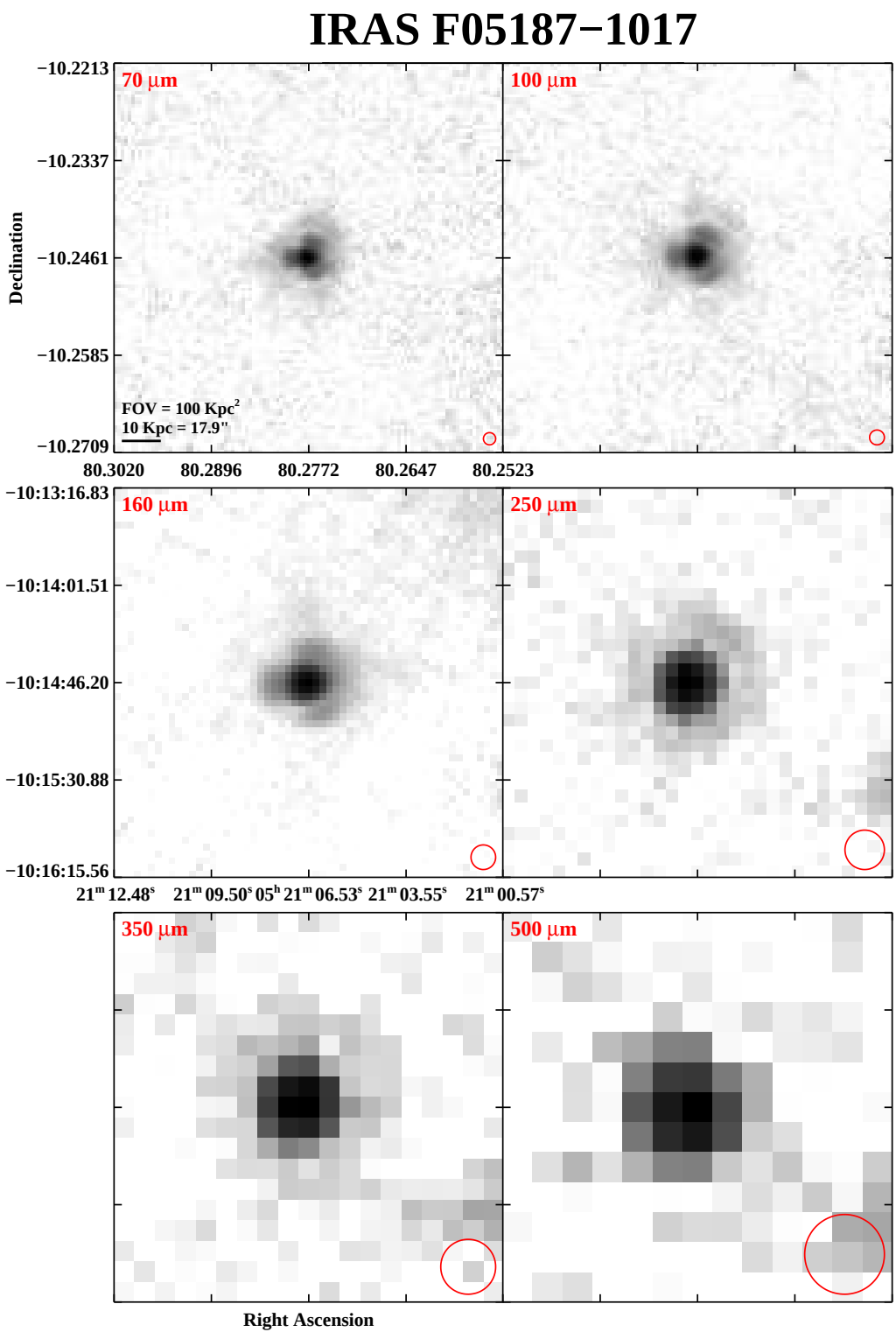

Figure 2.3 continued (page 56 of 209).

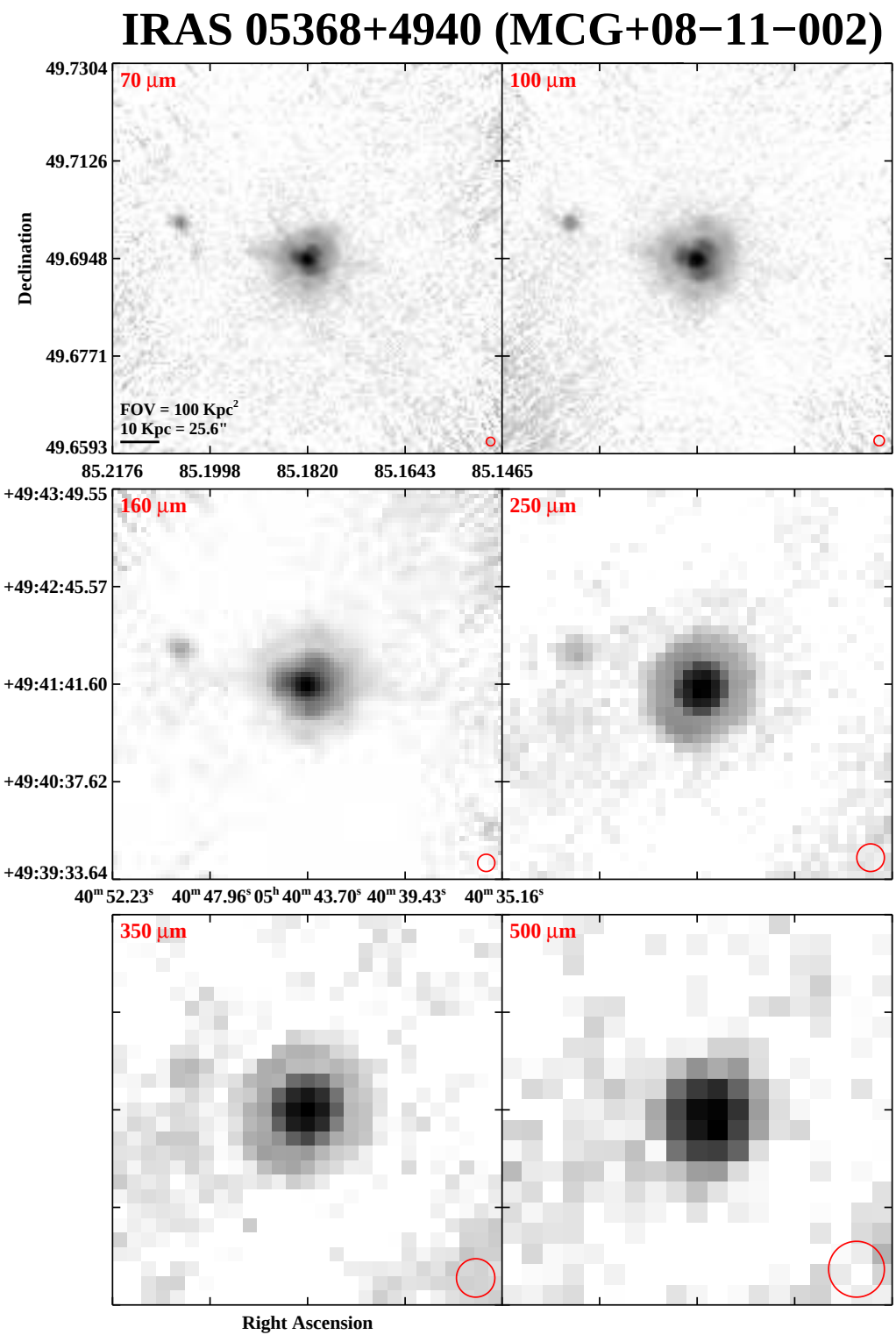

Figure 2.3 continued (page 57 of 209).

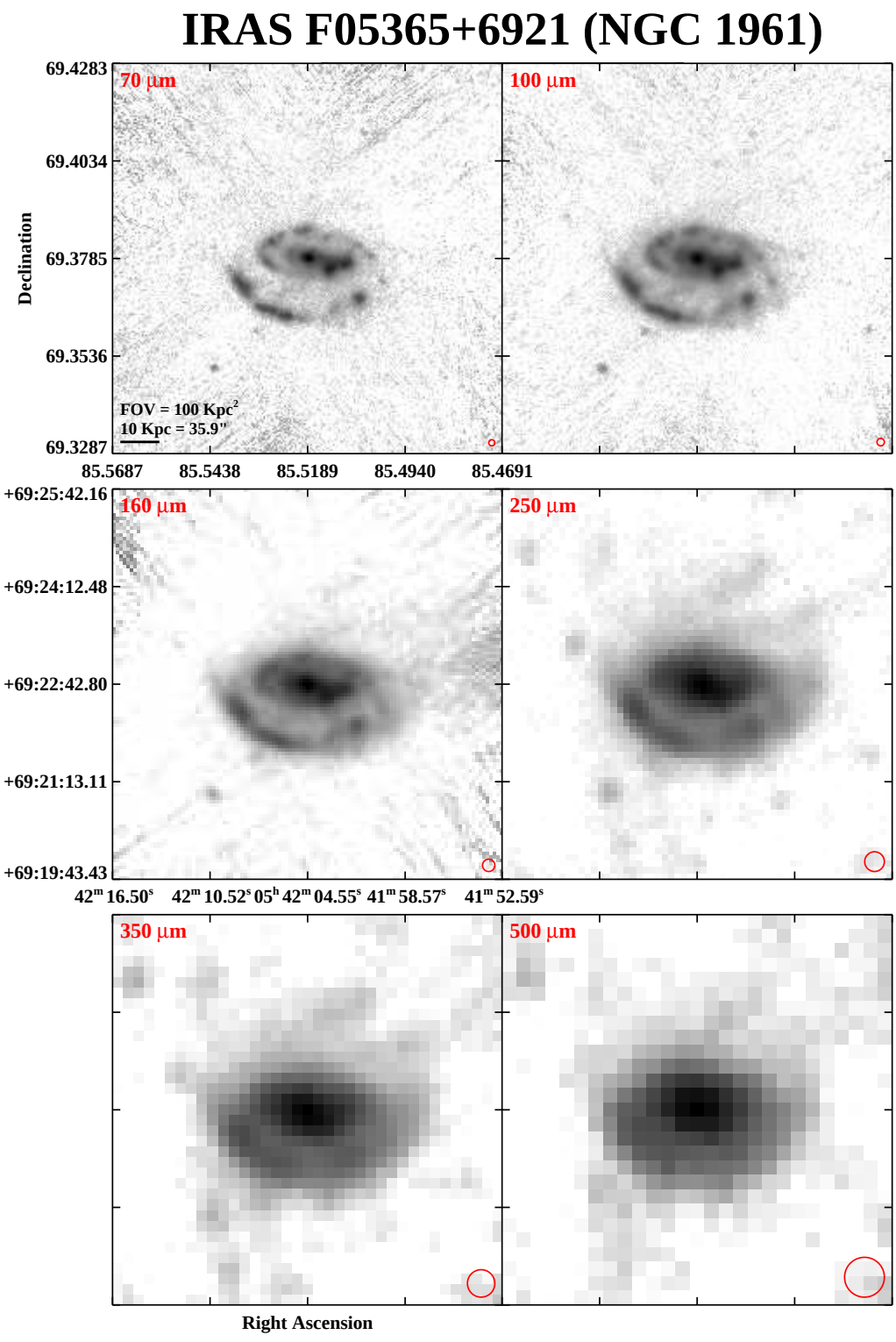

Figure 2.3 continued (page 58 of 209).

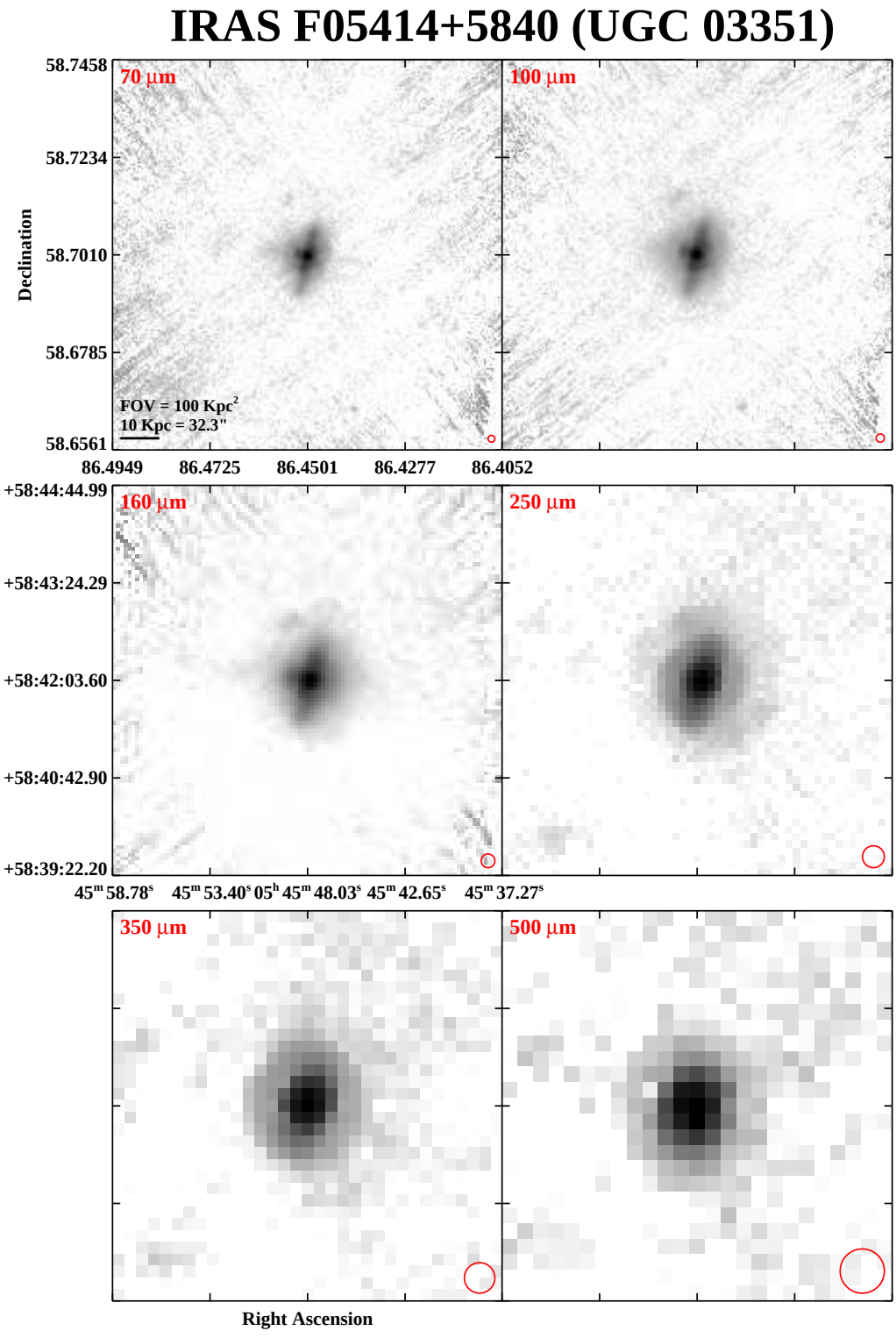

Figure 2.3 continued (page 59 of 209).

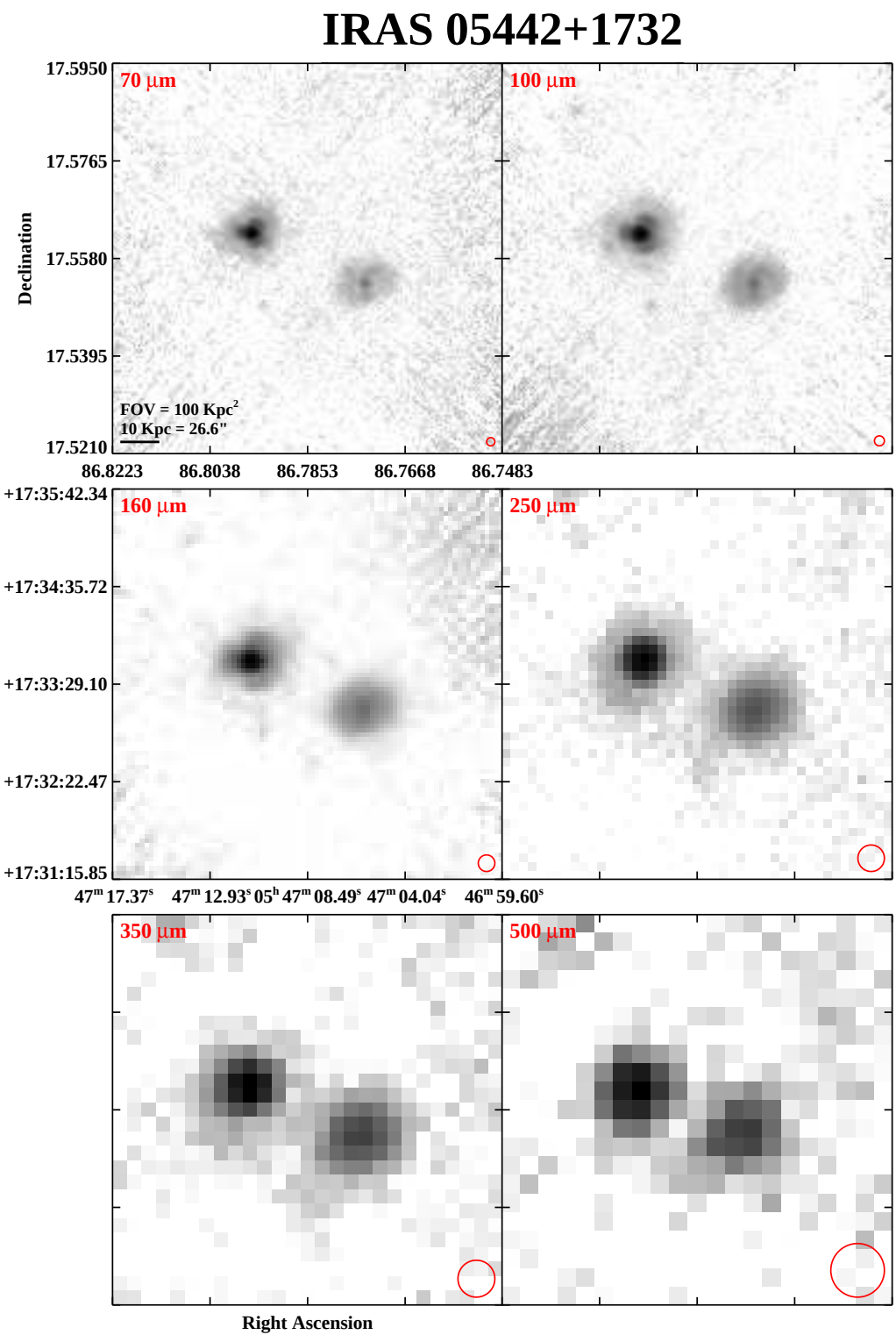

Figure 2.3 continued (page 60 of 209).

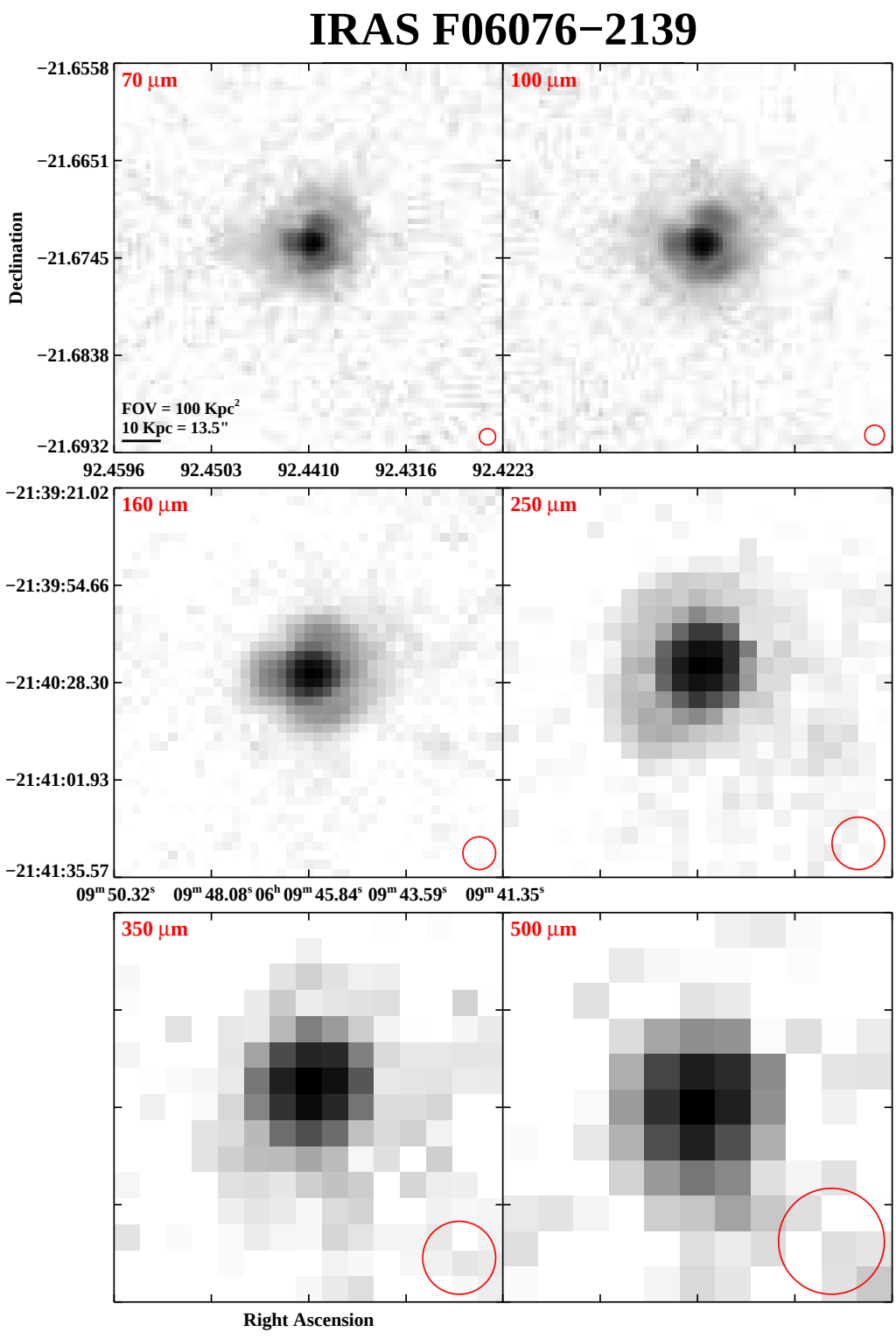

Figure 2.3 continued (page 61 of 209).

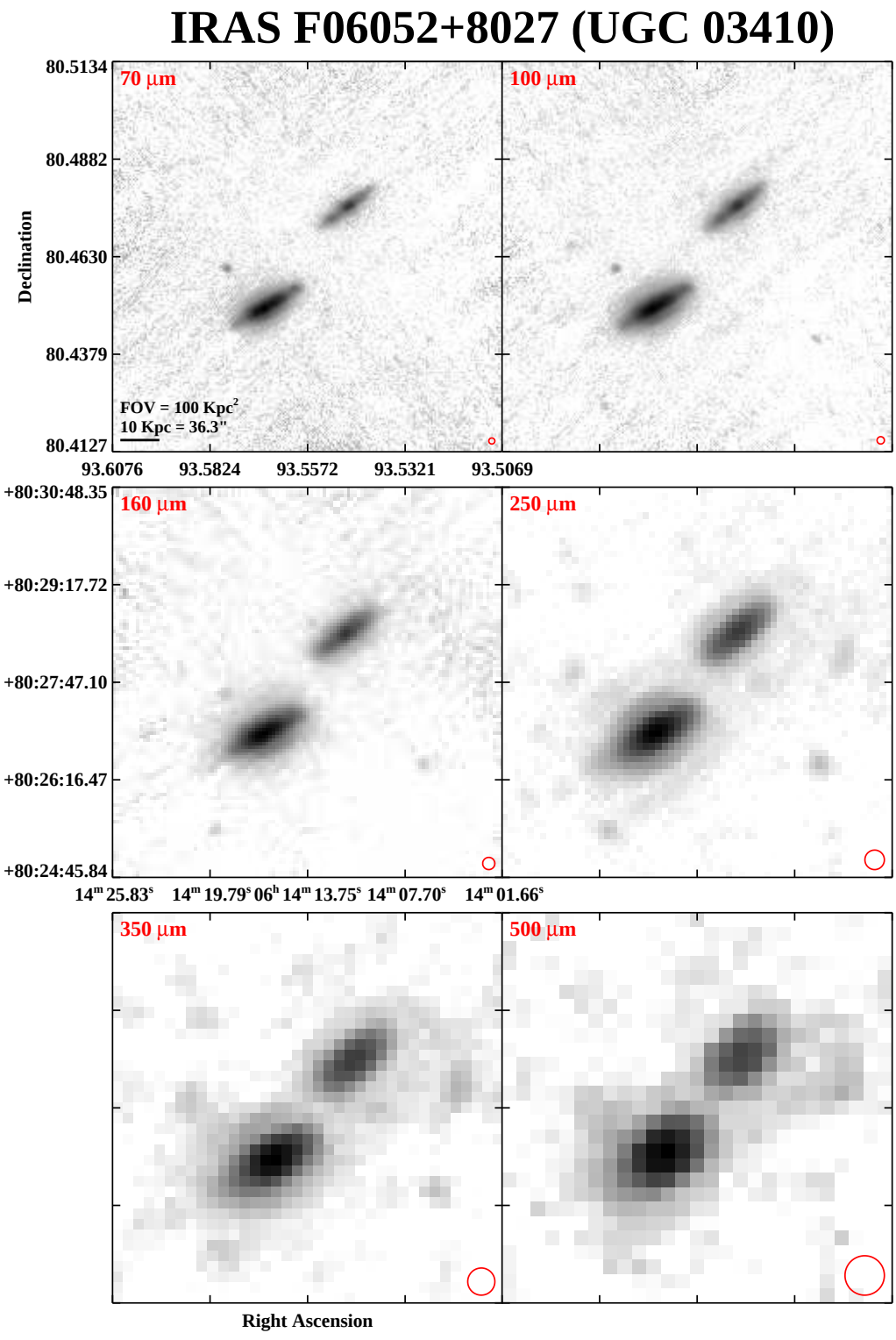

Figure 2.3 continued (page 62 of 209).

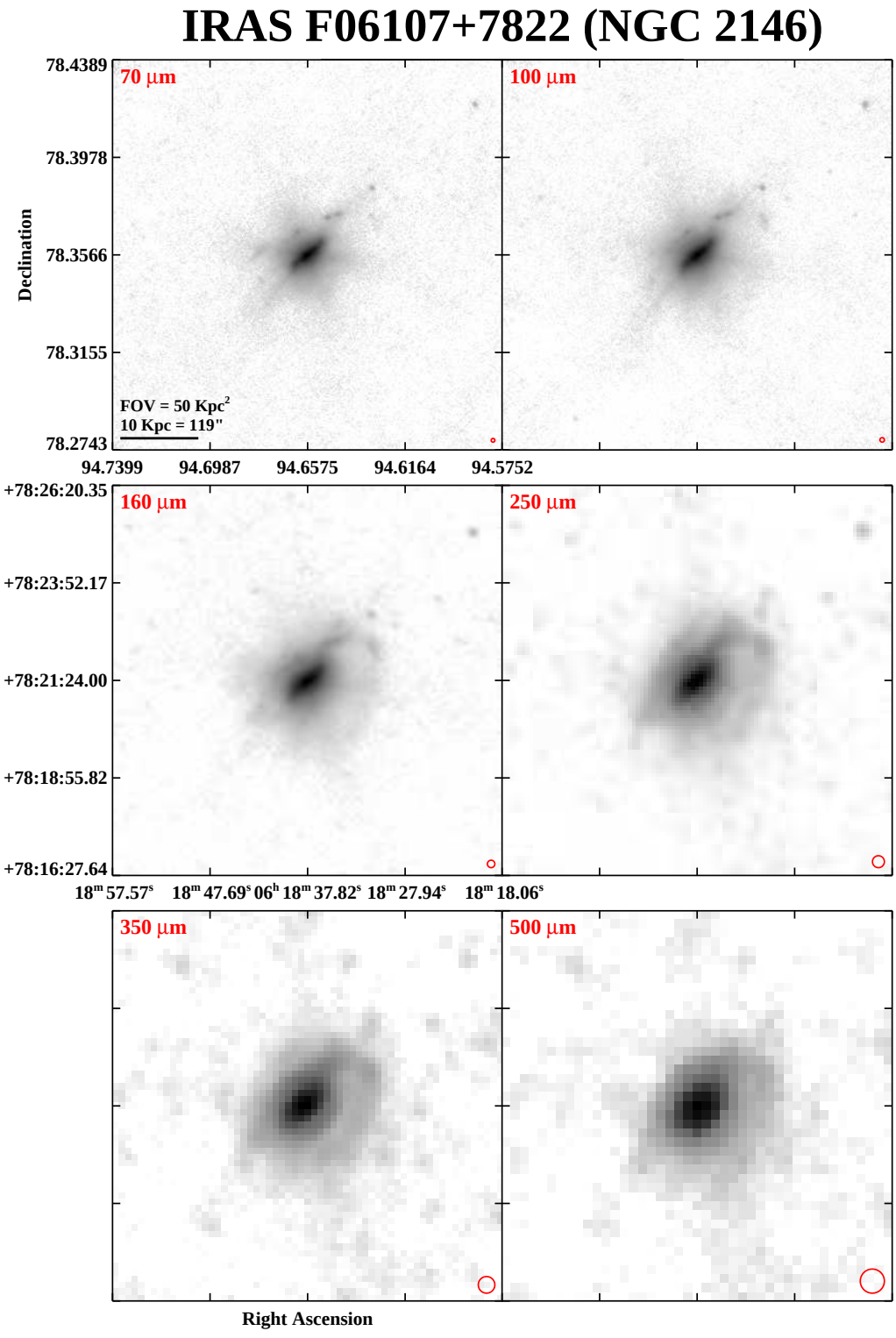

Figure 2.3 continued (page 63 of 209).

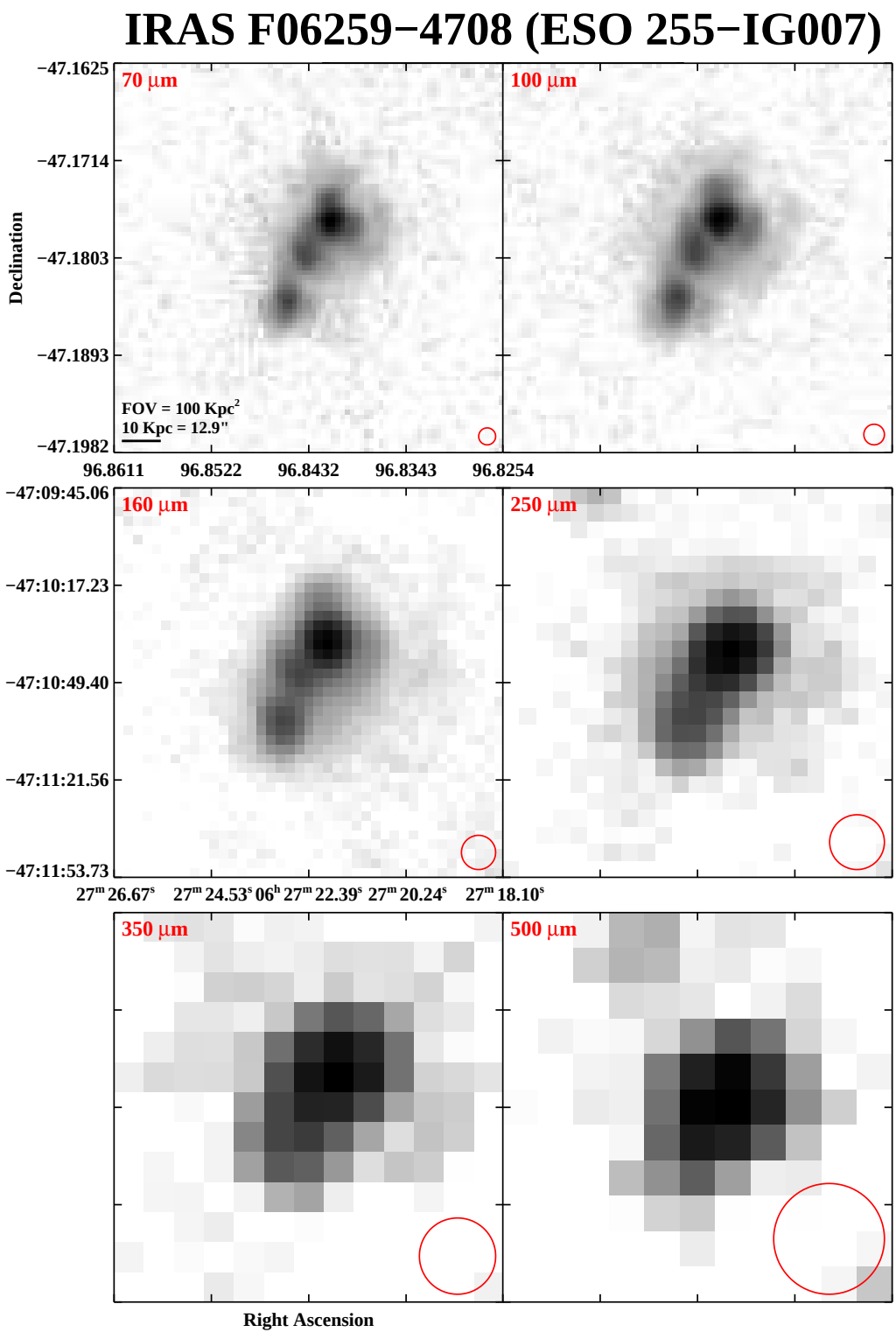

Figure 2.3 continued (page 64 of 209).

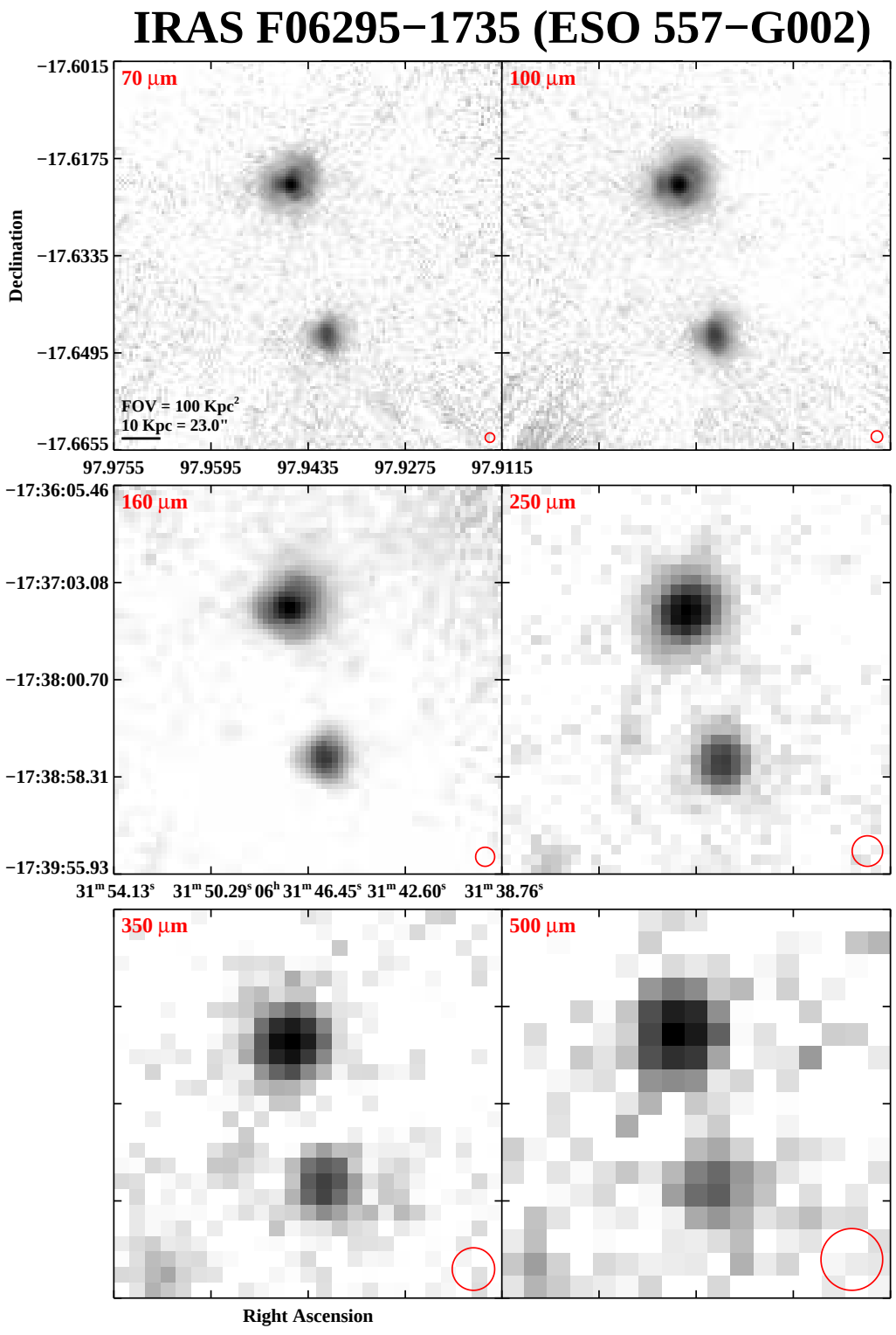

Figure 2.3 continued (page 65 of 209).

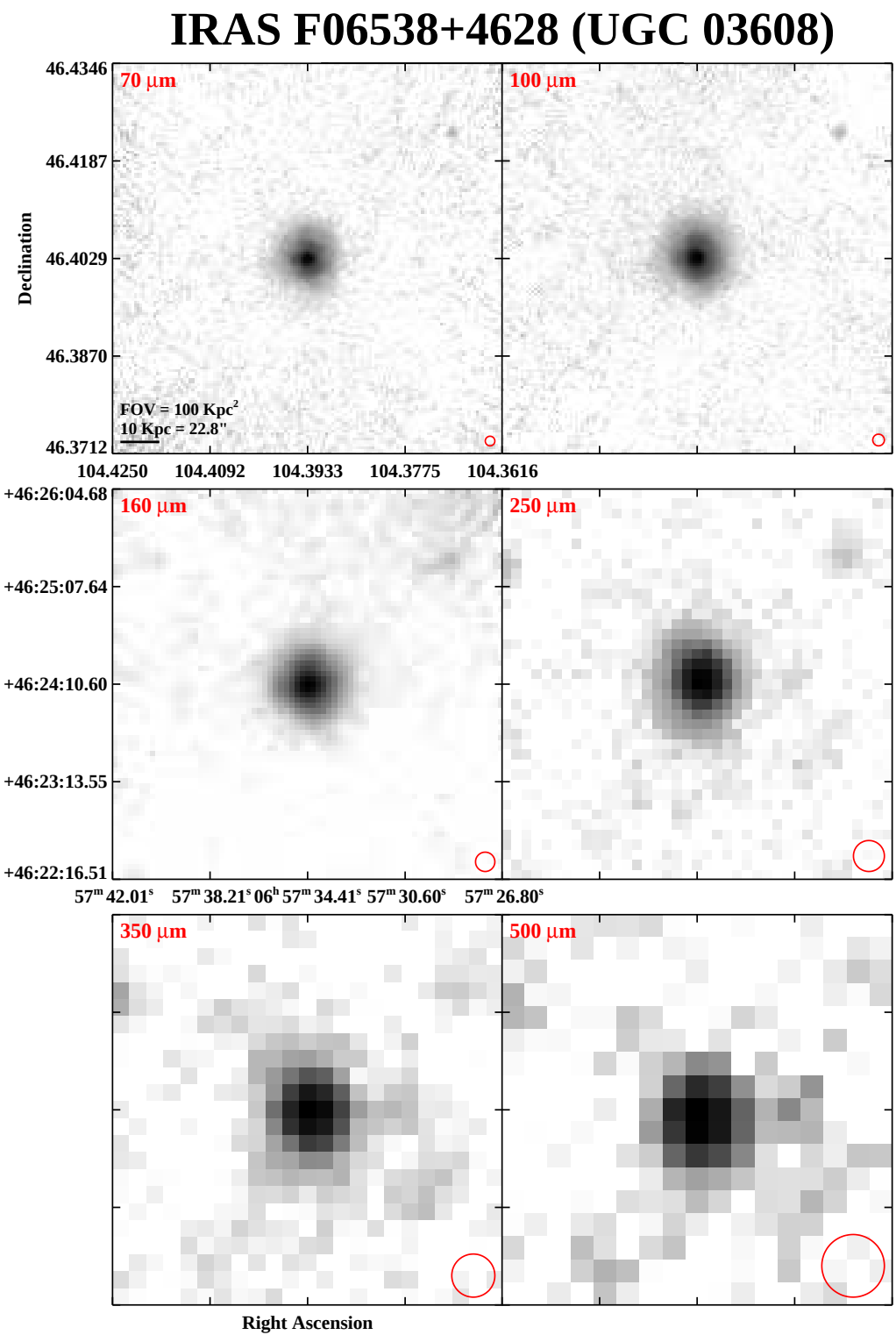

Figure 2.3 continued (page 66 of 209).

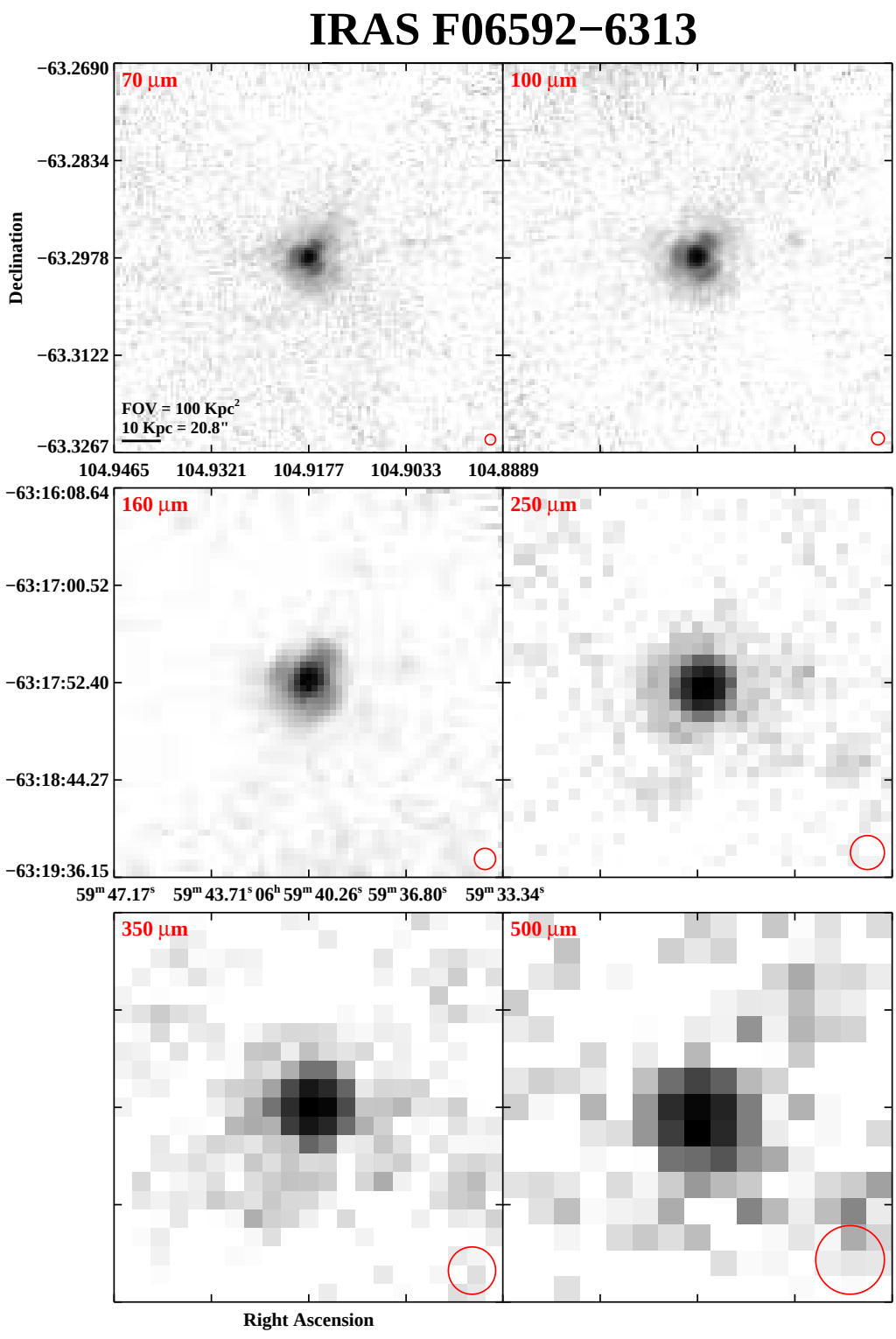

Figure 2.3 continued (page 67 of 209).

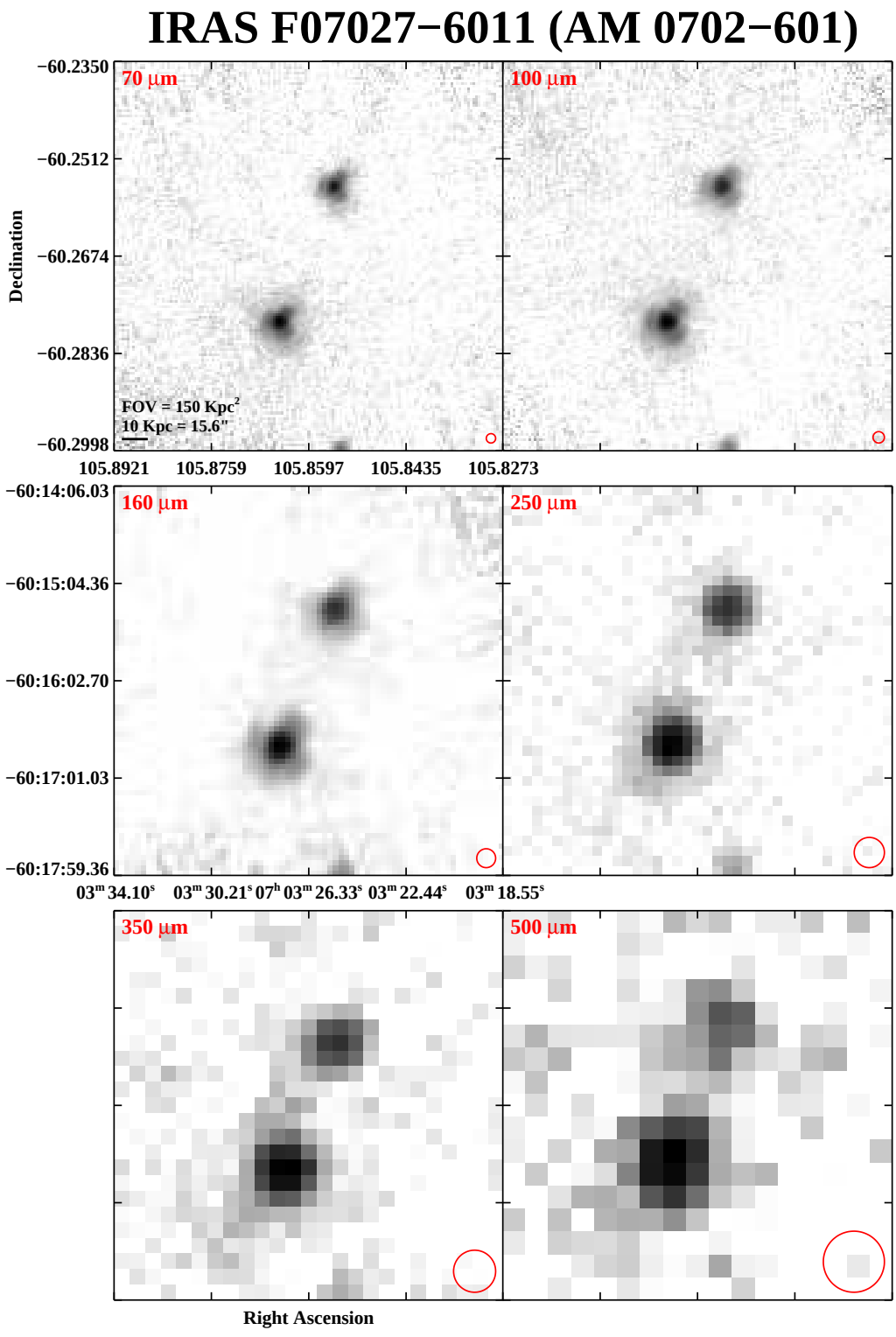

Figure 2.3 continued (page 68 of 209).

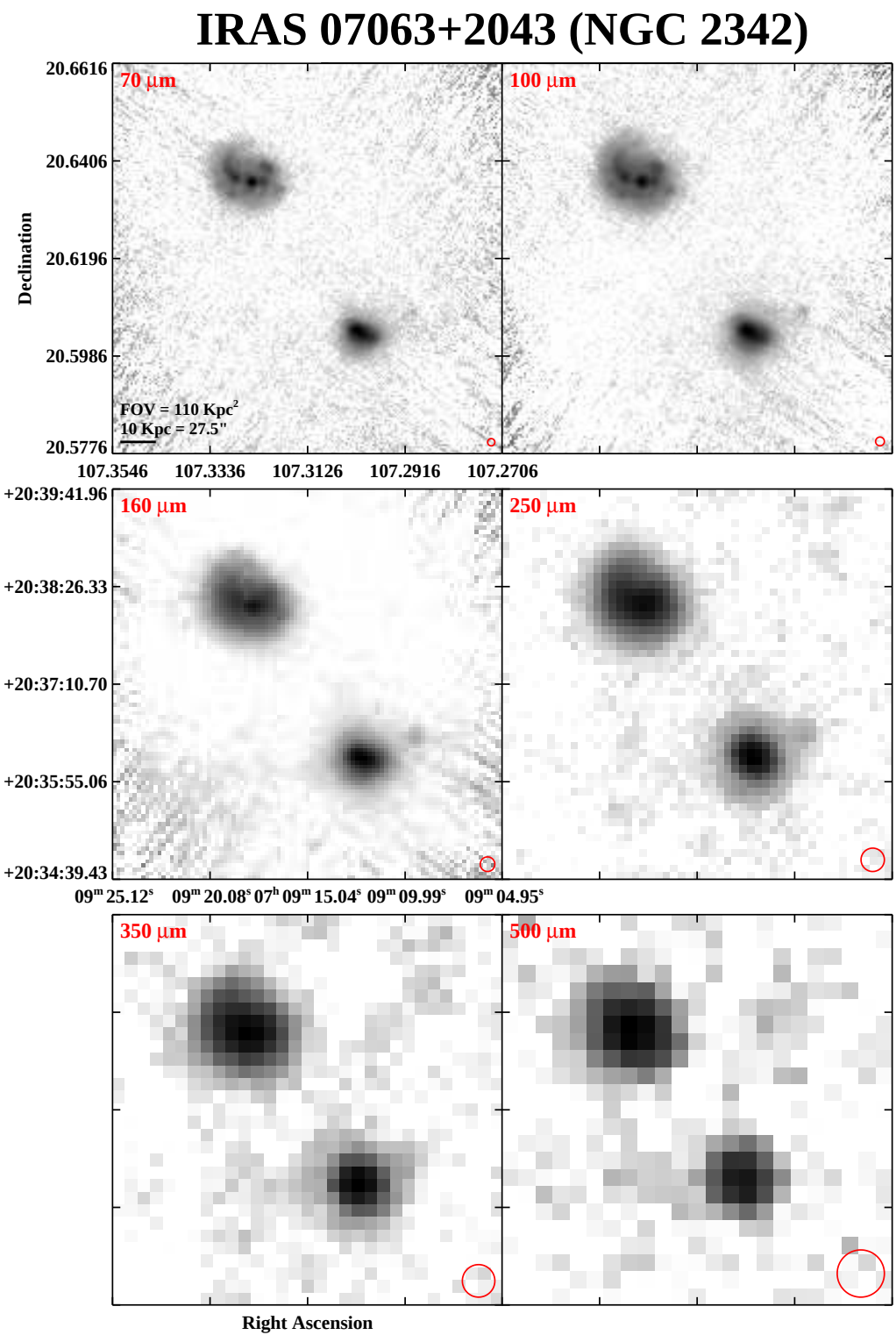

Figure 2.3 continued (page 69 of 209).

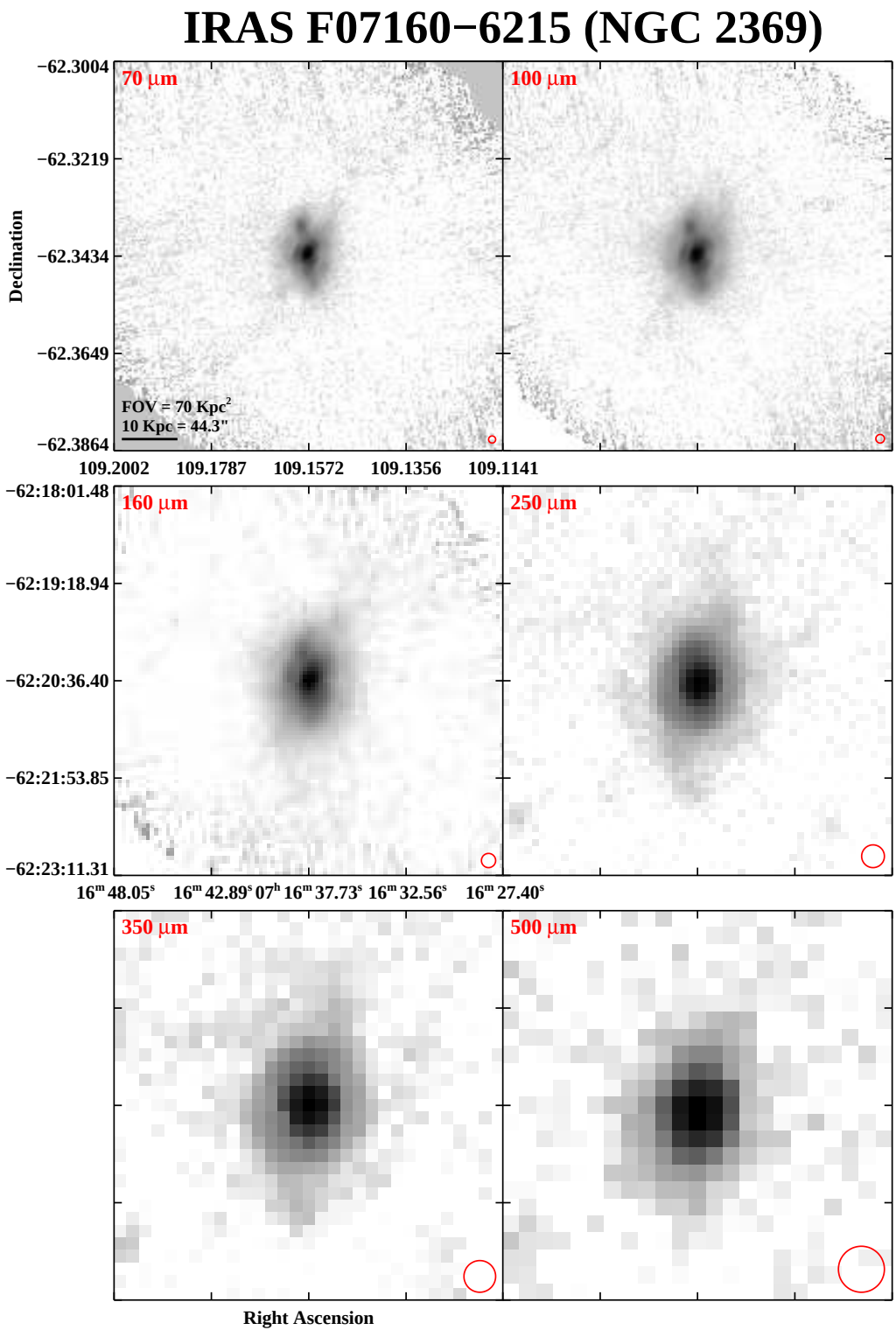

Figure 2.3 continued (page 70 of 209).

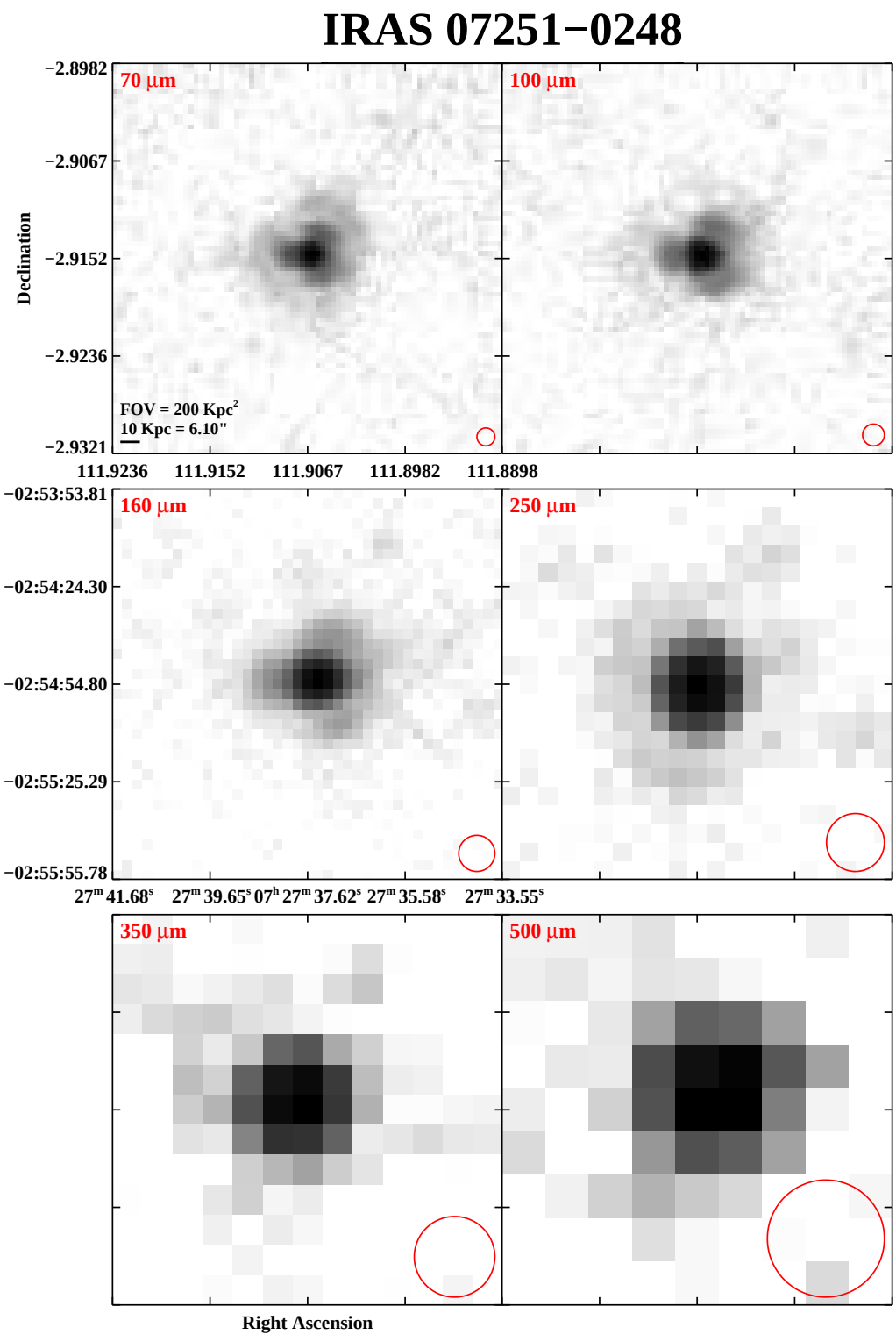

Figure 2.3 continued (page 71 of 209).

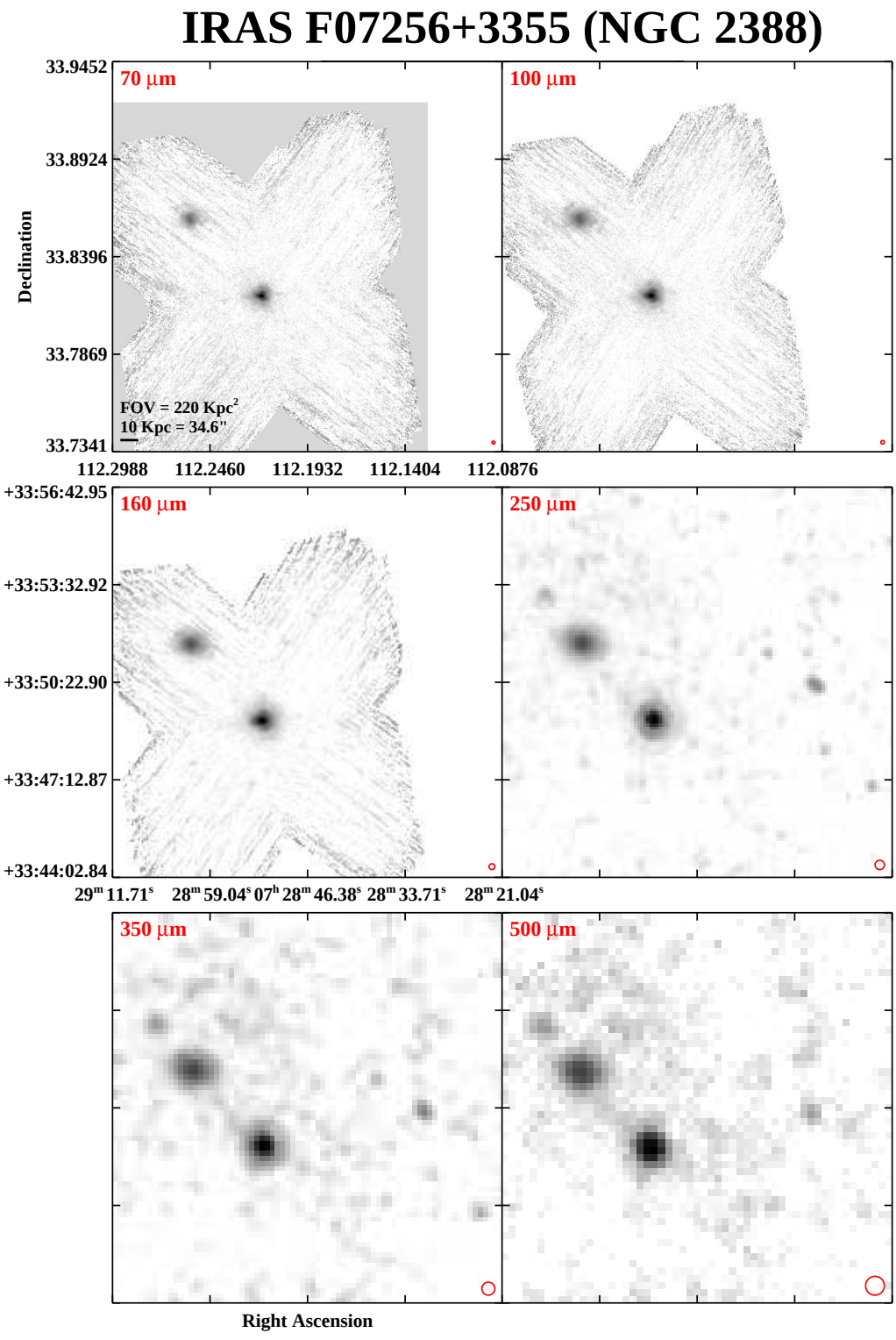

Figure 2.3 continued (page 72 of 209).

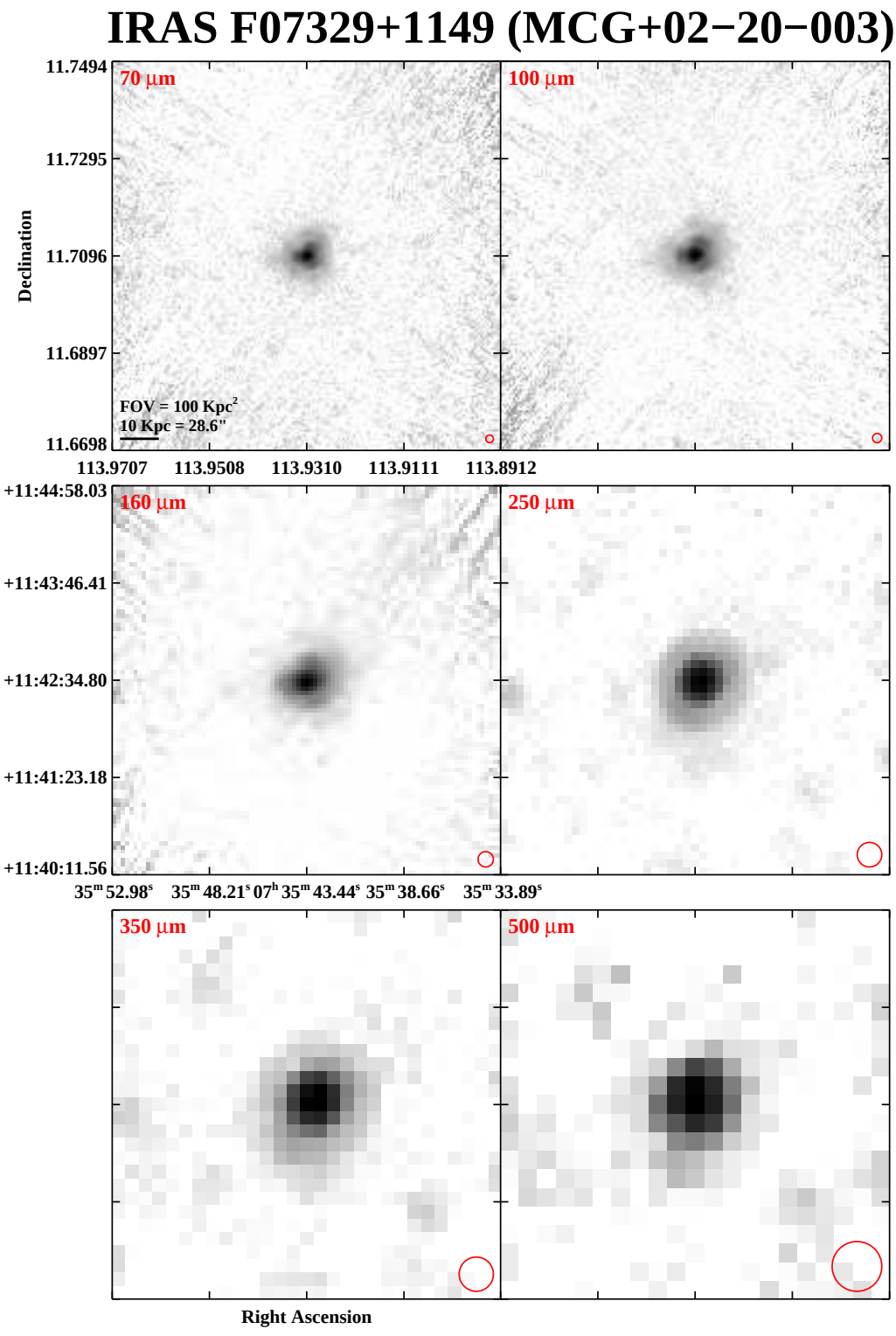

Figure 2.3 continued (page 73 of 209).

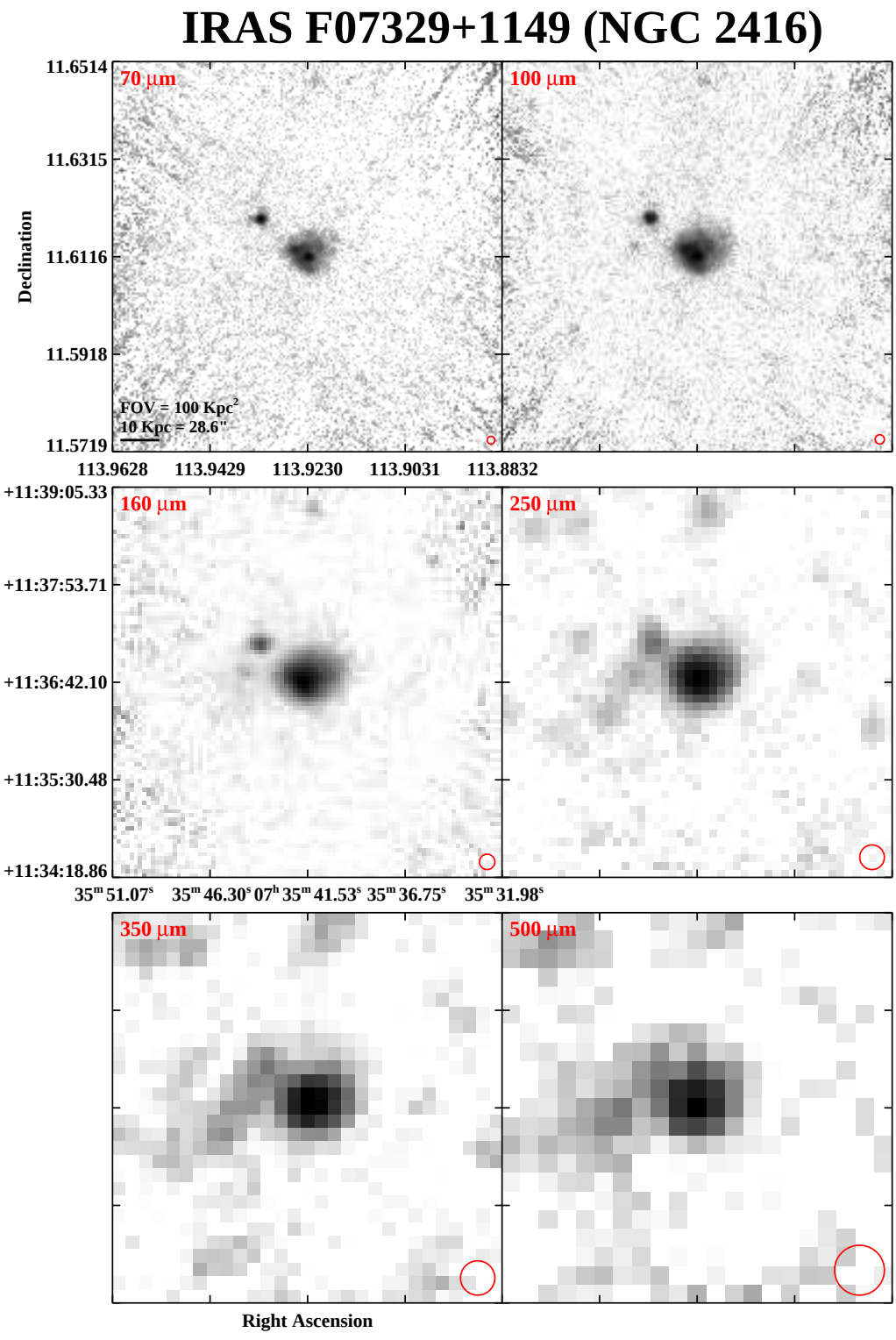

Figure 2.3 continued (page 74 of 209).

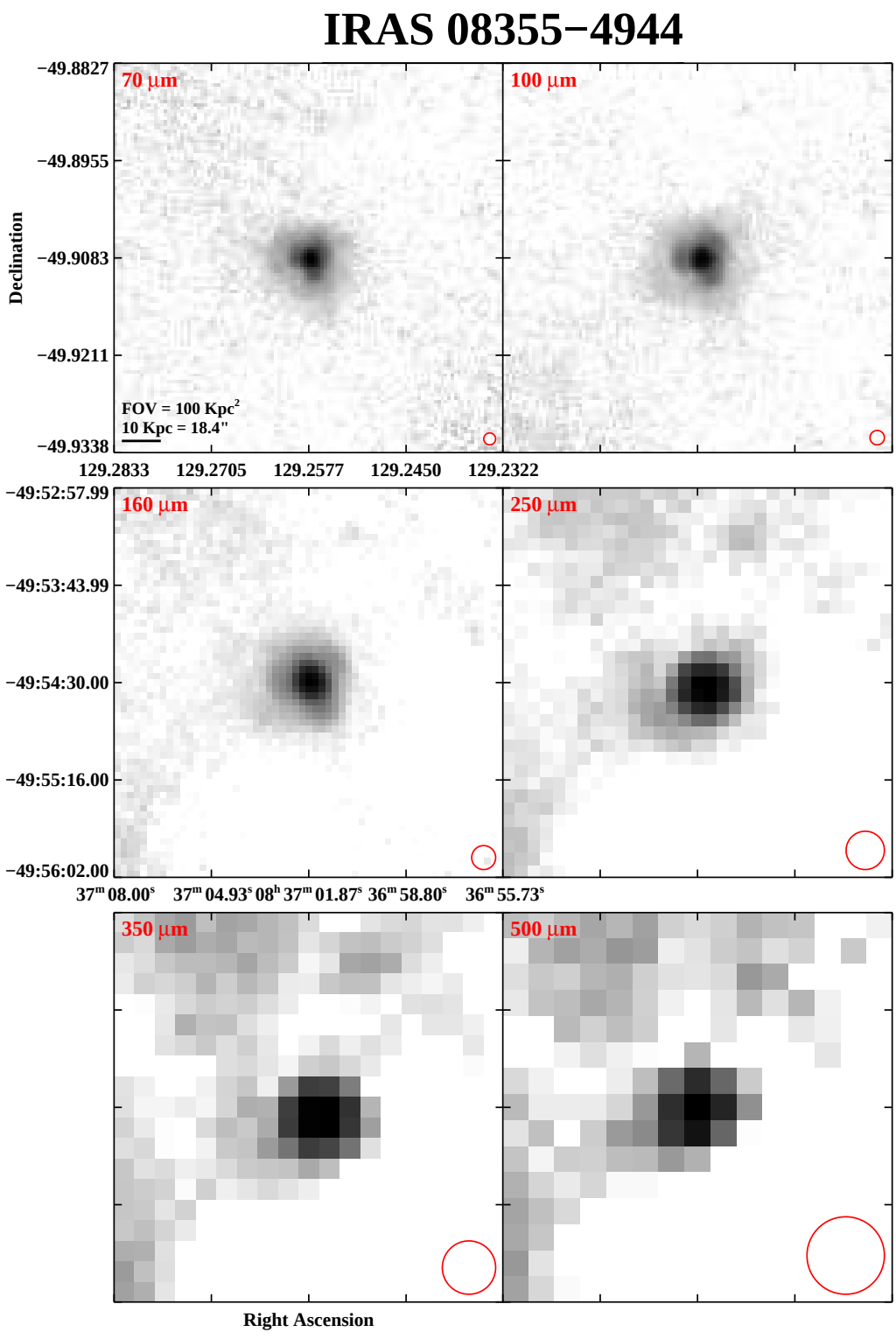

Figure 2.3 continued (page 75 of 209).

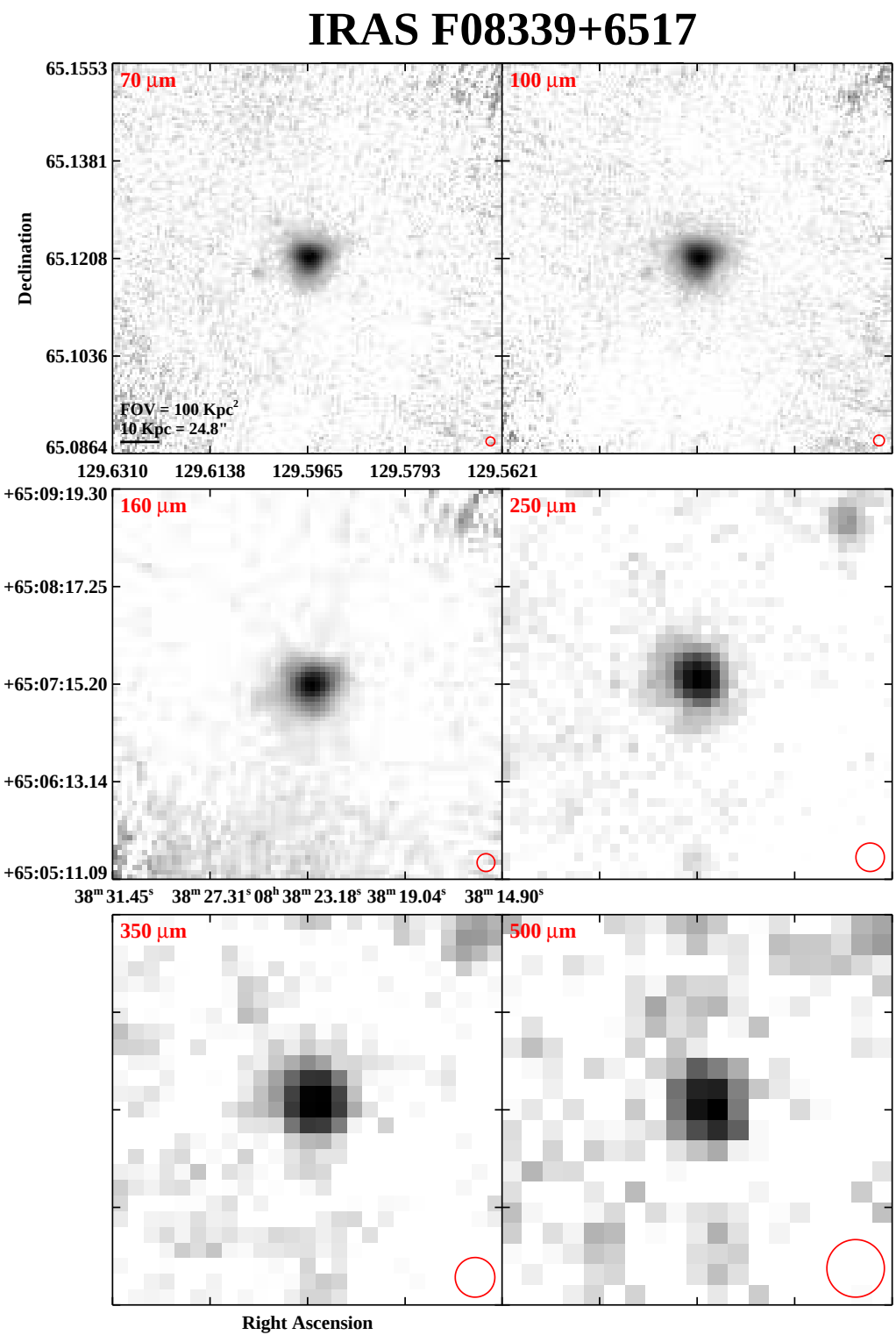

Figure 2.3 continued (page 76 of 209).

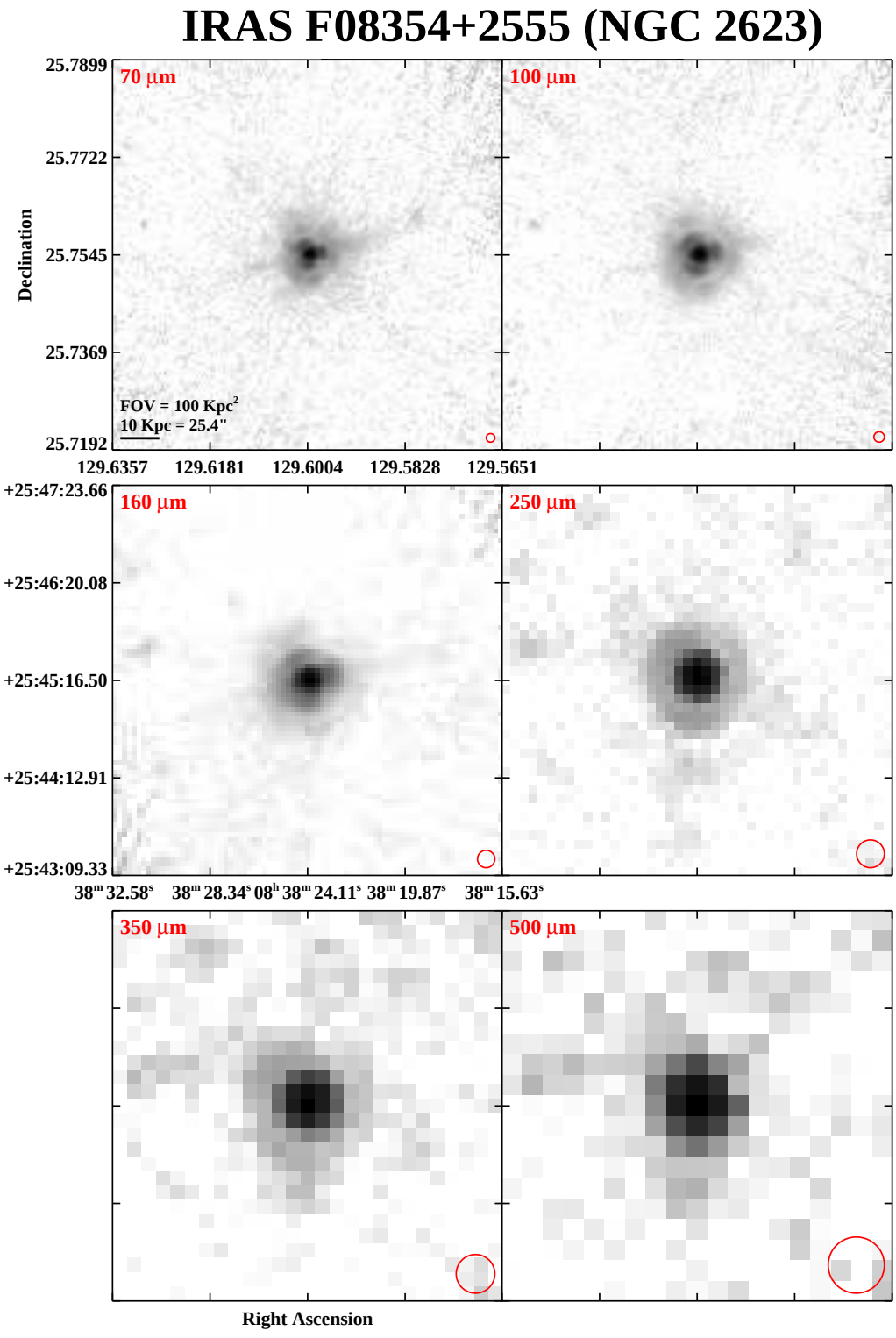

Figure 2.3 continued (page 77 of 209).

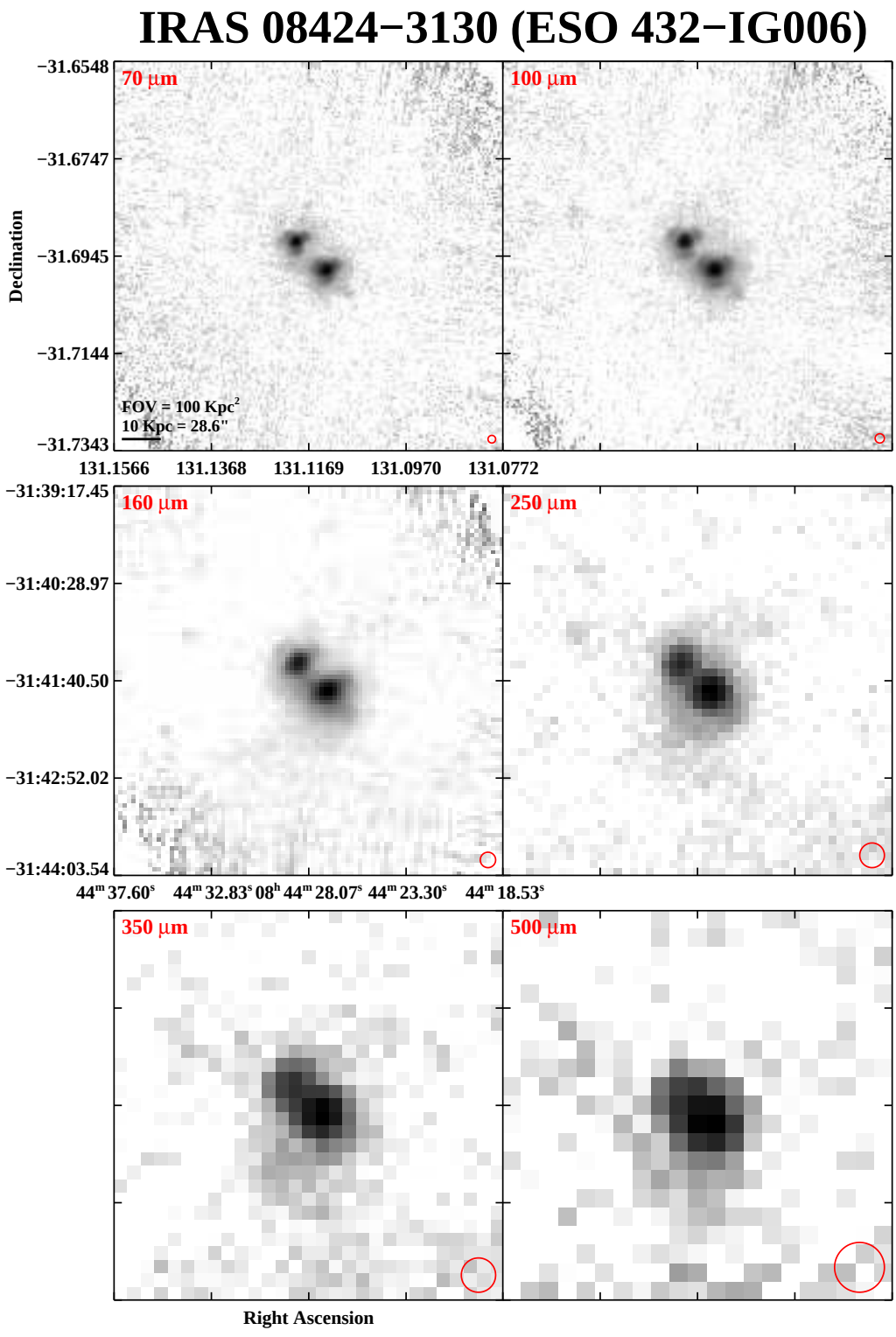

Figure 2.3 continued (page 78 of 209).

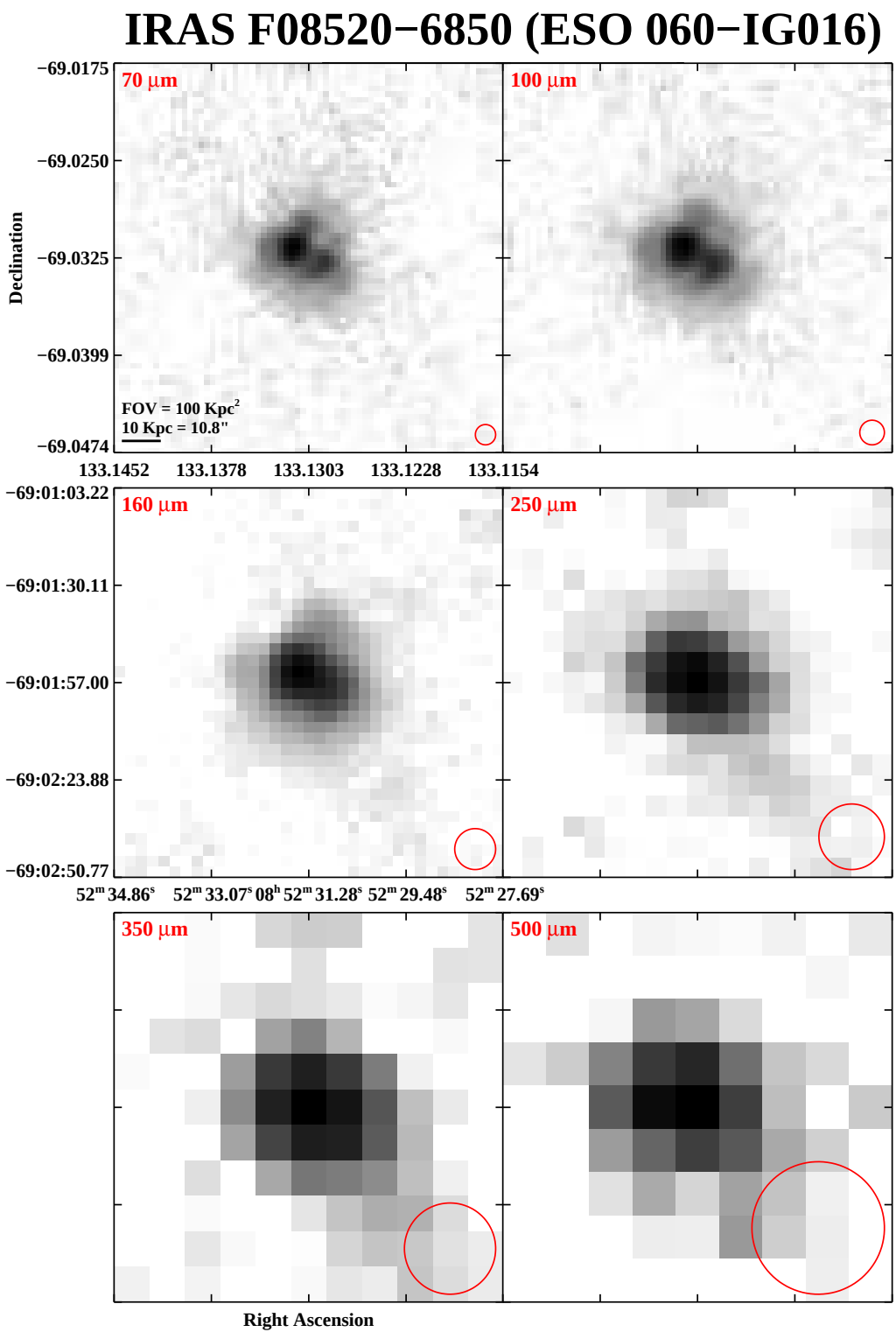

Figure 2.3 continued (page 79 of 209).

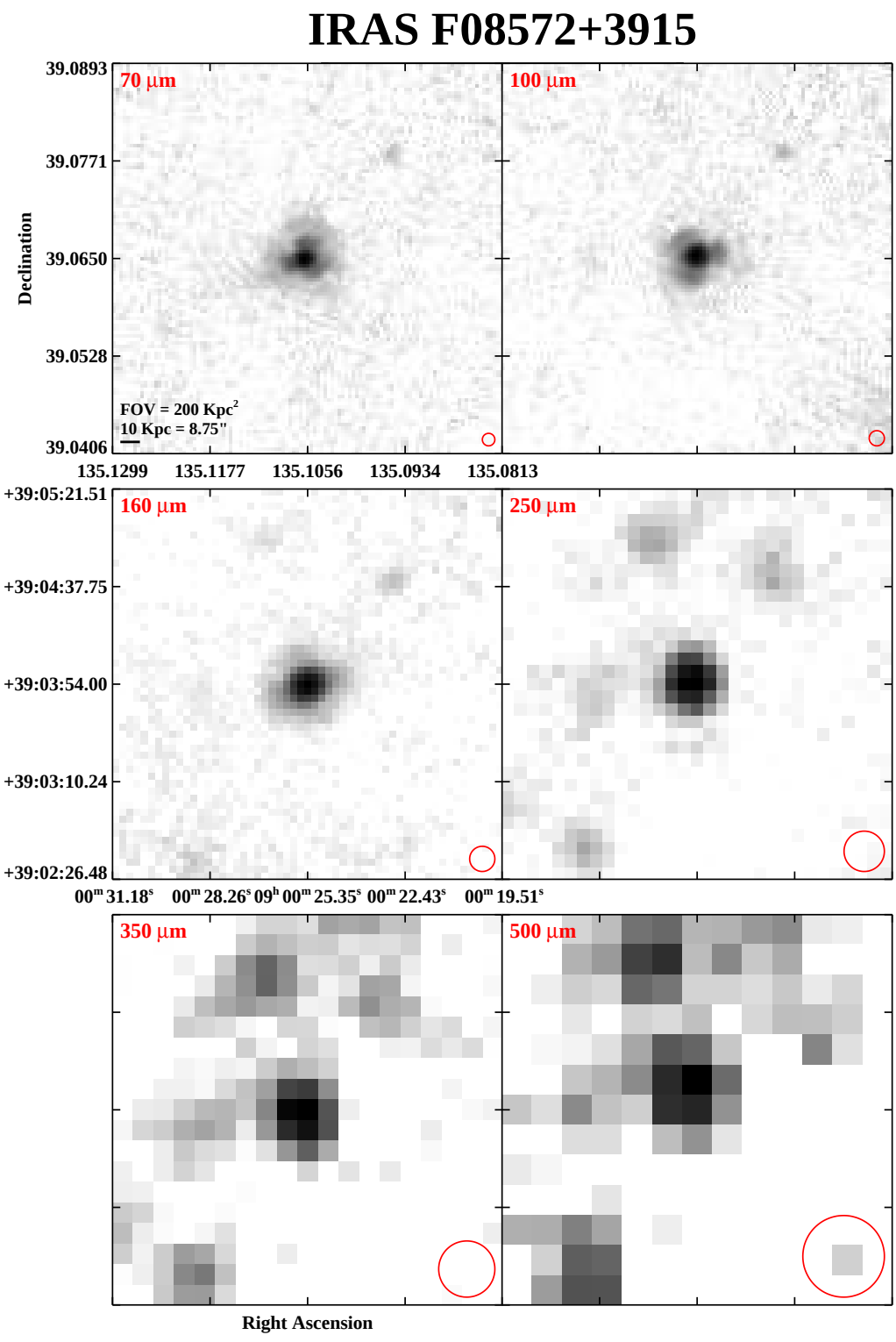

Figure 2.3 continued (page 80 of 209).

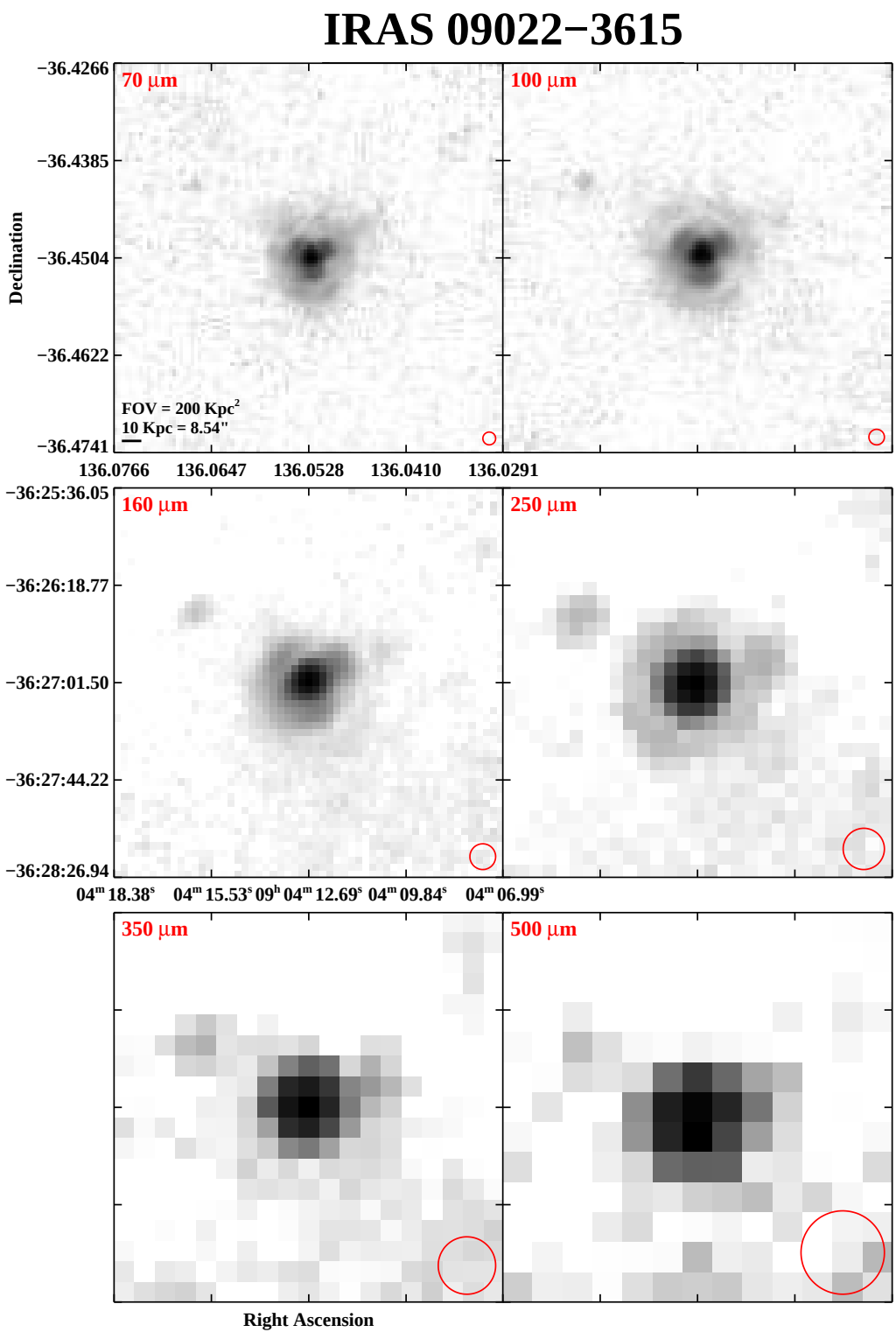

Figure 2.3 continued (page 81 of 209).

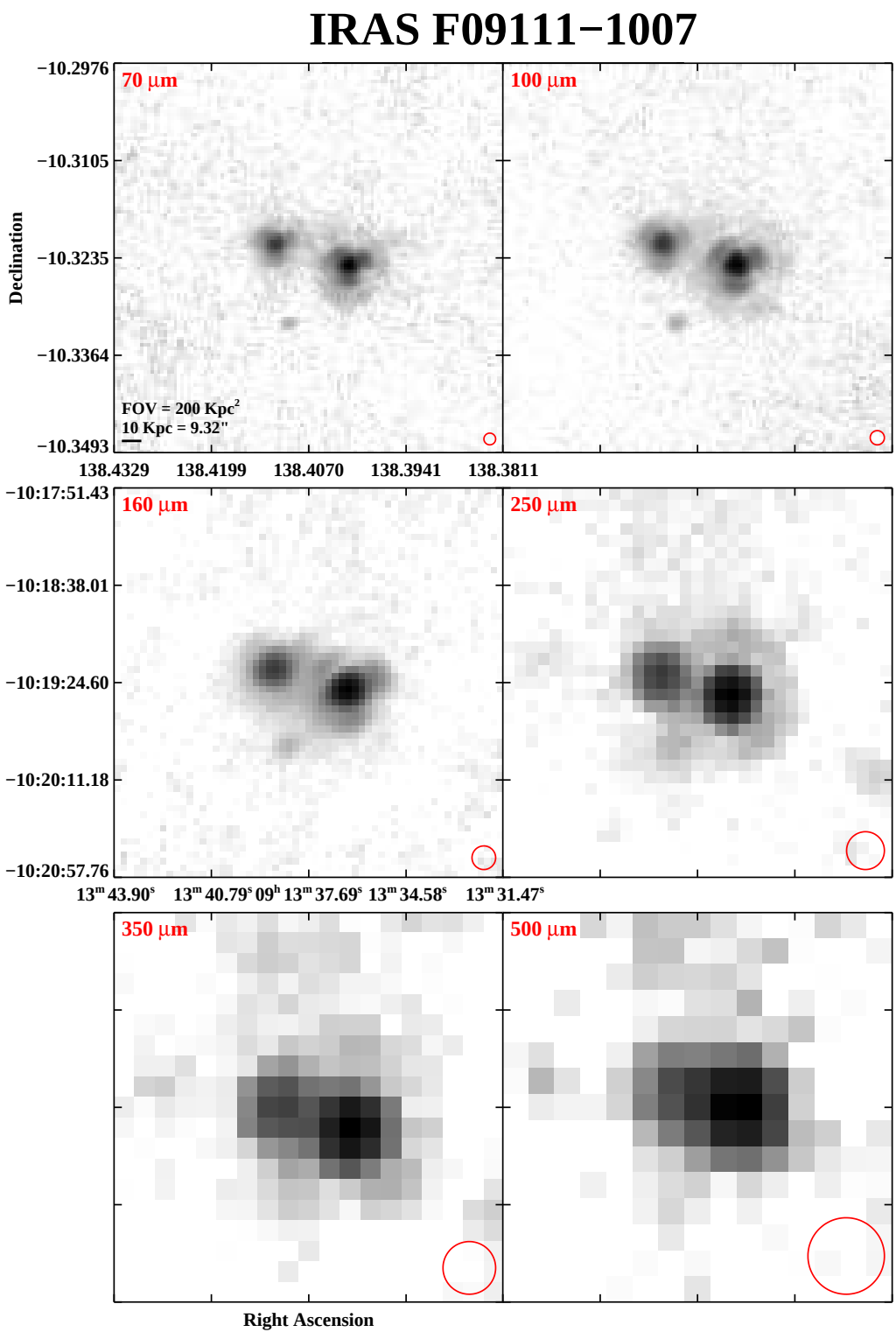

Figure 2.3 continued (page 82 of 209).

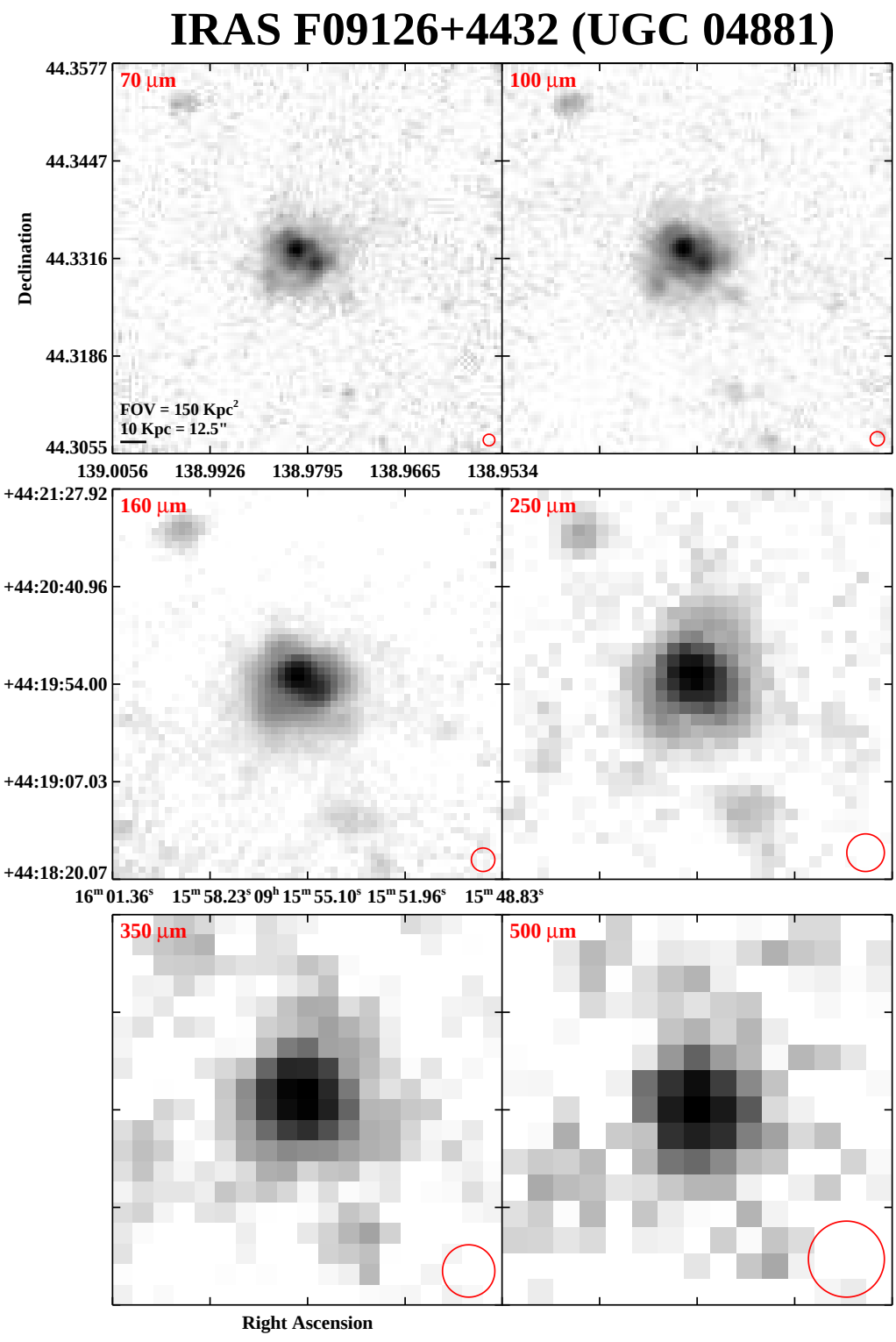

Figure 2.3 continued (page 83 of 209).

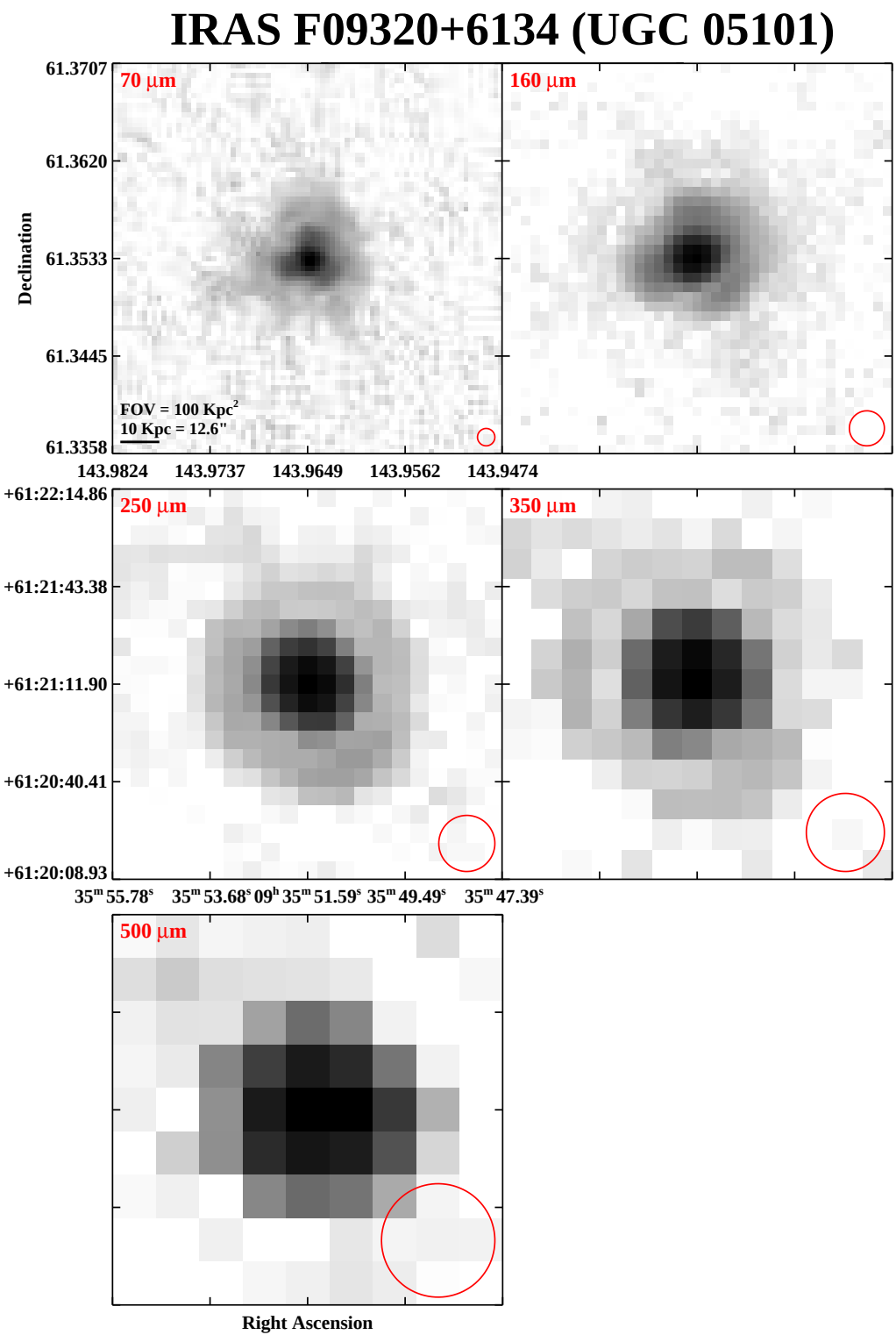

Figure 2.3 continued (page 84 of 209).

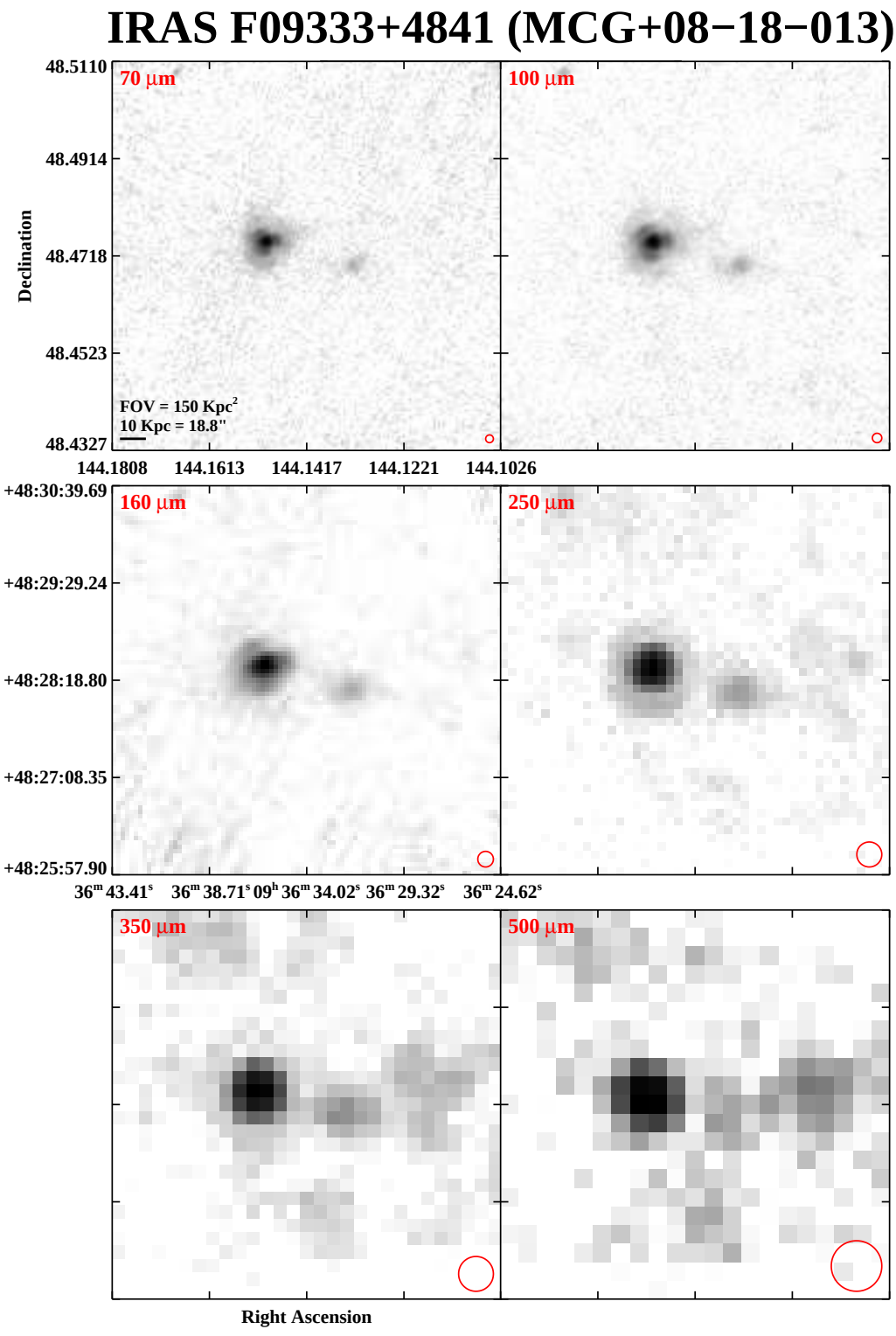

Figure 2.3 continued (page 85 of 209).

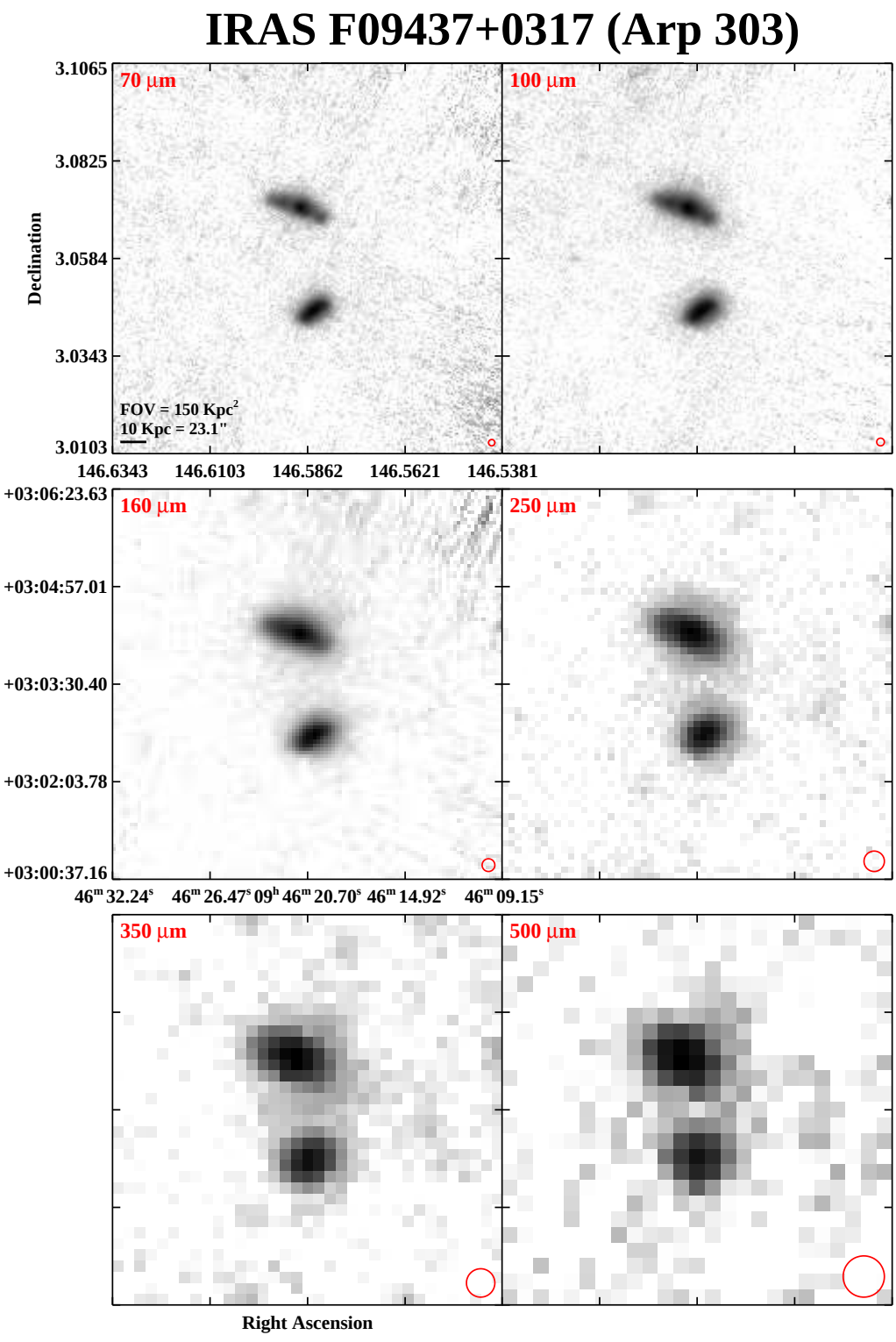

Figure 2.3 continued (page 86 of 209).

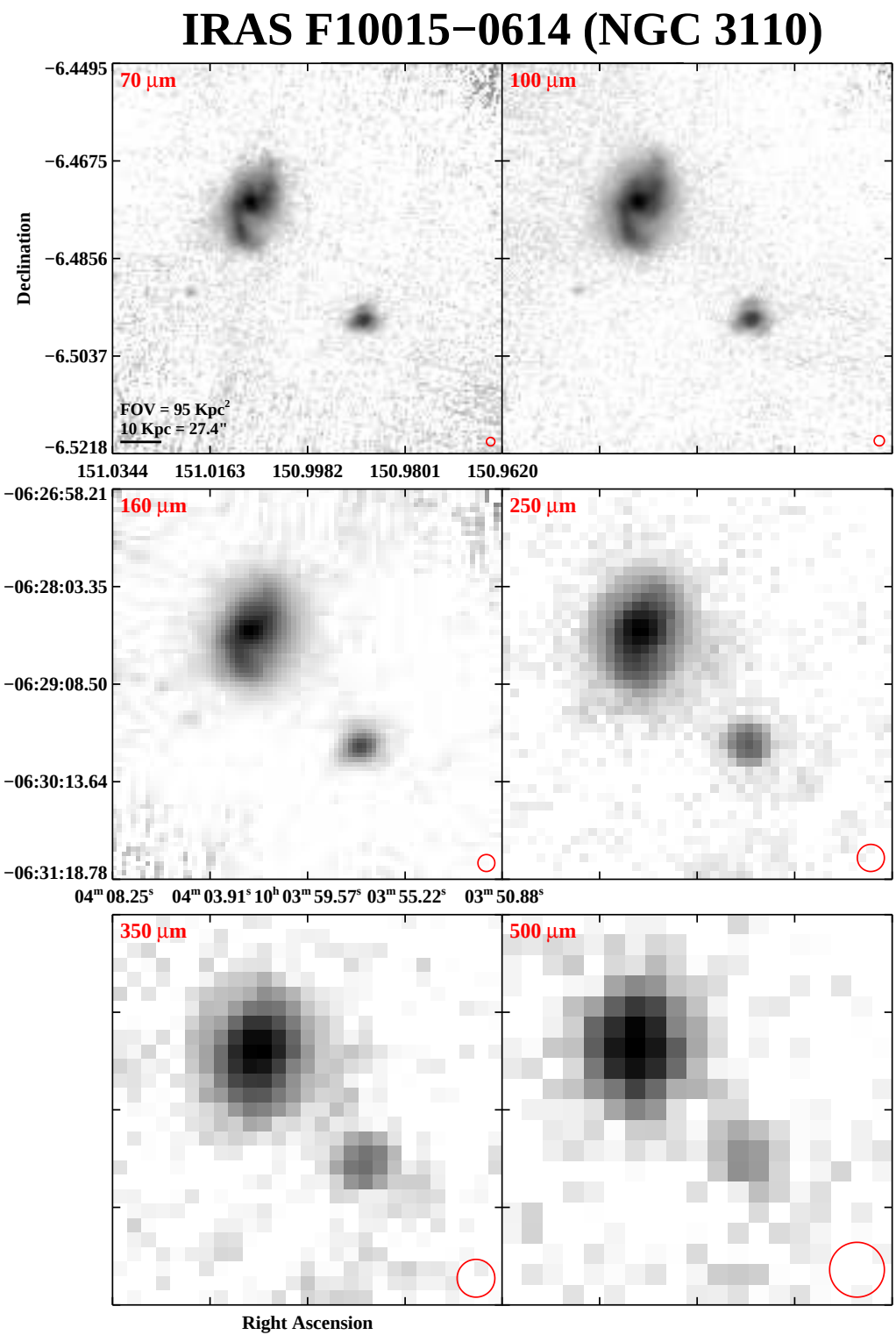

Figure 2.3 continued (page 87 of 209).

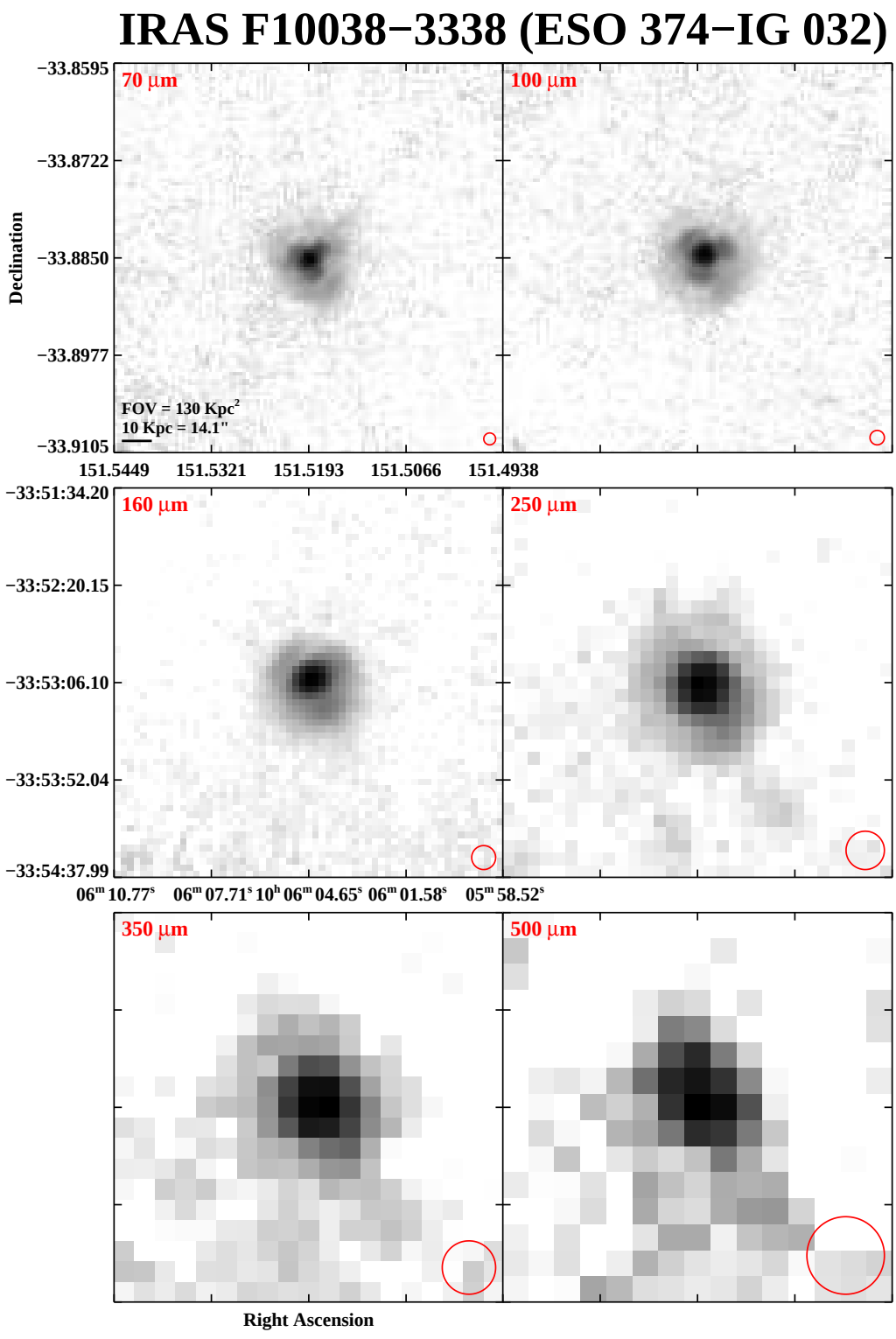

Figure 2.3 continued (page 88 of 209).

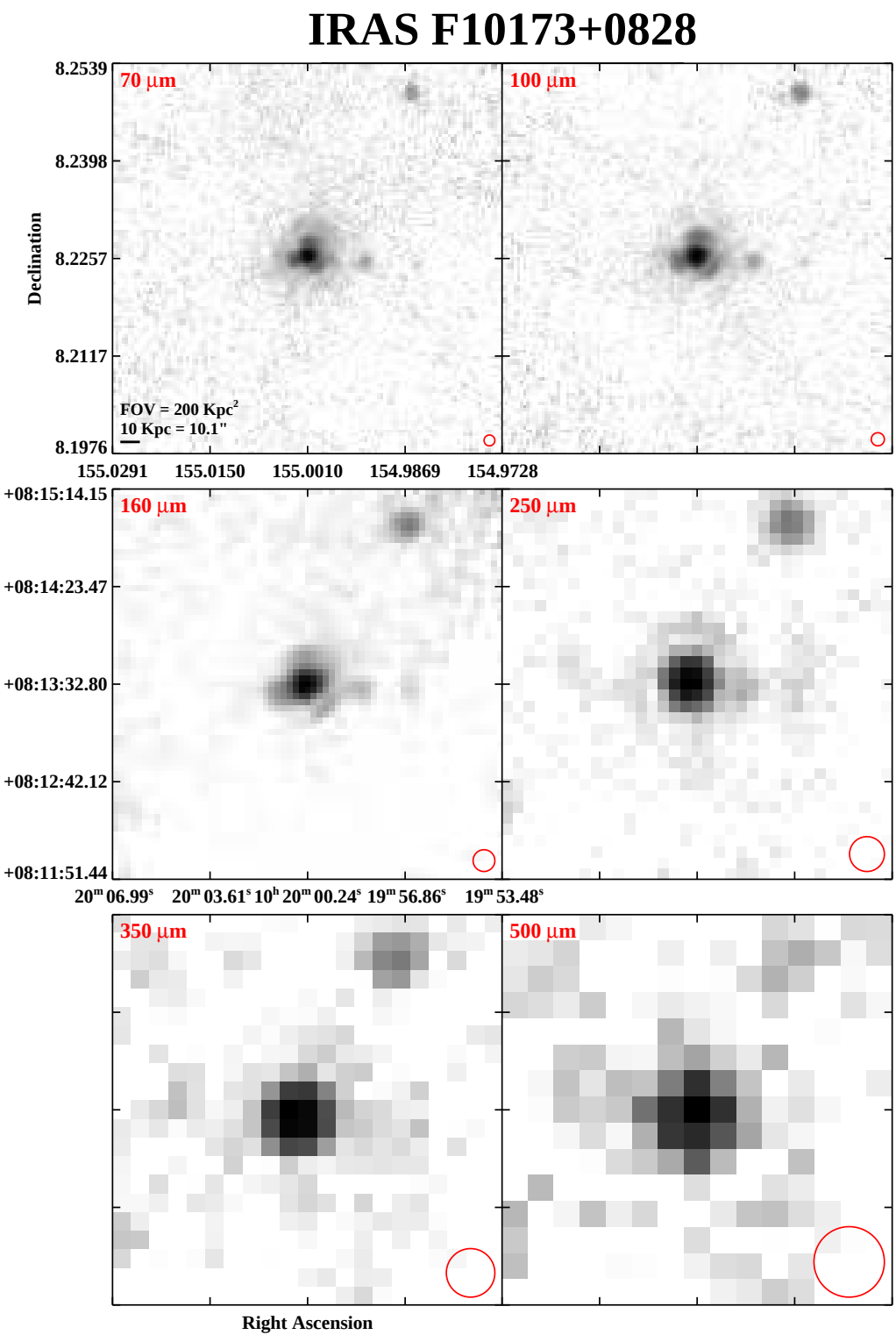

Figure 2.3 continued (page 89 of 209).

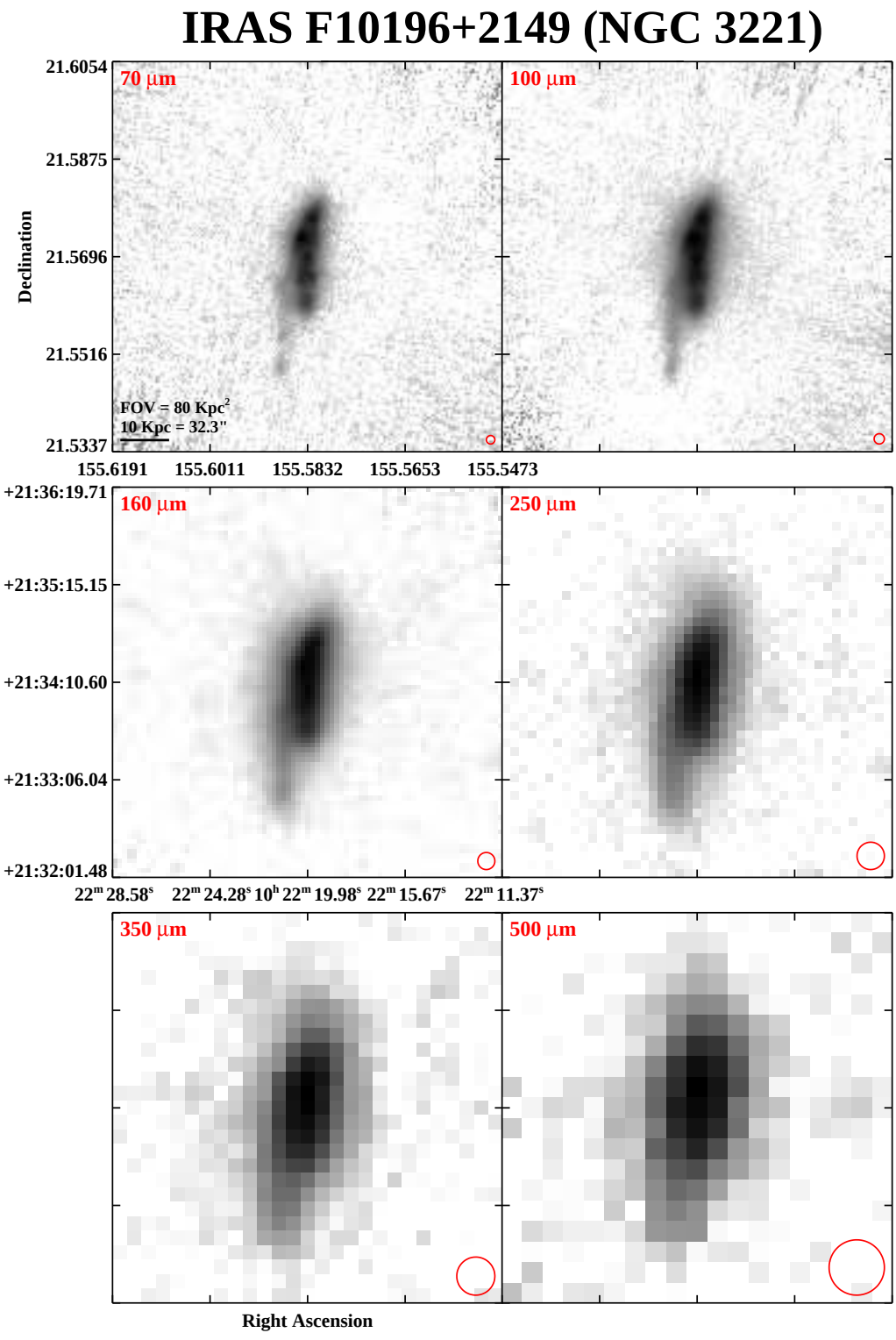

Figure 2.3 continued (page 90 of 209).

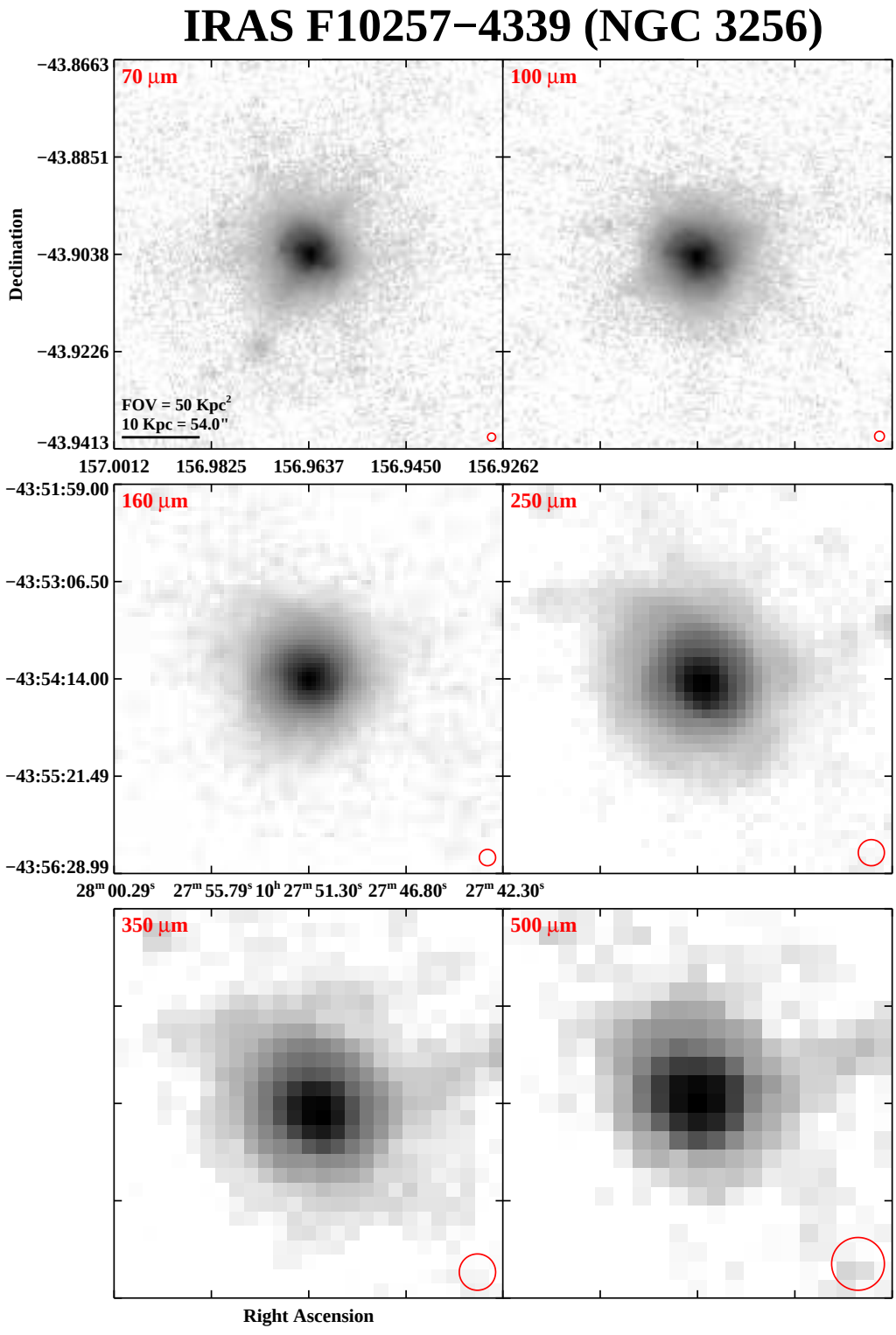

Figure 2.3 continued (page 91 of 209).

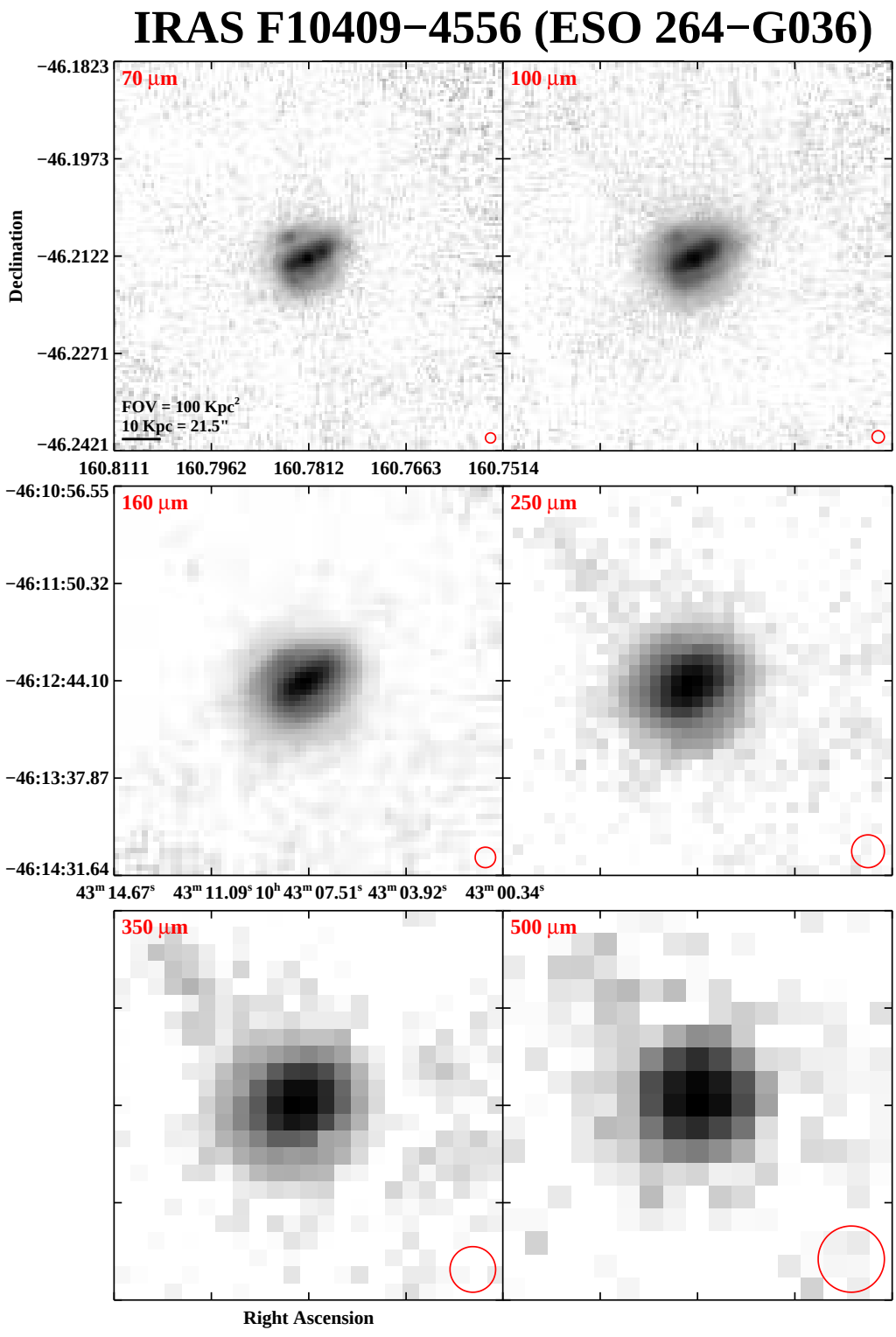

Figure 2.3 continued (page 92 of 209).

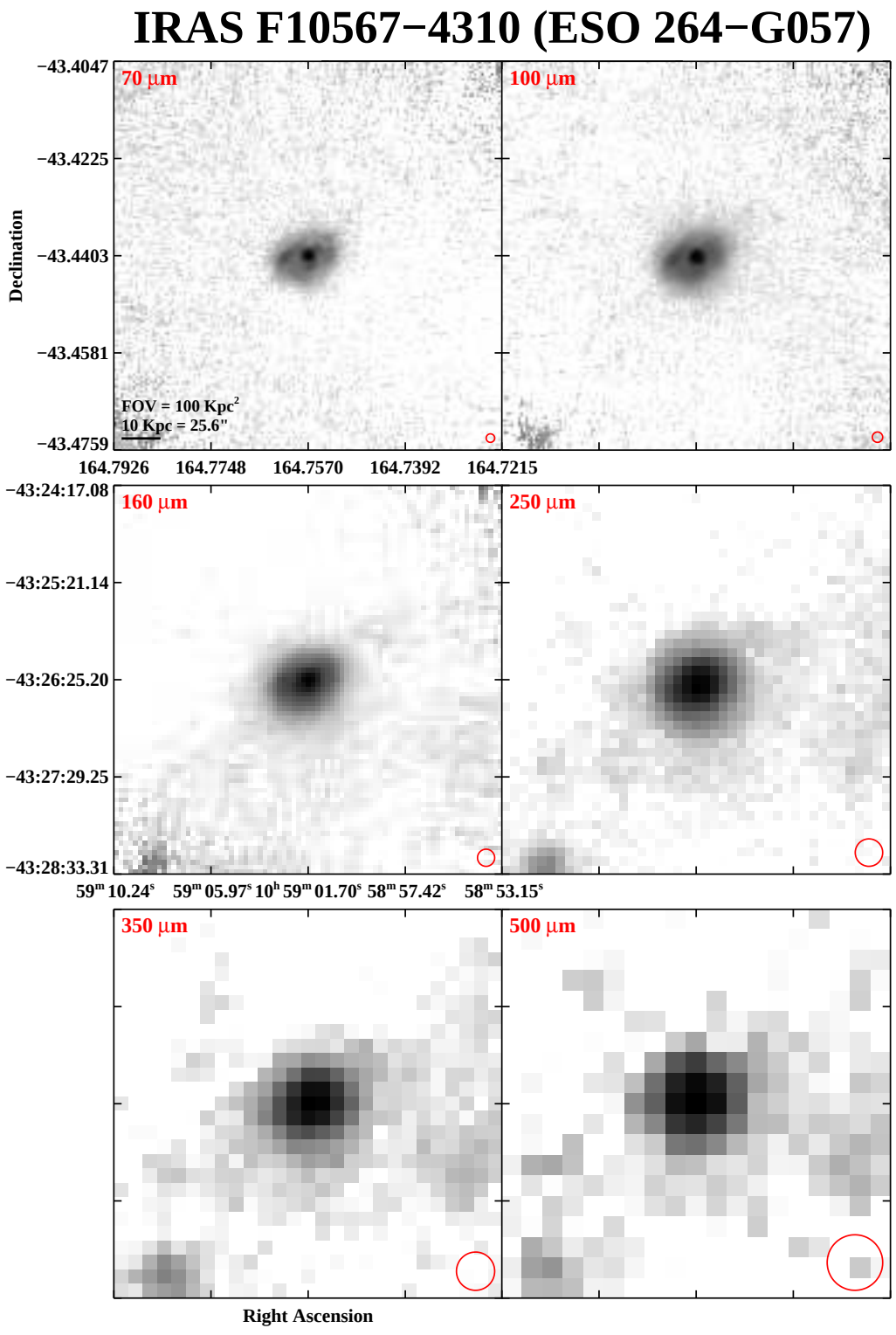

Figure 2.3 continued (page 93 of 209).

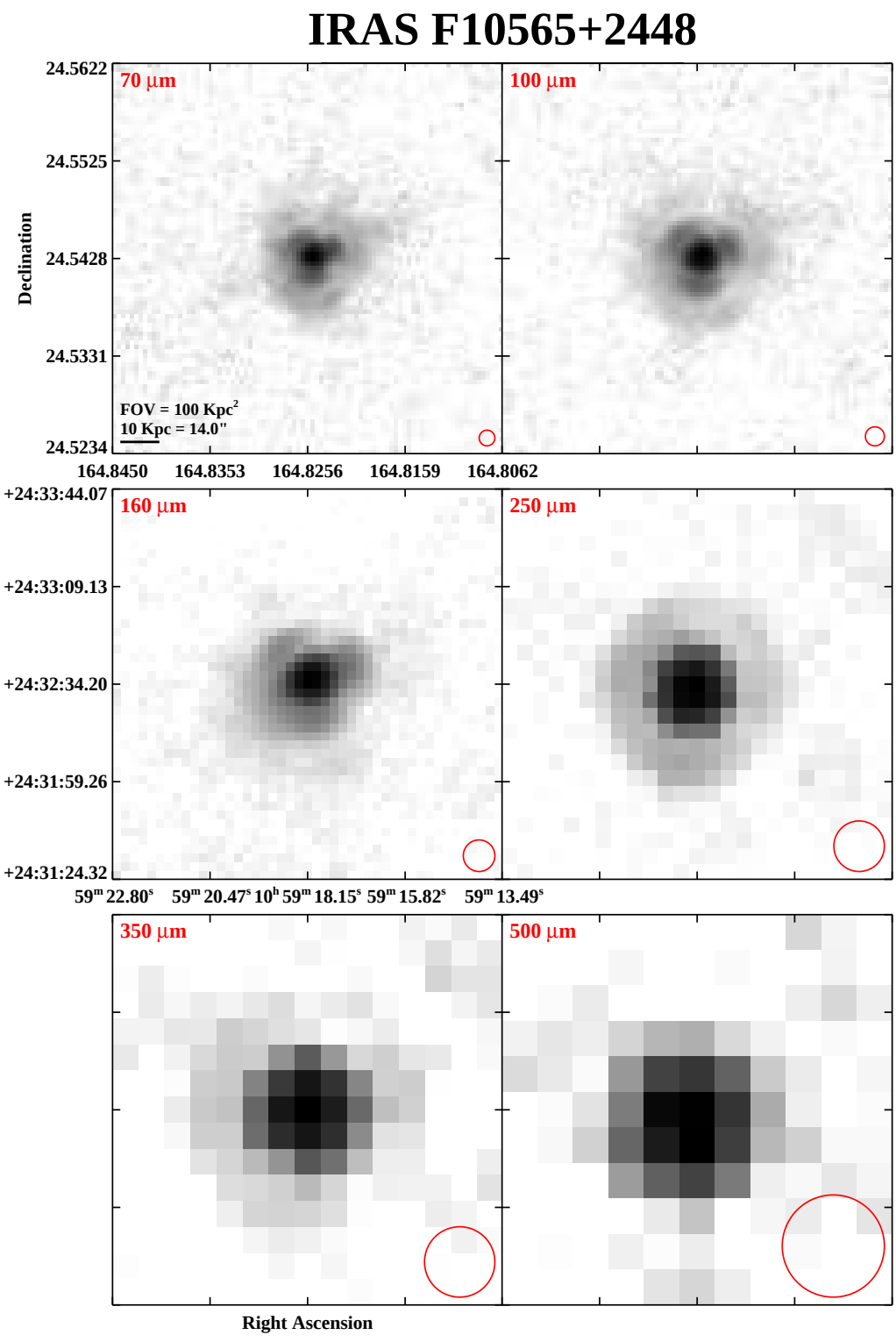

Figure 2.3 continued (page 94 of 209).

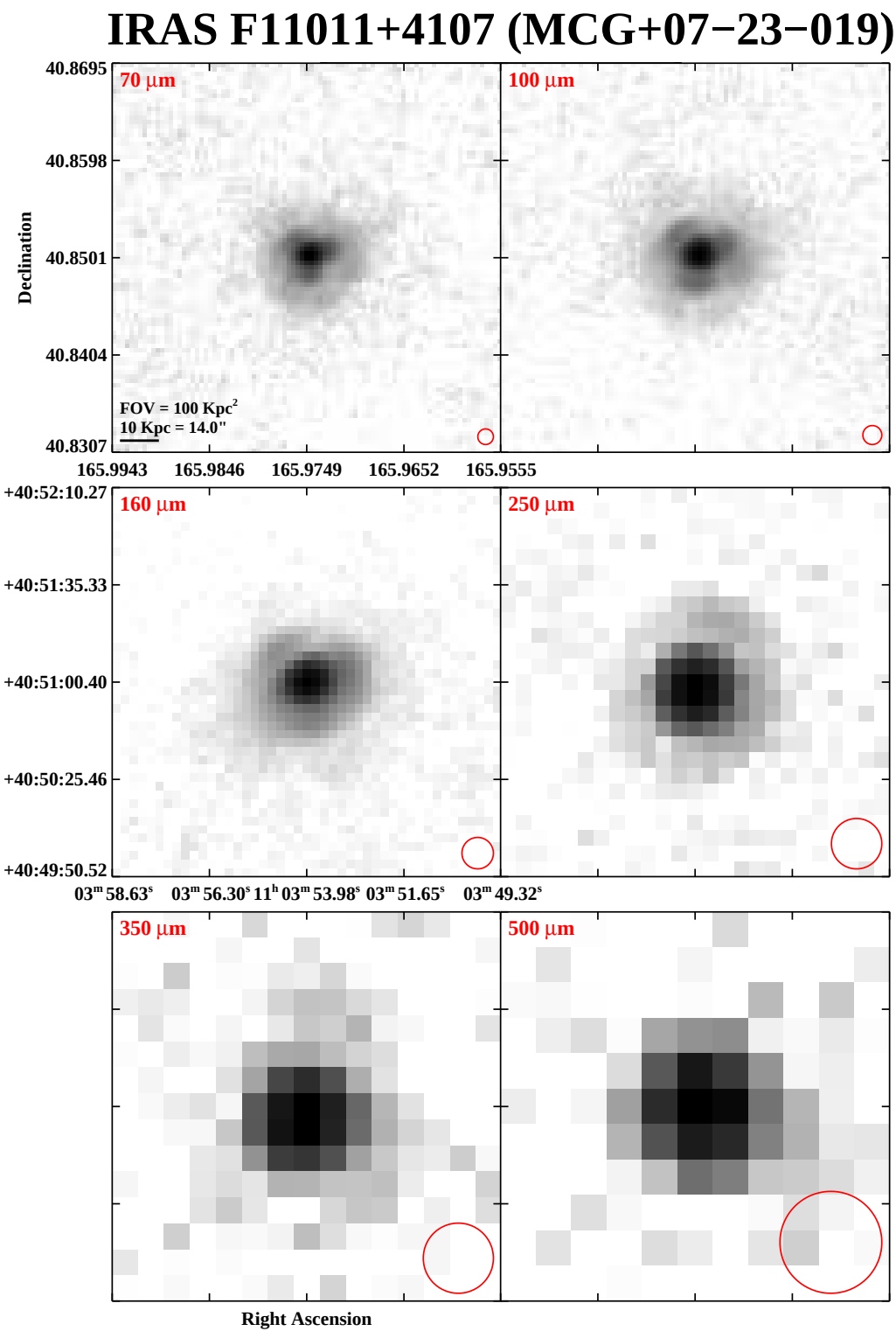

Figure 2.3 continued (page 95 of 209).

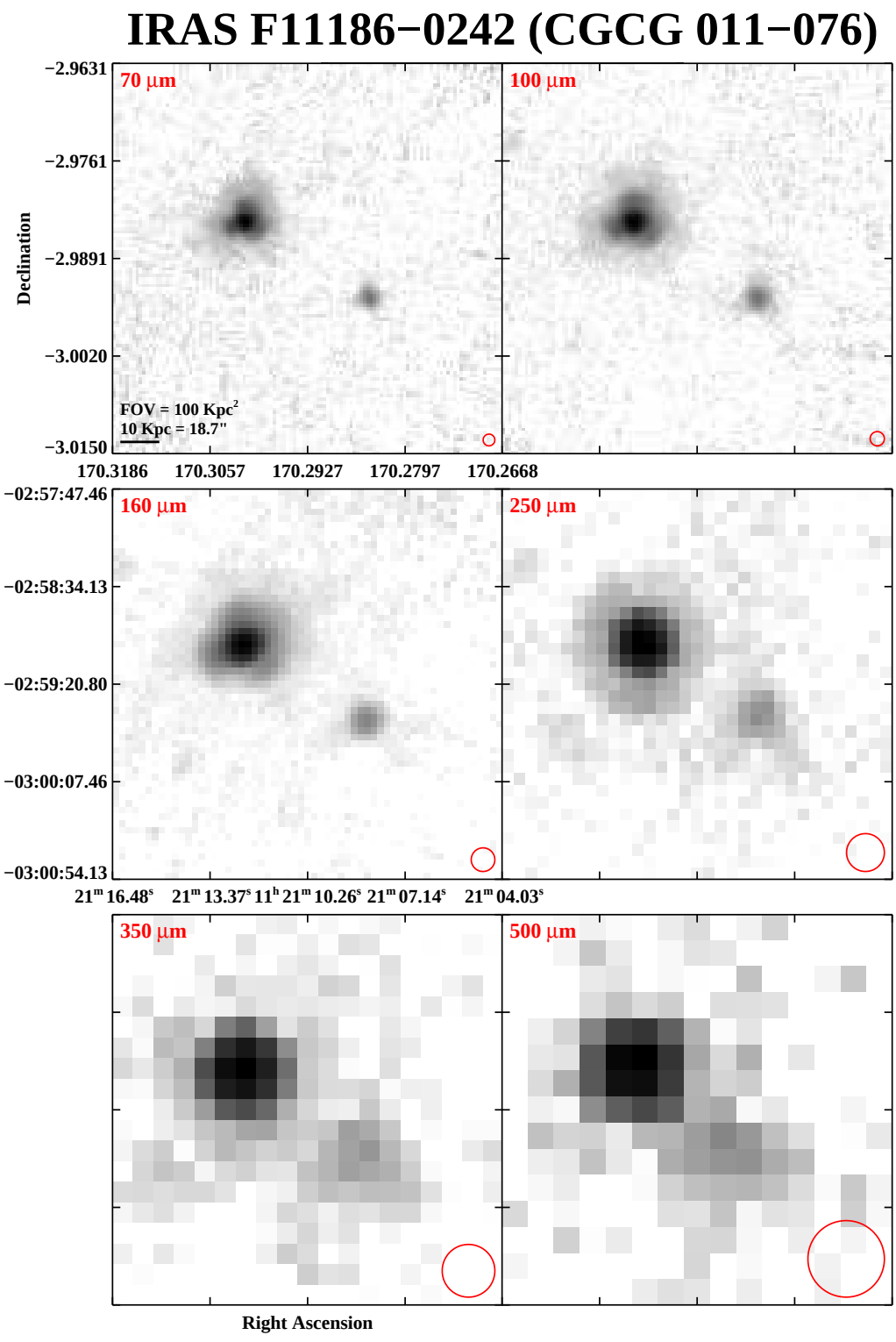

Figure 2.3 continued (page 96 of 209).

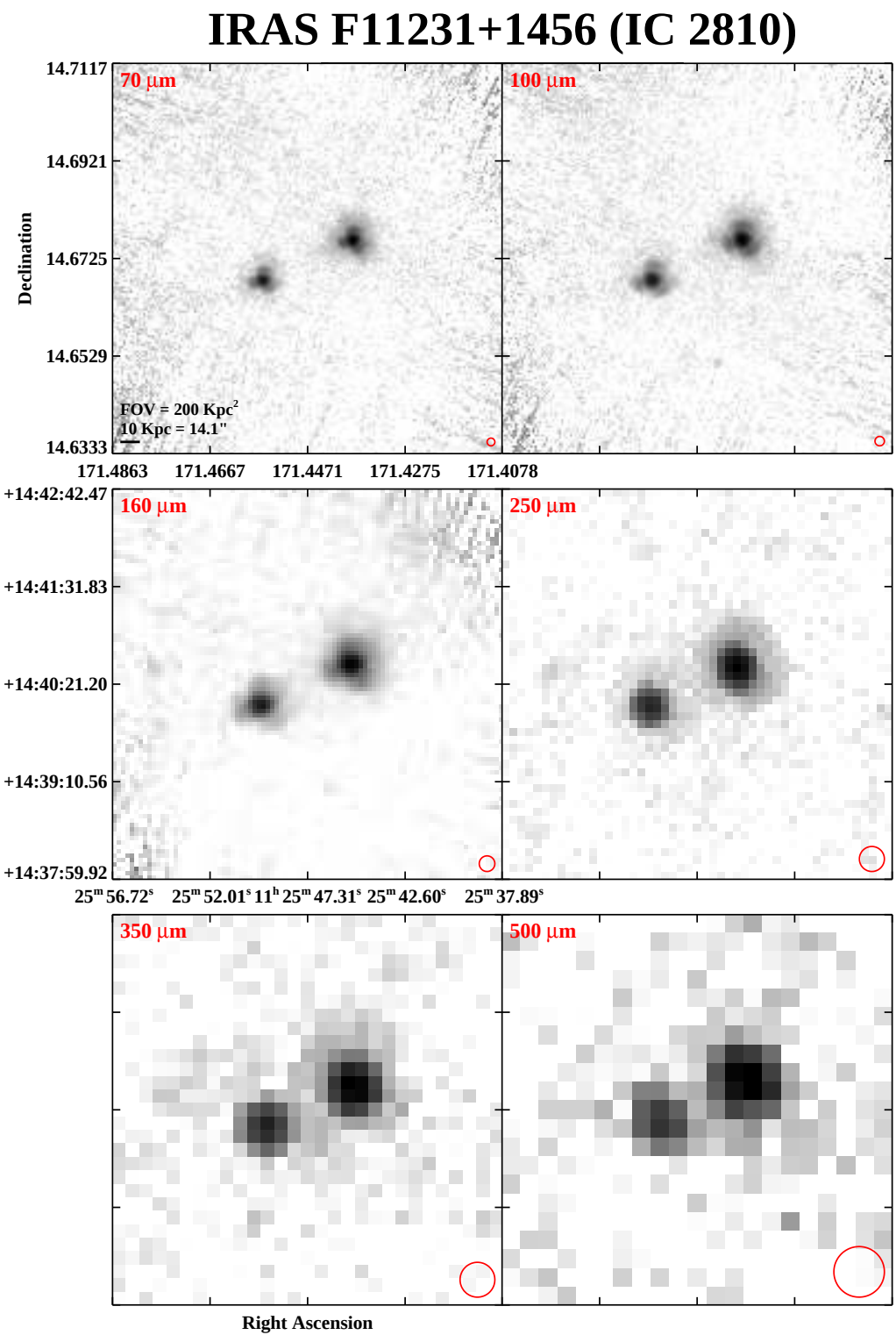

Figure 2.3 continued (page 97 of 209).

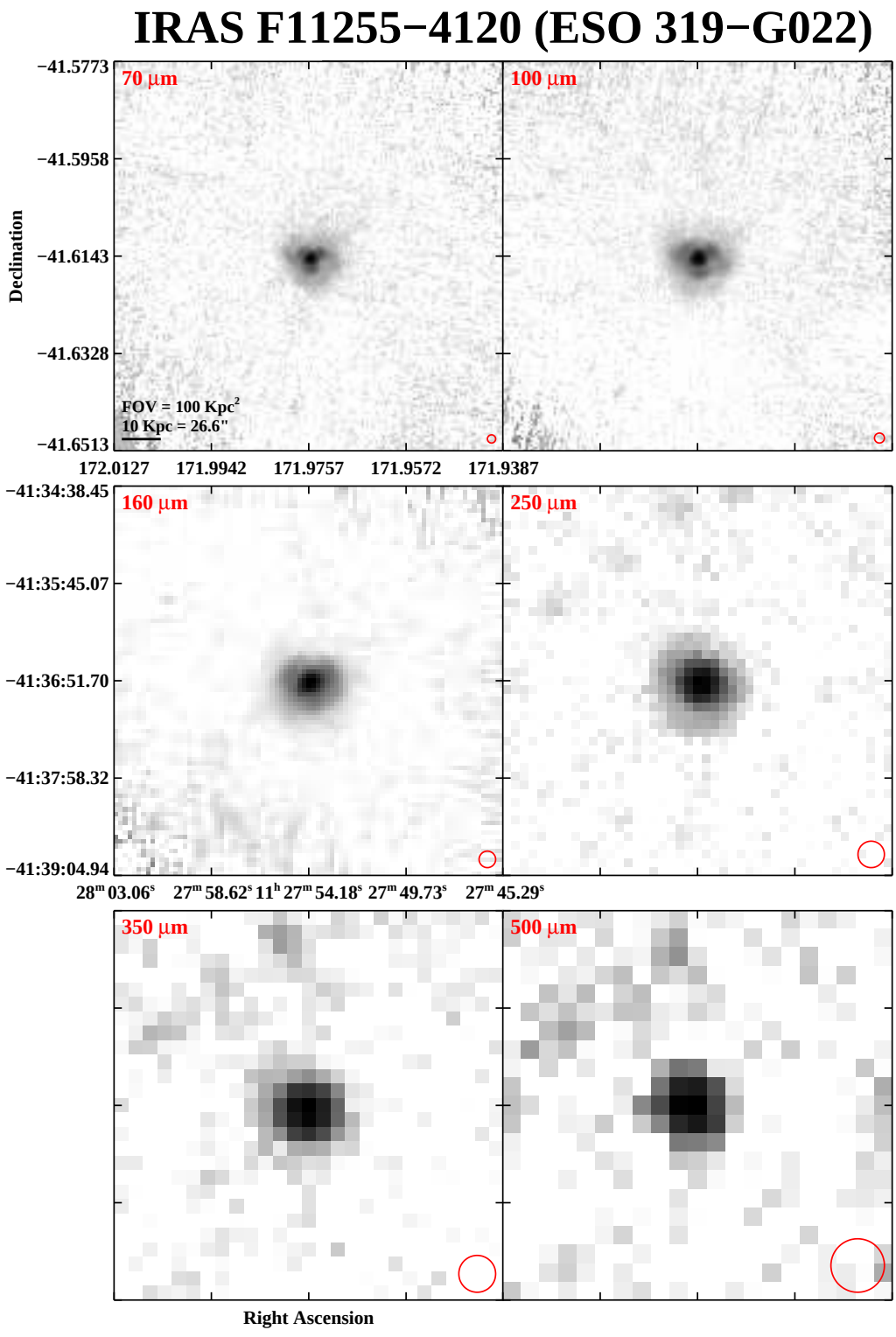

Figure 2.3 continued (page 98 of 209).

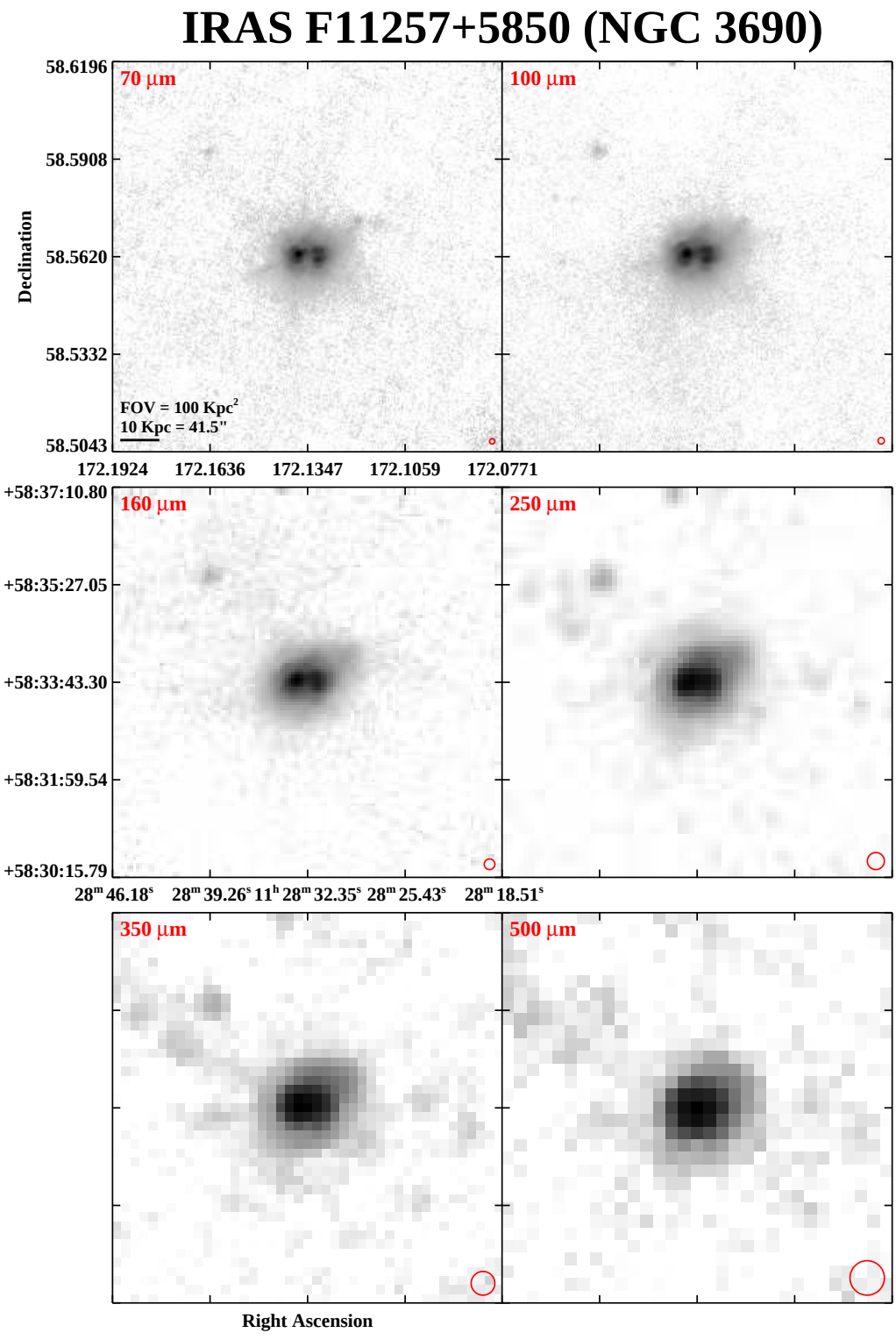

Figure 2.3 continued (page 99 of 209).

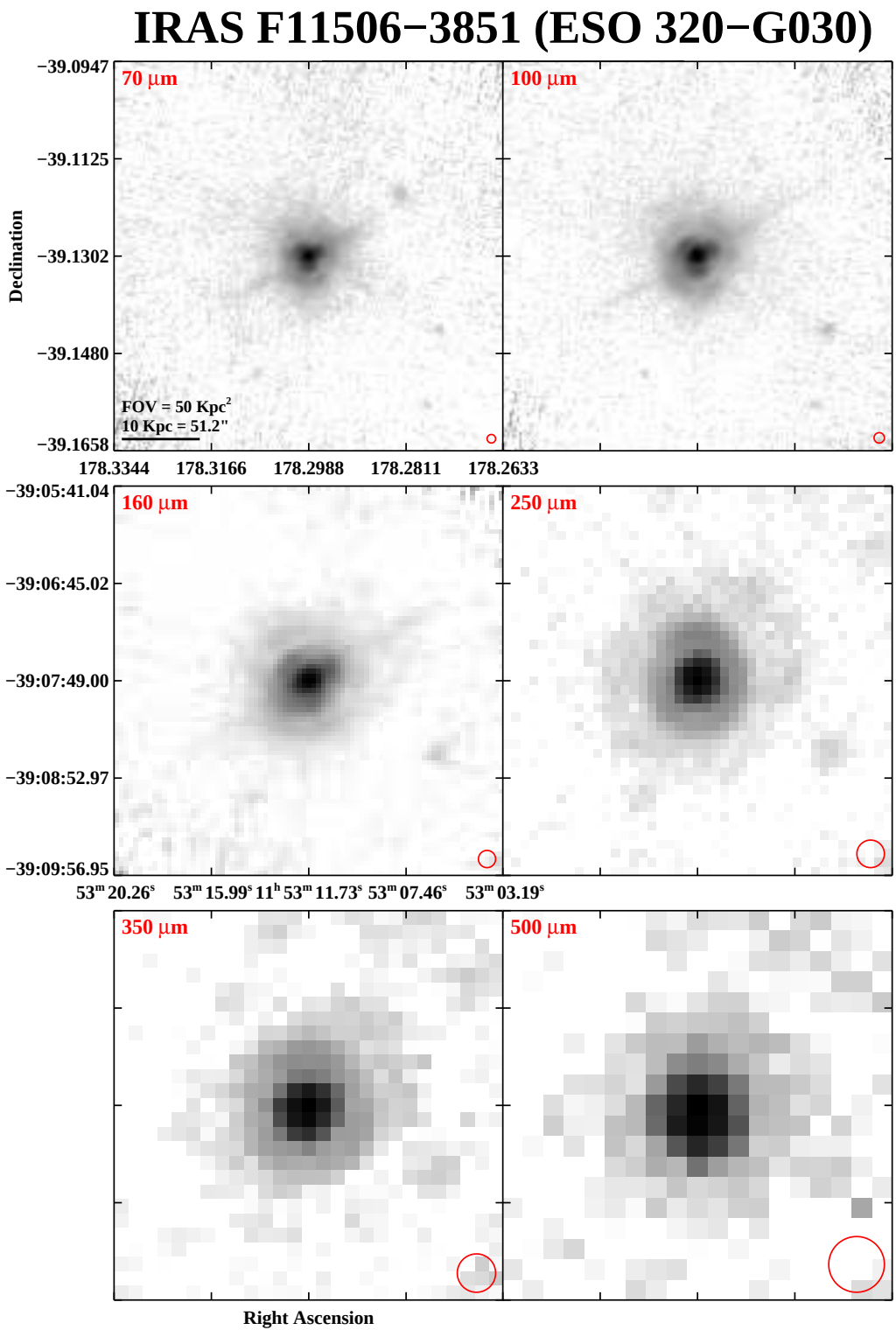

Figure 2.3 continued (page 100 of 209).

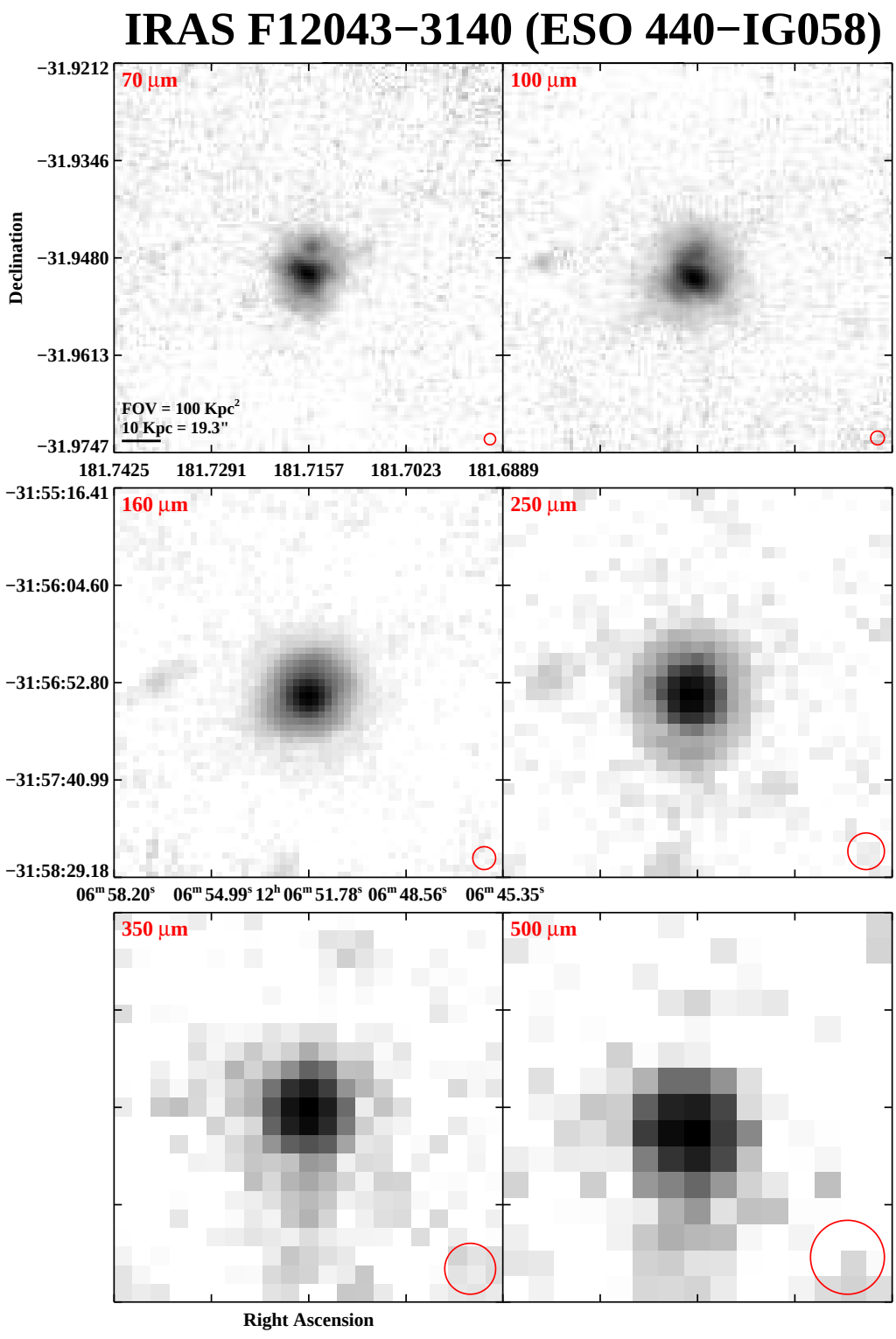

Figure 2.3 continued (page 101 of 209).

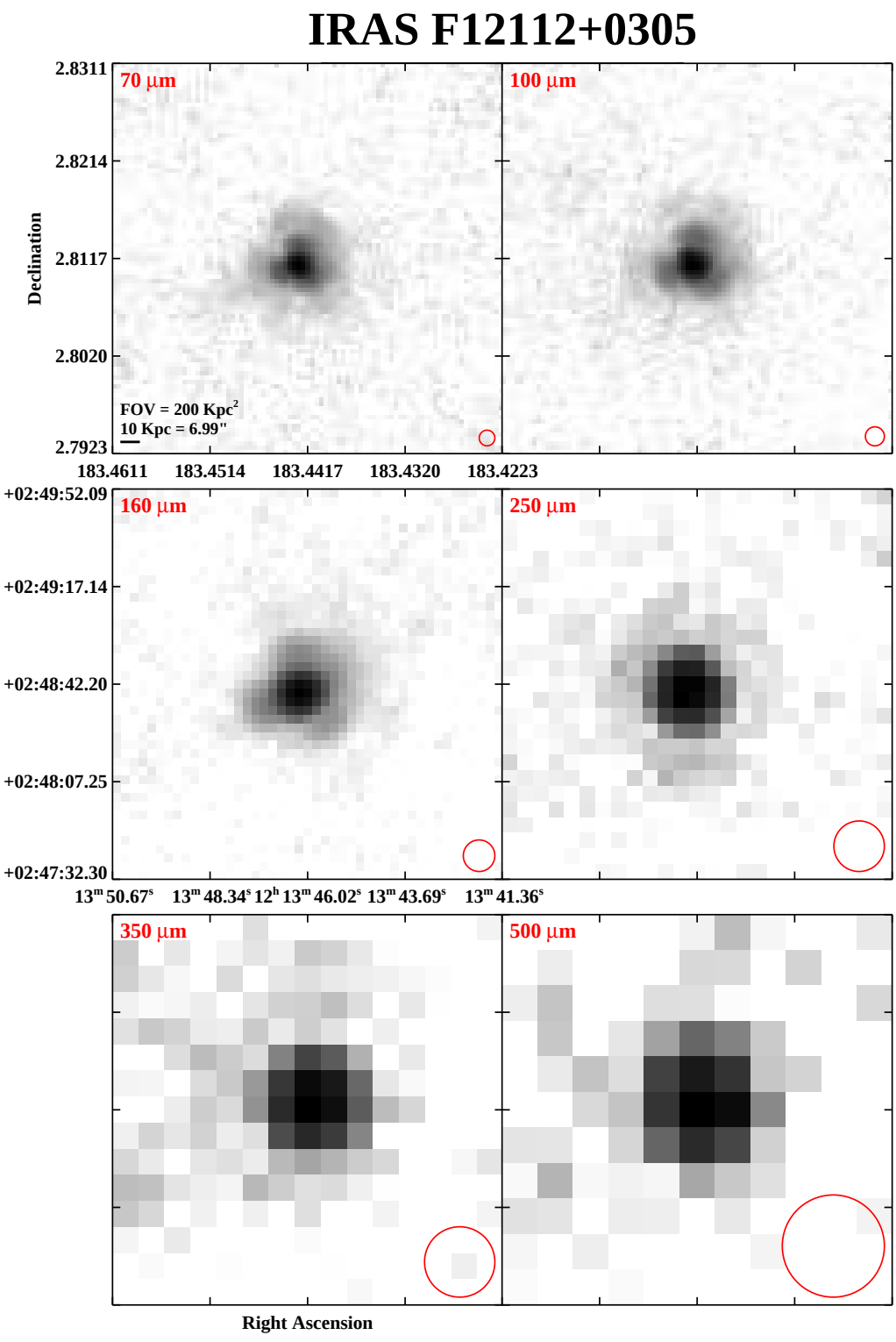

Figure 2.3 continued (page 102 of 209).

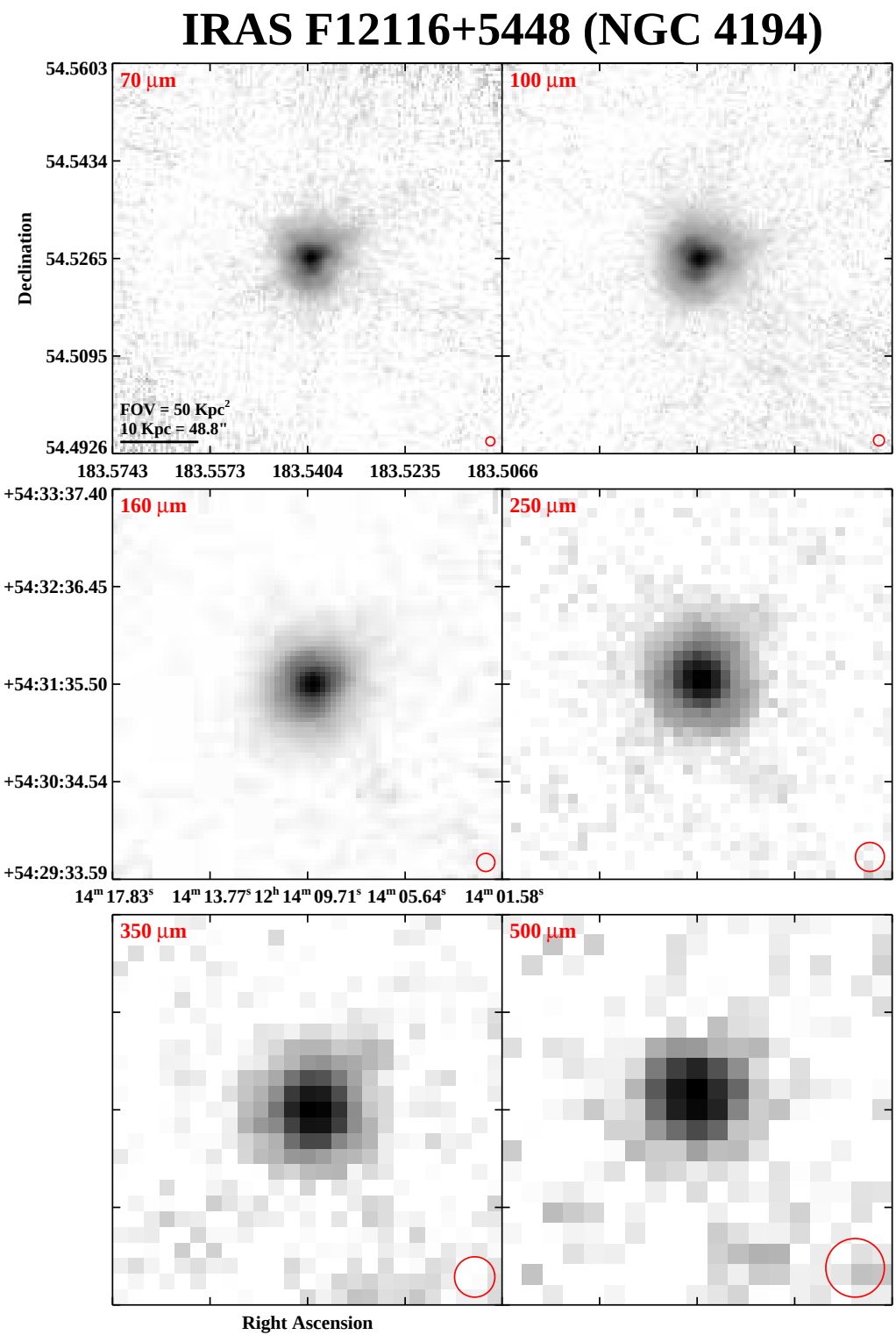

Figure 2.3 continued (page 103 of 209).

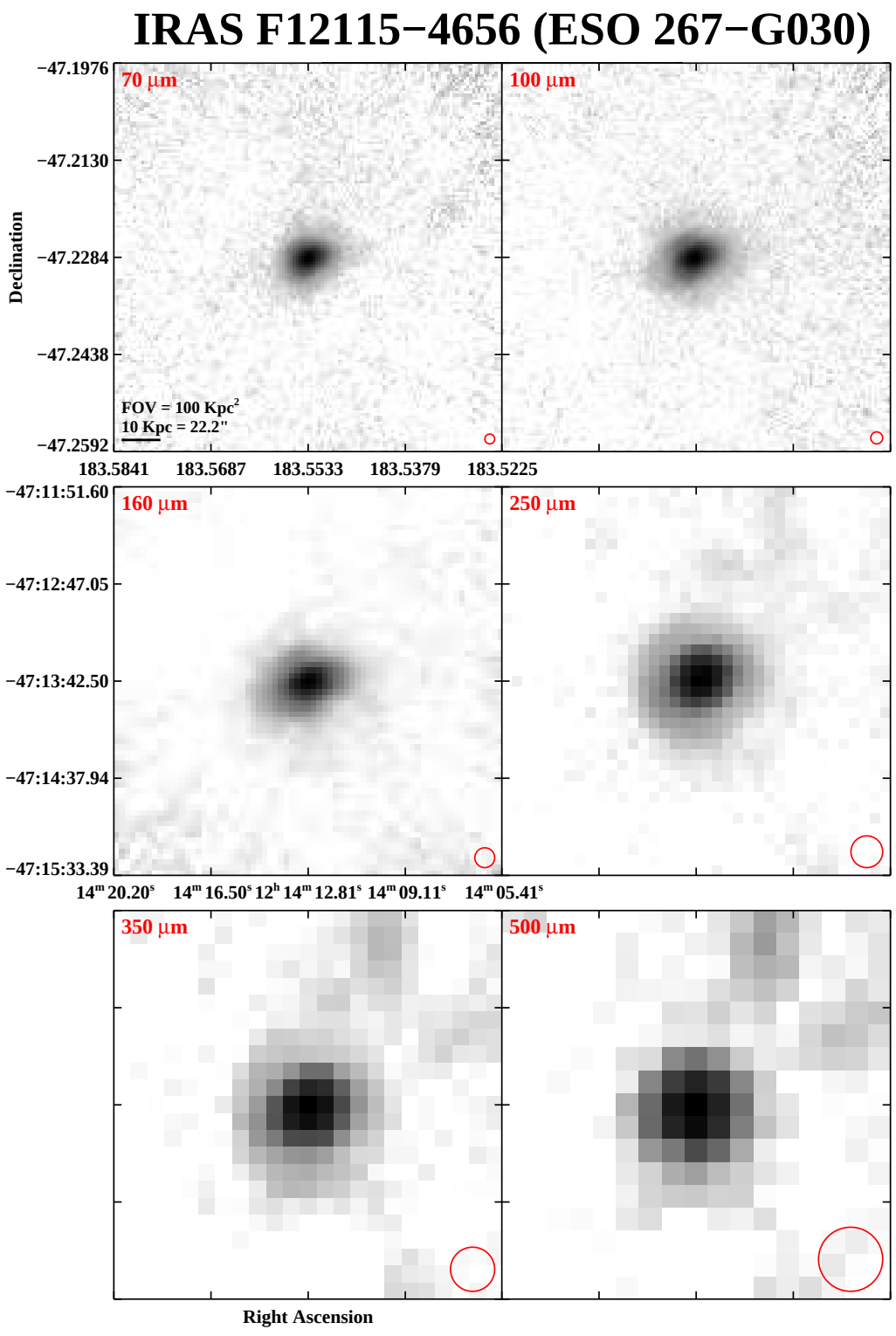

Figure 2.3 continued (page 104 of 209).

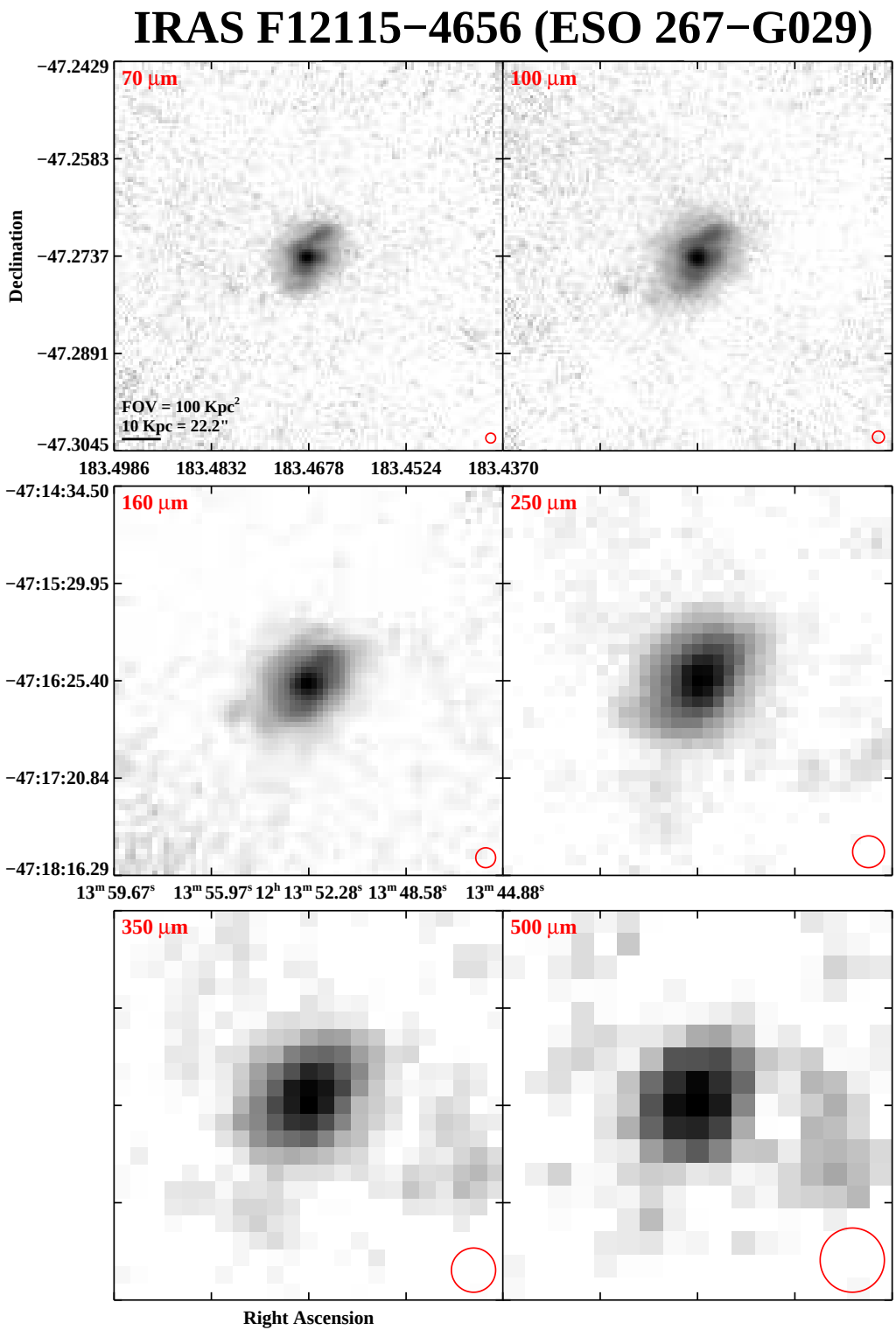

Figure 2.3 continued (page 105 of 209).

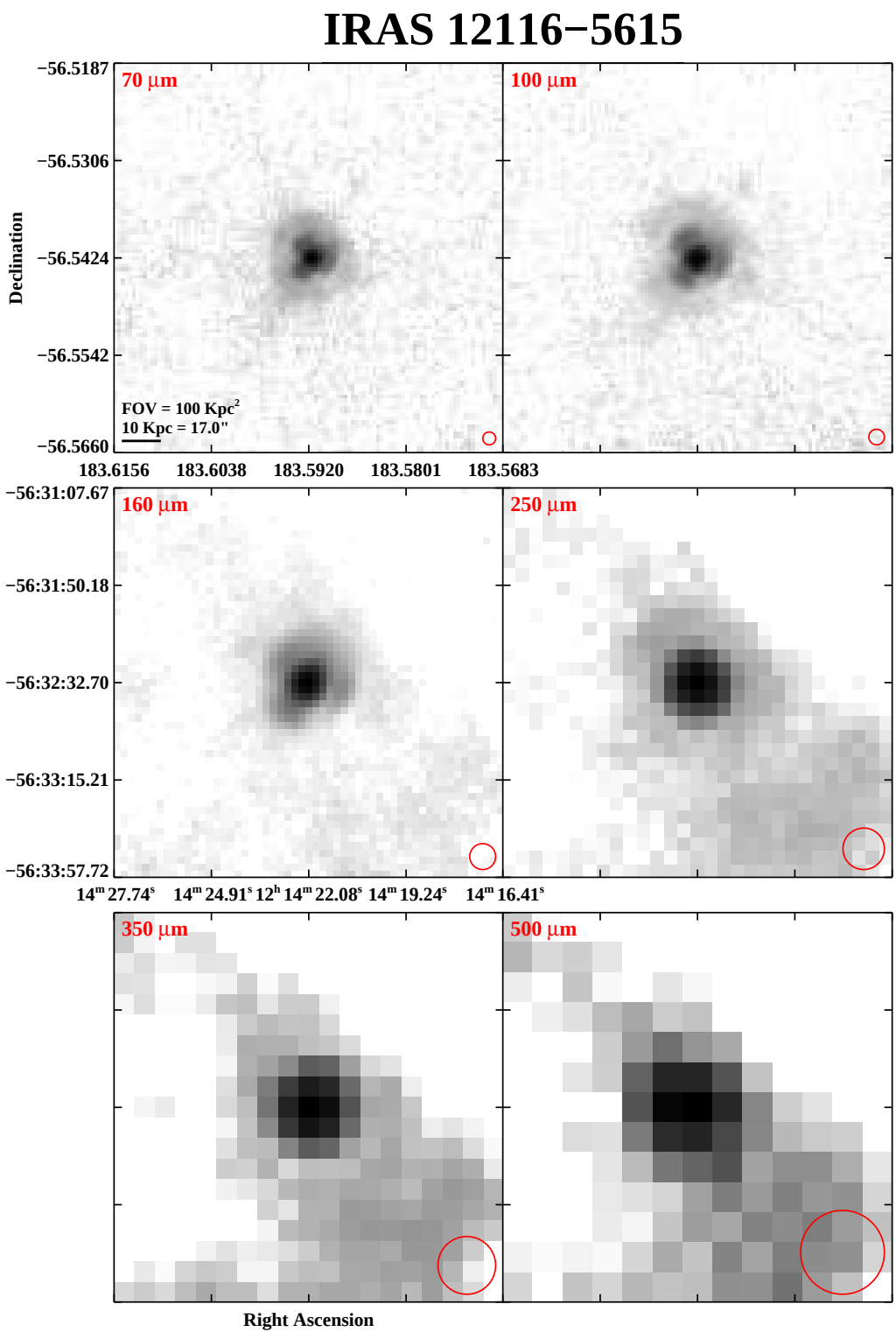

Figure 2.3 continued (page 106 of 209).

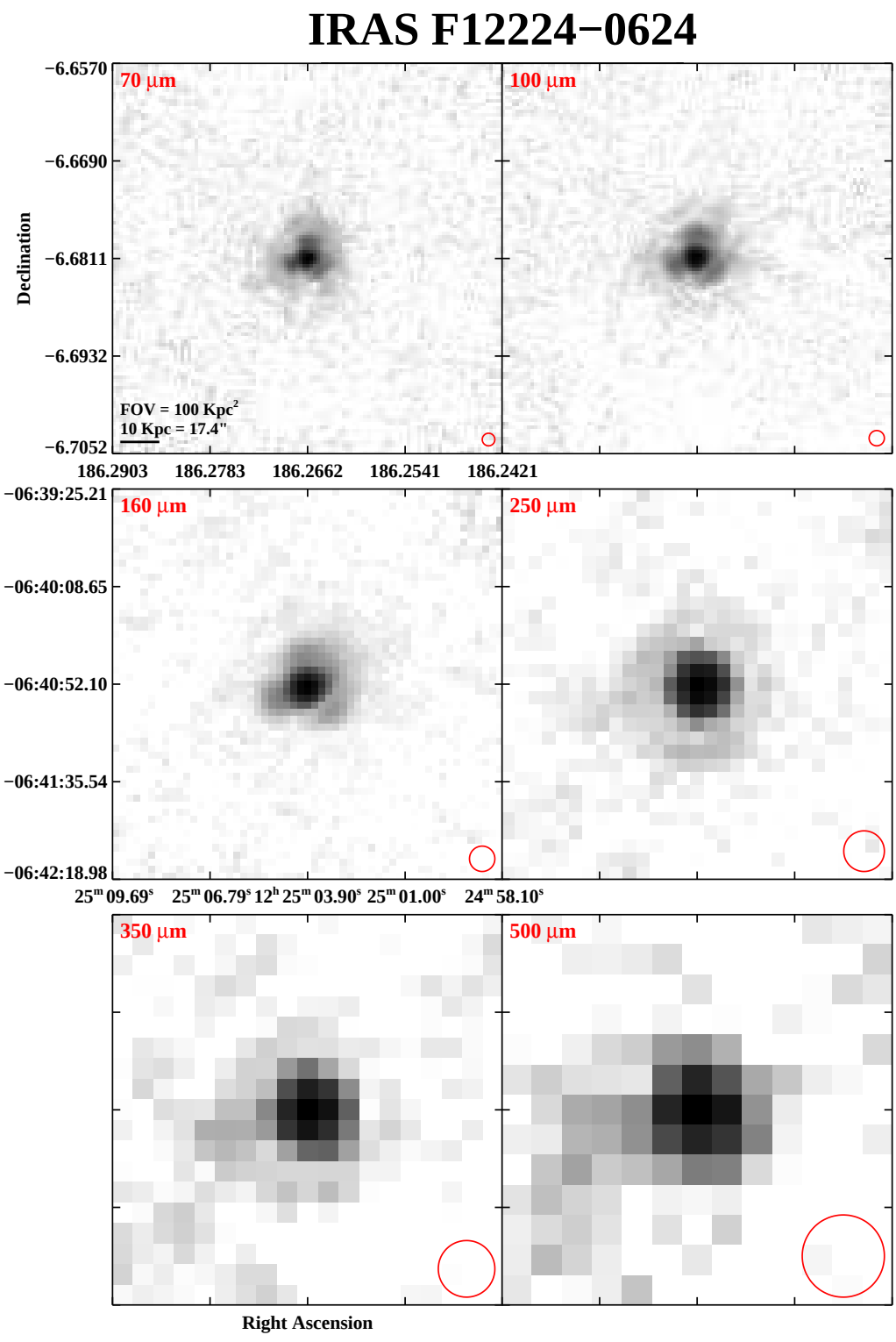

Figure 2.3 continued (page 107 of 209).

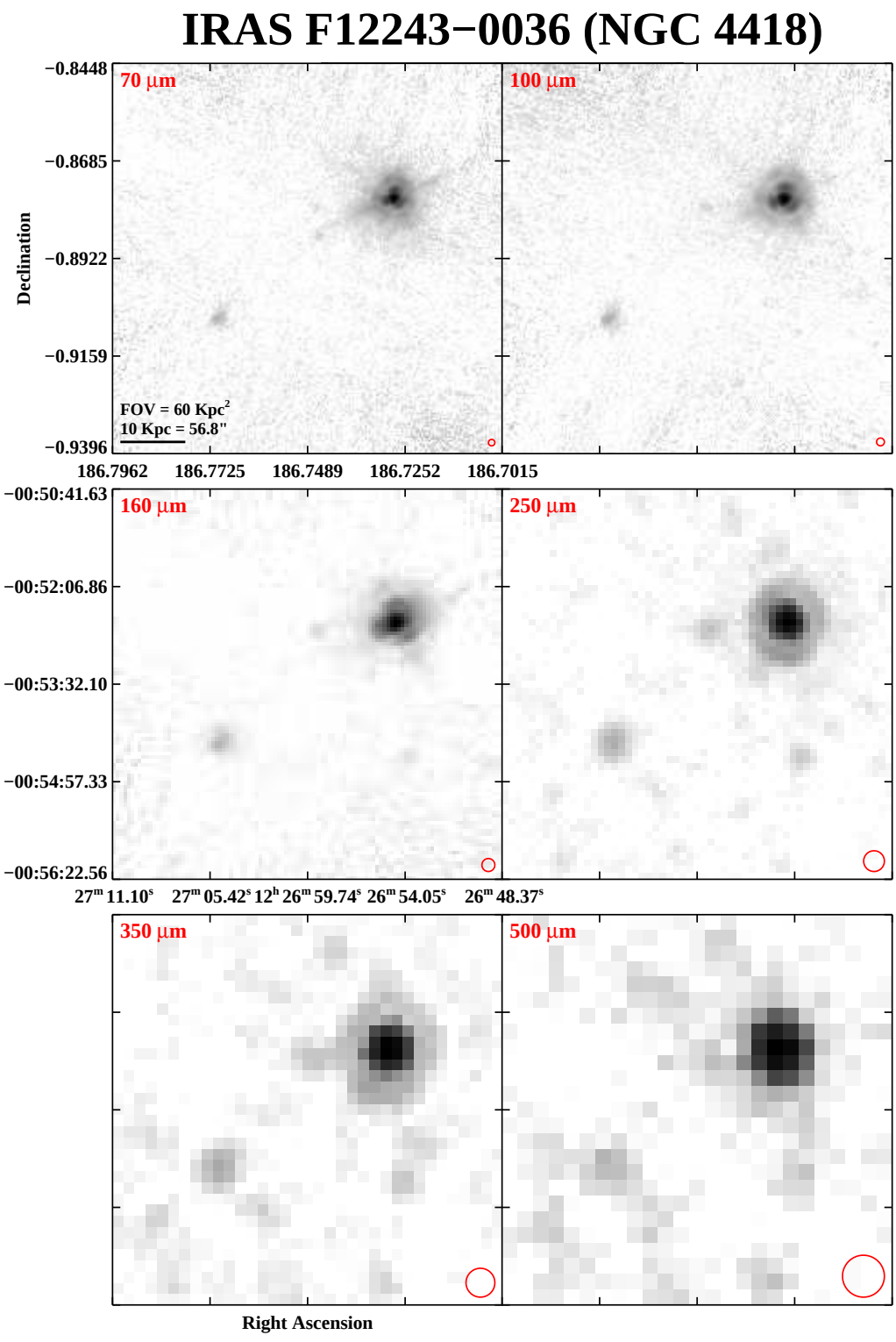

Figure 2.3 continued (page 108 of 209).

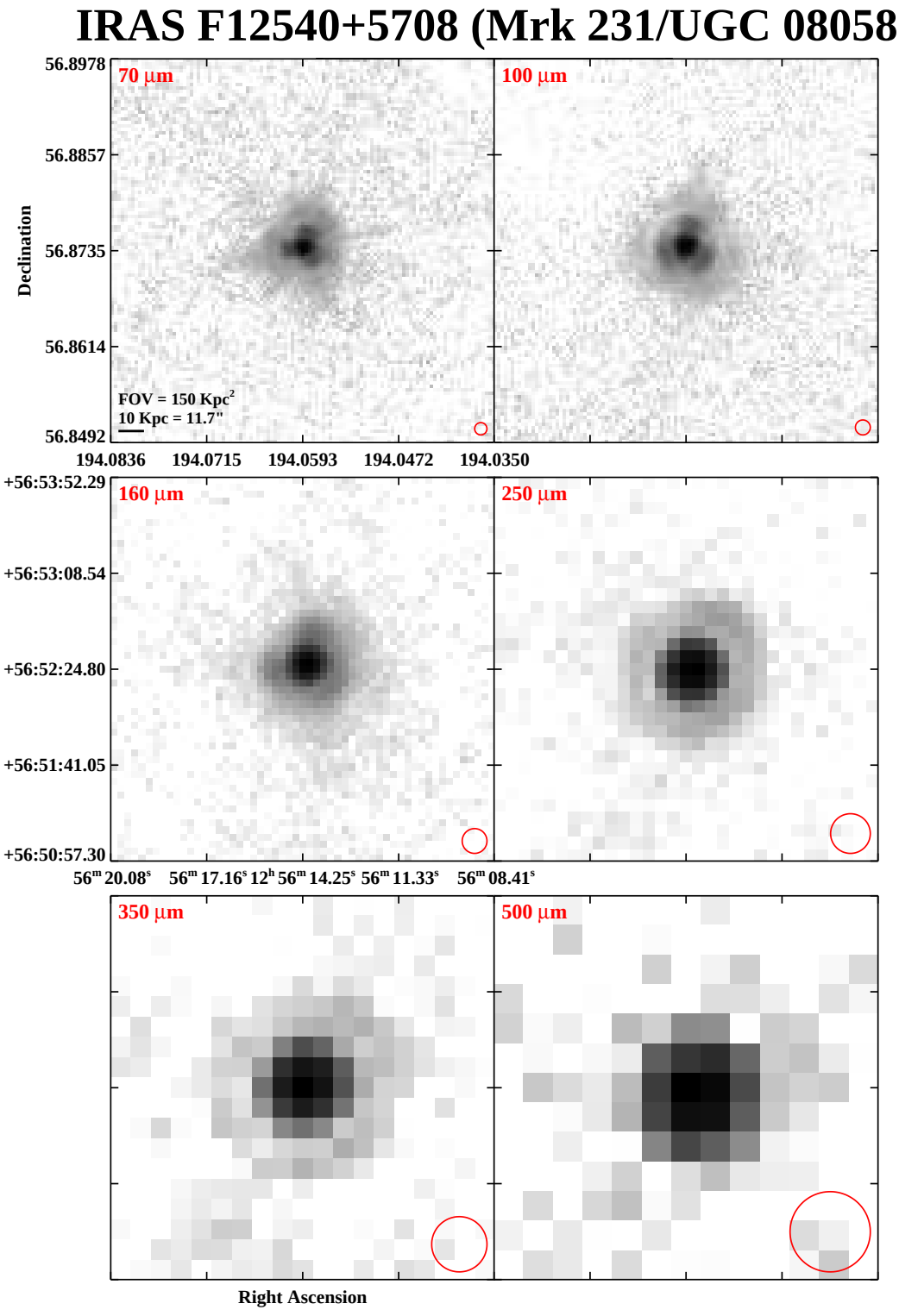

Figure 2.3 continued (page 109 of 209).

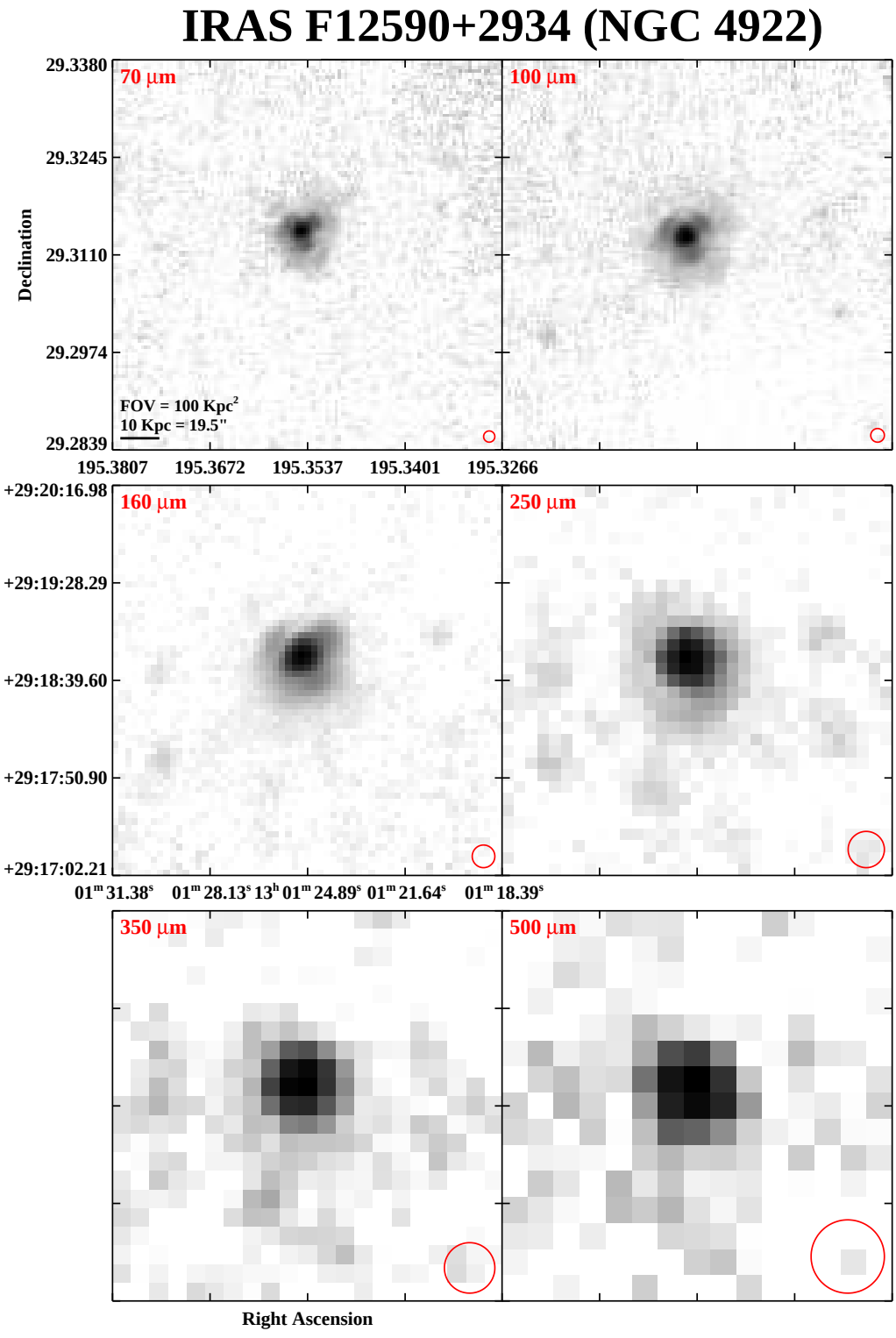

Figure 2.3 continued (page 110 of 209).

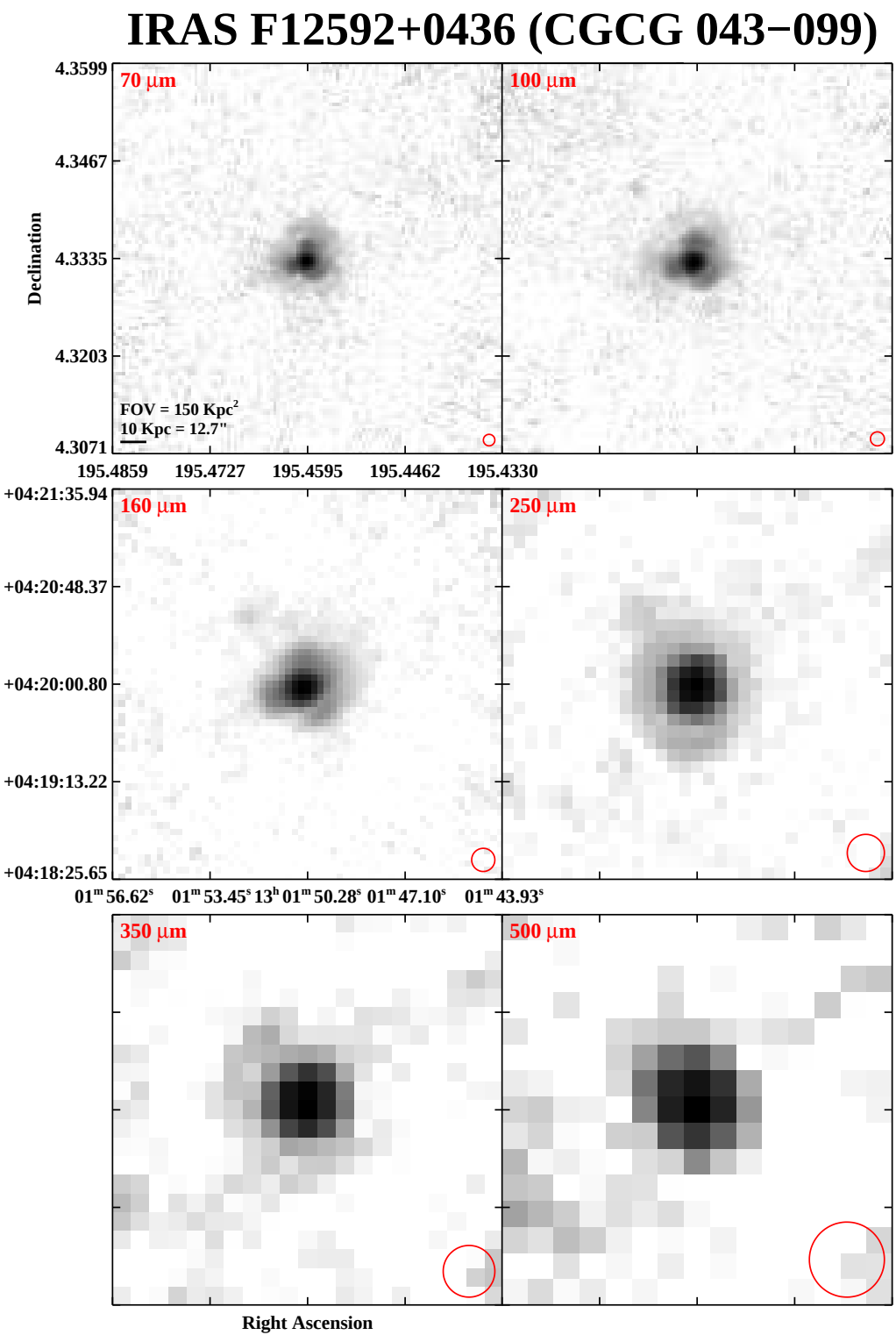

Figure 2.3 continued (page 111 of 209).

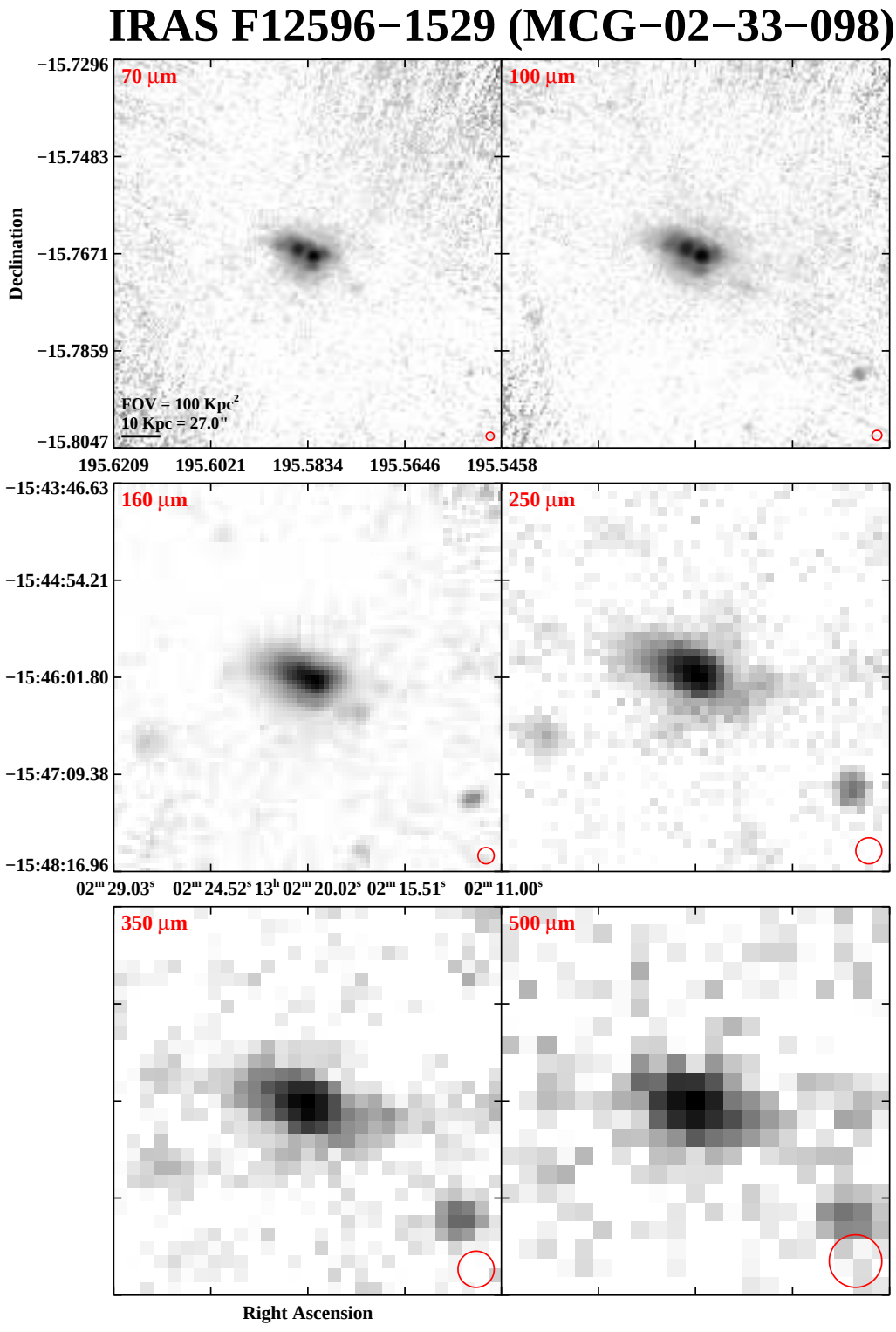

Figure 2.3 continued (page 112 of 209).

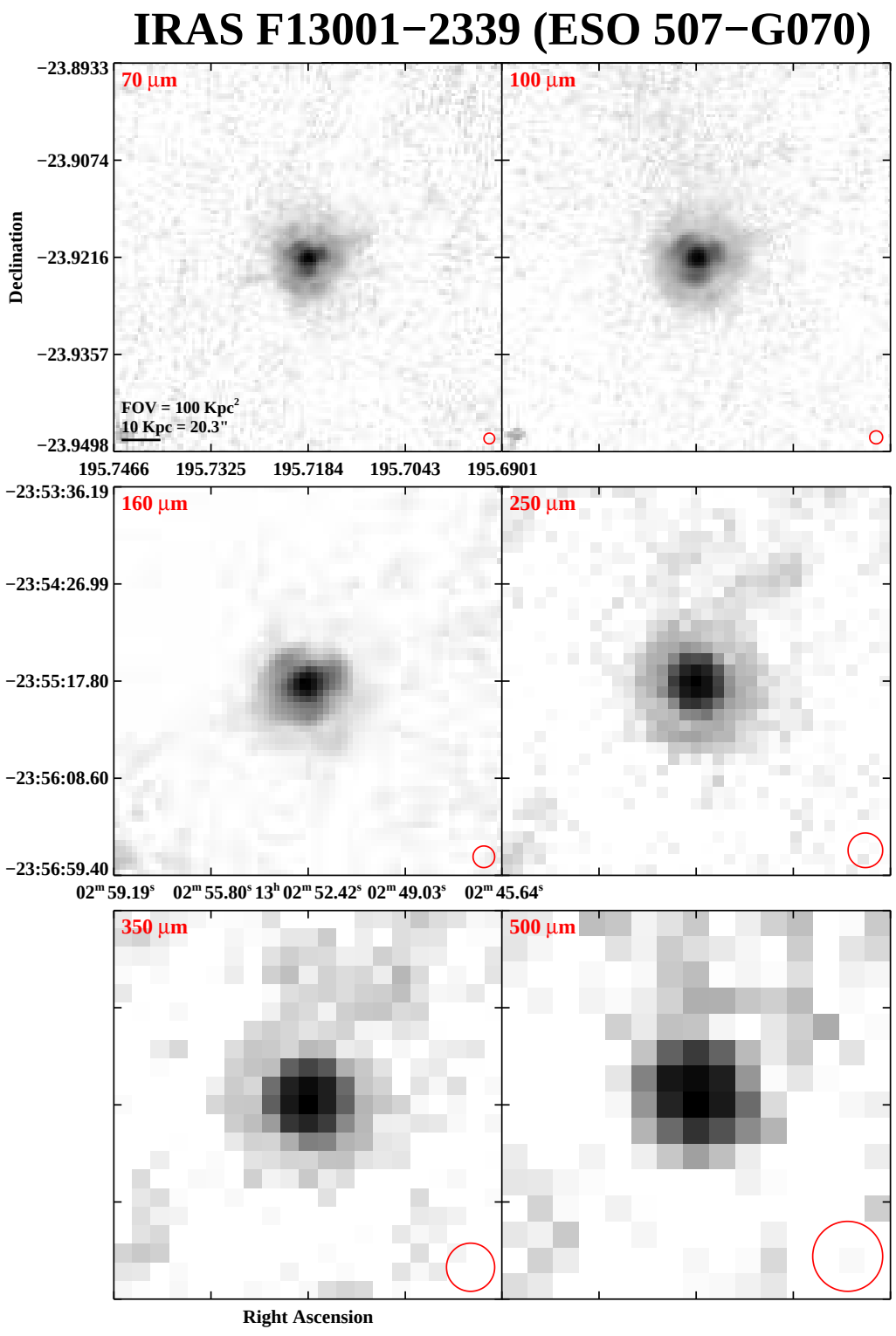

Figure 2.3 continued (page 113 of 209).

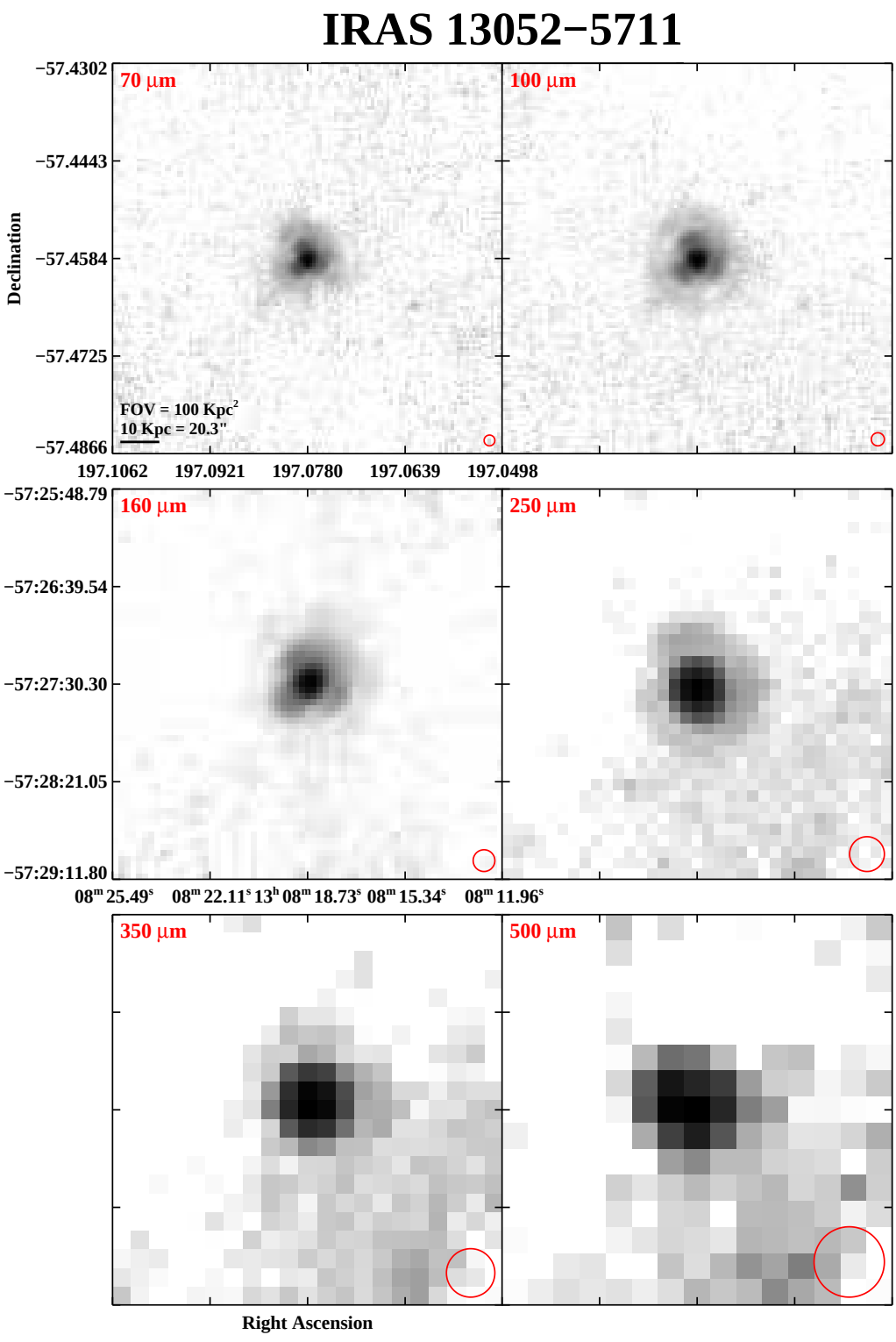

Figure 2.3 continued (page 114 of 209).

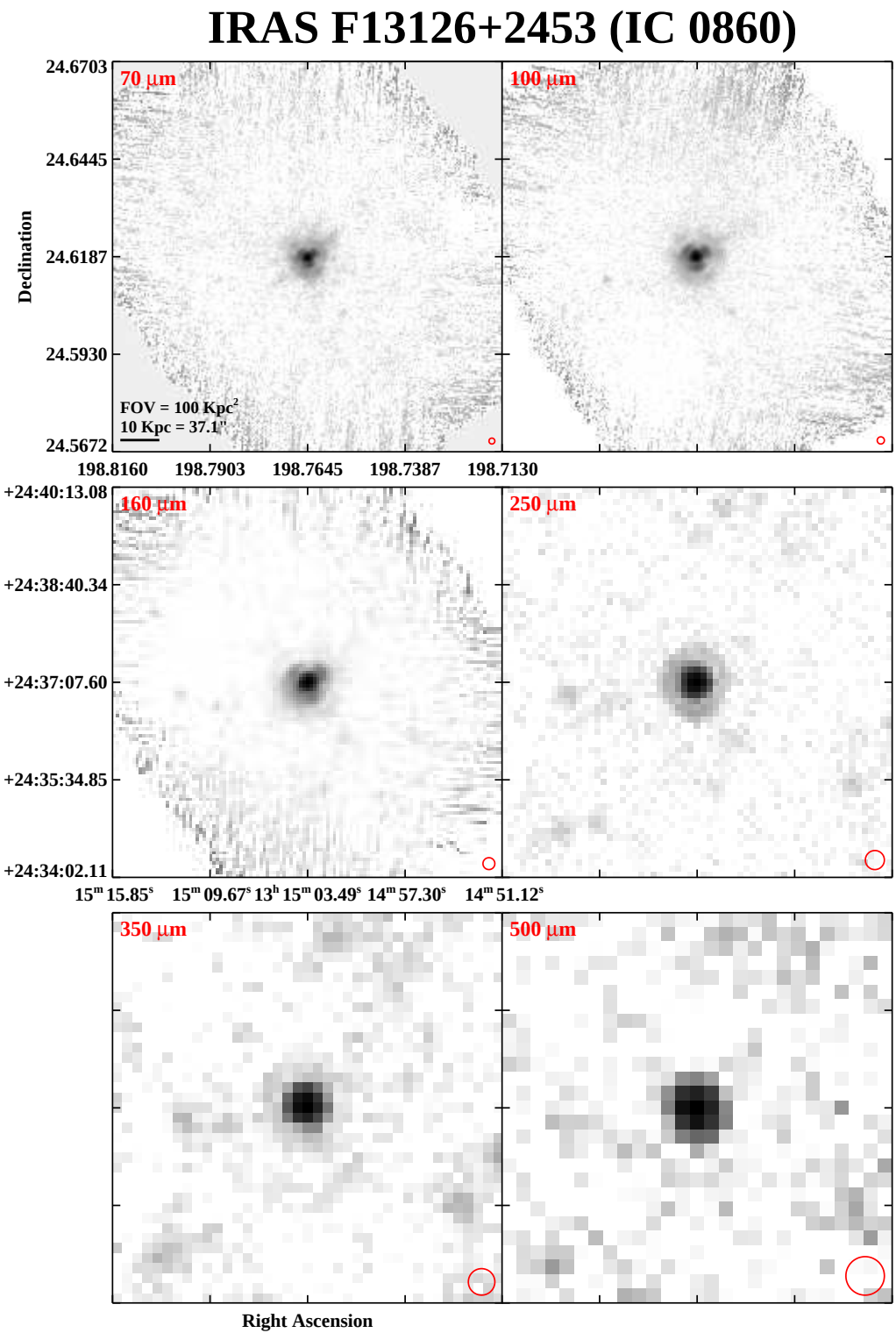

Figure 2.3 continued (page 115 of 209).

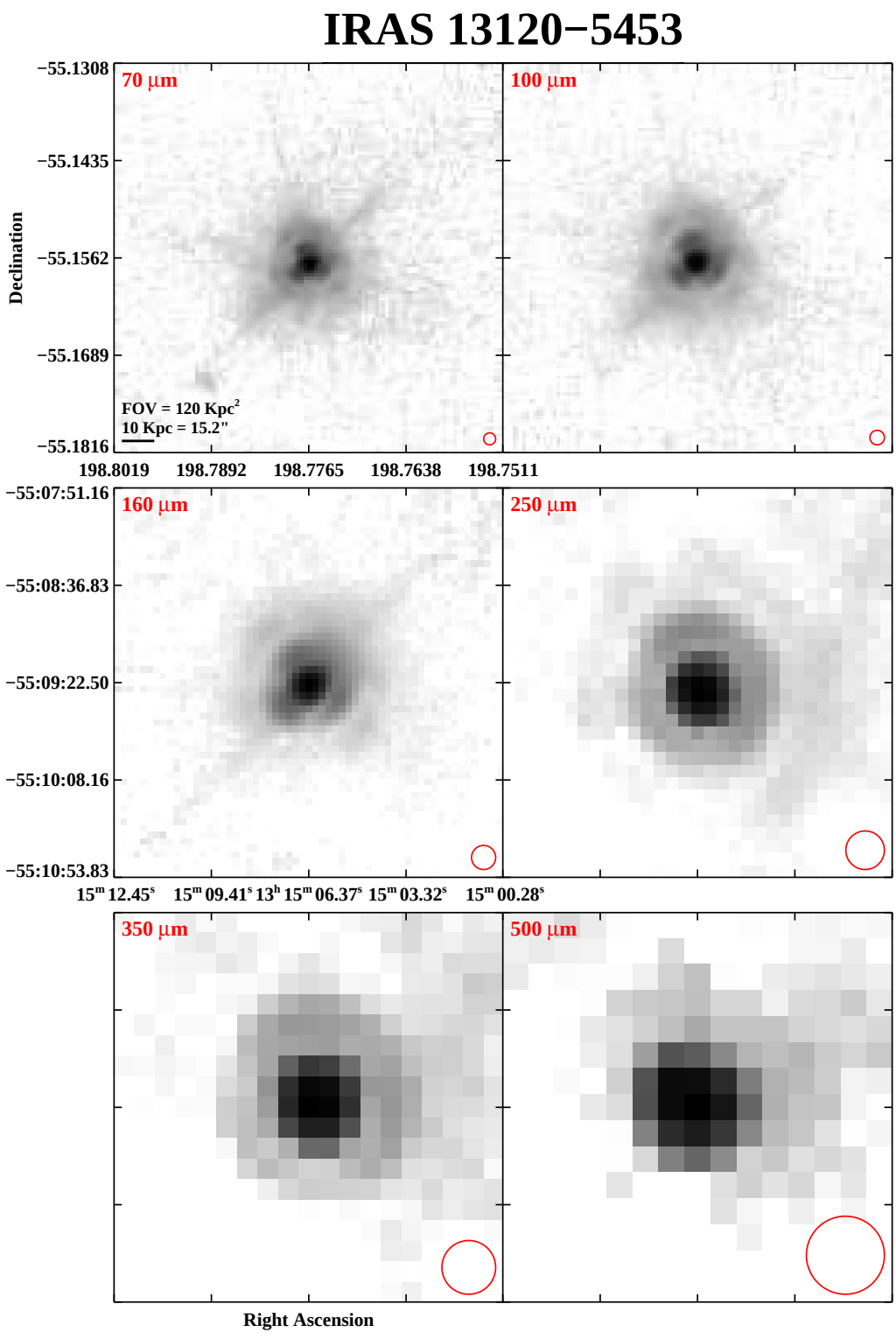

Figure 2.3 continued (page 116 of 209).

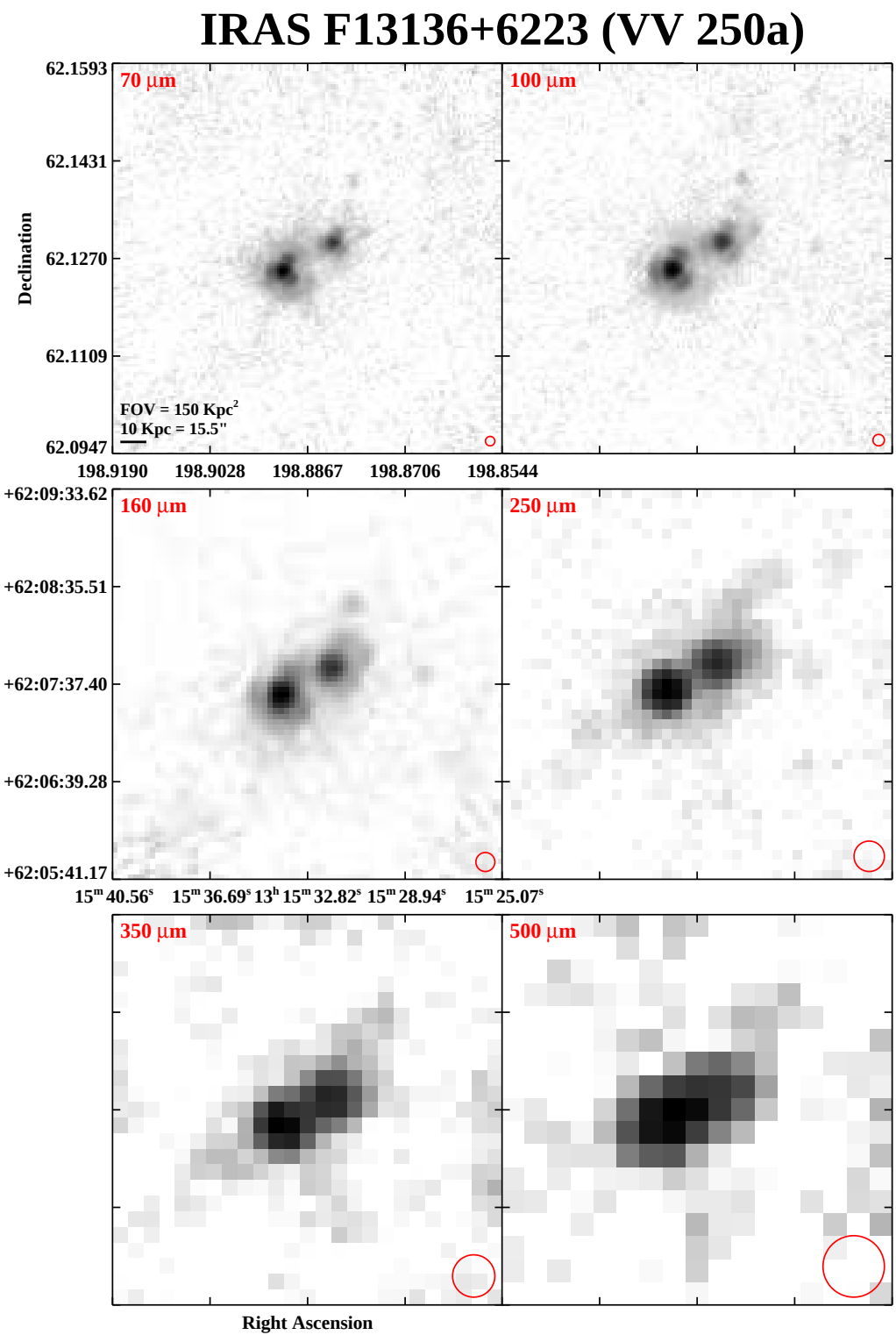

Figure 2.3 continued (page 117 of 209).

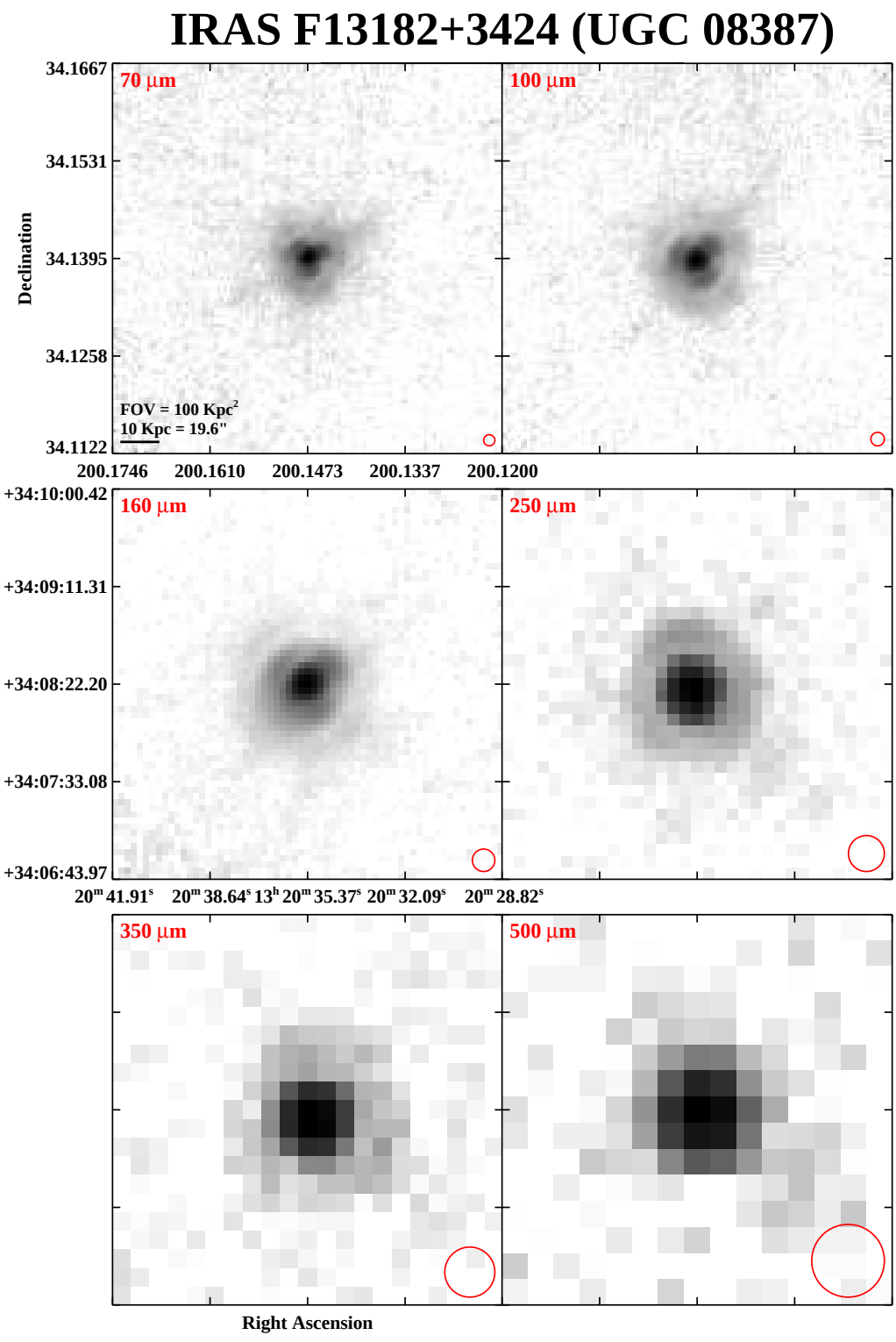

Figure 2.3 continued (page 118 of 209).

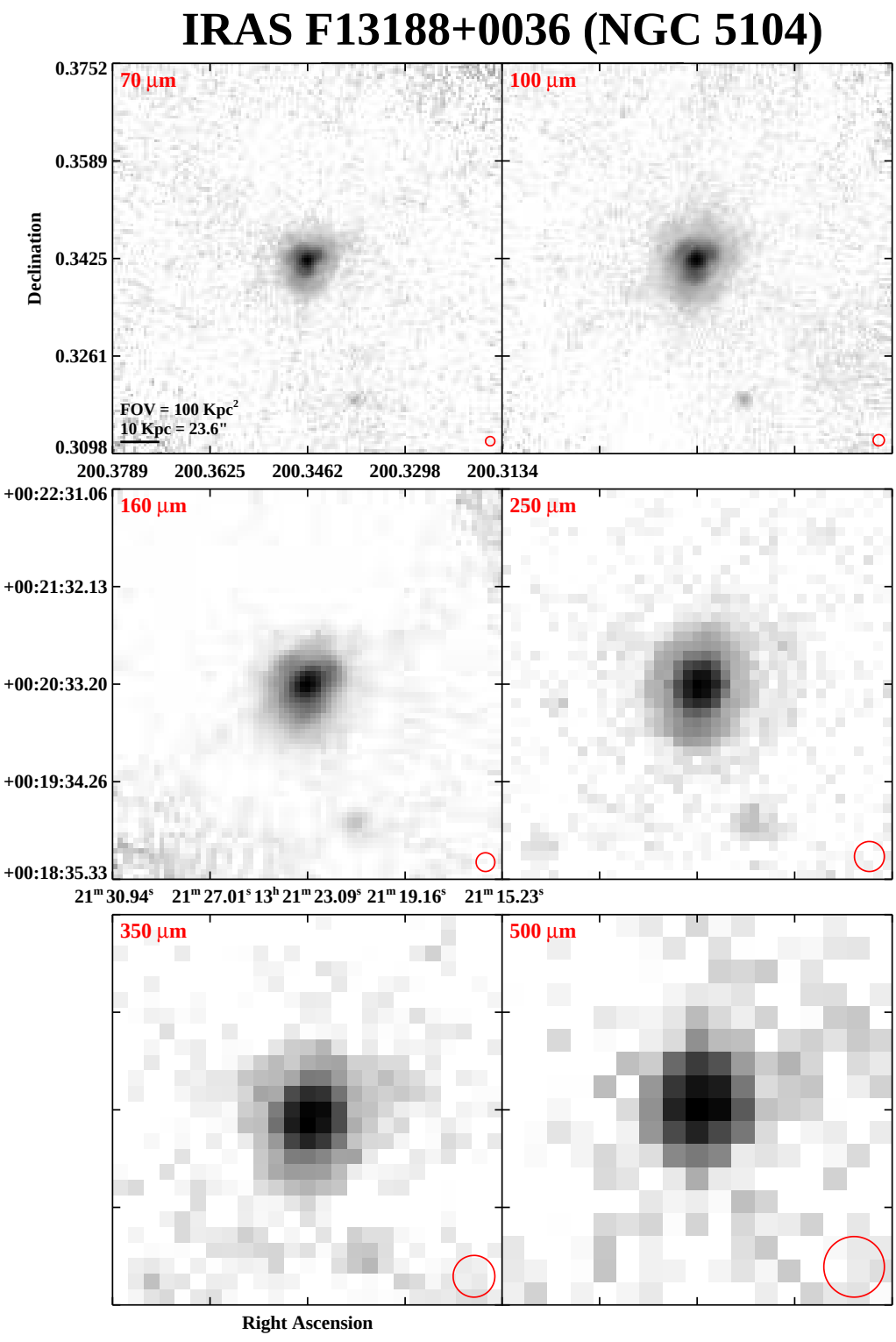

Figure 2.3 continued (page 119 of 209).

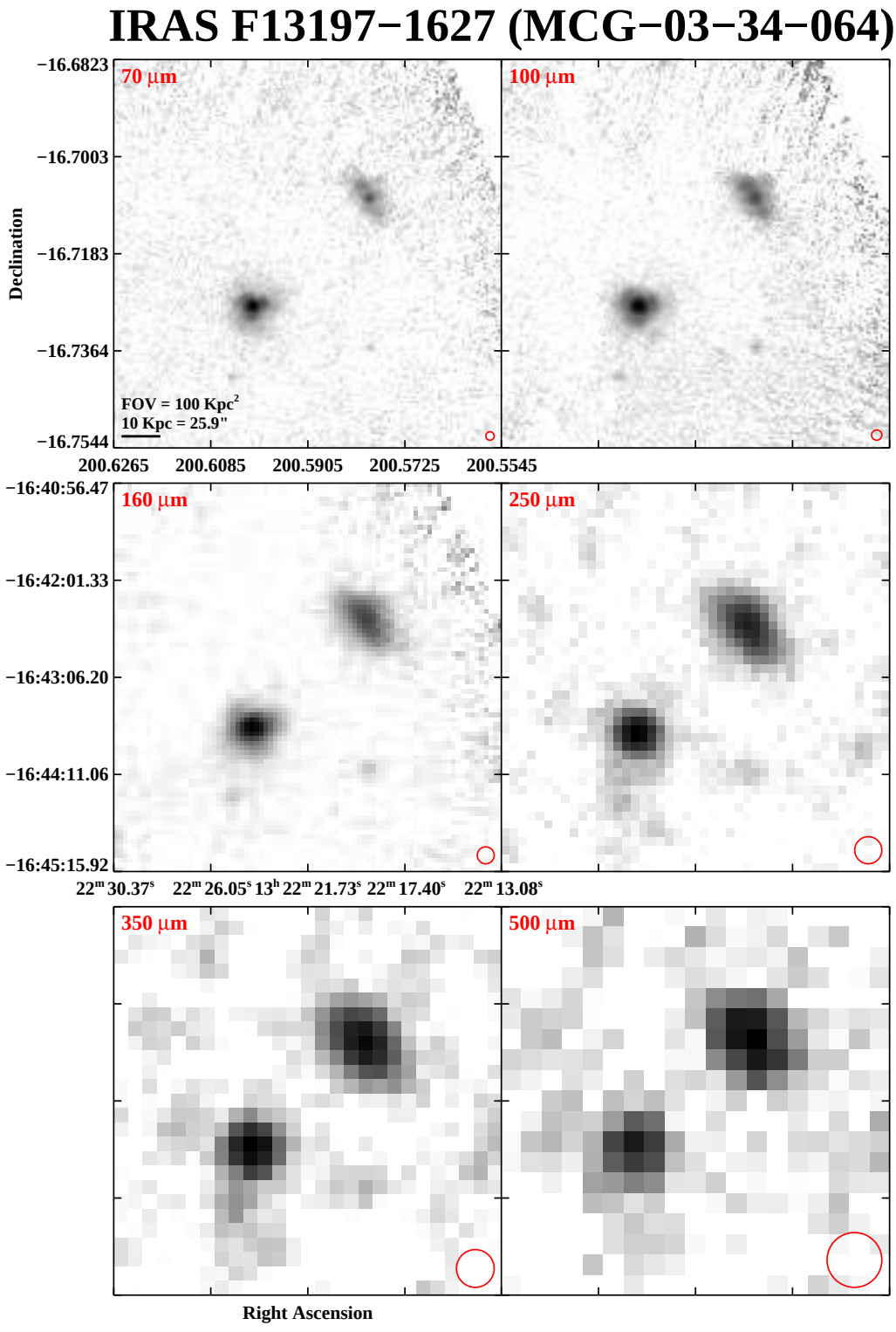

Figure 2.3 continued (page 120 of 209).

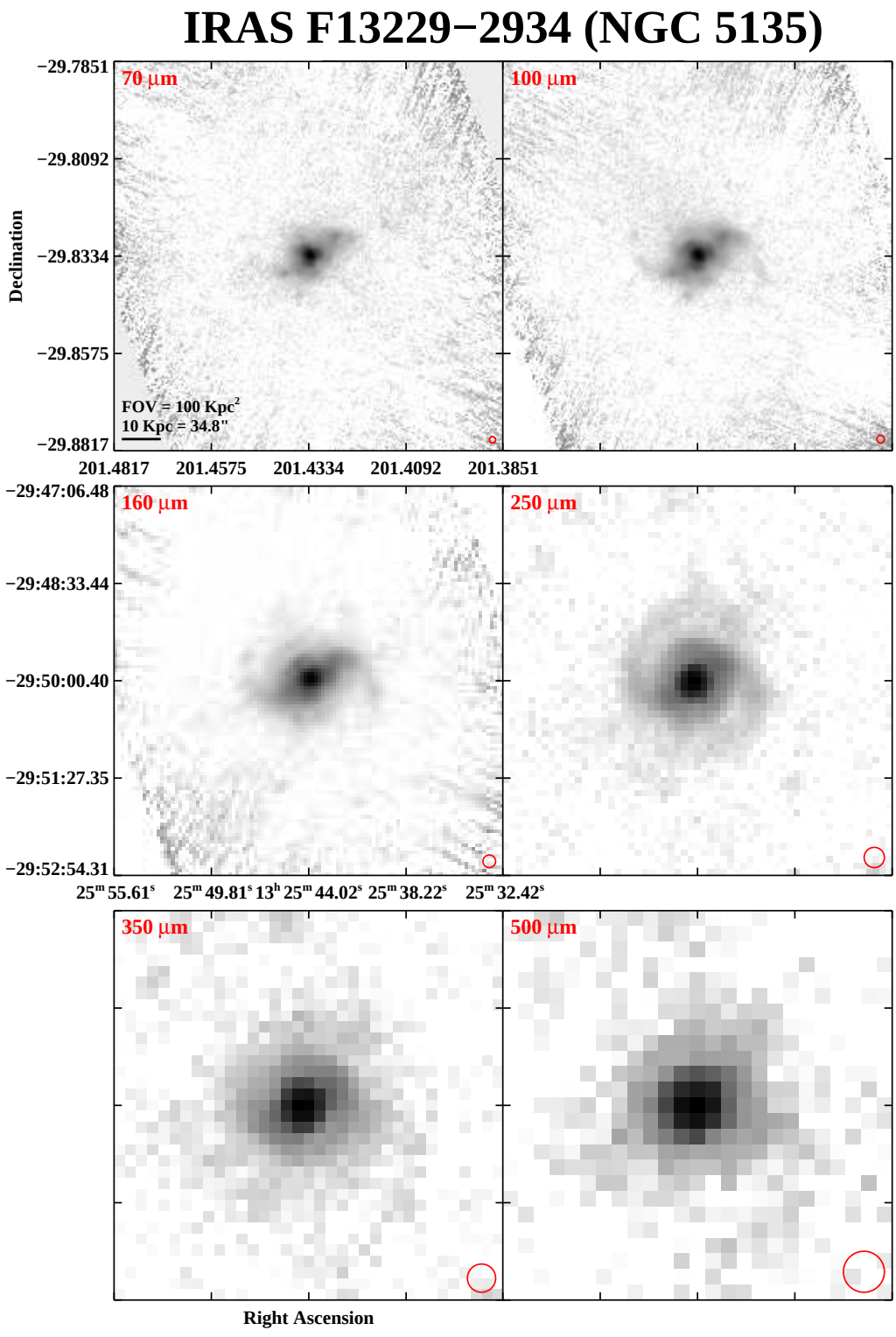

Figure 2.3 continued (page 121 of 209).

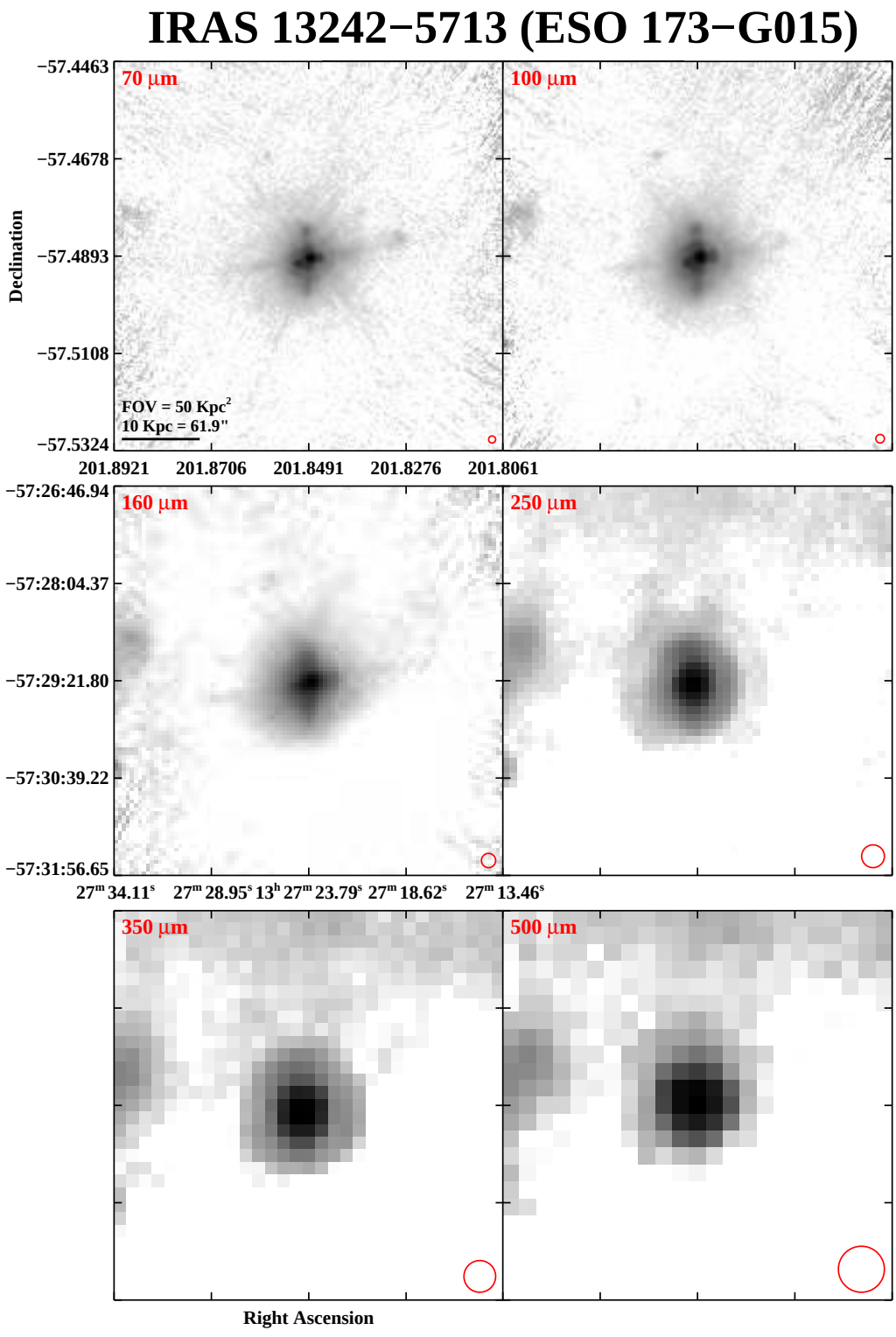

Figure 2.3 continued (page 122 of 209).

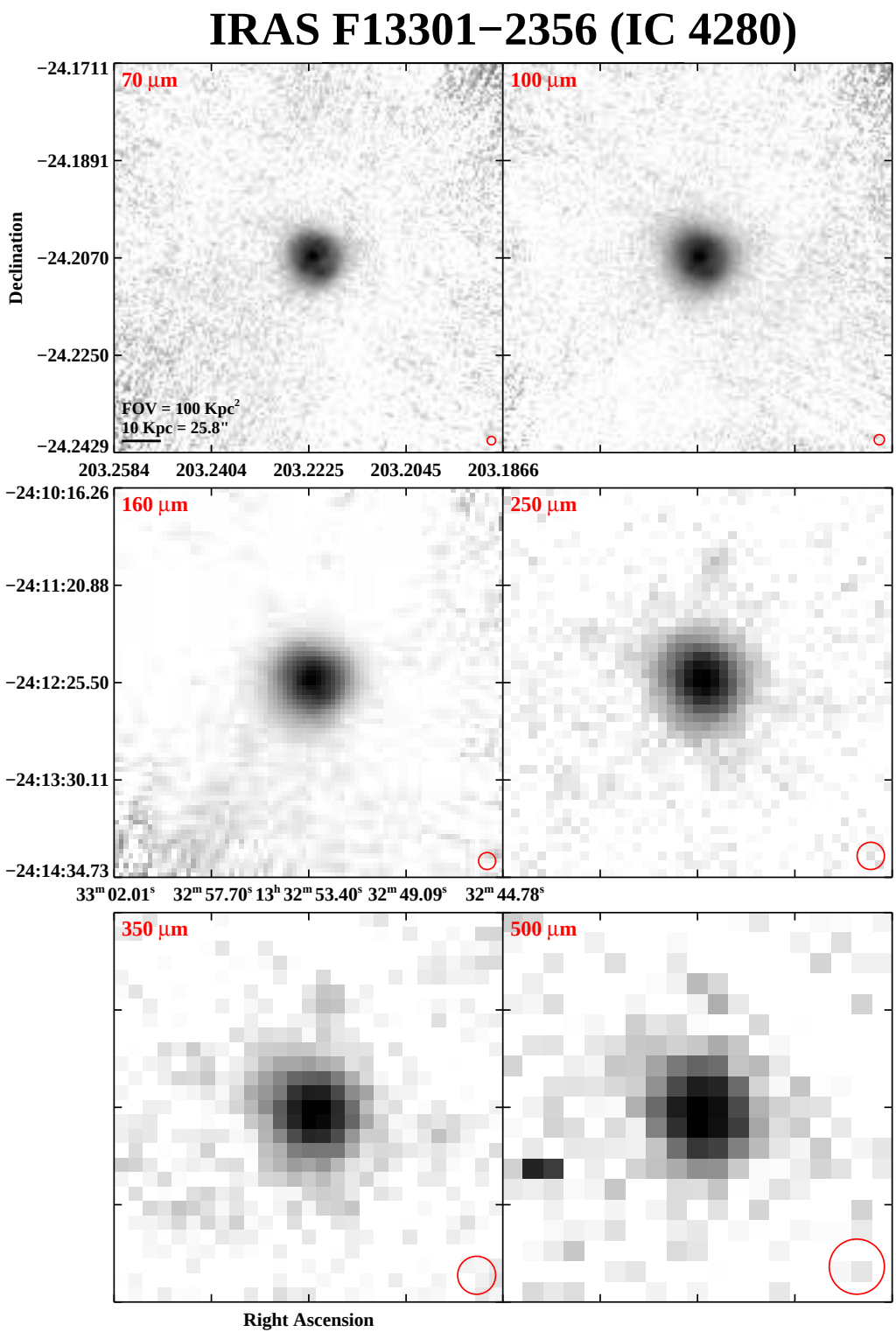

Figure 2.3 continued (page 123 of 209).

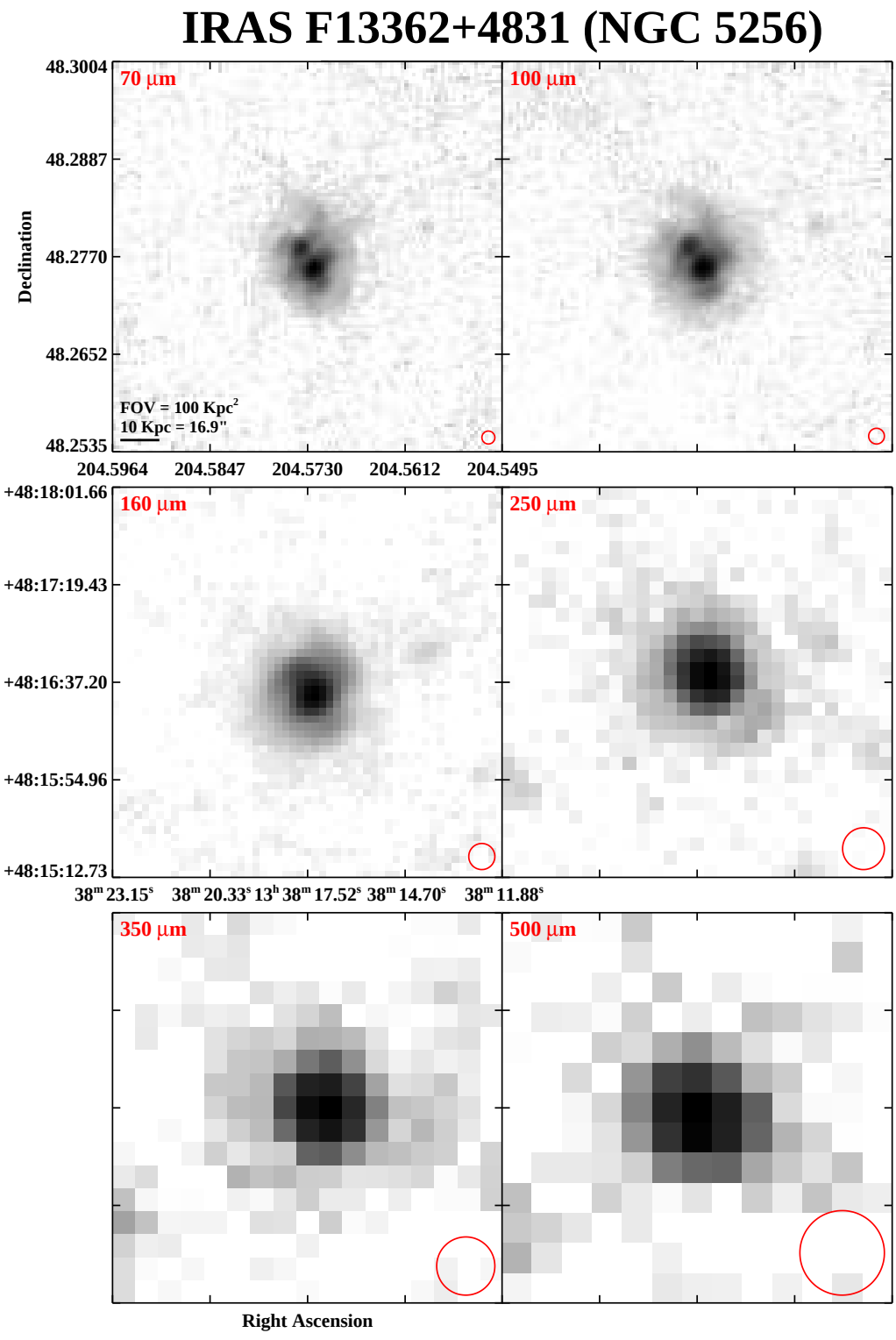

Figure 2.3 continued (page 124 of 209).

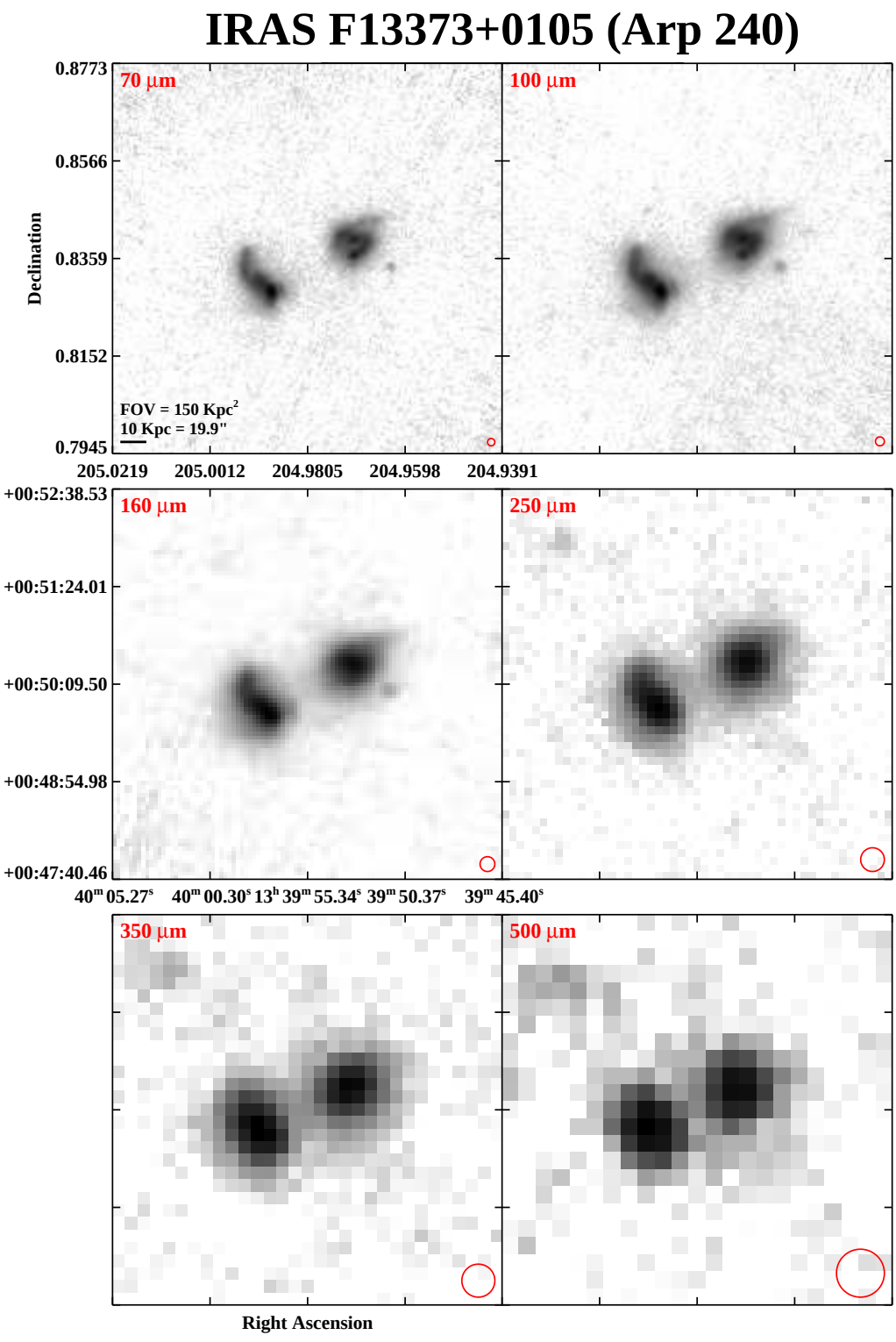

Figure 2.3 continued (page 125 of 209).

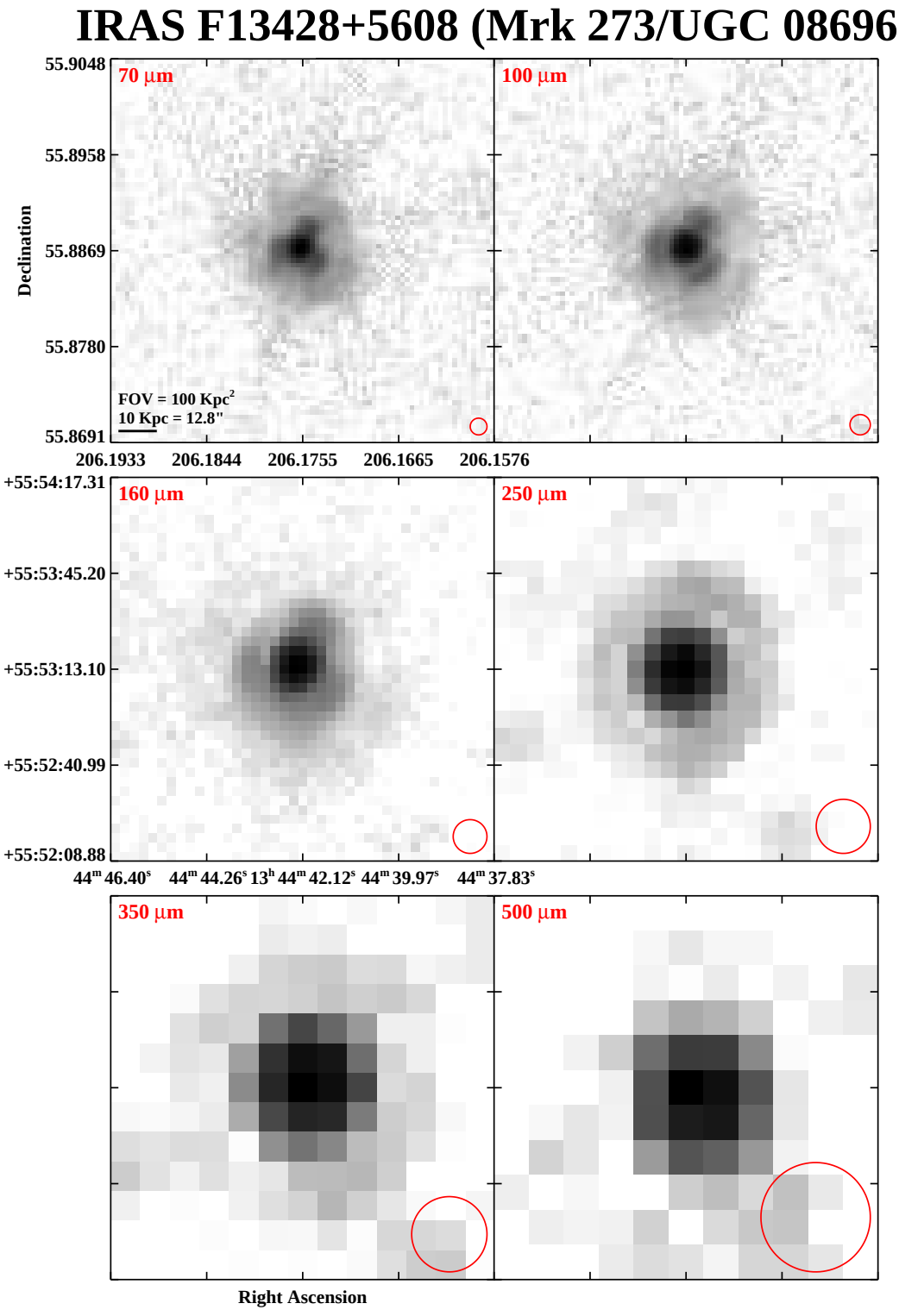

Figure 2.3 continued (page 126 of 209).

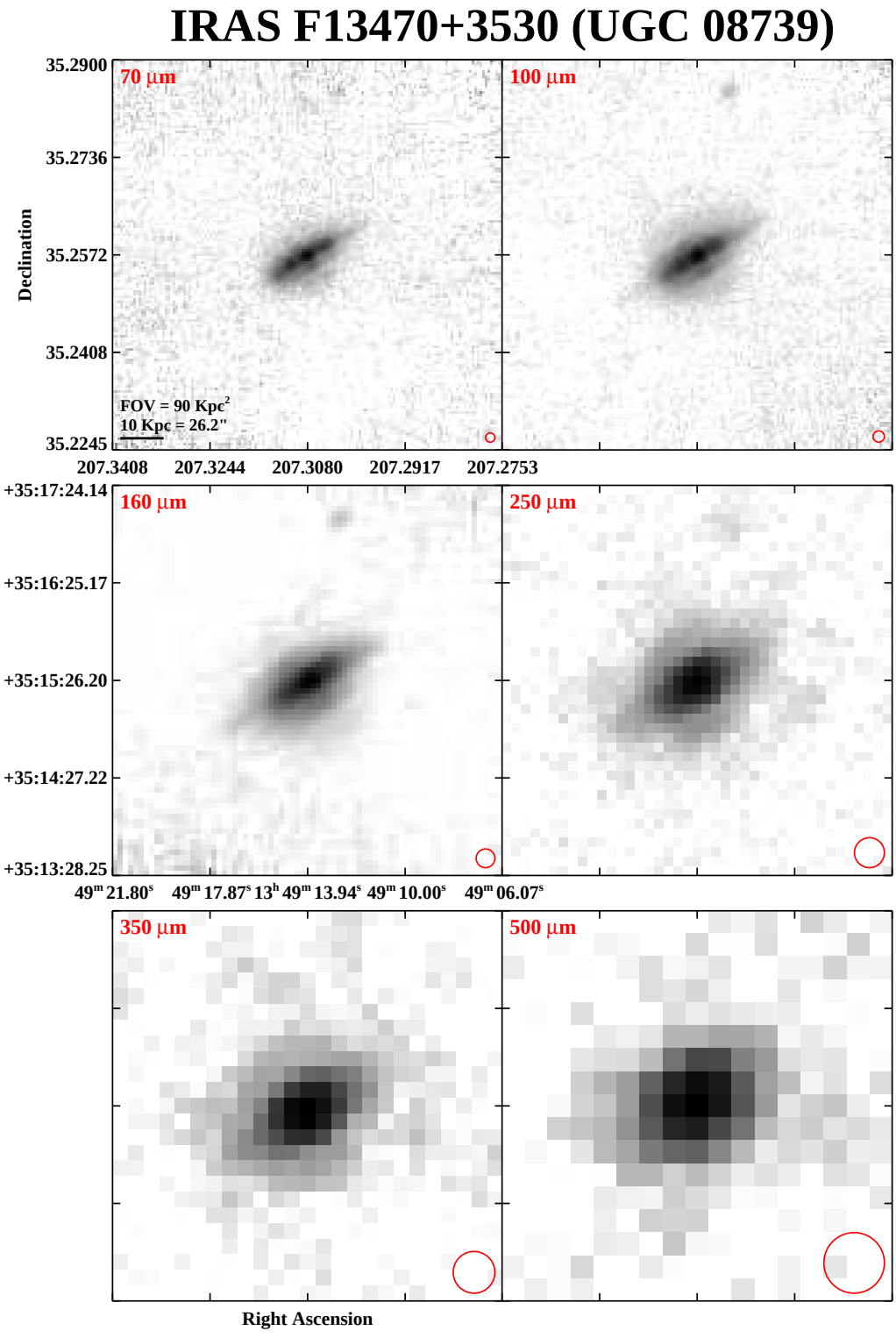

Figure 2.3 continued (page 127 of 209).

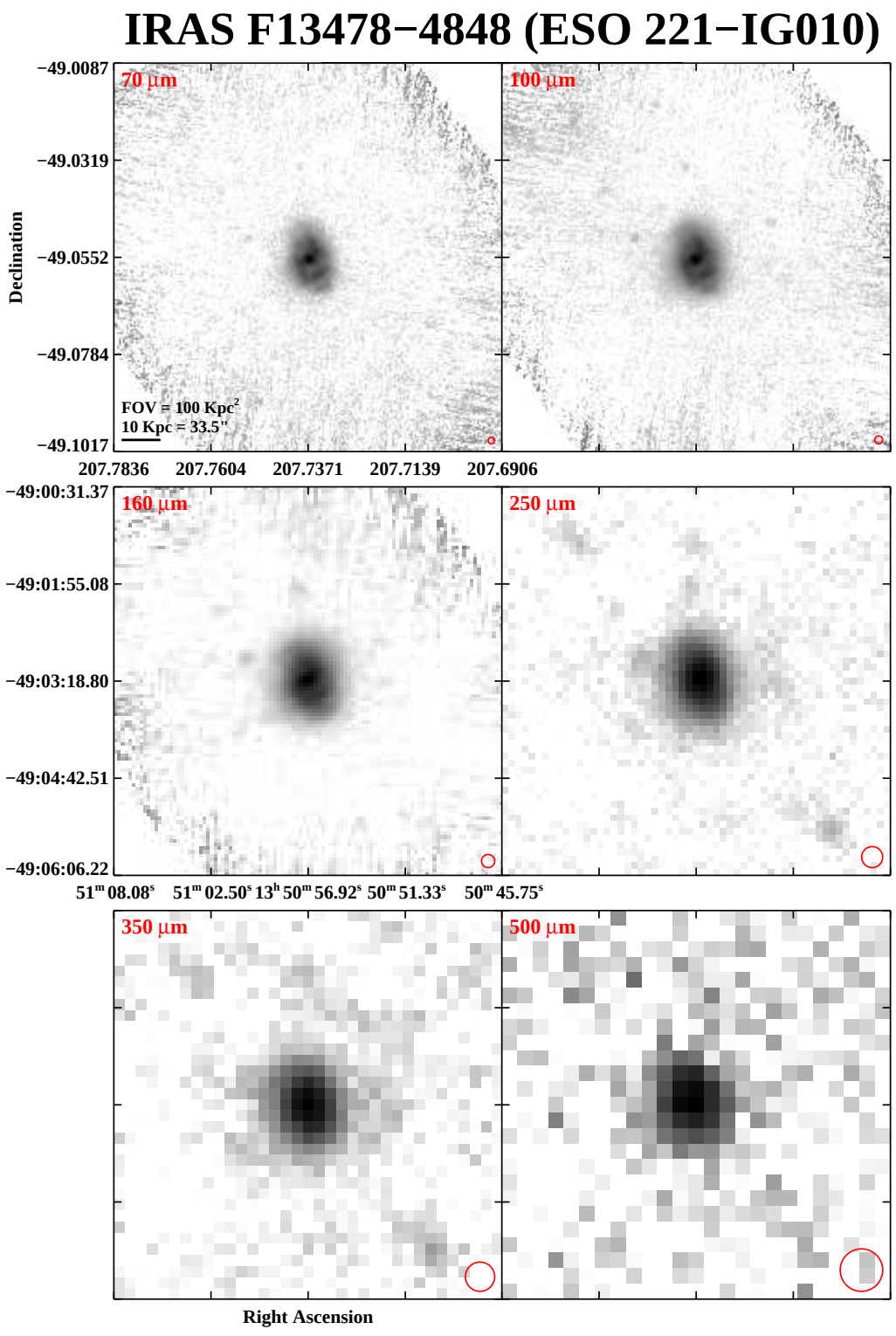

Figure 2.3 continued (page 128 of 209).

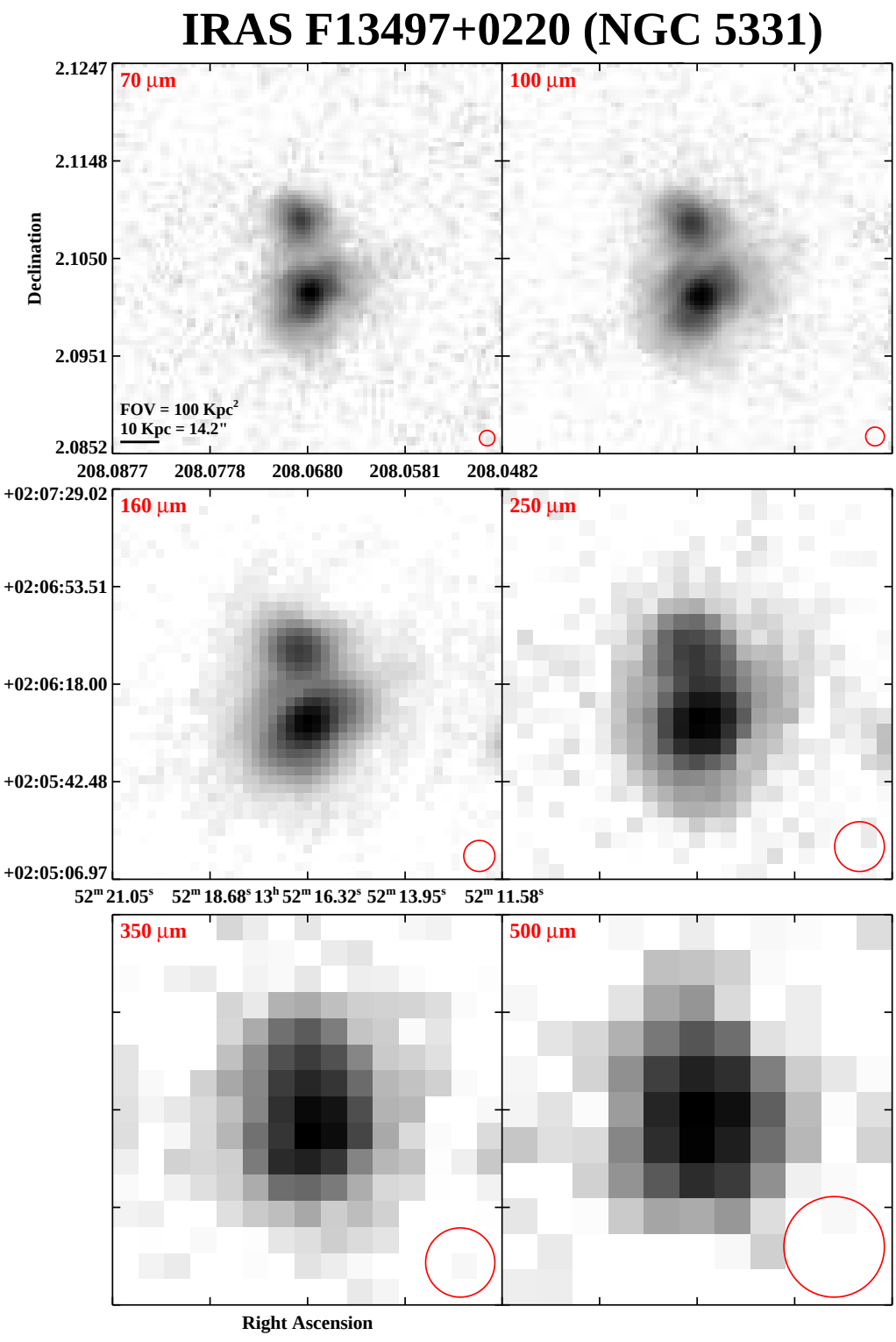

Figure 2.3 continued (page 129 of 209).

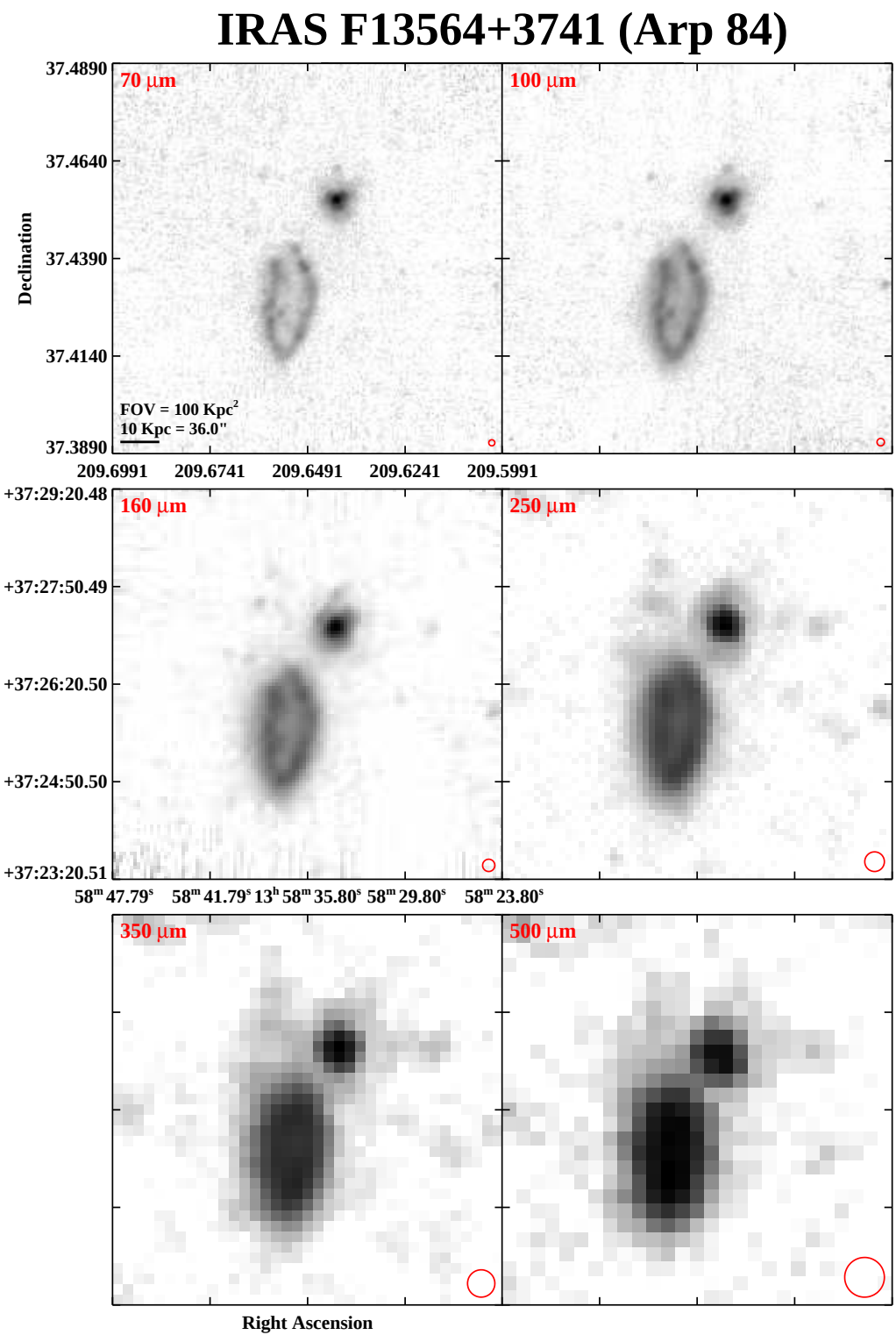

Figure 2.3 continued (page 130 of 209).

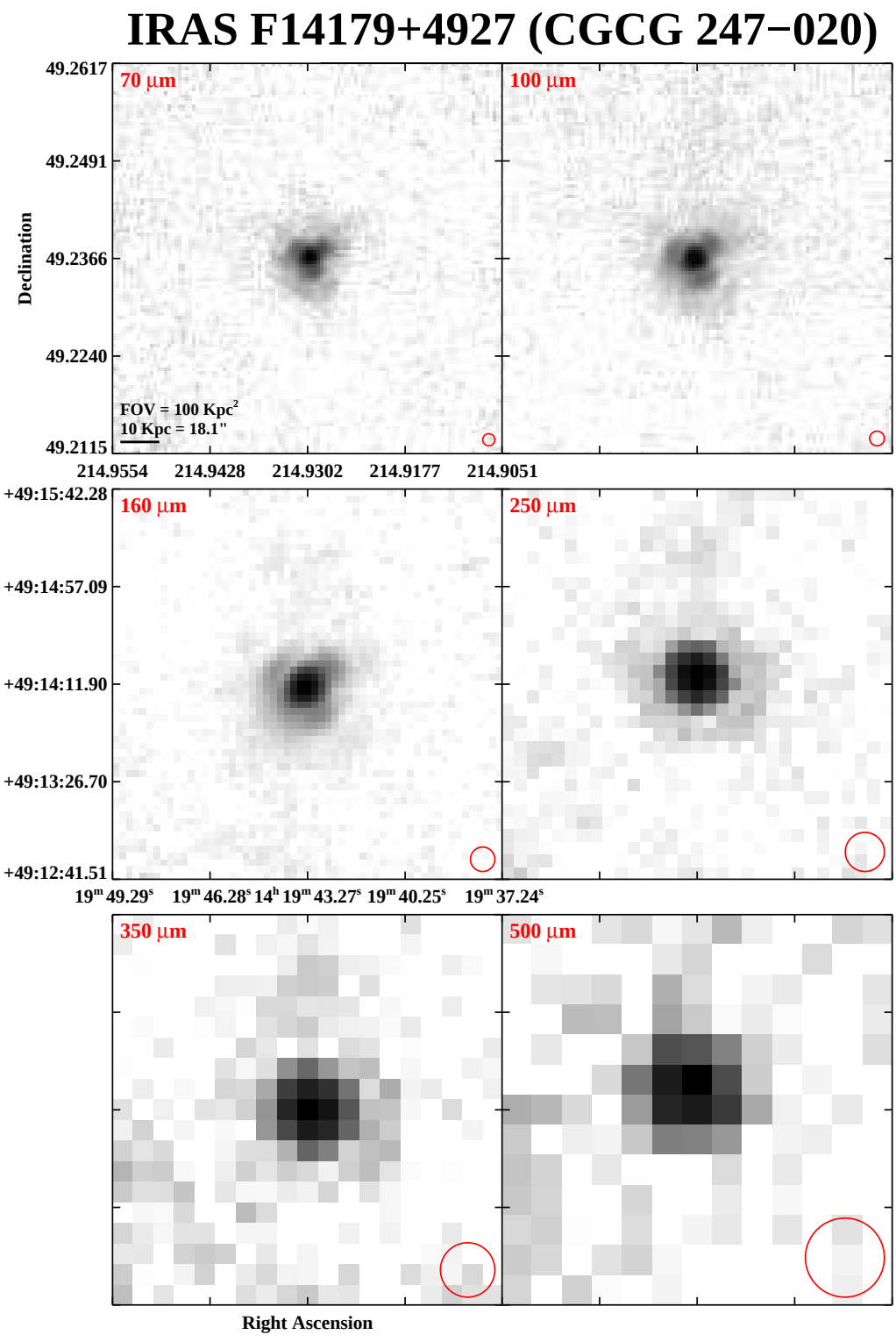

Figure 2.3 continued (page 131 of 209).

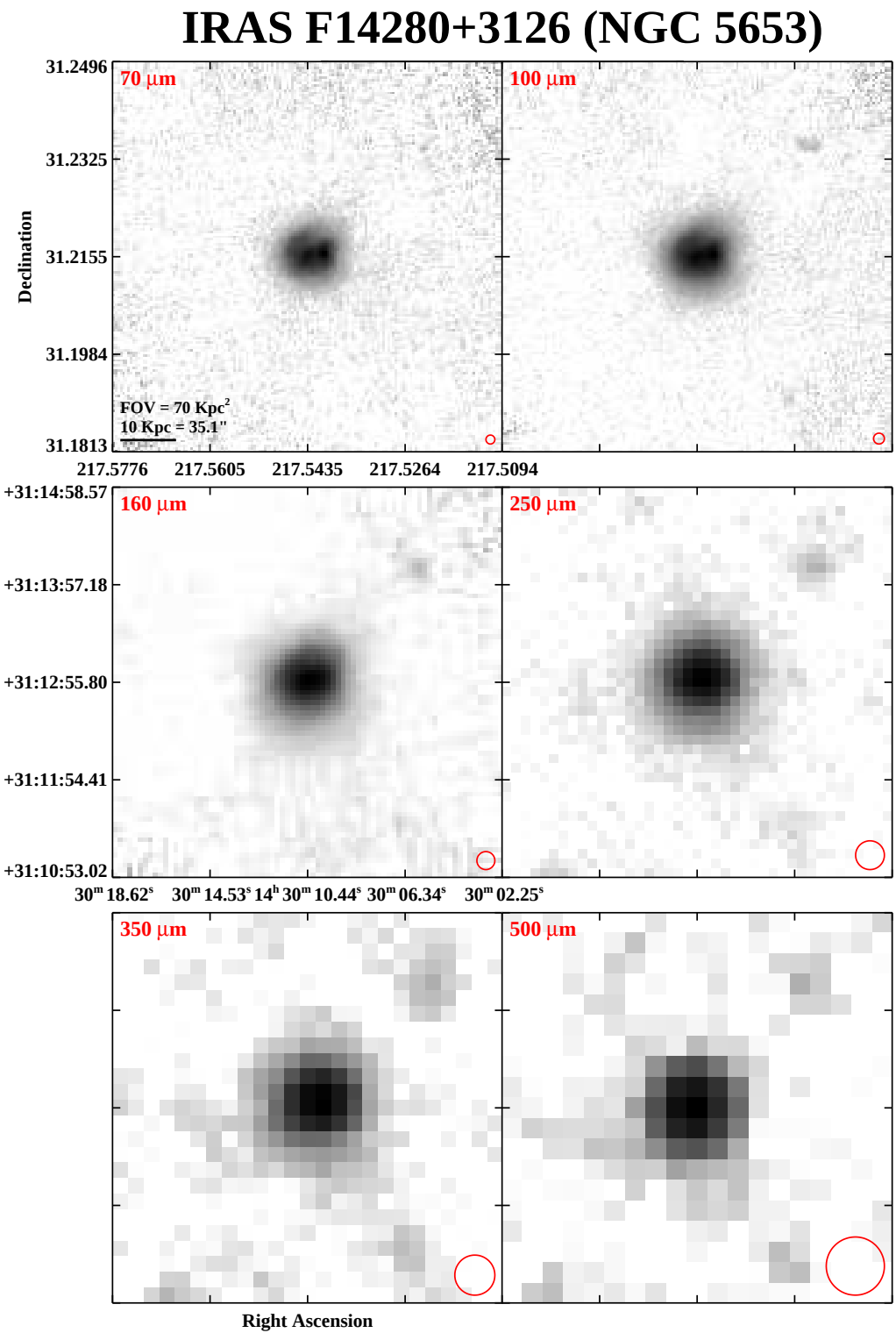

Figure 2.3 continued (page 132 of 209).

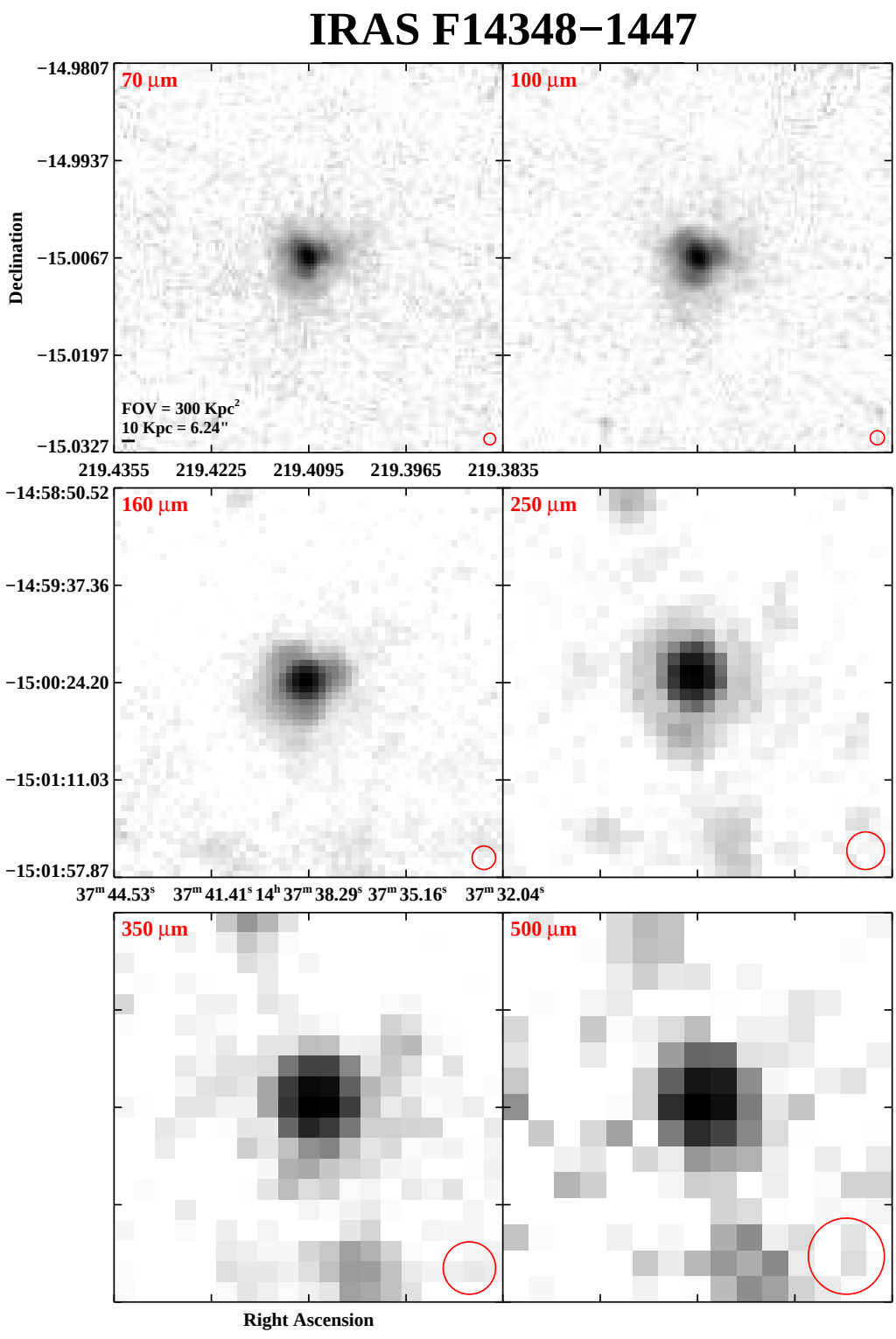

Figure 2.3 continued (page 133 of 209).

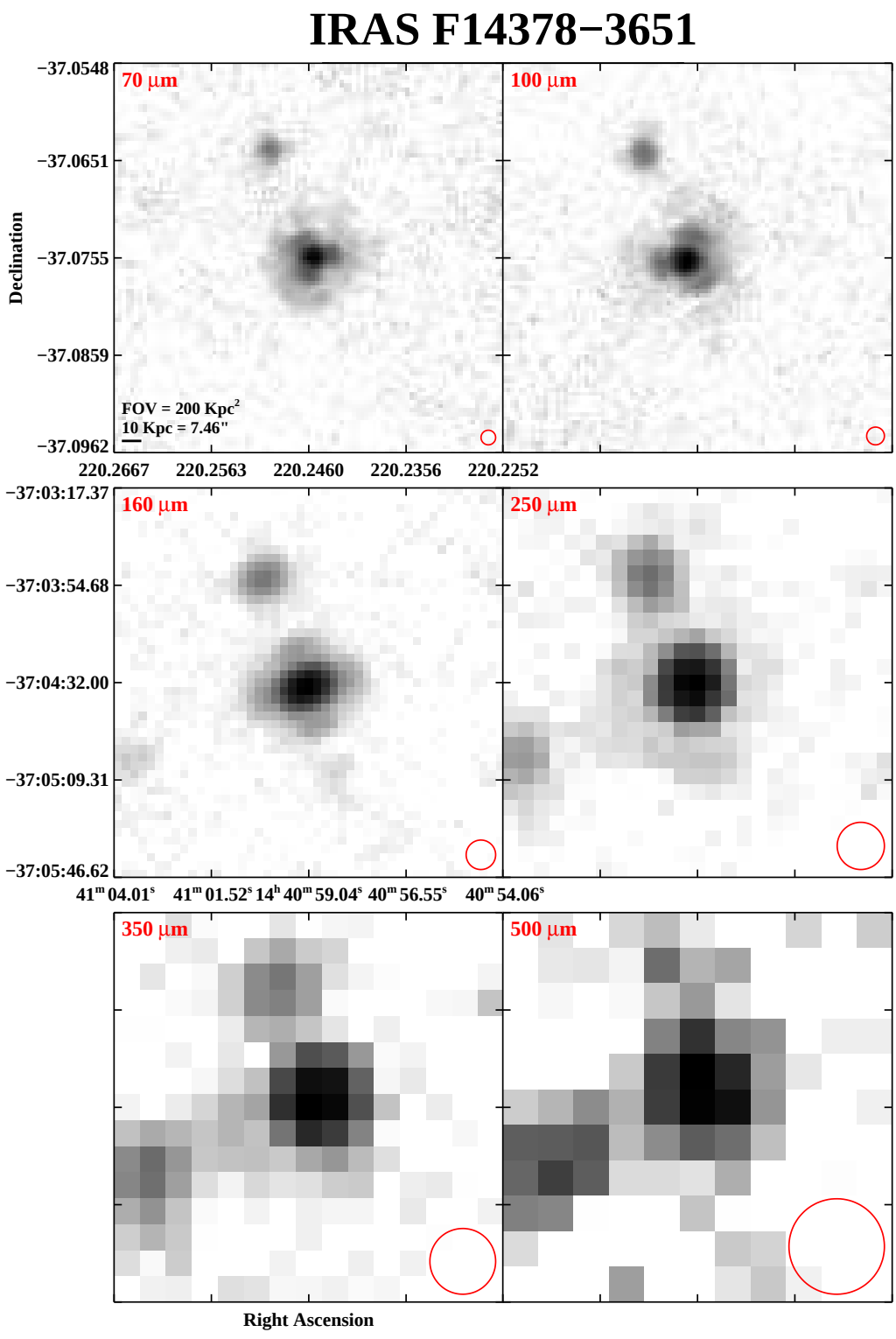

Figure 2.3 continued (page 134 of 209).

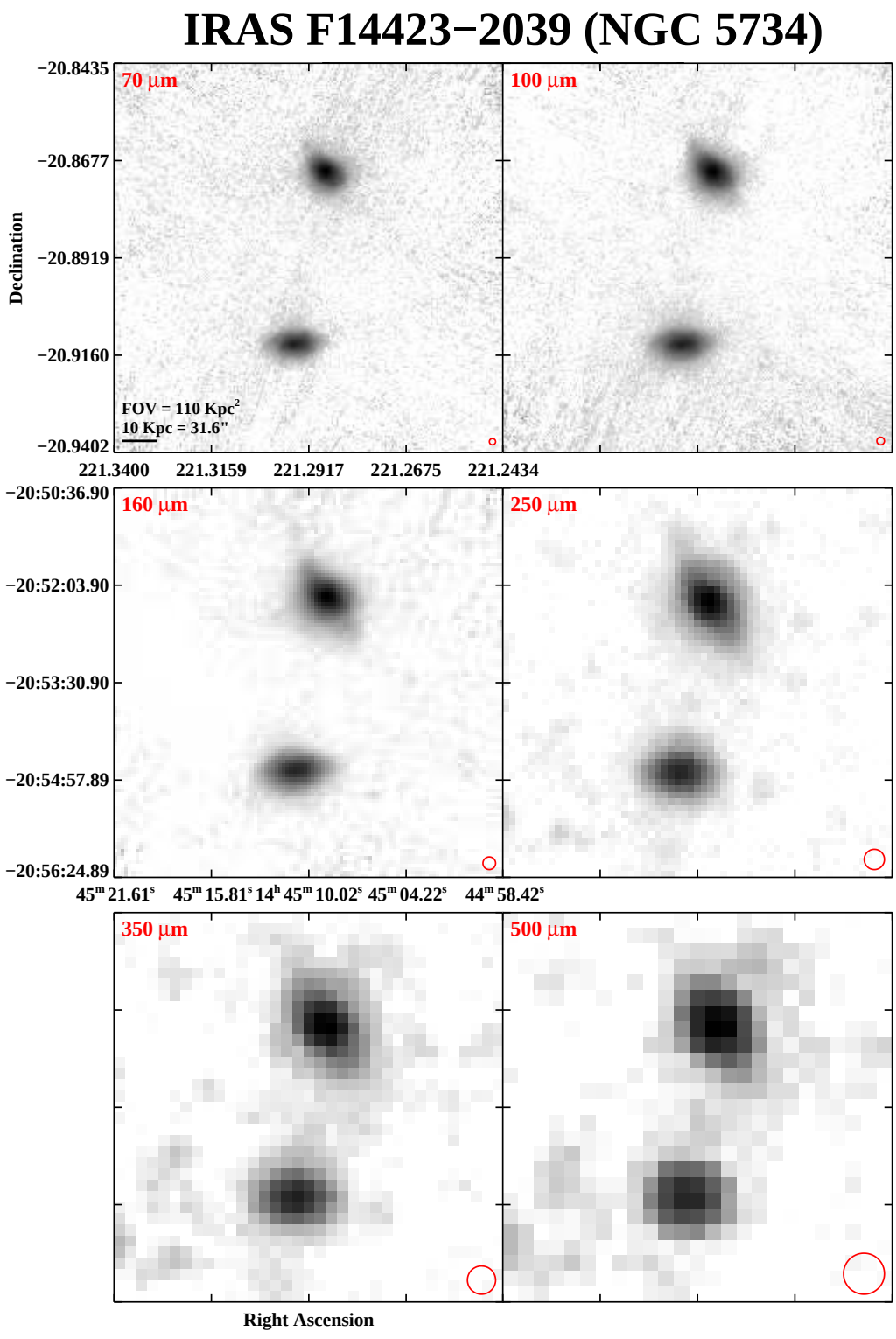

Figure 2.3 continued (page 135 of 209).

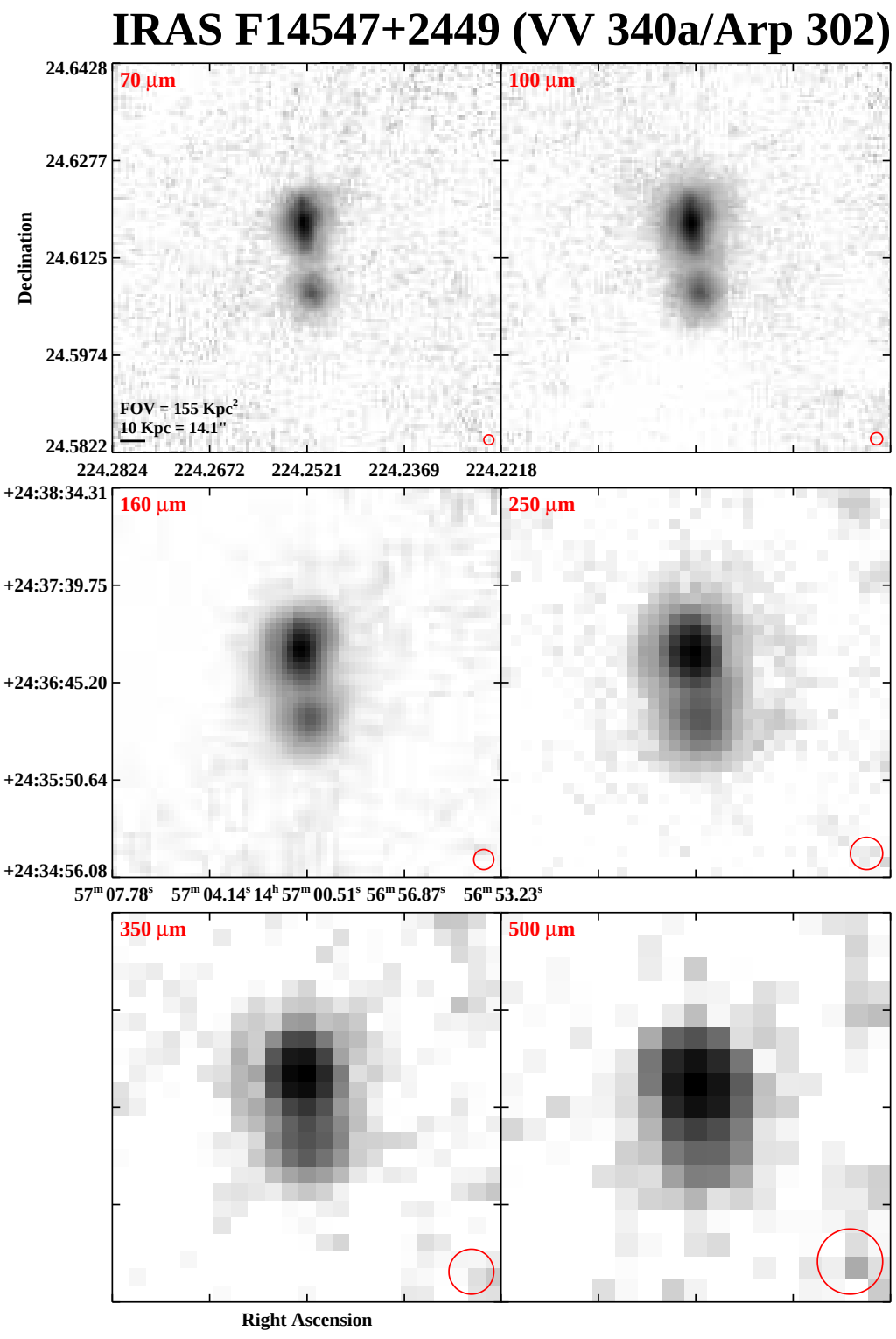

Figure 2.3 continued (page 136 of 209).

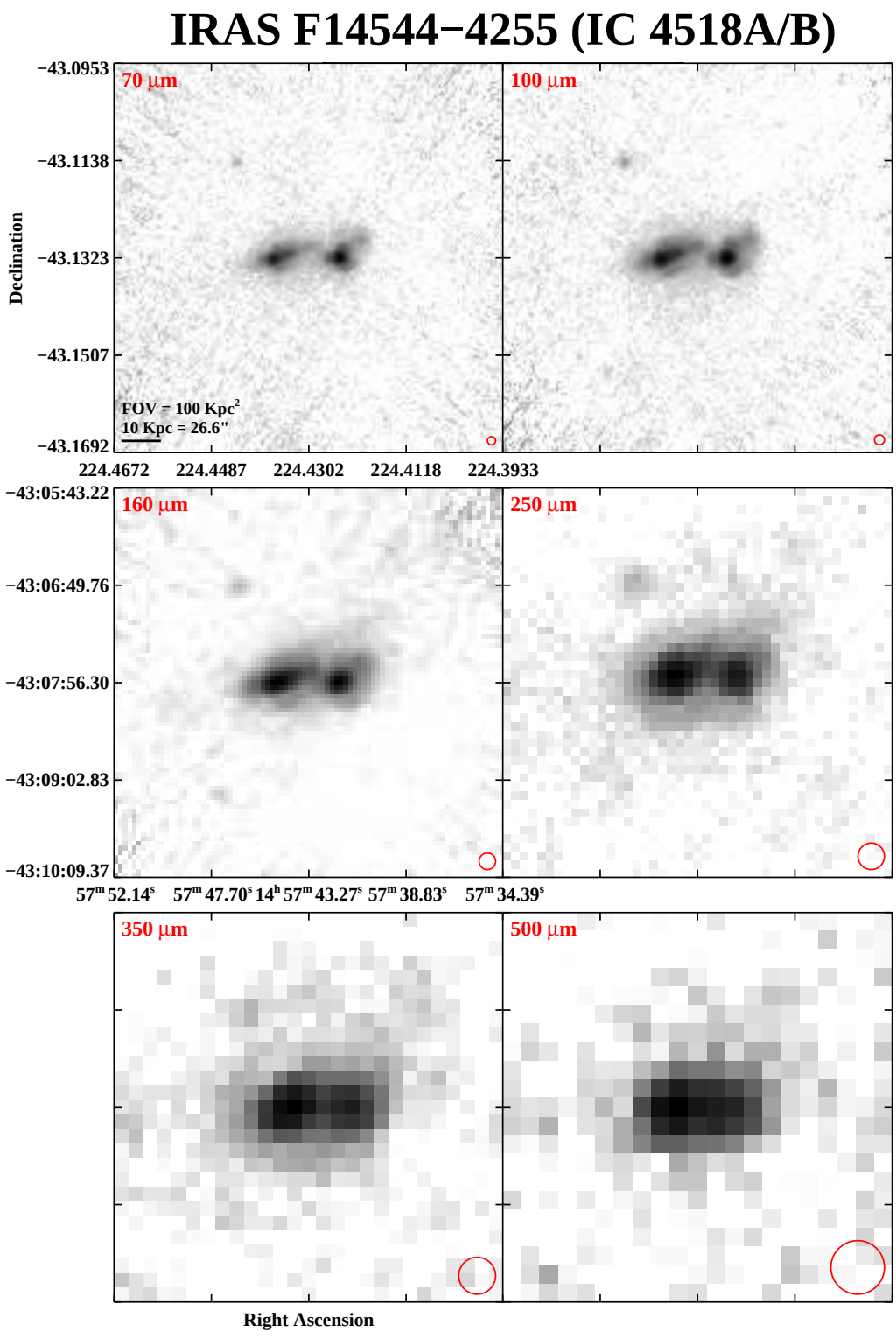

Figure 2.3 continued (page 137 of 209).

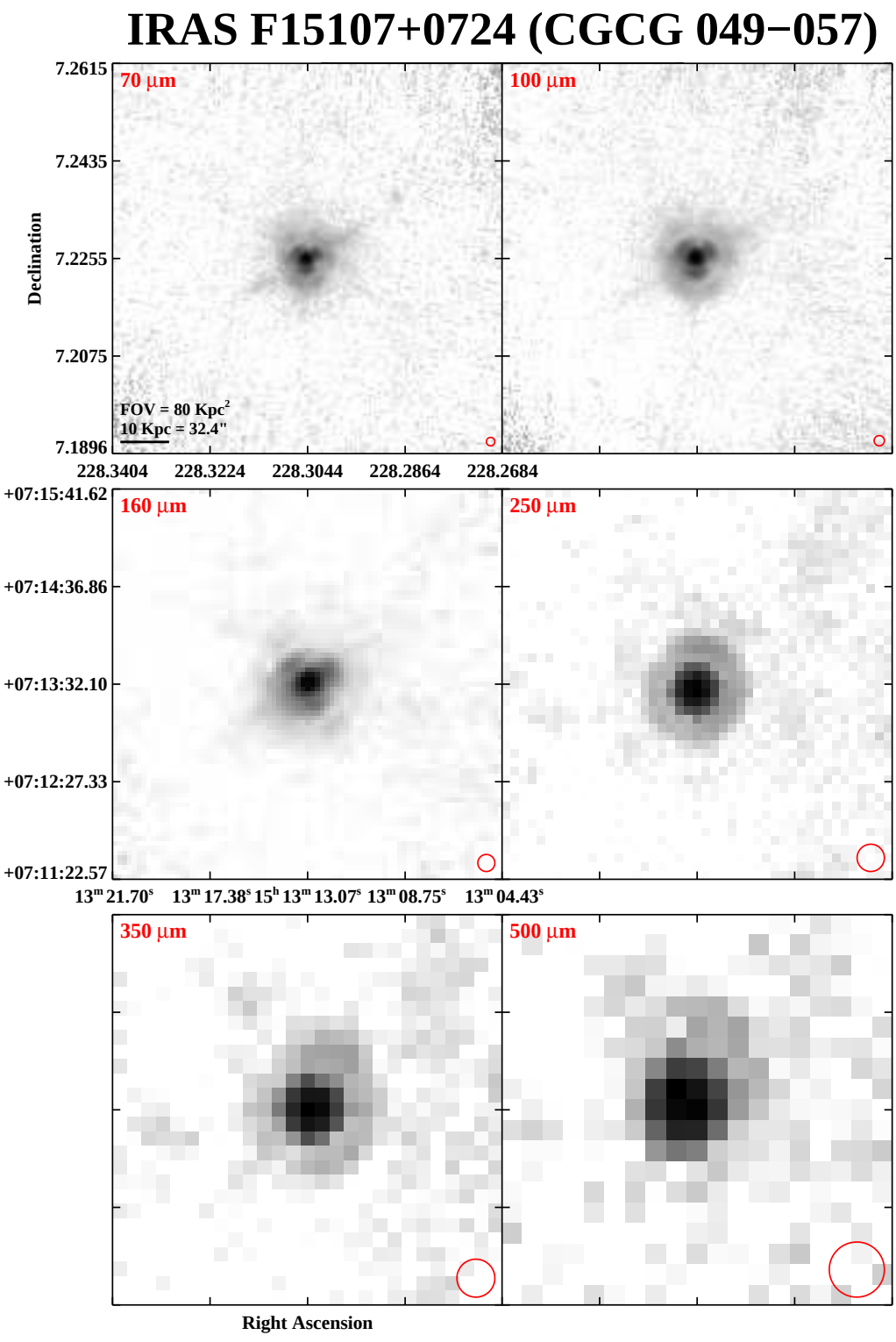

Figure 2.3 continued (page 138 of 209).

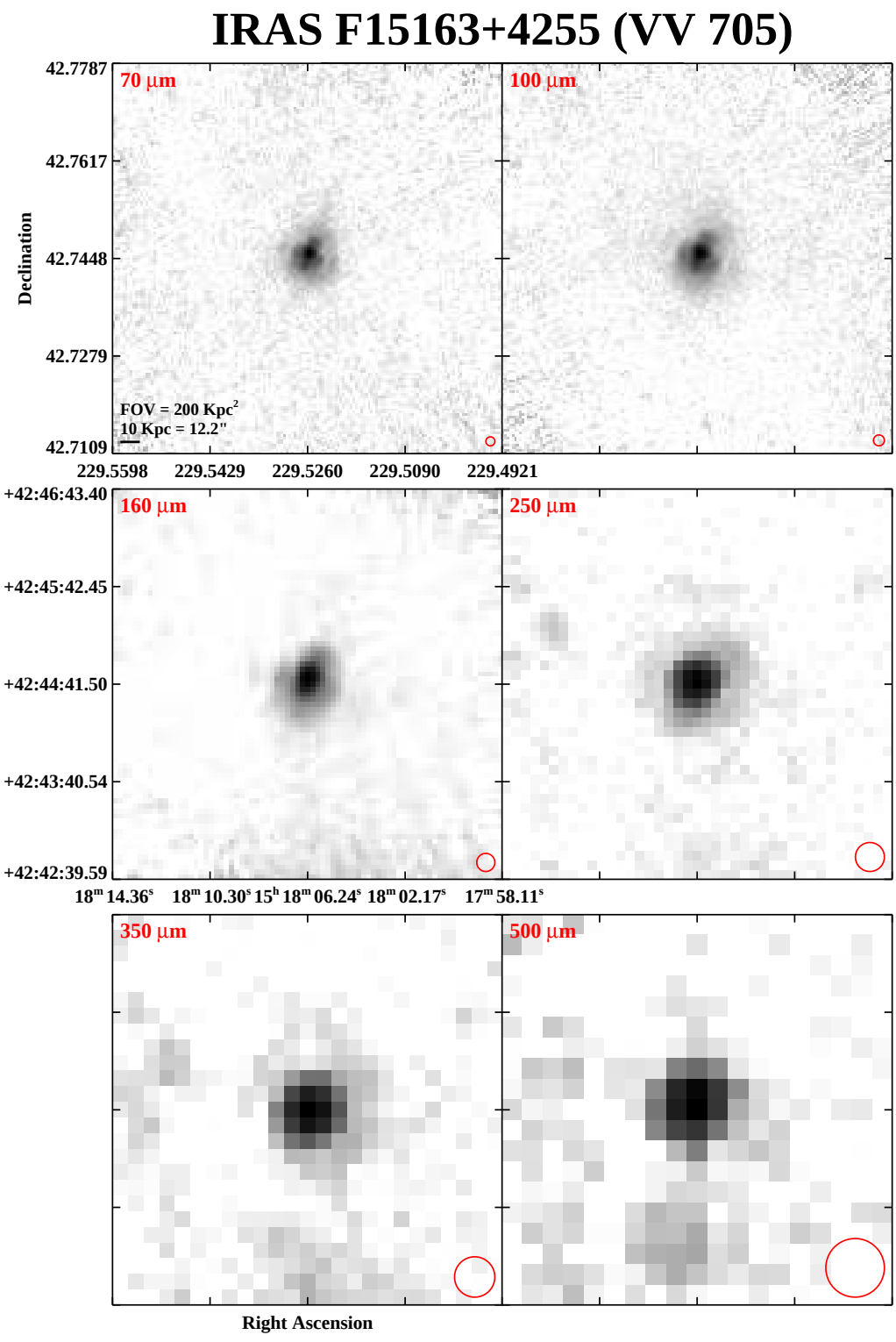

Figure 2.3 continued (page 139 of 209).

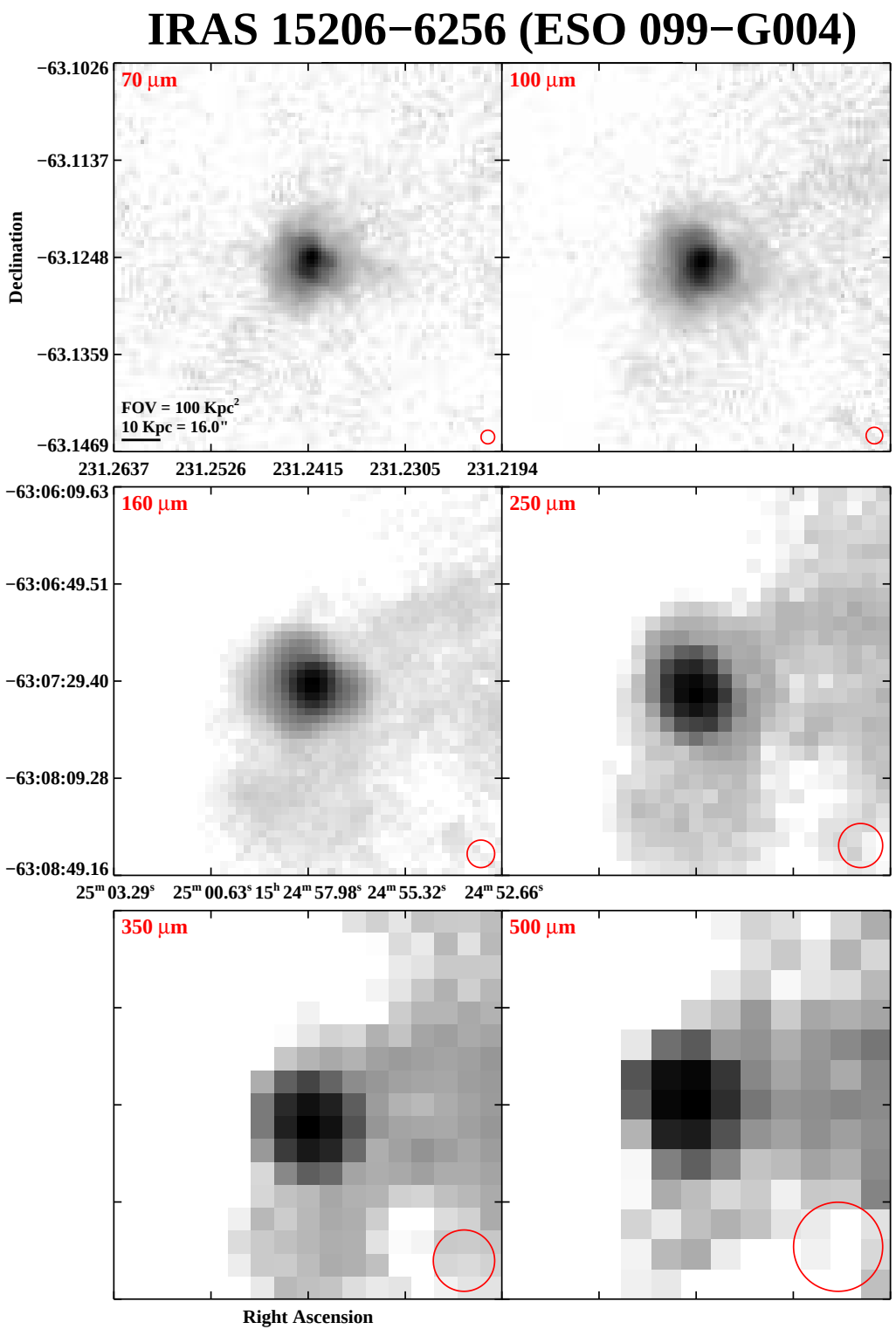

Figure 2.3 continued (page 140 of 209).

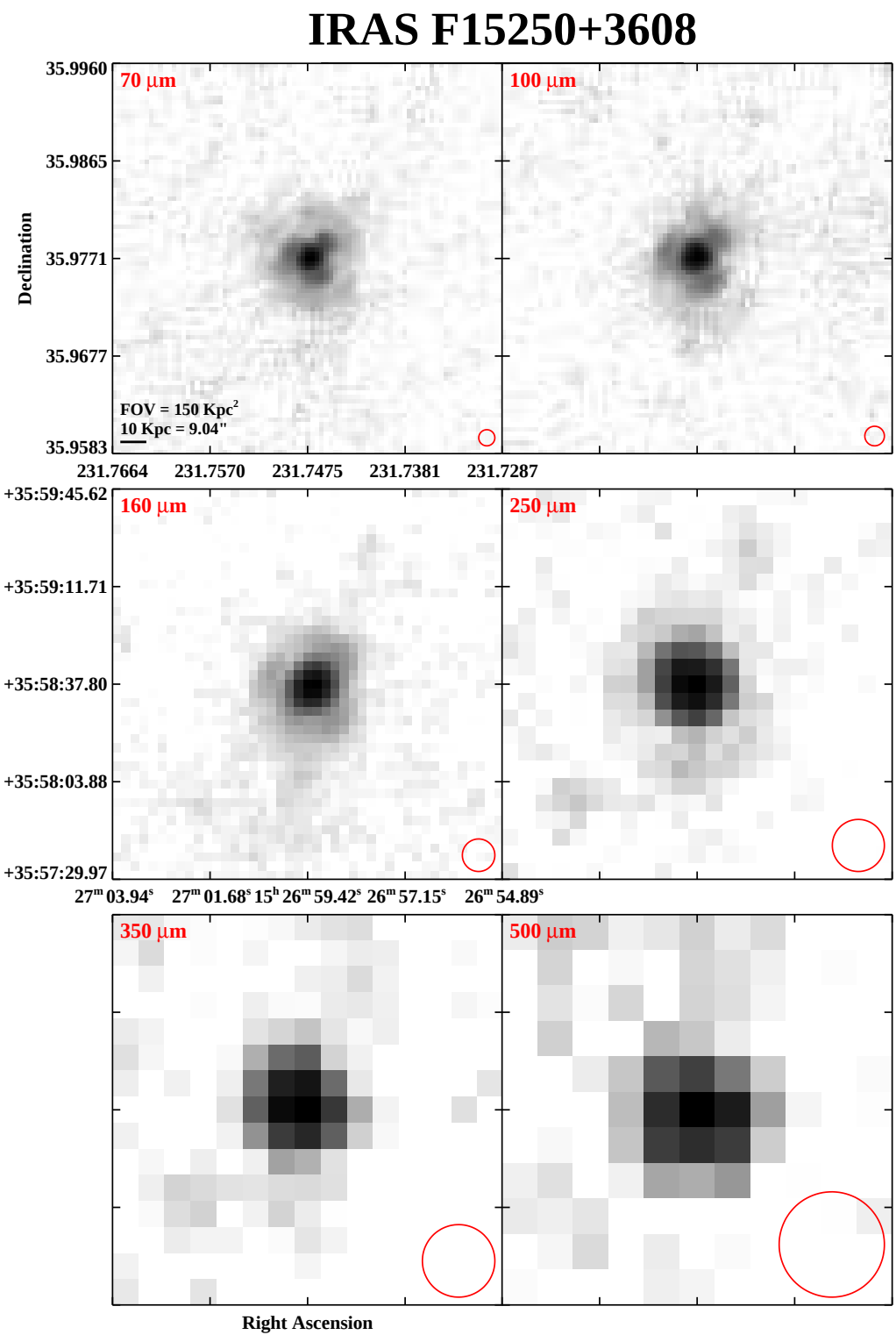

Figure 2.3 continued (page 141 of 209).

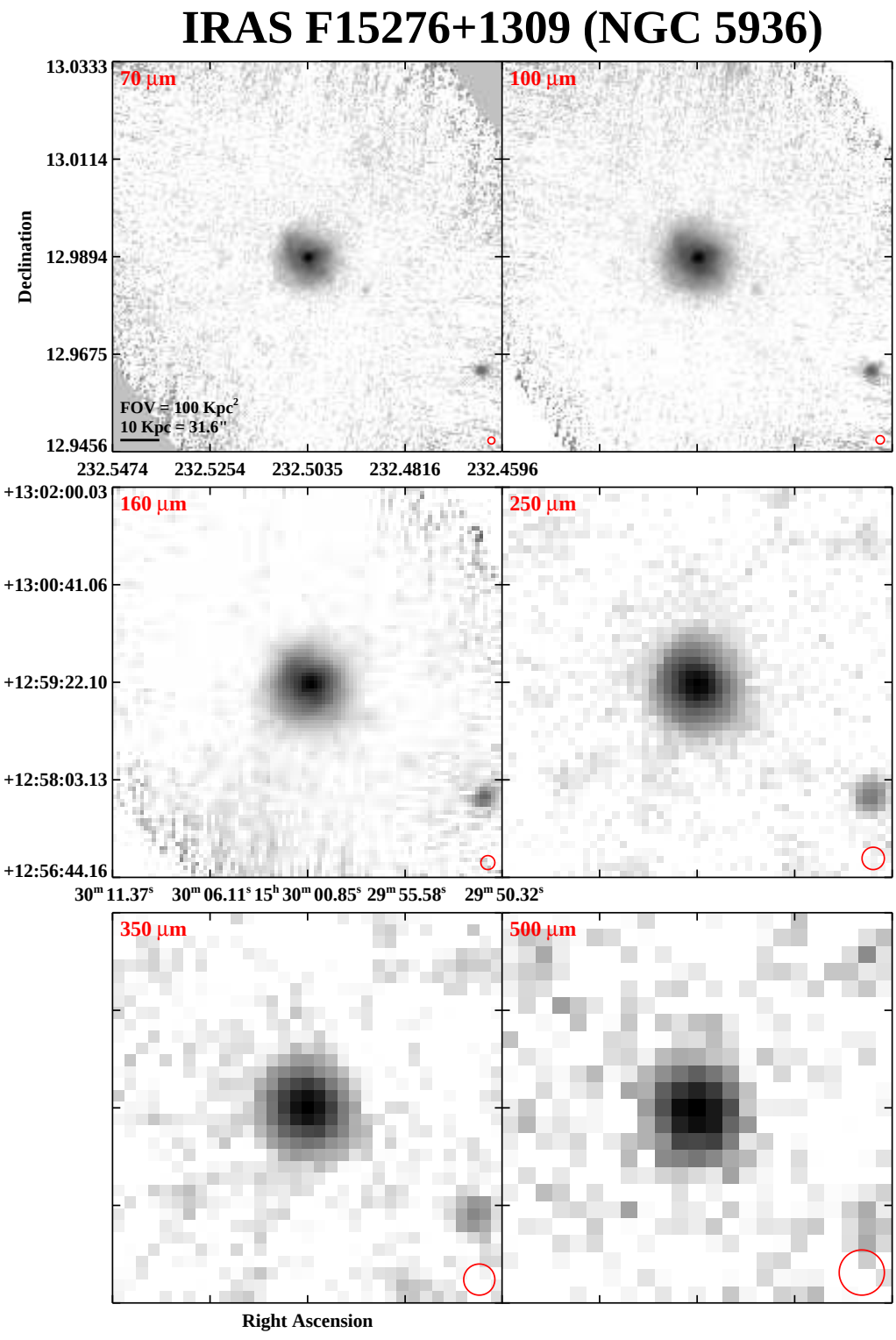

Figure 2.3 continued (page 142 of 209).

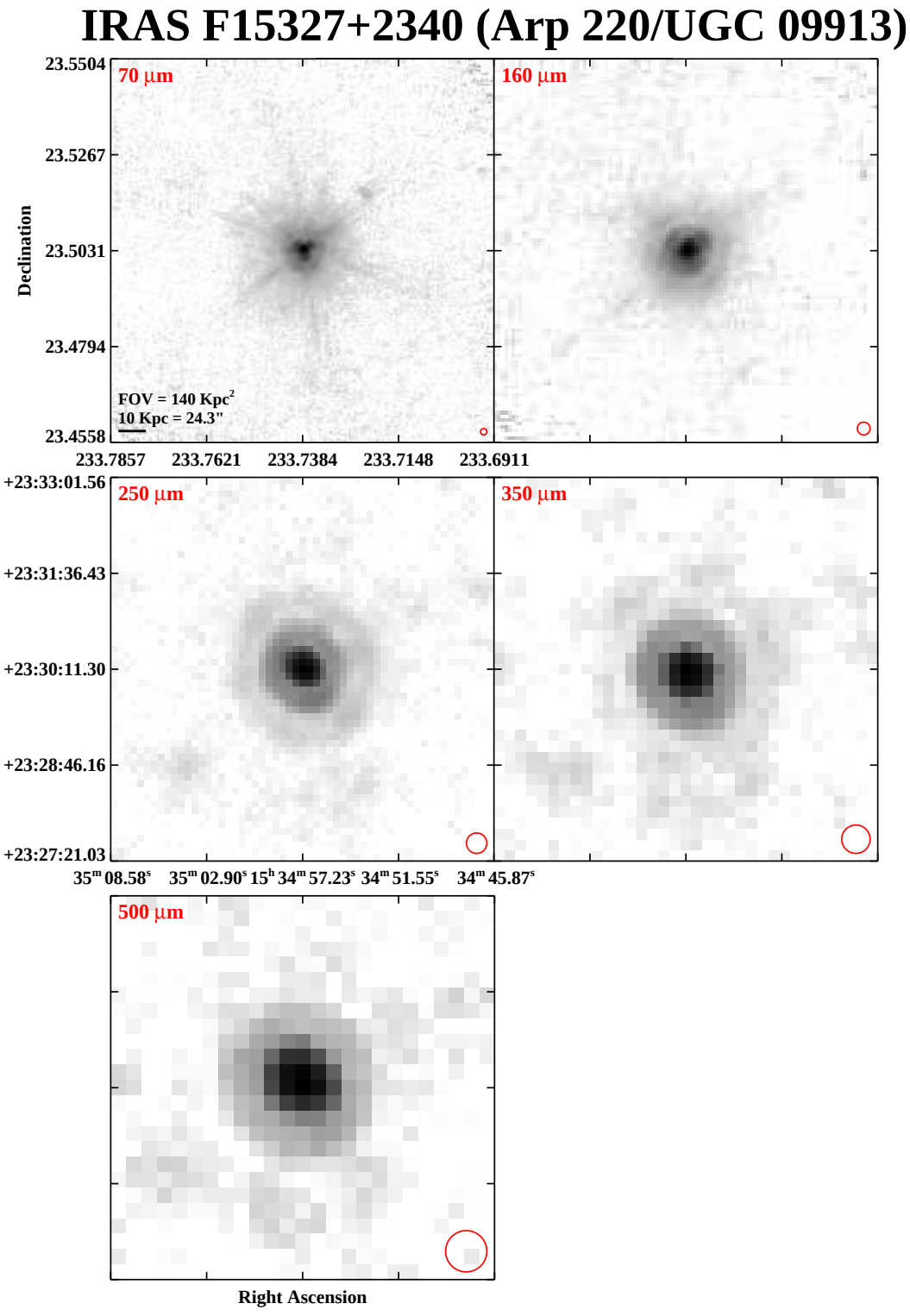

Figure 2.3 continued (page 143 of 209).

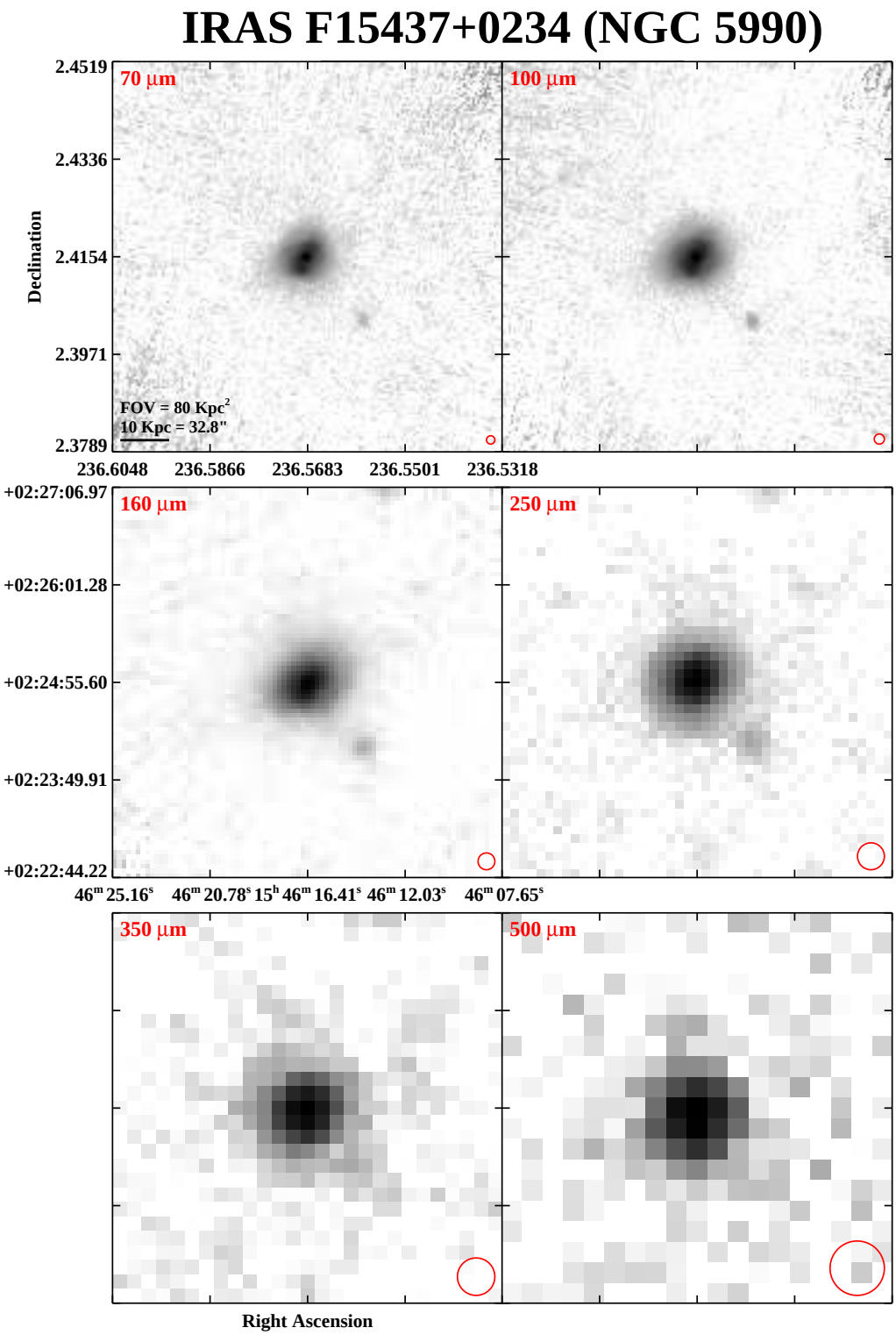

Figure 2.3 continued (page 144 of 209).

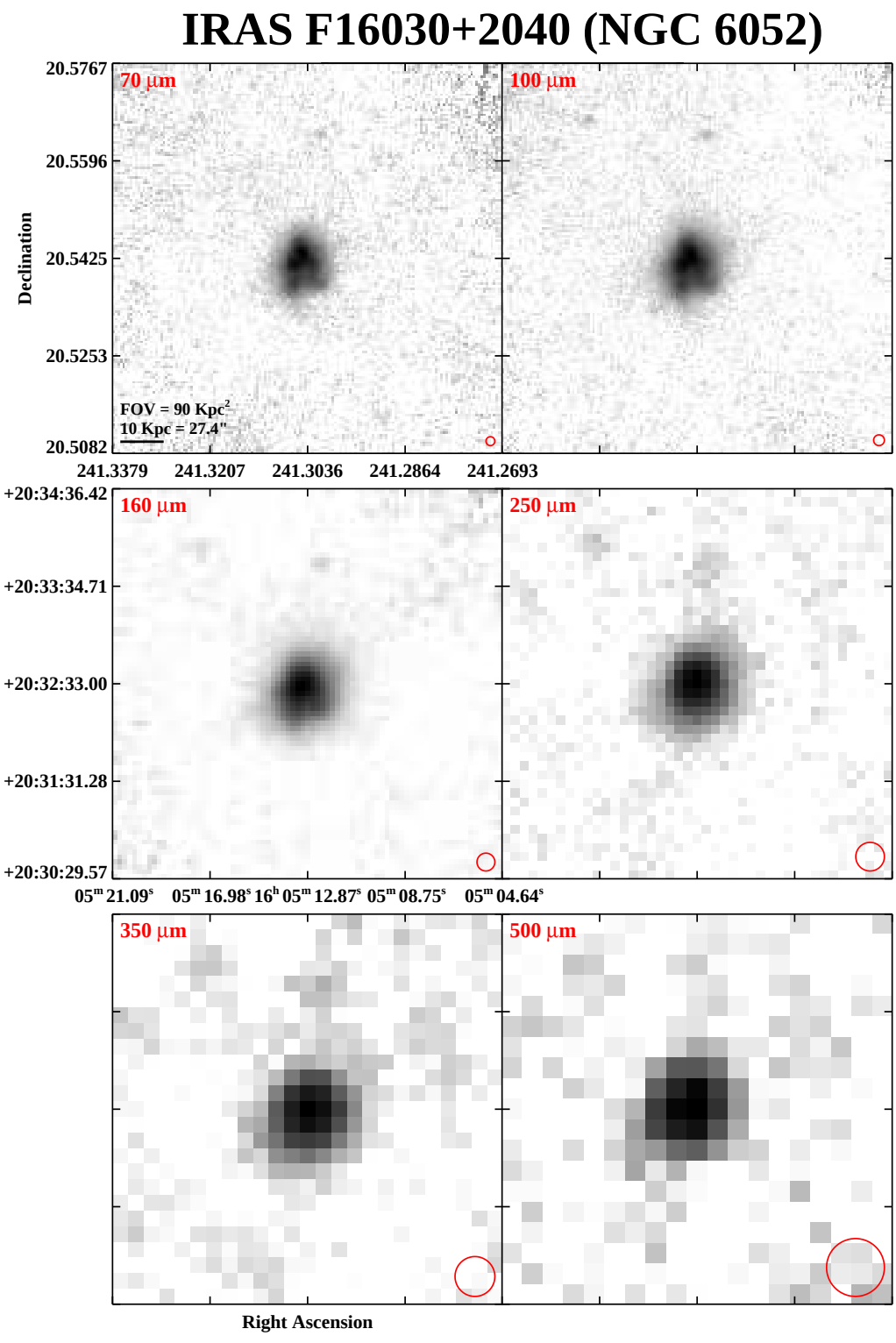

Figure 2.3 continued (page 145 of 209).

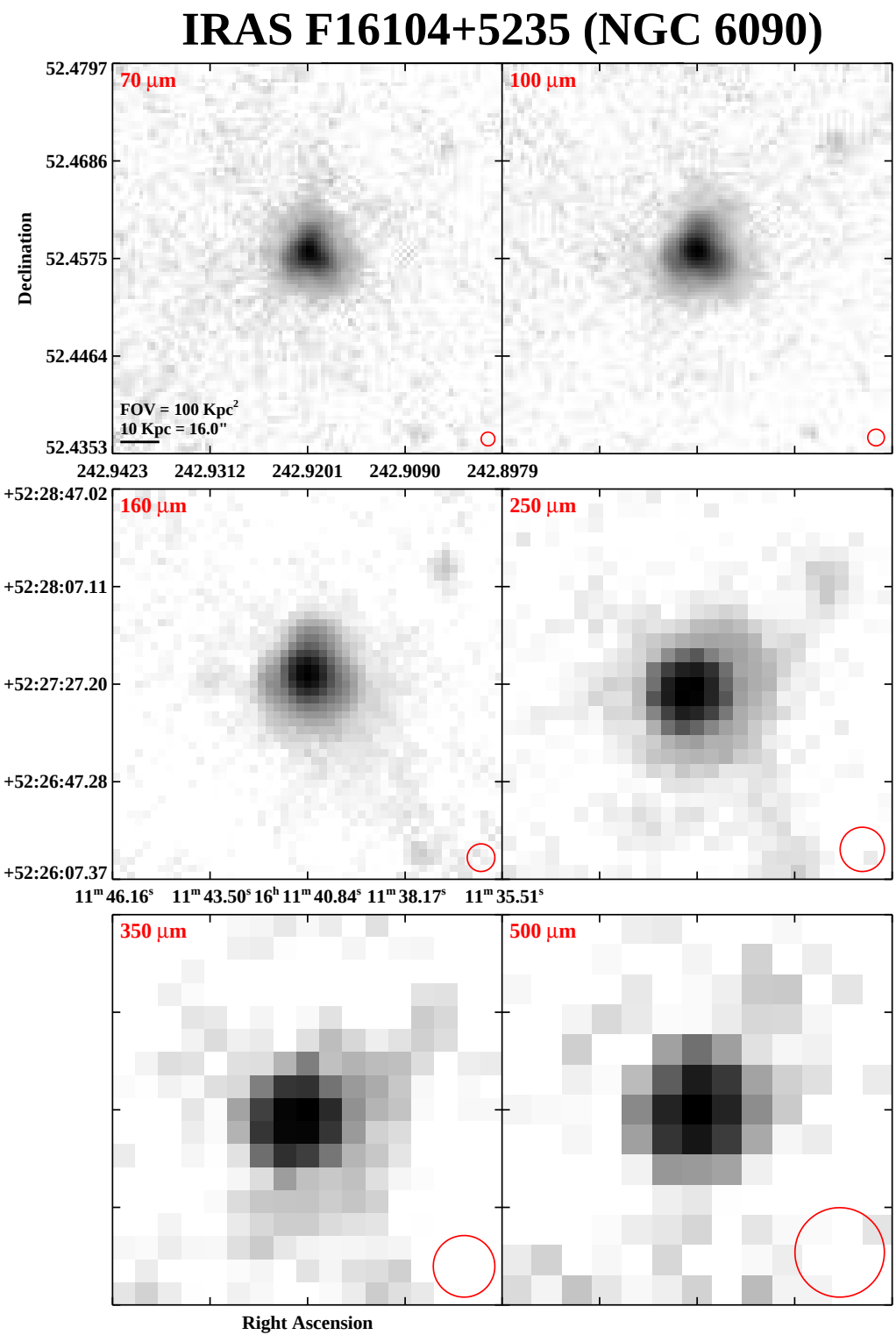

Figure 2.3 continued (page 146 of 209).

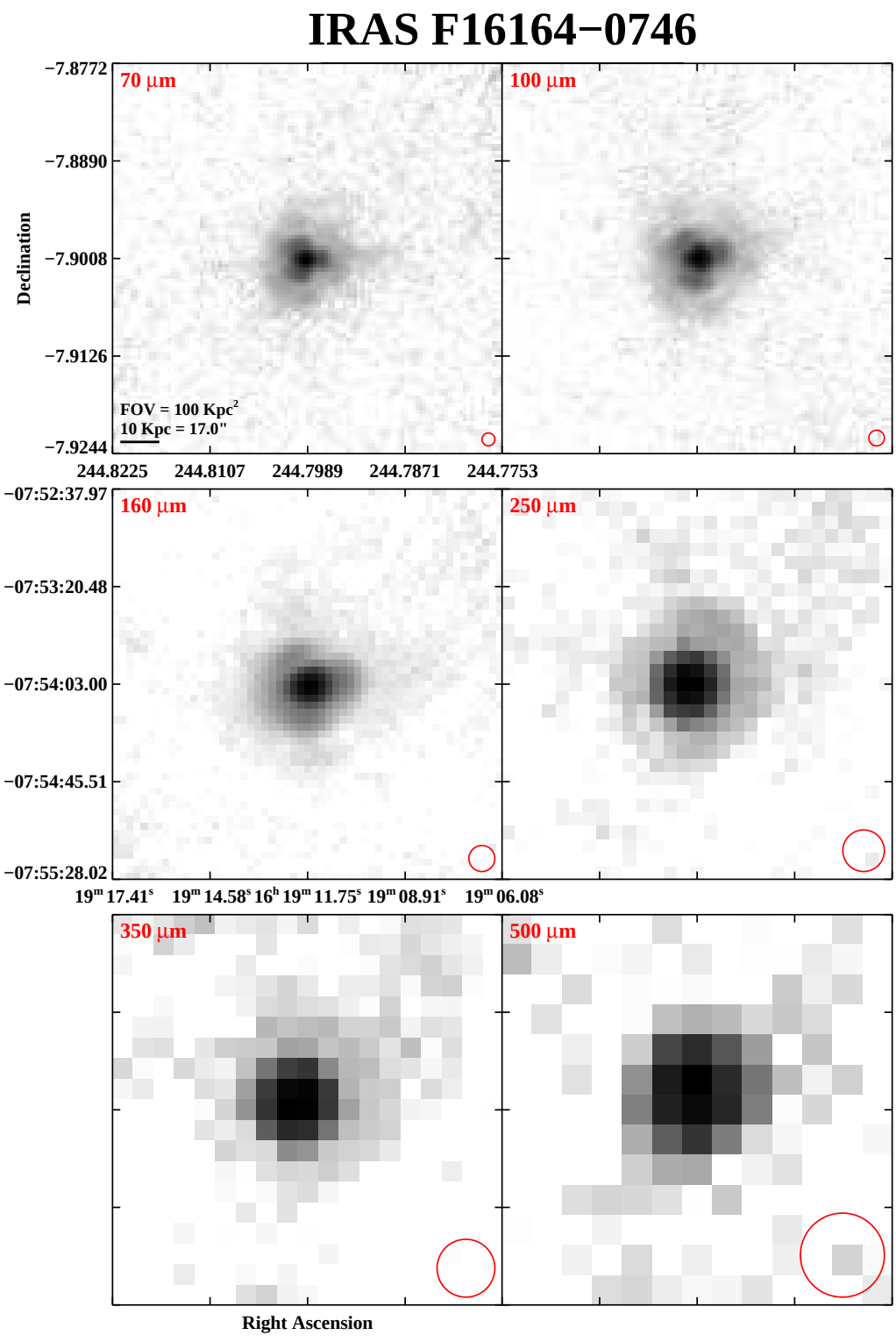

Figure 2.3 continued (page 147 of 209).

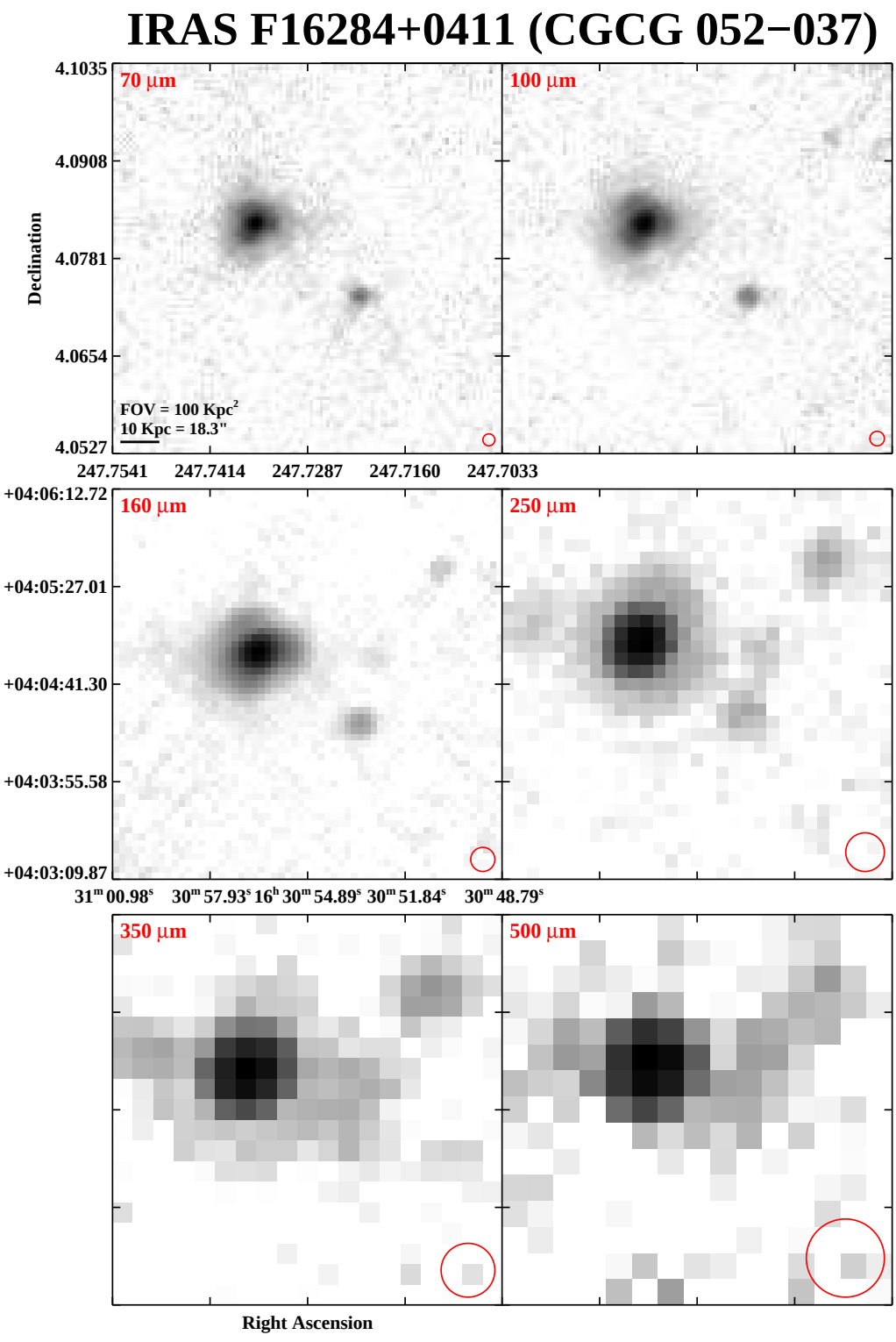

Figure 2.3 continued (page 148 of 209).

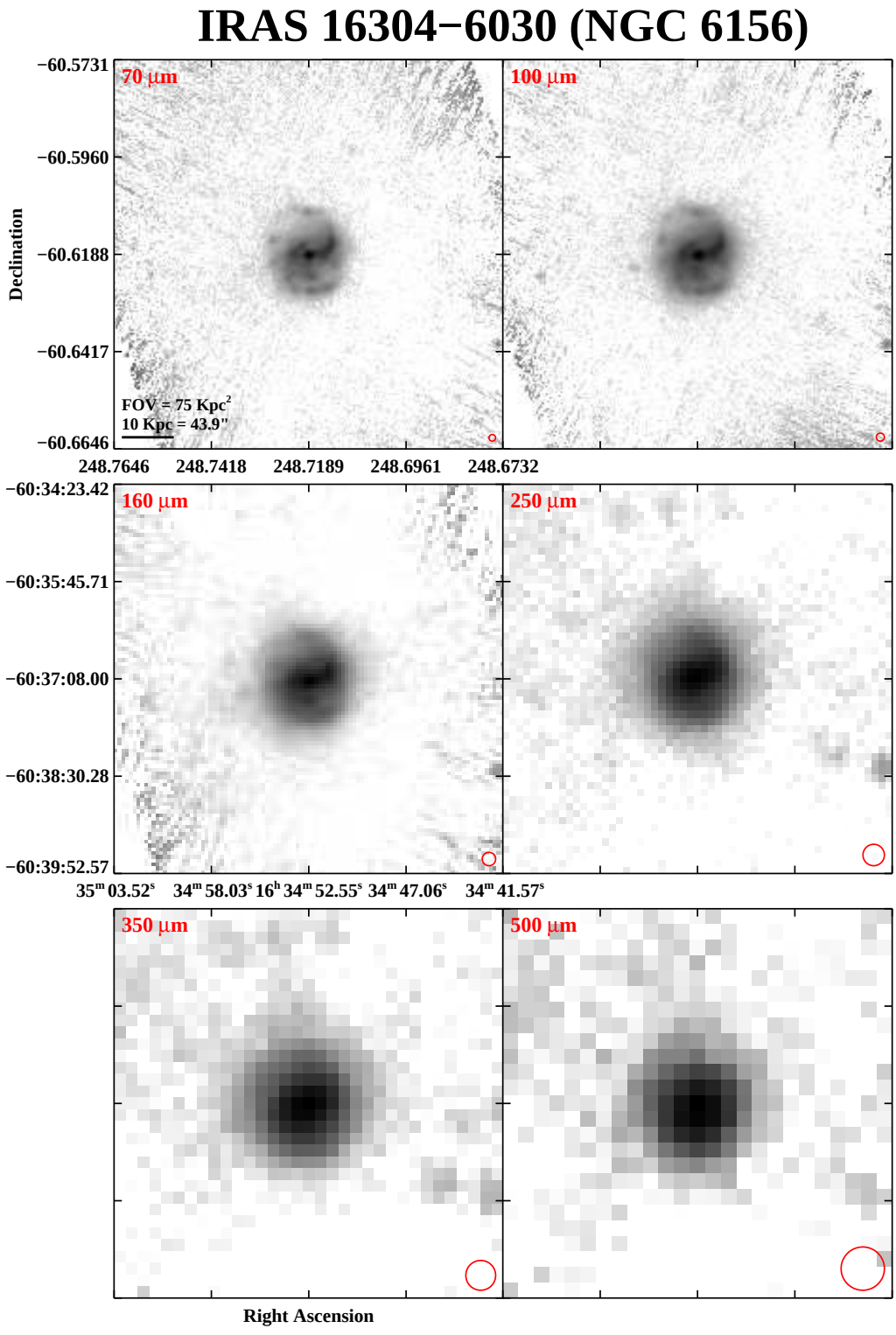

Figure 2.3 continued (page 149 of 209).

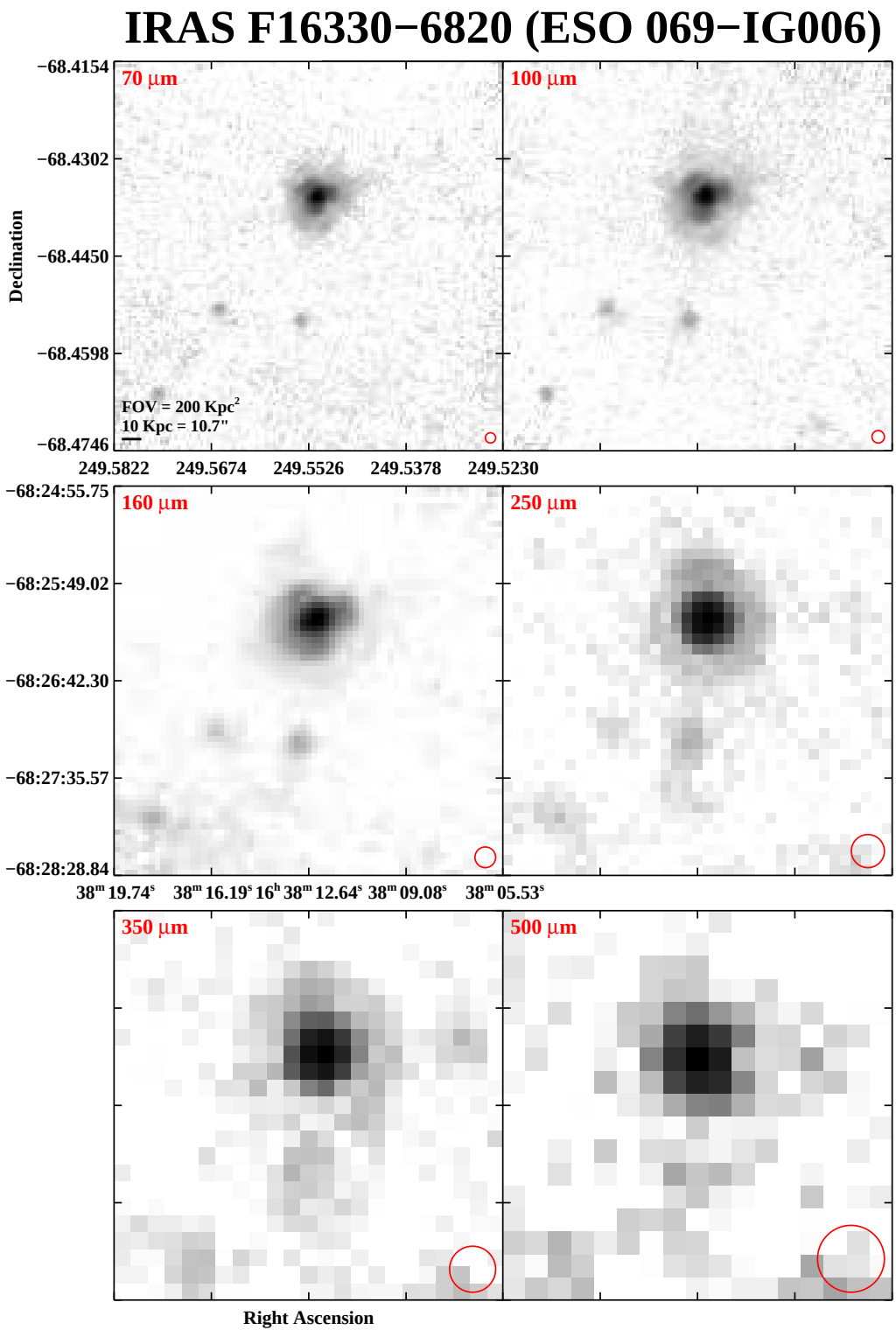

Figure 2.3 continued (page 150 of 209).

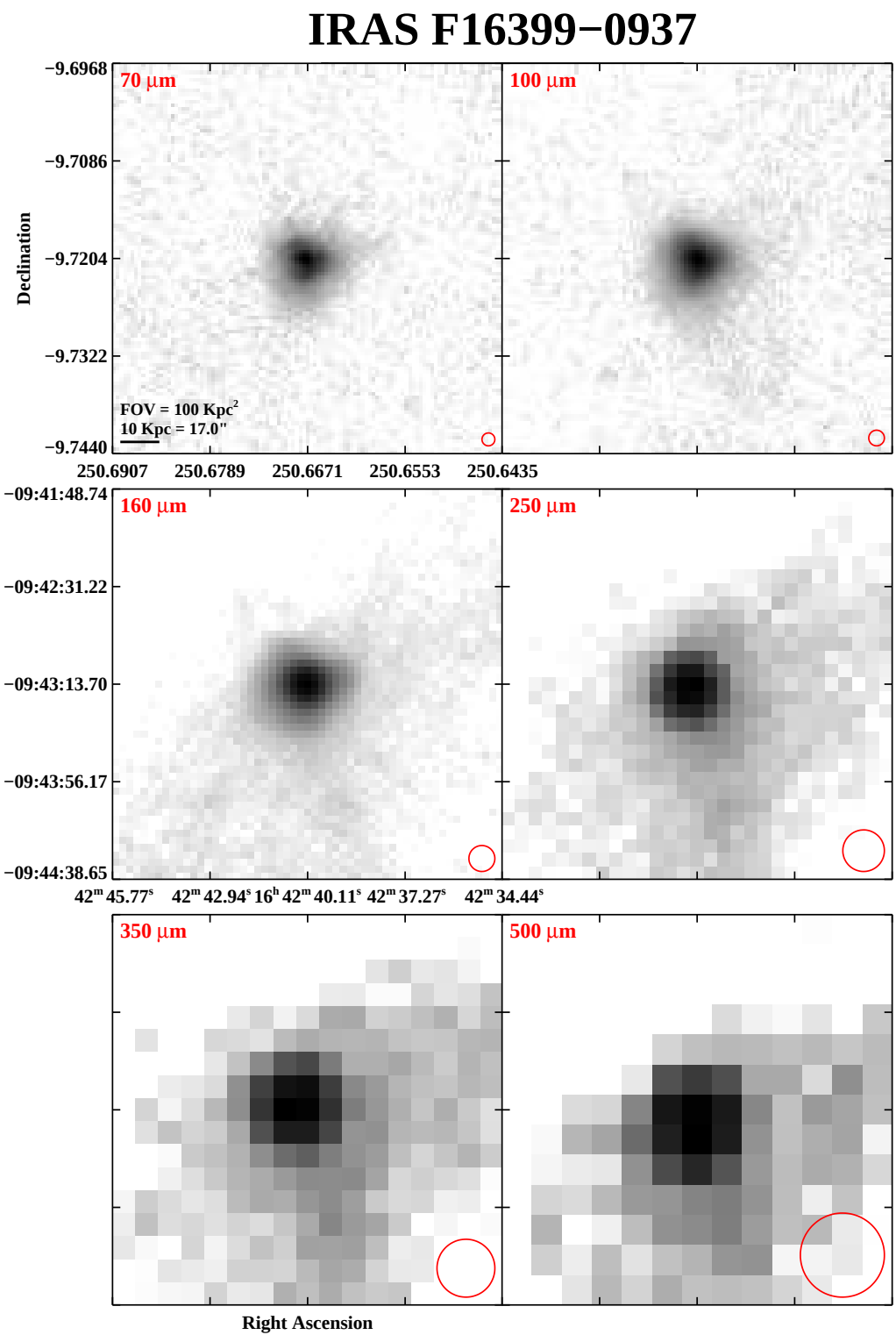

Figure 2.3 continued (page 151 of 209).

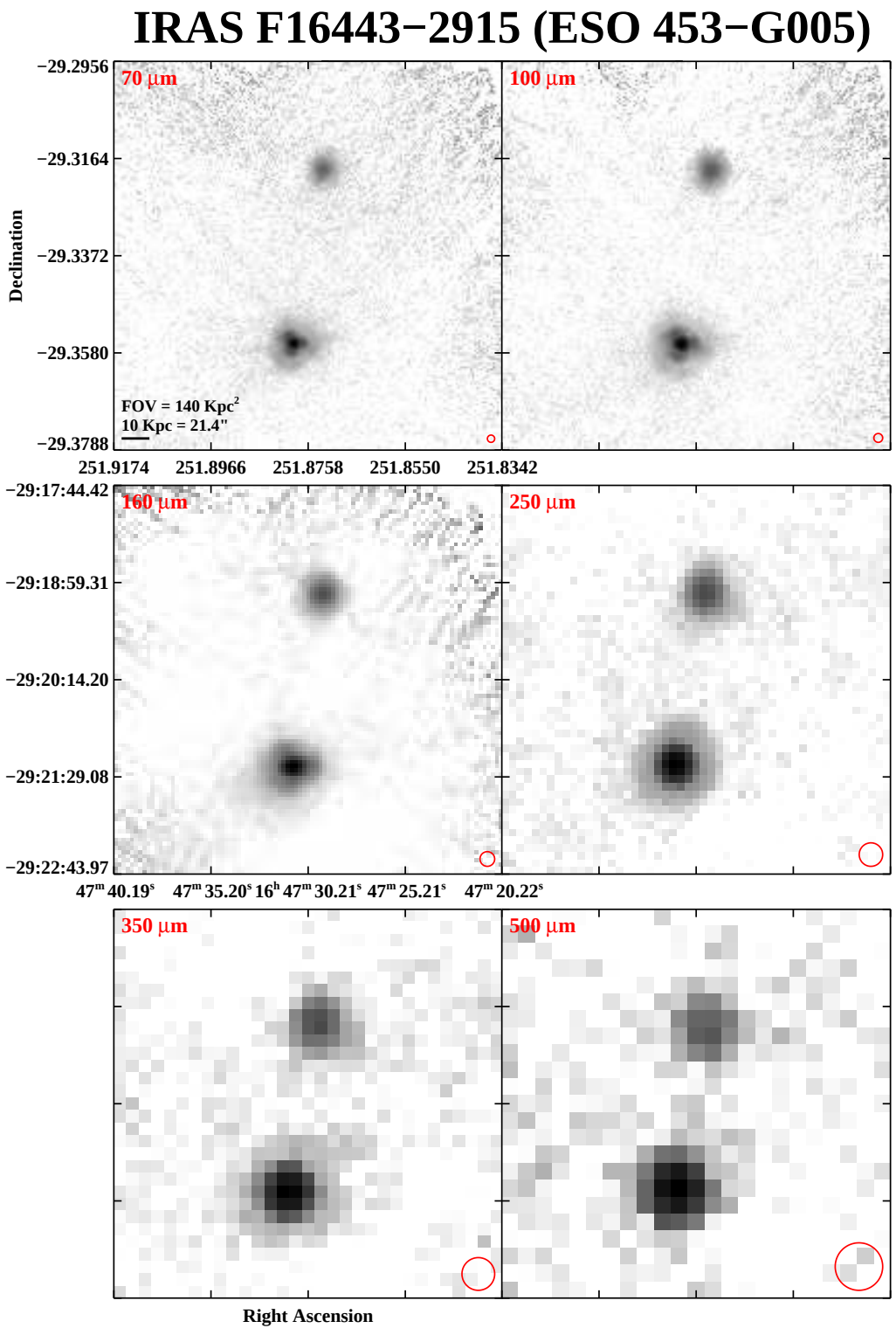

Figure 2.3 continued (page 152 of 209).

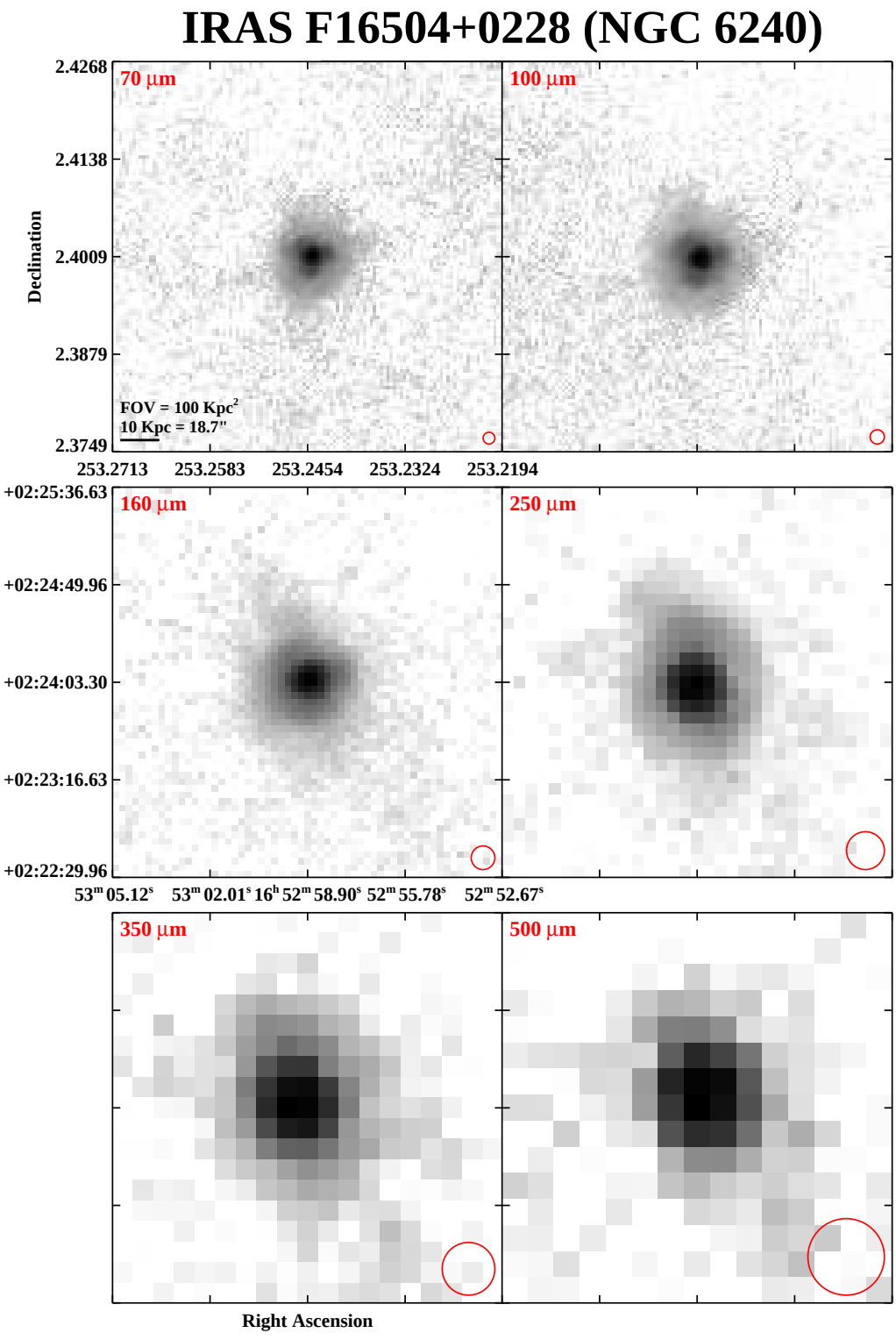

Figure 2.3 continued (page 153 of 209).

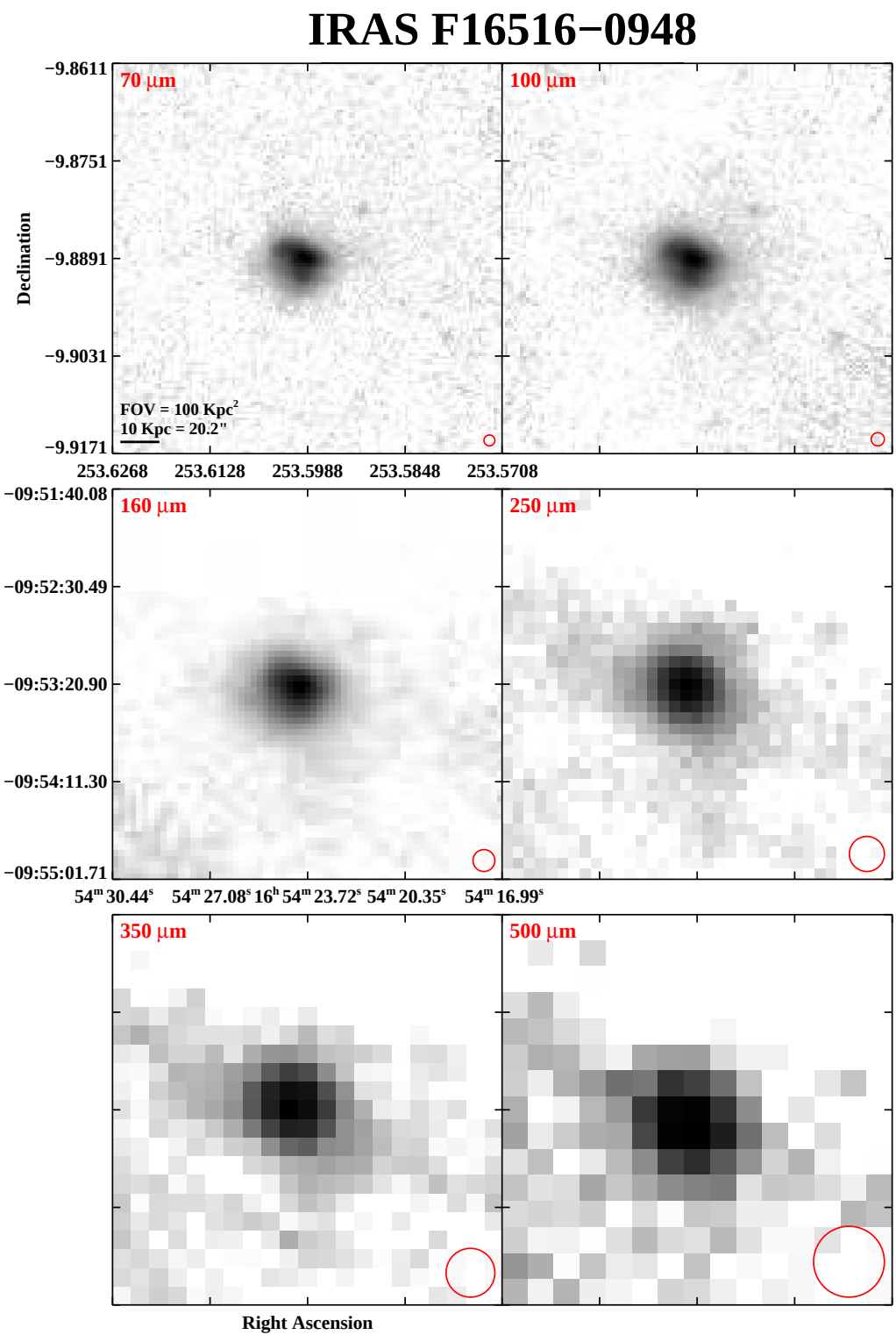

Figure 2.3 continued (page 154 of 209).

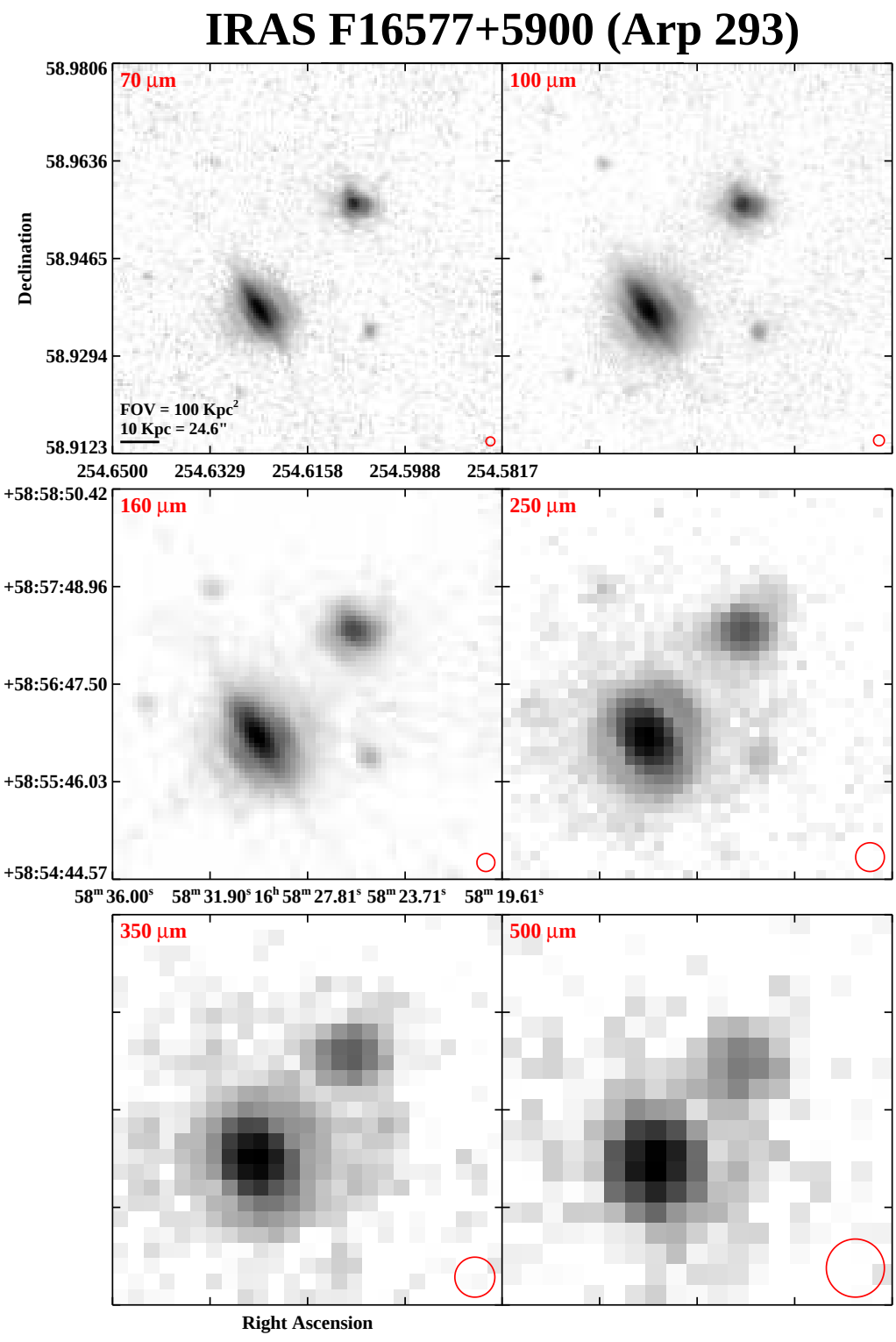

Figure 2.3 continued (page 155 of 209).

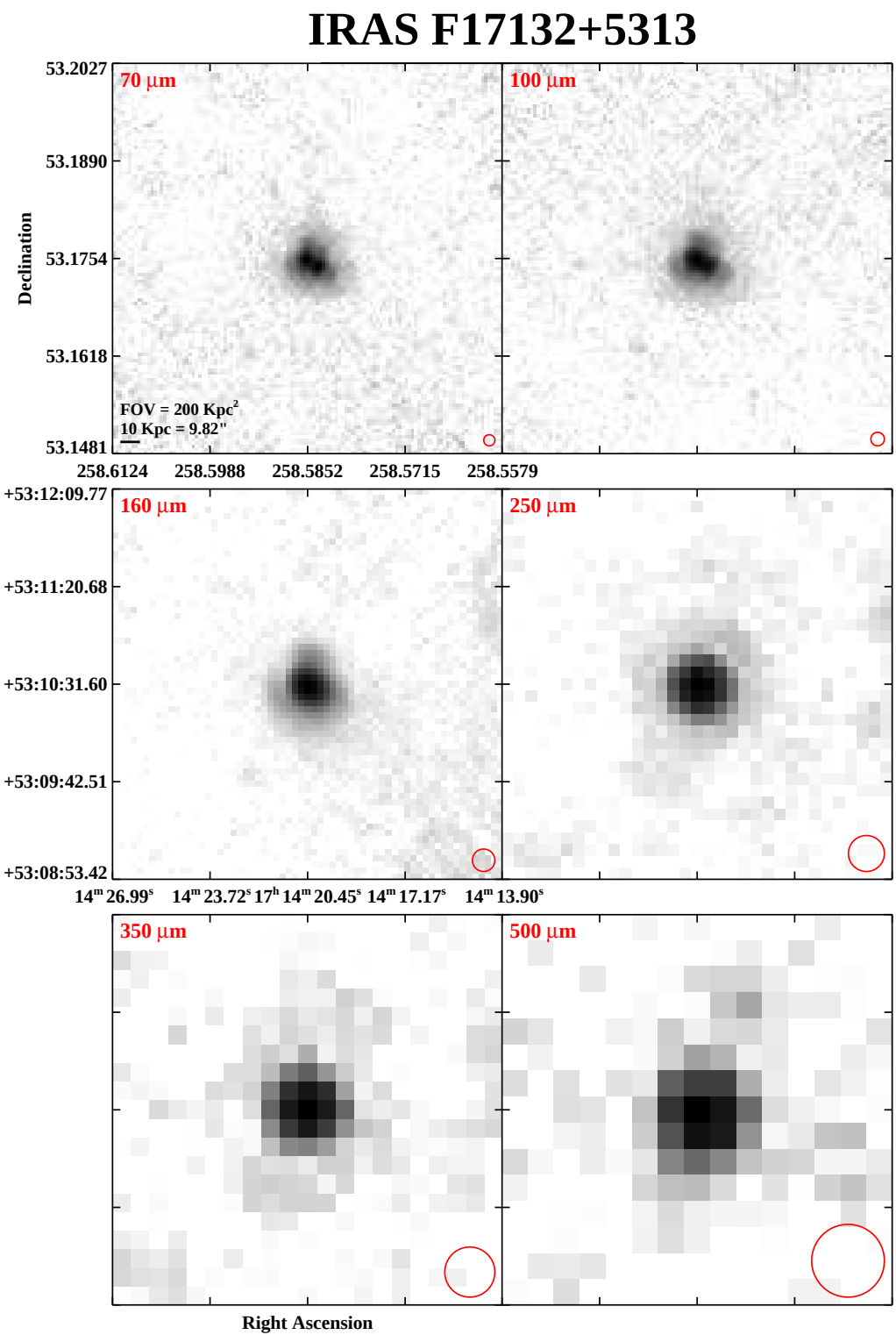

Figure 2.3 continued (page 156 of 209).

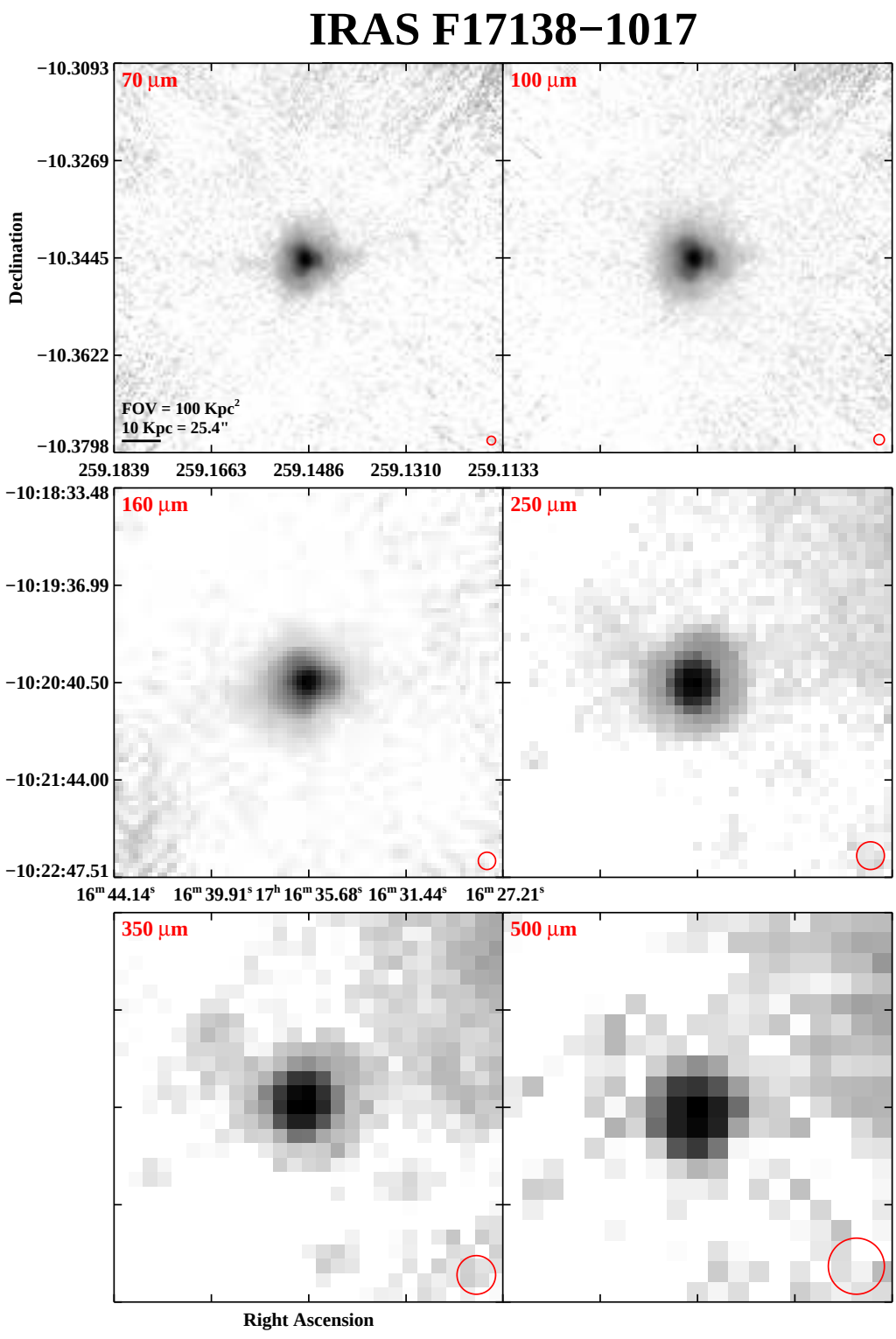

Figure 2.3 continued (page 157 of 209).

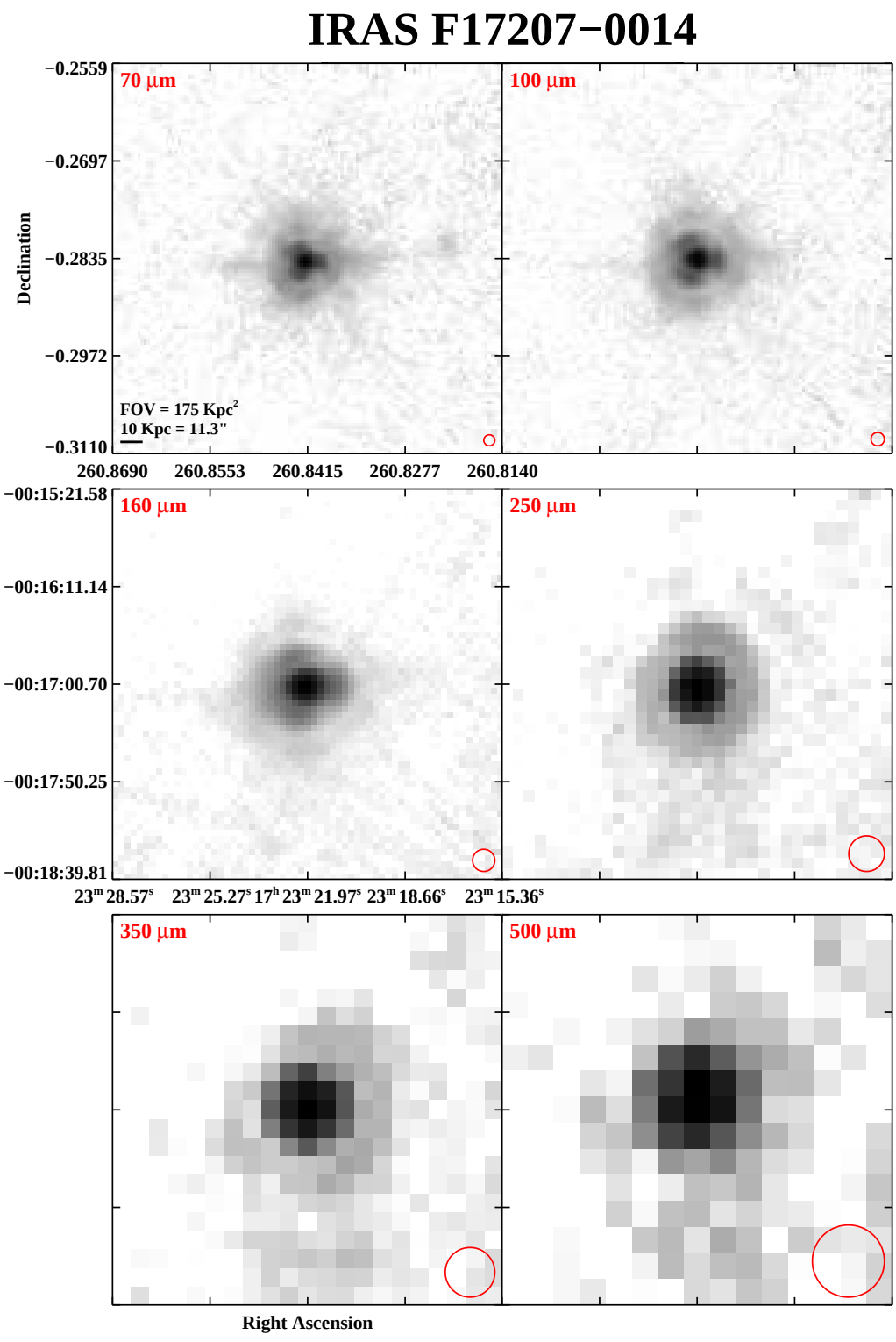

Figure 2.3 continued (page 158 of 209).

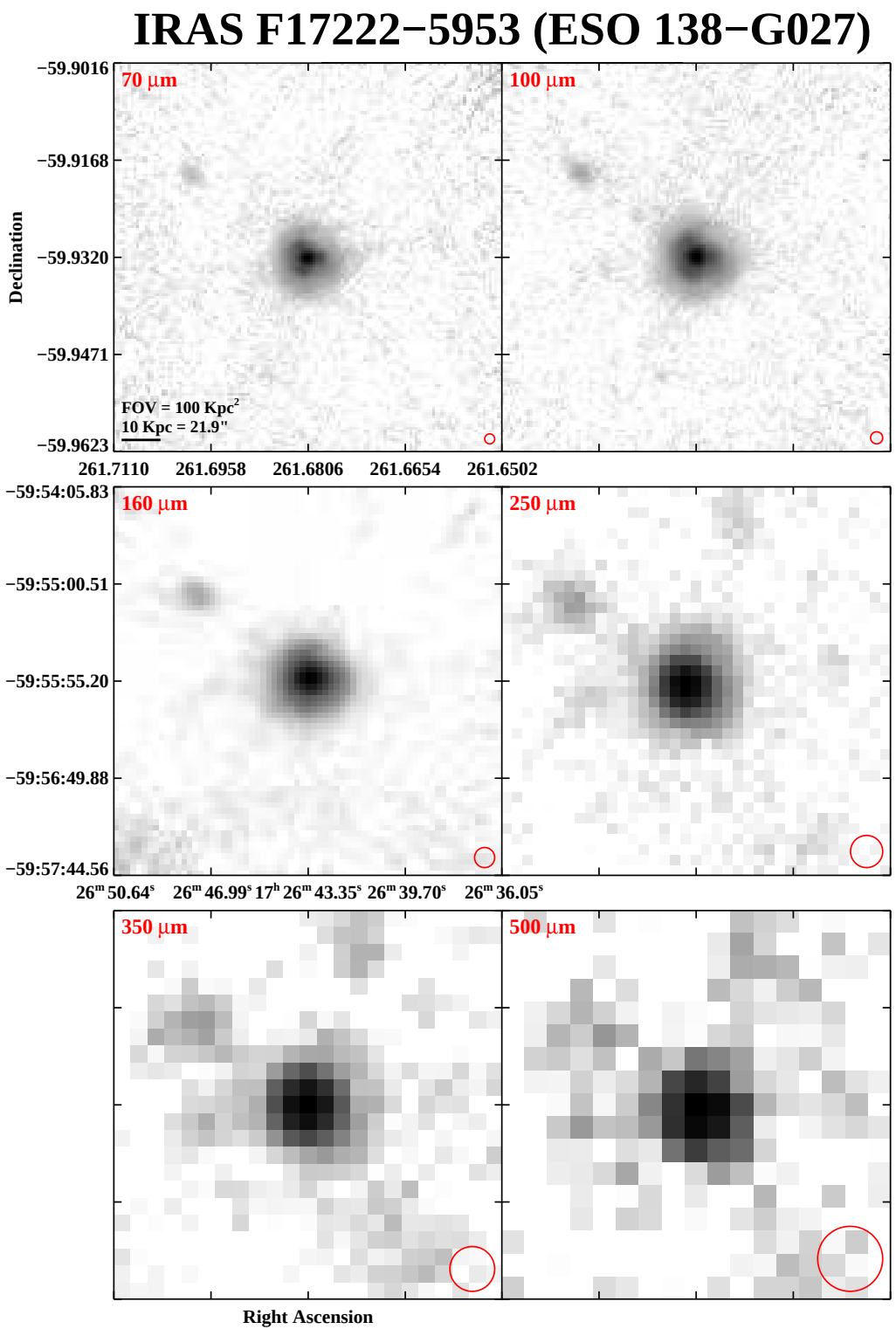

Figure 2.3 continued (page 159 of 209).

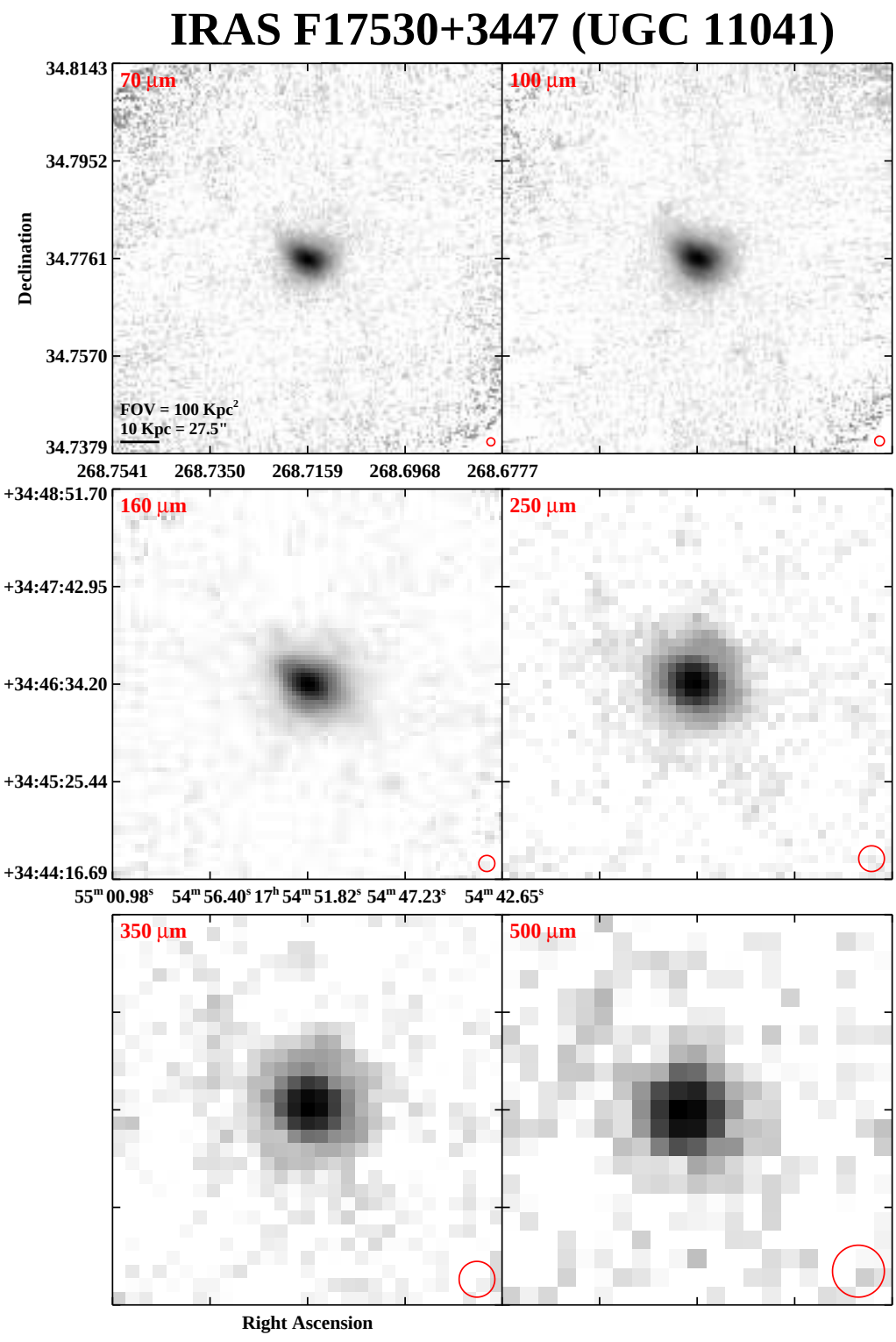

Figure 2.3 continued (page 160 of 209).

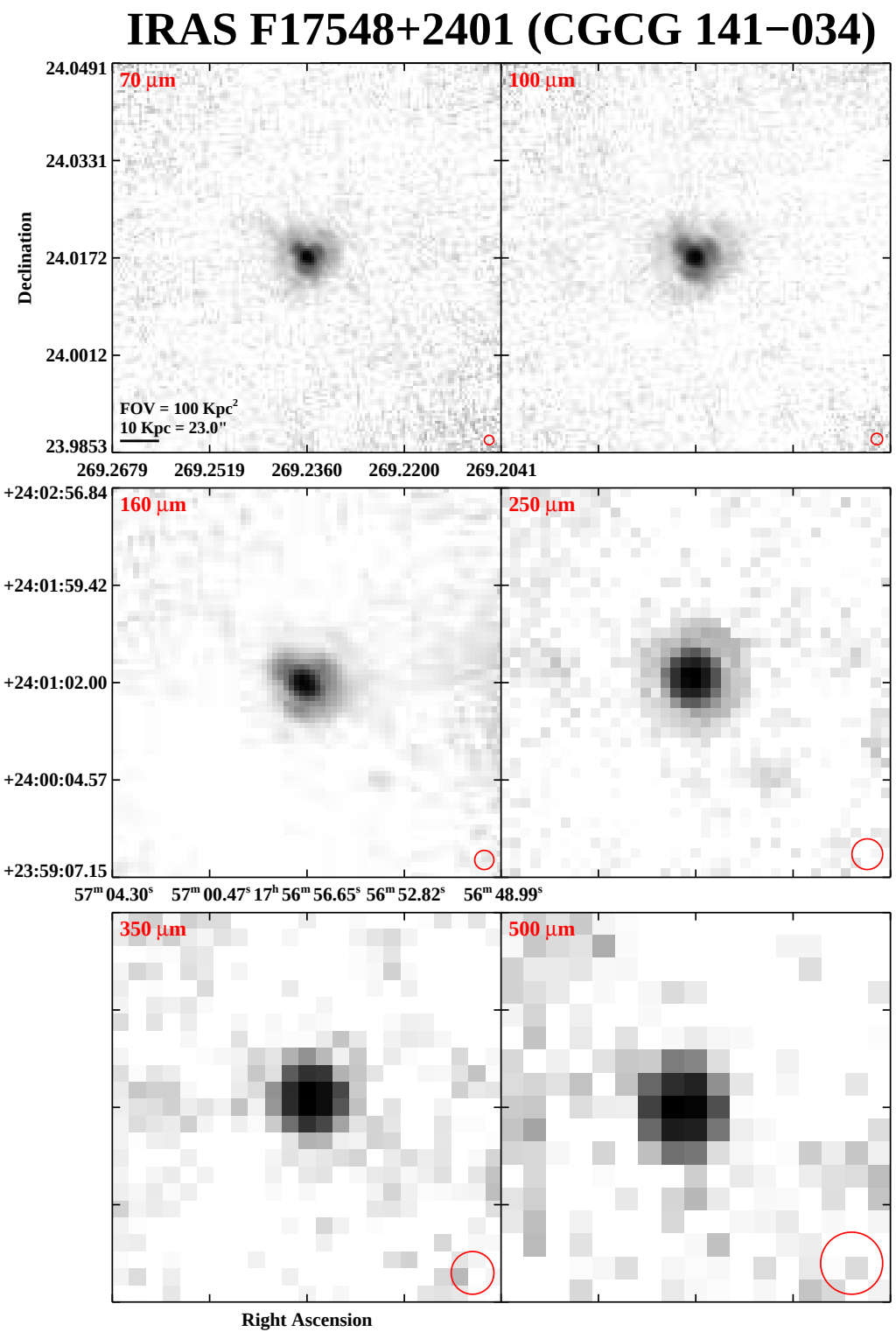

Figure 2.3 continued (page 161 of 209).

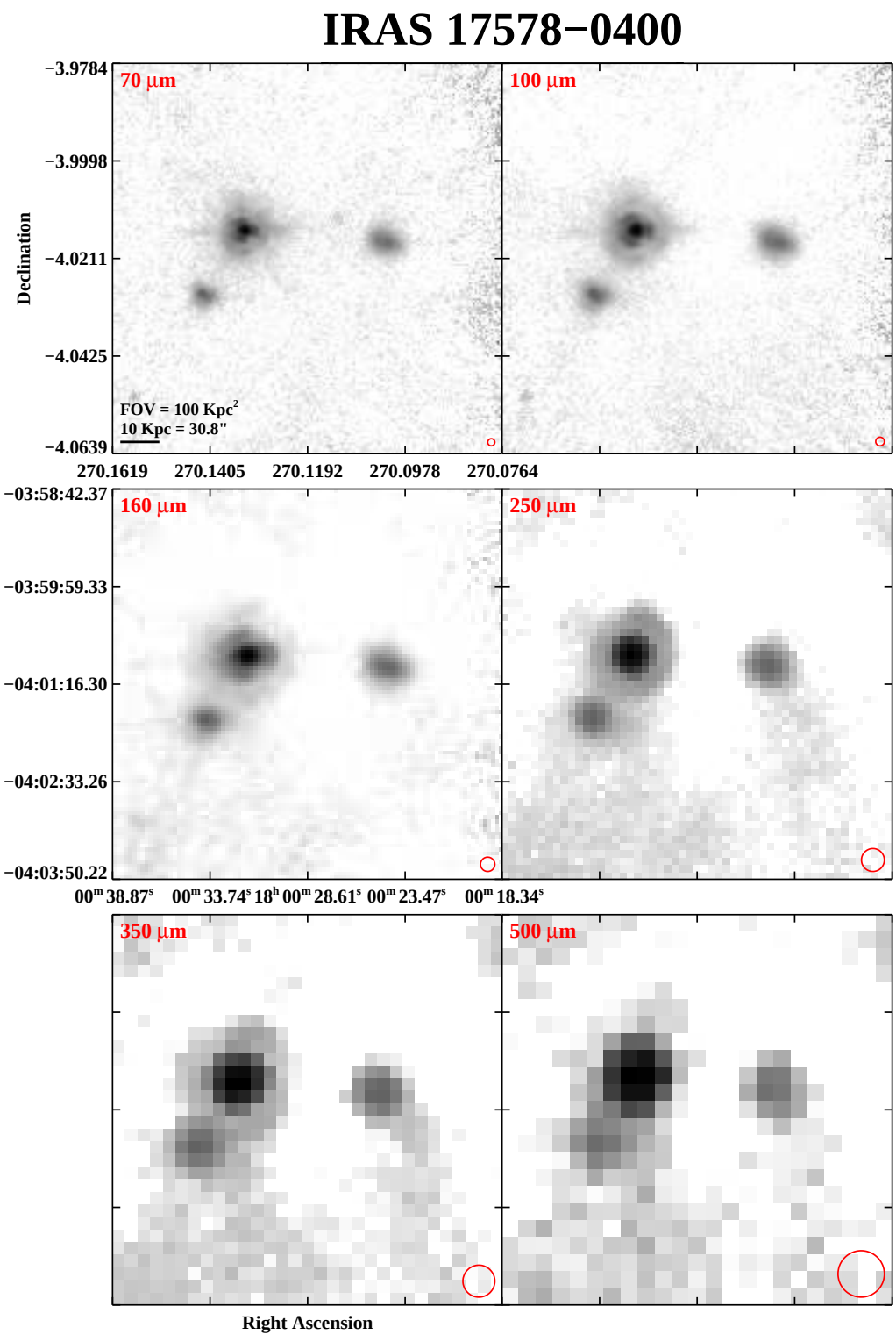

Figure 2.3 continued (page 162 of 209).

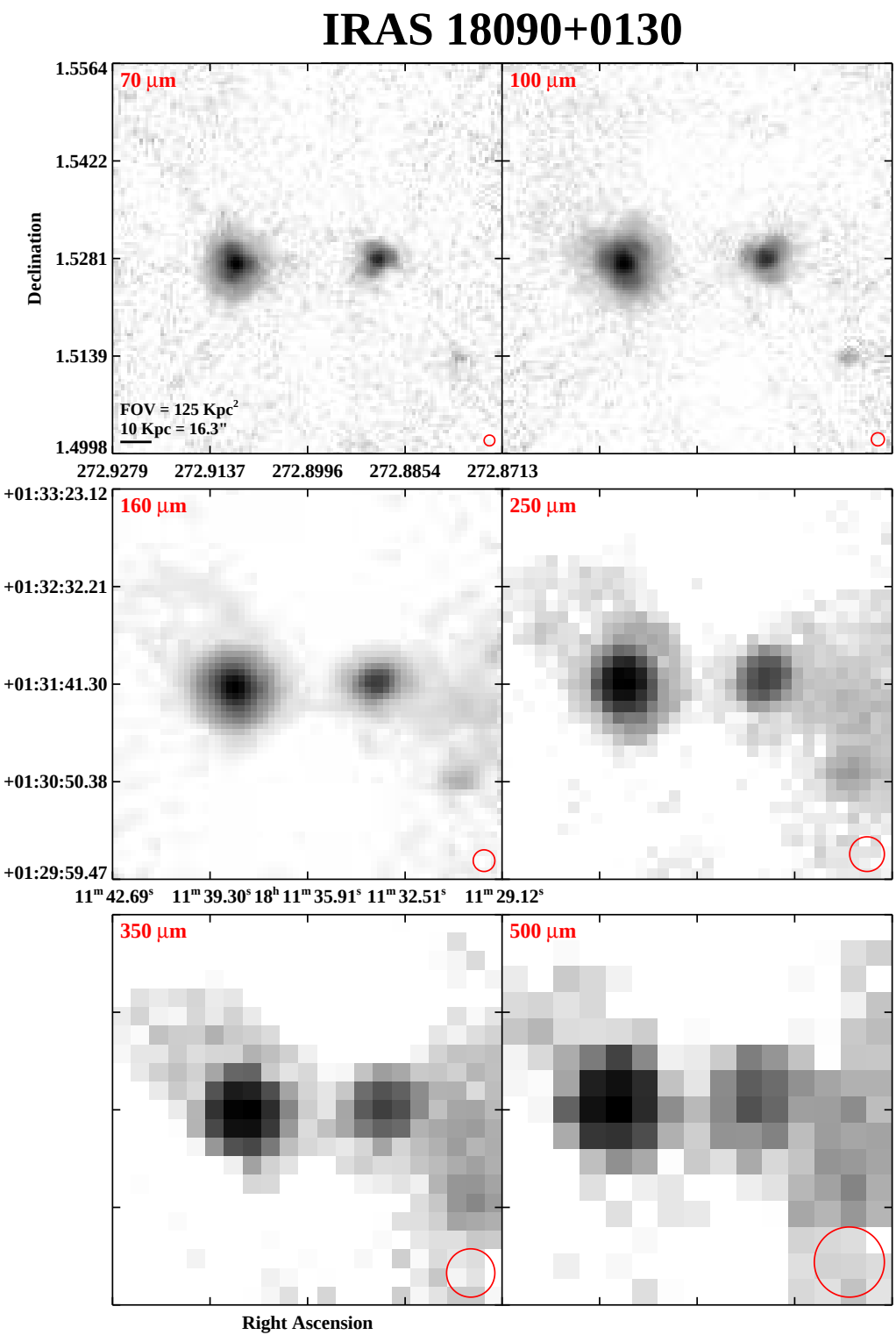

Figure 2.3 continued (page 163 of 209).

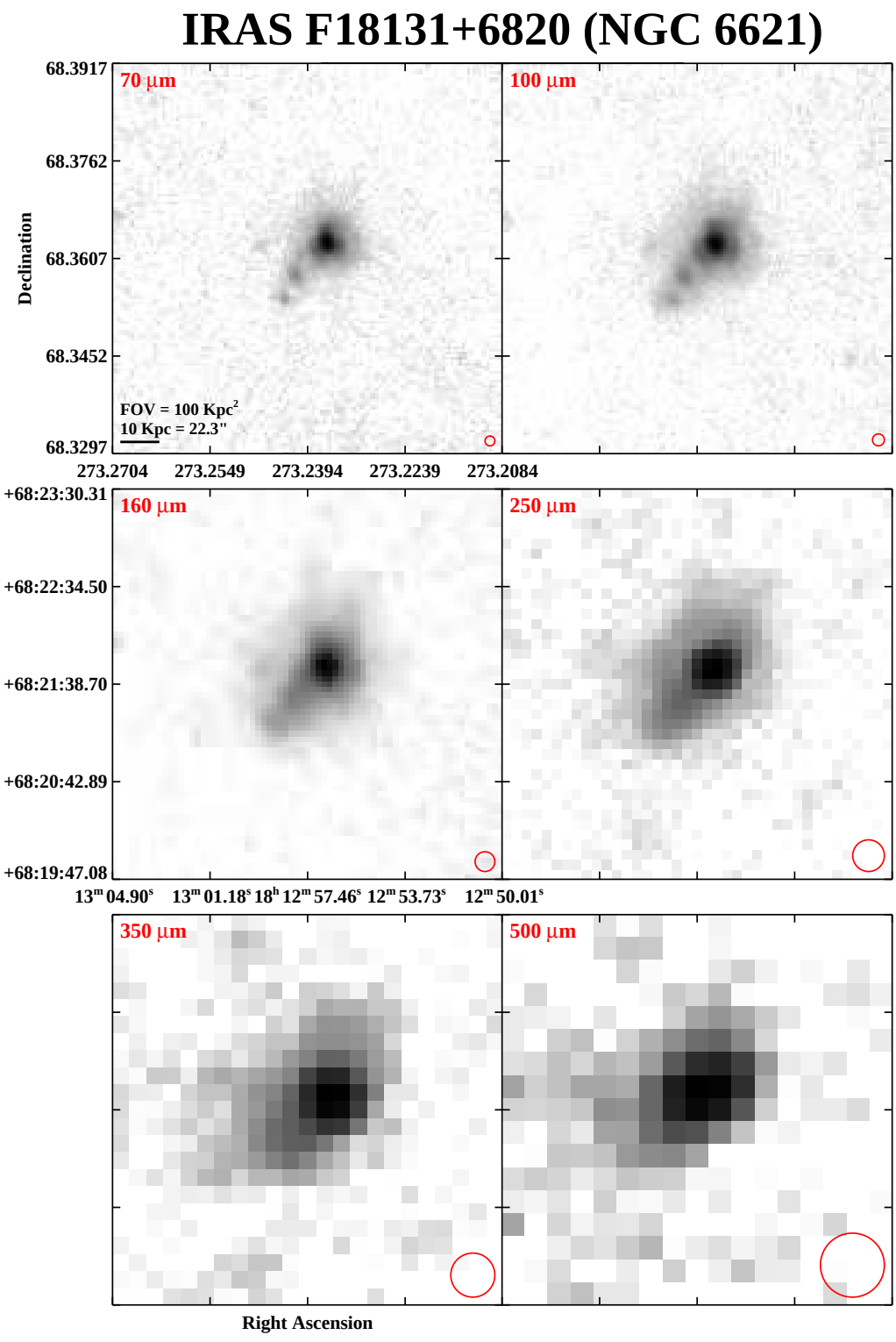

Figure 2.3 continued (page 164 of 209).

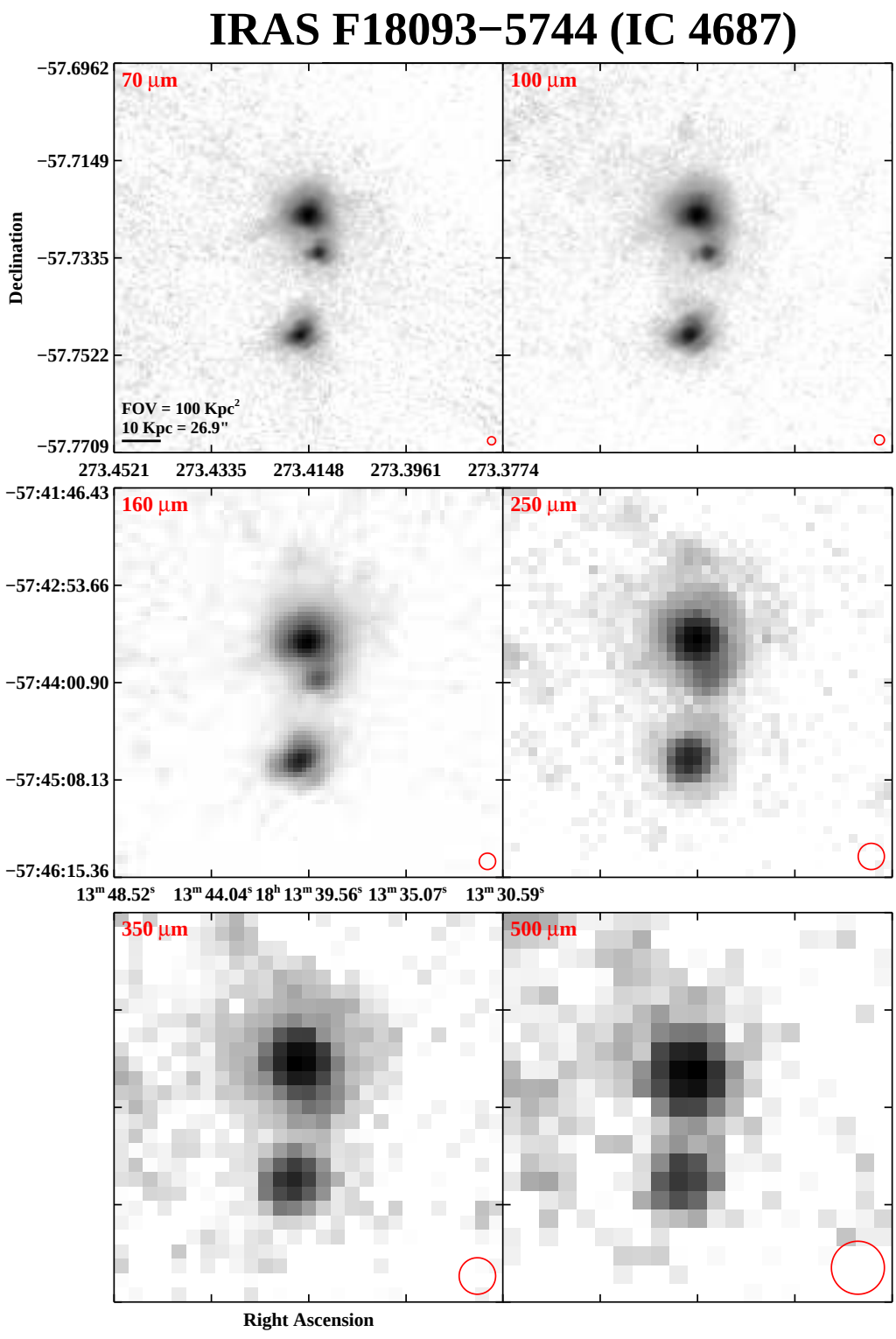

Figure 2.3 continued (page 165 of 209).

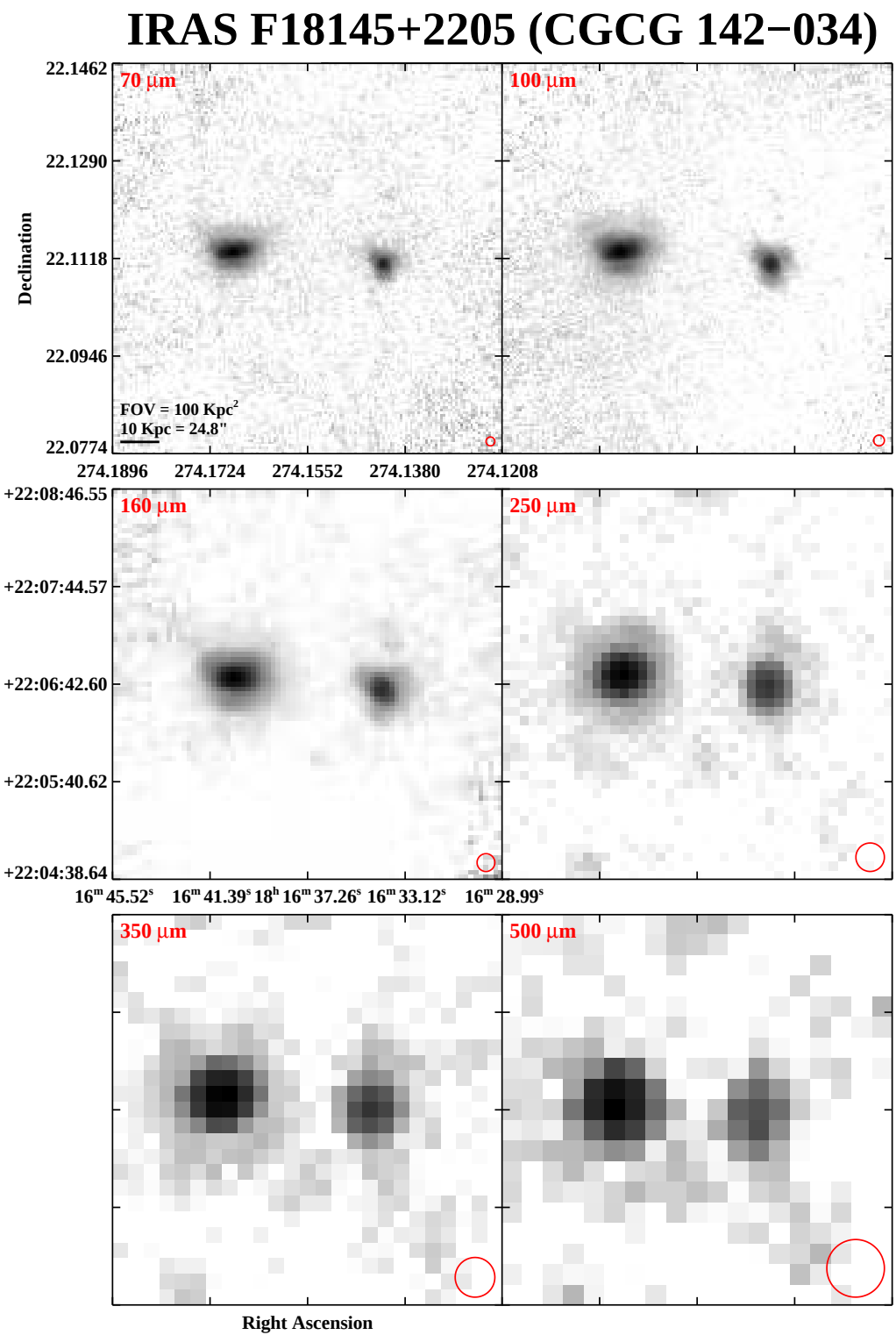

Figure 2.3 continued (page 166 of 209).

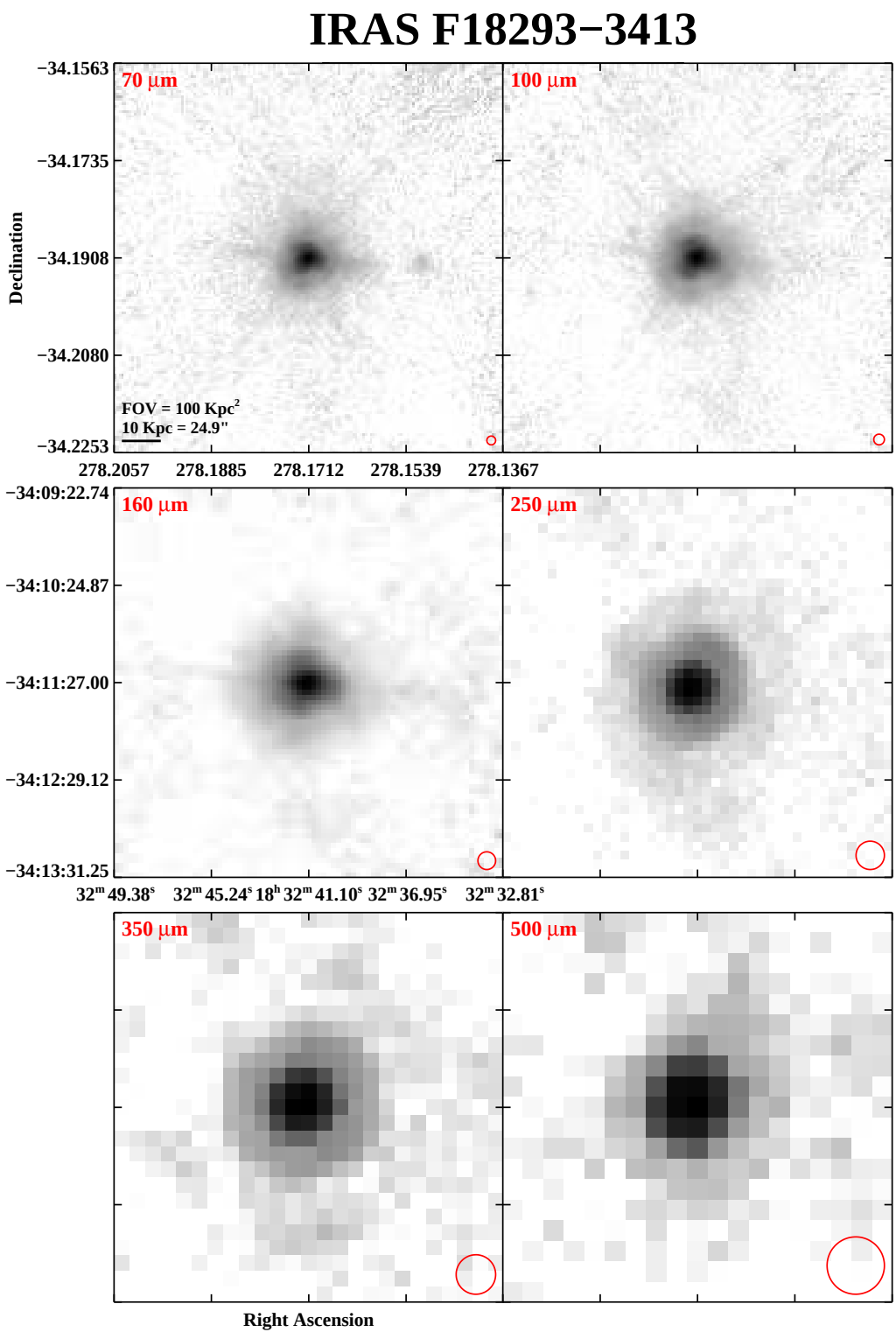

Figure 2.3 continued (page 167 of 209).

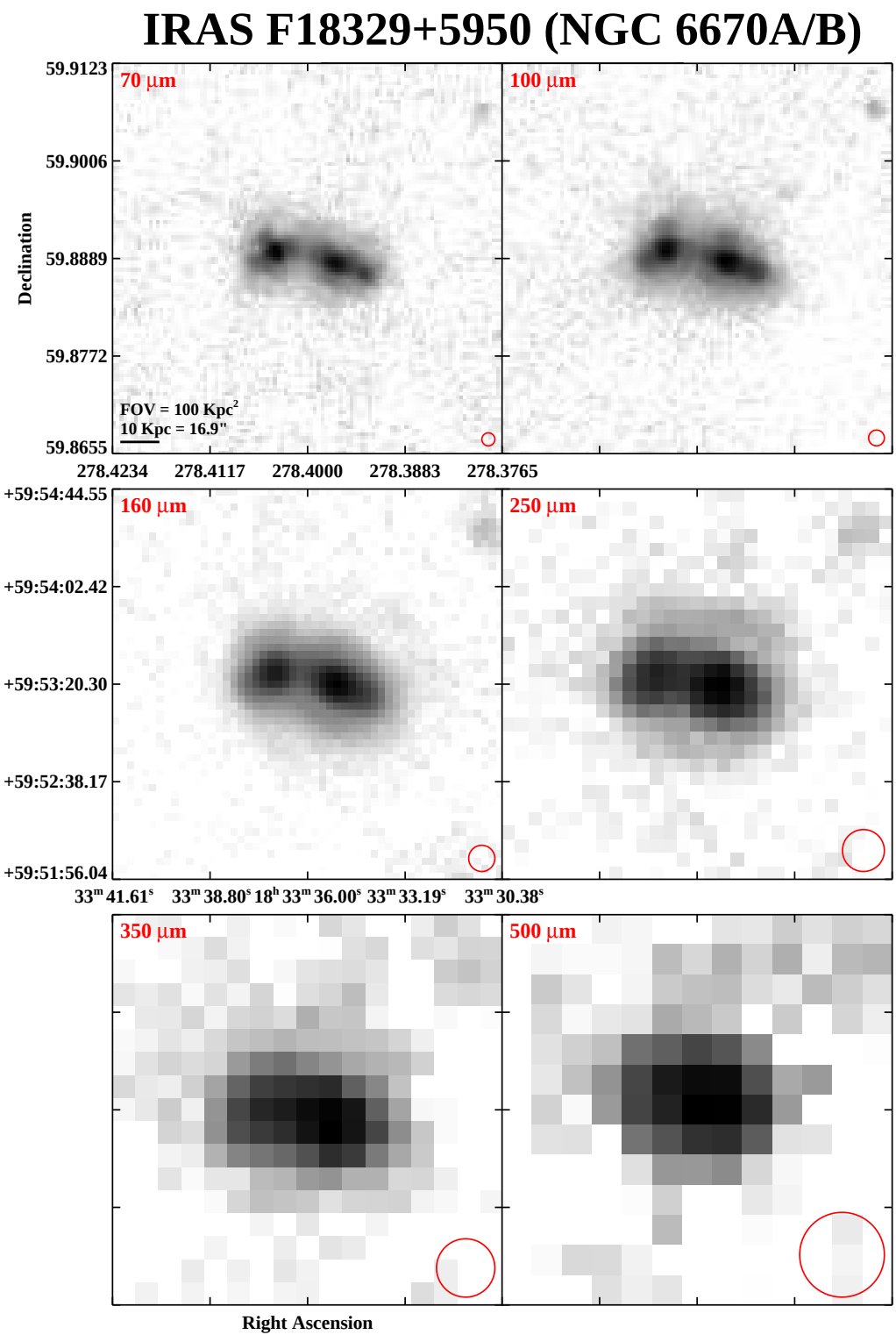

Figure 2.3 continued (page 168 of 209).

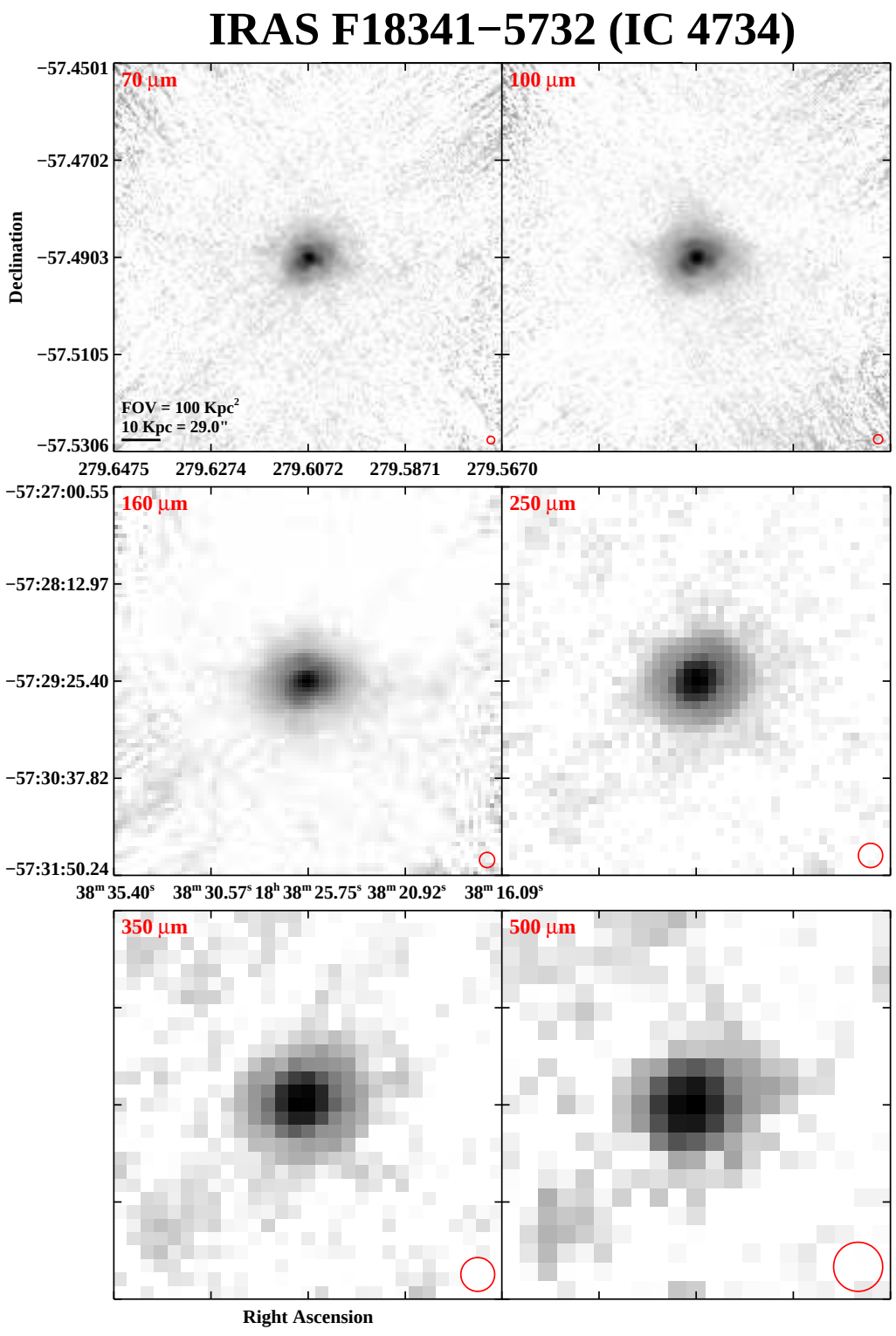

Figure 2.3 continued (page 169 of 209).

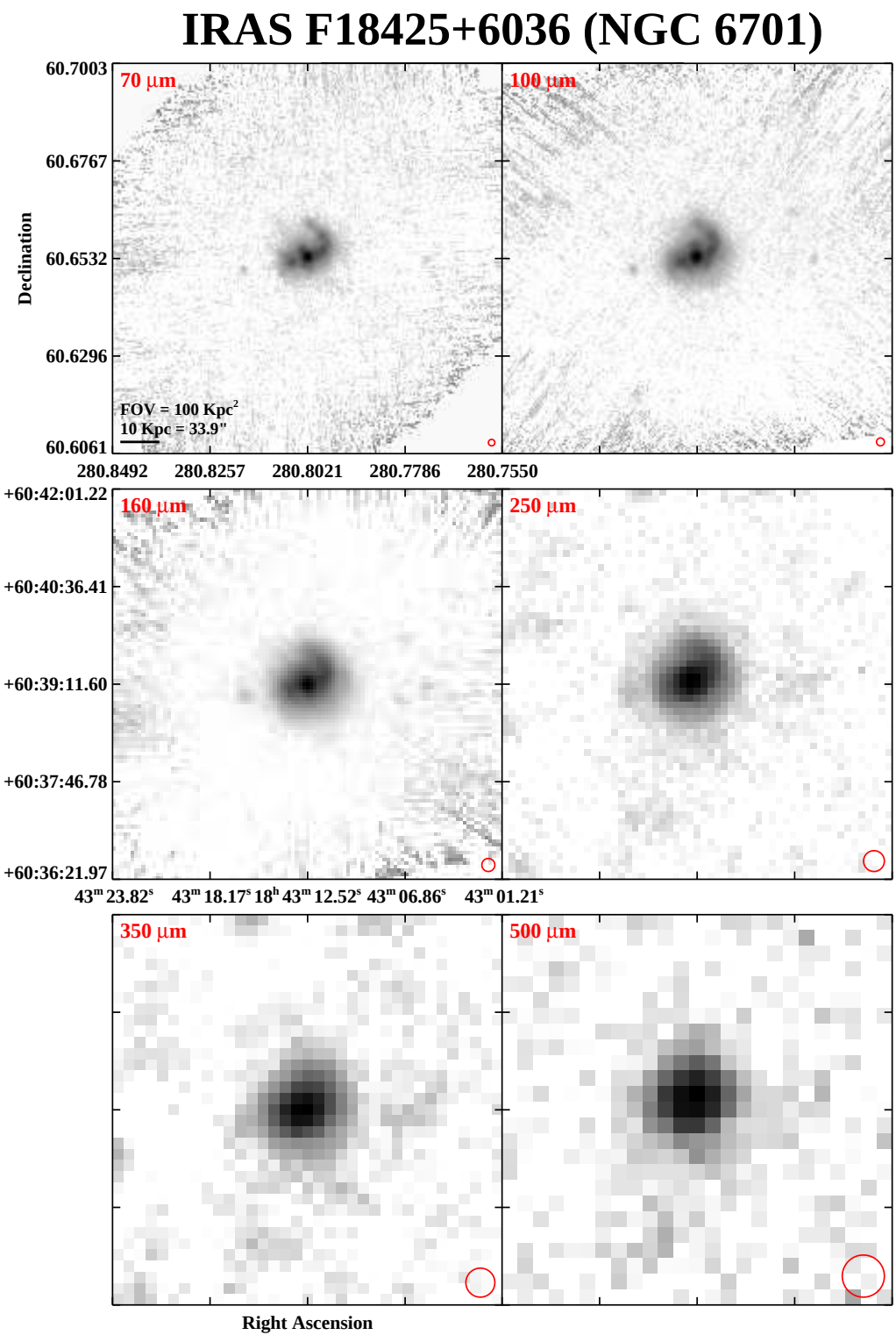

Figure 2.3 continued (page 170 of 209).

IRAS F19120+7320 (VV 414/NGC 6786/UGC 11415)

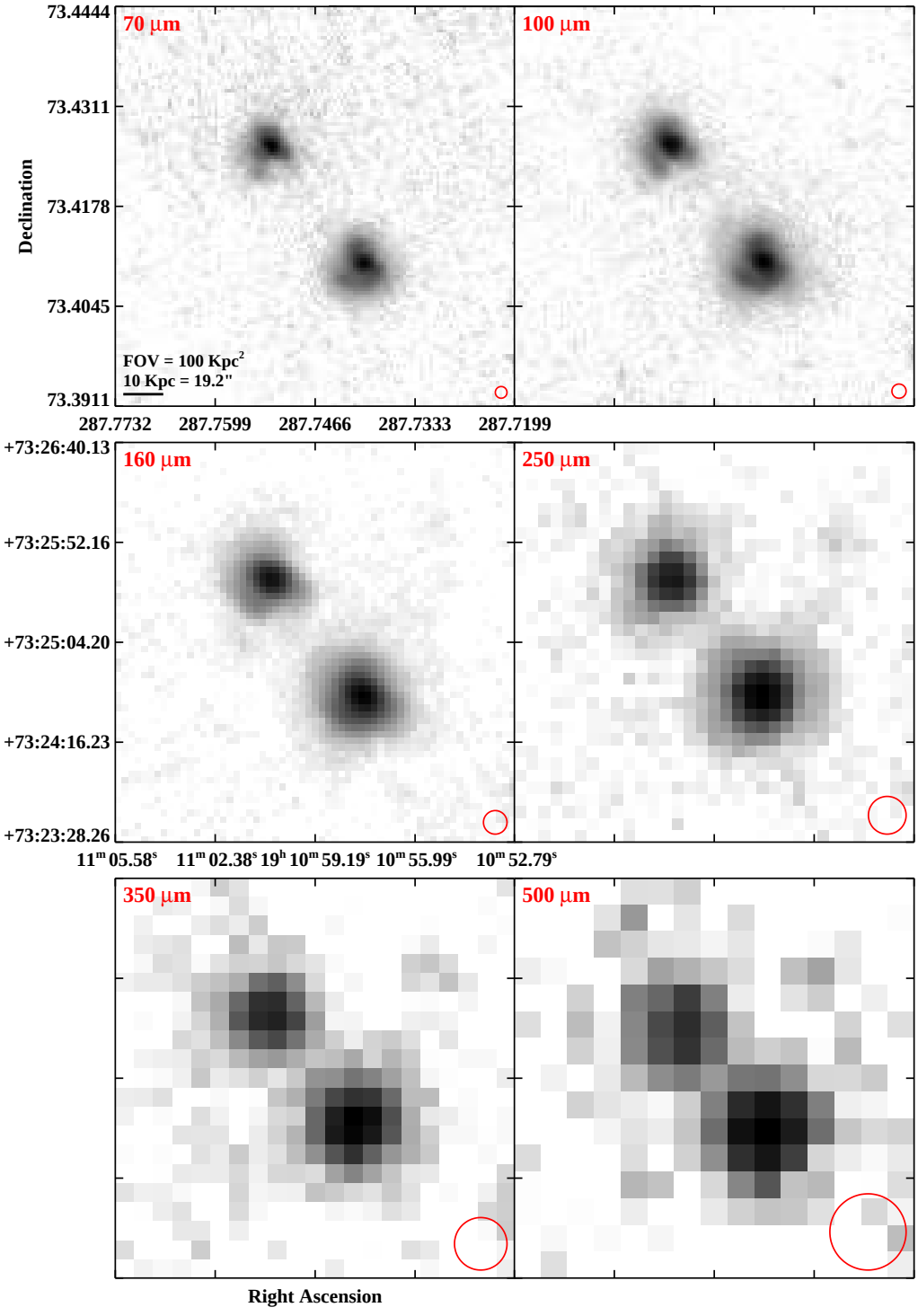

Figure 2.3 continued (page 171 of 209).

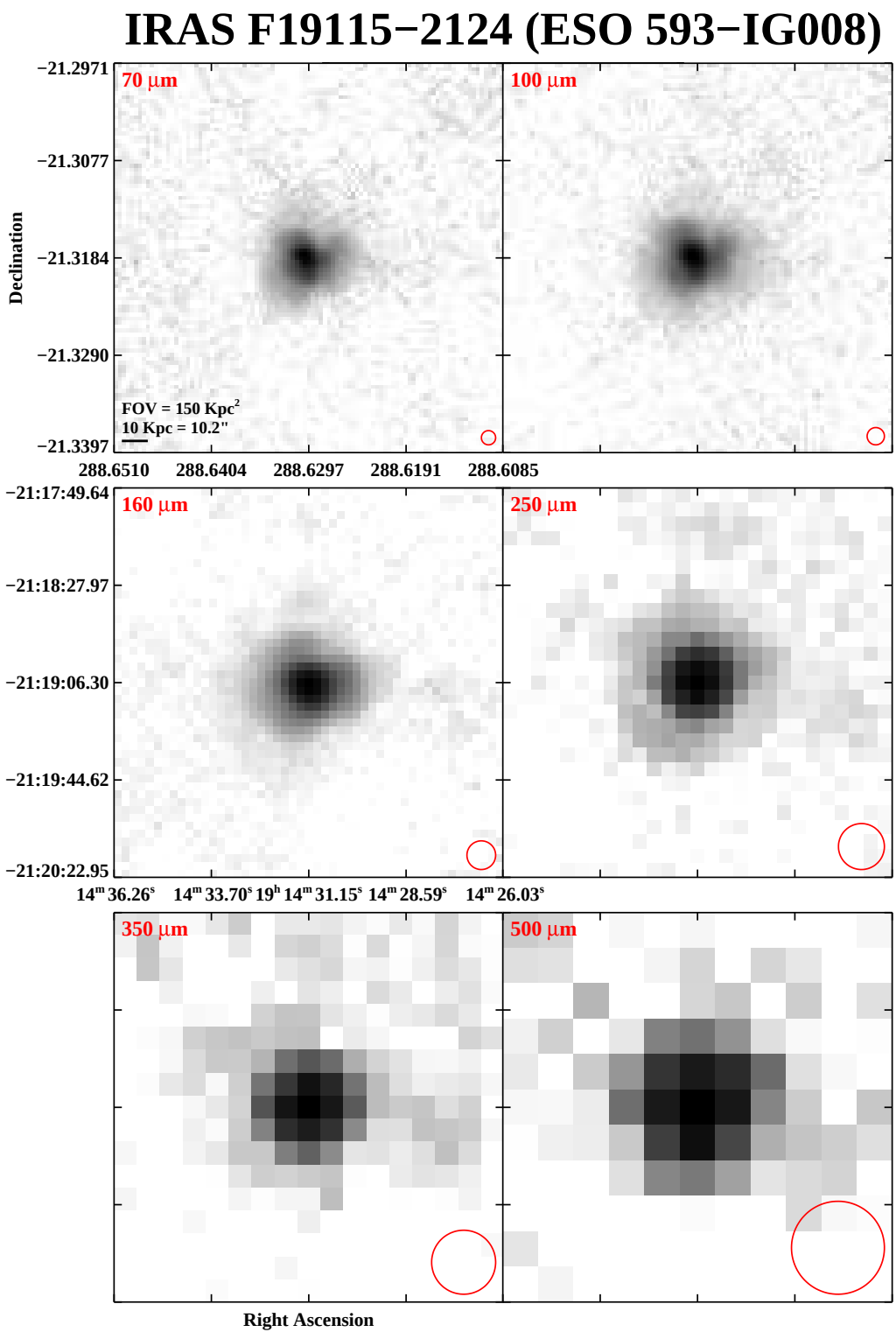

Figure 2.3 continued (page 172 of 209).

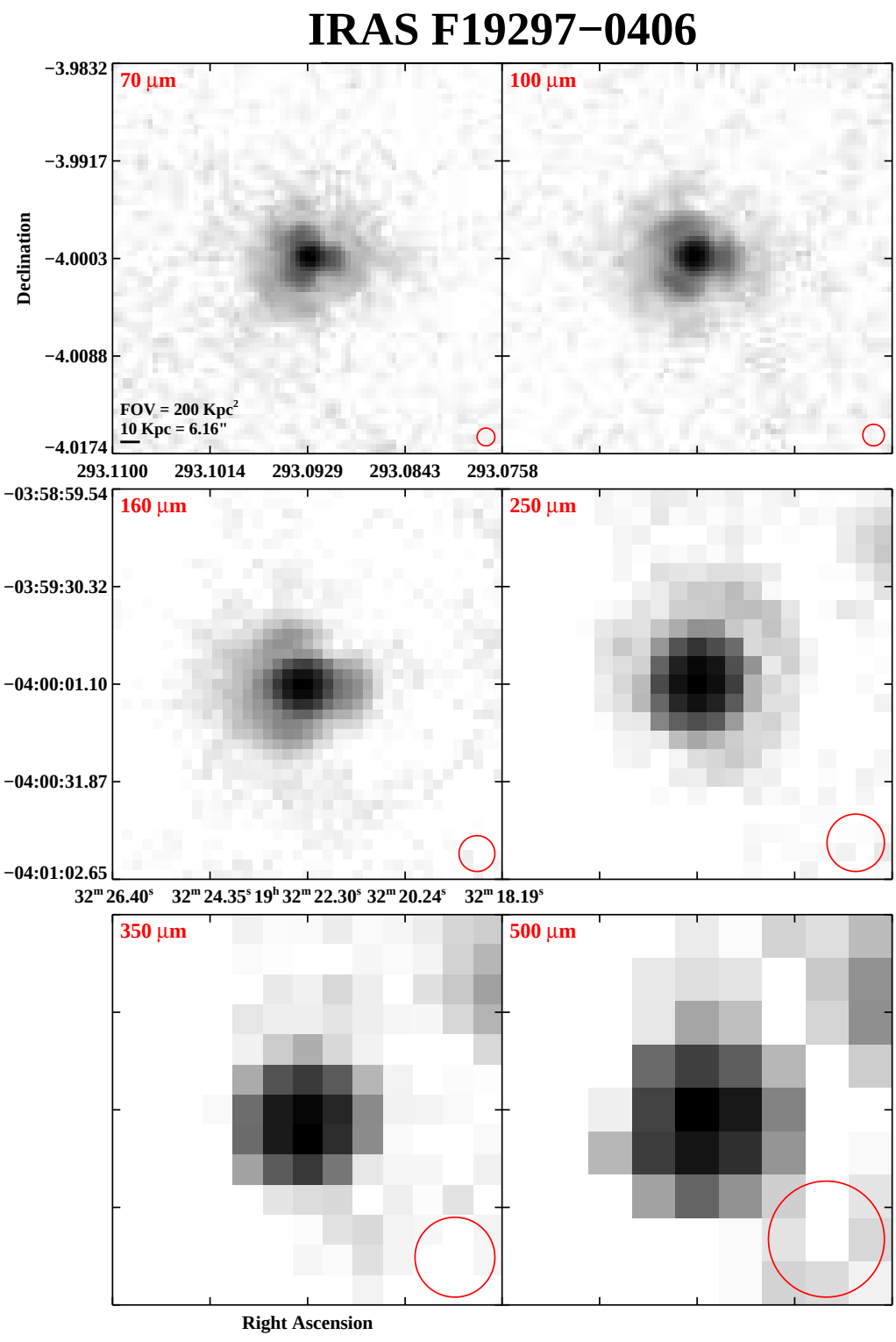

Figure 2.3 continued (page 173 of 209).

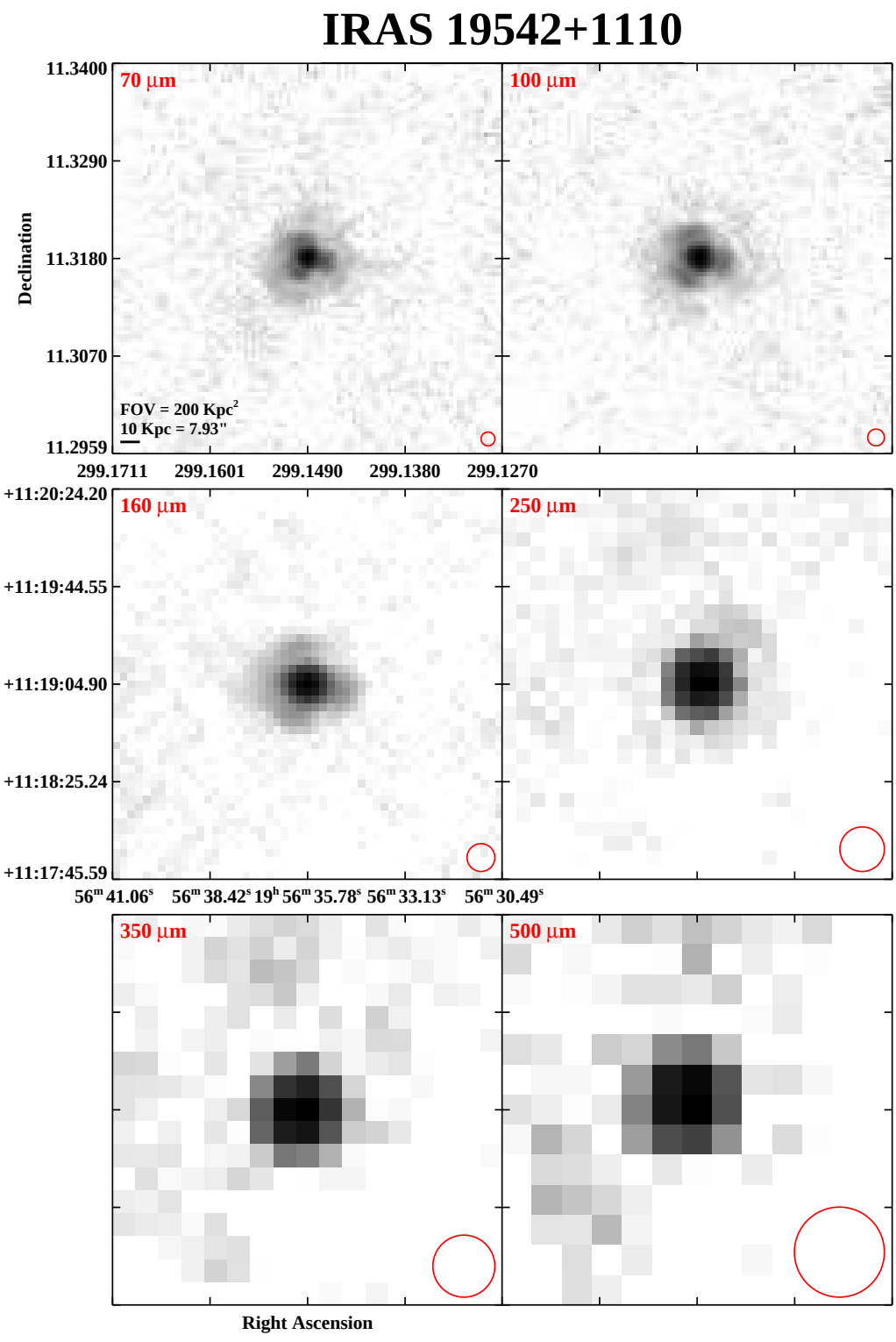

Figure 2.3 continued (page 174 of 209).

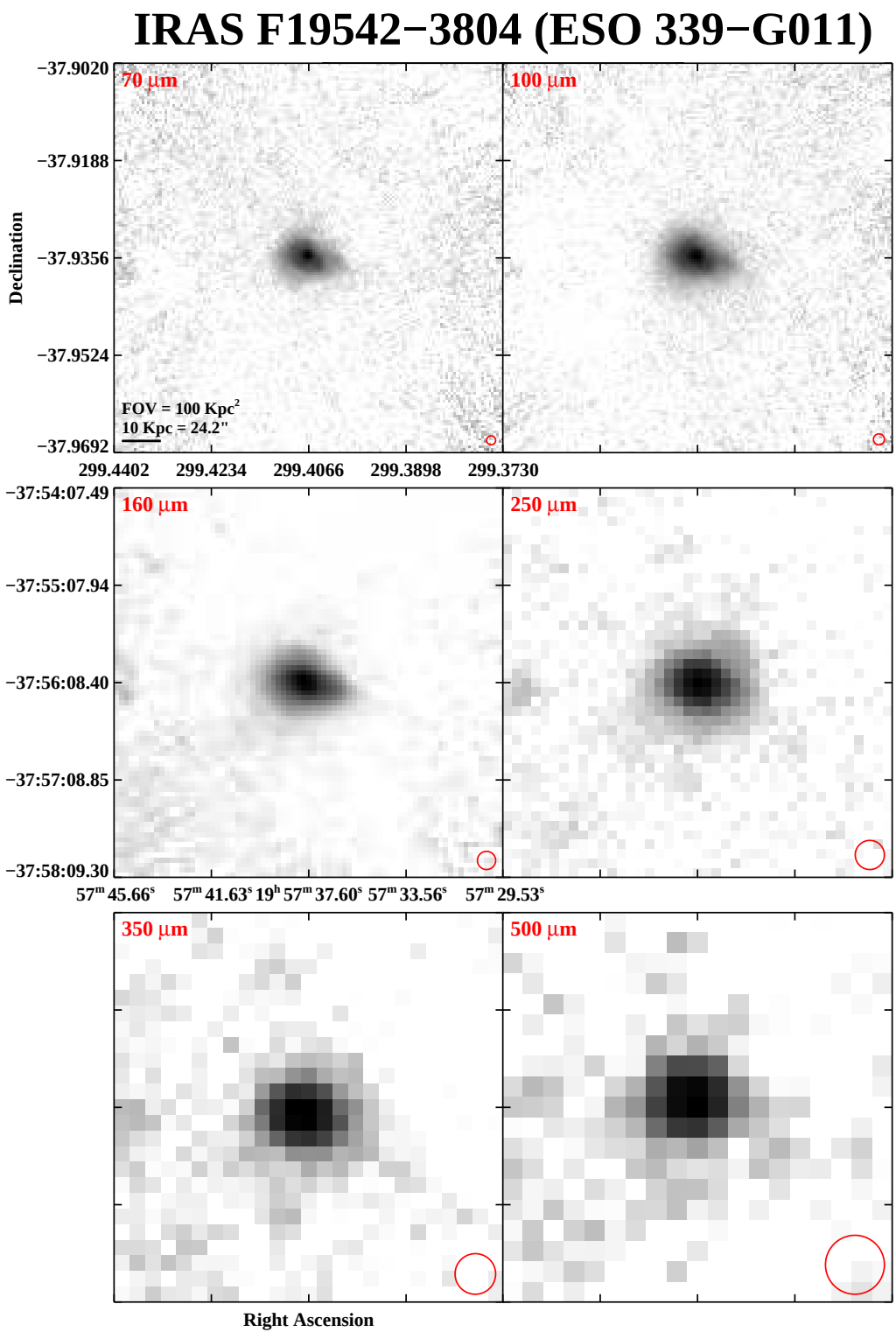

Figure 2.3 continued (page 175 of 209).

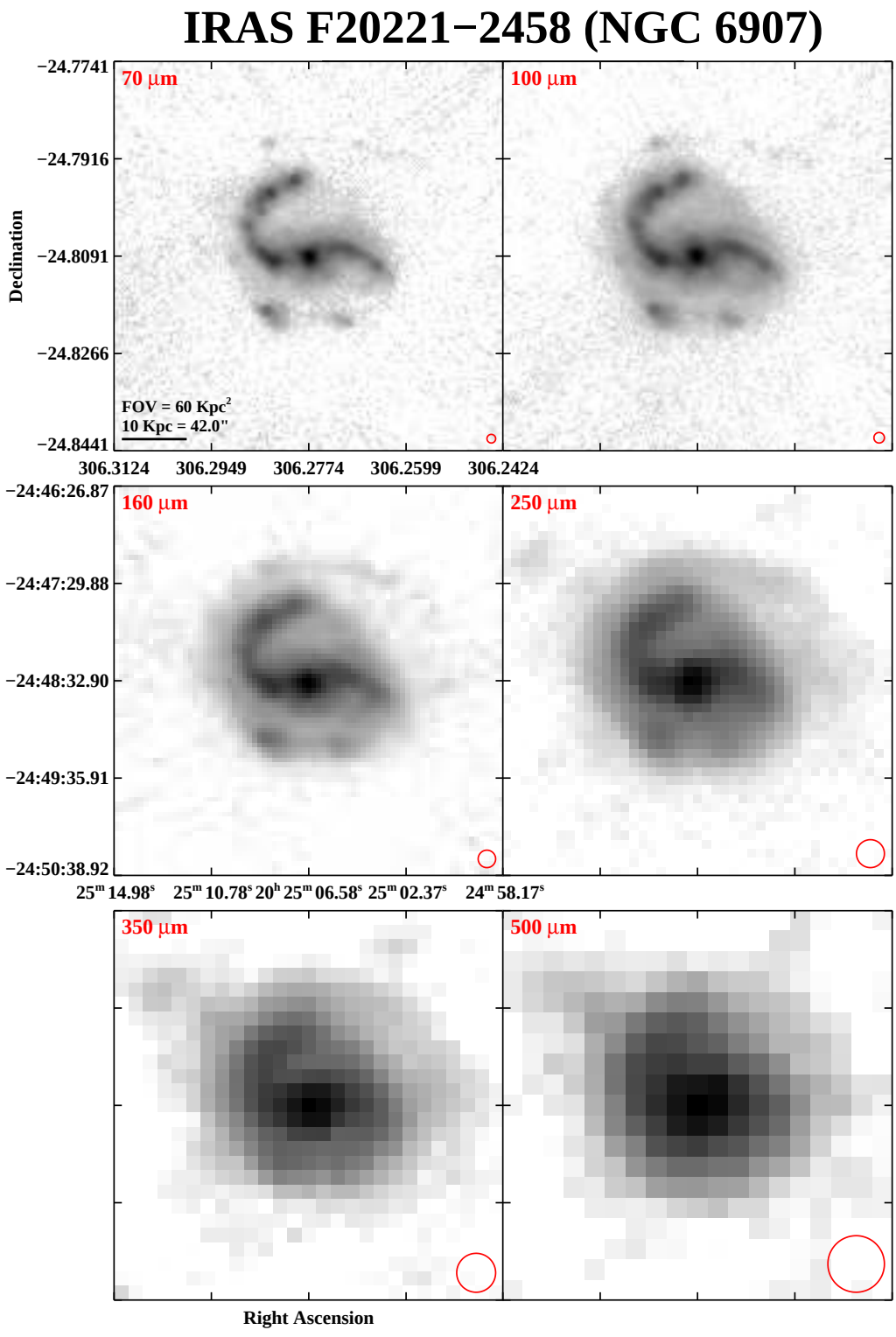

Figure 2.3 continued (page 176 of 209).

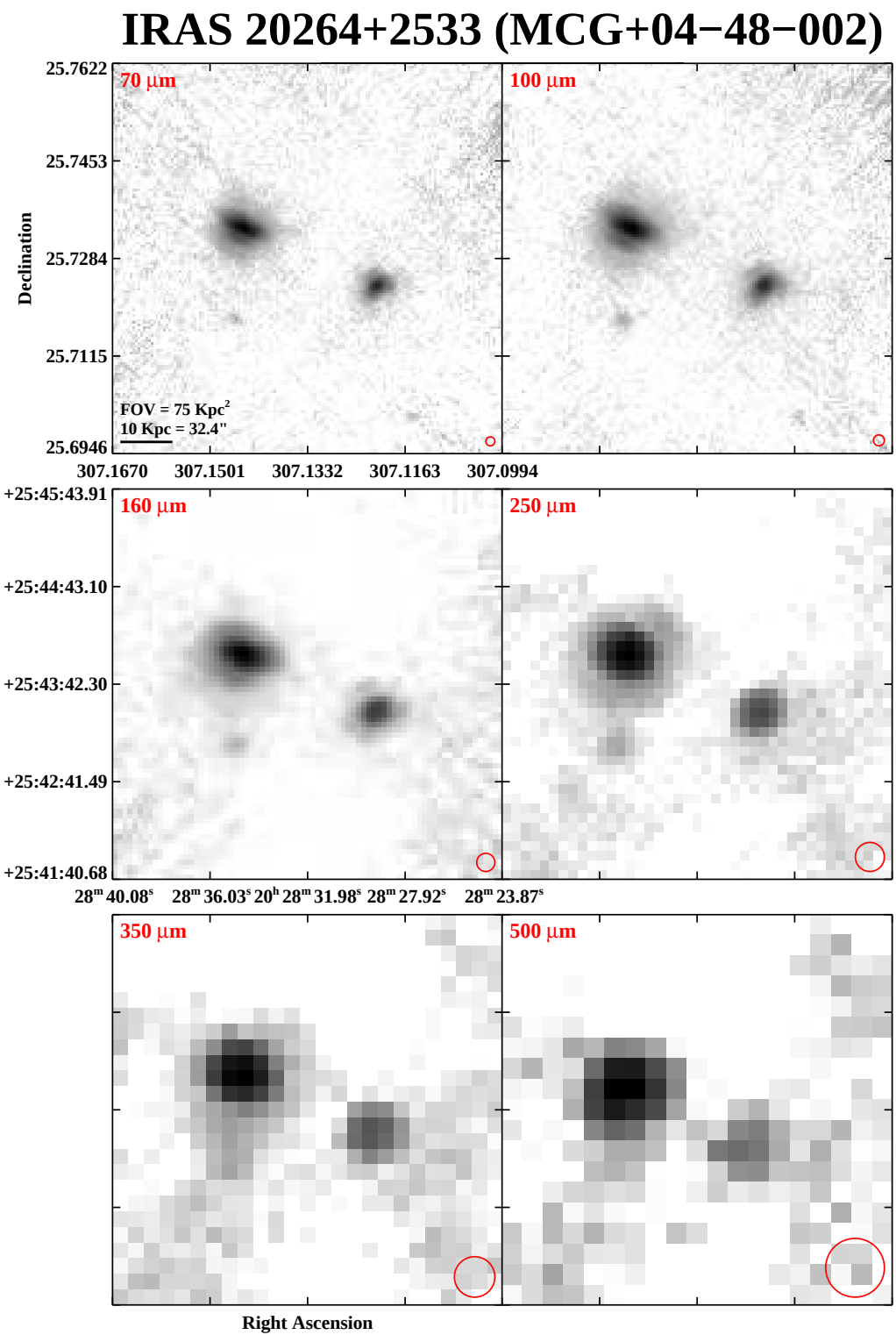

Figure 2.3 continued (page 177 of 209).

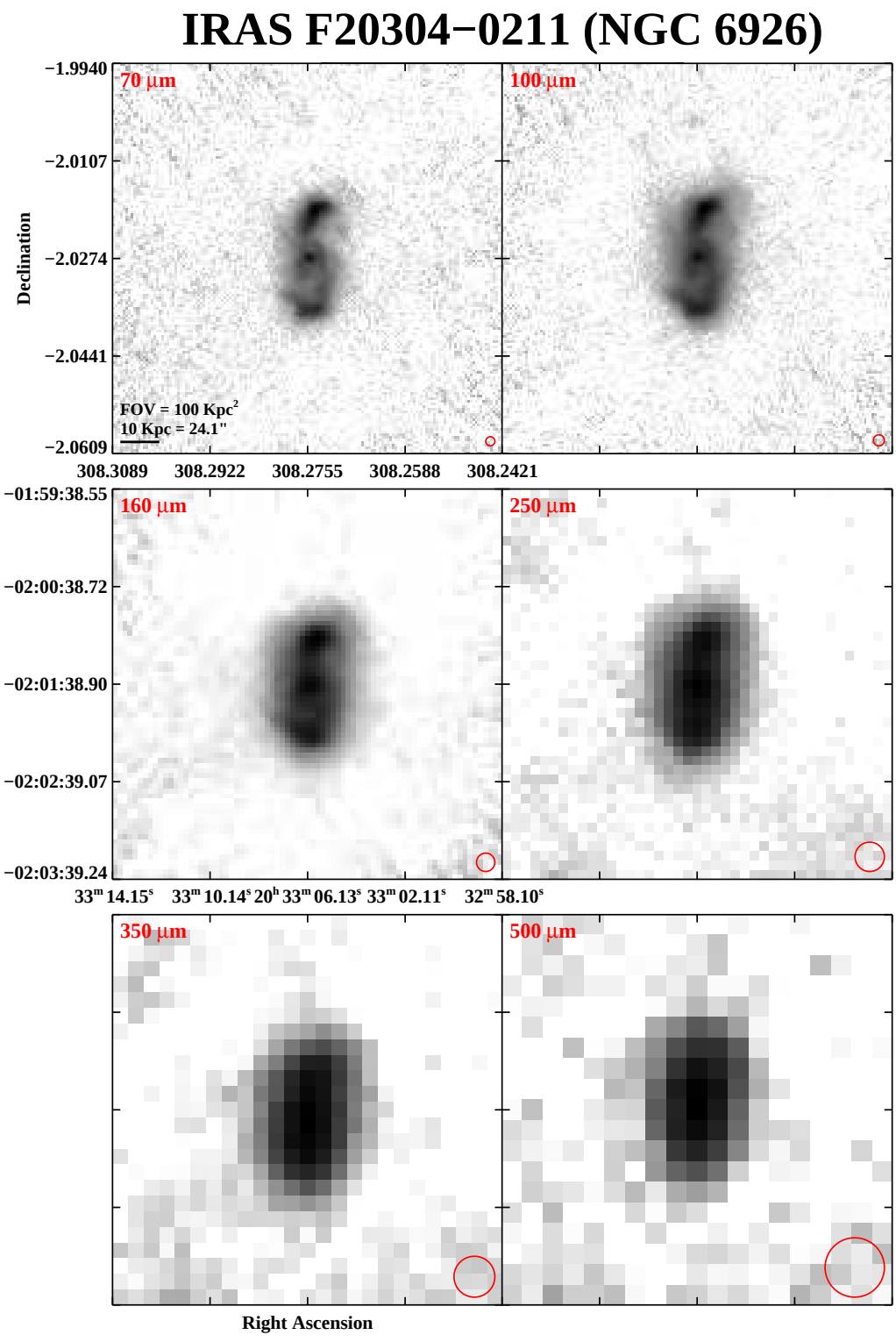

Figure 2.3 continued (page 178 of 209).

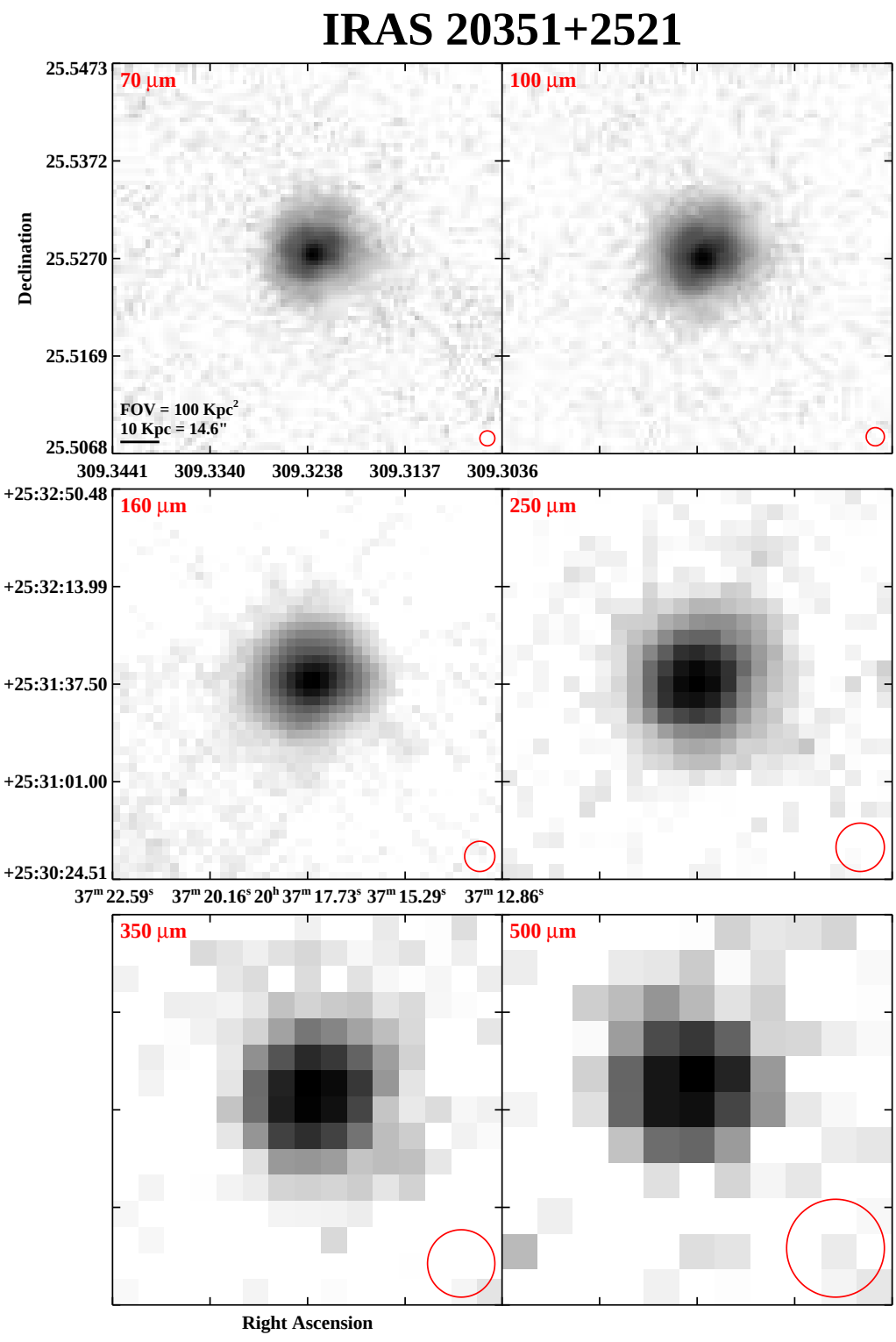

Figure 2.3 continued (page 179 of 209).

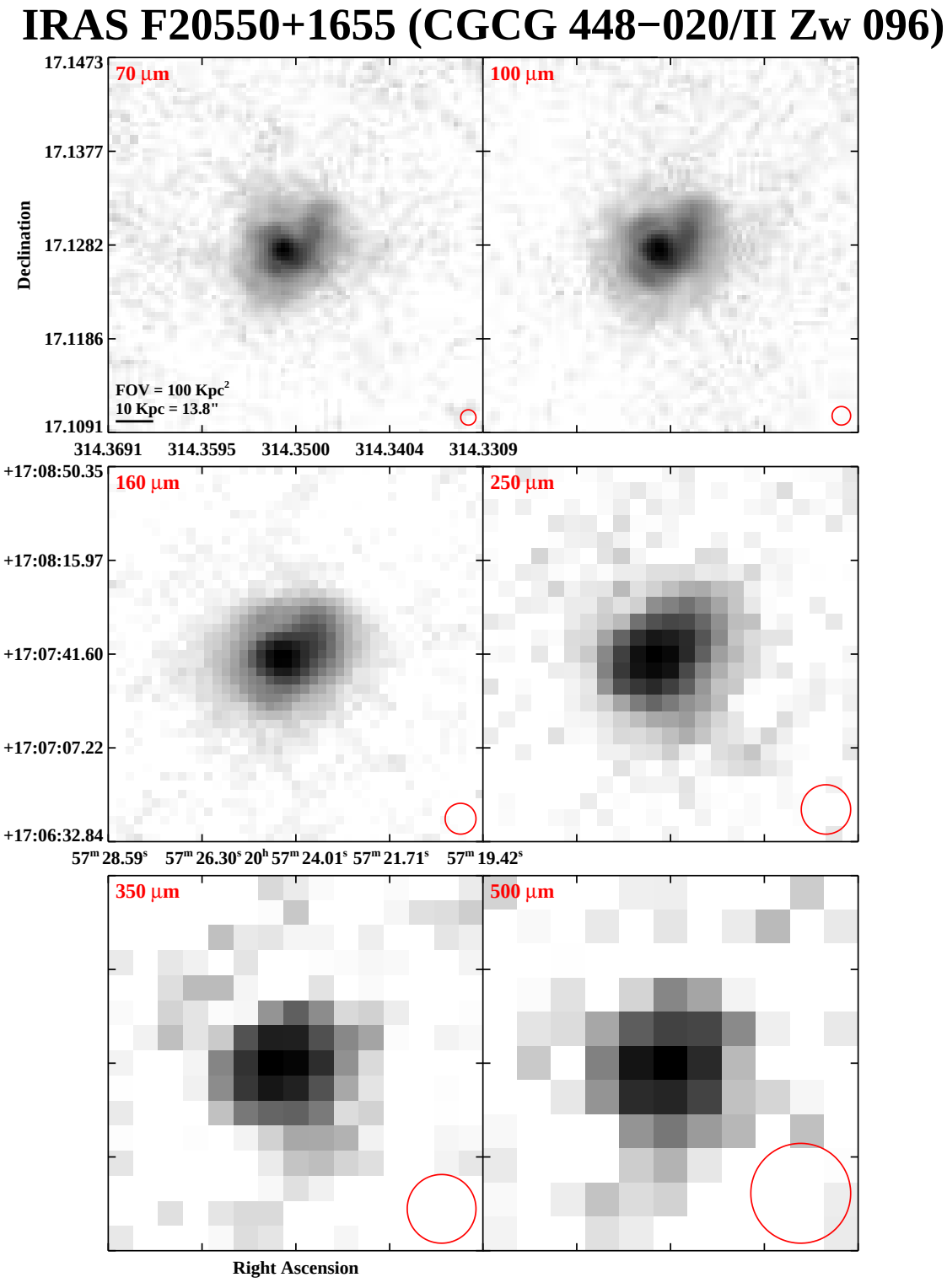

Figure 2.3 continued (page 180 of 209).

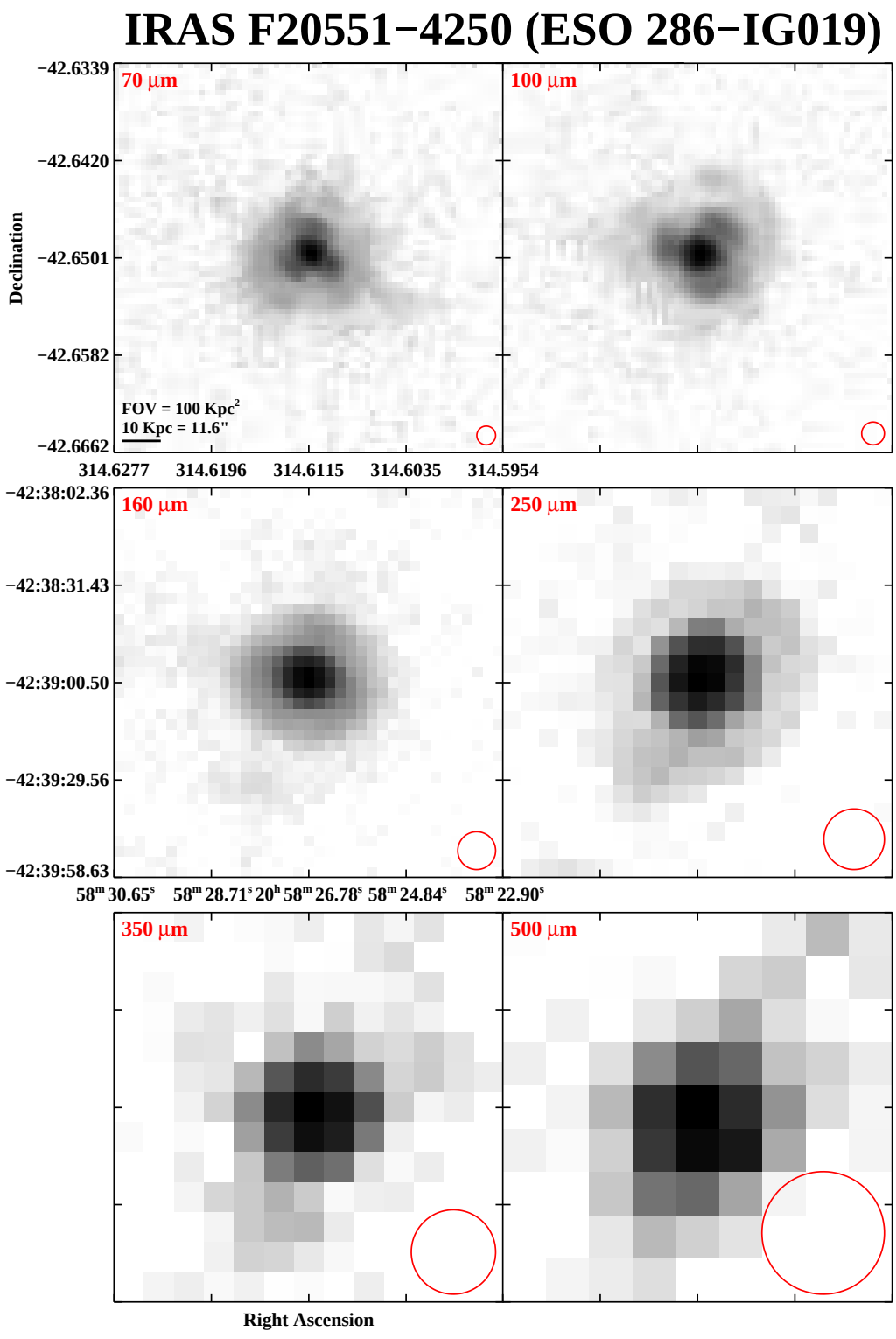

Figure 2.3 continued (page 181 of 209).

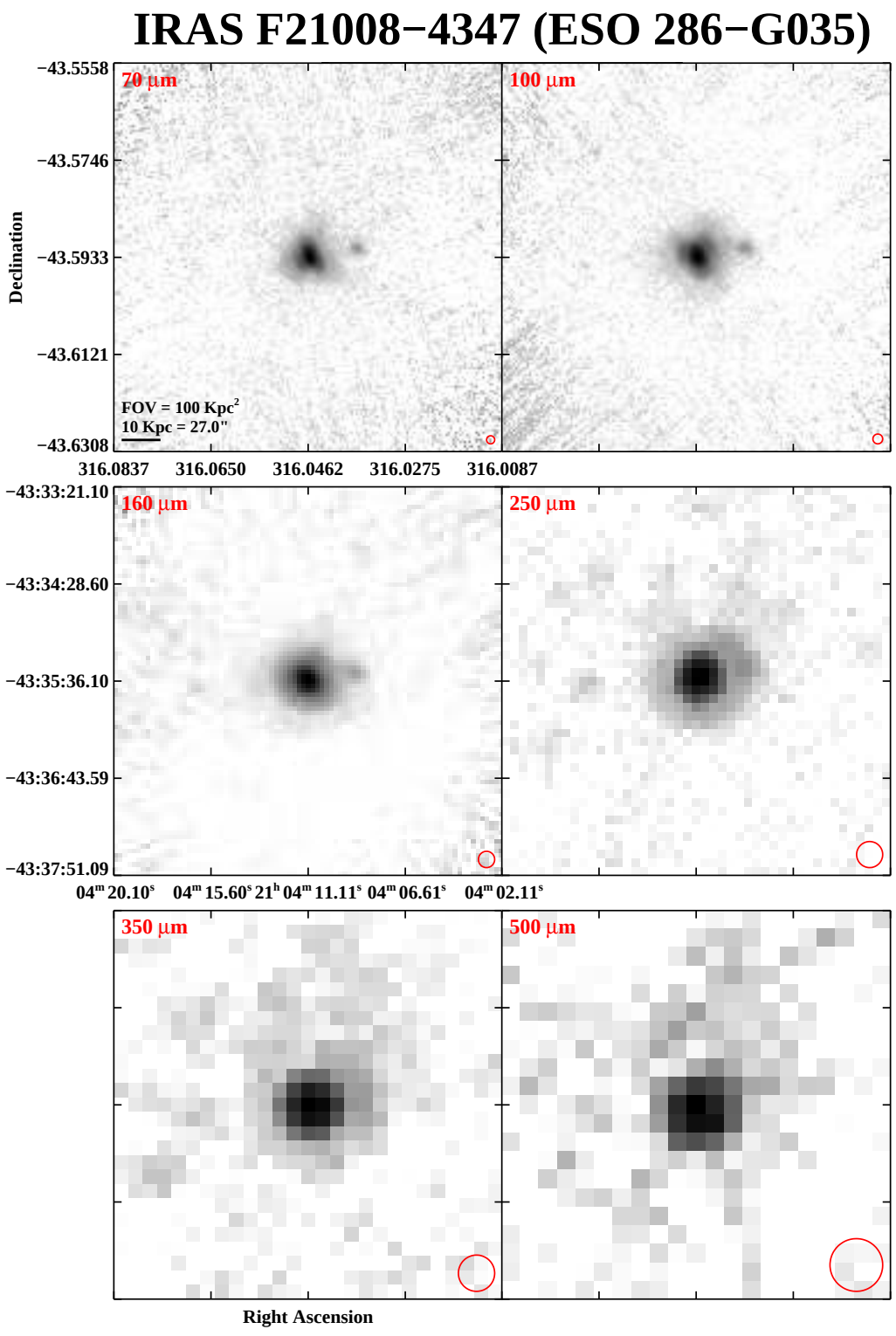

Figure 2.3 continued (page 182 of 209).

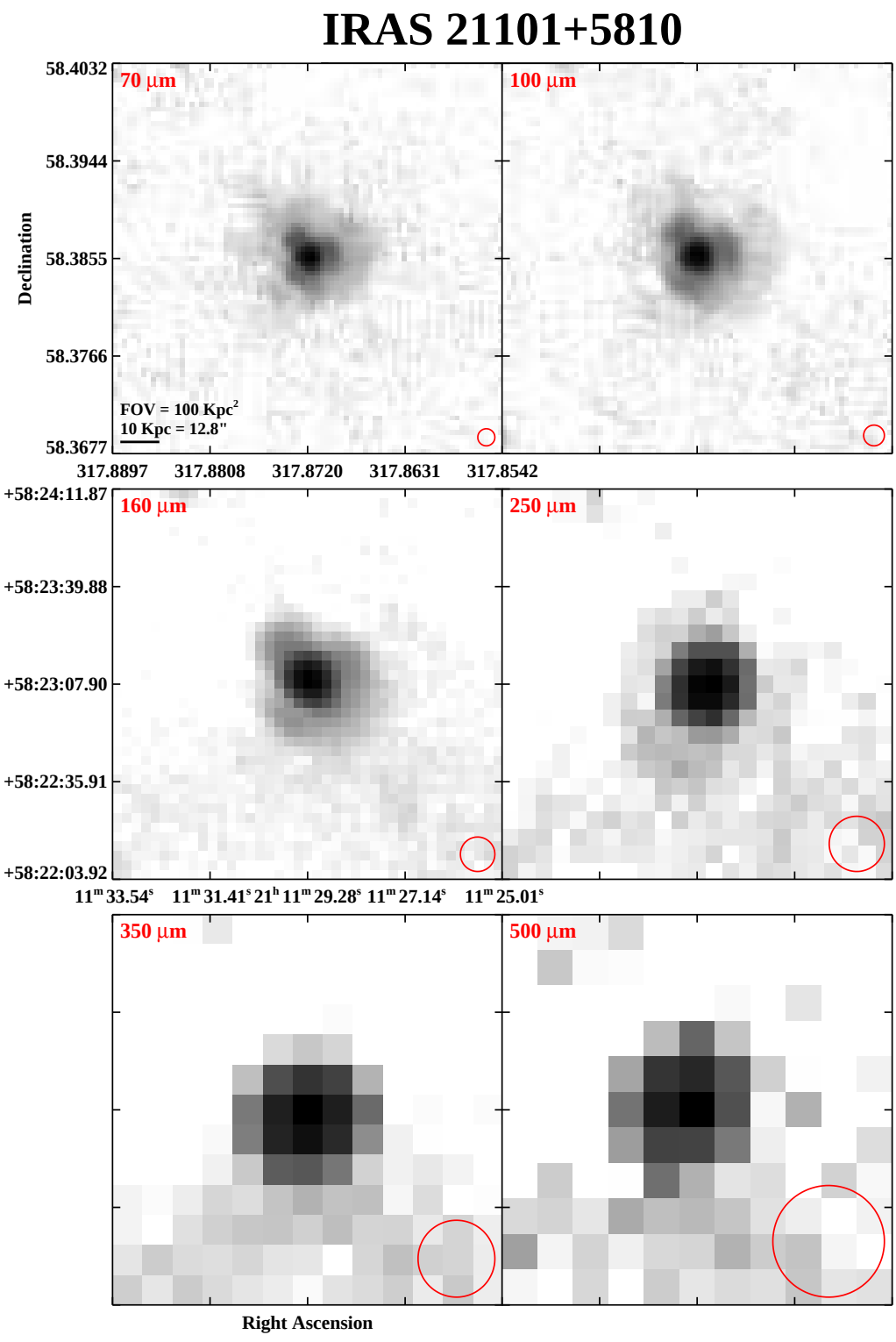

Figure 2.3 continued (page 183 of 209).

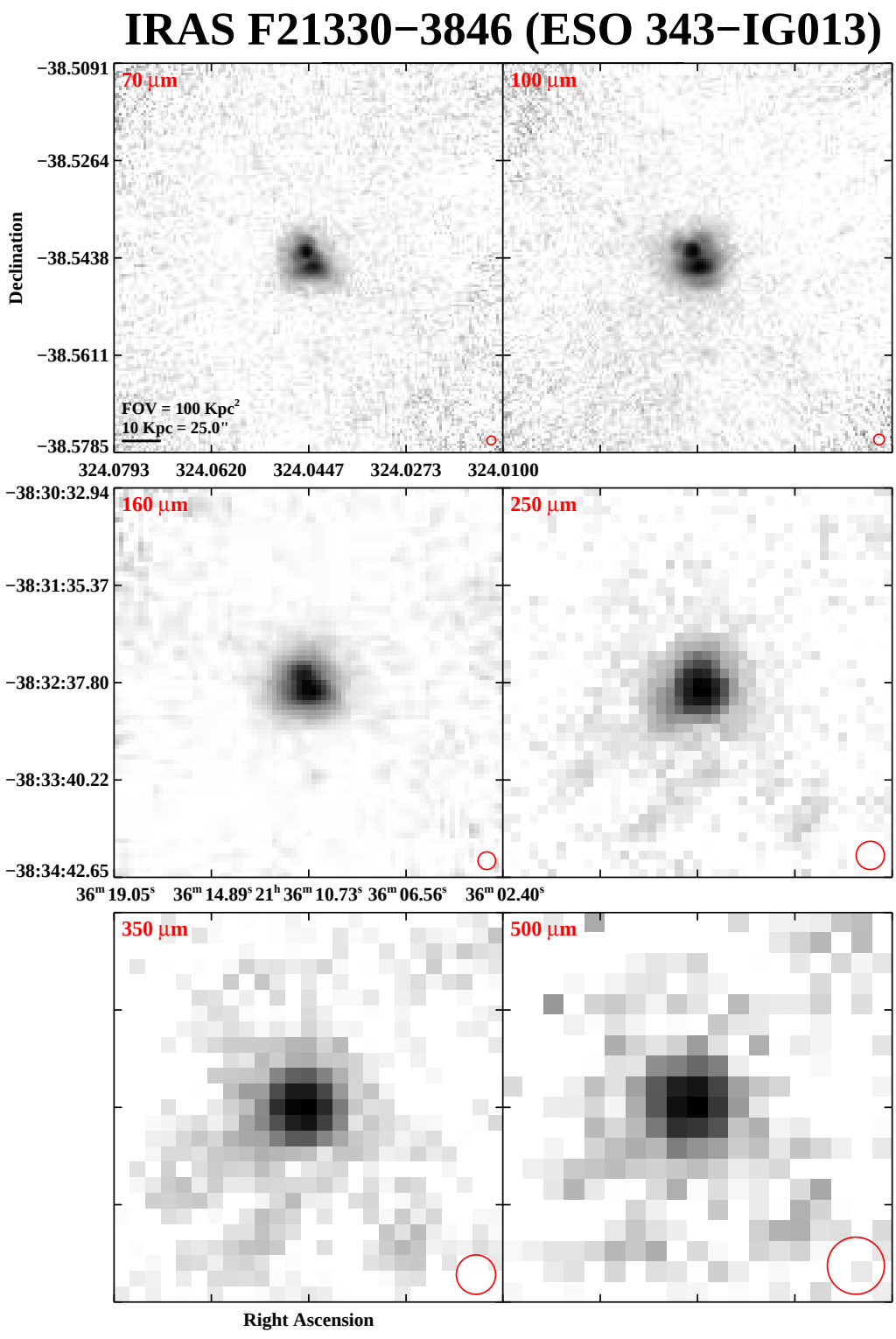

Figure 2.3 continued (page 184 of 209).

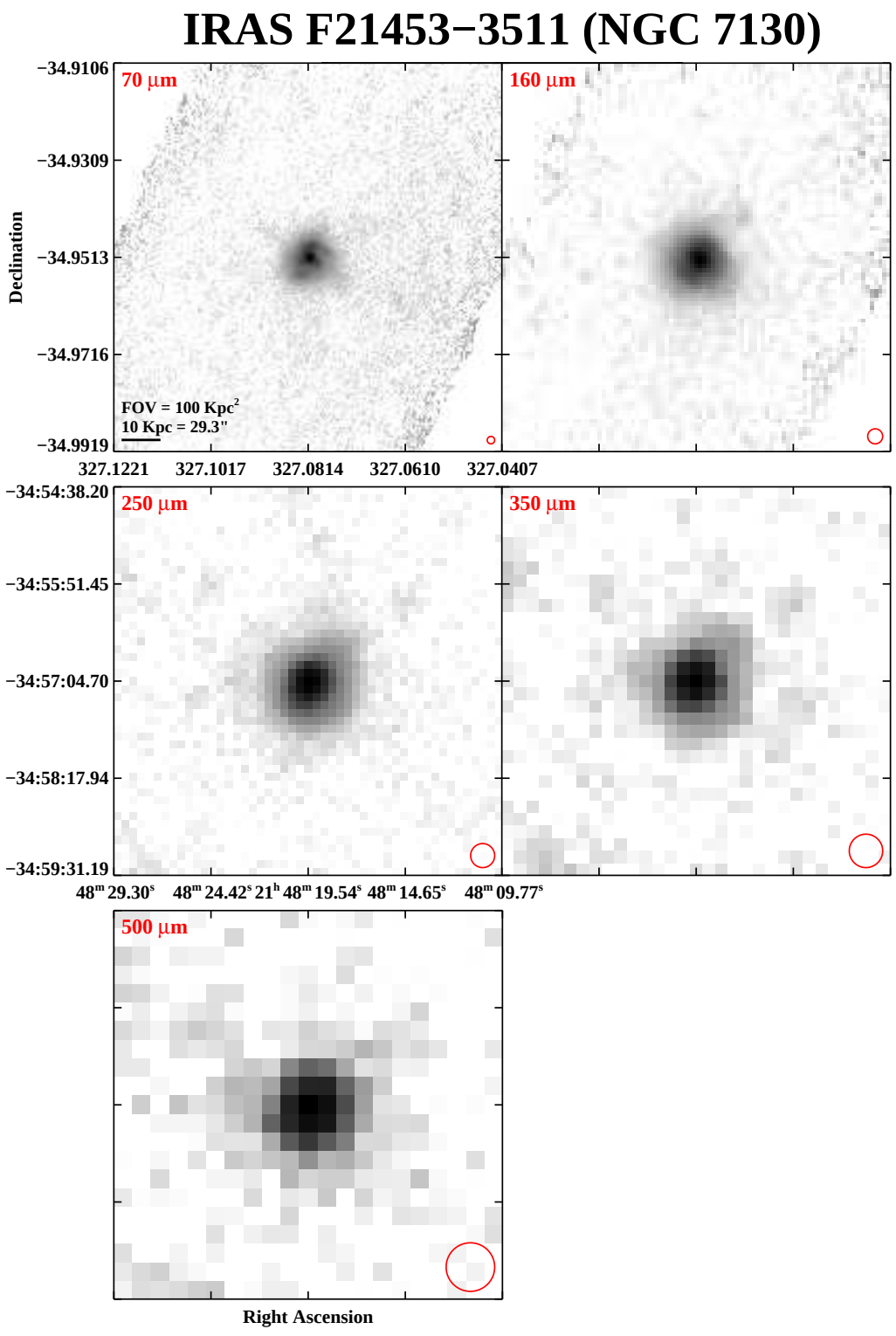

Figure 2.3 continued (page 185 of 209).

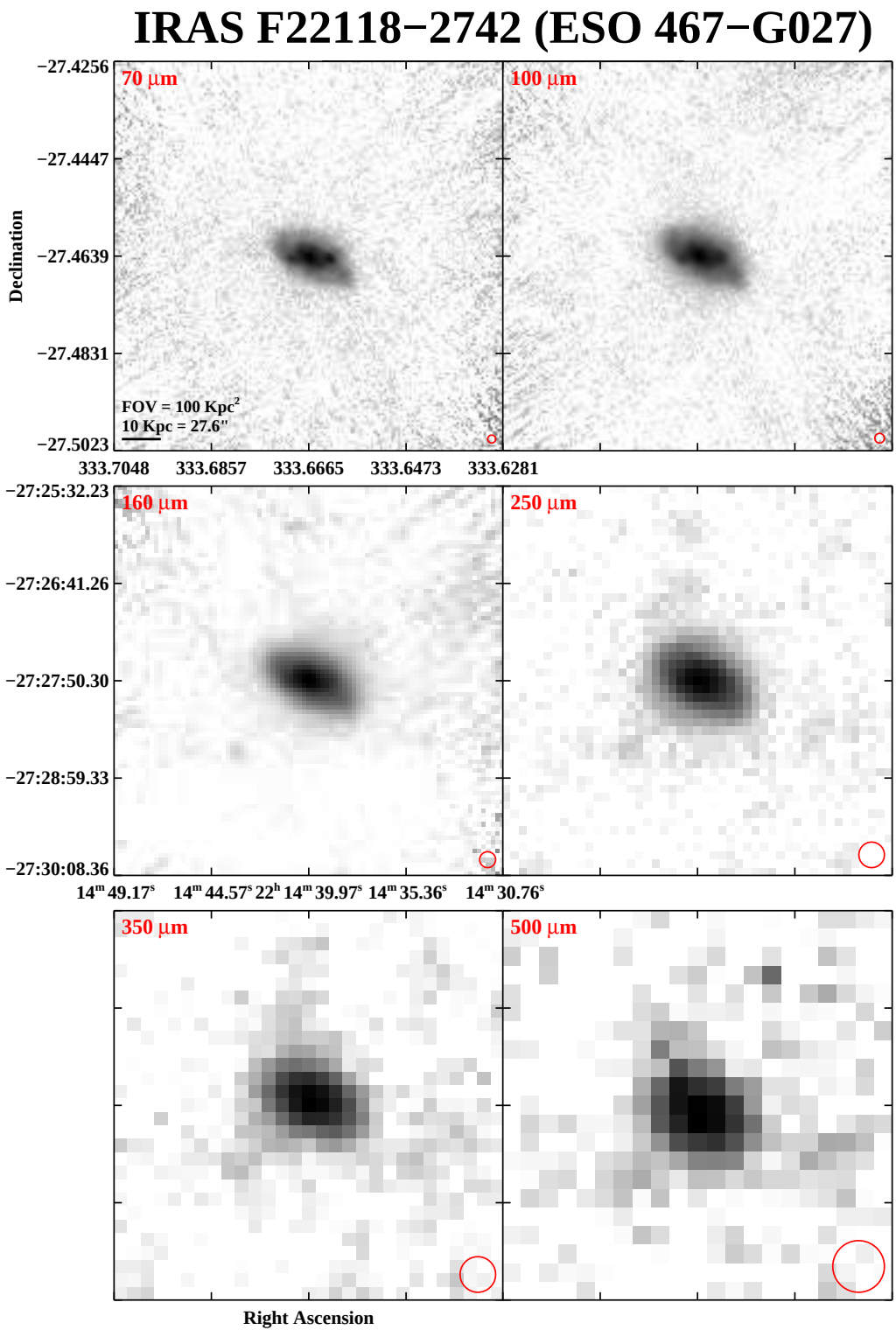

Figure 2.3 continued (page 186 of 209).

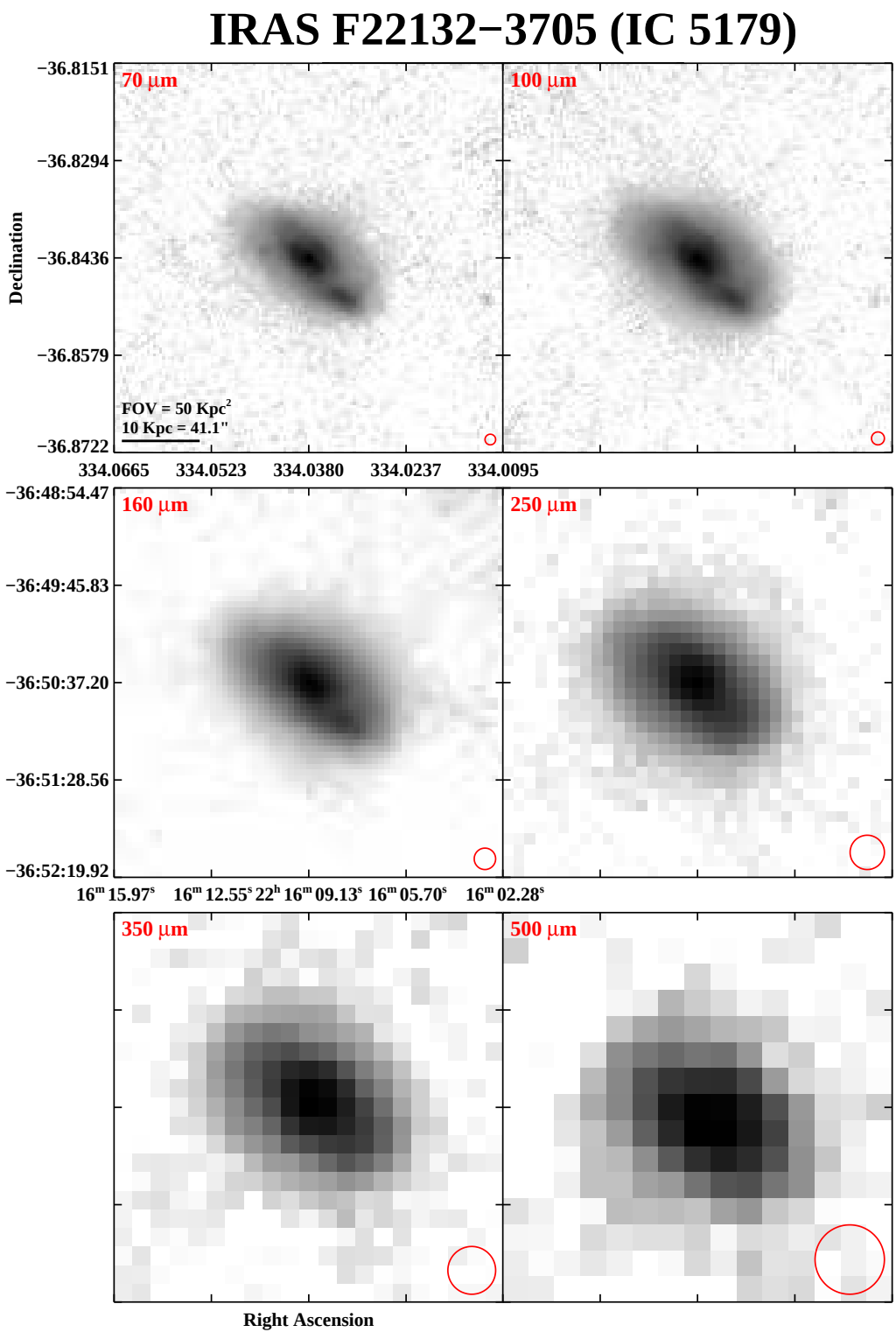

Figure 2.3 continued (page 187 of 209).

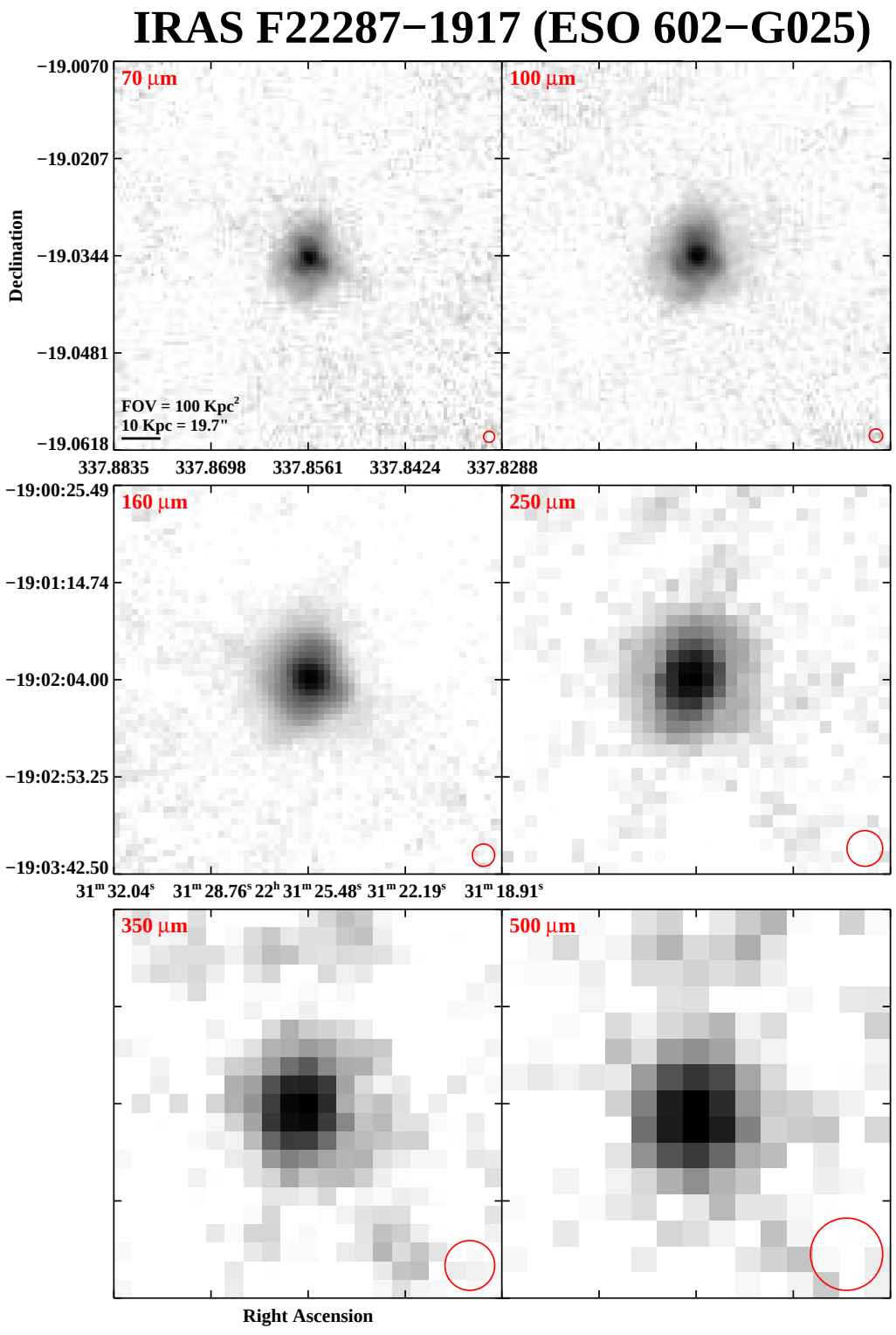

Figure 2.3 continued (page 188 of 209).

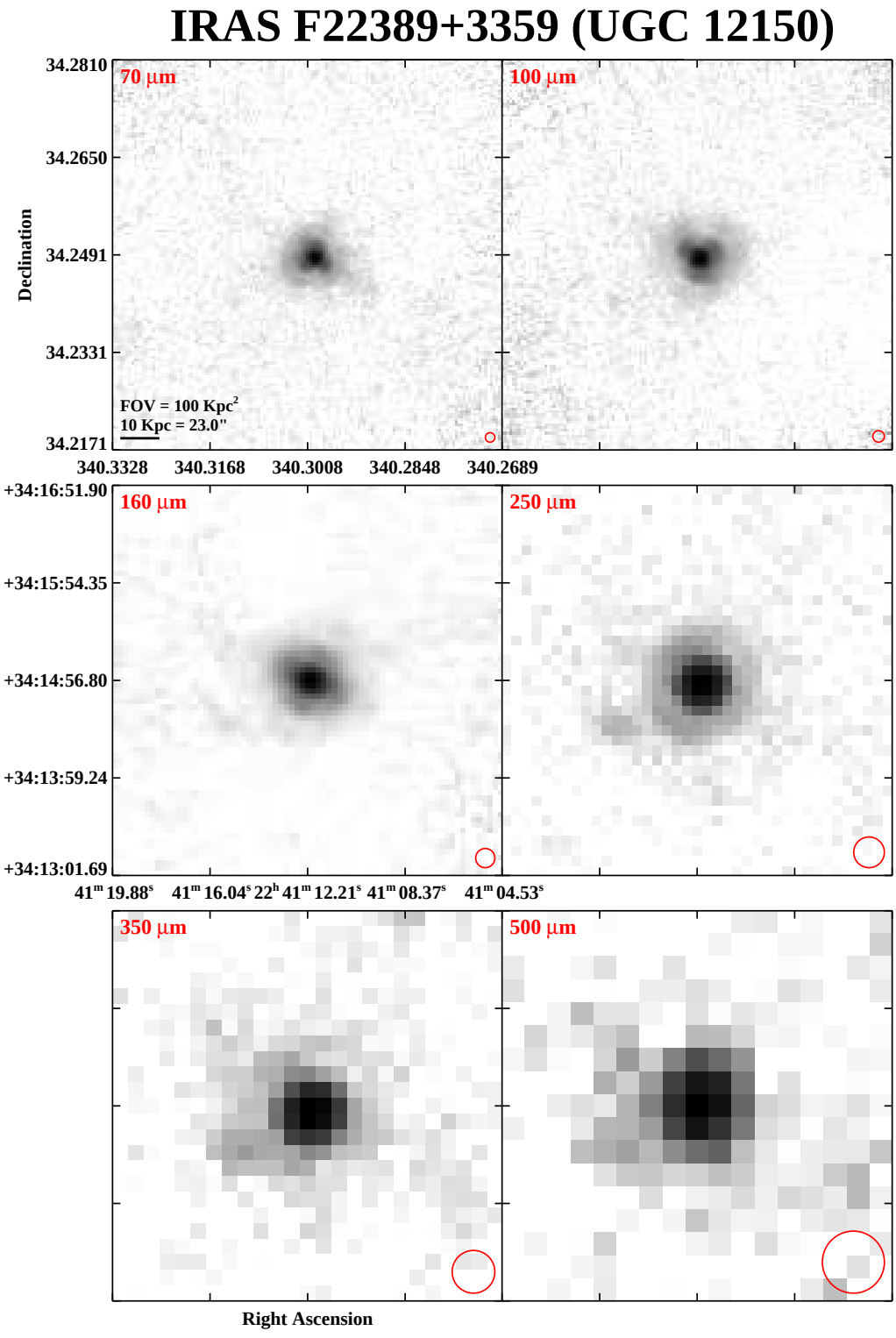

Figure 2.3 continued (page 189 of 209).

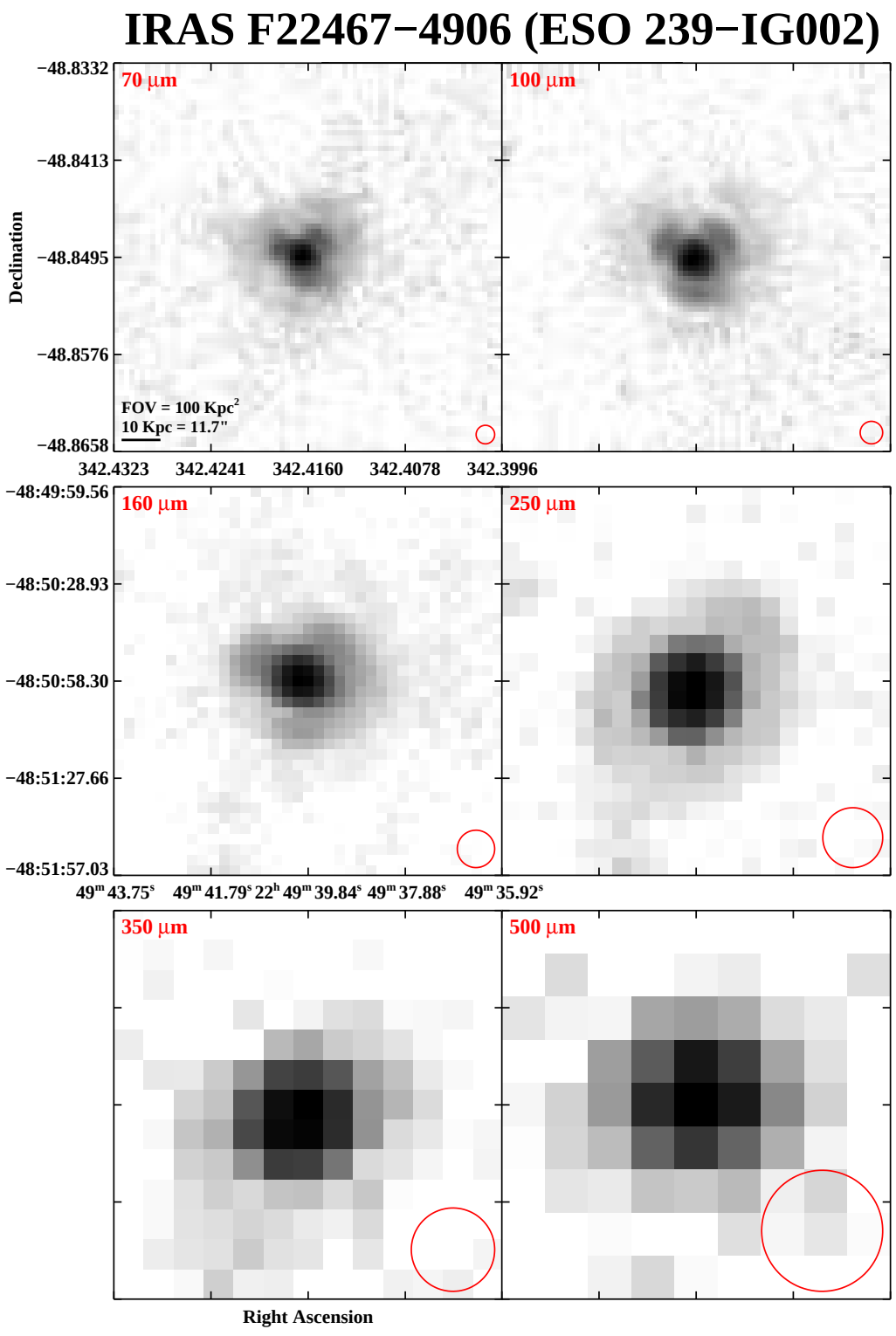

Figure 2.3 continued (page 190 of 209).

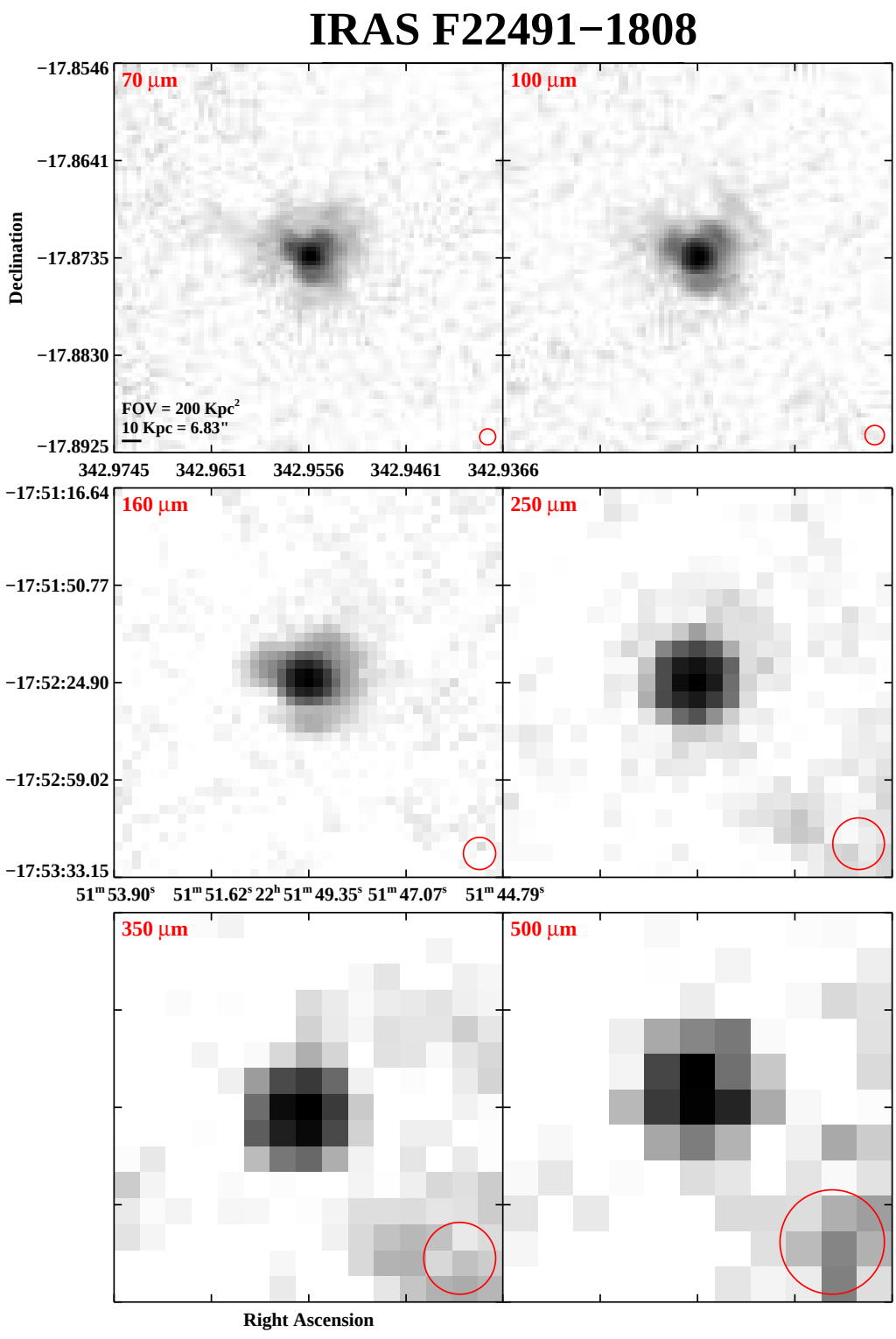

Figure 2.3 continued (page 191 of 209).

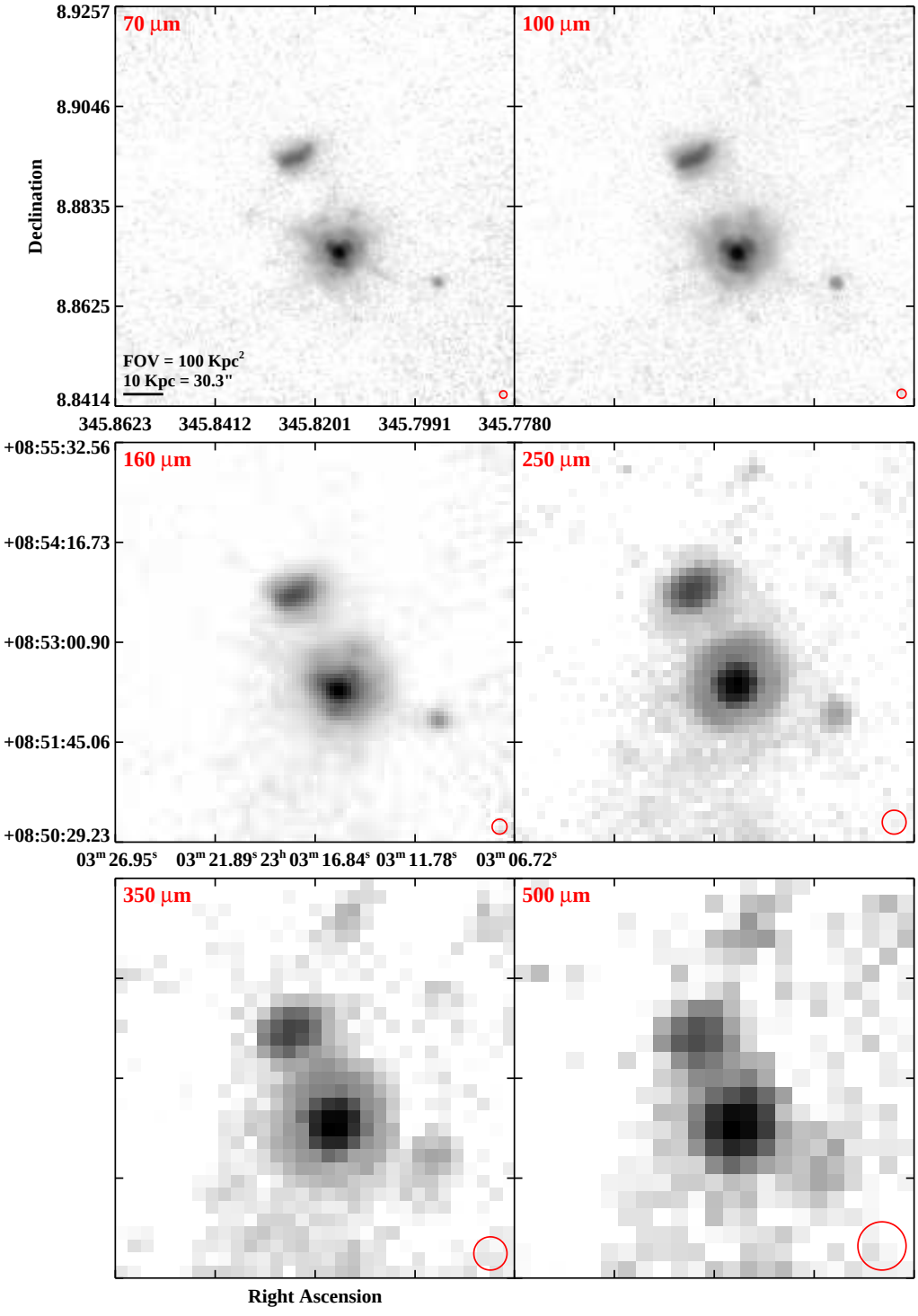

Figure 2.3 continued (page 192 of 209).

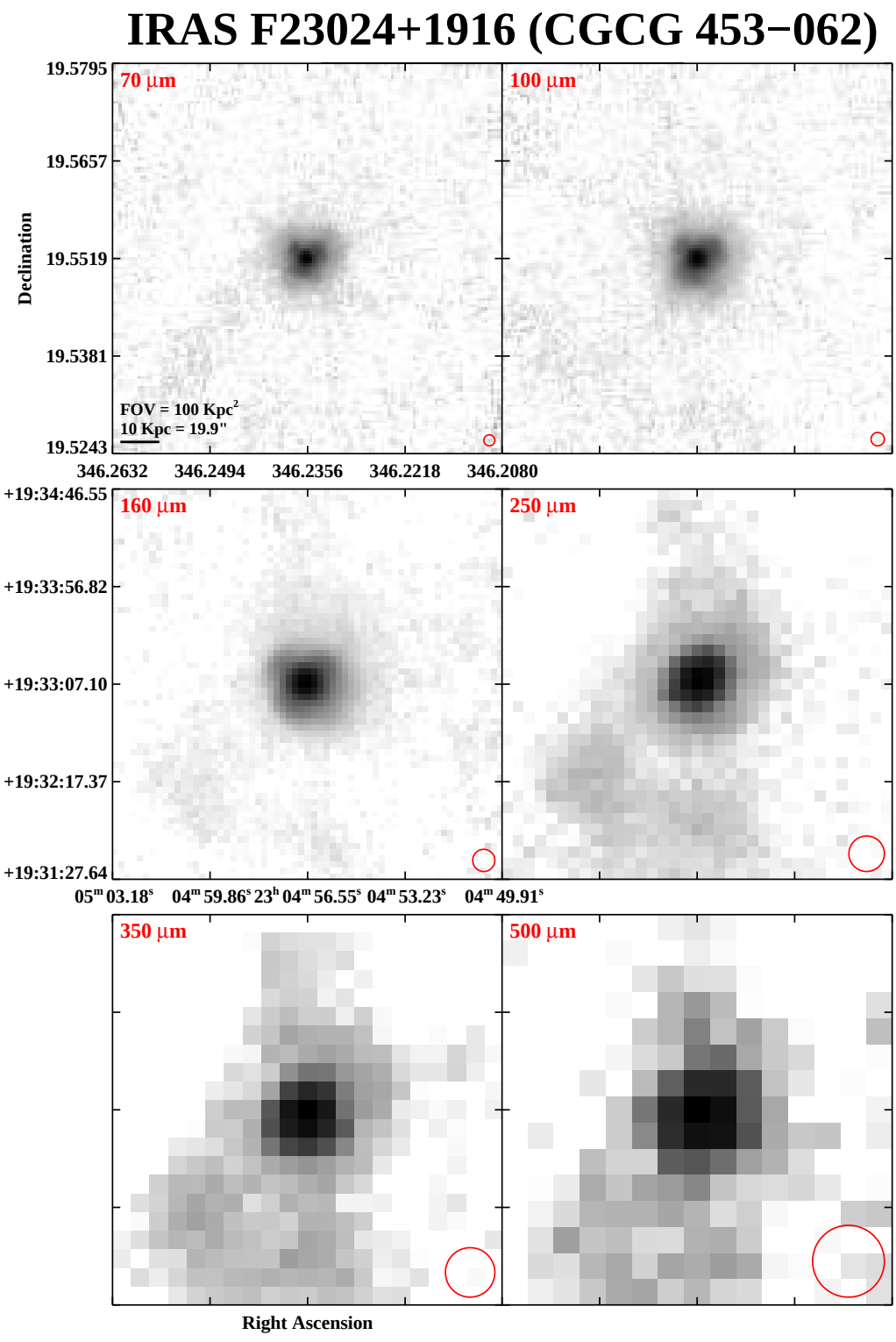

Figure 2.3 continued (page 193 of 209).

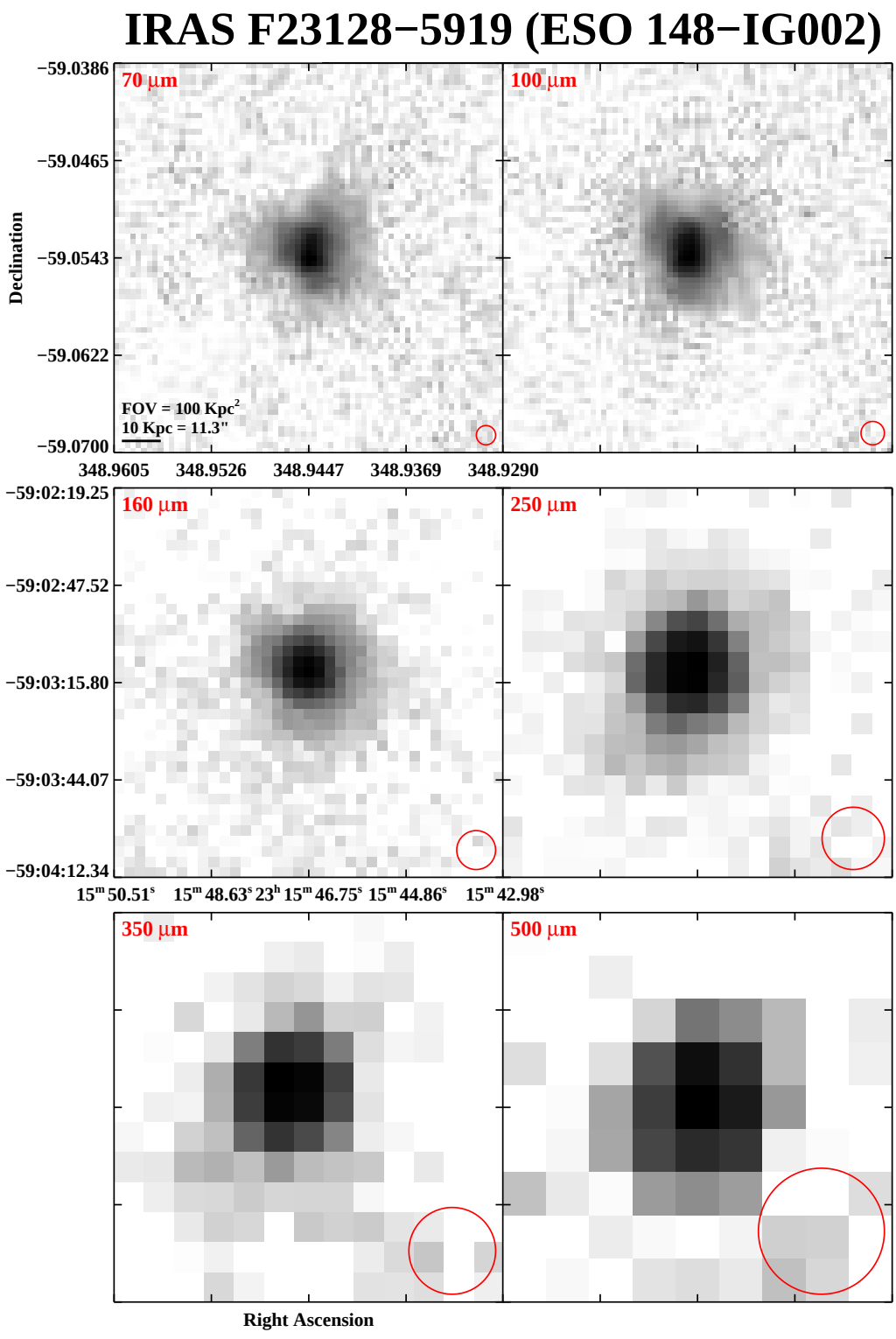

Figure 2.3 continued (page 194 of 209).

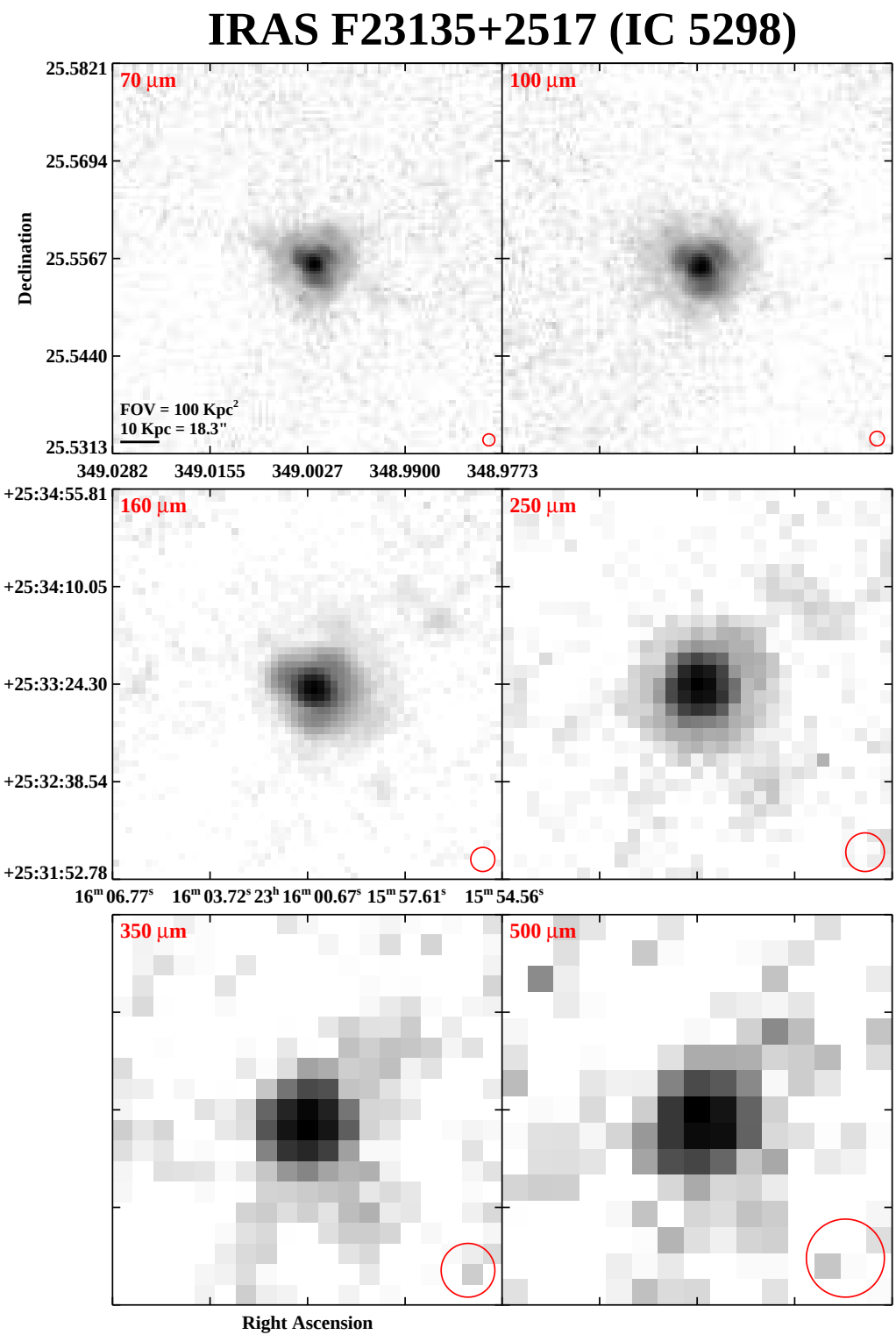

Figure 2.3 continued (page 195 of 209).

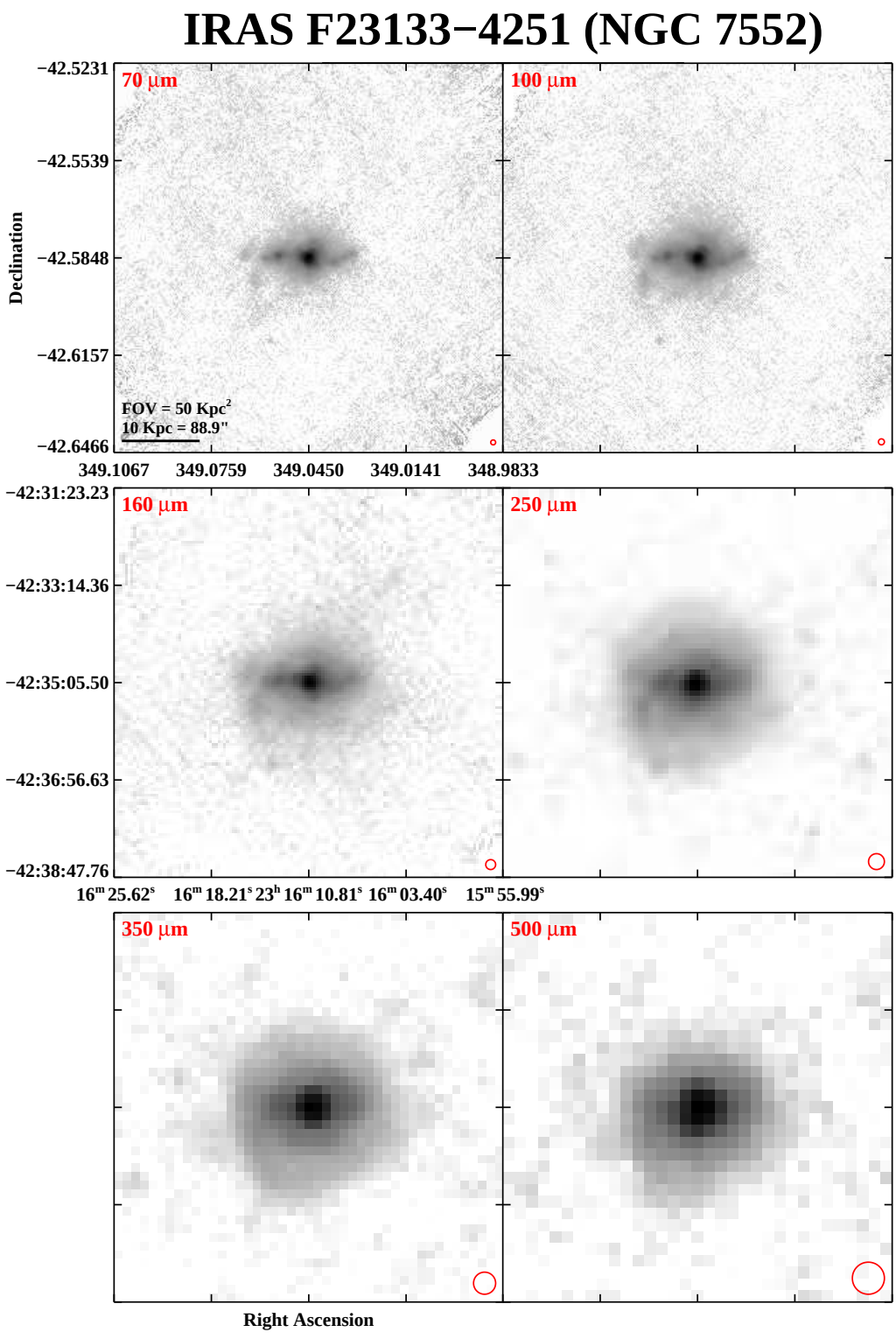

Figure 2.3 continued (page 196 of 209).

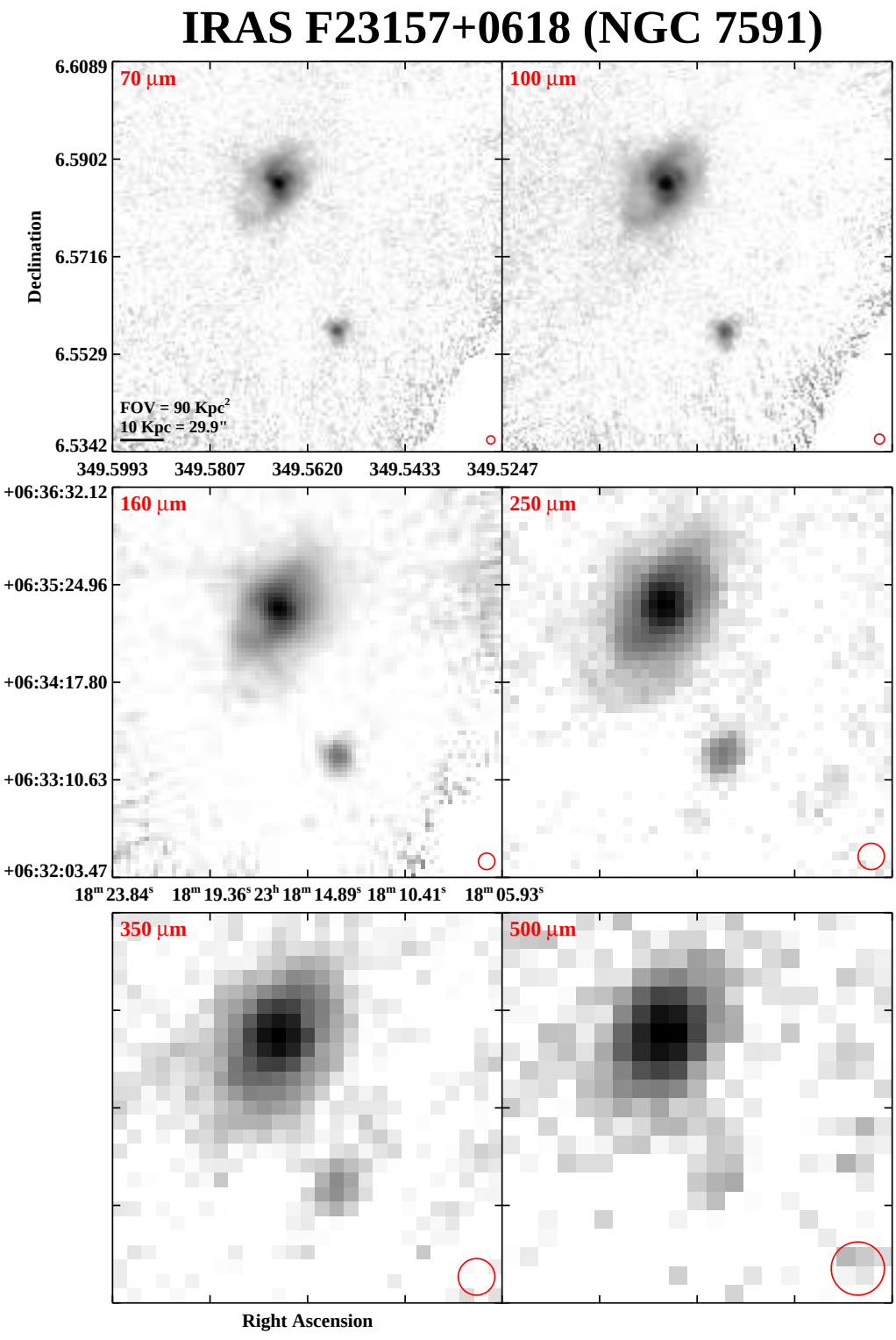

Figure 2.3 continued (page 197 of 209).

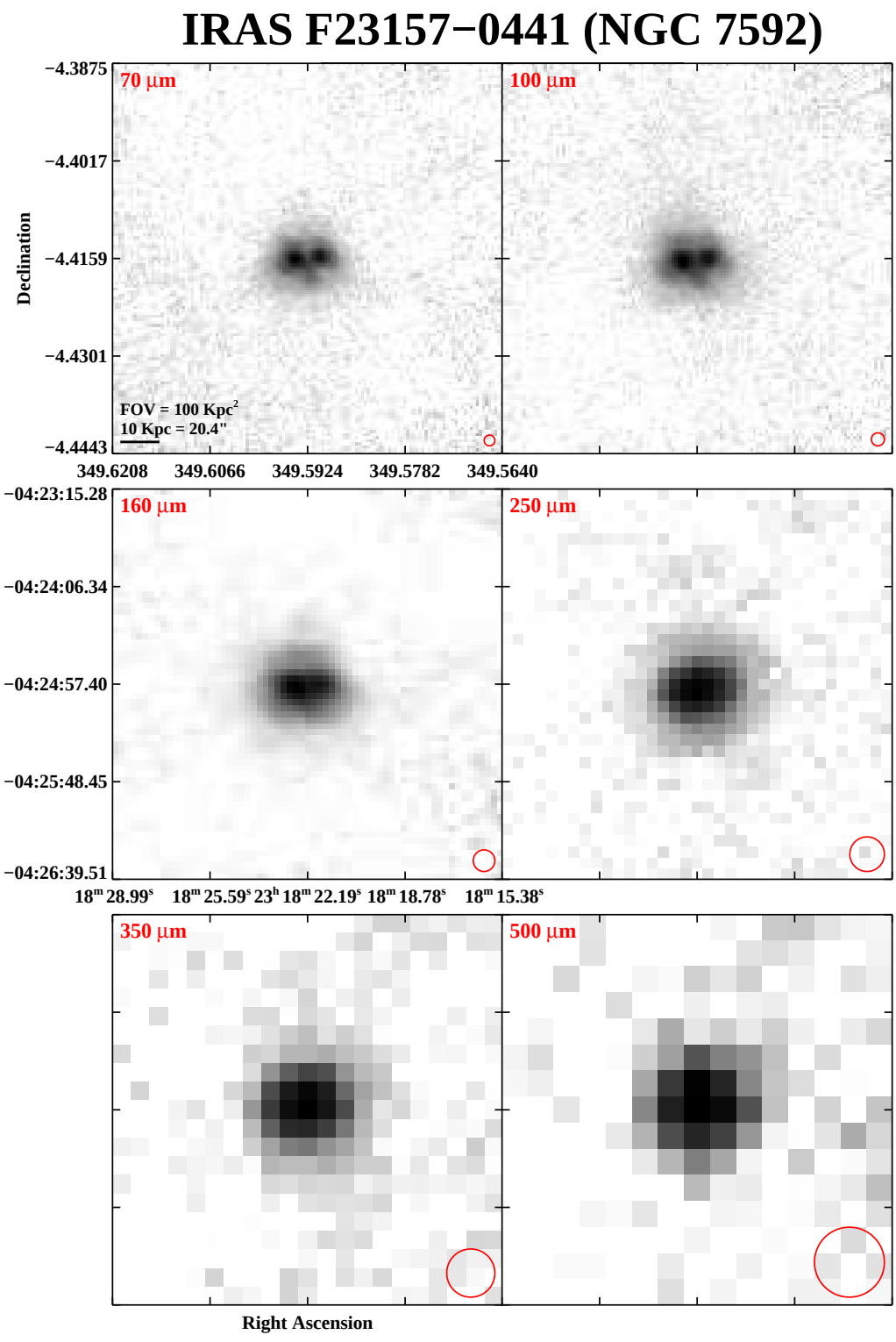

Figure 2.3 continued (page 198 of 209).

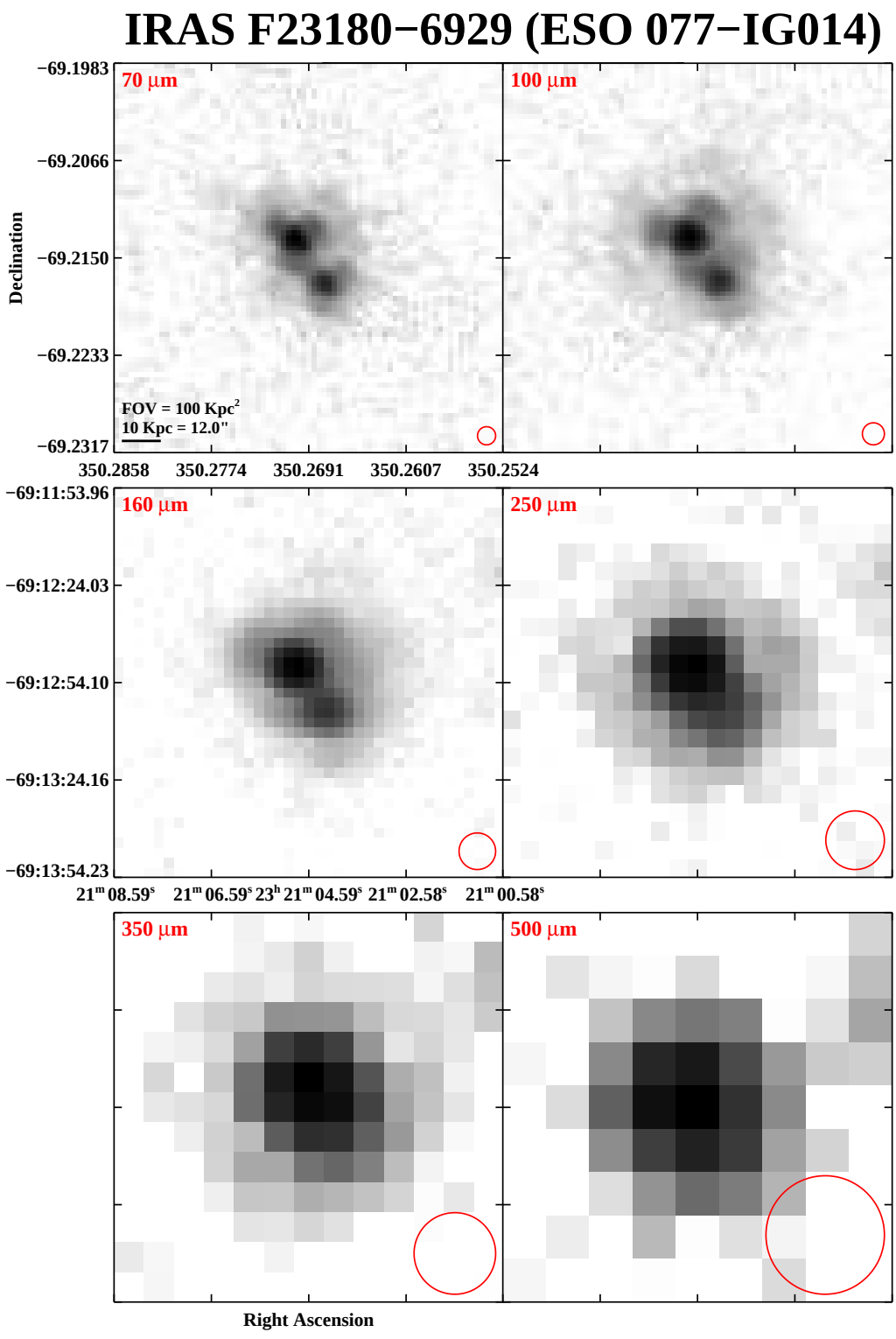

Figure 2.3 continued (page 199 of 209).

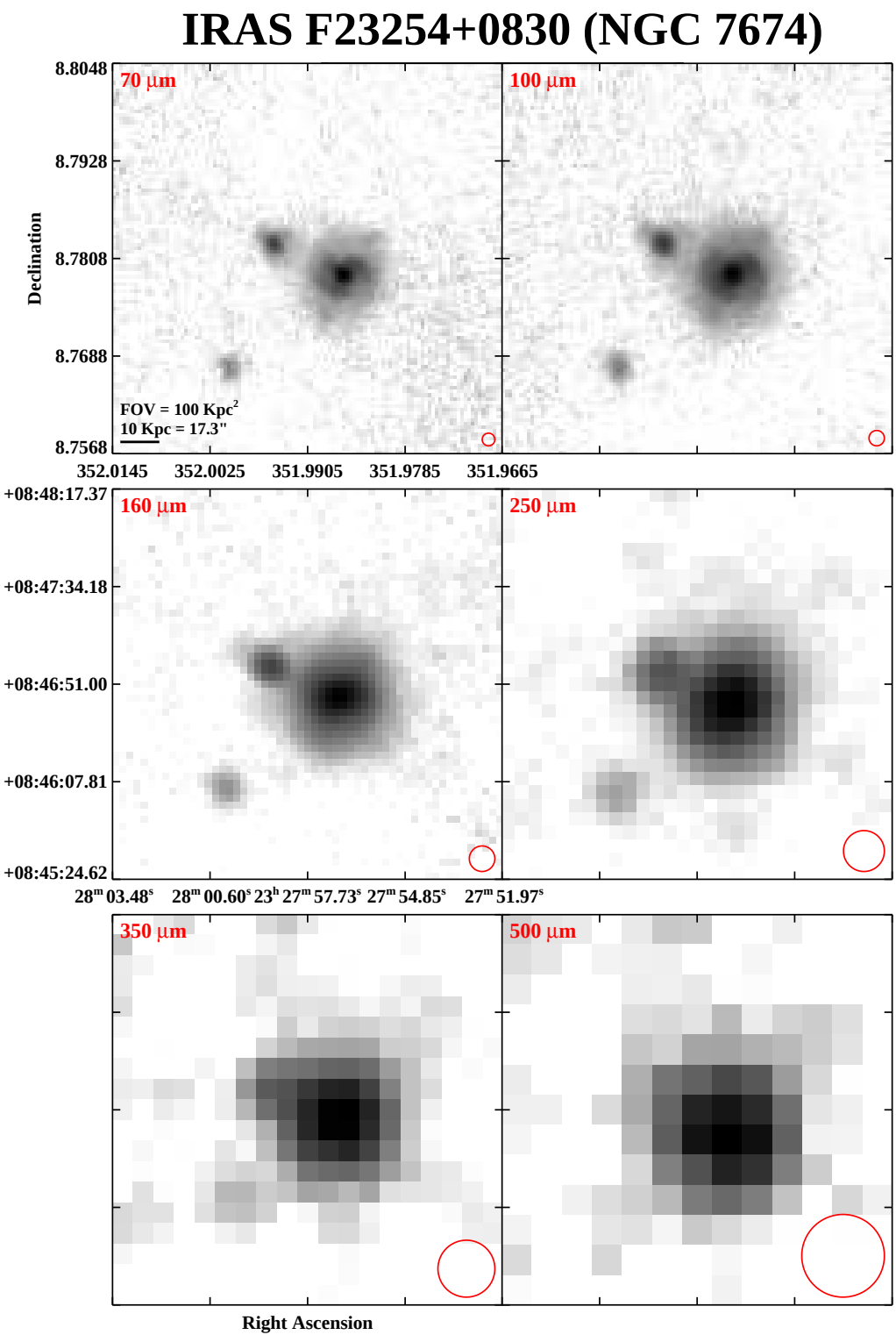

Figure 2.3 continued (page 200 of 209).

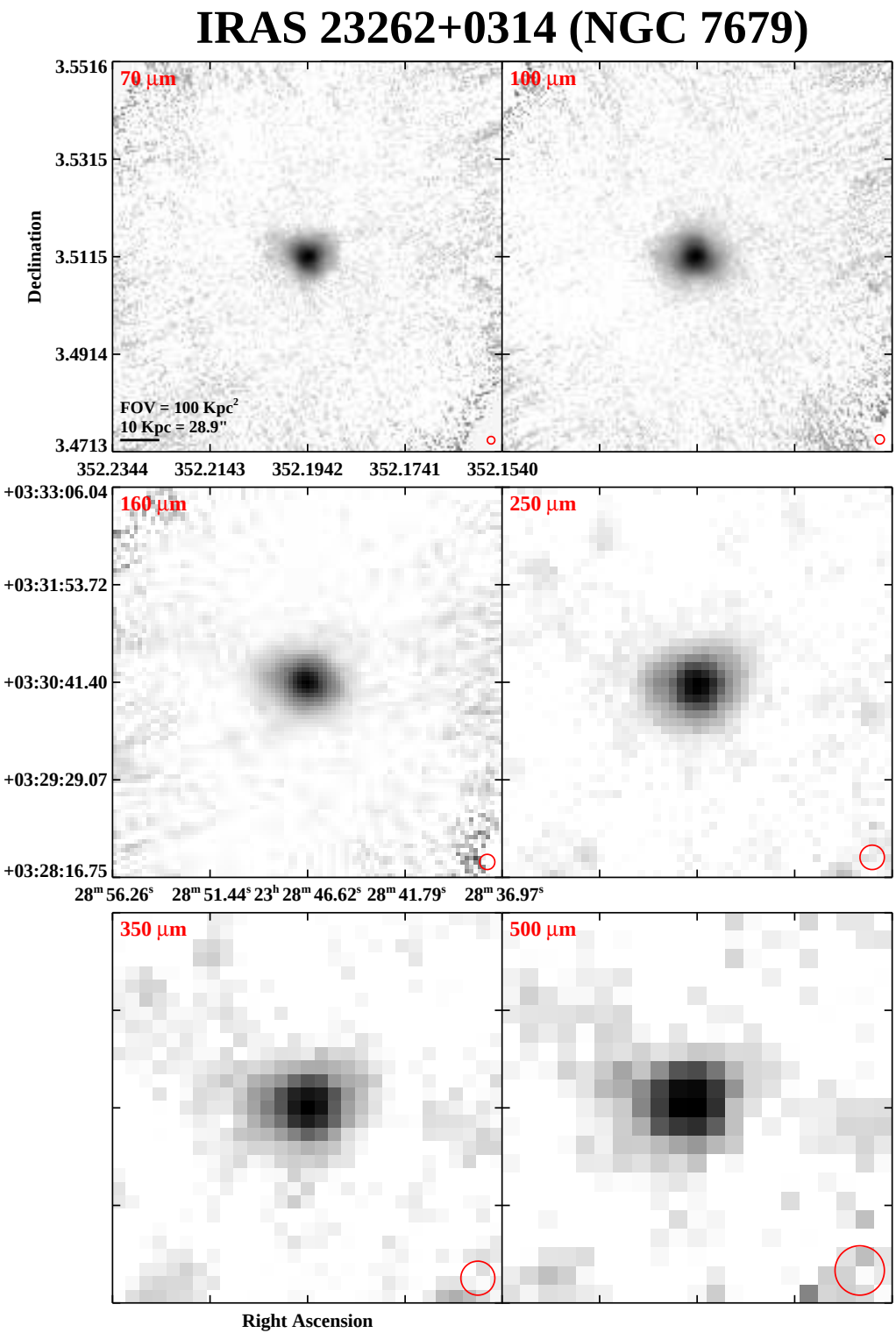

Figure 2.3 continued (page 201 of 209).

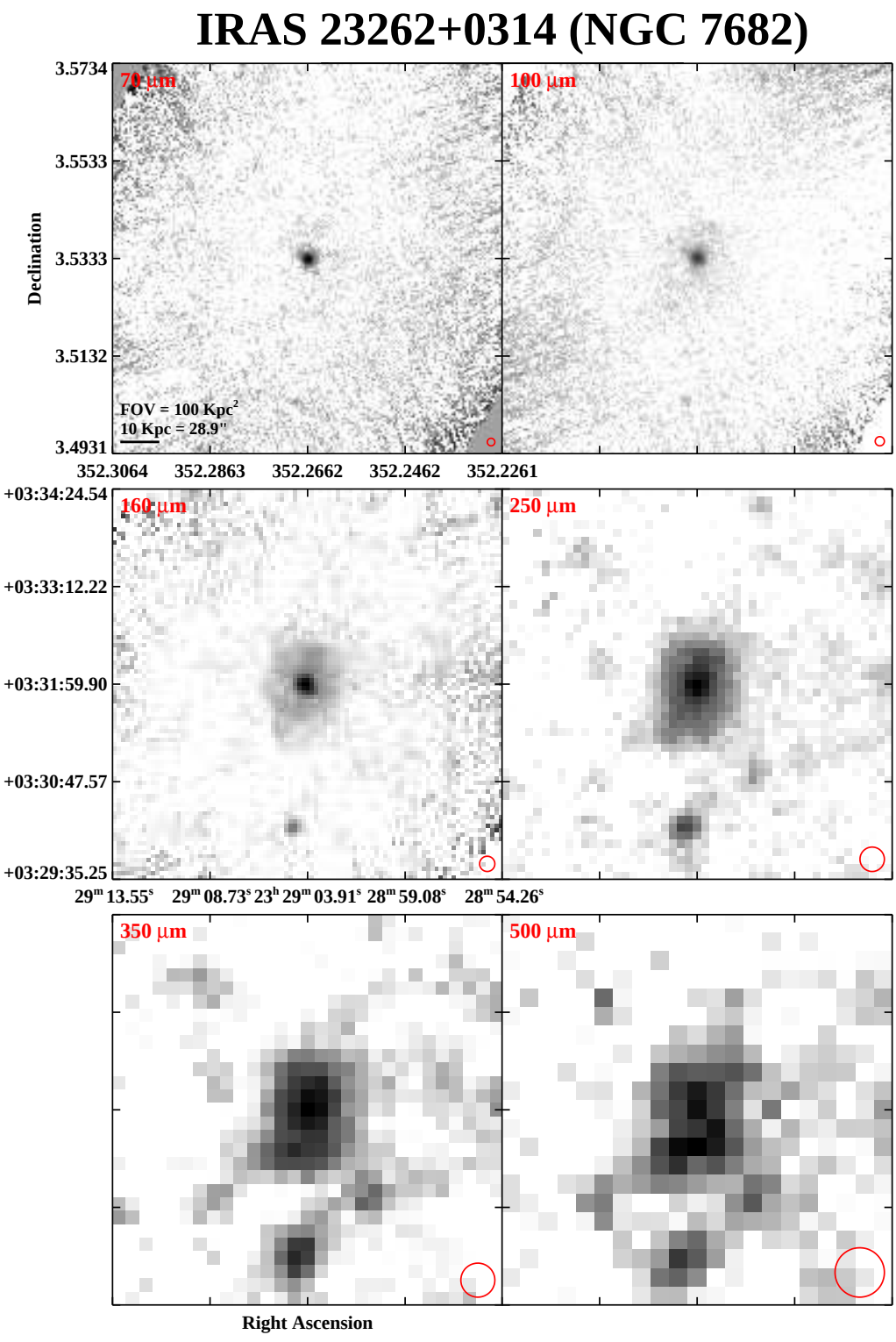

Figure 2.3 continued (page 202 of 209).

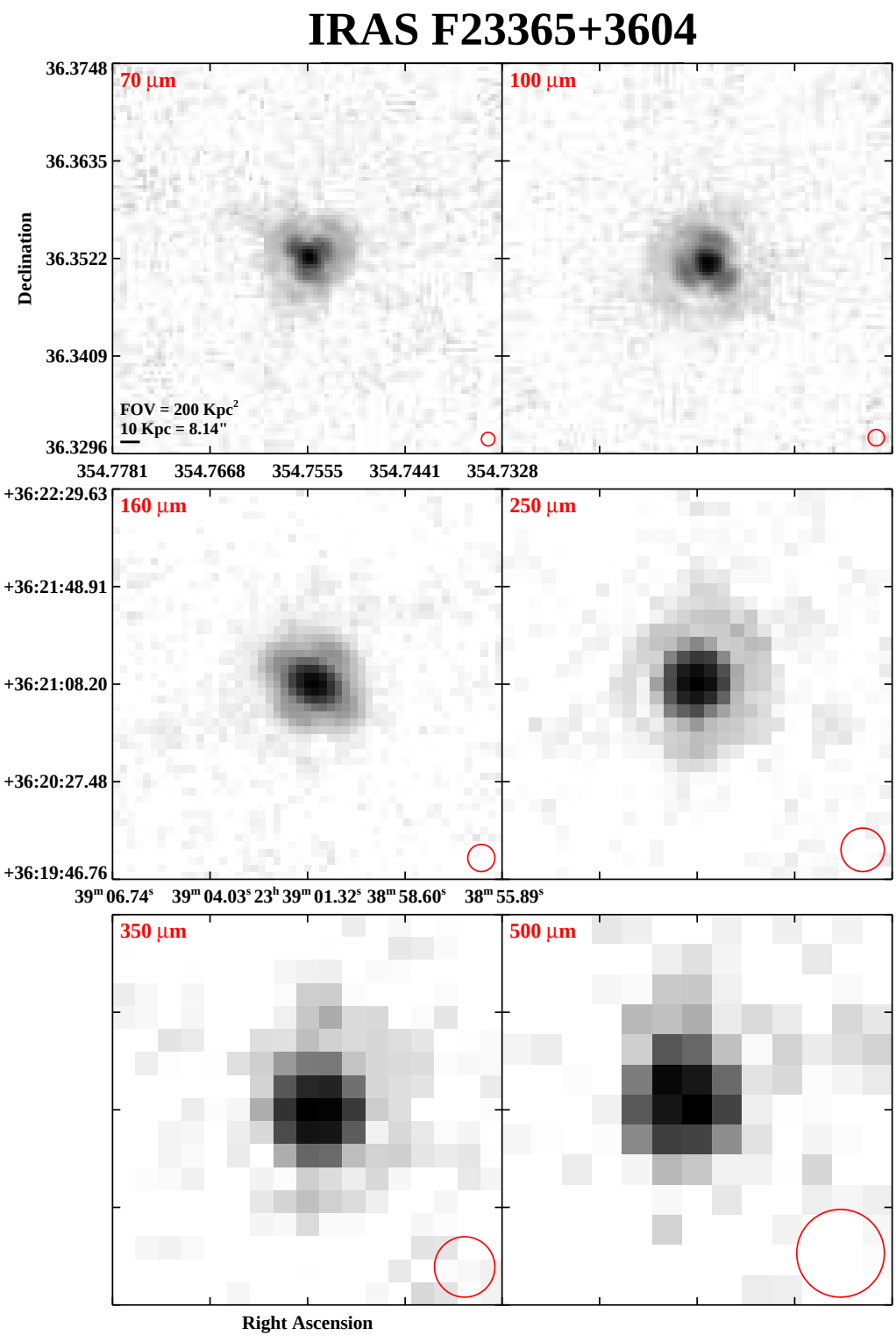

Figure 2.3 continued (page 203 of 209).

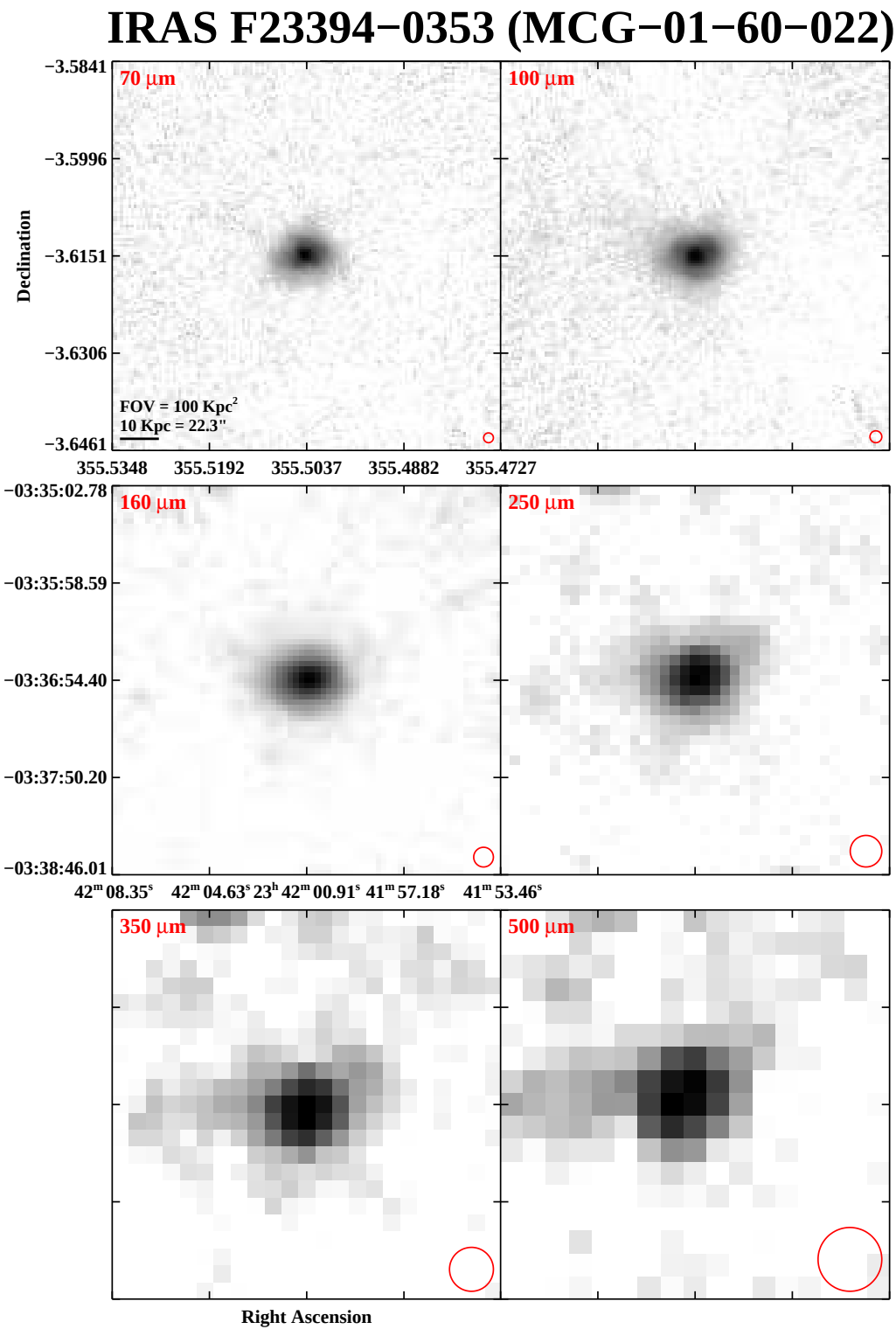

Figure 2.3 continued (page 204 of 209).

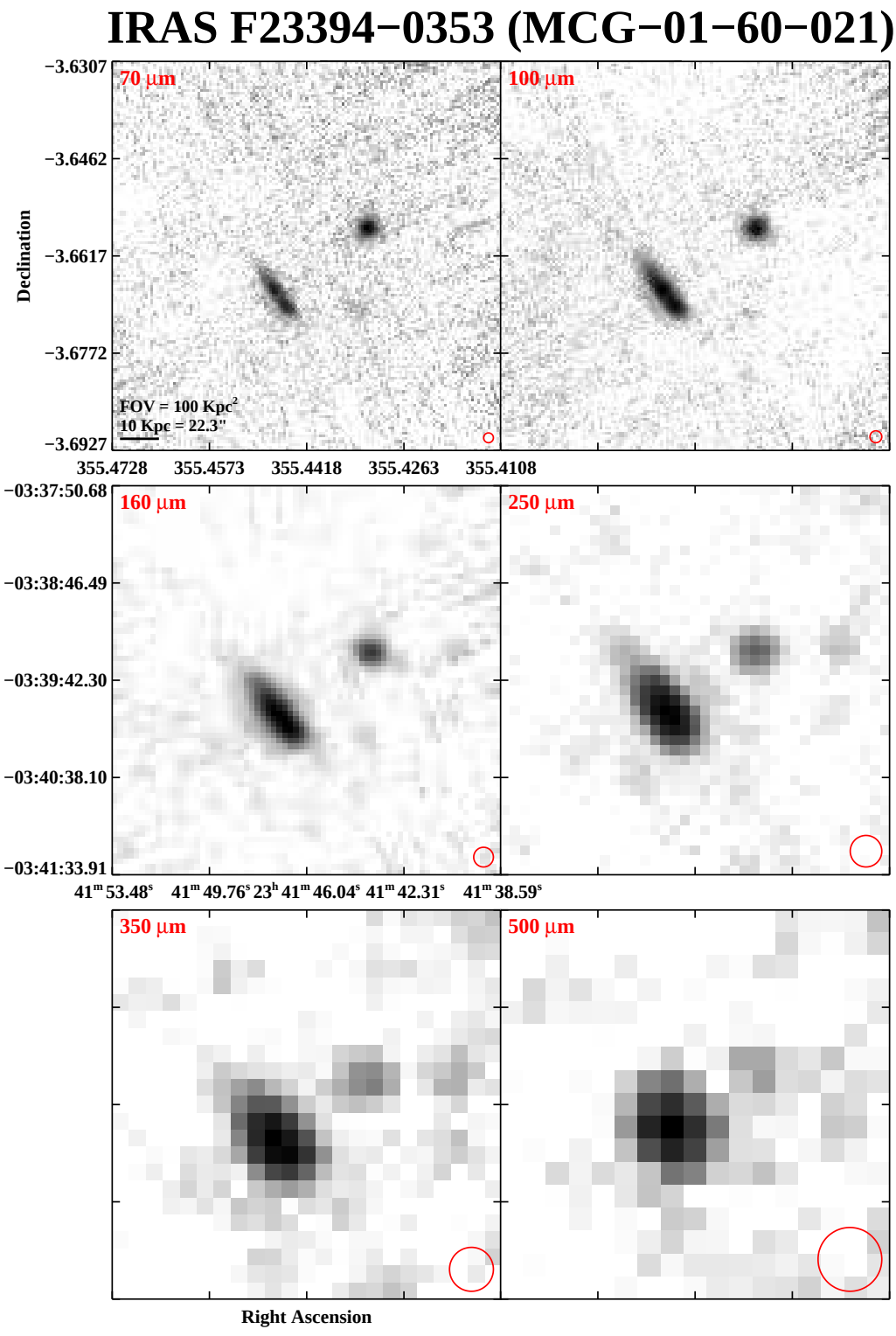

Figure 2.3 continued (page 205 of 209).

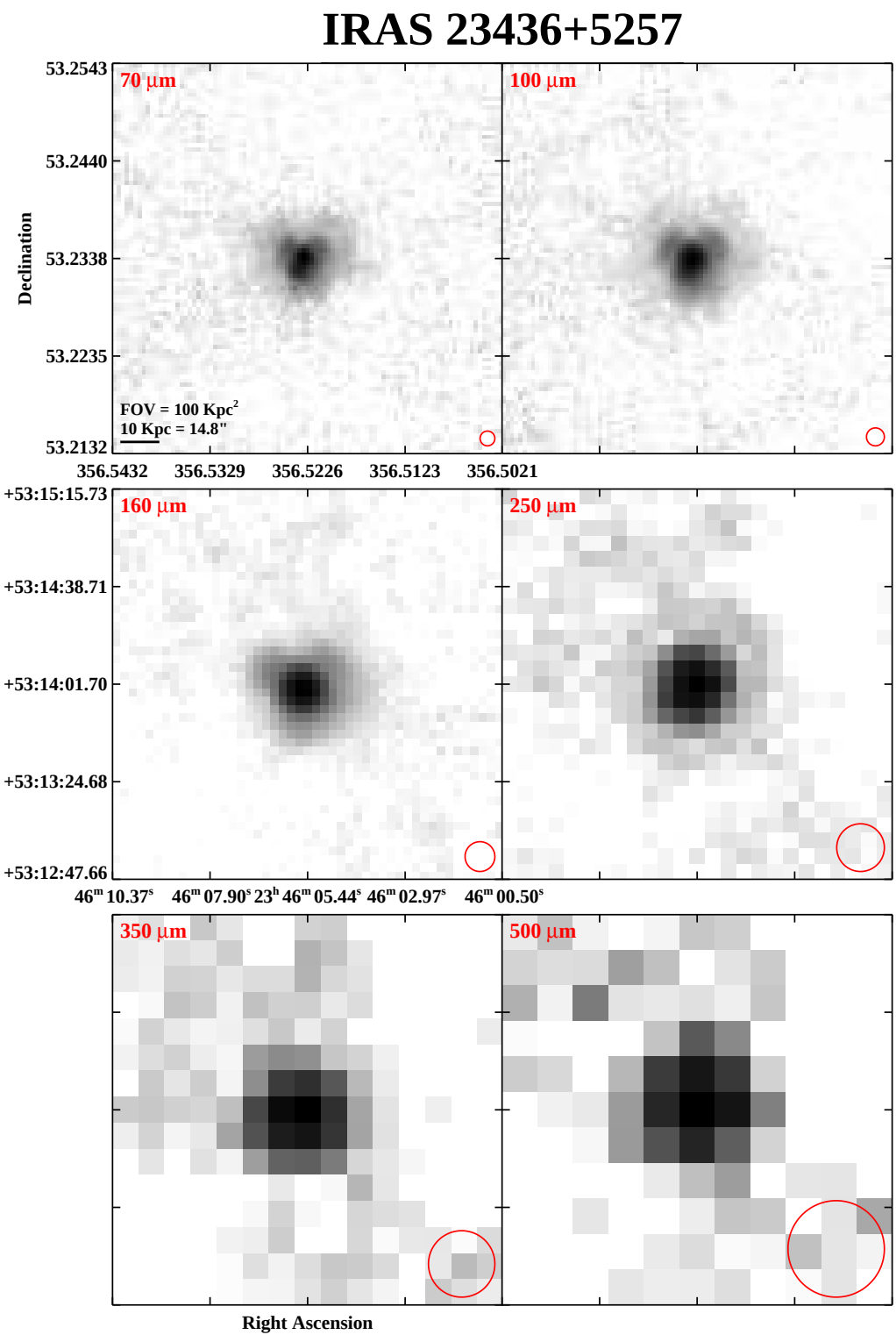

Figure 2.3 continued (page 206 of 209).

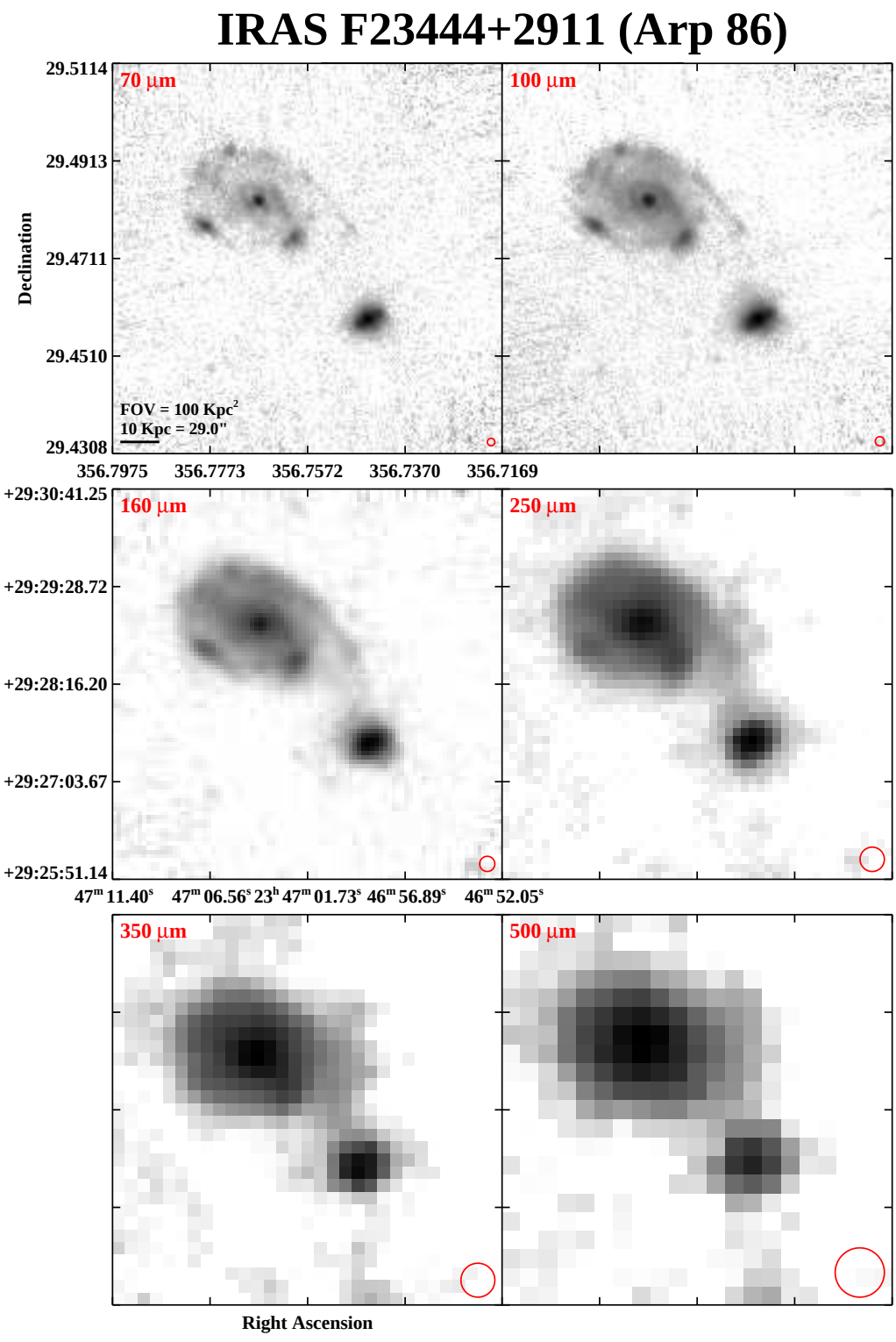

Figure 2.3 continued (page 207 of 209).

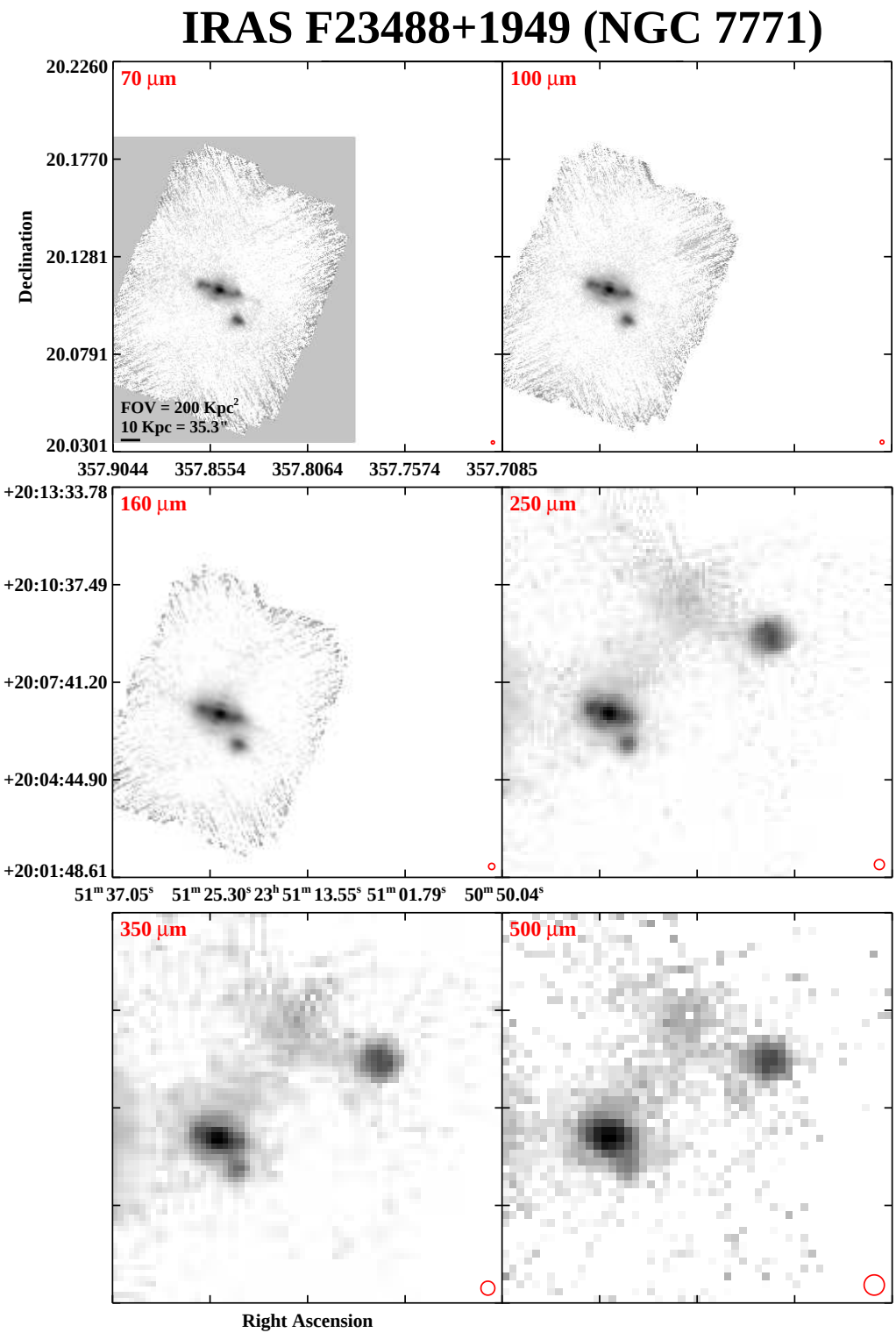

Figure 2.3 continued (page 208 of 209).

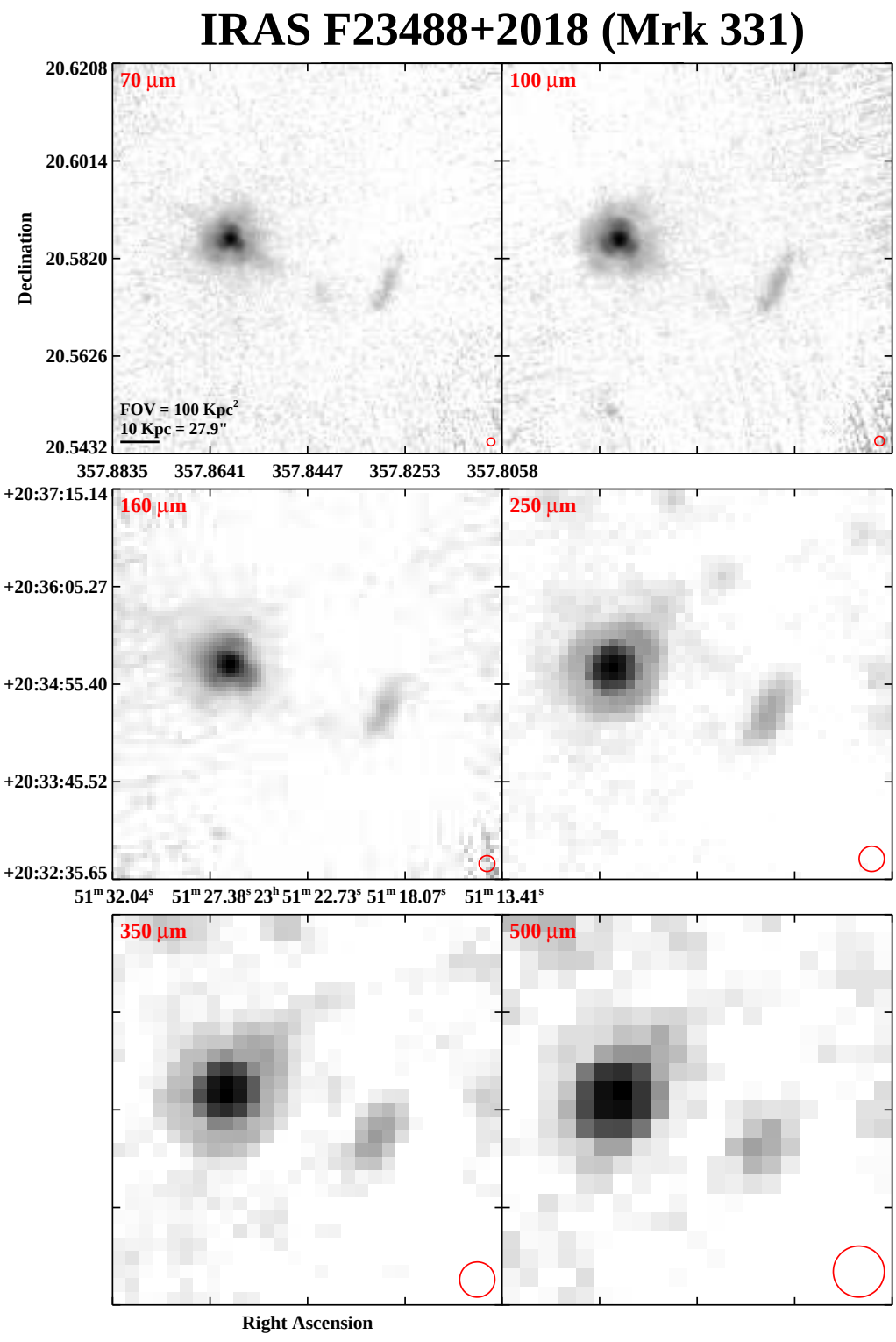

Figure 2.3 continued (page 209 of 209).

Instead we concluded that the best approach was to determine apertures by visual inspection, and subsequently check that we included all of the flux by plotting a curve of growth. We found that after subtracting any offset in the background levels, the curve of growth almost always flattens out at large radii, indicating a background flux contribution of zero. There are only a few small cases in the PACS data where the curve of growth does not flatten out, and in all cases this occurs when the object is very faint ($F_\lambda \lesssim 0.5$ Jy) and the background noise is more dominant. Curve of growth plots for the SPIRE data are also flat at large radii even for faint fluxes, again indicating robust background subtractions. In Figure 2.4 we show a set of representative curve-of-growth plots and apertures for IRAS F09111–1007 at different wavelengths. The photometry aperture is represented by the blue circle in the image and the blue line in the curve of growth plot below it. In order to facilitate comparison of matched aperture fluxes, all PACS aperture sizes are identical, while all SPIRE apertures are also identical, but larger than that of PACS. The aperture radius is typically set by the band with the largest beam size in which we can make a measurement for each instrument, which is usually the 160 μm channel for PACS and the 500 μm channel for SPIRE. We found that aperture radii encompassing approximately 95% of the total light gave the best tradeoff between including all of the flux but at the same time keeping the background error from getting too high. Although it is possible to use the same aperture size across all six bands (i.e., the SPIRE aperture size), the larger SPIRE aperture would encompass a significant amount of sky background for the higher resolution images (i.e., at 70 μm) and would introduce additional noise in our measurements. We therefore decided it was best to match the apertures for each instrument.

To accurately measure the flux of each galaxy the sky background must be subtracted from the measured flux. To do this we estimate the sky background in the annulus represented by the red circles in the image, which corresponds to the two red lines in the curve of growth plot. These background annuli were chosen to be as free from any source emission as possible. Within the `annularSkyAperturePhotometry` routine we used

the sky estimation algorithm from DAOPhot[6] to estimate the sky level, with the "fractional pixel" setting enabled. The background corrected flux density is then the total flux minus the product of the measured background level and the number of pixels within the target aperture.

We note that in some cases both component and total fluxes are measured for close pairs. These galaxies can be easily resolved and separated at shorter wavelengths, but become unresolved at longer wavelengths. In order to choose the best flux aperture, we carefully selected the radius at which the curve of growth was flattest. This is apparent in Figure 2.4 in the first two columns where the galaxy pair is easily resolved at 70 μm, but becomes marginally resolved at 160 μm. The third column in Figure 2.4 shows the curve of growth from a single large aperture encompassing the entire system, which includes faint extended flux missed by the individual component apertures. Finally since the galaxy pair is unresolved in the 350 μm and 500 μm SPIRE bands, we do not measure any component fluxes at those wavelengths. At 250 μm, component fluxes are still computed since they pair is still resolved. Every effort was made to measure as many marginally resolved systems as possible, while also providing a total flux measurement from one large aperture when necessary. We believe separately measuring component and total fluxes in cases such as this will be useful when the fractional flux contribution of each component is desired.

In Table 2.3 we present the table of monochromatic total flux density for each GOALS system in units of Jansky. Depending on the number of galaxies within a system, their apparent separation on the sky, and the beam size at that particular wavelength, the total *Herschel* flux for each system is calculated using one of three methods. In the simple case of single galaxy, the system flux is just the flux of that galaxy. In cases where there are two or more galaxies that are widely separated, the total flux is the sum of the component fluxes measured in separate apertures. Finally in cases where component galaxies are resolved but still overlapping (i.e., in Figure 2.4), the total system flux is obtained from a single large aperture encompassing all of the components. For triple and quadruple systems where two

[6]Adapted from the IDL AstroLib `mmm.pro` routine.

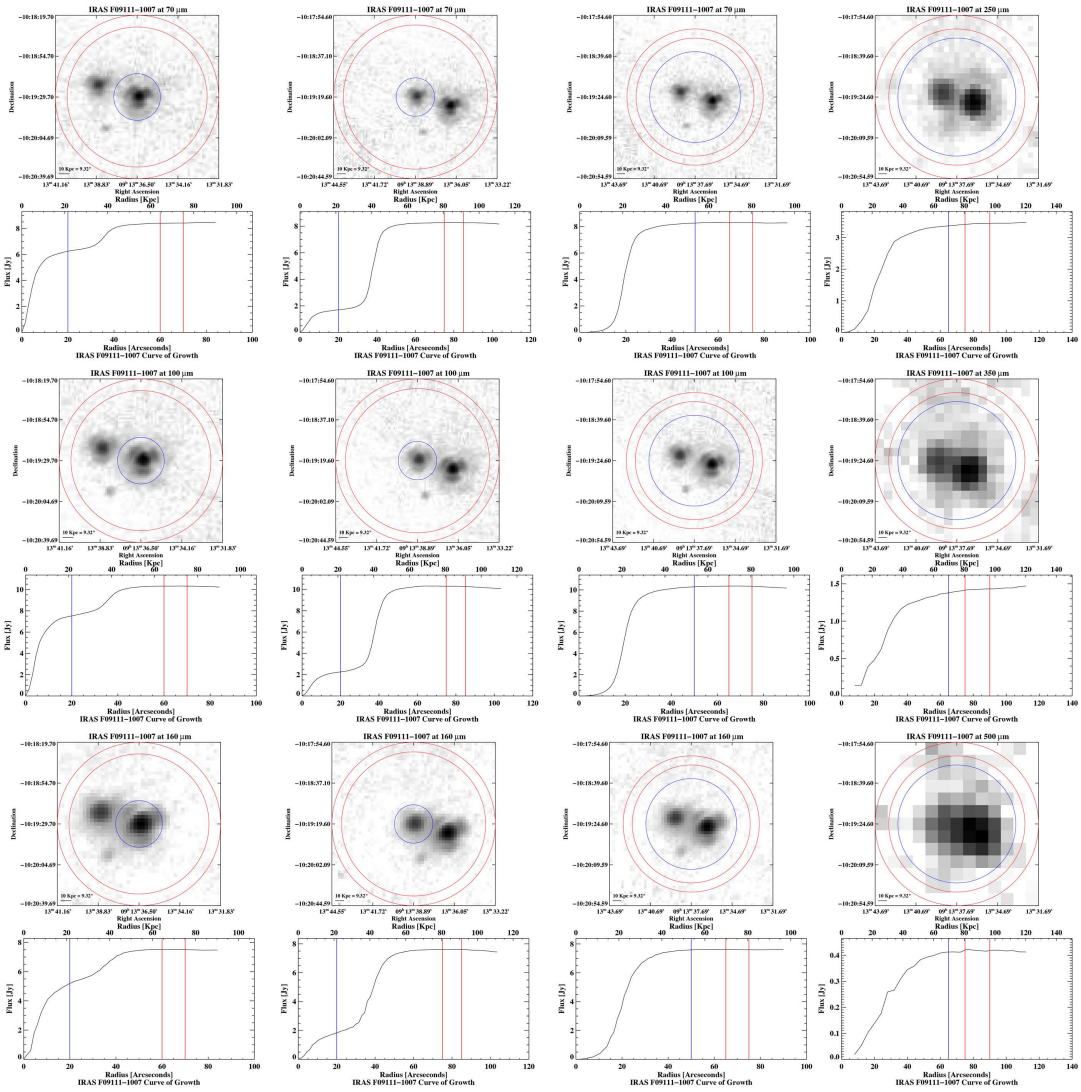

Figure 2.4 Twelve curve of growth plots for IRAS F09111–1007, which are representative for the entire GOALS sample. The blue circle in each image is the photometry aperture, while the red circles are the annuli from which the background is measured. These circles are represented in the curve of growth plot immediately below each image. The first column shows the PACS 70 μm, 100 μm, and 160 μm photometry apertures for the western component of the system. The second column shows the PACS photometry apertures for the eastern nucleus. The third column shows the PACS photometry apertures encompassing both galaxies which includes flux not in the component apertures, giving the total flux from this system. In the SPIRE bands, we only computed component fluxes at 250 μm since the galaxy pair is still resolved, however since the galaxies are essentially unresolved in the other two SPIRE bands, we only compute total fluxes at those two wavelengths. Note the fourth column only shows the total SPIRE apertures of both galaxies, and the individual 250 μm plots were omitted to keep the figure manageable.

galaxies are close and a third (or fourth) is far away (i.e., IRAS F02071–1023), the total system flux is calculated using a hybrid method: a single large aperture for the two close components, plus a second (or third) aperture around the far component(s). Since all of the total fluxes are calculated differently, we omit the coordinates and aperture radii in Table 2.3, but we include it in Tables 2.4 and 2.5 (see below).

In Table 2.3, Column (1) is the row reference number (corresponding to Tables 2.1, 2.2, 2.4, and 2.5) while column (2) is the IRAS name of the galaxy, ordered by ascending RA. Galaxies with the "F" prefix originate from the *IRAS* Faint Source Catalog, and galaxies with no "F" prefix are from the Point Source Catalog. Column (3) lists common optical counterpart names to the galaxy systems. Columns (4) – (6) are the total fluxes from the PACS instrument in units of Jy. Note that the four galaxies which lack 100 μm measurements are IRAS F02401-0013 (NGC 1068), IRAS F09320+6134 (UGC 05101), IRAS F15327+2340 (Arp 220), and IRAS F21453-3511 (NGC 7130). Columns (7) – (9) are the total fluxes from the SPIRE instrument in units of Jy.

In Table 2.4 we present the PACS monochromatic flux density in units of Jansky for each component measurable within each system, with the total system flux from Table 2.3 included for completeness on the last line for each system. For total fluxes that do not have an aperture size listed, the totals were calculated as the sum of the components. Likewise the RA and declination for these systems (on the totals line) represent the geometric midpoint between the companion galaxies. The column descriptions are (1) the row reference number, which corresponds to the same indices used in all of the other tables. Column (2) is the IRAS name of the galaxy, ordered by ascending RA. Column (3) is the individual name to that galaxy component. Note that galaxies prefixed by IRGP are from the catalog of newly defined infrared galaxy pairs defined in the companion *Spitzer*-GOALS paper by Mazzarella et al. (in prep.). Columns (4) – (5) are the coordinates of the aperture centers used. Lines where coordinates are listed but have no aperture radii are cases where the total flux is the sum of two widely separated components. These are the same 8 μm coordinates adopted in Mazzarella et al. (in prep.), however a few were slightly adjusted for the *Herschel* data.

Columns (6) – (7) are the aperture radii used for PACS photometry, in arcsec and kpc respectively. Columns (8) – (10) are the fluxes from the PACS instrument in units of Jy. Galaxy components that do not have flux measurements are too close to a companion galaxy to be resolved by PACS. The columns in Table 2.5 are identical to Table 2.4 except for the last three columns which are the fluxes for SPIRE. Likewise, galaxy components that do not have SPIRE fluxes are too close to a companion galaxy to be resolved by SPIRE.

2.6.1 PACS Aperture Photometry

In addition to measuring the flux, we must apply an aperture correction to account for flux outside of the aperture. The PACS aperture corrections are determined from observations of bright celestial standards, and the correction factors are included in the PACS calibration files distributed from the HSA. Within HIPE, the `photApertureCorrectionPointSource` task performs the aperture correction, where the input is the output product from the aperture photometry task. In addition a responsivity version must be specified, which for our data we used the most recent version (FM 7[7]). Since these aperture corrections are only applicable to point sources at each wavelength, we only apply the aperture correction to point sources within our sample. To identify the point sources, we performed PSF fitting of each source in our sample, and selected the objects with FWHM consistent with the corresponding point source FWHM in each PACS band. In Table 2.4 we denote the fluxes in which an aperture correction was applied by the superscript c. Typical (average) aperture correction values for the 70, 100, and 160 μm bands are 11.7%, 12.8%, and 15.5% of the uncorrected flux, respectively. The median values of the aperture correction values are less than a percent away from the averages. We do not flag aperture-corrected fluxes in Table 2.3 since many of the total fluxes are a combination of aperture-corrected and uncorrected fluxes.

[7]For a description, see section 2.3 of the PACS calibration framework document: `http://herschel.esac.esa.int/twiki/pub/Pacs/PacsCalibration/The_PACS_Calibration_Framework_-_issue_0.13.pdf`

Table 2.3 PACS and SPIRE Total Fluxes of GOALS Systems

			PACS			SPIRE		
#	IRAS Name	Optical Name	F_λ(70 μm) Jy	F_λ(100 μm) Jy	F_λ(160 μm) Jy	F_λ(250 μm) Jy	F_λ(350 μm) Jy	F_λ(500 μm) Jy
—	—	—						
1	F00073+2538	NGC 23	10.48 ± 0.52	14.26 ± 0.71	11.85 ± 0.59	5.311 ± 0.347	2.026 ± 0.134	0.718 ± 0.046
2	F00085-1223	NGC 34, Mrk 938	18.21 ± 0.84	17.68 ± 0.81	10.65 ± 0.48	3.573 ± 0.214	1.239 ± 0.075	0.339 ± 0.021
3	F00163-1039	Arp 256, MCG-02-01-051/2	8.038 ± 0.403	9.876 ± 0.495	7.496 ± 0.375	2.862 ± 0.189	1.209 ± 0.081	0.419 ± 0.033
4	F00344-3349	ESO 350-IG 038, Haro 11	6.195 ± 0.276	5.096 ± 0.228	2.341 ± 0.101	0.639 ± 0.038	0.216 ± 0.014	0.067 ± 0.006
5	F00402-2349	NGC 232	14.60 ± 0.56	20.00 ± 0.77	16.11 ± 0.60	6.397 ± 0.323	2.441 ± 0.124	0.703 ± 0.035
6	F00506+7248	MCG+12-02-001	25.31 ± 1.27	29.07 ± 1.45	20.34 ± 1.02	7.968 ± 0.485	2.793 ± 0.174	0.896 ± 0.057
7	F00548+4331	NGC 317B	10.91 ± 0.55	13.07 ± 0.65	9.945 ± 0.498	4.014 ± 0.266	1.600 ± 0.108	0.478 ± 0.039
8	F01053-1746	IC 1623, Arp 236	25.56 ± 1.28	29.28 ± 1.47	21.46 ± 1.08	8.991 ± 0.546	3.277 ± 0.201	1.023 ± 0.062
9	F01076-1707	MCG-03-04-014	8.996 ± 0.410	11.37 ± 0.51	8.758 ± 0.388	3.077 ± 0.187	1.181 ± 0.074	0.349 ± 0.023
10	F01159-4443	ESO 244-G012	9.934 ± 0.498	10.88 ± 0.54	7.735 ± 0.387	2.948 ± 0.194	1.155 ± 0.077	0.341 ± 0.025
11	F01173+1405	CGCG 436-030	11.71 ± 0.53	11.33 ± 0.51	6.907 ± 0.306	2.125 ± 0.128	0.770 ± 0.048	0.230 ± 0.015
12	F01325-3623	ESO 353-G020	10.58 ± 0.49	16.43 ± 0.75	15.26 ± 0.68	6.565 ± 0.408	2.621 ± 0.163	0.881 ± 0.056
13	F01341-3735	RR 032, ESO 297-G011/012	9.294 ± 0.300	12.45 ± 0.41	10.60 ± 0.36	4.107 ± 0.269	1.651 ± 0.110	0.522 ± 0.038
14	F01364-1042		7.395 ± 0.334	6.845 ± 0.307	3.989 ± 0.174	1.336 ± 0.080	0.517 ± 0.032	0.158 ± 0.011
15	F01417+1651	III Zw 035	14.74 ± 0.67	13.44 ± 0.61	7.770 ± 0.344	2.608 ± 0.156	0.995 ± 0.061	0.302 ± 0.019
16	F01484+2220	NGC 695	9.303 ± 0.466	13.24 ± 0.66	11.20 ± 0.56	4.959 ± 0.302	1.942 ± 0.120	0.655 ± 0.047
17	F01519+3640	UGC 01385	6.769 ± 0.302	8.267 ± 0.359	6.291 ± 0.253	2.537 ± 0.127	1.031 ± 0.055	0.279 ± 0.028
18	F02071-1023	NGC 838	36.90 ± 1.04	44.00 ± 1.22	34.54 ± 0.96	14.72 ± 0.54	5.799 ± 0.216	1.837 ± 0.070
19	F02070+3857	NGC 828	14.56 ± 0.73	24.95 ± 1.25	24.86 ± 1.24	12.78 ± 0.79	5.194 ± 0.324	1.621 ± 0.102
20	F02114+0456	IC 214	5.922 ± 0.287	8.032 ± 0.379	6.672 ± 0.310	3.038 ± 0.166	1.261 ± 0.071	0.421 ± 0.039
21	F02152+1418	NGC 877	16.11 ± 0.66	28.56 ± 1.21	31.25 ± 1.35	16.90 ± 1.10	7.291 ± 0.475	2.449 ± 0.162
22	F02203+3158	MCG+05-06-036	9.069 ± 0.320	13.03 ± 0.45	11.30 ± 0.37	4.206 ± 0.277	1.651 ± 0.111	0.529 ± 0.042
23	F02208+4744	UGC 01845	13.11 ± 0.59	17.48 ± 0.78	13.75 ± 0.60	5.036 ± 0.304	1.974 ± 0.121	0.563 ± 0.034
24	F02281-0309	NGC 958	8.261 ± 0.415	16.78 ± 0.84	19.75 ± 0.99	10.46 ± 0.68	4.532 ± 0.297	1.614 ± 0.114
25	F02345+2053	NGC 992	11.90 ± 0.60	16.25 ± 0.81	13.37 ± 0.67	5.906 ± 0.364	2.341 ± 0.145	0.734 ± 0.047
26	F02401-0013	NGC 1068	285.8 ± 14.3	$\cdots$	290.9 ± 14.5	117.9 ± 7.7	45.72 ± 2.97	14.40 ± 0.94
27	F02435+1253	UGC 02238	9.946 ± 0.498	15.33 ± 0.77	13.48 ± 0.67	6.147 ± 0.375	2.380 ± 0.148	0.756 ± 0.052
28	F02437+2122		6.927 ± 0.313	7.725 ± 0.347	5.027 ± 0.219	1.823 ± 0.106	0.658 ± 0.038	0.185 ± 0.012
28	F02437+2123[a]	2MASX J02464505+2133234	0.195 ± 0.014	0.541 ± 0.029	0.584 ± 0.031	0.491 ± 0.031	0.221 ± 0.015	0.079 ± 0.008
29	F02512+1446	UGC 02369	8.701 ± 0.436	10.36 ± 0.52	7.659 ± 0.383	3.096 ± 0.204	1.197 ± 0.080	0.382 ± 0.024

continued on the next page

Table 2.3. (continued) PACS and SPIRE Total Fluxes of GOALS Systems

			PACS			SPIRE		
#	IRAS Name	Optical Name	$F_\lambda(70\ \mu m)$	$F_\lambda(100\ \mu m)$	$F_\lambda(160\ \mu m)$	$F_\lambda(250\ \mu m)$	$F_\lambda(350\ \mu m)$	$F_\lambda(500\ \mu m)$
—	—	—	Jy	Jy	Jy	Jy	Jy	Jy
30	F03117+4151	UGC 02608	9.116 ± 0.456	11.57 ± 0.58	9.210 ± 0.461	4.135 ± 0.251	1.601 ± 0.099	0.518 ± 0.033
30	F03117+4151[a]	UGC 02612	0.575 ± 0.032	1.341 ± 0.069	1.660 ± 0.084	0.990 ± 0.061	0.429 ± 0.028	0.134 ± 0.012
31	F03164+4119	NGC 1275	6.807 ± 0.343	7.490 ± 0.377	5.691 ± 0.286	3.506 ± 0.217	2.851 ± 0.176	2.739 ± 0.168
32	F03217+4022		9.122 ± 0.412	10.84 ± 0.49	7.913 ± 0.345	3.134 ± 0.191	1.204 ± 0.075	0.358 ± 0.024
33	F03316-3618	NGC 1365	137.6 ± 6.9	221.5 ± 11.1	209.7 ± 10.5	103.7 ± 6.7	43.94 ± 2.86	15.63 ± 1.02
34	F03359+1523		7.170 ± 0.324	7.541 ± 0.339	4.878 ± 0.213	1.643 ± 0.099	0.599 ± 0.038	0.187 ± 0.013
35	F03514+1546	CGCG 465-012	6.673 ± 0.334	8.845 ± 0.443	6.946 ± 0.348	3.065 ± 0.186	1.130 ± 0.071	0.356 ± 0.025
35	F03514+1546[a]	CGCG 465-011	2.255 ± 0.114	3.804 ± 0.191	4.015 ± 0.201	2.188 ± 0.135	0.867 ± 0.056	0.310 ± 0.024
36	03582+6012		5.685 ± 0.285	5.922 ± 0.296	3.745 ± 0.188	1.598 ± 0.098	0.659 ± 0.044	0.158 ± 0.014
37	F04097+0525	UGC 02982	10.52 ± 0.53	16.86 ± 0.84	15.62 ± 0.78	7.324 ± 0.480	3.541 ± 0.223	1.068 ± 0.071
38	F04118-3207	ESO 420-G013	17.57 ± 0.81	22.28 ± 1.02	16.82 ± 0.75	6.401 ± 0.388	2.406 ± 0.148	0.669 ± 0.041
39	F04191-1855	ESO 550-IG 025	6.452 ± 0.323	8.676 ± 0.434	7.115 ± 0.356	3.273 ± 0.215	1.306 ± 0.087	0.449 ± 0.028
40	F04210-4042	NGC 1572	10.02 ± 0.50	16.45 ± 0.82	15.32 ± 0.77	7.368 ± 0.484	3.225 ± 0.199	1.028 ± 0.063
41	04271+3849		7.402 ± 0.371	10.97 ± 0.49	8.846 ± 0.385	3.815 ± 0.234	1.478 ± 0.093	0.453 ± 0.031
42	F04315-0840	NGC 1614	36.74 ± 1.70	37.00 ± 1.70	22.96 ± 1.04	7.291 ± 0.452	2.650 ± 0.165	0.748 ± 0.049
43	F04326+1904	UGC 03094	8.159 ± 0.409	12.77 ± 0.64	11.93 ± 0.60	5.210 ± 0.341	2.114 ± 0.140	0.663 ± 0.047
44	F04454-4838	ESO 203-IG001	6.125 ± 0.272	5.284 ± 0.233	2.945 ± 0.125	0.918 ± 0.053	0.339 ± 0.020	0.091 ± 0.007
45	F04502-3304	MCG-05-12-006	9.169 ± 0.414	10.35 ± 0.46	6.949 ± 0.303	2.454 ± 0.153	0.905 ± 0.059	0.266 ± 0.021
46	F05053-0805	NGC 1797	11.00 ± 0.51	13.49 ± 0.62	10.83 ± 0.48	4.438 ± 0.270	1.670 ± 0.103	0.534 ± 0.034
46	F05053-0805[a]	NGC 1799	0.402 ± 0.027	0.818 ± 0.044	0.954 ± 0.049	0.596 ± 0.044	0.315 ± 0.025	0.121 ± 0.014
47	F05054+1718	CGCG 468-002	10.43 ± 0.52	11.15 ± 0.56	7.394 ± 0.370	2.804 ± 0.185	1.015 ± 0.070	0.293 ± 0.024
48	05083+2441		7.576 ± 0.314	8.348 ± 0.333	5.716 ± 0.209	2.202 ± 0.146	0.824 ± 0.058	0.292 ± 0.024
49	F05081+7936	VII Zw 031	7.492 ± 0.338	10.12 ± 0.45	8.055 ± 0.351	3.130 ± 0.189	1.167 ± 0.072	0.349 ± 0.022
50	05129+5128		7.273 ± 0.329	7.655 ± 0.344	5.028 ± 0.219	1.771 ± 0.106	0.631 ± 0.038	0.196 ± 0.013
51	F05189-2524		13.53 ± 0.61	11.39 ± 0.51	6.180 ± 0.269	1.975 ± 0.118	0.729 ± 0.044	0.199 ± 0.014
52	F05187-1017		6.782 ± 0.309	8.595 ± 0.389	6.583 ± 0.292	2.721 ± 0.165	1.094 ± 0.068	0.327 ± 0.022
53	05368+4940	MCG+08-11-002	19.40 ± 0.88	26.93 ± 1.22	21.56 ± 0.95	8.341 ± 0.507	3.223 ± 0.198	0.948 ± 0.056
54	F05365+6921	NGC 1961	11.59 ± 0.58	26.26 ± 1.31	34.08 ± 1.71	19.59 ± 1.27	8.715 ± 0.567	3.076 ± 0.201
55	F05414+5840	UGC 03351	19.02 ± 0.95	31.33 ± 1.57	28.88 ± 1.44	13.70 ± 0.90	5.817 ± 0.359	1.858 ± 0.114
56	05442+1732		11.86 ± 0.49	13.91 ± 0.55	10.18 ± 0.37	4.194 ± 0.276	1.639 ± 0.110	0.578 ± 0.043

continued on the next page

Table 2.3. (continued) PACS and SPIRE Total Fluxes of GOALS Systems

			PACS			SPIRE		
#	IRAS Name	Optical Name	$F_\lambda(70\ \mu m)$	$F_\lambda(100\ \mu m)$	$F_\lambda(160\ \mu m)$	$F_\lambda(250\ \mu m)$	$F_\lambda(350\ \mu m)$	$F_\lambda(500\ \mu m)$
—	—	—	Jy	Jy	Jy	Jy	Jy	Jy
57	F06076-2139		7.554 ± 0.338	8.405 ± 0.373	5.664 ± 0.242	2.157 ± 0.129	0.863 ± 0.053	0.271 ± 0.017
58	F06052+8027	UGC 03410	12.42 ± 0.53	22.21 ± 0.92	23.59 ± 0.96	11.55 ± 0.60	4.528 ± 0.235	1.566 ± 0.077
59	F06107+7822	NGC 2146	198.7 ± 9.9	237.1 ± 11.9	174.4 ± 8.7	62.78 ± 4.08	22.89 ± 1.49	7.138 ± 0.465
60	F06259-4708	ESO 255-IG007	9.801 ± 0.491	10.67 ± 0.53	7.175 ± 0.359	2.764 ± 0.181	1.019 ± 0.068	0.289 ± 0.021
61	F06295-1735	ESO 557-G002	8.699 ± 0.335	10.29 ± 0.38	7.685 ± 0.279	3.006 ± 0.144	1.156 ± 0.057	0.345 ± 0.020
62	F06538+4628	UGC 03608	8.877 ± 0.444	10.62 ± 0.53	8.315 ± 0.416	3.593 ± 0.215	1.363 ± 0.083	0.429 ± 0.027
63	F06592-6313		6.904 ± 0.312	7.530 ± 0.338	5.027 ± 0.219	1.842 ± 0.113	0.755 ± 0.048	0.221 ± 0.017
64	F07027-6011	AM 0702-601	7.807 ± 0.260	9.229 ± 0.312	7.038 ± 0.228	2.540 ± 0.170	1.025 ± 0.072	0.309 ± 0.029
65	07063+2043	NGC 2342	17.64 ± 0.63	25.86 ± 0.93	22.26 ± 0.80	9.287 ± 0.443	3.761 ± 0.176	1.173 ± 0.057
66	F07160-6215	NGC 2369	26.90 ± 1.35	41.22 ± 2.06	37.55 ± 1.88	17.35 ± 1.14	7.181 ± 0.453	2.273 ± 0.143
67	07251-0248		7.024 ± 0.317	6.419 ± 0.288	3.878 ± 0.169	1.448 ± 0.087	0.561 ± 0.034	0.178 ± 0.012
68	F07256+3355	NGC 2388	24.48 ± 0.98[b]	32.84 ± 1.26[b]	27.76 ± 1.01[b]	12.02 ± 0.57[b]	4.632 ± 0.221[b]	1.537 ± 0.072[b]
69	F07329+1149	MCG+02-20-003	10.61 ± 0.48	13.13 ± 0.59	9.969 ± 0.437	4.071 ± 0.250	1.555 ± 0.095	0.503 ± 0.031
69	F07329+1149[a]	NGC 2416	0.897 ± 0.047	1.705 ± 0.086	1.956 ± 0.098	1.008 ± 0.066	0.436 ± 0.029	0.154 ± 0.010
70	08355-4944		10.25 ± 0.46	9.529 ± 0.428	5.637 ± 0.246	1.758 ± 0.105	0.622 ± 0.040	0.173 ± 0.015
71	F08339+6517		5.865 ± 0.294	6.163 ± 0.309	3.979 ± 0.200	1.267 ± 0.084	0.506 ± 0.031	0.148 ± 0.010
72	F08354+2555	NGC 2623	27.92 ± 1.27	28.46 ± 1.29	17.65 ± 0.78	5.929 ± 0.358	2.124 ± 0.130	0.589 ± 0.035
73	08424-3130	ESO 432-IG006	7.597 ± 0.381	9.841 ± 0.493	7.663 ± 0.384	3.117 ± 0.205	1.227 ± 0.082	0.363 ± 0.027
74	F08520-6850	ESO 060-IG016	5.468 ± 0.274	5.560 ± 0.278	3.496 ± 0.175	1.318 ± 0.088	0.613 ± 0.040	0.170 ± 0.014
75	F08572+3915		6.398 ± 0.282	4.452 ± 0.194	1.997 ± 0.084	0.521 ± 0.031	0.188 ± 0.014	0.042 ± 0.007
76	09022-3615		12.81 ± 0.58	13.14 ± 0.59	8.057 ± 0.351	2.588 ± 0.152	0.880 ± 0.051	0.243 ± 0.014
77	F09111-1007		8.314 ± 0.417	10.35 ± 0.52	7.726 ± 0.387	3.434 ± 0.225	1.357 ± 0.090	0.434 ± 0.030
78	F09126+4432	UGC 04881	7.311 ± 0.366	9.282 ± 0.465	7.433 ± 0.372	3.296 ± 0.217	1.360 ± 0.092	0.435 ± 0.029
79	F09320+6134	UGC 05101	15.34 ± 0.69	···	15.29 ± 0.65	6.138 ± 0.371	2.403 ± 0.148	0.755 ± 0.045
80	F09333+4841	MCG+08-18-013	7.463 ± 0.334	8.835 ± 0.388	6.737 ± 0.282	2.302 ± 0.152	0.935 ± 0.063	0.266 ± 0.021
81	F09437+0317	Arp 303, IC 0563/4	6.876 ± 0.244	12.37 ± 0.44	13.41 ± 0.48	6.772 ± 0.443	2.876 ± 0.190	0.916 ± 0.064
82	F10015-0614	NGC 3110	15.41 ± 0.69	22.94 ± 1.04	20.76 ± 0.95	8.670 ± 0.567	3.373 ± 0.223	1.042 ± 0.072
83	F10038-3338	ESO 374-IG 032	10.14 ± 0.46	8.693 ± 0.390	5.048 ± 0.220	1.837 ± 0.111	0.784 ± 0.049	0.266 ± 0.018
84	F10173+0828		6.298 ± 0.287	5.677 ± 0.257	3.169 ± 0.141	1.132 ± 0.068	0.501 ± 0.031	0.144 ± 0.011
85	F10196+2149	NGC 3221	10.43 ± 0.52	20.96 ± 1.05	24.06 ± 1.20	12.52 ± 0.82	5.352 ± 0.350	1.809 ± 0.120

continued on the next page

Table 2.3. (continued) PACS and SPIRE Total Fluxes of GOALS Systems

			PACS			SPIRE		
#	IRAS Name	Optical Name	F_λ(70 μm)	F_λ(100 μm)	F_λ(160 μm)	F_λ(250 μm)	F_λ(350 μm)	F_λ(500 μm)
—	—	—	Jy	Jy	Jy	Jy	Jy	Jy
86	F10257-4339	NGC 3256	120.3 ± 6.0	135.4 ± 6.8	93.48 ± 4.68	33.91 ± 2.21	12.16 ± 0.79	3.929 ± 0.242
87	F10409-4556	ESO 264-G036	7.974 ± 0.399	13.09 ± 0.65	13.10 ± 0.66	6.560 ± 0.429	2.658 ± 0.163	0.860 ± 0.052
88	F10567-4310	ESO 264-G057	6.910 ± 0.346	11.10 ± 0.56	10.41 ± 0.52	5.057 ± 0.331	2.124 ± 0.131	0.690 ± 0.043
89	F10565+2448		14.26 ± 0.64	15.80 ± 0.71	10.45 ± 0.46	3.643 ± 0.215	1.337 ± 0.078	0.381 ± 0.022
90	F11011+4107	MCG+07-23-019	8.484 ± 0.387	10.52 ± 0.48	7.825 ± 0.346	2.862 ± 0.172	1.098 ± 0.066	0.325 ± 0.021
91	F11186-0242	CGCG 011-076	6.742 ± 0.295	9.474 ± 0.406	8.312 ± 0.350	3.795 ± 0.252	1.653 ± 0.112	0.562 ± 0.042
92	F11231+1456	IC 2810	8.456 ± 0.283	11.40 ± 0.38	9.348 ± 0.297	3.820 ± 0.252	1.610 ± 0.108	0.544 ± 0.041
93	F11255-4120	ESO 319-G022	9.086 ± 0.414	10.53 ± 0.48	7.785 ± 0.344	3.088 ± 0.186	1.144 ± 0.070	0.319 ± 0.021
94	F11257+5850	NGC 3690, Arp 299	130.3 ± 6.5	118.3 ± 5.9	68.77 ± 3.44	21.85 ± 1.42	7.688 ± 0.502	2.273 ± 0.149
95	F11506-3851	ESO 320-G030	41.98 ± 1.97	49.14 ± 2.28	34.81 ± 1.59	13.02 ± 0.81	5.182 ± 0.324	1.608 ± 0.101
96	F12043-3140	ESO 440-IG058	8.197 ± 0.410	10.89 ± 0.54	8.693 ± 0.435	3.607 ± 0.238	1.323 ± 0.089	0.388 ± 0.028
97	F12112+0305		9.283 ± 0.419	9.241 ± 0.415	5.831 ± 0.254	1.974 ± 0.119	0.796 ± 0.049	0.226 ± 0.016
98	F12116+5448	NGC 4194	26.20 ± 1.21	26.14 ± 1.20	16.60 ± 0.75	5.315 ± 0.324	1.867 ± 0.115	0.549 ± 0.034
99	F12115-4656	ESO 267-G030	6.914 ± 0.346	10.26 ± 0.51	9.280 ± 0.464	4.509 ± 0.272	1.757 ± 0.107	0.598 ± 0.035
99	F12115-4656[a]	ESO 267-G029	5.725 ± 0.287	7.924 ± 0.397	7.143 ± 0.358	3.262 ± 0.213	1.350 ± 0.083	0.441 ± 0.028
100	12116-5615		11.76 ± 0.53	13.02 ± 0.58	8.808 ± 0.384	3.229 ± 0.195	1.268 ± 0.080	0.418 ± 0.028
101	F12224-0624		7.145 ± 0.323	7.761 ± 0.348	5.079 ± 0.221	1.972 ± 0.122	0.785 ± 0.050	0.271 ± 0.019
102	F12243-0036	NGC 4418	43.05 ± 1.98	34.46 ± 1.57	18.67 ± 0.83	6.631 ± 0.394	2.595 ± 0.152	0.930 ± 0.053
103	F12540+5708	UGC 08058, Mrk 231	34.87 ± 1.59	30.41 ± 1.37	16.93 ± 0.74	5.685 ± 0.343	2.007 ± 0.123	0.597 ± 0.036
104	F12590+2934	NGC 4922	6.763 ± 0.309	7.606 ± 0.345	5.283 ± 0.234	2.032 ± 0.122	0.727 ± 0.045	0.218 ± 0.015
105	F12592+0436	CGCG 043-099	6.538 ± 0.295	8.455 ± 0.379	6.675 ± 0.291	2.808 ± 0.171	1.055 ± 0.065	0.315 ± 0.020
106	F12596-1529	MCG-02-33-098	7.534 ± 0.377	8.490 ± 0.425	5.962 ± 0.299	2.654 ± 0.175	1.061 ± 0.072	0.330 ± 0.027
107	F13001-2339	ESO 507-G070	16.32 ± 0.75	16.90 ± 0.77	10.66 ± 0.47	3.747 ± 0.228	1.405 ± 0.087	0.451 ± 0.029
108	13052-5711		10.49 ± 0.48	13.55 ± 0.61	10.13 ± 0.45	3.819 ± 0.231	1.624 ± 0.101	0.422 ± 0.028
109	F13126+2453	IC 0860	19.67 ± 0.90	18.09 ± 0.82	10.66 ± 0.47	3.775 ± 0.228	1.523 ± 0.093	0.500 ± 0.030
110	13120-5453		50.72 ± 2.35	55.02 ± 2.53	34.97 ± 1.58	12.33 ± 0.75	4.396 ± 0.268	1.340 ± 0.079
111	F13136+6223	VV 250a	11.71 ± 0.59	11.16 ± 0.56	6.728 ± 0.337	2.429 ± 0.159	0.875 ± 0.059	0.273 ± 0.021
112	F13182+3424	UGC 08387	21.74 ± 1.00	25.82 ± 1.18	18.08 ± 0.81	6.356 ± 0.393	2.345 ± 0.146	0.646 ± 0.041
113	F13188+0036	NGC 5104	8.997 ± 0.410	13.54 ± 0.61	12.01 ± 0.53	5.266 ± 0.322	2.005 ± 0.124	0.658 ± 0.040
114	F13197-1627	MCG-03-34-064	6.179 ± 0.238	6.451 ± 0.234	5.199 ± 0.174	2.440 ± 0.108	1.016 ± 0.047	0.330 ± 0.017

continued on the next page

Table 2.3. (continued) PACS and SPIRE Total Fluxes of GOALS Systems

			PACS			SPIRE		
#	IRAS Name	Optical Name	$F_\lambda(70\ \mu m)$ Jy	$F_\lambda(100\ \mu m)$ Jy	$F_\lambda(160\ \mu m)$ Jy	$F_\lambda(250\ \mu m)$ Jy	$F_\lambda(350\ \mu m)$ Jy	$F_\lambda(500\ \mu m)$ Jy
—	—	—						
115	F13229-2934	NGC 5135	21.44 ± 1.07	31.12 ± 1.56	26.86 ± 1.34	12.37 ± 0.81	5.058 ± 0.333	1.577 ± 0.106
116	13242-5713	ESO 173-G015	97.67 ± 4.89	105.8 ± 5.3	71.63 ± 3.58	26.51 ± 1.74	9.706 ± 0.642	3.092 ± 0.194
117	F13301-2356	IC 4280	7.647 ± 0.383	12.97 ± 0.65	12.52 ± 0.63	5.631 ± 0.369	2.431 ± 0.150	0.771 ± 0.048
118	F13362+4831	NGC 5256	8.113 ± 0.406	9.692 ± 0.485	7.069 ± 0.354	2.757 ± 0.182	1.070 ± 0.073	0.336 ± 0.026
119	F13373+0105	Arp 240, NGC 5257/8	13.98 ± 0.50	21.58 ± 0.77	20.37 ± 0.72	9.434 ± 0.615	3.759 ± 0.246	1.259 ± 0.084
120	F13428+5608	UGC 08696, Mrk 273	24.46 ± 1.11	22.32 ± 1.00	12.74 ± 0.56	4.177 ± 0.252	1.531 ± 0.094	0.427 ± 0.026
121	F13470+3530	UGC 08739	8.163 ± 0.409	14.94 ± 0.75	15.87 ± 0.79	8.243 ± 0.540	3.405 ± 0.225	1.162 ± 0.073
122	F13478-4848	ESO 221-IG010	15.78 ± 0.79	21.63 ± 1.08	17.97 ± 0.90	7.116 ± 0.465	2.771 ± 0.183	0.917 ± 0.066
123	F13497+0220	NGC 5331	7.484 ± 0.375	11.27 ± 0.56	10.31 ± 0.52	5.010 ± 0.329	1.892 ± 0.126	0.673 ± 0.044
124	F13564+3741	Arp 84, NGC 5394/5	12.88 ± 0.44	20.72 ± 0.70	22.65 ± 0.81	11.93 ± 0.78	5.187 ± 0.338	1.856 ± 0.122
125	F14179+4927	CGCG 247-020	6.514 ± 0.326	7.450 ± 0.373	4.904 ± 0.246	1.789 ± 0.120	0.688 ± 0.048	0.175 ± 0.015
126	F14280+3126	NGC 5653	15.03 ± 0.69	22.88 ± 1.05	21.09 ± 0.95	8.748 ± 0.538	3.369 ± 0.207	0.994 ± 0.062
127	F14348-1447		8.260 ± 0.373	8.385 ± 0.376	5.475 ± 0.239	1.967 ± 0.117	0.728 ± 0.044	0.217 ± 0.014
128	F14378-3651		6.857 ± 0.305	6.661 ± 0.294	3.917 ± 0.167	1.376 ± 0.076	0.547 ± 0.030	0.158 ± 0.010
129	F14423-2039	NGC 5734	16.94 ± 0.62	27.32 ± 1.00	25.93 ± 0.96	11.61 ± 0.56	4.630 ± 0.217	1.582 ± 0.070
130	F14547+2449	VV 340a, Arp 302	8.788 ± 0.440	14.70 ± 0.74	13.89 ± 0.69	6.588 ± 0.432	2.617 ± 0.173	0.911 ± 0.062
131	F14544-4255	IC 4518A/B	9.106 ± 0.457	12.89 ± 0.65	12.29 ± 0.62	6.015 ± 0.394	2.427 ± 0.161	0.803 ± 0.056
132	F15107+0724	CGCG 049-057	27.65 ± 1.28	31.67 ± 1.45	21.83 ± 0.99	8.430 ± 0.528	3.225 ± 0.204	1.059 ± 0.068
133	F15163+4255	VV 705	9.027 ± 0.452	9.120 ± 0.456	5.581 ± 0.279	2.284 ± 0.137	0.863 ± 0.053	0.254 ± 0.016
134	15206-6256	ESO 099-G004	12.54 ± 0.57	14.61 ± 0.66	10.87 ± 0.47	3.970 ± 0.242	1.674 ± 0.109	0.505 ± 0.039
135	F15250+3608		7.158 ± 0.324	5.787 ± 0.260	3.031 ± 0.133	1.034 ± 0.061	0.385 ± 0.023	0.124 ± 0.008
136	F15276+1309	NGC 5936	10.75 ± 0.54	16.34 ± 0.82	14.97 ± 0.75	6.603 ± 0.431	2.715 ± 0.167	0.870 ± 0.056
137	F15327+2340	Arp 220, UGC 09913	139.2 ± 6.6	...	86.32 ± 3.99	30.87 ± 1.92	12.80 ± 0.80	3.865 ± 0.240
138	F15437+0234	NGC 5990	12.06 ± 0.60	16.81 ± 0.84	14.25 ± 0.71	6.071 ± 0.398	2.435 ± 0.150	0.831 ± 0.050
139	F16030+2040	NGC 6052	7.689 ± 0.385	10.16 ± 0.51	8.128 ± 0.407	3.317 ± 0.218	1.412 ± 0.088	0.483 ± 0.031
140	F16104+5235	NGC 6090	7.800 ± 0.352	9.269 ± 0.416	7.033 ± 0.307	2.666 ± 0.161	1.028 ± 0.063	0.288 ± 0.019
141	F16164-0746		13.29 ± 0.61	15.03 ± 0.68	10.21 ± 0.45	3.581 ± 0.220	1.266 ± 0.080	0.407 ± 0.028
142	F16284+0411	CGCG 052-037	9.151 ± 0.406	12.46 ± 0.55	10.04 ± 0.44	3.618 ± 0.240	1.423 ± 0.096	0.492 ± 0.036
143	16304-6030	NGC 6156	21.20 ± 1.06	32.32 ± 1.62	29.29 ± 1.47	12.91 ± 0.84	5.096 ± 0.334	1.678 ± 0.112
144	F16330-6820	ESO 069-IG006	9.444 ± 0.429	13.32 ± 0.60	10.75 ± 0.47	4.501 ± 0.266	1.788 ± 0.107	0.551 ± 0.033

continued on the next page

Table 2.3. (continued) PACS and SPIRE Total Fluxes of GOALS Systems

			PACS			SPIRE		
#	IRAS Name	Optical Name	F_λ(70 μm) Jy	F_λ(100 μm) Jy	F_λ(160 μm) Jy	F_λ(250 μm) Jy	F_λ(350 μm) Jy	F_λ(500 μm) Jy
—	—	—						
145	F16399-0937		9.368 ± 0.436	10.80 ± 0.50	8.302 ± 0.379	3.527 ± 0.218	1.333 ± 0.088	0.435 ± 0.034
146	F16443-2915	ESO 453-G005	13.83 ± 0.56	16.54 ± 0.64	12.61 ± 0.45	5.356 ± 0.262	2.175 ± 0.107	0.773 ± 0.038
147	F16504+0228	NGC 6240	26.48 ± 1.22	28.03 ± 1.28	19.00 ± 0.85	7.026 ± 0.437	2.834 ± 0.177	0.874 ± 0.056
148	F16516-0948		5.698 ± 0.286	8.243 ± 0.413	7.099 ± 0.356	3.353 ± 0.203	1.232 ± 0.079	0.434 ± 0.030
149	F16577+5900	NGC 6286, Arp 293	12.94 ± 0.55	22.53 ± 0.98	22.71 ± 0.99	11.60 ± 0.76	4.599 ± 0.303	1.495 ± 0.101
150	F17132+5313		6.210 ± 0.311	6.980 ± 0.349	5.474 ± 0.239	2.009 ± 0.122	0.780 ± 0.048	0.226 ± 0.016
151	F17138-1017		18.51 ± 0.86	21.72 ± 1.00	15.62 ± 0.70	5.423 ± 0.332	1.875 ± 0.117	0.531 ± 0.035
152	F17207-0014		38.09 ± 1.74	37.91 ± 1.72	23.07 ± 1.02	7.959 ± 0.485	2.907 ± 0.180	0.890 ± 0.054
153	F17222-5953	ESO 138-G027	9.930 ± 0.497	11.00 ± 0.55	8.861 ± 0.386	3.340 ± 0.202	1.240 ± 0.077	0.370 ± 0.025
154	F17530+3447	UGC 11041	7.636 ± 0.382	11.71 ± 0.59	10.97 ± 0.55	5.299 ± 0.322	2.103 ± 0.130	0.689 ± 0.042
155	F17548+2401	CGCG 141-034	8.282 ± 0.374	10.45 ± 0.47	7.845 ± 0.342	2.961 ± 0.183	0.998 ± 0.064	0.302 ± 0.021
156	17578-0400		34.70 ± 1.62	39.78 ± 1.84	27.58 ± 1.26	11.12 ± 0.65	4.300 ± 0.250	1.306 ± 0.078
157	18090+0130		9.912 ± 0.367	14.19 ± 0.53	12.24 ± 0.45	5.010 ± 0.242	1.869 ± 0.094	0.590 ± 0.033
158	F18131+6820	NGC 6621, Arp 81	8.257 ± 0.414	12.08 ± 0.60	11.24 ± 0.56	5.331 ± 0.350	2.159 ± 0.143	0.661 ± 0.048
159	F18093-5744	IC 4687	23.87 ± 1.19	28.18 ± 1.41	20.08 ± 1.00	8.029 ± 0.526	2.935 ± 0.196	0.928 ± 0.065
160	F18145+2205	CGCG 142-034	7.918 ± 0.315	12.44 ± 0.49	11.56 ± 0.45	5.753 ± 0.273	2.229 ± 0.108	0.712 ± 0.035
161	F18293-3413		45.71 ± 2.11	59.13 ± 2.71	45.84 ± 2.07	17.22 ± 1.07	6.454 ± 0.400	1.987 ± 0.122
162	F18329+5950	NGC 6670A/B	10.33 ± 0.52	13.92 ± 0.70	11.25 ± 0.56	4.664 ± 0.305	1.782 ± 0.118	0.537 ± 0.038
163	F18341-5732	IC 4734	19.06 ± 0.88	25.41 ± 1.16	20.51 ± 0.92	8.450 ± 0.525	3.257 ± 0.203	1.051 ± 0.066
164	F18425+6036	NGC 6701	12.91 ± 0.65	19.13 ± 0.96	16.80 ± 0.84	7.422 ± 0.485	2.863 ± 0.188	0.945 ± 0.059
165	F19120+7320	VV 414, NGC 6786	9.262 ± 0.296	11.90 ± 0.38	9.766 ± 0.309	4.003 ± 0.263	1.516 ± 0.102	0.568 ± 0.041
166	F19115-2124	ESO 593-IG008	7.972 ± 0.363	10.62 ± 0.48	8.597 ± 0.380	3.371 ± 0.203	1.278 ± 0.079	0.489 ± 0.030
167	F19297-0406		7.982 ± 0.400	8.114 ± 0.406	5.121 ± 0.257	1.833 ± 0.121	0.766 ± 0.046	0.225 ± 0.017
168	19542+1110		6.720 ± 0.300	6.516 ± 0.289	3.851 ± 0.165	1.265 ± 0.075	0.495 ± 0.030	0.126 ± 0.009
169	F19542-3804	ESO 339-G011	7.396 ± 0.340	10.69 ± 0.49	9.839 ± 0.440	4.448 ± 0.277	1.695 ± 0.108	0.591 ± 0.039
170	F20221-2458	NGC 6907	18.35 ± 0.92	31.39 ± 1.57	31.71 ± 1.59	16.38 ± 1.07	6.890 ± 0.448	2.378 ± 0.155
171	20264+2533	MCG+04-48-002	12.92 ± 0.53	17.71 ± 0.73	13.35 ± 0.55	5.719 ± 0.291	2.085 ± 0.112	0.669 ± 0.040
172	F20304-0211	NGC 6926	8.895 ± 0.446	15.94 ± 0.80	16.62 ± 0.83	7.808 ± 0.509	3.102 ± 0.204	0.998 ± 0.067
173	20351+2521		6.993 ± 0.350	9.142 ± 0.457	7.280 ± 0.364	3.280 ± 0.196	1.266 ± 0.077	0.347 ± 0.022
174	F20550+1655	CGCG 448-020, II Zw 096	11.79 ± 0.59	10.68 ± 0.53	6.199 ± 0.310	2.128 ± 0.140	0.810 ± 0.051	0.242 ± 0.018

continued on the next page

Table 2.3. (continued) PACS and SPIRE Total Fluxes of GOALS Systems

			PACS			SPIRE		
#	IRAS Name	Optical Name	F_λ(70 μm) Jy	F_λ(100 μm) Jy	F_λ(160 μm) Jy	F_λ(250 μm) Jy	F_λ(350 μm) Jy	F_λ(500 μm) Jy
—	—	—						
175	F20551-4250	ESO 286-IG019	12.64 ± 0.56	10.41 ± 0.46	5.749 ± 0.246	1.840 ± 0.111	0.631 ± 0.039	0.182 ± 0.013
176	F21008-4347	ESO 286-G035	9.498 ± 0.436	12.80 ± 0.58	10.42 ± 0.47	3.994 ± 0.242	1.470 ± 0.091	0.404 ± 0.026
177	21101+5810		8.068 ± 0.365	8.705 ± 0.391	5.753 ± 0.251	2.000 ± 0.122	0.749 ± 0.049	0.195 ± 0.015
178	F21330-3846	ESO 343-IG013	6.422 ± 0.322	8.031 ± 0.402	6.587 ± 0.330	2.721 ± 0.179	1.058 ± 0.072	0.354 ± 0.024
179	F21453-3511	NGC 7130	18.83 ± 0.94	···	19.68 ± 0.99	9.224 ± 0.571	3.549 ± 0.220	1.078 ± 0.068
180	F22118-2742	ESO 467-G027	7.027 ± 0.352	11.89 ± 0.59	11.53 ± 0.58	5.478 ± 0.358	2.083 ± 0.138	0.773 ± 0.050
181	F22132-3705	IC 5179	24.34 ± 1.22	37.57 ± 1.88	34.58 ± 1.73	14.97 ± 0.98	5.763 ± 0.377	1.892 ± 0.125
182	F22287-1917	ESO 602-G025	7.429 ± 0.339	10.36 ± 0.47	9.241 ± 0.409	3.991 ± 0.243	1.658 ± 0.103	0.488 ± 0.031
183	F22389+3359	UGC 12150	10.70 ± 0.48	14.70 ± 0.66	12.31 ± 0.54	5.086 ± 0.305	2.031 ± 0.121	0.611 ± 0.036
184	F22467-4906	ESO 239-IG002	8.041 ± 0.363	7.847 ± 0.352	4.975 ± 0.217	1.799 ± 0.107	0.700 ± 0.042	0.256 ± 0.016
185	F22491-1808		5.642 ± 0.252	4.975 ± 0.221	2.715 ± 0.116	0.841 ± 0.049	0.309 ± 0.018	0.082 ± 0.006
186	F23007+0836	NGC 7469, IC 5283, Arp 298	33.69 ± 1.43	40.18 ± 1.65	29.83 ± 1.16	11.16 ± 0.73	4.216 ± 0.278	1.266 ± 0.087
187	F23024+1916	CGCG 453-062	9.269 ± 0.422	11.42 ± 0.52	9.233 ± 0.409	4.418 ± 0.272	1.749 ± 0.111	0.609 ± 0.038
188	F23128-5919	ESO 148-IG002	11.97 ± 0.54	11.14 ± 0.50	6.028 ± 0.267	1.855 ± 0.110	0.655 ± 0.039	0.186 ± 0.013
189	F23135+2517	IC 5298	10.32 ± 0.47	11.53 ± 0.52	8.070 ± 0.357	3.042 ± 0.184	1.110 ± 0.069	0.336 ± 0.022
190	F23133-4251	NGC 7552	92.92 ± 4.65	116.3 ± 5.8	88.01 ± 4.40	35.64 ± 2.32	13.74 ± 0.90	4.226 ± 0.276
191	F23157+0618	NGC 7591	10.04 ± 0.47	14.49 ± 0.68	13.86 ± 0.65	7.067 ± 0.440	2.944 ± 0.186	0.973 ± 0.064
192	F23157-0441	NGC 7592	8.700 ± 0.435	10.44 ± 0.52	7.602 ± 0.380	2.916 ± 0.192	1.179 ± 0.073	0.355 ± 0.024
193	F23180-6929	ESO 077-IG014	6.716 ± 0.337	9.141 ± 0.458	7.056 ± 0.353	3.113 ± 0.205	1.254 ± 0.084	0.406 ± 0.025
194	F23254+0830	NGC 7674, HCG 96	5.865 ± 0.295	8.328 ± 0.418	7.663 ± 0.384	3.566 ± 0.232	1.424 ± 0.094	0.445 ± 0.031
195	23262+0314	NGC 7679	9.077 ± 0.413	11.74 ± 0.53	8.976 ± 0.397	3.367 ± 0.207	1.287 ± 0.079	0.496 ± 0.031
195	23262+0314[a]	NGC 7682	0.409 ± 0.028	0.770 ± 0.043	0.971 ± 0.051	0.746 ± 0.051	0.384 ± 0.029	0.151 ± 0.014
196	F23365+3604		8.070 ± 0.365	8.315 ± 0.373	5.222 ± 0.228	1.901 ± 0.113	0.707 ± 0.042	0.195 ± 0.012
197	F23394-0353	MCG-01-60-022	6.181 ± 0.279	8.292 ± 0.372	6.863 ± 0.299	2.932 ± 0.180	1.226 ± 0.076	0.402 ± 0.026
197	F23394-0353[a]	MCG-01-60-021, Mrk 933	0.722 ± 0.031	1.422 ± 0.056	1.988 ± 0.082	1.328 ± 0.087	0.555 ± 0.038	0.178 ± 0.014
198	23436+5257		6.576 ± 0.294	7.540 ± 0.335	5.213 ± 0.223	1.872 ± 0.112	0.684 ± 0.043	0.243 ± 0.017
199	F23444+2911	Arp 86, NGC 7752/3	7.612 ± 0.274	13.52 ± 0.50	15.05 ± 0.59	8.038 ± 0.524	3.524 ± 0.233	1.157 ± 0.080
200	F23488+1949	NGC 7771	27.61 ± 1.22[b]	43.18 ± 1.96[b]	40.13 ± 1.84[b]	18.97 ± 1.24[b]	7.501 ± 0.493[b]	2.366 ± 0.157[b]
201	F23488+2018	Mrk 331	21.31 ± 0.96	24.32 ± 1.08	17.46 ± 0.75	6.398 ± 0.375	2.410 ± 0.140	0.790 ± 0.044

Monochromatic PACS and SPIRE total fluxes in units of Jansky for each system in the GOALS sample. See §2.6 for the column descriptions.

We also experimented with applying these corrections to marginally resolved systems and systems with a point source and extended flux, however we found that the aperture corrections artificially boosted the flux by approximately 6% on average. This is because many of our objects have varying levels of flux contribution from the point source and extended component. Furthermore, the PACS team performed a careful surface brightness comparison[8] of PACS data with that of *IRAS* and *Spitzer* MIPS data on the same fields. By convolving, converting, and re-gridding the higher resolution PACS 70 μm to that of *IRAS* 60 μm and MIPS 70 μm, and the PACS 100 μm maps to that of *IRAS* 100 μm it was shown that there is no need to apply any pixel-to-pixel gain corrections to the PACS data. They also conclude that their point-source based calibration scheme is applicable in the case for extended sources. A similar conclusion is reached for the PACS red array[9]. Meléndez et al. (2014) also found in their *Herschel* PACS observations of the *Swift* BAT sample that aperture corrections on extended sources were negligible (less than 3%). Therefore we leave sources appearing extended or semi-extended in our sample unaltered by any aperture correction.

The absolute flux calibration of PACS uses models of five different late type standard stars with fluxes ranging between 0.6–15 Jy in the three photometric bands (Balog et al. 2014). In addition, ten different asteroids are also used to establish the flux calibration over the range of 0.1–300 Jy (Müller et al. 2014). For the standard stars, the absolute flux accuracy is within 3% at 70 μm and 100 μm, and within 5% at 160 μm. In addition, Uranus and Neptune were also observed for validation purposes with fluxes of up to several hundred Jy, however a 10% reduction due to nonlinearity in the detector response was observed. Taken altogether, the error in flux calibration is consistent to within 5% of the measured flux and takes into account flat-fielding, responsivity correction which includes the conversion of engineering units from volts to Jy pixel^{-1}, and gain drift correction which corrects for small drifts in gain with time (PACS Observer's Manual, and references therein).

[8]For more details see the *Herschel* technical note PICC-NHSC-TN-029.
[9]See technical note PICC-NHSC-TR-034.

Since PACS did not perform absolute measurements over the course of the mission, the fluxes are only measured relative to the zero level calculated by the mappers which is arbitrary.

In addition to the flux calibration uncertainty, we must also take into account the error from the background subtraction as well as the instrumental error. The error from the background subtraction is calculated in the following manner: first using the HIPE implementation of `DAOPhot` the 1-σ dispersion is calculated from all the pixels within the background annulus surrounding the target aperture. This is then multiplied by the square root of the total number of pixels within photometry aperture, under the assumption that the error in background subtraction of individual pixels are not correlated. On the other hand the instrumental error is calculated as the quadrature sum of all error pixels within the target aperture, using the error maps produced by the mapmaker. The total flux uncertainty is then calculated as the quadrature sum of all three error components.

We note that only two of the three galaxies in IRAS F07256+3355 (NGC 2388) were observed by PACS due to the smaller field of view, while SPIRE observed all three. Consequently the total fluxes in Table 2.3 for this system is the sum of only the two galaxies observed by both instruments, however SPIRE photometry of the third galaxy to the west is provided in the component flux table (Table 2.5). The same is also true for IRAS F23488+1949, with the third galaxy to the NNW of the closer pair.

2.6.2 SPIRE Aperture Photometry

The SPIRE 2-pass pipeline (see §2.4.2) produces a point-source calibrated map as the main output. However since many of our objects appear extended or marginally extended in our sample, and following the recommendation from the NASA Herschel Science Center (NHSC), we opted to use the extended-source calibrated maps from which we measured all of the fluxes. Both sets of maps are produced nearly identically, however the extended-source calibrated maps have relative gain factors applied to each bolometer's signal, which accounts for the small differences between the peak and integral of each individual bolometer's beam profile. This method helps reduce residual striping in maps with extended sources, since

Table 2.4 *Herschel* PACS Total and Component Fluxes of GOALS Systems

#	IRAS Name	Optical Name	RA	Dec.	Ang. Ap.	Phys. Ap.	$F_\lambda(70\ \mu m)$	$F_\lambda(100\ \mu m)$	$F_\lambda(160\ \mu m)$
—	—	—	HH:MM:SS	DD:MM:SS	$''$	kpc	Jy	Jy	Jy
1	F00073+2538	NGC 23	00 : 09 : 53.36	+ 25 : 55 : 27.7	45	13.81	10.48 ± 0.52	14.26 ± 0.71	11.85 ± 0.59
2	F00085-1223	NGC 34	00 : 11 : 06.56	− 12 : 06 : 28.2	45	17.78	18.21 ± 0.84^c	17.68 ± 0.81^c	10.65 ± 0.48^c
2	F00085-1223	NGC 35	00 : 11 : 10.51	− 12 : 01 : 14.9	···	···	···	···	···
2	F00085-1223		00 : 11 : 08.54	− 12 : 03 : 51.6	···	···	18.21 ± 0.84^c	17.68 ± 0.81^c	10.65 ± 0.48^c
3	F00163-1039	MCG-02-01-051	00 : 18 : 50.90	− 10 : 22 : 36.7	24	12.96	7.501 ± 0.329^c	8.382 ± 0.364^c	5.870 ± 0.244^c
3	F00163-1039	MCG-02-01-052	00 : 18 : 49.85	− 10 : 21 : 34.0	38	20.52	1.206 ± 0.062	2.081 ± 0.105	1.960 ± 0.099
3	F00163-1039	Arp 256	00 : 18 : 50.37	− 10 : 22 : 05.3	70	37.81	8.038 ± 0.403	9.876 ± 0.495	7.496 ± 0.375
4	F00344-3349	ESO 350-IG 038	00 : 36 : 52.49	− 33 : 33 : 17.2	27	11.18	6.195 ± 0.276^c	5.096 ± 0.228^c	2.341 ± 0.101^c
5	F00402-2349	NGC 232	00 : 42 : 45.83	− 23 : 33 : 41.0	35	15.49	12.23 ± 0.55^c	16.81 ± 0.75^c	13.53 ± 0.59^c
5	F00402-2349	NGC 235	00 : 42 : 52.82	− 23 : 32 : 27.8	35	15.49	2.371 ± 0.108^c	3.188 ± 0.144^c	2.581 ± 0.113^c
5	F00402-2349	RSCG 04	00 : 42 : 49.32	− 23 : 33 : 04.3	···	···	14.60 ± 0.56^c	20.00 ± 0.77^c	16.11 ± 0.60^c
6	F00506+7248	MCG+12-02-001	00 : 54 : 03.88	+ 73 : 05 : 05.9	50	16.41	25.31 ± 1.27	29.07 ± 1.45	20.34 ± 1.02
7	F00548+4331	NGC 317B	00 : 57 : 40.41	+ 43 : 47 : 32.5	28	10.06	11.63 ± 0.52^c	14.17 ± 0.63^c	···
7	F00548+4331	NGC 317A	00 : 57 : 39.04	+ 43 : 48 : 03.1	10	3.592	0.061 ± 0.005	0.085 ± 0.006	···
7	F00548+4331	NGC 317	00 : 57 : 39.72	+ 43 : 47 : 47.7	65	23.35	10.91 ± 0.55	13.07 ± 0.65	9.945 ± 0.498
8	F01053-1746	IC 1623A	01 : 07 : 46.79	− 17 : 30 : 27.4	···	···	···	···	···
8	F01053-1746	IC 1623B	01 : 07 : 47.59	− 17 : 30 : 24.2	···	···	···	···	···
8	F01053-1746	IC 1623	01 : 07 : 47.54	− 17 : 30 : 25.6	55	21.92	25.56 ± 1.28	29.28 ± 1.47	21.46 ± 1.08
9	F01076-1707	MCG-03-04-014	01 : 10 : 08.93	− 16 : 51 : 09.9	40	26.14	8.996 ± 0.410^c	11.37 ± 0.51^c	8.758 ± 0.388^c
10	F01159-4443	MCG-7-3-14	01 : 18 : 08.31	− 44 : 27 : 43.4	···	···	···	···	···
10	F01159-4443	MCG-7-3-13	01 : 18 : 08.23	− 44 : 28 : 00.4	···	···	···	···	···
10	F01159-4443	ESO 244-G012	01 : 18 : 08.27	− 44 : 27 : 51.9	45	19.13	9.934 ± 0.498	10.88 ± 0.54	7.735 ± 0.387
11	F01173+1405	CGCG 436-030	01 : 20 : 02.63	+ 14 : 21 : 42.3	40	15.94	11.71 ± 0.53^c	11.33 ± 0.51^c	6.907 ± 0.306^c
12	F01325-3623	ESO 353-G020	01 : 34 : 51.26	− 36 : 08 : 14.4	45	17.93	10.58 ± 0.49^c	16.43 ± 0.75^c	15.26 ± 0.68^c
13	F01341-3735	ESO 297-G 011	01 : 36 : 23.39	− 37 : 19 : 18.1	35	12.22	5.528 ± 0.250^c	8.316 ± 0.373^c	7.820 ± 0.341^c
13	F01341-3735	ESO 297-G 012	01 : 36 : 24.14	− 37 : 20 : 25.9	25	8.727	3.766 ± 0.166^c	4.130 ± 0.180^c	2.779 ± 0.116^c
13	F01341-3735	RR 032	01 : 36 : 23.76	− 37 : 19 : 51.9	···	···	9.294 ± 0.300^c	12.45 ± 0.41^c	10.60 ± 0.36^c
14	F01364-1042	IRAS F01364-1042	01 : 38 : 52.79	− 10 : 27 : 12.1	35	32.43	7.395 ± 0.334^c	6.845 ± 0.307^c	3.989 ± 0.174^c
15	F01417+1651	III Zw 035	01 : 44 : 30.56	+ 17 : 06 : 09.0	40	21.84	14.74 ± 0.67^c	13.44 ± 0.61^c	7.770 ± 0.344^c
16	F01484+2220	NGC 695	01 : 51 : 14.34	+ 22 : 34 : 56.0	45	28.45	9.303 ± 0.466	13.24 ± 0.66	11.20 ± 0.56

continued on the next page

Table 2.4. (continued) *Herschel* PACS Total and Component Fluxes of GOALS Systems

#	IRAS Name	Optical Name	RA	Dec.	Ang. Ap.	Phys. Ap.	$F_\lambda(70\ \mu m)$	$F_\lambda(100\ \mu m)$	$F_\lambda(160\ \mu m)$
—	—	—	HH:MM:SS	DD:MM:SS	$''$	kpc	Jy	Jy	Jy
17	F01519+3640	UGC 01385	01 : 54 : 53.82	+36 : 55 : 04.3	45	16.78	6.542 ± 0.301^c	7.828 ± 0.358^c	5.595 ± 0.251^c
17	F01519+3640	KUG 0152+366	01 : 55 : 01.75	+36 : 55 : 11.6	30	11.18	0.227 ± 0.018	0.439 ± 0.026	0.697 ± 0.037
17	F01519+3640	IRGP J015457.8+365508	01 : 54 : 57.78	+36 : 55 : 07.9	···	···	6.769 ± 0.302^c	8.267 ± 0.359^c	6.291 ± 0.253^c
18	F02071-1023	NGC 839	02 : 09 : 42.81	−10 : 11 : 02.0	50	12.92	13.70 ± 0.63^c	13.74 ± 0.63^c	8.861 ± 0.401^c
18	F02071-1023	NGC 838	02 : 09 : 38.66	−10 : 08 : 47.2	60	15.50	15.35 ± 0.72^c	18.26 ± 0.85^c	14.24 ± 0.65^c
18	F02071-1023	NGC 835	02 : 09 : 24.64	−10 : 08 : 09.3	40	10.34	7.041 ± 0.353	11.02 ± 0.55	10.19 ± 0.51
18	F02071-1023	NGC 833	02 : 09 : 20.87	−10 : 07 : 59.4	24	6.202	0.350 ± 0.027	0.590 ± 0.037	0.767 ± 0.043
18	F02071-1023	NGC 835/0833	02 : 09 : 24.64	−10 : 08 : 09.3	80	20.67	7.856 ± 0.397	11.99 ± 0.60	11.44 ± 0.57
18	F02071-1023	HCG 016	02 : 09 : 36.13	−10 : 09 : 32.6	···	···	36.90 ± 1.04^c	44.00 ± 1.22^c	34.54 ± 0.96^c
19	F02070+3857	NGC 828	02 : 10 : 09.53	+39 : 11 : 24.7	50	17.84	14.56 ± 0.73	24.95 ± 1.25	24.86 ± 1.24
20	F02114+0456	IC 0214	02 : 14 : 05.56	+05 : 10 : 23.7	40	23.74	5.708 ± 0.286	7.558 ± 0.378	6.174 ± 0.309
20	F02114+0456		02 : 13 : 55.99	+05 : 10 : 04.0	23	13.65	0.214 ± 0.015	0.474 ± 0.026	0.498 ± 0.027
20	F02114+0456	IRGP J021400.8+051014	02 : 14 : 00.77	+05 : 10 : 13.8	···	···	5.922 ± 0.287	8.032 ± 0.379	6.672 ± 0.310
21	F02152+1418	NGC 877	02 : 17 : 53.26	+14 : 31 : 18.4	48	12.31	3.303 ± 0.167	4.965 ± 0.249	4.741 ± 0.238
21	F02152+1418	NGC 876	02 : 17 : 59.68	+14 : 32 : 38.2	75	19.23	12.81 ± 0.64	23.60 ± 1.18	26.51 ± 1.33
21	F02152+1418	IRGP J021756.5+143158	02 : 17 : 56.46	+14 : 31 : 58.2	···	···	16.11 ± 0.66	28.56 ± 1.21	31.25 ± 1.35
22	F02203+3158	MCG+05-06-036	02 : 23 : 21.99	+32 : 11 : 48.8	30	19.74	6.814 ± 0.304^c	9.600 ± 0.426^c	8.152 ± 0.348^c
22	F02203+3158	MCG+05-06-035	02 : 23 : 18.97	+32 : 11 : 18.5	23	15.13	2.255 ± 0.099^c	3.426 ± 0.148^c	3.150 ± 0.130^c
22	F02203+3158	KPG 067	02 : 23 : 20.47	+32 : 11 : 33.6	···	···	9.069 ± 0.320^c	13.03 ± 0.45^c	11.30 ± 0.37^c
23	F02208+4744	UGC 01845	02 : 24 : 07.97	+47 : 58 : 11.9	35	11.03	13.11 ± 0.59^c	17.48 ± 0.78^c	13.75 ± 0.60^c
24	F02281-0309	NGC 958	02 : 30 : 42.84	−02 : 56 : 20.5	75	28.22	8.261 ± 0.415	16.78 ± 0.84	19.75 ± 0.99
25	F02345+2053	NGC 992	02 : 37 : 25.46	+21 : 06 : 02.8	50	13.67	11.90 ± 0.60	16.25 ± 0.81	13.37 ± 0.67
26	F02401-0013	NGC 1068	02 : 42 : 40.72	−00 : 00 : 47.9	170	13.02	285.8 ± 14.3	···	290.9 ± 14.5
27	F02435+1253	UGC 02238	02 : 46 : 17.46	+13 : 05 : 44.6	45	19.31	9.946 ± 0.498	15.33 ± 0.77	13.48 ± 0.67
28	F02437+2122	IRAS F02437+2122	02 : 46 : 39.13	+21 : 35 : 10.4	35	16.02	6.927 ± 0.313^c	7.725 ± 0.347^c	5.027 ± 0.219^c
28	F02437+2123[a]		02 : 46 : 45.05	+21 : 33 : 23.5	25	11.44	0.195 ± 0.014	0.541 ± 0.029	0.584 ± 0.031
29	F02512+1446	MCG+02-08-029	02 : 54 : 01.84	+14 : 58 : 15.7	···	···	···	···	···
29	F02512+1446	MCG+02-08-030	02 : 54 : 01.75	+14 : 58 : 36.4	···	···	···	···	···
29	F02512+1446	UGC 02369	02 : 54 : 01.79	+14 : 58 : 26.0	40	24.76	8.701 ± 0.436	10.36 ± 0.52	7.659 ± 0.383
30	F03117+4151	UGC 02608	03 : 15 : 01.47	+42 : 02 : 08.6	45	20.83	9.116 ± 0.456	11.57 ± 0.58	9.210 ± 0.461

continued on the next page

Table 2.4. (continued) *Herschel* PACS Total and Component Fluxes of GOALS Systems

#	IRAS Name	Optical Name	RA	Dec.	Ang. Ap.	Phys. Ap.	$F_\lambda(70\ \mu m)$	$F_\lambda(100\ \mu m)$	$F_\lambda(160\ \mu m)$
—	—	—	HH:MM:SS	DD:MM:SS	$''$	kpc	Jy	Jy	Jy
30	F03117+4151[a]	UGC 02612	03 : 15 : 14.58	+41 : 58 : 50.0	37	17.13	0.575 ± 0.032	1.341 ± 0.069	1.660 ± 0.084
31	F03164+4119	NGC 1275	03 : 19 : 48.18	+41 : 30 : 42.0	50	17.55	6.807 ± 0.343	7.490 ± 0.377	5.691 ± 0.286
32	F03217+4022	IRAS F03217+4022	03 : 25 : 05.37	+40 : 33 : 32.2	35	16.20	9.122 ± 0.412^c	10.84 ± 0.49^c	7.913 ± 0.345^c
33	F03316-3618	NGC 1365	03 : 33 : 36.40	−36 : 08 : 25.9	320	27.46	137.6 ± 6.9	221.5 ± 11.1	209.7 ± 10.5
34	F03359+1523	IRAS F03359+1523	03 : 38 : 47.07	+15 : 32 : 54.1	35	24.06	7.170 ± 0.324^c	7.541 ± 0.339^c	4.878 ± 0.213^c
35	F03514+1546[a]	CGCG 465-011	03 : 54 : 07.67	+15 : 59 : 24.3	40	17.47	2.255 ± 0.114	3.804 ± 0.191	4.015 ± 0.201
35	F03514+1546	CGCG 465-012	03 : 54 : 15.95	+15 : 55 : 43.4	35	15.29	6.673 ± 0.334	8.845 ± 0.443	6.946 ± 0.348
36	03582+6012	IRAS 03582+6012NE	04 : 02 : 32.99	+60 : 20 : 41.8	···	···	···	···	···
36	03582+6012	IRAS 03582+6012SW	04 : 02 : 31.97	+60 : 20 : 38.3	···	···	···	···	···
36	03582+6012	IRAS 03582+6012	04 : 02 : 32.47	+60 : 20 : 40.0	33	19.76	5.685 ± 0.285	5.922 ± 0.296	3.745 ± 0.188
37	F04097+0525	UGC 02982	04 : 12 : 22.68	+05 : 32 : 49.1	50	17.53	10.52 ± 0.53	16.86 ± 0.84	15.62 ± 0.78
38	F04118-3207	ESO 420-G013	04 : 13 : 49.70	−32 : 00 : 25.3	45	10.86	17.57 ± 0.81^c	22.28 ± 1.02^c	16.82 ± 0.75^c
39	F04191-1855	ESO 550-IG 025 NED01	04 : 21 : 20.08	−18 : 48 : 57.4	10	6.303	2.671 ± 0.104^c	3.663 ± 0.133^c	3.110 ± 0.096^c
39	F04191-1855	ESO 550-IG 025 NED02	04 : 21 : 20.02	−18 : 48 : 39.6	8	5.042	4.438 ± 0.160^c	5.781 ± 0.195^c	4.736 ± 0.125^c
39	F04191-1855	ESO 550-IG 025	04 : 21 : 20.04	−18 : 48 : 48.4	40	25.21	6.452 ± 0.323	8.676 ± 0.434	7.115 ± 0.356
40	F04210-4042	NGC 1572	04 : 22 : 42.81	−40 : 36 : 03.1	45	18.57	10.02 ± 0.50	16.45 ± 0.82	15.32 ± 0.77
41	04271+3849	IRAS 04271+3849	04 : 30 : 33.09	+38 : 55 : 47.8	35	13.20	7.402 ± 0.371	10.97 ± 0.49^c	8.846 ± 0.385^c
42	F04315-0840	NGC 1614	04 : 33 : 59.95	−08 : 34 : 46.6	50	15.93	36.74 ± 1.70^c	37.00 ± 1.70^c	22.96 ± 1.04^c
43	F04326+1904	UGC 03094	04 : 35 : 33.81	+19 : 10 : 18.0	50	24.46	8.159 ± 0.409	12.77 ± 0.64	11.93 ± 0.60
44	F04454-4838	ESO 203-IG001	04 : 46 : 49.55	−48 : 33 : 30.6	28	28.78	6.125 ± 0.272^c	5.284 ± 0.233^c	2.945 ± 0.125^c
45	F04502-3304	MCG-05-12-006	04 : 52 : 04.96	−32 : 59 : 26.0	35	13.29	9.169 ± 0.414^c	10.35 ± 0.46^c	6.949 ± 0.303^c
46	F05053-0805	NGC 1797	05 : 07 : 44.84	−08 : 01 : 08.7	45	13.44	11.00 ± 0.51^c	13.49 ± 0.62^c	10.83 ± 0.48^c
46	F05053-0805[a]	NGC 1799	05 : 07 : 44.59	−07 : 58 : 09.0	40	11.95	0.402 ± 0.027	0.818 ± 0.044	0.954 ± 0.049
47	F05054+1718	CGCG 468-002 NED01	05 : 08 : 19.71	+17 : 21 : 47.8	15	5.461	2.389 ± 0.099^c	2.941 ± 0.121^c	2.375 ± 0.087^c
47	F05054+1718	CGCG 468-002 NED02	05 : 08 : 21.21	+17 : 22 : 08.0	18	6.554	9.426 ± 0.402^c	9.891 ± 0.414^c	6.467 ± 0.251^c
47	F05054+1718	CGCG 468-002	05 : 08 : 20.46	+17 : 21 : 57.8	40	14.56	10.43 ± 0.52	11.15 ± 0.56	7.394 ± 0.370
48	05083+2441	IRAS 05083+2441	05 : 11 : 25.88	+24 : 45 : 18.2	30	13.79	6.982 ± 0.312^c	7.413 ± 0.329^c	4.739 ± 0.203^c
48	05083+2441		05 : 11 : 29.05	+24 : 46 : 04.0	30	13.79	0.594 ± 0.033	0.935 ± 0.049	0.977 ± 0.050
48	05083+2441	IRGP J051127.4+244539	05 : 11 : 27.46	+24 : 45 : 41.1	···	···	7.576 ± 0.314^c	8.348 ± 0.333^c	5.716 ± 0.209^c
49	F05081+7936	VII Zw 031	05 : 16 : 46.39	+79 : 40 : 12.9	35	36.69	7.492 ± 0.338^c	10.12 ± 0.45^c	8.055 ± 0.351^c

continued on the next page

Table 2.4. (continued) *Herschel* PACS Total and Component Fluxes of GOALS Systems

#	IRAS Name	Optical Name	RA	Dec.	Ang. Ap.	Phys. Ap.	$F_\lambda(70\ \mu m)$	$F_\lambda(100\ \mu m)$	$F_\lambda(160\ \mu m)$
—	—	—	HH:MM:SS	DD:MM:SS	$''$	kpc	Jy	Jy	Jy
50	05129+5128	IRAS 05129+5128	05 : 16 : 55.96	+ 51 : 31 : 56.9	35	19.29	7.273 ± 0.329^c	7.655 ± 0.344^c	5.028 ± 0.219^c
51	F05189-2524	IRAS F05189-2524	05 : 21 : 01.45	− 25 : 21 : 46.2	35	29.19	13.53 ± 0.61^c	11.39 ± 0.51^c	6.180 ± 0.269^c
52	F05187-1017	IRAS F05187-1017	05 : 21 : 06.53	− 10 : 14 : 46.2	40	22.38	6.782 ± 0.309^c	8.595 ± 0.389^c	6.583 ± 0.292^c
53	05368+4940	MCG+08-11-002	05 : 40 : 43.70	+ 49 : 41 : 41.6	40	15.63	19.40 ± 0.88^c	26.93 ± 1.22^c	21.56 ± 0.95^c
54	F05365+6921	NGC 1961	05 : 42 : 04.55	+ 69 : 22 : 42.8	120	33.45	11.59 ± 0.58	26.26 ± 1.31	34.08 ± 1.71
55	F05414+5840	UGC 03351	05 : 45 : 48.03	+ 58 : 42 : 03.6	53	16.42	19.02 ± 0.95	31.33 ± 1.57	28.88 ± 1.44
56	05442+1732	IRAS 05442+1732	05 : 47 : 11.20	+ 17 : 33 : 46.4	35	13.13	10.84 ± 0.49^c	11.95 ± 0.54^c	8.035 ± 0.350^c
56	05442+1732	UGC 03356	05 : 47 : 05.79	+ 17 : 33 : 11.9	35	13.13	1.026 ± 0.054	1.955 ± 0.099	2.141 ± 0.108
56	05442+1732	HIPASS J0547+17	05 : 47 : 08.49	+ 17 : 33 : 29.1	···	···	11.86 ± 0.49^c	13.91 ± 0.55^c	10.18 ± 0.37^c
57	F06076-2139	IRAS F06076-2139NW	06 : 09 : 45.74	− 21 : 40 : 24.5	···	···	···	···	···
57	F06076-2139	IRAS F06076-2139SE	06 : 09 : 45.95	− 21 : 40 : 32.1	···	···	···	···	···
57	F06076-2139	IRAS F06076-2139	06 : 09 : 45.84	− 21 : 40 : 28.3	30	22.30	7.554 ± 0.338^c	8.405 ± 0.373^c	5.664 ± 0.242^c
58	F06052+8027	UGC 03410	06 : 14 : 29.61	+ 80 : 26 : 59.6	52	14.34	10.34 ± 0.52	17.92 ± 0.90	18.52 ± 0.93
58	F06052+8027	UGC 03405	06 : 13 : 57.90	+ 80 : 28 : 34.7	45	12.41	2.083 ± 0.106	4.294 ± 0.216	5.071 ± 0.255
58	F06052+8027	KPG 108	06 : 14 : 13.75	+ 80 : 27 : 47.1	···	···	12.42 ± 0.53	22.21 ± 0.92	23.59 ± 0.96
59	F06107+7822	NGC 2146	06 : 18 : 37.82	+ 78 : 21 : 24.0	120	10.12	198.7 ± 9.9	237.1 ± 11.9	174.4 ± 8.7
60	F06259-4708	ESO 255-IG 007 NED01	06 : 27 : 21.70	− 47 : 10 : 36.2	···	···	···	···	···
60	F06259-4708	ESO 255-IG 007 NED02	06 : 27 : 22.55	− 47 : 10 : 47.3	···	···	···	···	···
60	F06259-4708	ESO 255-IG 007 NED03	06 : 27 : 23.09	− 47 : 11 : 02.6	···	···	···	···	···
60	F06259-4708	ESO 255-IG007	06 : 27 : 22.39	− 47 : 10 : 49.4	45	34.97	9.801 ± 0.491	10.67 ± 0.53	7.175 ± 0.359
61	F06295-1735	ESO 557-G002	06 : 31 : 47.20	− 17 : 37 : 16.6	40	17.36	7.144 ± 0.326^c	8.081 ± 0.366^c	6.001 ± 0.266^c
61	F06295-1735	ESO 557-G001	06 : 31 : 45.71	− 17 : 38 : 44.9	30	13.02	1.555 ± 0.079	2.208 ± 0.111	1.684 ± 0.085
61	F06295-1735	IRGP J063146.5-173802	06 : 31 : 46.45	− 17 : 38 : 00.7	···	···	8.699 ± 0.335^c	10.29 ± 0.38^c	7.685 ± 0.279^c
62	F06538+4628	UGC 3608	06 : 57 : 34.41	+ 46 : 24 : 10.6	40	17.53	8.877 ± 0.444	10.62 ± 0.53	8.315 ± 0.416
63	F06592-6313	IRAS F06592-6313	06 : 59 : 40.26	− 63 : 17 : 52.4	35	16.87	6.904 ± 0.312^c	7.530 ± 0.338^c	5.027 ± 0.219^c
64	F07027-6011	AM 0702-601 NED01	07 : 03 : 24.14	− 60 : 15 : 21.9	28	18.00	2.554 ± 0.114^c	2.700 ± 0.120^c	2.081 ± 0.089^c
64	F07027-6011	AM 0702-601 NED02	07 : 03 : 28.52	− 60 : 16 : 43.7	28	18.00	5.253 ± 0.234^c	6.529 ± 0.288^c	4.957 ± 0.210^c
64	F07027-6011	AM 0702-601	07 : 03 : 26.33	− 60 : 16 : 02.7	···	···	7.807 ± 0.260^c	9.229 ± 0.312^c	7.038 ± 0.228^c
65	07063+2043	NGC 2342	07 : 09 : 18.07	+ 20 : 38 : 10.2	55	20.00	9.528 ± 0.477	14.86 ± 0.74	13.45 ± 0.67
65	07063+2043	NGC 2341	07 : 09 : 12.01	+ 20 : 36 : 11.2	35	12.73	8.112 ± 0.406	11.00 ± 0.55	8.818 ± 0.441

continued on the next page

Table 2.4. (continued) *Herschel* PACS Total and Component Fluxes of GOALS Systems

#	IRAS Name	Optical Name	RA	Dec.	Ang. Ap.	Phys. Ap.	$F_\lambda(70\ \mu m)$	$F_\lambda(100\ \mu m)$	$F_\lambda(160\ \mu m)$
—	—	—	HH:MM:SS	DD:MM:SS	$''$	kpc	Jy	Jy	Jy
65	07063+2043	KPG 125	07 : 09 : 15.04	+ 20 : 37 : 10.7	···	···	17.64 ± 0.63	25.86 ± 0.93	22.26 ± 0.80
66	F07160-6215	NGC 2369	07 : 16 : 37.73	− 62 : 20 : 36.4	60	13.56	26.90 ± 1.35	41.22 ± 2.06	37.55 ± 1.88
67	07251-0248	IRAS 07251-0248	07 : 27 : 37.62	− 02 : 54 : 54.8	35	57.39	7.024 ± 0.317^{c}	6.419 ± 0.288^{c}	3.878 ± 0.169^{c}
68	F07256+3355	NGC 2389	07 : 29 : 04.59	+ 33 : 51 : 38.0	50	14.47	3.802 ± 0.194	6.412 ± 0.323	6.601 ± 0.332
68	F07256+3355	NGC 2388	07 : 28 : 53.44	+ 33 : 49 : 07.8	50	14.47	20.68 ± 0.96^{c}	26.43 ± 1.21^{c}	21.16 ± 0.96^{c}
68	F07256+3355	NGC 2385	07 : 28 : 28.17	+ 33 : 50 : 16.9	···	···	... [b]	... [b]	... [b]
68	F07256+3355	WBL 142	07 : 28 : 46.38	+ 33 : 50 : 22.9	···	···	24.48 ± 0.98^{c}	32.84 ± 1.26^{c}	27.76 ± 1.01^{c}
69	F07329+1149	MCG+02-20-003	07 : 35 : 43.44	+ 11 : 42 : 34.8	37	12.92	10.61 ± 0.48^{c}	13.13 ± 0.59^{c}	9.969 ± 0.437^{c}
69	F07329+1149[a]	NGC 2416	07 : 35 : 41.53	+ 11 : 36 : 42.1	32	11.17	0.897 ± 0.047	1.705 ± 0.086	1.956 ± 0.098
70	08355-4944	IRAS 08355-4944	08 : 37 : 01.87	− 49 : 54 : 30.0	35	19.02	10.25 ± 0.46^{c}	9.529 ± 0.428^{c}	5.637 ± 0.246^{c}
71	F08339+6517	IRAS F08339+6517	08 : 38 : 23.18	+ 65 : 07 : 15.2	45	18.13	5.865 ± 0.294	6.163 ± 0.309	3.979 ± 0.200
72	F08354+2555	NGC 2623	08 : 38 : 24.11	+ 25 : 45 : 16.5	40	15.73	27.92 ± 1.27^{c}	28.46 ± 1.29^{c}	17.65 ± 0.78^{c}
73	08424-3130	ESO 432-IG006SW	08 : 44 : 27.21	− 31 : 41 : 50.8	17	5.942	4.823 ± 0.204^{c}	6.700 ± 0.279^{c}	5.638 ± 0.215^{c}
73	08424-3130	ESO 432-IG006NE	08 : 44 : 28.93	− 31 : 41 : 30.3	14	4.894	3.469 ± 0.143^{c}	3.962 ± 0.160^{c}	2.783 ± 0.099^{c}
73	08424-3130	ESO 432-IG006	08 : 44 : 28.07	− 31 : 41 : 40.5	52	18.18	7.597 ± 0.381	9.841 ± 0.493	7.663 ± 0.384
74	F08520-6850	ESO 060-IG 016 NED01	08 : 52 : 32.07	− 69 : 01 : 54.8	···	···	···	···	···
74	F08520-6850	ESO 060-IG 016 NED02	08 : 52 : 30.50	− 69 : 01 : 59.2	···	···	···	···	···
74	F08520-6850	ESO 060-IG 016	08 : 52 : 31.28	− 69 : 01 : 57.0	33	30.69	5.468 ± 0.274	5.560 ± 0.278	3.496 ± 0.175
75	F08572+3915	IRAS F08572+3915	09 : 00 : 25.35	+ 39 : 03 : 54.0	25	28.57	6.398 ± 0.282^{c}	4.452 ± 0.194^{c}	1.997 ± 0.084^{c}
76	09022-3615	IRAS 09022-3615	09 : 04 : 12.69	− 36 : 27 : 01.5	35	40.96	12.81 ± 0.58^{c}	13.14 ± 0.59^{c}	8.057 ± 0.351^{c}
77	F09111-1007	2MASX J09133644-1019296	09 : 13 : 36.50	− 10 : 19 : 29.7	20	21.47	7.284 ± 0.315^{c}	8.923 ± 0.378^{c}	6.554 ± 0.262^{c}
77	F09111-1007	2MASX J09133888-1019196	09 : 13 : 38.89	− 10 : 19 : 19.6	20	21.47	2.003 ± 0.087^{c}	2.674 ± 0.114^{c}	2.327 ± 0.093^{c}
77	F09111-1007	IRAS F09111-1007	09 : 13 : 37.69	− 10 : 19 : 24.6	50	53.67	8.314 ± 0.417	10.35 ± 0.52	7.726 ± 0.387
78	F09126+4432	CGCG 209-036	09 : 15 : 44.49	+ 44 : 14 : 09.6	···	···	···	···	···
78	F09126+4432	UGC04881 NED01	09 : 15 : 55.52	+ 44 : 19 : 57.4	···	···	···	···	···
78	F09126+4432	UGC04881 NED02	09 : 15 : 54.69	+ 44 : 19 : 50.8	···	···	···	···	···
78	F09126+4432	UGC 04881	09 : 15 : 55.10	+ 44 : 19 : 54.0	45	35.93	7.311 ± 0.366	9.282 ± 0.465	7.433 ± 0.372
79	F09320+6134	UGC 05101	09 : 35 : 51.59	+ 61 : 21 : 11.9	30	23.82	15.34 ± 0.69^{c}	···	15.29 ± 0.65^{c}
80	F09333+4841	MCG+08-18-013	09 : 36 : 37.20	+ 48 : 28 : 27.7	37	19.70	7.330 ± 0.333^{c}	8.600 ± 0.387^{c}	6.416 ± 0.282^{c}
80	F09333+4841	MCG+08-18-012	09 : 36 : 30.86	+ 48 : 28 : 09.9	28	14.91	0.134 ± 0.023	0.235 ± 0.016	0.320 ± 0.019

continued on the next page

Table 2.4. (continued) *Herschel* PACS Total and Component Fluxes of GOALS Systems

#	IRAS Name	Optical Name	RA	Dec.	Ang. Ap.	Phys. Ap.	$F_\lambda(70\ \mu m)$	$F_\lambda(100\ \mu m)$	$F_\lambda(160\ \mu m)$
—	—	—	HH:MM:SS	DD:MM:SS	$''$	kpc	Jy	Jy	Jy
80	F09333+4841	CGCG 239-011	09 : 36 : 34.02	+ 48 : 28 : 18.8	···	···	7.463 ± 0.334^c	8.835 ± 0.388^c	6.737 ± 0.282^c
81	F09437+0317	IC 0564	09 : 46 : 21.10	+ 03 : 04 : 16.3	50	21.65	3.334 ± 0.168	6.625 ± 0.332	7.802 ± 0.391
81	F09437+0317	IC 0563	09 : 46 : 20.30	+ 03 : 02 : 44.7	40	17.32	3.542 ± 0.178	5.749 ± 0.288	5.604 ± 0.281
81	F09437+0317	Arp 303	09 : 46 : 20.70	+ 03 : 03 : 30.4	···	···	6.876 ± 0.244	12.37 ± 0.44	13.41 ± 0.48
82	F10015-0614	NGC 3110	10 : 04 : 02.11	− 06 : 28 : 29.5	50	18.23	13.81 ± 0.69	20.79 ± 1.04	18.91 ± 0.95
82	F10015-0614	MCG-01-26-013	10 : 03 : 57.03	− 06 : 29 : 47.7	30	10.94	1.597 ± 0.073^c	2.153 ± 0.097^c	1.852 ± 0.080^c
82	F10015-0614	IRGP J100359.6-062908	10 : 03 : 59.57	− 06 : 29 : 08.5	···	···	15.41 ± 0.69^c	22.94 ± 1.04^c	20.76 ± 0.95^c
83	F10038-3338	ESO 374-IG 032	10 : 06 : 04.65	− 33 : 53 : 06.1	35	24.76	10.14 ± 0.46^c	8.693 ± 0.390^c	5.048 ± 0.220^c
84	F10173+0828	IRAS F10173+0828	10 : 20 : 00.24	+ 08 : 13 : 32.8	40	39.46	6.298 ± 0.287^c	5.677 ± 0.257^c	3.169 ± 0.141^c
85	F10196+2149	NGC 3221	10 : 22 : 19.98	+ 21 : 34 : 10.6	95	29.43	10.43 ± 0.52	20.96 ± 1.05	24.06 ± 1.20
86	F10257-4339	NGC 3256	10 : 27 : 51.30	− 43 : 54 : 14.0	70	12.96	120.3 ± 6.0	135.4 ± 6.8	93.48 ± 4.68
87	F10409-4556	ESO 264-G036	10 : 43 : 07.51	− 46 : 12 : 44.1	45	20.92	7.974 ± 0.399	13.09 ± 0.65	13.10 ± 0.66
88	F10567-4310	ESO 264-G057	10 : 59 : 01.70	− 43 : 26 : 25.2	40	15.61	6.910 ± 0.346	11.10 ± 0.56	10.41 ± 0.52
89	F10565+2448	IRAS F10565+2448	10 : 59 : 18.15	+ 24 : 32 : 34.2	35	25.05	14.26 ± 0.64^c	15.80 ± 0.71^c	10.45 ± 0.46^c
90	F11011+4107	MCG+07-23-019	11 : 03 : 53.98	+ 40 : 51 : 00.4	40	28.62	8.484 ± 0.387^c	10.52 ± 0.48^c	7.825 ± 0.346^c
91	F11186-0242	CGCG 011-076	11 : 21 : 12.24	− 02 : 59 : 02.5	40	21.43	6.460 ± 0.295^c	8.954 ± 0.405^c	7.885 ± 0.349^c
91	F11186-0242	2MASX J11210825-0259399	11 : 21 : 08.29	− 02 : 59 : 39.2	27	14.46	0.281 ± 0.018^c	0.520 ± 0.026^c	0.427 ± 0.021^c
91	F11186-0242	IRGP J112110.3-025922	11 : 21 : 10.26	− 02 : 59 : 20.8	···	···	6.742 ± 0.295^c	9.474 ± 0.406^c	8.312 ± 0.350^c
92	F11231+1456	IC 2810	11 : 25 : 45.07	+ 14 : 40 : 36.0	30	21.23	5.703 ± 0.255^c	7.671 ± 0.341^c	6.251 ± 0.267^c
92	F11231+1456	MCG+03-29-044	11 : 25 : 49.55	+ 14 : 40 : 06.6	25	17.70	2.753 ± 0.122^c	3.734 ± 0.163^c	3.096 ± 0.130^c
92	F11231+1456	IRAS F11231+1456	11 : 25 : 47.31	+ 14 : 40 : 21.2	···	···	8.456 ± 0.283^c	11.40 ± 0.38^c	9.348 ± 0.297^c
93	F11255-4120	ESO 319-G022	11 : 27 : 54.18	− 41 : 36 : 51.7	40	15.01	9.086 ± 0.414^c	10.53 ± 0.48^c	7.785 ± 0.344^c
94	F11257+5850	UGC 6471	11 : 28 : 31.04	+ 58 : 33 : 40.5	···	···	···	···	···
94	F11257+5850	UGC 6472	11 : 28 : 33.67	+ 58 : 33 : 46.1	···	···	···	···	···
94	F11257+5850	NGC 3690	11 : 28 : 32.35	+ 58 : 33 : 43.3	75	18.07	130.3 ± 6.5	118.3 ± 5.9	68.77 ± 3.44
95	F11506-3851	ESO 320-G030	11 : 53 : 11.73	− 39 : 07 : 49.0	60	11.72	41.98 ± 1.97^c	49.14 ± 2.28^c	34.81 ± 1.59^c
96	F12043-3140	MCG-05-29-016	12 : 06 : 51.87	− 31 : 56 : 59.2	···	···	···	···	···
96	F12043-3140	MCG-05-29-017	12 : 06 : 51.70	− 31 : 56 : 46.4	···	···	···	···	···
96	F12043-3140	ESO 440-IG058	12 : 06 : 51.78	− 31 : 56 : 52.8	35	18.16	8.197 ± 0.410	10.89 ± 0.54	8.693 ± 0.435
97	F12112+0305	IRAS F12112+0305	12 : 13 : 46.02	+ 02 : 48 : 42.2	35	50.07	9.283 ± 0.419^c	9.241 ± 0.415^c	5.831 ± 0.254^c

continued on the next page

Table 2.4. (continued) *Herschel* PACS Total and Component Fluxes of GOALS Systems

#	IRAS Name	Optical Name	RA	Dec.	Ang. Ap.	Phys. Ap.	$F_\lambda(70\ \mu m)$	$F_\lambda(100\ \mu m)$	$F_\lambda(160\ \mu m)$
—	—	—	HH:MM:SS	DD:MM:SS	$''$	kpc	Jy	Jy	Jy
98	F12116+5448	NGC 4194	12 : 14 : 09.71	+ 54 : 31 : 35.5	50	10.25	26.20 ± 1.21^c	26.14 ± 1.20^c	16.60 ± 0.75^c
99	F12115-4656	ESO 267-G030	12 : 14 : 12.81	− 47 : 13 : 42.5	40	18.04	6.914 ± 0.346	10.26 ± 0.51	9.280 ± 0.464
99	F12115-4656[a]	ESO 267-G029	12 : 13 : 52.28	− 47 : 16 : 25.4	50	22.54	5.725 ± 0.287	7.924 ± 0.397	7.143 ± 0.358
100	12116-5615	IRAS 12116-5615	12 : 14 : 22.08	− 56 : 32 : 32.7	35	20.58	11.76 ± 0.53^c	13.02 ± 0.58^c	8.808 ± 0.384^c
101	F12224-0624	IRAS F12224-0624	12 : 25 : 03.90	− 06 : 40 : 52.1	35	20.14	7.145 ± 0.323^c	7.761 ± 0.348^c	5.079 ± 0.221^c
102	F12243-0036	NGC 4418	12 : 26 : 54.60	− 00 : 52 : 39.6	50	8.799	42.81 ± 1.98^c	34.12 ± 1.57^c	18.32 ± 0.83^c
102	F12243-0036	MCG+00-32-013	12 : 27 : 04.88	− 00 : 54 : 24.7	25	4.400	0.233 ± 0.018	0.337 ± 0.021	0.357 ± 0.018^c
102	F12243-0036	KPG 337	12 : 26 : 59.74	− 00 : 53 : 32.1	···	···	43.05 ± 1.98^c	34.46 ± 1.57^c	18.67 ± 0.83^c
103	F12540+5708	UGC 08058	12 : 56 : 14.25	+ 56 : 52 : 24.8	35	30.00	34.87 ± 1.59^c	30.41 ± 1.37^c	16.93 ± 0.74^c
104	F12590+2934	2MASX J13012450+2918306	13 : 01 : 25.27	+ 29 : 18 : 49.5	···	···	···	···	···
104	F12590+2934	FIRST J130125.2+291849	13 : 01 : 24.51	+ 29 : 18 : 29.8	···	···	···	···	···
104	F12590+2934	NGC 4922	13 : 01 : 24.89	+ 29 : 18 : 39.6	40	20.54	6.763 ± 0.309^c	7.606 ± 0.345^c	5.283 ± 0.234^c
105	F12592+0436	CGCG 043-099	13 : 01 : 50.28	+ 04 : 20 : 00.8	35	27.59	6.538 ± 0.295^c	8.455 ± 0.379^c	6.675 ± 0.291^c
106	F12596-1529	MCG-02-33-098SW	13 : 02 : 19.66	− 15 : 46 : 04.2	···	···	···	···	···
106	F12596-1529	MCG-02-33-098NE	13 : 02 : 20.38	− 15 : 45 : 59.6	···	···	···	···	···
106	F12596-1529	MCG-02-33-098	13 : 02 : 20.02	− 15 : 46 : 01.8	40	14.80	7.534 ± 0.377	8.490 ± 0.425	5.962 ± 0.299
107	F13001-2339	ESO 507-G070	13 : 02 : 52.42	− 23 : 55 : 17.8	43	21.16	16.32 ± 0.75^c	16.90 ± 0.77^c	10.66 ± 0.47^c
108	13052-5711	IRAS 13052-5711	13 : 08 : 18.73	− 57 : 27 : 30.3	38	18.72	10.49 ± 0.48^c	13.55 ± 0.61^c	10.13 ± 0.45^c
109	F13126+2453	IC 0860	13 : 15 : 03.49	+ 24 : 37 : 07.6	40	10.78	19.67 ± 0.90^c	18.09 ± 0.82^c	10.66 ± 0.47^c
110	13120-5453	IRAS 13120-5453	13 : 15 : 06.37	− 55 : 09 : 22.5	50	32.85	50.72 ± 2.35^c	55.02 ± 2.53^c	34.97 ± 1.58^c
111	F13136+6223	VV 250a	13 : 15 : 34.96	+ 62 : 07 : 29.2	21	13.55	10.70 ± 0.46^c	9.771 ± 0.417^c	5.513 ± 0.223^c
111	F13136+6223	VV 250b	13 : 15 : 30.69	+ 62 : 07 : 45.8	16	10.32	2.091 ± 0.088^c	2.730 ± 0.113^c	2.205 ± 0.082^c
111	F13136+6223	VV 250	13 : 15 : 32.82	+ 62 : 07 : 37.4	50	32.26	11.71 ± 0.59	11.16 ± 0.56	6.728 ± 0.337
112	F13182+3424	UGC 08387	13 : 20 : 35.37	+ 34 : 08 : 22.2	45	22.91	21.74 ± 1.00^c	25.82 ± 1.18^c	18.08 ± 0.81^c
113	F13188+0036	NGC 5104	13 : 21 : 23.09	+ 00 : 20 : 33.2	40	16.97	8.997 ± 0.410^c	13.54 ± 0.61^c	12.01 ± 0.53^c
114	F13197-1627	MCG-03-34-064	13 : 22 : 24.45	− 16 : 43 : 42.4	35	13.49	5.118 ± 0.232^c	4.863 ± 0.219^c	3.338 ± 0.146^c
114	F13197-1627	MCG-03-34-063	13 : 22 : 19.02	− 16 : 42 : 30.0	35	13.49	1.061 ± 0.057	1.588 ± 0.084	1.861 ± 0.095
114	F13197-1627	IRAS F13197-1627	13 : 22 : 21.73	− 16 : 43 : 06.2	···	···	6.179 ± 0.238^c	6.451 ± 0.234^c	5.199 ± 0.174^c
115	F13229-2934	NGC 5135	13 : 25 : 44.02	− 29 : 50 : 00.4	70	20.12	21.44 ± 1.07	31.12 ± 1.56	26.86 ± 1.34
116	13242-5713	ESO 173-G015	13 : 27 : 23.79	− 57 : 29 : 21.8	70	11.30	97.67 ± 4.89	105.8 ± 5.3	71.63 ± 3.58

continued on the next page

Table 2.4. (continued) *Herschel* PACS Total and Component Fluxes of GOALS Systems

#	IRAS Name	Optical Name	RA	Dec.	Ang. Ap.	Phys. Ap.	$F_\lambda(70\ \mu m)$	$F_\lambda(100\ \mu m)$	$F_\lambda(160\ \mu m)$
—	—	—	HH:MM:SS	DD:MM:SS	$''$	kpc	Jy	Jy	Jy
117	F13301-2356	IC 4280	13 : 32 : 53.40	− 24 : 12 : 25.5	45	17.41	7.647 ± 0.383	12.97 ± 0.65	12.52 ± 0.63
118	F13362+4831	KPG 388A	13 : 38 : 17.25	+ 48 : 16 : 32.9	···	···	···	···	···
118	F13362+4831	KPG 388B	13 : 38 : 17.79	+ 48 : 16 : 41.6	···	···	···	···	···
118	F13362+4831	NGC 5256	13 : 38 : 17.52	+ 48 : 16 : 37.2	40	23.68	8.113 ± 0.406	9.692 ± 0.485	7.069 ± 0.354
119	F13373+0105	NGC 5258	13 : 39 : 57.72	+ 00 : 49 : 53.0	45	22.65	7.311 ± 0.366	11.55 ± 0.58	11.03 ± 0.55
119	F13373+0105	NGC 5257	13 : 39 : 52.95	+ 00 : 50 : 25.9	43	21.64	6.664 ± 0.334	10.04 ± 0.50	9.350 ± 0.468
119	F13373+0105	Arp 240	13 : 39 : 55.34	+ 00 : 50 : 09.5	···	···	13.98 ± 0.50	21.58 ± 0.77	20.37 ± 0.72
120	F13428+5608	UGC 08696	13 : 44 : 42.12	+ 55 : 53 : 13.1	35	27.25	24.46 ± 1.11^c	22.32 ± 1.00^c	12.74 ± 0.56^c
121	F13470+3530	UGC 08739	13 : 49 : 13.94	+ 35 : 15 : 26.2	60	22.89	8.163 ± 0.409	14.94 ± 0.75	15.87 ± 0.79
122	F13478-4848	ESO 221-IG010	13 : 50 : 56.92	− 49 : 03 : 18.8	55	16.43	15.78 ± 0.79	21.63 ± 1.08	17.97 ± 0.90
123	F13497+0220	NGC 5331S	13 : 52 : 16.21	+ 02 : 06 : 05.1	17	12.32	6.750 ± 0.287^c	10.04 ± 0.42^c	···
123	F13497+0220	NGC 5331N	13 : 52 : 16.43	+ 02 : 06 : 30.9	13	9.151	1.496 ± 0.061^c	2.538 ± 0.101^c	···
123	F13497+0220	NGC 5331	13 : 52 : 16.32	+ 02 : 06 : 18.0	50	35.20	7.484 ± 0.375	11.27 ± 0.56	10.31 ± 0.52
124	F13564+3741	NGC 5395	13 : 58 : 37.96	+ 37 : 25 : 28.1	82	22.78	4.972 ± 0.251	10.61 ± 0.53	14.71 ± 0.74
124	F13564+3741	NGC 5394	13 : 58 : 33.64	+ 37 : 27 : 12.9	37	10.28	7.904 ± 0.358^c	10.11 ± 0.46^c	7.938 ± 0.348^c
124	F13564+3741	Arp 84	13 : 58 : 35.80	+ 37 : 26 : 20.5	···	···	12.88 ± 0.44^c	20.72 ± 0.70^c	22.65 ± 0.81^c
125	F14179+4927	CGCG 247-020	14 : 19 : 43.27	+ 49 : 14 : 11.9	35	19.36	6.514 ± 0.326	7.450 ± 0.373	4.904 ± 0.246
126	F14280+3126	NGC 5653W	14 : 30 : 09.67	+ 31 : 12 : 56.7	···	···	···	···	···
126	F14280+3126	NGC 5653E	14 : 30 : 10.44	+ 31 : 12 : 55.8	···	···	···	···	···
126	F14280+3126	NGC 5653	14 : 30 : 10.44	+ 31 : 12 : 55.8	50	14.25	15.03 ± 0.69^c	22.88 ± 1.05^c	21.09 ± 0.95^c
127	F14348-1447	IRAS F14378-1447 SW	14 : 37 : 38.28	− 15 : 00 : 24.2	···	···	···	···	···
127	F14348-1447	IRAS F14378-1447 NE	14 : 37 : 38.40	− 15 : 00 : 21.2	···	···	···	···	···
127	F14348-1447	IRAS F14348-1447	14 : 37 : 38.29	− 15 : 00 : 24.2	35	56.05	8.260 ± 0.373^c	8.385 ± 0.376^c	5.475 ± 0.239^c
128	F14378-3651	IRAS F14378-3651	14 : 40 : 59.04	− 37 : 04 : 32.0	28	37.52	6.857 ± 0.305^c	6.661 ± 0.294^c	3.917 ± 0.167^c
129	F14423-2039	NGC 5734	14 : 45 : 09.04	− 20 : 52 : 13.2	55	17.39	10.70 ± 0.54	17.42 ± 0.87	16.78 ± 0.84
129	F14423-2039	NGC 5743	14 : 45 : 11.02	− 20 : 54 : 48.6	45	14.22	6.246 ± 0.313	9.899 ± 0.495	9.151 ± 0.458
129	F14423-2039	IRGP J144510.0-205331	14 : 45 : 10.02	− 20 : 53 : 30.9	···	···	16.94 ± 0.62	27.32 ± 1.00	25.93 ± 0.96
130	F14547+2449	VV 340a	14 : 57 : 00.70	+ 24 : 37 : 05.8	25	17.76	7.488 ± 0.375	12.28 ± 0.61	11.16 ± 0.56
130	F14547+2449	VV 340b	14 : 57 : 00.32	+ 24 : 36 : 24.6	19	13.49	1.068 ± 0.054	1.873 ± 0.094	1.975 ± 0.099
130	F14547+2449	VV 340	14 : 57 : 00.51	+ 24 : 36 : 45.2	50	35.51	8.788 ± 0.440	14.70 ± 0.74	13.89 ± 0.69

continued on the next page

Table 2.4. (continued) *Herschel* PACS Total and Component Fluxes of GOALS Systems

#	IRAS Name	Optical Name	RA	Dec.	Ang. Ap.	Phys. Ap.	$F_\lambda(70\ \mu m)$	$F_\lambda(100\ \mu m)$	$F_\lambda(160\ \mu m)$
—	—	—	HH:MM:SS	DD:MM:SS	$''$	kpc	Jy	Jy	Jy
131	F14544-4255	IC 4518A	14 : 57 : 41.22	− 43 : 07 : 55.8	24	9.018	4.835 ± 0.242	5.842 ± 0.292	···
131	F14544-4255	IC 4518B	14 : 57 : 45.33	− 43 : 07 : 57.0	30	11.27	4.503 ± 0.202^c	7.678 ± 0.341^c	···
131	F14544-4255	IC 4518	14 : 57 : 43.27	− 43 : 07 : 56.3	65	24.42	9.106 ± 0.457	12.89 ± 0.65	12.29 ± 0.62
132	F15107+0724	CGCG 049-057	15 : 13 : 13.07	+ 07 : 13 : 32.1	50	15.44	27.65 ± 1.28^c	31.67 ± 1.45^c	21.83 ± 0.99^c
133	F15163+4255	VV 705 NED01	15 : 18 : 06.14	+ 42 : 44 : 45.0	···	···	···	···	···
133	F15163+4255	VV 705 NED02	15 : 18 : 06.34	+ 42 : 44 : 38.1	···	···	···	···	···
133	F15163+4255	VV 705	15 : 18 : 06.24	+ 42 : 44 : 41.5	35	28.71	9.027 ± 0.452	9.120 ± 0.456	5.581 ± 0.279
134	15206-6256	ESO 099-G004	15 : 24 : 57.98	− 63 : 07 : 29.4	35	21.94	12.54 ± 0.57^c	14.61 ± 0.66^c	10.87 ± 0.47^c
135	F15250+3608	IRAS F15250+3608	15 : 26 : 59.42	+ 35 : 58 : 37.8	35	38.71	7.158 ± 0.324^c	5.787 ± 0.260^c	3.031 ± 0.133^c
136	F15276+1309	NGC 5936	15 : 30 : 00.85	+ 12 : 59 : 22.1	50	15.83	10.75 ± 0.54	16.34 ± 0.82	14.97 ± 0.75
137	F15327+2340	UGC 09913	15 : 34 : 57.23	+ 23 : 30 : 11.3	70	28.78	139.2 ± 6.6^c	···	86.32 ± 3.99^c
138	F15437+0234	NGC 5990	15 : 46 : 16.41	+ 02 : 24 : 55.6	40	12.18	12.06 ± 0.60	16.81 ± 0.84	14.25 ± 0.71
139	F16030+2040	NGC 6052	16 : 05 : 12.87	+ 20 : 32 : 33.0	45	16.41	7.689 ± 0.385	10.16 ± 0.51	8.128 ± 0.407
140	F16104+5235	NGC 6090	16 : 11 : 40.84	+ 52 : 27 : 27.2	35	21.92	7.800 ± 0.352^c	9.269 ± 0.416^c	7.033 ± 0.307^c
141	F16164-0746	IRAS F16164-0746	16 : 19 : 11.75	− 07 : 54 : 03.0	40	23.52	13.29 ± 0.61^c	15.03 ± 0.68^c	10.21 ± 0.45^c
142	F16284+0411	CGCG 052-037	16 : 30 : 56.53	+ 04 : 04 : 58.7	40	21.87	8.910 ± 0.406^c	12.17 ± 0.55^c	9.839 ± 0.435^c
142	F16284+0411		16 : 30 : 53.25	+ 04 : 04 : 23.9	20	10.94	0.241 ± 0.013^c	0.285 ± 0.015^c	0.204 ± 0.010^c
142	F16284+0411	IRGP J163054.9+040441	16 : 30 : 54.89	+ 04 : 04 : 41.3	···	···	9.151 ± 0.406^c	12.46 ± 0.55^c	10.04 ± 0.44^c
143	16304-6030	NGC 6156	16 : 34 : 52.55	− 60 : 37 : 08.0	80	18.23	21.20 ± 1.06	32.32 ± 1.62	29.29 ± 1.47
144	F16330-6820	2MASX J16381190-6826080	16 : 38 : 11.85	− 68 : 26 : 08.2	40	37.54	9.407 ± 0.429^c	13.21 ± 0.60^c	10.62 ± 0.47^c
144	F16330-6820	2MASX J16381338-6827170	16 : 38 : 13.43	− 68 : 27 : 16.6	18	16.89	0.037 ± 0.007	0.110 ± 0.009	0.125 ± 0.008
144	F16330-6820	ESO 069-IG006	16 : 38 : 12.64	− 68 : 26 : 42.3	···	···	9.444 ± 0.429^c	13.32 ± 0.60^c	10.75 ± 0.47^c
145	F16399-0937	IRAS F16399-0937	16 : 42 : 40.11	− 09 : 43 : 13.7	55	32.37	9.368 ± 0.436^c	10.80 ± 0.50^c	8.302 ± 0.379^c
146	F16443-2915	ESO 453-G005	16 : 47 : 31.09	− 29 : 21 : 21.6	35	16.36	12.19 ± 0.55^c	13.95 ± 0.63^c	10.04 ± 0.44^c
146	F16443-2915	2MASX J16472937-2919067	16 : 47 : 29.34	− 29 : 19 : 06.8	30	14.02	1.645 ± 0.077^c	2.585 ± 0.117^c	2.569 ± 0.112^c
146	F16443-2915	IRGP J164730.2-292014	16 : 47 : 30.21	− 29 : 20 : 14.2	···	···	13.83 ± 0.56^c	16.54 ± 0.64^c	12.61 ± 0.45^c
147	F16504+0228	NGC 6240	16 : 52 : 58.90	+ 02 : 24 : 03.3	45	24.11	26.48 ± 1.22^c	28.03 ± 1.28^c	19.00 ± 0.85^c
148	F16516-0948	IRAS F16516-0948	16 : 54 : 23.72	− 09 : 53 : 20.9	45	22.32	5.698 ± 0.286	8.243 ± 0.413	7.099 ± 0.356
149	F16577+5900	NGC 6286	16 : 58 : 31.63	+ 58 : 56 : 13.3	55	22.37	10.73 ± 0.54	19.32 ± 0.97	19.71 ± 0.99
149	F16577+5900	NGC 6285	16 : 58 : 23.99	+ 58 : 57 : 21.7	35	14.24	2.210 ± 0.100^c	3.206 ± 0.144^c	2.998 ± 0.131^c

continued on the next page

Table 2.4. (continued) *Herschel* PACS Total and Component Fluxes of GOALS Systems

#	IRAS Name	Optical Name	RA	Dec.	Ang. Ap.	Phys. Ap.	$F_\lambda(70\ \mu m)$	$F_\lambda(100\ \mu m)$	$F_\lambda(160\ \mu m)$
—	—	—	HH:MM:SS	DD:MM:SS	$''$	kpc	Jy	Jy	Jy
149	F16577+5900	Arp 293	16 : 58 : 27.81	+58 : 56 : 47.5	···	···	12.94 ± 0.55^c	22.53 ± 0.98^c	22.71 ± 0.99^c
150	F17132+5313		17 : 14 : 19.79	+53 : 10 : 29.0	···	···	···	···	···
150	F17132+5313		17 : 14 : 20.45	+53 : 10 : 32.1	···	···	···	···	···
150	F17132+5313	IRAS F17132+5313	17 : 14 : 20.45	+53 : 10 : 31.6	35	35.65	6.210 ± 0.311	6.980 ± 0.349	5.474 ± 0.239^c
151	F17138-1017	IRAS F17138-1017	17 : 16 : 35.68	−10 : 20 : 40.5	50	19.68	18.51 ± 0.86^c	21.72 ± 1.00^c	15.62 ± 0.70^c
152	F17207-0014	IRAS F17207-0014	17 : 23 : 21.97	−00 : 17 : 00.7	40	35.31	38.09 ± 1.74^c	37.91 ± 1.72^c	23.07 ± 1.02^c
153	F17222-5953	ESO 138-G027	17 : 26 : 43.35	−59 : 55 : 55.2	35	16.00	9.930 ± 0.497	11.00 ± 0.55	8.861 ± 0.386^c
154	F17530+3447	UGC 11041	17 : 54 : 51.82	+34 : 46 : 34.2	45	16.36	7.636 ± 0.382	11.71 ± 0.59	10.97 ± 0.55
155	F17548+2401	CGCG 141-034	17 : 56 : 56.65	+24 : 01 : 02.0	35	15.24	8.282 ± 0.374^c	10.45 ± 0.47^c	7.845 ± 0.342^c
156	17578-0400	IRAS 17578-0400	18 : 00 : 31.86	−04 : 00 : 53.4	38	12.34	33.39 ± 1.52^c	36.93 ± 1.67^c	25.04 ± 1.10^c
156	17578-0400	2MASX J18003399-0401443	18 : 00 : 34.08	−04 : 01 : 43.9	25	8.121	1.889 ± 0.084^c	2.767 ± 0.121^c	2.520 ± 0.106^c
156	17578-0400	2MASX J18002449-0401023	18 : 00 : 24.29	−04 : 01 : 03.8	30	9.745	2.356 ± 0.119	3.177 ± 0.160	2.596 ± 0.131
156	17578-0400	2MASX J18003399-0401443	18 : 00 : 32.49	−04 : 01 : 13.1	65	21.11	32.34 ± 1.62	36.60 ± 1.83	24.98 ± 1.25
156	17578-0400	IRGP J1800301-040113	18 : 00 : 28.61	−04 : 01 : 16.3	···	···	34.70 ± 1.62	39.78 ± 1.84	27.58 ± 1.26
157	18090+0130	2MASX J18113842+0131397	18 : 11 : 38.42	+01 : 31 : 40.3	40	24.55	7.775 ± 0.354^c	11.32 ± 0.51^c	9.853 ± 0.436^c
157	18090+0130	2MASX J18113342+0131427	18 : 11 : 33.41	+01 : 31 : 42.4	25	15.34	2.136 ± 0.095^c	2.865 ± 0.125^c	2.389 ± 0.101^c
157	18090+0130	IRAS 18090+0130	18 : 11 : 35.91	+01 : 31 : 41.3	···	···	9.912 ± 0.367^c	14.19 ± 0.53^c	12.24 ± 0.45^c
158	F18131+6820	NGC 6621	18 : 12 : 55.39	+68 : 21 : 48.2	19	8.511	8.536 ± 0.366^c	11.77 ± 0.50^c	···
158	F18131+6820	NGC 6621SE	18 : 12 : 58.52	+68 : 21 : 29.4	9	4.032	0.273 ± 0.011^c	0.571 ± 0.020^c	···
158	F18131+6820	NGC 6622	18 : 12 : 59.68	+68 : 21 : 15.1	9	4.032	0.110 ± 0.005^c	0.252 ± 0.010^c	···
158	F18131+6820	Arp 81	18 : 12 : 57.46	+68 : 21 : 38.7	70	31.36	8.257 ± 0.414	12.08 ± 0.60	11.24 ± 0.56
159	F18093-5744	IC 4687	18 : 13 : 39.80	−57 : 43 : 30.7	21	7.809	16.56 ± 0.72^c	19.76 ± 0.84^c	···
159	F18093-5744	IC 4686	18 : 13 : 38.77	−57 : 43 : 57.3	13	4.834	2.821 ± 0.115^c	2.559 ± 0.102^c	···
159	F18093-5744	IC 4689	18 : 13 : 40.38	−57 : 44 : 54.3	35	13.01	5.817 ± 0.263^c	7.494 ± 0.336^c	5.616 ± 0.245^c
159	F18093-5744	KTS 57	18 : 13 : 38.91	−57 : 43 : 24.7	57	21.20	17.51 ± 0.88	20.08 ± 1.00	14.44 ± 0.72
159	F18093-5744	IRAS F18093-5744	18 : 13 : 39.56	−57 : 44 : 00.9	90	33.47	23.87 ± 1.19	28.18 ± 1.41	20.08 ± 1.00
160	F18145+2205	CGCG 142-034	18 : 16 : 40.69	+22 : 06 : 46.4	35	14.12	6.075 ± 0.304	9.564 ± 0.479	8.625 ± 0.432
160	F18145+2205	CGCG 142-033	18 : 16 : 33.83	+22 : 06 : 38.9	25	10.08	1.842 ± 0.082^c	2.874 ± 0.126^c	2.938 ± 0.123^c
160	F18145+2205	IRGP J1816372+220642	18 : 16 : 37.26	+22 : 06 : 42.6	···	···	7.918 ± 0.315^c	12.44 ± 0.49^c	11.56 ± 0.45^c
161	F18293-3413	IRAS F18293-3413	18 : 32 : 41.10	−34 : 11 : 27.0	50	20.12	45.71 ± 2.11^c	59.13 ± 2.71^c	45.84 ± 2.07^c

continued on the next page

Table 2.4. (continued) *Herschel* PACS Total and Component Fluxes of GOALS Systems

#	IRAS Name	Optical Name	RA	Dec.	Ang. Ap.	Phys. Ap.	$F_\lambda(70\ \mu m)$	$F_\lambda(100\ \mu m)$	$F_\lambda(160\ \mu m)$
—	—	—	HH:MM:SS	DD:MM:SS	$''$	kpc	Jy	Jy	Jy
162	F18329+5950	NGC 6670B	18 : 33 : 34.26	+59 : 53 : 17.9	18	10.68	5.462 ± 0.273	7.823 ± 0.391	6.439 ± 0.322
162	F18329+5950	NGC 6670A	18 : 33 : 37.74	+59 : 53 : 22.8	13	7.714	4.247 ± 0.213	4.800 ± 0.240	3.101 ± 0.155
162	F18329+5950	NGC 6670	18 : 33 : 36.00	+59 : 53 : 20.3	50	29.67	10.33 ± 0.52	13.92 ± 0.70	11.25 ± 0.56
163	F18341-5732	IC 4734	18 : 38 : 25.75	−57 : 29 : 25.4	45	15.53	19.06 ± 0.88^c	25.41 ± 1.16^c	20.51 ± 0.92^c
164	F18425+6036	NGC 6701	18 : 43 : 12.52	+60 : 39 : 11.6	50	14.74	12.91 ± 0.65	19.13 ± 0.96	16.80 ± 0.84
165	F19120+7320	NGC 6786	19 : 10 : 54.01	+73 : 24 : 36.0	33	17.20	5.146 ± 0.231^c	7.238 ± 0.323^c	6.199 ± 0.268^c
165	F19120+7320	UGC 11415	19 : 11 : 04.37	+73 : 25 : 32.5	30	15.64	4.117 ± 0.184^c	4.666 ± 0.207^c	3.568 ± 0.153^c
165	F19120+7320	VV 414	19 : 10 : 59.19	+73 : 25 : 04.2	···	···	9.262 ± 0.296^c	11.90 ± 0.38^c	9.766 ± 0.309^c
166	F19115-2124	ESO 593-IG008	19 : 14 : 31.15	−21 : 19 : 06.3	40	39.13	7.972 ± 0.363^c	10.62 ± 0.48^c	8.597 ± 0.380^c
167	F19297-0406	IRAS F19297-0406	19 : 32 : 22.30	−04 : 00 : 01.1	40	64.98	7.982 ± 0.400	8.114 ± 0.406	5.121 ± 0.257
168	19542+1110	IRAS 19542+1110	19 : 56 : 35.78	+11 : 19 : 04.9	30	37.83	6.720 ± 0.300^c	6.516 ± 0.289^c	3.851 ± 0.165^c
169	F19542-3804	ESO 339-G011	19 : 57 : 37.60	−37 : 56 : 08.4	45	18.61	7.396 ± 0.340^c	10.69 ± 0.49^c	9.839 ± 0.440^c
170	F20221-2458	NGC 6907	20 : 25 : 06.58	−24 : 48 : 32.9	80	19.04	18.35 ± 0.92	31.39 ± 1.57	31.71 ± 1.59
171	20264+2533	MCG+04-48-002	20 : 28 : 35.07	+25 : 44 : 00.3	40	12.33	10.36 ± 0.52	14.20 ± 0.71	10.81 ± 0.54
171	20264+2533	NGC 6921	20 : 28 : 28.90	+25 : 43 : 24.3	28	8.634	2.558 ± 0.114^c	3.510 ± 0.155^c	2.546 ± 0.108^c
171	20264+2533	IRGP J2028320+254342	20 : 28 : 31.98	+25 : 43 : 42.3	···	···	12.92 ± 0.53^c	17.71 ± 0.73^c	13.35 ± 0.55^c
172	F20304-0211	NGC 6926	20 : 33 : 06.13	−02 : 01 : 38.9	60	24.93	8.895 ± 0.446	15.94 ± 0.80	16.62 ± 0.83
173	20351+2521	IRAS 20351+2521	20 : 37 : 17.73	+25 : 31 : 37.5	35	23.98	6.993 ± 0.350	9.142 ± 0.457	7.280 ± 0.364
174	F20550+1655	CGCG 448-020NW	20 : 57 : 23.65	+17 : 07 : 44.1	···	···	···	···	···
174	F20550+1655	CGCG 448-020SEsw	20 : 57 : 24.09	+17 : 07 : 35.2	···	···	···	···	···
174	F20550+1655	CGCG 448-020SEne	20 : 57 : 24.38	+17 : 07 : 39.2	···	···	···	···	···
174	F20550+1655	CGCG 448-020	20 : 57 : 24.01	+17 : 07 : 41.6	40	29.09	11.79 ± 0.59	10.68 ± 0.53	6.199 ± 0.310
175	F20551-4250	ESO 286-IG019	20 : 58 : 26.78	−42 : 39 : 00.5	30	25.80	12.64 ± 0.56^c	10.41 ± 0.46^c	5.749 ± 0.246^c
176	F21008-4347	ESO 286-G035	21 : 04 : 11.11	−43 : 35 : 36.1	45	16.67	9.498 ± 0.436^c	12.80 ± 0.58^c	10.42 ± 0.47^c
177	21101+5810	IRAS 21101+5810	21 : 11 : 29.28	+58 : 23 : 07.9	35	27.35	8.068 ± 0.365^c	8.705 ± 0.391^c	5.753 ± 0.251^c
178	F21330-3846	ESO 343-IG 013 NED01	21 : 36 : 10.53	−38 : 32 : 42.8	···	···	···	···	···
178	F21330-3846	ESO 343-IG 013 NED02	21 : 36 : 10.93	−38 : 32 : 33.0	···	···	···	···	···
178	F21330-3846	ESO 343-IG013	21 : 36 : 10.73	−38 : 32 : 37.8	45	18.02	6.422 ± 0.322	8.031 ± 0.402	6.587 ± 0.330
179	F21453-3511	NGC 7130	21 : 48 : 19.54	−34 : 57 : 04.7	40	13.65	18.83 ± 0.94	···	19.68 ± 0.99
180	F22118-2742	ESO 467-G027	22 : 14 : 39.97	−27 : 27 : 50.3	50	18.11	7.027 ± 0.352	11.89 ± 0.59	11.53 ± 0.58

continued on the next page

Table 2.4. (continued) *Herschel* PACS Total and Component Fluxes of GOALS Systems

#	IRAS Name	Optical Name	RA	Dec.	Ang. Ap.	Phys. Ap.	$F_\lambda(70\ \mu m)$	$F_\lambda(100\ \mu m)$	$F_\lambda(160\ \mu m)$
—	—	—	HH:MM:SS	DD:MM:SS	$''$	kpc	Jy	Jy	Jy
181	F22132-3705	IC 5179	22 : 16 : 09.13	− 36 : 50 : 37.2	65	15.82	24.34 ± 1.22	37.57 ± 1.88	34.58 ± 1.73
182	F22287-1917	ESO 602-G025	22 : 31 : 25.48	− 19 : 02 : 04.0	40	20.30	7.429 ± 0.339^c	10.36 ± 0.47^c	9.241 ± 0.409^c
183	F22389+3359	UGC 12150	22 : 41 : 12.21	+ 34 : 14 : 56.8	35	15.20	10.70 ± 0.48^c	14.70 ± 0.66^c	12.31 ± 0.54^c
184	F22467-4906	ESO 239-IG002	22 : 49 : 39.84	− 48 : 50 : 58.3	35	29.80	8.041 ± 0.363^c	7.847 ± 0.352^c	4.975 ± 0.217^c
185	F22491-1808	IRAS F22491-1808	22 : 51 : 49.35	− 17 : 52 : 24.9	30	43.95	5.642 ± 0.252^c	4.975 ± 0.221^c	2.715 ± 0.116^c
186	F23007+0836	NGC 7469	23 : 03 : 15.64	+ 08 : 52 : 25.5	47	15.49	30.97 ± 1.43^c	35.76 ± 1.64^c	25.40 ± 1.14^c
186	F23007+0836	IC 5283	23 : 03 : 18.04	+ 08 : 53 : 36.5	33	10.88	2.719 ± 0.137	4.421 ± 0.221	4.434 ± 0.222
186	F23007+0836	Arp 298	23 : 03 : 16.84	+ 08 : 53 : 00.9	···	···	33.69 ± 1.43^c	40.18 ± 1.65^c	29.83 ± 1.16^c
187	F23024+1916	CGCG 453-062	23 : 04 : 56.55	+ 19 : 33 : 07.1	40	20.11	9.269 ± 0.422^c	11.42 ± 0.52^c	9.233 ± 0.409^c
188	F23128-5919	ESO 148-IG002	23 : 15 : 46.75	− 59 : 03 : 15.8	35	30.95	11.97 ± 0.54^c	11.14 ± 0.50^c	6.028 ± 0.267^c
189	F23135+2517	IC 5298	23 : 16 : 00.67	+ 25 : 33 : 24.3	40	21.86	10.32 ± 0.47^c	11.53 ± 0.52^c	8.070 ± 0.357^c
190	F23133-4251	NGC 7552	23 : 16 : 10.81	− 42 : 35 : 05.5	90	10.12	92.92 ± 4.65	116.3 ± 5.8	88.01 ± 4.40
191	F23157+0618	NGC 7591	23 : 18 : 16.25	+ 06 : 35 : 09.1	65	21.78	9.296 ± 0.466	13.59 ± 0.68	13.07 ± 0.65
191	F23157+0618	NGC 7591	23 : 18 : 13.52	+ 06 : 33 : 26.5	23	7.705	0.746 ± 0.035^c	0.897 ± 0.042^c	0.799 ± 0.035^c
191	F23157+0618	F23157+0618	23 : 18 : 14.89	+ 06 : 34 : 17.8	···	···	10.04 ± 0.47^c	14.49 ± 0.68^c	13.86 ± 0.65^c
192	F23157-0441	NGC 7592E	23 : 18 : 22.60	− 04 : 24 : 58.0	···	···	···	···	···
192	F23157-0441	NGC 7592W	23 : 18 : 21.78	− 04 : 24 : 57.0	···	···	···	···	···
192	F23157-0441	NGC 7592	23 : 18 : 22.19	− 04 : 24 : 57.4	40	19.59	8.700 ± 0.435	10.44 ± 0.52	7.602 ± 0.380
193	F23180-6929	ESO 077-IG 014 NED02	23 : 21 : 05.45	− 69 : 12 : 47.3	11	9.146	5.688 ± 0.225^c	7.545 ± 0.284^c	···
193	F23180-6929	ESO 077-IG 014 NED01	23 : 21 : 03.47	− 69 : 13 : 02.2	9	7.483	2.067 ± 0.078^c	2.828 ± 0.099^c	···
193	F23180-6929	ESO 077-IG014	23 : 21 : 04.59	− 69 : 12 : 54.1	40	33.26	6.716 ± 0.337	9.141 ± 0.458	7.056 ± 0.353
194	F23254+0830	NGC 7674	23 : 27 : 56.71	+ 08 : 46 : 44.3	28	16.21	5.489 ± 0.244^c	7.502 ± 0.331^c	···
194	F23254+0830	NGC 7674A	23 : 27 : 58.77	+ 08 : 46 : 57.9	11	6.368	0.718 ± 0.029^c	1.036 ± 0.039^c	···
194	F23254+0830	ARP 182	23 : 27 : 57.73	+ 08 : 46 : 51.0	70	40.52	5.865 ± 0.295	8.328 ± 0.418	7.663 ± 0.384
195	23262+0314	NGC 7679	23 : 28 : 46.62	+ 03 : 30 : 41.4	40	13.83	9.077 ± 0.413^c	11.74 ± 0.53^c	8.976 ± 0.397^c
195	23262+0314[a]	NGC 7682	23 : 29 : 03.91	+ 03 : 31 : 59.9	45	15.56	0.409 ± 0.028	0.770 ± 0.043	0.971 ± 0.051
196	F23365+3604	IRAS F23365+3604	23 : 39 : 01.32	+ 36 : 21 : 08.2	35	42.98	8.070 ± 0.365^c	8.315 ± 0.373^c	5.222 ± 0.228^c
197	F23394-0353	MCG-01-60-022	23 : 42 : 00.91	− 03 : 36 : 54.4	35	15.68	6.181 ± 0.279^c	8.292 ± 0.372^c	6.863 ± 0.299^c
197	F23394-0353[a]	MCG-01-60-021	23 : 41 : 47.33	− 03 : 40 : 01.7	37	16.57	0.399 ± 0.025	0.978 ± 0.051	1.577 ± 0.080
197	F23394-0353[a]	MRK 0933	23 : 41 : 43.69	− 03 : 39 : 26.5	25	11.20	0.323 ± 0.018^c	0.444 ± 0.022^c	0.411 ± 0.019^c

continued on the next page

Table 2.4. (continued) *Herschel* PACS Total and Component Fluxes of GOALS Systems

#	IRAS Name	Optical Name	RA	Dec.	Ang. Ap.	Phys. Ap.	$F_\lambda(70\ \mu m)$	$F_\lambda(100\ \mu m)$	$F_\lambda(160\ \mu m)$
—	—	—	HH:MM:SS	DD:MM:SS	$''$	kpc	Jy	Jy	Jy
197	F23394-0353	MCG-01-60-021	23 : 41 : 46.04	− 03 : 39 : 42.3	···	···	···	···	···
198	23436+5257	IRAS 23436+5257	23 : 46 : 05.44	+ 53 : 14 : 01.7	30	20.26	6.576 ± 0.294^{c}	7.540 ± 0.335^{c}	5.213 ± 0.223^{c}
199	F23444+2911	NGC 7752	23 : 47 : 04.84	+ 29 : 29 : 00.5	80	27.58	4.144 ± 0.211	8.625 ± 0.434	11.11 ± 0.56
199	F23444+2911	NGC 7753	23 : 46 : 58.62	+ 29 : 27 : 32.0	35	12.06	3.468 ± 0.174	4.891 ± 0.245	3.943 ± 0.198
199	F23444+2911	Arp 86	23 : 47 : 01.73	+ 29 : 28 : 16.2	···	···	7.612 ± 0.274	13.52 ± 0.50	15.05 ± 0.59
200	F23488+1949	NGC 7769	23 : 51 : 03.91	+ 20 : 09 : 01.7	···	···	... [b]	... [b]	... [b]
200	F23488+1949	NGC 7771	23 : 51 : 24.80	+ 20 : 06 : 42.2	47	13.33	24.12 ± 1.21	38.95 ± 1.95	36.67 ± 1.83
200	F23488+1949	NGC 7770	23 : 51 : 22.55	+ 20 : 05 : 49.2	30	8.508	3.493 ± 0.179	4.230 ± 0.215	3.451 ± 0.177
200	F23488+1949	KTG 82	23 : 51 : 23.67	+ 20 : 06 : 15.6	95	26.94	28.23 ± 1.41	43.77 ± 2.19	41.47 ± 2.07
201	F23488+2018	MRK 0331	23 : 51 : 26.77	+ 20 : 35 : 10.5	40	14.31	21.05 ± 0.96^{c}	23.93 ± 1.08^{c}	17.03 ± 0.75^{c}
201	F23488+2018	UGC 12812	23 : 51 : 18.69	+ 20 : 34 : 40.4	33	11.81	0.258 ± 0.022	0.387 ± 0.025	0.438 ± 0.026
201	F23488+2018	KPG 593	23 : 51 : 22.73	+ 20 : 34 : 55.4	···	···	21.31 ± 0.96^{c}	24.32 ± 1.08^{c}	17.46 ± 0.75^{c}

Monochromatic PACS fluxes in units of Jansky for the entire GOALS sample. These are component fluxes measurable for each system, with the total system flux from Table 2.3 included for completeness on the last line for each system. For total fluxes that do not have an aperture size, the totals were calculated as the sum of the components. Likewise the RA and dec. for these systems represent the midpoint between the companion galaxies. Galaxy components that do not have flux measurements are too close to a companion galaxy to be resolved by PACS. See §2.6 for the column descriptions. [a]These are very widely separated galaxy pairs that required two *Herschel* PACS observations. [b]This galaxy is part of a triple system, but is only visible in the SPIRE images. The total flux for this system does *not* include this galaxy. [c]These fluxes have an aperture correction factor applied.

the relative photometric gains between all of the bolometers is properly accounted for. In addition to applying the relative gains, the PMW and PLW channels are zero-point corrected by applying a constant offset based on the *Planck*-HFI maps (see §2.6.2). The overall calibration scheme for point and extended sources is described in Griffin et al. (2013).

The primary flux calibrator for SPIRE is Neptune, chosen because it has a well-understood submillimeter/FIR spectrum and is essentially a point source in the SPIRE beams. It is also bright enough from which high signal-to-noise measurements can be made, but not so bright that it would introduce non-linearity effects from the instrument. In order to calibrate the entire instrument, special 'fine scan' observations were taken such that each bolometer was scanned across Neptune in order to absolutely calibrate each bolometer. Repeated observations of Neptune also showed that there were no statistically significant changes in the detector responses over the mission. Further details on using Neptune as the primary SPIRE flux calibrator can be found in Bendo et al. (2013).

Since the vast majority of our sources have fluxes above 30 mJy, Pearson et al. (2014) recommends using either the timeline fitter or aperture photometry. Because a significant fraction of our sample contains marginally to very extended sources, as well as point sources, we opted to measure all of our SPIRE fluxes using the `annularSkyAperturePhotometry` task in HIPE in order to keep our measurements as uniform as possible. However this method results in the loss of flux outside the finite-sized aperture, for which an aperture correction is needed to fully account for all the flux. In the case of point sources, we applied the aperture correction by dividing our fluxes by the encircled energy fraction (EEF) amount corresponding to the aperture radius and SPIRE channel. The EEFs can be found in the SPIRE calibration files (accessible from within HIPE), and represents the ratio of flux (energy) inside the aperture divided by the true flux of the point source. As with the PACS aperture corrections, SPIRE fluxes in which an aperture correction was applied are denoted by a superscript c in Table 2.5, with average corrections of 10.1%, 10.3%, and 14.8% for the 250, 350, and 500 μm channels respectively. Similarly the median correction values are less than a percent difference from the averages.

In order to check the validity of our point source fluxes, we measured our fluxes a second time using the timeline source fitter on a subset of 65 objects that are point sources in all three SPIRE bands. The timeline fitter is the preferred method of obtaining point source fluxes on the SPIRE maps, since it works on the baseline subtracted, destriped, and deglitched Level 1 timelines of the data (which are calibrated in Jy/beam[10]). By using a Levenberg-Marquardt algorithm to fit a two dimensional circular or elliptical Gaussian function to the 2-D timeline data, the source can be modeled and the point source flux can be calculated from the 2-D fit. The advantage is it avoids any potential artifacts arising from the map-making process, such as smearing effects from pixelization. Because it does not use the Level 2 maps, source extraction is not necessary (i.e., aperture photometry), and there are no aperture corrections needed since the 2-D fit in principle takes into accounts all of the flux from the point source.

When we compared the aperture photometry results to the timeline fitter results, we found that they both agree very well at 250 μm and 350 μm with an average aperture/timeline flux ratio of 1.030 and 0.995 respectively, however the 500 μm channel had a slightly lower ratio of 0.93. To further check our results, we plotted the aperture/timeline flux ratio against the aperture photometry flux for all three bands, and found no statistically significant correlation in the flux ratio as a function of flux. However we do note in the 500 μm case, fluxes less than approximately 150 mJy appear to have a lower aperture/timeline flux ratio, whereas fluxes above that value have an average ratio close to unity. We believe this underestimation at faint fluxes is due to confusion noise, which was also observed in the SPIRE Map Making Test Report. Furthermore we note that the discrepancy in the 500 μm fluxes are still consistent within the typical flux errors ($\sim$15%). As a final check we also plotted the aperture/timeline ratio against the aperture photometry radius, and we again found no statistically significant correlation. From these tests our point source aperture photometry fluxes appear to be in good agreement with the results from the timeline fitter.

[10]See Dowell et al. (2010), §5.

In the case of semi-extended to extended sources, aperture corrections become more complex since the flux originates not from an unresolved source, but is seen instead as surface brightness distributed within an aperture. Although an aperture correction is needed for reasons similar to the point source case, Shimizu et al. (2016) found that their extended SPIRE fluxes for their *Swift* BAT sample did not need aperture corrections because they were negligible. To test this, they first convolved their 160 μm PACS data to the resolution of the three SPIRE bands, and then measured the fluxes on both the convolved and unconvolved images using the same SPIRE aperture sizes. Aperture corrections were then calculated as the ratio of the flux on the original PACS image divided by the flux obtained on the convolved image, with resulting median aperture corrections of 1.01, 0.98, and 0.98 for the 250 μm, 350 μm, and 500 μm channels respectively. This makes the assumption that the 160 μm and SPIRE fluxes originate from the same material within their galaxies. We also note that their aperture sizes are similar to ours, since their galaxy sample lies in the same redshift range. Ciesla et al. (2012) also showed by simulating in the worst-case scenario, a maximum aperture correction of 5% is needed at 500 μm. However this was done on an (intentionally) unphysical source that has a flat constant surface brightness, with a sharp drop to zero flux at a set radius. On more realistic sources they calculated aperture corrections of approximately $\lesssim$2%. As these corrections are very close to unity, we follow their precedent in only reporting the integrated, background subtracted flux for our extended sources.

To calculate the flux uncertainty for the SPIRE photometry, we follow a similar prescription we used for PACS. The first is a systematic error in the flux calibration related to the uncertainty in the models used for Neptune, which is the primary calibrator for SPIRE. These uncertainties, which are correlated across all three SPIRE bands, are currently quoted as 4%. The other source of uncertainty is a random uncertainty related to the ability to repeat flux density measurements of Neptune, which is 1.5% for all three bands. Altogether, these two sources of uncertainty are added linearly for a total of 5.5% error in the point source flux calibration. However in the case of extended emission calibration,

there is an additional error of 1% due to the current uncertainty in the measured beam area that is also added linearly. This error was recently improved from 4% with the release of the SPIRE calibration version 14_2. Therefore the total uncertainty in the extended source calibration scheme amounts to 6.5% of the background subtracted flux (Bendo et al. 2013).

To calculate our total flux uncertainties, we must also include any errors incurred from measuring and subtracting the background from the measured flux, as well as the instrumental error. To estimate the uncertainty from the background subtraction, we measure the 1-σ dispersion of the flux in each pixel within the annular area used for our background measurements. This is then multiplied by the square root of the number of pixels within the photometry aperture (which can be a fractional amount) to obtain the error in background measurement. The instrumental error is calculated by summing in quadrature the pixels within the aperture on the error map generated by the pipeline. We note this underestimates the error because the noise is correlated between pixels. Our final SPIRE flux uncertainties are then computed as the quadrature sum of all three sources of error. In the case where the total system flux is the sum of two (or more) components, the flux uncertainty is the quadrature sum of each galaxy component's flux error.

SPIRE Zero-Point Correction

Due to the large radiative contribution of *Herschel*'s optical components (230 Jy, 250 Jy, 270 Jy for the PSW, PMW, PLW channels respectively), SPIRE can only measure the relative flux on the sky, i.e., the flux of the target minus the background level. During data reduction the SPIRE maps are generated such that the background is approximately normalized to zero, which makes it impossible to determine the absolute flux of the target. However to recover the absolute flux we used the all-sky maps from the *Planck* mission (modified to have a spatial resolution of $8'$ FWHM), since the Planck-HFI 857 GHz and 545 GHz filters match fairly well to the *Herschel* 350 μm and 500 μm band passes respectively (see Fig. 5.16 in the SPIRE handbook). These corrections become more important in sources with very extended flux, since some of the diffuse low surface-brightness flux may be subtracted out.

Table 2.5 *Herschel* SPIRE Total and Component Fluxes of GOALS Systems

#	IRAS Name	Optical Name	RA	Dec.	Ang. Ap.	Phys. Ap.	$F_\lambda(250\ \mu m)$	$F_\lambda(350\ \mu m)$	$F_\lambda(500\ \mu m)$
—	—	—	HH:MM:SS	DD:MM:SS	$''$	kpc	Jy	Jy	Jy
1	F00073+2538	NGC 23	00 : 09 : 53.36	+ 25 : 55 : 27.7	70	21.48	5.311 ± 0.347	2.026 ± 0.134	0.718 ± 0.046^c
2	F00085-1223	NGC 34	00 : 11 : 06.56	− 12 : 06 : 28.2	55	21.73	3.573 ± 0.214^c	1.239 ± 0.075^c	0.339 ± 0.021^c
2	F00085-1223	NGC 35	00 : 11 : 10.51	− 12 : 01 : 14.9	···	···	···	···	···
2	F00085-1223	IRGP J001108.5-120351	00 : 11 : 08.54	− 12 : 03 : 51.6	···	···	3.573 ± 0.214^c	1.239 ± 0.075^c	0.339 ± 0.021^c
3	F00163-1039	MCG-02-01-051	00 : 18 : 50.90	− 10 : 22 : 36.7	···	···	···	···	···
3	F00163-1039	MCG-02-01-052	00 : 18 : 49.85	− 10 : 21 : 34.0	···	···	···	···	···
3	F00163-1039	Arp 256	00 : 18 : 50.37	− 10 : 22 : 05.3	80	43.21	2.862 ± 0.189	1.209 ± 0.081	0.419 ± 0.033
4	F00344-3349	ESO 350-IG 038	00 : 36 : 52.49	− 33 : 33 : 17.2	35	14.49	0.639 ± 0.038^c	0.216 ± 0.014^c	0.067 ± 0.006^c
5	F00402-2349	NGC 232	00 : 42 : 45.83	− 23 : 33 : 41.0	53	23.46	5.299 ± 0.317^c	2.011 ± 0.121^c	0.578 ± 0.033^c
5	F00402-2349	NGC 235	00 : 42 : 52.82	− 23 : 32 : 27.8	45	19.92	1.098 ± 0.065^c	0.431 ± 0.026^c	0.125 ± 0.009^c
5	F00402-2349	RSCG 04	00 : 42 : 49.32	− 23 : 33 : 04.3	···	···	6.397 ± 0.323^c	2.441 ± 0.124^c	0.703 ± 0.035^c
6	F00506+7248	MCG+12-02-001	00 : 54 : 03.88	+ 73 : 05 : 05.9	60	19.69	7.968 ± 0.485^c	2.793 ± 0.174^c	0.896 ± 0.057^c
7	F00548+4331	NGC 317B	00 : 57 : 40.41	+ 43 : 47 : 32.5	···	···	···	···	···
7	F00548+4331	NGC 317A	00 : 57 : 39.04	+ 43 : 48 : 03.1	···	···	···	···	···
7	F00548+4331	NGC 317	00 : 57 : 39.72	+ 43 : 47 : 47.7	75	26.94	4.014 ± 0.266	1.600 ± 0.108	0.478 ± 0.039
8	F01053-1746	IC 1623A	01 : 07 : 46.79	− 17 : 30 : 27.4	···	···	···	···	···
8	F01053-1746	IC 1623B	01 : 07 : 47.59	− 17 : 30 : 24.2	···	···	···	···	···
8	F01053-1746	IC 1623	01 : 07 : 47.54	− 17 : 30 : 25.6	60	23.91	8.991 ± 0.546^c	3.277 ± 0.201^c	1.023 ± 0.062^c
9	F01076-1707	MCG-03-04-014	01 : 10 : 08.93	− 16 : 51 : 09.9	53	34.64	3.077 ± 0.187^c	1.181 ± 0.074^c	0.349 ± 0.023^c
10	F01159-4443	MCG-7-3-14	01 : 18 : 08.31	− 44 : 27 : 43.4	···	···	···	···	···
10	F01159-4443	MCG-7-3-13	01 : 18 : 08.23	− 44 : 28 : 00.4	···	···	···	···	···
10	F01159-4443	ESO 244-G012	01 : 18 : 08.27	− 44 : 27 : 51.9	55	23.38	2.948 ± 0.194	1.155 ± 0.077	0.341 ± 0.025
11	F01173+1405	CGCG 436-030	01 : 20 : 02.63	+ 14 : 21 : 42.3	55	21.92	2.125 ± 0.128^c	0.770 ± 0.048^c	0.230 ± 0.015^c
12	F01325-3623	ESO 353-G020	01 : 34 : 51.26	− 36 : 08 : 14.4	70	27.90	6.565 ± 0.408^c	2.621 ± 0.163^c	0.881 ± 0.056^c
13	F01341-3735	ESO 297-G 011	01 : 36 : 23.39	− 37 : 19 : 18.1	40	13.96	3.446 ± 0.203^c	···	···
13	F01341-3735	ESO 297-G 012	01 : 36 : 24.14	− 37 : 20 : 25.9	25	8.727	0.969 ± 0.053^c	···	···
13	F01341-3735	RR 032	01 : 36 : 23.76	− 37 : 19 : 51.9	75	26.18	4.107 ± 0.269	1.651 ± 0.110	0.522 ± 0.038
14	F01364-1042	IRAS F01364-1042	01 : 38 : 52.79	− 10 : 27 : 12.1	45	41.69	1.336 ± 0.080^c	0.517 ± 0.032^c	0.158 ± 0.011^c
15	F01417+1651	III Zw 035	01 : 44 : 30.56	+ 17 : 06 : 09.0	50	27.30	2.608 ± 0.156^c	0.995 ± 0.061^c	0.302 ± 0.019^c
16	F01484+2220	NGC 695	01 : 51 : 14.34	+ 22 : 34 : 56.0	60	37.93	4.959 ± 0.302^c	1.942 ± 0.120^c	0.655 ± 0.047^c

continued on the next page

Table 2.5. (continued) *Herschel* SPIRE Total and Component Fluxes of GOALS Systems

#	IRAS Name	Optical Name	RA	Dec.	Ang. Ap.	Phys. Ap.	$F_\lambda(250\ \mu m)$	$F_\lambda(350\ \mu m)$	$F_\lambda(500\ \mu m)$
—	—	—	HH:MM:SS	DD:MM:SS	$''$	kpc	Jy	Jy	Jy
17	F01519+3640	UGC 01385	01 : 54 : 53.82	+36 : 55 : 04.3	50	18.64	1.956 ± 0.120^c	0.811 ± 0.050^c	0.203 ± 0.022^c
17	F01519+3640	KUG 0152+366	01 : 55 : 01.75	+36 : 55 : 11.6	50	18.64	0.581 ± 0.043	0.221 ± 0.022	0.076 ± 0.017
17	F01519+3640	IRGP J015457.8+365508	01 : 54 : 57.78	+36 : 55 : 07.9	···	···	2.537 ± 0.127^c	1.031 ± 0.055^c	0.279 ± 0.028^c
18	F02071-1023	NGC 839	02 : 09 : 42.81	−10 : 11 : 02.0	75	19.38	3.134 ± 0.193^c	1.145 ± 0.071^c	0.354 ± 0.023^c
18	F02071-1023	NGC 838	02 : 09 : 38.66	−10 : 08 : 47.2	83	21.45	5.962 ± 0.368^c	2.293 ± 0.142^c	0.755 ± 0.047^c
18	F02071-1023	NGC 835	02 : 09 : 24.64	−10 : 08 : 09.3	33	8.527	4.933 ± 0.278^c	1.916 ± 0.104^c	···
18	F02071-1023	NGC 833	02 : 09 : 20.87	−10 : 07 : 59.4	27	6.977	0.448 ± 0.030	0.213 ± 0.015	···
18	F02071-1023	NGC 835/0833	02 : 09 : 24.64	−10 : 08 : 09.3	85	21.96	5.629 ± 0.348^c	2.360 ± 0.146^c	0.728 ± 0.046^c
18	F02071-1023	HCG 016	02 : 09 : 36.13	−10 : 09 : 32.6	···	···	14.72 ± 0.54^c	5.799 ± 0.216^c	1.837 ± 0.070^c
19	F02070+3857	NGC 828	02 : 10 : 09.53	+39 : 11 : 24.7	80	28.55	12.78 ± 0.79^c	5.194 ± 0.324^c	1.621 ± 0.102^c
20	F02114+0456	IC 0214	02 : 14 : 05.56	+05 : 10 : 23.7	60	35.60	2.659 ± 0.163^c	1.053 ± 0.068^c	0.352 ± 0.033^c
20	F02114+0456		02 : 13 : 55.99	+05 : 10 : 04.0	45	26.70	0.379 ± 0.028^c	0.208 ± 0.019^c	0.069 ± 0.021^c
20	F02114+0456	IRGP J021400.8+051014	02 : 14 : 00.77	+05 : 10 : 13.8	···	···	3.038 ± 0.166^c	1.261 ± 0.071^c	0.421 ± 0.039^c
21	F02152+1418	NGC 877	02 : 17 : 53.26	+14 : 31 : 18.4	56	14.36	2.579 ± 0.168	1.138 ± 0.075	0.396 ± 0.028
21	F02152+1418	NGC 876	02 : 17 : 59.68	+14 : 32 : 38.2	85	21.80	13.91 ± 0.90	5.730 ± 0.373	1.962 ± 0.129
21	F02152+1418	IRGP J021756.5+143158	02 : 17 : 56.46	+14 : 31 : 58.2	150	38.47	16.90 ± 1.10	7.291 ± 0.475	2.449 ± 0.162
22	F02203+3158	MCG+05-06-036	02 : 23 : 21.99	+32 : 11 : 48.8	33	21.71	3.352 ± 0.192^c	···	···
22	F02203+3158	MCG+05-06-035	02 : 23 : 18.97	+32 : 11 : 18.5	24	15.79	1.390 ± 0.074^c	···	···
22	F02203+3158	KPG 067	02 : 23 : 20.47	+32 : 11 : 33.6	65	42.76	4.206 ± 0.277	1.651 ± 0.111	0.529 ± 0.042
23	F02208+4744	UGC 01845	02 : 24 : 07.97	+47 : 58 : 11.9	50	15.76	5.036 ± 0.304^c	1.974 ± 0.121^c	0.563 ± 0.034^c
24	F02281-0309	NGC 958	02 : 30 : 42.84	−02 : 56 : 20.5	90	33.86	10.46 ± 0.68	4.532 ± 0.297	1.614 ± 0.114
25	F02345+2053	NGC 992	02 : 37 : 25.46	+21 : 06 : 02.8	70	19.14	5.906 ± 0.364^c	2.341 ± 0.145^c	0.734 ± 0.047^c
26	F02401-0013	NGC 1068	02 : 42 : 40.72	−00 : 00 : 47.9	200	15.32	117.9 ± 7.7	45.72 ± 2.97	14.40 ± 0.94
27	F02435+1253	UGC 02238	02 : 46 : 17.46	+13 : 05 : 44.6	60	25.74	6.147 ± 0.375^c	2.380 ± 0.148^c	0.756 ± 0.052^c
28	F02437+2122	IRAS F02437+2122	02 : 46 : 39.13	+21 : 35 : 10.4	35	16.02	1.823 ± 0.106^c	0.658 ± 0.038^c	0.185 ± 0.012^c
28	F02437+2123[a]		02 : 46 : 45.05	+21 : 33 : 23.5	40	18.31	0.491 ± 0.031^c	0.221 ± 0.015^c	0.079 ± 0.008^c
29	F02512+1446	MCG+02-08-029	02 : 54 : 01.84	+14 : 58 : 15.7	···	···	···	···	···
29	F02512+1446	MCG+02-08-030	02 : 54 : 01.75	+14 : 58 : 36.4	···	···	···	···	···
29	F02512+1446	UGC 02369	02 : 54 : 01.79	+14 : 58 : 26.0	50	30.96	3.096 ± 0.204	1.197 ± 0.080	0.382 ± 0.024^c
30	F03117+4151	UGC 02608	03 : 15 : 01.47	+42 : 02 : 08.6	60	27.78	4.135 ± 0.251^c	1.601 ± 0.099^c	0.518 ± 0.033^c

continued on the next page

Table 2.5. (continued) *Herschel* SPIRE Total and Component Fluxes of GOALS Systems

#	IRAS Name	Optical Name	RA	Dec.	Ang. Ap.	Phys. Ap.	$F_\lambda(250\ \mu m)$	$F_\lambda(350\ \mu m)$	$F_\lambda(500\ \mu m)$
—	—	—	HH:MM:SS	DD:MM:SS	$''$	kpc	Jy	Jy	Jy
30	F03117+4151[a]	UGC 02612	03 : 15 : 14.58	+41 : 58 : 50.0	45	20.83	0.990 ± 0.061[c]	0.429 ± 0.028[c]	0.134 ± 0.012[c]
31	F03164+4119	NGC 1275	03 : 19 : 48.18	+41 : 30 : 42.0	75	26.33	3.506 ± 0.217[c]	2.851 ± 0.176[c]	2.739 ± 0.168[c]
32	F03217+4022	IRAS F03217+4022	03 : 25 : 05.37	+40 : 33 : 32.2	55	25.46	3.134 ± 0.191[c]	1.204 ± 0.075[c]	0.358 ± 0.024[c]
33	F03316-3618	NGC 1365	03 : 33 : 36.40	−36 : 08 : 25.9	360	30.89	103.7 ± 6.7	43.94 ± 2.86	15.63 ± 1.02
34	F03359+1523	IRAS F03359+1523	03 : 38 : 47.07	+15 : 32 : 54.1	50	34.37	1.643 ± 0.099[c]	0.599 ± 0.038[c]	0.187 ± 0.013[c]
35	F03514+1546[a]	CGCG 465-011	03 : 54 : 07.67	+15 : 59 : 24.3	60	26.21	2.188 ± 0.135[c]	0.867 ± 0.056[c]	0.310 ± 0.024[c]
35	F03514+1546	CGCG 465-012	03 : 54 : 15.95	+15 : 55 : 43.4	55	24.02	3.065 ± 0.186[c]	1.130 ± 0.071[c]	0.356 ± 0.025[c]
36	03582+6012	IRAS 03582+6012NE	04 : 02 : 32.99	+60 : 20 : 41.8	···	···	···	···	···
36	03582+6012	IRAS 03582+6012SW	04 : 02 : 31.97	+60 : 20 : 38.3	···	···	···	···	···
36	03582+6012	IRAS 03582+6012	04 : 02 : 32.47	+60 : 20 : 40.0	43	25.75	1.598 ± 0.098[c]	0.659 ± 0.044[c]	0.158 ± 0.014[c]
37	F04097+0525	UGC 02982	04 : 12 : 22.68	+05 : 32 : 49.1	90	31.55	7.324 ± 0.480	3.541 ± 0.223[c]	1.068 ± 0.071[c]
38	F04118-3207	ESO 420-G013	04 : 13 : 49.70	−32 : 00 : 25.3	55	13.28	6.401 ± 0.388[c]	2.406 ± 0.148[c]	0.669 ± 0.041[c]
39	F04191-1855	ESO 550-IG 025 NED01	04 : 21 : 20.08	−18 : 48 : 57.4	···	···	···	···	···
39	F04191-1855	ESO 550-IG 025 NED02	04 : 21 : 20.02	−18 : 48 : 39.6	···	···	···	···	···
39	F04191-1855	ESO 550-IG 025	04 : 21 : 20.04	−18 : 48 : 48.4	60	37.82	3.273 ± 0.215	1.306 ± 0.087	0.449 ± 0.028[c]
40	F04210-4042	NGC 1572	04 : 22 : 42.81	−40 : 36 : 03.1	65	26.82	7.368 ± 0.484	3.225 ± 0.199[c]	1.028 ± 0.063[c]
41	04271+3849	IRAS 04271+3849	04 : 30 : 33.09	+38 : 55 : 47.8	60	22.63	3.815 ± 0.234[c]	1.478 ± 0.093[c]	0.453 ± 0.031[c]
42	F04315-0840	NGC 1614	04 : 33 : 59.95	−08 : 34 : 46.6	70	22.30	7.291 ± 0.452[c]	2.650 ± 0.165[c]	0.748 ± 0.049[c]
43	F04326+1904	UGC 03094	04 : 35 : 33.81	+19 : 10 : 18.0	65	31.80	5.210 ± 0.341	2.114 ± 0.140	0.663 ± 0.047
44	F04454-4838	ESO 203-IG001	04 : 46 : 49.55	−48 : 33 : 30.6	33	33.92	0.918 ± 0.053[c]	0.339 ± 0.020[c]	0.091 ± 0.007[c]
45	F04502-3304	MCG-05-12-006	04 : 52 : 04.96	−32 : 59 : 26.0	65	24.67	2.454 ± 0.153[c]	0.905 ± 0.059[c]	0.266 ± 0.021[c]
46	F05053-0805	NGC 1797	05 : 07 : 44.84	−08 : 01 : 08.7	60	17.92	4.438 ± 0.270[c]	1.670 ± 0.103[c]	0.534 ± 0.034[c]
46	F05053-0805[a]	NGC 1799	05 : 07 : 44.59	−07 : 58 : 09.0	60	17.92	0.596 ± 0.044	0.315 ± 0.025[c]	0.121 ± 0.014[c]
47	F05054+1718	CGCG 468-002 NED01	05 : 08 : 19.71	+17 : 21 : 47.8	···	···	···	···	···
47	F05054+1718	CGCG 468-002 NED02	05 : 08 : 21.21	+17 : 22 : 08.0	···	···	···	···	···
47	F05054+1718	CGCG 468-002	05 : 08 : 20.46	+17 : 21 : 57.8	50	18.20	2.804 ± 0.185	1.015 ± 0.070	0.293 ± 0.024
48	05083+2441	IRAS 05083+2441	05 : 11 : 25.88	+24 : 45 : 18.2	37	17.01	1.672 ± 0.099[c]	0.613 ± 0.036[c]	0.198 ± 0.013[c]
48	05083+2441		05 : 11 : 29.05	+24 : 46 : 04.0	36	16.55	0.573 ± 0.040	0.290 ± 0.020[c]	0.103 ± 0.011[c]
48	05083+2441	IRGP J051127.4+244539	05 : 11 : 27.46	+24 : 45 : 41.1	70	32.17	2.202 ± 0.146	0.824 ± 0.058	0.292 ± 0.024
49	F05081+7936	VII Zw 031	05 : 16 : 46.39	+79 : 40 : 12.9	55	57.65	3.130 ± 0.189[c]	1.167 ± 0.072[c]	0.349 ± 0.022[c]

continued on the next page

Table 2.5. (continued) *Herschel* SPIRE Total and Component Fluxes of GOALS Systems

#	IRAS Name	Optical Name	RA	Dec.	Ang. Ap.	Phys. Ap.	$F_\lambda(250\ \mu m)$	$F_\lambda(350\ \mu m)$	$F_\lambda(500\ \mu m)$
—	—	—	HH:MM:SS	DD:MM:SS	$''$	kpc	Jy	Jy	Jy
50	05129+5128	IRAS 05129+5128	05 : 16 : 55.96	+ 51 : 31 : 56.9	45	24.81	1.771 ± 0.106^c	0.631 ± 0.038^c	0.196 ± 0.013^c
51	F05189-2524	IRAS F05189-2524	05 : 21 : 01.45	− 25 : 21 : 46.2	40	33.36	1.975 ± 0.118^c	0.729 ± 0.044^c	0.199 ± 0.014^c
52	F05187-1017	IRAS F05187-1017	05 : 21 : 06.53	− 10 : 14 : 46.2	50	27.97	2.721 ± 0.165^c	1.094 ± 0.068^c	0.327 ± 0.022^c
53	05368+4940	MCG+08-11-002	05 : 40 : 43.70	+ 49 : 41 : 41.6	55	21.49	8.341 ± 0.507^c	3.223 ± 0.198^c	0.948 ± 0.056^c
54	F05365+6921	NGC 1961	05 : 42 : 04.55	+ 69 : 22 : 42.8	140	39.03	19.59 ± 1.27	8.715 ± 0.567	3.076 ± 0.201
55	F05414+5840	UGC 03351	05 : 45 : 48.03	+ 58 : 42 : 03.6	70	21.69	13.70 ± 0.90	5.817 ± 0.359^c	1.858 ± 0.114^c
56	05442+1732	IRAS 05442+1732	05 : 47 : 11.20	+ 17 : 33 : 46.4	43	16.14	2.878 ± 0.172^c	1.005 ± 0.061^c	0.322 ± 0.021^c
56	05442+1732	UGC 03356	05 : 47 : 05.79	+ 17 : 33 : 11.9	43	16.14	1.376 ± 0.091	0.577 ± 0.040	0.207 ± 0.016
56	05442+1732	HIPASS J0547+17	05 : 47 : 08.49	+ 17 : 33 : 29.1	90	33.77	4.194 ± 0.276	1.639 ± 0.110	0.578 ± 0.043
57	F06076-2139	IRAS F06076-2139NW	06 : 09 : 45.74	− 21 : 40 : 24.5	···	···	···	···	···
57	F06076-2139	IRAS F06076-2139SE	06 : 09 : 45.95	− 21 : 40 : 32.1	···	···	···	···	···
57	F06076-2139	IRAS F06076-2139	06 : 09 : 45.84	− 21 : 40 : 28.3	50	37.16	2.157 ± 0.129^c	0.863 ± 0.053^c	0.271 ± 0.017^c
58	F06052+8027	UGC 03410	06 : 14 : 29.61	+ 80 : 26 : 59.6	68	18.76	8.771 ± 0.571	3.428 ± 0.223	1.222 ± 0.074^c
58	F06052+8027	UGC 03405	06 : 13 : 57.90	+ 80 : 28 : 34.7	50	13.79	2.782 ± 0.181	1.100 ± 0.072	0.343 ± 0.024
58	F06052+8027	KPG 108	06 : 14 : 13.75	+ 80 : 27 : 47.1	···	···	11.55 ± 0.60	4.528 ± 0.235	1.566 ± 0.077^c
59	F06107+7822	NGC 2146	06 : 18 : 37.82	+ 78 : 21 : 24.0	150	12.65	62.78 ± 4.08	22.89 ± 1.49	7.138 ± 0.465
60	F06259-4708	ESO 255-IG 007 NED01	06 : 27 : 21.70	− 47 : 10 : 36.2	···	···	···	···	···
60	F06259-4708	ESO 255-IG 007 NED02	06 : 27 : 22.55	− 47 : 10 : 47.3	···	···	···	···	···
60	F06259-4708	ESO 255-IG 007 NED03	06 : 27 : 23.09	− 47 : 11 : 02.6	···	···	···	···	···
60	F06259-4708	ESO 255-IG007	06 : 27 : 22.39	− 47 : 10 : 49.4	60	46.63	2.764 ± 0.181	1.019 ± 0.068	0.289 ± 0.021
61	F06295-1735	ESO 557-G002	06 : 31 : 47.20	− 17 : 37 : 16.6	45	19.53	2.247 ± 0.135^c	0.857 ± 0.052^c	0.250 ± 0.017^c
61	F06295-1735	ESO 557-G001	06 : 31 : 45.71	− 17 : 38 : 44.9	43	18.66	0.759 ± 0.052	0.299 ± 0.023	0.095 ± 0.011
61	F06295-1735	IRGP J063146.5-173802	06 : 31 : 46.45	− 17 : 38 : 00.7	···	···	3.006 ± 0.144^c	1.156 ± 0.057^c	0.345 ± 0.020^c
62	F06538+4628	UGC 3608	06 : 57 : 34.41	+ 46 : 24 : 10.6	50	21.91	3.593 ± 0.215^c	1.363 ± 0.083^c	0.429 ± 0.027^c
63	F06592-6313	IRAS F06592-6313	06 : 59 : 40.26	− 63 : 17 : 52.4	55	26.50	1.842 ± 0.113^c	0.755 ± 0.048^c	0.221 ± 0.017^c
64	F07027-6011	AM 0702-601 NED01	07 : 03 : 24.14	− 60 : 15 : 21.9	43	27.64	0.874 ± 0.054^c	0.344 ± 0.024^c	0.096 ± 0.012^c
64	F07027-6011	AM 0702-601 NED02	07 : 03 : 28.52	− 60 : 16 : 43.7	50	32.14	1.991 ± 0.121^c	0.816 ± 0.051^c	0.292 ± 0.020^c
64	F07027-6011	AM 0702-601	07 : 03 : 26.33	− 60 : 16 : 02.7	90	57.86	2.540 ± 0.170	1.025 ± 0.072	0.309 ± 0.029
65	07063+2043	NGC 2342	07 : 09 : 18.07	+ 20 : 38 : 10.2	65	23.63	5.856 ± 0.382	2.328 ± 0.153	0.742 ± 0.050
65	07063+2043	NGC 2341	07 : 09 : 12.01	+ 20 : 36 : 11.2	50	18.18	3.431 ± 0.225	1.433 ± 0.086^c	0.431 ± 0.027^c

continued on the next page

Table 2.5. (continued) *Herschel* SPIRE Total and Component Fluxes of GOALS Systems

#	IRAS Name	Optical Name	RA	Dec.	Ang. Ap.	Phys. Ap.	$F_\lambda(250\ \mu m)$	$F_\lambda(350\ \mu m)$	$F_\lambda(500\ \mu m)$
—	—	—	HH:MM:SS	DD:MM:SS	$''$	kpc	Jy	Jy	Jy
65	07063+2043	KPG 125	07 : 09 : 15.04	+ 20 : 37 : 10.7	···	···	9.287 ± 0.443	3.761 ± 0.176^{c}	1.173 ± 0.057^{c}
66	F07160-6215	NGC 2369	07 : 16 : 37.73	− 62 : 20 : 36.4	95	21.46	17.35 ± 1.14	7.181 ± 0.453^{c}	2.273 ± 0.143^{c}
67	07251-0248	IRAS 07251-0248	07 : 27 : 37.62	− 02 : 54 : 54.8	45	73.78	1.448 ± 0.087^{c}	0.561 ± 0.034^{c}	0.178 ± 0.012^{c}
68	F07256+3355	NGC 2389	07 : 29 : 04.59	+ 33 : 51 : 38.0	78	22.58	3.538 ± 0.231	1.395 ± 0.091	0.520 ± 0.035
68	F07256+3355	NGC 2388	07 : 28 : 53.44	+ 33 : 49 : 07.8	85	24.60	8.484 ± 0.525^{c}	3.237 ± 0.201^{c}	1.017 ± 0.063^{c}
68	F07256+3355	NGC 2385	07 : 28 : 28.17	+ 33 : 50 : 16.9	37	10.71	0.379 ± 0.025^{b}	0.184 ± 0.012^{b}	$0.057 \pm 0.005^{b,c}$
68	F07256+3355	WBL 142	07 : 28 : 46.38	+ 33 : 50 : 22.9	···	···	12.02 ± 0.57^{c}	4.632 ± 0.221^{c}	1.537 ± 0.072^{c}
69	F07329+1149	MCG+02-20-003	07 : 35 : 43.44	+ 11 : 42 : 34.8	70	24.43	4.071 ± 0.250^{c}	1.555 ± 0.095^{c}	0.503 ± 0.031^{c}
69	F07329+1149[a]	NGC 2416	07 : 35 : 41.53	+ 11 : 36 : 42.1	42	14.66	1.008 ± 0.066	0.436 ± 0.029	0.154 ± 0.010^{c}
70	08355-4944	IRAS 08355-4944	08 : 37 : 01.87	− 49 : 54 : 30.0	40	21.74	1.758 ± 0.105^{c}	0.622 ± 0.040^{c}	0.173 ± 0.015^{c}
71	F08339+6517	IRAS F08339+6517	08 : 38 : 23.18	+ 65 : 07 : 15.2	45	18.13	1.267 ± 0.084	0.506 ± 0.031^{c}	0.148 ± 0.010^{c}
72	F08354+2555	NGC 2623	08 : 38 : 24.11	+ 25 : 45 : 16.5	50	19.66	5.929 ± 0.358^{c}	2.124 ± 0.130^{c}	0.589 ± 0.035^{c}
73	08424-3130	ESO 432-IG006SW	08 : 44 : 27.21	− 31 : 41 : 50.8	···	···	···	···	···
73	08424-3130	ESO 432-IG006NE	08 : 44 : 28.93	− 31 : 41 : 30.3	···	···	···	···	···
73	08424-3130	ESO 432-IG006	08 : 44 : 28.07	− 31 : 41 : 40.5	65	22.72	3.117 ± 0.205	1.227 ± 0.082	0.363 ± 0.027
74	F08520-6850	ESO 060-IG 016 NED01	08 : 52 : 32.07	− 69 : 01 : 54.8	···	···	···	···	···
74	F08520-6850	ESO 060-IG 016 NED02	08 : 52 : 30.50	− 69 : 01 : 59.2	···	···	···	···	···
74	F08520-6850	ESO 060-IG 016	08 : 52 : 31.28	− 69 : 01 : 57.0	60	55.79	1.318 ± 0.088	0.613 ± 0.040^{c}	0.170 ± 0.014^{c}
75	F08572+3915	IRAS F08572+3915	09 : 00 : 25.35	+ 39 : 03 : 54.0	35	39.99	0.521 ± 0.031^{c}	0.188 ± 0.014^{c}	0.042 ± 0.007^{c}
76	09022-3615	IRAS 09022-3615	09 : 04 : 12.69	− 36 : 27 : 01.5	40	46.81	2.588 ± 0.152^{c}	0.880 ± 0.051^{c}	0.243 ± 0.014^{c}
77	F09111-1007	2MASX J09133644-1019296	09 : 13 : 36.50	− 10 : 19 : 29.7	20	21.47	2.615 ± 0.134^{c}	···	···
77	F09111-1007	2MASX J09133888-1019196	09 : 13 : 38.89	− 10 : 19 : 19.6	20	21.47	1.001 ± 0.051^{c}	···	···
77	F09111-1007	IRAS F09111-1007	09 : 13 : 37.69	− 10 : 19 : 24.6	65	69.77	3.434 ± 0.225	1.357 ± 0.090	0.434 ± 0.030
78	F09126+4432	CGCG 209-036	09 : 15 : 44.49	+ 44 : 14 : 09.6	···	···	···	···	···
78	F09126+4432	UGC04881 NED01	09 : 15 : 55.52	+ 44 : 19 : 57.4	···	···	···	···	···
78	F09126+4432	UGC04881 NED02	09 : 15 : 54.69	+ 44 : 19 : 50.8	···	···	···	···	···
78	F09126+4432	UGC 04881	09 : 15 : 55.10	+ 44 : 19 : 54.0	60	47.91	3.296 ± 0.217	1.360 ± 0.092	0.435 ± 0.029^{c}
79	F09320+6134	UGC 05101	09 : 35 : 51.59	+ 61 : 21 : 11.9	53	42.09	6.138 ± 0.371^{c}	2.403 ± 0.148^{c}	0.755 ± 0.045^{c}
80	F09333+4841	MCG+08-18-013	09 : 36 : 37.20	+ 48 : 28 : 27.7	37	19.70	2.320 ± 0.135^{c}	0.872 ± 0.049^{c}	···
80	F09333+4841	MCG+08-18-012	09 : 36 : 30.86	+ 48 : 28 : 09.9	28	14.91	0.187 ± 0.015	0.100 ± 0.009	···

continued on the next page

Table 2.5. (continued) *Herschel* SPIRE Total and Component Fluxes of GOALS Systems

#	IRAS Name	Optical Name	RA	Dec.	Ang. Ap.	Phys. Ap.	$F_\lambda(250\ \mu m)$	$F_\lambda(350\ \mu m)$	$F_\lambda(500\ \mu m)$
—	—	—	HH:MM:SS	DD:MM:SS	$''$	kpc	Jy	Jy	Jy
80	F09333+4841	CGCG 239-011	09 : 36 : 34.02	+ 48 : 28 : 18.8	75	39.92	2.302 ± 0.152	0.935 ± 0.063	0.266 ± 0.021
81	F09437+0317	IC 0564	09 : 46 : 21.10	+ 03 : 04 : 16.3	55	23.81	4.181 ± 0.274	1.800 ± 0.119	0.593 ± 0.041
81	F09437+0317	IC 0563	09 : 46 : 20.30	+ 03 : 02 : 44.7	50	21.65	2.696 ± 0.177	1.065 ± 0.071	0.345 ± 0.025
81	F09437+0317	Arp 303	09 : 46 : 20.70	+ 03 : 03 : 30.4	90	38.96	6.772 ± 0.443	2.876 ± 0.190	0.916 ± 0.064
82	F10015-0614	NGC 3110	10 : 04 : 02.11	− 06 : 28 : 29.5	67	24.43	7.794 ± 0.509	3.226 ± 0.198^c	1.000 ± 0.062^c
82	F10015-0614	MCG-01-26-013	10 : 03 : 57.03	− 06 : 29 : 47.7	40	14.58	0.647 ± 0.041^c	0.264 ± 0.020^c	0.075 ± 0.009^c
82	F10015-0614	IRGP J100359.6-062908	10 : 03 : 59.57	− 06 : 29 : 08.5	110	40.10	8.670 ± 0.567	3.373 ± 0.223	1.042 ± 0.072
83	F10038-3338	ESO 374-IG 032	10 : 06 : 04.65	− 33 : 53 : 06.1	55	38.90	1.837 ± 0.111^c	0.784 ± 0.049^c	0.266 ± 0.018^c
84	F10173+0828	IRAS F10173+0828	10 : 20 : 00.24	+ 08 : 13 : 32.8	45	44.40	1.132 ± 0.068^c	0.501 ± 0.031^c	0.144 ± 0.011^c
85	F10196+2149	NGC 3221	10 : 22 : 19.98	+ 21 : 34 : 10.6	110	34.08	12.52 ± 0.82	5.352 ± 0.350	1.809 ± 0.120
86	F10257-4339	NGC 3256	10 : 27 : 51.30	− 43 : 54 : 14.0	85	15.74	33.91 ± 2.21	12.16 ± 0.79	3.929 ± 0.242^c
87	F10409-4556	ESO 264-G036	10 : 43 : 07.51	− 46 : 12 : 44.1	60	27.90	6.560 ± 0.429	2.658 ± 0.163^c	0.860 ± 0.052^c
88	F10567-4310	ESO 264-G057	10 : 59 : 01.70	− 43 : 26 : 25.2	60	23.42	5.057 ± 0.331	2.124 ± 0.131^c	0.690 ± 0.043^c
89	F10565+2448	IRAS F10565+2448	10 : 59 : 18.15	+ 24 : 32 : 34.2	43	30.77	3.643 ± 0.215^c	1.337 ± 0.078^c	0.381 ± 0.022^c
90	F11011+4107	MCG+07-23-019	11 : 03 : 53.98	+ 40 : 51 : 00.4	45	32.20	2.862 ± 0.172^c	1.098 ± 0.066^c	0.325 ± 0.021^c
91	F11186-0242	CGCG 011-076	11 : 21 : 12.24	− 02 : 59 : 02.5	40	21.43	3.521 ± 0.209^c	1.382 ± 0.080^c	···
91	F11186-0242		11 : 21 : 08.29	− 02 : 59 : 39.2	23	12.32	0.265 ± 0.016^c	0.121 ± 0.009^c	···
91	F11186-0242	IRGP J112110.3-025922	11 : 21 : 10.26	− 02 : 59 : 20.8	100	53.57	3.795 ± 0.252	1.653 ± 0.112	0.562 ± 0.042
92	F11231+1456	IC 2810	11 : 25 : 45.07	+ 14 : 40 : 36.0	44	31.14	2.713 ± 0.162^c	1.142 ± 0.068^c	···
92	F11231+1456	MCG+03-29-044	11 : 25 : 49.55	+ 14 : 40 : 06.6	37	26.19	1.324 ± 0.078^c	0.561 ± 0.033^c	···
92	F11231+1456	IRAS F11231+1456	11 : 25 : 47.31	+ 14 : 40 : 21.2	90	63.70	3.820 ± 0.252	1.610 ± 0.108	0.544 ± 0.041
93	F11255-4120	ESO 319-G022	11 : 27 : 54.18	− 41 : 36 : 51.7	50	18.76	3.088 ± 0.186^c	1.144 ± 0.070^c	0.319 ± 0.021^c
94	F11257+5850	UGC 6471	11 : 28 : 31.04	+ 58 : 33 : 40.5	···	···	···	···	···
94	F11257+5850	UGC 6472	11 : 28 : 33.67	+ 58 : 33 : 46.1	···	···	···	···	···
94	F11257+5850	NGC 3690	11 : 28 : 32.35	+ 58 : 33 : 43.3	90	21.69	21.85 ± 1.42	7.688 ± 0.502	2.273 ± 0.149
95	F11506-3851	ESO 320-G030	11 : 53 : 11.73	− 39 : 07 : 49.0	80	15.63	13.02 ± 0.81^c	5.182 ± 0.324^c	1.608 ± 0.101^c
96	F12043-3140	MCG-05-29-016	12 : 06 : 51.87	− 31 : 56 : 59.2	···	···	···	···	···
96	F12043-3140	MCG-05-29-017	12 : 06 : 51.70	− 31 : 56 : 46.4	···	···	···	···	···
96	F12043-3140	ESO 440-IG058	12 : 06 : 51.78	− 31 : 56 : 52.8	50	25.94	3.607 ± 0.238	1.323 ± 0.089	0.388 ± 0.028
97	F12112+0305	IRAS F12112+0305	12 : 13 : 46.02	+ 02 : 48 : 42.2	45	64.38	1.974 ± 0.119^c	0.796 ± 0.049^c	0.226 ± 0.016^c

continued on the next page

Table 2.5. (continued) *Herschel* SPIRE Total and Component Fluxes of GOALS Systems

#	IRAS Name	Optical Name	RA	Dec.	Ang. Ap.	Phys. Ap.	$F_\lambda(250\ \mu m)$	$F_\lambda(350\ \mu m)$	$F_\lambda(500\ \mu m)$
—	—	—	HH:MM:SS	DD:MM:SS	$''$	kpc	Jy	Jy	Jy
98	F12116+5448	NGC 4194	12 : 14 : 09.71	+54 : 31 : 35.5	60	12.30	5.315 ± 0.324^c	1.867 ± 0.115^c	0.549 ± 0.034^c
99	F12115-4656	ESO 267-G030	12 : 14 : 12.81	−47 : 13 : 42.5	60	27.05	4.509 ± 0.272^c	1.757 ± 0.107^c	0.598 ± 0.035^c
99	F12115-4656[a]	ESO 267-G029	12 : 13 : 52.28	−47 : 16 : 25.4	70	31.56	3.262 ± 0.213	1.350 ± 0.083^c	0.441 ± 0.028^c
100	12116-5615	IRAS 12116-5615	12 : 14 : 22.08	−56 : 32 : 32.7	45	26.46	3.229 ± 0.195^c	1.268 ± 0.080^c	0.418 ± 0.028^c
101	F12224-0624	IRAS F12224-0624	12 : 25 : 03.90	−06 : 40 : 52.1	65	37.41	1.972 ± 0.122^c	0.785 ± 0.050^c	0.271 ± 0.019^c
102	F12243-0036	NGC 4418	12 : 26 : 54.60	−00 : 52 : 39.6	65	11.44	6.447 ± 0.393^c	2.498 ± 0.152^c	0.885 ± 0.053^c
102	F12243-0036	MCG+00-32-013	12 : 27 : 04.88	−00 : 54 : 24.7	40	7.039	0.184 ± 0.013^c	0.097 ± 0.007^c	0.044 ± 0.006^c
102	F12243-0036	KPG 337	12 : 26 : 59.74	−00 : 53 : 32.1	···	···	6.631 ± 0.394^c	2.595 ± 0.152^c	0.930 ± 0.053^c
103	F12540+5708	UGC 08058	12 : 56 : 14.25	+56 : 52 : 24.8	50	42.86	5.685 ± 0.343^c	2.007 ± 0.123^c	0.597 ± 0.036^c
104	F12590+2934		13 : 01 : 25.27	+29 : 18 : 49.5	···	···	···	···	···
104	F12590+2934		13 : 01 : 24.51	+29 : 18 : 29.8	···	···	···	···	···
104	F12590+2934	NGC 4922	13 : 01 : 24.89	+29 : 18 : 39.6	50	25.67	2.032 ± 0.122^c	0.727 ± 0.045^c	0.218 ± 0.015^c
105	F12592+0436	CGCG 043-099	13 : 01 : 50.28	+04 : 20 : 00.8	60	47.30	2.808 ± 0.171^c	1.055 ± 0.065^c	0.315 ± 0.020^c
106	F12596-1529	MCG-02-33-098SW	13 : 02 : 19.66	−15 : 46 : 04.2	···	···	···	···	···
106	F12596-1529	MCG-02-33-098NE	13 : 02 : 20.38	−15 : 45 : 59.6	···	···	···	···	···
106	F12596-1529	MCG-02-33-098	13 : 02 : 20.02	−15 : 46 : 01.8	70	25.89	2.654 ± 0.175	1.061 ± 0.072	0.330 ± 0.027
107	F13001-2339	ESO 507-G070	13 : 02 : 52.42	−23 : 55 : 17.8	55	27.06	3.747 ± 0.228^c	1.405 ± 0.087^c	0.451 ± 0.029^c
108	13052-5711	IRAS 13052-5711	13 : 08 : 18.73	−57 : 27 : 30.3	50	24.63	3.819 ± 0.231^c	1.624 ± 0.101^c	0.422 ± 0.028^c
109	F13126+2453	IC 0860	13 : 15 : 03.49	+24 : 37 : 07.6	50	13.48	3.775 ± 0.228^c	1.523 ± 0.093^c	0.500 ± 0.030^c
110	13120-5453	IRAS 13120-5453	13 : 15 : 06.37	−55 : 09 : 22.5	60	39.42	12.33 ± 0.75^c	4.396 ± 0.268^c	1.340 ± 0.079^c
111	F13136+6223	VV 250a	13 : 15 : 34.96	+62 : 07 : 29.2	···	···	···	···	···
111	F13136+6223	VV 250b	13 : 15 : 30.69	+62 : 07 : 45.8	···	···	···	···	···
111	F13136+6223	VV 250	13 : 15 : 32.82	+62 : 07 : 37.4	70	45.17	2.429 ± 0.159	0.875 ± 0.059	0.273 ± 0.021
112	F13182+3424	UGC 08387	13 : 20 : 35.37	+34 : 08 : 22.2	65	33.09	6.356 ± 0.393^c	2.345 ± 0.146^c	0.646 ± 0.041^c
113	F13188+0036	NGC 5104	13 : 21 : 23.09	+00 : 20 : 33.2	60	25.45	5.266 ± 0.322^c	2.005 ± 0.124^c	0.658 ± 0.040^c
114	F13197-1627	MCG-03-34-064	13 : 22 : 24.45	−16 : 43 : 42.4	40	15.42	1.235 ± 0.073^c	0.459 ± 0.028^c	0.120 ± 0.009^c
114	F13197-1627	MCG-03-34-063	13 : 22 : 19.02	−16 : 42 : 30.0	55	21.20	1.205 ± 0.080	0.557 ± 0.038	0.210 ± 0.015^c
114	F13197-1627	IRAS F13197-1627	13 : 22 : 21.73	−16 : 43 : 06.2	···	···	2.440 ± 0.108^c	1.016 ± 0.047^c	0.330 ± 0.017^c
115	F13229-2934	NGC 5135	13 : 25 : 44.02	−29 : 50 : 00.4	100	28.75	12.37 ± 0.81	5.058 ± 0.333	1.577 ± 0.106
116	13242-5713	ESO 173-G015	13 : 27 : 23.79	−57 : 29 : 21.8	80	12.92	26.51 ± 1.74	9.706 ± 0.642	3.092 ± 0.194^c

continued on the next page

Table 2.5. (continued) *Herschel* SPIRE Total and Component Fluxes of GOALS Systems

#	IRAS Name	Optical Name	RA	Dec.	Ang. Ap.	Phys. Ap.	$F_\lambda(250\ \mu m)$	$F_\lambda(350\ \mu m)$	$F_\lambda(500\ \mu m)$
—	—	—	HH:MM:SS	DD:MM:SS	$''$	kpc	Jy	Jy	Jy
117	F13301-2356	IC 4280	13 : 32 : 53.40	− 24 : 12 : 25.5	65	25.15	5.631 ± 0.369	2.431 ± 0.150^c	0.771 ± 0.048^c
118	F13362+4831	KPG 388A	13 : 38 : 17.25	+ 48 : 16 : 32.9	···	···	···	···	···
118	F13362+4831	KPG 388B	13 : 38 : 17.79	+ 48 : 16 : 41.6	···	···	···	···	···
118	F13362+4831	NGC 5256	13 : 38 : 17.52	+ 48 : 16 : 37.2	60	35.52	2.757 ± 0.182	1.070 ± 0.073	0.336 ± 0.026
119	F13373+0105	NGC 5258	13 : 39 : 57.72	+ 00 : 49 : 53.0	45	22.65	4.933 ± 0.323	1.954 ± 0.129	0.670 ± 0.039^c
119	F13373+0105	NGC 5257	13 : 39 : 52.95	+ 00 : 50 : 25.9	45	22.65	4.175 ± 0.273	1.649 ± 0.109	0.645 ± 0.037^c
119	F13373+0105	Arp 240	13 : 39 : 55.34	+ 00 : 50 : 09.5	90	45.29	9.434 ± 0.615	3.759 ± 0.246	1.259 ± 0.084
120	F13428+5608	UGC 08696	13 : 44 : 42.12	+ 55 : 53 : 13.1	55	42.82	4.177 ± 0.252^c	1.531 ± 0.094^c	0.427 ± 0.026^c
121	F13470+3530	UGC 08739	13 : 49 : 13.94	+ 35 : 15 : 26.2	80	30.52	8.243 ± 0.540	3.405 ± 0.225	1.162 ± 0.073^c
122	F13478-4848	ESO 221-IG010	13 : 50 : 56.92	− 49 : 03 : 18.8	75	22.40	7.116 ± 0.465	2.771 ± 0.183	0.917 ± 0.066
123	F13497+0220	NGC 5331S	13 : 52 : 16.21	+ 02 : 06 : 05.1	···	···	···	···	···
123	F13497+0220	NGC 5331N	13 : 52 : 16.43	+ 02 : 06 : 30.9	···	···	···	···	···
123	F13497+0220	NGC 5331	13 : 52 : 16.32	+ 02 : 06 : 18.0	80	56.32	5.010 ± 0.329	1.892 ± 0.126	0.673 ± 0.044^c
124	F13564+3741	NGC 5395	13 : 58 : 37.96	+ 37 : 25 : 28.1	88	24.45	8.647 ± 0.562	3.819 ± 0.249	1.370 ± 0.090
124	F13564+3741	NGC 5394	13 : 58 : 33.64	+ 37 : 27 : 12.9	42	11.67	3.255 ± 0.191^c	1.273 ± 0.073^c	0.404 ± 0.023^c
124	F13564+3741	Arp 84	13 : 58 : 35.80	+ 37 : 26 : 20.5	140	38.89	11.93 ± 0.78	5.187 ± 0.338	1.856 ± 0.122
125	F14179+4927	CGCG 247-020	14 : 19 : 43.27	+ 49 : 14 : 11.9	45	24.89	1.789 ± 0.120	0.688 ± 0.048	0.175 ± 0.015
126	F14280+3126	NGC 5653W	14 : 30 : 09.67	+ 31 : 12 : 56.7	···	···	···	···	···
126	F14280+3126	NGC 5653E	14 : 30 : 10.44	+ 31 : 12 : 55.8	···	···	···	···	···
126	F14280+3126	NGC 5653	14 : 30 : 10.44	+ 31 : 12 : 55.8	70	19.95	8.748 ± 0.538^c	3.369 ± 0.207^c	0.994 ± 0.062^c
127	F14348-1447	IRAS F14378-1447 SW	14 : 37 : 38.28	− 15 : 00 : 24.2	···	···	···	···	···
127	F14348-1447	IRAS F14378-1447 NE	14 : 37 : 38.40	− 15 : 00 : 21.2	···	···	···	···	···
127	F14348-1447	IRAS F14348-1447	14 : 37 : 38.29	− 15 : 00 : 24.2	45	72.06	1.967 ± 0.117^c	0.728 ± 0.044^c	0.217 ± 0.014^c
128	F14378-3651	IRAS F14378-3651	14 : 40 : 59.04	− 37 : 04 : 32.0	30	40.20	1.376 ± 0.076^c	0.547 ± 0.030^c	0.158 ± 0.010^c
129	F14423-2039	NGC 5734	14 : 45 : 09.04	− 20 : 52 : 13.2	70	22.13	7.553 ± 0.492	2.899 ± 0.189	0.988 ± 0.060^c
129	F14423-2039	NGC 5743	14 : 45 : 11.02	− 20 : 54 : 48.6	60	18.97	4.055 ± 0.264	1.731 ± 0.105^c	0.593 ± 0.036^c
129	F14423-2039	IRGP J144510.0-205331	14 : 45 : 10.02	− 20 : 53 : 30.9	···	···	11.61 ± 0.56	4.630 ± 0.217^c	1.582 ± 0.070^c
130	F14547+2449	VV 340a	14 : 57 : 00.70	+ 24 : 37 : 05.8	···	···	···	···	···
130	F14547+2449	VV 340b	14 : 57 : 00.32	+ 24 : 36 : 24.6	···	···	···	···	···
130	F14547+2449	VV 340	14 : 57 : 00.51	+ 24 : 36 : 45.2	80	56.82	6.588 ± 0.432	2.617 ± 0.173	0.911 ± 0.062

continued on the next page

Table 2.5. (continued) *Herschel* SPIRE Total and Component Fluxes of GOALS Systems

#	IRAS Name	Optical Name	RA	Dec.	Ang. Ap.	Phys. Ap.	$F_\lambda(250\ \mu m)$	$F_\lambda(350\ \mu m)$	$F_\lambda(500\ \mu m)$
—	—	—	HH:MM:SS	DD:MM:SS	$''$	kpc	Jy	Jy	Jy
131	F14544-4255	IC 4518A	14 : 57 : 41.22	− 43 : 07 : 55.8	···	···	···	···	···
131	F14544-4255	IC 4518B	14 : 57 : 45.33	− 43 : 07 : 57.0	···	···	···	···	···
131	F14544-4255	IC 4518	14 : 57 : 43.27	− 43 : 07 : 56.3	90	33.82	6.015 ± 0.394	2.427 ± 0.161	0.803 ± 0.056
132	F15107+0724	CGCG 049-057	15 : 13 : 13.07	+ 07 : 13 : 32.1	80	24.71	8.430 ± 0.528^c	3.225 ± 0.204^c	1.059 ± 0.068^c
133	F15163+4255	VV 705 NED01	15 : 18 : 06.14	+ 42 : 44 : 45.0	···	···	···	···	···
133	F15163+4255	VV 705 NED02	15 : 18 : 06.34	+ 42 : 44 : 38.1	···	···	···	···	···
133	F15163+4255	VV 705	15 : 18 : 06.24	+ 42 : 44 : 41.5	50	41.02	2.284 ± 0.137^c	0.863 ± 0.053^c	0.254 ± 0.016^c
134	15206-6256	ESO 099-G004	15 : 24 : 57.98	− 63 : 07 : 29.4	45	28.21	3.970 ± 0.242^c	1.674 ± 0.109^c	0.505 ± 0.039^c
135	F15250+3608	IRAS F15250+3608	15 : 26 : 59.42	+ 35 : 58 : 37.8	40	44.23	1.034 ± 0.061^c	0.385 ± 0.023^c	0.124 ± 0.008^c
136	F15276+1309	NGC 5936	15 : 30 : 00.85	+ 12 : 59 : 22.1	70	22.16	6.603 ± 0.431	2.715 ± 0.167^c	0.870 ± 0.056^c
137	F15327+2340	UGC 09913	15 : 34 : 57.23	+ 23 : 30 : 11.3	90	37.00	30.87 ± 1.92^c	12.80 ± 0.80^c	3.865 ± 0.240^c
138	F15437+0234	NGC 5990	15 : 46 : 16.41	+ 02 : 24 : 55.6	60	18.27	6.071 ± 0.398	2.435 ± 0.150^c	0.831 ± 0.050^c
139	F16030+2040	NGC 6052	16 : 05 : 12.87	+ 20 : 32 : 33.0	60	21.87	3.317 ± 0.218	1.412 ± 0.088^c	0.483 ± 0.031^c
140	F16104+5235	NGC 6090	16 : 11 : 40.84	+ 52 : 27 : 27.2	55	34.45	2.666 ± 0.161^c	1.028 ± 0.063^c	0.288 ± 0.019^c
141	F16164-0746	IRAS F16164-0746	16 : 19 : 11.75	− 07 : 54 : 03.0	60	35.28	3.581 ± 0.220^c	1.266 ± 0.080^c	0.407 ± 0.028^c
142	F16284+0411	CGCG 052-037	16 : 30 : 56.53	+ 04 : 04 : 58.7	40	21.87	3.771 ± 0.224^c	···	···
142	F16284+0411	2MASX J16305326+0404243	16 : 30 : 53.25	+ 04 : 04 : 23.9	20	10.94	0.111 ± 0.008^c	···	···
142	F16284+0411	IRGP J163054.9+040441	16 : 30 : 54.89	+ 04 : 04 : 41.3	70	38.28	3.618 ± 0.240	1.423 ± 0.096	0.492 ± 0.036
143	16304-6030	NGC 6156	16 : 34 : 52.55	− 60 : 37 : 08.0	100	22.79	12.91 ± 0.84	5.096 ± 0.334	1.678 ± 0.112
144	F16330-6820	2MASX J16381190-6826080	16 : 38 : 11.85	− 68 : 26 : 08.2	55	51.62	4.374 ± 0.266^c	1.729 ± 0.107^c	0.527 ± 0.033^c
144	F16330-6820	2MASX J16381338-6827170	16 : 38 : 13.43	− 68 : 27 : 16.6	25	23.46	0.128 ± 0.012	0.058 ± 0.008	0.024 ± 0.005
144	F16330-6820	ESO 069-IG006	16 : 38 : 12.64	− 68 : 26 : 42.3	···	···	4.501 ± 0.266^c	1.788 ± 0.107^c	0.551 ± 0.033^c
145	F16399-0937	IRAS F16399-0937	16 : 42 : 40.11	− 09 : 43 : 13.7	60	35.31	3.527 ± 0.218^c	1.333 ± 0.088^c	0.435 ± 0.034^c
146	F16443-2915	ESO 453-G005	16 : 47 : 31.09	− 29 : 21 : 21.6	55	25.70	4.150 ± 0.252^c	1.635 ± 0.101^c	0.575 ± 0.035^c
146	F16443-2915	2MASX J16472937-2919067	16 : 47 : 29.34	− 29 : 19 : 06.8	50	23.37	1.206 ± 0.074^c	0.539 ± 0.035^c	0.199 ± 0.015^c
146	F16443-2915	IRGP J164730.2-292014	16 : 47 : 30.21	− 29 : 20 : 14.2	···	···	5.356 ± 0.262^c	2.175 ± 0.107^c	0.773 ± 0.038^c
147	F16504+0228	NGC 6240	16 : 52 : 58.90	+ 02 : 24 : 03.3	80	42.86	7.026 ± 0.437^c	2.834 ± 0.177^c	0.874 ± 0.056^c
148	F16516-0948	IRAS F16516-0948	16 : 54 : 23.72	− 09 : 53 : 20.9	55	27.28	3.353 ± 0.203^c	1.232 ± 0.079^c	0.434 ± 0.030^c
149	F16577+5900	NGC 6286	16 : 58 : 31.63	+ 58 : 56 : 13.3	50	20.34	9.311 ± 0.611	3.969 ± 0.239^c	1.307 ± 0.075^c
149	F16577+5900	NGC 6285	16 : 58 : 23.99	+ 58 : 57 : 21.7	40	16.27	1.435 ± 0.086^c	0.556 ± 0.034^c	0.189 ± 0.013^c

continued on the next page

Table 2.5. (continued) *Herschel* SPIRE Total and Component Fluxes of GOALS Systems

#	IRAS Name	Optical Name	RA	Dec.	Ang. Ap.	Phys. Ap.	$F_\lambda(250\ \mu m)$	$F_\lambda(350\ \mu m)$	$F_\lambda(500\ \mu m)$
—	—	—	HH:MM:SS	DD:MM:SS	$''$	kpc	Jy	Jy	Jy
149	F16577+5900	Arp 293	16 : 58 : 27.81	+58 : 56 : 47.5	130	52.88	11.60 ± 0.76	4.599 ± 0.303	1.495 ± 0.101
150	F17132+5313		17 : 14 : 19.79	+53 : 10 : 29.0	···	···	···	···	···
150	F17132+5313		17 : 14 : 20.45	+53 : 10 : 32.1	···	···	···	···	···
150	F17132+5313	IRAS F17132+5313	17 : 14 : 20.45	+53 : 10 : 31.6	55	56.02	2.009 ± 0.122^c	0.780 ± 0.048^c	0.226 ± 0.016^c
151	F17138-1017	IRAS F17138-1017	17 : 16 : 35.68	−10 : 20 : 40.5	60	23.62	5.423 ± 0.332^c	1.875 ± 0.117^c	0.531 ± 0.035^c
152	F17207-0014	IRAS F17207-0014	17 : 23 : 21.97	−00 : 17 : 00.7	55	48.56	7.959 ± 0.485^c	2.907 ± 0.180^c	0.890 ± 0.054^c
153	F17222-5953	ESO 138-G027	17 : 26 : 43.35	−59 : 55 : 55.2	55	25.14	3.340 ± 0.202^c	1.240 ± 0.077^c	0.370 ± 0.025^c
154	F17530+3447	UGC 11041	17 : 54 : 51.82	+34 : 46 : 34.2	60	21.82	5.299 ± 0.322^c	2.103 ± 0.130^c	0.689 ± 0.042^c
155	F17548+2401	CGCG 141-034	17 : 56 : 56.65	+24 : 01 : 02.0	60	26.12	2.961 ± 0.183^c	0.998 ± 0.064^c	0.302 ± 0.021^c
156	17578-0400	IRAS 17578-0400	18 : 00 : 31.86	−04 : 00 : 53.4	40	12.99	8.913 ± 0.529^c	3.443 ± 0.200^c	1.091 ± 0.062^c
156	17578-0400	2MASX J18003399-0401443	18 : 00 : 34.08	−04 : 01 : 43.9	27	8.770	1.313 ± 0.072^c	0.531 ± 0.032^c	0.187 ± 0.012^c
156	17578-0400	2MASX J18002449-0401023	18 : 00 : 24.29	−04 : 01 : 03.8	45	14.62	1.292 ± 0.080^c	0.575 ± 0.039^c	0.188 ± 0.016^c
156	17578-0400	2MASX J18003399-0401443	18 : 00 : 32.49	−04 : 01 : 13.1	70	22.74	9.824 ± 0.647	3.725 ± 0.247	1.118 ± 0.077
156	17578-0400	IRGP J1800301-040113	18 : 00 : 28.61	−04 : 01 : 16.3	···	···	11.12 ± 0.65^c	4.300 ± 0.250^c	1.306 ± 0.078^c
157	18090+0130	2MASX J18113842+0131397	18 : 11 : 38.42	+01 : 31 : 40.3	50	30.69	3.802 ± 0.229^c	1.451 ± 0.090^c	0.465 ± 0.030^c
157	18090+0130	2MASX J18113342+0131427	18 : 11 : 33.41	+01 : 31 : 42.4	40	24.55	1.208 ± 0.078^c	0.418 ± 0.029^c	0.124 ± 0.015^c
157	18090+0130	IRAS 18090+0130	18 : 11 : 35.91	+01 : 31 : 41.3	···	···	5.010 ± 0.242^c	1.869 ± 0.094^c	0.590 ± 0.033^c
158	F18131+6820	NGC 6621	18 : 12 : 55.39	+68 : 21 : 48.2	···	···	···	···	···
158	F18131+6820	NGC 6621SE	18 : 12 : 58.52	+68 : 21 : 29.4	···	···	···	···	···
158	F18131+6820	NGC 6622	18 : 12 : 59.68	+68 : 21 : 15.1	···	···	···	···	···
158	F18131+6820	Arp 81	18 : 12 : 57.46	+68 : 21 : 38.7	85	38.08	5.331 ± 0.350	2.159 ± 0.143	0.661 ± 0.048
159	F18093-5744	IC 4687	18 : 13 : 39.80	−57 : 43 : 30.7	···	···	···	···	···
159	F18093-5744	IC 4686	18 : 13 : 38.77	−57 : 43 : 57.3	···	···	···	···	···
159	F18093-5744	IC 4689	18 : 13 : 40.38	−57 : 44 : 54.3	38	14.13	2.154 ± 0.127^c	0.807 ± 0.047^c	0.252 ± 0.017^c
159	F18093-5744	KTS 57	18 : 13 : 38.91	−57 : 43 : 24.7	55	20.45	5.488 ± 0.360	2.026 ± 0.135	0.585 ± 0.041
159	F18093-5744	IRAS F18093-5744	18 : 13 : 39.56	−57 : 44 : 00.9	110	40.90	8.029 ± 0.526	2.935 ± 0.196	0.928 ± 0.065
160	F18145+2205	CGCG 142-034	18 : 16 : 40.69	+22 : 06 : 46.4	50	20.17	4.308 ± 0.259^c	1.687 ± 0.103^c	0.536 ± 0.033^c
160	F18145+2205	CGCG 142-033	18 : 16 : 33.83	+22 : 06 : 38.9	40	16.13	1.445 ± 0.087^c	0.542 ± 0.034^c	0.176 ± 0.013^c
160	F18145+2205	IRGP J1816372+220642	18 : 16 : 37.26	+22 : 06 : 42.6	···	···	5.753 ± 0.273^c	2.229 ± 0.108^c	0.712 ± 0.035^c
161	F18293-3413	IRAS F18293-3413	18 : 32 : 41.10	−34 : 11 : 27.0	70	28.17	17.22 ± 1.07^c	6.454 ± 0.400^c	1.987 ± 0.122^c

continued on the next page

Table 2.5. (continued) *Herschel* SPIRE Total and Component Fluxes of GOALS Systems

#	IRAS Name	Optical Name	RA	Dec.	Ang. Ap.	Phys. Ap.	$F_\lambda(250\ \mu m)$	$F_\lambda(350\ \mu m)$	$F_\lambda(500\ \mu m)$
—	—	—	HH:MM:SS	DD:MM:SS	$''$	kpc	Jy	Jy	Jy
162	F18329+5950	NGC 6670B	18 : 33 : 34.26	+59 : 53 : 17.9	···	···	···	···	···
162	F18329+5950	NGC 6670A	18 : 33 : 37.74	+59 : 53 : 22.8	···	···	···	···	···
162	F18329+5950	NGC 6670	18 : 33 : 36.00	+59 : 53 : 20.3	60	35.60	4.664 ± 0.305	1.782 ± 0.118	0.537 ± 0.038
163	F18341-5732	IC 4734	18 : 38 : 25.75	−57 : 29 : 25.4	75	25.89	8.450 ± 0.525^c	3.257 ± 0.203^c	1.051 ± 0.066^c
164	F18425+6036	NGC 6701	18 : 43 : 12.52	+60 : 39 : 11.6	70	20.63	7.422 ± 0.485	2.863 ± 0.188	0.945 ± 0.059^c
165	F19120+7320	NGC 6786	19 : 10 : 54.01	+73 : 24 : 36.0	45	23.45	2.685 ± 0.160^c	1.040 ± 0.063^c	0.360 ± 0.022^c
165	F19120+7320	UGC 11415	19 : 11 : 04.37	+73 : 25 : 32.5	33	17.20	1.487 ± 0.086^c	0.597 ± 0.034^c	0.219 ± 0.013^c
165	F19120+7320	VV 414	19 : 10 : 59.19	+73 : 25 : 04.2	90	46.91	4.003 ± 0.263	1.516 ± 0.102	0.568 ± 0.041
166	F19115-2124	ESO 593-IG008	19 : 14 : 31.15	−21 : 19 : 06.3	50	48.92	3.371 ± 0.203^c	1.278 ± 0.079^c	0.489 ± 0.030^c
167	F19297-0406	IRAS F19297-0406	19 : 32 : 22.30	−04 : 00 : 01.1	40	64.98	1.833 ± 0.121	0.766 ± 0.046^c	0.225 ± 0.017^c
168	19542+1110	IRAS 19542+1110	19 : 56 : 35.78	+11 : 19 : 04.9	40	50.44	1.265 ± 0.075^c	0.495 ± 0.030^c	0.126 ± 0.009^c
169	F19542-3804	ESO 339-G011	19 : 57 : 37.60	−37 : 56 : 08.4	80	33.08	4.448 ± 0.277^c	1.695 ± 0.108^c	0.591 ± 0.039^c
170	F20221-2458	NGC 6907	20 : 25 : 06.58	−24 : 48 : 32.9	120	28.57	16.38 ± 1.07	6.890 ± 0.448	2.378 ± 0.155
171	20264+2533	MCG+04-48-002	20 : 28 : 35.07	+25 : 44 : 00.3	50	15.42	4.709 ± 0.284^c	1.724 ± 0.108^c	0.558 ± 0.038^c
171	20264+2533	NGC 6921	20 : 28 : 28.90	+25 : 43 : 24.3	40	12.33	1.009 ± 0.063^c	0.361 ± 0.027^c	0.111 ± 0.014^c
171	20264+2533	IRGP J2028320+254342	20 : 28 : 31.98	+25 : 43 : 42.3	···	···	5.719 ± 0.291^c	2.085 ± 0.112^c	0.669 ± 0.040^c
172	F20304-0211	NGC 6926	20 : 33 : 06.13	−02 : 01 : 38.9	70	29.08	7.808 ± 0.509	3.102 ± 0.204	0.998 ± 0.067
173	20351+2521	IRAS 20351+2521	20 : 37 : 17.73	+25 : 31 : 37.5	50	34.25	3.280 ± 0.196^c	1.266 ± 0.077^c	0.347 ± 0.022^c
174	F20550+1655	CGCG 448-020NW	20 : 57 : 23.65	+17 : 07 : 44.1	···	···	···	···	···
174	F20550+1655	CGCG 448-020SEsw	20 : 57 : 24.09	+17 : 07 : 35.2	···	···	···	···	···
174	F20550+1655	CGCG 448-020SEne	20 : 57 : 24.38	+17 : 07 : 39.2	···	···	···	···	···
174	F20550+1655	CGCG 448-020	20 : 57 : 24.01	+17 : 07 : 41.6	50	36.36	2.128 ± 0.140	0.810 ± 0.051^c	0.242 ± 0.018^c
175	F20551-4250	ESO 286-IG019	20 : 58 : 26.78	−42 : 39 : 00.5	55	47.30	1.840 ± 0.111^c	0.631 ± 0.039^c	0.182 ± 0.013^c
176	F21008-4347	ESO 286-G035	21 : 04 : 11.11	−43 : 35 : 36.1	55	20.37	3.994 ± 0.242^c	1.470 ± 0.091^c	0.404 ± 0.026^c
177	21101+5810	IRAS 21101+5810	21 : 11 : 29.28	+58 : 23 : 07.9	45	35.17	2.000 ± 0.122^c	0.749 ± 0.049^c	0.195 ± 0.015^c
178	F21330-3846	ESO 343-IG 013 NED01	21 : 36 : 10.53	−38 : 32 : 42.8	···	···	···	···	···
178	F21330-3846	ESO 343-IG 013 NED02	21 : 36 : 10.93	−38 : 32 : 33.0	···	···	···	···	···
178	F21330-3846	ESO 343-IG013	21 : 36 : 10.73	−38 : 32 : 37.8	55	22.03	2.721 ± 0.179	1.058 ± 0.072	0.354 ± 0.024^c
179	F21453-3511	NGC 7130	21 : 48 : 19.54	−34 : 57 : 04.7	75	25.60	9.224 ± 0.571^c	3.549 ± 0.220^c	1.078 ± 0.068^c
180	F22118-2742	ESO 467-G027	22 : 14 : 39.97	−27 : 27 : 50.3	70	25.35	5.478 ± 0.358	2.083 ± 0.138	0.773 ± 0.050^c

continued on the next page

Table 2.5. (continued) *Herschel* SPIRE Total and Component Fluxes of GOALS Systems

#	IRAS Name	Optical Name	RA	Dec.	Ang. Ap.	Phys. Ap.	$F_\lambda(250\ \mu m)$	$F_\lambda(350\ \mu m)$	$F_\lambda(500\ \mu m)$
—	—	—	HH:MM:SS	DD:MM:SS	$''$	kpc	Jy	Jy	Jy
181	F22132-3705	IC 5179	22 : 16 : 09.13	− 36 : 50 : 37.2	90	21.90	14.97 ± 0.98	5.763 ± 0.377	1.892 ± 0.125
182	F22287-1917	ESO 602-G025	22 : 31 : 25.48	− 19 : 02 : 04.0	60	30.46	3.991 ± 0.243^c	1.658 ± 0.103^c	0.488 ± 0.031^c
183	F22389+3359	UGC 12150	22 : 41 : 12.21	+ 34 : 14 : 56.8	45	19.55	5.086 ± 0.305^c	2.031 ± 0.121^c	0.611 ± 0.036^c
184	F22467-4906	ESO 239-IG002	22 : 49 : 39.84	− 48 : 50 : 58.3	45	38.31	1.799 ± 0.107^c	0.700 ± 0.042^c	0.256 ± 0.016^c
185	F22491-1808	IRAS F22491-1808	22 : 51 : 49.35	− 17 : 52 : 24.9	35	51.28	0.841 ± 0.049^c	0.309 ± 0.018^c	0.082 ± 0.006^c
186	F23007+0836	NGC 7469	23 : 03 : 15.64	+ 08 : 52 : 25.5	52	17.14	9.561 ± 0.575^c	3.554 ± 0.216^c	1.084 ± 0.063^c
186	F23007+0836	IC 5283	23 : 03 : 18.04	+ 08 : 53 : 36.5	35	11.54	1.997 ± 0.132	0.771 ± 0.053	0.235 ± 0.018
186	F23007+0836	Arp 298	23 : 03 : 16.84	+ 08 : 53 : 00.9	90	29.67	11.16 ± 0.73	4.216 ± 0.278	1.266 ± 0.087
187	F23024+1916	CGCG 453-062	23 : 04 : 56.55	+ 19 : 33 : 07.1	60	30.17	4.418 ± 0.272^c	1.749 ± 0.111^c	0.609 ± 0.038^c
188	F23128-5919	ESO 148-IG002	23 : 15 : 46.75	− 59 : 03 : 15.8	40	35.37	1.855 ± 0.110^c	0.655 ± 0.039^c	0.186 ± 0.013^c
189	F23135+2517	IC 5298	23 : 16 : 00.67	+ 25 : 33 : 24.3	50	27.32	3.042 ± 0.184^c	1.110 ± 0.069^c	0.336 ± 0.022^c
190	F23133-4251	NGC 7552	23 : 16 : 10.81	− 42 : 35 : 05.5	130	14.62	35.64 ± 2.32	13.74 ± 0.90	4.226 ± 0.276
191	F23157+0618	NGC 7591	23 : 18 : 16.25	+ 06 : 35 : 09.1	90	30.15	6.716 ± 0.440	2.813 ± 0.185	0.917 ± 0.063
191	F23157+0618	NGC 7591	23 : 18 : 13.52	+ 06 : 33 : 26.5	35	11.73	0.351 ± 0.024^c	0.131 ± 0.012^c	0.056 ± 0.010^c
191	F23157+0618	F23157+0618	23 : 18 : 14.89	+ 06 : 34 : 17.8	···	···	7.067 ± 0.440^c	2.944 ± 0.186^c	0.973 ± 0.064^c
192	F23157-0441	NGC 7592E	23 : 18 : 22.60	− 04 : 24 : 58.0	···	···	···	···	···
192	F23157-0441	NGC 7592W	23 : 18 : 21.78	− 04 : 24 : 57.0	···	···	···	···	···
192	F23157-0441	NGC 7592	23 : 18 : 22.19	− 04 : 24 : 57.4	55	26.93	2.916 ± 0.192	1.179 ± 0.073^c	0.355 ± 0.024^c
193	F23180-6929	ESO 077-IG 014 NED02	23 : 21 : 05.45	− 69 : 12 : 47.3	···	···	···	···	···
193	F23180-6929	ESO 077-IG 014 NED01	23 : 21 : 03.47	− 69 : 13 : 02.2	···	···	···	···	···
193	F23180-6929	ESO 077-IG014	23 : 21 : 04.59	− 69 : 12 : 54.1	50	41.57	3.113 ± 0.205	1.254 ± 0.084	0.406 ± 0.025^c
194	F23254+0830	NGC 7674	23 : 27 : 56.71	+ 08 : 46 : 44.3	···	···	···	···	···
194	F23254+0830	NGC 7674A	23 : 27 : 58.77	+ 08 : 46 : 57.9	···	···	···	···	···
194	F23254+0830	ARP 182	23 : 27 : 57.73	+ 08 : 46 : 51.0	75	43.42	3.566 ± 0.232	1.424 ± 0.094	0.445 ± 0.031
195	23262+0314	NGC 7679	23 : 28 : 46.62	+ 03 : 30 : 41.4	70	24.20	3.367 ± 0.207^c	1.287 ± 0.079^c	0.496 ± 0.031^c
195	23262+0314[a]	NGC 7682	23 : 29 : 03.91	+ 03 : 31 : 59.9	70	24.20	0.746 ± 0.051	0.384 ± 0.029	0.151 ± 0.014
196	F23365+3604	IRAS F23365+3604	23 : 39 : 01.32	+ 36 : 21 : 08.2	45	55.26	1.901 ± 0.113^c	0.707 ± 0.042^c	0.195 ± 0.012^c
197	F23394-0353	MCG-01-60-022	23 : 42 : 00.91	− 03 : 36 : 54.4	70	31.36	2.932 ± 0.180^c	1.226 ± 0.076^c	0.402 ± 0.026^c
197	F23394-0353[a]	MCG-01-60-021	23 : 41 : 47.33	− 03 : 40 : 01.7	38	17.02	1.074 ± 0.070	0.457 ± 0.030	0.177 ± 0.010^c
197	F23394-0353[a]	MRK 0933	23 : 41 : 43.69	− 03 : 39 : 26.5	32	14.33	0.184 ± 0.012^c	0.069 ± 0.006^c	0.023 ± 0.004^c

continued on the next page

Table 2.5. (continued) *Herschel* SPIRE Total and Component Fluxes of GOALS Systems

#	IRAS Name	Optical Name	RA	Dec.	Ang. Ap.	Phys. Ap.	$F_\lambda(250\ \mu m)$	$F_\lambda(350\ \mu m)$	$F_\lambda(500\ \mu m)$
—	—	—	HH:MM:SS	DD:MM:SS	$''$	kpc	Jy	Jy	Jy
197	F23394-0353	MCG-01-60-021	23 : 41 : 46.04	− 03 : 39 : 42.3	70	31.36	1.328 ± 0.087	0.555 ± 0.038	0.178 ± 0.014
198	23436+5257	IRAS 23436+5257	23 : 46 : 05.44	+ 53 : 14 : 01.7	40	27.01	1.872 ± 0.112^{c}	0.684 ± 0.043^{c}	0.243 ± 0.017^{c}
199	F23444+2911	NGC 7752	23 : 47 : 04.84	+ 29 : 29 : 00.5	90	31.02	6.964 ± 0.454	3.220 ± 0.211	1.102 ± 0.073
199	F23444+2911	NGC 7753	23 : 46 : 58.62	+ 29 : 27 : 32.0	45	15.51	1.898 ± 0.113^{c}	0.717 ± 0.044^{c}	0.240 ± 0.015^{c}
199	F23444+2911	Arp 86	23 : 47 : 01.73	+ 29 : 28 : 16.2	150	51.71	8.038 ± 0.524	3.524 ± 0.233	1.157 ± 0.080
200	F23488+1949	NGC 7769	23 : 51 : 03.91	+ 20 : 09 : 01.7	55	15.60	5.017 ± 0.329^{b}	1.878 ± 0.126^{b}	$0.703 \pm 0.044^{b,}$
200	F23488+1949	NGC 7771	23 : 51 : 24.80	+ 20 : 06 : 42.2	45	12.76	16.35 ± 1.07	6.181 ± 0.407	···
200	F23488+1949	NGC 7770	23 : 51 : 22.55	+ 20 : 05 : 49.2	23	6.523	1.461 ± 0.077^{c}	0.500 ± 0.027^{c}	···
200	F23488+1949	KTG 82	23 : 51 : 23.67	+ 20 : 06 : 15.6	100	28.36	18.97 ± 1.24	7.501 ± 0.493	2.366 ± 0.157
201	F23488+2018	MRK 0331	23 : 51 : 26.77	+ 20 : 35 : 10.5	65	23.26	6.145 ± 0.375^{c}	2.282 ± 0.139^{c}	0.729 ± 0.044^{c}
201	F23488+2018	UGC 12812	23 : 51 : 18.69	+ 20 : 34 : 40.4	45	16.10	0.253 ± 0.019	0.128 ± 0.011	0.061 ± 0.006^{c}
201	F23488+2018	KPG 593	23 : 51 : 22.73	+ 20 : 34 : 55.4	···	···	6.398 ± 0.375^{c}	2.410 ± 0.140^{c}	0.790 ± 0.044^{c}

Monochromatic SPIRE fluxes in units of Jansky for the entire GOALS sample. These are component fluxes measurable for each system, with the total system flux from Table 2.3 included for completeness on the last line for each system. For total fluxes that do not have an aperture size, the totals were calculated as the sum of the components. Likewise the RA and dec. for these systems represent the midpoint between the companion galaxies. Galaxy components that do not have flux measurements are too close to a companion galaxy to be resolved by SPIRE. See §2.6 for the column descriptions. [a]These are very widely separated galaxy pairs that required two *Herschel* PACS observations. [b]This galaxy is part of a triple system, but is only visible in the SPIRE images. The total flux for this system does *not* include this galaxy. [c]These fluxes have an aperture correction factor applied.

Bertincourt et al. (2016) performed an in-depth analysis of SPIRE and HFI data on the same fields, and found a very high degree of linearity between the two datasets, as well as a good agreement in the relative calibrations between the two instruments. The zero-points of the *Planck* maps are derived assuming that the zero-point of the Galactic emission can be defined as zero dust emission for a null HI column density[11]. The final step is to apply a slight gain correction to the *Planck* maps, which for our data we used the NHSC recommended gain factors of 0.989 and 1.02 for the 857 GHz and 545 GHz channels, respectively. The *Planck* calibration uncertainty for both channels is 10%. Using the all-sky *Planck* data, zero-point corrections are applied as flux offsets over the entire SPIRE map, and do not affect the SPIRE flux calibrations (which is background subtracted). We note that these zero point corrections were only applied to the 350 μm and 500 μm channels only, and the 250 μm maps were not corrected since there is no overlap with *Planck*.

2.6.3 Distribution of *Herschel* Fluxes

In Figure 2.5 we show the distribution of fluxes from our *Herschel* program in each of the three PACS and SPIRE photometer bands. The histogram x-axis range and binning for each band was selected in order to meaningfully show the data. The fluxes shown here are all 1657 measured fluxes, comprising both component and total fluxes, and do not include total system fluxes that are the sum of the component fluxes. The x-axis of each panel is shown in units of log(Jy) to encompass the wide dynamic range of fluxes measured within the data.

As expected the fluxes are generally higher in the three PACS bands, while they are lower in the SPIRE bands due to the Rayleigh-Jeans tail of the galaxy's SED. The number of measured fluxes and bin sizes are indicated for each band, as well as the minimum and maximum fluxes. The galaxies with the highest fluxes are all nearby (IRAS F02401–0013/NGC 1068, IRAS F03316–3618/NGC 1365, and IRAS F06107+7822/NGC 2146)

[11]See the Explanatory Supplement to the Planck 2013 results: http://wiki.cosmos.esa.int/planckpla/index.php/CMB_and_astrophysical_component_maps#Thermal_dust_emission

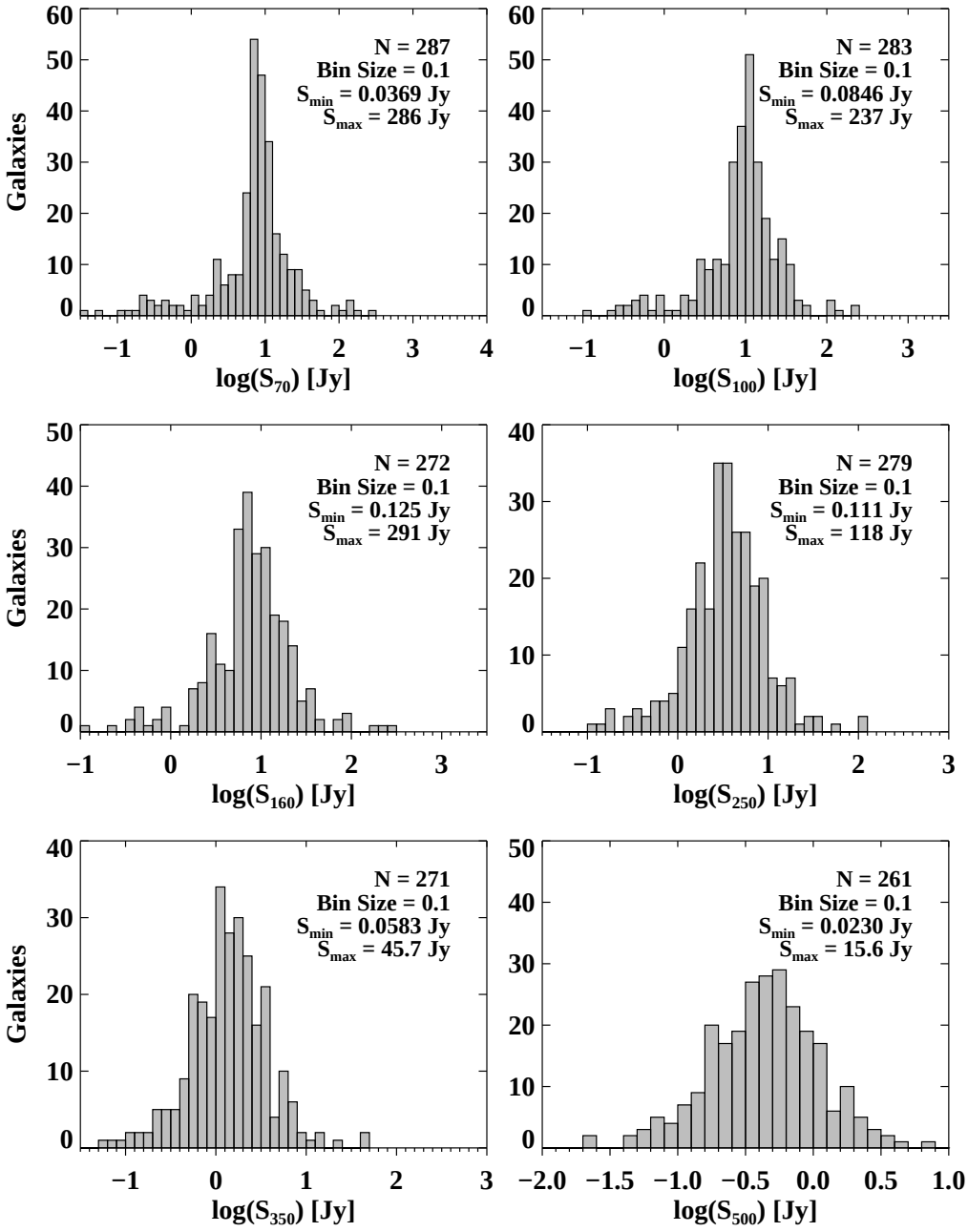

Figure 2.5 Histogram plot of the *Herschel* PACS and SPIRE fluxes from our sample. The histogram range for each band was fine tuned in order to meaningfully show the data. The fluxes shown here are all the actual measured fluxes, consisting of component and total fluxes. The x-axis of each panel is shown in units of log(Jy) to encompass the wide dynamic range of fluxes measured within the data.

and tend to be quite extended in the *Herschel* maps, with the exception of NGC 2146 which appears to be more concentrated than the other two in the PACS 70 μm and 100 μm channels. On the other hand the faintest measured fluxes in the PACS bands are well within the "faint" flux regime for PACS data reduction (see §2.4.1).

2.7 Discussion

2.7.1 Comparison of PACS Fluxes to Previous Missions

One important check is to compare our new PACS 100 μm fluxes to the legacy *IRAS* 100 μm fluxes published in Sanders et al. (2003), since the central wavelengths of both instruments are the same. In Figure 2.6 we show the filter transmission curves for PACS and *IRAS* in blue and red respectively. Before comparing the fluxes measured from each telescope, several constraints must be used to ensure a meaningful comparison. Importantly, we only selected objects that either appear as single galaxies in the PACS 100 μm maps, or have component galaxies close enough such that it is only marginally resolved (or not at all) by PACS. We note that the *IRAS* 100 μm channel has a FWHM beamsize of $\sim 4'$, which is significantly larger than the PACS 100 μm beamsize of $6\farcs8$, therefore any unresolved system in PACS would certainly appear unresolved to *IRAS*. Second, we also applied an aperture correction for point source objects in the PACS 100 μm maps, however we did not apply a color correction to any of our fluxes (see §2.7.3). The latter point would be needed to stay in accordance with how Sanders et al. (2003) measured the *IRAS* RBGS fluxes (see also Soifer et al. 1989), to ensure as accurate of a comparison as possible[12]. Importantly, these objects span the entire range of 100 μm fluxes within the GOALS sample, and represent the entire spectrum of source morphology from point source to very extended objects.

In the upper panel of Figure 2.7 we plot the 100 μm PACS/IRAS flux ratio as a function of the *IRAS* 100 μm flux for 128 GOALS objects satisfying our criteria (corresponding to 64% of our sample). The red line represents the unweighted average of the ratio which

[12]The *IRAS* data reduction pipeline also assumes a power law spectral index of -1, which is the same as PACS and SPIRE.

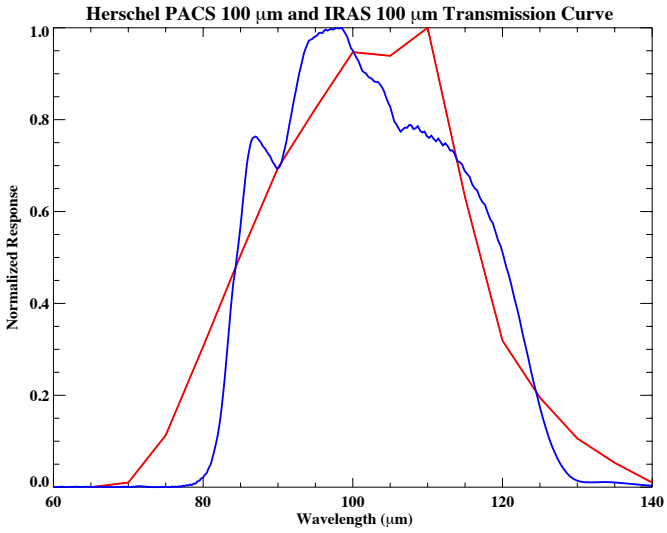

Figure 2.6 The normalized transmission curves of the 100 μm band passes for *Herschel*-PACS in blue and *IRAS* in red.

is 1.012, with dashed lines representing the 1-σ scatter of 0.09. On the other hand the median of the PACS/IRAS ratio is 1.006. Additionally we see no variation in the flux ratio except for fluxes above ∼100 Jy, where our PACS fluxes are slightly higher. The IRAS names of these six galaxies are F03316–3618, F06107+7822, F10257–4339, F11257+5850, 13242–5713, and F23133–4251. Of these six sources the two with the highest PACS/IRAS ratios, F03316–3618 (NGC 1365) and F06107+7822 (NGC 2146), are large galaxies with optical sizes of $11\farcm2 \times 6\farcm2$ and $6\farcm0 \times 3\farcm4$. Their fluxes could be underestimated by IRAS since they were computed assuming point source photometry, however once we exclude these two systems, there doesn't appear to be any PACS excess left in the bright sources. Overall, there is a broad agreement in fluxes between our *Herschel* data and the *IRAS* data, to within measurement errors (∼5–10% for PACS).

Additionally we also compared the PACS 70 μm fluxes to the *IRAS* 60 μm fluxes, however because of the difference in wavelength, we first had to interpolate the *IRAS* 60 μm measurement to 70 μm. To do this, we first estimated the power law index to the nearest whole number on the short-wavelength side of the SED bump using the *IRAS* 60

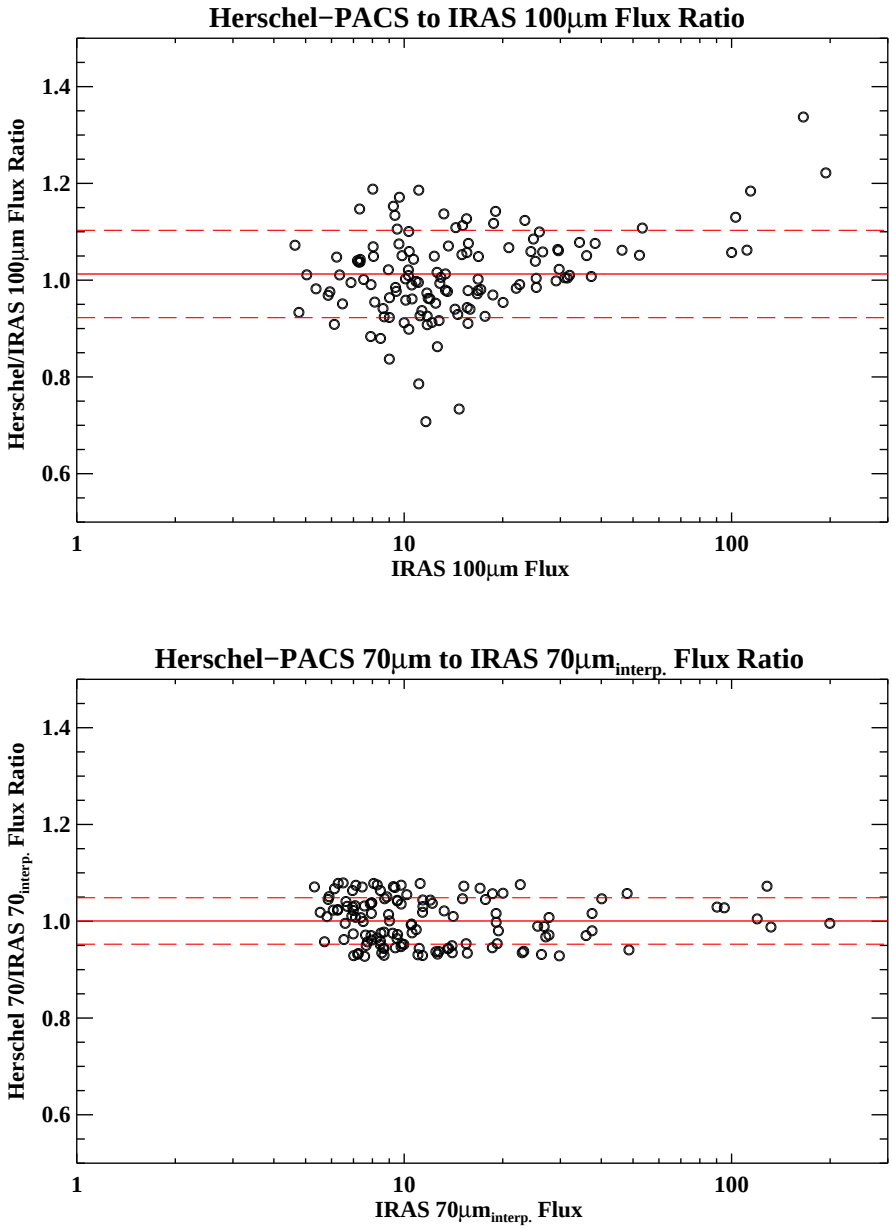

Figure 2.7 *Upper panel*: The *Herschel*-PACS 100 μm to *IRAS* 100 μm flux ratio plotted as a function of the *IRAS* 100 μm flux for 128 of our galaxies carefully chosen to be single objects, or if the system has multiple components they are too close to be distinguishable by PACS at 100 μm. These galaxies represent the entire spectrum of very extended emission, to point sources as seen by PACS. The mean ratio represented by the red line is 1.012, with the dashed red lines representing the 1-σ scatter of 0.09. The median ratio is 1.006. Error bars were omitted to keep the plot readable. *Lower panel*: Same as the upper panel but for the *Herschel*-PACS 70 μm data compared to the interpolated IRAS 70 μm flux. The mean ratio is 1.001 with a 1-σ scatter of 0.04, and a median ratio of 1.00. The agreement between the PACS 70 μm and interpolated *IRAS* 70 μm fluxes is excellent.

μm and PACS 70 μm fluxes[13]. To interpolate the *IRAS* 60 μm flux to 70 μm, we divided the *IRAS* 60 μm fluxes by multiplicative factors corresponding to each power law index found in Table 2 of the *Herschel* technical note PICC-ME-TN-038. These factors were calculated by the PACS team to convert PACS fluxes to other key wavelengths and vice versa based on SED shape. We then plotted the ratio of the PACS 70 μm flux to the interpolated *IRAS* 70 μm flux as a function of the *IRAS* flux, shown in the bottom panel of Figure 2.7. The average flux ratio represented by the red line is 1.001 with a 1-σ scatter of 0.04 (dashed lines), and the median ratio is 1.00. The agreement between the PACS and *IRAS* data in this case is exquisite, with an even tighter relation than the 100 μm comparison throughout the entire flux range.

Another comparison is to perform a similar analysis using GOALS data from the *Spitzer* MIPS instrument at 70 and 160 μm (Mazzarella et al. in prep.). Unfortunately, many of the images from that program suffer from saturation and other image quality issues that make it impossible to draw a meaningful comparison. As a result we have agreed that the PACS 70 and 160 μm data will completely supersede the corresponding MIPS data.

The results here are also similar to the analysis done in the *Herschel* technical note SAp-PACS-MS-0718-11, where extended source fluxes were compared between PACS to *Spitzer*-MIPS and *IRAS*. Although they found an average PACS/IRAS 100 μm flux ratio of 1.32, their dispersion in the flux ratio is very similar to our results in Figure 2.7. We note that their analysis was done on HIPE 6, where the PACS responsivity was not well understood resulting in much higher flux ratios than our result.

2.7.2 Comparison of SPIRE Fluxes Measured From Different Calibration Versions

To check the consistency of our SPIRE fluxes we compared the measured fluxes of our SPIRE data reduced using three different SPIRE calibrations: `SPIRECAL_10_1`, `SPIRECAL_13_1`, and the latest version `SPIRECAL_14_2`. In Figure 2.8 we show six histograms of the fractional

[13]We did not use the *IRAS* 100 μm flux as that is right on the peak of the SED, which would systematically underestimate the power law index.

percentage change in flux between each calibration version for each of the bands. In order to facilitate as direct of a comparison as possible, we use the uncorrected fluxes computed directly by the `annularSkyAperturePhotometry` task in HIPE, which are not aperture or color corrected. The histograms show as a general trend towards longer wavelengths, a larger variance in the percent change in flux. This is again due to the long wavelength Rayleigh-Jeans tail of the galaxy's SED, where the fainter fluxes are affected more by instrument uncertainties.

In the histogram comparing `SPIRECAL_10_1` and `SPIRECAL_13_1` (Fig. 2.8, first column), the general trend is an increase in the measured flux by an unweighted average of approximately 1.45%, 0.91%, and 1.19% of the `SPIRECAL_13_1` flux, for the 250 μm, 350 μm, and 500 μm channels. The shape of the histogram distribution is very close to Gaussian in each case, however the 250 μm channel shows a slight positive skewness. The main updates in the calibration and data reduction pipeline are improved absolute flux calibrations of Neptune, and a better algorithm in destriping the data and removal of image artifacts.

In the second column of Figure 2.8 we show the histogram of measured fluxes between `SPIRECAL_13_1`, and the latest version `SPIRECAL_14_2`. The only change was an update to the absolute flux calibration of the instrument, which resulted in an even smaller change in the average flux: 0.24%, –0.19%, and 0.25% for the 250 μm, 350μm, and 500 μm channels respectively. SPIRE maps reduced using the two previous calibration versions are available upon request.

2.7.3 Caveats

In this section we detail several cautionary notes on using the data presented in this chapter.

Color Corrections

By convention both of the PACS and SPIRE data reduction packages consider a flux calibration of the form νF_ν = constant (i.e., a spectral index of -1). Since the *Herschel* photometry for the GOALS sample covers a wide range of wavelengths, and therefore

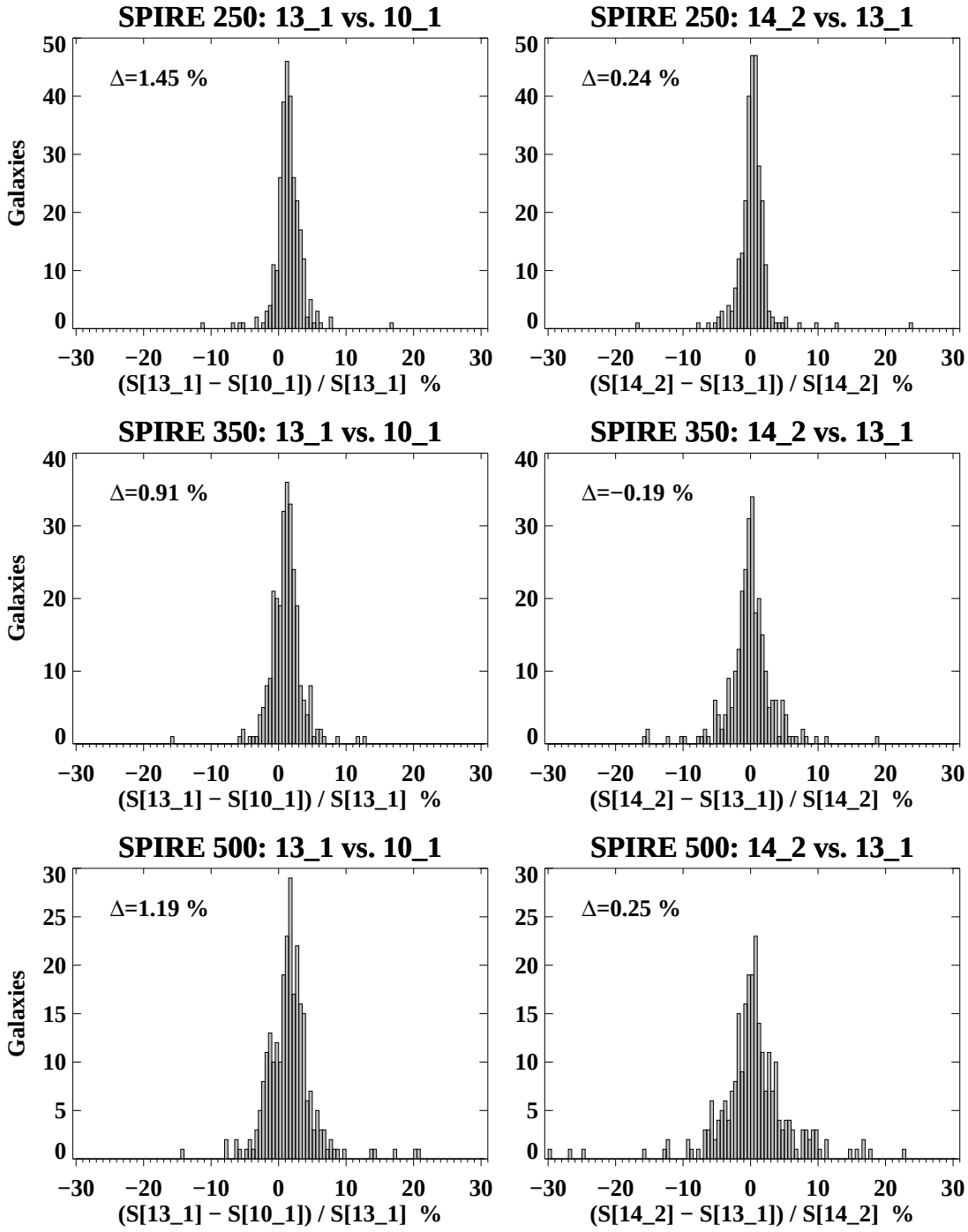

Figure 2.8 Histogram plots comparing the percent change in flux between SPIRECAL_10_1 vs. SPIRECAL_13_1 in the first column, and SPIRECAL_13_1 vs. SPIRECAL_14_2 in the second column. The values in each panel represent the unweighted average percent change between each calibration version.

different parts of the galaxy's SED, the color correction factor changes as a function of wavelength, as well as weaker dependence on infrared luminosity (due to a change in the dust temperature). This is because the effective beam area of each instrument changes slightly for different spectral indices. For PACS the color correction factors are listed on the NHSC website[14], and are applied to the fluxes by *dividing* the factor for the appropriate power law exponent. The SPIRE color correction factors are listed in the online SPIRE data reduction guide[15] in Table 6.16 and are to be *multiplied*.

For this work, we have decided to forego applying a color correction for both PACS and SPIRE fluxes. This would otherwise require a detailed analysis involving a multi-component SED fit for each galaxy to derive the spectral slope at each observed *Herschel* band, which is outside the current scope of this chapter. This decision was agreed upon for both the *Herschel* and *Spitzer* (Mazzarella et al. in prep.) data for the GOALS sample. Flux changes due to color corrections for PACS bands are up to ∼3%, and for SPIRE bands up to ∼6% for extended sources, which is less than or equal to the absolute calibration uncertainty of both instruments. However we note for point sources, the SPIRE color correction can be higher, which we estimate to be ∼15% for a spectral index of $\alpha = 4$. If a photometric precision of within a few percent is desired, we strongly recommend users of the *Herschel*-GOALS data to include color corrections to the aperture photometry presented in this chapter.

PACS Saturation Limits

Since galaxies within GOALS sample are very bright in the far-infrared, there is a small chance that some of our images exhibit saturation issues in a few of our *Herschel* maps. For the PACS photometer there are two types of saturations. Hard saturation occurs when the signal after the readout electronics are outside the dynamic range of the analog-to-digital converter. On the other hand soft saturation arises from saturation of the readout electronics itself. Taking into account both effects, the point source saturation limits are 220 Jy, 510 Jy, and 1125 Jy for the 70 μm, 100 μm, and 160 μm passbands respectively.

[14] `https://nhscsci.ipac.caltech.edu/pacs/docs/ PACS_photometer_colorcorrectionfactors.txt`
[15] `http://herschel.esac.esa.int/hcss-doc-14.0/print/ spire_drg/spire_drg.pdf`

Fortunately for our sample, the latter two passbands have saturation limits well above our maximum measured fluxes of 248 Jy and 301 Jy for the 100 μm and 160 μm channels. For the 70 μm channel, the nearby galaxy F02401–0013 has a total measured flux of 290 Jy which is above the saturation limit, and F06107+7822 which has a flux of 205 Jy and is close to the saturation limit. However both appear very extended at 70 μm, and in checking the saturation masks in the time-ordered data cubes we found no significant number of pixels were masked due to saturation.

Correlated Noise in PACS Data

Nine of our PACS maps exhibit residual correlated noise resembling low-level ripples in both the scan and cross-scan directions for only the blue camera (70 μm and 100 μm). Of these maps three of them only have this effect on the edges of the map, and do not affect the photometry or map quality. Unfortunately for the other six maps the current processing techniques in Jscanam, Unimap, and MADMap fail to remove it. One example of this is the 100 μm map of F03316–3618. However we emphasize that these are very low-level effects, and do not significantly affect the quality of the photometry[16], which we estimate to be on the few percent level. This was calculated by first placing ten random apertures on empty sky on each map, then measuring the standard deviation in the flux per pixel on the affected maps. This is then multiplied by the number of pixels within the photometry aperture.

2.8 Summary

In this chapter we have presented broad band *Herschel* imaging for the entire GOALS sample in Figure 2.3. Total system fluxes, PACS component fluxes, and SPIRE component fluxes (where possible) are also computed in all six *Herschel* bands in Tables 2.3, 2.4, and 2.5 respectively. Particular care was taken in producing archival quality atlas maps using the best data reduction codes and algorithms available at the time. The data presented here are thus far the highest resolution, most sensitive and comprehensive far-infrared imaging

[16]These image artifacts are taken into account when calculating the uncertainty in flux.

survey of the nearest luminous infrared galaxies. For many of these objects, this work presents the first imaging data and reliable photometry at wavelengths beyond ∼200 μm in the submillimeter regime.

1. All 201 GOALS objects were detected in all three *Herschel* PACS (70, 100, and 160 μm) and all three SPIRE (250, 350, 500 μm) bands. The FOV of the PACS and SPIRE images are sufficient and sensitive enough to detect the full extent of the far-infrared emission for even the widest pair separations. Only two GOALS systems have full SPIRE coverage but lack PACS coverage of a third distant component (NGC 2385 in F07256+3355, and NGC 7769 in F23488+1949). In addition, four galaxies observed outside of our *Herschel* program lack 100 μm data since they were not observed by those programs.

2. The image quality of the data are superb and were cleaned using the most up to date reduction routines and calibration files from the *Herschel* Science Center. None of the images suffer from any saturation effects, major striping, or other image quality issues that may arise from scan-based observations. Aperture corrections were applied only to point sources, while no color corrections were applied to any objects. Furthermore the SPIRE 350 μm and 500 μm maps were zero-point corrected using data from the *Planck* observations.

3. The resolution is sufficient to resolve individual components of many pairs and interacting/merging systems in our sample, particularly at the shorter wavelengths where the PACS 70 μm FWHM band has a beamsize of $5\farcs6$. On the other hand wider pairs can still be resolved even at the longer wavelength SPIRE bands.

4. Comparing our PACS 70 and 100 μm fluxes to the legacy *IRAS* 60 and 100 μm measurements respectively, we found an excellent agreement (to within error) across our flux range as well as object morphologies ranging from point sources to extended systems.

5. The PACS 70 μm and 160 μm data within this work supersede the reported fluxes and maps from the MIPS instrument on *Spitzer* (see Mazzarella et al. in prep.) due to the better sensitivity, resolution, and lack of image artifacts in the *Herschel* data.

In conjunction with datasets from other infrared telescopes (i.e., *Spitzer*, *WISE*), the *Herschel* data from this chapter will allow us for the first time to construct accurate spectral energy distributions in the infrared ($\sim$3–500 μm) for the entire GOALS sample, which will be presented in several forthcoming papers. The FITS files for the image mosaics constructed and presented in this atlas are being made available in the Infrared Science Archive (IRSA)[17]. Metadata for the images are also being folded into the NASA/IPAC Extragalactic Database (NED)[18] to simplify searches in context with other data in NED, including links to the FITS files at IRSA.

[17] `http://irsa.ipac.caltech.edu/data/GOALS/overview.html`
[18] `http://ned.ipac.caltech.edu/`

References

Armus, L., Mazzarella, J. M., Evans, A. S., Surace, J. A., Sanders, D. B., Iwasawa, K., Frayer, D. T., Howell, J. H., Chan, B., Petric, A., Vavilkin, T., Kim, D. C., Haan, S., Inami, H., Murphy, E. J., Appleton, P. N., Barnes, J. E., Bothun, G., Bridge, C. R., Charmandaris, V., Jensen, J. B., Kewley, L. J., Lord, S., Madore, B. F., Marshall, J. A., Melbourne, J. E., Rich, J., Satyapal, S., Schulz, B., Spoon, H. W. W., Sturm, E., U, V., Veilleux, S., & Xu, K. 2009, PASP, 121, 559

Balog, Z., Müller, T., Nielbock, M., Altieri, B., Klaas, U., Blommaert, J., Linz, H., Lutz, D., Moór, A., Billot, N., Sauvage, M., & Okumura, K. 2014, Experimental Astronomy, 37, 129

Barbey, N., Sauvage, M., Starck, J.-L., Ottensamer, R., & Chanial, P. 2011, A&A, 527, A102

Bendo, G. J., Griffin, M. J., Bock, J. J., Conversi, L., Dowell, C. D., Lim, T., Lu, N., North, C. E., Papageorgiou, A., Pearson, C. P., Pohlen, M., Polehampton, E. T., Schulz, B., Shupe, D. L., Sibthorpe, B., Spencer, L. D., Swinyard, B. M., Valtchanov, I., & Xu, C. K. 2013, MNRAS, 433, 3062

Bertincourt, B., Lagache, G., Martin, P. G., Schulz, B., Conversi, L., Dassas, K., Maurin, L., Abergel, A., Beelen, A., Bernard, J.-P., Crill, B. P., Dole, H., Eales, S., Gudmundsson, J. E., Lellouch, E., Moreno, R., & Perdereau, O. 2016, A&A, 588, A107

Cantalupo, C. M., Borrill, J. D., Jaffe, A. H., Kisner, T. S., & Stompor, R. 2010, ApJS, 187, 212

Chu, J. K., Sanders, D. B., Larson, K. L., Mazzarella, J. M., Howell, J. H., Díaz-Santos, T., Xu, K. C., Paladini, R., Schulz, B., Shupe, D., Appleton, P., Armus, L., Billot, N., Chan, B. H. P., Evans, A. S., Fadda, D., Frayer, D. T., Haan, S., Ishida, C. M., Iwasawa, K., Kim, D.-C., Lord, S., Murphy, E., Petric, A., Privon, G. C., Surace, J. A., & Treister, E. 2017, ApJS, 229, 25

Ciesla, L., Boselli, A., Smith, M. W. L., Bendo, G. J., Cortese, L., Eales, S., Bianchi, S., Boquien, M., Buat, V., Davies, J., Pohlen, M., Zibetti, S., Baes, M., Cooray, A., De Looze, I., di Serego Alighieri, S., Galametz, M., Gomez, H. L., Lebouteiller, V., Madden, S. C., Pappalardo, C., Remy, A., Spinoglio, L., Vaccari, M., Auld, R., & Clements, D. L. 2012, A&A, 543, A161

Condon, J. J., Helou, G., Sanders, D. B., & Soifer, B. T. 1990, ApJS, 73, 359

—. 1996, ApJS, 103, 81

Díaz-Santos, T., Armus, L., Charmandaris, V., Lu, N., Stierwalt, S., Stacey, G., Malhotra, S., van der Werf, P. P., Howell, J. H., Privon, G. C., Mazzarella, J. M., Goldsmith, P. F., Murphy, E. J., Barcos-Muñoz, L., Linden, S. T., Inami, H., Larson, K. L., Evans, A. S., Appleton, P., Iwasawa, K., Lord, S., Sanders, D. B., & Surace, J. A. 2017, ApJ, 846, 32

Díaz-Santos, T., Armus, L., Charmandaris, V., Stacey, G., Murphy, E. J., Haan, S., Stierwalt, S., Malhotra, S., Appleton, P., Inami, H., Magdis, G. E., Elbaz, D., Evans, A. S., Mazzarella, J. M., Surace, J. A., van der Werf, P. P., Xu, C. K., Lu, N., Meijerink, R., Howell, J. H., Petric, A. O., Veilleux, S., & Sanders, D. B. 2014, ApJ, 788, L17

Díaz-Santos, T., Armus, L., Charmandaris, V., Stierwalt, S., Murphy, E. J., Haan, S., Inami, H., Malhotra, S., Meijerink, R., Stacey, G., Petric, A. O., Evans, A. S., Veilleux, S., van der Werf, P. P., Lord, S., Lu, N., Howell, J. H., Appleton, P., Mazzarella, J. M.,

Surace, J. A., Xu, C. K., Schulz, B., Sanders, D. B., Bridge, C., Chan, B. H. P., Frayer, D. T., Iwasawa, K., Melbourne, J., & Sturm, E. 2013, ApJ, 774, 68

Dowell, C. D., Pohlen, M., Pearson, C., Griffin, M., Lim, T., Bendo, G. J., Benielli, D., Bock, J. J., Chanial, P., Clements, D. L., Conversi, L., Ferlet, M., Fulton, T., Gastaud, R., Glenn, J., Grundy, T., Guest, S., King, K. J., Leeks, S. J., Levenson, L., Lu, N., Morris, H., Nguyen, H., O'Halloran, B., Oliver, S., Panuzzo, P., Papageorgiou, A., Polehampton, E., Rigopoulou, D., Roussel, H., Schneider, N., Schulz, B., Schwartz, A., Shupe, D. L., Sibthorpe, B., Sidher, S., Smith, A. J., Swinyard, B. M., Trichas, M., Valtchanov, I., Woodcraft, A. L., Xu, C. K., & Zhang, L. 2010, in Proc. SPIE, Vol. 7731, Space Telescopes and Instrumentation 2010: Optical, Infrared, and Millimeter Wave, 773136

Dunne, L., Eales, S., Edmunds, M., Ivison, R., Alexander, P., & Clements, D. L. 2000, MNRAS, 315, 115

Griffin, M. J., Abergel, A., Abreu, A., Ade, P. A. R., André, P., Augueres, J.-L., Babbedge, T., Bae, Y., Baillie, T., Baluteau, J.-P., Barlow, M. J., Bendo, G., Benielli, D., Bock, J. J., Bonhomme, P., Brisbin, D., Brockley-Blatt, C., Caldwell, M., Cara, C., Castro-Rodriguez, N., Cerulli, R., Chanial, P., Chen, S., Clark, E., Clements, D. L., Clerc, L., Coker, J., Communal, D., Conversi, L., Cox, P., Crumb, D., Cunningham, C., Daly, F., Davis, G. R., de Antoni, P., Delderfield, J., Devin, N., di Giorgio, A., Didschuns, I., Dohlen, K., Donati, M., Dowell, A., Dowell, C. D., Duband, L., Dumaye, L., Emery, R. J., Ferlet, M., Ferrand, D., Fontignie, J., Fox, M., Franceschini, A., Frerking, M., Fulton, T., Garcia, J., Gastaud, R., Gear, W. K., Glenn, J., Goizel, A., Griffin, D. K., Grundy, T., Guest, S., Guillemet, L., Hargrave, P. C., Harwit, M., Hastings, P., Hatziminaoglou, E., Herman, M., Hinde, B., Hristov, V., Huang, M., Imhof, P., Isaak, K. J., Israelsson, U., Ivison, R. J., Jennings, D., Kiernan, B., King, K. J., Lange, A. E., Latter, W., Laurent, G., Laurent, P., Leeks, S. J., Lellouch, E., Levenson, L., Li, B., Li, J., Lilienthal, J., Lim, T., Liu, S. J., Lu, N., Madden, S., Mainetti, G., Marliani, P., McKay, D., Mercier, K., Molinari, S., Morris, H., Moseley, H., Mulder, J., Mur, M., Naylor, D. A., Nguyen, H.,

O'Halloran, B., Oliver, S., Olofsson, G., Olofsson, H.-G., Orfei, R., Page, M. J., Pain, I., Panuzzo, P., Papageorgiou, A., Parks, G., Parr-Burman, P., Pearce, A., Pearson, C., Pérez-Fournon, I., Pinsard, F., Pisano, G., Podosek, J., Pohlen, M., Polehampton, E. T., Pouliquen, D., Rigopoulou, D., Rizzo, D., Roseboom, I. G., Roussel, H., Rowan-Robinson, M., Rownd, B., Saraceno, P., Sauvage, M., Savage, R., Savini, G., Sawyer, E., Scharmberg, C., Schmitt, D., Schneider, N., Schulz, B., Schwartz, A., Shafer, R., Shupe, D. L., Sibthorpe, B., Sidher, S., Smith, A., Smith, A. J., Smith, D., Spencer, L., Stobie, B., Sudiwala, R., Sukhatme, K., Surace, C., Stevens, J. A., Swinyard, B. M., Trichas, M., Tourette, T., Triou, H., Tseng, S., Tucker, C., Turner, A., Vaccari, M., Valtchanov, I., Vigroux, L., Virique, E., Voellmer, G., Walker, H., Ward, R., Waskett, T., Weilert, M., Wesson, R., White, G. J., Whitehouse, N., Wilson, C. D., Winter, B., Woodcraft, A. L., Wright, G. S., Xu, C. K., Zavagno, A., Zemcov, M., Zhang, L., & Zonca, E. 2010, A&A, 518, L3

Griffin, M. J., North, C. E., Schulz, B., Amaral-Rogers, A., Bendo, G., Bock, J., Conversi, L., Conley, A., Dowell, C. D., Ferlet, M., Glenn, J., Lim, T., Pearson, C., Pohlen, M., Sibthorpe, B., Spencer, L., Swinyard, B., & Valtchanov, I. 2013, MNRAS, 434, 992

Howell, J. H., Armus, L., Mazzarella, J. M., Evans, A. S., Surace, J. A., Sanders, D. B., Petric, A., Appleton, P., Bothun, G., Bridge, C., Chan, B. H. P., Charmandaris, V., Frayer, D. T., Haan, S., Inami, H., Kim, D.-C., Lord, S., Madore, B. F., Melbourne, J., Schulz, B., U, V., Vavilkin, T., Veilleux, S., & Xu, K. 2010, ApJ, 715, 572

Ishida, C. M. 2004, PhD thesis, UNIVERSITY OF HAWAI'I

Iwasawa, K., Sanders, D. B., Teng, S. H., U, V., Armus, L., Evans, A. S., Howell, J. H., Komossa, S., Mazzarella, J. M., Petric, A. O., Surace, J. A., Vavilkin, T., Veilleux, S., & Trentham, N. 2011, A&A, 529, A106

Kim, D., Sanders, D. B., Veilleux, S., Mazzarella, J. M., & Soifer, B. T. 1995, ApJS, 98, 129

Lu, N., Zhao, Y., Díaz-Santos, T., Xu, C. K., Gao, Y., Armus, L., Isaak, K. G., Mazzarella, J. M., van der Werf, P. P., Appleton, P. N., Charmandaris, V., Evans, A. S., Howell, J., Iwasawa, K., Leech, J., Lord, S., Petric, A. O., Privon, G. C., Sanders, D. B., Schulz, B., & Surace, J. A. 2017, ApJS, 230, 1

Lu, N., Zhao, Y., Xu, C. K., Gao, Y., Armus, L., Mazzarella, J. M., Isaak, K. G., Petric, A. O., Charmandaris, V., Díaz-Santos, T., Evans, A. S., Howell, J., Appleton, P., Inami, H., Iwasawa, K., Leech, J., Lord, S., Sanders, D. B., Schulz, B., Surace, J., & van der Werf, P. P. 2014, ApJ, 787, L23

Lu, N., Zhao, Y., Xu, C. K., Gao, Y., Díaz-Santos, T., Charmandaris, V., Inami, H., Howell, J., Liu, L., Armus, L., Mazzarella, J. M., Privon, G. C., Lord, S. D., Sanders, D. B., Schulz, B., & van der Werf, P. P. 2015, ApJ, 802, L11

Meléndez, M., Mushotzky, R. F., Shimizu, T. T., Barger, A. J., & Cowie, L. L. 2014, ApJ, 794, 152

Miville-Deschênes, M.-A. & Lagache, G. 2005, ApJS, 157, 302

Mould, J. R., Hughes, S. M. G., Stetson, P. B., Gibson, B. K., Huchra, J. P., Freedman, W. L., Kennicutt, Jr., R. C., Bresolin, F., Ferrarese, L., Ford, H. C., Graham, J. A., Han, M., Hoessel, J. G., Illingworth, G. D., Kelson, D. D., Macri, L. M., Madore, B. F., Phelps, R. L., Prosser, C. F., Rawson, D., Saha, A., Sakai, S., Sebo, K. M., Silbermann, N. A., & Turner, A. M. 2000, ApJ, 528, 655

Müller, T., Balog, Z., Nielbock, M., Lim, T., Teyssier, D., Olberg, M., Klaas, U., Linz, H., Altieri, B., Pearson, C., Bendo, G., & Vilenius, E. 2014, Experimental Astronomy, 37, 253

Nguyen, H. T., Schulz, B., Levenson, L., Amblard, A., Arumugam, V., Aussel, H., Babbedge, T., Blain, A., Bock, J., Boselli, A., Buat, V., Castro-Rodriguez, N., Cava, A., Chanial, P., Chapin, E., Clements, D. L., Conley, A., Conversi, L., Cooray, A., Dowell,

C. D., Dwek, E., Eales, S., Elbaz, D., Fox, M., Franceschini, A., Gear, W., Glenn, J., Griffin, M., Halpern, M., Hatziminaoglou, E., Ibar, E., Isaak, K., Ivison, R. J., Lagache, G., Lu, N., Madden, S., Maffei, B., Mainetti, G., Marchetti, L., Marsden, G., Marshall, J., O'Halloran, B., Oliver, S. J., Omont, A., Page, M. J., Panuzzo, P., Papageorgiou, A., Pearson, C. P., Perez Fournon, I., Pohlen, M., Rangwala, N., Rigopoulou, D., Rizzo, D., Roseboom, I. G., Rowan-Robinson, M., Scott, D., Seymour, N., Shupe, D. L., Smith, A. J., Stevens, J. A., Symeonidis, M., Trichas, M., Tugwell, K. E., Vaccari, M., Valtchanov, I., Vigroux, L., Wang, L., Ward, R., Wiebe, D., Wright, G., Xu, C. K., & Zemcov, M. 2010, A&A, 518, L5

Ott, S. 2010, in Astronomical Society of the Pacific Conference Series, Vol. 434, Astronomical Data Analysis Software and Systems XIX, ed. Y. Mizumoto, K.-I. Morita, & M. Ohishi, 139

Patanchon, G., Ade, P. A. R., Bock, J. J., Chapin, E. L., Devlin, M. J., Dicker, S., Griffin, M., Gundersen, J. O., Halpern, M., Hargrave, P. C., Hughes, D. H., Klein, J., Marsden, G., Martin, P. G., Mauskopf, P., Netterfield, C. B., Olmi, L., Pascale, E., Rex, M., Scott, D., Semisch, C., Truch, M. D. P., Tucker, C., Tucker, G. S., Viero, M. P., & Wiebe, D. V. 2008, ApJ, 681, 708

Pearson, C., Lim, T., North, C., Bendo, G., Conversi, L., Dowell, D., Griffin, M., Jin, T., Laporte, N., Papageorgiou, A., Schulz, B., Shupe, D., Smith, A. J., & Xu, K. 2014, Experimental Astronomy, 37, 175

Piazzo, L., Calzoletti, L., Faustini, F., Pestalozzi, M., Pezzuto, S., Elia, D., di Giorgio, A., & Molinari, S. 2015, MNRAS, 447, 1471

Pilbratt, G. L., Riedinger, J. R., Passvogel, T., Crone, G., Doyle, D., Gageur, U., Heras, A. M., Jewell, C., Metcalfe, L., Ott, S., & Schmidt, M. 2010, A&A, 518, L1

Poglitsch, A., Waelkens, C., Geis, N., Feuchtgruber, H., Vandenbussche, B., Rodriguez, L., Krause, O., Renotte, E., van Hoof, C., Saraceno, P., Cepa, J., Kerschbaum, F.,

Agnèse, P., Ali, B., Altieri, B., Andreani, P., Augueres, J.-L., Balog, Z., Barl, L., Bauer, O. H., Belbachir, N., Benedettini, M., Billot, N., Boulade, O., Bischof, H., Blommaert, J., Callut, E., Cara, C., Cerulli, R., Cesarsky, D., Contursi, A., Creten, Y., De Meester, W., Doublier, V., Doumayrou, E., Duband, L., Exter, K., Genzel, R., Gillis, J.-M., Grözinger, U., Henning, T., Herreros, J., Huygen, R., Inguscio, M., Jakob, G., Jamar, C., Jean, C., de Jong, J., Katterloher, R., Kiss, C., Klaas, U., Lemke, D., Lutz, D., Madden, S., Marquet, B., Martignac, J., Mazy, A., Merken, P., Montfort, F., Morbidelli, L., Müller, T., Nielbock, M., Okumura, K., Orfei, R., Ottensamer, R., Pezzuto, S., Popesso, P., Putzeys, J., Regibo, S., Reveret, V., Royer, P., Sauvage, M., Schreiber, J., Stegmaier, J., Schmitt, D., Schubert, J., Sturm, E., Thiel, M., Tofani, G., Vavrek, R., Wetzstein, M., Wieprecht, E., & Wiezorrek, E. 2010, A&A, 518, L2

Roussel, H. 2013, PASP, 125, 1126

Sanders, D. B., Mazzarella, J. M., Kim, D., Surace, J. A., & Soifer, B. T. 2003, AJ, 126, 1607

Sanders, D. B., Scoville, N. Z., & Soifer, B. T. 1991, ApJ, 370, 158

Shimizu, T. T., Meléndez, M., Mushotzky, R. F., Koss, M. J., Barger, A. J., & Cowie, L. L. 2016, MNRAS, 456, 3335

Skrutskie, M. F., Cutri, R. M., Stiening, R., Weinberg, M. D., Schneider, S., Carpenter, J. M., Beichman, C., Capps, R., Chester, T., Elias, J., Huchra, J., Liebert, J., Lonsdale, C., Monet, D. G., Price, S., Seitzer, P., Jarrett, T., Kirkpatrick, J. D., Gizis, J. E., Howard, E., Evans, T., Fowler, J., Fullmer, L., Hurt, R., Light, R., Kopan, E. L., Marsh, K. A., McCallon, H. L., Tam, R., Van Dyk, S., & Wheelock, S. 2006, AJ, 131, 1163

Soifer, B. T., Boehmer, L., Neugebauer, G., & Sanders, D. B. 1989, AJ, 98, 766

Stierwalt, S., Armus, L., Surace, J. A., Inami, H., Petric, A. O., Diaz-Santos, T., Haan, S., Charmandaris, V., Howell, J., Kim, D. C., Marshall, J., Mazzarella, J. M., Spoon,

H. W. W., Veilleux, S., Evans, A., Sanders, D. B., Appleton, P., Bothun, G., Bridge, C. R., Chan, B., Frayer, D., Iwasawa, K., Kewley, L. J., Lord, S., Madore, B. F., Melbourne, J. E., Murphy, E. J., Rich, J. A., Schulz, B., Sturm, E., Vavilkin, T., & Xu, K. 2013, ApJS, 206, 1

Zhao, Y., Lu, N., Xu, C. K., Gao, Y., Lord, S., Howell, J., Isaak, K. G., Charmandaris, V., Diaz-Santos, T., Appleton, P., Evans, A., Iwasawa, K., Leech, J., Mazzarella, J., Petric, A. O., Sanders, D. B., Schulz, B., Surace, J., & van der Werf, P. P. 2013, ApJ, 765, L13

Zhao, Y., Lu, N., Xu, C. K., Gao, Y., Lord, S. D., Charmandaris, V., Diaz-Santos, T., Evans, A., Howell, J., Petric, A. O., van der Werf, P. P., & Sanders, D. B. 2016, ApJ, 819, 69

Chapter 3

The 3–500 μm Spectral Energy Distributions of Local Luminous Infrared Galaxies

Note: *This chapter to be submitted to the Astrophysical Journal Letters as Chu, J. K.; Sanders, D. B.; et al.*

Abstract

We present median infrared (3–500 μm) spectral energy distributions (SEDs) binned by total infrared luminosity in 0.25 dex increments spanning $\log(L_{\rm IR}/L_{\odot}) = 11.0$–12.6, for the complete sample of 201 luminous infrared galaxies (LIRGs) in the Great Observatories All-Sky LIRG Survey (GOALS). The SEDs were compiled using survey data of the GOALS galaxies obtained with *IRAS*, *Spitzer Space Telescope*, *Wide-field Infrared Survey Explorer* and *Herschel Space Observatory* . We also compiled similar data on galaxies with lower $L_{\rm IR}$ in the KINGFISH sample for comparison. The overall shapes of the median SEDs for the GOALS galaxies at $\lambda > 100$ μm are similar, with a mean submillimeter (250–500 μm) spectral index, $F \propto \nu^{\alpha}$, of $\alpha = 4 \pm 0.12$, and a luminosity peak at $\lambda_{\rm peak} \sim 100$ μm for sources with $\log(L_{\rm IR}/L_{\odot}) \approx 11.0$. Towards higher $L_{\rm IR}$, the peak smoothly shifts to shorter far-infrared wavelengths to $\lambda_{\rm peak} \sim 60$ μm for sources with $\log(L_{\rm IR}/L_{\odot}) > 12.0$. The overall behavior of the median GOALS SEDs at $\lambda < 100$ μm are slightly more complex, in particular at luminosities $\log(L_{\rm IR}/L_{\odot}) \geq 11.75$, where the broad silicate features centered at $\sim$10 μm and $\sim$18 μm appear to depress the overall emission in the mid-infrared, making

the appearance of excess emission at longer infrared wavelengths. We also compare our new GOALS SEDs with the most widely used SED templates that are currently available in the literature. Our new results suggest that all previously published model SEDs for LIRGs need to be modified to properly reflect the latest observations, and that searches for high-redshift LIRGs based on assumed rest-frame, broadband infrared colors can be improved by using our new results for the GOALS galaxies.

3.1 Introduction

In a recent paper (Chu et al. 2017, *Herschel*-GOALS), we presented far-infrared images and photometry for the complete sample of 201 extragalactic objects in the Great Observatories All-Sky LIRG Survey (GOALS[1], Armus et al. 2009) that were observed with both the PACS and SPIRE instruments onboard the *Herschel Space Observatory*. This letter uses these data to construct far-infrared (FIR) spectral energy distributions (SEDs) for each target and to characterize the overall shapes and variations of the median SEDs as a function of total infrared luminosity, $L_{\rm IR} \equiv L(8 - 1000\ \mu{\rm m})$.

To obtain a more complete picture of the far-infrared SEDs of local LIRGs, we have added data from the *Spitzer Space Telescope*, *Wide-field Infrared Survey Explorer*, and *Infrared Astronomical Satellite*, to provide broadband photometry covering the wavelength range 3–500 μm. These photometric measurements were extracted in a consistent manner using common field centers and consistent aperture masks (i.e., U et al. 2012), which is important when dealing with LIRGs where a large fraction of the sources show extensive non-axisymmetric features characteristic of strong interactions and mergers (i.e., tidal bridges and tails, shells and ripples, etc.). To contrast the SEDs for LIRGs with the SEDs of lower infrared luminosity galaxies, we also present SEDs for galaxies in the nearby, volume-limited KINGFISH sample, where the data have been extracted from Dale et al. (2017). We use a reference cosmology of $\Omega_\Lambda = 0.72, \Omega_{\rm m} = 0.28$ and $H_0 = 70$ km sec.$^{-1}$ Mpc^{-1}, however

[1] `http://goals.ipac.caltech.edu/`

we also take into account local non-cosmological effects by using the three-attractor model of Mould et al. (2000).

3.2 The GOALS Sample

The GOALS sample comprises 179 LIRGs ($11 \leq \log(L_{\rm IR}/L_{\odot}) < 12$) and 22 ULIRGs ($12 \leq \log(L_{\rm IR}/L_{\odot}) < 13$) in the local universe, with a median and maximum redshift of $\langle z \rangle = 0.021$ and 0.0876 respectively. The GOALS galaxies are the 201 most luminous galaxies with $\log(L_{\rm IR}/L_{\odot}) \geq 11.0$ in the Revised Bright Galaxy Sample (RBGS, Sanders et al. 2003), a flux limited sample selected by their *IRAS* 60 μm flux with Galactic latitudes above $|b| > 5^{\circ}$. As a complete sample of infrared-bright galaxies, GOALS also represents a complete picture of different interaction stages such as isolated galaxies, minor mergers, and major mergers. The nearby nature of this sample means it can be studied in detail at all wavelengths from X-ray to radio.

3.3 Observations

We briefly summarize the observations used in this chapter which combine data spanning over thirty years of infrared space missions. In Figure 3.1, we show all of the filter curves for the available data, color-coded by mission and/or instrument. As a result of our dedicated observing campaigns, we have achieved a very high degree of uniformity in our rich multi-wavelength dataset.

The *Infrared Astronomical Satellite* (Neugebauer et al. 1984), was the first space observatory sensitive enough at mid- and far-infrared wavelengths to detect a large population of local luminous infrared galaxies, resulting in the GOALS sample. For this chapter we use the final reprocessed *IRAS* fluxes from Sanders et al. (2003), which includes the Pass 3 calibration of the *IRAS* Level 1 archive and have flux measurements made in a more consistent manner than the previous $\rm BGS_1$+$\rm BGS_2$ sample (Soifer et al. 1986, 1987, 1989; Sanders et al. 1995). Since the *WISE* 12 μm and *Herschel* 100 μm observations (see

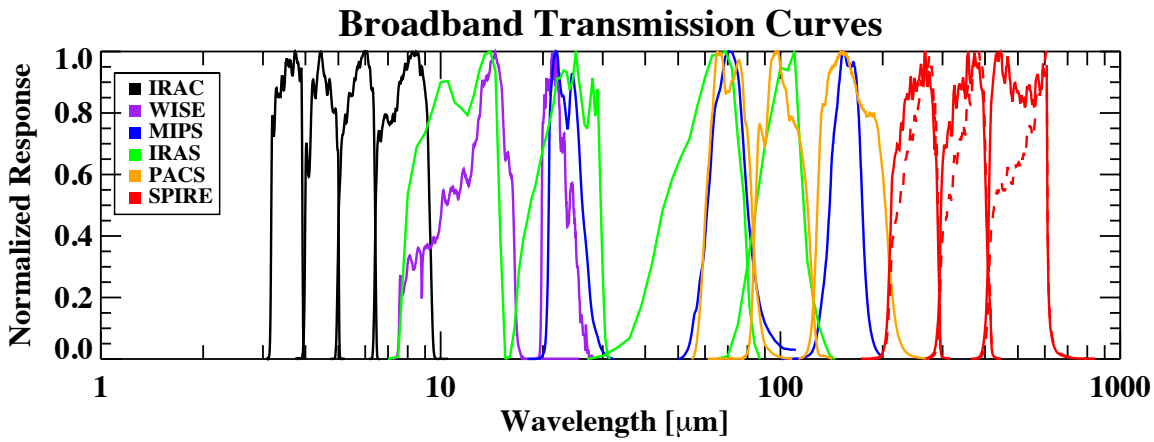

Figure 3.1 From left to right, the four *Spitzer*-IRAC bands are centered at 3.6, 4.5, 5.8, and 8 μm in black, the three *IRAS* bands are centered at 12, 25, 60, and 100 μm in green, the two *WISE* bands are centered at 12 μm (W3) and 22 μm (W4) in purple, the three *Spitzer*-MIPS bands at 24, 70, and 160 μm in blue, the three *Herschel*-PACS bands are centered at 70, 100, and 160 μm in orange, and the three *Herschel*-SPIRE bands centered at 250, 350, and 500 μm in red. We do not use the *Spitzer*-MIPS 24 μm photometry because its filter curve is very similar to the *WISE* 22 μm filter, and also because it is close to the *IRAS* 25 μm photometry (see Mazzarella et al. in preparation). We omit the *IRAS* 100 μm point since it is superseded by *Herschel*-PACS. For the SPIRE bands (red), the point source response is shown with a solid curve, while the extended source response is shown with a dashed curve. Note the large difference in response for the SPIRE 500 μm transmission curve.

below) have much higher angular resolutions and sensitivities, we use those data in place of the *IRAS* 12 and 100 μm photometry in our analysis.

The *Spitzer* (Werner et al. 2004) data for the entire GOALS sample include both Infrared Array Camera (IRAC, Fazio et al. 2004) observations at 3.4, 4.5, 5.8, and 8 μm as well Multiband Imaging Photometer for *Spitzer* (MIPS, Rieke et al. 2004) observations at 24, 70, and 160 μm (Mazzarella et al. in prep). Due to the image quality issues with the MIPS 70 and 160 μm data, most notably source saturation on the detector arrays, we use the *Herschel*-PACS 70 and 160 μm data instead. Although the 24 μm data quality is very good, we don't include those fluxes since its filter is very similar to the *WISE* W4 filter at 22 μm, and also because 24 μm is very close to the *IRAS* 25 μm point.

Data from *WISE* (Wright et al. 2010), an all-sky mid-infrared (MIR) survey telescope, are also incorporated to help fill in the complex MIR part of the SED. Since the two shortest bands of *WISE* correspond very closely to the two shortest IRAC bands, we only include the W3 12 μm and W4 22 μm photometry. The fluxes were extracted from the AllWISE catalog by feeding in a list of input coordinates for the entire GOALS sample. A combination of extended source photometry, profile-fitted photometry, and "standard aperture" photometry were used depending on the source morphology with respect to the PSF of the W3 and W4 bands, which are $6\farcs7$ and $11\farcs8$ FWHM respectively. We then perform a very small aperture and color correction, as detailed by the WISE Explanatory Supplement. Due to the uncertainty in the calibration of the W4 relative spectral response, we include an additional -10% correction for very red sources since many of them have steeply rising MIR spectra (see Stierwalt et al. 2013).

The *Herschel Space Observatory* (Pilbratt et al. 2010) provides the final piece needed to construct infrared SEDs of the GOALS sample. The complete atlas and measured photometry (including both total system and component fluxes) is described in Chu et al. (2017), and consists of Photoconductor Array Camera and Spectrometer (PACS, Poglitsch et al. 2010) imaging at 70, 100, and 160 μm, and Spectral and Photometric Imaging Receiver (SPIRE, Griffin et al. 2010) imaging at 250, 350, and 500 μm. A total of 169 and 160 targets were observed by PACS and SPIRE respectively, while the remaining 32 and 41 PACS and SPIRE targets respectively were obtained from other programs.

Because we are combining data from many different space missions, it is important that all of the photometry are consistent and properly cross-calibrated. Starting with the *Herschel* data, Chu et al. (2017) showed that the PACS 100 μm data agree very well with the *IRAS* 100 μm photometry, with an average Herschel/IRAS flux ratio of 1.01. The same is true for the PACS 70 μm data when compared to the *IRAS* 60 μm flux interpolated to 70 μm. Comparing the *WISE* 12 μm fluxes to the corresponding *IRAS* 12 μm fluxes, we found an average WISE/IRAS ratio of 0.63 with a large scatter due to the significantly wider *IRAS* 12 μm filter. Furthermore both filter curves span the complex emission and

absorption features near 10 μm, causing the large scatter. The average WISE 22/IRAS 25 μm flux ratio is 0.68, again lower because of the narrower FWHM of the *WISE* filter. The scatter is much lower ($\sigma \approx 0.1$) since there are no significant narrow spectral features. However both broadband photometry points match very well with the spectral slopes found in our *Spitzer*-IRS MIR spectra. Finally, a detailed analysis by Jarrett et al. (2011) showed an excellent agreement between the *Spitzer* photometric system and the *WISE* calibration, to within 4.5% and 5.7% for the *WISE* 12 and 22 μm bands from observations of the north and south ecliptic poles.

3.4 Results

In Figure 3.2 we present the median-averaged 3–500 μm SEDs of the GOALS sample after dividing the sample into six $L_{\rm IR}$ bins, each spanning 0.25 dex from $10^{11} L_{\odot}$ to $10^{12.6} L_{\odot}$. On the x-axis we plot the wavelength and on the y-axis is $\log(\nu L_{\nu}/L_{\odot})$. In order from lowest to highest $L_{\rm IR}$ the bins contain 64, 58, 38, 19, 13, and 9 galaxy systems, with the decrease in number towards higher $L_{\rm IR}$ to be expected since the most luminous objects are the rarest, and GOALS is a flux-limited sample. In addition to the LIRGs and ULIRGs from GOALS, we include multi-wavelength photometry from the sub-LIRG ($\log(L_{\rm IR}/L_{\odot}) < 11.0$) KINGFISH sample in Dale et al. (2017), which adds an additional 31 galaxies between the $\log(L_{\rm IR}/L_{\odot})$ ranges of 9.75 to 10.75 in increments of 0.25 dex (5–7 objects per bin). The $\log(L_{\rm IR}/L_{\odot}) = 10.75 - 11$ bin was omitted because there were only two objects within that range. The median-averaged luminosities and associated 1-σ dispersions for each $L_{\rm IR}$ bin and wavelength are presented in Table 1. In Appendix A I present the full SED for each GOALS system. Since we only present the broadband photometry here, we emphasize that the lines connecting each point only serves to guide the reader's eye, and should not be interpreted as the actual SED shape between the photometric points, especially at near- and mid-infrared wavelengths.

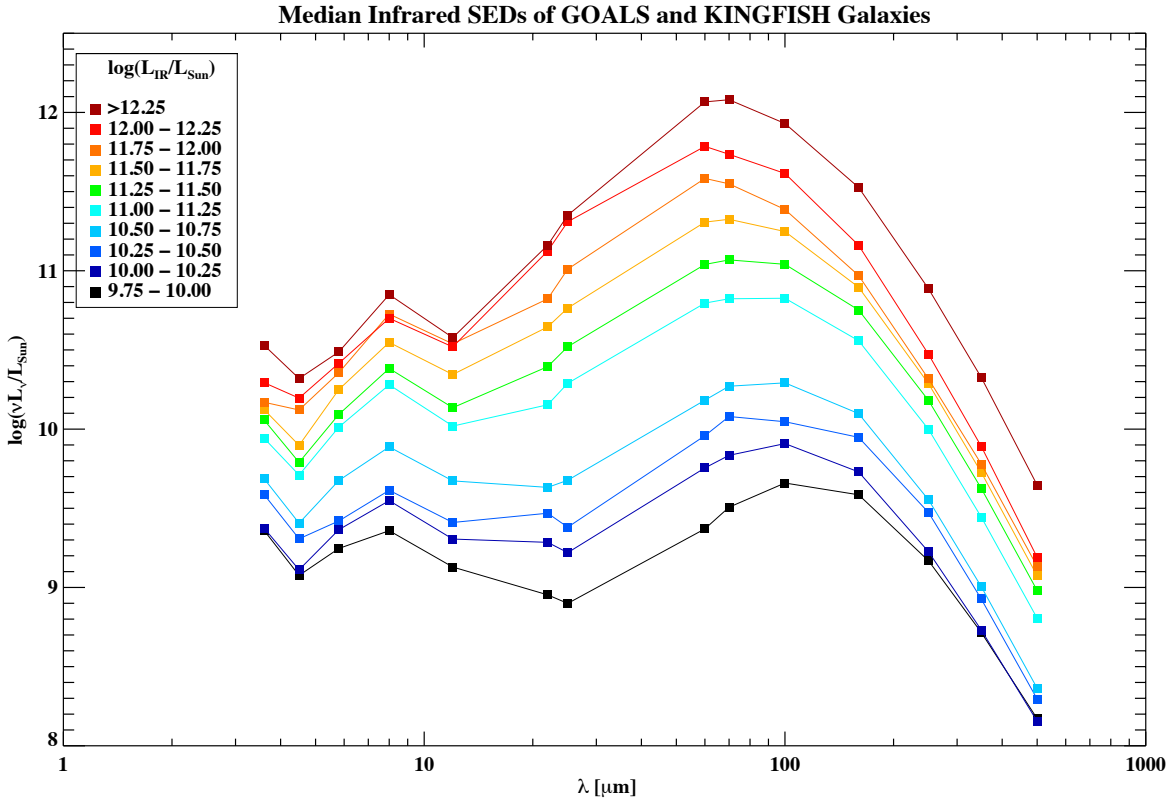

Figure 3.2 The median-averaged 3–500 μm SEDs from each of the six GOALS bins (each spanning 0.25 dex in $\log(L_{\rm IR}/L_{\odot})$). Additionally, we include 31 sub-LIRG galaxies from the KINGFISH sample also binned by 0.25 dex, however we do not include the $\log(L_{\rm IR}/L_{\odot}) = 10.75$ to 11 bin as only two objects satisfy that criteria.

Table 3.1 Median Infrared Luminosity Densities: $\lambda \leq 25$ μm

$\log(L_{\rm IR}/L_\odot)$ Bin	$\nu L_{3.6}$	$\nu L_{4.5}$	$\nu L_{5.8}$	νL_{8}	νL_{12}	νL_{22}	νL_{25}
—	$\log(\nu L_\nu/L_\odot)$	$\log(\nu L_\nu/L_\odot)$	$\log(\nu L_\nu/L_\odot)$	$\log(\nu L_\nu/L_\odot)$	$\log(\nu L_\nu/L_\odot)$	$\log(\nu L_\nu/L_\odot)$	$\log(\nu L_\nu/L_\odot)$
$9.75-10.00$	9.36 ± 0.53	9.08 ± 0.52	9.25 ± 0.37	9.36 ± 0.29	9.13 ± 0.26	8.95 ± 0.20	8.90 ± 0.24
$10.00-10.25$	9.37 ± 0.25	9.11 ± 0.20	9.36 ± 0.24	9.55 ± 0.25	9.31 ± 0.26	9.28 ± 0.28	9.22 ± 0.26
$10.25-10.50$	9.59 ± 0.27	9.31 ± 0.26	9.42 ± 0.28	9.61 ± 0.34	9.41 ± 0.31	9.47 ± 0.27	9.38 ± 0.25
$10.50-10.75$	9.69 ± 0.26	9.41 ± 0.24	9.68 ± 0.18	9.89 ± 0.12	9.67 ± 0.10	9.63 ± 0.10	9.68 ± 0.13
$11.00-11.25$	9.94 ± 0.24	9.71 ± 0.23	10.01 ± 0.26	10.28 ± 0.24	10.02 ± 0.22	10.15 ± 0.14	10.29 ± 0.13
$11.25-11.50$	10.06 ± 0.25	9.79 ± 0.27	10.09 ± 0.25	10.38 ± 0.24	10.14 ± 0.27	10.39 ± 0.23	10.52 ± 0.21
$11.50-11.75$	10.12 ± 0.25	9.90 ± 0.25	10.25 ± 0.25	10.55 ± 0.22	10.34 ± 0.24	10.65 ± 0.18	10.76 ± 0.16
$11.75-12.00$	10.17 ± 0.33	10.12 ± 0.33	10.36 ± 0.41	10.73 ± 0.35	10.54 ± 0.36	10.82 ± 0.19	11.01 ± 0.17
$12.00-12.25$	10.29 ± 0.24	10.20 ± 0.36	10.42 ± 0.55	10.70 ± 0.25	10.52 ± 0.26	11.12 ± 0.20	11.31 ± 0.17
>12.25	10.53 ± 0.37	10.32 ± 0.43	10.49 ± 0.53	10.85 ± 0.33	10.58 ± 0.36	11.16 ± 0.28	11.35 ± 0.22

Table 3.1 Median Infrared Luminosity Densities *(continued)*: $\lambda > 25$ μm

$\log(L_{\rm IR}/L_\odot)$ Bin	νL_{60}	νL_{70}	νL_{100}	νL_{160}	νL_{250}	νL_{350}	νL_{500}
—	$\log(\nu L_\nu/L_\odot)$	$\log(\nu L_\nu/L_\odot)$	$\log(\nu L_\nu/L_\odot)$	$\log(\nu L_\nu/L_\odot)$	$\log(\nu L_\nu/L_\odot)$	$\log(\nu L_\nu/L_\odot)$	$\log(\nu L_\nu/L_\odot)$
$9.75-10.00$	9.37 ± 0.24	9.51 ± 0.23	9.66 ± 0.23	9.59 ± 0.23	9.17 ± 0.24	8.72 ± 0.24	8.17 ± 0.25
$10.00-10.25$	9.76 ± 0.26	9.83 ± 0.28	9.91 ± 0.29	9.73 ± 0.37	9.23 ± 0.42	8.73 ± 0.44	8.15 ± 0.45
$10.25-10.50$	9.96 ± 0.32	10.08 ± 0.28	10.05 ± 0.23	9.95 ± 0.24	9.47 ± 0.26	8.93 ± 0.26	8.30 ± 0.27
$10.50-10.75$	10.18 ± 0.10	10.27 ± 0.05	10.29 ± 0.07	10.10 ± 0.17	9.55 ± 0.23	9.01 ± 0.26	8.36 ± 0.29
$11.00-11.25$	10.80 ± 0.08	10.82 ± 0.10	10.83 ± 0.11	10.56 ± 0.16	10.00 ± 0.21	9.44 ± 0.22	8.81 ± 0.24
$11.25-11.50$	11.04 ± 0.11	11.07 ± 0.12	11.04 ± 0.14	10.75 ± 0.17	10.18 ± 0.19	9.63 ± 0.20	8.98 ± 0.22
$11.50-11.75$	11.31 ± 0.08	11.33 ± 0.10	11.25 ± 0.12	10.90 ± 0.15	10.29 ± 0.19	9.73 ± 0.20	9.07 ± 0.22
$11.75-12.00$	11.58 ± 0.06	11.55 ± 0.08	11.39 ± 0.13	10.97 ± 0.18	10.32 ± 0.20	9.78 ± 0.20	9.13 ± 0.21
$12.00-12.25$	11.79 ± 0.10	11.74 ± 0.08	11.61 ± 0.12	11.16 ± 0.16	10.47 ± 0.21	9.89 ± 0.23	9.19 ± 0.25
>12.25	12.07 ± 0.06	12.08 ± 0.07	11.93 ± 0.07	11.53 ± 0.07	10.89 ± 0.08	10.33 ± 0.09	9.65 ± 0.10

3.5 Discussion

3.5.1 Median SEDs as a Function of $L_{\rm IR}$

Generally speaking, one notable trend in Figure 3.2 is that the higher $L_{\rm IR}$ bins have SED peaks at shorter wavelengths than lower luminosity galaxies. At submillimeter wavelengths ($\lambda \gtrsim 250$ μm) all of the LIRG and ULIRG bins have very similar spectral slopes, approximately following a $F \propto \nu^{4\pm0.12}$ relation. The top two sub-LIRG bins also have a submillimeter spectral slope of approximately 4, whereas the two lower bins have shallower spectral slopes of 3.3 and 3.6 for the 9.75−10 and 10−10.25 bins respectively.

Figure 3.2 also shows how similar the submillimeter luminosities are for all of the GOALS bins except the very top bin, with a maximum difference of about 0.5 dex. However by 60 μm there is a larger difference in luminosity between the five bins, with a spread that increases to about 1 dex. The brightest GOALS bin, which includes the most extreme galaxies such as Arp 220 and Mrk 231, is noticeably extra-luminous at all FIR and submillimeter wavelengths ($\lambda \gtrsim 60$ μm) than the next brightest bin. This is remarkable given that an average increase in $L_{\rm IR}$ of ∼0.25 dex produces a marked increase of ∼0.4 dex in the FIR and submillimeter luminosity. This may be due to an additional warm dust component being starburst heated only at the highest luminosities, while the cool dust heated by the interstellar radiation field is staying at about the same luminosity. However at near- and mid-infrared wavelengths the top bin has luminosities almost the same as the next $L_{\rm IR}$ bin below it, suggesting that AGN heating (and thus AGN activity) is nearly the same by the time these galaxies reach the ULIRG phase. Another possibility is that the original *IRAS* $L_{\rm IR}$ estimates (see Perault 1987) at ULIRG luminosities are not as accurate, since they were estimated using only *IRAS* measurements. This will be directly addressed in our next paper where we will perform SED fitting for each galaxy and calculate a more accurate $L_{\rm IR}$.

3.5.2 Comparisons to SED Templates in the Literature

Before the availability of *Herschel* FIR and submillimeter data, many studies needing FIR SEDs of galaxies were forced to rely heavily on SED models. By using four archetypical galaxies – Arp 220, NGC 6090, M82, and M51, each representing ULIRGs, LIRGs, starbursts, and normal galaxies respectively, Chary & Elbaz (2001) (hereafter CE01) interpolated and derived 0.1–1000 μm SEDs for a $\log(L_{\rm IR}/L_{\odot})$ range of 8.3–13.6. To construct their final SED templates, they interpolated the models using templates that best fit the MIR (4–20 μm) and far-infrared (20–1000 μm) separately between the four galaxies, then joined them together to produce the final SED template. Rieke et al. (2009, hereafter R09) used a similar approach using additional data from *Spitzer* IRAC, IRS, and MIPS.

In Figure 3.3 we show our full infrared GOALS SEDs with both models. The CE01 curves were calculated identically as our data: for each galaxy the closest matching CE01 template was selected and the resulting ensemble of corresponding SEDs were median-averaged within each bin. The R09 models were calculated as the average of two models bracketing each bin, since they only give models at 0.25 dex intervals in $L_{\rm IR}$. The gray shaded portions represent the 1-σ dispersion in luminosity for each photometric point, and indicates the spread in SED shape for that bin. On the bottom of each panel we plot the residuals of both templates minus our data.

There are several bins in Figure 3.3 where both match quite well to the data at $\lambda \gtrsim 100$ μm, namely the $\log(L_{\rm IR}/L_{\odot}) = 11.5$–$11.75$ and $\log(L_{\rm IR}/L_{\odot}) > 12.25$ bins. This is most likely due to the fact that two of the four archetypes in CE01 have infrared luminosities within that $L_{\rm IR}$ range, namely Arp 220 and NGC 6090. A similar plot for the sub-LIRG sample also reveals the same behavior, where the CE01 archetype M82 ($\log(L_{\rm IR}/L_{\odot}) = 10.77$) matches very well with the corresponding KINGFISH $L_{\rm IR}$ bin. On the other hand the R09 models behave similar to CE01 at low luminosities, however they increasingly overestimate the FIR peak towards higher $L_{\rm IR}$. It is also notable that both models are essentially identical beyond 100 μm.

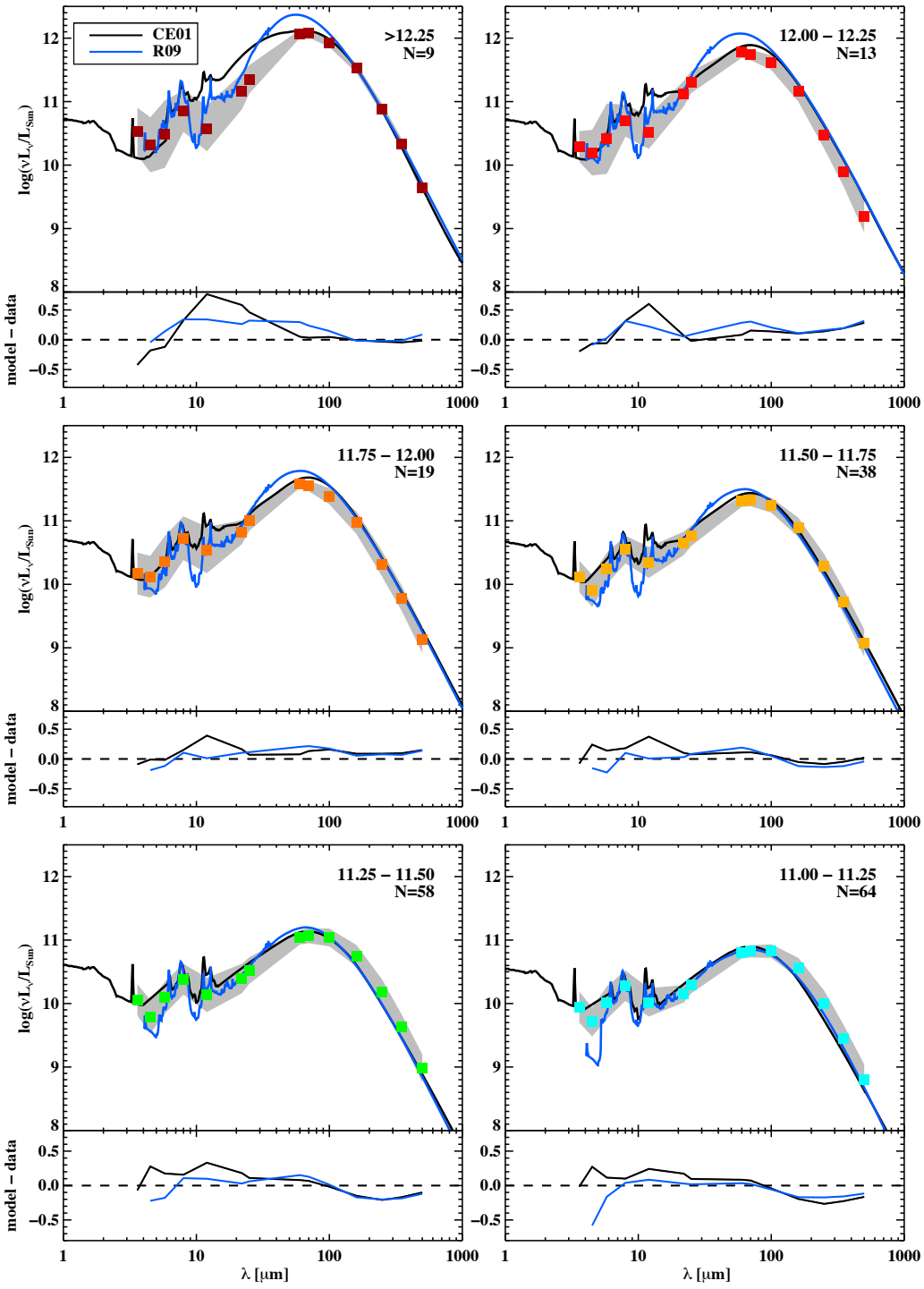

Figure 3.3 The median-averaged 3−500 μm SEDs of the galaxies by $L_{\rm IR}$, with the CE01 (black) and R09 (dark blue) models. The luminosity range and number of objects within each bin is indicated on the upper right. The grey shading represents the 1-σ dispersion in luminosity flux density. On the bottom we plot the difference of each model minus our data, where the dashed line indicates a difference of 0.

Overall the CE01 SED templates do reproduce the correct shape and slope of the FIR emission and lie within the 1 sigma dispersion of our data, despite noticeable vertical offsets in some of the bins. Both models in Figure 3.3 from lowest to highest $L_{\rm IR}$ don't quite match our data at wavelengths beyond $\sim$100 μm. This can be explained by the fact that both models generated their SEDs by interpolating between different IR luminosities, and was done in an approximately linear fashion at far-infrared and submillimeter wavelengths. In contrast, the increase in luminosity in our FIR/submillimeter data is not linear as we show in Figure 3.2, causing the observed oscillatory under- and over-prediction of both models relative to the data.

The MIR is less robust for CE01 with a tendency to overestimate the actual luminosity due to the presence of the 10 μm and 18 μm silicate absorption feature, especially for the three brightest bin. In addition the models for the top $L_{\rm IR}$ bin have a significantly wider FIR peak in contrast to the lower $L_{\rm IR}$ bins. The peak wavelength of the FIR bump also seemingly varies in relation to our data, both underestimating and overestimating the true peak. However the MIR spectral slopes of the R09 models agree very well with our data and appear to include the 18 μm silicate feature, despite a positive offset in the highest bin.

3.5.3 The $L_{\rm IR}$-Color Relation

An alternative way of examining SED trends as a function of $L_{\rm IR}$ is to plot the $L_{\rm IR}$ *vs.* MIR or FIR color, shown in Figure 3.4. The top two panels show the 22/70 μm and 22/100 μm flux ratio as a function of IR luminosity, while the bottom panels show the 70/100 μm and 70/250 μm ratios. In each panel the flux ratios are shown for every galaxy or galaxy system from both GOALS and KINGFISH with gray circles and triangles respectively, with medians plotted as red and blue stars respectively. The vertical error bars on each median point indicates the 1-σ dispersion for data in that bin. In black we plot the templates of CE01, and in green are the SED models of R09. Due to the uncertainty in R09's models above $10^{12.5} L_{\odot}$, we plot dashed lines at those luminosities.

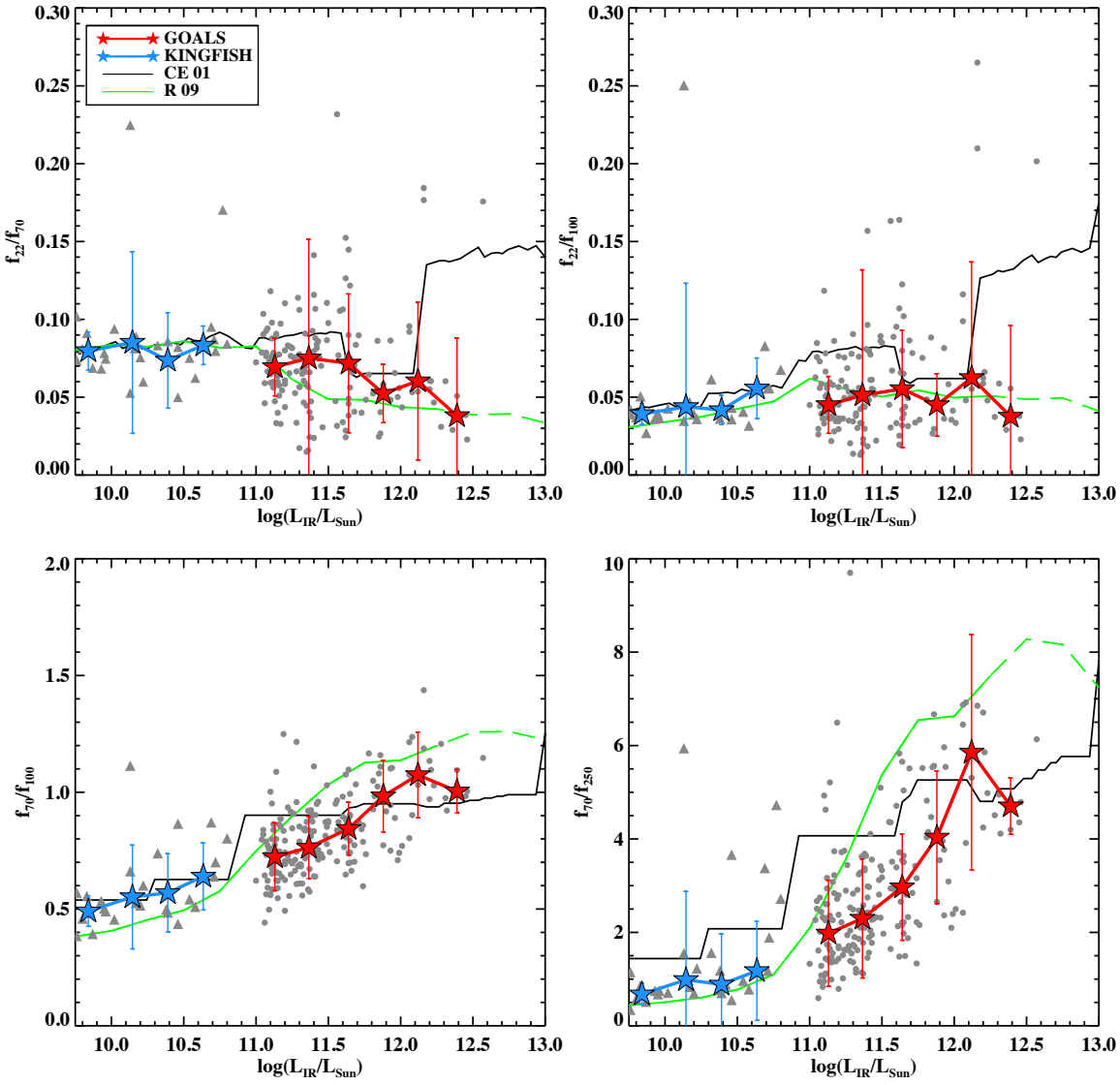

Figure 3.4 Mid- and far-infrared colors of the GOALS sample plotted as a function of the total $L_{\rm IR}$. The median flux ratio of each $L_{\rm IR}$ bin is plotted as red (blue) stars, with the individual ratios of each object plotted as gray circles (triangles) for the GOALS (KINGFISH) sample. The vertical bars on each median point represent the 1-σ dispersion of the colors in that bin. The black and green lines represent the model predictions of CE01 and R09 respectively. The dashed part of R09's models at high $L_{\rm IR}$ represent a high level of uncertainty in their predictions, as cautioned in their paper.

The R09 models match the sub-LIRGs from KINGFISH quite well for all of the colors, except for the 70/100 color where there is a noticeable under-prediction by ∼20% (compared to the median). CE01 on the other hand also agrees quite well with the sub-LIRGs, except for the 70/250 ratio where it over-predicts by ∼50%. At LIRG and ULIRG luminosities, the differences between each set of models and our data become more complex. R09 noticeably over-predicts in both the 70/100 and 70/250 flux ratios by up to 2× compared to the median, while it agrees quite well with the 22/100 flux ratio, and to a lesser degree the 22/70 flux ratio. On the other hand CE01 has better but not perfect agreement in the 70/100 flux ratio, however like R09 they also over-predict the 70/250 color ratio. This is not surprising since both CE01 and R09 had *IRAS* data from which to derive their templates so their predictions are relatively reasonable up to 100 μm. In the top two panels, CE01 again tracks somewhat closely with the GOALS data, however there is a clear jump in CE01's ratio at the top $L_{\rm IR}$ bin up to 3× the median of our data. This is due to an overestimate in the MIR flux as we show in Figure 3.3.

In the bottom two panels of Figure 3.4 there is an increase in FIR color ratio until it peaks at around the ULIRG threshold ($L_{\rm IR} = 10^{12} L_{\odot}$), which also has the largest dispersion. This indicates that as galaxy mergers progress and increase their FIR output (Larson et al. 2016), they become bluer around the SED peak. This is simply a consequence of the SED peak moving to shorter wavelengths as one moves towards higher infrared luminosities. Furthermore at the highest infrared luminosities where the galaxies are mostly advanced mergers with merging nuclei, they appear to become redder again. To be sure we weren't biased by the 70 μm data, we analyzed and obtained similar results using the 100 μm photometry.

In the MIR the color ratios indicate a downward (redder) trend for the 22/70 color, and a nearly constant 22/100 color ratio. The latter seems to indicate that on average, the spectral slope between 22 and 100 microns on average doesn't vary much between $10^{9.75} L_{\odot}$ to $10^{12.5} L_{\odot}$. We also note that three galaxies at the highest luminosities with very blue

colors relative to the rest of the sample are IRAS F01589-2524, IRAS F08572+3915, and Mrk 231.

3.6 Summary

In this chapter we present for the first time the median 3–500 μm SEDs for the complete sample of 201 LIRGs in GOALS. We also include for comparison 31 objects with lower infrared luminosity from the KINGFISH local-volume galaxy sample. Our main results can be summarized as follows:

1. Galaxies with $\log(L_{\rm IR}/L_{\odot}) \geq 10.25$ have a similar submillimeter (λ = 250–500 μm) spectral index, $F \propto \nu^{\alpha}$ with $\alpha = 4 \pm 0.12$, while less luminous galaxies have slightly shallower spectral slopes.

2. The far-infrared SEDs of local LIRGs peak in the wavelength range $\lambda \sim$ 60–100 μm, where $\lambda_{\rm peak}$ shifts systematically to shorter wavelength with increasing $L_{\rm IR}$.

3. At wavelengths shorter than $\lambda_{\rm peak}$, the shapes of the SEDs are more complex. At the highest luminosities of $\log(L_{\rm IR}/L_{\odot}) \geq 11.75$, broad absorption features appear to depress the emission in the mid-infrared ($\lambda \sim$ 8–25 μm), which makes the appearance of excess emission at longer wavelengths.

4. At wavelengths longer than $\lambda_{\rm peak}$, the SED models of Chary & Elbaz (2001) and Rieke et al. (2009) either underestimate or overestimate our data, due to the quasi-linear method in which they derived their models. However as we show in Figure 3.2 the FIR and submillimeter luminosities do not increase linearly with increasing $L_{\rm IR}$.

5. Comparisons of our new SEDs with widely used templates in the literature show that previous assumptions about infrared colors can systematically overestimate the actual color by as much as a factor of 3$\times$ from the median color.

6. We provide a table of median broadband luminosities corresponding to the median SEDs in the luminosity bins of $L_{\rm IR}$ presented in Figure 3.2. These new data should be used to carry out improved searches for LIRGs in the more distant universe.

In a follow-up paper we will present a more detailed analysis of the infrared SEDs of LIRGs by combining the broadband photometry data presented here with mid-infrared (λ = 5–35 μm) spectroscopy from *Spitzer*-IRS. The combined dataset will then be used to provide more accurate SEDs templates for LIRGs that can be downloaded for public use.

References

Armus, L., Mazzarella, J. M., Evans, A. S., Surace, J. A., Sanders, D. B., Iwasawa, K., Frayer, D. T., Howell, J. H., Chan, B., Petric, A., Vavilkin, T., Kim, D. C., Haan, S., Inami, H., Murphy, E. J., Appleton, P. N., Barnes, J. E., Bothun, G., Bridge, C. R., Charmandaris, V., Jensen, J. B., Kewley, L. J., Lord, S., Madore, B. F., Marshall, J. A., Melbourne, J. E., Rich, J., Satyapal, S., Schulz, B., Spoon, H. W. W., Sturm, E., U, V., Veilleux, S., & Xu, K. 2009, PASP, 121, 559

Chary, R. & Elbaz, D. 2001, ApJ, 556, 562

Chu, J. K., Sanders, D. B., Larson, K. L., Mazzarella, J. M., Howell, J. H., Díaz-Santos, T., Xu, K. C., Paladini, R., Schulz, B., Shupe, D., Appleton, P., Armus, L., Billot, N., Chan, B. H. P., Evans, A. S., Fadda, D., Frayer, D. T., Haan, S., Ishida, C. M., Iwasawa, K., Kim, D.-C., Lord, S., Murphy, E., Petric, A., Privon, G. C., Surace, J. A., & Treister, E. 2017, ApJS, 229, 25

Dale, D. A., Cook, D. O., Roussel, H., Turner, J. A., Armus, L., Bolatto, A. D., Boquien, M., Brown, M. J. I., Calzetti, D., De Looze, I., Galametz, M., Gordon, K. D., Groves, B. A., Jarrett, T. H., Helou, G., Herrera-Camus, R., Hinz, J. L., Hunt, L. K., Kennicutt, R. C., Murphy, E. J., Rest, A., Sandstrom, K. M., Smith, J.-D. T., Tabatabaei, F. S., & Wilson, C. D. 2017, ApJ, 837, 90

Fazio, G. G., Hora, J. L., Allen, L. E., Ashby, M. L. N., Barmby, P., Deutsch, L. K., Huang, J.-S., Kleiner, S., Marengo, M., Megeath, S. T., Melnick, G. J., Pahre, M. A., Patten,

B. M., Polizotti, J., Smith, H. A., Taylor, R. S., Wang, Z., Willner, S. P., Hoffmann, W. F., Pipher, J. L., Forrest, W. J., McMurty, C. W., McCreight, C. R., McKelvey, M. E., McMurray, R. E., Koch, D. G., Moseley, S. H., Arendt, R. G., Mentzell, J. E., Marx, C. T., Losch, P., Mayman, P., Eichhorn, W., Krebs, D., Jhabvala, M., Gezari, D. Y., Fixsen, D. J., Flores, J., Shakoorzadeh, K., Jungo, R., Hakun, C., Workman, L., Karpati, G., Kichak, R., Whitley, R., Mann, S., Tollestrup, E. V., Eisenhardt, P., Stern, D., Gorjian, V., Bhattacharya, B., Carey, S., Nelson, B. O., Glaccum, W. J., Lacy, M., Lowrance, P. J., Laine, S., Reach, W. T., Stauffer, J. A., Surace, J. A., Wilson, G., Wright, E. L., Hoffman, A., Domingo, G., & Cohen, M. 2004, ApJS, 154, 10

Griffin, M. J., Abergel, A., Abreu, A., Ade, P. A. R., André, P., Augueres, J.-L., Babbedge, T., Bae, Y., Baillie, T., Baluteau, J.-P., Barlow, M. J., Bendo, G., Benielli, D., Bock, J. J., Bonhomme, P., Brisbin, D., Brockley-Blatt, C., Caldwell, M., Cara, C., Castro-Rodriguez, N., Cerulli, R., Chanial, P., Chen, S., Clark, E., Clements, D. L., Clerc, L., Coker, J., Communal, D., Conversi, L., Cox, P., Crumb, D., Cunningham, C., Daly, F., Davis, G. R., de Antoni, P., Delderfield, J., Devin, N., di Giorgio, A., Didschuns, I., Dohlen, K., Donati, M., Dowell, A., Dowell, C. D., Duband, L., Dumaye, L., Emery, R. J., Ferlet, M., Ferrand, D., Fontignie, J., Fox, M., Franceschini, A., Frerking, M., Fulton, T., Garcia, J., Gastaud, R., Gear, W. K., Glenn, J., Goizel, A., Griffin, D. K., Grundy, T., Guest, S., Guillemet, L., Hargrave, P. C., Harwit, M., Hastings, P., Hatziminaoglou, E., Herman, M., Hinde, B., Hristov, V., Huang, M., Imhof, P., Isaak, K. J., Israelsson, U., Ivison, R. J., Jennings, D., Kiernan, B., King, K. J., Lange, A. E., Latter, W., Laurent, G., Laurent, P., Leeks, S. J., Lellouch, E., Levenson, L., Li, B., Li, J., Lilienthal, J., Lim, T., Liu, S. J., Lu, N., Madden, S., Mainetti, G., Marliani, P., McKay, D., Mercier, K., Molinari, S., Morris, H., Moseley, H., Mulder, J., Mur, M., Naylor, D. A., Nguyen, H., O'Halloran, B., Oliver, S., Olofsson, G., Olofsson, H.-G., Orfei, R., Page, M. J., Pain, I., Panuzzo, P., Papageorgiou, A., Parks, G., Parr-Burman, P., Pearce, A., Pearson, C., Pérez-Fournon, I., Pinsard, F., Pisano, G., Podosek, J., Pohlen, M., Polehampton, E. T., Pouliquen, D., Rigopoulou, D., Rizzo, D., Roseboom, I. G., Roussel, H., Rowan-

Robinson, M., Rownd, B., Saraceno, P., Sauvage, M., Savage, R., Savini, G., Sawyer, E., Scharmberg, C., Schmitt, D., Schneider, N., Schulz, B., Schwartz, A., Shafer, R., Shupe, D. L., Sibthorpe, B., Sidher, S., Smith, A., Smith, A. J., Smith, D., Spencer, L., Stobie, B., Sudiwala, R., Sukhatme, K., Surace, C., Stevens, J. A., Swinyard, B. M., Trichas, M., Tourette, T., Triou, H., Tseng, S., Tucker, C., Turner, A., Vaccari, M., Valtchanov, I., Vigroux, L., Virique, E., Voellmer, G., Walker, H., Ward, R., Waskett, T., Weilert, M., Wesson, R., White, G. J., Whitehouse, N., Wilson, C. D., Winter, B., Woodcraft, A. L., Wright, G. S., Xu, C. K., Zavagno, A., Zemcov, M., Zhang, L., & Zonca, E. 2010, A&A, 518, L3

Jarrett, T. H., Cohen, M., Masci, F., Wright, E., Stern, D., Benford, D., Blain, A., Carey, S., Cutri, R. M., Eisenhardt, P., Lonsdale, C., Mainzer, A., Marsh, K., Padgett, D., Petty, S., Ressler, M., Skrutskie, M., Stanford, S., Surace, J., Tsai, C. W., Wheelock, S., & Yan, D. L. 2011, ApJ, 735, 112

Larson, K. L., Sanders, D. B., Barnes, J. E., Ishida, C. M., Evans, A. S., U, V., Mazzarella, J. M., Kim, D.-C., Privon, G. C., Mirabel, I. F., & Flewelling, H. A. 2016, ApJ, 825, 128

Mould, J. R., Hughes, S. M. G., Stetson, P. B., Gibson, B. K., Huchra, J. P., Freedman, W. L., Kennicutt, Jr., R. C., Bresolin, F., Ferrarese, L., Ford, H. C., Graham, J. A., Han, M., Hoessel, J. G., Illingworth, G. D., Kelson, D. D., Macri, L. M., Madore, B. F., Phelps, R. L., Prosser, C. F., Rawson, D., Saha, A., Sakai, S., Sebo, K. M., Silbermann, N. A., & Turner, A. M. 2000, ApJ, 528, 655

Neugebauer, G., Habing, H. J., van Duinen, R., Aumann, H. H., Baud, B., Beichman, C. A., Beintema, D. A., Boggess, N., Clegg, P. E., de Jong, T., Emerson, J. P., Gautier, T. N., Gillett, F. C., Harris, S., Hauser, M. G., Houck, J. R., Jennings, R. E., Low, F. J., Marsden, P. L., Miley, G., Olnon, F. M., Pottasch, S. R., Raimond, E., Rowan-Robinson, M., Soifer, B. T., Walker, R. G., Wesselius, P. R., & Young, E. 1984, ApJ, 278, L1

Perault, M. 1987, PhD thesis, PhD thesis, Univ. Paris , (1987)

Pilbratt, G. L., Riedinger, J. R., Passvogel, T., Crone, G., Doyle, D., Gageur, U., Heras, A. M., Jewell, C., Metcalfe, L., Ott, S., & Schmidt, M. 2010, A&A, 518, L1

Poglitsch, A., Waelkens, C., Geis, N., Feuchtgruber, H., Vandenbussche, B., Rodriguez, L., Krause, O., Renotte, E., van Hoof, C., Saraceno, P., Cepa, J., Kerschbaum, F., Agnèse, P., Ali, B., Altieri, B., Andreani, P., Augueres, J.-L., Balog, Z., Barl, L., Bauer, O. H., Belbachir, N., Benedettini, M., Billot, N., Boulade, O., Bischof, H., Blommaert, J., Callut, E., Cara, C., Cerulli, R., Cesarsky, D., Contursi, A., Creten, Y., De Meester, W., Doublier, V., Doumayrou, E., Duband, L., Exter, K., Genzel, R., Gillis, J.-M., Grözinger, U., Henning, T., Herreros, J., Huygen, R., Inguscio, M., Jakob, G., Jamar, C., Jean, C., de Jong, J., Katterloher, R., Kiss, C., Klaas, U., Lemke, D., Lutz, D., Madden, S., Marquet, B., Martignac, J., Mazy, A., Merken, P., Montfort, F., Morbidelli, L., Müller, T., Nielbock, M., Okumura, K., Orfei, R., Ottensamer, R., Pezzuto, S., Popesso, P., Putzeys, J., Regibo, S., Reveret, V., Royer, P., Sauvage, M., Schreiber, J., Stegmaier, J., Schmitt, D., Schubert, J., Sturm, E., Thiel, M., Tofani, G., Vavrek, R., Wetzstein, M., Wieprecht, E., & Wiezorrek, E. 2010, A&A, 518, L2

Rieke, G. H., Alonso-Herrero, A., Weiner, B. J., Pérez-González, P. G., Blaylock, M., Donley, J. L., & Marcillac, D. 2009, ApJ, 692, 556

Rieke, G. H., Young, E. T., Engelbracht, C. W., Kelly, D. M., Low, F. J., Haller, E. E., Beeman, J. W., Gordon, K. D., Stansberry, J. A., Misselt, K. A., Cadien, J., Morrison, J. E., Rivlis, G., Latter, W. B., Noriega-Crespo, A., Padgett, D. L., Stapelfeldt, K. R., Hines, D. C., Egami, E., Muzerolle, J., Alonso-Herrero, A., Blaylock, M., Dole, H., Hinz, J. L., Le Floc'h, E., Papovich, C., Pérez-González, P. G., Smith, P. S., Su, K. Y. L., Bennett, L., Frayer, D. T., Henderson, D., Lu, N., Masci, F., Pesenson, M., Rebull, L., Rho, J., Keene, J., Stolovy, S., Wachter, S., Wheaton, W., Werner, M. W., & Richards, P. L. 2004, ApJS, 154, 25

Sanders, D. B., Egami, E., Lipari, S., Mirabel, I. F., & Soifer, B. T. 1995, AJ, 110, 1993

Sanders, D. B., Mazzarella, J. M., Kim, D., Surace, J. A., & Soifer, B. T. 2003, AJ, 126, 1607

Soifer, B. T., Boehmer, L., Neugebauer, G., & Sanders, D. B. 1989, AJ, 98, 766

Soifer, B. T., Sanders, D. B., Madore, B. F., Neugebauer, G., Danielson, G. E., Elias, J. H., Lonsdale, C. J., & Rice, W. L. 1987, ApJ, 320, 238

Soifer, B. T., Sanders, D. B., Neugebauer, G., Danielson, G. E., Lonsdale, C. J., Madore, B. F., & Persson, S. E. 1986, ApJ, 303, L41

Stierwalt, S., Armus, L., Surace, J. A., Inami, H., Petric, A. O., Diaz-Santos, T., Haan, S., Charmandaris, V., Howell, J., Kim, D. C., Marshall, J., Mazzarella, J. M., Spoon, H. W. W., Veilleux, S., Evans, A., Sanders, D. B., Appleton, P., Bothun, G., Bridge, C. R., Chan, B., Frayer, D., Iwasawa, K., Kewley, L. J., Lord, S., Madore, B. F., Melbourne, J. E., Murphy, E. J., Rich, J. A., Schulz, B., Sturm, E., Vavilkin, T., & Xu, K. 2013, ApJS, 206, 1

U, V., Sanders, D. B., Mazzarella, J. M., Evans, A. S., Howell, J. H., Surace, J. A., Armus, L., Iwasawa, K., Kim, D.-C., Casey, C. M., Vavilkin, T., Dufault, M., Larson, K. L., Barnes, J. E., Chan, B. H. P., Frayer, D. T., Haan, S., Inami, H., Ishida, C. M., Kartaltepe, J. S., Melbourne, J. L., & Petric, A. O. 2012, ApJS, 203, 9

Werner, M. W., Roellig, T. L., Low, F. J., Rieke, G. H., Rieke, M., Hoffmann, W. F., Young, E., Houck, J. R., Brandl, B., Fazio, G. G., Hora, J. L., Gehrz, R. D., Helou, G., Soifer, B. T., Stauffer, J., Keene, J., Eisenhardt, P., Gallagher, D., Gautier, T. N., Irace, W., Lawrence, C. R., Simmons, L., Van Cleve, J. E., Jura, M., Wright, E. L., & Cruikshank, D. P. 2004, ApJS, 154, 1

Wright, E. L., Eisenhardt, P. R. M., Mainzer, A. K., Ressler, M. E., Cutri, R. M., Jarrett, T., Kirkpatrick, J. D., Padgett, D., McMillan, R. S., Skrutskie, M., Stanford, S. A., Cohen, M., Walker, R. G., Mather, J. C., Leisawitz, D., Gautier, III, T. N., McLean, I.,

Benford, D., Lonsdale, C. J., Blain, A., Mendez, B., Irace, W. R., Duval, V., Liu, F., Royer, D., Heinrichsen, I., Howard, J., Shannon, M., Kendall, M., Walsh, A. L., Larsen, M., Cardon, J. G., Schick, S., Schwalm, M., Abid, M., Fabinsky, B., Naes, L., & Tsai, C.-W. 2010, AJ, 140, 1868

Chapter 4

Spatial Decomposition of the Radio-Infrared Correlation in Luminous Infrared Galaxies

Note: *This chapter to be submitted to the Astrophysical Journal as Chu, J. K. and Sanders, D. B.*

Abstract

We present an analysis of the radio-infrared correlation in 85 galaxies from the Great Observatories All-Sky LIRG Survey (GOALS) sample. Previous studies have shown that a tight linear radio-infrared correlation exists in normal nearby galaxies, where high angular resolution radio maps were found to spatially correlate with the distribution of far-infrared luminosity within a galaxy. Since the GOALS sample is composed of the most infrared-luminous interacting galaxies, we use this sample to characterize the behavior of the radio-infrared correlation in conditions not found in normal galaxies. By utilizing the superior $6''$ beam size of *Spitzer*'s MIPS 24 μm imaging band and the VLA B array 20 cm atlases from Condon et al. (1990 and 1996), we calculate the MIR to radio flux ratio q_{24}, for the nuclear component as well as the whole galaxy. We find that on average the nuclear q_{24} value is smaller than the q_{24} over the entire galaxy by a factor of 81% due to an enhancement of the radio flux in the nucleus. Furthermore galaxies with a total infrared luminosity greater than $10^{11.6} L_{\odot}$ show an even larger discrepancy of up to an order of magnitude between the nuclear and total q_{24} values. This is a strong indication that these galaxies contain

powerful AGN nuclei that severely depress their nuclear q_{24} ratio, and challenges previous claims that radio maps are a suitable proxy for unavailable high-resolution infrared maps.

4.1 Introduction

The well-established radio-infrared correlation was first observed in very nearby star forming galaxies, and subsequently shown to hold over five orders of magnitude in luminosity from nearby galaxies (such as normal spirals, starbursts, dwarf galaxies, and Seyfert galaxies; Condon 1992; Yun et al. 2001; Bell 2003) to high redshift objects (Appleton et al. 2004; Seymour et al. 2009). The radio-infrared correlation q is essentially a (positive) linear relation obtained by dividing a galaxy's far-infrared (FIR) luminosity by its radio continuum flux. An investigation by Walterbos & Schwering (1987) of M31 showed that, when comparing *IRAS* 60 μm and 100 μm maps to 11 cm radio maps, the spatial distribution of warm dust best matches that of the radio continuum. A number of other galaxies exhibiting similar spatial correlations were later found by Beck & Golla (1988), who investigated the radial distributions of the radio and FIR emission in these systems.

A simple and straightforward explanation of this relation is that the observed correlation is an indicator of the recent star formation history in a galaxy. This would provide the mechanism to both heat interstellar dust from hot massive stars, as well as generate relativistic electrons and accelerate cosmic rays from subsequent supernovae. The dust would cool off by re-radiating its energy in the FIR regime of the electromagnetic spectrum, while a thermal contribution from dusty H II regions plus non-thermal relativistic electrons and cosmic rays would emit synchrotron radiation in the radio continuum.

Its most striking feature however, is how tightly correlated and linear the relation appears at least superficially over a wide range of objects and conditions. Hence further studies of it were geared towards refining the tightness of the correlation, such as Condon et al. (1991b) on luminous infrared galaxies and Roy et al. (1992) on Seyfert 2 galaxies. Wunderlich & Klein (1988) mentioned that temporal effects are one possible mechanism in

which the radio-infrared correlation may deviate from a "tight" linear correlation. There are two possible evolutionary paths: first that the number of hot OB stars has significantly decreased at the end of a starburst while the relativistic electrons resulting from supernovae would still be stored in the interstellar medium (ISM), since the lifetime of the non-thermal radio emission is considerably longer than that of the FIR radiation. The second possibility being the reverse, in which the starburst was so recent that the there is a time lag between the onset of thermal FIR emission and the non-thermal radio emission due to the lack of supernovae. However Wunderlich et al. (1987) found that if they considered galaxies with dust temperatures above and below $T_d = 30$K, which corresponds to high and low star formation rates (SFR) respectively, there was only a small difference in the correlation.

Another measure of the SFR can be obtained by observing a galaxy's CO emission, since it is a tracer of H_2 molecular gas. This would also imply a tight correlation between the CO luminosity with the FIR luminosity. This was in fact observed and successfully detected by Young et al. (1984) and Sanders & Mirabel (1985), although they found the dispersion to be much larger than the spread observed in the radio-infrared correlation. However this may not be related to how well star formation correlates with FIR luminosity, but instead it may be due to the fact that CO is not a completely reliable indicator of star formation. Instead the high dispersion in the CO-FIR relation may be a result of varying conditions and optical depth effects rather than anything intrinsic about the SFR.

For galaxies that noticeably deviate from the "tight" radio-infrared correlation, different analyses were undertaken to linearize them, such as Roy et al. (1992) who attempted to linearize a sample of 9 Seyfert 2 galaxies by subtracting the core radio component from the total radio emission. They believed that Seyfert 2 galaxies had normal star forming disks with a radio-loud active galactic nucleus (AGN) embedded in the nucleus. Condon et al. (1991a) also attempted to produce a tighter correlation in spirals by introducing a two-component disk model: a radio-loud component containing young massive stars that heats the warm dust and the cool cirrus dust, plus an older population of stars that is radio quiet.

Recently, studies such as Dumas et al. (2011) have concentrated mostly on lower luminosity galaxies. They found that the radio-infrared correlation varied depending on the location in the nearby spiral M51. Particularly they show that the 24 μm and 20 cm emission was linear within the spiral arms and globally over the entire galaxy, but was sub-linear in the interarm regions and over-linear in the central 3.5 kpc. Hughes et al. (2006) obtained slightly different results in the Large Magellanic Cloud (LMC), and found that the radio-infrared correlation was most robust in regions where thermal radio emission dominates over the non-thermal component. Interestingly they found that the overall correlation in the LMC is non-linear: In bright star forming regions the radio power appears to increase faster than the FIR component (sub-linear), whereas a steeper (super-linear) relation applies more generally across the LMC.

However unlike M51 and the LMC, bright infrared galaxies are particularly interesting in context of the radio-infrared correlation, which is the focus of this paper. Their high infrared (IR) luminosities provide an interesting environment to examine how the radio-infrared correlation behaves in these objects, which are formed from the violent mergers and interactions of two or more galaxies. Luminous infrared galaxies (LIRGs) are galaxies with a FIR luminosity of $10^{11} L_{\odot} \leq L_{\rm IR} < 10^{12} L_{\odot}$, while ultra-luminous infrared galaxies (ULIRGs) emit anywhere from $10^{12} L_{\odot} \leq L_{\rm IR} < 10^{13} L_{\odot}$. The *Infrared Astronomical Satellite* (*IRAS*, Neugebauer et al. 1984) found tens of thousands of these objects in the infrared, but because it could not resolve them, it was impossible to map the spatial distribution of the infrared flux. However with the launch of the *Spitzer Space Telescope*, we now have mid-infrared (MIR) maps of these objects with a resolution of several arcseconds, a huge improvement over the *IRAS* resolution of several arcminutes. In this paper we examine the correlation of infrared to radio flux over different spatial scales, and compare our results to standard optical spectral classifications (BPT diagrams, Baldwin et al. 1981; Veilleux & Osterbrock 1987; Kewley et al. 2001; Kauffmann et al. 2003; Kewley et al. 2006). In §2 we describe our sample and data reduction, and in §3 we discuss our data analysis process. §4 will cover our main results, and in §5 we interpret our results.

Throughout this paper we adopt the Benchmark Model for cosmology, with $H_0 = 72$ km sec^{-1} Mpc^{-1}, $\Omega_M = 0.27$, and $\Omega_\Lambda = 0.73$.

4.2 Sample Selection and Data Reduction

4.2.1 The GOALS Sample

The Great Observatories All-Sky LIRG Survey combines both imaging and spectroscopic data for a complete set of 201 LIRGs and ULIRGs selected from the *IRAS* Revised Bright Galaxy Sample (RBGS, Sanders et al. 2003). The 629 RBGS galaxies are a complete sample of extragalactic sources with an *IRAS* 60 μm flux above 5.24 Jy, covering the entire sky above and below a Galactic latitude of $|b| > 5°$. The spatial constraint is imposed to reduce possible confusion with foreground infrared dust emission from within the Milky Way. Furthermore the RBGS is a complete sample spanning the full spectrum of galaxy types, from low-luminosity ($L < 10^{10.5} L_\odot$) isolated gas-rich spirals to violently interacting galaxy pairs among the LIRGs and ULIRGs, as well as including numerous galaxies optically classified as Seyfert 1, Seyfert 2, low ionization narrow emission-line region (LINER), composite (both AGN and starbursts present) and starburst (H II) galaxies. The median redshift of the sample is about 0.008, with a maximum redshift of 0.088 (the ULIRG Mrk 231).

Within the RBGS sample, a total of 179 LIRGs and 22 ULIRGs (i.e., galaxies with $L \geq 10^{11} L_\odot$) were selected for the GOALS sample (Armus et al. 2009), which represents a statistically complete local sample of infrared-luminous galaxies that serves as an analog to higher redshift systems (i.e., Cowie et al. 2004). Therefore these objects represent a complete picture of galaxy evolution and the generation of FIR radiation throughout all the major interaction stages that we can observe. This sample was chosen because these galaxies have been imaged in almost every wavelength, including VLA 20 cm (Condon et al. 1990 and 1996), CO and HCN (Sanders et al. 1991), sub-millimeter images (Dunne et al. 2000), near-infrared images from 2MASS (Skrutskie et al. 2006), optical and K-band imaging

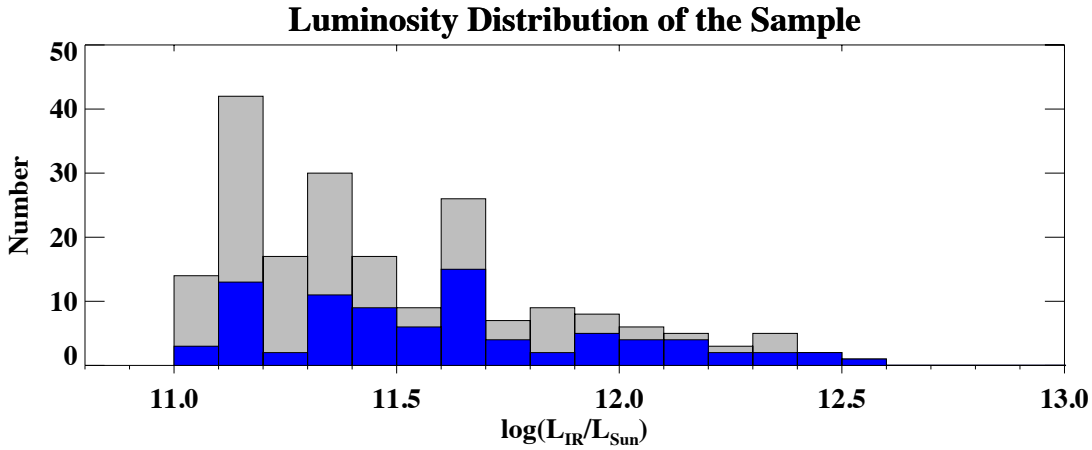

Figure 4.1 The luminosity distribution of our sample in blue over the entire GOALS sample (grey). Our sample covers the entire luminosity range between $10^{11} L_{\odot}$ to $10^{12.5} L_{\odot}$, i.e., all of the LIRGs and ULIRGs.

(Ishida 2004), as well as space-based observations from *Spitzer Space Telescope* (IRAC and MIPS), *Hubble Space Telescope* (WFPC2, ACS, NICMOS), *GALEX* (NUV and FUV), and *Chandra X-ray Observatory* (ACIS). Out of these 201 galaxies, we further selected a subset of 85 sources (42%) that were observed with the VLA, since the southern limit of observation is at a declination of about $-45°$. A comparison of the luminosity distribution of our 85 galaxies (hereafter referred to as "our sample") to that of GOALS in Figure 4.1 reveals that our sample still spans the full luminosity range and is not biased in any way. Thus our sample should be a reliable representation of the full GOALS sample since these galaxies do not have any preferential properties in any one part of the sky.

4.2.2 Data Reduction

Spitzer MIPS 24 μm Maps

The Multiband Imaging Photometer for *Spitzer* (MIPS, Rieke et al. 2004) observations for 176 of the GOALS sources were obtained between October 2004 and September 2005 through the Cycle 1 General Observing (GO) program (PID #3672). The remaining 27

targets were obtained through the *Spitzer* Reserved Observation Catalog (ROC), and are now included in the public *Spitzer* archive.

Each observation consisted of multiple 3-4 second integrations to insure adequate redundancy in case of cosmic ray hits or bad pixels. In addition 2-3 mapping cycles were used to correct for transient effects in the detectors. For small sources with D $< 2'$, small-field photometry Astronomical Observation Requests (AORs) were used along with the minimum 3 second exposure to obtain high signal-to-noise data for very bright galaxies. This is crucial for our study since a saturation of the nucleus can only provide a lower limit on the 24 μm flux. The net on-target integration time is 48 seconds per pointing, with a point source sensitivity of approximately 0.5 mJy. Sources or systems larger than $2'$ were observed in large-scale photometry mode with one to a few individual pointings.

The GOALS team performed all of the data reduction and post-processing. The Basic Calibrated Data (BCD) pipeline products tend to exhibit artifacts due to very bright galaxy nuclei for many of the targets. Some of these features include a weak "jailbars" effect in the BCDs, which reflects different readout gains rather than saturation. For strong "jailbars" due to saturation the frames were not included in the final mosaic. In some cases dark latents (1-2% depressions in responsitivity) are visible for sources brighter than approximately 18 Jy. These two effects were corrected where possible by using the self-calibration procedure provided by the Spitzer Science Center (SSC). Residual gradients on the 1-2% level were also present in the 24 μm images for large mosaics where the MOPEX routine `overlap` was used. In addition, optical distortion can induce variations of $2 - 10\%$ across the frame in some cases. The post-BCD pipeline program MOPEX was used to correct this problem. The final 24 μm mosaics were then assembled by the `overlap` routine. Furthermore both datasets from the GO and ROC were processed identically. More information on the *Spitzer* MIPS data reduction can be found in Mazzarella et al. (in preparation) and in the MIPS Instrument Handbook.

The absolute calibration of MIPS is in fact more uncertain than the actual measurement uncertainties. For 24 μm this uncertainty is approximately 5% (MIPS Instrument

Handbook). Comparisons of the total fluxes obtained in this paper with the fluxes reported by Mazzarella et al. (in preparation) do indeed vary by a little less than 5%. The astrometric solutions were obtained by matching foreground stars and converted into the world coordinate system (WCS), and have an approximate 1σ uncertainty of about $0\farcs7$ (Mazzarella et al. in preparation).

VLA 20 cm Maps

Condon et al. (1990, hereafter "C90") mapped 313 of the RBGS sources at 1.49 GHz (20.1 cm) in the A, B, and C array configurations between November 1987 and February 1989. The remaining 187 sources observable by the VLA were mapped in 1993 using the B, BnC, and C array at 1.425 GHz (21 cm), a frequency that suffers less from interference than does 1.49 GHz (Condon et al. 1996, hereafter "C96").

For our analysis we chose the B array configuration since it gives us a beam size of $5'' - 8''$, which is similar to the $6''$ beam size of our 24 μm data. In addition the B array is more sensitive to diffuse radio emission from star-forming galaxies than the A array is, which has a beam size of $1\farcs5$-$2\farcs8$. However we do have one object (VV 340a) for which we only have the A array data for, and it has a beam size of $1\farcs5$. The variation in beam sizes for a particular array arises from the fact that different observation declinations produce different sized elliptical beam sizes, however the data were first restored to a circular Gaussian shape before analysis.

Each observation from C90 typically consisted of two "snapshot" scans about 4 minutes long, spaced by approximately 2 hours to improve the (u, v) coverage. A single "snapshot" scan of about 3 minutes was used for the 1.425 GHz data in C96. For both datasets C90 and C96 used 3C 38 and 3C 286 were used as amplitude calibrators, and nearby unresolved sources were monitored for phase calibrations. The sources were then identified in the primary beam from the calibrated wide-field (u, v) data and self-calibrated. Finally the data were CLEANed, residual fringes were clipped, and the final maps were restored with circular Gaussian beams and corrected for primary-beam attenuation (Condon et al. 1990).

The RMS map noise σ_n is between 0.1-0.2 mJy per beam solid angle Ω_b, which implies that the noise contribution to the error in S is approximately $\sigma_n\sqrt{\Omega/\Omega_b}$, where Ω is the solid angle of the source. Thus the approximate RMS confusion error in S for a source in our sample should be $\sigma_S \approx \sqrt{270\Omega_b S}$ mJy where Ω_b is in steradians (Condon 1987). For a beam size of about $6''$ and a representative source flux density of roughly 50 mJy the flux errors are around 2 μJy. The intensity-proportion calibration errors are no more than 5%. As a comparison the fluxes obtained in this paper are on average within 5% of the fluxes reported in C90 and C96. Finally the radio position errors for all but the most extended sources are less than $1''$, on par with the astrometric uncertainty from MIPS.

4.3 Data Analysis

First we precessed the radio data from B1950 into J2000 coordinates using the `jprecess` routine, assuming a proper motion of exactly zero. Since we do not know *a priori* if the radio and infrared peaks would coincide, we used the WCS information from both datasets to align the maps. In fact we see that in most cases the peaks do coincide within the reported astrometric errors. Our next step was to pinpoint the center of the galaxy using the radio data. Since 24 μm radiation is still susceptible to absorption (i.e., from silicates) we chose to not use the infrared peak in each galaxy. A good example of this can be seen in Arp 220 (Figure 4.2, No. 64), where there are two apparent peaks in the 24 μm map. The radio peak on the other hand has a very low optical depth and can be taken as the center of the galaxy.

To find the center, we first obtained rough coordinates for each galaxy through the online catalog Vizier, and selected a region encompassing $\pm 2'$ in RA and declination from the coordinate. We then ran a routine to automatically locate the radio peak within the selected $4' \times 4'$ frame. Unfortunately we were not able to automatically identify the correct center for about 25% of our sample, which required us to manually select the radio peak for these galaxies. The radio peaks are plotted in Figure 4.2 as red crosses, and we also estimate

its uncertainty to be less than $1''$. This implies a maximum alignment error of about $1''.2$ between the MIPS and VLA maps, assuming their errors are random and independent. For galaxies with two distinct components, we chose the stronger peak as the main galaxy.

We then plotted both the radio (blue) and infrared (black) contour maps together in Figure 4.2 and confirmed that the radio peaks were close to the infrared peaks for all the galaxies. We chose to plot 20 contour levels divided equally between the maximum and minimum values in each respective map. We note that there were significant negative contour levels found in the radio data, which are indicated as dotted curves on each map. These artifacts are due to post-processing effects and self-calibration procedures. In addition the beam sizes for both the infrared (black) and radio (blue) maps are plotted in the upper left side for comparison. The MIPS 24 μm beam size is always fixed at $6''$, while the VLA beam size can be 5–$8''$. Note that VV 340a was only observed with the A array, and has a beam size of $1''.5$.

We then performed fixed circular aperture photometry centered on the radio peak for both the radio and infrared data. We chose the largest beam size for each galaxy to be the smallest flux extraction aperture. Since our 24 μm data is limited to $6''$, the smallest apertures were either $6''$, $7''$, or $8''$ in diameter, depending on the beam size of the radio data. We then proceeded to measure the flux in an aperture $9''$ in diameter, with each subsequent aperture being $3''$ larger (in diameter) than the previous. The maximum aperture size was determined by the size of the galaxy, but small enough to avoid contamination from companion galaxies. Note that for each aperture, we apply the appropriate aperture corrections and measure the entire flux falling within that aperture and not the flux within the annulus. To be sure our flux measurements are not affected by errors in the WCS alignment, we performed a Monte Carlo simulation by randomly offsetting the aperture center within $1''.2$ of the radio peak, and found the fluxes to vary by less than $\sim$5%.

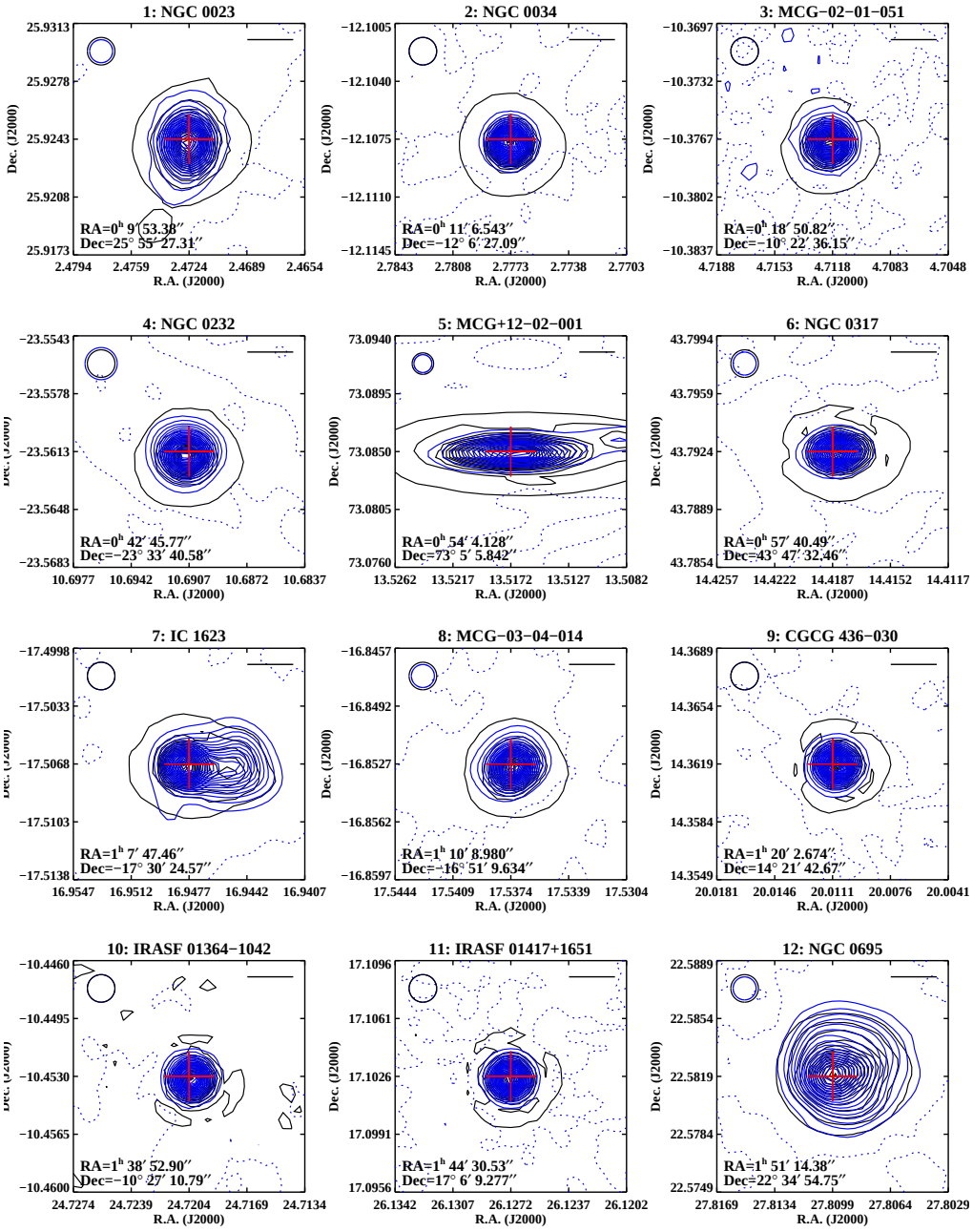

Figure 4.2 On the following pages we show in order of increasing RA the MIPS 24 μm and VLA 20 cm contours plotted in black and blue, respectively. The center of each galaxy as determined by the radio peak is indicated by the red cross, and in cases where there are two distinct components, we select the stronger radio peak to be the center. Negative radio contours are indicated by the dotted curves. Beam sizes for both the infrared and radio maps are shown in the upper left and have the same color scheme. Finally the 10″ scale bar is indicated in the upper right. On all of the plots north is up and east is to the left. Note that NGC 5653 has several vertical lines due to image artifacts that do not affect the photometry.

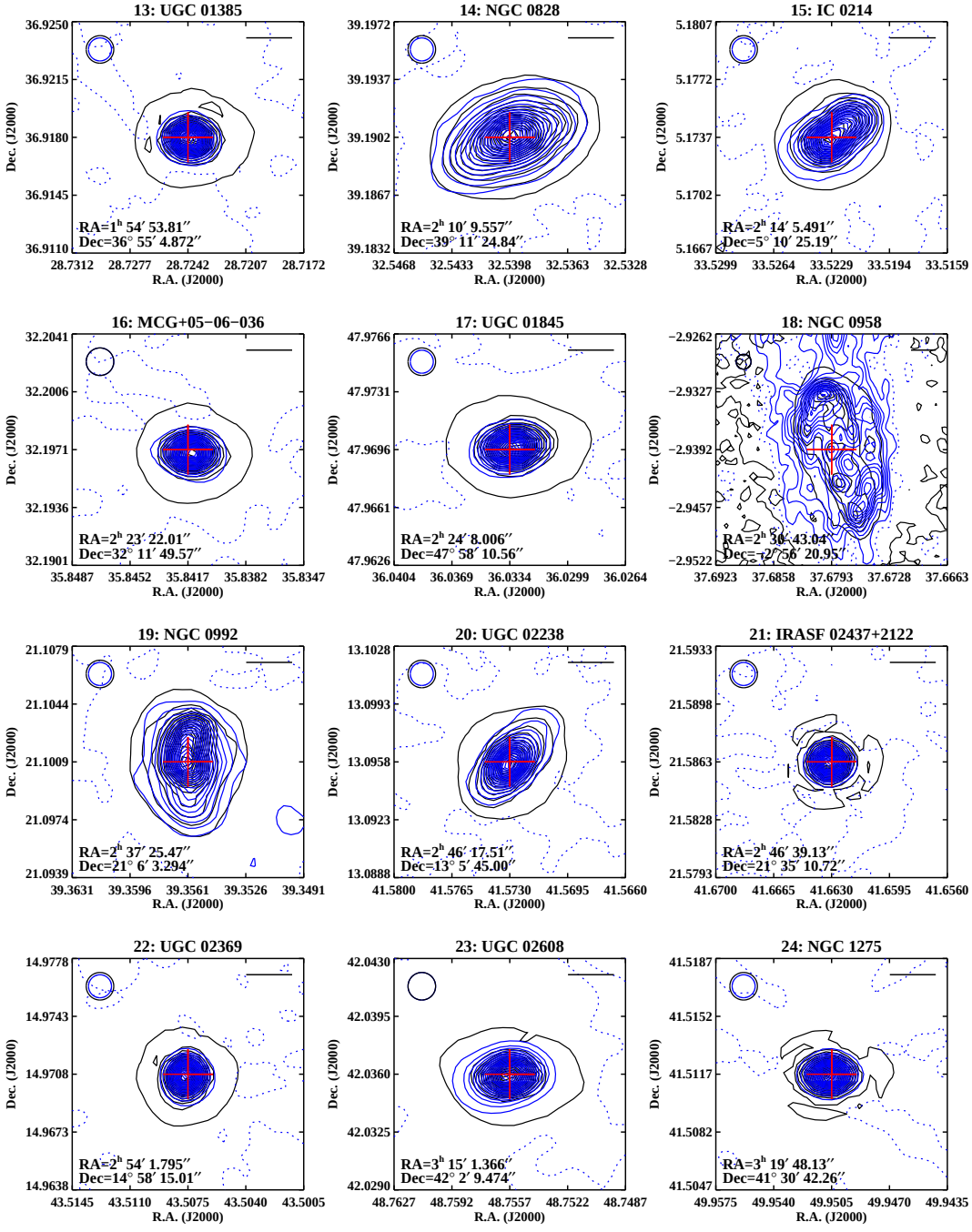

Figure 4.2 continued (page 2 of 7).

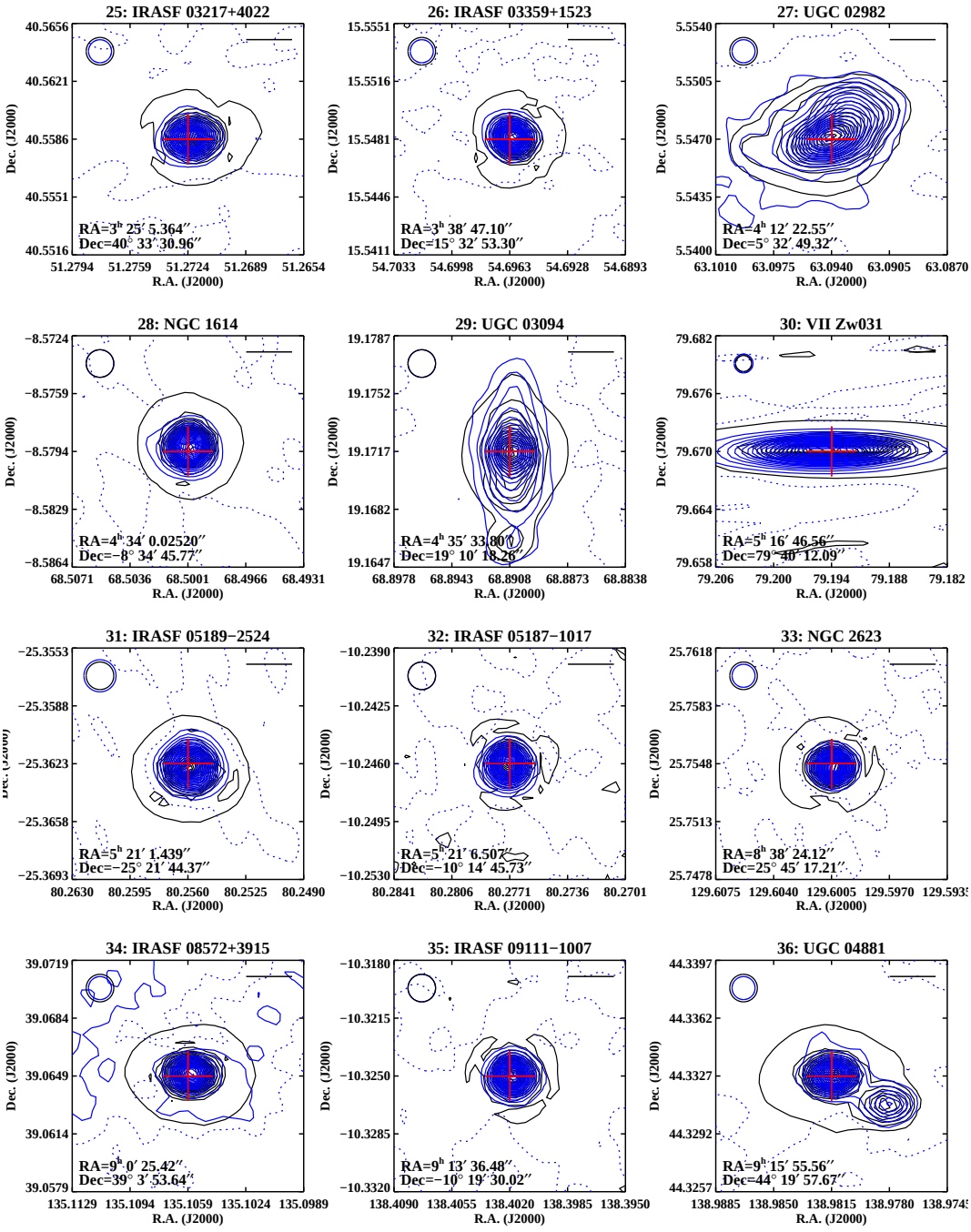

Figure 4.2 continued (page 3 of 7).

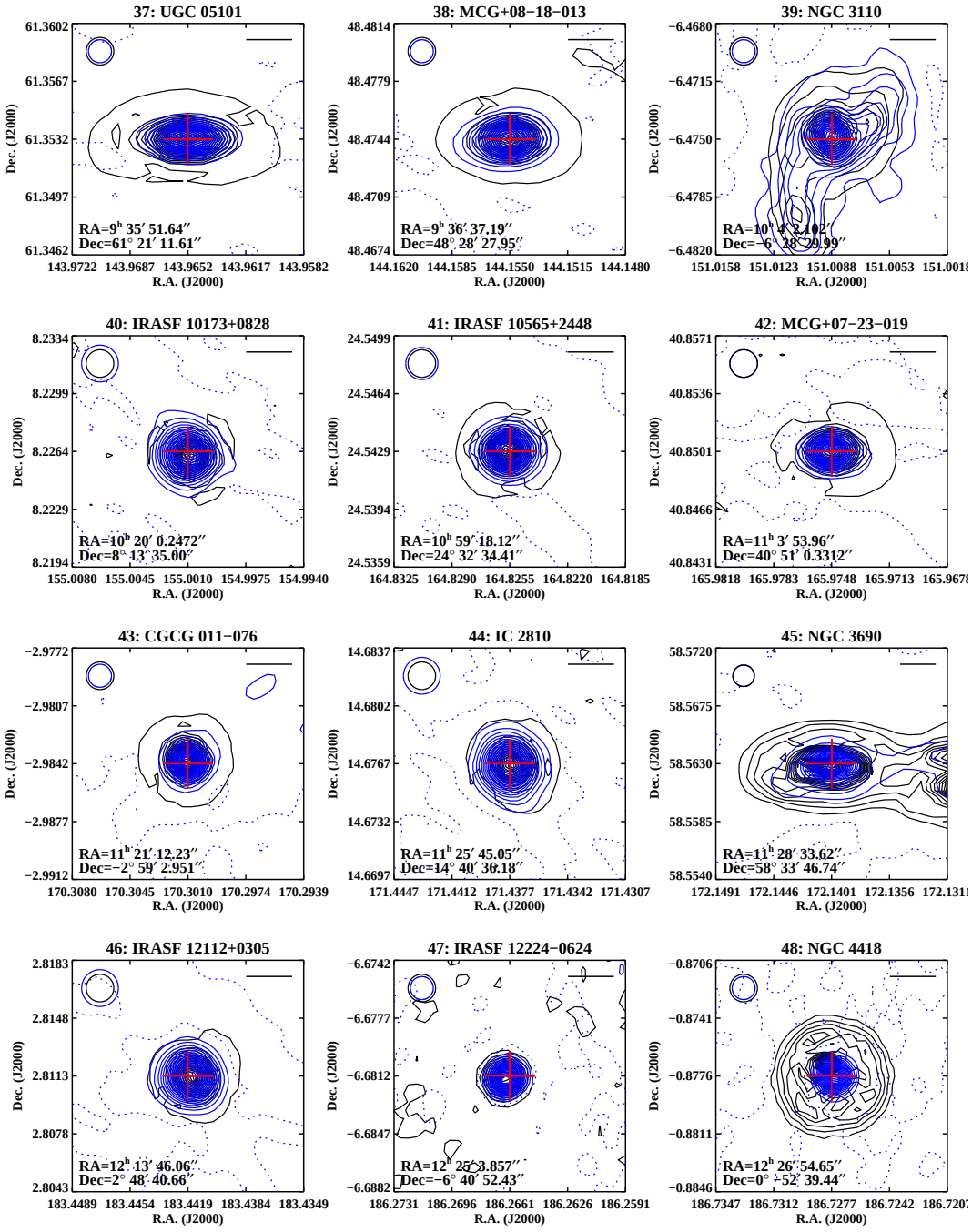

Figure 4.2 continued (page 4 of 7).

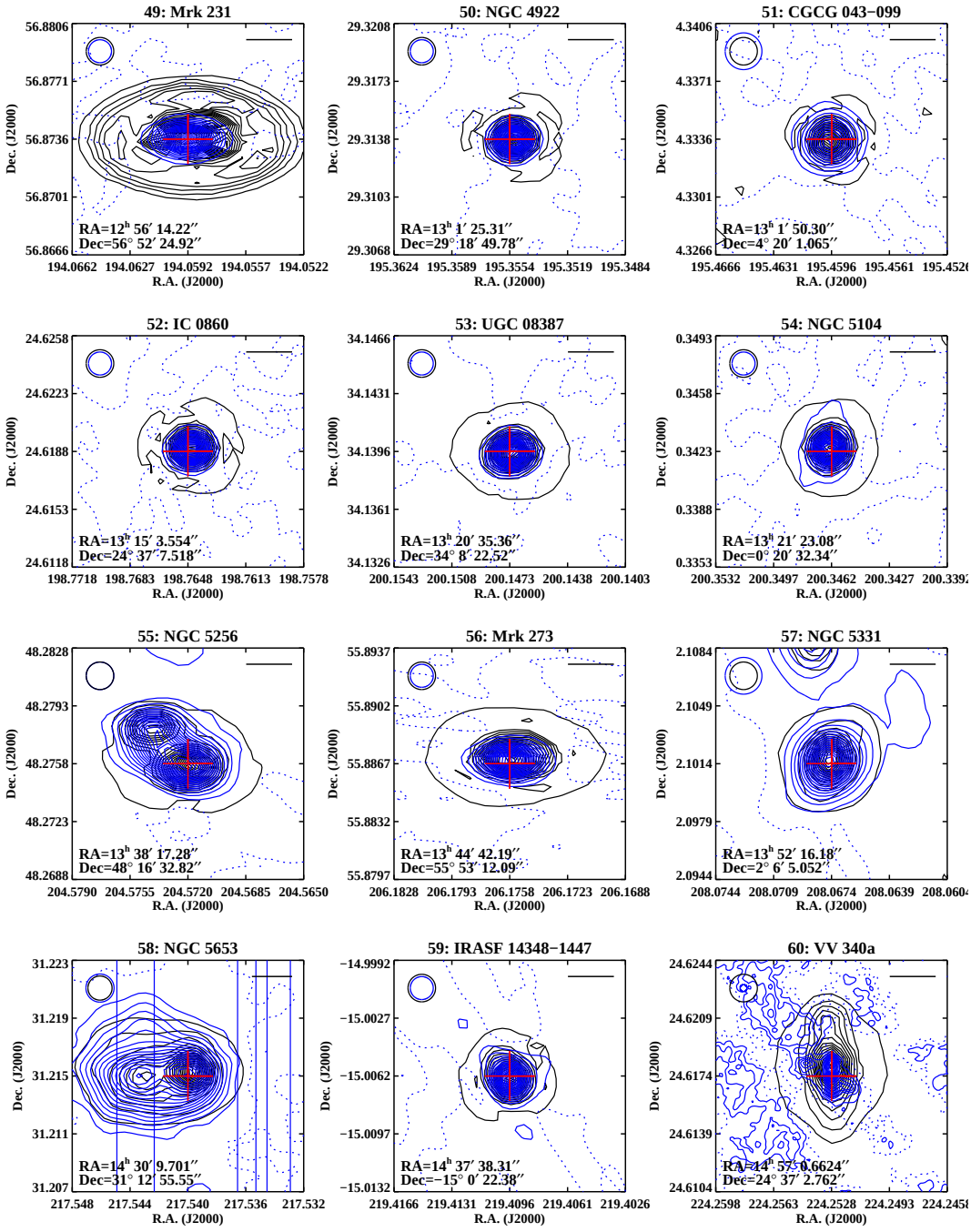

Figure 4.2 continued (page 5 of 7).

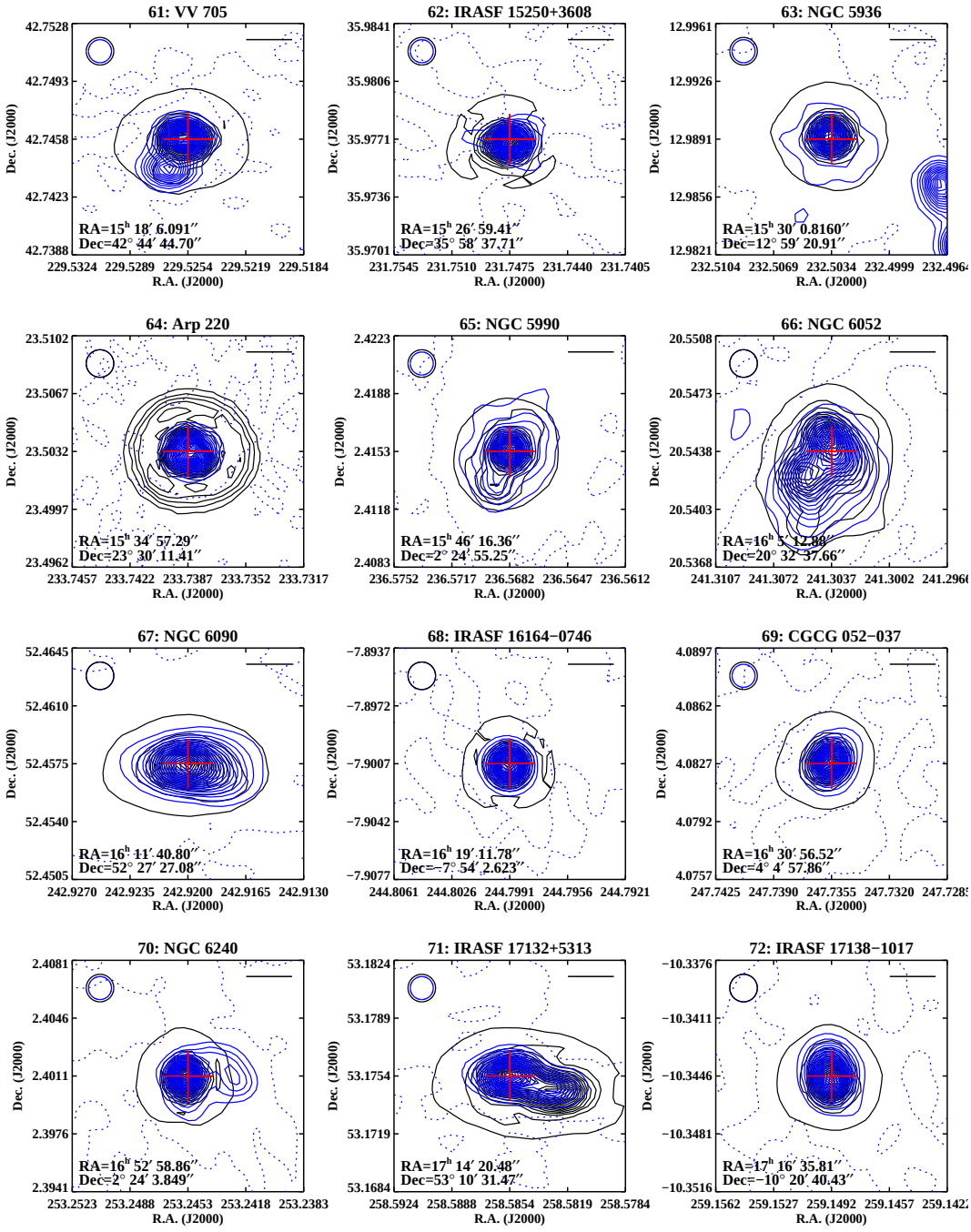

Figure 4.2 continued (page 6 of 7).

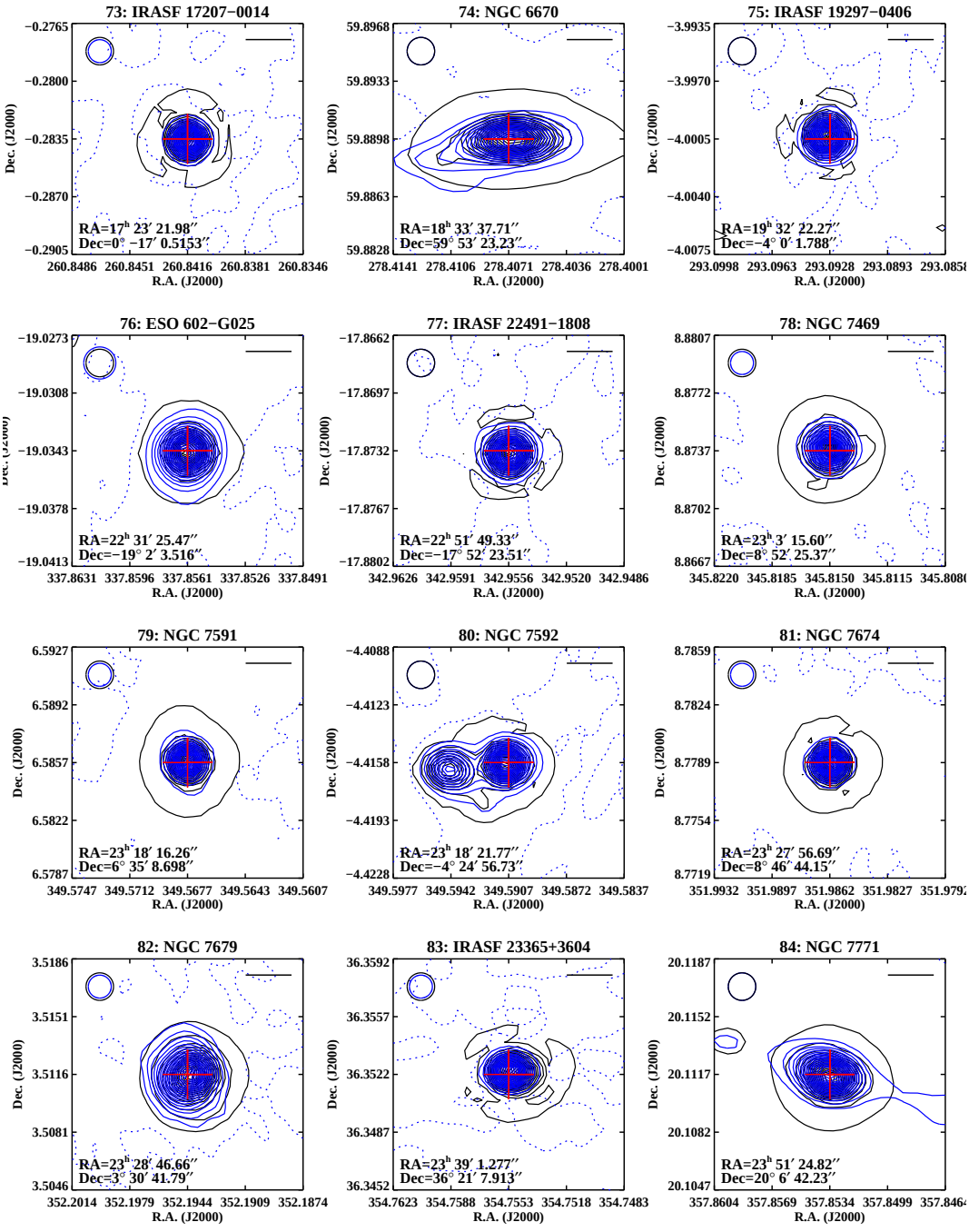

Figure 4.2 continued (page 7 of 7).

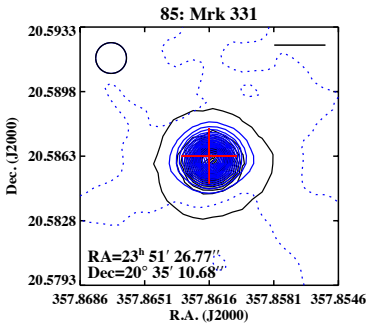

Figure 4.2 continued.

Using these measurements we constructed the curve of growth for each galaxy, shown in Figure 4.3. Following the same convention as in Figure 4.2, the infrared data is plotted in black while the radio data is in blue. As one would expect the measured flux is lower at small diameters, while at large diameters the flux corresponds to the total flux from the galaxy. Since the radio data contained some significant negative flux contours, we terminated the flux measurements when the background noise started to dominate. For a few galaxies such as IRAS F12224-0624 we could not get very many points due to a concentrated radio core with negative contour levels very close to the source (cf. Figure 4.2, No. 47). Out of our entire sample only 5 galaxies have radio curves of growth with 4 or less points (corresponding to 15″in diameter), however all galaxies were measured out to at least 12″. In Table 4.1 we present our full sample with the coordinates of the galaxy center, the infrared and radio fluxes, and the VLA beam sizes.

In addition to the measured infrared and radio fluxes, we also plot the flux ratio

$$q_{24}(D) \equiv \frac{F_{24\mu\mathrm{m}}(D)}{F_{20\mathrm{cm}}(D)} \tag{4.1}$$

for each aperture diameter D in green. We already see that $q_{24}(D)$ can vary substantially depending on the galaxy. It is interesting to note that $q_{24}(D)$ for Mrk 231 (Figure 4.3, No. 49), the brightest galaxy in our sample at $10^{12.51} L_{\odot}$, changes by a whole order of magnitude. Another interesting object is NGC 1275 (Figure 4.3, No. 24) , otherwise known

Table 4.1 Radio and Infrared Fluxes

#	GOALS Name	RA (J2000)	Dec. (J2000)	$F(24\ \mu m)$	$F(20\ cm)$	L_{IR}	VLA Beam Size	Optical Classification
—	—	HH MM SS	DD MM SS	mJy	mJy	$\log(L_{IR}/L_{\odot})$	$''$	—
(1)	(2)	(3)	(4)	(5)	(6)	(7)	(8)	(9)
1	NGC 0023	00 09 53.4	+25 55 27.3	828.7	57.9	11.05	5	C
2	NGC 0034	00 11 06.5	–12 06 27.1	1756.4	57.1	11.44	6	S2
3	MCG-02-01-051	00 18 50.8	–10 22 36.1	975.0	34.3	11.87	6	H
4	NGC 0232	00 42 45.8	–23 33 40.6	811.6	53.1	11.30	7	C
5	MCG+12-02-001	00 54 04.1	+73 05 05.8	2715.8	52.5	11.44	5	U
6	NGC 0317	00 57 40.5	+43 47 32.5	800.3	58.8	11.11	5	U
7	IC 1623	01 07 47.5	–17 30 24.6	2832.0	214.0	11.65	6	H
8	MCG-03-04-014	01 10 09.0	–16 51 09.6	698.9	61.5	11.63	6	C
9	CGCG 436-030	01 20 02.7	+14 21 42.7	1172.5	49.3	11.63	6	H
10	IRASF 01364-1042	01 38 52.9	–10 27 10.8	242.8	18.9	11.76	6	L
11	IRASF 01417+1651	01 44 30.5	+17 06 09.3	730.1	41.6	11.56	6	H
12	NGC 0695	01 51 14.4	+22 34 54.8	677.0	100.4	11.63	5	H
13	UGC 01385	01 54 53.8	+36 55 04.9	754.9	19.1	10.99	5	C
14	NGC 0828	02 10 09.6	+39 11 24.8	839.3	107.7	11.31	5	U
15	IC 0214	02 14 05.5	+05 10 25.2	497.9	43.2	11.37	5	U
16	MCG+05-06-036	02 23 22.0	+32 11 49.6	491.1	34.5	11.59	5	U
17	UGC 01845	02 24 08.0	+47 58 10.6	829.4	62.6	11.07	5	U
18	NGC 0958	02 30 43.0	–02 56 21.0	497.6	54.1	11.17	6	H
19	NGC 0992	02 37 25.5	+21 06 03.3	1036.3	62.4	11.02	5	U
20	UGC 02238	02 46 17.5	+13 05 45.0	491.3	60.7	11.26	5	C
21	IRASF 02437+2122	02 46 39.1	+21 35 10.7	433.3	15.2	11.11	5	S2
22	UGC 02369	02 54 01.8	+14 58 15.0	1086.5	55.0	11.60	5	C
23	UGC 02608	03 15 01.4	+42 02 09.5	1153.4	105.6	11.35	6	U
24	NGC 1275	03 19 48.1	+41 30 42.3	3043.3	24246.6	11.20	5	U
25	IRASF 03217+4022	03 25 05.4	+40 33 31.0	646.5	35.7	11.28	5	U
26	IRASF 03359+1523	03 38 47.1	+15 32 53.3	402.6	21.3	11.47	5	H
27	UGC 02982	04 12 22.6	+05 32 49.3	595.7	80.6	11.13	5	H
28	NGC 1614	04 34 00.0	–08 34 45.8	6165.4	128.6	11.60	6	C
29	UGC 03094	04 35 33.8	+19 10 18.3	597.2	80.2	11.35	6	U
30	VII Zw031	05 16 46.6	+79 40 12.1	469.7	41.5	11.94	7	U

continued on the next page

Table 4.1. (continued) Radio and Infrared Fluxes

#	GOALS Name	RA (J2000)	Dec. (J2000)	$F(24\ \mu m)$	$F(20\ cm)$	L_{IR}	VLA Beam Size	Optical Classification
—	—	HH MM SS	DD MM SS	mJy	mJy	$\log(L_{IR}/L_{\odot})$	$''$	—
(1)	(2)	(3)	(4)	(5)	(6)	(7)	(8)	(9)
31	IRASF 05189-2524	05 21 01.4	–25 21 44.4	2380.1	27.8	12.11	7	S2
32	IRASF 05187-1017	05 21 06.5	–10 14 45.7	142.8	30.1	11.23	6	L
33	NGC 2623	08 38 24.1	+25 45 17.2	1324.3	91.1	11.54	5	L
34	IRASF 08572+3915	09 00 25.4	+39 03 53.6	1337.0	9.2	12.10	5	C
35	IRASF 09111-1007	09 13 36.5	–10 19 30.0	303.9	30.7	12.00	6	U
36	UGC 04881	09 15 55.6	+44 19 57.7	404.9	40.3	11.69	5	C
37	UGC 05101	09 35 51.6	+61 21 11.6	759.2	151.9	11.95	5	S2
38	MCG+08-18-012	09 36 37.2	+48 28 27.9	531.1	35.6	11.28	6	C
39	NGC 3110	10 04 02.1	–06 28 30.0	989.5	111.7	11.31	5	H
40	IRASF 10173+0828	10 20 00.2	+08 13 35.0	250.2	10.7	11.80	8	U
41	IRASF 10565+2448	10 59 18.1	+24 32 34.4	925.1	56.0	12.02	7	C
42	MCG+07-23-019	11 03 54.0	+40 51 00.3	243.8	24.2	11.61	5	U
43	CGCG 011-076	11 21 12.2	–02 59 03.0	614.6	42.0	11.37	5	C
44	IC 2810	11 25 45.1	+14 40 36.2	294.6	17.4	11.59	8	C
45	NGC 3690	11 28 33.6	+58 33 46.7	17677.8	424.6	11.88	6	H
46	IRASF 12112+0305	12 13 46.1	+02 48 40.7	344.2	23.8	12.28	8	S2
47	IRASF 12224-0624	12 25 03.9	–06 40 52.4	149.5	7.7	11.27	5	S2
48	NGC 4418	12 26 54.6	–00 52 39.4	3764.4	40.2	11.08	5	U
49	Mrk 231	12 56 14.2	+56 52 24.9	3840.3	239.3	12.51	5	S1
50	NGC 4922	13 01 25.3	+29 18 49.8	1118.3	34.4	11.32	5	S2
51	CGCG 043-099	13 01 50.3	+04 20 01.1	300.4	29.3	11.62	8	U
52	IC 0860	13 15 03.6	+24 37 07.5	864.7	34.0	11.17	5	U
53	UGC 08387	13 20 35.4	+34 08 22.5	1013.3	100.3	11.67	5	C
54	NGC 5104	13 21 23.1	+00 20 32.3	527.5	34.1	11.20	5	C
55	NGC 5256	13 38 17.3	+48 16 32.8	810.9	114.2	11.49	6	C
56	Mrk 273	13 44 42.2	+55 53 12.1	1756.8	137.1	12.14	5	S2
57	NGC 5331	13 52 16.2	+02 06 05.1	415.4	38.4	11.59	8	U
58	NGC 5653	14 30 09.7	+31 12 55.6	1077.5	52.5	11.06	7	H
59	IRASF 14348-1447	14 37 38.3	–15 00 22.4	366.8	42.8	12.30	5	C
60	VV 340a	14 57 00.7	+24 37 02.8	317.3	62.8	11.67	1.5	H

continued on the next page

Table 4.1. (continued) Radio and Infrared Fluxes

#	GOALS Name	RA (J2000)	Dec. (J2000)	$F(24\ \mu m)$	$F(20\ cm)$	L_{IR}	VLA Beam Size	Optical Classification
—	—	HH MM SS	DD MM SS	mJy	mJy	$\log(L_{IR}/L_{\odot})$	$''$	—
(1)	(2)	(3)	(4)	(5)	(6)	(7)	(8)	(9)
61	VV 705	15 18 06.1	+42 44 44.7	1129.3	47.2	11.89	5	C
62	IRASF 15250+3608	15 26 59.4	+35 58 37.7	1008.5	14.6	12.02	5	C
63	NGC 5936	15 30 00.8	+12 59 20.9	984.3	52.6	11.07	5	C
64	Arp 220	15 34 57.3	+23 30 11.4	3619.7	316.3	12.21	6	L
65	NGC 5990	15 46 16.4	+02 24 55.3	1217.3	55.5	11.06	5	S2
66	NGC 6052	16 05 12.9	+20 32 37.7	661.7	73.2	11.02	6	H
67	NGC 6090	16 11 40.8	+52 27 27.1	904.4	51.5	11.51	6	H
68	IRASF 16164-0746	16 19 11.8	–07 54 02.6	468.7	67.1	11.55	6	S2
69	CGCG 052-037	16 30 56.5	+04 04 57.9	686.9	30.6	11.38	5	H
70	NGC 6240	16 52 58.9	+02 24 03.9	2846.1	392.6	11.85	5	L
71	IRASF 17132+5313	17 14 20.5	+53 10 31.5	459.9	25.5	11.89	5	H
72	IRASF 17138-1017	17 16 35.8	–10 20 40.4	1608.9	68.4	11.42	6	U
73	IRASF 17207-0014	17 23 22.0	–00 17 00.5	1117.0	102.1	12.39	5	H
74	NGC 6670	18 33 37.7	+59 53 23.2	842.3	56.7	11.60	6	H
75	IRASF 19297-0406	19 32 22.3	–04 00 01.8	379.1	25.5	12.37	6	C
76	ESO 602-G025	22 31 25.5	–19 02 03.5	575.9	36.3	11.27	7	C
77	IRASF 22491-1808	22 51 49.3	–17 52 23.5	401.3	6.0	12.11	6	H
78	NGC 7469	23 03 15.6	+08 52 25.4	3566.0	180.5	11.59	5	S1
79	NGC 7591	23 18 16.3	+06 35 08.7	636.4	47.7	11.05	5	S2
80	NGC 7592	23 18 21.8	–04 24 56.7	791.3	57.7	11.33	6	H
81	NGC 7674	23 27 56.7	+08 46 44.2	1470.6	225.4	11.50	5	S2
82	NGC 7679	23 28 46.7	+03 30 41.8	848.5	45.7	11.05	5	S2
83	IRASF 23365+3604	23 39 01.3	+36 21 07.9	599.2	24.7	12.13	5	C
84	NGC 7771	23 51 24.8	+20 06 42.2	1284.6	140.5	11.34	6	C
85	Mrk 331	23 51 26.8	+20 35 10.7	1901.6	68.8	11.41	6	H

The columns are (1) the row number; (2) galaxies as identified in the GOALS sample; (3) right ascension of the radio peak; (4) declination of the radio peak; (5) the total 24 μmflux measured in mJy; (6) the total VLA 20 cm flux measured in mJy; (7) the infrared (8–1000 μm) luminosity, measured in $\log(L/L_{\odot})$; (8) the VLA beam size diameter, measured in arcseconds; (9) the optical classifications from Yuan et al. (2010). H is starburst, C is composite, S1 is Seyfert 1, S2 is Seyfert 2, and L is LINER. U indicates a galaxy for which we do not have a classification for.

as Centaurus A. The measured radio flux is approximately 8 times higher than the infrared flux due to the large radio lobes emanating from the central black hole.

Finally in Figure 4.4 we plot the 20 cm flux on the x-axis versus the 24 μm flux on the y-axis, for both the nuclear region (6″, 7″, or 8″) and the whole galaxy. For the best fit lines we assumed a flux uncertainty of 5%, which yielded a power law index of around 0.6. However we note that in both plots, the correlation is quite loose and that there is no preferential scatter based on optical spectral classifications. These optical classifications were obtained from Yuan et al. (2010), who used BPT diagnostic diagrams to classify galaxies into AGN, low ionization narrow emission-line region (LINER) galaxies, star forming and AGN composites, and pure star forming galaxies. It appears that AGNs are just as likely to be found in the upper right portion of the relation as star forming and composite galaxies.

4.4 Results

Since we now have the high resolution MIR data that *IRAS* lacked, we can separately compute q_{24} for the nuclear and disk components of each galaxy. We plot q_{24} as a function of the IR luminosity and the spectral type in Figure 4.5 and calculate q_{24} for three different regions: the central aperture (nuclear region), the annulus between the first aperture radius (6″, 7″, or 8″) and 12″ (disk component), and the whole galaxy. This analysis will allow us to examine how q_{24} behaves differently in the nucleus as a function of several different key galaxy properties.

At first glance there appears to be little difference between the plots. The amount of scatter as measured by σ are all very similar, however if we examine the mean and median of q_{24}, we notice a trend in which it increases with larger apertures. This is in fact also visible in Figure 4.4, where the power law index increases going from the nuclear region to the total galaxy.

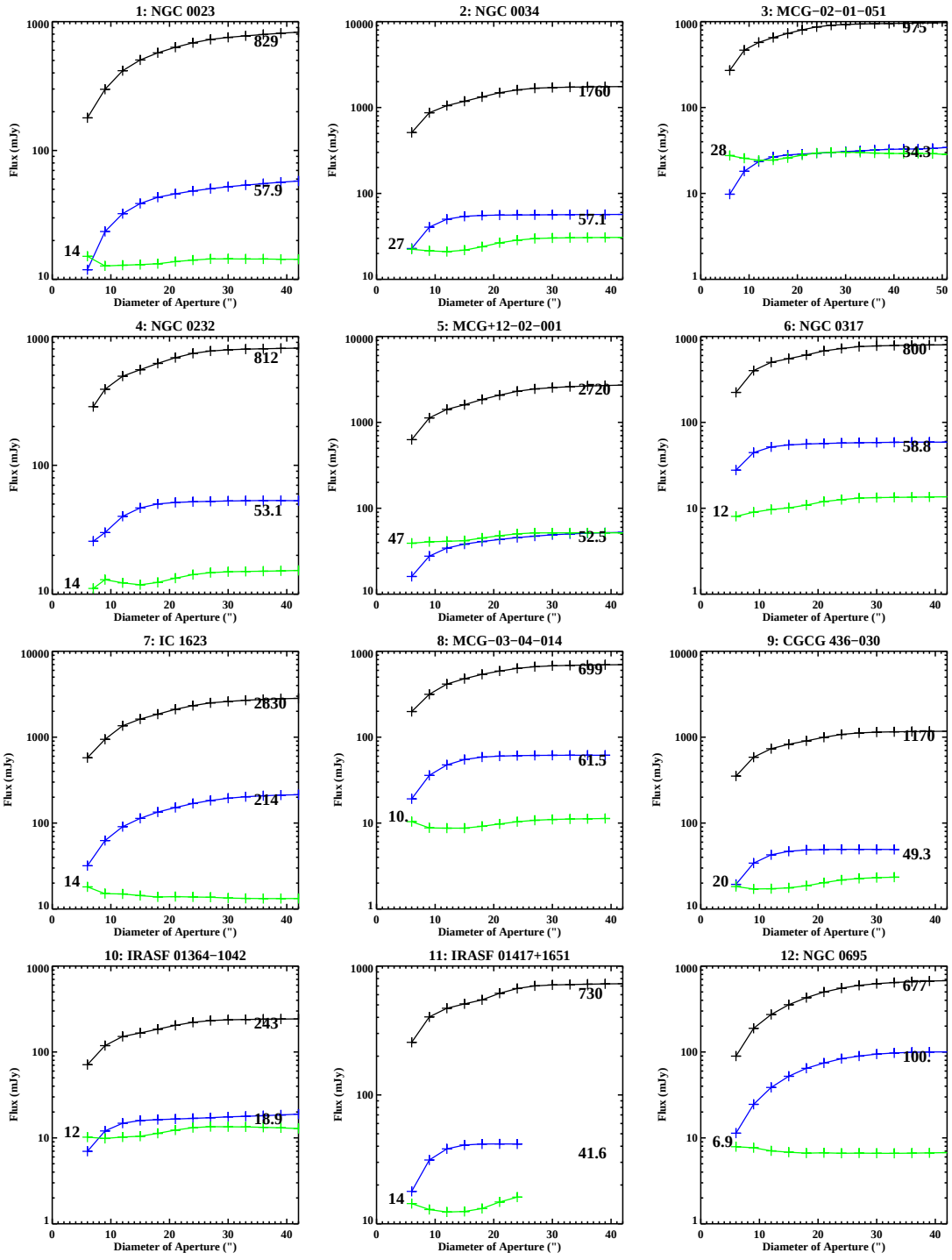

Figure 4.3 On the following pages we show in order of increasing RA the curves of growth calculated for each galaxy. Following the convention in Figure 4.2, the infrared data is in black, and the radio data is in blue. The total flux over the entire galaxy detected at each wavelength is shown on the right side of the plot. The ratio q_{24} as a function of the full aperture diameter is shown in green, with the average q_{24} value on the left side. The green curve illustrates how q_{24} changes as we increase the aperture size centered on the radio peak.

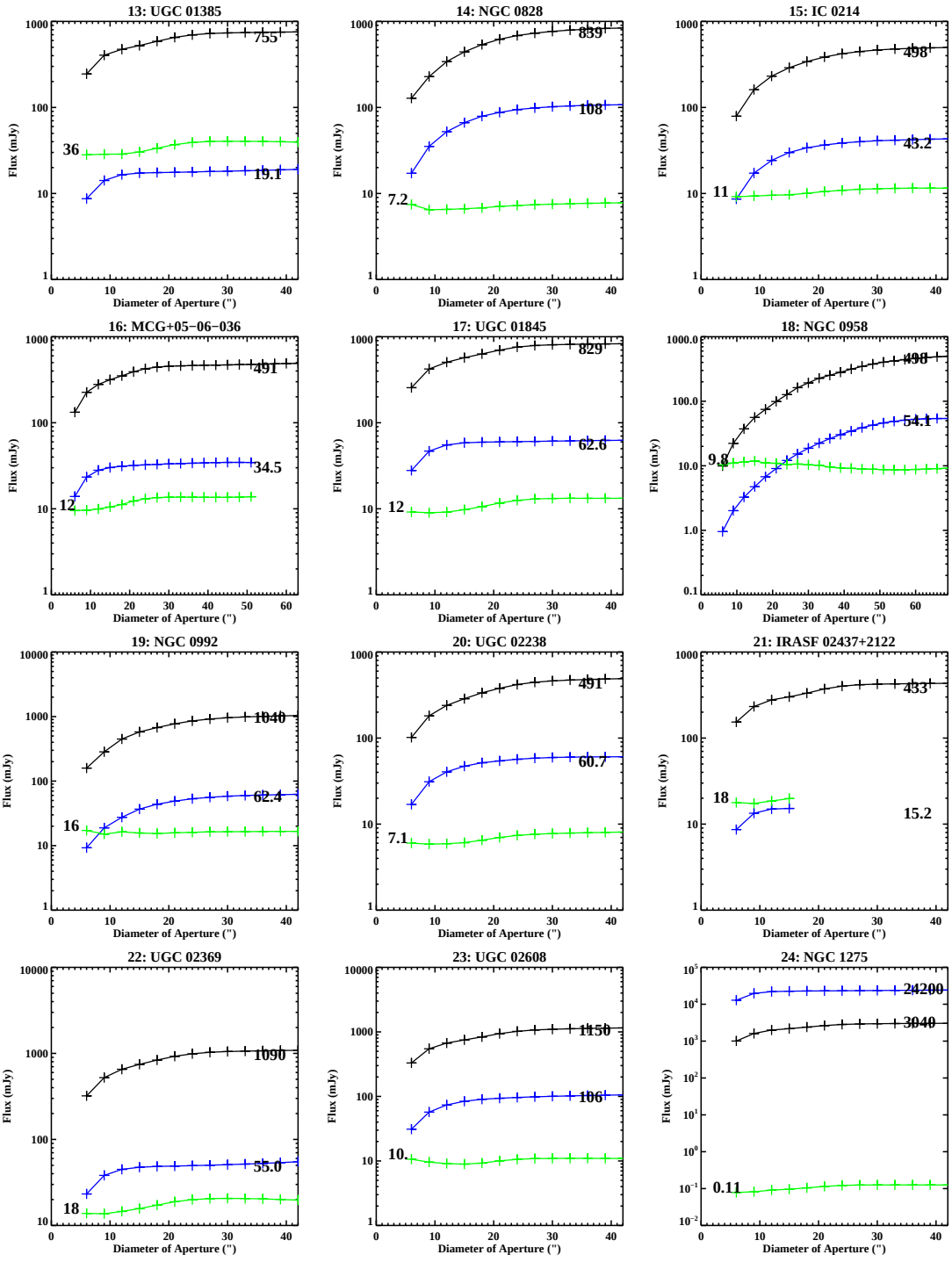

Figure 4.3 continued (page 2 of 7).

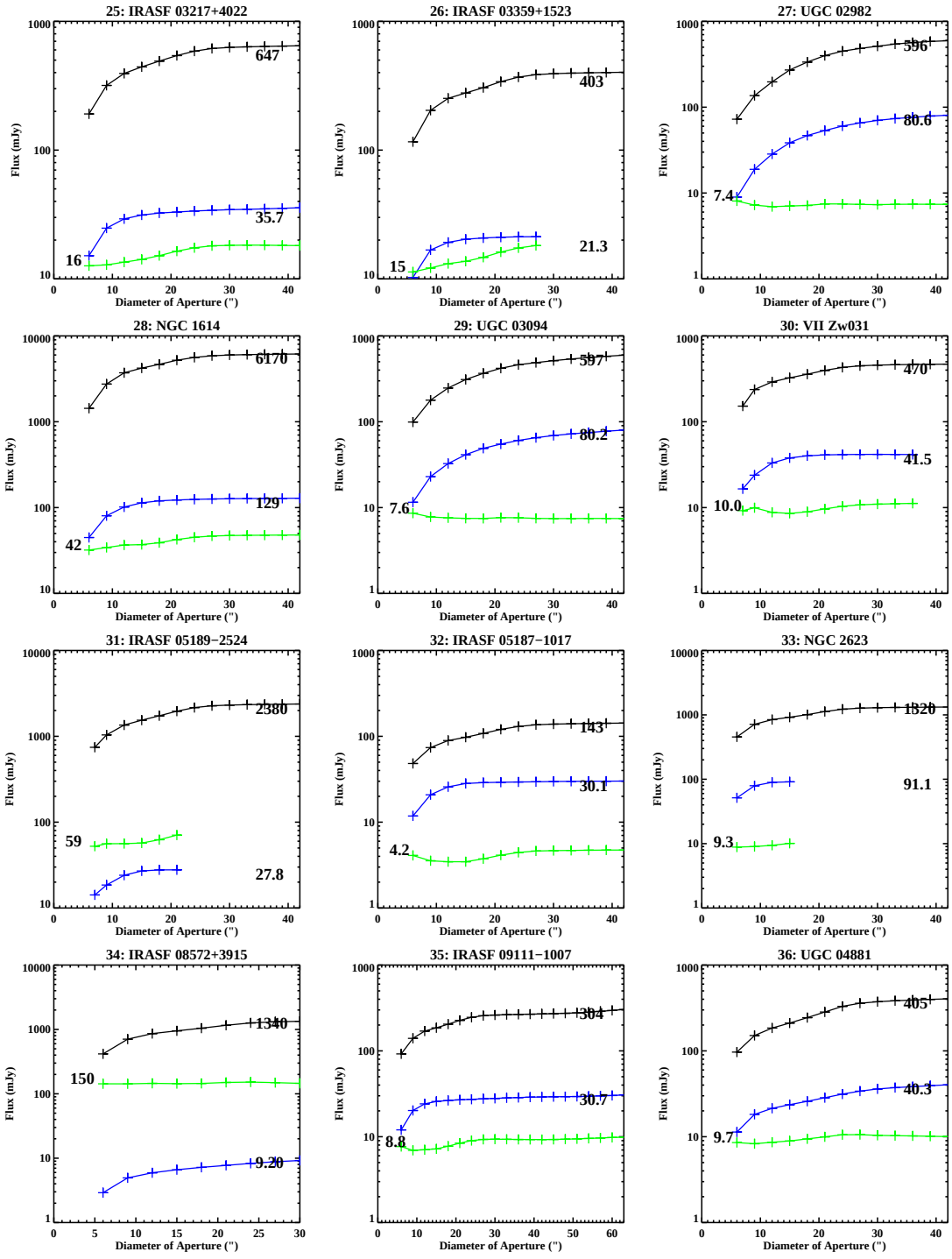

Figure 4.3 continued (page 3 of 7).

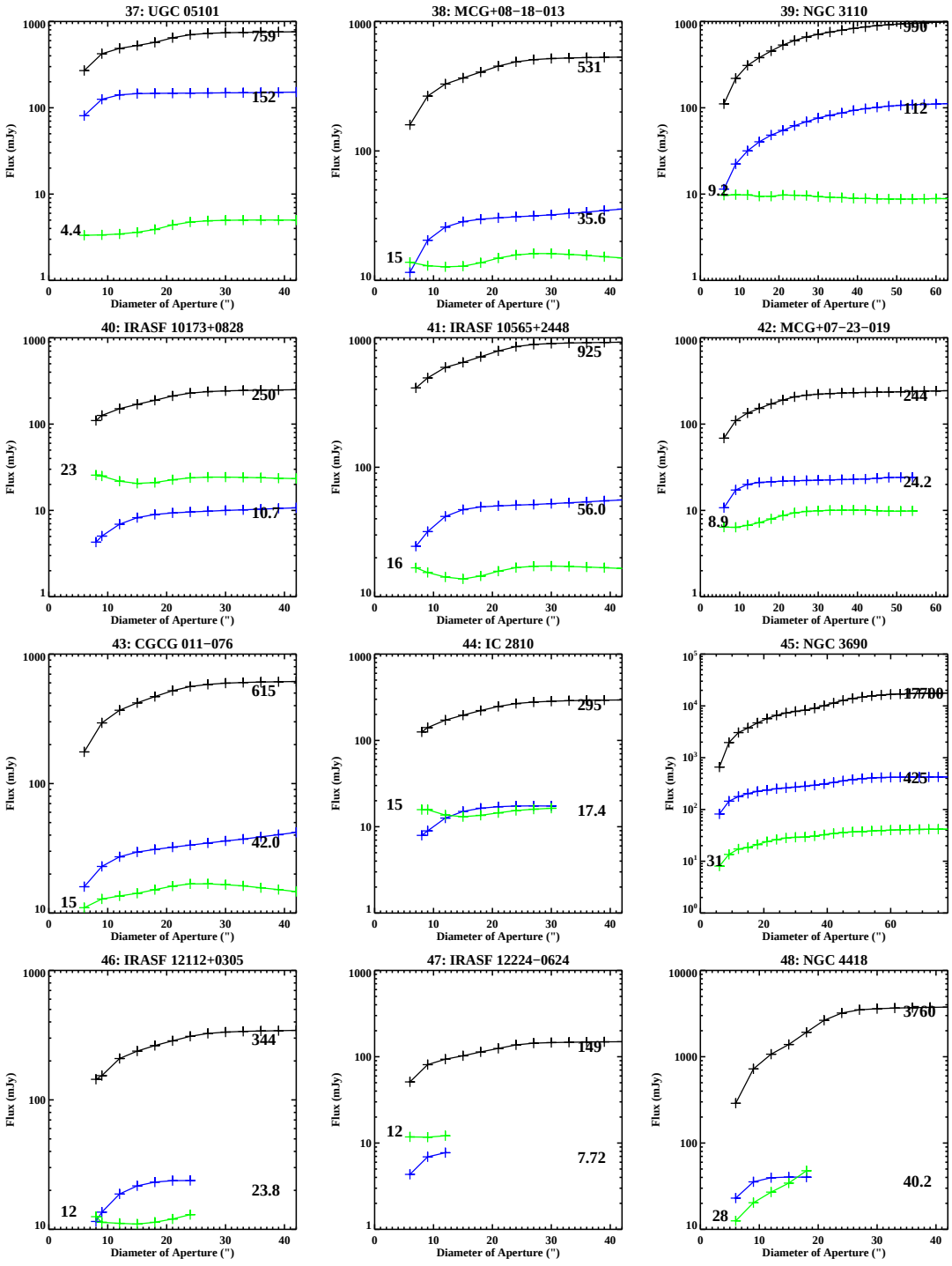

Figure 4.3 continued (page 4 of 7).

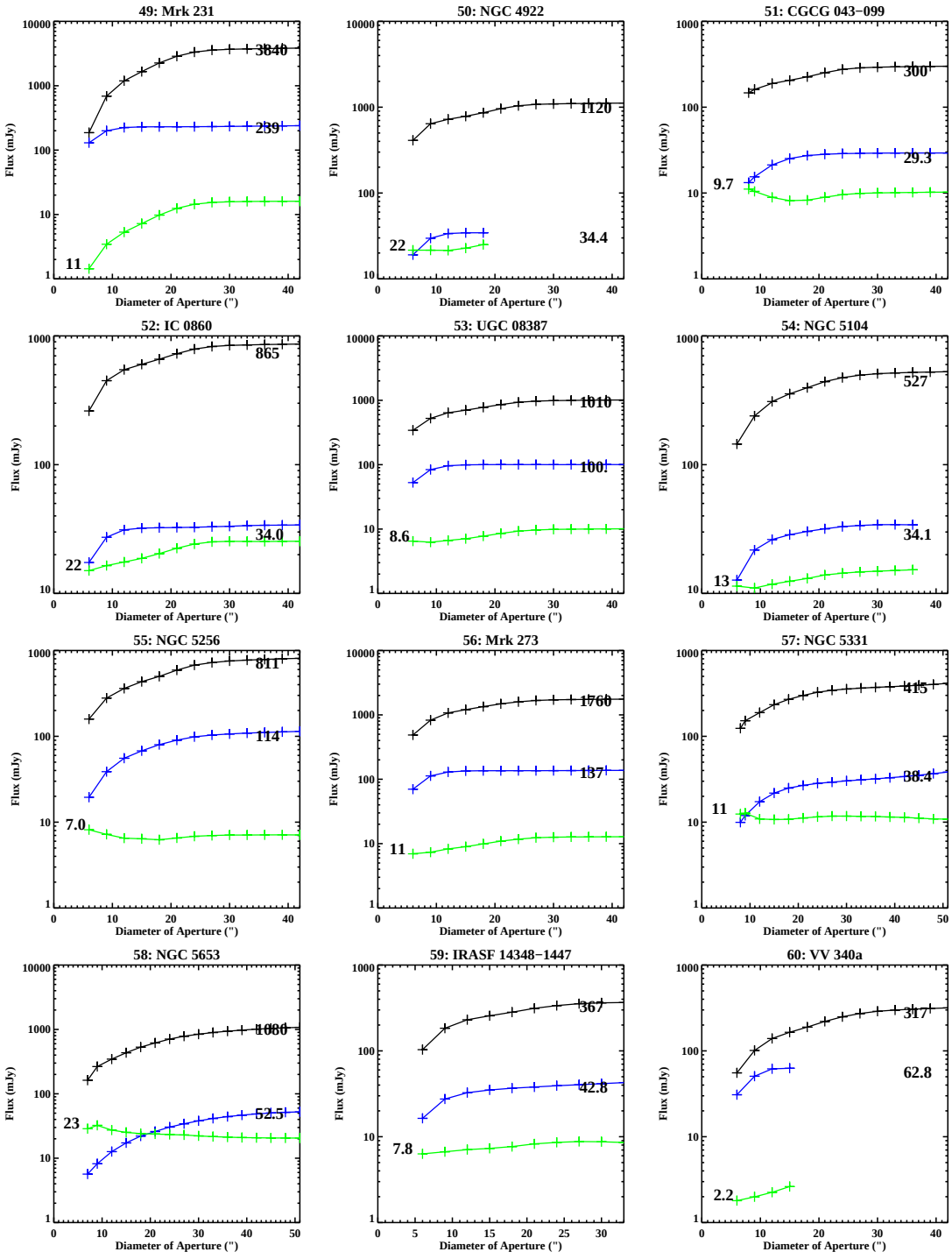

Figure 4.3 continued (page 5 of 7).

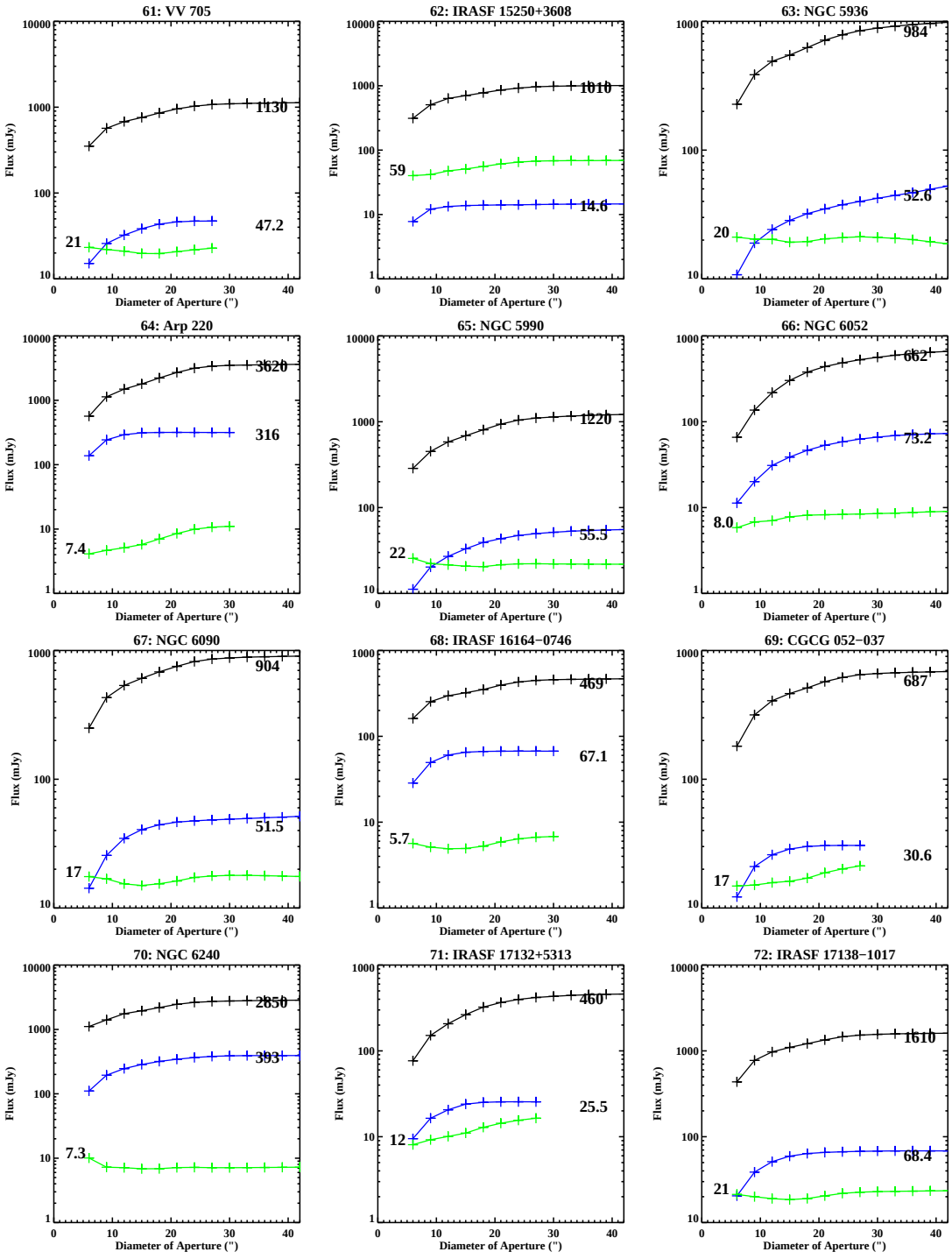

Figure 4.3 continued (page 6 of 7).

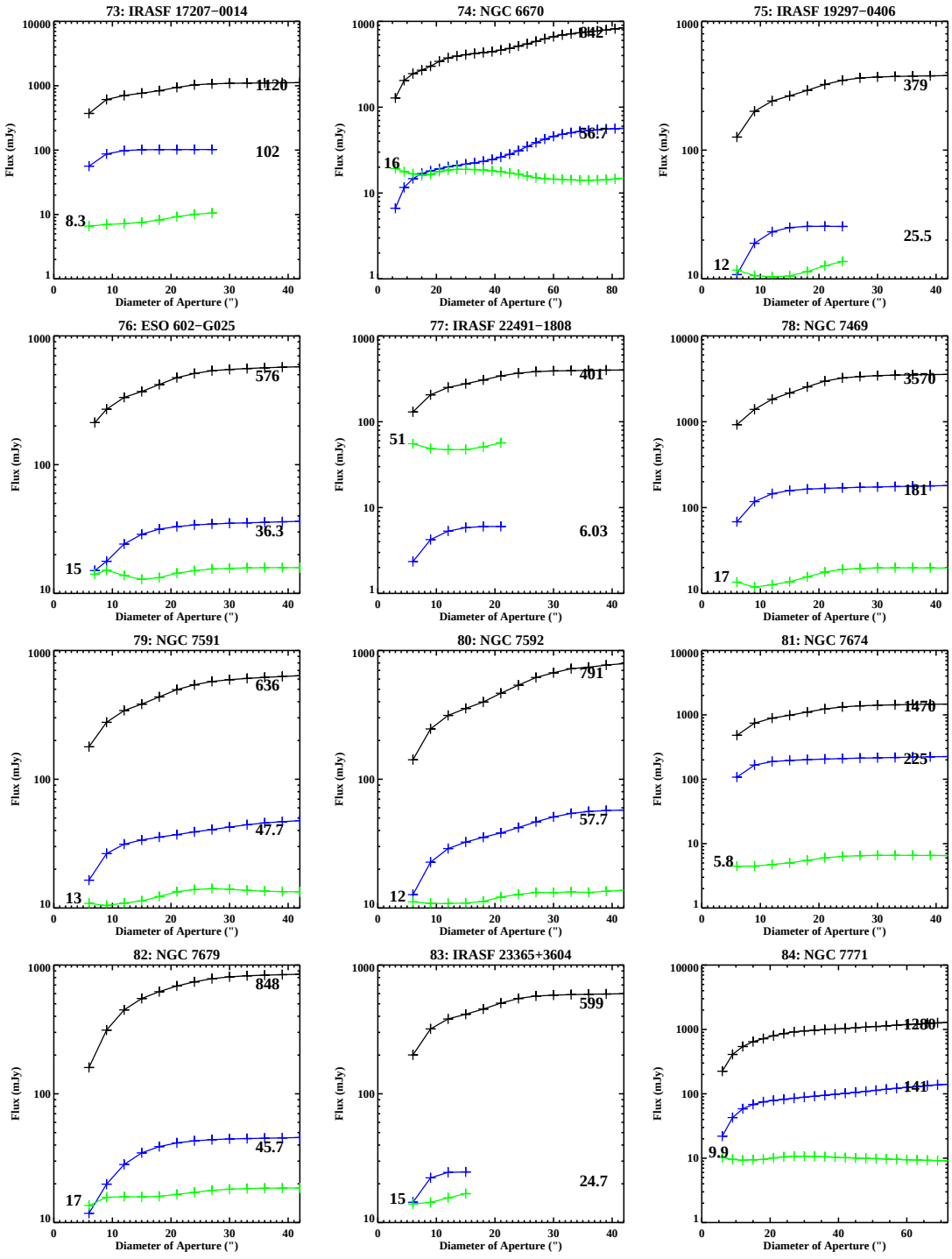

Figure 4.3 continued (page 7 of 7).

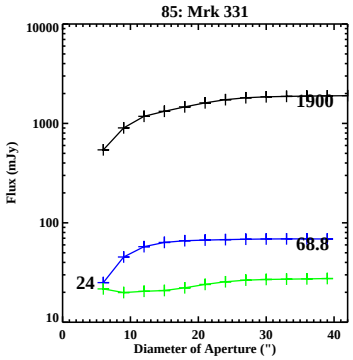

Figure 4.3 continued.

A more meaningful way of showing any changes in q_{24} is to simply take the ratio. If there are no changes in q_{24} between the nuclear region and total galaxy flux, then we would expect the ratio to be exactly 1. In Figure 4.6 we calculate the ratio of the central $q_{24,\mathrm{nuc}}$ over $q_{24,\mathrm{total}}$ for the entire galaxy. Several trends become noticeable: the majority of the sample have a $q_{24,\mathrm{nuc}}/q_{24,\mathrm{total}}$ ratio below 1, implying that the central q_{24} is in fact lower. This is due to the fact that either the radio flux in the center of the galaxy is higher, or the MIR flux in the center is lower, thus pushing down q_{24}. On average we found that the nuclear q_{24} ratio is approximately 81% lower than the total q_{24}.

The most interesting feature in Figure 4.6 is the behavior of galaxies with a FIR luminosity greater than $10^{11.6}L_{\odot}$. These galaxies noticeably dip below the $q_{24,\mathrm{nuc}}/q_{24,\mathrm{total}} = 1$ line, and increase in severity as L_{IR} increases, whereas for galaxies below $10^{11.6}L_{\odot}$ they lie fairly distributed around a $q_{24,\mathrm{nuc}}/q_{24,\mathrm{total}} = 0.81$. There also appears to be a lack of trend with respect to spectral type; even galaxies classified as starbursts are heavily depressed above $10^{11.6}L_{\odot}$. An interesting object is NGC 4418, which has an infrared luminosity of $10^{11.08}L_{\odot}$, but has a highly depressed central to total q_{24} ratio of about 0.14. The only plausible explanation for this is a lower than normal $q_{24,\mathrm{nuc}}$ for the central aperture compared to $q_{24,\mathrm{total}}$.

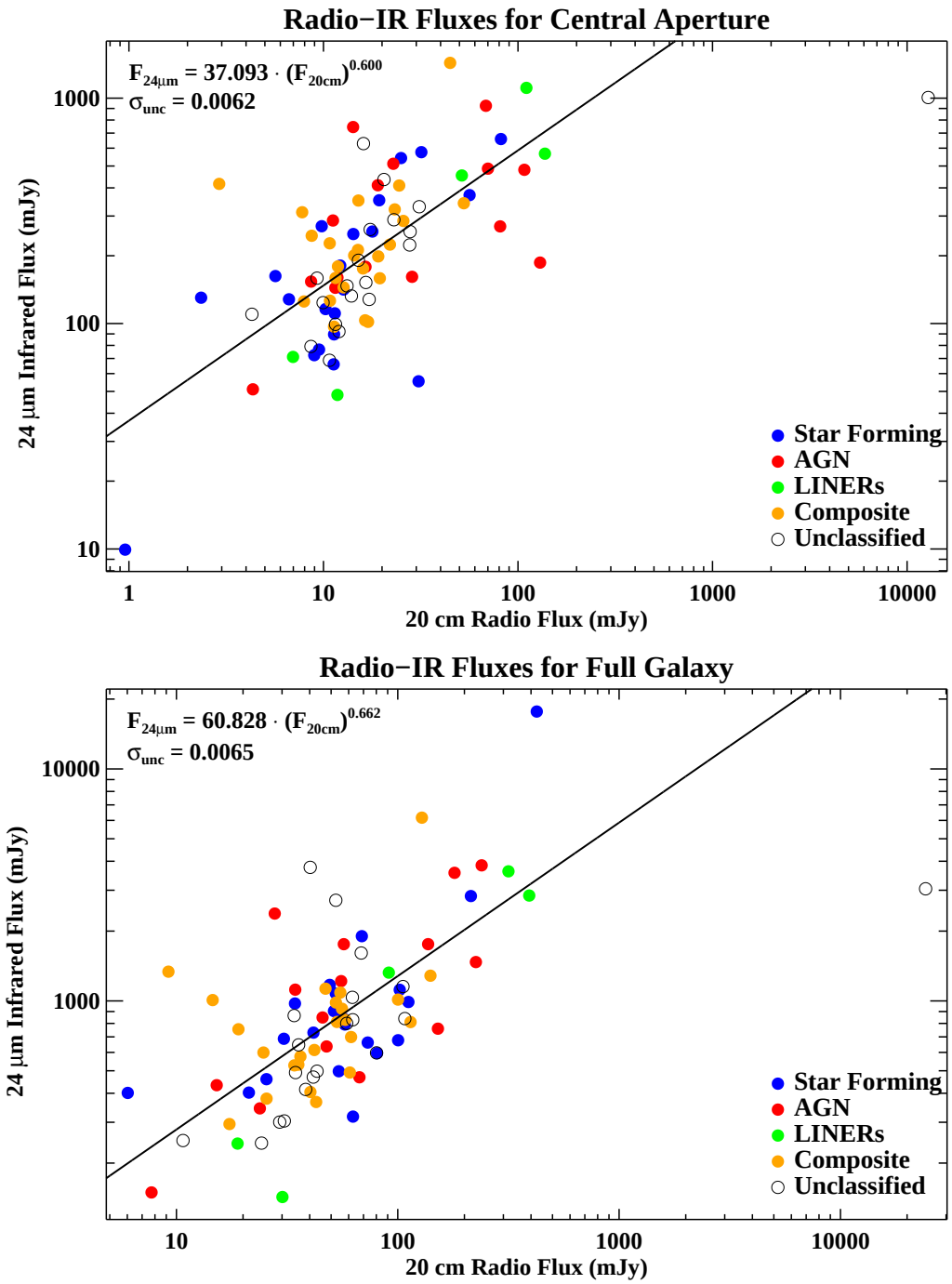

Figure 4.4 We plot the 24 μm flux vs. the 20 cm radio continuum flux for our entire sample. The top panel shows the radio-infrared correlation for the central extraction aperture (6″, 7″, or 8″), while we plot the total flux from each galaxy on the bottom panel. We can already see that there is a small difference in logarithmic slope between the data. σ_{unc} is the uncertainty in the power law index. In our fit we did not include NGC 1275 (Centaurus A), as it lies on the far right hand side of both plots.

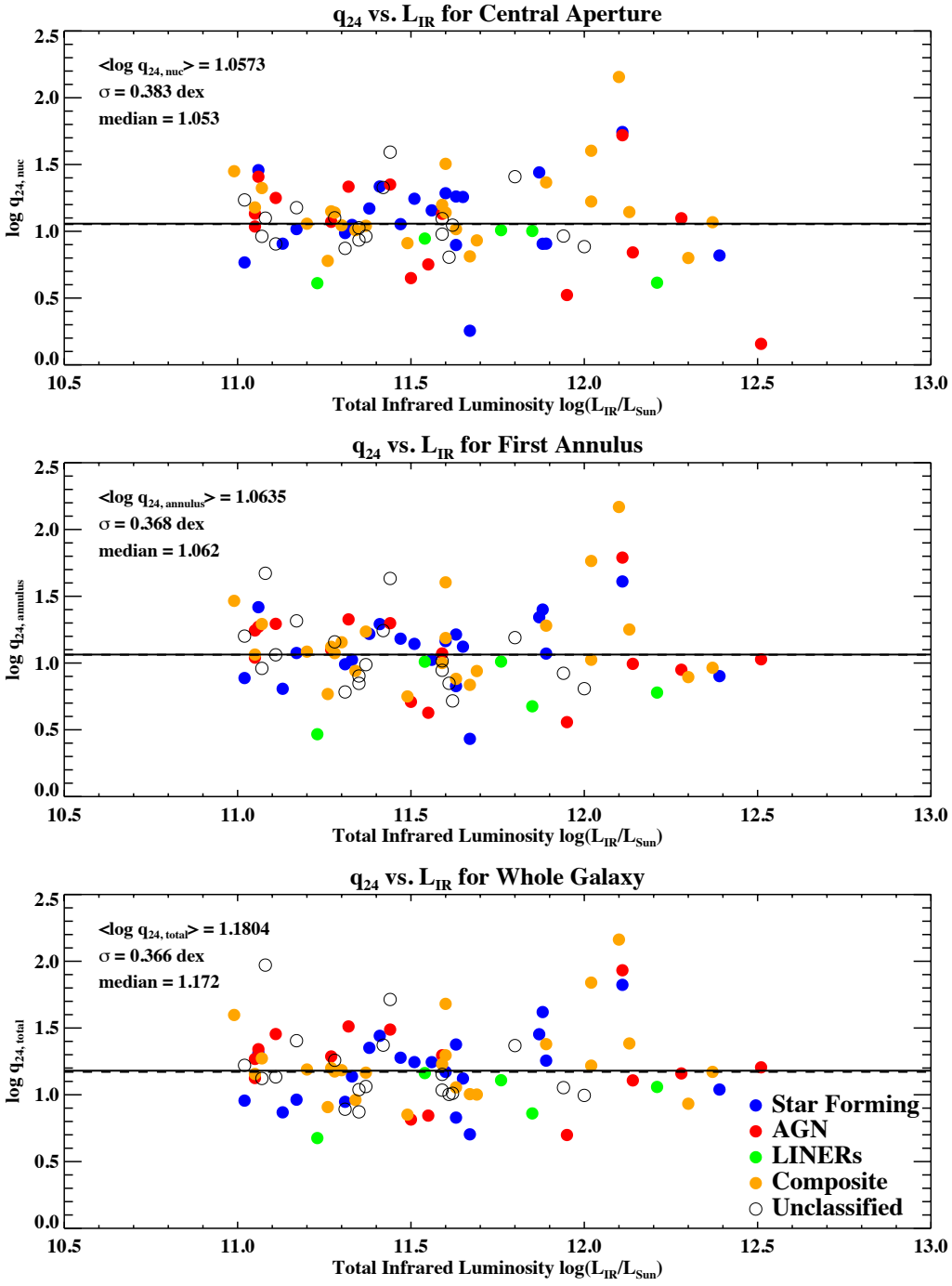

Figure 4.5 The calculated q_{24} ratio vs. $L_{\rm IR}$ for the central aperture, first annulus (see text), and entire galaxy. The mean (solid line) and median (dashed line) are computed for each plot, as well as the dispersion in the vertical direction. It is apparent that as we increase the extraction aperture, both the mean and median increase, but the dispersion remains almost identical.

4.5 Discussion

4.5.1 The Observed Variation in q_{24}

The depression in the nuclear to total q_{24} ratio is best interpreted as the presence of an AGN in the center of the galaxy. Since the AGN is typically quite concentrated in the nucleus of a galaxy, measurements of q_{24} in the central aperture would be different from that measured over the entire galaxy. As one begins to include fluxes from larger apertures, any differences in the nuclear q_{24} from the overall value is diluted quickly. This can be seen in several galaxies such as NGC 4418 and most dramatically for Mrk 231 in Figure 4.3. In fact by looking at the radio curve of growth for Mrk 231, we see that the radio power has already reached about 50% of its full strength at the smallest aperture. For comparison, the infrared power at the *same* aperture is only 5% of the total infrared flux, a whole order of magnitude smaller than in the radio. This is clearly seen in Figure 4.6, where Mrk 231's (an AGN with $L = 10^{12.51} L_{\odot}$) central to total q_{24} ratio is at about 0.1.

However it is unclear if this depression in the nuclear q_{24} with respect to the total q_{24} is due to a radio excess, or an infrared deficit. In the first case a radio excess over the infrared emission can be explained by the presence of a radio loud AGN core that dominates over radio emission from the disk. That is to say, there exists a strong radio point source (due to the AGN) embedded within a more diffuse radio emission in the disk. On the other hand, a deficit in infrared flux can also explain why the nuclear q_{24} value is lower. The MIPS 24 μm channel encompasses a very broad and shallow silicate absorption feature centered at 18 μm that extends well into the 24 μm passband. There have been some evidence that this absorption is most pronounced in dust enshrouded AGN galaxies (i.e., Type 2 AGN), where the silicate features are believed to originate from the inner illuminated side of the dust torus surrounding the black hole (see Hatziminaoglou et al. 2015, and references therein). Because it is impossible to ascertain if this is due to a radio excess or infrared deficit, from this point on we consider only the fact that the nuclear q_{24} value is different between the nucleus and entire galaxy. This uncertainty will be resolved once we have

access to the high resolution *Herschel* FIR maps that are not contaminated by this feature, and IRS MIR spectra which would reveal the presence or absence of a silicate absorption feature.

It is interesting to note that the break at $\log(L_{\rm IR}/L_{\odot}) = 11.6$ corresponds to the luminosity above which *all* LIRGs are found to be advanced major mergers of gas-rich spiral disks, which is similar to what Ishida (2004) found. At lower infrared luminosities (i.e., $\log(L_{\rm IR}/L_{\odot}) = 11.0 - 11.6$) they found a mixture of galaxy types including ∼50% minor mergers, ∼20% large spirals, and ∼30% major mergers in the early stages of their merger history. It seems reasonable to assume that objects with $\log(L_{\rm IR}/L_{\odot}) < 11.6$ are less likely to have built up strong gas concentrations in their nuclei, and that AGN fueling is still secondary to more widespread starburst activity. That the mean $q_{24,\rm nuc}/q_{24,\rm total}$ ratio is still less than 1 would seem to indicate that an AGN is typically present in these lower luminosity systems, but that it is not until one reaches the more advanced stages of gas-rich major mergers where one begins to see the AGN begin to produce a more prominent effect on q_{24}.

When we examine objects such as Mrk 231 that are above $\sim 10^{11.6} L_{\odot}$, we indeed see that $q_{24,\rm nuc}/q_{24,\rm total}$ tends to be smaller than galaxies below the luminosity threshold. The optically classified LINER Arp 220 (with $\log(L_{\rm IR}/L_{\odot}) = 12.21$) also lies quite low compared to the rest of the galaxies in Figure 4.6. Arp 220 is a noteworthy galaxy that is most likely a merging system with a double nucleus. In fact for most of the galaxies in this luminosity range, the q_{24} ratio seems to generally increase as one increases the aperture diameter. This is readily apparent in the average q_{24} values for the nuclear, first annulus, and total galaxy in Figure 4.5. Galaxies such as Arp 220 ($10^{12.21} L_{\odot}$), IRASF 05189-2524 ($10^{12.11} L_{\odot}$), Mrk 231 ($10^{12.51} L_{\odot}$), and IRASF 17132+5313 ($10^{11.89} L_{\odot}$) show an especially large change. These results agree with the conclusions made by Ishida (2004) where all galaxies above $10^{11.6} L_{\odot}$ are in an advanced merger stage, since a powerful AGN from the nucleus would diminish the nuclear q_{24} value. Furthermore we note that the drop in $q_{24,\rm nuc}/q_{24,\rm total}$ increases with

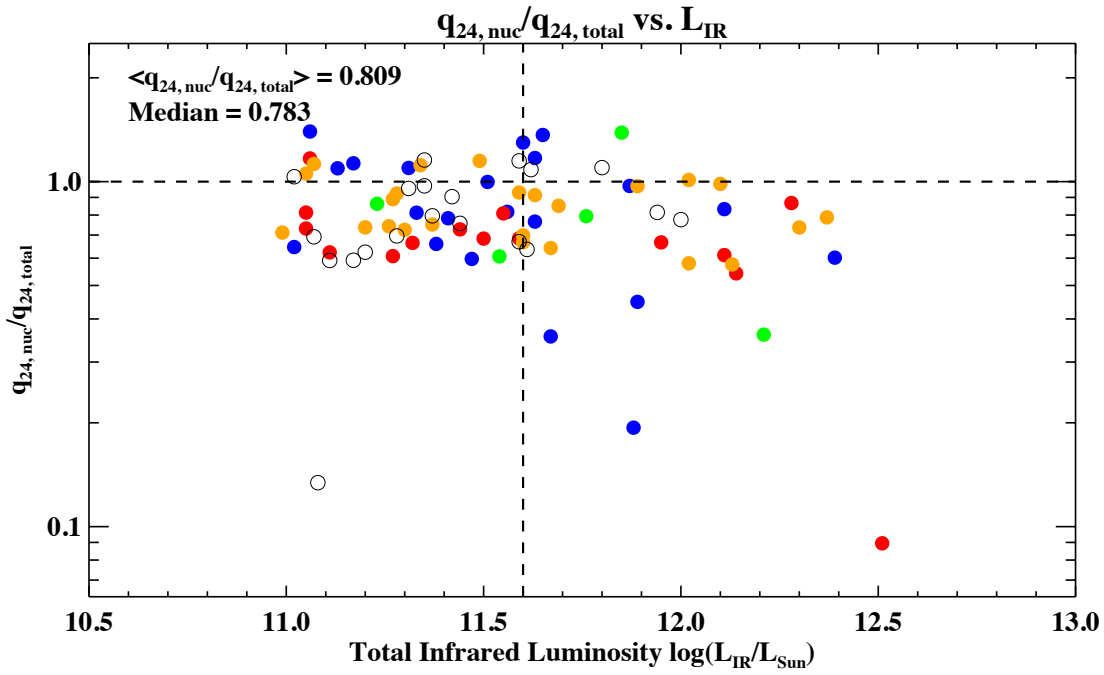

Figure 4.6 The ratio of the nuclear region ($q_{24,\mathrm{nuc}}$) to the entire galaxy ($q_{24,\mathrm{total}}$). Most galaxies below a luminosity of $10^{11.6} L_{\odot}$ appear to have a ratio less than 1, but consistently average around a ratio of 0.8. However for galaxies above $10^{11.6} L_{\odot}$, the galaxies have increasingly lower ratios as L_{IR} increases. Mrk 231 is the AGN with the highest L_{IR}, and Arp 220 is the LINER with a luminosity of $10^{12.21} L_{\odot}$. The only galaxy below $10^{11.6} L_{\odot}$ with a very low ratio is NGC 4418. It is noteworthy that starbursts between $10^{11.6} L_{\odot}$ and $10^{11.9} L_{\odot}$ have very low ratios despite their optical classification.

higher luminosity, indicating that these are the most violently interacting systems with the most powerful AGN.

Below a luminosity of $10^{11.6} L_{\odot}$ we see that essentially all the galaxies have a central to total q_{24} ratio of close to 0.8 in Figure 4.6, again consistent with what Ishida (2004) found. Unlike the higher luminosity objects which have a much larger dispersion (roughly an order of magnitude), these galaxies appear quite flat over a luminosity range of a little over half a decade. This seems to imply that there is a roughly constant relation between the nuclear and total q_{24} for these galaxies. There also seems to be no clear trend with respect to spectral class, although there is a higher fraction of starburst galaxies above 1.

Furthermore, other studies of (U)LIRGs have shown that the size of the infrared source in a galaxy becomes smaller for galaxies with very high luminosities (Condon et al. 1990, 1996). Normally this would mitigate the observed drop in the $q_{24,\mathrm{nuc}}/q_{24,\mathrm{total}}$ ratio above $10^{11.6} L_{\odot}$ in Figure 4.6, since an increase in the nuclear-infrared flux would increase the $q_{24,\mathrm{nuc}}$ ratio, but this is not evident in our data. Although it is theoretically possible to plot the ratio of $q_{24,\mathrm{disk}}$ to $q_{24,\mathrm{total}}$, we do not know *a priori* if we are really extracting the disk's flux since many of our objects have double nuclei. It is likely that when calculating the q_{24} of a particular annular region, radiation from one nucleus can contaminate what would otherwise be flux from a non-AGN component (i.e., star forming regions).

Overall the evidence points towards a major intensification of *both* starburst and AGN activity at higher FIR luminosities (i.e., Figure 4.4). As galaxies collide and begin to coalesce, massive tidal disruptions push gas towards the centers of the merging disks, which in turn intensifies AGN activity and alters the nuclear q_{24} with respect to the rest of the galaxy. At the same time, strong shocks propagating through the interstellar medium induce rapid star formation, which can over a short timescale generate an intense UV radiation field that heats up nearby dust. This heated dust then re-radiates almost all of its energy away in the FIR. In the nucleus the AGN similarly heats up the dust surrounding the supermassive black hole, which additionally contributes to the IR flux. Subsequent supernova shocks from the deaths of massive stars would also contribute to the disk's radio flux (from both thermal

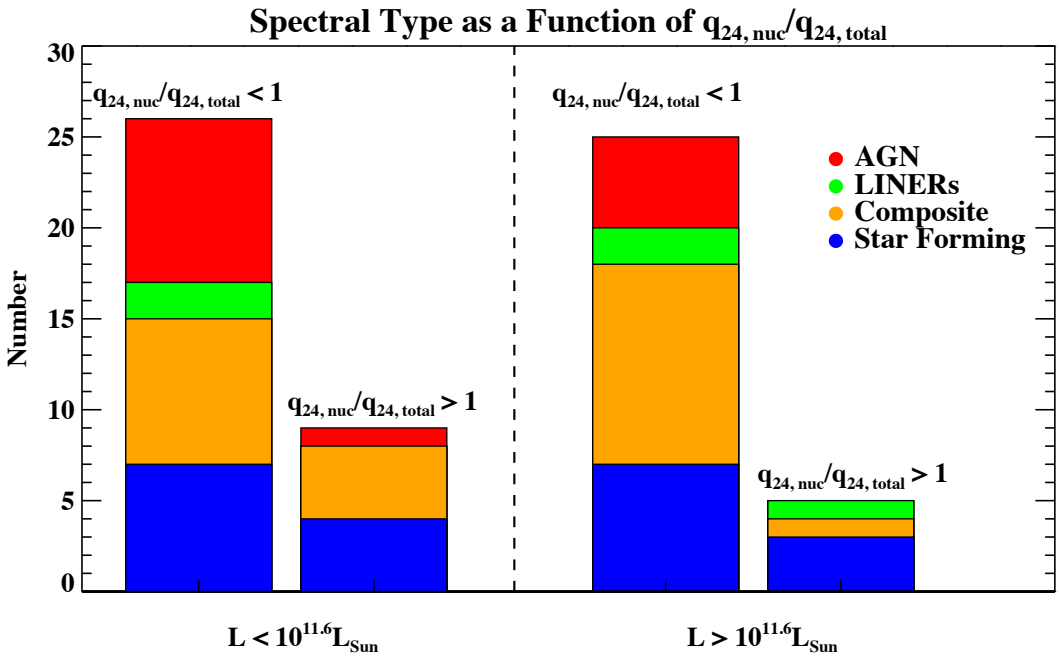

Figure 4.7 A bar chart showing the distribution of galaxies with known optical classifications (65) within each region as a function of spectral type. Immediately we see that almost all of the optically classified AGN in both luminosity bins have central to total q_{24} ratios less than 1. Composites make up a fair amount of galaxies both above and below 1 for $L < 10^{11.6} L_{\odot}$, but for the high luminosity bin virtually all of the composites are below ($q_{24,\mathrm{nuc}}/q_{24,\mathrm{total}} < 1$). This suggests that galaxies above $10^{11.6} L_{\odot}$ have a powerful AGN regardless of its spectral type. Finally it is not surprising to note that in both luminosity bins, there is a higher fraction of star forming galaxies with a ratio above 1 than below.

and non-thermal sources), while a radio loud core from the AGN increases the nuclear radio flux. Quantitatively the q_{24} ratio would vary dramatically between the nucleus and disk due to either a very powerful radio core or a deep MIR silicate absorption feature from the torus surrounding the black hole.

In order to investigate how the nuclear to total q_{24} varies as a function of L_{IR} and optical spectral type, we divide Figure 4.6 into four regions above and below a ratio of 1 and also below and above $10^{11.6} L_{\odot}$ (dashed lines in Figure 4.6). In Figure 4.7 we show the number of occurrences of each spectral type within each of these four regions. We see that for galaxies below $10^{11.6} L_{\odot}$, there is a higher fraction of starbursts (44%) out of all galaxies above a

ratio of 1, implying that their nuclei are relatively quiescent. The composites on the other hand are spread roughly equally below and above 1 (31% and 44% of the < 1 and > 1 bins, respectively), since they have a comparable contribution from both starbursts and AGN. We further note that those galaxies optically classified as AGN make up a substantial fraction (35%) of all galaxies with a ratio below 1 (in the low luminosity bin), which supports the evidence that they host an AGN. In fact almost all of the AGN in this luminosity range are below 1, with only one object with a ratio $q_{24,\mathrm{nuc}}/q_{24,\mathrm{total}} > 1$.

In the high luminosity bin, we see a similar effect: all of the AGN have a central to total q_{24} ratio less than 1. However in this case almost all of the composite galaxies are below 1 as well. This may be a result that, although there is active star formation occurring in the disk, there is also a very powerful AGN in the nucleus that pushes its central to total q_{24} ratio below 1. This suggests most galaxies above $10^{11.6} L_{\odot}$ have a powerful AGN regardless of its optical spectral type. Similar to the lower luminosity galaxies, the optically classified starbursts tend to dominate (60%) in the few galaxies that are above 1. Overall, we see that of the 65 galaxies we have optical classifications for, only 14 (21%) are above 1, whereas the majority of the galaxies have a depressed nuclear q_{24} ratio.

4.5.2 Comparison with *IRAS* Data

Given the ∼arcminute resolution of *IRAS*, it was impossible to resolve the nuclear and disk components in our sample before the launch of *Spitzer*. As a comparison, the infrared maps from *IRAS* would actually appear larger than the map sizes in Figure 4.2. Thus it was not surprising when Condon et al. (1991b) plotted the radio-infrared correlation for a sample of 40 LIRGs with $L > 10^{11.25} L_{\odot}$, they obtained a q value that was roughly constant across a whole decade in luminosity. We reproduce this observation for our data using the final *IRAS* fluxes (Sanders et al. 2003) in the top panel of Figure 4.8, using the original definition of q:

$$q_{80} \equiv \frac{2.58 \cdot S_{60\mu\mathrm{m}} + S_{100\mu\mathrm{m}}}{S_{20\mathrm{cm}}} \tag{4.2}$$

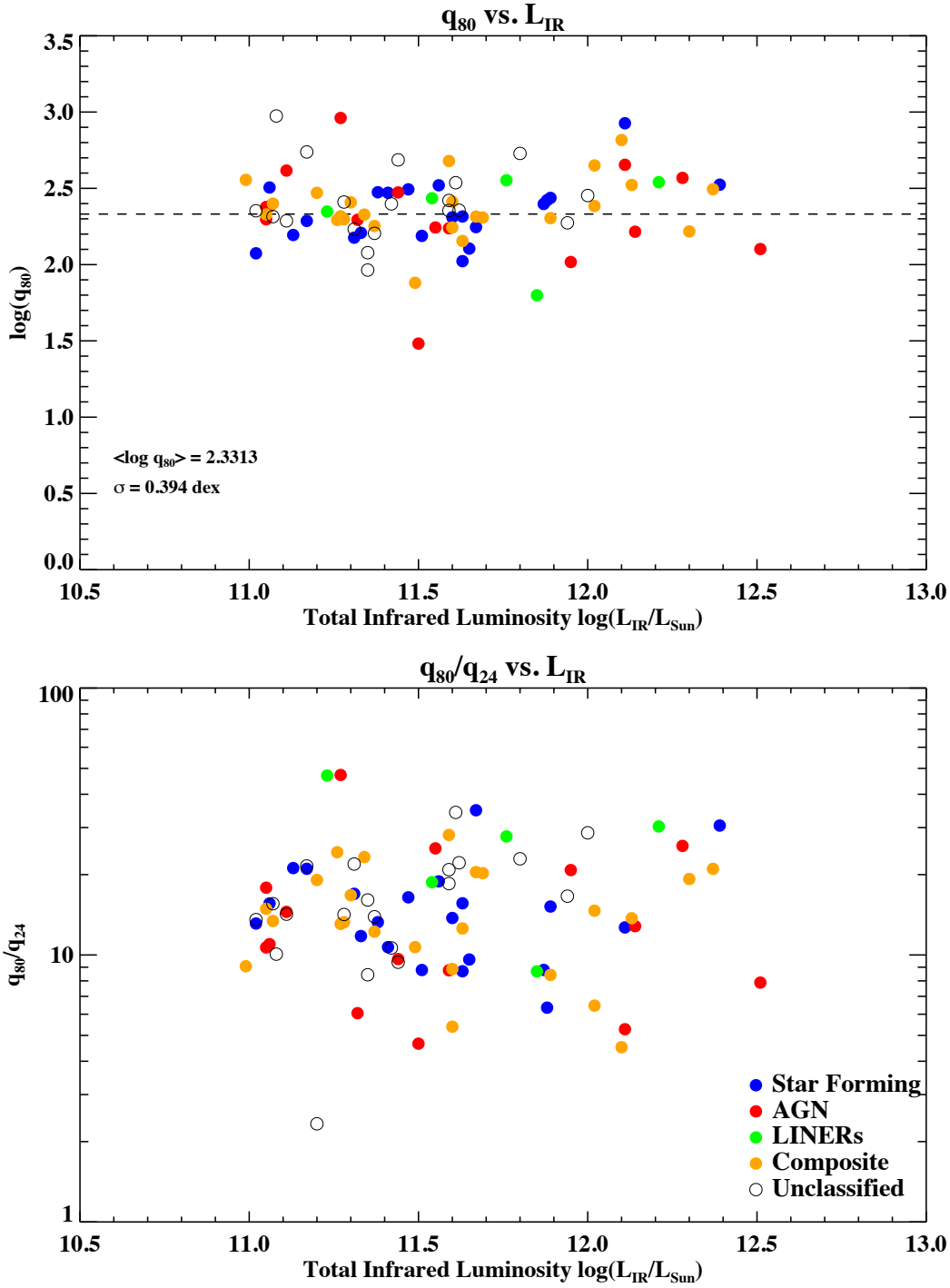

Figure 4.8 The radio-infrared correlation using the original definition, but using the final *IRAS* fluxes. On the top panel we show how q_{80} varies over $L_{\rm IR}$. Note that the dispersion of 0.394 dex is very similar to the dispersion we obtained for q_{24} in the bottom panel of Figure 4.5. On the bottom panel we show the ratio of q_{80}/q_{24}, and see that the ratio does not vary at all over the entire luminosity range.

where $S_{60\mu m}$ and $S_{100\mu m}$ are the *IRAS* 60 μm and 100 μm flux densities, respectively, and q_{80} is an interpolated flux density representing the galaxy's FIR flux (Condon et al. 1991b). Comparing the *IRAS* fluxes of our data in Figure 4.8 to Figure 4 in Condon et al. (1991b), we see that the data and scatter indeed look the same.

If we then compare q_{80} vs. $L_{\rm IR}$ (Figure 4.8) with q_{24} vs. $L_{\rm IR}$ (bottom panel of Figure 4.5) for the entire galaxy, the data look quite similar in logarithm space. The dispersion of the data points in the vertical direction are essentially the same, measuring 0.366 dex and 0.394 dex for q_{24} and q_{80} respectively. Thus if we only consider a galaxy's global fluxes, which was what *IRAS* could only do, then the radio-infrared correlation seems to hold. However, because *IRAS* lacked the ability to differentiate between the nuclear and disk component, any differences in the nuclear-infrared flux was *masked* by the total global flux of the galaxy. On the other hand, we utilized MIPS 24 μm data because it has just enough resolution to resolve the nuclei of our galaxies, and had a long enough wavelength to detect warm dust. In Figure 4.8, bottom panel, we show the ratio of MIPS 24 μm to the *IRAS* 80 μm total fluxes. From this we see that within a certain amount of scatter, the correlation between the *total* q_{24} and q_{80} values appear to be flat and does not vary over the entire luminosity range. Thus our 24 μm data is a reliable substitute for the FIR "80 μm" flux from *IRAS*.

4.6 Summary

Previous studies have found the radio-infrared correlation to be tightly constrained over several orders of magnitude in luminosity if one were to only use total FIR fluxes. We observe 85 galaxies from the GOALS sample in an effort to characterize the behavior of the infrared to radio flux ratio q on galactic scales in luminous infrared galaxies. We summarize our findings as follows:

1. Although the radio-infrared correlation appears to hold if one uses only the total flux and make a few corrections (i.e., Condon et al. 1991a), when we look at the actual *spatial* distribution of mid-infrared and radio emission in luminous infrared galaxies,

the correlation breaks down especially in the nucleus. We find a large fraction (78%) of galaxies within our sample to have a smaller q_{24} value in the nucleus than if we were to compute q_{24} for the entire galaxy. Thus care must be taken if one wishes to substitute high resolution radio interferometric data for unavailable mid-infrared maps of galaxies. The evidence clearly points to a complex behavior of q_{24} on the scale of galactic structures. However the origin of this depressed nuclear q_{24} value is unclear, as it can be due to a radio excess or infrared deficit in the nucleus.

2. We observe a break in the nuclear to total q_{24} ratio in our sample of 85 galaxies at a luminosity of $10^{11.6} L_{\odot}$ (Figure 4.6). It appears that for very high luminosity objects such as Mrk 231, the nuclear q_{24} value can be up to an order of magnitude smaller than that of the entire galaxy, which is strong evidence for powerful AGN. Furthermore this effect on galaxies above $10^{11.6} L_{\odot}$ is not only seen in optically classified Seyferts, but composites and starbursts seem just as likely to contain luminous AGN. On the other hand galaxies below $10^{11.6} L_{\odot}$ seem to be more well-behaved: the nuclear q_{24} value is on average about 81% of the galaxy's total q_{24}, which suggests they still have a mild contribution from AGN. Overall this suggests that a luminosity of $10^{11.6} L_{\odot}$ is a special turning point in galaxy evolution.

3. Our data show that optically classified AGNs across our entire luminosity range of $10^{11} L_{\odot}$ to $10^{12.5} L_{\odot}$ almost always have a central to total q_{24} ratio below 1 (Figure 4.7). We also find that starburst galaxies below $10^{11.6} L_{\odot}$ in general tend to have central to total q_{24} ratios around or above 1, which implies that they lack a significant AGN contribution and tend to be more quiescent.

4.7 Addendum

Since the original work was done using the 24 μm images, we have reduced and published the *Herschel* FIR images as described in Chapter 2. In this section we describe our initial results using the high resolution FIR maps obtained using the *Herschel* PACS instrument

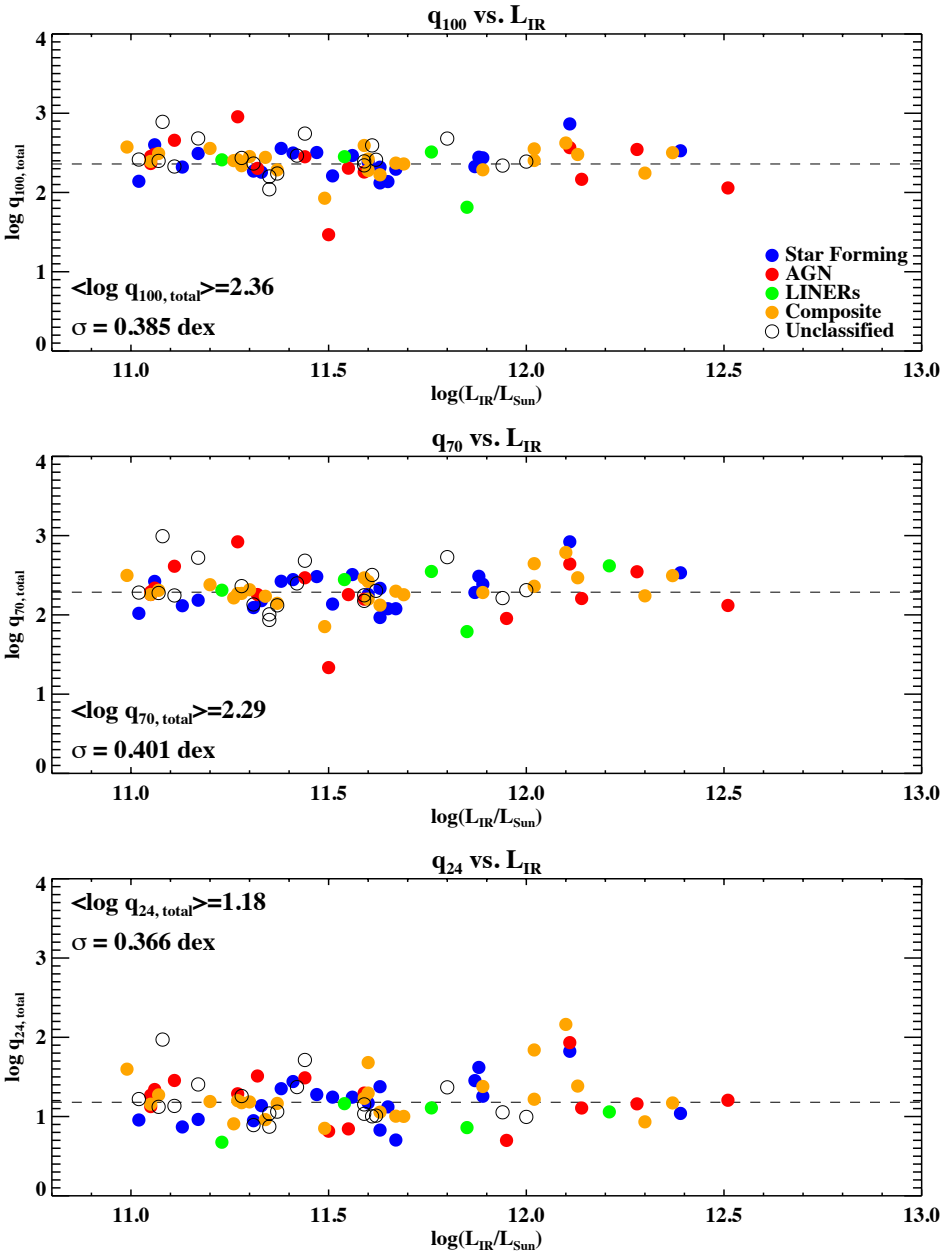

Figure 4.9 The calculated q_{100}, q_{70}, and q_{24} ratios vs. $L_{\rm IR}$ for the entire galaxy. The mean (dashed line) is computed for each plot, as well as the dispersion in the vertical direction. The observed increase in the q value from 24 to 100 μm is due to the longer wavelengths probing closer to the IR SED peak.

at 70 and 100 μm. At both of these wavelengths, the *Herschel* maps have the same full width half maximum (FWHM) beam sizes as the *Spitzer* 24 μm images (6$''$). In Figure 4.9 we show the total value of q_{70} and q_{100} as a function of $L_{\rm IR}$ and color coded by the optical spectral type, with q_{24} on the bottom panel for reference. We find that like q_{24}, there are no trends in the q_{70} and q_{100} ratios that correlate with $L_{\rm IR}$ or optical spectral type. In addition we calculate the average q value at each wavelength, where we find it to increase as a function of wavelength. This is to be expected since the longer wavelengths are close to the peak of the infrared SED. The average q_{80} ratio of 2.33 in Figure 4.8 is also exactly in between the average q_{70} and q_{100} ratios (2.29 and 2.36 respectively), which shows that Equation 4.2 is a reasonable estimate of the FIR emission using the *IRAS* 60 and 100 μm fluxes. Finally the dispersions at each wavelength are also very similar, suggesting that all three bands are probing the same dust component.

Since we are most interested in determining the nuclear to total q ratio using the true FIR flux, we examine the fluxes measured using the same apertures as we did on the 24 μm maps, namely the nuclear and total fluxes. In Figure 4.10 we show the nuclear to total q ratios for the PACS 70 and 100 μm data, as well as the 24 μm ratio from Figure 4.6. Immediately it is obvious that the 70 and 100 μm data similarly show that most of the galaxies have $q_{\rm nuc}/q_{\rm total}$ ratios less than 1, similar to the result at 24 μm. However what is surprising is that neither of the PACS bands show the break in the $q_{24,{\rm nuc}}/q_{24,{\rm total}}$ ratio at $L_{\rm IR} = 10^{11.6} L_{\odot}$. This result strongly suggests that the break in the nuclear to total q_{24} ratio in Figure 4.6 is a result of a deficit in infrared flux, most likely due to the broad 18 μm silicate absorption feature.

To further confirm this we examine the nuclear spectra of the entire GOALS sample ($\sim$240 total nuclei) from *Spitzer*-IRS described in Stierwalt et al. (2013), which covers the MIR wavelength range from 5–35 μm. In Figure 4.11 we show the median averaged MIR spectra for all of the GOALS systems, binned into 0.25 dex intervals of total infrared luminosity (six bins total). Indeed there appears to be an absorption feature (most likely due to silicates) between $\sim$15–25 μm for the highest luminosity (U)LIRGs that affects the

24 μm passband (which encompasses $\sim$21–26 μm, FWHM). Therefore we conclude that the break in Figure 4.6 is due to absorption in the mid infrared in the nuclei of the brightest (U)LIRGs, rather than a radio excess.

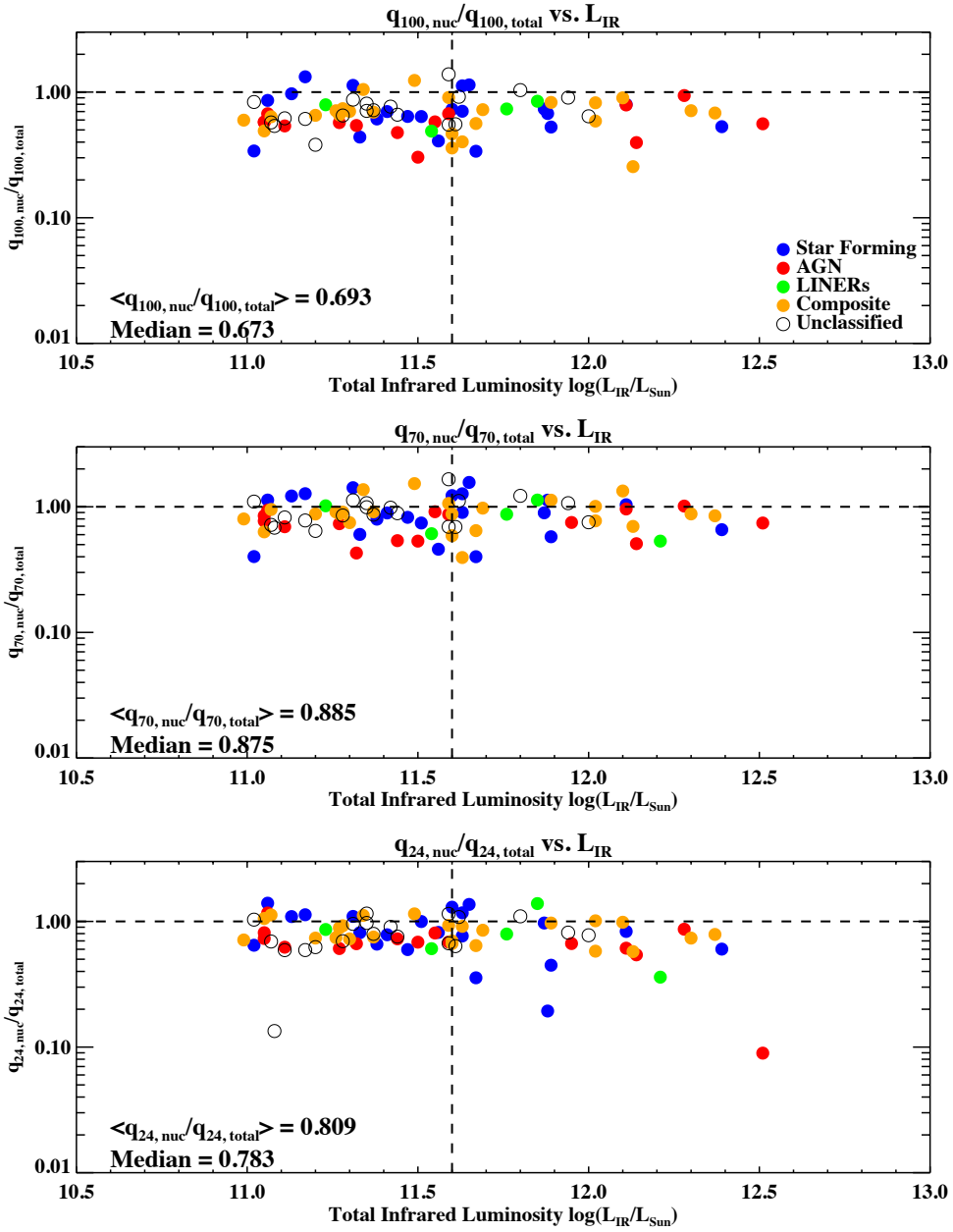

Figure 4.10 The nuclear to total ratios for q_{100}, q_{70}, and q_{24} as a function of $L_{\rm IR}$ and color coded by optical spectral classification. The mean is computed for each plot, as well as the dispersion in the vertical direction. The horizontal dashed line indicates where the nuclear q ratio equals the q value computed over the entire galaxy, while the vertical line indicates the luminosity above which we observe a decrease in the 24 μm nuclear to total q ratio. While there appears to be a break in the 24 μm nuclear to total q ratio, this is not seen at longer wavelengths.

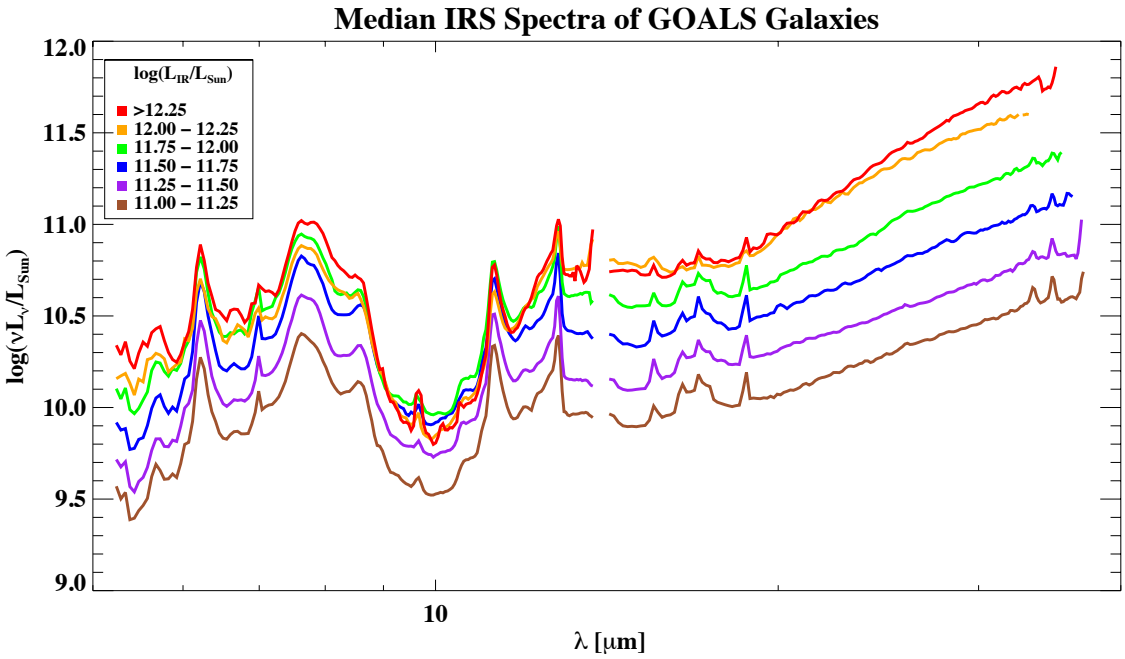

Figure 4.11 The median IRS spectra for the GOALS sample, divided into IR luminosity bins of 0.25 dex. The three highest $L_{\rm IR}$ bins show a significant amount of absorption between $\sim$15–25 μm, while the lower luminosity bins do not show much evidence of absorption in this wavelength range. In comparison the MIPS 24 μm filter covers the wavelengths between 21–26 μm at FWHM.

References

Appleton, P. N., Fadda, D. T., Marleau, F. R., Frayer, D. T., Helou, G., Condon, J. J., Choi, P. I., Yan, L., Lacy, M., Wilson, G., Armus, L., Chapman, S. C., Fang, F., Heinrichson, I., Im, M., Jannuzi, B. T., Storrie-Lombardi, L. J., Shupe, D., Soifer, B. T., Squires, G., & Teplitz, H. I. 2004, ApJS, 154, 147

Armus, L., Mazzarella, J. M., Evans, A. S., Surace, J. A., Sanders, D. B., Iwasawa, K., Frayer, D. T., Howell, J. H., Chan, B., Petric, A., Vavilkin, T., Kim, D. C., Haan, S., Inami, H., Murphy, E. J., Appleton, P. N., Barnes, J. E., Bothun, G., Bridge, C. R., Charmandaris, V., Jensen, J. B., Kewley, L. J., Lord, S., Madore, B. F., Marshall, J. A., Melbourne, J. E., Rich, J., Satyapal, S., Schulz, B., Spoon, H. W. W., Sturm, E., U, V., Veilleux, S., & Xu, K. 2009, PASP, 121, 559

Baldwin, J. A., Phillips, M. M., & Terlevich, R. 1981, PASP, 93, 5

Beck, R. & Golla, G. 1988, A&A, 191, L9

Bell, E. F. 2003, ApJ, 586, 794

Condon, J. J. 1987, ApJS, 65, 485

—. 1992, ARA&A, 30, 575

Condon, J. J., Anderson, M. L., & Helou, G. 1991a, ApJ, 376, 95

Condon, J. J., Helou, G., Sanders, D. B., & Soifer, B. T. 1990, ApJS, 73, 359

—. 1996, ApJS, 103, 81

Condon, J. J., Huang, Z., Yin, Q. F., & Thuan, T. X. 1991b, ApJ, 378, 65

Cowie, L. L., Barger, A. J., Fomalont, E. B., & Capak, P. 2004, ApJ, 603, L69

Dumas, G., Schinnerer, E., Tabatabaei, F. S., Beck, R., Velusamy, T., & Murphy, E. 2011, AJ, 141, 41

Dunne, L., Eales, S., Edmunds, M., Ivison, R., Alexander, P., & Clements, D. L. 2000, MNRAS, 315, 115

Hatziminaoglou, E., Hernán-Caballero, A., Feltre, A., & Piñol Ferrer, N. 2015, ApJ, 803, 110

Hughes, A., Wong, T., Ekers, R., Staveley-Smith, L., Filipovic, M., Maddison, S., Fukui, Y., & Mizuno, N. 2006, MNRAS, 370, 363

Ishida, C. M. 2004, PhD thesis, UNIVERSITY OF HAWAI'I

Kauffmann, G., Heckman, T. M., Tremonti, C., Brinchmann, J., Charlot, S., White, S. D. M., Ridgway, S. E., Brinkmann, J., Fukugita, M., Hall, P. B., Ivezić, Ž., Richards, G. T., & Schneider, D. P. 2003, MNRAS, 346, 1055

Kewley, L. J., Dopita, M. A., Sutherland, R. S., Heisler, C. A., & Trevena, J. 2001, ApJ, 556, 121

Kewley, L. J., Groves, B., Kauffmann, G., & Heckman, T. 2006, MNRAS, 372, 961

Neugebauer, G., Habing, H. J., van Duinen, R., Aumann, H. H., Baud, B., Beichman, C. A., Beintema, D. A., Boggess, N., Clegg, P. E., de Jong, T., Emerson, J. P., Gautier, T. N., Gillett, F. C., Harris, S., Hauser, M. G., Houck, J. R., Jennings, R. E., Low, F. J., Marsden, P. L., Miley, G., Olnon, F. M., Pottasch, S. R., Raimond, E., Rowan-Robinson, M., Soifer, B. T., Walker, R. G., Wesselius, P. R., & Young, E. 1984, ApJ, 278, L1

Rieke, G. H., Young, E. T., Engelbracht, C. W., Kelly, D. M., Low, F. J., Haller, E. E., Beeman, J. W., Gordon, K. D., Stansberry, J. A., Misselt, K. A., Cadien, J., Morrison, J. E., Rivlis, G., Latter, W. B., Noriega-Crespo, A., Padgett, D. L., Stapelfeldt, K. R., Hines, D. C., Egami, E., Muzerolle, J., Alonso-Herrero, A., Blaylock, M., Dole, H., Hinz, J. L., Le Floc'h, E., Papovich, C., Pérez-González, P. G., Smith, P. S., Su, K. Y. L., Bennett, L., Frayer, D. T., Henderson, D., Lu, N., Masci, F., Pesenson, M., Rebull, L., Rho, J., Keene, J., Stolovy, S., Wachter, S., Wheaton, W., Werner, M. W., & Richards, P. L. 2004, ApJS, 154, 25

Roy, A. L., Norris, R. P., Allen, D. A., Troup, E. R., & Kesteven, M. J. 1992, in Astronomical Society of the Pacific Conference Series, Vol. 31, Relationships Between Active Galactic Nuclei and Starburst Galaxies, ed. A. V. Filippenko, 83–+

Sanders, D. B., Mazzarella, J. M., Kim, D., Surace, J. A., & Soifer, B. T. 2003, AJ, 126, 1607

Sanders, D. B. & Mirabel, I. F. 1985, ApJ, 298, L31

Sanders, D. B., Scoville, N. Z., & Soifer, B. T. 1991, ApJ, 370, 158

Seymour, N., Huynh, M., Dwelly, T., Symeonidis, M., Hopkins, A., McHardy, I. M., Page, M. J., & Rieke, G. 2009, MNRAS, 398, 1573

Skrutskie, M. F., Cutri, R. M., Stiening, R., Weinberg, M. D., Schneider, S., Carpenter, J. M., Beichman, C., Capps, R., Chester, T., Elias, J., Huchra, J., Liebert, J., Lonsdale, C., Monet, D. G., Price, S., Seitzer, P., Jarrett, T., Kirkpatrick, J. D., Gizis, J. E., Howard, E., Evans, T., Fowler, J., Fullmer, L., Hurt, R., Light, R., Kopan, E. L., Marsh, K. A., McCallon, H. L., Tam, R., Van Dyk, S., & Wheelock, S. 2006, AJ, 131, 1163

Stierwalt, S., Armus, L., Surace, J. A., Inami, H., Petric, A. O., Diaz-Santos, T., Haan, S., Charmandaris, V., Howell, J., Kim, D. C., Marshall, J., Mazzarella, J. M., Spoon, H. W. W., Veilleux, S., Evans, A., Sanders, D. B., Appleton, P., Bothun, G., Bridge, C. R.,

Chan, B., Frayer, D., Iwasawa, K., Kewley, L. J., Lord, S., Madore, B. F., Melbourne, J. E., Murphy, E. J., Rich, J. A., Schulz, B., Sturm, E., Vavilkin, T., & Xu, K. 2013, ApJS, 206, 1

Veilleux, S. & Osterbrock, D. E. 1987, ApJS, 63, 295

Walterbos, R. A. M. & Schwering, P. B. W. 1987, A&A, 180, 27

Wunderlich, E. & Klein, U. 1988, A&A, 206, 47

Wunderlich, E., Wielebinski, R., & Klein, U. 1987, A&AS, 69, 487

Young, J. S., Kenney, J., Lord, S. D., & Schloerb, F. P. 1984, ApJ, 287, L65

Yuan, T., Kewley, L. J., & Sanders, D. B. 2010, ApJ, 709, 884

Yun, M. S., Reddy, N. A., & Condon, J. J. 2001, ApJ, 554, 803

Chapter 5

Rest-Frame Optical Emission Line Diagnostics of Luminous Infrared Galaxies at $z \sim 2.3$

Note: *This chapter to be submitted to the Astrophysical Journal as Chu, J. K.; Sanders, D. B.; Kewley, L. J.; and Yuan, T.-T.*

Abstract

We present Keck I/MOSFIRE observations on the rest-frame optical spectra of (ultra-)luminous infrared galaxies [(U)LIRGs], AGN, and star forming galaxies between $2 \leq z \leq 2.6$ in the COSMOS field. The (U)LIRGs were selected by their *Herschel* and/or 24 μm detection, the AGN were selected by their IRAC colors or X-ray detection, and the star-forming galaxies were selected by their sBzK colors. We compare our spectroscopic redshifts to the photometric redshifts in the COSMOS2015 catalog, and find a general agreement with $\sigma_{\Delta z/(1+z)} = 0.088$ for our sample, a catastrophic failure rate of 7.2%, and no difference due to different sample selection. Using our sample of 151 galaxies spanning the stellar mass range of $10^{9.5}$ to $10^{11.6}$ $M_{\odot}$ where we securely detect at least three lines in Hβ, [O III], Hα, and [N II], we investigate the location of (U)LIRGs relative to the main star-forming branch on the $z \sim 2.3$ BPT diagram. We find that the (U)LIRGs occupy a different location on the BPT diagram than the star-forming sequence, with notably higher log([N II]/Hα) flux ratios, and a large dispersion in log([O III]/Hβ) skewed towards lower ratios. We also identify 12 IR selected objects that additionally harbor AGN. By including

AGN and star forming galaxies from other NIR surveys at the same redshift, we recover the $z \simeq 2$ star forming sequence and AGN mixing sequence, and show that our (U)LIRGs occupy the region between them with characteristics resembling both populations. This suggests that IR luminous galaxies at these redshifts are not only actively forming stars, but many of them host AGNs as well. We then assess how local BPT classification lines perform and conclude that they should not be used at $z = 2$. Finally, we examine the mass-excitation (MEx) diagram and show that AGN and star forming galaxies are not well separated, with (U)LIRGs occupying both regions. Together, these results suggest that many of our $z \sim 2.3$ (U)LIRGs harbor an AGN, similar to their lower redshift cousins.

5.1 Introduction

After the initial discovery of luminous and ultra-luminous infrared galaxies (LIRGs: $L_{\rm IR} \geq 10^{11} L_{\odot}$, ULIRGs: $L_{\rm IR} \geq 10^{12} L_{\odot}$, or (U)LIRGs collectively; Kleinmann & Low 1970b,a; Rieke & Low 1972), it was shown that many of these galaxies, especially the most luminous ones are undergoing an extreme burst of star formation and/or also harbor an active galactic nucleus (AGN). Sanders & Mirabel (1996) put forth the idea that these (U)LIRGs are the result of major galaxy-galaxy mergers (i.e., Toomre & Toomre 1972): as two gas-rich spiral galaxies begin to collide, tidal disruptions and associated shocks between the galaxies induce an episode of rapid star formation throughout both galaxies (i.e., Kennicutt et al. 1987; Barnes 2004). As both galaxies begin to coalesce into a single galaxy, the starburst is accompanied by gas and dust fueling the central black hole, producing an AGN signature and further increasing the energy output of the galaxy (i.e., Veilleux et al. 2009). The infrared (IR) luminosity originates from the dust absorbing the ultraviolet (UV) and optical light emitted by star formation and/or the AGN, and re-emitting the energy at IR wavelengths. This scenario is supported in the local universe where it was found that the fraction of (U)LIRGs hosting AGNs increases with $L_{\rm IR}$ (Veilleux et al. 1995) and that the merger fraction also increases with $L_{\rm IR}$ (i.e., Sanders et al. 1988a; Kim 1995; Veilleux

et al. 2002). In addition Larson et al. (2016) showed using a morphological analysis that the most advanced mergers are also the most luminous infrared galaxies, and Yuan et al. (2010) showed that the most luminous nearby systems ($z \lesssim 0.3$) also harbor powerful AGN. Finally Sanders et al. (1988b) was the first to suggest an evolutionary link between the ULIRG phase where gas and dust completely enshrouds the central black hole, and optically selected quasi-stellar objects (QSOs). This is evident from studying the space density of local ULIRGs, where Soifer et al. (1987) found that they had similar luminosities and space densities as QSOs.

While (U)LIRGs are relatively rare in the local universe, they become increasingly more common at high redshift (i.e., Casey et al. 2012). At the same time multiple studies have shown that both star formation and AGN activity increases with redshift, peaking around $z \sim 2$ (Reddy et al. 2008; Madau & Dickinson 2014; Ueda et al. 2014; Bourne et al. 2017), which corresponds to when the universe was only ∼3 Gyr old. Other studies similarly conclude that approximately half of today's stellar mass in galaxies appear to be in place by $z \sim 1$ (i.e., Drory et al. 2005; Pozzetti et al. 2007; Pérez-González et al. 2008), while the AGN space density peaks close to $z \sim 2$ (i.e., Brusa et al. 2011; Aird et al. 2015). Furthermore Casey et al. (2012) showed that the star formation rate density (SFRD) is increasingly dominated by (U)LIRGs above $z \sim 0.6$, while the SFRD contribution from normal star forming galaxies (i.e., those without a significant IR luminosity) appears to decrease as a function of redshift. By $z \sim 2$ the contribution to the SFRD from (U)LIRGs is at least ∼3 times larger than from normal star forming galaxies, making them an important class of galaxies to understand at high redshifts.

Although studies of (U)LIRGs up to $z \sim 1$ (i.e., Kartaltepe et al. 2010; Juneau et al. 2013) reveal that they are somewhat similar to what is found locally, it is still unclear what the relative strengths of starbursts and/or AGN are in (U)LIRGs at $z \sim 2$, or "cosmic noon." To address this question we turn to the strong emission lines of elements such as hydrogen, nitrogen, and oxygen in the rest-frame optical regime (3000–7000 Å), which can reveal detailed information on the physical conditions of gas in the interstellar medium

(ISM) as well as the nature of the ionizing source(s). Optical emission line diagnostics, or "BPT" diagrams (Baldwin et al. 1981) are one of the most powerful tools available for studying the rest-frame optical spectra of local galaxies. This method uses the ratios of optical emission line fluxes, such as that of [N II]λ6584/Hα vs. [O III]λ5007/Hβ as a way of classifying emission-line galaxies since they are sensitive to the hardness of the ionizing radiation field. This is crucial since AGN emission is typically harder than that produced by pure star formation, and can be easily used to separate AGN-dominated galaxies from H II (starburst) galaxies.

The wealth of optical spectroscopy data from the Sloan Digital Sky Survey (SDSS; York et al. 2000) has revolutionized these classification schemes by revealing clearly formed branches of star forming galaxies and AGN on the BPT diagram (Kewley et al. 2006). However the first purely theoretical classification scheme on the BPT diagrams was derived by Kewley et al. (2001, henceforth K01). By combining modern stellar population synthesis codes, shock models, and photoionization simulations, they were able to differentiate between starburst-dominated and AGN-dominated galaxies on the BPT diagram. Kauffmann et al. (2003) further refined the classification scheme by adding a composite region to the [N II] BPT diagram, where the AGN and star formation contribution to the ionizing radiation field is comparable to each other. Recently, Kewley et al. (2013, henceforth K13) extended their predictions of the BPT diagram out to higher redshifts, and showed that they were able to differentiate between starburst-dominated and AGN-dominated galaxies out to $z = 3$.

Until recently, rest-frame optical spectroscopy of $z \sim 2$ galaxies were fairly limited in scope (i.e., Erb et al. 2006; Kriek et al. 2008; Hainline et al. 2009; Yoshikawa et al. 2010) owing to the faintness of these objects, the amount of telescope time needed, and the difficulties of near-IR spectroscopic observations. However with the advent of recent NIR multi-object spectrographs such as MOSFIRE (McLean et al. 2012) and KMOS (Sharples et al. 2014), we are now poised construct large samples of rest-frame optical spectra of $z \sim 2$ galaxies. Several surveys are already underway such as the Keck Baryonic Structure

Survey (KBSS; Rudie et al. 2012; Steidel et al. 2014) and MOSFIRE Deep Evolution Survey (MOSDEF; Kriek et al. 2015), where both primarily rely on (rest-frame) UV and/or optical selection techniques. However in this chapter we carry out the first exclusive survey on the ISM properties of infrared selected (U)LIRGs at $z \sim 2.3$. Furthermore we select our own control sample of AGN and star forming galaxies and compare them to our (U)LIRGs as well as other UV/optically selected samples. In §5.2 and §5.3 we describe our sample selection and observations, and in §5.4 we present our results. We discuss the result of our BPT analysis in §5.5, and present it in the context of ancillary data and other $z \sim 2$ surveys in §5.6. We summarize our results in §5.7. Throughout this chapter we assume a ΛCDM cosmology with $H_0 = 70$ km s^{-1}, $\Omega_m = 0.27$, and $\Lambda = 0.73$.

5.2 Sample Selection

The Cosmic Evolution Survey field (COSMOS; Scoville et al. 2007) is an ideal laboratory to study the properties of emission-line galaxies due to its existing and extensive multi-wavelength coverage including observations from JVLA, *Herschel Space Observatory*, *Spitzer Space Telescope*, *GALEX*, *Chandra X-ray Observatory*, *XMM Newton*, and 30 photometric bands between the UV and NIR. It is also the largest deep field covering an unprecedented 2 deg^2, allowing us to capture many more rare objects that may be missed in surveys with smaller areas. As well as being equatorial (centered at J2000 α=10h 00m 28.6s, δ=2d 12m 21s), the COSMOS field was chosen for its relatively low Galactic dust extinction ($\langle E(B-V)\rangle \simeq 0.02$), low *IRAS* 100 μm background for an equatorial field its size, and lack of bright radio, UV, and X-ray sources.

The redshift range of our survey was selected based on the available filters on MOSFIRE, the strong emission lines of interest, and the spectroscopic survey efficiency desired. At $2 \leq z \leq 2.61$, Hβ λ4861 Å and [O III] $\lambda\lambda$4959, 5007 Å conveniently shifts into the H-band while Hα λ6563 Å, [N II] $\lambda\lambda$6548, 6584 Å, and [S II] $\lambda\lambda$6717, 6731 Å shifts into the K-band, allowing us to capture all of the main BPT emission lines with only two sets of observations.

The redshifts of our candidates were either determined from spectroscopic redshifts in the zCOSMOS (Lilly et al. 2007, 2017 in prep.) and FMOS COSMOS (Silverman et al. 2015) surveys, or using the photometric redshifts from the COSMOS2015 catalog (Laigle et al. 2016). The photometric redshifts are calculated using SED templates that are fit to fluxes in 30 bands, covering the near-UV (2300 Å) to the mid-infrared (8 μm) for precise redshifts. Finally we impose a magnitude limit of $K_s \leq 23.1$ (AB) as determined by the MOSFIRE exposure time calculator, to ensure that we detect the main emission lines with sufficient signal to noise ratios. In order to include as many emission line galaxies as possible, we constructed our sample using five different selection methods.

5.2.1 Herschel and 24 μm Selection

We selected IR bright galaxies, i.e. (U)LIRGs, in the COSMOS field based on *Herschel Space Observatory* (Pilbratt et al. 2010) observations because it is ideally suited to detect the extreme infrared luminosities of these systems. Even at $z \sim 2$, the *Herschel* bandpasses are still probing the rest-frame FIR regime of the SED where (U)LIRGs emit the most of their bolometric luminosities. *Herschel* FIR observations of the COSMOS field were taken using the PACS instrument (Poglitsch et al. 2010) at 100 and 160 μm under the PACS Evolutionary Probe program (PEP; Lutz et al. 2011), while the submillimeter data at 250, 350, and 500 μm were taken by SPIRE (Griffin et al. 2010) as part of the *Herschel* Multi-tiered Extragalactic Survey (HerMES; Oliver et al. 2012).

We use the catalog generated by Lee et al. (2013), where their ∼4200 *Herschel* sources (over the entire field) were identified using 24 μm priors from our COSMOS-*Spitzer* program Sanders et al. (2007). In order for a source to be considered real, we require every *Herschel* detection to have a minimum SNR of 3 in at least two *Herschel* bands. However due to the drop in sensitivity as one moves to higher redshifts, we found only 272 (U)LIRGs over the entire field that satisfied our redshift and magnitude criteria, resulting in a very low surface density of possible targets to observe.

Due to the stringent requirement and low number of sources directly detected by *Herschel*, we relaxed our constraints to include objects detected in only one *Herschel* band, and objects detected by *Spitzer*-MIPS at 24 μm. The latter provides a much deeper coverage with more than 39,000 sources with $S_{24} > 80$ μJy at the 90% completeness limit (Le Floc'h et al. 2009). This allows us to add an additional 1450 (U)LIRGs that satisfies our redshift and magnitude criteria. Although 24 μm does not directly probe the FIR at $z \sim 2.3$, the mid-infrared has been shown to correlate strongly in general with the total infrared luminosity (Rieke et al. 2009). Furthermore we emphasize that this selection method was designed to be complementary to that of other surveys at similar redshifts which are currently based on rest-frame UV and/or B-band selection, whereas our targets were selected based on their $\sim$10–100 μm emission. This is critical as this class of galaxies, with even a moderate amount of dust obscuration, may be missed by pure optical selection methods.

5.2.2 AGN Selection

In addition to IR luminous galaxies, we include in our sample AGN selected by both *Spitzer*-IRAC colors and X-ray detections. This is important in constructing an unbiased sample, as Azadi et al. (2017) showed that MIR AGN identification tends to bias against the most massive galaxies, while a pure X-ray selection showed possible bias towards more dusty host galaxies.

AGN selection by their *Spitzer*-IRAC colors (e.g., Stern et al. 2005; Lacy et al. 2007) rely primarily on detecting the blackbody radiation from the hot dust surrounding the supermassive black hole (SMBH). In the absence of an AGN, the SEDs of galaxies typically display a prominent dip between the 1.6 μm stellar emission bump and the FIR emission from star-forming heated dust ($T_{\rm SF,dust} \simeq 25 - 50$ K). However if a galaxy hosts and AGN, dust in the circumnuclear torus can be heated to very high temperatures ($T_{\rm AGN,dust} \simeq 1000 - 1500$ K) where it radiates in the MIR. If the AGN luminosity is comparable to the host galaxy, then the superposition of the blackbody radiation from the

AGN-heated dust will fill in this dip and produce a red, power-law like thermal continuum across the IRAC bands (i.e., Elvis et al. 1994). This will be visible to the observer as long as the obscuring medium is optically thin to MIR radiation, regardless of optical or UV extinction.

Donley et al. (2012) identified ∼1500 AGN sources in the COSMOS field using a revised IRAC-based selection criteria. By plotting the IRAC colors $\log(S_{5.8}/S_{3.6})$ vs. $\log(S_8/S_{4.5})$, they showed that the most secure AGN detections lie along a locus of pure power-law SEDs. This selection method was designed to be both highly complete and reliable, while excluding high redshift star-forming galaxies identified using other color selection criteria (i.e., BzK or Lyman break galaxies). Furthermore Mendez et al. (2013) confirmed this result using a combination of multiple mid-IR and X-ray surveys at varying depths. From the catalog provided by Donley et al. (2012), we selected a total of 266 IRAC-detected AGN that satisfy our redshift and magnitude criteria. Although this method recovers 75% of total sources detected in *XMM*-COSMOS (Hasinger et al. 2007), it cannot effectively identify low-luminosity AGN with host-dominated MIR SEDs, and also appears to be incomplete to luminous but extremely obscured AGN. Mendez et al. (2013) conducted a separate study and also came to the same conclusion, and additionally found that this fraction increases to 90% when compared against the deepest X-ray data available. A traditional X-ray selection therefore remains an important tool for identifying AGN missed in the MIR.

Unlike optical or infrared selection methods, X-ray AGN surveys do not suffer from heavy contamination by non-active galaxies, and is efficient in selecting low-luminosity and obscured AGN up to equivalent hydrogen column densities approaching the Compton-thick regime. We select our X-ray sources from Civano et al. (2012), who matched the 1761 sources in the central 0.9 deg^2 of the field (*Chandra*-COSMOS; Elvis et al. 2009) to optical and infrared counterparts using the "likelihood ratio" technique (Sutherland & Saunders 1992). Apart from using a simple match of the positional offset between sources in different catalogs, the likelihood ratio technique also takes into account for each possible optical/IR counterpart the probability that it is a real or spurious association. This powerful statistical

method allows for a much better characterization and higher success rate for the final sample of identifications. For the C-COSMOS dataset, Civano et al. (2012) reported that 97% of the X-ray sources have a positive identification, from which we identified 206 X-ray AGN of interest, bringing us up to a total of 472 AGN within our redshift range.

5.2.3 Star-Forming Galaxies

The BzK selection method (Daddi et al. 2004) is primarily used to separate high-redshift galaxies at $1.4 \lesssim z \lesssim 2.5$ from lower redshift galaxies and field stars. They demonstrated in the $(B-z)$ vs. $(z-K_s)$ color-color space that high redshift star-forming galaxies, and low-redshift galaxies are well separated at $z \simeq 1.4$. This makes it possible and relatively straight-forward to accumulate large samples of galaxies using only three photometric bands. Furthermore, the separation of star-forming (sBzK) as opposed to passively evolving galaxies (pBzK) above $z > 1.4$ relies on the [O II] $\lambda\lambda 3727, 3729$ Å and the 4000 Å break ($D_n(4000)$), both of which are spectral signatures of active star formation. The advantage to this method is that it recovers many moderately obscured star-forming galaxies at high redshifts that traditional rest-frame UV-selection methods miss. This is crucial since a complete and unbiased sample of (non IR-luminous) star-forming galaxies is needed to compare with infrared luminous galaxies.

For our study we have combined the B_J and z^+ photometry taken on Subaru Suprime-Cam (Taniguchi et al. 2007) with the K_s data taken on the UltraVISTA telescope (McCracken et al. 2012) to construct the BzK diagram. The K_s photometry was measured with a $2''$ diameter aperture with a 5σ detection limit of 23.7 mag (AB) over 1.7 deg^2 of the field[1]. Following the photometric corrections outlined in McCracken et al. (2010) and applying a magnitude cut at $K_s \leq 23.1$ mag (AB), we identified a total of ∼40,000 star-forming BzK galaxies, of which 8011 were within our redshift range.

[1]Based only on the UltraVISTA DR1 data. With the DR2 released in 2012, the final 3σ depth is 24.5 and 25.2 mag (AB) in the deep and ultra-deep stripes respectively.

5.2.4 The Full Sample

Since many of our objects may be detected by two or more selection methods, we first matched everything to our optical catalog. From there we assigned a classification to each object such that they would be considered as in descending order: (U)LIRGs (*Herschel* and/or 24 μm selected), AGN (X-ray and/or IRAC selected), and star forming galaxies (sBzK selected). For example, if a galaxy is detected in both the AGN and sBzK sample, it would be considered an AGN. We note that our selection method is not mutually exclusive, for instance an AGN galaxy may also be a (U)LIRG, however it would be classified as a (U)LIRG given our priorities[2]. From this we arrive at the final count of 1722 (U)LIRGs, 135 AGN, and 6344 star-forming galaxies in our sample.

5.3 Observations and Data Reduction

5.3.1 Mask Design Strategy

Spectroscopic observations were performed using the Multi-Object Spectrograph for Infrared Exploration (MOSFIRE; McLean et al. 2010, 2012) on Keck I. Briefly, MOSFIRE is a cassegrain-mounted NIR (YJHK) multi-object spectrograph capable of remotely and quickly reconfiguring its focal plane Configurable Slit Unit (CSU) in a matter of minutes ($\sim$15 min. for a full mask reconfiguration). The CSU comprises 46 pairs of opposing bars that can form slits within a $6\farcm11 \times 6\farcm11$ field of view on the sky, although slits placed near the edges in the dispersion direction will suffer from reduced wavelength coverage. For this reason our slit masks were designed with slits only in the central $3\farcm3 \times 6\farcm12$ (dispersion $\times$ spatial) region[3]. Each opposing pair of bars can produce a single slit length of $7\farcs1$ in the spatial direction, or if longer slits are desired, multiple bars can be combined to produce slit lengths in multiples of $7\farcs5$ increments. Equipped with the latest HAWAII2-RG detector

[2]Indeed, we did find 12 galaxies to be classified as both.

[3]Within this reduced area, we only lose a maximum of $\sim$20% in wavelength coverage for slits near the edges in the dispersion direction. Slits near the edges in the spatial direction are unaffected.

with an on-sky plate scale of $0.1798''$/pixel[4], MOSFIRE delivers a spectral resolution of $R \sim 3600$ in the H-band (1.465 – 1.799 μm) and K-band (1.953 – 2.398 μm) with a standard slit size of $0\farcs7$ on the sky.

Our mask designs were generated using the Java-based MOSFIRE Automatic GUI-based Mask Application (MAGMA) software (version 1.1). In order to maximize the number of targets on a given mask, we began by selecting broad regions in COSMOS with as many of our candidate targets as possible. Using an input master catalog constructed as described in §5.2, we ran MAGMA which iterates through three different positional variables (RA, dec., and PA) to find the optimal on-sky mask position maximizing our priority. This was first done in a coarse manner, whereby MAGMA searched over a typical parameter space of $\pm 3'$ in ΔRA and Δdec. in steps of $\sim$1-2$''$ at all position angles (1° steps). A second (or more) MAGMA run was then done using the results from the first pass, this time with a finer search grid of $\pm 45''$ in ΔRA and Δdec. in steps of $\sim 0.5''$, and all position angles. In addition, we required at least 4 alignment stars to be present in the mask design for accurate placement of the mask on the sky. Since spectroscopic observations in the NIR require us to dither our individual exposures in the spatial direction, we chose the default nod amplitude of $\pm 1\farcs5$ along the slit, with $2\farcs5$ of dither space towards the slit edges. In practice, as long as our objects are less than $\sim 1''$ in size, we can expect our slits to cover the entire target. Finally we chose the default slit width of $0\farcs7$, which provides a good trade-off between reaching our fainter targets while retaining good spectral resolution.

The final results of each mask design were then inspected by eye, and in a few cases we were able to manually squeeze an additional target onto the mask. Our target prioritization was done in the same order described in §5.2.4, placing the greatest priority on the *Herschel* objects, followed by the 24 μm objects, AGN, and finally the sBzK-selected objects. Within the same selection method, greater weight was placed on objects for which we had secure spectroscopic redshifts, while objects with only photometric redshifts that had a large error had the least priority. Because of the way we prioritized our targets, and

[4]Only in the spatial axis. In the dispersion axis, an additional anamorphic multiplicative factor of 1.335 and 1.357 is needed for YJ and HK bands respectively.

the number of objects within our different sub-samples, a typical mask would be evenly split between (U)LIRGs (of which 2-5 were *Herschel*-detected) and star-forming galaxies, with anywhere between 0-3 AGN. Each of our masks have on average ∼24 objects (not including serendipitous detections), which is less than the maximum possible of 46 objects due to our source distribution on the sky and dither space requirements. This resulted in the assignment of multiple bars to an individual object in some cases.

5.3.2 MOSFIRE Observations

A total of 15 masks were observed in both H- and K-band over seven nights from 2014 to 2016 (PI: Chu), with one night completely lost due to weather. In Figure 5.1 we show the footprints of all of the observed masks overlaid on the COSMOS i^+-band mosaic from Subaru (Taniguchi et al. 2007), while in Table 5.1 we list all of our mask configurations and observing conditions. Each mask is labeled with the coarse MAGMA run (first number) followed by a version (second number) corresponding to the fine search run.

Standard afternoon calibrations were executed before each night of observing, which includes arc and flat observations for each mask and filter combination. A thermal flat was taken for K-band to correct for thermal emission which is visible at the long-wavelength end of the filter. For the science exposures we adopted the recommended integration times of 120 s and 180 s per frame for H- and K-band respectively, which the MOSFIRE instrument team found to be the best trade-off between exposure cadence and the effect of detector noise. This is because the rapidly-varying intensities of telluric OH emission features (a few percent over ∼30 s) drives one towards shorter exposures, while longer exposures allows one to overcome detector read noise in the low background between the OH lines. To further reduce noise, each exposure was nondestructively read in 16 pairs (Fowler sampling) which resulted in a readout noise of 5.8 electrons (rms) and a gain of 2.15 electrons/count.

Our total integration times for each mask and band are listed in Table 5.1. From the MOSFIRE exposure time calculator we determined that H-band required 48 min. of integration time to reach a SNR of ∼5 for a line flux of $\sim 5 \cdot 10^{-18}$ ergs s^{-1} cm^{-2}. In

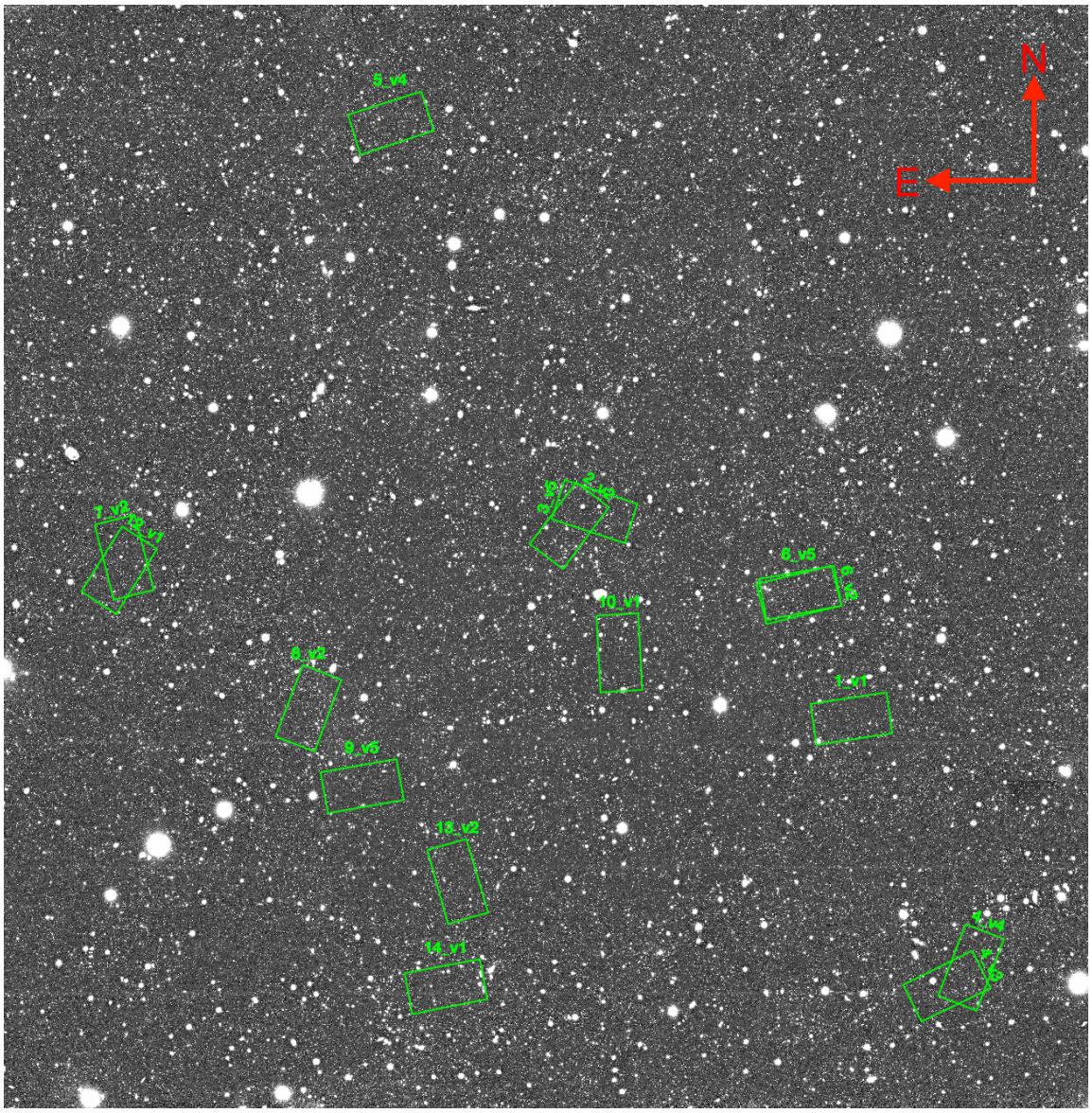

Figure 5.1 A visual representation of our observed MOSFIRE masks in the COSMOS field, the field of view here spans RA= $09^h57^m35^s$ to $10^h03^m20^s$, and dec. $= 1°28'30''$ to $2°56'20''$, where North is up and East is left. Each mask is $3.'3$ wide and $6.'12$ long, superimposed on top of the Subaru SuprimeCam i^+ band image (Taniguchi et al. 2007). For masks 6_v2 and 6_v5, the latter mask is the rectangle that is slightly higher on the left side relative to the former.

K-band a total integration time of 84 min. was required to reach the same depth and SNR, due to differences in telescope + instrument efficiencies. Each set of observations were taken using an ABBA dither pattern with $\pm 1.5''$ offsets to properly subtract out telluric emission features. However in an effort to improve our H-band detection rates, for the two nights in 2016 we increased our H-band integration times to $\sim$84 min. while keeping K-band approximately the same. In addition, four masks were re-observed to improve our line sensitivities down to $\sim 3.5 \cdot 10^{-18}$ ergs s^{-1} cm^{-2} (at the same SNR) for objects not detected in the first observation. To design these masks, targets that were already detected in the first mask were removed, and MAGMA was ran again to optimize mask placement. One pair of masks (cosmos_6_v2 and cosmos_6_v5) is nearly the same because of bad weather when the first mask was observed.

For each night we observed an A0V star near the beginning and end of the night at airmasses close to our observations to derive a flux response spectrum and for telluric corrections. In the 2014 and 2015 observing seasons, these stars were observed using three slit bars placed in the middle of the CSU mask. Unfortunately this configuration was insufficient in covering the entire wavelength range targeted by some of the slits. To remedy this on the two nights in 2016, we observed the telluric stars using the `long2pos` mask, which consists of two 3-segment long slits that are offset $\pm 1.5'$ from the center. The telluric star is then observed using an ABBA pattern in both slits to cover the entire wavelength range.

5.3.3 MOSFIRE Data Reduction

Data reduction and processing were performed using the latest version of the python-based MOSFIRE Data Reduction Pipeline (MOSDRP) released in 2016, which produces background-subtracted, spatially rectified, and wavelength-calibrated 2D spectra from the raw FITS files. Each mask is reduced using a "driver" script which calls all of the file lists and controls all of the pipeline steps for a specific mask/band combination. The first step in the pipeline is to generate a pixel flat and trace the slit edges. However because in K-band the dome emits some thermal radiation that is visible at the longest wavelengths (a

Table 5.1 Keck I MOSFIRE Observations

Mask Name	UT Obs. Date	Mask Center Coordinates		Mask PA[a]	Integration Time		Avg. FWHM Seeing		N_{gal}[b]
		Right Ascension	Declination		H-Band	K-Band	H-Band	K-Band	
—	YYYY–MM–DD	HH MM SS	DD MM SS	°	min.	min.	″	″	—
cosmos_1_v1	2014–02–09	09h 58m 50.14s	01d 59m 25.00s	−81.0	48	84	0.6	0.5	29
cosmos_2_v2	2016–02–17	10h 00m 20.11s	02d 14m 48.00s	−37.0	84	84	0.7	0.8	26
cosmos_3_v5	2014–02–09	10h 00m 12.13s	02d 15m 55.42s	+72.0	48	84	0.5	0.4	26
cosmos_4_v3	2014–02–08	09h 58m 19.75s	01d 38m 03.50s	−64.0	48	84	0.8	0.6	31
cosmos_4_v4	2015–01–31	09h 58m 12.00s	01d 39m 33.50s	−21.0	48	78	0.6	0.6	28
cosmos_5_v4	2015–01–31	10h 01m 17.13s	02d 46m 54.15s	−72.0	48	60	0.7	0.7	33
cosmos_6_v2	2014–02–08	09h 59m 06.45s	02d 09m 27.40s	−79.5	48	84	1.3	0.9	26
cosmos_6_v5	2015–01–31	09h 59m 06.91s	02d 09m 16.40s	−76.0	48	78	0.7	0.8	28
cosmos_7_v2	2016–02–18	10h 02m 42.20s	02d 12m 16.40s	+14.0	80	84	0.7	0.7	26
cosmos_8_v2	2014–02–09	10h 01m 43.33s	02d 00m 14.80s	−21.0	48	54	0.4	0.5	29
cosmos_9_v5	2016–02–18	10h 01m 26.29s	01d 54m 01.90s	−80.0	96	96	0.8	0.8	24
cosmos_10_v1	2015–02–01	10h 00m 04.21s	02d 04m 39.00s	+3.0	48	78	0.7	0.9	23
cosmos_12_v1	2016–02–17	10h 02m 43.86s	02d 11m 13.90s	−32.0	92	102	0.9	1.1	25
cosmos_13_v2	2015–02–01	10h 00m 55.91s	01d 46m 26.50s	+16.0	48	78	0.6	0.7	23
cosmos_14_v1	2015–02–01	10h 00m 59.54s	01d 38m 03.60s	−79.0	48	78	0.7	0.8	27

The MOSFIRE observing log for each mask configuration. [a]The mask position angle on the sky measured in degrees counterclockwise from the vertical orientation. [b]The number of galaxies observed in each mask, including serendipitous detections.

few hundred counts), we perform an additional step to subtract "thermal flat" observations from the flat data. These thermal flats were taken just like normal flats but with the flat lamps turned off.

Next all of our science frames are combined so that we may interactively determine our wavelength calibration solution using the night sky lines at the center of the slit. Outlying lines that are greater than ∼0.15 Å are deleted from the wavelength solution, resulting in typical residuals of ∼0.07 Å (rms) for the final solution. After this is done for each object, MOSDRP uses the initial wavelength solution to automatically fit the rest of each slit, then applies the full 2D wavelength solution to the combined science frame. However due to the paucity of night sky lines at the long wavelength side of K-band, we use Ne arc lamp observations to accurately calibrate those wavelengths. Since the light path taken by the night sky lines and the arc lamps slightly differ (<1 pixel on the detector), we first calibrate using night sky lines, then use those initial solutions to calibrate the lines from the Ne lamp. Once both solutions are obtained, they are combined and applied to the 2D science frames.

MOSDRP next performs a background subtraction to remove contributions from the atmosphere. The background subtraction step produces several files in this case, the most important ones being rectified FITS files containing the signal, integration time, variance, and signal to noise. At this point we examine each of the signal files to be sure that each slit was correctly rectified and wavelength-calibrated. The final step is to shift and combine the different nod positions to produce the final 2D spectrum. In our case where we use the ABBA nod pattern, the FITS files are combined as: $(A-B)+(B-A)_{\mathrm{shifted}}$, where "shifted" in our case is $3''$. This operation produces a single positive trace surrounded by two negative traces for each object in the slit. Finally, data reduction for the telluric observations were done in a very similar manner to our science data.

Subsequent 1D spectrum extraction, telluric correction, and flux calibration was performed using the MOSFIT code developed for the ZFIRE survey (Nanayakkara et al. 2016). First we extracted the 1D spectrum of the standard star from the wavelength-calibrated 2D spectrum. We then removed the intrinsic Hydrogen absorption lines in the

stellar atmosphere by using Gaussian fits to the line profiles, then used the fitted profile to interpolate over the absorption feature. The resulting spectrum was then divided by a theoretical blackbody function corresponding to the surface temperature of an A0 star (T∼10,000 K). Next the spectrum was normalized and smoothed to create a sensitivity curve, which is the total system response as a function of wavelength due to atmospheric absorption, telescope sensitivities, and the response function of MOSFIRE. The sensitivity curve was then divided into both the science frames and the standard star observations.

The flux conversion factor was derived by comparing our observed spectrum to the specific 2MASS magnitude for that star. This factor was then applied to the science frames to produce the final flux-calibrated 2D spectrum. This simple flux calibration method does not consider slit-loss where the systematic error is about 20–30%. Because this work focuses on emission line ratios, the absolute errors of flux calibration do not affect on our results. To extract the 1D spectrum, we visually searched each slit for the target and any serendipitous detections, using the original mask design parameters to aid in finding the expected position of our objects. This method also allows us to identify any false-positive features that may show up in our 2D spectra. If the object is visible in our 2D spectrum (i.e., if emission lines or a continuum is present), the code will determine the optimal extraction aperture using the FWHM of the spatial profile. If the object is too faint or undetected, we set the extraction aperture to be the FWHM of a point source based on the seeing conditions for that mask.

5.4 Results

After 1D spectrum extraction, we used SpecPro (Masters & Capak 2011) to measure the redshifts of our galaxies. In Figure 5.2 we show five examples of our final spectra for a variety of sources with their corresponding spectroscopic redshifts in both H- and K-band around the emission lines of interest. Once we determined the redshifts, we fit the observed emission lines with Gaussian profiles to measure the line fluxes. In Figure 5.2 we show

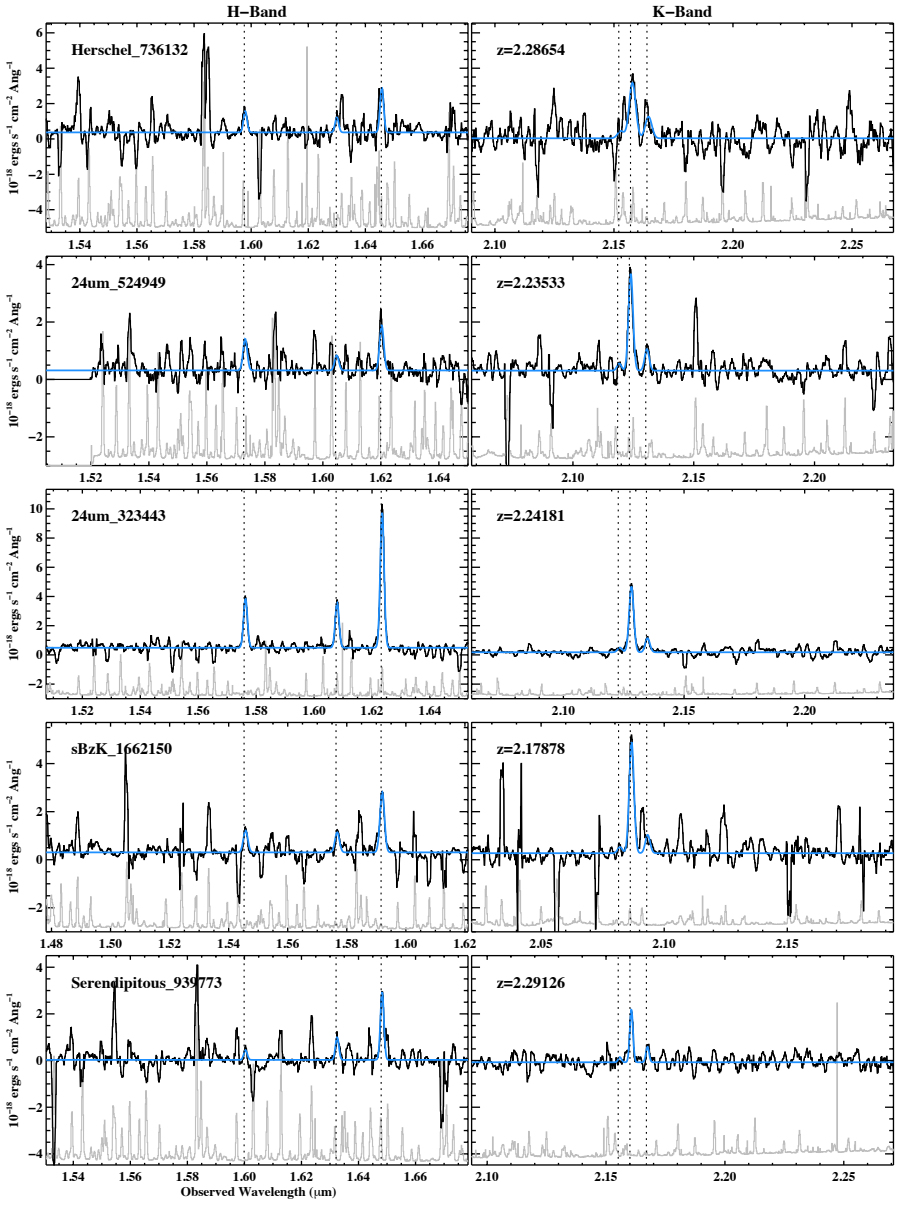

Figure 5.2 Example 1D spectra around emission lines of interest from our MOSFIRE observations, where each row is one object. The left side is the H-band observation where the dotted lines represent detections in (from left to right) Hβ λ4861, [O III] λ4959, and [O III] λ5007 Å. The right side is the corresponding K-band data, where the dotted lines represent (from left to right) [N II] λ6548, Hα λ6563, and [N II] λ6584 Å. The black lines represent the un-smoothed data, while the blue represents the continuum + emission line fits. The grey error spectrum is also plotted offset from the data itself. The bottom row shows a serendipitously-detected object with all four emission lines, that wasn't present in any of our selection methods. In Figure 5.6 this object clearly lies above the $z = 2.3$ maximum starburst line on the BPT diagram.

our emission line fits in blue, while the grey spectrum below represents the error spectrum which we used to calculate the flux error. In cases where there was insufficient SNR to measure an emission line flux, we used the error spectrum to calculate the 1σ upper limit to the flux.

Over our entire program we obtained the spectra on a total of 365 objects, consisting of 36 *Herschel*, 139 24 μm, 12 AGN, and 136 sBzK-selected objects. In addition we detected 10 serendipitous galaxies which we were able to classify into one of the aforementioned selection methods, and 32 serendipitous galaxies that did not fall into any of our classifications. In Figure 5.3 we show the redshift distribution for all targets with secure redshifts in the top panel, as well as the redshift distribution for each selection method. The median redshift for both the (U)LIRG and star forming samples is $z = 2.19$ and an average of $z = 2.23$. On the bottom panel we show the redshift distribution for those galaxies in which we detect all four BPT emission lines. The AGN in the bottom plot are all also detected in the IR, so they are double-counted in the histogram.

In Figure 5.3 there is a very sharp jump in the number of objects in the redshift bin $[2.10, 2.15]$. Upon further examination we found a total of 25 galaxies with redshifts between 2.10 to 2.14 spread across two different mask footprints, with 13 and 12 in each region, which we will refer to as Clusters 1 and 2 respectively. Furthermore we individually examined each spectrum and confirmed that the redshifts were not misidentified due to residual telluric sky features since all but one object had multiple emission lines. On the sky Clusters 1 and 2 are centered at the approximate coordinates $(\alpha, \delta) =$ (09h 58m 13s, 01d 39m 05s), and $(\alpha, \delta) =$ (10h 02m 42s, 02d 12m 07s) respectively. Both have projected diameters of ~ 150" which corresponds to 1.27 and 1.18 Mpc at their respective redshifts. Searches through the literature did not reveal any known structures at those coordinates and redshift. In Cluster 1 one of the galaxies is farther to the southeast, so we do not consider that source to be included in the galaxy cluster, leaving us with 12 members in the cluster. The average redshift for Clusters 1 and 2 are $\langle z \rangle = 2.1025$ and $\langle z \rangle = 2.1331$, with a 1σ dispersion of $2.333758 \cdot 10^{-3}$ and $7.06029 \cdot 10^{-3}$ respectively assuming a Gaussian distribution.

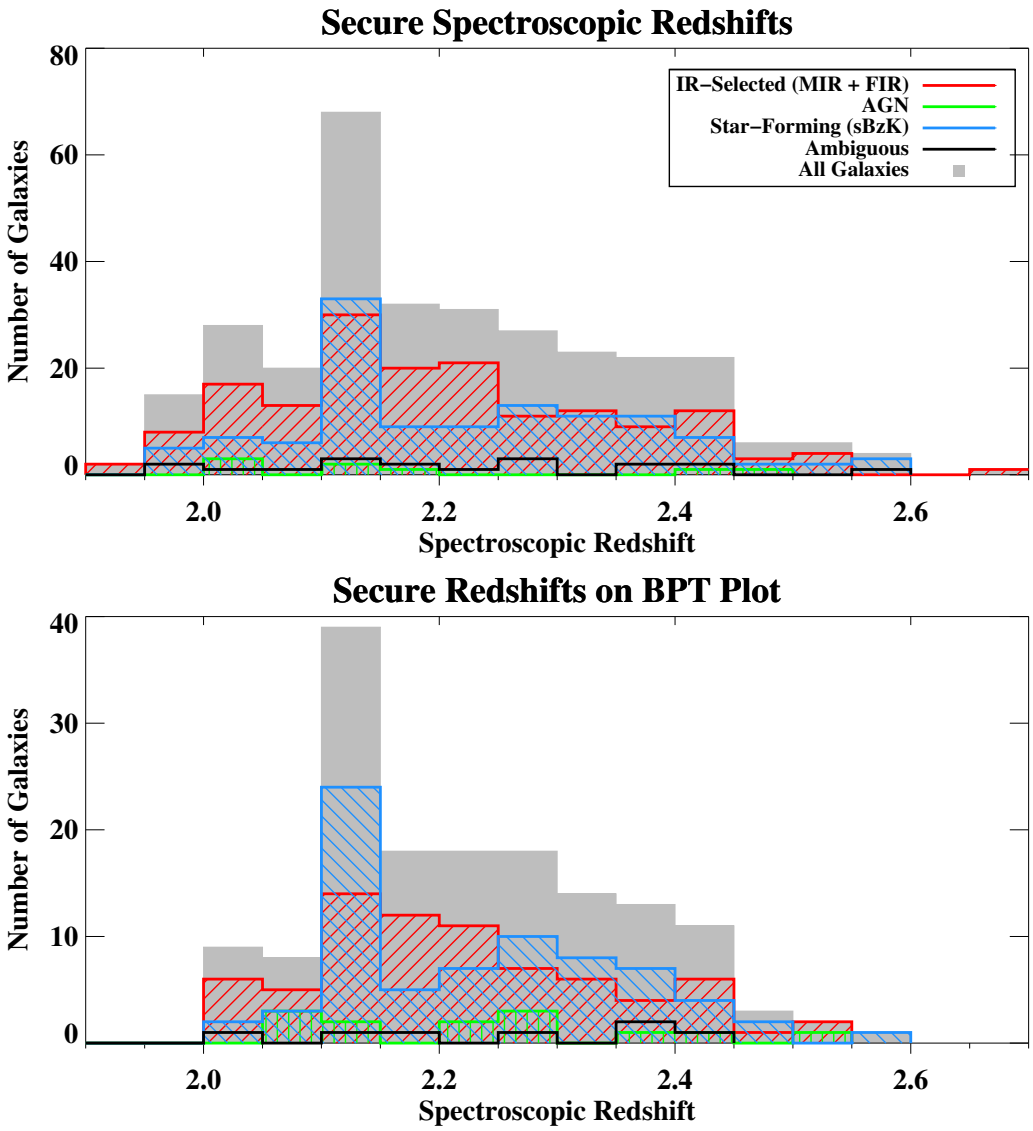

Figure 5.3 The redshift distribution for all targets with secure redshifts (top panel), and for those targets with 3 or more lines with SNR $\geq$ 3 for Hα, [N II], [O III], and Hβ (lower panel). In each histogram the red, green, blue lines represent IR, AGN, and star-forming selected galaxies respectively, while the grey histogram represents the sum of all objects. The 12 AGN that were also cross-identified in our infrared catalogs (see §5.5) are plotted on the bottom panel, however they do not contribute to the total histogram in grey.

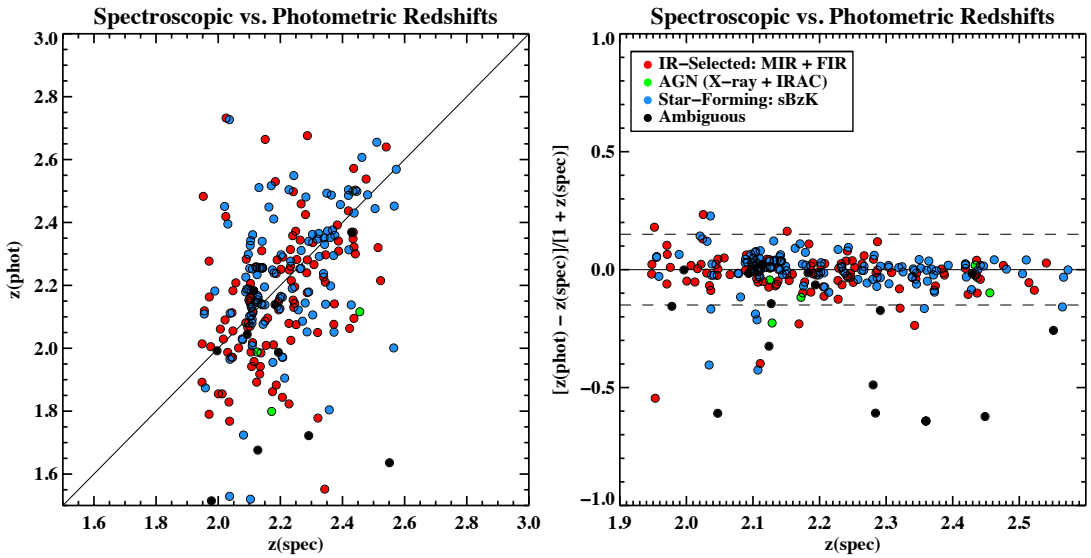

Figure 5.4 Comparison of our spectroscopic redshifts to the photometric redshifts from Laigle et al. (2016). *Left*: Plot of $z_{\rm spec}$ *vs.* $z_{\rm phot}$ for all of our sources, color-coded by selection method. We also plot the line where $z_{\rm spec} = z_{\rm phot}$. *Right*: Plot of $z_{\rm spec}$ *vs.* $\Delta z/(1+z_{\rm spec})$ where Δz is defined to be $z_{\rm phot} - z_{\rm spec}$. Anything outside of the two dashed lines represents a catastrophic failure.

We also assessed the quality of photometric redshifts in the COSMOS2015 catalog (Laigle et al. 2016) compared to our spectroscopic redshifts. By using the latest 30-band imaging observations executed on the COSMOS field from near-UV through the mid-IR, they computed precise photometric redshifts for over half a million objects. Photo-z's for X-ray selected objects were obtained from the *Chandra*-COSMOS Legacy Survey catalog of Marchesi et al. (2016). In Figure 5.4, left panel we show our spectroscopic redshift compared to the photometric redshift for our objects, color-coded by our selection method. A fairly large scatter is observed with an average $|\Delta z| = |z_{\rm phot} - z_{\rm spec}| = 0.22$. In the right panel of Figure 5.4 we show $\Delta z/(1+z_{\rm spec})$ as a function of $z_{\rm spec}$, where there are no obvious trends with redshift. In addition, we calculated $\sigma_{\Delta z/(1+z)}$ for our sample to be 0.088, with little variation between our different selection methods. Furthermore the catastrophic failure rate, defined to be $|\Delta z|/(1+z_{\rm spec}) > 0.15$, is 7.2% for our entire sample. These figures

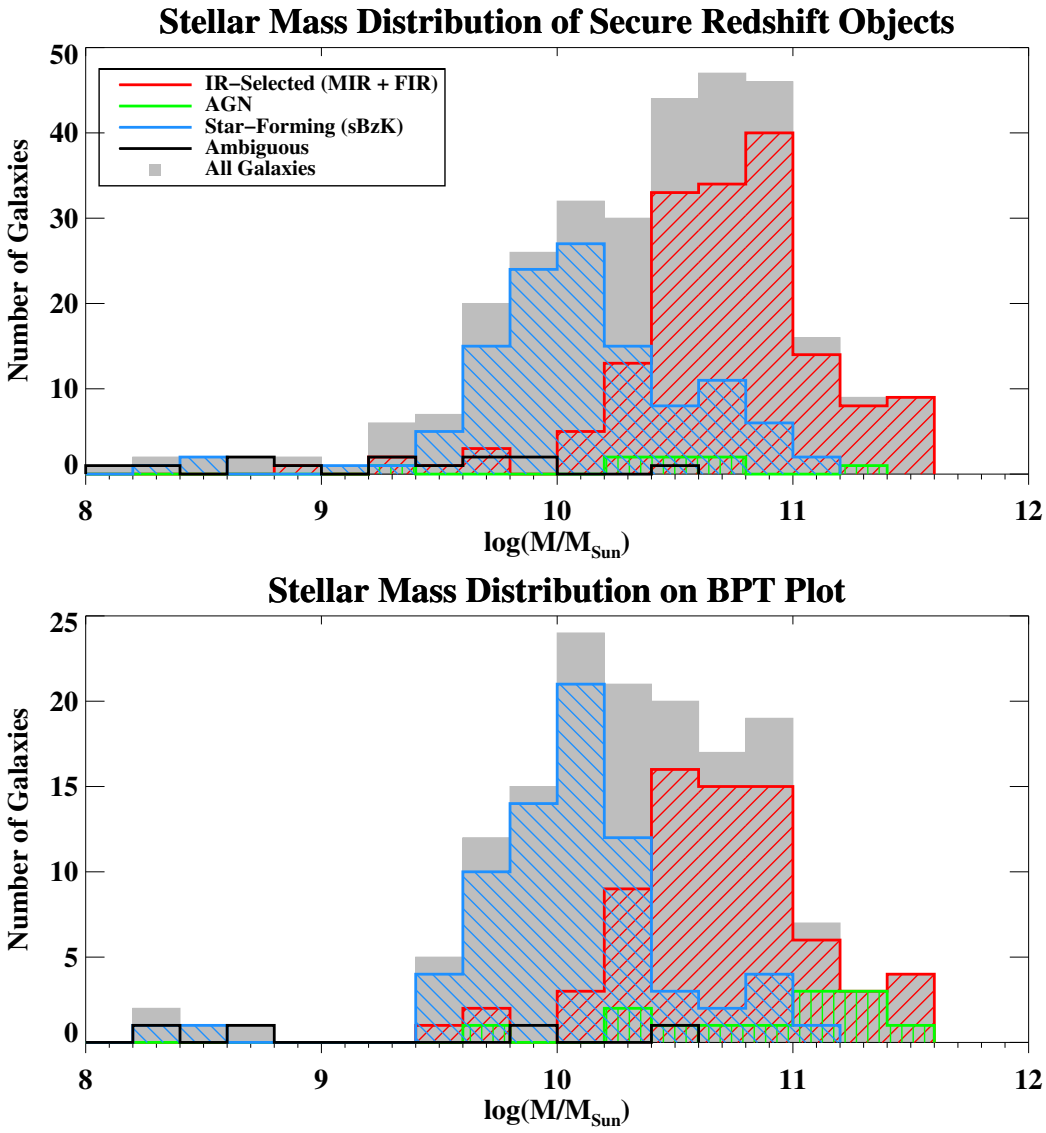

Figure 5.5 Same as Figure 5.3 but for the stellar mass distribution.

are roughly similar to what Laigle et al. (2016) report in their comparisons to other $z \sim 2$ spectroscopic surveys.

In Figure 5.5 we show the stellar mass distribution of our sample, which we extracted from the COSMOS2015 catalog. These stellar masses were derived from fitting the stellar population synthesis models of Bruzual & Charlot (2003) to the observed photometry using the publicly available LePhare code, following the methods described in Ilbert et al. (2015). For the X-ray sources we used the stellar masses of Suh et al. (2017), which were derived from multi-component AGN + star formation SED fits to the observed photometry. The top panel shows the overall mass distribution for all targets with a secure redshift, as well as the mass distribution of each selection method. It is apparent here that our *Herschel* and 24 μm selection on average have higher masses than our sBzK objects, reaching up to $10^{11.6} M_{\odot}$. The median stellar mass for the star forming galaxies is $10^{10.1} M_{\odot}$, while for the (U)LIRG sample the median is $10^{10.7} M_{\odot}$. This is also reflected in the bottom panel where the IR-selected objects are biased towards higher stellar masses. Overall our sample encompasses galaxy stellar masses from about $10^{9.5}$ to $10^{11.6}$ solar masses.

5.5 Rest-Frame Optical Excitation Properties of IR Luminous Galaxies at $z \sim 2.3$

One of the primary goals of our survey is to investigate the rest-frame optical properties of (U)LIRGs at $z \sim 2.3$ on the BPT diagram. In Figure 5.6 we show the BPT diagram for our 151 sources having at least 3 emission lines detected with sufficient SNR, color coded by their selection method. Out of these, 74 have detections in all four lines, consisting of 38 (U)LIRGs, 34 sBzK-selected galaxies, and 2 serendipitously detected galaxies that lack any classification. Within the 38 (U)LIRGs 10 are *Herschel*-selected while the rest were selected by their 24 μm emission. The remaining 77 galaxies with 3 detected lines and 1 line limit is composed of 33 (U)LIRGs of which 4 are *Herschel*-selected, 39 sBzK, and 5

unclassified galaxies. The majority of these 77 objects have upper flux limits in either Hβ or [N II], which are the fainter lines in H- and K-band respectively.

We plot in greyscale the distribution of local galaxies from SDSS for comparison, where the star-forming sequence forms the left part of the "butterfly," and the AGN branch (or mixing sequence) forming the right side. However at high redshifts the position of the star-forming branch shifts due to a combination of a larger ionization parameter, electron density, and/or a harder EUV radiation field, while the AGN mixing sequence shifts due to the metallicity of the narrow-line region (NLR), the shape of the AGN's ionizing radiation field, and the ionization parameter (Kewley et al. 2013). As expected our data shows a shift towards higher log[O III]/Hβ at fixed log[N II]/Hα ratios compared to the SDSS galaxies. We discuss this in more detail in §5.6.2.

Perhaps the most interesting result is that many of the (U)LIRGs occupy a different location on the BPT diagram than the optically selected (sBzK) sample, suggesting that they are not purely forming stars. In particular Figure 5.6 shows that many (U)LIRGs have noticeably higher log[N II]/Hα ratios than our sBzK-selected galaxies, and also a larger distribution in log[O III]/Hβ. Many of the (U)LIRGs also have lower log[O III]/Hβ ratios than the sBzK sample as well. To be sure our *Herschel* and 24 μm selections are probing the same population, we denote the *Herschel*-selected galaxies on the BPT diagram with orange crosses. It is clear in Figure 5.6 that the overall distribution of both IR selected samples is essentially identical. This suggests that a pure optical selection such as our sBzK technique may not sufficiently sample the full range of galaxies on the star forming sequence. We discuss this point further in §5.6.1. It is also unclear what the amount of AGN contribution in (U)LIRGs may be, since many of these objects clearly lie outside of the star forming sequence.

To address this question, in Figure 5.6 we denote 12 (U)LIRGs with green squares which were also detected to harbor AGN based on their IRAC colors and/or X-ray detection. Of these 12 objects, 3 are *Herschel* sources, and of these 2 were detected by IRAC and the third detected by both IRAC and in X-rays. The other 9 AGN are 24 μm sources with 6

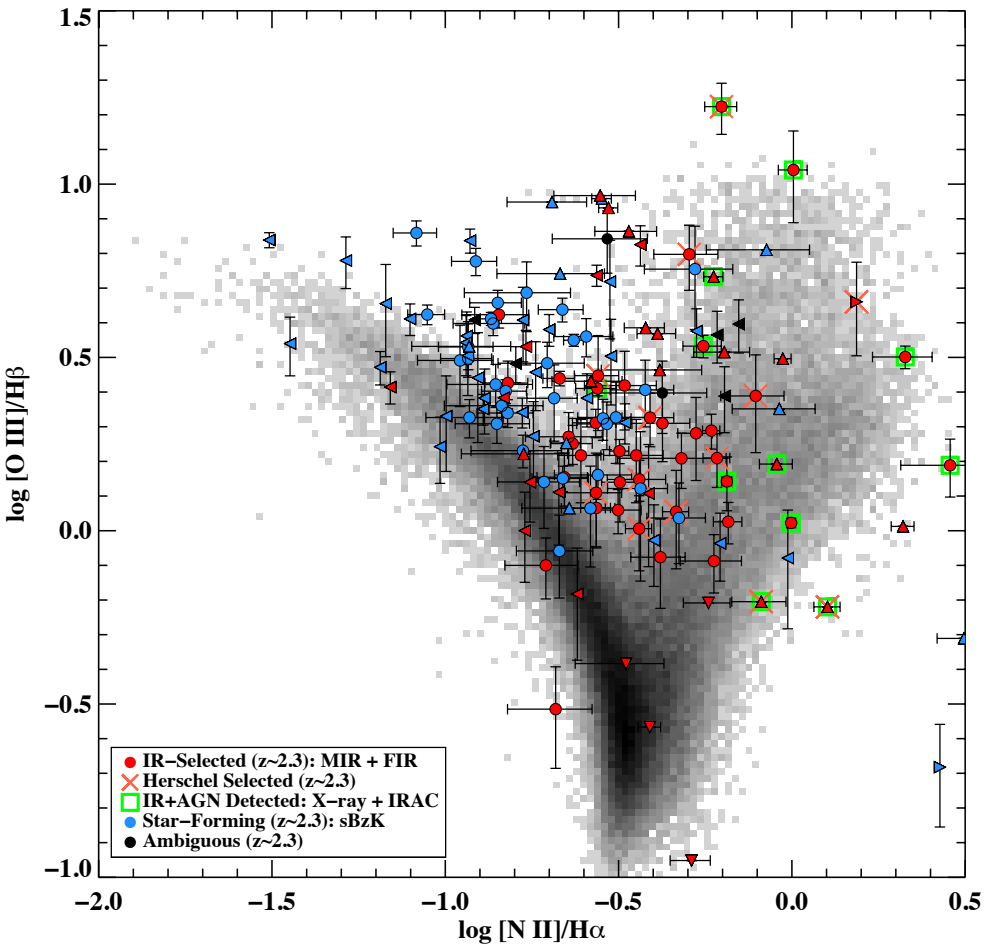

Figure 5.6 The BPT diagram of our 151 objects at $z \sim 2.3$, of which 38 (U)LIRGs, 34 star-forming, and 2 unclassified galaxies were securely detected in all four lines, overlaid on top of the SDSS sample in greyscale. We also include 33 (U)LIRG, 39 star-forming, and 5 unclassified galaxies with a single limit in any of the four lines represented by triangles. In addition we denote using green squares the 12 (U)LIRGs which are also detected by either the X-ray or IRAC AGN selection techniques. Also plotted is the $z = 0$ maximum starburst line (dashed pink) from K01, and the semi-empirical Kauffmann et al. (2003) line (dotted pink) dividing starburst and composite galaxies. We also include the $z = 2.3$ star forming sequence from K13. While our sBzK-selected galaxies (blue) mostly fall below the $z = 2.3$ maximum starburst line as expected, our IR-selected objects (red) are notably biased towards the higher-metallicity end of the star-forming branch, with many objects also extending into the AGN branch.

detected by IRAC, 1 detected in X-rays, and 2 detected by both AGN selection techniques. All 12 of these AGN have high log[N II]/Hα ratios with a median of -0.09 that significantly separates them from the sBzK-selected galaxies, however they have a large distribution in their log[O III]/Hβ ratios. This supports the conclusion drawn by Coil et al. (2015) that one can use the log[N II]/Hα alone to identify AGN within a galaxy sample.

With our current data, it appears that the AGN mixing sequence begins at a significantly higher log[O III]/Hβ ratio at $z \sim 2.3$ (by $\sim$0.7 dex) than it does for the local galaxies as predicted by K13. This is primarily due to differences in the physical conditions of ISMs in these high redshift galaxies. For example a harder radiation field may be responsible for the increase in the log[O III]/Hβ ratio because there are more photons available to ionize [O III]. However other factors can also affect both line ratios, such as the ionization parameter, metallicity, and electron density, making it difficult to determine the exact cause(s) of these shifts. In addition, many (U)LIRGs possess AGN characteristics and appear off the star forming sequence populating the region between the high metallicity end of the star forming branch and the AGN branch, suggesting that many of these objects have comparable contributions from both star formation and AGN to their global spectra. Notably, there are quite a few (U)LIRGs that were not previously classified as AGN hosts but have optical line ratios indicative of AGN.

5.6 Discussion

5.6.1 Comparisons With Other $z \sim 2.3$ Samples

Given the wealth of data collected by recent NIR spectroscopic surveys, it is now possible to construct a picture of what the $z \sim 2.3$ BPT diagram looks like. In Figure 5.7 we show our data along with all publicly available $z \sim 2.3$ datasets where [O III]/Hβ and [N II]/Hα were measured, including 161 star forming galaxies and 7 AGN all optically/UV-selected in KBSS (Steidel et al. 2014), 34 X-ray and IRAC AGN from MOSDEF (Coil et al. 2015; Azadi et al. 2017), and 5 dusty star forming galaxies (DSFGs) selected by their 450 μm or

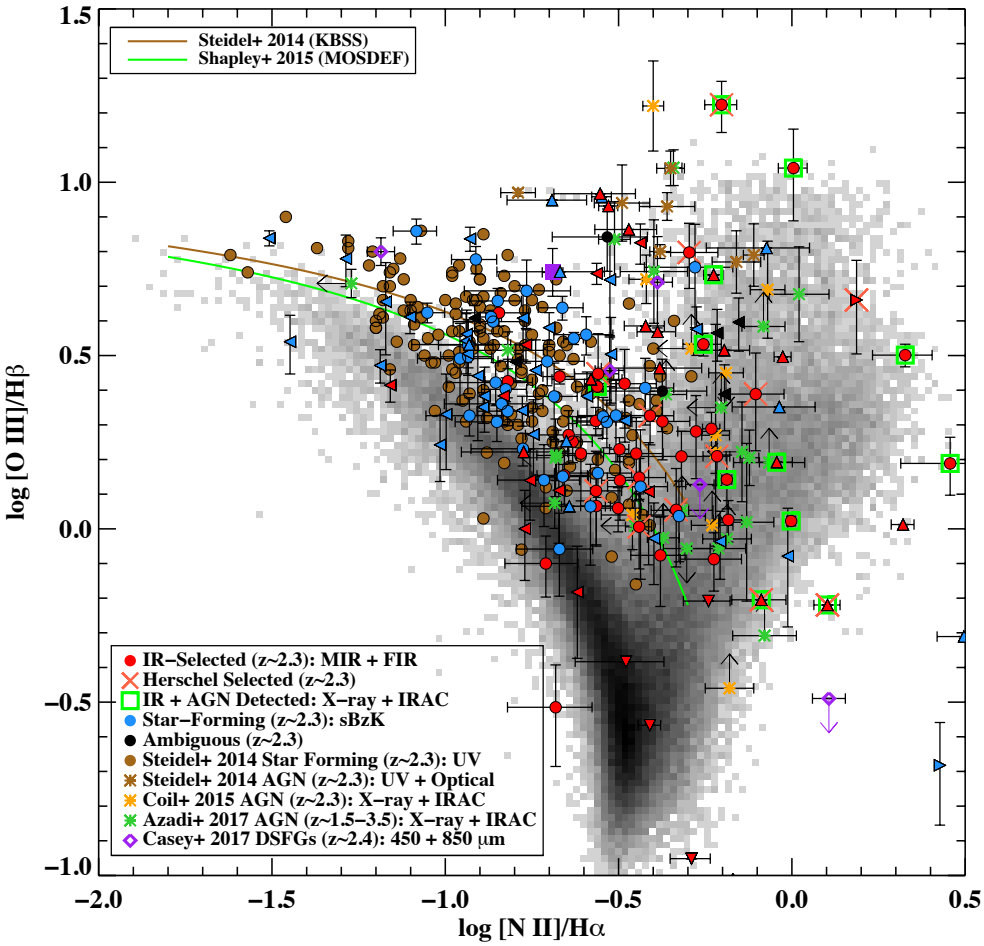

Figure 5.7 The BPT diagram of our sources along with the data from all other publicly available $z \sim 2.3$ surveys, including UV-selected star-forming galaxies in KBSS (Steidel et al. 2014), AGN from MOSDEF (Coil et al. 2015; Azadi et al. 2017), and DSFGs (Casey et al. 2017). The KBSS sample also includes a few AGN which we denote as asterisks in the plot. Note we only include X-ray and/or IRAC detected AGN from Azadi et al. (2017). Although their AGN sample spans a redshift range between $1.5 \lesssim z \lesssim 3.5$, the bulk of their AGN lie between $2 \lesssim z \lesssim 3$ (see their Figure 6). We also include the star-forming branch as reported by both Steidel et al. (2014, brown line) and Shapley et al. (2015, green line). Finally, we also include a data point from Casey et al. (2017) representing the composite spectrum of DSFGs as a filled purple square.

850 μm emission from Casey et al. (2017). In addition we plot the derived fit to the star forming sequence from both KBSS in brown and MOSDEF in green.

Rest-Frame Optically Selected Galaxies

Examining the optically selected galaxies from our sample compared to that of KBSS in Figure 5.7 (brown points and curve), both agree very well and follow approximately the same relationship on the star forming sequence. This is not too surprising since the KBSS selection technique is mainly a rest-frame optical and/or UV selection. One small difference is that the KBSS data extend further to the upper left part of the diagram, however this can be explained by the fact that the mass distributions of our sample goes down to $10^{9.5}$ $M_{\odot}$, while KBSS probes all the way down to 10^{9} $M_{\odot}$ (see Fig. 4 of Strom et al. (2017)). Given the well-known correlation between the mass and average metallicity of a galaxy (i.e., the MZ relationship) this implies that the KBSS sample probes galaxies with lower metallicities which lie on the upper left side of the star forming sequence. Otherwise at the high-mass end, our optically-selected targets have roughly the same maximum mass as KBSS ($\sim 10^{11.3}$ $M_{\odot}$).

To show this formally, we fit our sBzK galaxies with a functional form similar to that found in the literature:

$$\log\,[\mathrm{OIII}]/\mathrm{H}\beta = \frac{p_0}{\log\,[\mathrm{NII}]/\mathrm{H}\alpha - p_1} + p_2. \tag{5.1}$$

However to avoid divergent fit parameters, we adopt $p_0 = 0.61$ which is the same value used to fit the local star forming abundance sequence in K13. Using the IDL routine `MPFIT` (Markwardt 2009) we determined the best-fit parameters to Equation 5.1 to be

$$\log\,[\mathrm{OIII}]/\mathrm{H}\beta = \frac{0.61}{\log\,[\mathrm{NII}]/\mathrm{H}\alpha - 0.36} + 1.06 \tag{5.2}$$

which is shown in Figure 5.8 and is valid over the log[N II]/Hα interval $[-1.3, -0.3]$. We note here that one galaxy was excluded from the fit, due to its very high log[O III]/Hβ and

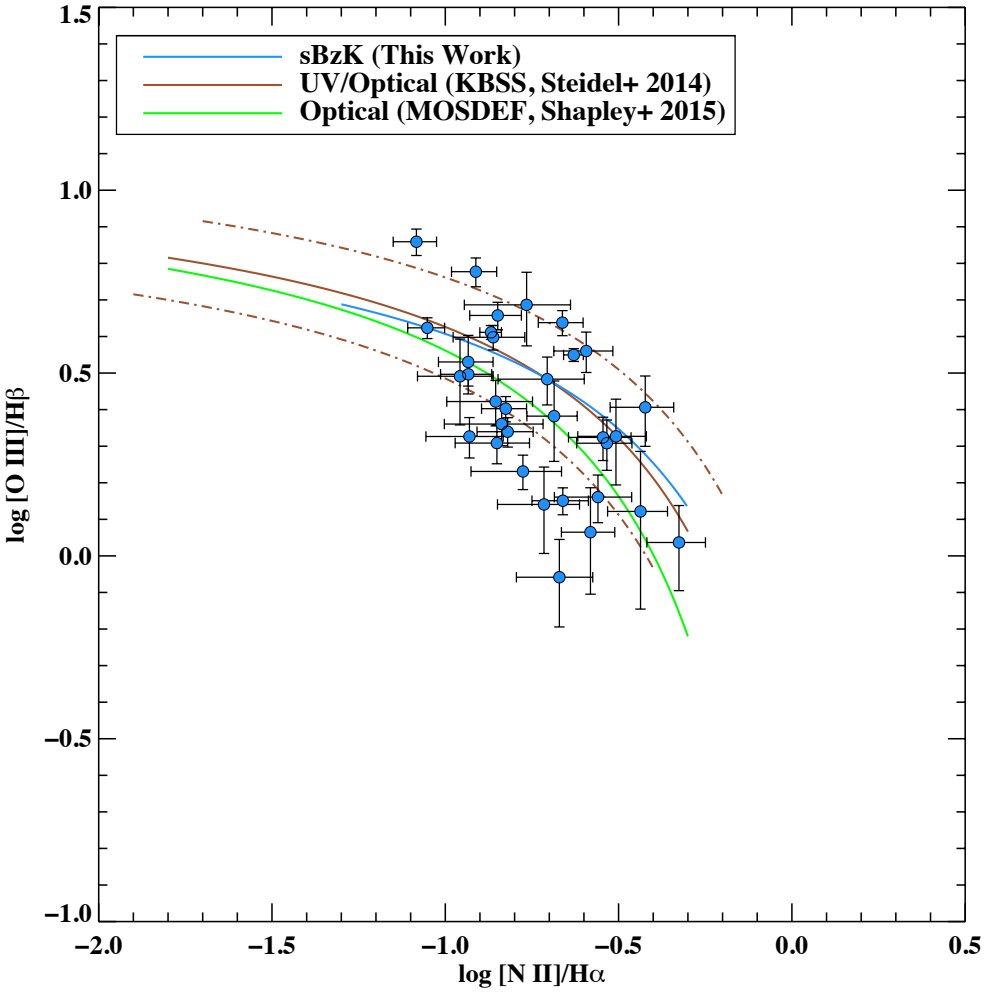

Figure 5.8 The derived fit (blue line) for our sBzK galaxies securely detected in all four emission lines (blue points) on the BPT diagram. We include the fits from two other $z \sim 2.3$ samples (KBSS and MOSDEF) for comparison. The dash-dot KBSS curve represents the ± 0.12 dex intrinsic scatter about their fit. It is clear that our fit and individual data points are consistent with both results.

log[N II]/Hα ratios that suggest the presence of an AGN. Our fit agrees quite well with both the KBSS and MOSDEF results, with $\chi^2/\nu = 13.8$ for the best-fit model. However since we are also interested in the intrinsic scatter of our data, we assume that the total 1-sigma dispersion of each data point is the quadrature sum of the measurement error and the intrinsic scatter (i.e., the uncertainties are independent of each other). Therefore to calculate the intrinsic scatter we estimate the additional amount of uncertainty that needs to be added to the measurement errors to attain $\chi^2/\nu \simeq 1$. We find that our intrinsic scatter to be 0.12 dex which is very similar to the SDSS galaxies, and is slightly less than the value quoted for KBSS (0.18 dex, Strom et al. 2017).

On the other hand MOSDEF is primarily an H-band selection down to a limiting magnitude of 24.5 (AB) (Kriek et al. 2015), and their mass distribution also goes lower than our optically-selected galaxies to about $10^9 M_\odot$. Shapley et al. (2015) performed an initial analysis of 53 of these galaxies on the BPT diagram, and showed that their offset (Figure 5.7, green line) from Steidel et. al.'s data can be explained due to a different distribution of galaxy stellar mass. Specifically, they showed that the fit to their low mass galaxies (26 objects with $M_* \leq 10^{10.11} M_\odot$) was virtually indistinguishable from the KBSS curve, while the high mass fit showed no significant offset from the local SDSS relation. Although the sample size of our secure sBzK detections is too small to perform a similar analysis, the derived fit for our data also appears to loosely resemble their low mass galaxies.

Rest-Frame IR Selected Galaxies

Similar to the results in §5.5, the most striking difference between our (U)LIRGs and the MOSDEF and KBSS star-forming galaxies is the near segregation between their loci on the BPT diagram. As we show in Figures 5.7 and 5.9 the optically selected galaxies across all samples only reach a maximum log[N II]/Hα ratio of about -0.4. However many of the (U)LIRGs clearly have larger log[N II]/Hα ratios, up to as high as 0 and a few beyond even that. It is important to mention here that the stellar mass distribution of the MOSDEF galaxies also reaches $10^{11.5} M_\odot$, similar to our IR selected sample. This suggests that despite

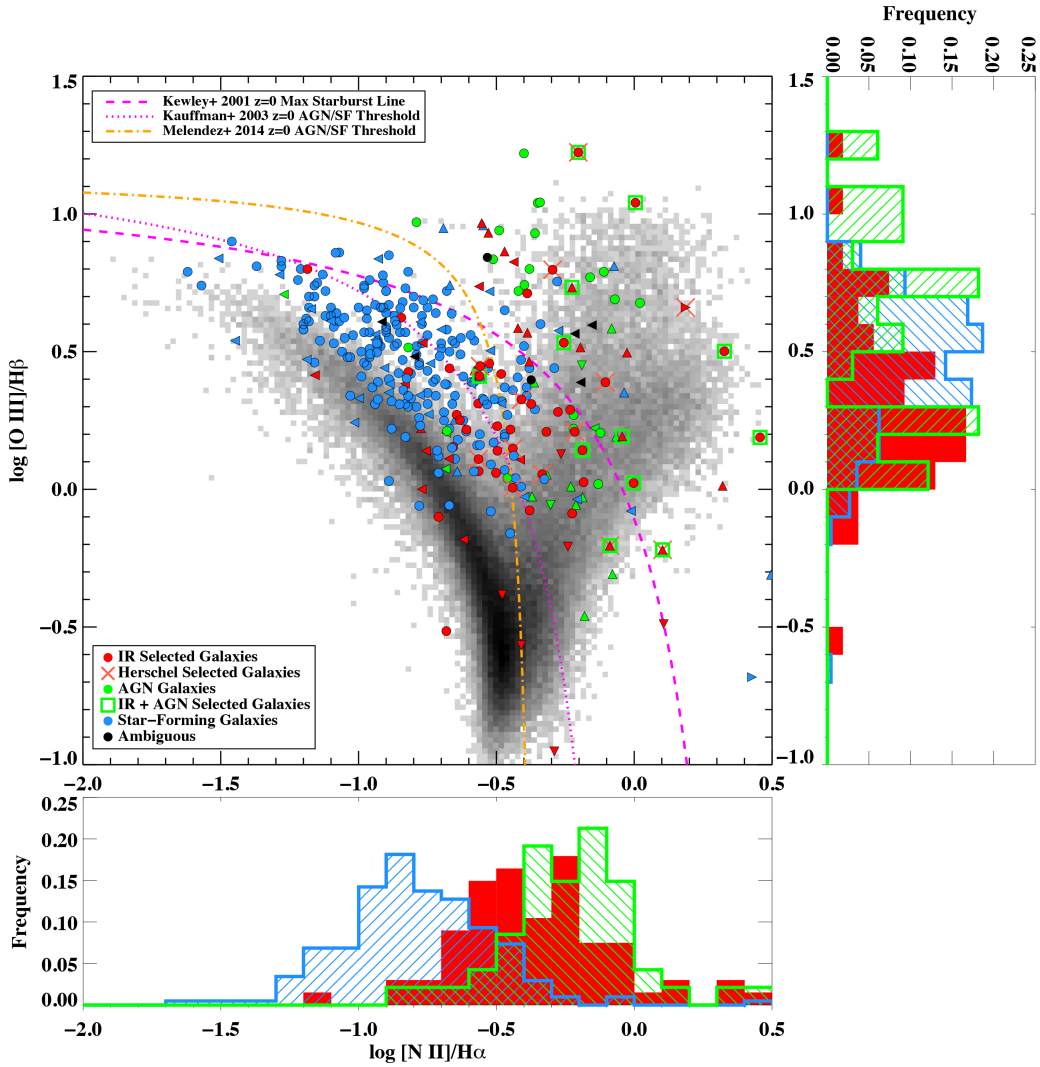

Figure 5.9 We show the BPT diagram of our sources plus those from published data classified by selection method, overlaid on top of the SDSS sample. The bottom histogram shows fractional distribution in the log [N II]/Hα ratio for each of the three selection methods. The histogram on the right shows the fractional distribution in log [O III]/Hβ ratio for each selection method. In blue are galaxies selected by sBzK (this work) and KBSS UV/optically selected star-forming galaxies (Steidel et al. 2014). The (U)LIRGs from our sample and DSFGs (Casey et al. 2017) are plotted in red. In green are the AGN from MOSDEF (Coil et al. 2015; Azadi et al. 2017) and a few AGN from KBSS. IR selected galaxies that also have an AGN signature are included in both IR and AGN samples (green squares). Measurements with a single limit are included, but only in the histogram (axis) where there is no limit. The IR-selected objects have a noticeably different log [N II]/Hα distribution from the star-forming sample, tending towards higher ratios that are more similar to AGN-selected objects. In the log [O III]/Hβ histogram, the IR-selected objects are biased more towards smaller line ratios than the star-forming galaxies. Finally we include the $z = 0$ demarcation lines of Kewley et al. (2001), Kauffmann et al. (2003), and Meléndez et al. (2014).

the fact both samples (IR and optical) have similar mass distributions, the ISM properties of (U)LIRGs are substantially different from those selected by KBSS and MOSDEF. This highlights the important point that understanding the sample selection criteria of high redshift galaxies is critical in assembling a full census of galaxies in the early universe.

In the rest-frame of these galaxies, our *Herschel* and 24 μm selection is sensitive to the $\sim$10–100 μm wavelength range of their SED which is usually dominated by obscured star formation, and in some instances a powerful (obscured) AGN. In addition the 5 DSFGs from Casey et. al. are also included since they were selected by their rest-frame far-IR emission. This selection criteria is sensitive to dust obscured galaxies whereby the dust reprocesses optical/UV radiation from a strong ionizing source (or sources) and re-emits the energy in the IR. As a whole these galaxies were most likely missed because of their very red optical colors, especially since MOSDEF's H-band selection at $z = 2.3$ roughly corresponds to a rest-frame B-band selection. Again it is clear that although these two samples have similar stellar masses, their internal physical properties are intrinsically different due to the different rest-frame wavelengths used to select them.

AGN

In the local universe it is well-known that the (intrinsically) brightest (U)LIRGs harbor powerful AGN which moves them towards the upper right of the BPT diagram. However at high redshifts we do not yet have definitive classification lines between pure star forming systems and those with AGN, although in §5.6.2 we briefly explore how different classification lines perform at $z \sim 2.3$. Instead we can compare where (U)LIRGs appear on the BPT diagram to the location of AGN identified *a priori* using other AGN selection techniques.

In Figure 5.10 we recover the $z \sim 2.3$ AGN branch using all of the KBSS and MOSDEF AGN, along with the 12 AGN from our sample for a total of 53 AGN. Nearly all of the AGN have log[N II]/H$\alpha \gtrsim -0.5$ and occupy more than an order of magnitude in the log[O III]/Hβ direction from -0.2 to 1.2. Most of the AGN occupy this predominantly vertical sequence

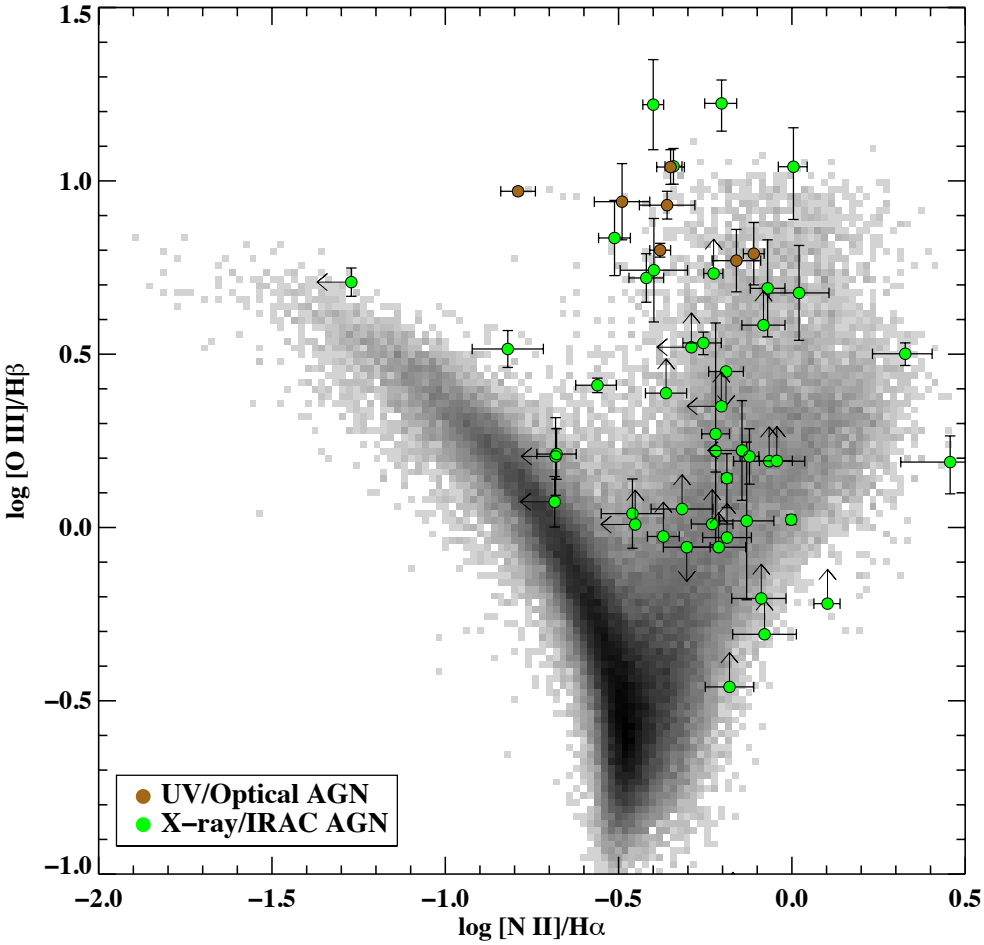

Figure 5.10 The BPT diagram of all AGN from our sample, KBSS, and MOSDEF. Shown in green are the AGN detected in X-ray or by IRAC colors, while the brown points signify those detected in the UV/optical. The local SDSS galaxies are also shown for comparison.

which somewhat matches the local SDSS AGN shown in greyscale. Interestingly, at the bottom of the AGN branch (where it joins the star forming sequence) the high redshift AGN matches perfectly with the local AGN branch. However at the upper end of the AGN branch many of the AGN have noticeably smaller [N II]/Hα ratios compared to the local AGN, possibly because they are more metal-poor. This suggests that the evolution in the [N II]/Hα ratio at high redshift is largely insensitive to AGN strength, with many AGN having ratios between $-0.5 \lesssim$ log[N II]/Hα $\lesssim 0.2$ across a large range in log[O III]/Hβ. However, it's also noteworthy that there are several AGN in Figure 5.9 with log[N II]/Hα ratios less than -0.5 (8 total, 3 with upper limits on [N II]). These AGN are very interesting since 6 of them lie within the $z \sim 2.3$ star forming locus, and would otherwise be classified as purely star forming. The other 2 AGN lie at a high log[O III]/Hβ ratio such that it does not fall on the star forming sequence.

In Figure 5.10 there is also an apparent difference in AGN selection criteria at high redshift. The 7 KBSS AGN (brown circles) are concentrated at high log[N II]/Hα *and* log[O III]/Hβ ratios, whereas AGN selected via X-ray and IRAC (green circles) occupy a much larger range in log[O III]/Hβ. This is intimately tied to how Steidel et. al. identified their AGN by using the presence of rest-frame UV emission lines (such as C IV$\lambda\lambda$ 1548, 1550 Å and N V$\lambda\lambda$ 1238, 1242 Å), which are indicative of the presence of high ionization species that cannot be produced by stellar radiation fields (see i.e., Hainline et al. 2011). This of course implies that the line of sight to the AGN is relatively dust free, otherwise the UV radiation would be attenuated very quickly by intervening dust between the black hole and the observer. On the other hand the MOSDEF (and our) AGN were all either X-ray or IRAC selected, both of which are sensitive to a much wider range of obscured and unobscured AGN phenomena. Hence, it may be that the Steidel et. al. objects represent the most powerful AGN in which the dust around it has been photo-dissociated, allowing the UV photons to escape. Since this effect takes time it may be that these UV/optically selected AGN are older than the ones detected by the other two methods. Again this underscores how sample selection can introduce biases in the sample.

Comparing the Three Samples

Using the star forming and AGN loci we can now examine where an infrared selected sample fits on the BPT diagram. To better visualize the distribution of objects with different selection criteria, in Figure 5.9 we plot the BPT diagram again but with galaxies color coded by how they were selected. In blue we show galaxies that were selected by any optical and/or UV methods, in red we show rest-frame IR selected objects from *Herschel* and 24 μm and the 5 submillimeter DSFGs of Casey et. al., and in green we show all of the AGN. We also include the local SDSS data as reference. Figure 5.9 makes quite clear that many of the (U)LIRGs exhibit optical emission-line properties similar to AGN hosts, much like (U)LIRGs in the local universe.

To better quantify the distribution in line ratios between the different samples, we construct histogram densities for both the log[O III]/Hβ and log[N II]/Hα ratios with a bin size of 0.1 dex in Figure 5.9. Galaxies with a single limit in one of the four lines are included in the histogram, but only in the line ratio for which both lines are securely detected. For the [N II]/Hα ratio this resulted in 62, 204, and 47 galaxies in the IR-selected, star forming, and AGN samples respectively. For the [O III]/Hβ ratio there are 51, 225, and 33 IR-selected, star forming, and AGN galaxies respectively. In the log[N II]/Hα histogram it is clear that (U)LIRGs (red) on average have a higher ratio than the star forming galaxies (blue). In fact the (U)LIRG distribution of log[N II]/Hα ratios resemble AGN more so than the star forming galaxies. This is further confirmed when we calculated the median log[N II]/Hα ratios of each sample to be -0.39, -0.81, and -0.21 for the IR-selected, star forming, and AGN galaxies respectively.

In the log[O III]/Hβ axis the distributions are less distinct due to the degeneracy in [O III]/Hβ between the star forming and AGN branches. Nevertheless, the (U)LIRGs appear to systematically have lower log[O III]/Hβ ratios on average compared to the optically selected sample, with a median value of 0.26 compared to 0.5. On the other hand the AGN appear to be scattered over a large range of log[O III]/Hβ as discussed earlier. If we look at the dispersions of each sample, we see that the IR selected objects and AGN have a

1-sigma spread of 0.31 and 0.37 respectively. Compared to the 1-sigma value of 0.23 for the star forming sample, it is clear that not all of the IR selected objects reside in the star forming sequence. Taken together these results suggest that high redshift (U)LIRGs effectively straddle the region between the star forming and AGN population on the BPT diagram.

Shocks

The positions of objects on the BPT diagram may be affected by shocks within the ISMs of these galaxies, caused by for instance outflows from star formation or AGN activity. K13 showed that at high redshift, the effect of shocks would be to move galaxies toward the left on the BPT diagram thus mimicking the line ratios of AGN, because the shocked gas enhances red forbidden transitions such as [N II] and [S II]. To model this, they considered the cases of slow shocks ($v \lesssim 200$ km s^{-1}) and fast shocks ($v \gtrsim 200$ km s^{-1}). In the slow shock case, the photoionization front due to the shocked gas lags behind the actual shock front, which produces line ratios directly dependent on the shock velocity. For fast shocks, the photoionization front travels faster than the shock front and pre-ionizes the gas, and can significantly contribute to optical emission lines. In Figure 7 of K13, they show the positions of a galaxy as a function of shock velocity in the case where they are completely dominated by shock excitation. Of course these are only maximum theoretical predictions, and in reality galaxies with shocks would lie somewhere between the star forming sequence and the maximum shock models, forming a shock mixing sequence. As a result fast shocks in star forming galaxies will masquerade as a composite starburst-AGN galaxy at high redshifts, while slow shocks may appear as high metallicity starbursts.

This is important in the interpretation of our data because there are numerous kinematic and spectroscopic evidence of shocks in high redshift galaxies (see i.e., Steidel et al. 2010; Yuan et al. 2012), hinting that it may be a common phenomenon. Indeed many (U)LIRGs in Figure 5.9 appear to occupy areas on the BPT diagram that could have some degree of shock contribution to the optical emission lines. Specifically the (U)LIRGs that are

farther "along" the star forming sequence may be evidence for slow shocks, while non-AGN (U)LIRGs with high log[N II]/Hα ratios may have some contribution from fast shocks. This makes it difficult to disentangle galaxies with shocked ISMs from those harboring AGN, therefore future integral field observations of these (U)LIRGs would be needed to determine whether or not shocks significantly contribute to the emission lines.

On the other hand the vast majority of optically selected galaxies do not appear to exhibit much evidence of any shock excitation. There are a few ($\sim$10) that do not lie on the star forming sequence, and it is difficult to tell at this point if they are indeed due to shocks, or if it is because they harbor an as yet undetected AGN. Nevertheless it remains clear that shocks play a negligible role in optically selected galaxies at $z \sim 2.3$, and instead they follow a tight star forming sequence. It is important to mention that this result also applies to the KBSS data, which spans a wide range in star formation rates ($\log(\mathrm{SFR}/M_{\odot}\mathrm{yr}^{-1}) =$ 0.5–2.5).

5.6.2 Comparisons With Theoretical BPT Classification Schemes

Although there currently aren't any starburst-AGN classification lines for the BPT diagram at high redshift, we briefly assess how effective the local calibrations of the classification lines are at $z \sim 2.3$. We also examined the four limiting scenarios from K13 which correspond to galaxies with "normal" or "extreme" ISM conditions with "metal-rich" or "metal-poor" AGN NLR regions.

In the local universe, considerable progress has been made in understanding the behavior of starbursts and AGN on the BPT diagram. In Figure 5.9 we compare two sets of local classification schemes, the first are the maximum starburst line from K01 (dashed magenta) and the starburst-AGN composite line of Kauffmann et al. (2003) (dotted magenta), and the second is the starburst-AGN line from Meléndez et al. (2014) (dash-dot orange). In the first case, the K01 and Kauffmann lines clearly misclassify many galaxies on the star forming sequence to be starburst-AGN composites (in between the lines), although most of the AGN still lie above the Kauffmann line. The Meléndez et al. (2014) line does a better

job by including most of the star forming sequence, although it still misclassifies some of the star forming galaxies at the high metallicity end of the star forming sequence. At this point it is difficult to tell since we lack a statistically large sample of AGN. In addition neither classification scheme is able to separate the few bona fide AGN that fall within the $z \sim 2.3$ star forming sequence. Thus we conclude that local BPT classification lines in general should not be used to separate starbursts and AGN at high redshift.

In K13, they attempted to model the positions of the star forming sequence and AGN branch on the BPT diagram based on different limiting assumptions in their properties. For the star forming sequence, the ISM conditions in the galaxy can either have conditions similar to local ($z \sim 0$) galaxies (normal ISM), or the ISM may have a larger ionization parameter and a denser ISM, and/or a harder ionizing radiation field (extreme ISM). On the other hand the AGN NLR may have reached the level of chemical enrichment seen in local galaxies (metal-rich), or it may coevolve with the ISM as a function of redshift (metal-poor). From these four cases there are a total of four resulting scenarios, corresponding to normal ISM with metal-rich NLR (Scenario 1), normal ISM with metal-poor NLR (Scenario 2), extreme ISM with metal rich NLR (Scenario 3), and extreme ISM with metal poor NLR (Scenario 4).

In Figure 5.11 we show all of the available data plotted with the $z \sim 2.3$ predictions for each limiting case, with blue lines representing the approximate boundaries of the predicted star forming sequence, and red lines representing the boundaries of the AGN branch. It is immediately obvious that Scenario 1, which essentially corresponds to local galaxies, is not appropriate for galaxies at $z \simeq 2$. The star forming galaxies form a branch that is clearly offset towards higher log[O III]/Hβ and/or log[N II]/Hα relative to the local star-forming sequence. This has of course been long suspected and now confirmed through multiple studies, including this work. The AGN on the other hand extend vertically (as discussed in §5.6.1) and brackets both above and below the AGN boundaries. Scenario 2 assumes a normal ISM coupled with a metal-poor NLR, which only changes the shape and location of the AGN branch relative to Scenario 1. A lower metallicity in the NLR moves the AGN

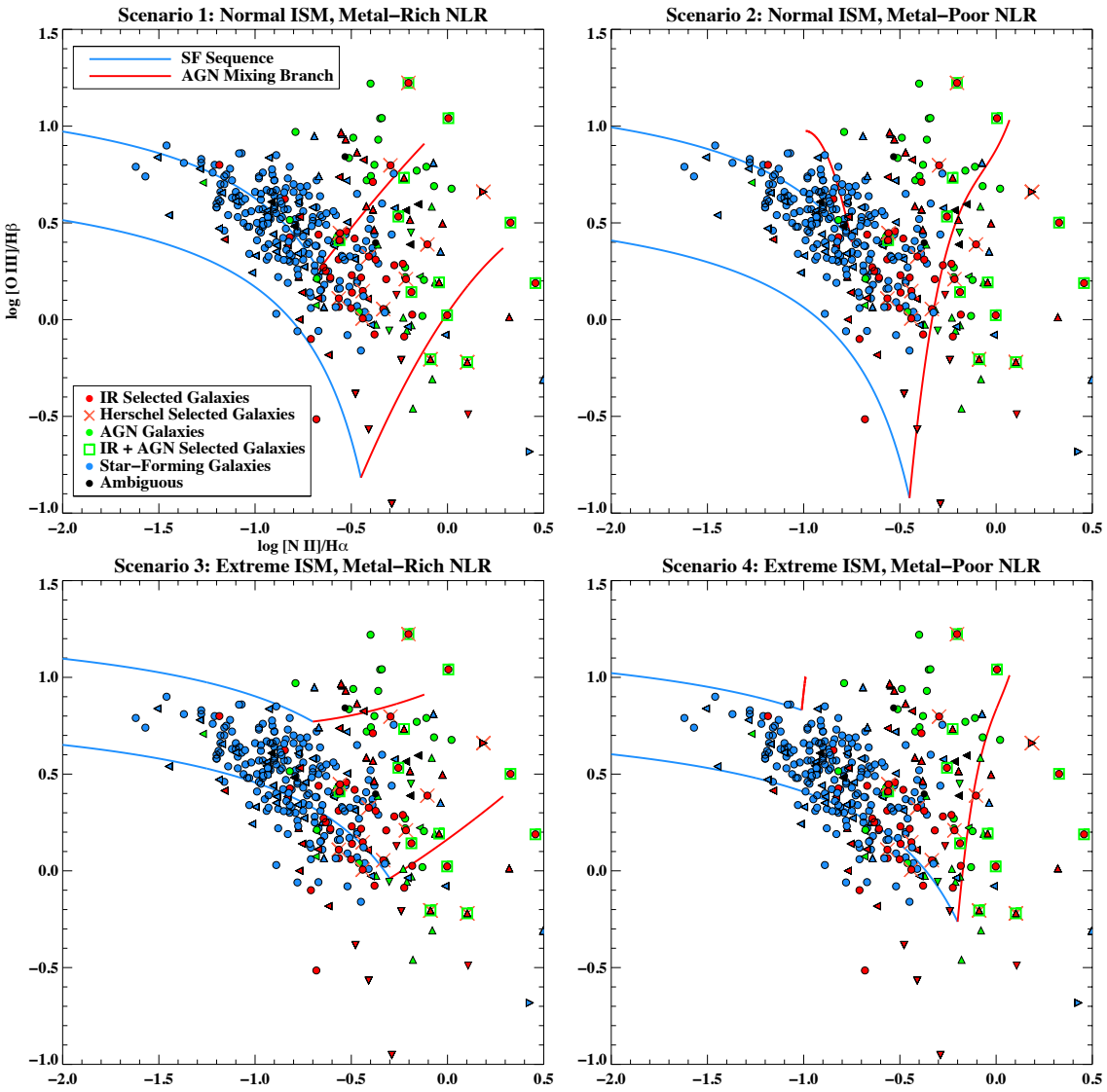

Figure 5.11 Similar to Figure 5.9 we show the BPT diagram of all sources color coded by selection criteria, with each of K13's Scenarios plotted as well.

branch to the left, which captures many of our high log[O III]/Hβ and log[N II]/Hα AGN, however misses many objects with high log[N II]/Hα and moderate log[O III]/Hβ ratios.

In Scenario 3 they assume a high redshift extreme ISM and an AGN NLR that has already been chemically enriched to levels seen in local galaxies, while Scenario 4 assumes a metal-poor AGN that coevolves with the rest of the galaxy. Generally speaking K13 showed that at very low NLR metallicities (i.e. Scenarios 2 and 4), the AGN models produced model spectra with a lower spread but high ratio in [O III]/Hβ, while the [N II]/Hα ratio becomes smaller. Presumably this is due to nitrogen becoming a primary nucleosynthetic element at low metallicity, while the decrease in oxygen abundance is offset by a rise in the the electron temperature. In the case of extreme ISM and high NLR metallicity (Scenario 3), since the AGN NLR is assumed to have the same metallicity as local AGN, the AGN mixing sequence is approximately the merger of the local SDSS mixing branch with the high redshift star forming sequence. However similar to Scenario 1, the metal-rich NLR assumption in Scenario 3 results in missing many AGN above and below the AGN boundaries.

On the other hand the extreme ISM conditions of Scenarios 3 and 4 slightly over-predicts the location of the star forming sequence, with a number of galaxies falling below the lower star forming branch boundary. This suggests that ISM conditions in high redshift star forming galaxies are not as extreme as predicted by K13, possibly because they are a mixture of galaxies with normal, intermediate, and extreme ISM conditions. Averaged together their mean ISM properties would result in the star forming branch to lie between the local relation and that predicted by K13. It also appears that the "slope" in the star forming data points is not as shallow as predicted by K13, but are instead similar to the "slope" for local galaxies. Overall these points suggest that the star forming sequence boundary as predicted by K13 falls somewhere between their $z = 0$ and $z = 2.3$ models.

The positions of the AGN boundaries in Scenario 4 appears to capture the most number of AGN at $z \sim 2.3$, missing approximately only 11 of the 53 AGN. However the presence of these 11 AGN to the left of the boundary suggests that at least some AGN have enriched to the levels seen in local NLRs. This is plausible as a small minority of galaxies may evolve

fast enough to have metallicities comparable to local AGN. However with the current sample size of high redshift AGN it is not yet possible to make a definitive statement.

5.6.3 The Stellar Mass-Excitation Relation

The stellar mass-excitation (MEx) diagram was developed by Juneau et al. (2011) as an alternative method to separate starbursts and AGN in situations where the [N II]/Hα ratio cannot be easily measured (i.e., at $z > 0.4$ where it redshifts out of the optical regime), by using the quantity of stellar mass instead. Juneau et al. (2014) further refined their classification lines and provided an equation to calculate the horizontal shift ($\Delta \log(M/M_{\odot})$) needed for high redshift samples. The reason for the shift is twofold, first high redshift spectroscopic surveys are affected by selection effects due to emission line detection limits, which shifts the entire bivariate distribution (and corresponding demarcation line) to higher masses as the line luminosity limit is increased. Second, they also assume an evolution in $L^{*}_{\mathrm{H}\alpha}$ (i.e., the break in the Hα luminosity function) as a way to parametrize changes in the global SFRD, which they assume depends on redshift according to $(1+z)^{2.27}$. Combining the redshift dependence of $L^{*}_{\mathrm{H}\alpha}(z)$ with a given line luminosity limit, they map a $z = 2$ galaxy[5] that is a certain distance away from $L^{*}_{\mathrm{H}\alpha,z=2}$ to a corresponding low redshift SDSS galaxy the same distance away from $L^{*}_{\mathrm{H}\alpha,z=0}$. They then derive the shift in the demarcation line using the resulting ensemble of SDSS galaxies.

Using their Equation B1, a line flux limit of roughly 5×10^{-18} ergs s^{-1} cm^{-2} at the median redshift of $z = 2.23$ we derive a horizontal shift of $\Delta \log(M/M_{\odot}) = +0.23$ which is similar to what Coil et al. (2015) derived. In Figure 5.12 we show the MEx diagram for our sources as well as those from KBSS and MOSDEF, along with the demarcation line shifted by +0.23 (dotted curves) as described above. Immediately it's clear this is insufficient at separating star forming and AGN galaxies since the majority of the star forming galaxies fall either in the MEx intermediate or MEx AGN regions. Alternatively, Coil et. al. proposed using a larger shift of $\Delta \log(M/M_{\odot}) = +0.75$ which we show in Figure 5.12 as the dashed

[5]We only use $z = 2$ as an example redshift here.

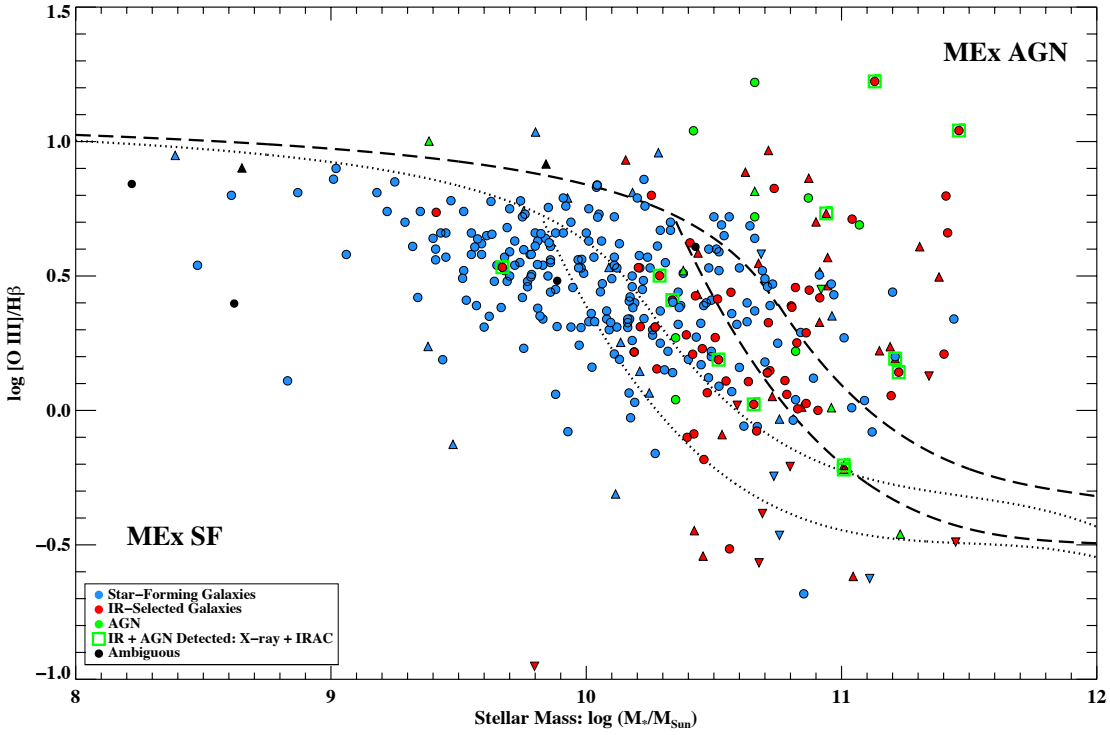

Figure 5.12 The mass-excitation (MEx) diagram at $z \simeq 2.3$. The dotted line represents a $\Delta \log(M/M_{\odot}) = +0.23$ shift of the star-forming/AGN demarcation line at $z = 0$, as calculated by equation B1 in Juneau et al. (2014), assuming a flux limit of 5×10^{-18} ergs s^{-1} cm^{-2} and a median redshift of $z = 2.23$, with a $(1 + z)^{2.27}$ evolution in the luminosity function. The dashed line represents Coil et al. (2015)'s suggestion of $\Delta \log(M/M_{\odot}) = +0.75$, which does a better job at separating star-forming galaxies (blue points) from the AGN (green points and squares). The IR selected objects on the other hand clearly straddle both the star-forming and AGN regions of the MEx diagram.

curve, and Strom et. al. suggested an even more extreme shift of $\Delta \log(M/M_{\odot}) \gtrsim 1.0$ to cleanly separate their (UV-selected) AGN and star forming galaxies. In Figure 5.12 the former appears to better separate out the AGN with most of the AGN identified *a priori* falling in the MEx AGN or close to the MEx intermediate regions. However there are several (U)LIRGs identified to harbor AGN that clearly lie in regions otherwise dominated by star forming galaxies. As a result, it appears that a line luminosity limit and evolution in the cosmic SFRD are insufficient in explaining the dramatic shift towards higher masses. In fact Coil et al. (2015) suggests that this may be due to a metallicity effect, since at a given stellar mass the metallicity decreases as a function of redshift, or put another away, at constant metallicity a positive shift in stellar mass is needed as redshift is increased. Since the MEx diagram was originally calibrated at low redshifts, the demarcation line would need to be shifted in the positive (mass) direction commensurate with the MZ relation at that redshift.

Given the discussion above we adopt $\Delta \log(M/M_{\odot}) = 0.75$ for the demarcation line. Using this and the loci of star forming and AGN galaxies on the MEx diagram, it is also notable that our (U)LIRGs appear to straddle the region between these two populations, much like on the BPT diagram. In fact some of the (U)LIRGs have lower limits in Hβ which suggests an even higher [O III]/Hβ ratio placing them securely in the MEx AGN region, while many of the rest occupy the MEx intermediate region in between. This again confirms the conclusion from our BPT diagram, that many (U)LIRGs at high redshifts appear to have both star formation as well as an AGN.

5.7 Summary

In this chapter we examine for the first time the rest-frame optical spectra of luminous infrared galaxies at $z \sim 2.3$ using data from Keck I/MOSFIRE. We select emission line galaxies in the COSMOS field using five different selection criteria for (U)LIRGs, AGN, and star forming galaxies. Using our spectra we conclude the following:

1. We compare our spectroscopic redshifts to the photometric redshifts in the COSMOS2015 catalog (Laigle et al. 2016), and find a general agreement between them with $\sigma_{\Delta z/(1+z)} = 0.088$, and a catastrophic failure rate of 7.2%. In addition we find no difference in these values across different sample selection criteria.

2. We report the serendipitous discovery of two new unrelated galaxy clusters at redshifts $\langle z \rangle = 2.1025$ and $\langle z \rangle = 2.1331$ each with 12 members, centered at approximately $(\alpha, \delta) =$ (09h 58m 13s, 01d 39m 05s), and $(\alpha, \delta) =$ (10h 02m 42s, 02d 12m 07s) respectively. The projected diameter of each cluster is approximately 1.27 Mpc and 1.18 Mpc respectively.

3. Using our 151 galaxies where we detect at least three lines in Hβ, [O III], Hα, and [N II], we show that our sBzK selected star forming galaxies lie above the local SDSS star forming abundance sequence on the log[O III]/Hβ vs. log[N II]/Hα BPT diagram, and is very similar to the UV and/or optically selected galaxies of KBSS and MOSDEF.

4. We found that the distribution of (U)LIRGs on the BPT diagram lie in a different location than the bulk of optically selected star forming galaxies, with higher log[N II]/Hα ratios on average. In addition (U)LIRGs possess a larger spread in their log[O III]/Hβ ratios compared to the optical sample, with lower average ratios. We additionally identify 12 (U)LIRGs which were also detected to harbor AGN via their IRAC colors or X-ray detection. These objects have a high average log[N II]/Hα ratio of -0.09, and occupy the same region as AGN from other high redshift surveys. Overall, this suggests that (U)LIRGs are powered by a combination of star formation as well as an AGN, straddling the region on the BPT diagram between pure star forming and AGN-dominated galaxies. This also shows that our rest-frame infrared $\sim$10–100 μm selection criteria results in a sample that has markedly different properties than a rest-frame optical B-band selection such as that of MOSDEF and KBSS, despite probing the same stellar mass range.

5. We recover the AGN branch on the $z \sim 2.3$ BPT diagram, and note that its shape and location are somewhat similar to local AGN in the SDSS sample. However unlike the local AGN branch, at high redshift it is noticeably more vertical, implying the [N II]/Hα ratio is less sensitive to AGN strength. Furthermore we show how different AGN selection criteria affects their location on the BPT diagram. Specifically AGN selected by the presence of rest-UV emission lines tend to have high ratios in both log[N II]/Hα and log[O III]/Hβ, whereas those selected by IRAC colors or in X-ray have high log[N II]/Hα with a large (more than an order of magnitude) distribution in their log[O III]/Hβ ratios. We attribute this to the fact that X-ray and IRAC selection methods are sensitive to a much wider range in AGN obscuration than a UV/optical selection. It is also likely that a UV/optical selection is more sensitive to the most powerful AGN, and/or older AGN that have had time to photo-dissociate the dust surrounding it.

6. We examine how well local starburst-AGN classification lines perform on our high redshift data, and conclude that the theoretical lines of Kewley et al. (2001) and Kauffmann et al. (2003) should not be used at high redshift to separate pure star forming, composite, and and AGN galaxies. The more recent classification line of Meléndez et al. (2014) is better and successfully separates most AGN from the star forming sequence, however it misses some AGN that appear to have pure star forming line ratios, and may still miss galaxies at the high metallicity end of the star forming branch. We also assess the four limiting scenarios of Kewley et al. (2013) in the context of the available data, and conclude that ISM conditions at $z \sim 2.3$ are not as extreme as predicted, and that there appears to be both metal-rich and metal-poor AGN. However more high redshift AGN are needed to further confirm this. We also found their "Scenario 4" which corresponds to a larger ionization parameter, denser ISM, and/or harder ionizing radiation field with a metal poor AGN narrow line region has the best agreement with the data, however it still misses a moderate number of AGN with very high log[N II]/Hα ratios.

7. Finally we examine the stellar mass-excitation (MEx) diagram at $z \sim 2.3$, and show that star forming galaxies and AGN are only somewhat separated in this diagnostic, even with a $\Delta \log(M/M_{\odot}) = +0.75$ shift of the $z = 0$ demarcation line. We found several IRAC and X-ray detected objects to appear in the region otherwise dominated by optical star forming galaxy sample. We also show that our (U)LIRGs occupy the MEx intermediate region between the star forming and AGN, confirming again that these are starburst-AGN composite systems.

References

Aird, J., Coil, A. L., Georgakakis, A., Nandra, K., Barro, G., & Pérez-González, P. G. 2015, MNRAS, 451, 1892

Azadi, M., Coil, A. L., Aird, J., Reddy, N., Shapley, A., Freeman, W. R., Kriek, M., Leung, G. C. K., Mobasher, B., Price, S. H., Sanders, R. L., Shivaei, I., & Siana, B. 2017, ApJ, 835, 27

Baldwin, J. A., Phillips, M. M., & Terlevich, R. 1981, PASP, 93, 5

Barnes, J. E. 2004, MNRAS, 350, 798

Bourne, N., Dunlop, J. S., Merlin, E., Parsa, S., Schreiber, C., Castellano, M., Conselice, C. J., Coppin, K. E. K., Farrah, D., Fontana, A., Geach, J. E., Halpern, M., Knudsen, K. K., Michałowski, M. J., Mortlock, A., Santini, P., Scott, D., Shu, X. W., Simpson, C., Simpson, J. M., Smith, D. J. B., & van der Werf, P. P. 2017, MNRAS, 467, 1360

Brusa, M., Gilli, R., Civano, F., Comastri, A., Fiore, R., & Vignali, C. 2011, Memorie della Societa Astronomica Italiana Supplementi, 17, 106

Bruzual, G. & Charlot, S. 2003, MNRAS, 344, 1000

Casey, C. M., Berta, S., Béthermin, M., Bock, J., Bridge, C., Budynkiewicz, J., Burgarella, D., Chapin, E., Chapman, S. C., Clements, D. L., Conley, A., Conselice, C. J., Cooray, A., Farrah, D., Hatziminaoglou, E., Ivison, R. J., le Floc'h, E., Lutz, D., Magdis, G., Magnelli, B., Oliver, S. J., Page, M. J., Pozzi, F., Rigopoulou, D., Riguccini, L.,

Roseboom, I. G., Sanders, D. B., Scott, D., Seymour, N., Valtchanov, I., Vieira, J. D., Viero, M., & Wardlow, J. 2012, ApJ, 761, 140

Casey, C. M., Cooray, A., Killi, M., Capak, P., Chen, C.-C., Hung, C.-L., Kartaltepe, J., Sanders, D. B., & Scoville, N. Z. 2017, ApJ, 840, 101

Civano, F., Elvis, M., Brusa, M., Comastri, A., Salvato, M., Zamorani, G., Aldcroft, T., Bongiorno, A., Capak, P., Cappelluti, N., Cisternas, M., Fiore, F., Fruscione, A., Hao, H., Kartaltepe, J., Koekemoer, A., Gilli, R., Impey, C. D., Lanzuisi, G., Lusso, E., Mainieri, V., Miyaji, T., Lilly, S., Masters, D., Puccetti, S., Schawinski, K., Scoville, N. Z., Silverman, J., Trump, J., Urry, M., Vignali, C., & Wright, N. J. 2012, ApJS, 201, 30

Coil, A. L., Aird, J., Reddy, N., Shapley, A. E., Kriek, M., Siana, B., Mobasher, B., Freeman, W. R., Price, S. H., & Shivaei, I. 2015, ApJ, 801, 35

Daddi, E., Cimatti, A., Renzini, A., Fontana, A., Mignoli, M., Pozzetti, L., Tozzi, P., & Zamorani, G. 2004, ApJ, 617, 746

Donley, J. L., Koekemoer, A. M., Brusa, M., Capak, P., Cardamone, C. N., Civano, F., Ilbert, O., Impey, C. D., Kartaltepe, J. S., Miyaji, T., Salvato, M., Sanders, D. B., Trump, J. R., & Zamorani, G. 2012, ApJ, 748, 142

Drory, N., Salvato, M., Gabasch, A., Bender, R., Hopp, U., Feulner, G., & Pannella, M. 2005, ApJ, 619, L131

Elvis, M., Civano, F., Vignali, C., Puccetti, S., Fiore, F., Cappelluti, N., Aldcroft, T. L., Fruscione, A., Zamorani, G., Comastri, A., Brusa, M., Gilli, R., Miyaji, T., Damiani, F., Koekemoer, A. M., Finoguenov, A., Brunner, H., Urry, C. M., Silverman, J., Mainieri, V., Hasinger, G., Griffiths, R., Carollo, M., Hao, H., Guzzo, L., Blain, A., Calzetti, D., Carilli, C., Capak, P., Ettori, S., Fabbiano, G., Impey, C., Lilly, S., Mobasher, B., Rich, M., Salvato, M., Sanders, D. B., Schinnerer, E., Scoville, N., Shopbell, P., Taylor, J. E., Taniguchi, Y., & Volonteri, M. 2009, ApJS, 184, 158

Elvis, M., Wilkes, B. J., McDowell, J. C., Green, R. F., Bechtold, J., Willner, S. P., Oey, M. S., Polomski, E., & Cutri, R. 1994, ApJS, 95, 1

Erb, D. K., Steidel, C. C., Shapley, A. E., Pettini, M., Reddy, N. A., & Adelberger, K. L. 2006, ApJ, 647, 128

Griffin, M. J., Abergel, A., Abreu, A., Ade, P. A. R., André, P., Augueres, J.-L., Babbedge, T., Bae, Y., Baillie, T., Baluteau, J.-P., Barlow, M. J., Bendo, G., Benielli, D., Bock, J. J., Bonhomme, P., Brisbin, D., Brockley-Blatt, C., Caldwell, M., Cara, C., Castro-Rodriguez, N., Cerulli, R., Chanial, P., Chen, S., Clark, E., Clements, D. L., Clerc, L., Coker, J., Communal, D., Conversi, L., Cox, P., Crumb, D., Cunningham, C., Daly, F., Davis, G. R., de Antoni, P., Delderfield, J., Devin, N., di Giorgio, A., Didschuns, I., Dohlen, K., Donati, M., Dowell, A., Dowell, C. D., Duband, L., Dumaye, L., Emery, R. J., Ferlet, M., Ferrand, D., Fontignie, J., Fox, M., Franceschini, A., Frerking, M., Fulton, T., Garcia, J., Gastaud, R., Gear, W. K., Glenn, J., Goizel, A., Griffin, D. K., Grundy, T., Guest, S., Guillemet, L., Hargrave, P. C., Harwit, M., Hastings, P., Hatziminaoglou, E., Herman, M., Hinde, B., Hristov, V., Huang, M., Imhof, P., Isaak, K. J., Israelsson, U., Ivison, R. J., Jennings, D., Kiernan, B., King, K. J., Lange, A. E., Latter, W., Laurent, G., Laurent, P., Leeks, S. J., Lellouch, E., Levenson, L., Li, B., Li, J., Lilienthal, J., Lim, T., Liu, S. J., Lu, N., Madden, S., Mainetti, G., Marliani, P., McKay, D., Mercier, K., Molinari, S., Morris, H., Moseley, H., Mulder, J., Mur, M., Naylor, D. A., Nguyen, H., O'Halloran, B., Oliver, S., Olofsson, G., Olofsson, H.-G., Orfei, R., Page, M. J., Pain, I., Panuzzo, P., Papageorgiou, A., Parks, G., Parr-Burman, P., Pearce, A., Pearson, C., Pérez-Fournon, I., Pinsard, F., Pisano, G., Podosek, J., Pohlen, M., Polehampton, E. T., Pouliquen, D., Rigopoulou, D., Rizzo, D., Roseboom, I. G., Roussel, H., Rowan-Robinson, M., Rownd, B., Saraceno, P., Sauvage, M., Savage, R., Savini, G., Sawyer, E., Scharmberg, C., Schmitt, D., Schneider, N., Schulz, B., Schwartz, A., Shafer, R., Shupe, D. L., Sibthorpe, B., Sidher, S., Smith, A., Smith, A. J., Smith, D., Spencer, L., Stobie, B., Sudiwala, R., Sukhatme, K., Surace, C., Stevens, J. A., Swinyard, B. M., Trichas, M.,

Tourette, T., Triou, H., Tseng, S., Tucker, C., Turner, A., Vaccari, M., Valtchanov, I., Vigroux, L., Virique, E., Voellmer, G., Walker, H., Ward, R., Waskett, T., Weilert, M., Wesson, R., White, G. J., Whitehouse, N., Wilson, C. D., Winter, B., Woodcraft, A. L., Wright, G. S., Xu, C. K., Zavagno, A., Zemcov, M., Zhang, L., & Zonca, E. 2010, A&A, 518, L3

Hainline, K. N., Shapley, A. E., Greene, J. E., & Steidel, C. C. 2011, ApJ, 733, 31

Hainline, K. N., Shapley, A. E., Kornei, K. A., Pettini, M., Buckley-Geer, E., Allam, S. S., & Tucker, D. L. 2009, ApJ, 701, 52

Hasinger, G., Cappelluti, N., Brunner, H., Brusa, M., Comastri, A., Elvis, M., Finoguenov, A., Fiore, F., Franceschini, A., Gilli, R., Griffiths, R. E., Lehmann, I., Mainieri, V., Matt, G., Matute, I., Miyaji, T., Molendi, S., Paltani, S., Sanders, D. B., Scoville, N., Tresse, L., Urry, C. M., Vettolani, P., & Zamorani, G. 2007, ApJS, 172, 29

Ilbert, O., Arnouts, S., Le Floc'h, E., Aussel, H., Bethermin, M., Capak, P., Hsieh, B.-C., Kajisawa, M., Karim, A., Le Fèvre, O., Lee, N., Lilly, S., McCracken, H. J., Michel-Dansac, L., Moutard, T., Renzini, M. A., Salvato, M., Sanders, D. B., Scoville, N., Sheth, K., Silverman, J. D., Smolčić, V., Taniguchi, Y., & Tresse, L. 2015, A&A, 579, A2

Juneau, S., Bournaud, F., Charlot, S., Daddi, E., Elbaz, D., Trump, J. R., Brinchmann, J., Dickinson, M., Duc, P.-A., Gobat, R., Jean-Baptiste, I., Le Floc'h, É., Lehnert, M. D., Pacifici, C., Pannella, M., & Schreiber, C. 2014, ApJ, 788, 88

Juneau, S., Dickinson, M., Alexander, D. M., & Salim, S. 2011, ApJ, 736, 104

Juneau, S., Dickinson, M., Bournaud, F., Alexander, D. M., Daddi, E., Mullaney, J. R., Magnelli, B., Kartaltepe, J. S., Hwang, H. S., Willner, S. P., Coil, A. L., Rosario, D. J., Trump, J. R., Weiner, B. J., Willmer, C. N. A., Cooper, M. C., Elbaz, D., Faber, S. M., Frayer, D. T., Kocevski, D. D., Laird, E. S., Monkiewicz, J. A., Nandra, K., Newman, J. A., Salim, S., & Symeonidis, M. 2013, ApJ, 764, 176

Kartaltepe, J. S., Sanders, D. B., Le Floc'h, E., Frayer, D. T., Aussel, H., Arnouts, S., Ilbert, O., Salvato, M., Scoville, N. Z., Surace, J., Yan, L., Brusa, M., Capak, P., Caputi, K., Carollo, C. M., Civano, F., Elvis, M., Faure, C., Hasinger, G., Koekemoer, A. M., Lee, N., Lilly, S., Liu, C. T., McCracken, H. J., Schinnerer, E., Smolčić, V., Taniguchi, Y., Thompson, D. J., & Trump, J. 2010, ApJ, 709, 572

Kauffmann, G., Heckman, T. M., Tremonti, C., Brinchmann, J., Charlot, S., White, S. D. M., Ridgway, S. E., Brinkmann, J., Fukugita, M., Hall, P. B., Ivezić, Ž., Richards, G. T., & Schneider, D. P. 2003, MNRAS, 346, 1055

Kennicutt, Jr., R. C., Roettiger, K. A., Keel, W. C., van der Hulst, J. M., & Hummel, E. 1987, AJ, 93, 1011

Kewley, L. J., Dopita, M. A., Leitherer, C., Davé, R., Yuan, T., Allen, M., Groves, B., & Sutherland, R. 2013, ApJ, 774, 100

Kewley, L. J., Dopita, M. A., Sutherland, R. S., Heisler, C. A., & Trevena, J. 2001, ApJ, 556, 121

Kewley, L. J., Groves, B., Kauffmann, G., & Heckman, T. 2006, MNRAS, 372, 961

Kim, D.-C. 1995, PhD thesis, UNIVERSITY OF HAWAII.

Kleinmann, D. E. & Low, F. J. 1970a, ApJ, 161, L203

—. 1970b, ApJ, 159, L165

Kriek, M., Shapley, A. E., Reddy, N. A., Siana, B., Coil, A. L., Mobasher, B., Freeman, W. R., de Groot, L., Price, S. H., Sanders, R., Shivaei, I., Brammer, G. B., Momcheva, I. G., Skelton, R. E., van Dokkum, P. G., Whitaker, K. E., Aird, J., Azadi, M., Kassis, M., Bullock, J. S., Conroy, C., Davé, R., Kereš, D., & Krumholz, M. 2015, ApJS, 218, 15

Kriek, M., van Dokkum, P. G., Franx, M., Illingworth, G. D., Marchesini, D., Quadri, R., Rudnick, G., Taylor, E. N., Förster Schreiber, N. M., Gawiser, E., Labbé, I., Lira, P., & Wuyts, S. 2008, ApJ, 677, 219

Lacy, M., Petric, A. O., Sajina, A., Canalizo, G., Storrie-Lombardi, L. J., Armus, L., Fadda, D., & Marleau, F. R. 2007, AJ, 133, 186

Laigle, C., McCracken, H. J., Ilbert, O., Hsieh, B. C., Davidzon, I., Capak, P., Hasinger, G., Silverman, J. D., Pichon, C., Coupon, J., Aussel, H., Le Borgne, D., Caputi, K., Cassata, P., Chang, Y.-Y., Civano, F., Dunlop, J., Fynbo, J., Kartaltepe, J. S., Koekemoer, A., Le Fèvre, O., Le Floc'h, E., Leauthaud, A., Lilly, S., Lin, L., Marchesi, S., Milvang-Jensen, B., Salvato, M., Sanders, D. B., Scoville, N., Smolcic, V., Stockmann, M., Taniguchi, Y., Tasca, L., Toft, S., Vaccari, M., & Zabl, J. 2016, ApJS, 224, 24

Larson, K. L., Sanders, D. B., Barnes, J. E., Ishida, C. M., Evans, A. S., U, V., Mazzarella, J. M., Kim, D.-C., Privon, G. C., Mirabel, I. F., & Flewelling, H. A. 2016, ApJ, 825, 128

Le Floc'h, E., Aussel, H., Ilbert, O., Riguccini, L., Frayer, D. T., Salvato, M., Arnouts, S., Surace, J., Feruglio, C., Rodighiero, G., Capak, P., Kartaltepe, J., Heinis, S., Sheth, K., Yan, L., McCracken, H. J., Thompson, D., Sanders, D., Scoville, N., & Koekemoer, A. 2009, ApJ, 703, 222

Lee, N., Sanders, D. B., Casey, C. M., Scoville, N. Z., Hung, C.-L., Le Floc'h, E., Ilbert, O., Aussel, H., Capak, P., Kartaltepe, J. S., Roseboom, I., Salvato, M., Aravena, M., Berta, S., Bock, J., Oliver, S. J., Riguccini, L., & Symeonidis, M. 2013, ApJ, 778, 131

Lilly, S. J., Le Fèvre, O., Renzini, A., Zamorani, G., Scodeggio, M., Contini, T., Carollo, C. M., Hasinger, G., Kneib, J.-P., Iovino, A., Le Brun, V., Maier, C., Mainieri, V., Mignoli, M., Silverman, J., Tasca, L. A. M., Bolzonella, M., Bongiorno, A., Bottini, D., Capak, P., Caputi, K., Cimatti, A., Cucciati, O., Daddi, E., Feldmann, R., Franzetti, P., Garilli, B., Guzzo, L., Ilbert, O., Kampczyk, P., Kovac, K., Lamareille, F., Leauthaud, A., Borgne, J.-F. L., McCracken, H. J., Marinoni, C., Pello, R., Ricciardelli, E., Scarlata, C., Vergani, D., Sanders, D. B., Schinnerer, E., Scoville, N., Taniguchi, Y., Arnouts, S., Aussel, H., Bardelli, S., Brusa, M., Cappi, A., Ciliegi, P., Finoguenov, A., Foucaud, S., Franceschini, R., Halliday, C., Impey, C., Knobel, C., Koekemoer, A., Kurk, J.,

Maccagni, D., Maddox, S., Marano, B., Marconi, G., Meneux, B., Mobasher, B., Moreau, C., Peacock, J. A., Porciani, C., Pozzetti, L., Scaramella, R., Schiminovich, D., Shopbell, P., Smail, I., Thompson, D., Tresse, L., Vettolani, G., Zanichelli, A., & Zucca, E. 2007, ApJS, 172, 70

Lutz, D., Poglitsch, A., Altieri, B., Andreani, P., Aussel, H., Berta, S., Bongiovanni, A., Brisbin, D., Cava, A., Cepa, J., Cimatti, A., Daddi, E., Dominguez-Sanchez, H., Elbaz, D., Förster Schreiber, N. M., Genzel, R., Grazian, A., Gruppioni, C., Harwit, M., Le Floc'h, E., Magdis, G., Magnelli, B., Maiolino, R., Nordon, R., Pérez García, A. M., Popesso, P., Pozzi, F., Riguccini, L., Rodighiero, G., Saintonge, A., Sanchez Portal, M., Santini, P., Shao, L., Sturm, E., Tacconi, L. J., Valtchanov, I., Wetzstein, M., & Wieprecht, E. 2011, A&A, 532, A90

Madau, P. & Dickinson, M. 2014, ARA&A, 52, 415

Marchesi, S., Civano, F., Elvis, M., Salvato, M., Brusa, M., Comastri, A., Gilli, R., Hasinger, G., Lanzuisi, G., Miyaji, T., Treister, E., Urry, C. M., Vignali, C., Zamorani, G., Allevato, V., Cappelluti, N., Cardamone, C., Finoguenov, A., Griffiths, R. E., Karim, A., Laigle, C., LaMassa, S. M., Jahnke, K., Ranalli, P., Schawinski, K., Schinnerer, E., Silverman, J. D., Smolcic, V., Suh, H., & Trakhtenbrot, B. 2016, ApJ, 817, 34

Markwardt, C. B. 2009, in Astronomical Society of the Pacific Conference Series, Vol. 411, Astronomical Data Analysis Software and Systems XVIII, ed. D. A. Bohlender, D. Durand, & P. Dowler, 251

Masters, D. & Capak, P. 2011, PASP, 123, 638

McCracken, H. J., Capak, P., Salvato, M., Aussel, H., Thompson, D., Daddi, E., Sanders, D. B., Kneib, J.-P., Willott, C. J., Mancini, C., Renzini, A., Cook, R., Le Fèvre, O., Ilbert, O., Kartaltepe, J., Koekemoer, A. M., Mellier, Y., Murayama, T., Scoville, N. Z., Shioya, Y., & Tanaguchi, Y. 2010, ApJ, 708, 202

McCracken, H. J., Milvang-Jensen, B., Dunlop, J., Franx, M., Fynbo, J. P. U., Le Fèvre, O., Holt, J., Caputi, K. I., Goranova, Y., Buitrago, F., Emerson, J. P., Freudling, W., Hudelot, P., López-Sanjuan, C., Magnard, F., Mellier, Y., Møller, P., Nilsson, K. K., Sutherland, W., Tasca, L., & Zabl, J. 2012, A&A, 544, A156

McLean, I. S., Steidel, C. C., Epps, H., Matthews, K., Adkins, S., Konidaris, N., Weber, B., Aliado, T., Brims, G., Canfield, J., Cromer, J., Fucik, J., Kulas, K., Mace, G., Magnone, K., Rodriguez, H., Wang, E., & Weiss, J. 2010, in Society of Photo-Optical Instrumentation Engineers (SPIE) Conference Series, Vol. 7735, Society of Photo-Optical Instrumentation Engineers (SPIE) Conference Series

McLean, I. S., Steidel, C. C., Epps, H. W., Konidaris, N., Matthews, K. Y., Adkins, S., Aliado, T., Brims, G., Canfield, J. M., Cromer, J. L., Fucik, J., Kulas, K., Mace, G., Magnone, K., Rodriguez, H., Rudie, G., Trainor, R., Wang, E., Weber, B., & Weiss, J. 2012, in Proc. SPIE, Vol. 8446, Ground-based and Airborne Instrumentation for Astronomy IV, 84460J

Meléndez, M., Heckman, T. M., Martínez-Paredes, M., Kraemer, S. B., & Mendoza, C. 2014, MNRAS, 443, 1358

Mendez, A. J., Coil, A. L., Aird, J., Diamond-Stanic, A. M., Moustakas, J., Blanton, M. R., Cool, R. J., Eisenstein, D. J., Wong, K. C., & Zhu, G. 2013, ApJ, 770, 40

Nanayakkara, T., Glazebrook, K., Kacprzak, G. G., Yuan, T., Tran, K.-V., Spitler, L., Kewley, L., Straatman, C., Cowley, M., Fisher, D., Labbe, I., Tomczak, A., Allen, R., & Alcorn, L. 2016, ApJ, 828, 21

Oliver, S. J., Bock, J., Altieri, B., Amblard, A., Arumugam, V., Aussel, H., Babbedge, T., Beelen, A., Béthermin, M., Blain, A., Boselli, A., Bridge, C., Brisbin, D., Buat, V., Burgarella, D., Castro-Rodríguez, N., Cava, A., Chanial, P., Cirasuolo, M., Clements, D. L., Conley, A., Conversi, L., Cooray, A., Dowell, C. D., Dubois, E. N., Dwek, E., Dye, S., Eales, S., Elbaz, D., Farrah, D., Feltre, A., Ferrero, P., Fiolet, N., Fox, M.,

Franceschini, A., Gear, W., Giovannoli, E., Glenn, J., Gong, Y., González Solares, E. A., Griffin, M., Halpern, M., Harwit, M., Hatziminaoglou, E., Heinis, S., Hurley, P., Hwang, H. S., Hyde, A., Ibar, E., Ilbert, O., Isaak, K., Ivison, R. J., Lagache, G., Le Floc'h, E., Levenson, L., Faro, B. L., Lu, N., Madden, S., Maffei, B., Magdis, G., Mainetti, G., Marchetti, L., Marsden, G., Marshall, J., Mortier, A. M. J., Nguyen, H. T., O'Halloran, B., Omont, A., Page, M. J., Panuzzo, P., Papageorgiou, A., Patel, H., Pearson, C. P., Pérez-Fournon, I., Pohlen, M., Rawlings, J. I., Raymond, G., Rigopoulou, D., Riguccini, L., Rizzo, D., Rodighiero, G., Roseboom, I. G., Rowan-Robinson, M., Sánchez Portal, M., Schulz, B., Scott, D., Seymour, N., Shupe, D. L., Smith, A. J., Stevens, J. A., Symeonidis, M., Trichas, M., Tugwell, K. E., Vaccari, M., Valtchanov, I., Vieira, J. D., Viero, M., Vigroux, L., Wang, L., Ward, R., Wardlow, J., Wright, G., Xu, C. K., & Zemcov, M. 2012, MNRAS, 424, 1614

Pérez-González, P. G., Trujillo, I., Barro, G., Gallego, J., Zamorano, J., & Conselice, C. J. 2008, ApJ, 687, 50

Pilbratt, G. L., Riedinger, J. R., Passvogel, T., Crone, G., Doyle, D., Gageur, U., Heras, A. M., Jewell, C., Metcalfe, L., Ott, S., & Schmidt, M. 2010, A&A, 518, L1

Poglitsch, A., Waelkens, C., Geis, N., Feuchtgruber, H., Vandenbussche, B., Rodriguez, L., Krause, O., Renotte, E., van Hoof, C., Saraceno, P., Cepa, J., Kerschbaum, F., Agnèse, P., Ali, B., Altieri, B., Andreani, P., Augueres, J.-L., Balog, Z., Barl, L., Bauer, O. H., Belbachir, N., Benedettini, M., Billot, N., Boulade, O., Bischof, H., Blommaert, J., Callut, E., Cara, C., Cerulli, R., Cesarsky, D., Contursi, A., Creten, Y., De Meester, W., Doublier, V., Doumayrou, E., Duband, L., Exter, K., Genzel, R., Gillis, J.-M., Grözinger, U., Henning, T., Herreros, J., Huygen, R., Inguscio, M., Jakob, G., Jamar, C., Jean, C., de Jong, J., Katterloher, R., Kiss, C., Klaas, U., Lemke, D., Lutz, D., Madden, S., Marquet, B., Martignac, J., Mazy, A., Merken, P., Montfort, F., Morbidelli, L., Müller, T., Nielbock, M., Okumura, K., Orfei, R., Ottensamer, R., Pezzuto, S., Popesso, P., Putzeys, J., Regibo, S., Reveret, V., Royer, P., Sauvage, M., Schreiber, J., Stegmaier, J.,

Schmitt, D., Schubert, J., Sturm, E., Thiel, M., Tofani, G., Vavrek, R., Wetzstein, M., Wieprecht, E., & Wiezorrek, E. 2010, A&A, 518, L2

Pozzetti, L., Bolzonella, M., Lamareille, F., Zamorani, G., Franzetti, P., Le Fèvre, O., Iovino, A., Temporin, S., Ilbert, O., Arnouts, S., Charlot, S., Brinchmann, J., Zucca, E., Tresse, L., Scodeggio, M., Guzzo, L., Bottini, D., Garilli, B., Le Brun, V., Maccagni, D., Picat, J. P., Scaramella, R., Vettolani, G., Zanichelli, A., Adami, C., Bardelli, S., Cappi, A., Ciliegi, P., Contini, T., Foucaud, S., Gavignaud, I., McCracken, H. J., Marano, B., Marinoni, C., Mazure, A., Meneux, B., Merighi, R., Paltani, S., Pellò, R., Pollo, A., Radovich, M., Bondi, M., Bongiorno, A., Cucciati, O., de la Torre, S., Gregorini, L., Mellier, Y., Merluzzi, P., Vergani, D., & Walcher, C. J. 2007, A&A, 474, 443

Reddy, N. A., Steidel, C. C., Pettini, M., Adelberger, K. L., Shapley, A. E., Erb, D. K., & Dickinson, M. 2008, ApJS, 175, 48

Rieke, G. H., Alonso-Herrero, A., Weiner, B. J., Pérez-González, P. G., Blaylock, M., Donley, J. L., & Marcillac, D. 2009, ApJ, 692, 556

Rieke, G. H. & Low, F. J. 1972, ApJ, 176, L95

Rudie, G. C., Steidel, C. C., Trainor, R. F., Rakic, O., Bogosavljević, M., Pettini, M., Reddy, N., Shapley, A. E., Erb, D. K., & Law, D. R. 2012, ApJ, 750, 67

Sanders, D. B. & Mirabel, I. F. 1996, ARA&A, 34, 749

Sanders, D. B., Salvato, M., Aussel, H., Ilbert, O., Scoville, N., Surace, J. A., Frayer, D. T., Sheth, K., Helou, G., Brooke, T., Bhattacharya, B., Yan, L., Kartaltepe, J. S., Barnes, J. E., Blain, A. W., Calzetti, D., Capak, P., Carilli, C., Carollo, C. M., Comastri, A., Daddi, E., Ellis, R. S., Elvis, M., Fall, S. M., Franceschini, A., Giavalisco, M., Hasinger, G., Impey, C., Koekemoer, A., Le Fèvre, O., Lilly, S., Liu, M. C., McCracken, H. J., Mobasher, B., Renzini, A., Rich, M., Schinnerer, E., Shopbell, P. L., Taniguchi, Y., Thompson, D. J., Urry, C. M., & Williams, J. P. 2007, ApJS, 172, 86

Sanders, D. B., Soifer, B. T., Elias, J. H., Madore, B. F., Matthews, K., Neugebauer, G., & Scoville, N. Z. 1988a, ApJ, 325, 74

Sanders, D. B., Soifer, B. T., Elias, J. H., Neugebauer, G., & Matthews, K. 1988b, ApJ, 328, L35

Scoville, N., Aussel, H., Brusa, M., Capak, P., Carollo, C. M., Elvis, M., Giavalisco, M., Guzzo, L., Hasinger, G., Impey, C., Kneib, J.-P., LeFevre, O., Lilly, S. J., Mobasher, B., Renzini, A., Rich, R. M., Sanders, D. B., Schinnerer, E., Schminovich, D., Shopbell, P., Taniguchi, Y., & Tyson, N. D. 2007, ApJS, 172, 1

Shapley, A. E., Reddy, N. A., Kriek, M., Freeman, W. R., Sanders, R. L., Siana, B., Coil, A. L., Mobasher, B., Shivaei, I., Price, S. H., & de Groot, L. 2015, ApJ, 801, 88

Sharples, R., Bender, R., Agudo Berbel, A., Bennett, R., Bezawada, N., Castillo, R., Cirasuolo, M., Clark, P., Davidson, G., Davies, R., Davies, R., Dubbeldam, M., Fairley, A., Finger, G., Schreiber, N. F., Genzel, R., Haefner, R., Hess, A., Jung, I., Lewis, I., Montgomery, D., Murray, J., Muschielok, B., Pirard, J., Ramsay, S., Rees, P., Richter, J., Robertson, D., Robson, I., Rolt, S., Saglia, R., Saviane, I., Schlichter, J., Schmidtobreik, L., Segovia, A., Smette, A., Tecza, M., Todd, S., Wegner, M., & Wiezorrek, E. 2014, in Proc. SPIE, Vol. 9147, Ground-based and Airborne Instrumentation for Astronomy V, 91470W

Silverman, J. D., Kashino, D., Sanders, D., Kartaltepe, J. S., Arimoto, N., Renzini, A., Rodighiero, G., Daddi, E., Zahid, J., Nagao, T., Kewley, L. J., Lilly, S. J., Sugiyama, N., Baronchelli, I., Capak, P., Carollo, C. M., Chu, J., Hasinger, G., Ilbert, O., Juneau, S., Kajisawa, M., Koekemoer, A. M., Kovac, K., Le Fèvre, O., Masters, D., McCracken, H. J., Onodera, M., Schulze, A., Scoville, N., Strazzullo, V., & Taniguchi, Y. 2015, ApJS, 220, 12

Soifer, B. T., Sanders, D. B., Madore, B. F., Neugebauer, G., Danielson, G. E., Elias, J. H., Lonsdale, C. J., & Rice, W. L. 1987, ApJ, 320, 238

Steidel, C. C., Erb, D. K., Shapley, A. E., Pettini, M., Reddy, N., Bogosavljević, M., Rudie, G. C., & Rakic, O. 2010, ApJ, 717, 289

Steidel, C. C., Rudie, G. C., Strom, A. L., Pettini, M., Reddy, N. A., Shapley, A. E., Trainor, R. F., Erb, D. K., Turner, M. L., Konidaris, N. P., Kulas, K. R., Mace, G., Matthews, K., & McLean, I. S. 2014, ApJ, 795, 165

Stern, D., Eisenhardt, P., Gorjian, V., Kochanek, C. S., Caldwell, N., Eisenstein, D., Brodwin, M., Brown, M. J. I., Cool, R., Dey, A., Green, P., Jannuzi, B. T., Murray, S. S., Pahre, M. A., & Willner, S. P. 2005, ApJ, 631, 163

Strom, A. L., Steidel, C. C., Rudie, G. C., Trainor, R. F., Pettini, M., & Reddy, N. A. 2017, ApJ, 836, 164

Suh, H., Civano, F., Hasinger, G., Lusso, E., Lanzuisi, G., Marchesi, S., Trakhtenbrot, B., Allevato, V., Cappelluti, N., Capak, P. L., Elvis, M., Griffiths, R. E., Laigle, C., Lira, P., Riguccini, L., Rosario, D. J., Salvato, M., Schawinski, K., & Vignali, C. 2017, ApJ, 841, 102

Sutherland, W. & Saunders, W. 1992, MNRAS, 259, 413

Taniguchi, Y., Scoville, N., Murayama, T., Sanders, D. B., Mobasher, B., Aussel, H., Capak, P., Ajiki, M., Miyazaki, S., Komiyama, Y., Shioya, Y., Nagao, T., Sasaki, S. S., Koda, J., Carilli, C., Giavalisco, M., Guzzo, L., Hasinger, G., Impey, C., LeFevre, O., Lilly, S., Renzini, A., Rich, M., Schinnerer, E., Shopbell, P., Kaifu, N., Karoji, H., Arimoto, N., Okamura, S., & Ohta, K. 2007, ApJS, 172, 9

Toomre, A. & Toomre, J. 1972, ApJ, 178, 623

Ueda, Y., Akiyama, M., Hasinger, G., Miyaji, T., & Watson, M. G. 2014, ApJ, 786, 104

Veilleux, S., Kim, D.-C., & Sanders, D. B. 2002, ApJS, 143, 315

Veilleux, S., Kim, D.-C., Sanders, D. B., Mazzarella, J. M., & Soifer, B. T. 1995, ApJS, 98, 171

Veilleux, S., Rupke, D. S. N., Kim, D., Genzel, R., Sturm, E., Lutz, D., Contursi, A., Schweitzer, M., Tacconi, L. J., Netzer, H., Sternberg, A., Mihos, J. C., Baker, A. J., Mazzarella, J. M., Lord, S., Sanders, D. B., Stockton, A., Joseph, R. D., & Barnes, J. E. 2009, ApJS, 182, 628

York, D. G., Adelman, J., Anderson, Jr., J. E., Anderson, S. F., Annis, J., Bahcall, N. A., Bakken, J. A., Barkhouser, R., Bastian, S., Berman, E., Boroski, W. N., Bracker, S., Briegel, C., Briggs, J. W., Brinkmann, J., Brunner, R., Burles, S., Carey, L., Carr, M. A., Castander, F. J., Chen, B., Colestock, P. L., Connolly, A. J., Crocker, J. H., Csabai, I., Czarapata, P. C., Davis, J. E., Doi, M., Dombeck, T., Eisenstein, D., Ellman, N., Elms, B. R., Evans, M. L., Fan, X., Federwitz, G. R., Fiscelli, L., Friedman, S., Frieman, J. A., Fukugita, M., Gillespie, B., Gunn, J. E., Gurbani, V. K., de Haas, E., Haldeman, M., Harris, F. H., Hayes, J., Heckman, T. M., Hennessy, G. S., Hindsley, R. B., Holm, S., Holmgren, D. J., Huang, C.-h., Hull, C., Husby, D., Ichikawa, S.-I., Ichikawa, T., Ivezić, Ž., Kent, S., Kim, R. S. J., Kinney, E., Klaene, M., Kleinman, A. N., Kleinman, S., Knapp, G. R., Korienek, J., Kron, R. G., Kunszt, P. Z., Lamb, D. Q., Lee, B., Leger, R. F., Limmongkol, S., Lindenmeyer, C., Long, D. C., Loomis, C., Loveday, J., Lucinio, R., Lupton, R. H., MacKinnon, B., Mannery, E. J., Mantsch, P. M., Margon, B., McGehee, P., McKay, T. A., Meiksin, A., Merelli, A., Monet, D. G., Munn, J. A., Narayanan, V. K., Nash, T., Neilsen, E., Neswold, R., Newberg, H. J., Nichol, R. C., Nicinski, T., Nonino, M., Okada, N., Okamura, S., Ostriker, J. P., Owen, R., Pauls, A. G., Peoples, J., Peterson, R. L., Petravick, D., Pier, J. R., Pope, A., Pordes, R., Prosapio, A., Rechenmacher, R., Quinn, T. R., Richards, G. T., Richmond, M. W., Rivetta, C. H., Rockosi, C. M., Ruthmansdorfer, K., Sandford, D., Schlegel, D. J., Schneider, D. P., Sekiguchi, M., Sergey, G., Shimasaku, K., Siegmund, W. A., Smee, S., Smith, J. A., Snedden, S., Stone, R., Stoughton, C., Strauss, M. A., Stubbs, C., SubbaRao, M., Szalay, A. S., Szapudi, I., Szokoly, G. P., Thakar, A. R., Tremonti, C., Tucker, D. L., Uomoto, A., Vanden Berk, D., Vogeley, M. S., Waddell, P., Wang, S.-i., Watanabe, M., Weinberg, D. H., Yanny, B., Yasuda, N., & SDSS Collaboration. 2000,

AJ, 120, 1579

Yoshikawa, T., Akiyama, M., Kajisawa, M., Alexander, D. M., Ohta, K., Suzuki, R., Tokoku, C., Uchimoto, Y. K., Konishi, M., Yamada, T., Tanaka, I., Omata, K., Nishimura, T., Koekemoer, A. M., Brandt, N., & Ichikawa, T. 2010, ApJ, 718, 112

Yuan, T., Kewley, L. J., & Sanders, D. B. 2010, ApJ, 709, 884

Yuan, T.-T., Kewley, L. J., Swinbank, A. M., & Richard, J. 2012, ApJ, 759, 66

Chapter 6

Summary and Future Work

The primary goal of this dissertation has been to investigate the multi-wavelength properties of luminous infrared galaxies using the latest generation of world class astronomical facilities and instruments. In particular this is the first in-depth study of nearby (U)LIRGs utilizing high resolution far-infrared and submillimeter imaging data. In addition I also conducted the first statistical study investigating the rest-frame optical emission line properties of (U)LIRGs at $z \sim 2.3$ where they are many times more numerous than in the local universe. Below I summarize the main results from each chapter.

6.1 The Great Observatories All-Sky LIRG Survey: *Herschel* Image Atlas and Aperture Photometry

In Chapter 2 I presented the complete atlas of *Herschel* broadband imaging for the entire GOALS sample at 70, 100, 160, 250, 350, and 500 μm, which has been published as Chu et al. (2017) in the *Astrophysical Journal Supplement Series*. Each map was carefully processed and checked for maximal image quality to ensure a legacy-quality dataset using the most up to date processing techniques and calibration files (Figure 2.3). The maps do not suffer from any major image quality issues that may arise from scan-based observations such as major striping, background gradients, or saturation effects. In addition all 201 GOALS objects were detected in all six wavelength bands, while the field of view of all the maps

are large and sensitive enough to detect the full extent of the far-infrared and submillimeter emission. Furthermore the resolution of *Herschel* is high enough to resolve many individual components of interacting systems, particularly at 70 and 100 μm. On the other hand the resolution at submillimeter wavelengths is still sufficient to resolve wider galaxy pairs.

In addition I performed aperture photometry for each system as well as component fluxes where possible (Tables 2.3, 2.4, and 2.5). I then compared the *Herschel* 70 and 100 μm fluxes to the well-calibrated *IRAS* 60 and 100 μm measurements from Sanders et al. (2003), and found an excellent agreement at all flux levels and object morphologies (Figure 2.7). For many of these galaxies this chapter presents the first, high resolution imaging and reliable photometric measurements in the far-infrared and submillimeter. The final, reduced images are available on the Infrared Science Archive (IRSA) for use by the general astronomical community.

6.2 The 3–500 μm Spectral Energy Distributions of Local Luminous Infrared Galaxies

In Chapter 3 I used the *Herschel* data from the preceding chapter in conjunction with infrared data from *IRAS*, *Spitzer*, and *WISE* to construct the infrared spectral energy distribution between 3–500 μm. Combining the GOALS data with similar data on the KINGFISH sample of sub-luminous infrared galaxies (those with $L_{\rm IR} < 10^{11} L_{\odot}$), I compared the properties of the SEDs with respect to their total infrared luminosity, submillimeter luminosity and spectral index, infrared color, and to previous SED models from the literature (Figure 3.2).

By dividing all of the galaxies into infrared luminosity bin sizes of 0.25 dex, I find that all galaxies with infrared luminosities above $\sim 10^{10.25} L_{\odot}$ have nearly the same spectral slope of approximately $F \propto \nu^{4\pm0.12}$, while galaxies less luminous than that threshold (down to $10^{9.75} L_{\odot}$) have noticeably shallower indices of approximately $F \propto \nu^{3.4}$. Additionally, for galaxies with total infrared luminosities between $10^{11} L_{\odot}$ and $10^{12.25} L_{\odot}$, their submillimeter

luminosities are nearly the same with a maximum difference of ~ 0.5 dex. This implies that the cold dust component probed by the submillimeter is very similar for a wide range in total infrared luminosity. However for the brightest infrared luminosity bin ($L_{\rm IR} > 10^{12.25} L_{\odot}$) the submillimeter luminosity at all wavelengths is 0.4 dex higher than the next brightest luminosity bin, which suggests that an additional warm dust component is being heated only in the most luminous systems. In addition I find that the peak wavelength in the far-infrared shifts from ~ 100 μm at $L_{\rm IR} \approx 10^{11} L_{\odot}$ to ~ 60 μm at $L_{\rm IR} \approx 10^{12.5} L_{\odot}$.

In addition I showed that the SED models of Chary & Elbaz (2001) and Rieke et al. (2009) all reasonably predict the correct SED shapes of (U)LIRGs, with the exception being in the mid-infrared (Figure 3.3). At the highest luminosities where $\log(L_{\rm IR}/L_{\odot}) \geq 11.75$, the 18 μm broad silicate absorption feature appears to depress the emission in the mid-infrared ($\lambda \sim 8$–25 μm). This makes the appearance of excess emission at longer wavelengths, which is what we also observed in Chapter 4. This feature was not included in the templates of Chary & Elbaz (2001) since they did not have *Spitzer*-IRS data, however it is accounted for by Rieke et al. (2009). Otherwise the models lie within the 1-σ dispersion of the data at far-infrared and submillimeter wavelengths, although there are small but noticeable systematic offsets below and above the data as a function of $L_{\rm IR}$. This is due to the approximately linear method in which they interpolated their model SEDs, whereas our new data clearly show a nonlinear increase in the far-infrared and submillimeter luminosities.

I also examined the far-infrared and submillimeter color, or flux ratio for both the GOALS and KINGFISH samples. I computed the $L_{\rm IR}$-color relation at two mid-infrared wavelengths (f_{22}/f_{70} and f_{22}/f_{100}) and two far-infrared wavelengths (f_{70}/f_{100} and f_{70}/f_{250}), and compared them to the model predictions of Chary & Elbaz (2001) and Rieke et al. (2009) (Figure 3.4). In general I find the sub-LIRGs to agree reasonably well with both models in the mid- and far-infrared, except in the f_{70}/f_{250} flux ratio where it can overestimate the true color by a factor of ~ 2. This is most likely because these models were derived before the availability of accurate submillimeter fluxes from *Herschel*. In the (U)LIRG regime both models tend to predict bluer far-infrared colors (higher flux ratios) than the data by

up to 2× compared to the median of our data. In the mid-infrared both models agree reasonably well with the (U)LIRG data except at the highest luminosity, where Chary & Elbaz (2001) overestimates the flux ratio by 3× due to the aforementioned 18 μm absorption feature. Additionally I find that as $L_{\rm IR}$ is increased up to about $10^{12.25} L_{\odot}$, the f_{70}/f_{100} and f_{70}/f_{250} flux ratios both increase, which implies their far-infrared colors become bluer on average. However the most luminous galaxies above $10^{12.25} L_{\odot}$ appear to become redder again, which is normally the most dust-enshrouded stage of a galaxy merger. Finally I provide a table of median broadband luminosities corresponding to the median SEDs in the luminosity bins of $L_{\rm IR}$ presented in Figure 3.2. This chapter clearly shows the need for updated SEDs of (U)LIRGs, which I further discuss in §6.5.

6.3 Spatial Decomposition of the Radio-Infrared Correlation in Luminous Infrared Galaxies

In Chapter 4 I used the *Spitzer* and *Herschel* GOALS data to explore the spatial distribution of the radio-infrared correlation in (U)LIRGs. Previous studies have found a tight correlation between the infrared to radio flux ratio q that extends over several orders magnitude in luminosity, however many of these studies were restricted to only total fluxes (and hence ratios) of galaxies. In this chapter I used the high resolution 24 μm maps from *Spitzer*, 70 and 100 μm maps from *Herschel*, and VLA 20 cm maps to investigate if the correlation holds on galactic scales in (U)LIRGs (Figures 4.2 and 4.3). To do this I computed the q value separately for the nuclear region and for the total galaxy, and then computed the ratio $q_{\rm nuc}/q_{\rm total}$. I find that most of the (U)LIRGs have a smaller $q_{\rm nuc}$ value at 24, 70, and 100 μm compared to $q_{\rm total}$ (Figure 4.10). This clearly points to a complex behavior in the q value over different spatial components of a galaxy, and care must be used if one wishes to infer the distribution of mid-infrared emission using radio maps.

Above an infrared luminosity of $10^{11.6} L_{\odot}$, I observed a marked reduction in the $q_{24,\rm nuc}/q_{24,\rm total}$ ratio as $L_{\rm IR}$ is increased (Figure 4.10). This trend is seen not only in optically

selected (i.e., BPT diagram) Seyferts, but includes starbursts and composite systems as well. Below this luminosity threshold the $q_{24,\mathrm{nuc}}/q_{24,\mathrm{total}}$ ratio appears to be constant with an average ratio of 81%. On the other hand the nuclear to total q ratios for the 70 and 100 μm data do not show this depression at any L_{IR}, which implies the observed depression in the $q_{24,\mathrm{nuc}}/q_{24,\mathrm{total}}$ ratio above $10^{11.6}L_{\odot}$ is due to a deficit in mid-infrared flux, and not an excess in radio emission. This deficit arises from the broad 18 μm silicate absorption feature which is roughly proportional to the AGN strength, and since the most IR luminous galaxies have the most powerful AGN, it is most pronounced at higher L_{IR}. By plotting the average *Spitzer* IRS spectra (5–35 μm) of these galaxies in different bins of L_{IR}, we confirmed that the galaxies above $10^{11.6}L_{\odot}$ have a very prominent absorption feature extending well into the *Spitzer* 24 μm passband (Figure 4.11).

6.4 Rest-Frame Optical Emission Line Diagnostics of Luminous Infrared Galaxies at $z \sim 2.3$

In Chapter 5 I examined the rest-frame optical emission line properties of (U)LIRGs at $z \sim 2.3$ in the COSMOS field. The motivation for this study is to determine what powers high redshift (U)LIRGs, whether it is due to starbursts, AGN, or both. To do this I selected (U)LIRGs using a *Herschel* and 24 μm selection, star forming galaxies using the BzK color-color selection technique, and AGN using an X-ray and *Spitzer*-IRAC selection method. Using observations taken on Keck I/MOSFIRE, we show that the our star forming selected galaxies lie above the local SDSS star forming abundance sequence on the log[O III]/Hβ vs. log[N II]/Hα BPT diagram, and is very similar to the UV and/or optically selected galaxies of KBSS (Steidel et al. 2014; Strom et al. 2017) and MOSDEF (Shapley et al. 2015) (Figure 5.8).

More interestingly, I found the distribution of (U)LIRGs on the BPT diagram to lie in a different location than the bulk of optically selected star forming galaxies, with higher log[N II]/Hα ratios on average (Figure 5.9). In the log[O III]/Hβ ratio, (U)LIRGs displayed

a much larger dispersion than the control sample of star forming galaxies. Of the 71 (U)LIRGs that were detected, we found 12 which were also detected by one or both of our AGN selection criteria. These objects have a high average log[N II]/Hα ratio of -0.09, and occupy the same region as AGN in the MOSDEF and KBSS samples. Overall this suggests that (U)LIRGs are powered by a combination of intense star formation as well as AGN. This also shows that a rest-frame infrared ($\sim$10–100 μm) selection criteria results in a sample that has markedly different properties than a rest-frame optical or UV selection method, despite having the same stellar mass range.

Using the data I obtained in conjunction with data from KBSS and MOSDEF, I show that the $z \sim 2.3$ AGN branch on the BPT diagram is somewhat similar to local AGN in the SDSS sample (Figure 5.10). However unlike the local galaxies, the $z \sim 2.3$ AGN branch is noticeably more vertical, which implies the log[N II]/Hα ratio is less sensitive to AGN strength. Furthermore I show how AGN selected based on the presence of rest-UV lines tend to have high ratios in both log[N II]/Hα and log[O III]/Hβ, whereas those selected by IRAC colors or in X-ray have a similarly high log[N II]/Hα, but with a large dispersion in their log[O III]/Hβ ratios. This is attributed to the fact that the X-ray and IRAC selection techniques are sensitive to a much wider range in AGN obscuration than a UV selection. This also implies that a UV/optical selection is more sensitive to the most powerful AGN, and/or older AGN that have had time to photo-dissociate the dust surrounding it.

I also assessed how well local starburst-AGN classification lines perform on the high redshift BPT diagram, and conclude that the theoretical lines of Kewley et al. (2001) and Kauffmann et al. (2003) should not be used at high redshift to separate pure star forming, composite, and AGN galaxies (Figure 5.9). On the other hand the more recent $z = 0$ demarcation line of Meléndez et al. (2014) is better and successfully separates most AGN from the star forming sequence, however it misses some AGN that appear to have pure star forming line ratios, and may still miss galaxies at the high metallicity end of the star forming branch. We also investigated how well the four limiting scenarios of Kewley et al. (2013) fit our data, and conclude that ISM conditions at $z \sim 2.3$ are not as extreme as predicted

(Figure 5.11). Their "Scenario 4" which corresponds to "extreme ISM conditions" (i.e., a larger ionization parameter, denser ISM, and/or harder ionizing radiation field) with a metal poor AGN narrow line region has the best agreement with the data, however it still misses a moderate number of AGN with very high log[N II]/Hα ratios. Finally I examined the $z \sim 2.3$ mass-excitation (MEx) diagram and show that the star forming galaxies and AGN are only somewhat separated in this diagnostic, and does not appear to be as robust as what Juneau et al. (2014) found (Figure 5.12). However the (U)LIRGs occupy the "MEx intermediate" region between the star forming and AGN, confirming again that these are starburst-AGN composite systems.

6.5 Future Work

This dissertation has investigated the multi-wavelength properties of luminous infrared galaxies in both the nearby and distant universe. In the case of local (U)LIRGs, it is clear that an updated set of SED templates is needed to replace the existing models, which were developed before the availability of accurate far-infrared data from *Herschel*. With our new data it is no longer necessary to approximate the far-infrared and submillimeter luminosities in (U)LIRGs. Thus one immediate avenue for future work is to derive new infrared and submillimeter SED templates of luminous infrared galaxies as a function of $L_{\rm IR}$ using our new data. This will involve the SED fitting of the photometry presented in Chapter 3 using existing codes such as that of Casey (2012). These fits will also naturally allow one to derive accurate bulk properties of (U)LIRGs such as their infrared luminosities, dust masses, and effective dust temperatures. In addition one can also examine the relation between the 8 μm luminosity and the total infrared luminosity, where for example Elbaz et al. (2011) found local galaxies to deviate from a log-linear relationship. Finally this work will also be critical in providing more accurate and complete infrared SEDs to model high redshift galaxies.

In the distant universe where (U)LIRGs are the dominant sites of star formation, the next step would be to compute dust-corrected Hα-based star formation rates and far-infrared-based star formation rates for (U)LIRGs with no AGN signature, and compare both quantities to their stellar masses. For galaxies only detected at mid-infrared but not far-infrared wavelengths, one can use the new 3–500 μm infrared SEDs described above to estimate their total $L_{\rm IR}$, and hence the far-infrared star formation rate. Recent studies have shown a "main sequence" correlation to exist for star forming galaxies (i.e., Noeske et al. 2007), and it would be interesting to compare the main sequence using SFRs derived in two different ways. Additionally Chapter 5 mentions how shocks can play a large role in high redshift galaxies and produce AGN-like signatures on the BPT diagram. In order to resolve whether or not the apparent AGN-like properties of (U)LIRGs is due to shocks or AGN, one can obtain adaptive optics corrected, near-infrared integral field observations on a few of the (U)LIRGs in my sample. This would allow a study on the spatial distribution of the log[N II]/Hα and log[O III]/Hβ ratios. If the elevated log[N II]/Hα ratios are due to shocks, this would be manifested throughout the disk of the galaxy, whereas if it was due to an AGN it would be centrally concentrated in the nucleus.

Another possible study is to perform an analysis similar to Chapter 5 on the infrared selected galaxies from the completed Subaru FMOS-COSMOS survey, comprising of rest-frame optical spectra on more than 3000 galaxies at $z \sim 1.6$ in the COSMOS field. This large sample will allow us to construct a complete picture of the BPT diagram at $z \sim 1.6$, and will be interesting to compare to my higher redshift MOSFIRE results. Combined with existing studies at $z \sim 1$ and below, these studies would collectively trace the evolution of emission line galaxies on the BPT diagram over 75% of the age of the universe. In summary, luminous infrared galaxies play an important role in galaxy evolution throughout cosmic time, and although this dissertation has revealed new insights into their nature, much work still needed in understanding the physical processes responsible for driving them.

References

Casey, C. M. 2012, MNRAS, 425, 3094

Chary, R. & Elbaz, D. 2001, ApJ, 556, 562

Chu, J. K., Sanders, D. B., Larson, K. L., Mazzarella, J. M., Howell, J. H., Díaz-Santos, T., Xu, K. C., Paladini, R., Schulz, B., Shupe, D., Appleton, P., Armus, L., Billot, N., Chan, B. H. P., Evans, A. S., Fadda, D., Frayer, D. T., Haan, S., Ishida, C. M., Iwasawa, K., Kim, D.-C., Lord, S., Murphy, E., Petric, A., Privon, G. C., Surace, J. A., & Treister, E. 2017, ApJS, 229, 25

Elbaz, D., Dickinson, M., Hwang, H. S., Díaz-Santos, T., Magdis, G., Magnelli, B., Le Borgne, D., Galliano, F., Pannella, M., Chanial, P., Armus, L., Charmandaris, V., Daddi, E., Aussel, H., Popesso, P., Kartaltepe, J., Altieri, B., Valtchanov, I., Coia, D., Dannerbauer, H., Dasyra, K., Leiton, R., Mazzarella, J., Alexander, D. M., Buat, V., Burgarella, D., Chary, R.-R., Gilli, R., Ivison, R. J., Juneau, S., Le Floc'h, E., Lutz, D., Morrison, G. E., Mullaney, J. R., Murphy, E., Pope, A., Scott, D., Brodwin, M., Calzetti, D., Cesarsky, C., Charlot, S., Dole, H., Eisenhardt, P., Ferguson, H. C., Förster Schreiber, N., Frayer, D., Giavalisco, M., Huynh, M., Koekemoer, A. M., Papovich, C., Reddy, N., Surace, C., Teplitz, H., Yun, M. S., & Wilson, G. 2011, A&A, 533, A119

Juneau, S., Bournaud, F., Charlot, S., Daddi, E., Elbaz, D., Trump, J. R., Brinchmann, J., Dickinson, M., Duc, P.-A., Gobat, R., Jean-Baptiste, I., Le Floc'h, É., Lehnert, M. D., Pacifici, C., Pannella, M., & Schreiber, C. 2014, ApJ, 788, 88

Kauffmann, G., Heckman, T. M., Tremonti, C., Brinchmann, J., Charlot, S., White, S. D. M., Ridgway, S. E., Brinkmann, J., Fukugita, M., Hall, P. B., Ivezić, Ž., Richards, G. T., & Schneider, D. P. 2003, MNRAS, 346, 1055

Kewley, L. J., Dopita, M. A., Leitherer, C., Davé, R., Yuan, T., Allen, M., Groves, B., & Sutherland, R. 2013, ApJ, 774, 100

Kewley, L. J., Dopita, M. A., Sutherland, R. S., Heisler, C. A., & Trevena, J. 2001, ApJ, 556, 121

Meléndez, M., Heckman, T. M., Martínez-Paredes, M., Kraemer, S. B., & Mendoza, C. 2014, MNRAS, 443, 1358

Noeske, K. G., Weiner, B. J., Faber, S. M., Papovich, C., Koo, D. C., Somerville, R. S., Bundy, K., Conselice, C. J., Newman, J. A., Schiminovich, D., Le Floc'h, E., Coil, A. L., Rieke, G. H., Lotz, J. M., Primack, J. R., Barmby, P., Cooper, M. C., Davis, M., Ellis, R. S., Fazio, G. G., Guhathakurta, P., Huang, J., Kassin, S. A., Martin, D. C., Phillips, A. C., Rich, R. M., Small, T. A., Willmer, C. N. A., & Wilson, G. 2007, ApJ, 660, L43

Rieke, G. H., Alonso-Herrero, A., Weiner, B. J., Pérez-González, P. G., Blaylock, M., Donley, J. L., & Marcillac, D. 2009, ApJ, 692, 556

Sanders, D. B., Mazzarella, J. M., Kim, D., Surace, J. A., & Soifer, B. T. 2003, AJ, 126, 1607

Shapley, A. E., Reddy, N. A., Kriek, M., Freeman, W. R., Sanders, R. L., Siana, B., Coil, A. L., Mobasher, B., Shivaei, I., Price, S. H., & de Groot, L. 2015, ApJ, 801, 88

Steidel, C. C., Rudie, G. C., Strom, A. L., Pettini, M., Reddy, N. A., Shapley, A. E., Trainor, R. F., Erb, D. K., Turner, M. L., Konidaris, N. P., Kulas, K. R., Mace, G., Matthews, K., & McLean, I. S. 2014, ApJ, 795, 165

Strom, A. L., Steidel, C. C., Rudie, G. C., Trainor, R. F., Pettini, M., & Reddy, N. A. 2017, ApJ, 836, 164

Appendix A

The 3–500 μm Spectral Energy Distribution Library for the Full GOALS Sample

In this appendix I present the individual spectral energy distributions for each of the 201 systems in the GOALS sample (in ascending right ascension) that were used to construct the median SEDs described in Section 3.4. Briefly, the *Spitzer* IRAC bands at 3.6, 4.5, 5.8, and 8 μm were obtained from the companion *Spitzer*-GOALS atlas paper (Mazzarella et al. in prep.), while the mid-infrared 12 and 22 μm photometry were obtained from the publicly available AllWISE catalog. Furthermore the *IRAS* photometry at 12, 25, 60, and 100 μm were obtained from Sanders et al. (2003), while the *Herschel* data at 70, 100, 160, 250, 350, and 500 μm are from Chu et al. (2017). In addition for completeness, I include available *Spitzer* Infrared Spectrograph (IRS, Houck et al. 2004) mid-infrared spectroscopy between 5–35 μm for the majority of the sample, which is described in Stierwalt et al. (2013). Together these data represent the most complete view of the nearest luminous infrared galaxies.

Because the mid-infrared spectra were taken in long slit mode on the nucleus of each galaxy and thus did not cover the entire galaxy, the spectra were corrected by adding a constant offset to the entire spectrum. This offset was computed by comparing the mid-infrared 22 and 25 μm broadband photometry points to the corresponding fluxes in the IRS data. The spectra were then offset such that the broadband photometry and spectra match.

Although it is also theoretically possible to use the 8 and 12 μm photometry, in practice this is complicated by the fact that both of these wavelengths bracket the deep 9.7 μm silicate absorption feature, and would also include complex polycyclic aromatic hydrocarbon (PAH) emission lines. The strengths of these spectral features can vary spatially over the galaxy, thus making any scaling of the spectra very complex.

Furthermore because there is a small fraction of galaxies ($\sim$ 17%) that do not have *WISE* 12 μm measurements, I use the *IRAS* 12 μm fluxes in its place which are represented by upside down triangles in the SED library. Because the *IRAS* 12 μm filter is significantly wider than the corresponding *WISE* filter (see Figure 3.1), it tends to overestimate the true *WISE* flux, however it is still included for completeness. Finally we do not include photometric error bars on the four *Spitzer* IRAC points because they were not available at this time.

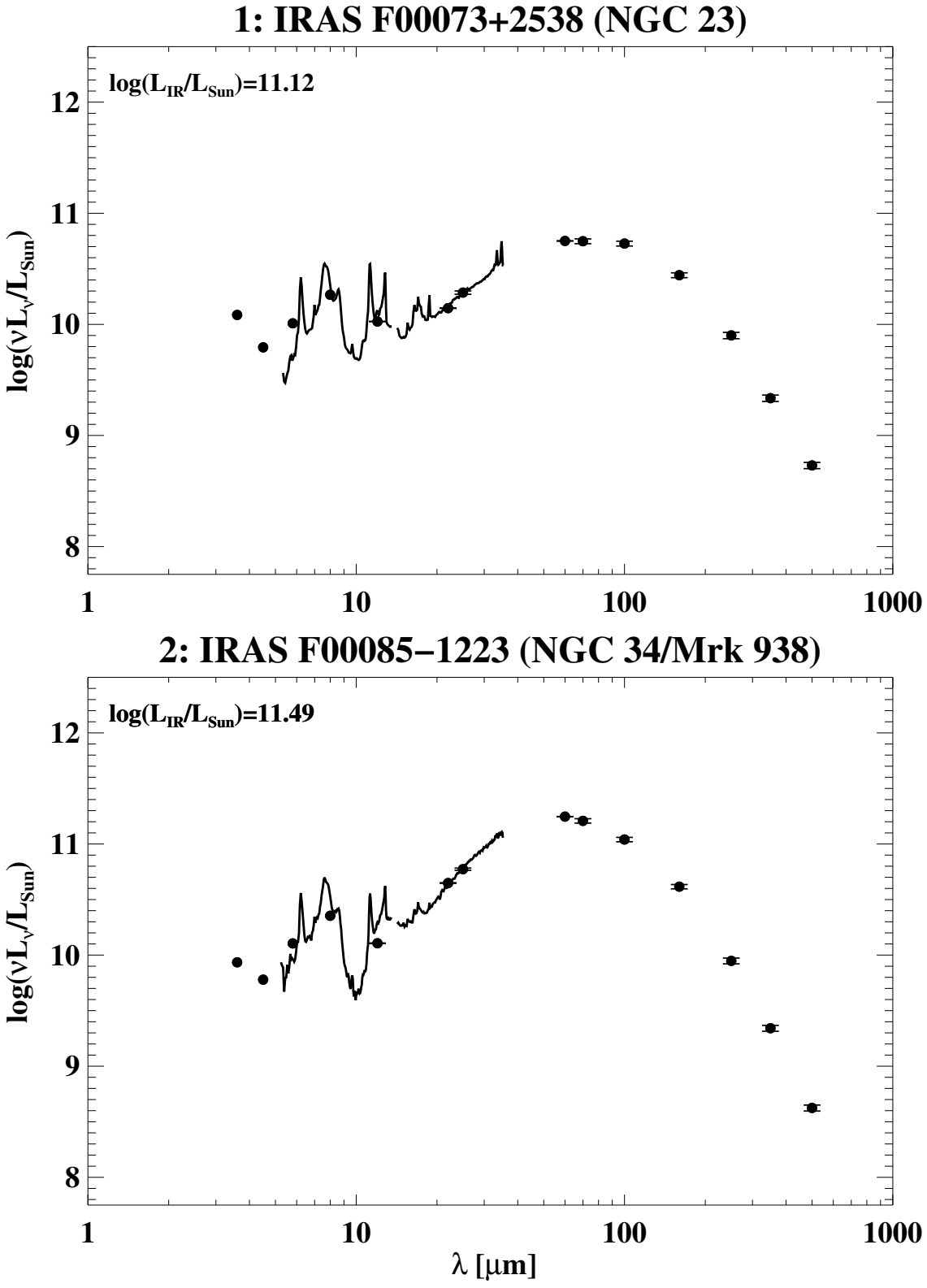

Figure A.1 The 3–500 μm spectral energy distribution library for the GOALS sample.

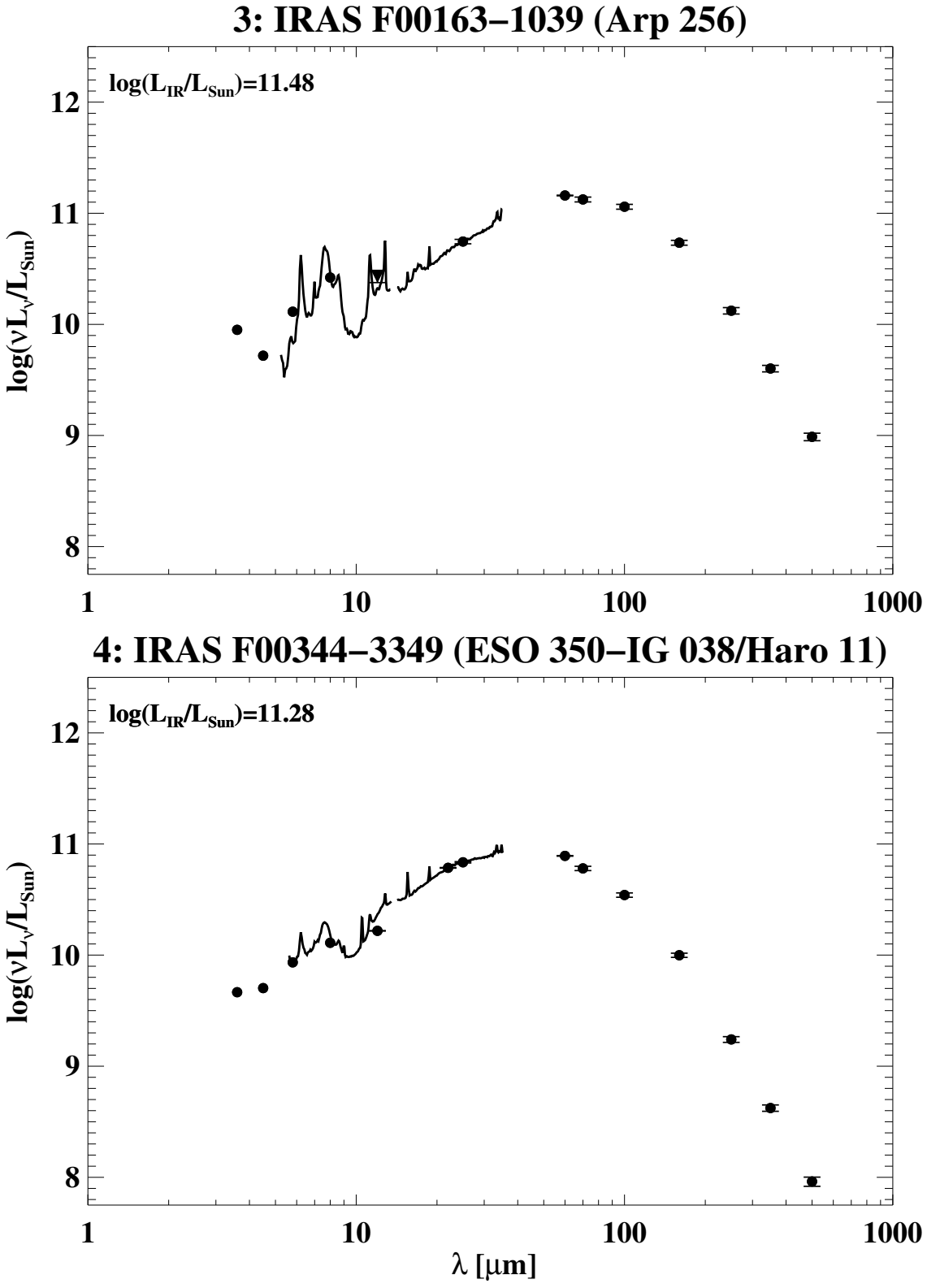

Figure A.1 continued (page 2 of 101).

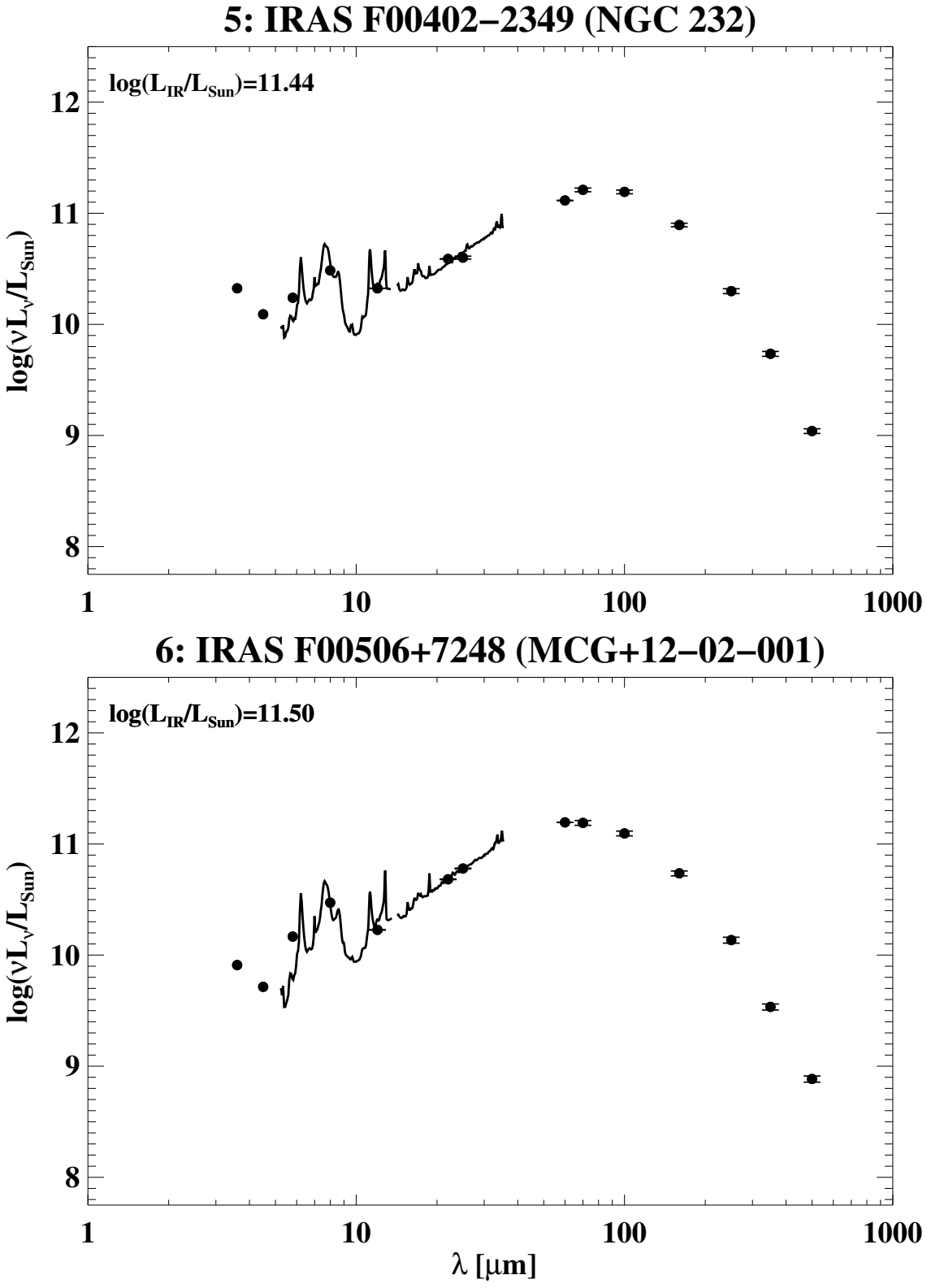

Figure A.1 continued (page 3 of 101).

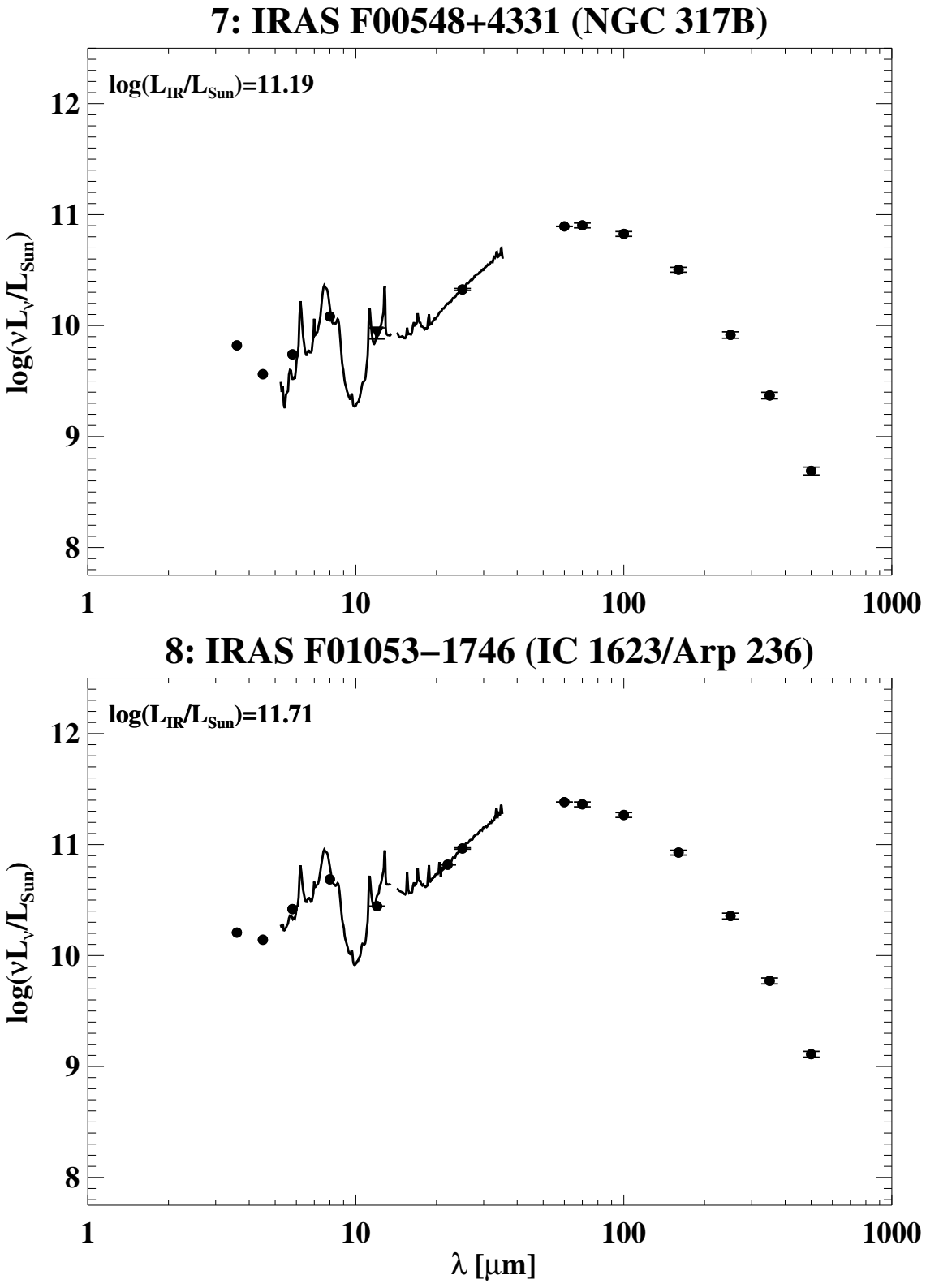

Figure A.1 continued (page 4 of 101).

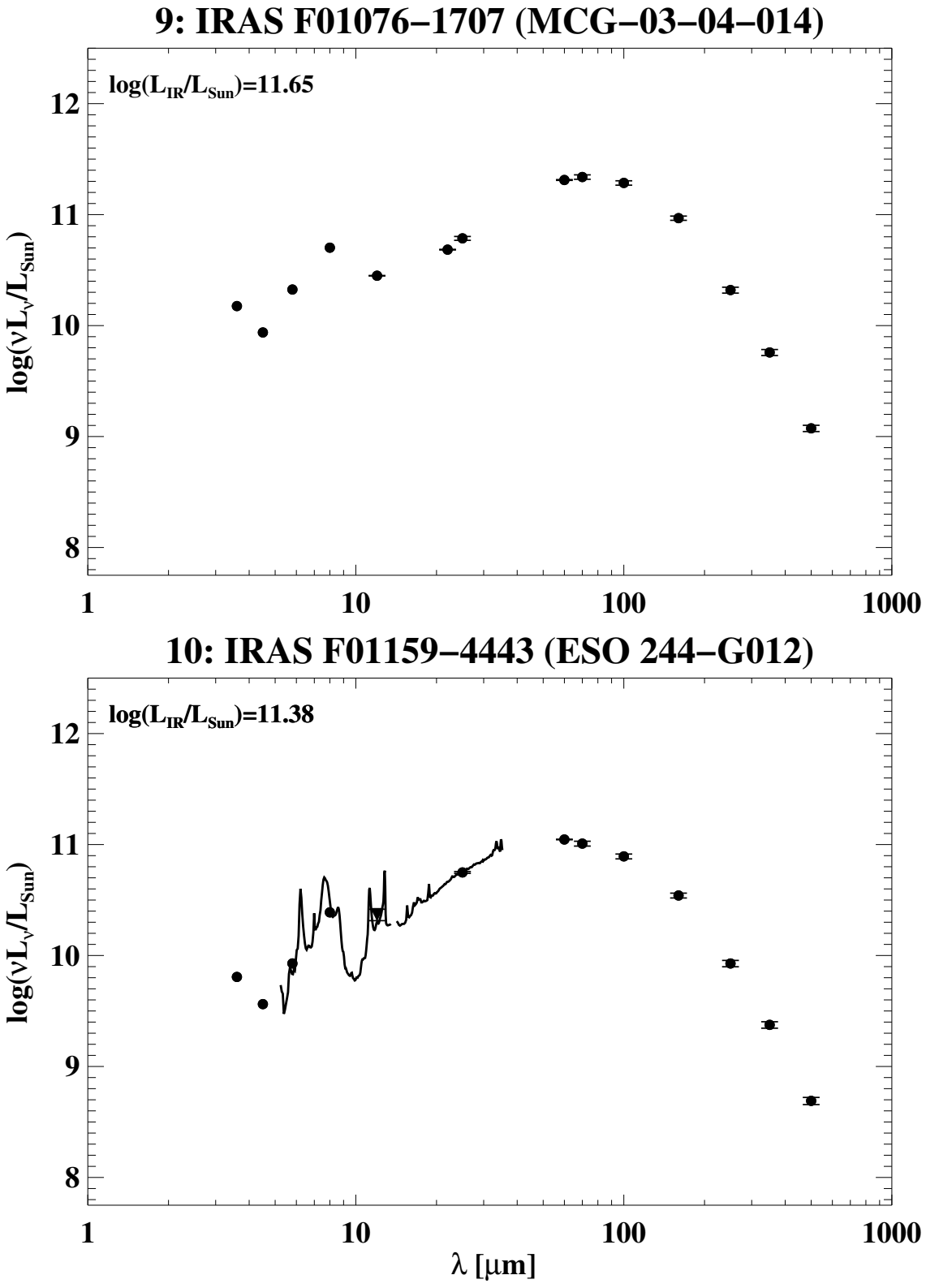

Figure A.1 continued (page 5 of 101).

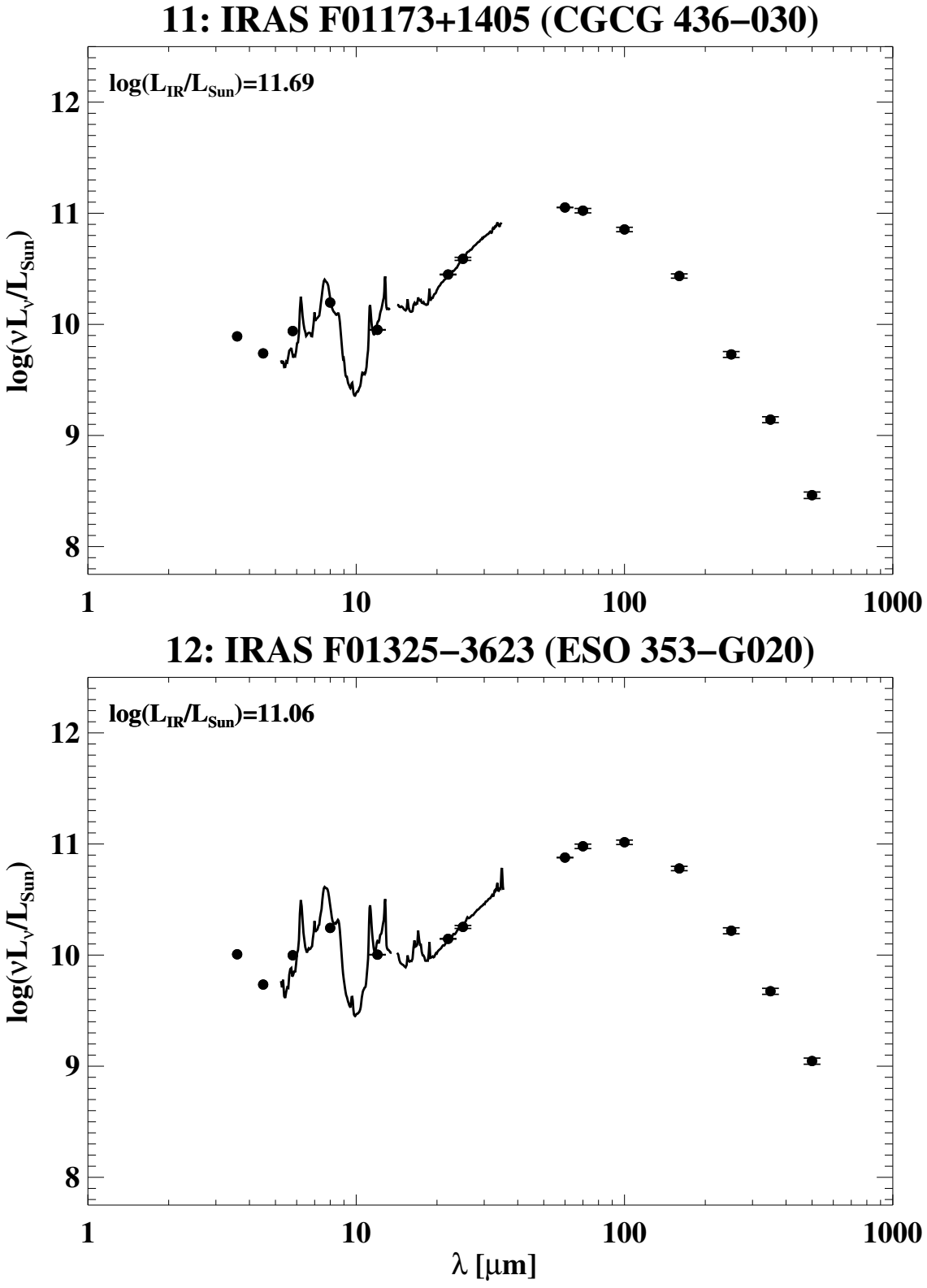

Figure A.1 continued (page 6 of 101).

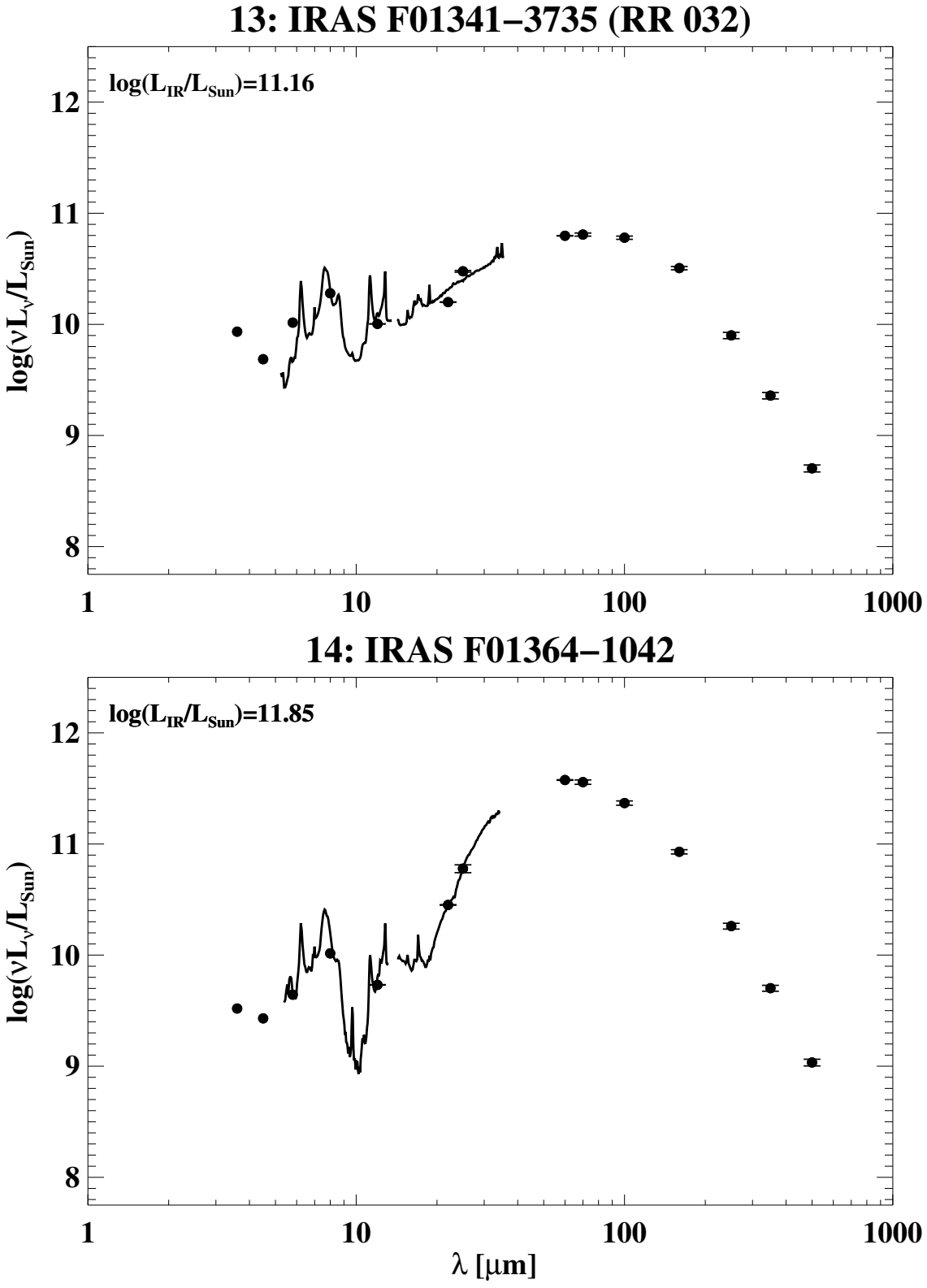

Figure A.1 continued (page 7 of 101).

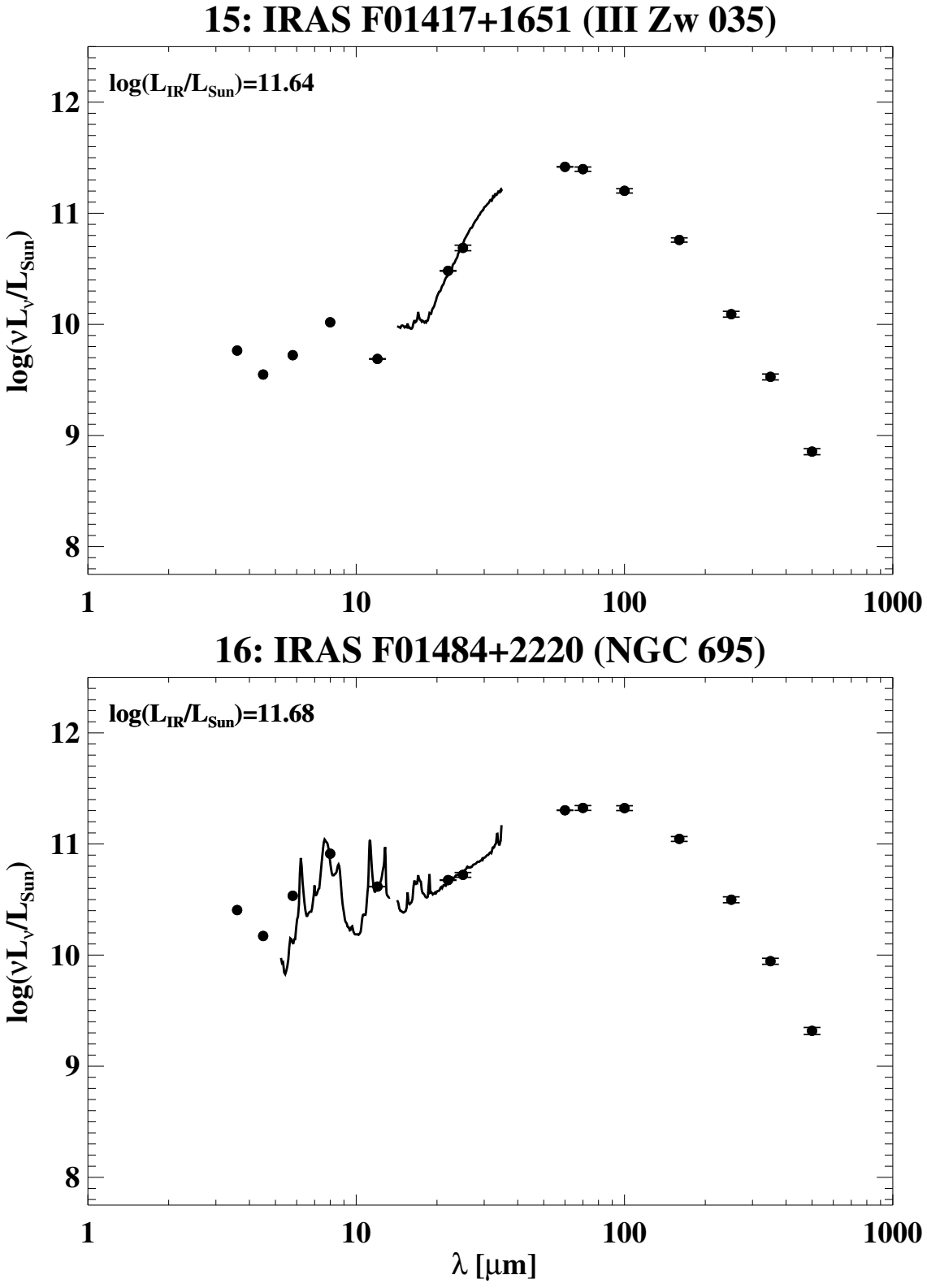

Figure A.1 continued (page 8 of 101).

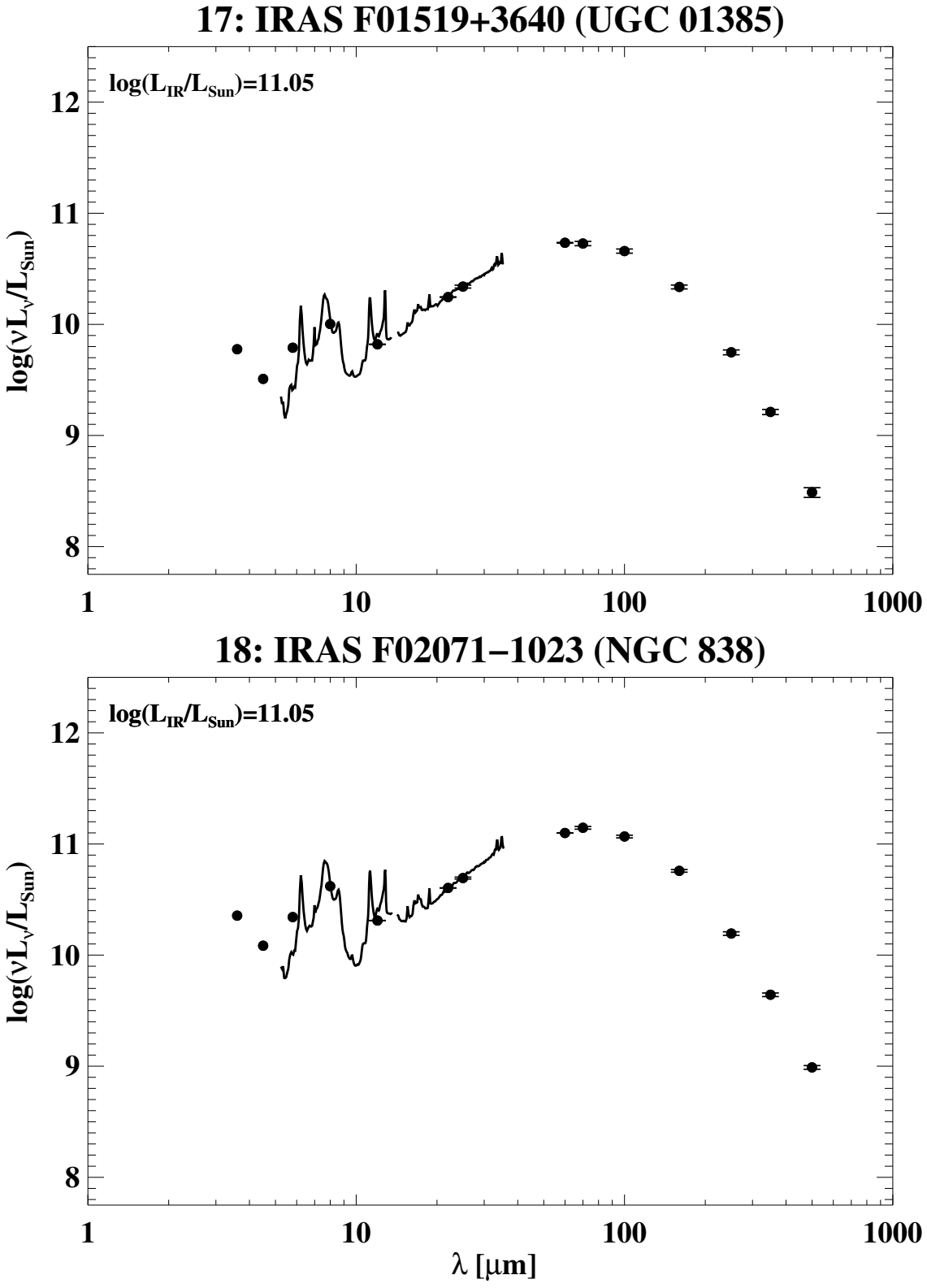

Figure A.1 continued (page 9 of 101).

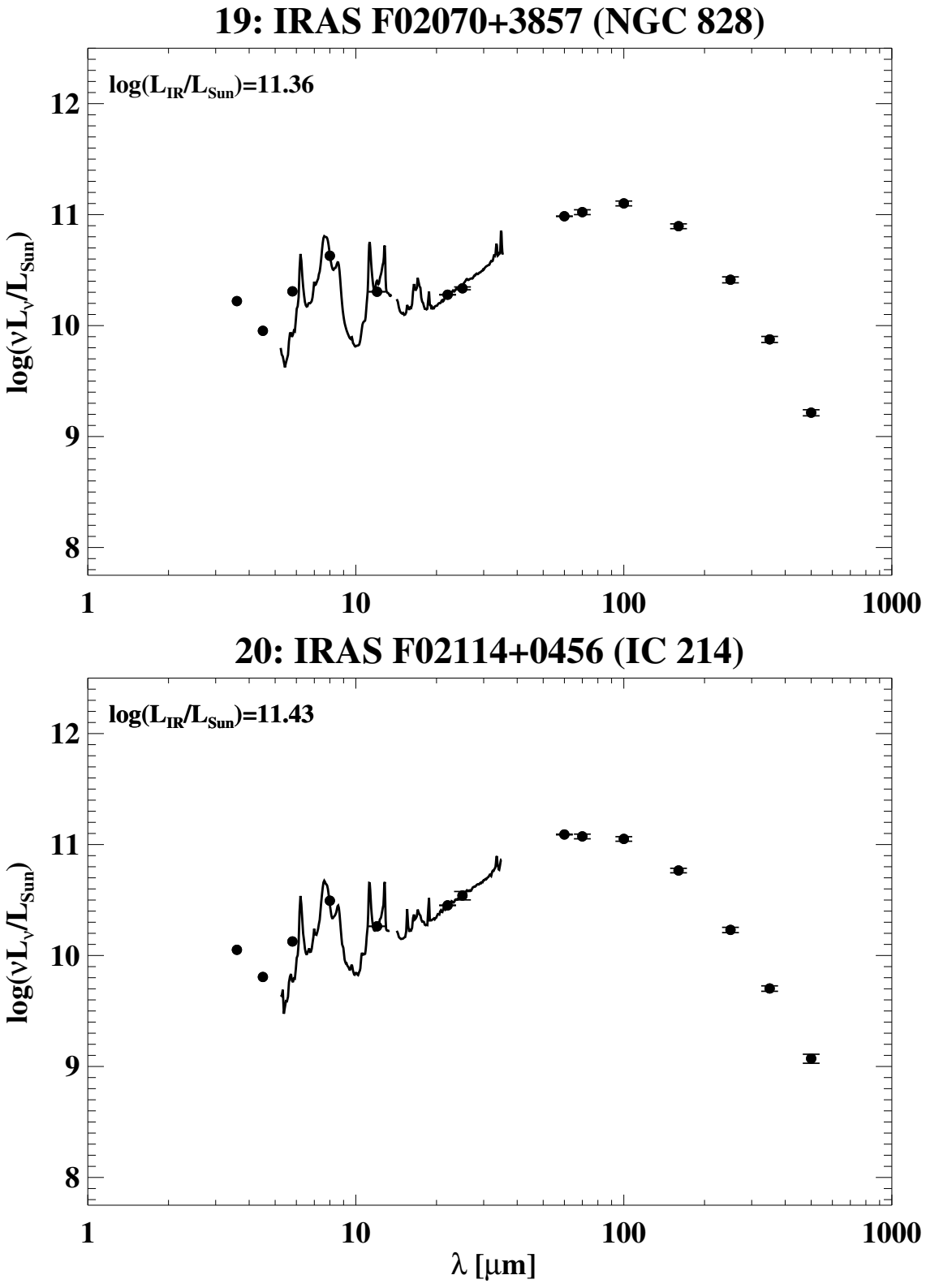

Figure A.1 continued (page 10 of 101).

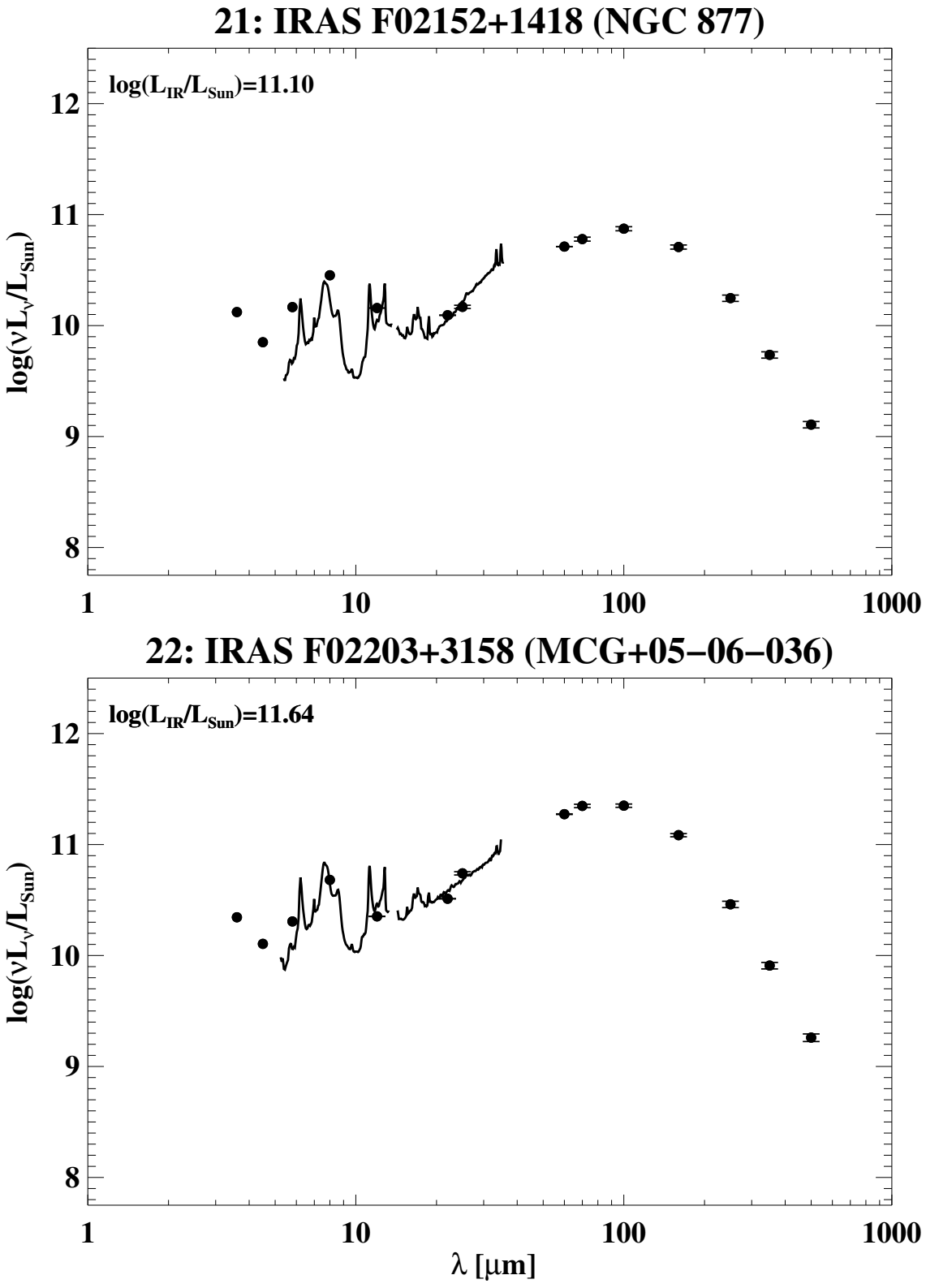

Figure A.1 continued (page 11 of 101).

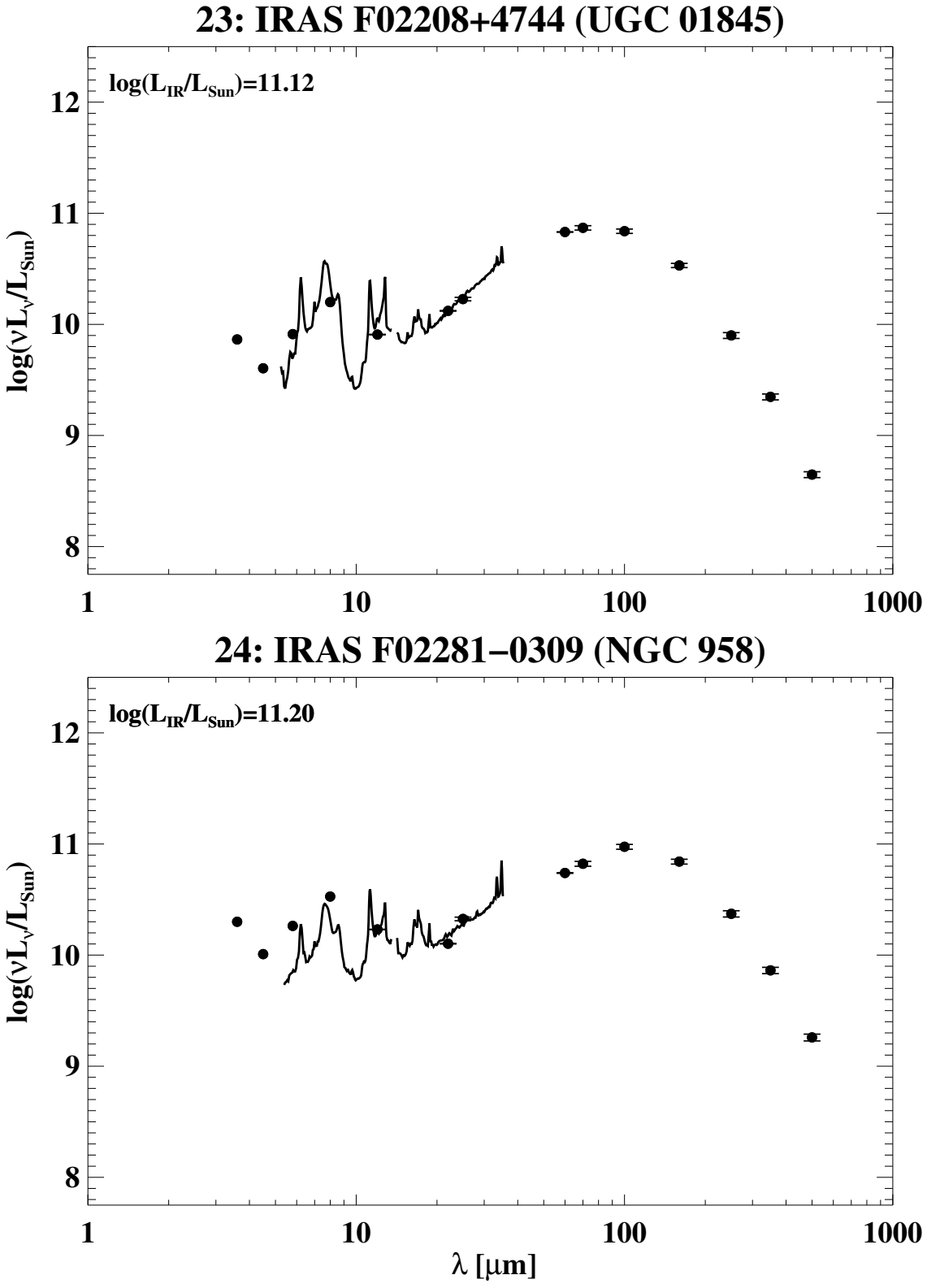

Figure A.1 continued (page 12 of 101).

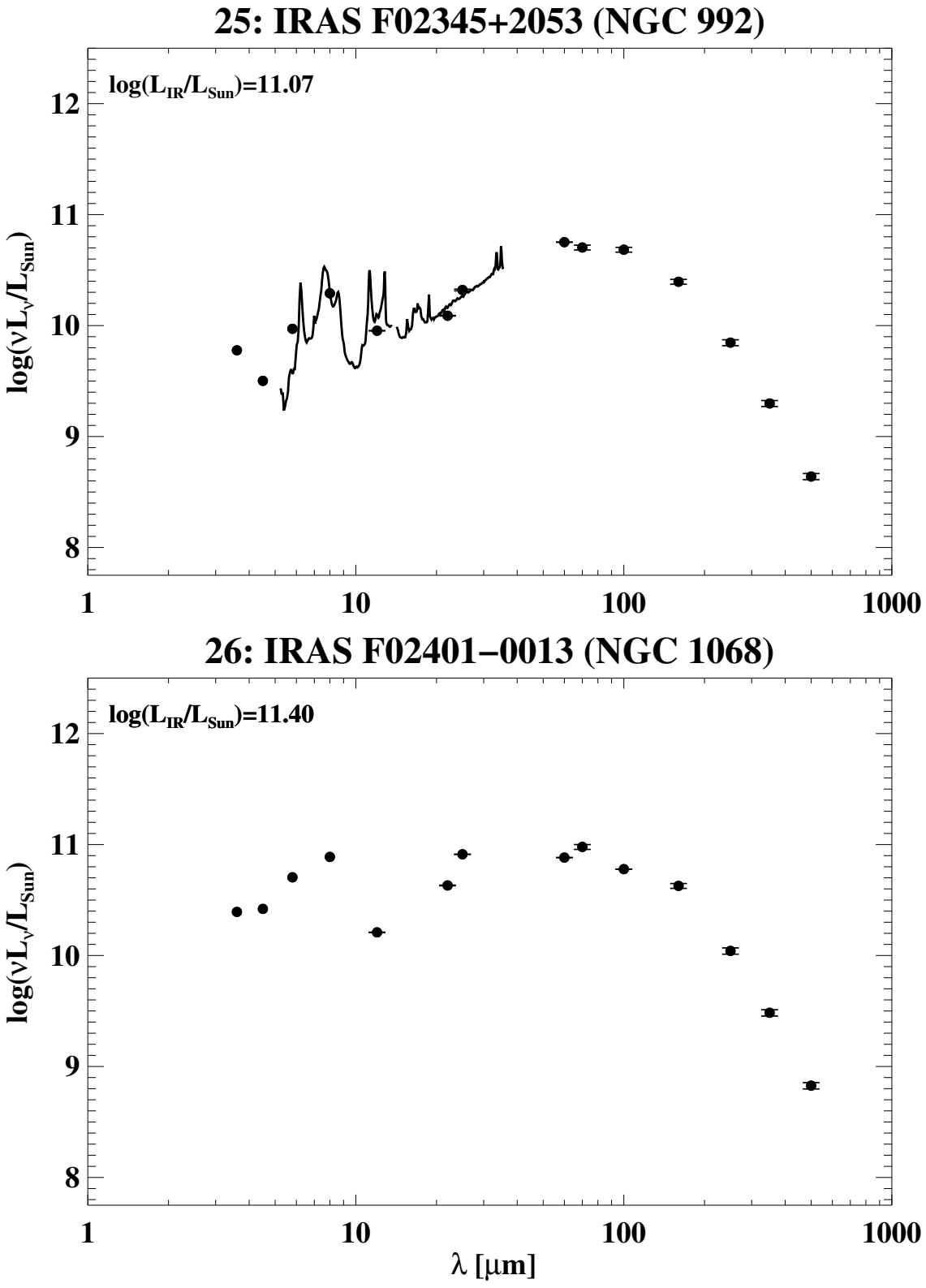

Figure A.1 continued (page 13 of 101).

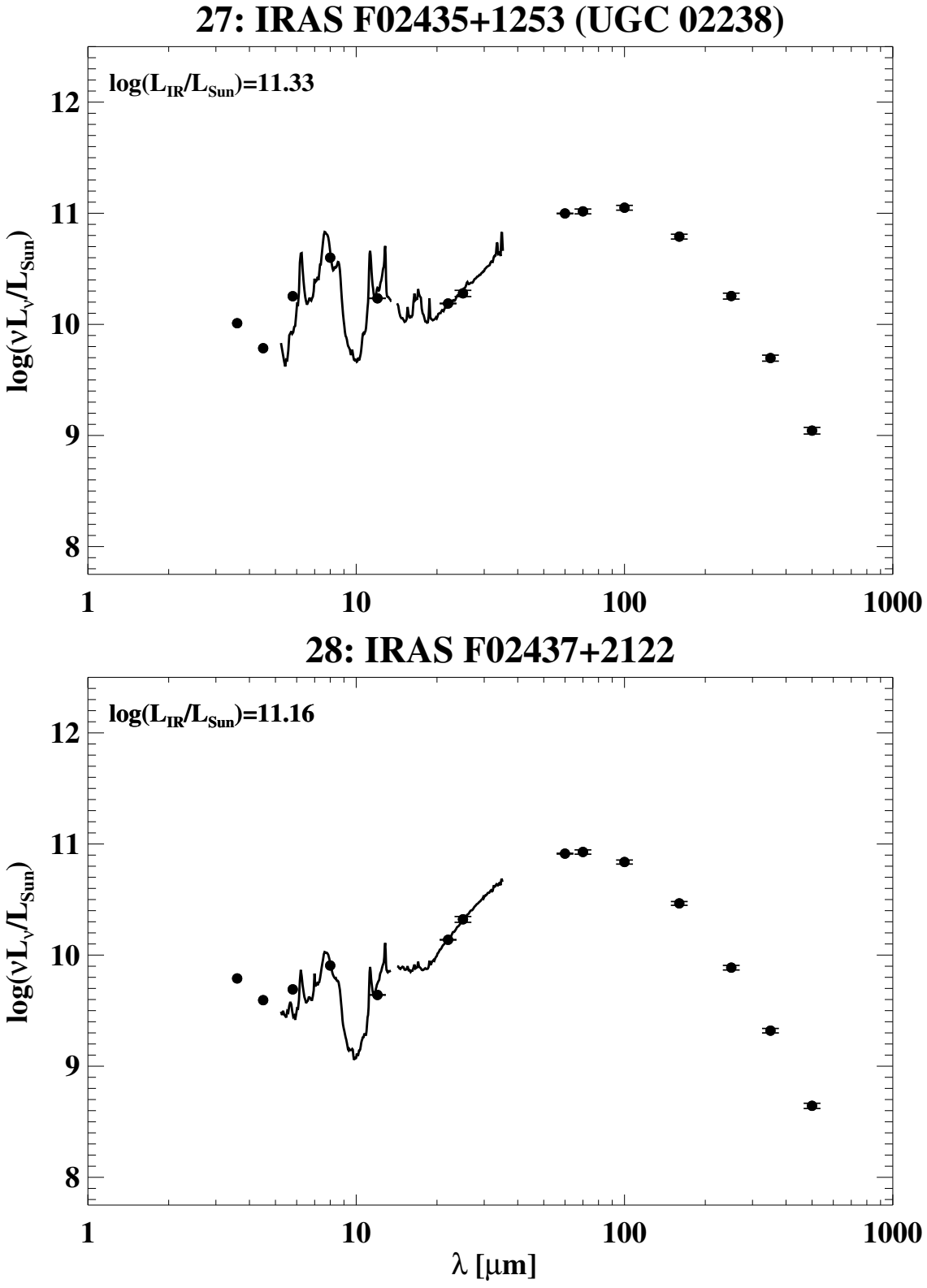

Figure A.1 continued (page 14 of 101).

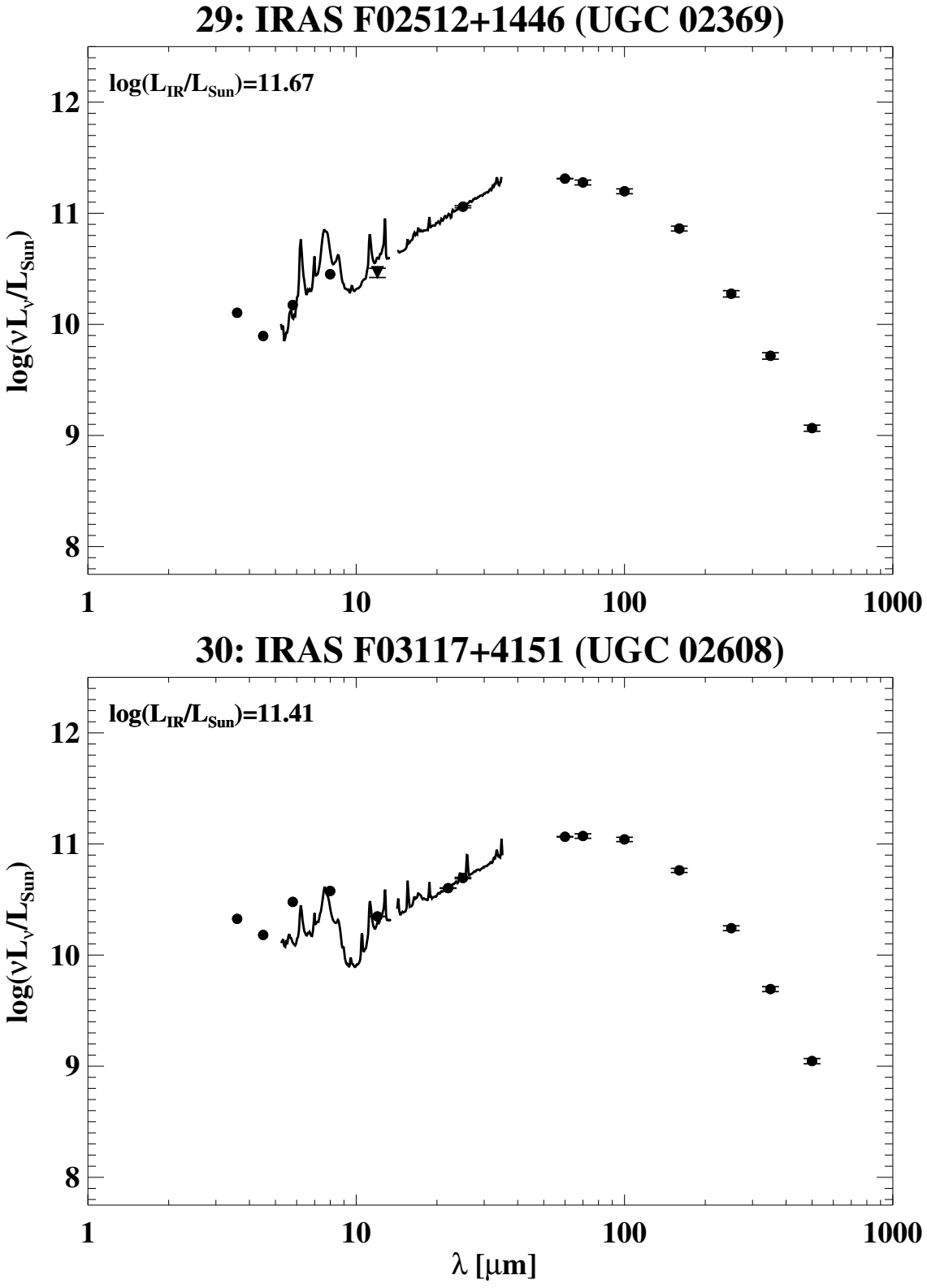

Figure A.1 continued (page 15 of 101).

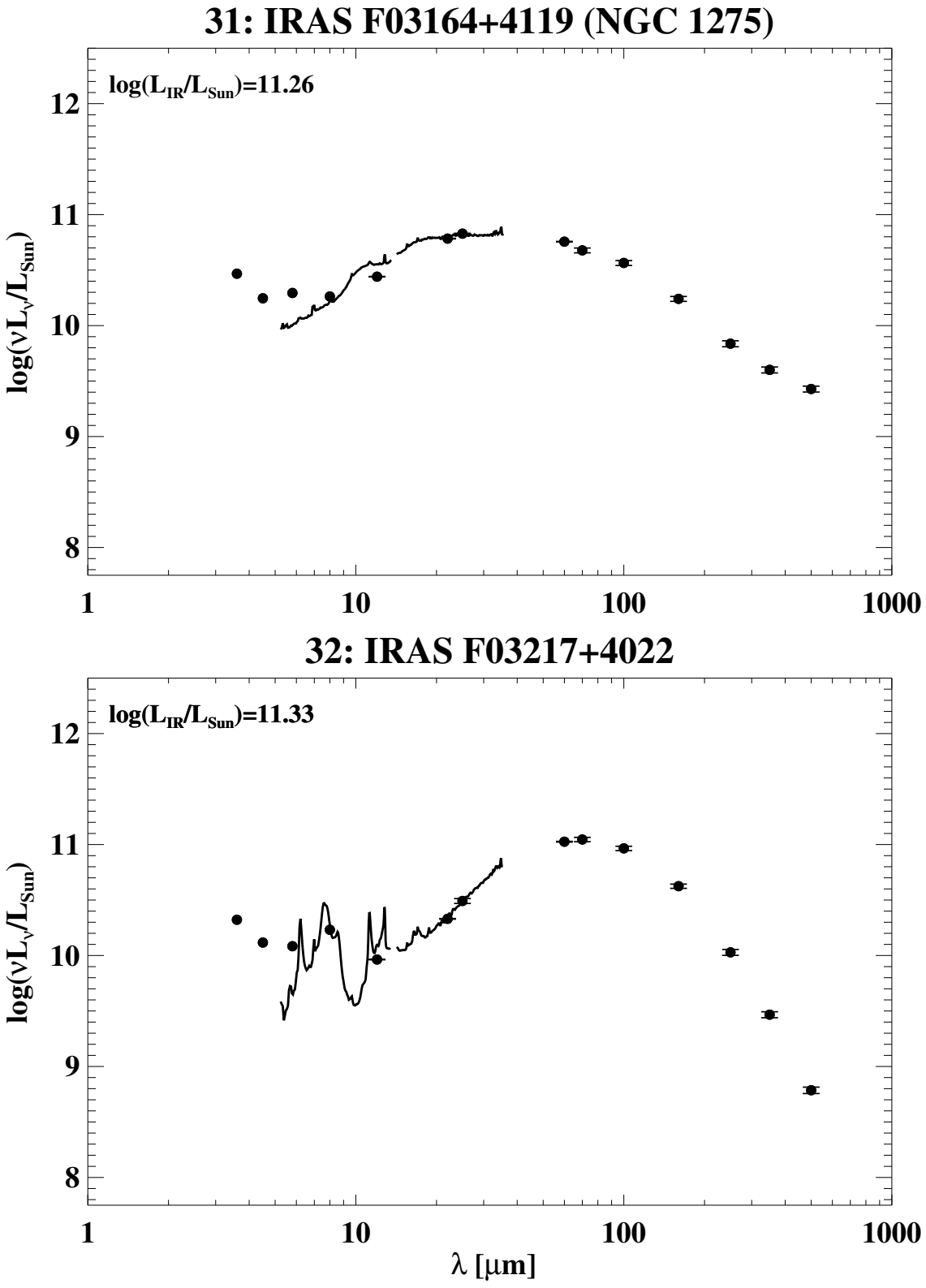

Figure A.1 continued (page 16 of 101).

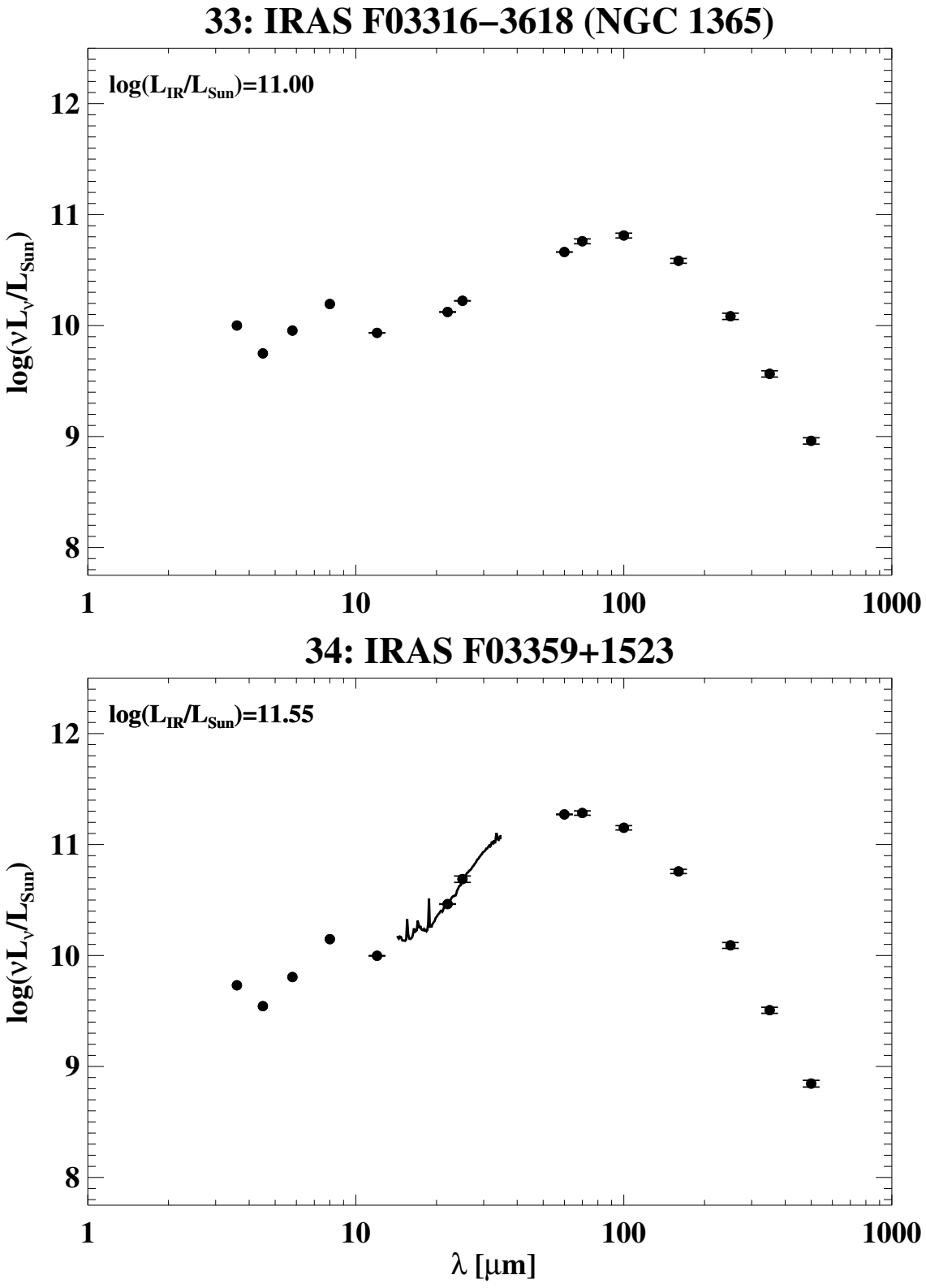

Figure A.1 continued (page 17 of 101).

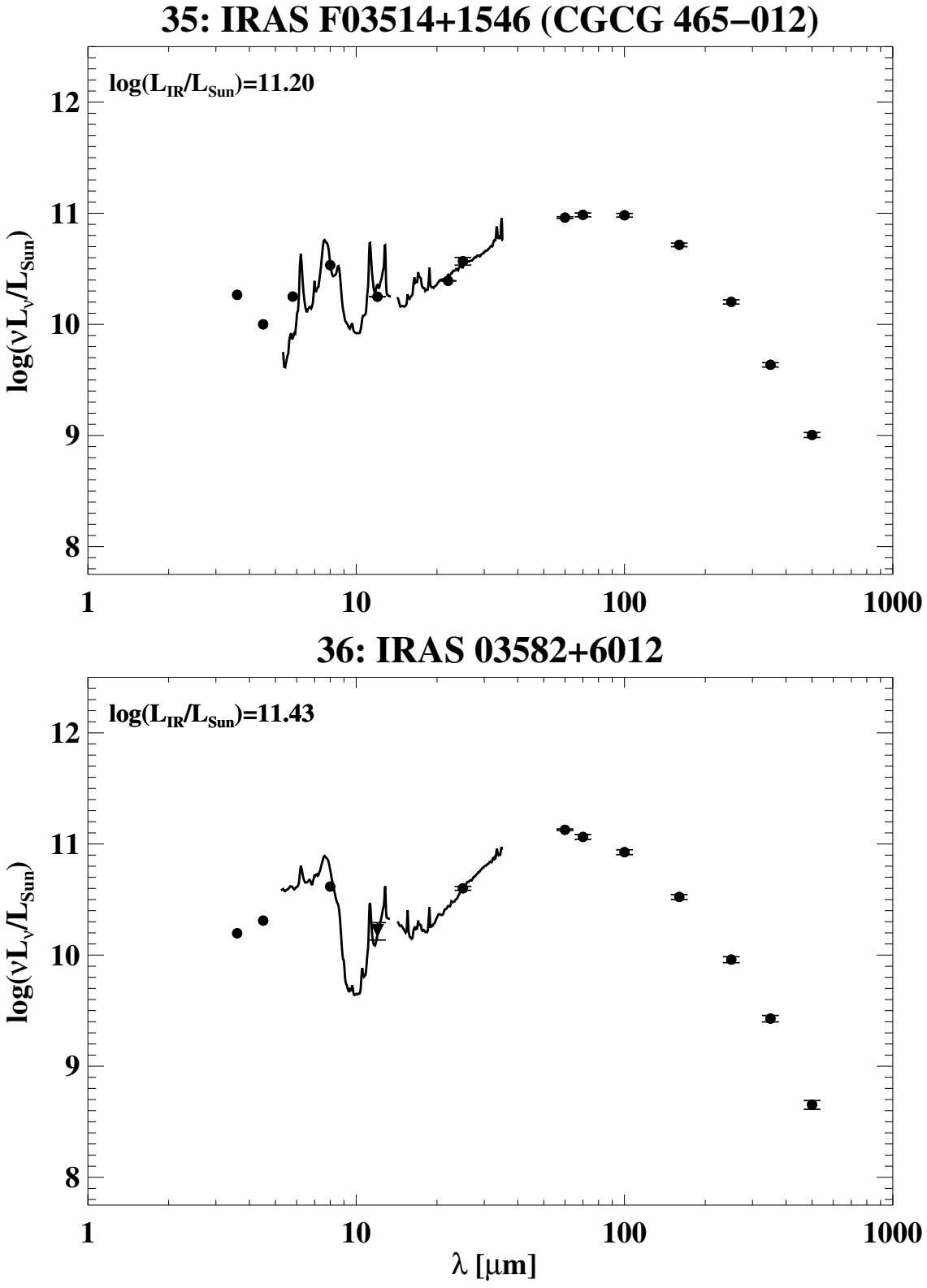

Figure A.1 continued (page 18 of 101).

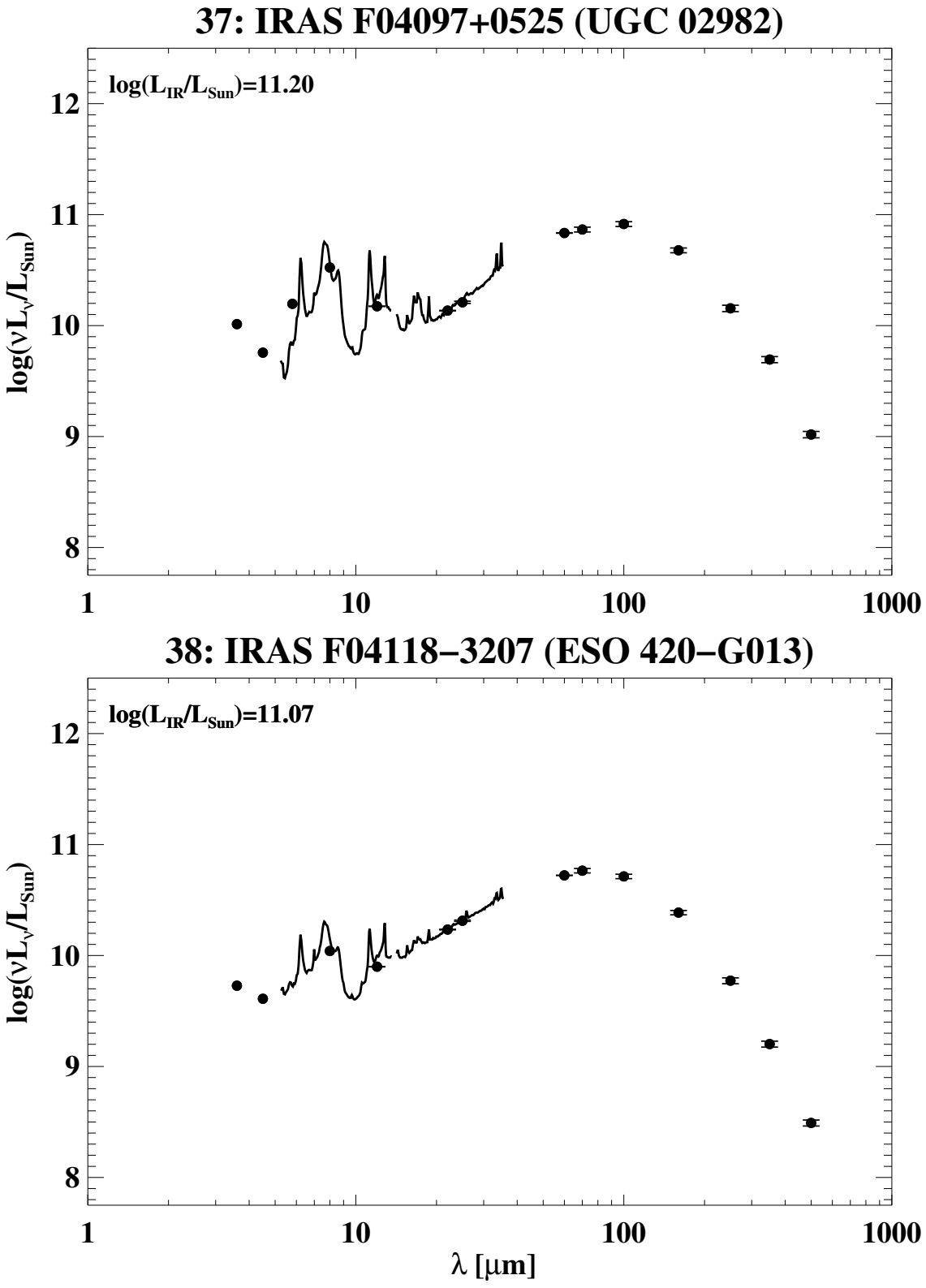

Figure A.1 continued (page 19 of 101).

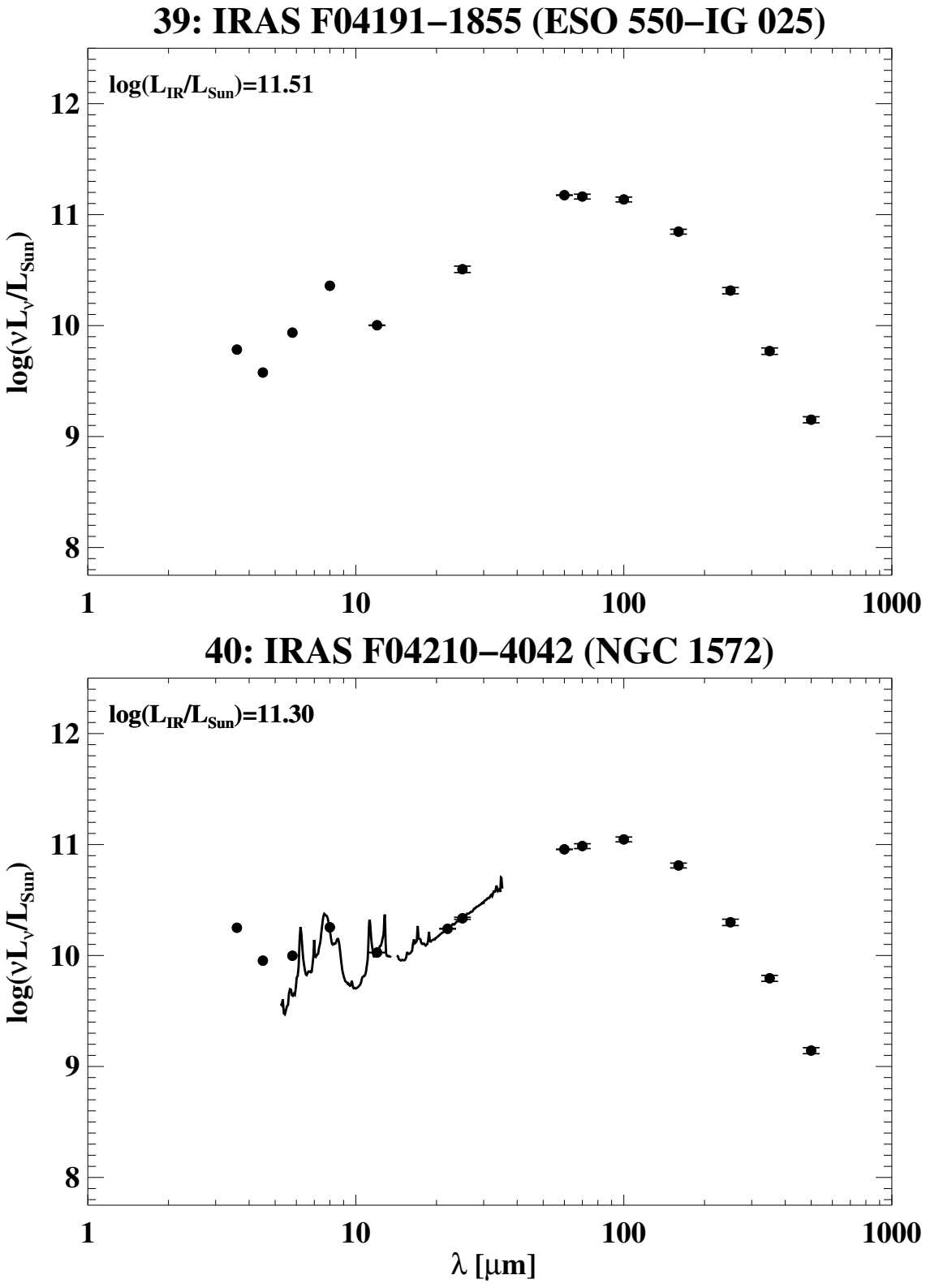

Figure A.1 continued (page 20 of 101).

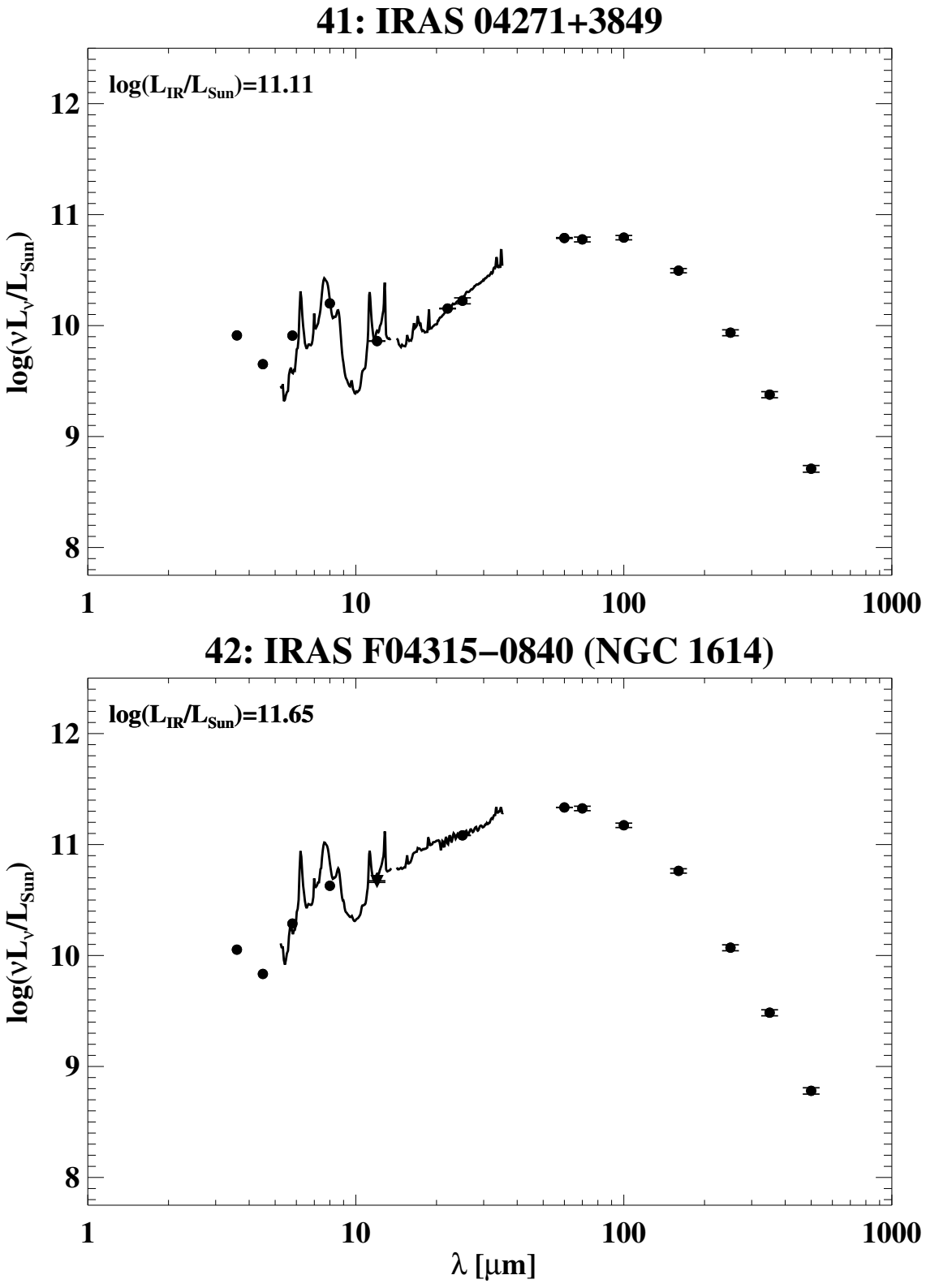

Figure A.1 continued (page 21 of 101).

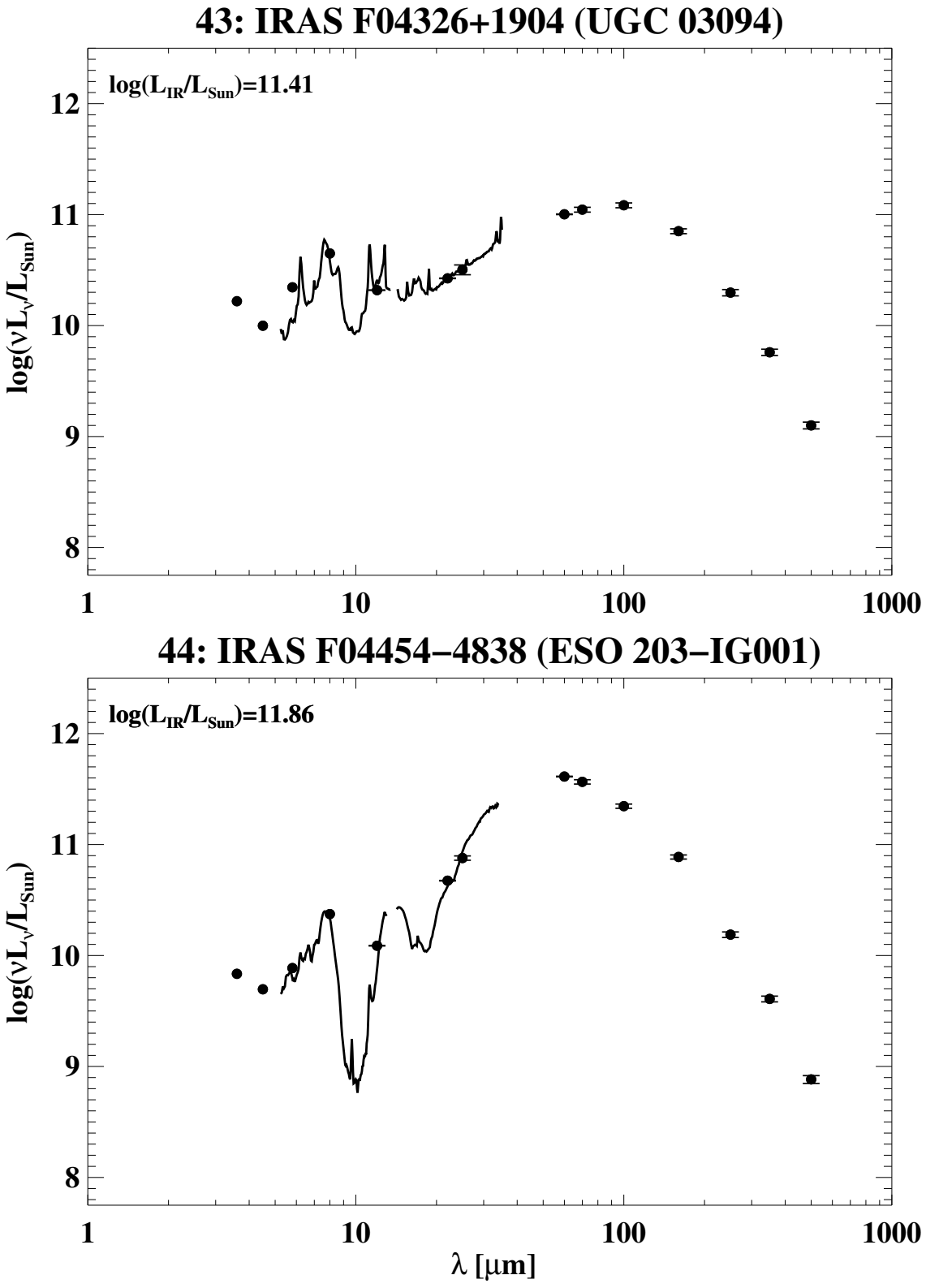

Figure A.1 continued (page 22 of 101).

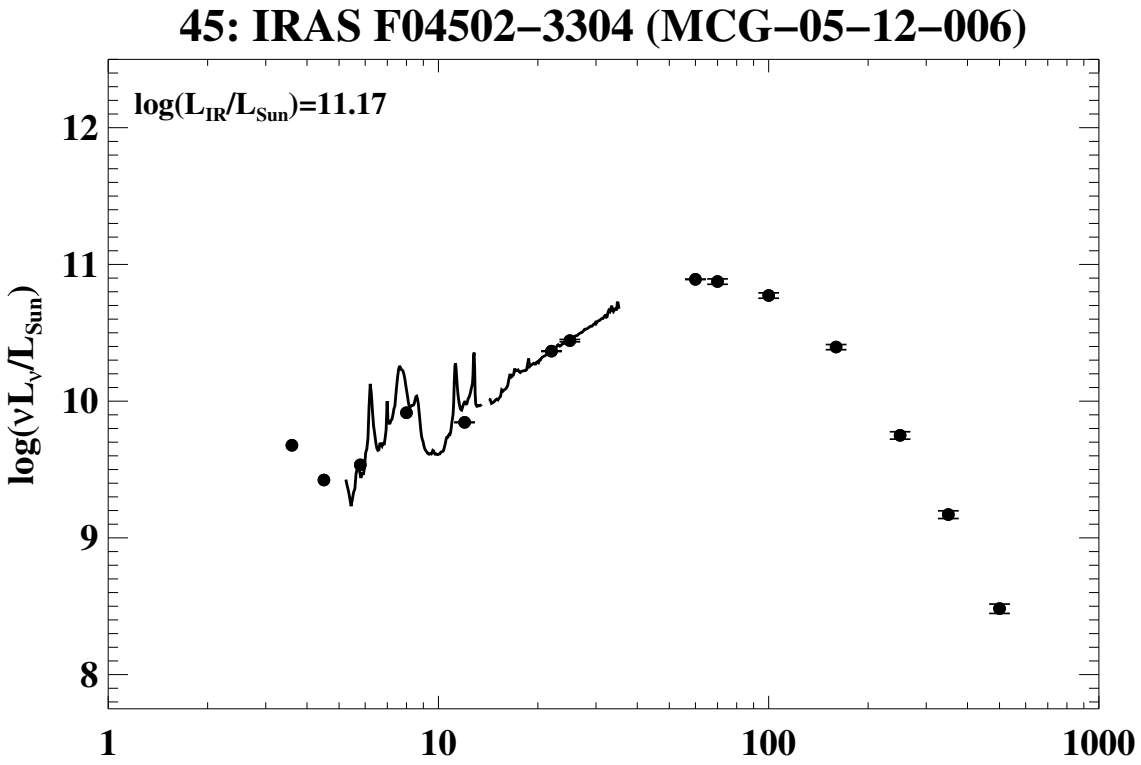

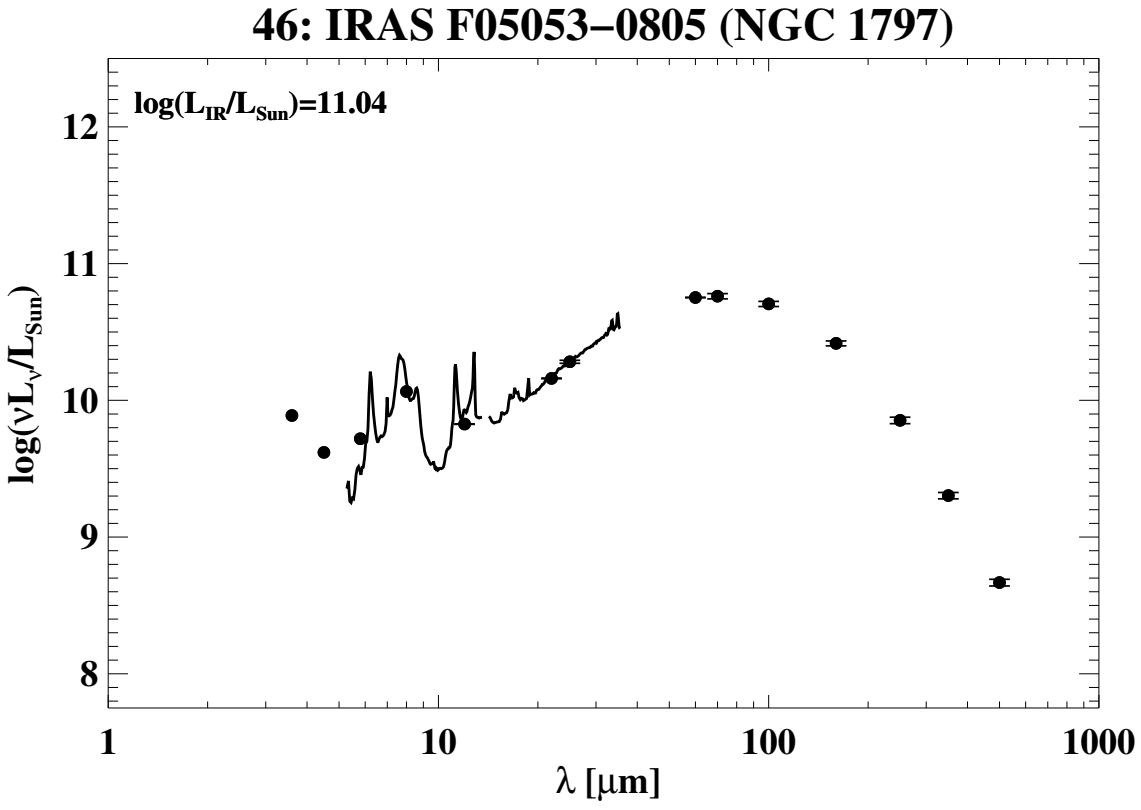

Figure A.1 continued (page 23 of 101).

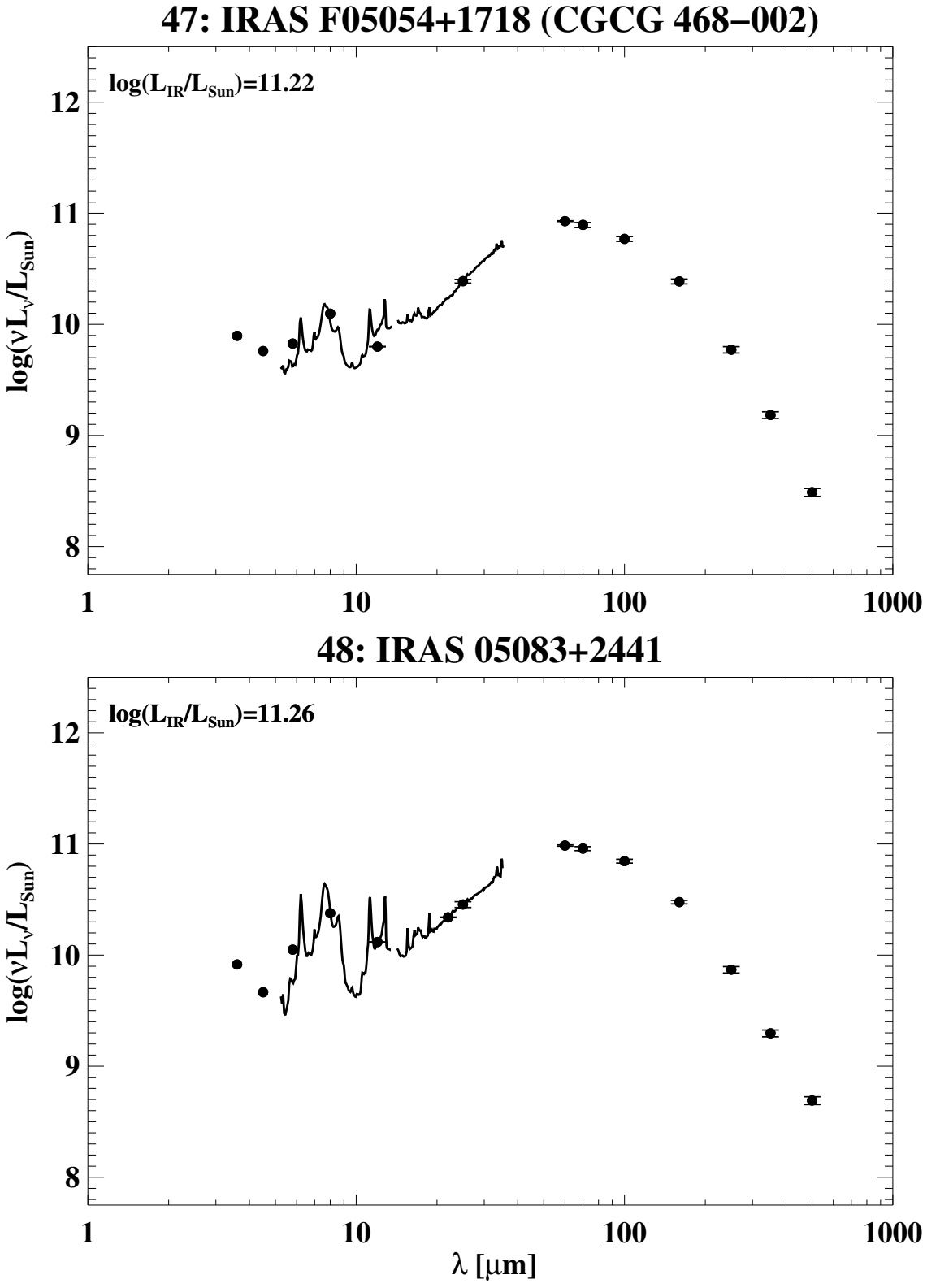

Figure A.1 continued (page 24 of 101).

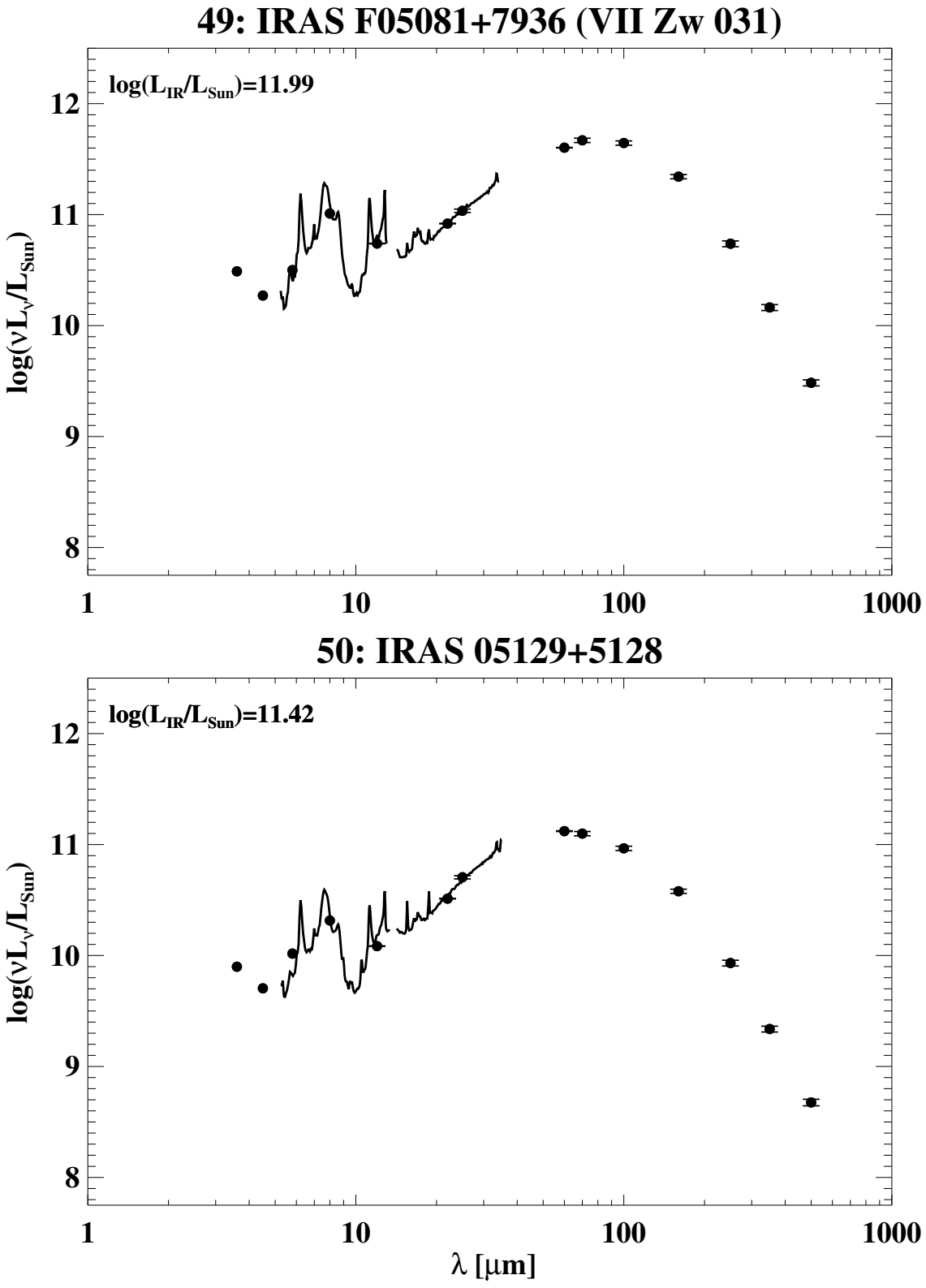

Figure A.1 continued (page 25 of 101).

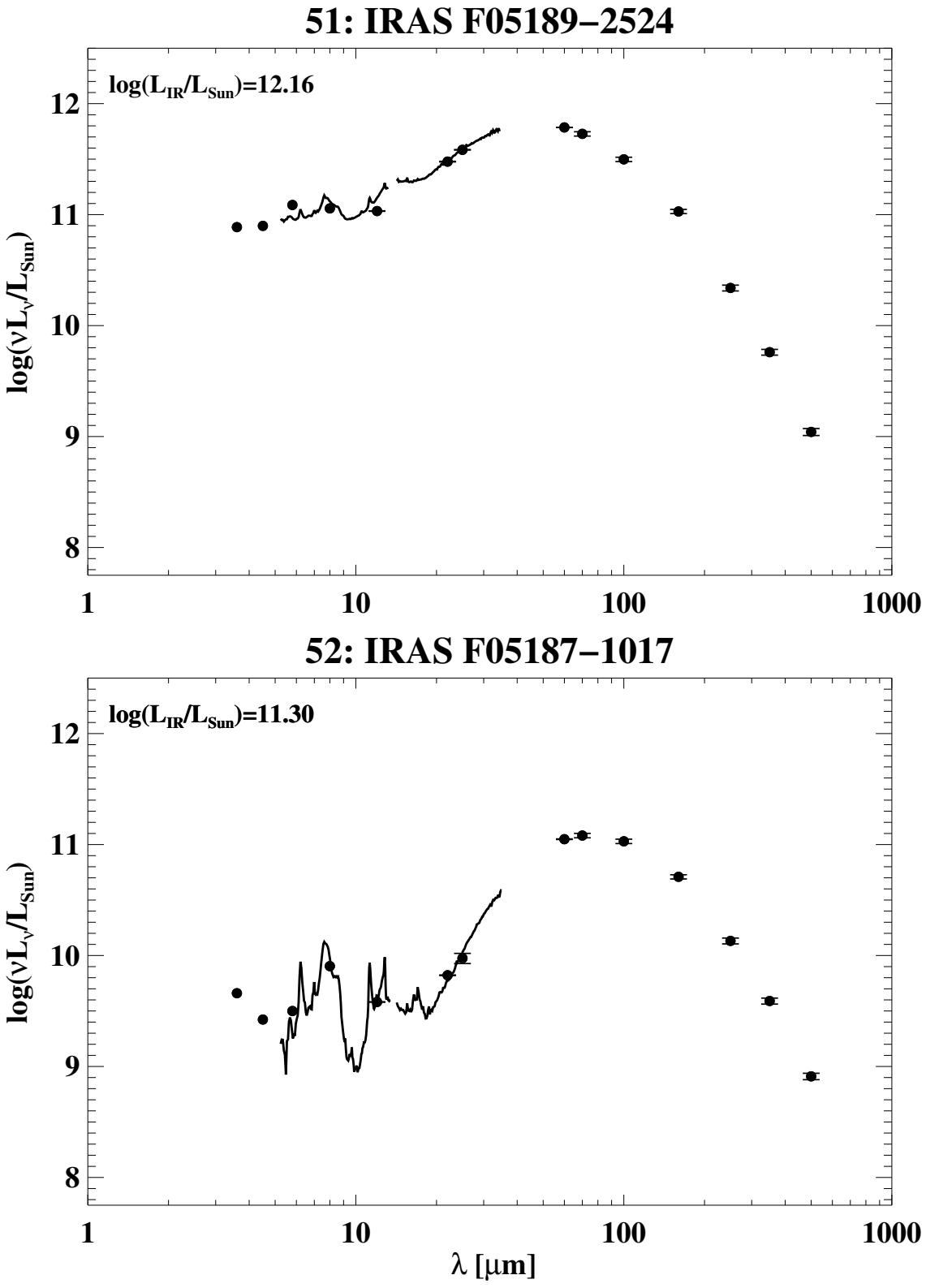

Figure A.1 continued (page 26 of 101).

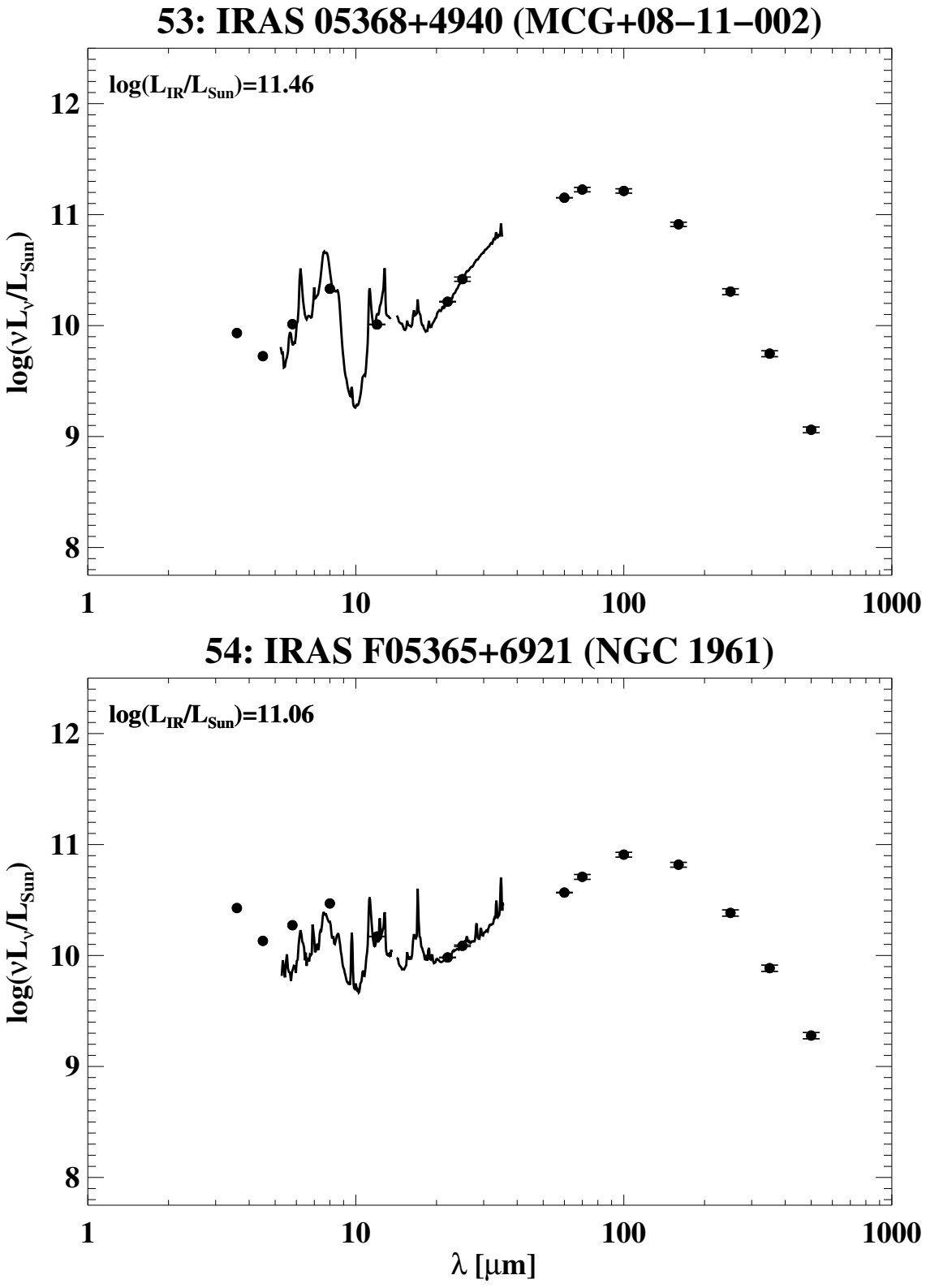

Figure A.1 continued (page 27 of 101).

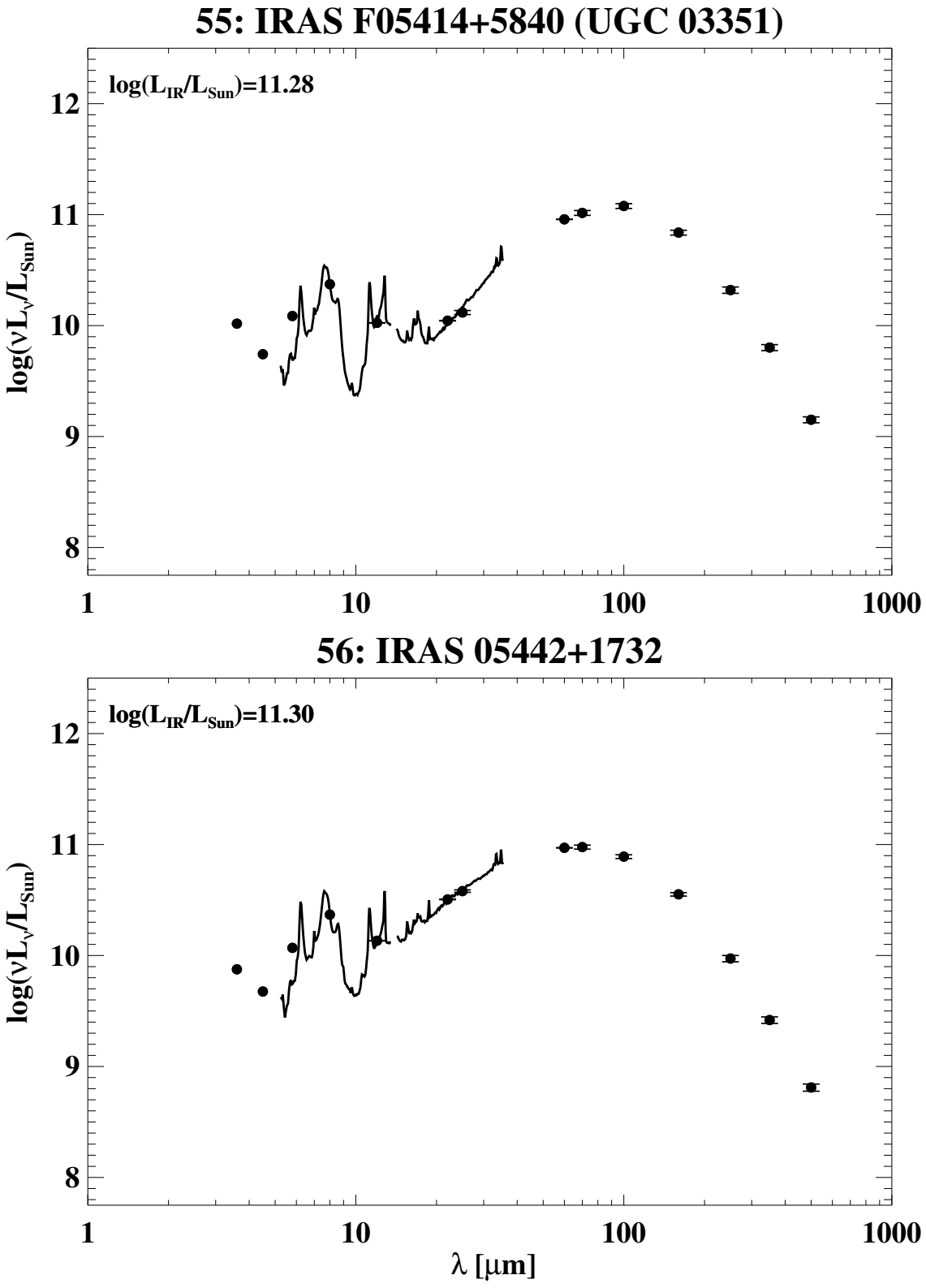

Figure A.1 continued (page 28 of 101).

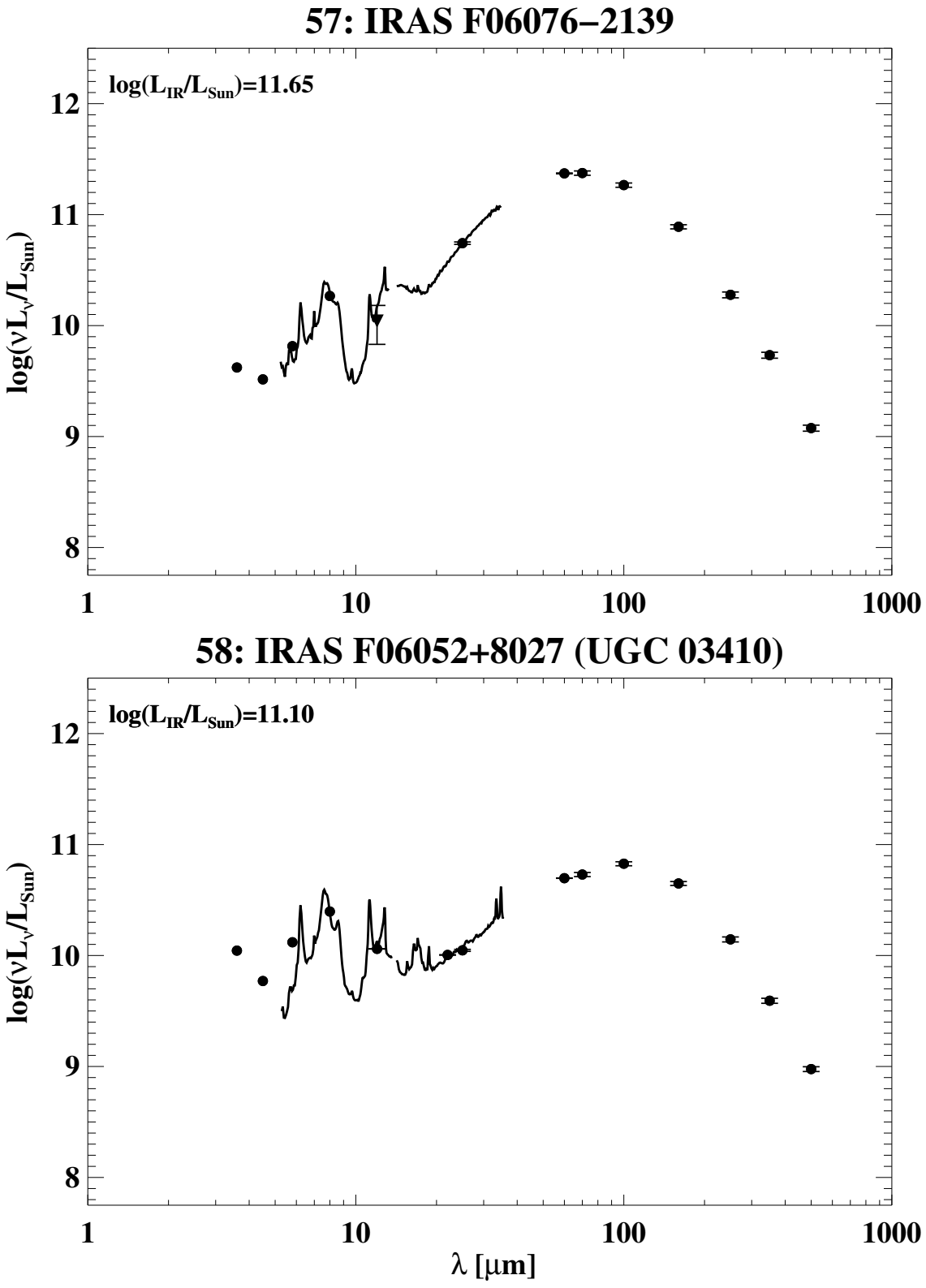

Figure A.1 continued (page 29 of 101).

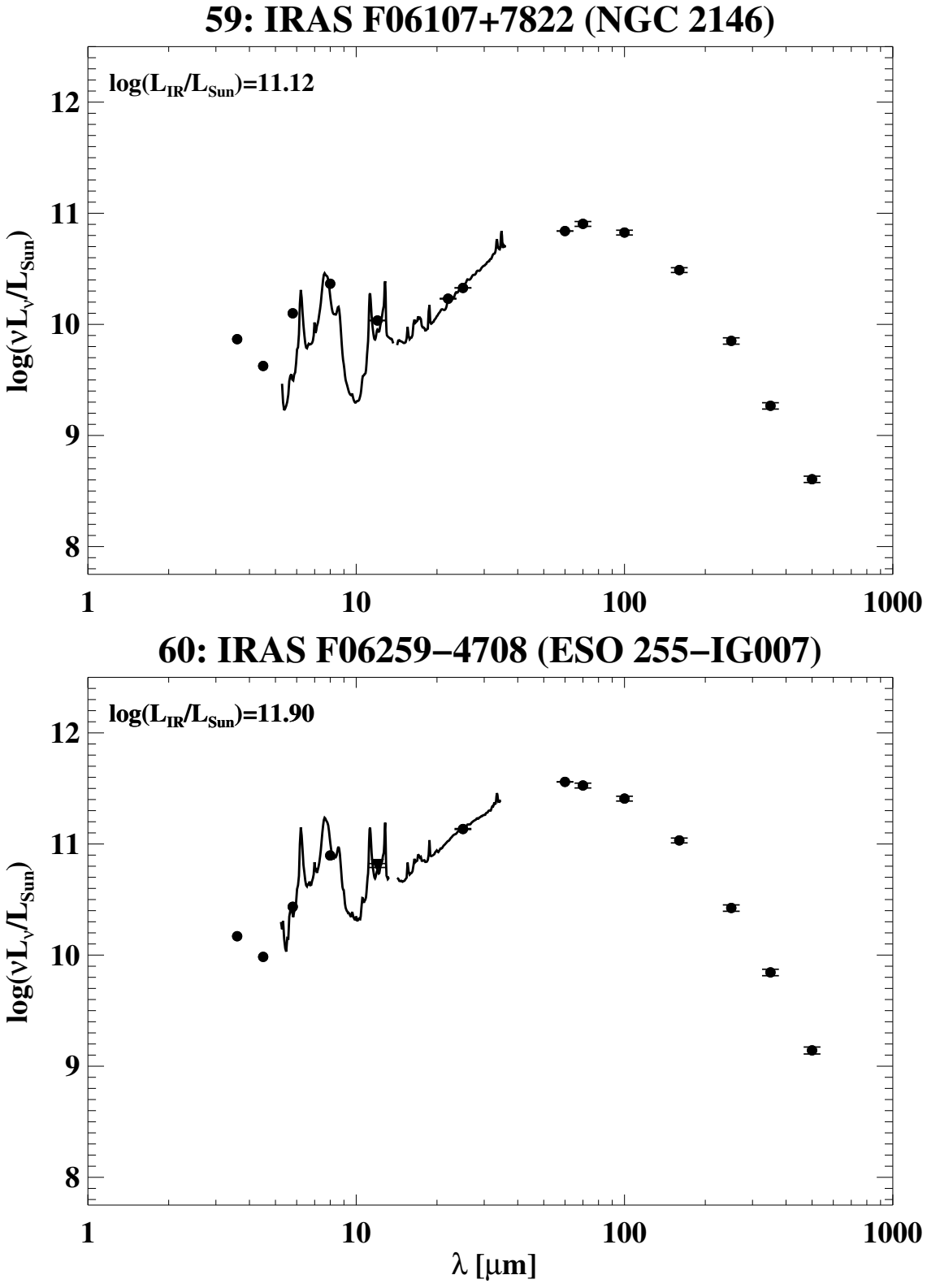

Figure A.1 continued (page 30 of 101).

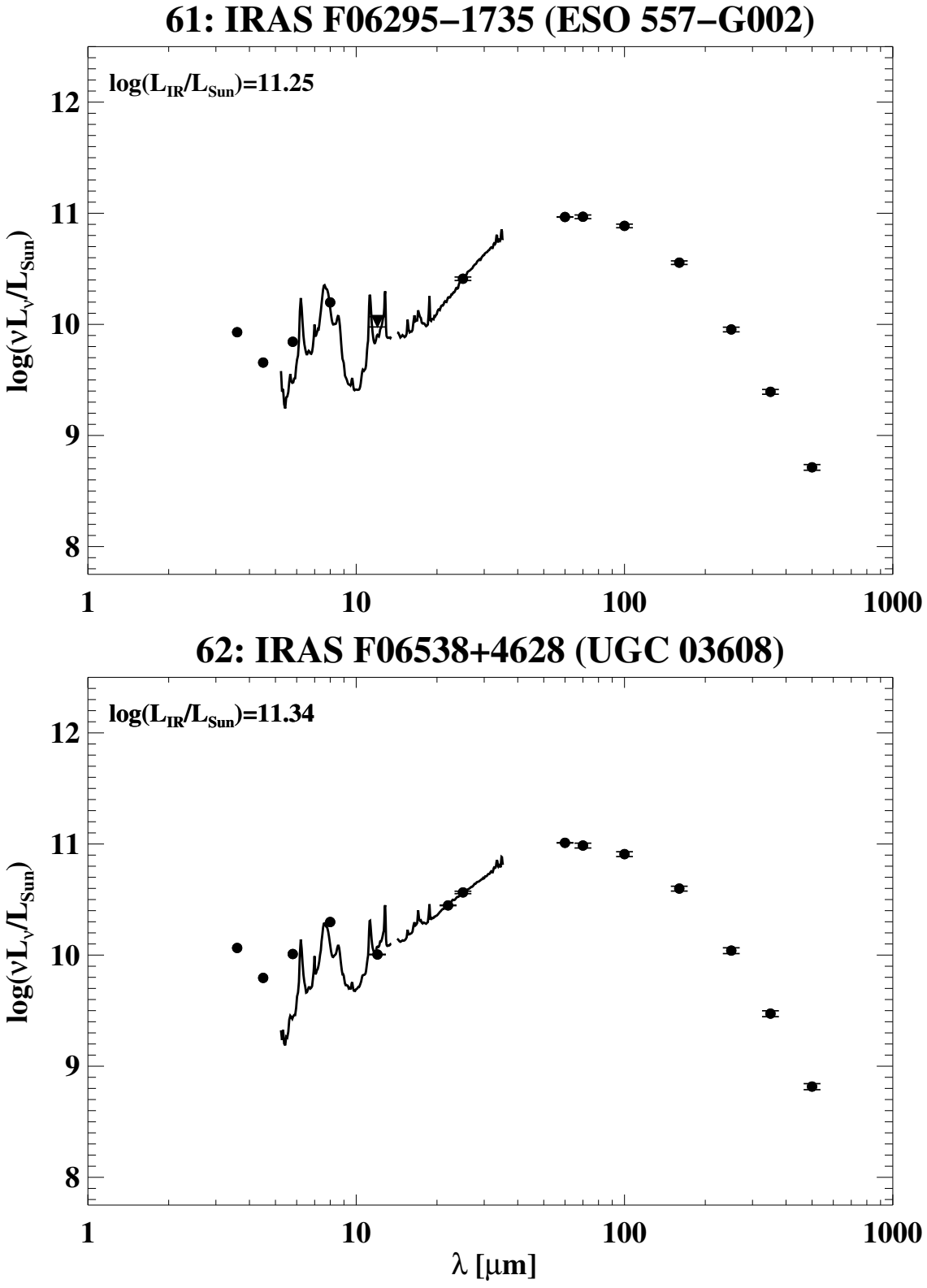

Figure A.1 continued (page 31 of 101).

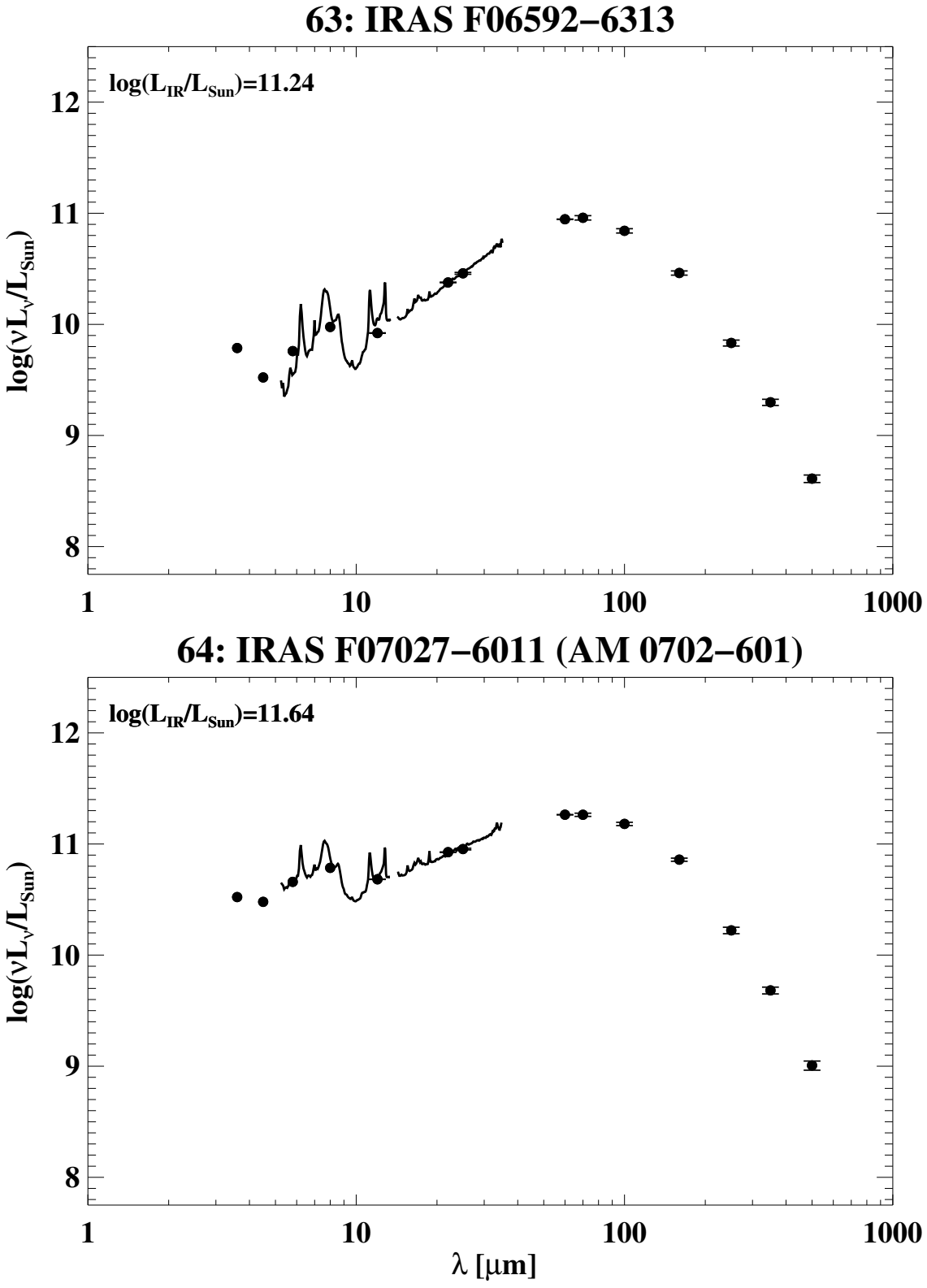

Figure A.1 continued (page 32 of 101).

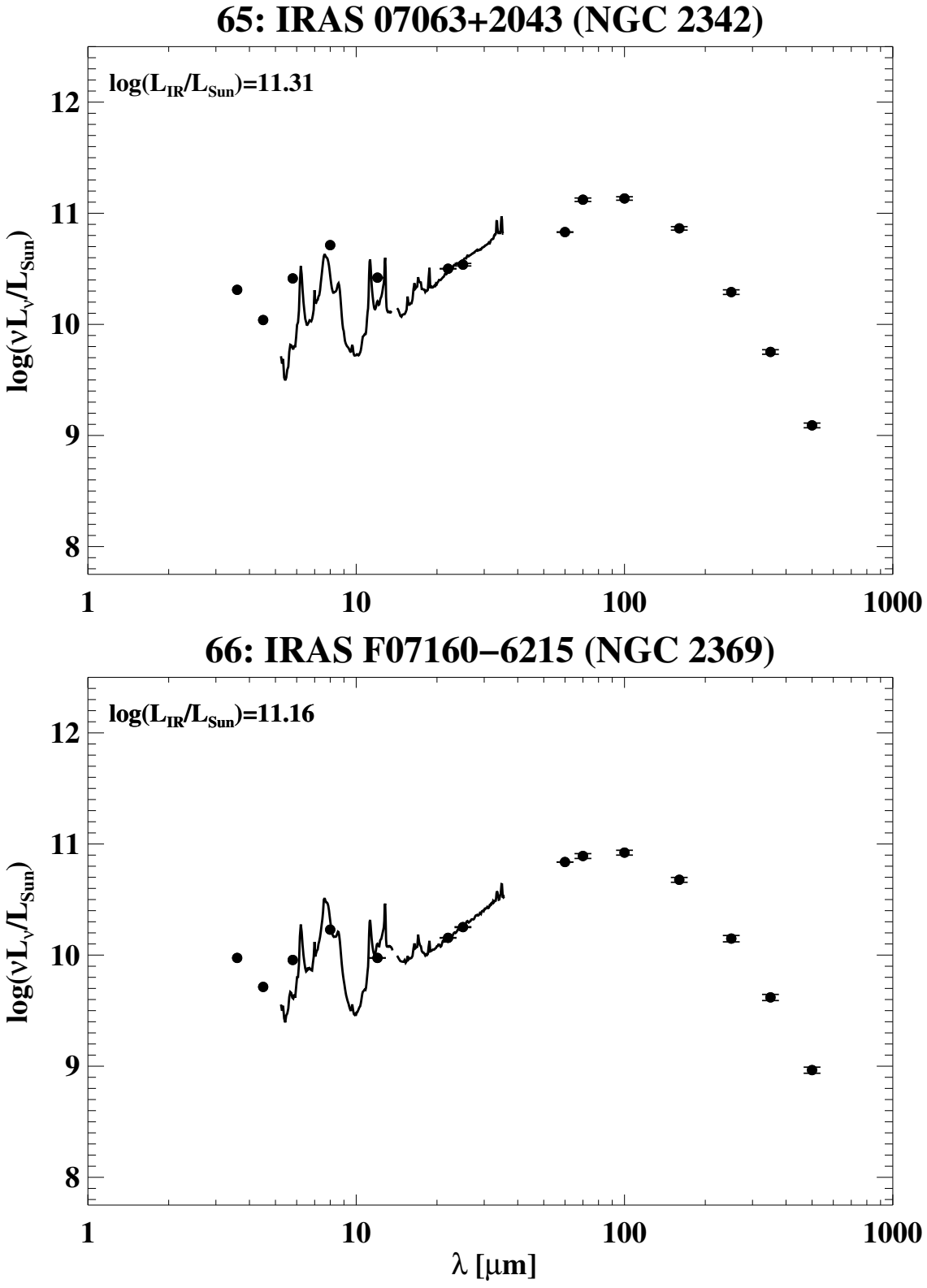

Figure A.1 continued (page 33 of 101).

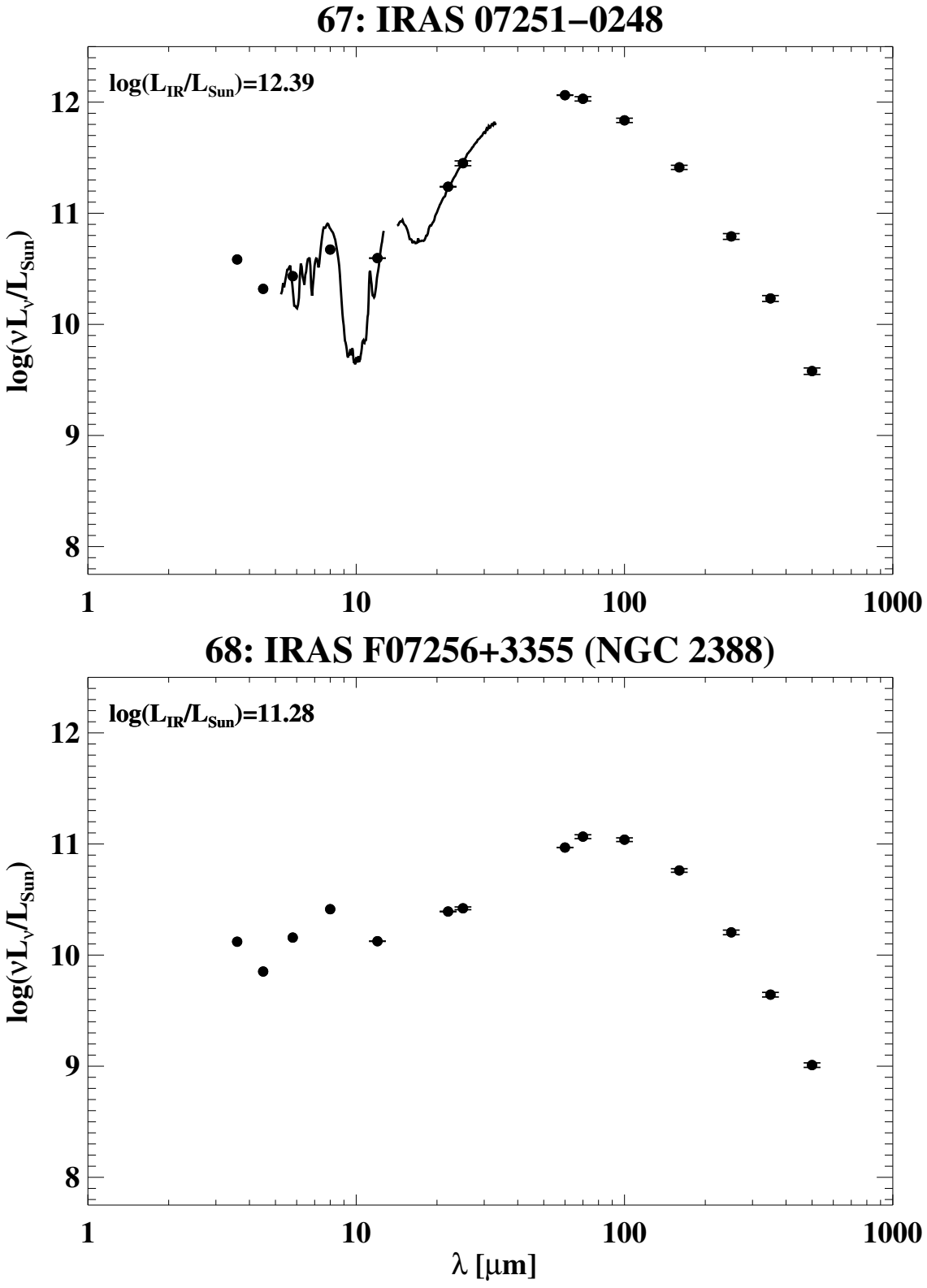

Figure A.1 continued (page 34 of 101).

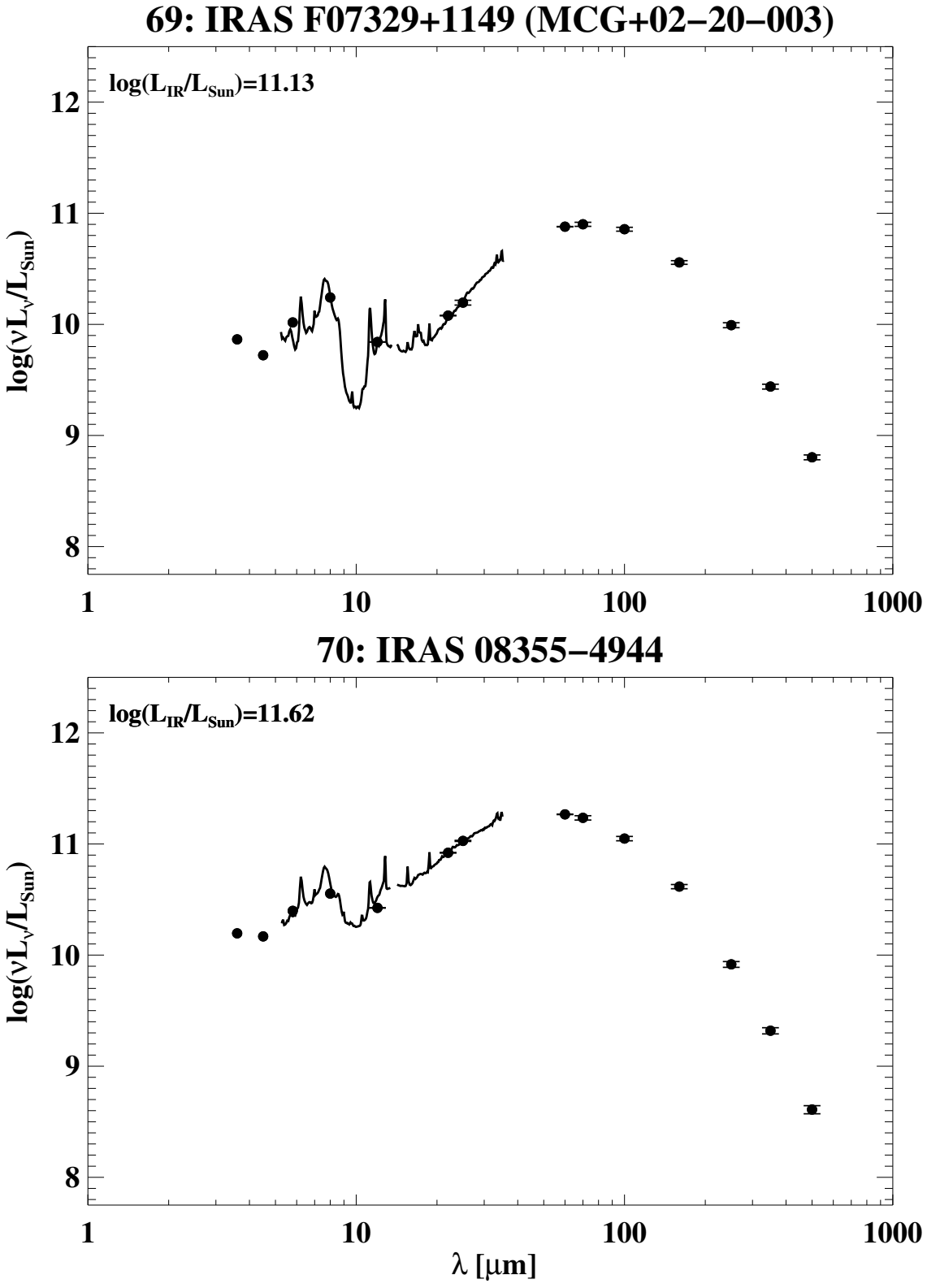

Figure A.1 continued (page 35 of 101).

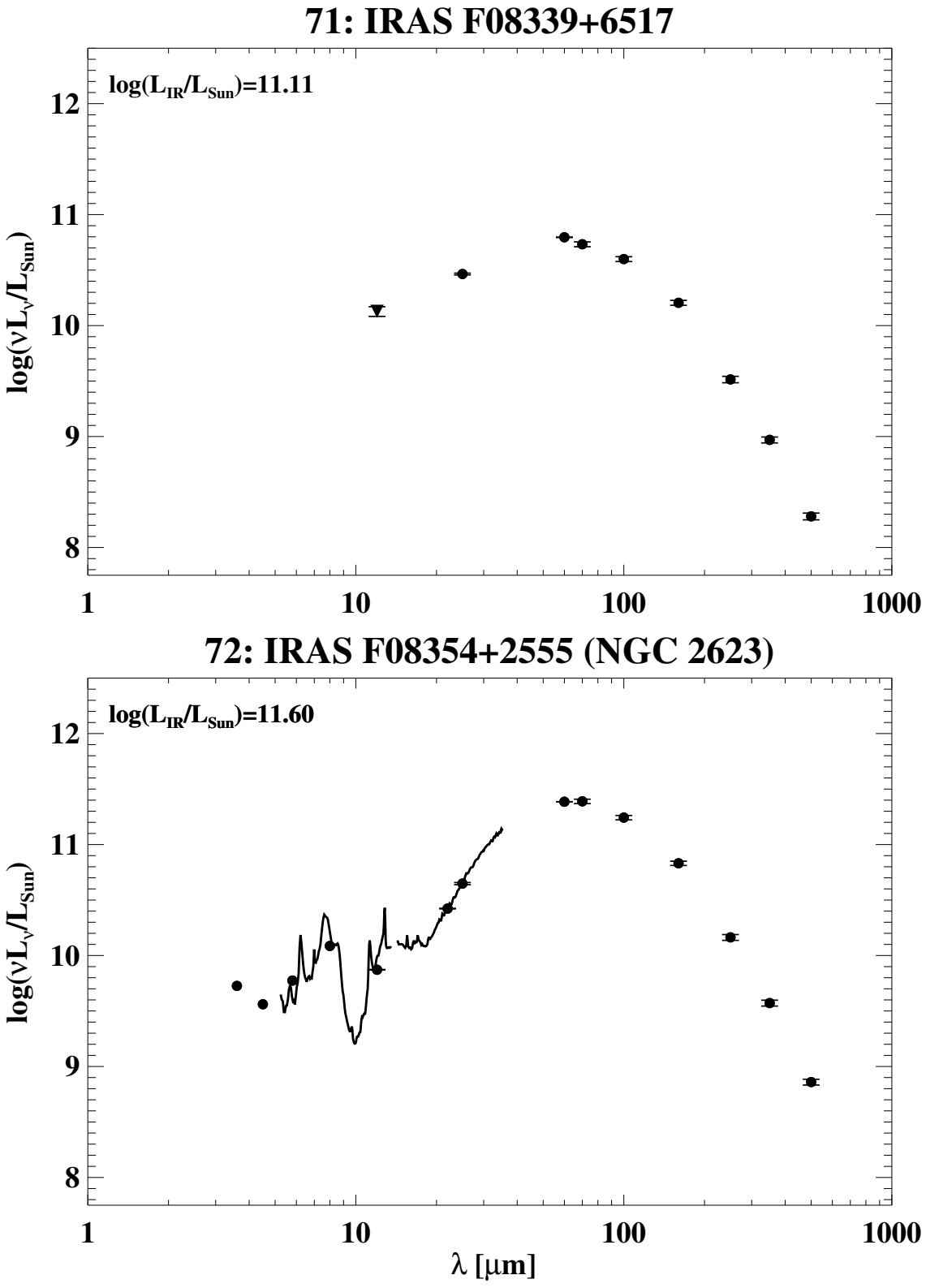

Figure A.1 continued (page 36 of 101).

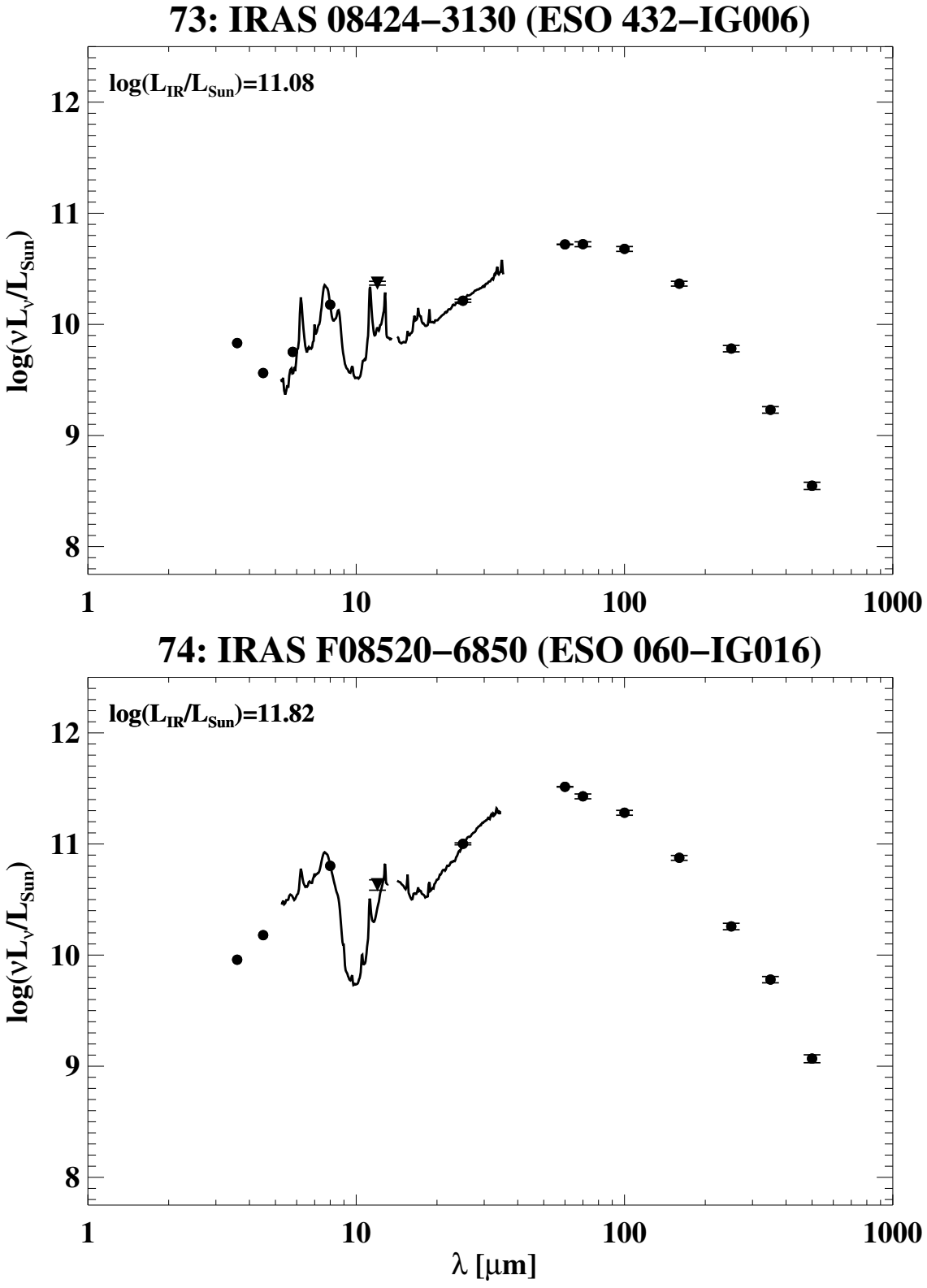

Figure A.1 continued (page 37 of 101).

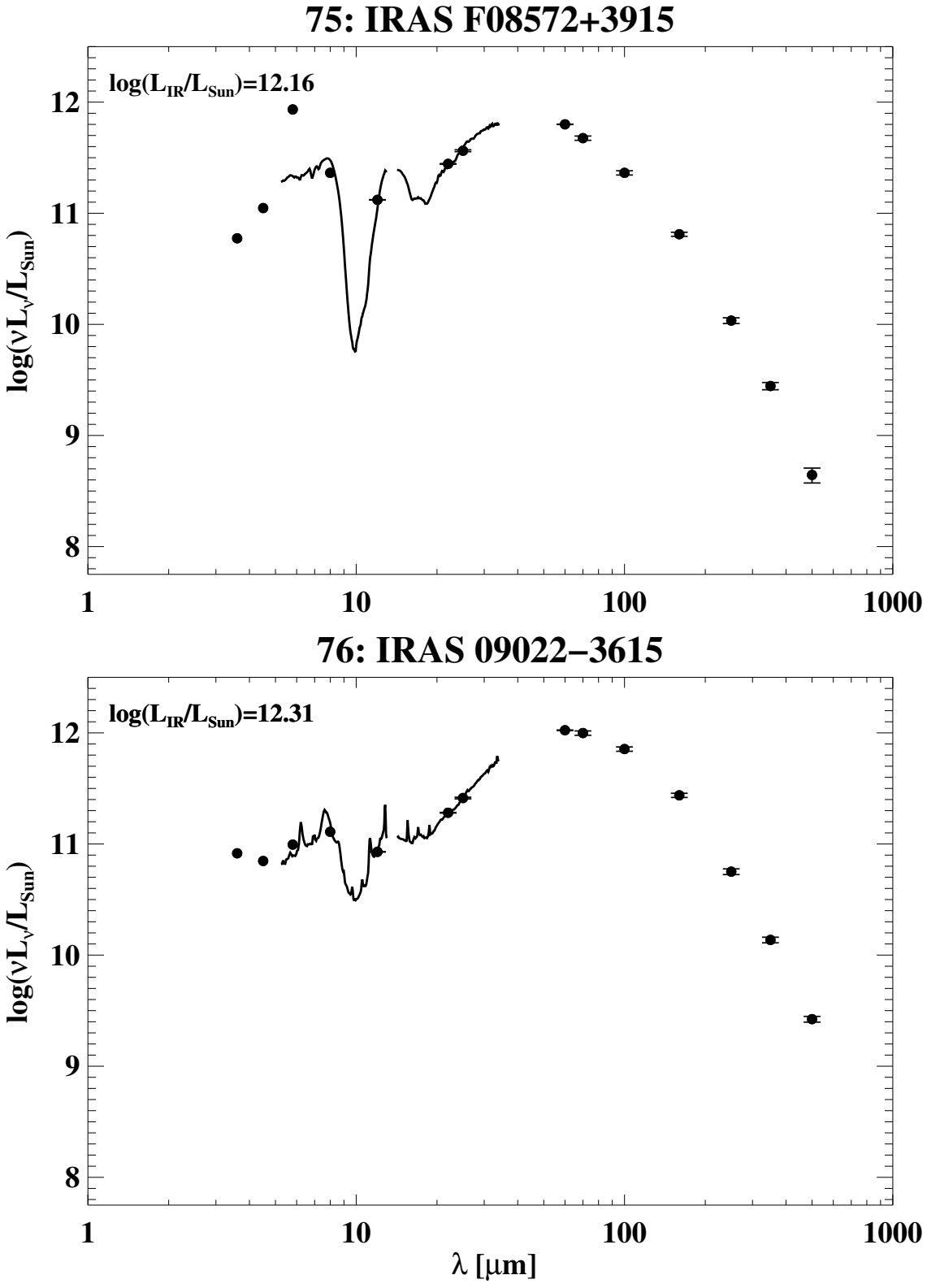

Figure A.1 continued (page 38 of 101).

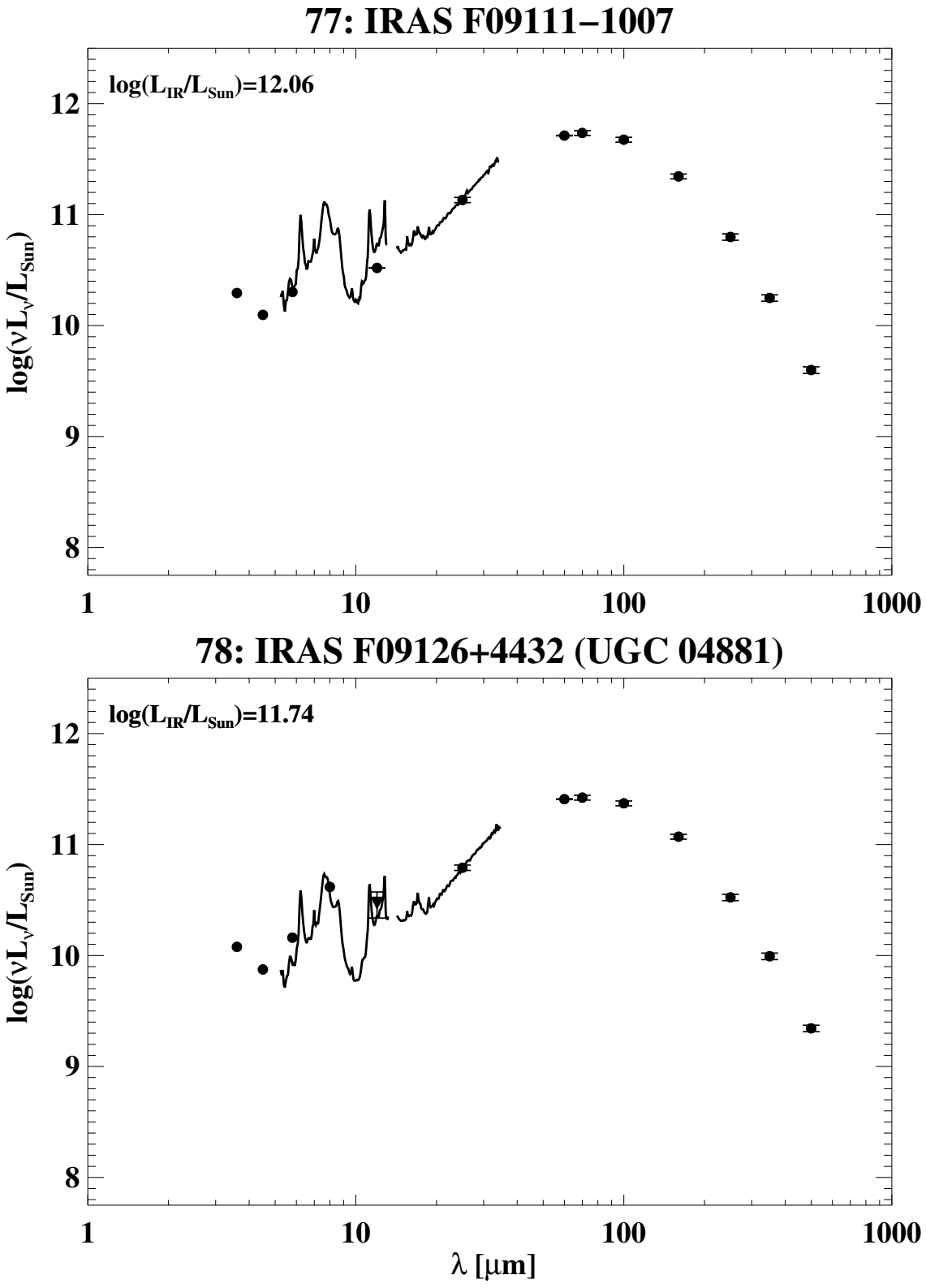

Figure A.1 continued (page 39 of 101).

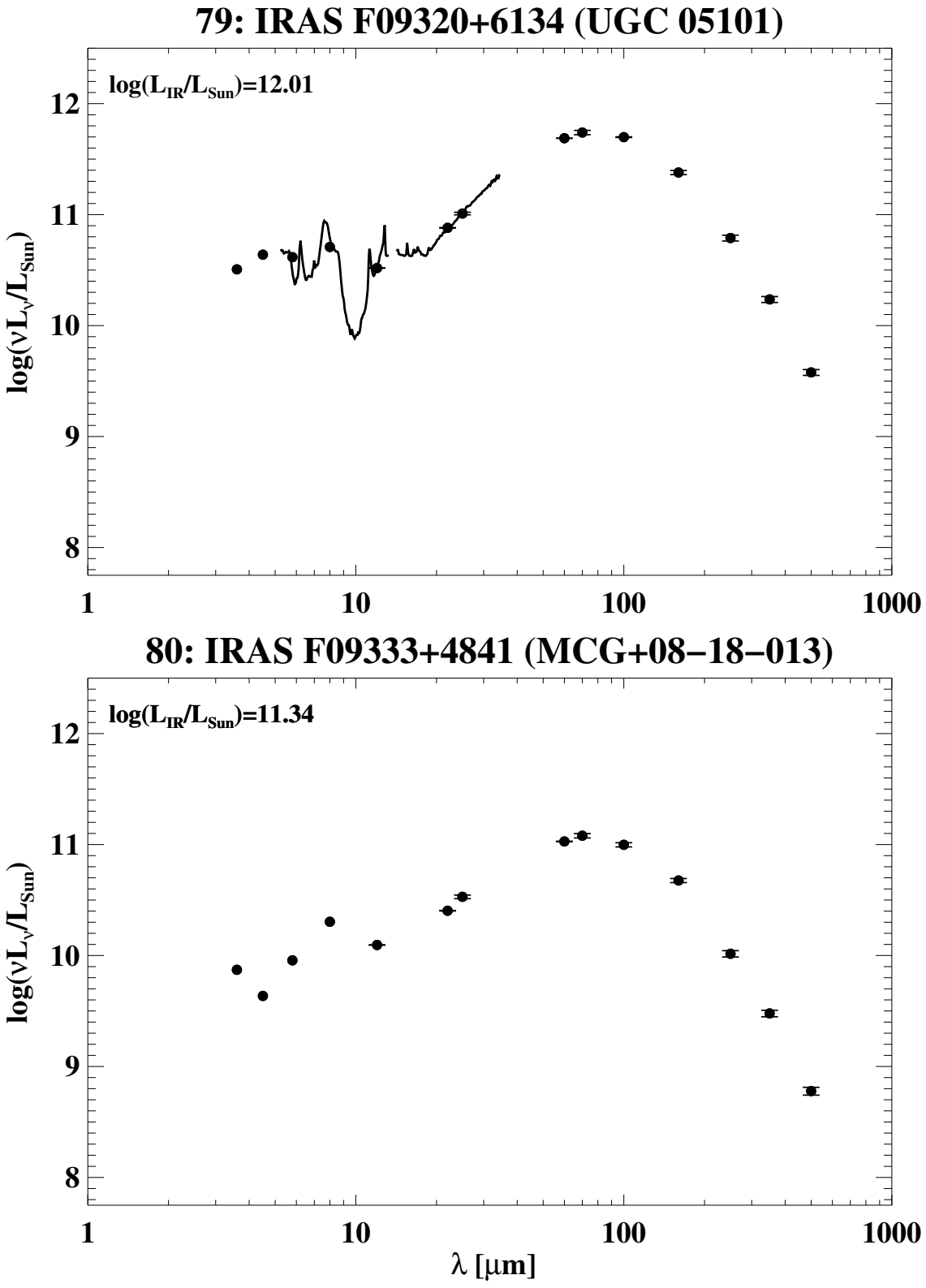

Figure A.1 continued (page 40 of 101).

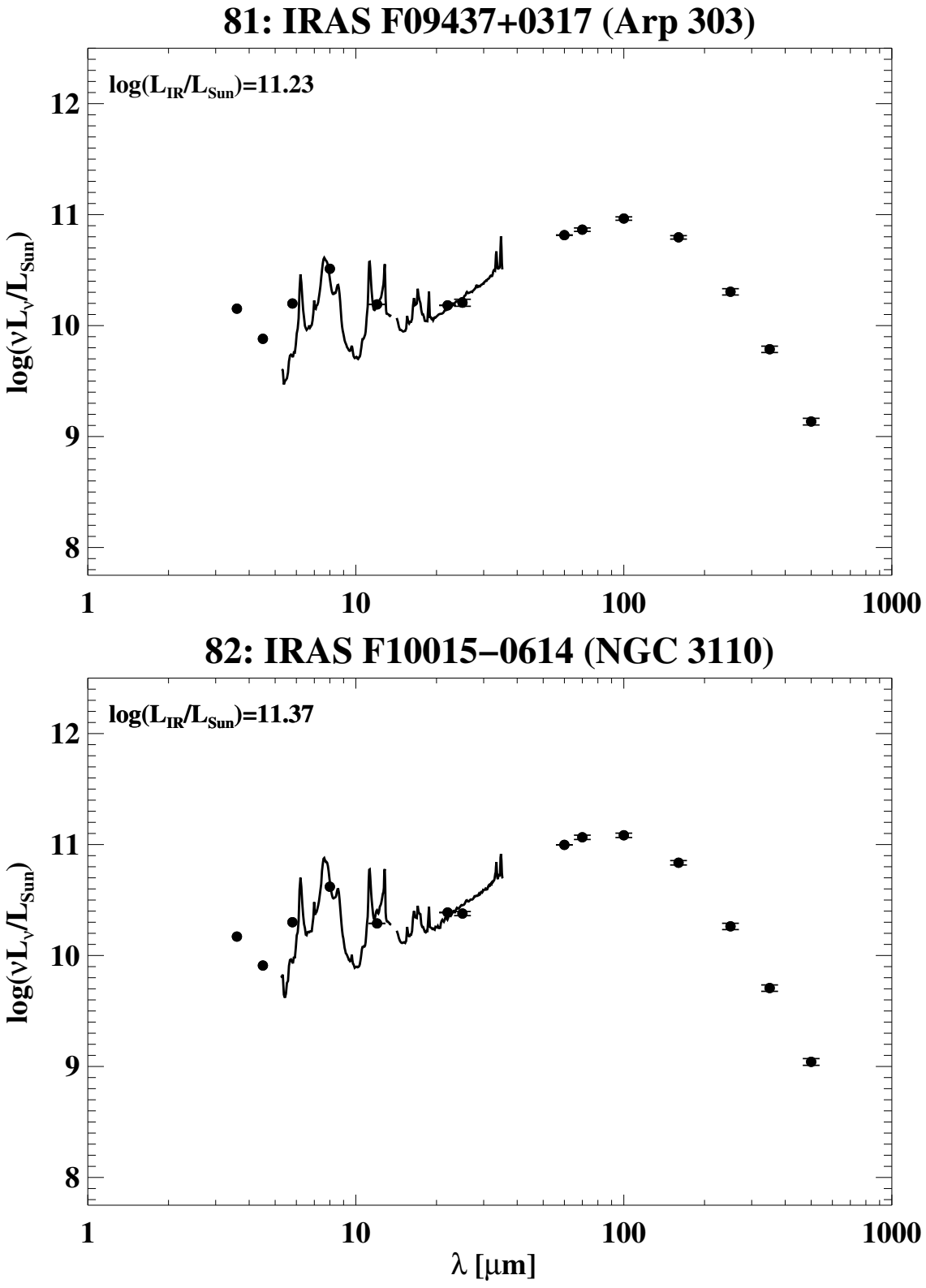

Figure A.1 continued (page 41 of 101).

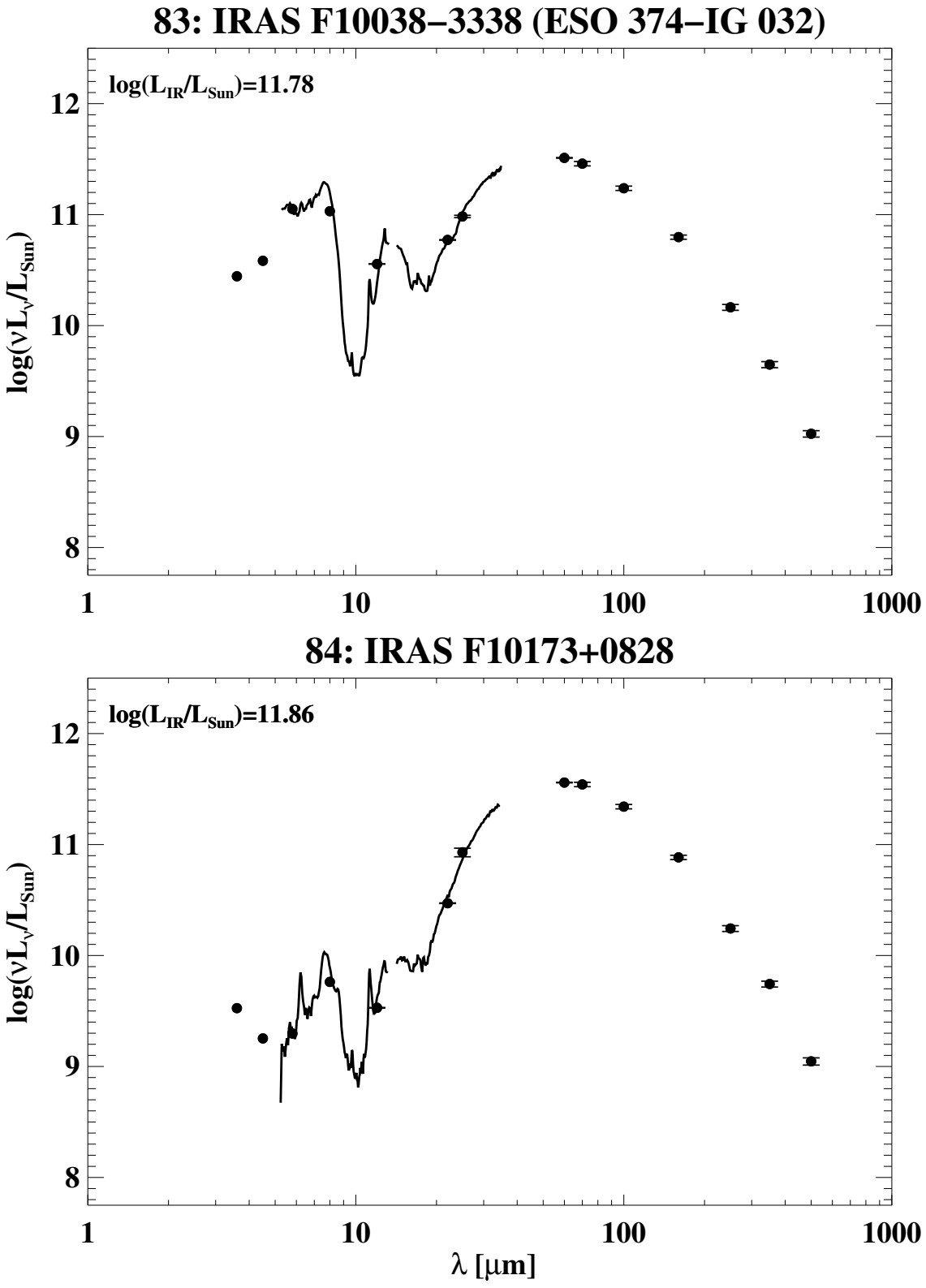

Figure A.1 continued (page 42 of 101).

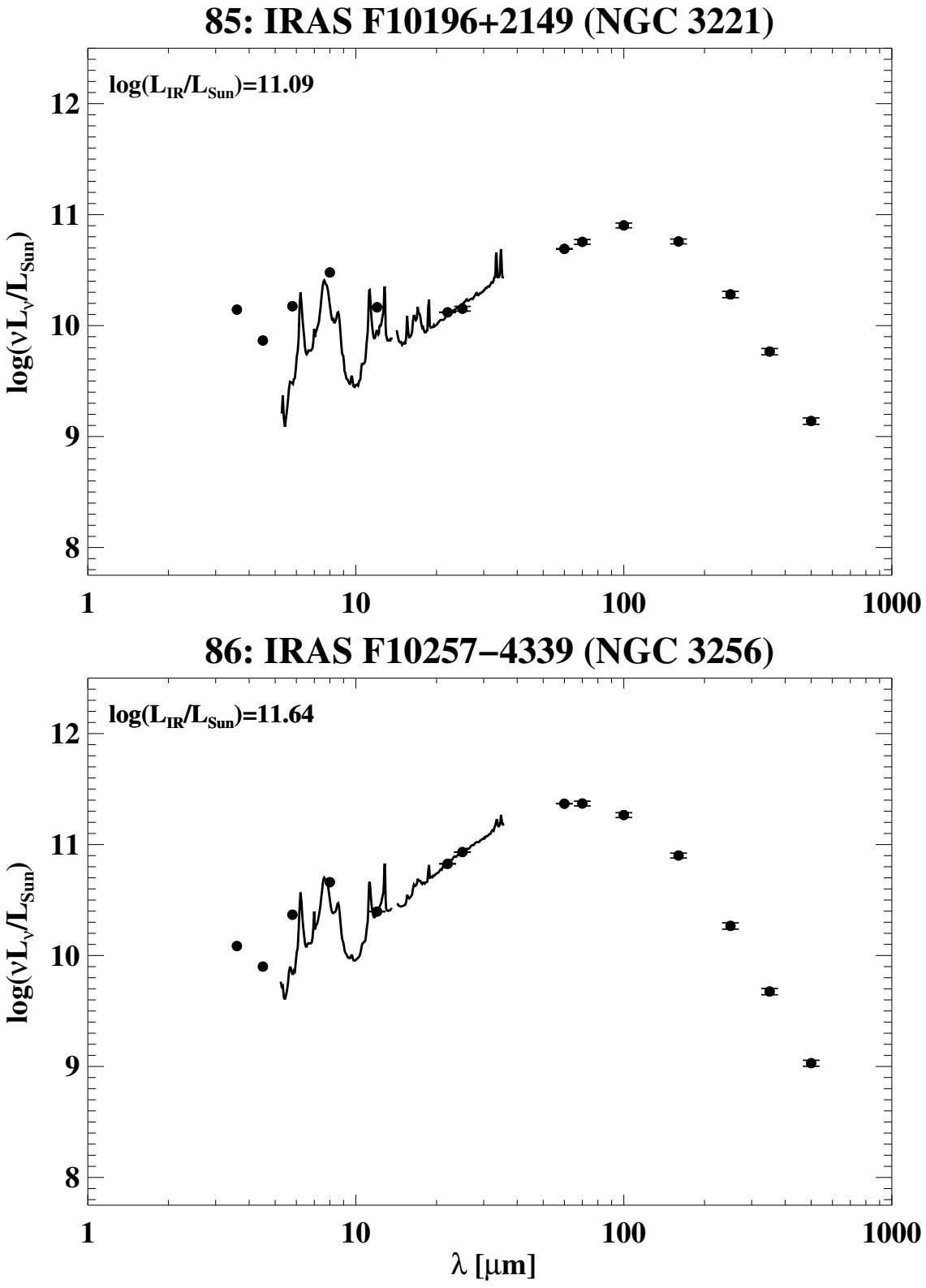

Figure A.1 continued (page 43 of 101).

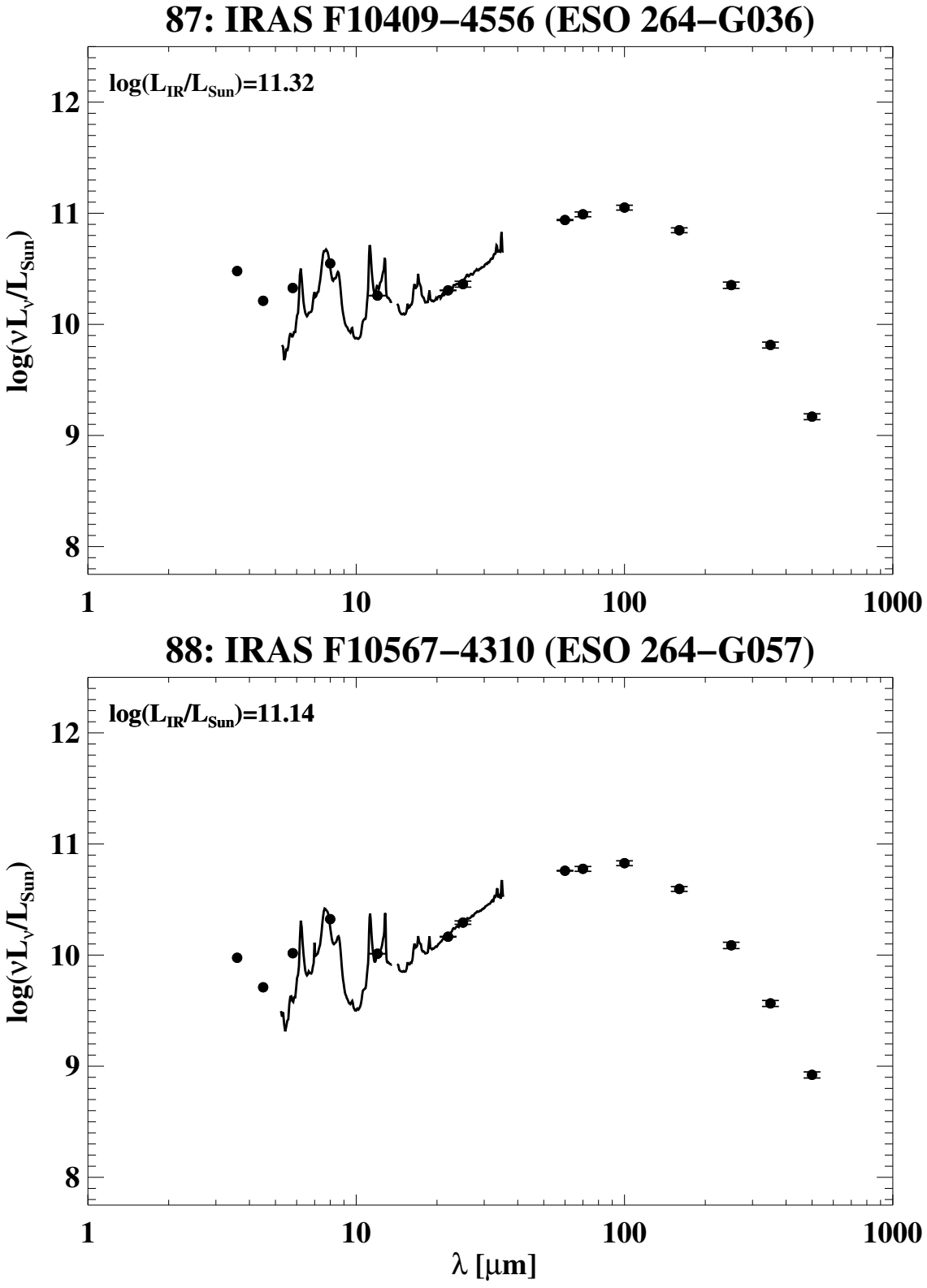

Figure A.1 continued (page 44 of 101).

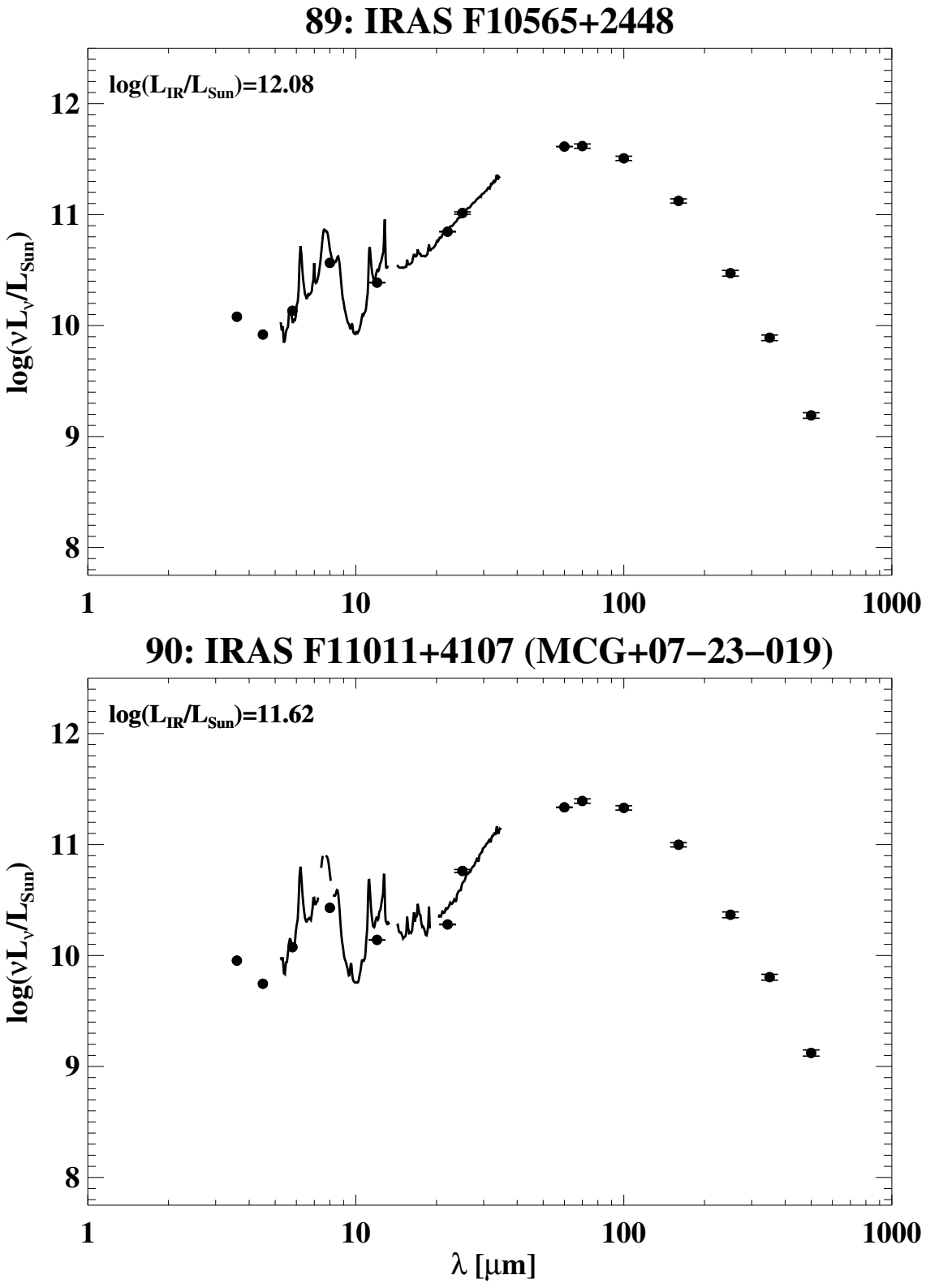

Figure A.1 continued (page 45 of 101).

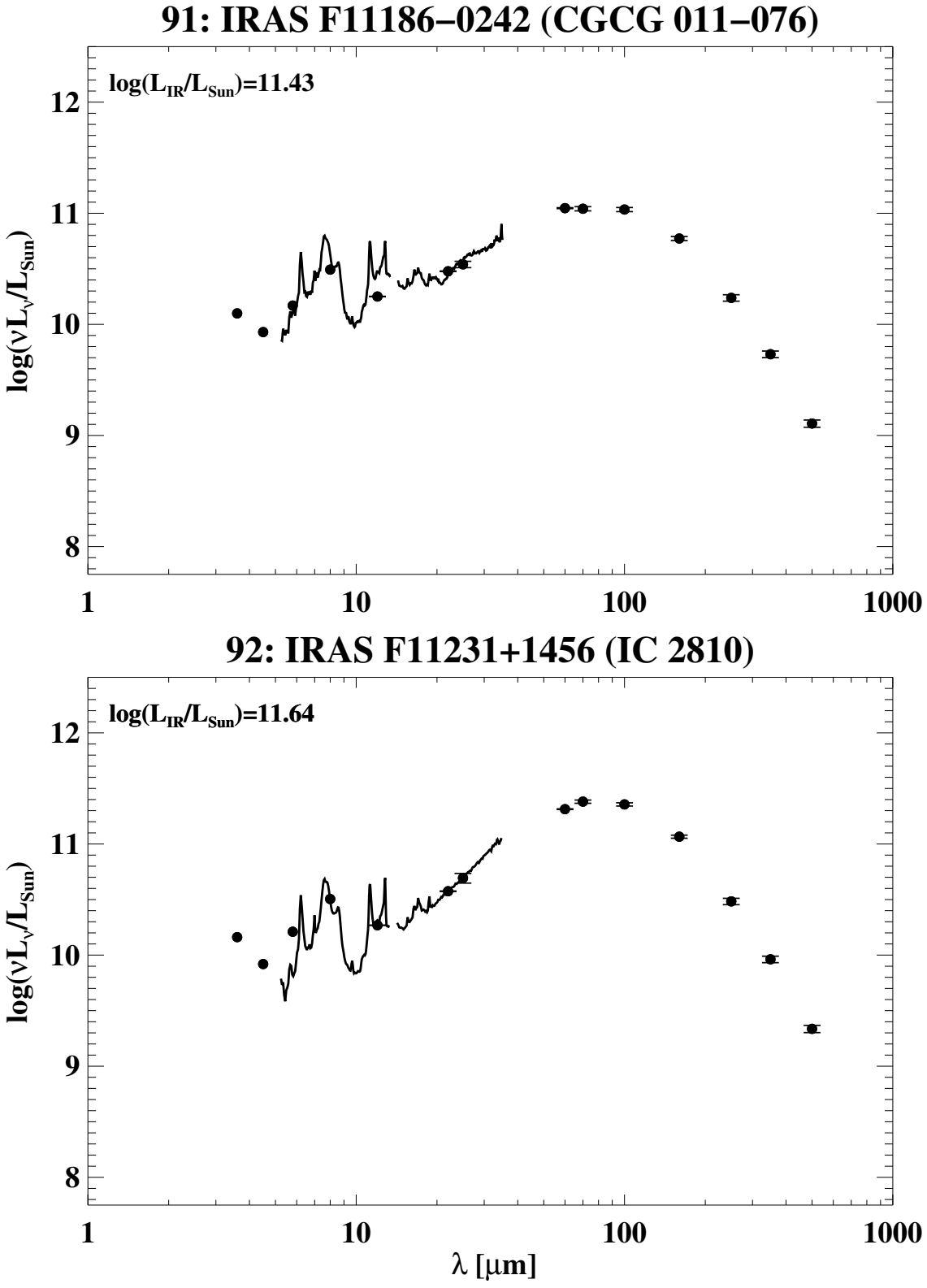

Figure A.1 continued (page 46 of 101).

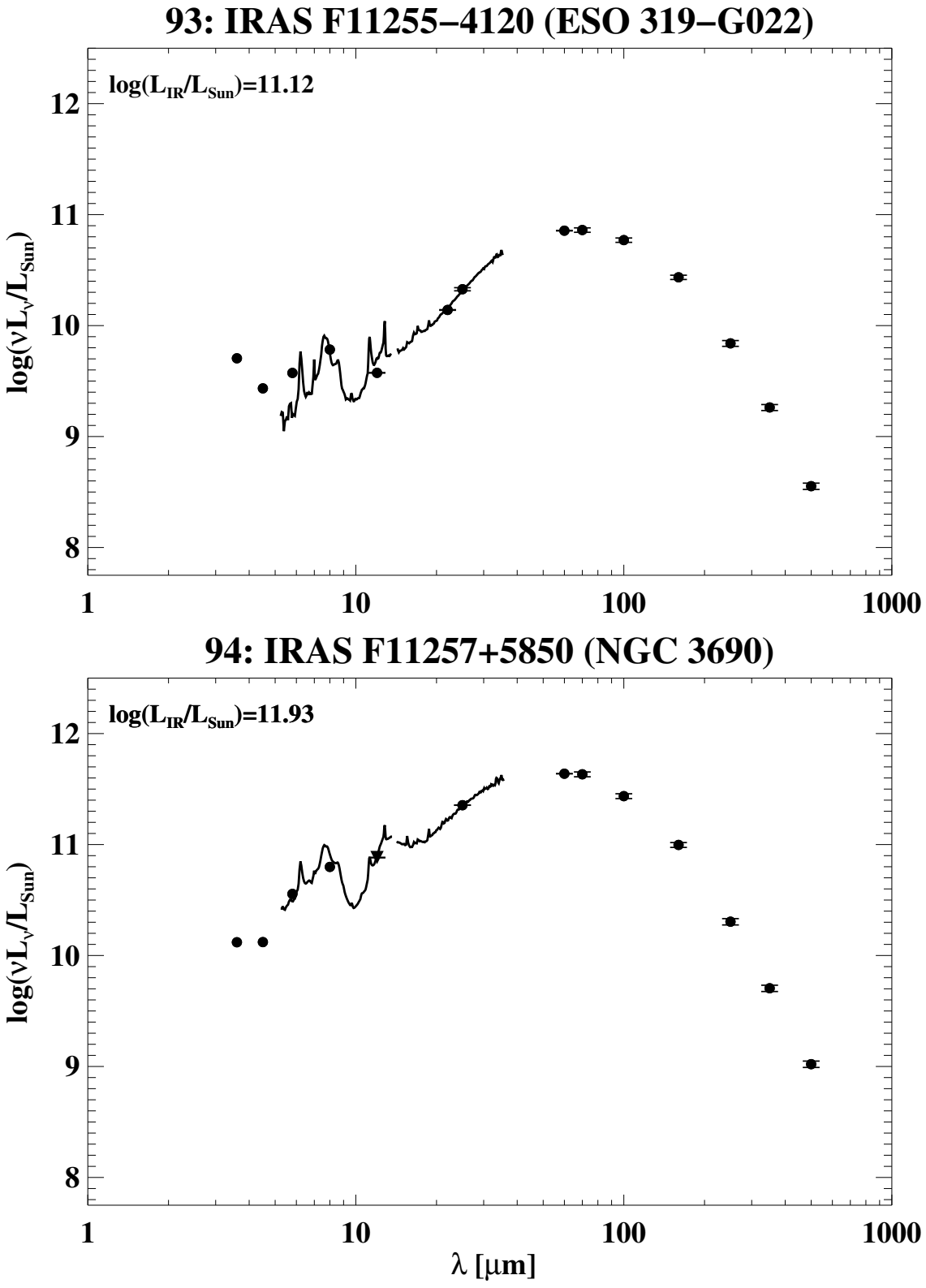

Figure A.1 continued (page 47 of 101).

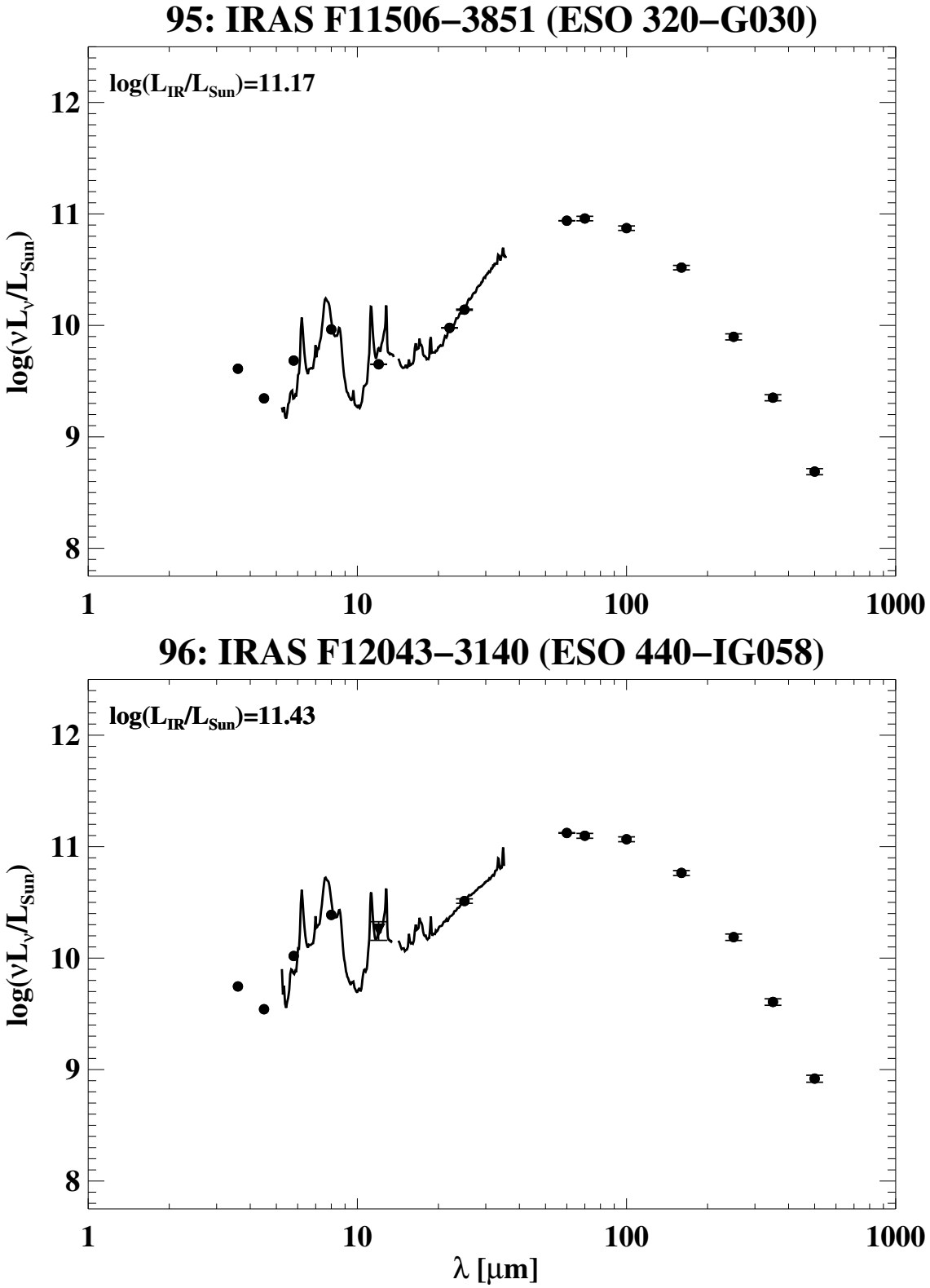

Figure A.1 continued (page 48 of 101).

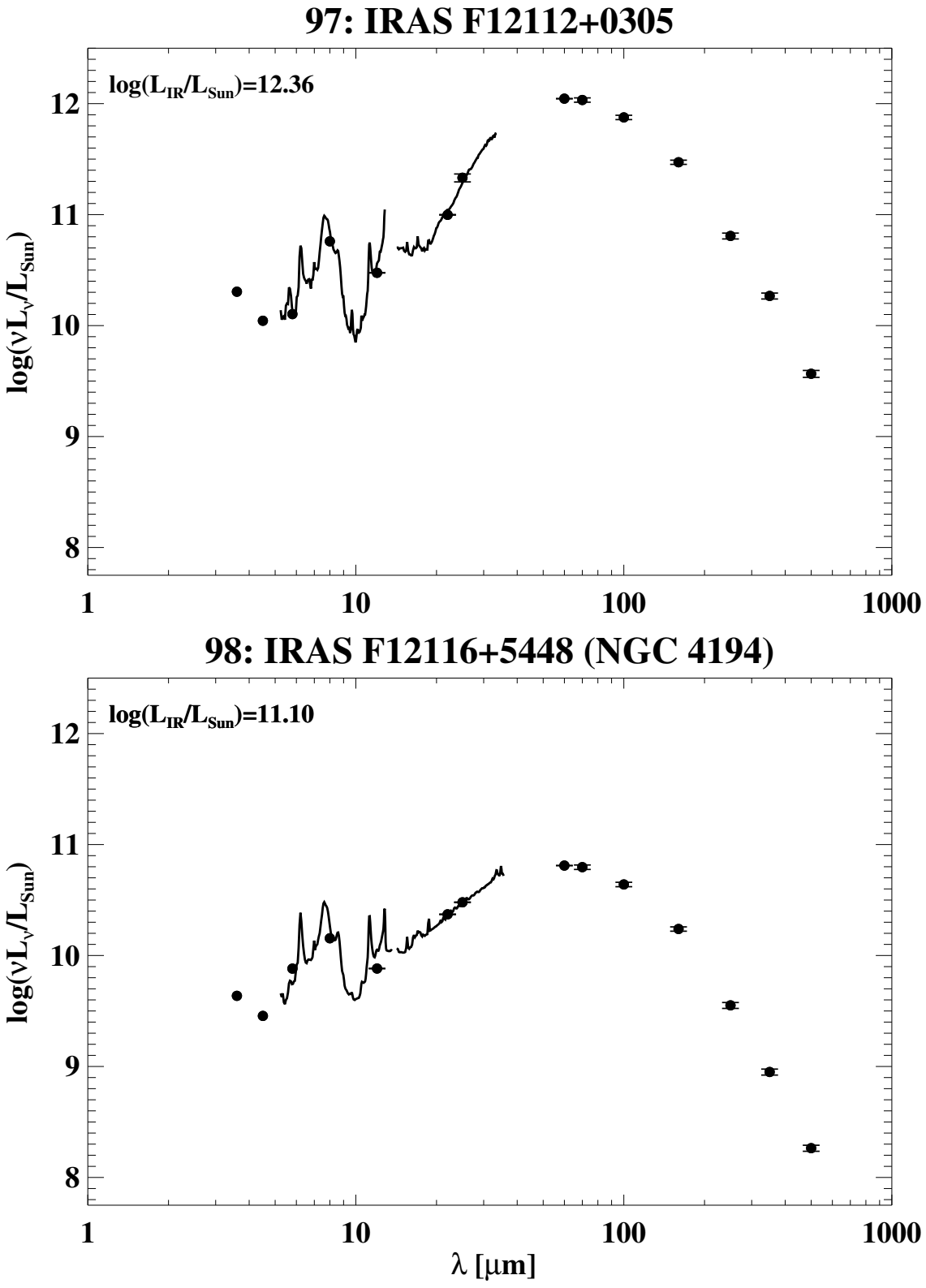

Figure A.1 continued (page 49 of 101).

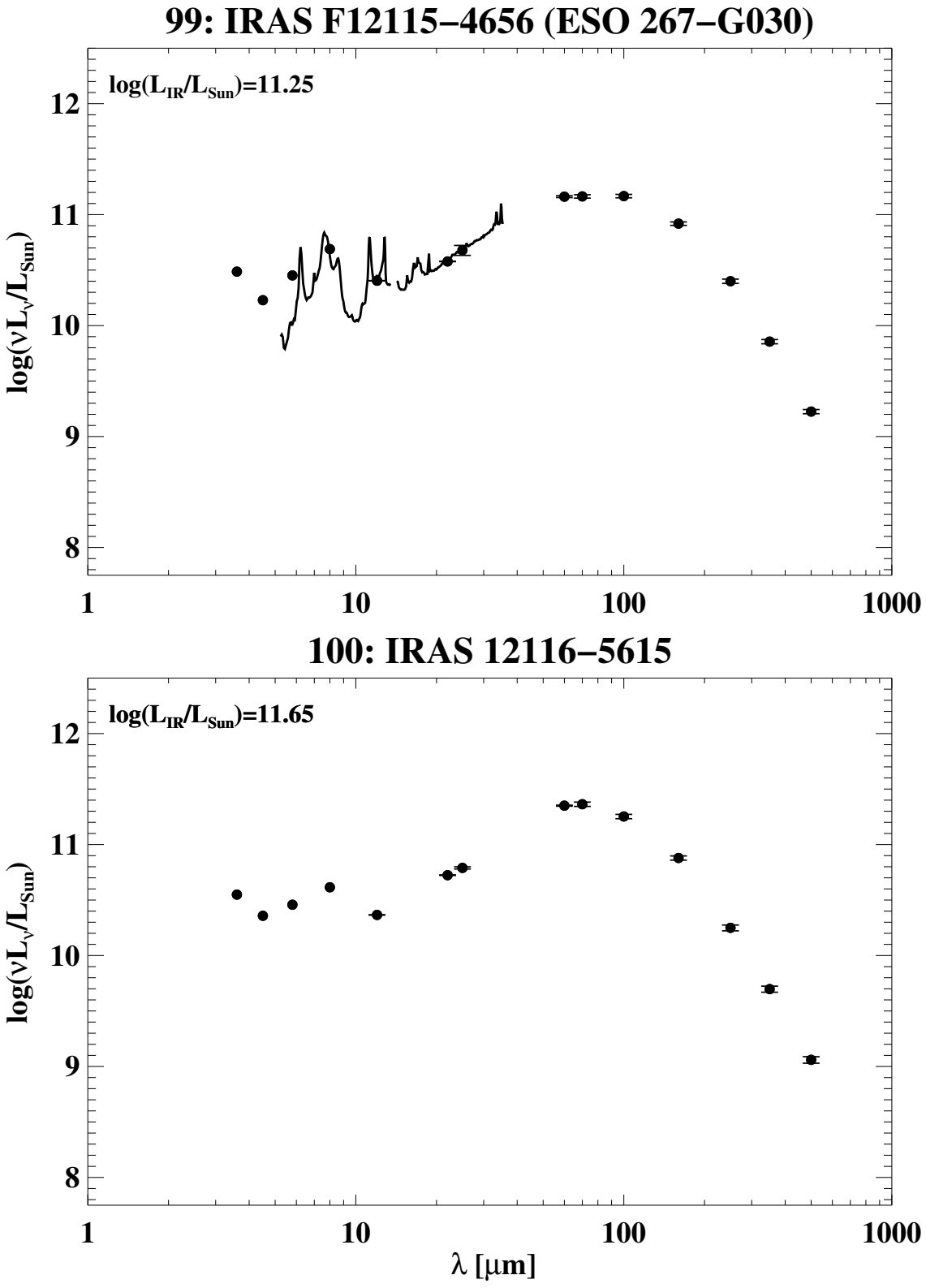

Figure A.1 continued (page 50 of 101).

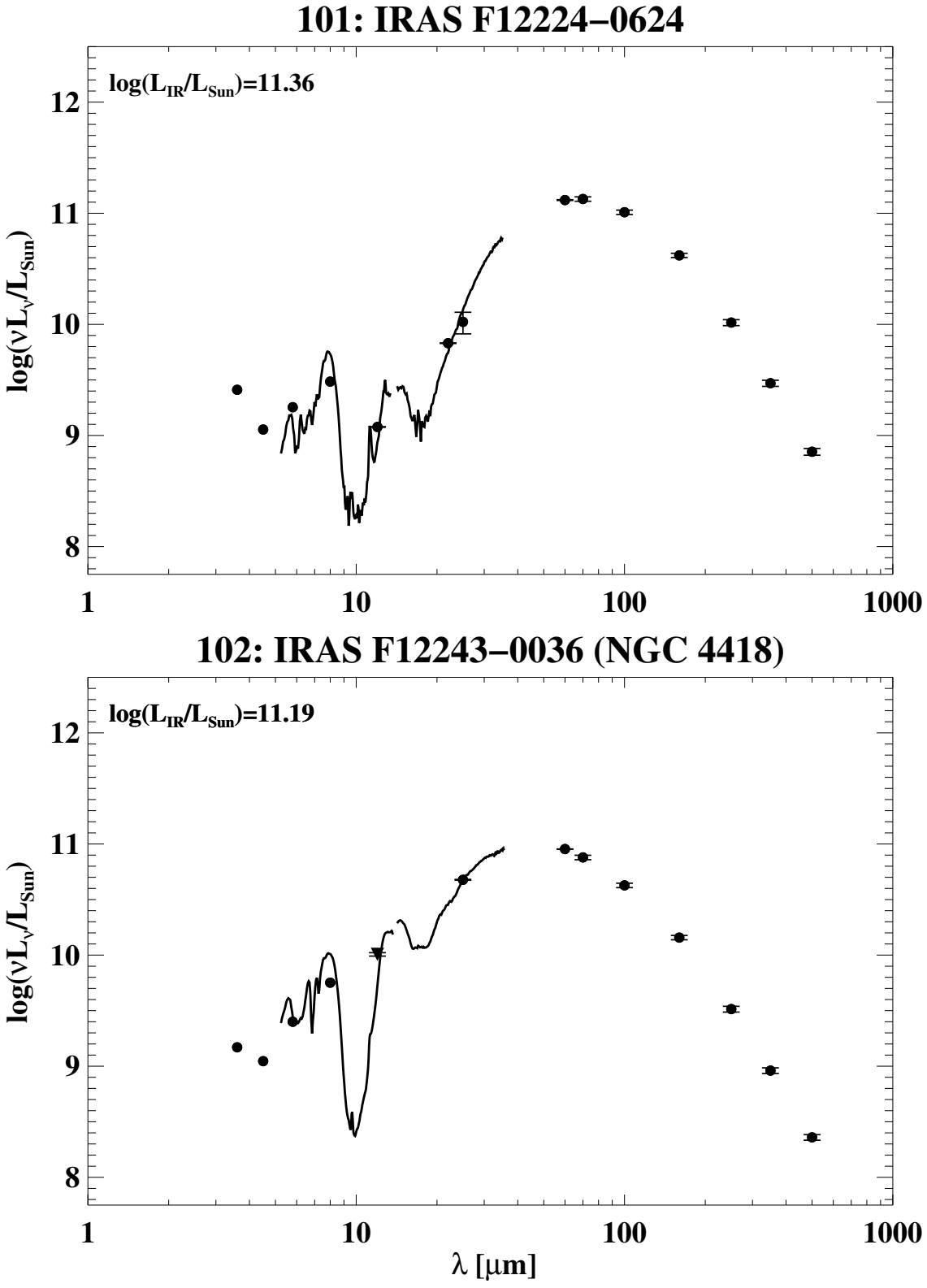

Figure A.1 continued (page 51 of 101).

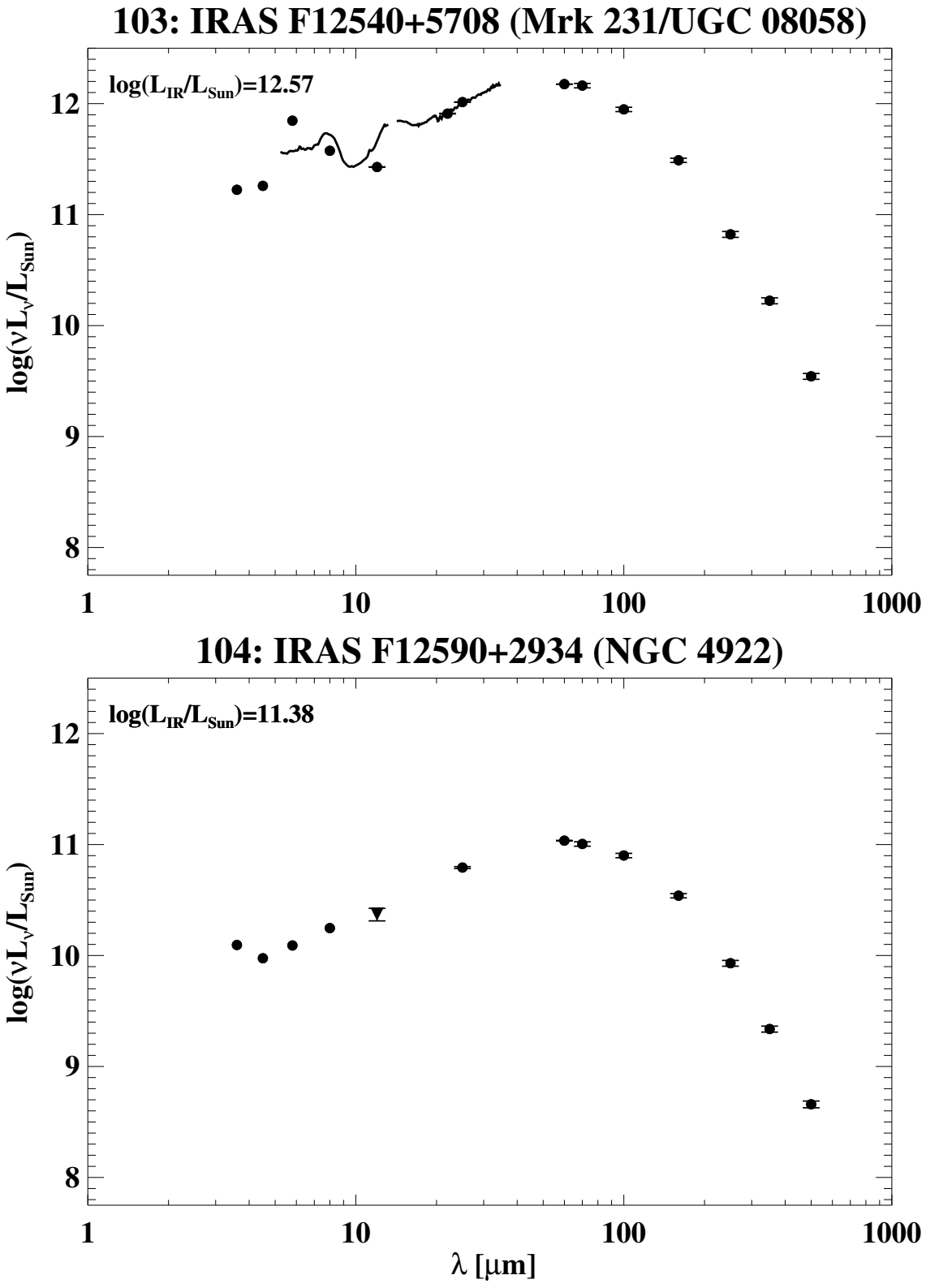

Figure A.1 continued (page 52 of 101).

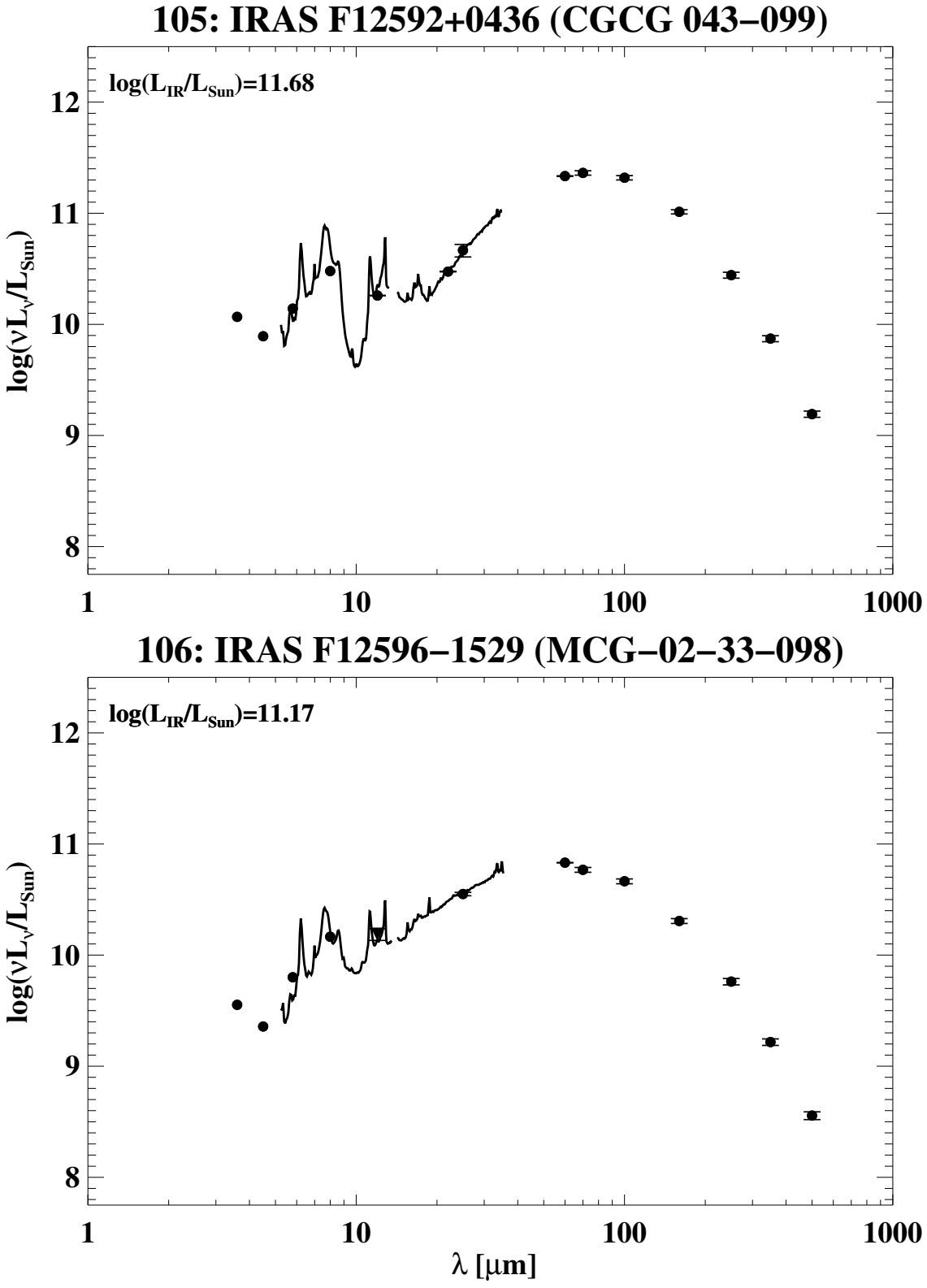

Figure A.1 continued (page 53 of 101).

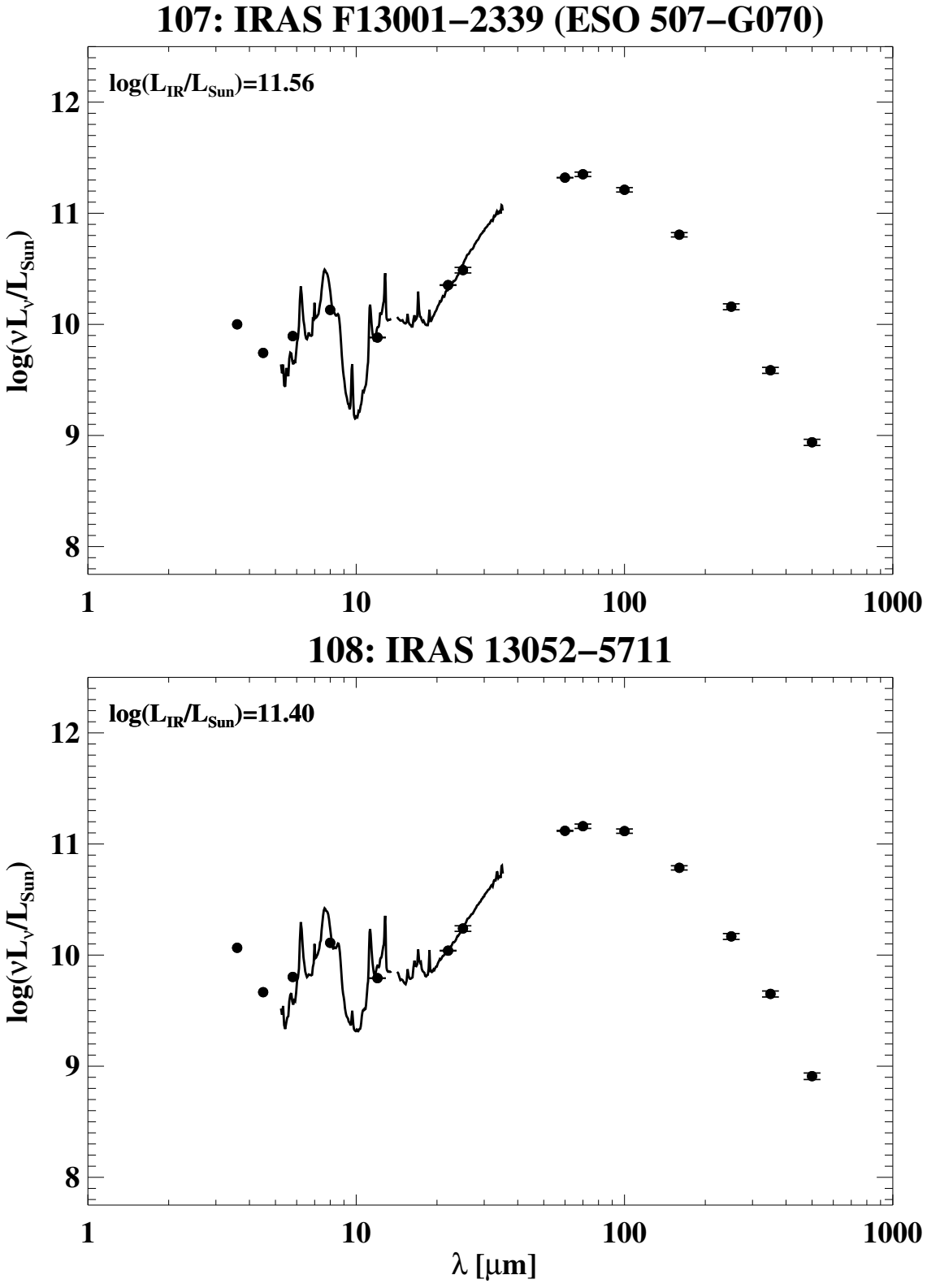

Figure A.1 continued (page 54 of 101).

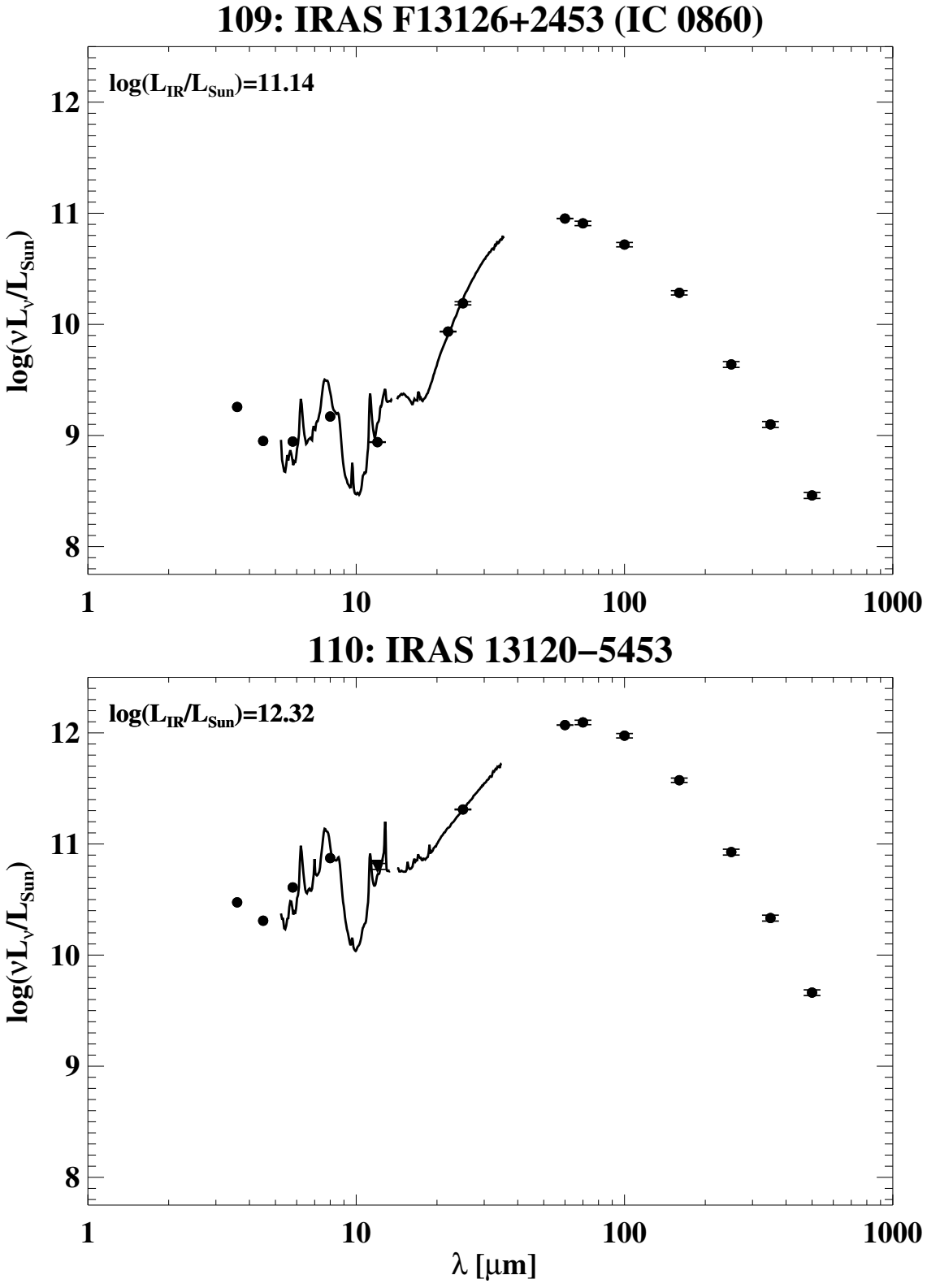

Figure A.1 continued (page 55 of 101).

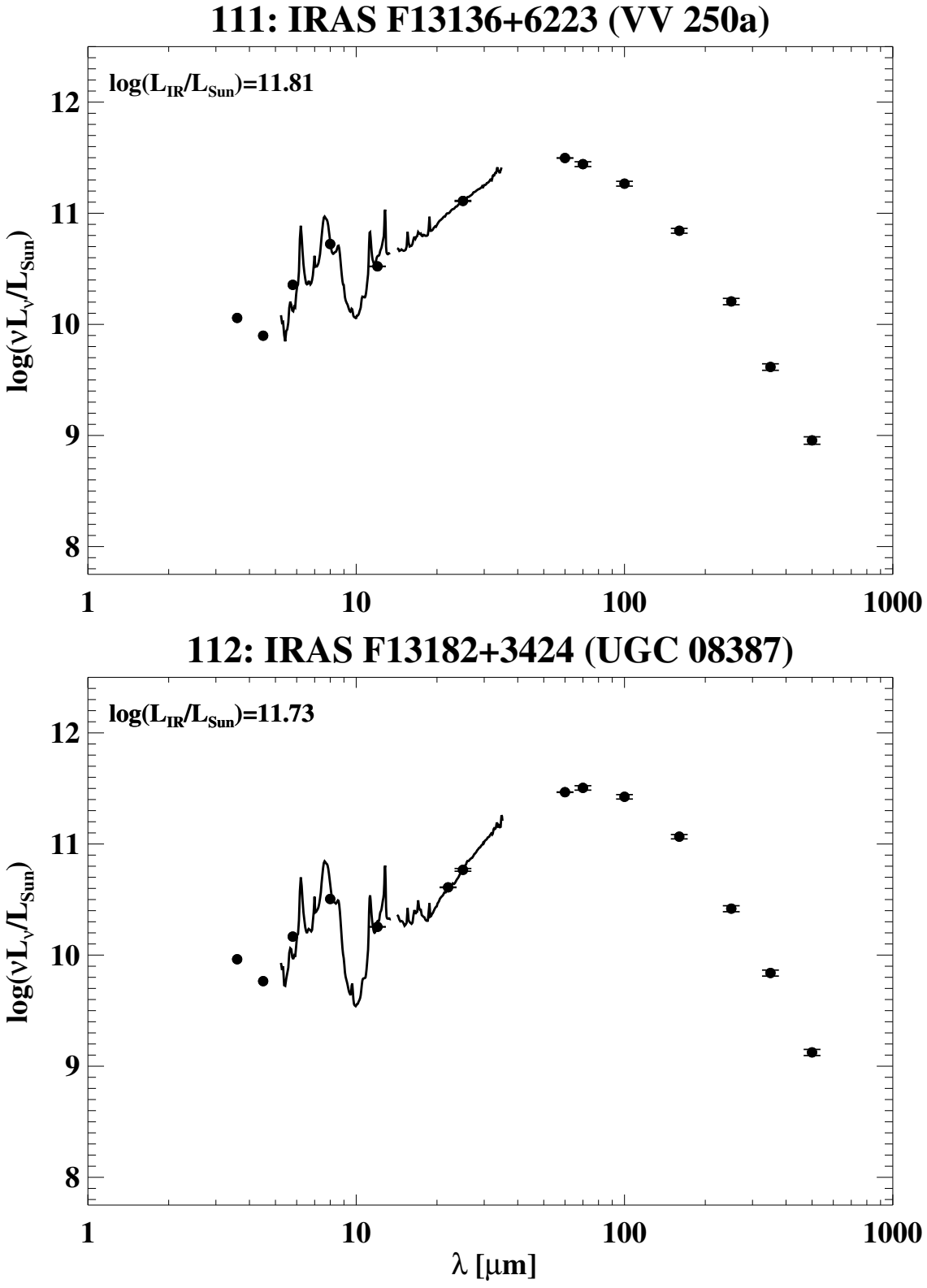

Figure A.1 continued (page 56 of 101).

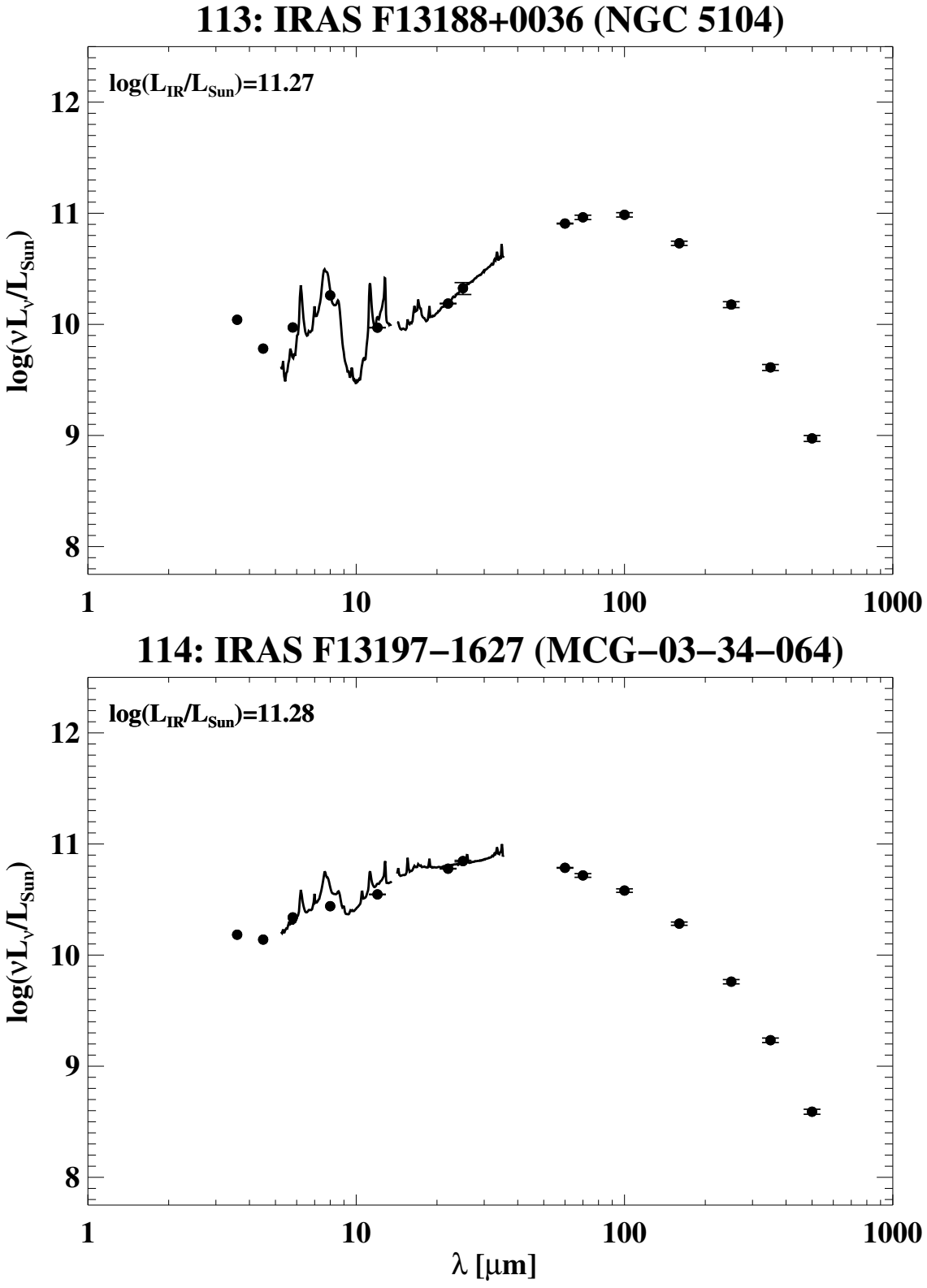

Figure A.1 continued (page 57 of 101).

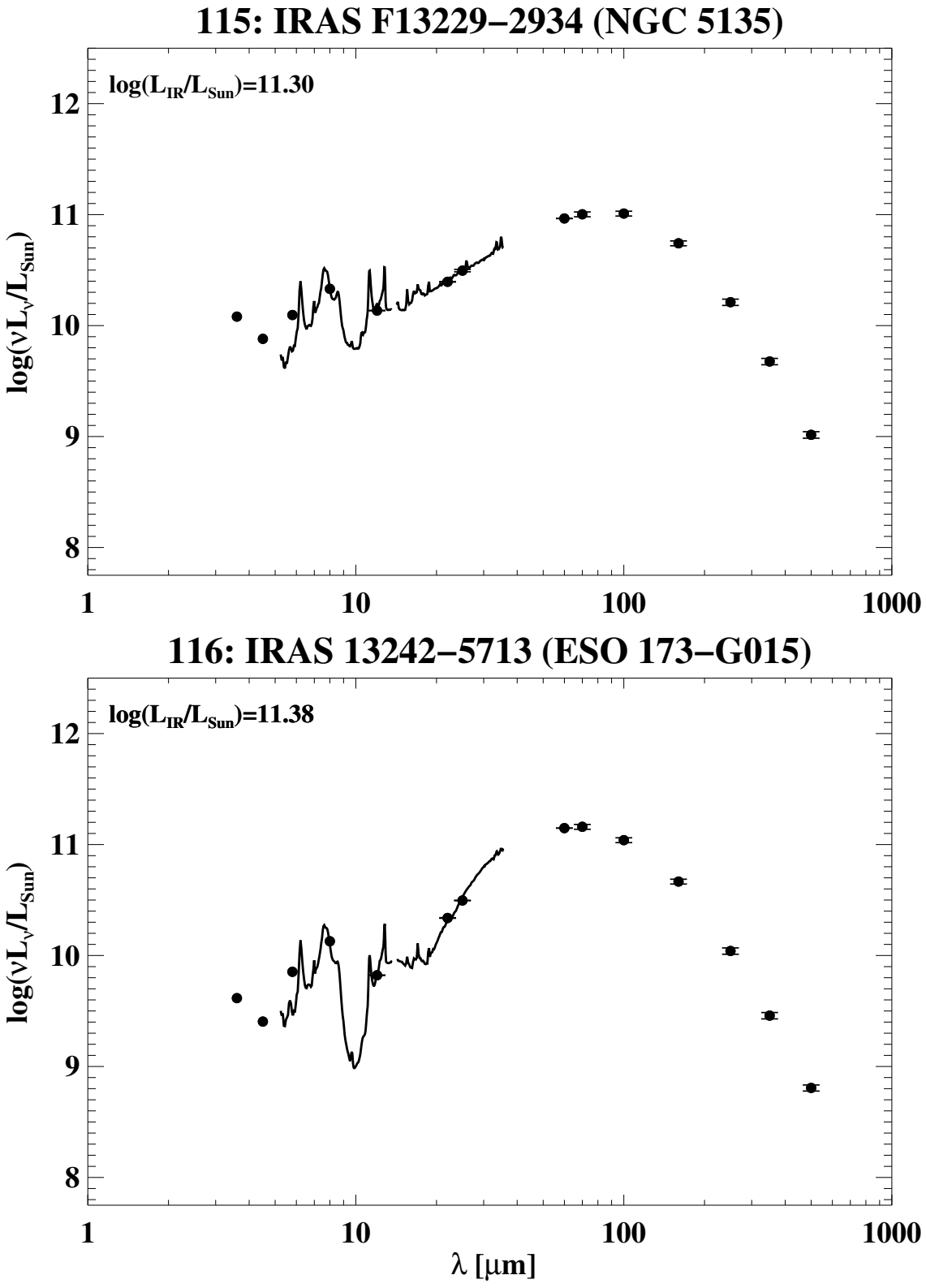

Figure A.1 continued (page 58 of 101).

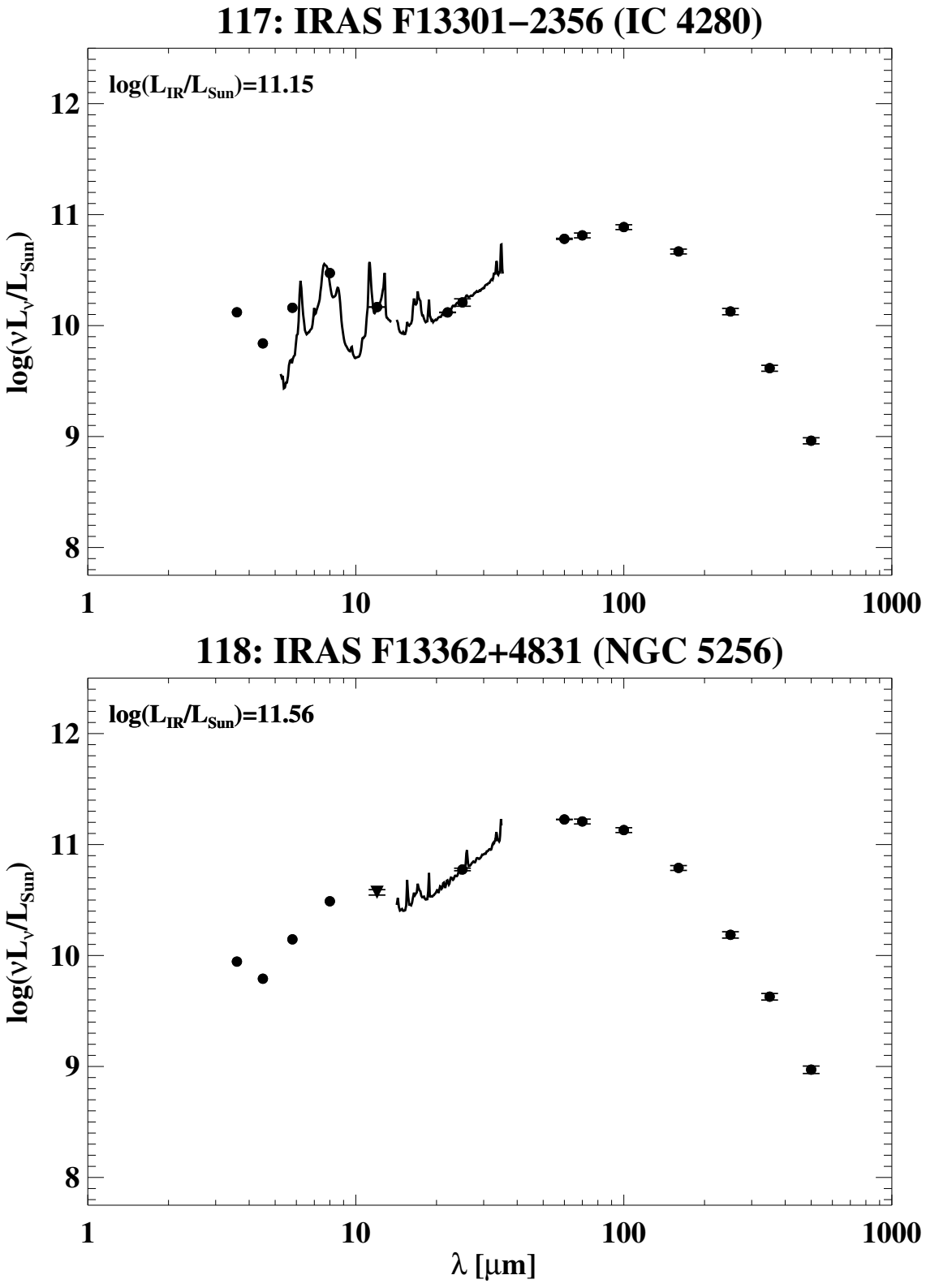

Figure A.1 continued (page 59 of 101).

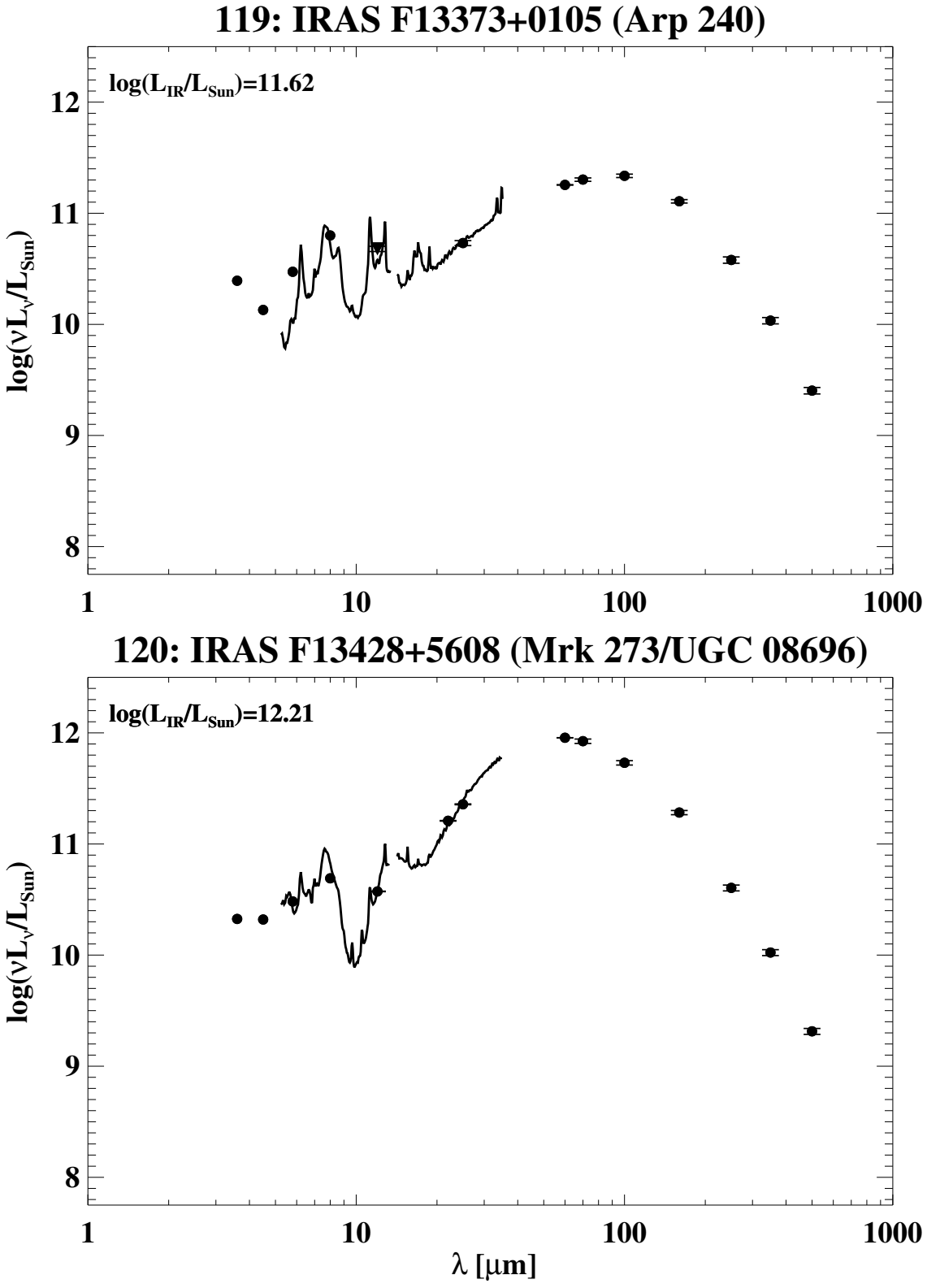

Figure A.1 continued (page 60 of 101).

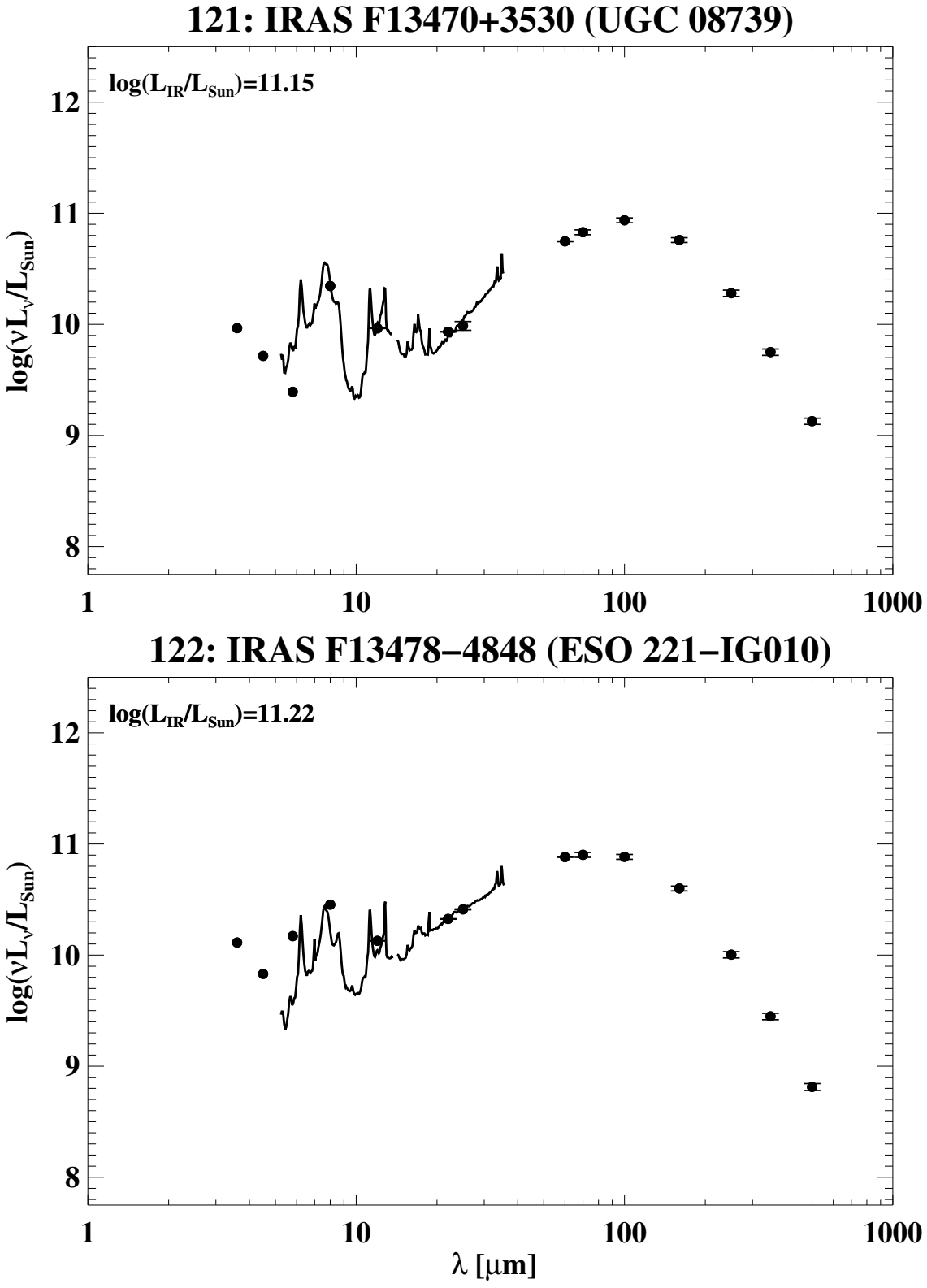

Figure A.1 continued (page 61 of 101).

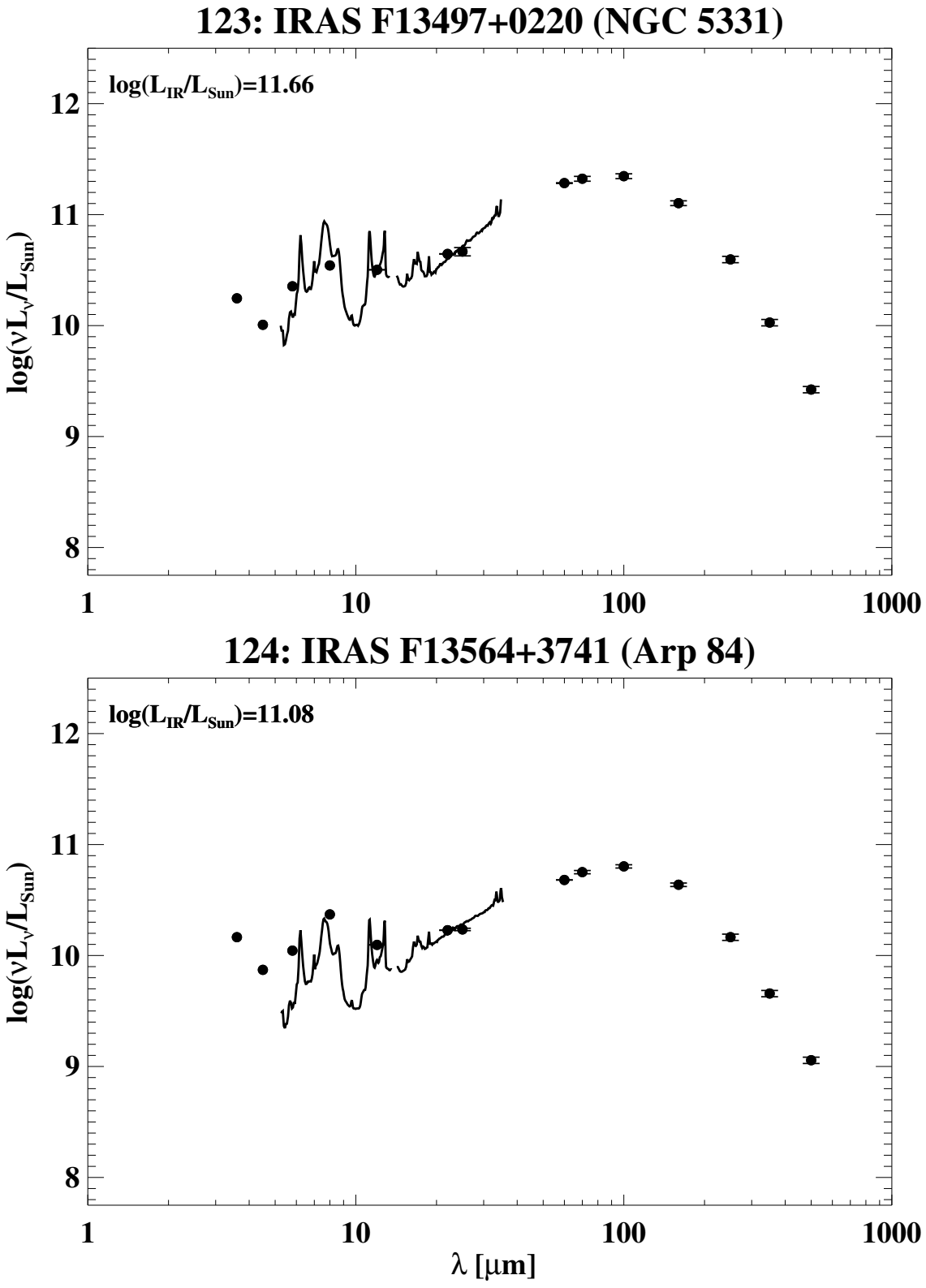

Figure A.1 continued (page 62 of 101).

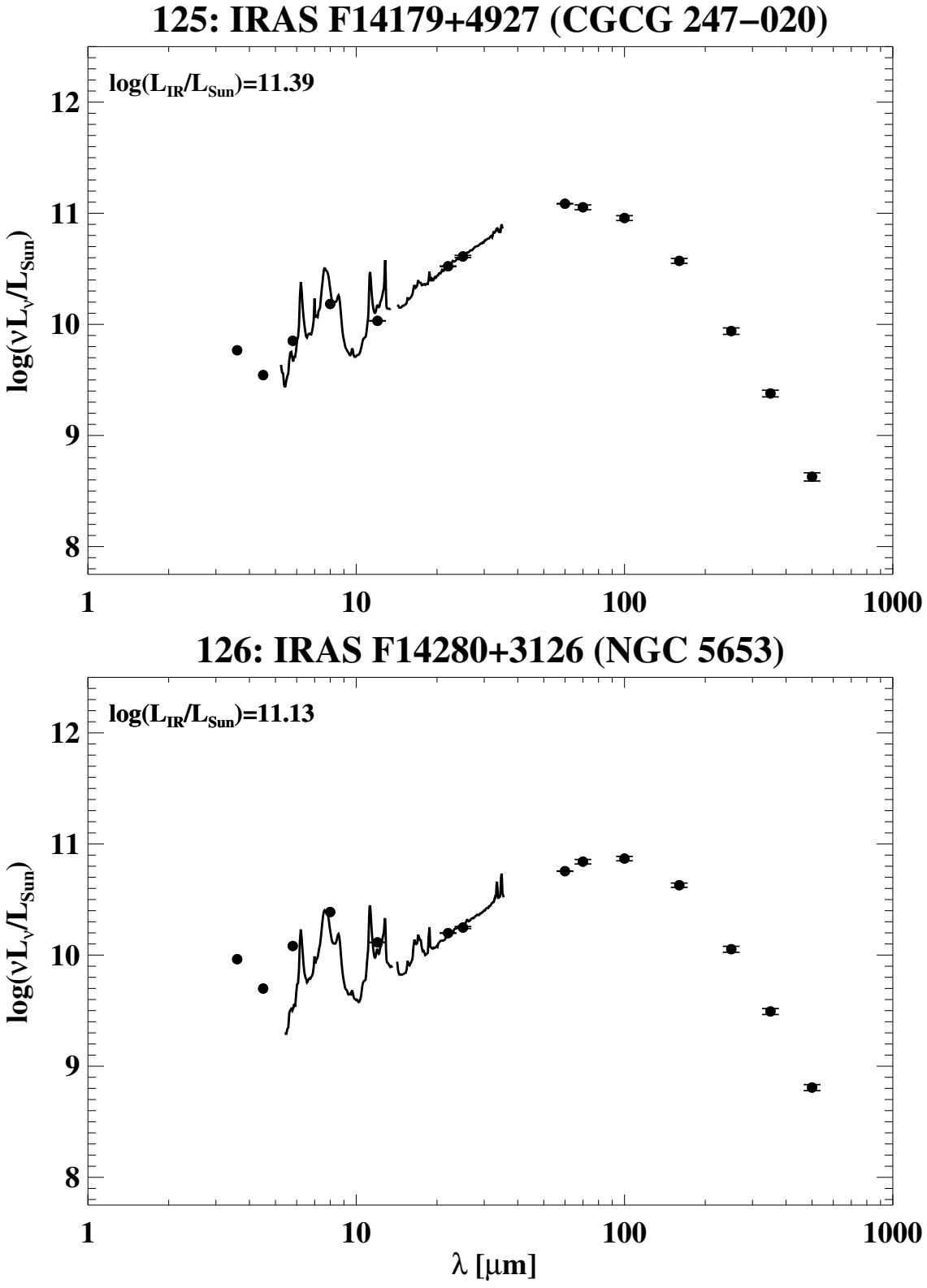

Figure A.1 continued (page 63 of 101).

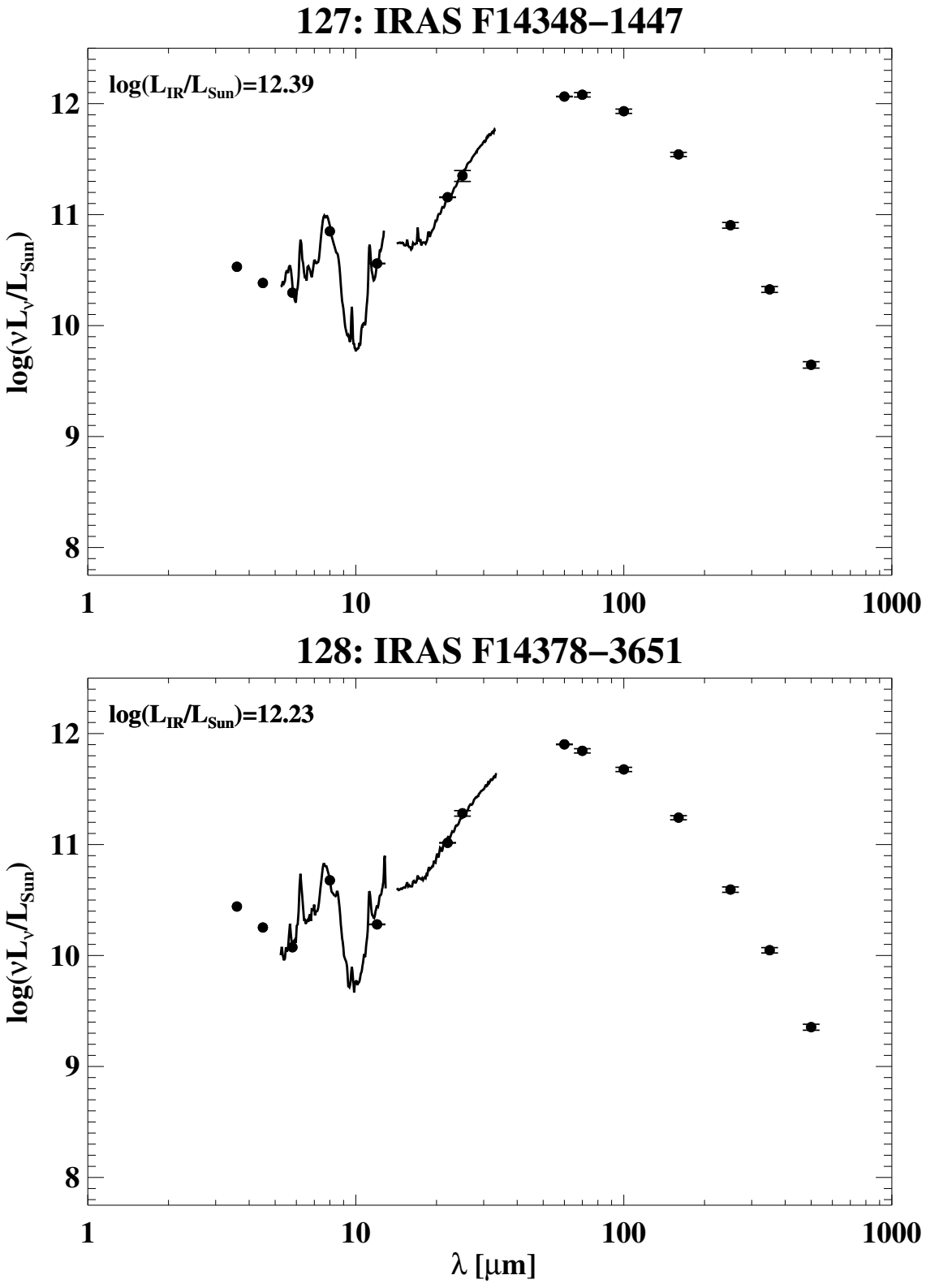

Figure A.1 continued (page 64 of 101).

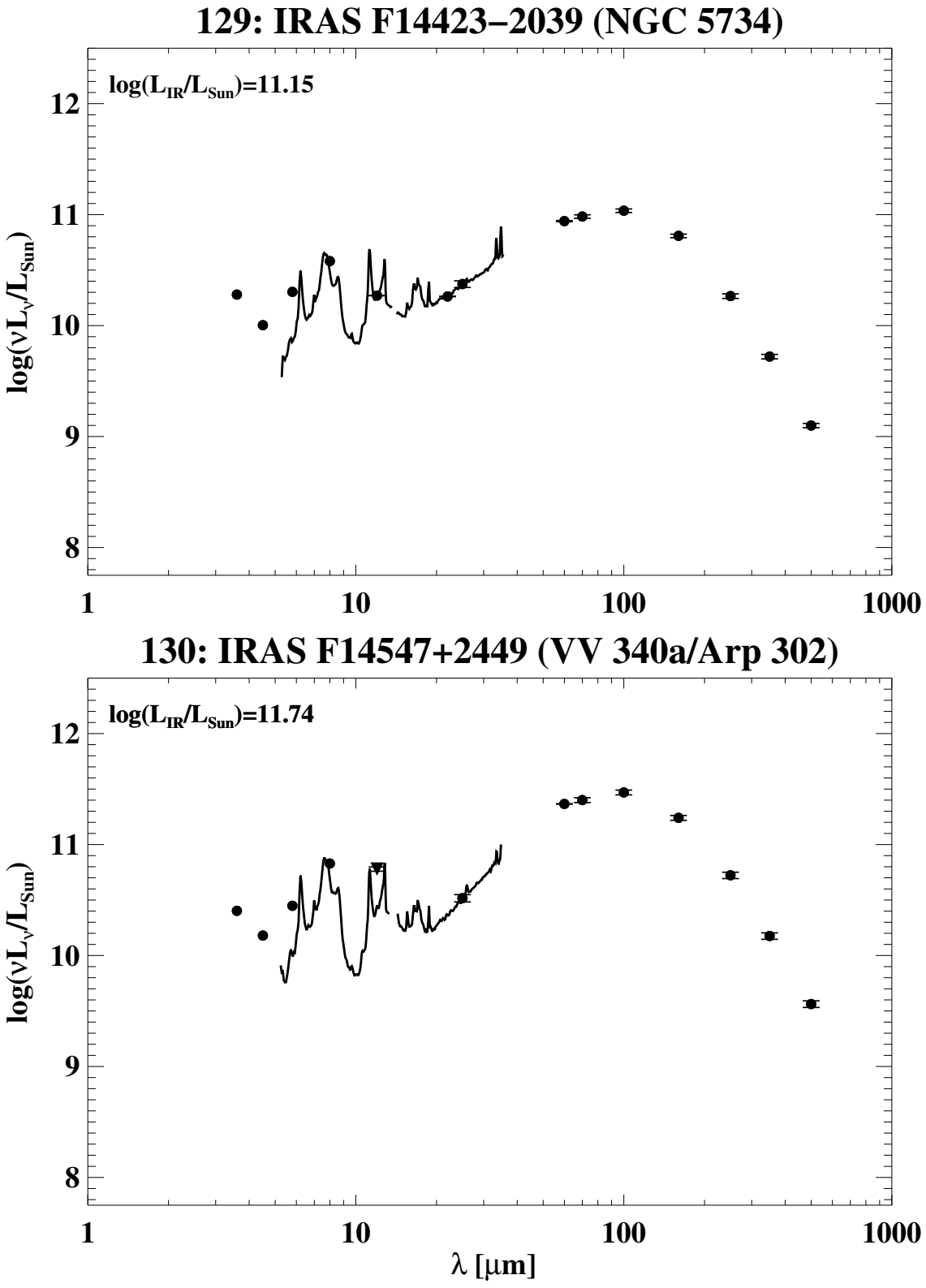

Figure A.1 continued (page 65 of 101).

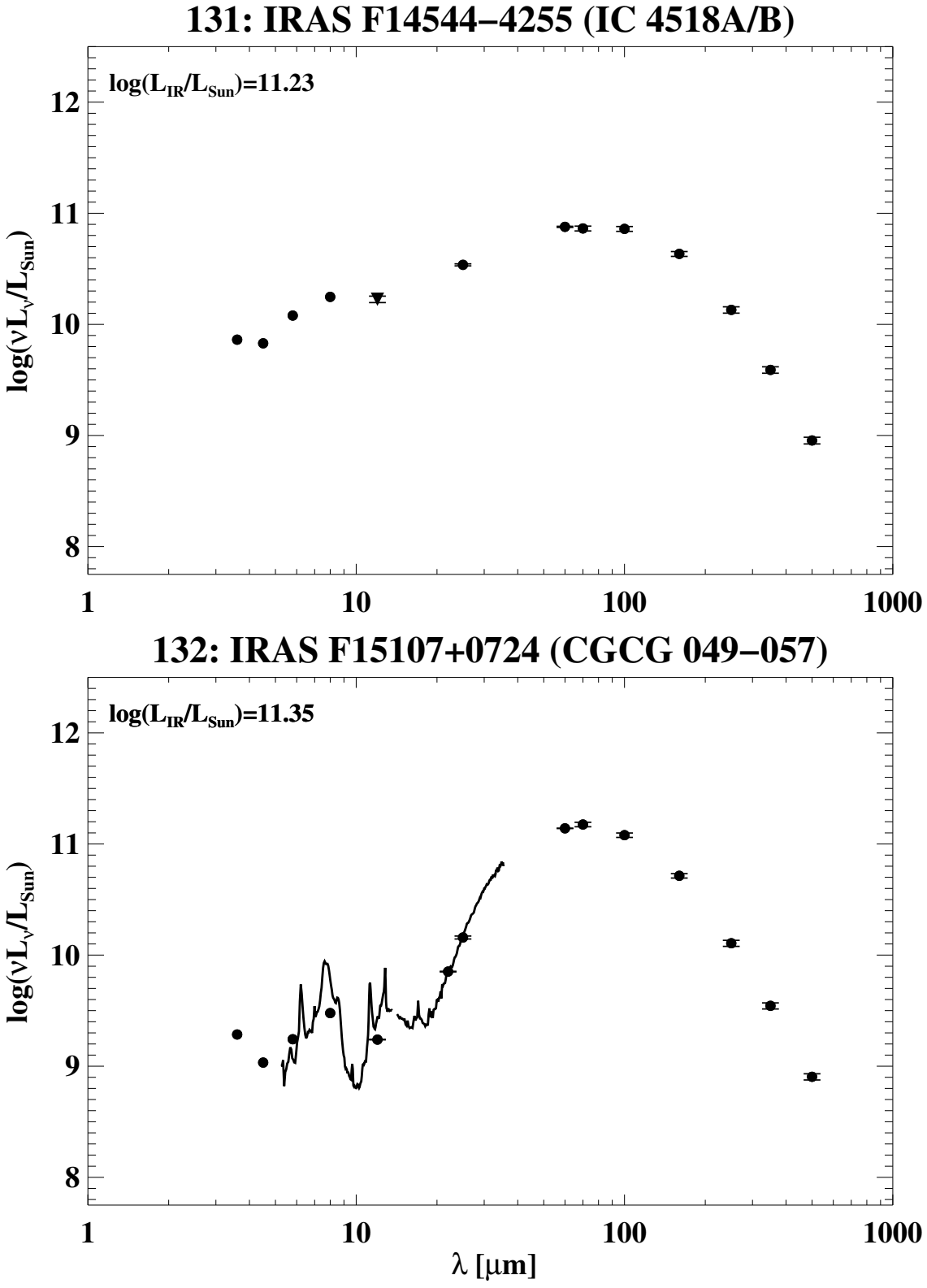

Figure A.1 continued (page 66 of 101).

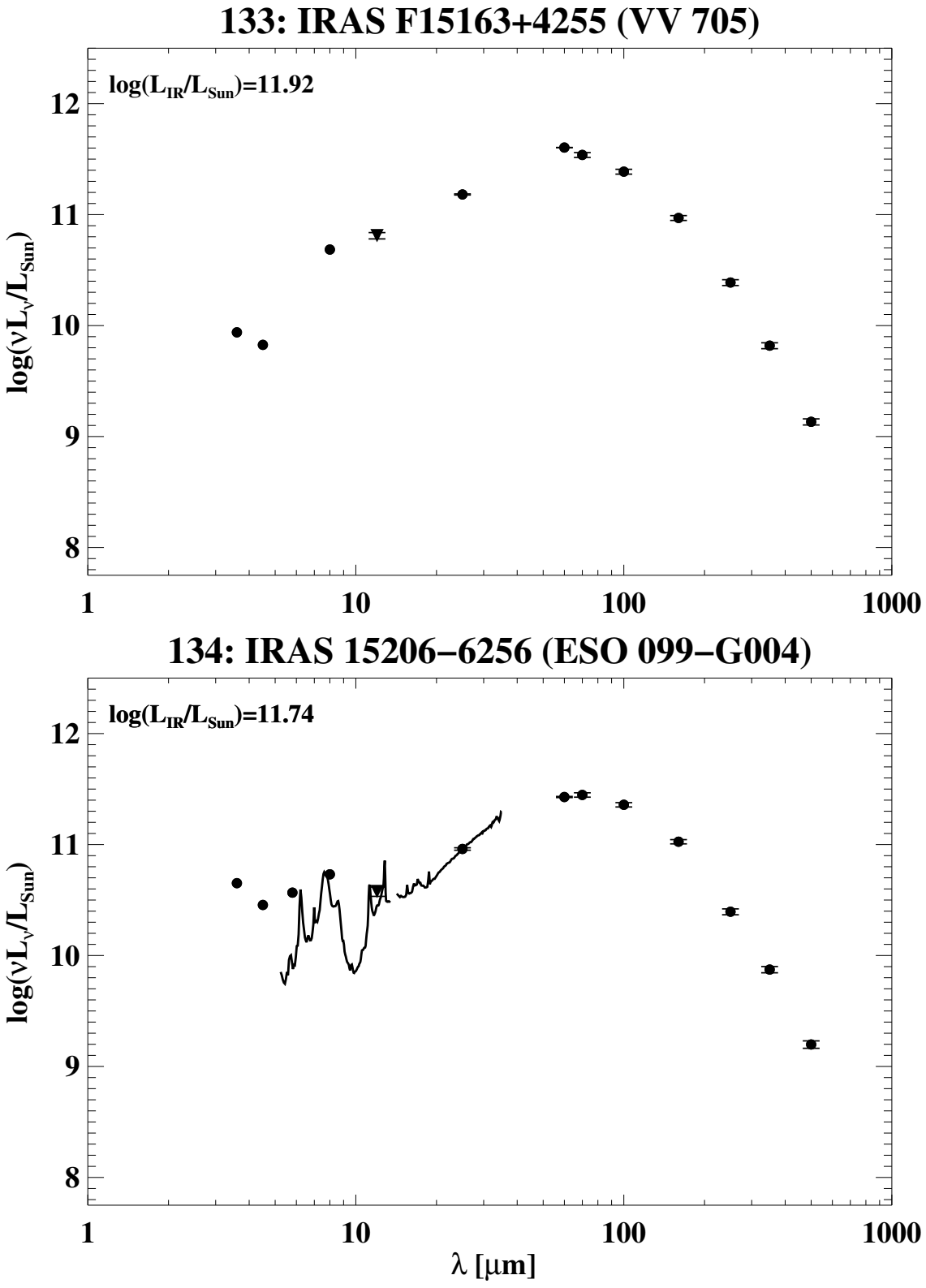

Figure A.1 continued (page 67 of 101).

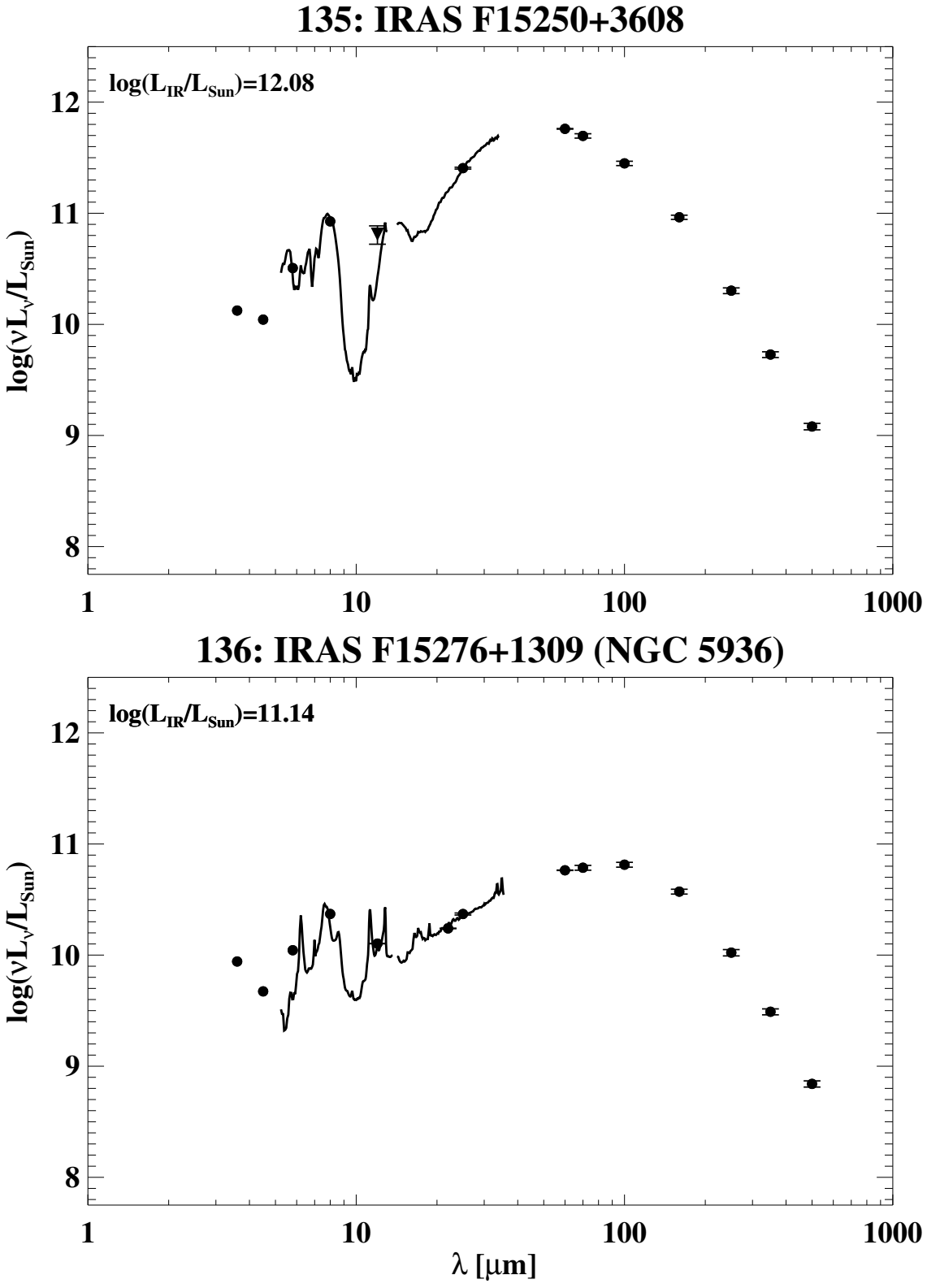

Figure A.1 continued (page 68 of 101).

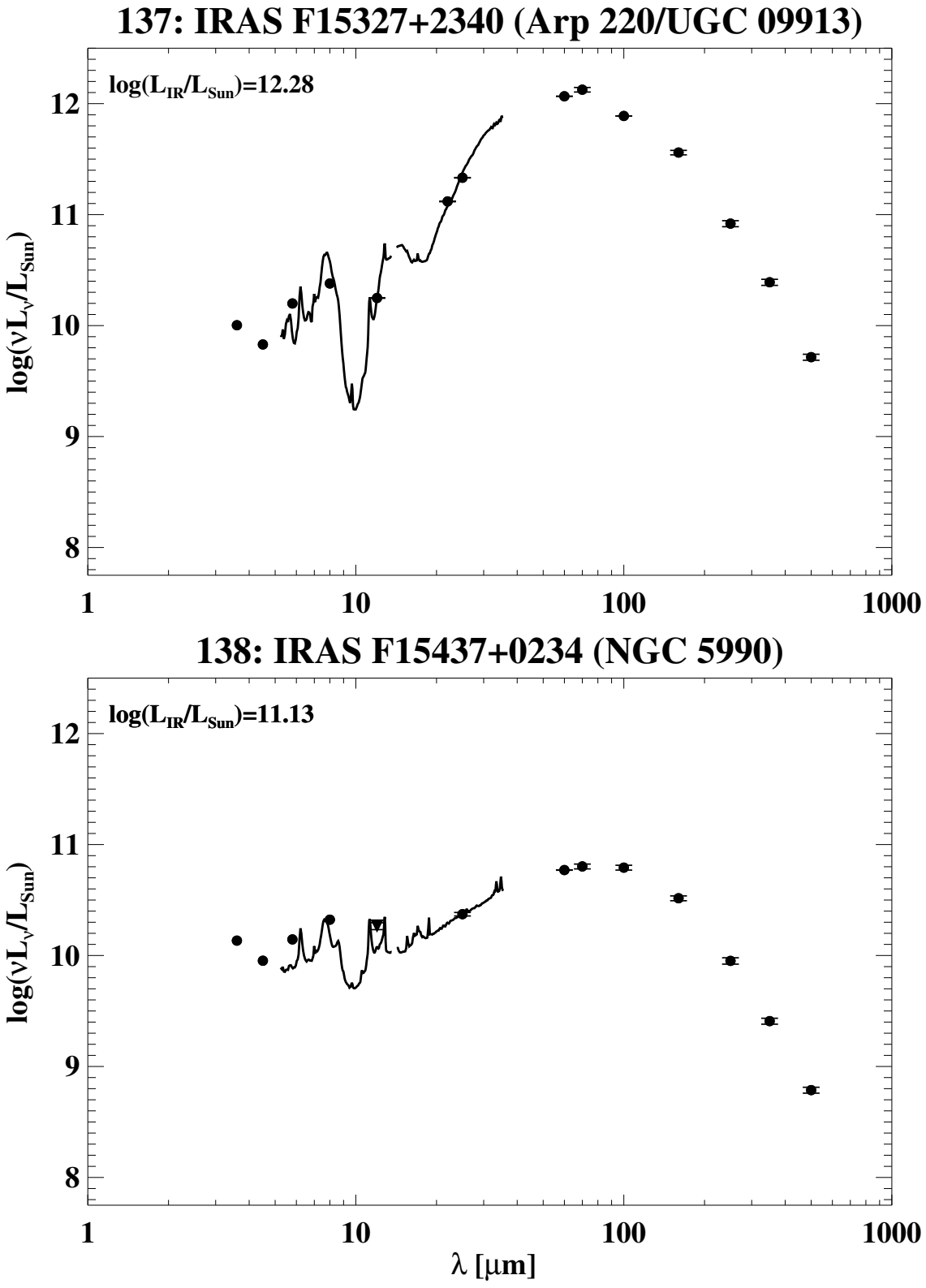

Figure A.1 continued (page 69 of 101).

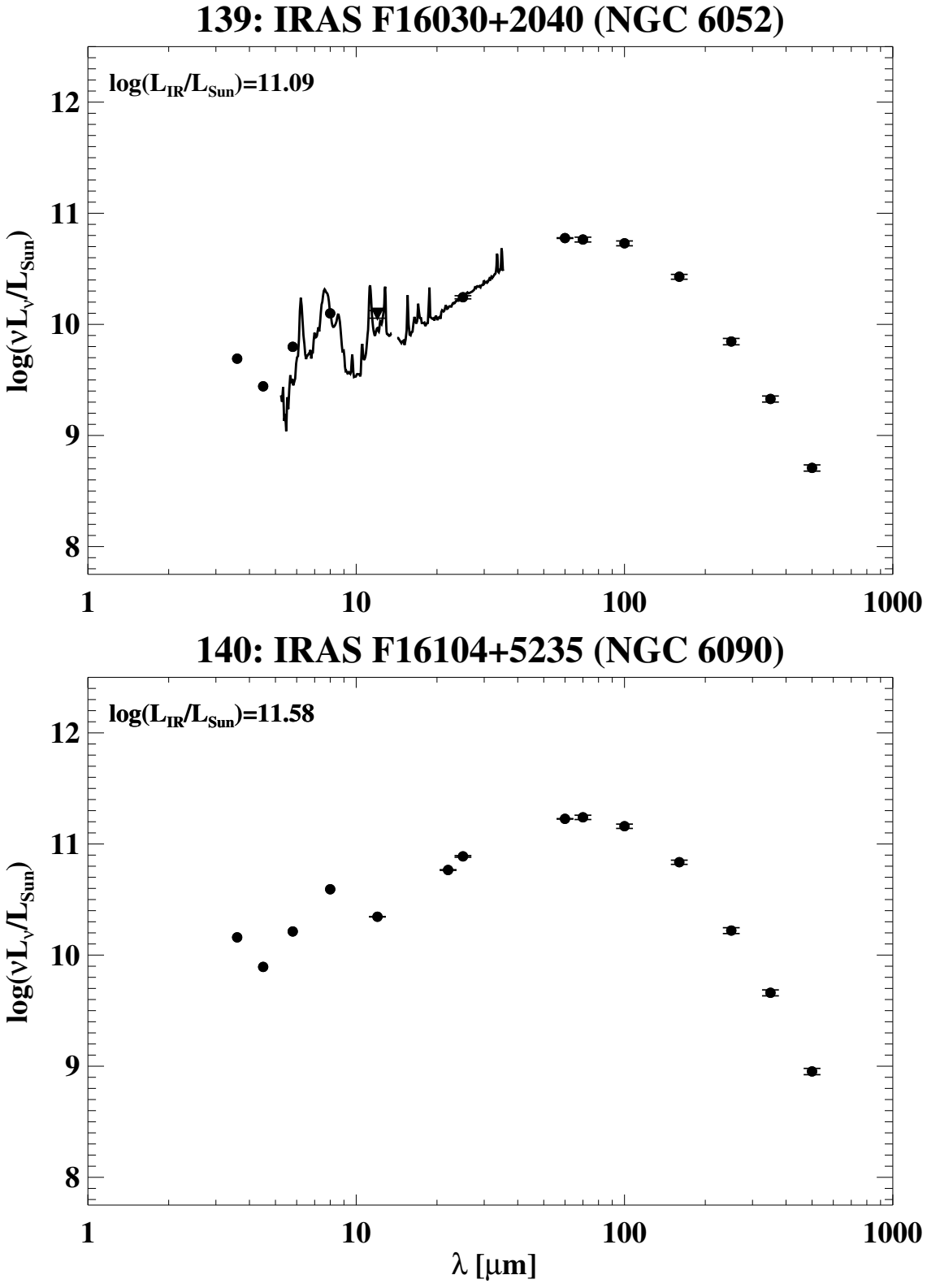

Figure A.1 continued (page 70 of 101).

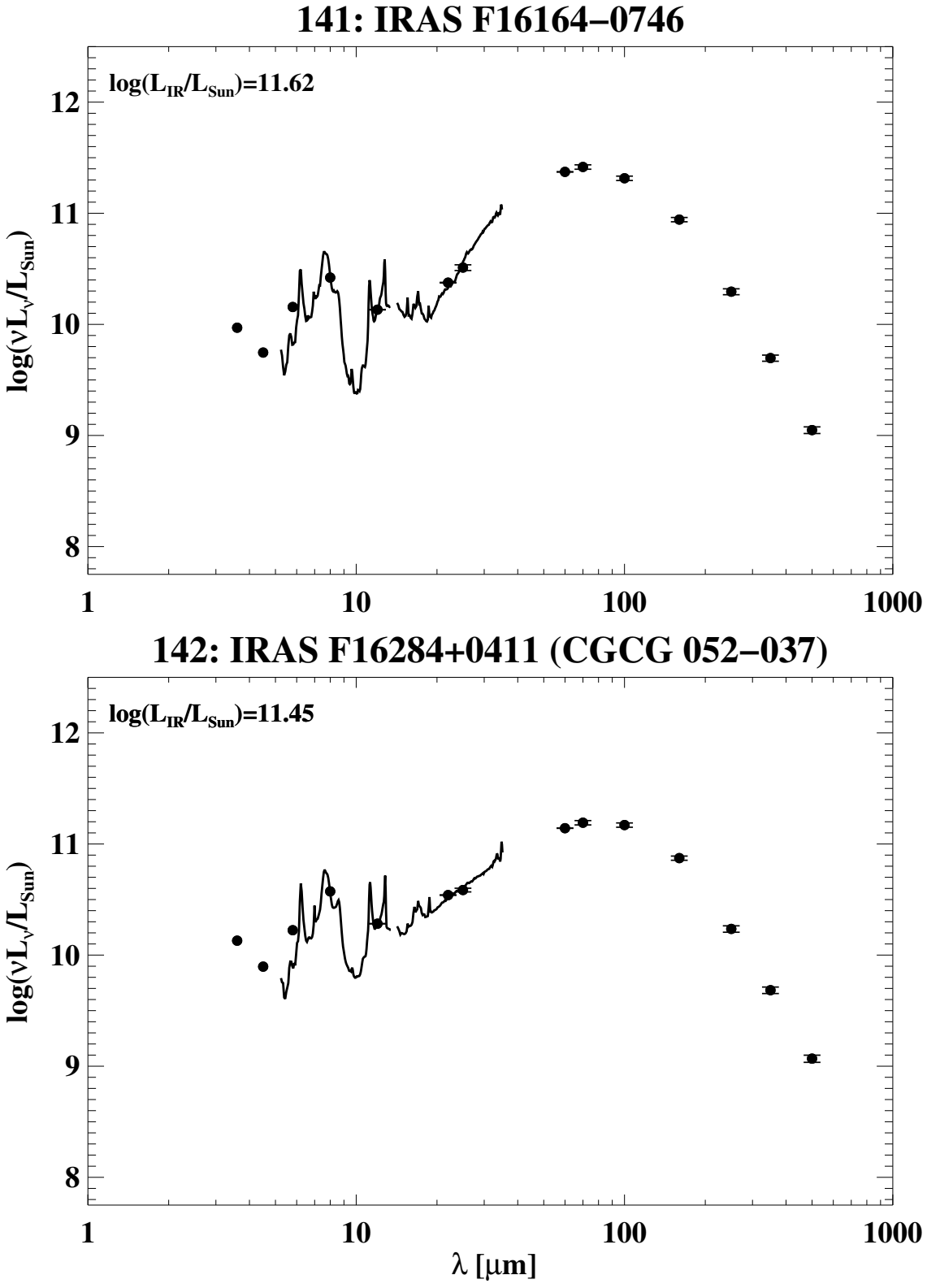

Figure A.1 continued (page 71 of 101).

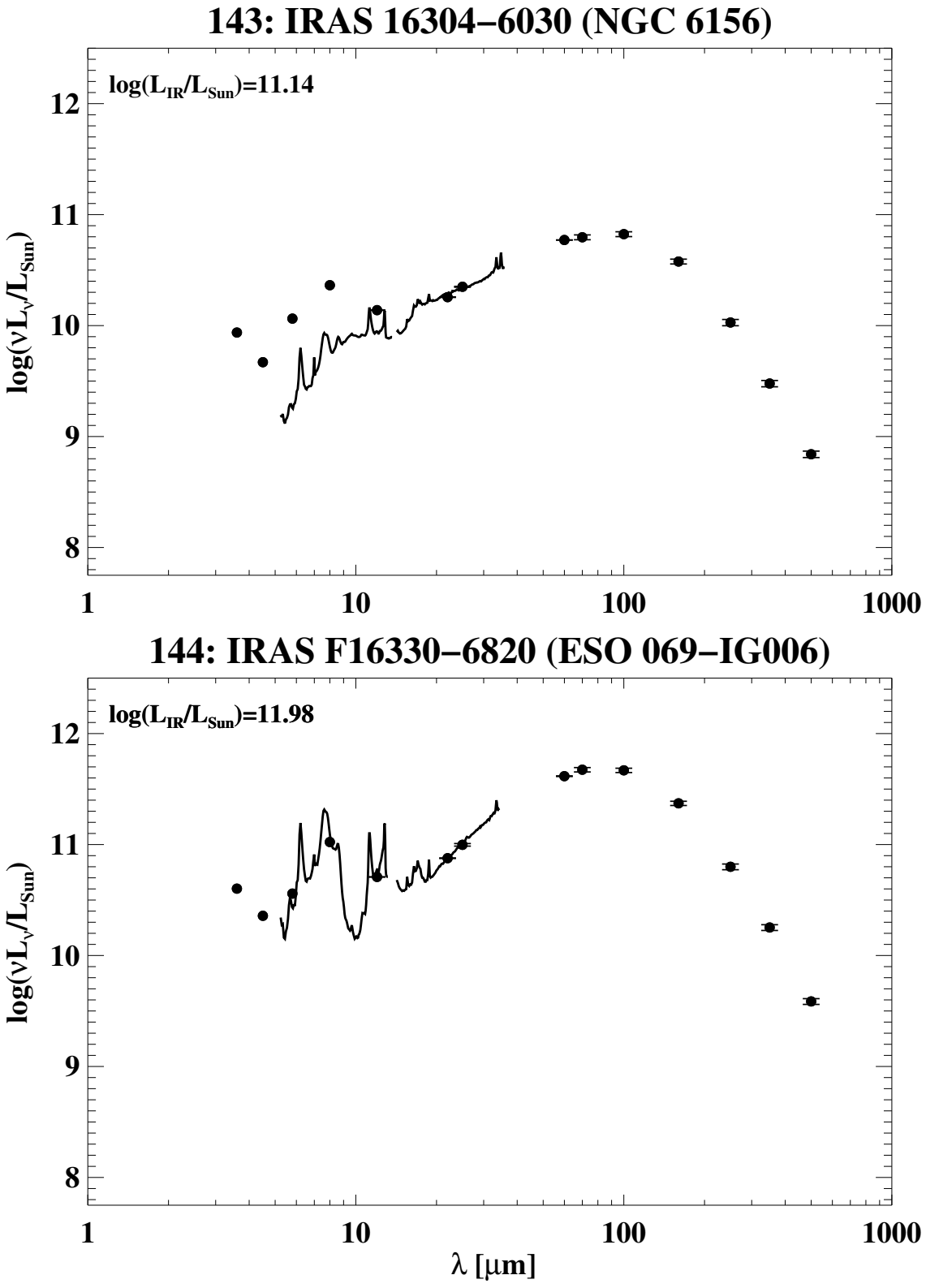

Figure A.1 continued (page 72 of 101).

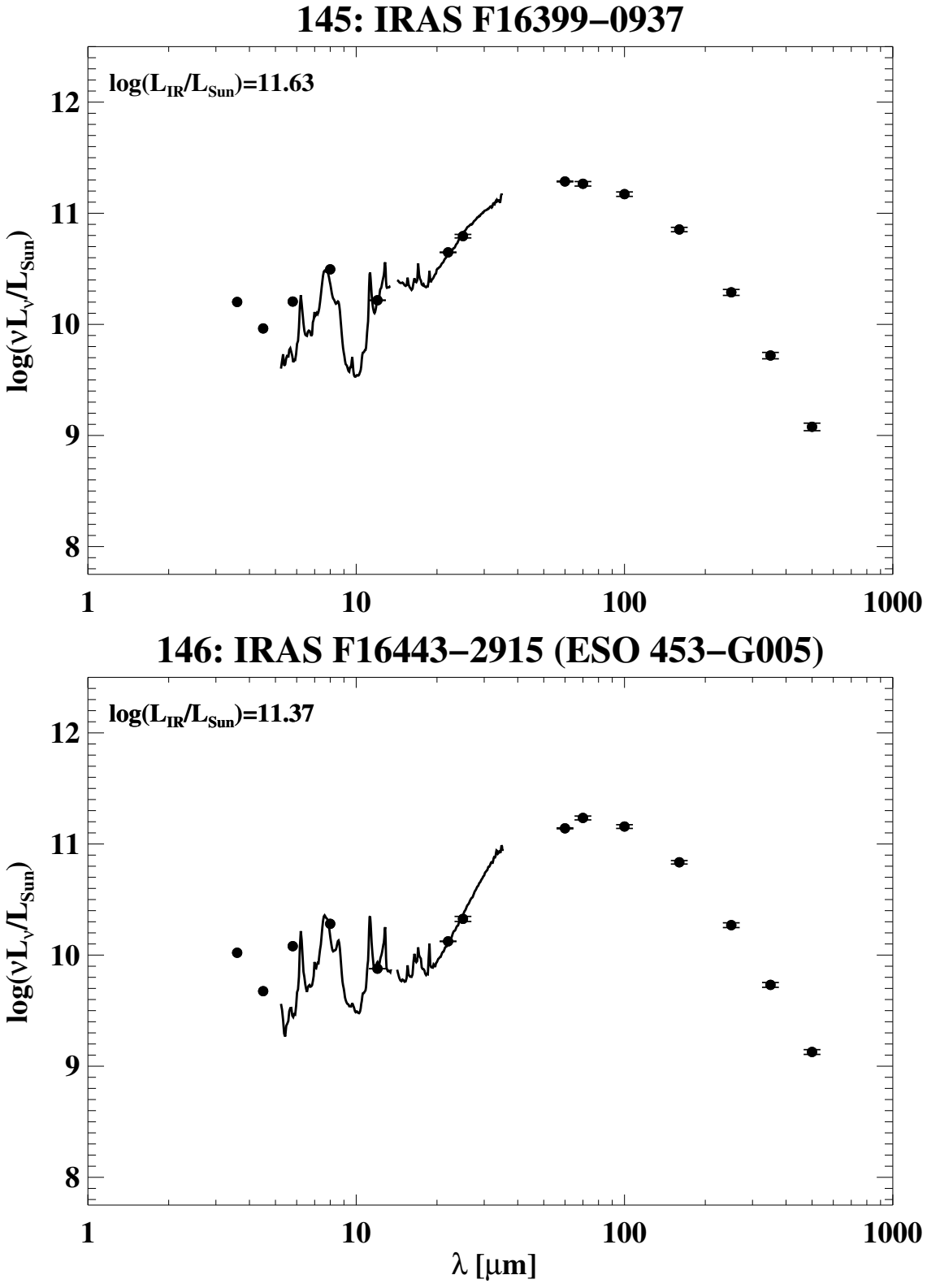

Figure A.1 continued (page 73 of 101).

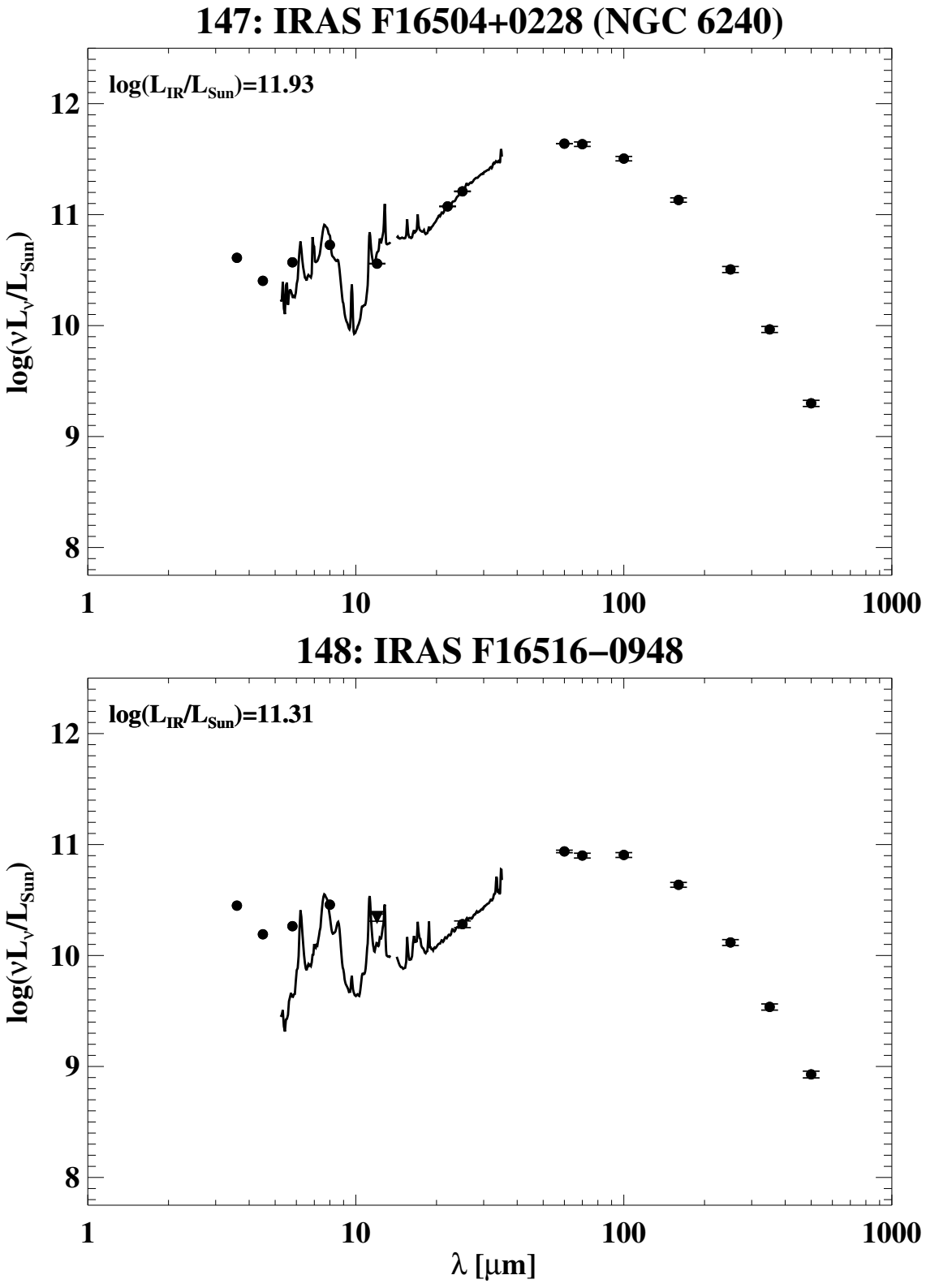

Figure A.1 continued (page 74 of 101).

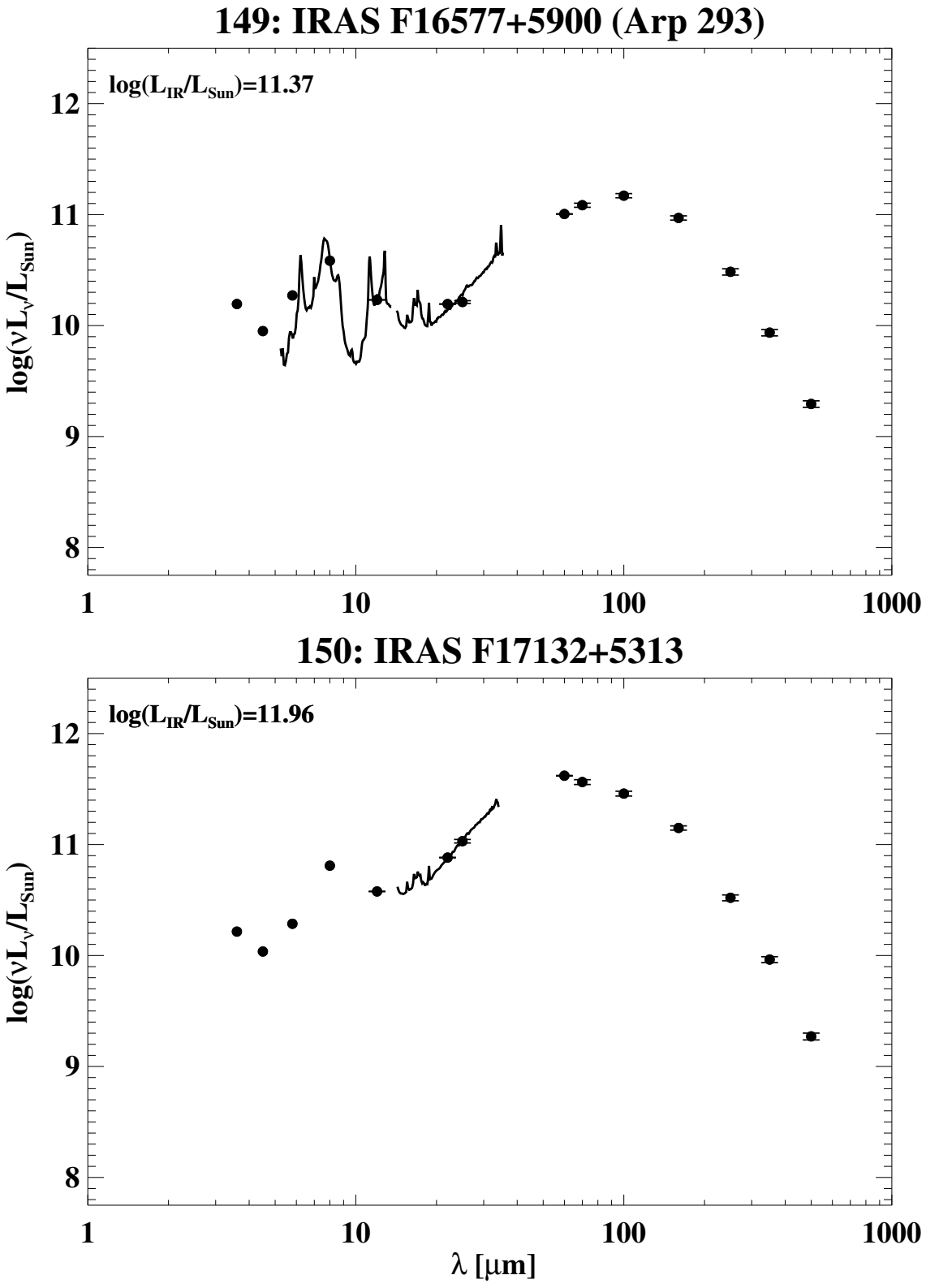

Figure A.1 continued (page 75 of 101).

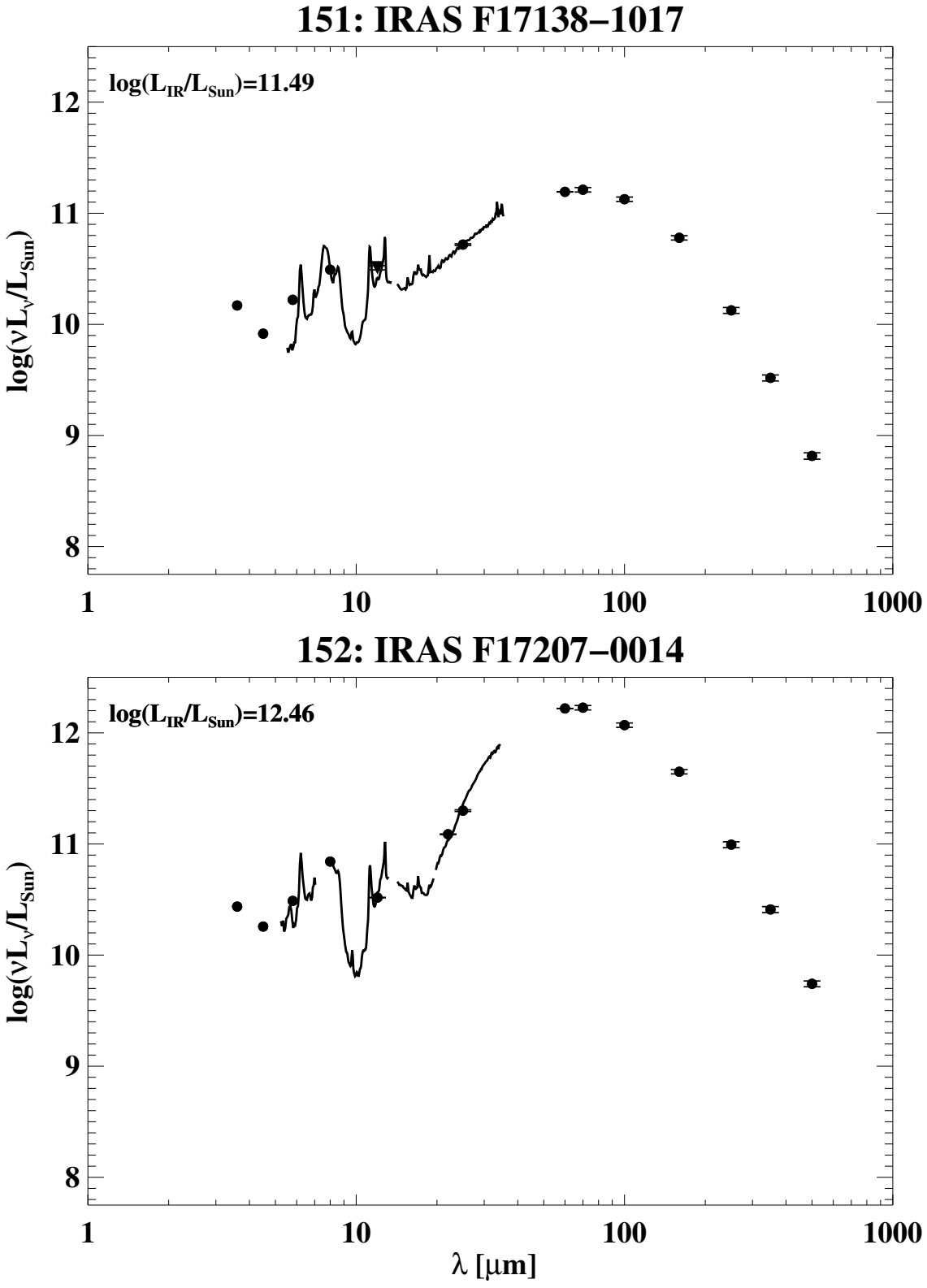

Figure A.1 continued (page 76 of 101).

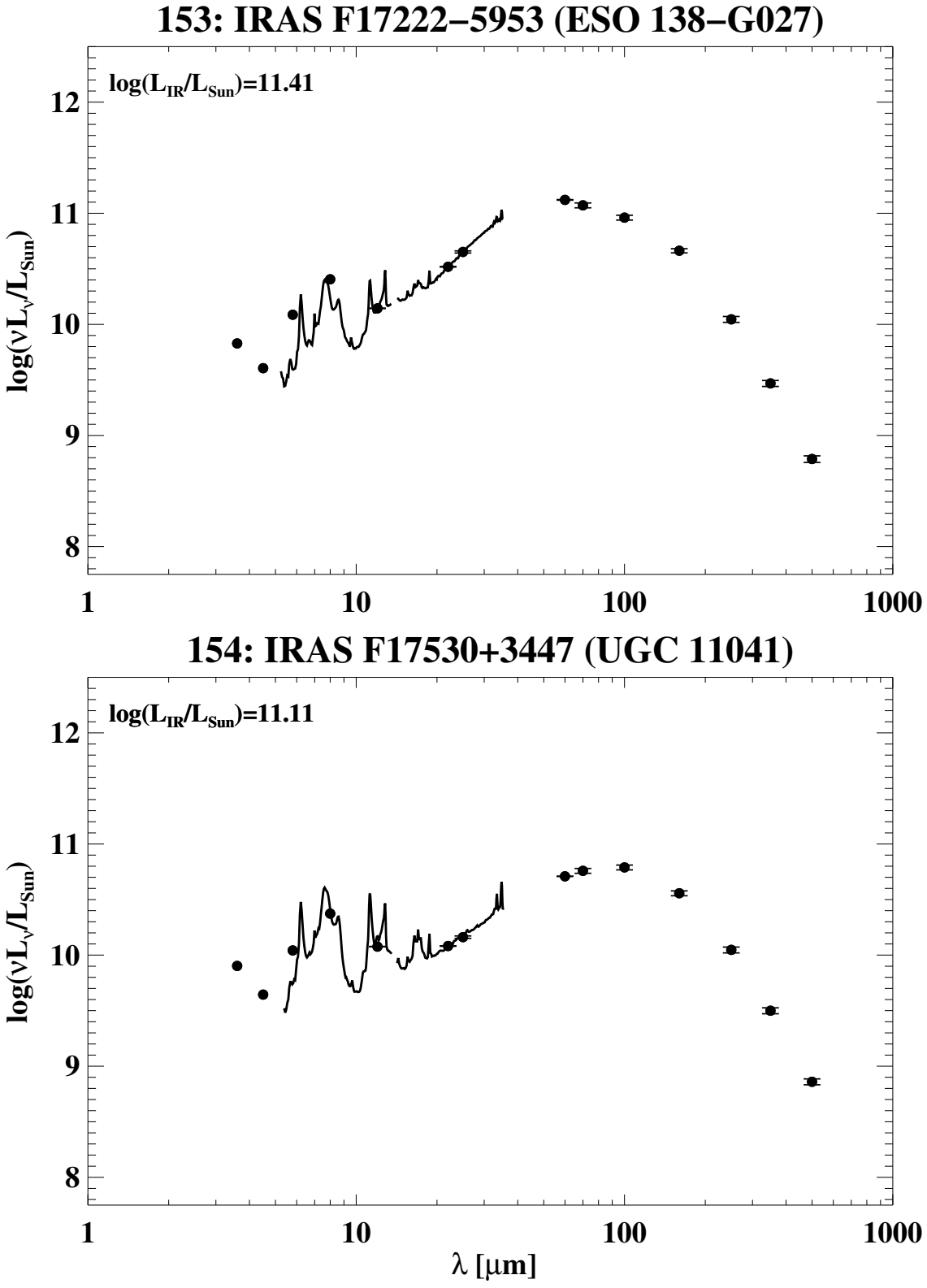

Figure A.1 continued (page 77 of 101).

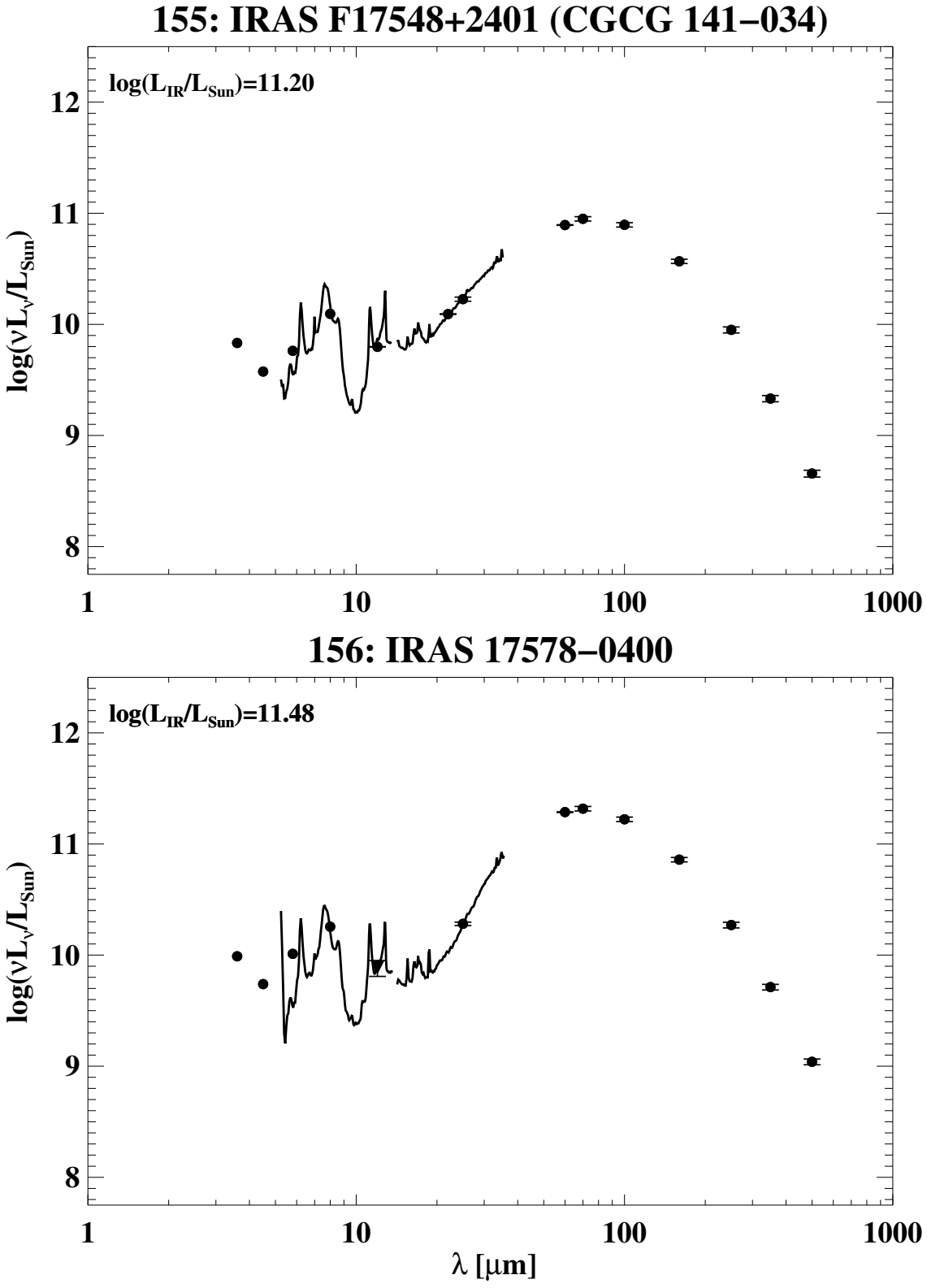

Figure A.1 continued (page 78 of 101).

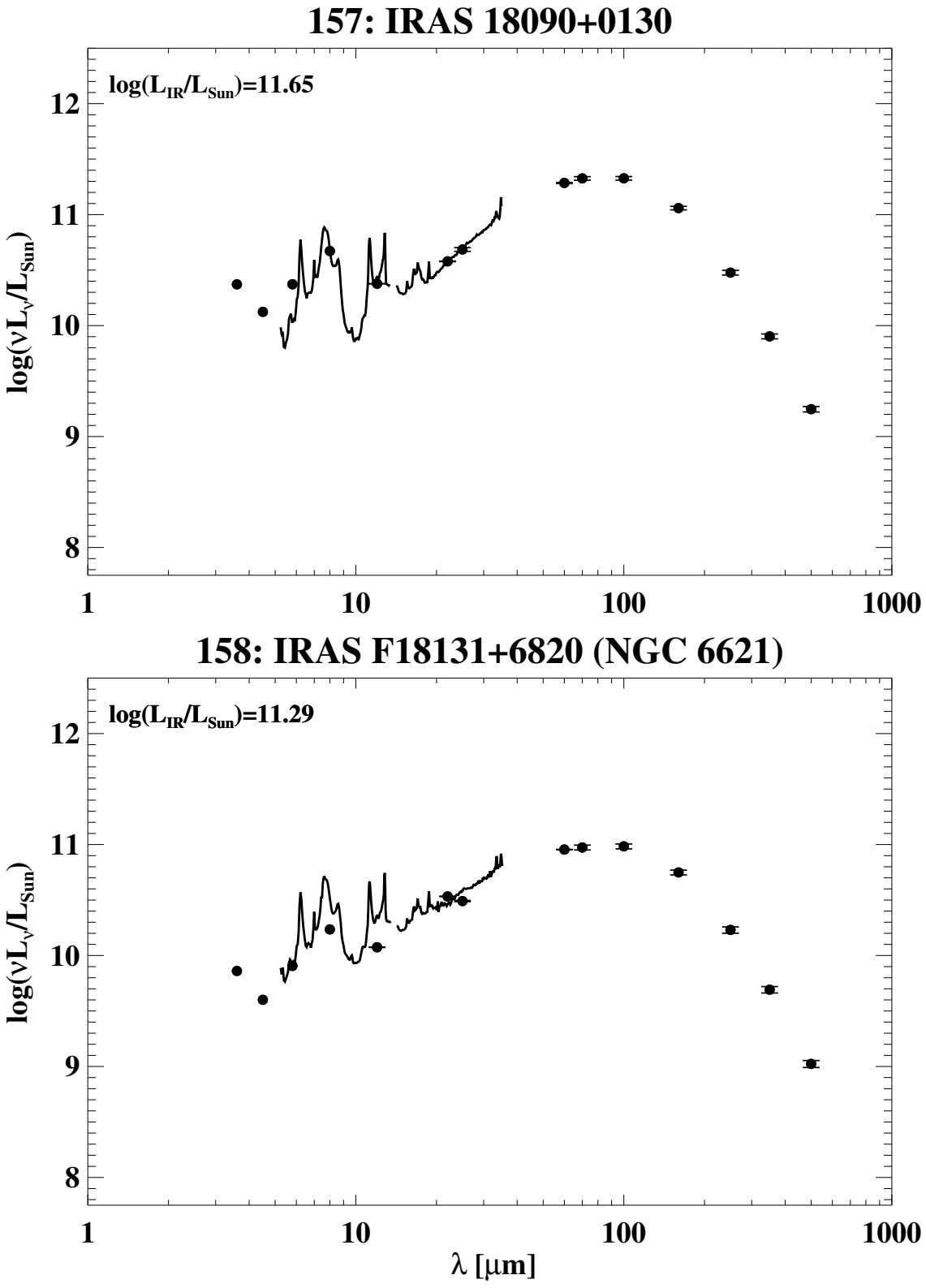

Figure A.1 continued (page 79 of 101).

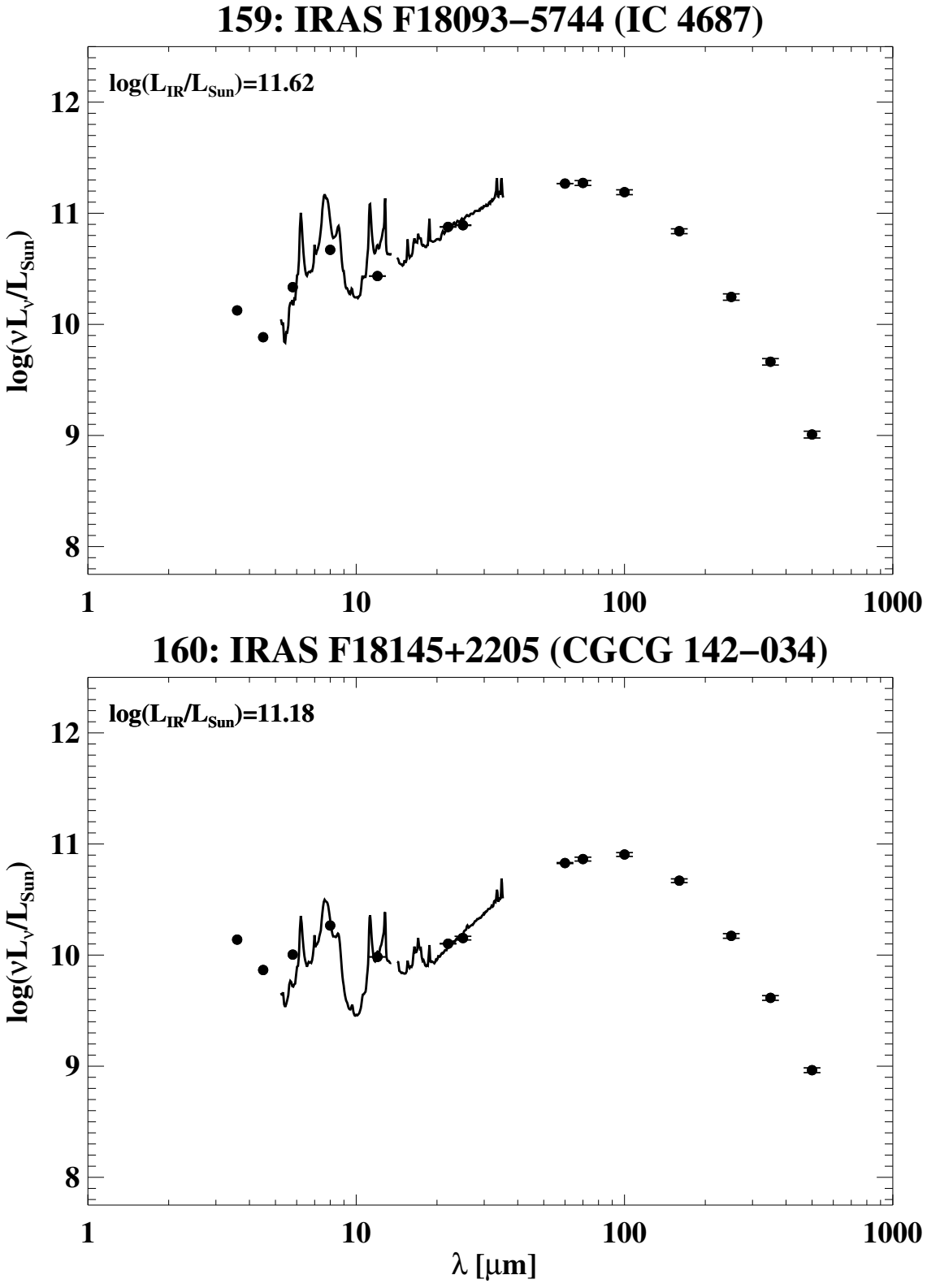

Figure A.1 continued (page 80 of 101).

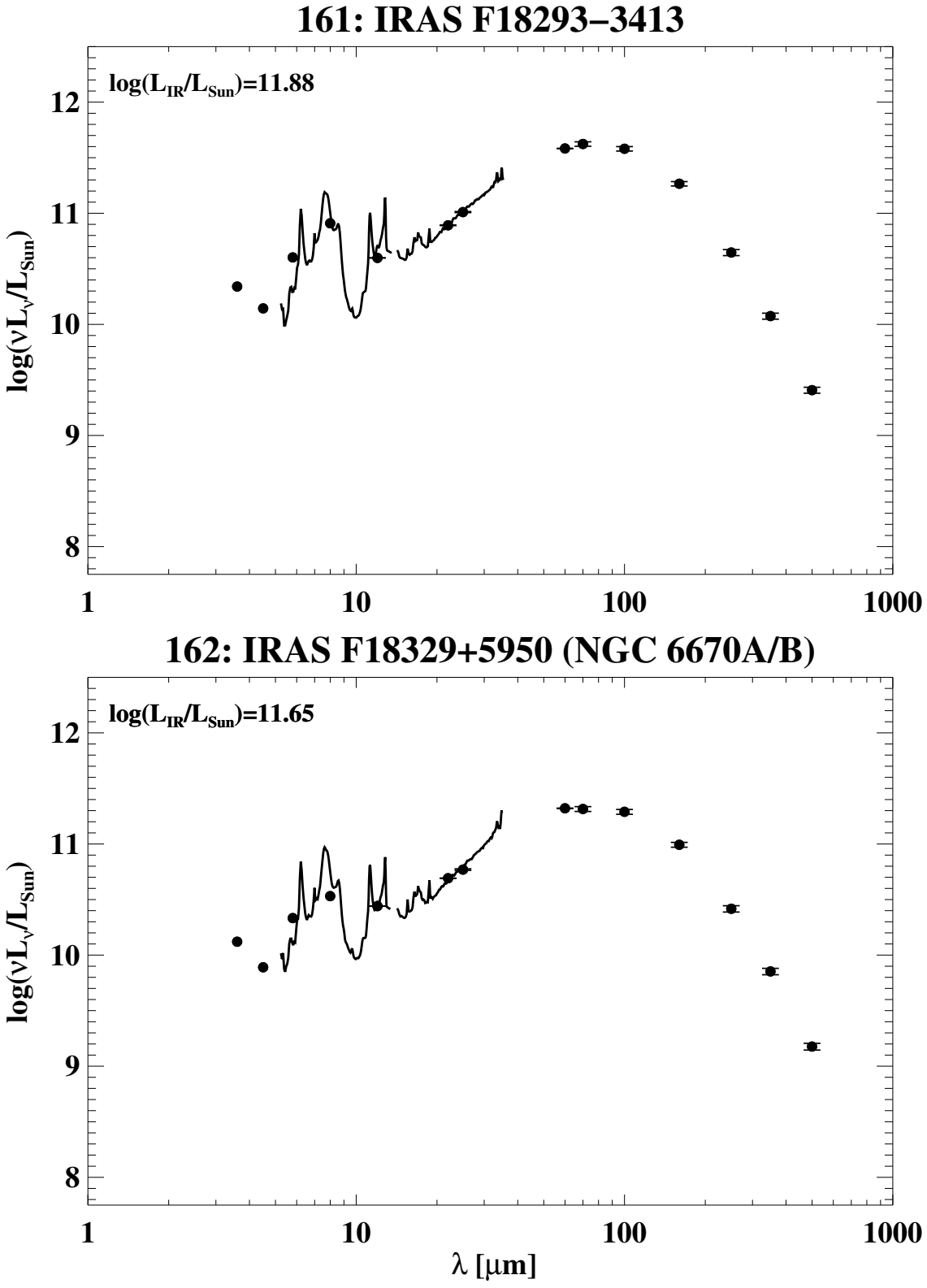

Figure A.1 continued (page 81 of 101).

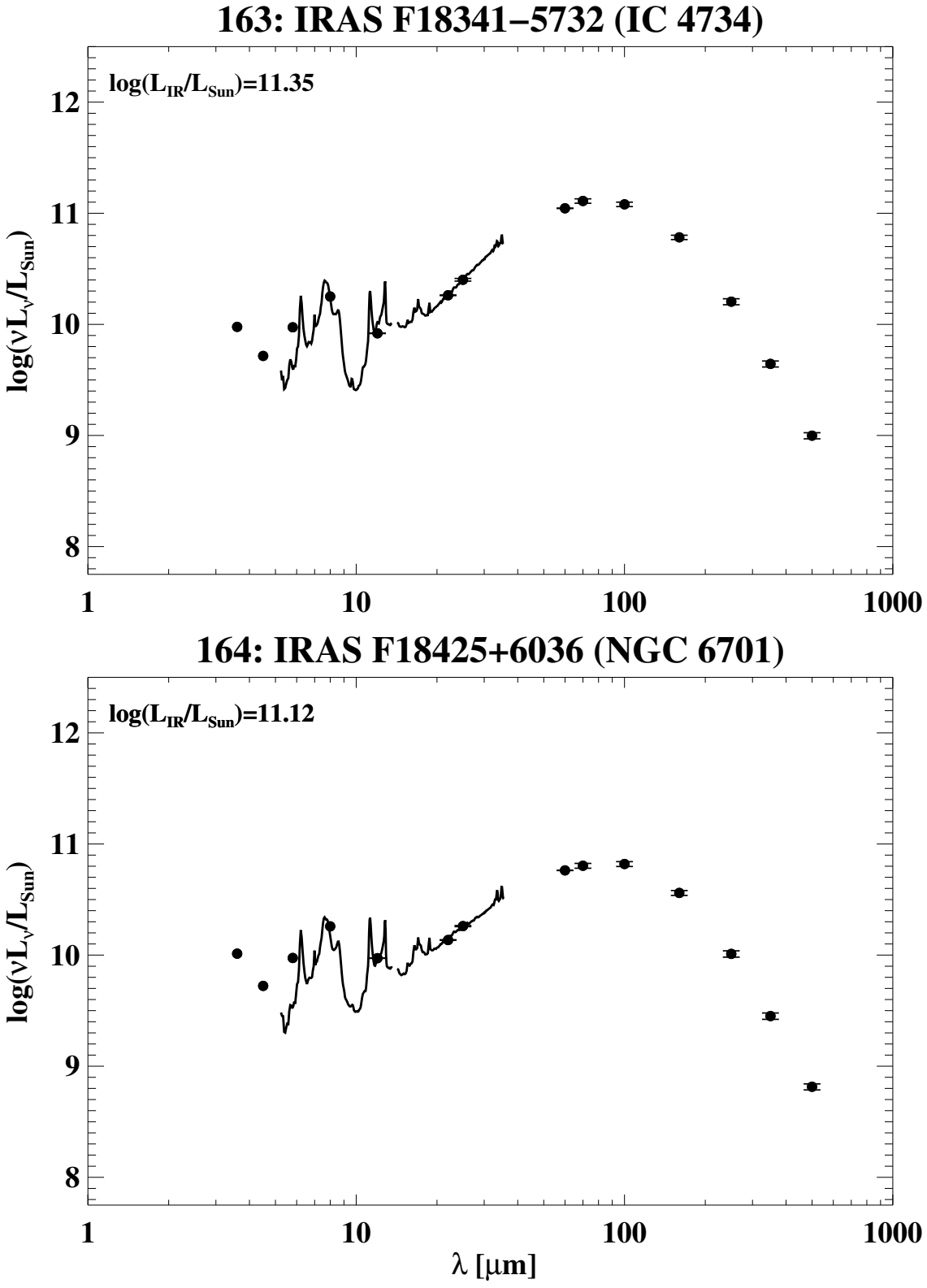

Figure A.1 continued (page 82 of 101).

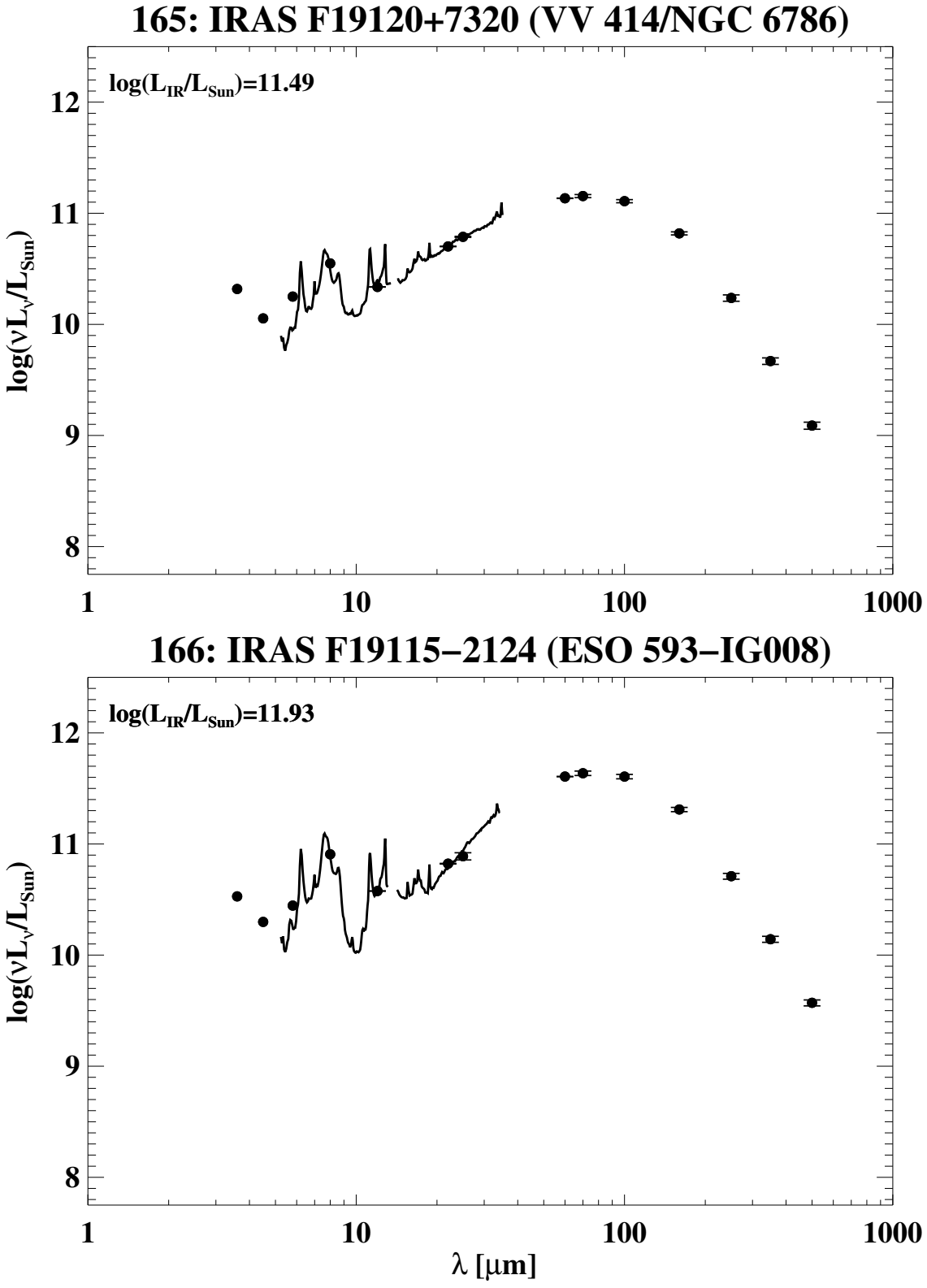

Figure A.1 continued (page 83 of 101).

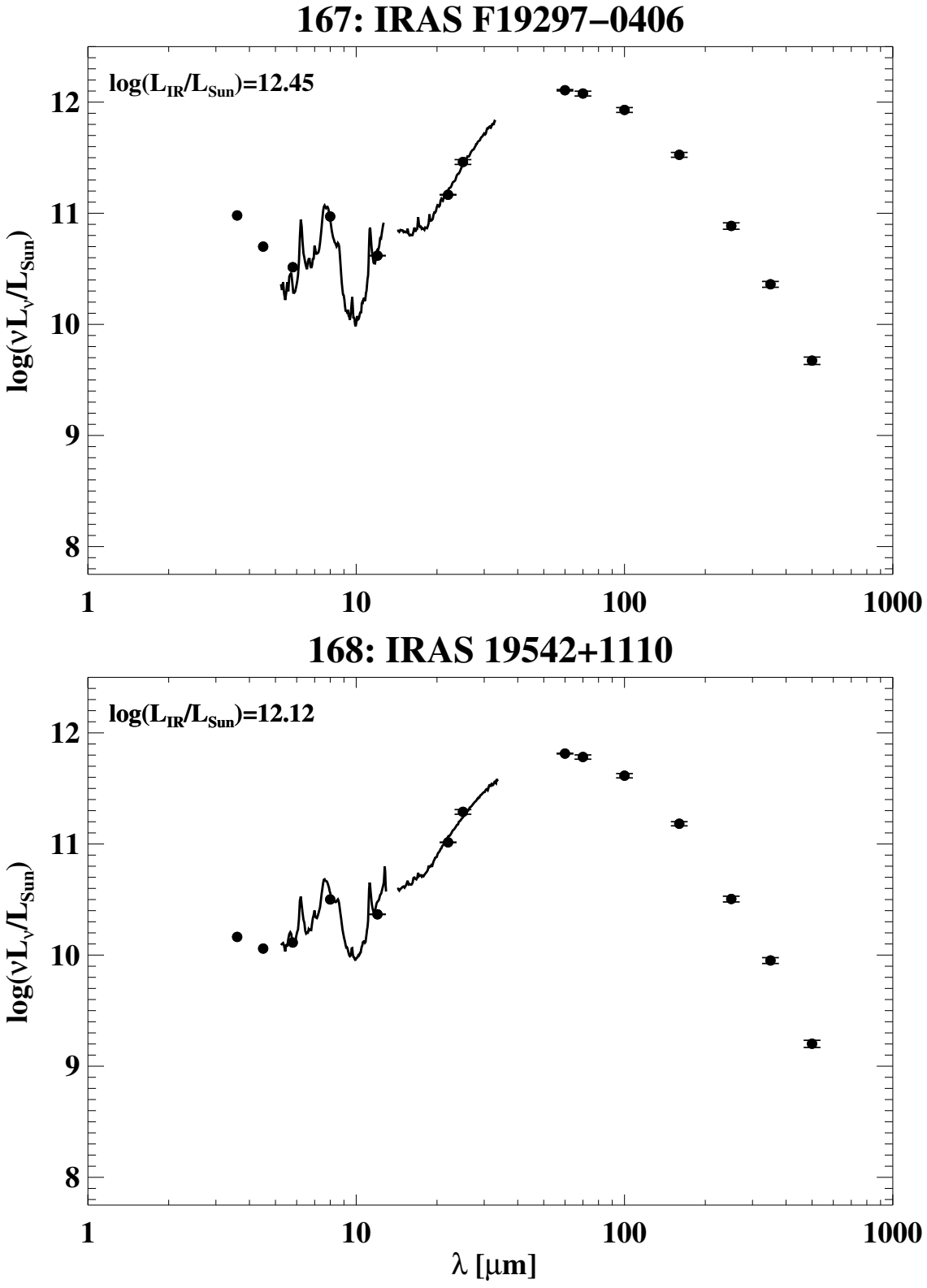

Figure A.1 continued (page 84 of 101).

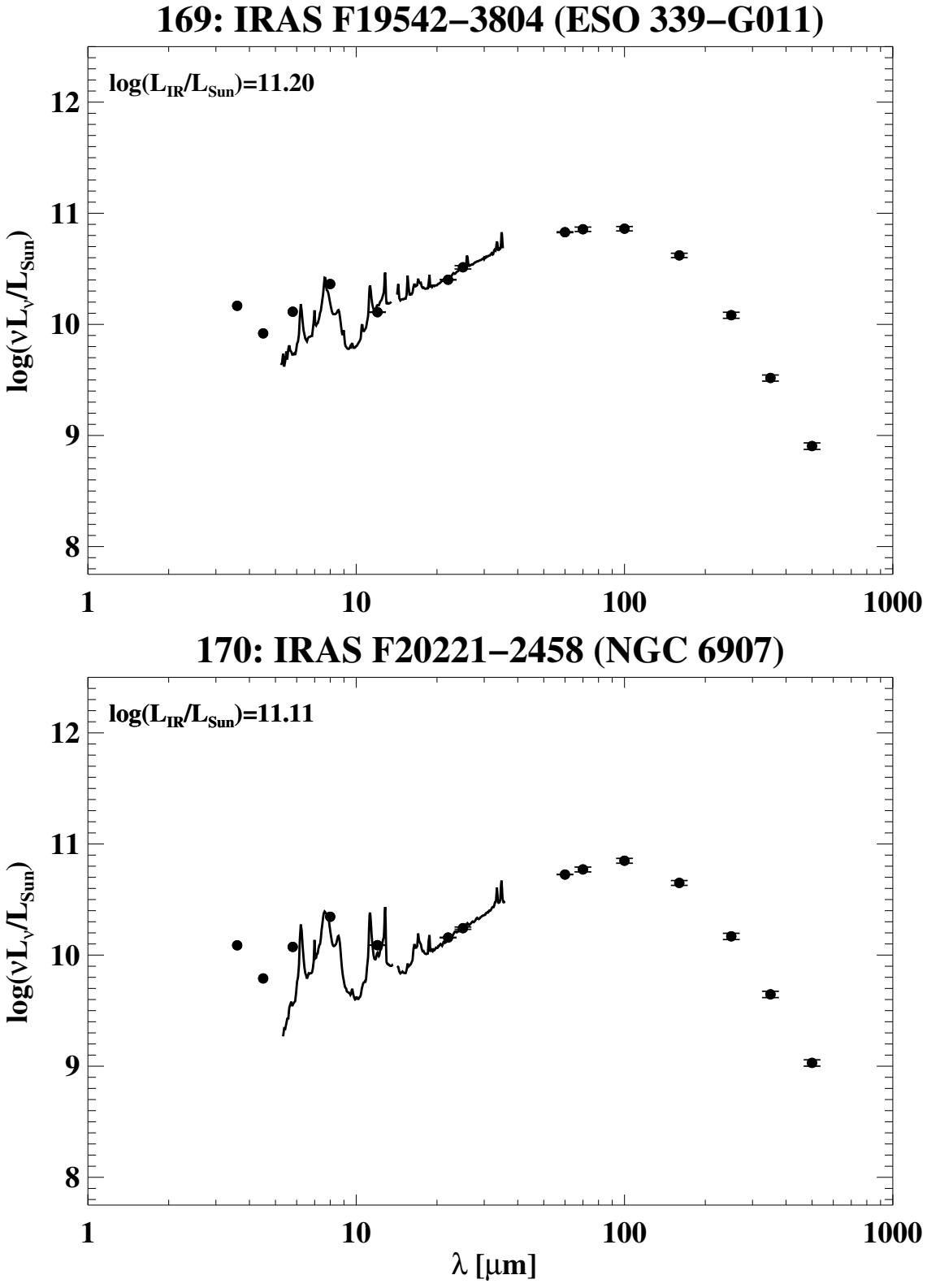

Figure A.1 continued (page 85 of 101).

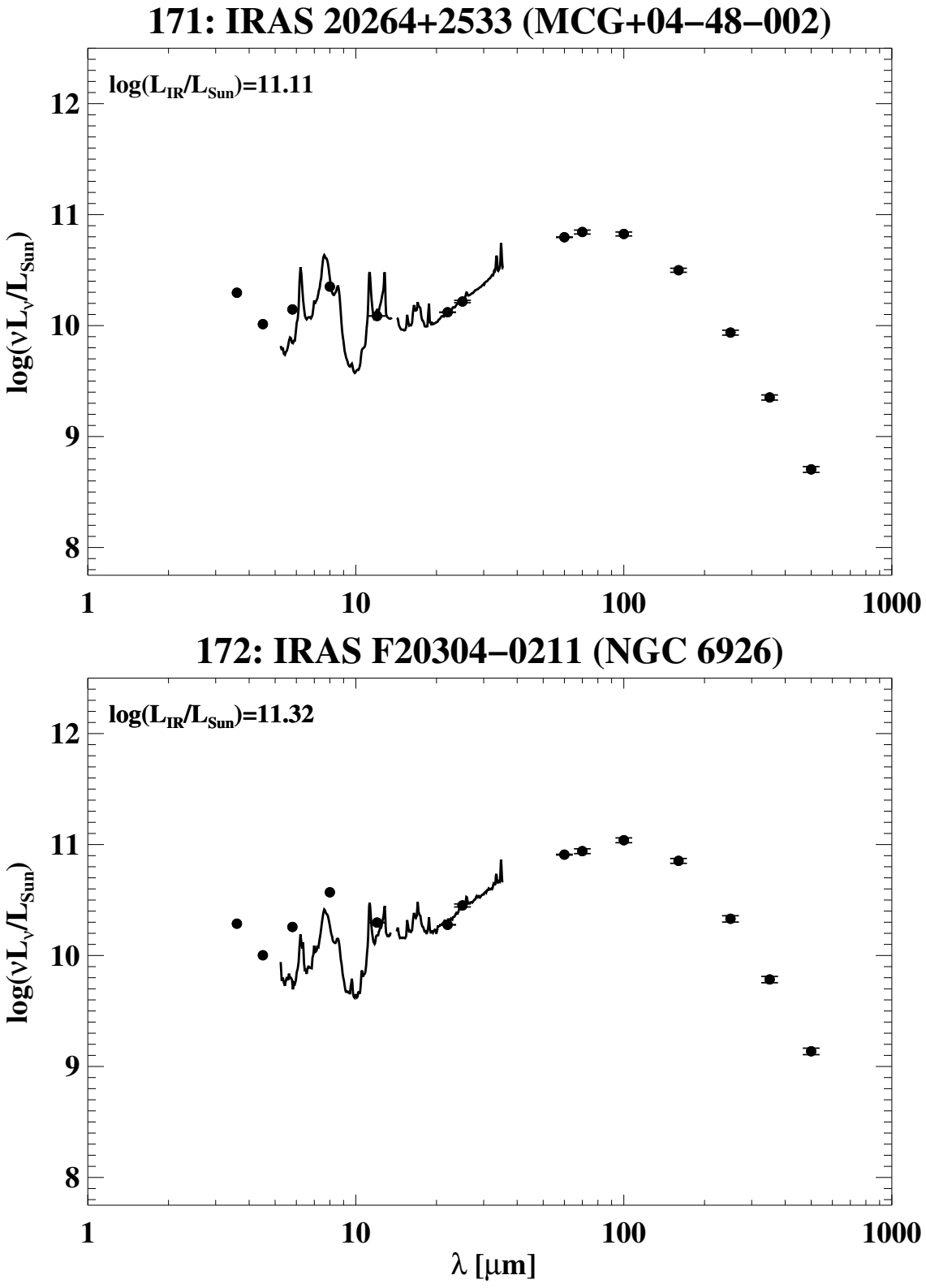

Figure A.1 continued (page 86 of 101).

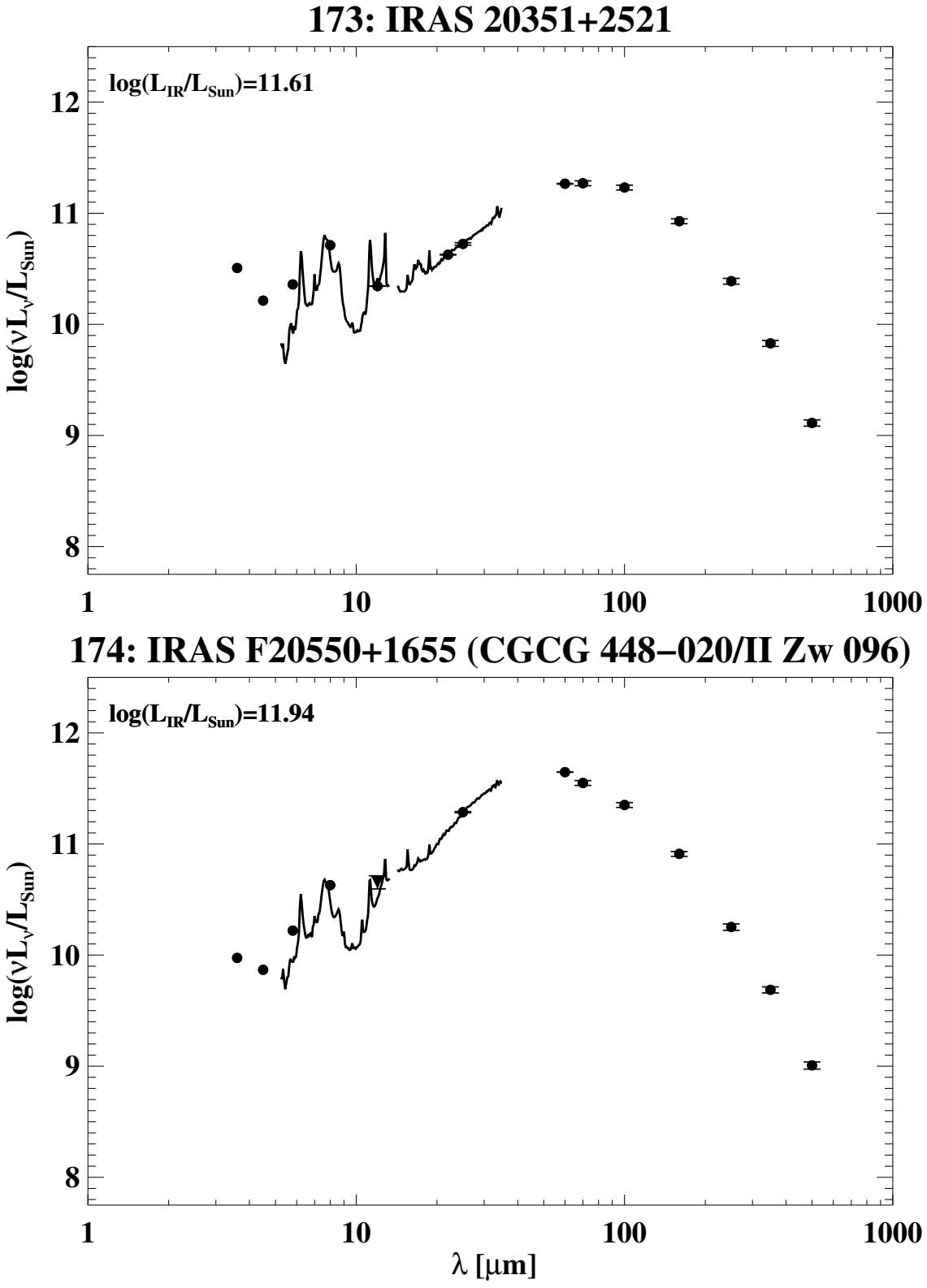

Figure A.1 continued (page 87 of 101).

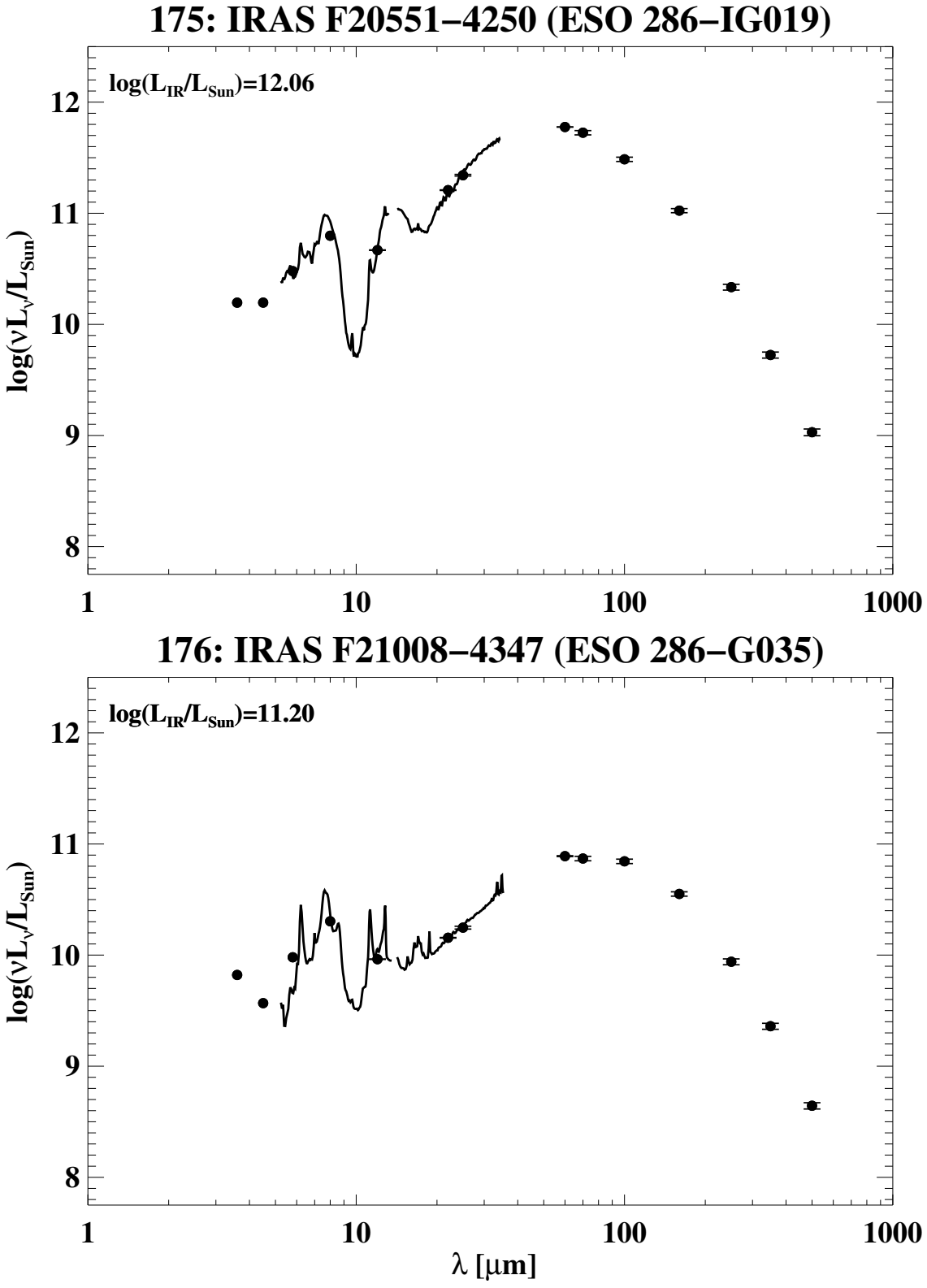

Figure A.1 continued (page 88 of 101).

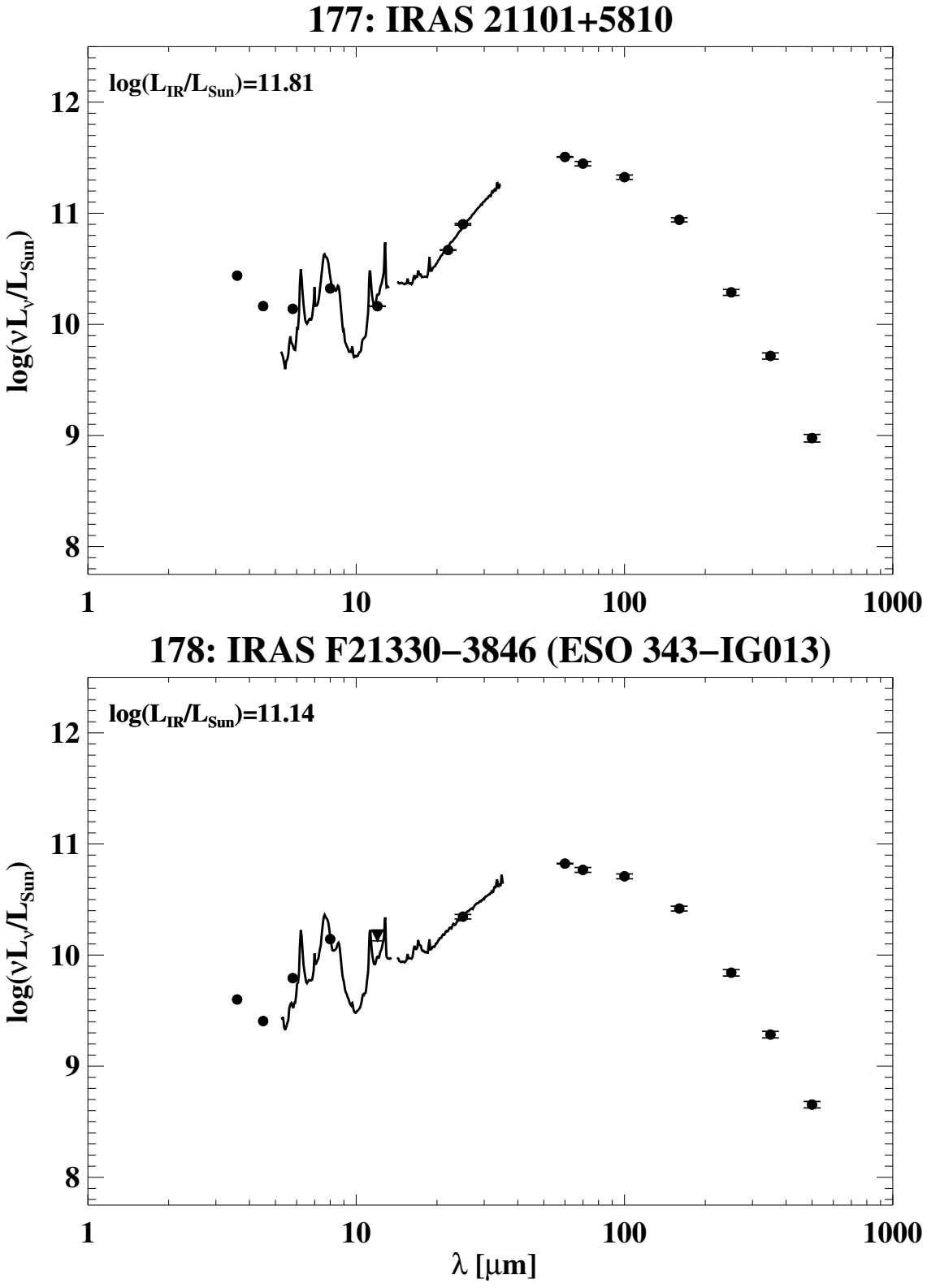

Figure A.1 continued (page 89 of 101).

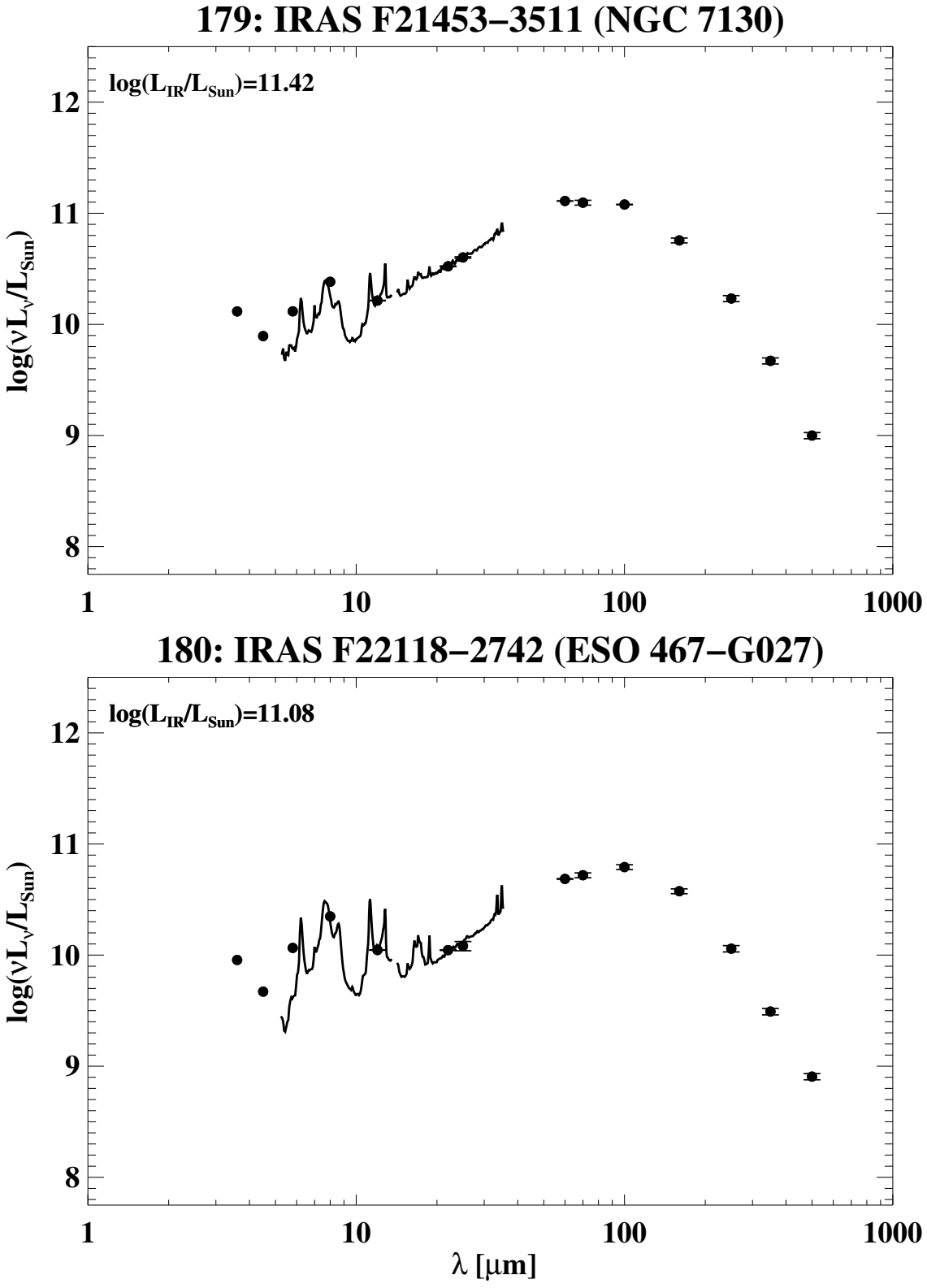

Figure A.1 continued (page 90 of 101).

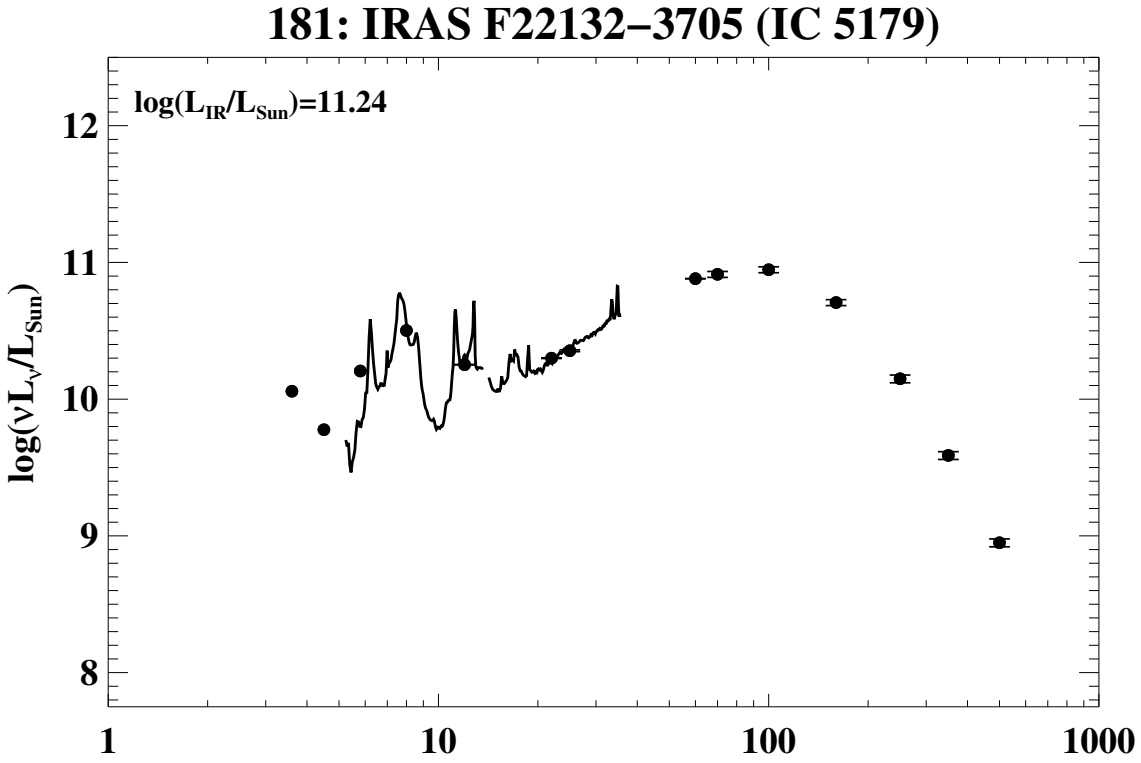

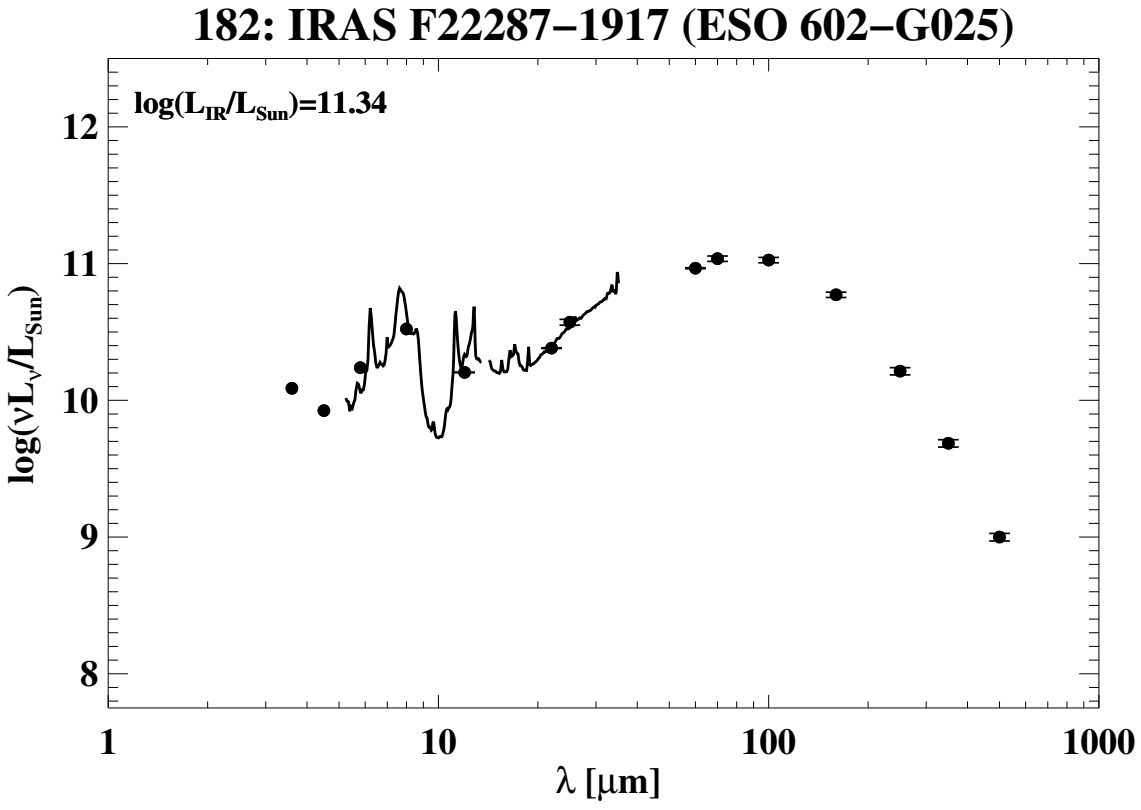

Figure A.1 continued (page 91 of 101).

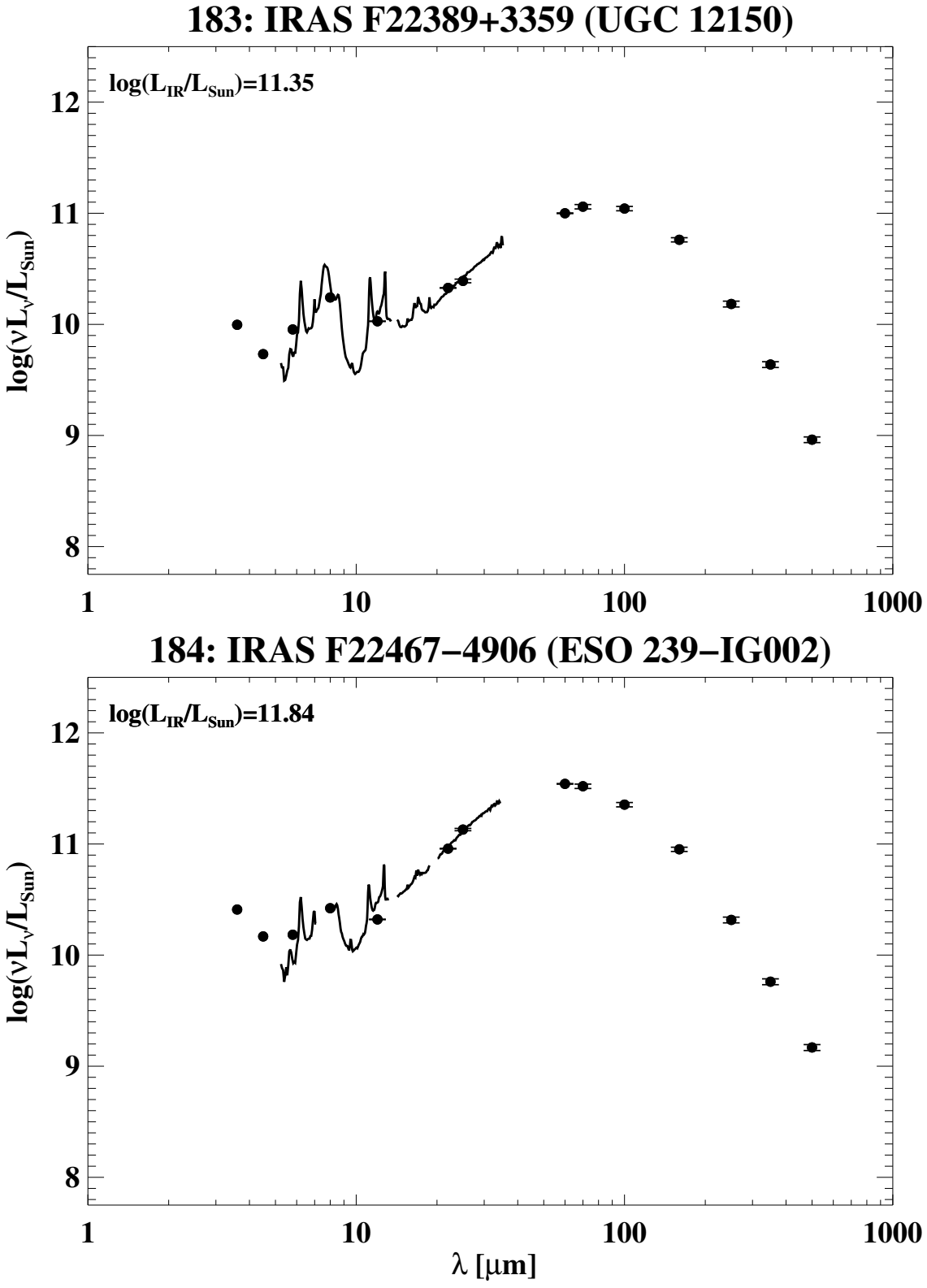

Figure A.1 continued (page 92 of 101).

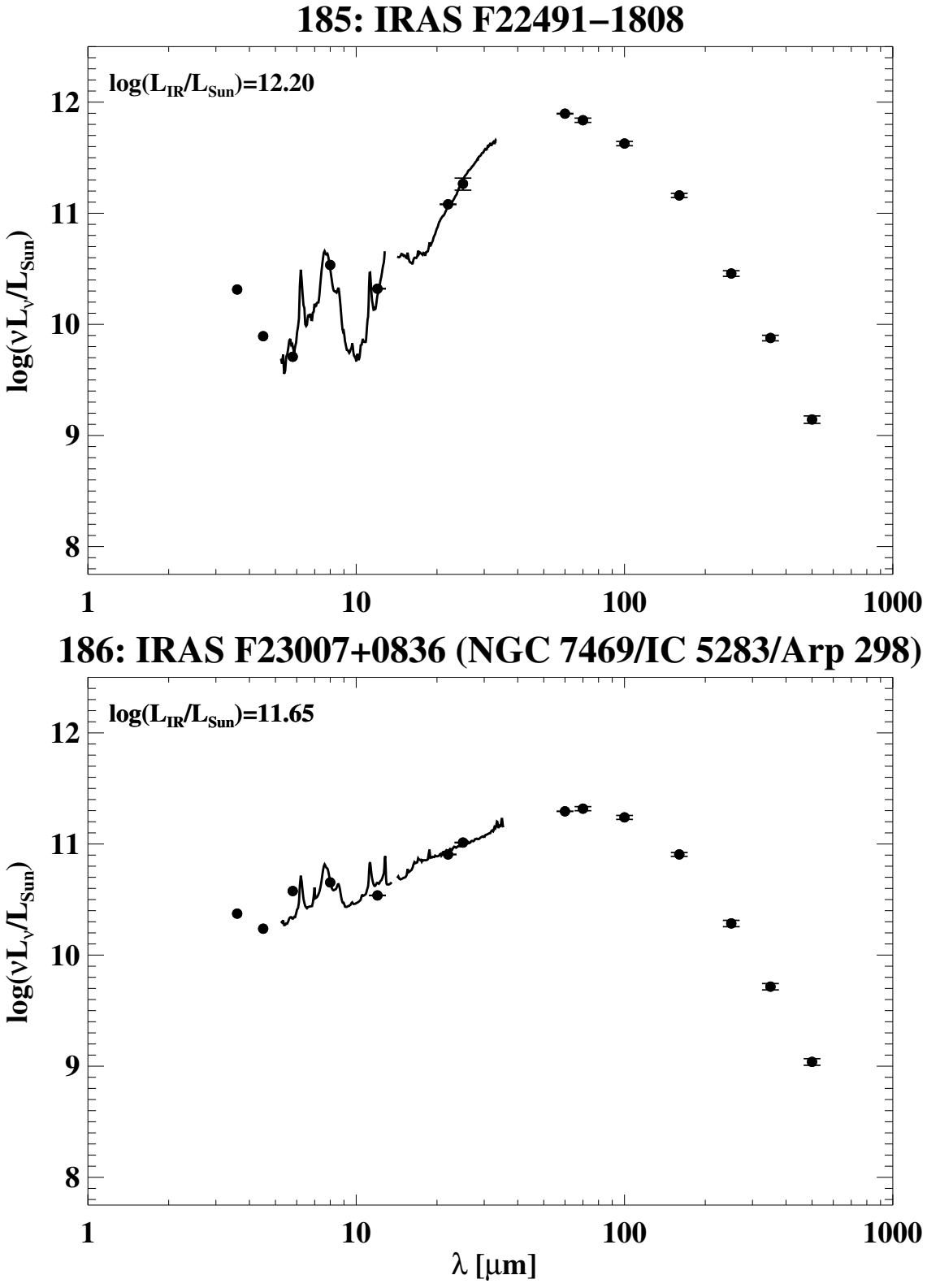

Figure A.1 continued (page 93 of 101).

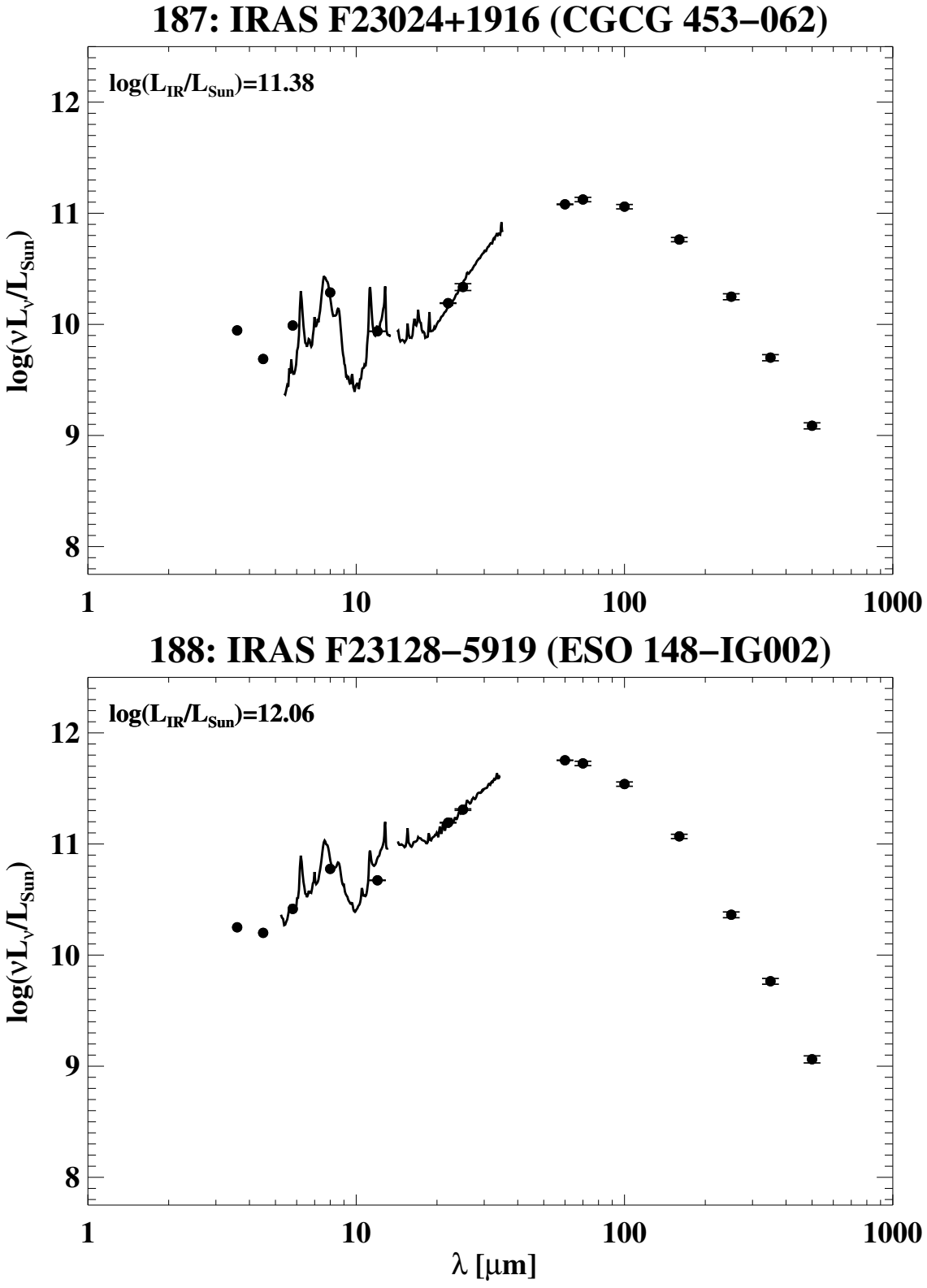

Figure A.1 continued (page 94 of 101).

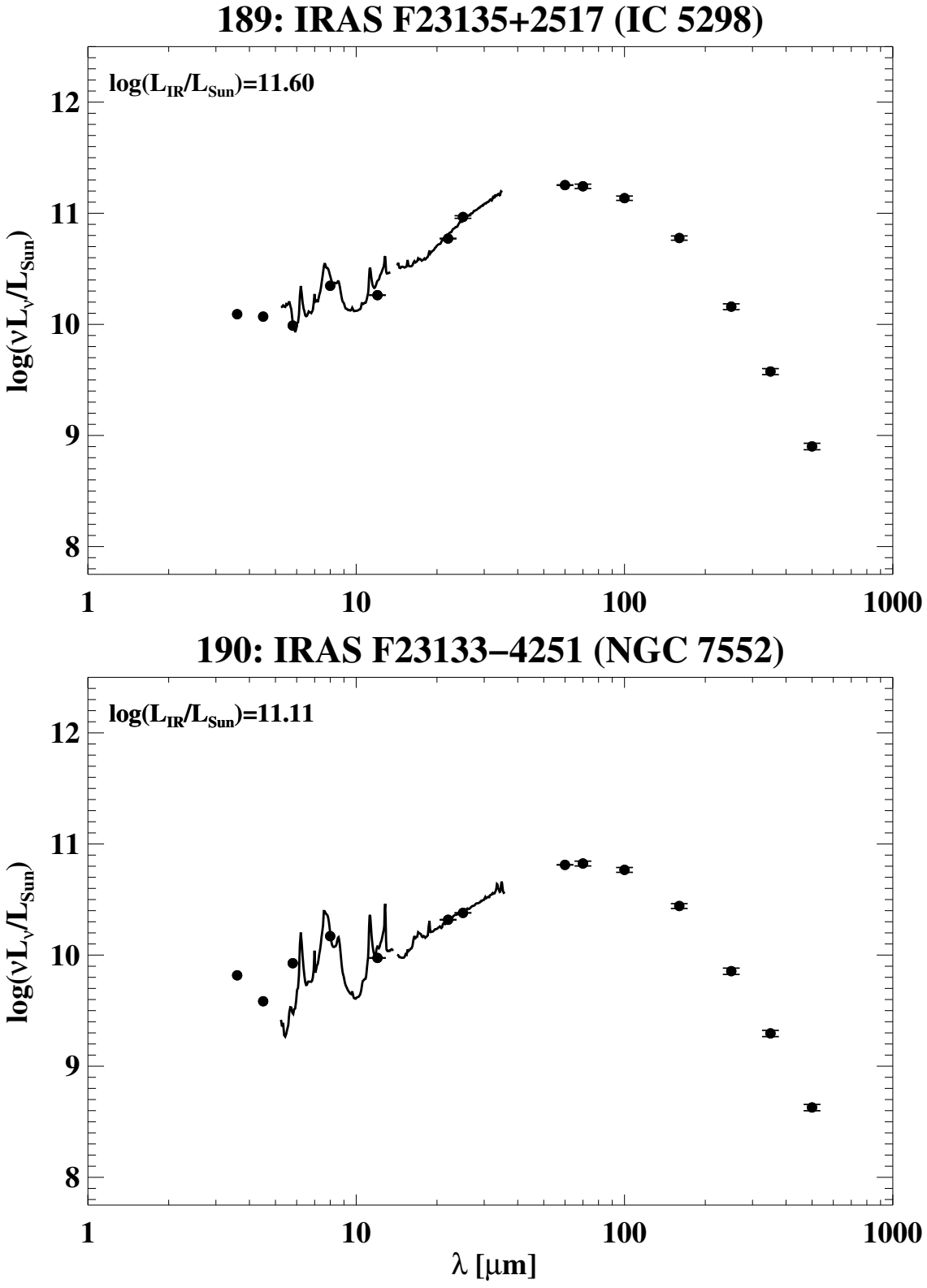

Figure A.1 continued (page 95 of 101).

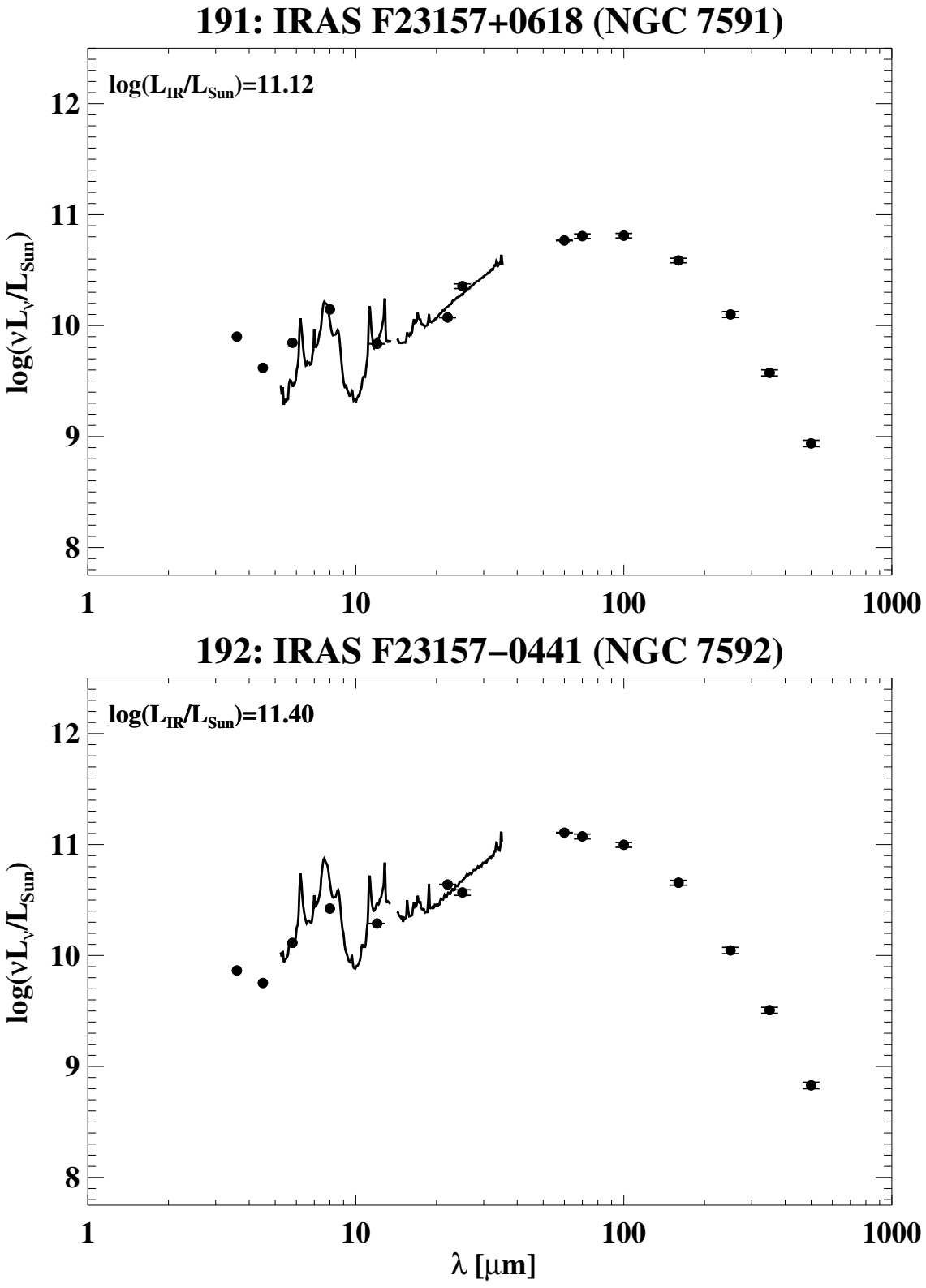

Figure A.1 continued (page 96 of 101).

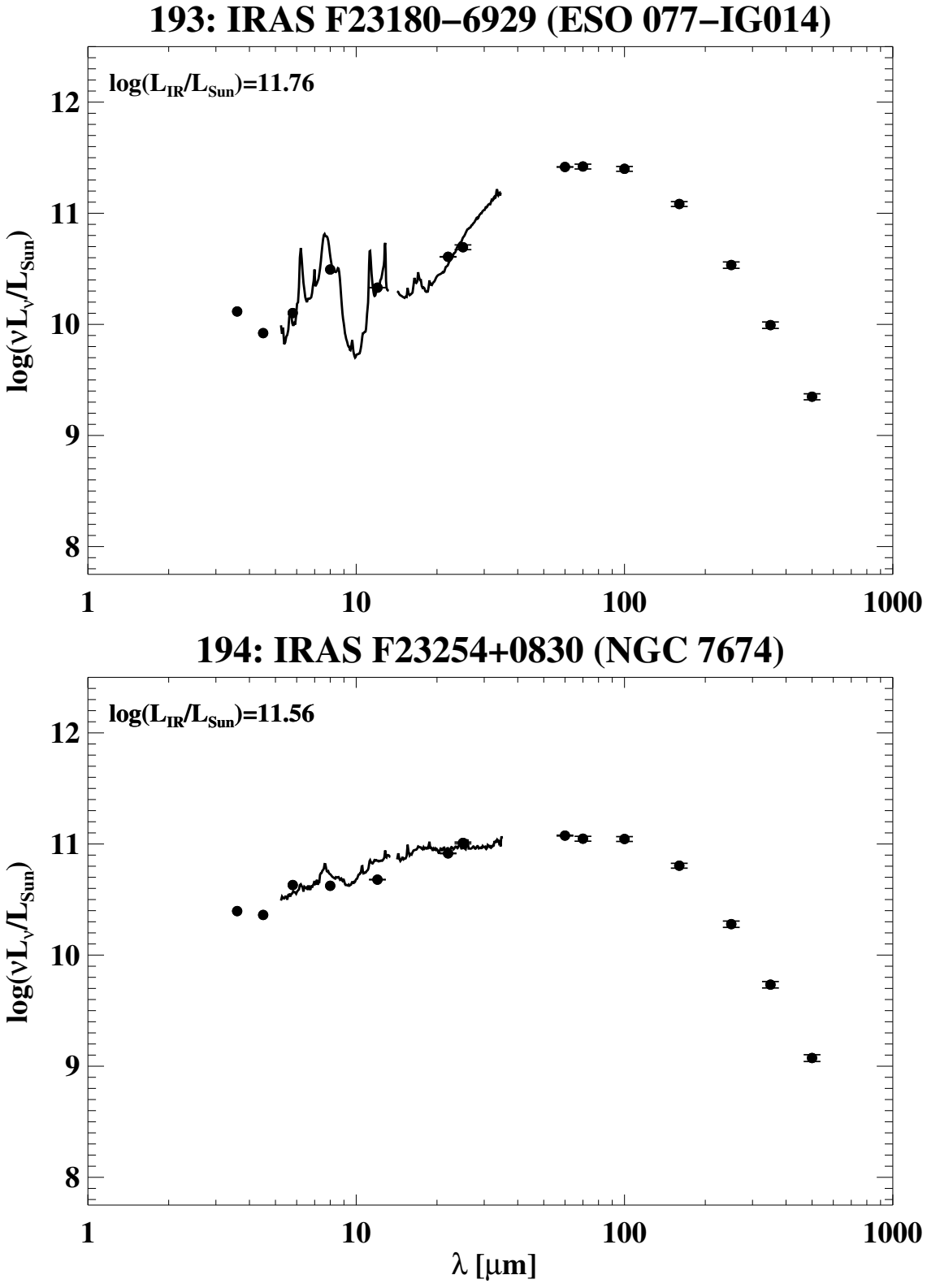

Figure A.1 continued (page 97 of 101).

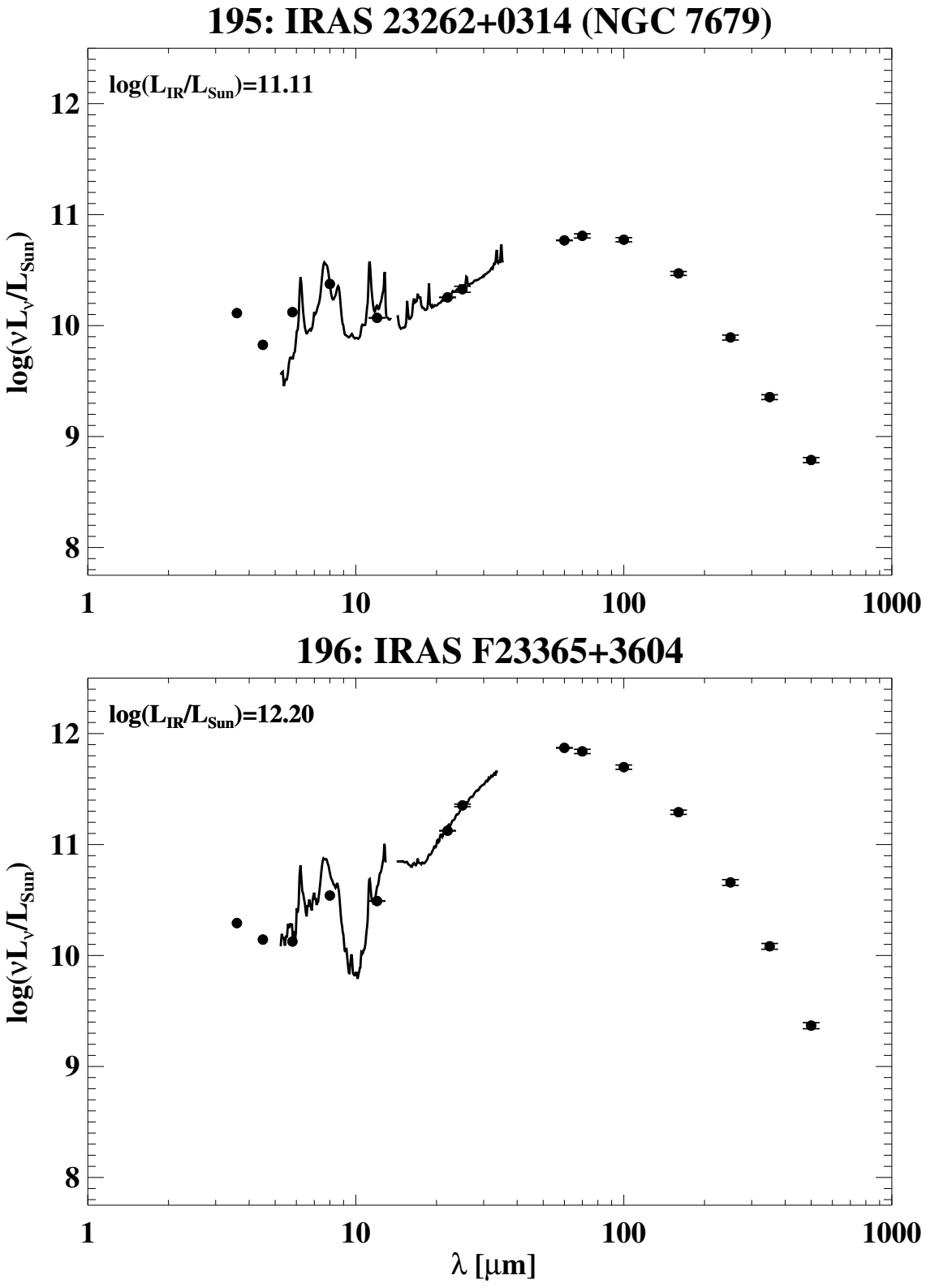

Figure A.1 continued (page 98 of 101).

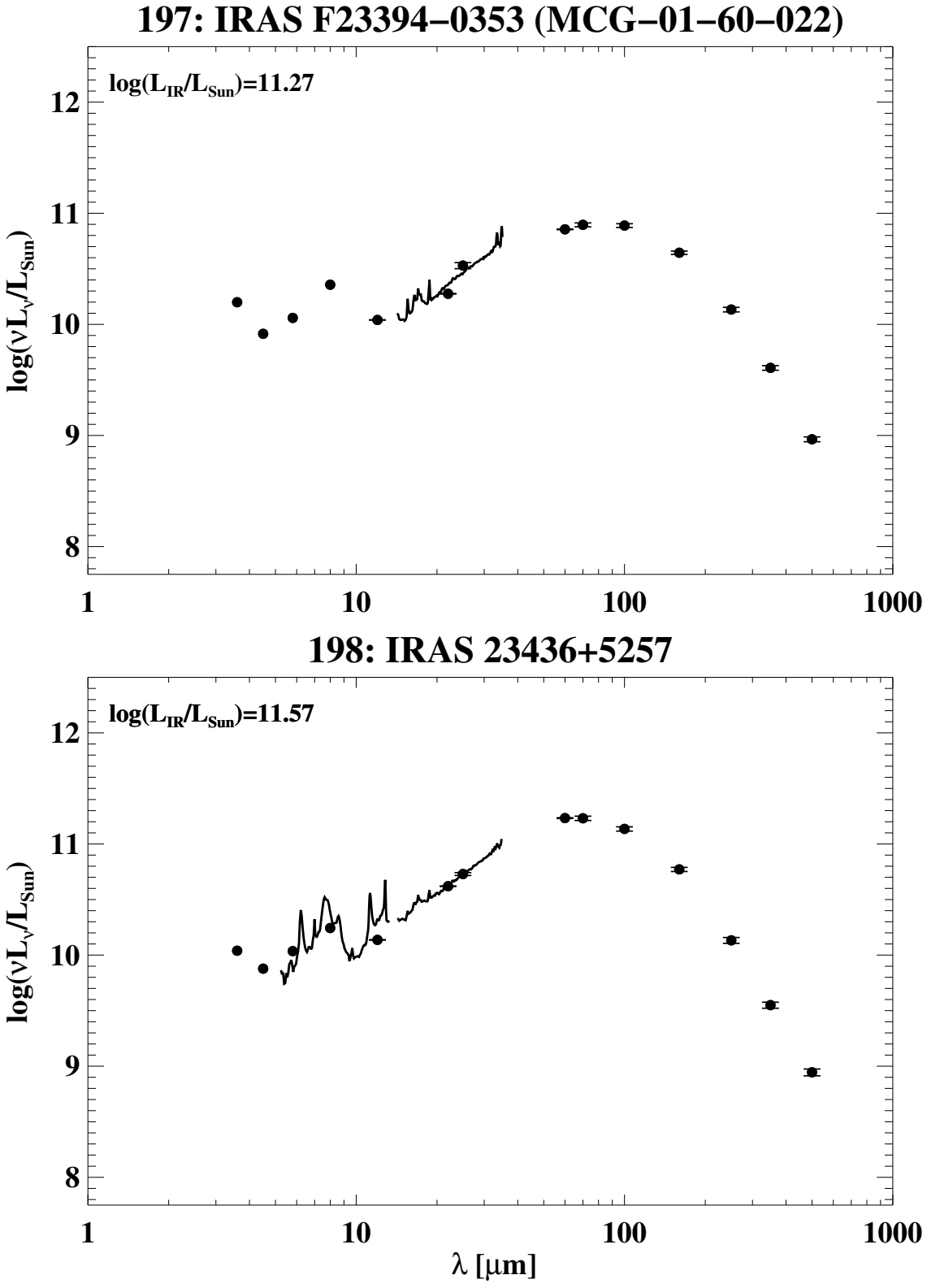

Figure A.1 continued (page 99 of 101).

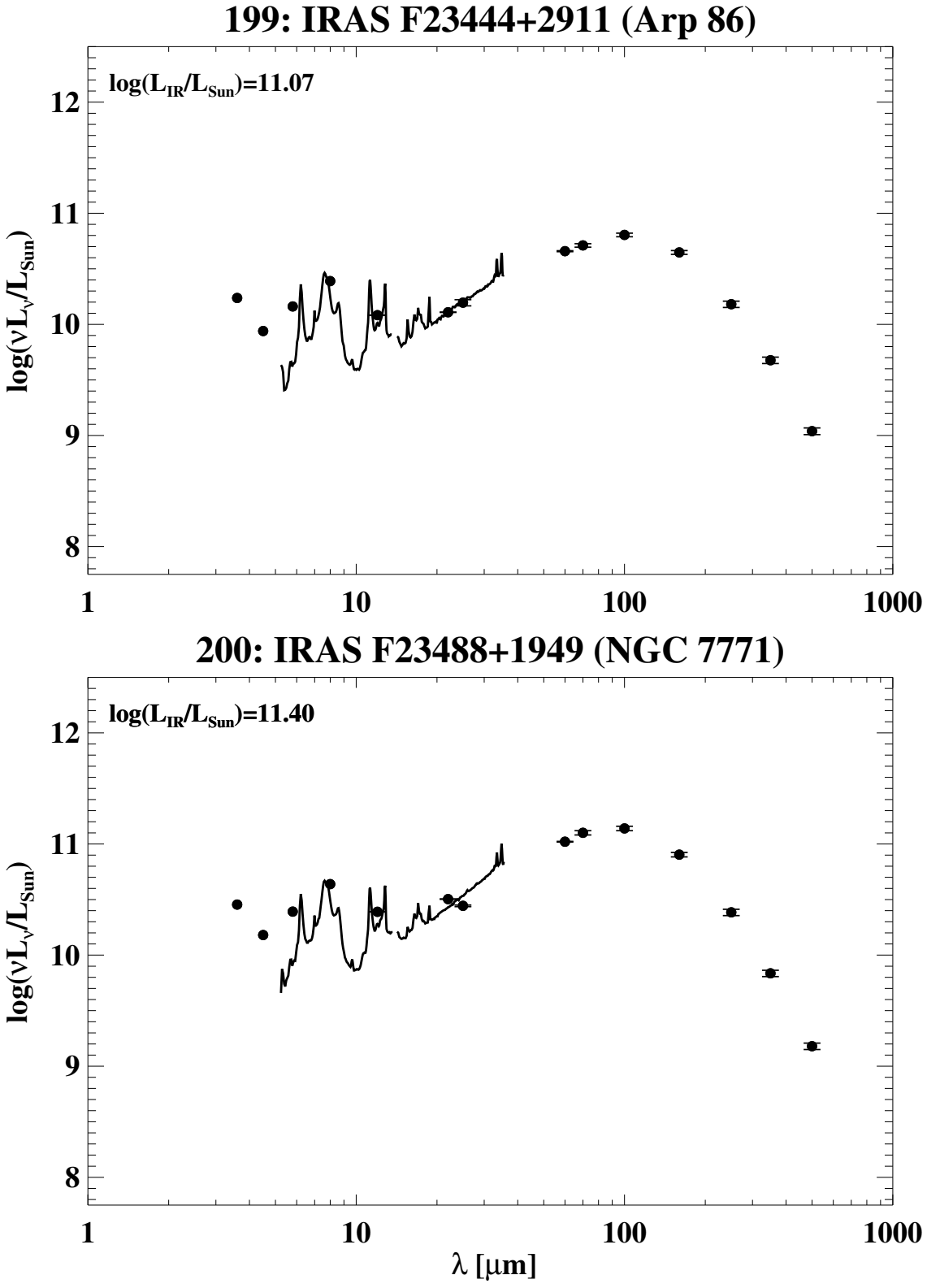

Figure A.1 continued (page 100 of 101).

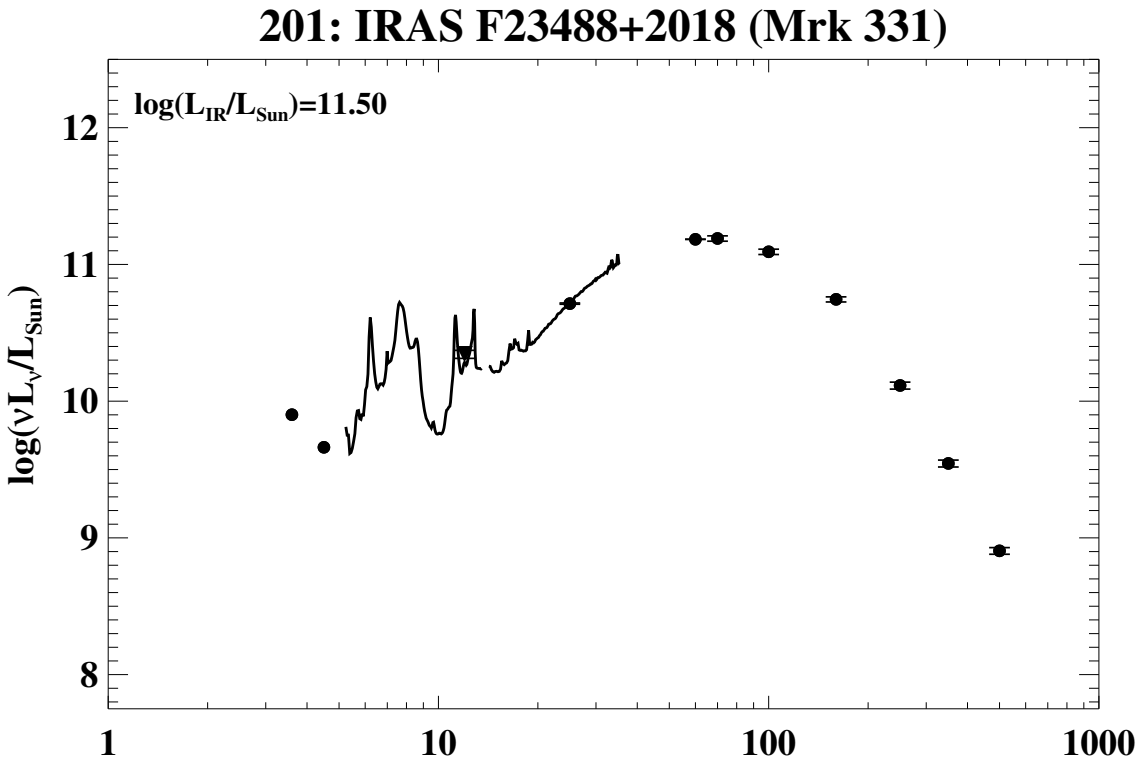

Figure A.1 continued (page 101 of 101).

References

Chu, J. K., Sanders, D. B., Larson, K. L., Mazzarella, J. M., Howell, J. H., Díaz-Santos, T., Xu, K. C., Paladini, R., Schulz, B., Shupe, D., Appleton, P., Armus, L., Billot, N., Chan, B. H. P., Evans, A. S., Fadda, D., Frayer, D. T., Haan, S., Ishida, C. M., Iwasawa, K., Kim, D.-C., Lord, S., Murphy, E., Petric, A., Privon, G. C., Surace, J. A., & Treister, E. 2017, ApJS, 229, 25

Houck, J. R., Roellig, T. L., van Cleve, J., Forrest, W. J., Herter, T., Lawrence, C. R., Matthews, K., Reitsema, H. J., Soifer, B. T., Watson, D. M., Weedman, D., Huisjen, M., Troeltzsch, J., Barry, D. J., Bernard-Salas, J., Blacken, C. E., Brandl, B. R., Charmandaris, V., Devost, D., Gull, G. E., Hall, P., Henderson, C. P., Higdon, S. J. U., Pirger, B. E., Schoenwald, J., Sloan, G. C., Uchida, K. I., Appleton, P. N., Armus, L., Burgdorf, M. J., Fajardo-Acosta, S. B., Grillmair, C. J., Ingalls, J. G., Morris, P. W., & Teplitz, H. I. 2004, ApJS, 154, 18

Sanders, D. B., Mazzarella, J. M., Kim, D., Surace, J. A., & Soifer, B. T. 2003, AJ, 126, 1607

Stierwalt, S., Armus, L., Surace, J. A., Inami, H., Petric, A. O., Diaz-Santos, T., Haan, S., Charmandaris, V., Howell, J., Kim, D. C., Marshall, J., Mazzarella, J. M., Spoon, H. W. W., Veilleux, S., Evans, A., Sanders, D. B., Appleton, P., Bothun, G., Bridge, C. R., Chan, B., Frayer, D., Iwasawa, K., Kewley, L. J., Lord, S., Madore, B. F., Melbourne, J. E., Murphy, E. J., Rich, J. A., Schulz, B., Sturm, E., Vavilkin, T., & Xu, K. 2013, ApJS, 206, 1